佐证材料目录

一、学科竞赛获奖目录（26 项）.....1
二、教学成果奖目录（4 项）.....22
三、实验室化学试剂信息库及应用证明.....25
四、“三废”处理发表成果及应用证明.....29
五、实验教学模式改革及成果.....32
六、教学改革项目(10 项).....36
七、教学改革论文(15 篇).....49
八、指导大学生创新创业项目目录(66 项).....81
九、指导学生发表论文(42 篇).....163
十、教材目录（2 部）.....224
十一、专著(5 部).....227
十二、专利(3 项).....231
十三、科研项目(9 项）.....235
十四、高级别科研论文目录(14 篇 SCI 论文).....250
十五、科研论文(32 篇).....296
十六、实验室安全培训及考试.....386
十七、联合培养协议.....388
十八、校企合作成果.....389
十九、化学专业获批黑龙江省一流本科专业建设点.....390
二十、光电功能材料实验室获批黑龙江省重点实验室.....391

学科竞赛获奖目录（26 项）

1、2021 年第七届中国国际“互联网+”大学生创新创业大赛获国家级铜奖两项。（2 项）

2、2021 年 iCAN 全国大学生创新创业大赛黑龙江省赛区选拔赛获一等奖一项、二等奖一项、三等奖一项。（3 项）

3、2021 年“建行杯”第七届黑龙江省“互联网+”大学生创新创业大赛获省级金奖两项、银奖两项、铜奖四项。（8 项）

4、2021 年“天正设计杯”化工设计大赛获国家二等奖一项、东北赛区一等奖一项。（2 项）

5、2021 年全国大学生化工实验大赛获东北赛区二等奖一项。（1 项）

6、2020 年第十二届工银融 e 联“挑战杯”黑龙江省大学生创业计划竞赛获省级银奖一项。（1 项）

7、2020 年“建行杯”第六届黑龙江省“互联网+”大学生创新创业大赛获省级金奖一项、铜奖一项。（2 项）

8、2019 年“建行杯”第五届黑龙江省“互联网+”大学生创新创业大赛获省级银奖一项。（1 项）

9、2019 年“欧倍尔杯”黑龙江省第二届大学生化工实验竞赛获省级二等奖一项。（1 项）

10、2018 年“建行杯”第四届黑龙江省“互联网+”大学生创新创业大赛获省级二等奖一项。（1 项）

11、2018 年全国高校商业精英挑战赛第六届创新创业竞赛获国家级二等奖一项。（1 项）

12、2017 年内地与港澳地区数字经济创新创业竞赛获银质奖一项。（1 项）

13、2017 年“建行杯”第三届黑龙江省“互联网+”大学生创新创业大赛获省级三等奖一项。（1 项）

14、2017 年第十五届“挑战杯”黑龙江省大学生课外学术科技作品竞赛省级三等奖一项。（1 项）

1、2021 年第七届中国国际“互联网+”大学生创新创业大赛获国家级铜奖两项

获奖证书

Certificate of Award

孙艺元、何坦莹、焦晶楠、沈勇、魏雨鑫、张咏琪

你们的作品《以“铜”为“汞”:PVC催化剂的绿色原料革命——走好汞催化剂替代之路》，在第七届中国国际“互联网+”大学生创新创业大赛中荣获铜奖

指导老师：邵艳秋、郑友进、吕晓芳、李鸿嘉

特发此证，以资鼓励。

主办单位：教育部、中央统战部、中央网络安全和信息化委员会办公室、国家发展和改革委员会、工业和信息化部、人力资源和社会保障部、农业农村部、中国科学院、中国工程院、国家知识产权局、国家乡村振兴局、共青团中央、江西省人民政府

承办单位：南昌大学、南昌市人民政府

中国国际“互联网+”大学生创新创业大赛组织委员会

二〇二一年十月

编号：2021100926

获奖证书

Certificate of Award

赵晖、孙浩轩、吕月珩、李思聪、郝俊萍、白雪、
李爽、贠欣雨、那艾嘉、周蕊、宋晨曦

你们的作品《光洁士：空心微珠为载体的纳米光催化剂——新一代高效环境净化产品》，在第七届中国国际“互联网+”大学生创新创业大赛中荣获铜奖

指导老师：郝国栋、李鸿嘉、刘玉峰、吕晓芳、柴宝杰、
王虎、周波、韩驰、王明磊、郝春丽

特发此证，以资鼓励。

主办单位：教育部、中央统战部、中央网络安全和信息化委员会办公室、国家发展和改革委员会、
工业和信息化部、人力资源和社会保障部、农业农村部、中国科学院、中国工程院、
国家知识产权局、国家乡村振兴局、共青团中央、江西省人民政府

承办单位：南昌大学、南昌市人民政府

中国国际“互联网+”大学生创新创业大赛组织委员会
二〇二一年十月

中国国际“互联网+”大学生创新创业大赛 组织委员会

编号：2021100925

2、2021 年 iCAN 全国大学生创新创业大赛黑龙江省赛区选拔赛获一等奖一项、二等奖一项、三等奖一项

AWARDS
证书编号：iCAN2021HLJ140
2021年iCAN全国大学生创新创业大赛黑龙江赛区选拔赛
iCAN Innovation Contest 2021（HEILONGJIANG）
三 等 奖
参赛作品：钢表面 TD-SNC 法制备陶瓷膜层
参赛单位：牡丹江师范学院
团队成员：惠子玥 夏万杰 马宇航
指导老师：郝国栋 邵长斌
iCAN全国大学生创新创业大赛组织委员会
2021年10月

3、2021 年“建行杯”第七届黑龙江省“互联网+”大学生创新创业大赛获省级金奖两项、银奖两项、铜奖四项

获奖证书

孙艺元、何坦莹、焦晶楠、沈勇、魏雨鑫、张咏琪：

你们的作品《以“铜”为“汞”:PVC催化剂的绿色原料革命——走好汞催化剂替代之路》荣获“建行杯”第七届黑龙江“互联网+”大学生创新创业大赛

金 奖

指导教师：邵艳秋、郑友进、吕晓芳、李鸿嘉

黑龙江省教育厅
2021年8月6日

获奖证书

赵晖、郝俊萍、李思聪、吕月珩、孙浩轩：

你们的作品《光洁士：空心微珠为载体的纳米光催化剂-新一代高效环境净化产品》荣获“建行杯”第七届黑龙江“互联网+”大学生创新创业大赛

金 奖

指导教师：郝国栋、李鸿嘉、王虎、韩驰、王明磊

黑龙江省教育厅
2021年8月6日

获 奖 证 书

和凯宇、金云鹏、傅靖晗、岳子怡、武琳、李林、朱钰华：

你们的作品《化锈为漆——克服“各种不利条件”的金属防腐涂料》荣获“建行杯”第七届黑龙江“互联网+”大学生创新创业大赛

银 奖

指导教师：蒋舰、周波、吕晓芳、李鸿嘉

黑龙江省教育厅
2021年8月6日

获 奖 证 书

金云鹏、和凯宇、赵旭、杨楠、吴远江、郭子钰、朱钰华：

你们的作品《“聚本安涂”——“明星”材料的重防腐涂料革新之路》荣获“建行杯”第七届黑龙江“互联网+”大学生创新创业大赛

银 奖

指导教师：蒋舰、吕晓芳、李鸿嘉、韩东

黑龙江省教育厅
2021年8月6日

获 奖 证 书

罗丽妍、白雪、刘璐、卢欣禹、贾文清、谭云亓、姚金兰、李雅慧、王嘉怡、陈忠艳：

你们的作品《轻金属表面的双极微弧氧化——打造更美价也廉的模件》荣获“建行杯”第七届黑龙江“互联网+”大学生创新创业大赛

铜 奖

指导教师：郝国栋、王虎、李鸿嘉、王明磊

黑龙江省教育厅
2021年8月6日

获 奖 证 书

董瑞、夏万杰、惠子玥、周爽、马宇航、张亮、张佳琪：

你们的作品《钢表面TD-SNC法陶瓷膜层的制备》荣获“建行杯”第七届黑龙江“互联网+”大学生创新创业大赛

铜 奖

指导教师：邵长斌、郝国栋、周波

黑龙江省教育厅
2021年8月6日

获 奖 证 书

党文浩、李玉竹、张岩、孙丽楠、宋佳：

你们的作品《变废为宝：木耳菌糠有机化处理》荣获“建行杯”第七届黑龙江“互联网+”大学生创新创业大赛

铜 奖

指导教师：苏爽月、廉波、刘婷婷

黑龙江省教育厅
2021年8月6日

获 奖 证 书

董惠敏、刘越、冀雪儿、李敬怡、沈静丽、潘德任：

你们的作品《东北地区土壤综合治理与应用》荣获“建行杯”第七届黑龙江“互联网+”大学生创新创业大赛

铜 奖

指导教师：苏爽月、姜力

黑龙江省教育厅
2021年8月6日

4、2021 年“天正设计杯”化工设计大赛获国家二等奖一项、东北赛区一等奖一项

荣誉证书

CERTIFICATE OF HONOR

"天正设计杯"第十五届全国大学生化工设计竞赛

贰等奖

获奖学校：牡丹江师范学院

获奖学生：弓栅栅、彭先林、姚欣欣、雒炜轩、李爽

指导教师：王超宇、邢乐红、姜力

中国化工学会

中国化工教育协会

二〇二一年八月

荣誉证书

CERTIFICATE OF HONOR

2021 年东北赛区大学生化工设计竞赛

壹等奖

获奖学校：牡丹江师范学院

获奖学生：弓栅栅、彭先林、姚欣欣、雒炜轩、李爽

指导教师：王超宇、邢乐红、姜力

中国化工学会

中国化工教育协会

二〇二一年八月

5、2021 年全国大学生化工实验大赛获东北赛区二等奖一项

荣誉证书

2021年全国大学生化工实验大赛东北赛区选拔赛

二等奖

获奖学校：牡丹江师范学院

获奖学生：曾坤　刘羽　张宇

指导教师：邢乐红

中国化工教育协会

二〇二一年七月

6、2020 年第十二届工银融 **e** 联“挑战杯”黑龙江省大学生创业计划竞赛获省级银奖一项

获奖证书

魏 敏、董 瑞、李雨桐 同学：

你（们）的项目《 环保无甲醛水性酚醛树脂胶粘剂 》

在第十二届工银融 e联 “挑战杯”黑龙江省大学生创业计划竞赛中荣获：

银 奖

指导教师：蒋舰

特颁此证，以资鼓励。

共青团黑龙江省委员会 黑龙江省教育厅 黑龙江省科学技术协会 黑龙江省学生联合会

二〇二〇年九月

7、2020 年“建行杯”第六届黑龙江省“互联网+”大学生创新创业大赛获省级金奖一项、铜奖一项

获奖证书

魏敏、杨薇、金云鹏、
张博、韩惠如、于佳：

你们的作品《环保聚苯胺重防腐涂料》荣获“建行杯”第六届黑龙江省“互联网+”大学生创新创业大赛

金奖

指导教师：蒋舰、张晓祥

黑龙江省教育厅
2020年8月31日

获奖证书

董瑞、张敬新、张亮、王澳、李雨桐：

你们的作品《析氢阴极材料》荣获“建行杯”第六届黑龙江省“互联网+”大学生创新创业大赛

铜奖

指导教师：邢乐红、李想

黑龙江省教育厅
2020年8月31日

8、2019 年“建行杯”第五届黑龙江省“互联网+”大学生创新创业大赛获省级银奖一项

获奖证书

金云鹏、何春雨、惠婉婷、黄宇硕：

你们的作品《水性带锈转锈防腐涂料》荣获“建行杯”第五届黑龙江省“互联网+”大学生创新创业大赛

银 奖

黑龙江省教育厅

指导老师：蒋 舰、蔡 雪、邵艳秋、左明辉

2019 年 8 月 26 日

9、2019 年“欧倍尔杯”黑龙江省第二届大学生化工实验竞赛获省级二等奖一项

荣誉证书

2019年“欧倍尔杯”黑龙江省第二届大学生化工实验竞赛

省二等奖

获奖学校：牡丹江师范学院

获奖学生：陈浩楠、孙美微、李若男

指导教师：蔡　雪、李鋆婧、赵　玥、邵艳秋

黑龙江省化工学会　　黑龙江省普通高等学校创新创业教育指导委员会

二〇一九年七月

10、2018 年“建行杯”第四届黑龙江省“互联网+”大学生创新创业大赛获省级二等奖一项

获奖证书

金云鹏 王宇杭 赵薪淼 张秀彪:

你们的作品《绿色环保水性汽车内饰胶》荣获“建行杯”第四届黑龙江省互联网+大学生创新创业大赛

二等奖

指导教师：蒋舰 周波 蔡雪 左明辉

黑龙江省教育厅

2018年8月28日

11、2018 年全国高校商业精英挑战赛第六届创新创业竞赛获国家级二等奖一项

证 书

牡丹江师范学院的参赛作品《年产 500 吨水性环保内饰胶》

荣获 2018 年全国高校商业精英挑战赛第六届创新创业竞赛全国总决赛二等奖。

团队学生成员：张梓彤 马悦 张秀彪 李贺若 邢北奇 吴淋

优秀指导教师：蒋靓 蔡雪

二〇一八年五月二十二日

12、2017 年内地与港澳地区数字经济创新创业竞赛获银质奖一项

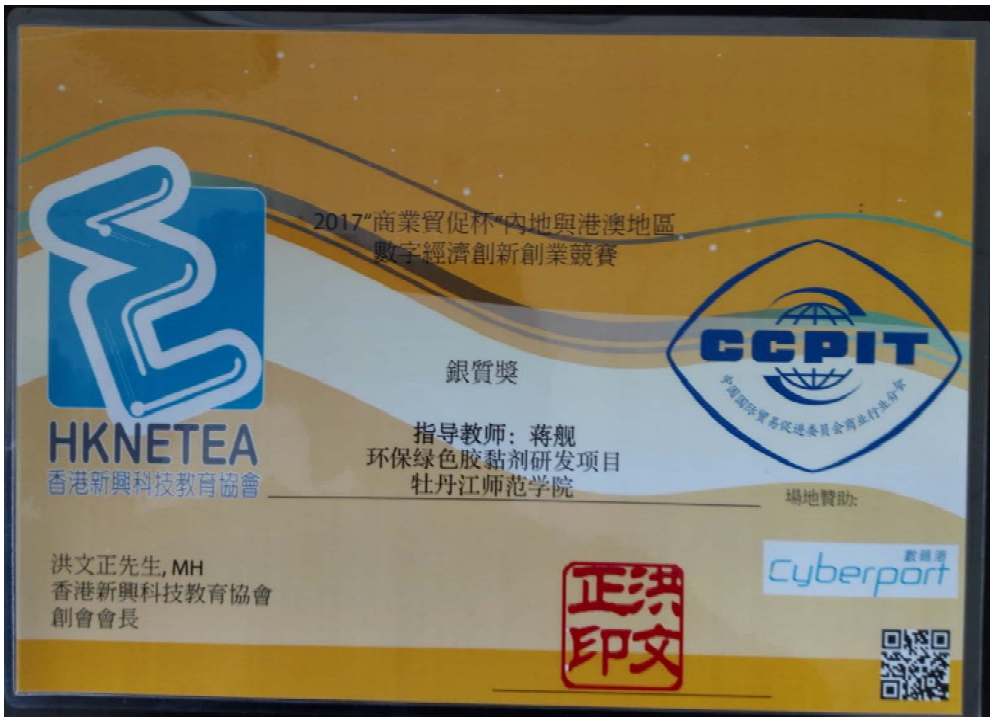

13、2017 年“建行杯”第三届黑龙江省“互联网+”大学生创新创业大赛获省级三等奖一项

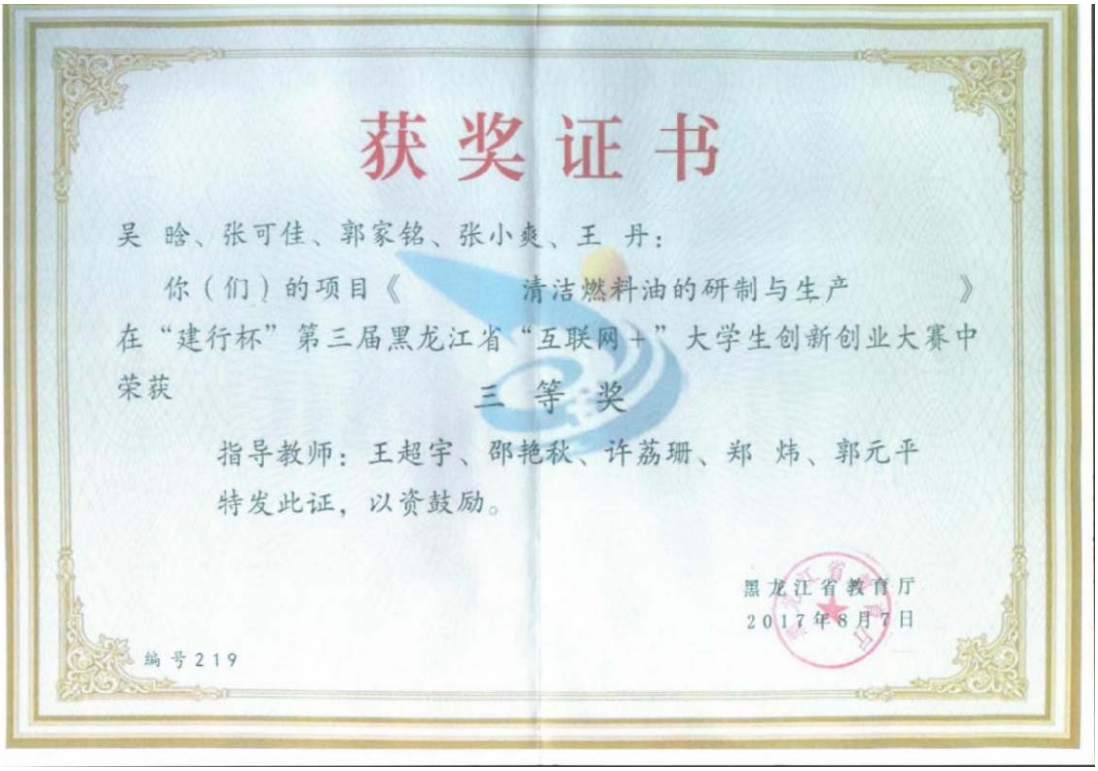

获奖证书

吴 晗、张可佳、郭家铭、张小爽、王 丹：

你（们）的项目《 清洁燃料油的研制与生产 》

在“建行杯”第三届黑龙江省“互联网+”大学生创新创业大赛中

荣获 三 等 奖

指导教师：王超宇、邵艳秋、许荔珊、郑 炜、郭元平

特发此证，以资鼓励。

黑龙江省教育厅

2017年8月7日

编号219

14、2017 年第十五届“挑战杯”黑龙江省大学生课外学术科技作品竞赛省级三等奖一项

荣誉证书

HONORARY CREDENTIAL

吴晗、郭家铭、张小爽、张可佳、王丹 同学：

你们的项目《清洁燃料油的研制与生产》，荣获第十五届“挑战杯”黑龙江省大学生课外学术科技作品竞赛

三 等 奖

共青团黑龙江省委员会　黑龙江省教育厅　黑龙江省科技厅　黑龙江省科学技术协会　黑龙江省社会科学院　黑龙江省学生联合会

2017 年 7 月 31 日

教学成果奖目录（4 项）

1、2021 年《基于学生创新能力培养的实验室管理体系建设与实验室教学改革》获校教学成果一等奖

2、2020 年《基于课程-实验-项目-服务联动的分析化学教学实践研究》获校教学成果二等奖

3、2017 年《以培养学生创新实践能力为核心的应用化学实践教学体系改革与实践》获校教学成果一等奖

4、2011 年《高师分析化学课程教学改革探究》获校教学成果二等奖

1、2021 年《基于学生创新能力培养的实验室管理体系建设与实验室教学改革》获校教学成果一等奖

院内公示

关于2022年度校级教学成果奖及推荐参评省级教学成果奖的公示

发布人：[redacted]　　2022-05-22

各单位：

按照黑龙江省教育厅发布《关于做好2022年黑龙江省高等教育和职业教育教学成果奖评审工作的通知》《2022年高等教育省级教学成果奖评审工作安排》要求，结合《关于公布2021年教学成果奖评审结果的通知》，现将2022年度校级教学成果奖及推荐参评省级教学成果奖结果公示如下：

项目名称	主持人	申报单位	获奖等级
创新、协同、共享：乡村振兴背景下地方高校乡村小学教师培养模式建构与实践	于海英	教育科学学院	一等奖
审判庭搬进校园——法学类专业政产学研协同育人的改革与实践研究	李学锋	法学院	
东北抗联精神育人体系的构建与实施	陈君	东北抗联学院	
“五点筑实，四体深化，三维推进”：地方高校专创融合人才培养的改革与实践	吕晓芳	招生就业处	
[redacted]	[redacted]	数学科学学院	
基于学生创新能力培养的实验室管理体系建设与实验教学改革	邵艳秋	化学化工学院	

2、2020 年基于课程-实验-项目-服务联动的分析化学教学实践研究获校教学成果二等奖

3、2017 年以培养学生创新实践能力为核心的应用化学实践教学体系改革与实践获校教学成果一等奖

左明辉 崔术新 邵长斌 陈玉锋 肖同欣 蔡雪 王冰

你们的 以培养学生创新实践能力为核心的应用化学实践教学体系改革与实践 获得牡丹江师范学院 2017 年教学成果 一 等奖。

牡丹江师范学院

二〇一七年十一月

4、2011 年高师分析化学课程教学改革探究获校教学成果二等奖

荣誉证书

邵艳秋 任玉兰 刘素娟 罗玉杰

你的《高师分析化学课程教学改革探究》获牡丹江师范学院二〇一一年教学成果二等奖。

牡丹江师范学院

二〇一一年十月二十五日

实验室化学试剂信息库

甲类，乙类化学试剂明细.xlsx
QQ浏览器文件服务

所有化学试剂汇总表 | 无机试剂 | 有机试剂

	A	B	
1	1	己烷	全部出
2	2	二硫化碳	12瓶，
3	3	苯	15瓶，
4	4	甲苯	全部出
5	5	甲醇	49瓶，
6	6	95%乙醇	0库存
7	7	灯用酒精	66瓶，
8	8	无水乙醇	150瓶
9	9	乙醚	23瓶，
10	10	乙酸甲酯	2瓶，
11	11	丙酮	19瓶，
12	12	黄磷	7瓶，
13	13	金属钾	2.5瓶，
14	14	金属钠	3瓶，
15	15	金属钙	1瓶，
16	16	氢化钠	1瓶，
17	17	氯酸钾	20瓶，
18	18	氯酸钠	5瓶，

K34

编辑 | 格式转换

2020.01.03年现存危化品排查...
QQ浏览器文件服务

Sheet1 | Sheet2 | Sheet3

	A	B	C
1	学院		化学
2		名称	数量（
3		胡椒醛	2
4		乙酸酐	4
5		三氯甲烷（氯仿）	15
6		乙醚	18
7		丙酮	4
8		2-丁酮（甲基乙基酮）	14
9		高锰酸钾	88
10		硫酸	38
11		盐酸	47
12		苯	13
13		灯用酒精	19
14		二硫化碳	12
15		甲醇	33
16		氯酸钾	18

J7

编辑 | 格式转换

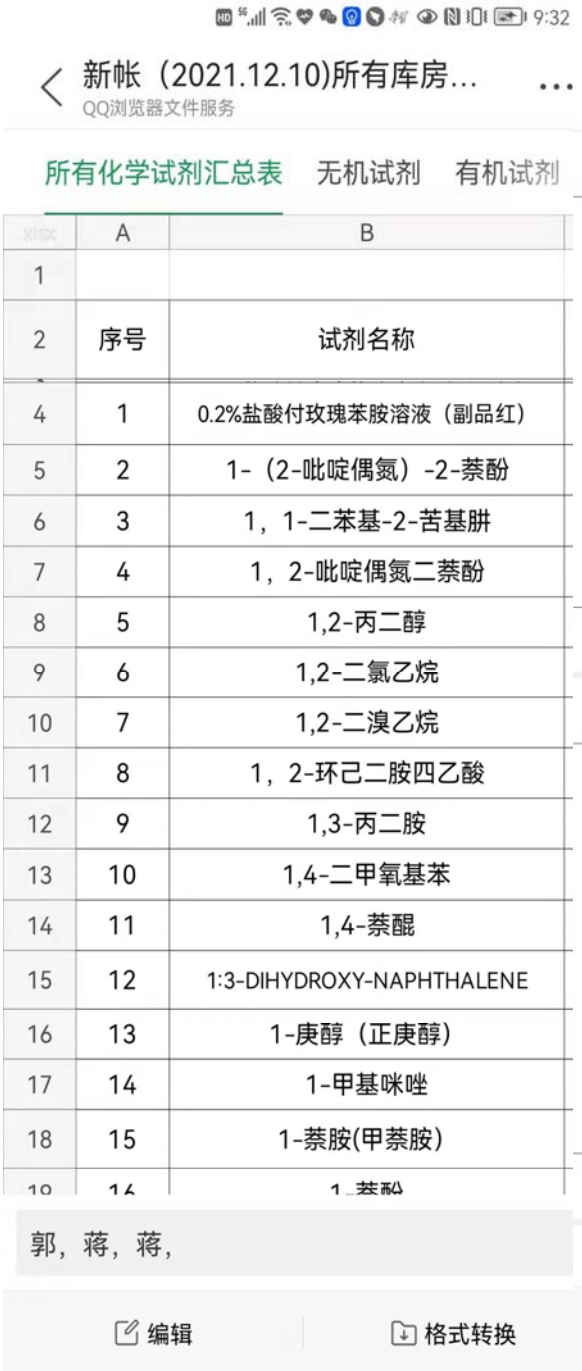

新帐（2021.12.10)所有库房...
QQ浏览器文件服务

所有化学试剂汇总表　无机试剂　有机试剂

	A	B
1		
2	序号	试剂名称
4	1	0.2%盐酸付玫瑰苯胺溶液（副品红）
5	2	1-（2-吡啶偶氮）-2-萘酚
6	3	1，1-二苯基-2-苦基肼
7	4	1，2-吡啶偶氮二萘酚
8	5	1,2-丙二醇
9	6	1,2-二氯乙烷
10	7	1,2-二溴乙烷
11	8	1，2-环己二胺四乙酸
12	9	1,3-丙二胺
13	10	1,4-二甲氧基苯
14	11	1,4-萘醌
15	12	1:3-DIHYDROXY-NAPHTHALENE
16	13	1-庚醇（正庚醇）
17	14	1-甲基咪唑
18	15	1-萘胺(甲萘胺)
19	16	1-萘酚

郭，蒋，蒋，

编辑　格式转换

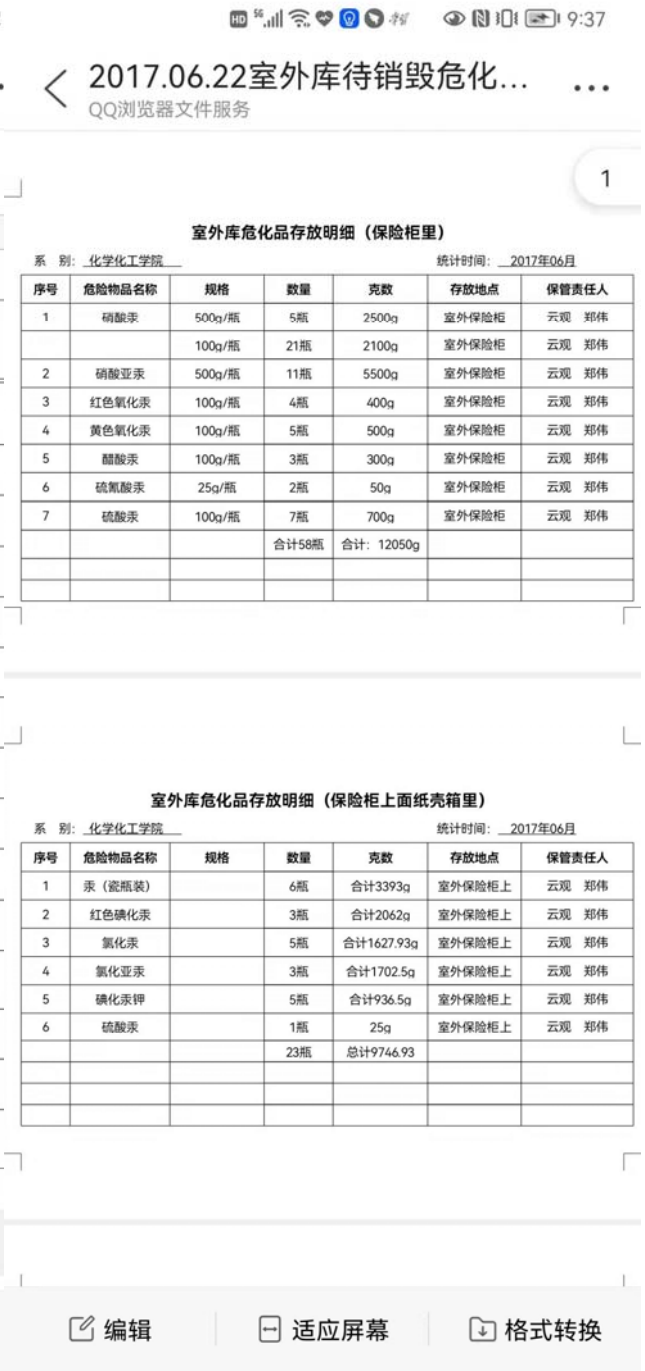

2017.06.22室外库待销毁危化...
QQ浏览器文件服务

1

室外库危化品存放明细（保险柜里）

系　别：化学化工学院　　统计时间：2017年06月

序号	危险物品名称	规格	数量	克数	存放地点	保管责任人
1	硝酸汞	500g/瓶	5瓶	2500g	室外保险柜	云观　郑伟
		100g/瓶	21瓶	2100g	室外保险柜	云观　郑伟
2	硝酸亚汞	500g/瓶	11瓶	5500g	室外保险柜	云观　郑伟
3	红色氧化汞	100g/瓶	4瓶	400g	室外保险柜	云观　郑伟
4	黄色氧化汞	100g/瓶	5瓶	500g	室外保险柜	云观　郑伟
5	醋酸汞	100g/瓶	3瓶	300g	室外保险柜	云观　郑伟
6	硫氰酸汞	25g/瓶	2瓶	50g	室外保险柜	云观　郑伟
7	硫酸汞	100g/瓶	7瓶	700g	室外保险柜	云观　郑伟
			合计58瓶	合计：12050g		

室外库危化品存放明细（保险柜上面纸壳箱里）

系　别：化学化工学院　　统计时间：2017年06月

序号	危险物品名称	规格	数量	克数	存放地点	保管责任人
1	汞（瓷瓶装）		6瓶	合计3393g	室外保险柜上	云观　郑伟
2	红色碘化汞		3瓶	合计2062g	室外保险柜上	云观　郑伟
3	氯化汞		5瓶	合计1627.93g	室外保险柜上	云观　郑伟
4	氯化亚汞		3瓶	合计1702.5g	室外保险柜上	云观　郑伟
5	碘化汞钾		5瓶	合计936.5g	室外保险柜上	云观　郑伟
6	硫酸汞		1瓶	25g	室外保险柜上	云观　郑伟
			23瓶	总计9746.93		

编辑　适应屏幕　格式转换

应用证明

项目名称	易燃易爆化学品试剂电子信息库
应用单位	牡丹江大学食品药品学院
技术应用起始时间	2018 年 11 月

食品药品专业每天都要使用各种各样的化学药品，而药品库化学试剂种类数量繁多，在这数以千计的化学药品中，有些试剂具有不同程度的爆炸、易燃、助燃、毒害、腐蚀和放射性等危险特性，使用前都要现百度某种试剂是否是易燃易爆试剂，还要确定网上信息的真实性，参考牡丹江师范学院化学化工学院提供的化学试剂电子信息库及易燃易爆化学品试剂电子信息库，能够很快查到试剂存放位置并且是否是易燃易爆试剂，非常方便和适用。

牡丹江大学食品药品学院

2019-06-20

应用证明

项目名称	易燃易爆化学品试剂电子信息库
应用单位	四平市食品药品检验所
技术应用起始时间	2018.11-现在

药检行业每天都要使用各种各样的化学药品，而药品库化学试剂种类数量繁多，在这数以千计的化学药品中，有些试剂具有不同程度的爆炸、易燃、助燃、毒害、腐蚀和放射性等危险特性，使用前都要现百度某种试剂是否是易燃易爆试剂，还要确定网上信息的真实性，参考牡丹江师范学院化学化工学院提供的化学试剂电子信息库及易燃易爆化学品试剂电子信息库，能够很快查到试剂存放位置并且是否易燃易爆试剂，非常方便和适用。

四平市食品药品检验所

2019-06-20

“三废”处理发表成果及应用证明

应用证明

项目名称	实验“三废”处理办法
应用单位	宁安市市场监督管理局
技术应用起始时间	2019 年 10 月

宁安市市场监督管理局是牡丹江师范学院化学化工学院的实习就业基地，多年来为我单位做了大量的仪器使用培训和实验技术指导。在我们工作实践中一直研究实验产生的“三废”处理办法，始终没有解决，2019 年化学化工学院学生在我单位实习期间，实验操作中对无机、有机实验产生的废物处理办法收到很好的效果，非常适用，我们将他们的做法收藏并用在实践中，在解决环保要求的同时也提升实验的安全性、节约性。

宁安市市场监督管理局

2022.5.20

高校化学实验室常见无机废液的处理方法

邵艳秋，姜封庆，蔡雪，谭荣欣
(牡丹江师范学院化学化工学院，黑龙江牡丹江 157011)

[摘要]高校化学实验室每年都需要进行大量的无机实验，无机实验所产生有害无机废液对地球环境污染严重，该文主要介绍我校实验室所产生的无机废液，根据其化学性质进行了简单分类并提出环保安全的处理方法。

[关键词]实验室；无机废液；处理方法
[中图分类号]G4 [文献标识码]A [文章编号]1007-1865(2019)05-0263-01

Treatment Methods of Common Inorganic Waste Liquid in University Chemistry Laboratory

Shao Yanqiu, Jiang Fengqing, Cai Xue, Tan Rongxin
(Department of Chemistry, MudanjiangNormalUniversity, Mudanjiang 157011, China)

Abstract: A large number of inorganic experiments are carried out every year in chemical laboratories of colleges and universities. The harmful inorganic waste liquid produced by inorganic experiments has seriously polluted the earth environment.

Keywords: laboratory; inorganic waste; processing method

无机废液的处理是高校实验室三废处理中最难以解决的问题。首先无机废液的种类繁多，实验室在处理上有较大难度；其次，无机实验产生无机废液的数量较大；最后，高校缺乏系统的实验室废液处理的相关教育[1]，使得学生对于废液处理的并没有形成一个科学严谨的态度，导致学生做完实验直接将废液倒进实验室下水道，造成下水管道污染甚至对周围水质造成极大的影响[2]，该文根据高校实验室中常见无机废液的种类和特点整理出了相应的处理方法。

1 无机化学实验废液的产生及分类

高校化学实验室所产生的废液按其来源可以分为容器洗涤液和未反应完全或者新产生的实验余液。实验所产生余液的性质复杂，种类繁多，需要严格按要求处理。废液按成分一般可分为无机废液、有机废液和生化废液[3]。其中，对环境污染最为严重的是无机废液[4]，主要包括含有铬、铅、镉、氰、银、钡、铜、汞等废液。另外，实验室产生的酸碱废液也对环境也会造成一定的影响。这些废液对生活用水及环境危害极大[5]。因此，我校对无机化学实验产生的废液处理问题高度重视，采取了实验室自行处理及分类存放找专门机构集中处理的方式。本文根据无机废液的性质及相关文献介绍总结出了我们实验课所产生废液的自行处理方法。

2 无机实验废液处理的一般原则

实验教学倡导将绿色化学[6]、环保化学、安全化学[7]等理念融入教学之中。在制定教学大纲时根据国家专业目录培养学生的技能要求，尽量选择毒性小、污染少，废液排放量小、废液种类少、废液处理容易的实验项目以减少对环境的污染[8-9]。另外，在学生培养过程中加强学生对废液处理、废物循环再利用以及减少废物排放量的认识，强化环保化学理念。

要不断强化微型实验在教学中的实际应用，在能得到同样实验现象和实验结论的前提下，尽量减少实验耗材，所排放废液也会大大减少。所以我们在教学过程中根据具体实验要求尽量选择微型实验，从而降低实验室废液处理的压力。

对于排放的废液要按照小心收集、准确分类、安全存放和严格处理的要求进行处理。

优先选择花费小、操作简单、绿色安全的处理方法，而且要高度重视废液的回收再利用问题[10]。

3 无机实验废液处理的对策及方法

我校无机实验产生的废液种类主要有含铬、铅、镉、汞、银、钡、铜、锌、酸碱废液等几类，参照文献结合自身实验条件采取以下处理办法。

3.1 酸碱废液的处理

无机化学实验通常会产生酸性和碱性的物质，这类废液直接排放会造成水 pH 值的改变。如果水质酸度过高，会造成实验室管道腐蚀。一般在处理这类废液时先看其浓度，如果浓度较低，可稀释后直接排放，如果浓度过高，则需定期进行中和处理，达到国家污水排放标准(GB8978-1996)[11]后再进行排放。

3.2 含铬废液的处理

铬酸洗液是实验室常用的洗液，也是无机实验中含铬废液的主要产生来源；醋酸铬(Ⅱ)水合物的制备实验会产生含铬废液。其中 Cr(Ⅵ)是 Cr(Ⅲ)的毒性的 100 倍，所以，实验室废液处理一般是把高价铬离子转化为低价铬离子，水中 Cr(Ⅵ)排放要小于 0.5 ppm。一般处理方法是用铁氧体法除去铬，在含铬废液中加入硫酸亚铁作为还原剂，从而把高价铬还原为低价铬，pH 值调节后生成铬的氢氧化物沉淀，进行统一焚烧处理，剩余废液可简单稀释后直接倒入下水道。

3.3 含银废液的处理

含银废液中回收银的方法有很多，如沉淀法、电解法和离子交换法等，但最主要的是沉淀法。无机化学实验中常见非金属阴离子的分离与鉴定、常见阳离子的分离与鉴定、P区非金属元素(一)、P区非金属元素(二)和离子的鉴定和未知物的鉴别等实验产生含银废液，用沉淀法处理含银废液方便适用。此方法是在废液中加入Na_2SO_4等含有SO_4^{2-}的溶液，将废液中的Ag^+完全转化为相对应的Ag_2SO_4沉淀，然后进行过滤回收处理。各高校在无机实验中会产生大量的含银废液，可以在实验后对其进行集中的处理。

3.4 含铅、镉废液的处理

含铅废液和含镉废液也是化学实验室经常产生的毒性很强的无机废液，产生铅、镉废液的实验有碘化铅溶度积的测定、常见阳离子的分离与鉴定、P 区非金属元素(一)、P 区非金属元素(二)、离子的鉴定和未知物的鉴别、氢气的制备和铜相对原子量的测定等实验都产生铅、镉废液。实验室一般可以把废液中毒性强的铅离子和镉离子转化为无毒性的沉淀。首先把碱性物质加入到含铅、镉废液的废液中，然后调节废液的 pH 值为 8~10，加入共沉淀剂 $FeSO_4$，使废液中的铅离子和镉离子生成相对应的沉淀物，最后把沉淀物进行焚烧处理[12]。

3.5 含汞废液的处理

离子的鉴定和未知物的鉴别这个实验产生汞废液。实验室处理废液的办法是调节废液的 pH 值至碱性，然后把大量的 Na_2S 加入到含汞废液中，从而使有毒的汞离子转化为无毒的沉淀。最后再加入大量的 Na_2S 和 $FeSO_4$ 使其完全生成沉淀，静置 10 min 后，离心过滤的上层清液中汞离子浓度远低于排放标准后，可以安全的排放到外界，而所产生的沉淀则需要积累到一定数量后统一进行焚烧处理。

(下转第 262 页)

[收稿日期] 2019-01-28
[基金项目] 牡丹江师范学院教改项目(18-XJ20064)；黑龙江省教育厅科研备案项目(1352MSYB006)；牡丹江师范学院科研项目(JG2017001)
[作者简介] 邵艳秋(1969-)，女，吉林长春人，博士，主要研究方向为实验室建设与管理。

(C)1994-2019 China Academic Journal Electronic Publishing House. All rights reserved. http://www.cnki.net

有机化学实验中废液及固废的处理

云　观[1]，陈佳丽[2]，蒋　舰[1]，邵艳秋[1]

（1. 牡丹江师范学院 化学化工学院，黑龙江 牡丹江　157011；2. 牡丹江龙江环保供水有限公司，黑龙江 牡丹江　157011）

摘要：本文总结了我校本科有机化学实验的实验项目及产生的废液、固废，并进行分类。通过中和至无毒化、蒸馏再利用、转化为其它实验的反应原料等环保安全的方法处理产生的废液、固废，可以减少有机化学实验对环境的污染，并且可以降低实验成本。

关键词：有机化学实验；废液；固废；处理办法

中图分类号：X703；X705　　文献标识码：B　　文章编号：1008－021X(2020)05－0257－02

DOI:10.19319/j.cnki.issn.1008-021x.2020.05.100

Treatment of Liquid and Solid Wastes in Organic Chemistry Experiments

Yun Guan[1], *Chen Jiali*[2], *Jiang Jian*[1], *Shao Yanqiu*[1]

(1. College of Chemistry and Chemical Engineering, Mudanjiang Normal University, Mudanjiang　157011, China;
2. Mudanjiang Longjiang Environmental Protection Water Supply Co., Ltd., Mudanjiang　157011, China)

Abstract: This paper summarizes the experimental items of organic chemistry experiment and the waste liquid and solid waste, and classifies them. The environmental protection and safety methods such as neutralization to non－toxicization, distillation and reuse, and conversion into other experimental reaction materials to deal with the waste liquid and solid waste can reduce the environmental pollution caused by organic chemistry experiments and reduce the experimental cost.

Key words: organic chemistry experiment; waste liquid; solid waste; treatment method

有机化学实验是本科教学中化学、生物、医学、高分子和材料科学等多专业的专业基础课，在有机化学实验中大多数实验都会产生废液及固废，如果在实验结束后不能及时处理实验产生的废弃物，将会对人体健康和环境造成危害和污染。目前绿色化学实验呼声渐高[1-3]，进行环境无害的化学实验是化学实验教学领域的长期目标。本文主要介绍了本校本科有机化学相关实验时产生的废液、固废和处理办法。

1　有机化学实验中产生的废液及固废种类

根据现阶段本院本科生使用的教材[4]，将其进行的全部有机化学实验的题目及废液固废类型进行了汇总，如表 1 所示。

表 1　有机化学实验项目及产生的主要废液固废

Table 1　Organic chemistry experiment topic and main waste liquid and solid waste

序号	实验项目	产生的主要废液及固废
序号	实验项目	产生的主要废液及固废
1	熔点的测定	液体石蜡
2	液态有机化合物折光率的测定	无
3	柱层析	无水乙醇、三氧化二铝粉料
4	重结晶提纯法	乙酰苯胺、活性炭
5	蒸馏和沸点测定	无水乙醇
6	分馏	丙酮、无水乙醇
7	环己烯的制备	环己烯、氯化钙
8	溴乙烷的制备	溴乙烷、硫酸
9	乙酸乙酯的制备	乙酸乙酯、硫酸镁
10	减压蒸馏	乙酸正丁酯
11	乙酰苯胺的制备	乙酰苯胺、乙酸、锌粉
12	茶叶中生物碱的提取	咖啡因、乙醇、茶叶
13	肉桂酸的合成	肉桂酸、苯甲醛
14	正丁醚的合成	正丁醚、硫酸、氯化钙
15	乙酸正丁酯的合成	乙酸正丁酯、乙酸、正丁醇、硫酸、硫酸镁
16	脲醛树脂的合成	脲醛树脂
17	甲基橙的合成	甲基橙、乙醇、乙醚
18	阿司匹林的制备	水杨酸
19	洗涤灵的制备	十二烷基硫酸钠

2　废液、固废类型及处理办法

2.1　废液及固废类型

2.1.1　干燥剂型

在实验环己烯的制备、乙酸乙酯的制备、正丁醚的合成、乙酸正丁酯的合成中，产生的氯化钙、硫酸镁废弃物均作为产品干燥时的干燥剂使用。这两种化学品在使用后均变为结晶水合物状态。

2.1.2　催化剂型

在正丁醚的合成实验和乙酸正丁酯的合成实验中，浓硫酸作为催化剂使用，在实验过程中会经过分液漏斗分出，成为废液。

2.1.3　反应原料型

在实验乙酰苯胺的制备、阿司匹林的制备、乙酸正丁酯、肉桂酸的制备中，乙酸、锌粉、水杨酸、正丁醇、苯甲醛五种有机物由于未完全反应，在进行除杂时，以杂质的形式被蒸馏或过滤出来形成废物。在实验茶叶中生物碱的提取中，乙醇作为萃取咖啡因的溶剂，在后期蒸馏时需蒸馏出大部分乙醇，成为废液。在实验溴乙烷的制备中，浓硫酸作为反应原料，过量和溴化钠进行反应，反应结束后剩余的硫酸分液漏斗分出，成为废液。

收稿日期：2019－12－17

基金项目：黑龙江省高等教育教学改革一般研究项目(SJGY20190688)

作者简介：云　观(1992—)，助教，研究方向为有机化学与生物化学。

(C)1994-2020 China Academic Journal Electronic Publishing House. All rights reserved.　http://www.cnki.net

实验教学模式改革及成果

上传到“云端”班课的实验录制 PPT：

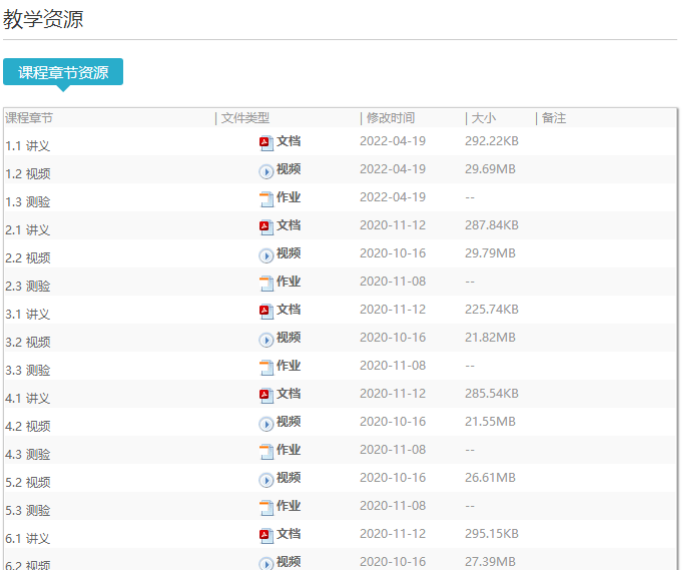

基于云班课的物理化学实验混合式教学模式探索

贾林艳，韩俊凤，左明辉，邵长斌，陈玉锋，邵艳秋

（牡丹江师范学院 化学化工学院，黑龙江 牡丹江　157011）

摘要：混合式教学模式已成为高校教学改革的趋势之一。针对目前物理化学实验教学现状及存在的问题，探索基于云班课的混合式教学，详细阐述了传统教学与混合式教学的过程，混合式教学模式在物理化学实验教学中的应用，使得学生学习的积极性提高，创新能力和实践能力增强，课堂效率和教学效果大大提高。

关键词：混合式教学；物理化学实验；云班课

中图分类号：G642.423　　文献标识码：A　　文章编号：1008-021X(2021)01-0217-02

DOI:10.19319/j.cnki.issn.1008-021x.2021.01.096

Research on the Application of Mixed Teaching in Physical Chemistry Experiment Course Based on Cloud Class Platform

Jia Linyan, Han Junfeng, Zuo Minghui, Shao Changbin, Chen Yufeng, Shao Yanqiu

(College of Chemistry and Chemical Engineering, Mudanjiang Normal University, Mudanjiang　157011, China)

Abstract: Mixed teaching has become one of the important trends in the teaching development of college curriculum. Considering current situation and existing problems, mixed teaching in physical chemistry experiment course has been researched based on cloud class platform. The comparison on teaching process has been expounded between traditional teaching and mixed teaching. The new teaching mode not only has stimulated interest in learning, strengthened practical and innovation ability, but also has been effectively improved the quality of teaching.

Key words: mixed teaching; physical chemistry experiment; cloud class

随着互联网技术的快速发展，电脑、智能手机的普及，各种线上教学平台应运而生，为混合式教学提供了必备条件。教师必须跟上时代的步伐，利用“互联网 +”平台，创新教学理念和教学方式[1]。混合式教学是目前教学改革的趋势之一，它是将传统教学与线上教学相结合的教学模式，是互联网与教育相融合的产物[2]。该教学模式既可以发挥教师的引导、启发、监控教学过程作用，又能够充分体现学生作为学习过程主体的主动性、积极性与创造性[3]。选择一个适宜的线上平台是决定混合式教学效果的重要因素。

云班课是一款免费移动智能教学 APP，很大程度上解除了教师在选择时的费用之忧，该软件有教师端和学生端，教师可以上传各种教学资源、创建题库、创建活动、进行轻直播等。上传的教学资源可以是文档和视频等资料；创建活动包括答疑探讨、测试、问卷调查、头脑风暴、作业任务等活动。

物理化学实验需要综合运用物理和化学的原理与技术，方法与仪器，以及数学运算工具，是一门理论性、实践性、综合性和研究性很强的课程[4]，学生需掌握实验的基本原理、基本方法，通过实验的完成和数据处理，提高学生发现问题、分析问题和解决问题的能力，在实验中加强对学生的科研和创新能力的培养。

1　传统教学模式

由于受实验仪器台套数的限制，目前我校物理化学实验课程采用大循环模式，每个实验班 16 人左右，每个实验有 4 套仪器，即一位教师指导 16 人完成 4 个实验。教学模式可分为以下几个步骤：

1.1　学生课前预习

课前要求学生写预习报告。由于物理化学实验涉及的原理和实验技术较为深奥难懂，学生看教材很枯燥，大部分学生只是对照实验讲义采取摘抄的方式完成预习报告交差而已，对实验仪器设备的使用方法没有感官的认识，对实验每一步预期的测定结果及现象并没有系统了解，并未达到预习的目的，所以其实是对实验一无所知走进实验室。

1.2　课上实验

基本上采用灌输式教学模式。教师对实验目的、原理和实验步骤一一讲解，进行仪器操作演示，学生机械式地听讲。然后学生“抓中药式”按教材的实验步骤完成实验。由于前期预习不够充分，所以对实验过程出现的实验现象、测定的数据规律没有认识，当测定结果出现很大偏差时不能及时发现问题仍旧机械地做下去，最后得出错误的结论。

1.3　课后总结

下课后学生根据测定的实验结果处理实验数据，完成实验报告。由于实验数据处理有的较为复杂，有些学生不能自己独立完成，甚至有个别学生抄袭别人的报告一交了之。对实验中出现的误差不能认真分析。

1.4　课程考核方式

近年来已多次对实验成绩考核进行改革，但预习实验报告和实验报考仍占考核成绩地权重较高。这两部分都包含实验目的、实验原理、实验仪器与药品、实验步骤，学生基本上都是照书摘抄，数据处理和误差分析部分很多学生也是课后相互借鉴完成，无法实现培养学生独立进行数据处理、分析问题解决问题等能力的目标。

可以看出，传统的物理化学实验教学过程是以教师为中心，学生处于被动接受的地位，积极性不高，教学效果较差。因此，教师需要适应时代的发展，对实验教学进行改革与创新。

2　基于云班课的混合式教学模式

由于云班课具有使用便捷，师生均可随时随地在手机上使

收稿日期：2020-09-23

基金项目：牡丹江师范学院教学改革项目（19-XJ21029）（JK-2020014）；黑龙江省高等教育教学改革一般研究项目（SJGY20190688）

作者简介：贾林艳（1971—），女，博士，牡丹江师范学院教授，硕士生导师，主要从事物理化学教学及稀土发光材料研究。

(C)1994-2021 China Academic Journal Electronic Publishing House. All rights reserved.　http://www.cnki.net

17:37
...0.0K/s
分析化学实验
多选
从本地上传
网页链接
资源库
调序
高锰酸钾标准溶液的配制与标定...
19
93KB
13 人查看
允许下载 10.22 08:31 发布
2 经验
微信图片_20181022082356
97KB
13 人查看
允许下载 10.22 08:31 发布
2 经验
微信图片_20181022082324
87KB
13 人查看
允许下载 10.22 08:31 发布
2 经验
操作评分标准
1
EDTA标准溶液的配制与标定，水的总...
13
微信图片_20180929104755
104KB
14 人查看
允许下载 09.29 10:56 发布
2 经验
资源
成员
活动
消息
详情

17:36
...1.3K/s
分析化学实验
多选
从本地上传
网页链接
资源库
调序
未分组
5
分析化学实验心得体会分享
14
f95ca19f15e1652cdbb7c6becf51d5d0
8.42MB | 00:01:04
13 人查看
允许下载 12.03 15:58 发布
2 经验
ed22ec6520189bd...b647f773e271be
2.71MB | 00:00:20
13 人查看
允许下载 12.03 15:58 发布
2 经验
ea778b22c959931...f889f9656b4b31
7.82MB | 00:01:01
13 人查看
允许下载 12.03 15:58 发布
2 经验
d1a0908490effb...e0962d6abeedad
6.28MB | 00:00:48
13 人查看
允许下载 12.03 15:57 发布
2 经验
baaf9a9f80bfc1d6fa6fcca86159b4d0
资源
成员
活动
消息
详情

17:33
...0.4K/s
分析化学实验
课堂表现
全部 12
未开始 0
进行中 0
已结束 12
实验报告
作业活动 请拍照...定过氧化氢的含量）
14 人参与 20 经验 已结束
作业活动 请拍照...分光光度法测定铁）
14 人参与 20 经验 已结束
作业活动 请拍照...量法测定镍的含量）
14 人参与 20 经验 已结束
作业活动 请拍照...法测定铜盐中的铜）
14 人参与 20 经验 已结束
作业活动 请拍照上...的测定（莫尔法））
14 人参与 20 经验 已结束
预习报告
作业活动 请拍照...分光光度法测定铁）
14 人参与 20 经验 已结束
作业活动 请拍照...量法测定镍的含量）
资源
成员
添加活动
消息
详情

17:32
...0.0K/s
历史
11月16日08时27分选人活动
gy1工艺17赵美琪
+3 经验
2017023039
2018-11-16
11月16日08时23分选人活动
张靖扬
+8 经验
2017023061
2018-11-16
11月16日08时04分选人活动
刘艳阳
+10 经验
2017023035
2018-11-16
11月02日08时42分选人活动
杜金鑫
+4 经验
2017023047
2018-11-02
11月02日08时40分选人活动
gy1工艺26候珍莉
+4 经验

文章编号:1003-6180(2020)01-0075-03

移动 APP 辅助教学:分析化学实验“七步教学法”

刘素娟,邵艳秋,任玉兰,苏爽月,赵 宇
(牡丹江师范学院 化学化工学院,黑龙江 牡丹江 157011)

摘 要:提出手机移动 APP 蓝墨云班课与分析化学实验课程深度融合的“七步教学法”.“七步教学法”分为课前预习过关测试、课堂提问激发兴趣、厉性惩罚奖励剥夺、实验操作拍照上传、及时表扬慎用批评、实验报告批改及时、课后总结提升内化.教学成果表明,“七步教学法”能有效激发学生的学习兴趣,充分调动学生学习积极性,提高学生学习自主性,线上与线下学习结合更加紧密,取得了较好的教学效果.

关键词:移动 APP;分析化学实验;七步教学法
DOI:10.13815/j.cnki.jmtc(ns).2020.01.017
[中图分类号]G642 [文献标志码]A

Mobile APP Assisted Teaching: "Seven-step Teaching Method" for Analytical Chemistry Experiment

LIU Sujuan, SHAO Yanqiu, REN Yulan, SU Shuangyue, ZHAO Yu
(College of Chemistry and Chemical Engineering, Mudanjiang Normal University, Mudanjiang 157011, China)

Abstract: This paper proposed a "seven-step teaching method" that integrates mobile APP blue ink cloud class with analytical chemistry experiment course. "Seven-step teaching method" was divided into pre-class pass test, classroom questions to stimulate interest, negative punishment and reward deprivation, experimental operation photos uploaded, timely praise and criticism, experimental report correction timely, after-class summary to improve internalization. The teaching results showed that the "seven-step teaching method" can effectively stimulate students' interest in learning, fully mobilize students' learning enthusiasm, and improve their autonomy in learning. The combination of online and offline learning was more closely, and had achieved a better teaching effect.

Key words: Mobile APP; Analytical Chemistry Experiment; Seven-step Teaching Method

收稿日期:2019-06-20
基金项目:黑龙江省青年科学基金项目(QC2014C009);牡丹江师范学院教改项目(18-XJ20066)
作者简介:刘素娟(1981-),女,山东郓城人.副教授,硕士,硕士生导师,主要从事分析化学和材料合成研究;邵艳秋(1969-),女,黑龙江牡丹江人.教授,博士,主要从事材料合成研究;任玉兰(1971-),女,黑龙江牡丹江人.教授,博士,主要从事材料合成研究.

(C)1994-2020 China Academic Journal Electronic Publishing House. All rights reserved. http://www.cnki.net

教学改革项目（共 10 项）

1.基于学生创新能力培养的实验管理体系建设与实验教学改革

黑龙江省教学改革项目（结项）　　负责人：邵艳秋

2.“双创型”大学生实践能力培养模式研究-以化学人才培养模式为例　　黑龙江省教学改革项目（在研）　　负责人：邵艳秋

3.分析化学

牡丹江师范学院教育教学改革“金科”建设专项　　负责人：邵艳秋

4.基于学生创新能力培养的实验管理体系建设与实验教学改革

牡丹江师范学院教育教学改革重点项目（结项）　　负责人：邵艳秋

5.能力培养视域下分析化学实验教学优化研究

牡丹江师范学院教学改革项目　　负责人：邵艳秋

6.分析化学案例教学研究

牡丹江师范学院案例教学专项教学改革项目　　负责人：邵艳秋

7.高等师范院校化学专业《分析化学》课程体系改革与实践研究

牡丹江师范学院教学改革项目　　负责人：邵艳秋

8.化工原理

牡丹江师范学院教学改革•课程思政项目　　负责人：邢乐红

9.工程教育专业认证背景下地方高校化工创新人才培养模式的研究与探索　　牡丹江师范学院校级一般项目　　负责人：邢乐红

10.有机化学

牡丹江师范学院专项项目　　负责人：蒋舰

邵艳秋教学改革项目（共 7 项）

1.基于学生创新能力培养的实验管理体系建设与实验教学改革

黑龙江省教学改革项目（结项）　　负责人：邵艳秋

2.“双创型”大学生实践能力培养模式研究-以化学人才培养模式为例　　黑龙江省教学改革项目（在研）　　负责人：邵艳秋

3.分析化学

牡丹江师范学院教育教学改革“金科”建设专项　　负责人：邵艳秋

4.基于学生创新能力培养的实验管理体系建设与实验教学改革

牡丹江师范学院教育教学改革项目　　负责人：邵艳秋

5.能力培养视域下分析化学实验教学优化研究

牡丹江师范学院教学改革项目　　负责人：邵艳秋

6.分析化学案例教学研究

牡丹江师范学院案例教学专项教学改革项目　　负责人：邵艳秋

7.高等师范院校化学专业《分析化学》课程体系改革与实践研究

牡丹江师范学院教学改革项目　　负责人：邵艳秋

3.基于学生创新能力培养的实验管理体系建设与实验教学改革

黑龙江省教学改革项目　　负责人：邵艳秋

2019年度高等教育教学改革一般研究项目备案汇总表

序号	高校名称	项目名称	项目编号	项目负责人	成员1	成员2	成员3	成员4	备注
1	大庆师范学院	基于工程教育专业认证的化工专业应用型人才实践能力培养研究	SJGY20190001	何丹凤	周付江	邓进军	陈成	刘超	
2	大庆师范学院	按类招生分流培养背景下计算机类专业教学“金课”建设的探索和实践	SJGY20190002	王健	刘雅喆	李梓	许有军		
3	大庆师范学院	应用型本科院校经管类专业第二课堂活动支撑系统的研究与实践	SJGY20190003	孙伟仁	徐珉钰	刘楠	邬德林	张平	
4	大庆师范学院	工程专业认证视域下生物制药专业人才培养模式研究	SJGY20190004	任国领	张志国	赵晓菊	闫立地	殷亚杰	
5	大庆师范学院	“双创型”人才培养视阈下的大学商务英语专业课程设置研究	SJGY20190005	刘晓旭	何明霞	王芳	尚艳辉	黄丽双	
6	大庆师范学院	打造工科系列专业选修课线上线下混合式金课的研究与实践	SJGY20190006	林芳	张丽丽	孙影	齐风河	王凤娠	
7	大庆师范学院	应用型人才培养视角下法学专业实践教学“整合模式”研究	SJGY20190007	刘锐	陈超	史黎	张媛	赵静	
8	大庆师范学院	“新工科”背景下以专业创新人才培养为导向的大学物理课程教学改革研究	SJGY20190008	王玉玲	张宏伟	何巍巍	成宝芝	徐权	
9	大庆师范学院	教师资格认证背景下卓越教师职前培养模式创新研究	SJGY20190009	孙玉红	赵丽	徐晶	原昊	刘玲	
10	大庆师范学院	专业认证背景下汽车服务工程专业人才培养模式创新的研究与实践	SJGY20190010	赵大伟	王馨玉	董云峰	刘永皓	徐权	
11	大庆师范学院	高校钢琴课程“教、练、赛、演”一体化教学模式改革与实践	SJGY20190011	刘菁菁	李轶男	王宇婧	修金毓	张宁	
12	东北林业大学	“互联网+高等教育”新形态下包装材料学课程教学改革的研究与实践	SJGY20190012	张群利	刘兵	陈春晟	郑权	张希栋	
13	东北林业大学	森林工程“一流专业”建设的研究与实践	SJGY20190013	侯卫萍	李耀翔	辛颖	薛伟	狄海廷	
14	东北林业大学	新时代党建引领“三全育人”模式探索与实践	SJGY20190014	郑燕	王宇	付书朋	申晓腾	杨林光	
15	东北林业大学	基于“工程教育专业认证”OBE导向的三相异步电机拆装课程设计实验项目教学改革	SJGY20190015	王金聪	谢永华	杨林光	张延林	张澎涛	
688	牡丹江师范学院	基于学生创新能力培养的实验管理体系建设与实验教学改革	SJGY20190688	邵艳秋	蔡雪	云观	邢乐红	蒋舰	
689	牡丹江师范学院	UGS模式下卓越教师培养模式的理论和实践研究	SJGY20190689	杨洋	乔世文	赵杰	李旭	滕巧玲	
690	牡丹江师范学院	新时代背景下地方高校导师队伍建设有效途径探索与实践	SJGY20190690	张冰	李殿伟	才忠喜	薛巨泉	郝忠彬	
691	牡丹江医学院	应用型医学院校基础医学整合课程运行中模块化教学团队的建设与实践	SJGY20190691	杨旭芳	李丽	冯华	陈培	王莞	

523	牡丹江师范学院	区域师范本科院校两级教学管理机制与策略的研究与实践	SJGY20190680	韩驰	张衷平	李旭	林创		
524	牡丹江师范学院	法学教育校政协同育人的理论与实践研究	SJGY20190682	李学锋	褚清清	谌雪燕	王伟	徐忠颖	
525	牡丹江师范学院	基于学生创新能力培养的实验管理体系建设与实验教学改革	SJGY20190688	邵艳秋	蔡雪	云观	邢乐红	蒋舰	

2.“双创型”大学生实践能力培养模式研究-以化学人才培养模式为例　　黑龙江省教学改革项目　　负责人：邵艳秋

附件 2

项目编号：_____

黑龙江省高等教育教学改革项目
立项申报书

项目名称：“双创型”大学生实践能力培养模式研究—以化学人才培养模式为例

主 持 人：邵艳秋

学校名称：牡丹江师范学院

申请日期：2021.12.21

项目类别：一般研究项目

联系电话：13614608351

牡丹江师范学院

3.分析化学

牡丹江师范学院教育教学改革“金科”建设专项　　负责人：邵艳秋

申请类别
2

牡丹江师范学院
教育教学改革·“金课”建设专项

申　请　书

项目名称 _____分析化学_____

项目负责人_____邵艳秋_____

专业类代码_____070301_____

学院（部门）__化学化工学院_____

牡丹江师范学院教务处

二〇二〇年四月

4.基于学生创新能力培养的实验管理体系建设与实验教学改革

牡丹江师范学院教育教学改革项目　　负责人：邵艳秋

附件 3：

项目编号：_____

牡丹江师范学院教育教学改革项目

立项申报书

项目名称：基于学生创新能力培养的实验管理体系建设与实验教学改革

主 持 人：邵艳秋

单位名称：化学化工学院

团队归属（或职能归属）：化学基础课程教学团队

申请时间：2018 年 6 月 24 日

项目类别：重大委托项目

联系电话：13614608351

项目组主要成员（不含主持人）					
姓名	出生年月	工作单位	专业技术职务	学历学位	项目分工
蔡　雪	1974 年 1 月	化学化工学院	教授	博士研究生	课题运作和组织
云　观	1992 年 8 月	化学化工学院	助教	大学本科	实验管理体制研究与实践
邢乐红	1983 年 11 月	化学化工学院	副教授	博士研究生	实验教学改革与实践
蒋　靓	1973 年 3 月	化学化工学院	讲师	博士研究生	实验教学改革与实践
赵　宇	1989 年 8 月	化学化工学院	助教	硕士研究生	实验教学改革与实践

牡丹江师范学院制

1

5.能力培养视域下分析化学实验教学优化研究

牡丹江师范学院教学改革项目　　负责人：邵艳秋

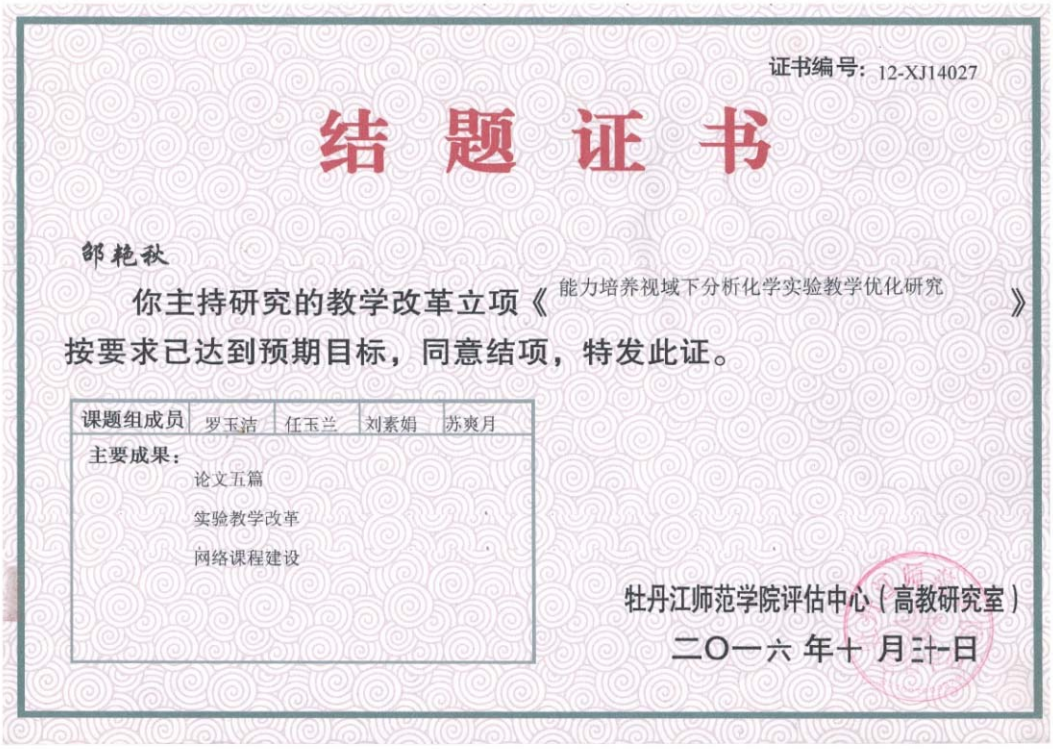

证书编号：12-XJ14027

结 题 证 书

邵艳秋

你主持研究的教学改革立项《能力培养视域下分析化学实验教学优化研究》按要求已达到预期目标，同意结项，特发此证。

课题组成员	罗玉洁	任玉兰	刘素娟	苏爽月

主要成果：

论文五篇

实验教学改革

网络课程建设

牡丹江师范学院评估中心（高教研究室）

二〇一六 年十 月三十日

6.分析化学案例教学研究

牡丹江师范学院案例教学专项教学改革项目　　负责人：邵艳秋

编号：

牡丹江师范学院
案例教学专项教学改革项目

申　　报　　表

项目名称：分析化学案例教学研究
主 持 人：邵艳秋
申请单位：化学化工学院
申报时间：2013 年 9 月 16
联系电话：（办）0453-6511219
（手机）13614608351
E_ mail：邵艳秋

牡丹江师范学院
二〇一三年九月

7.高等师范院校化学专业《分析化学》课程体系改革与实践研究

牡丹江师范学院教学改革项目　　负责人：邵艳秋

编号：09YY-09293

结 题 证 书

邵艳秋你主持研究的教学改革课题《高等师范院校化学专业《分析化学》课程体系改革与实践研究》按要求已达到预期目标，同意结题，特发此证。

课题组成员	罗玉杰	任玉兰	刘素娟	
主要成果： 论文4篇 核心1篇				

负责人签字：

牡丹江师范学院教务处

二〇一一 年七 月十 日

邢乐红教学改革项目（共 2 项）

1.化工原理

牡丹江师范学院教学改革•课程思政项目　　负责人：邢乐红

2.工程教育专业认证背景下地方高校化工创新人才培养模式的研究与探索　牡丹江师范学院校级一般项目　　负责人：邢乐红

1.化工原理

牡丹江师范学院教学改革•课程思政项目　　负责人：邢乐红

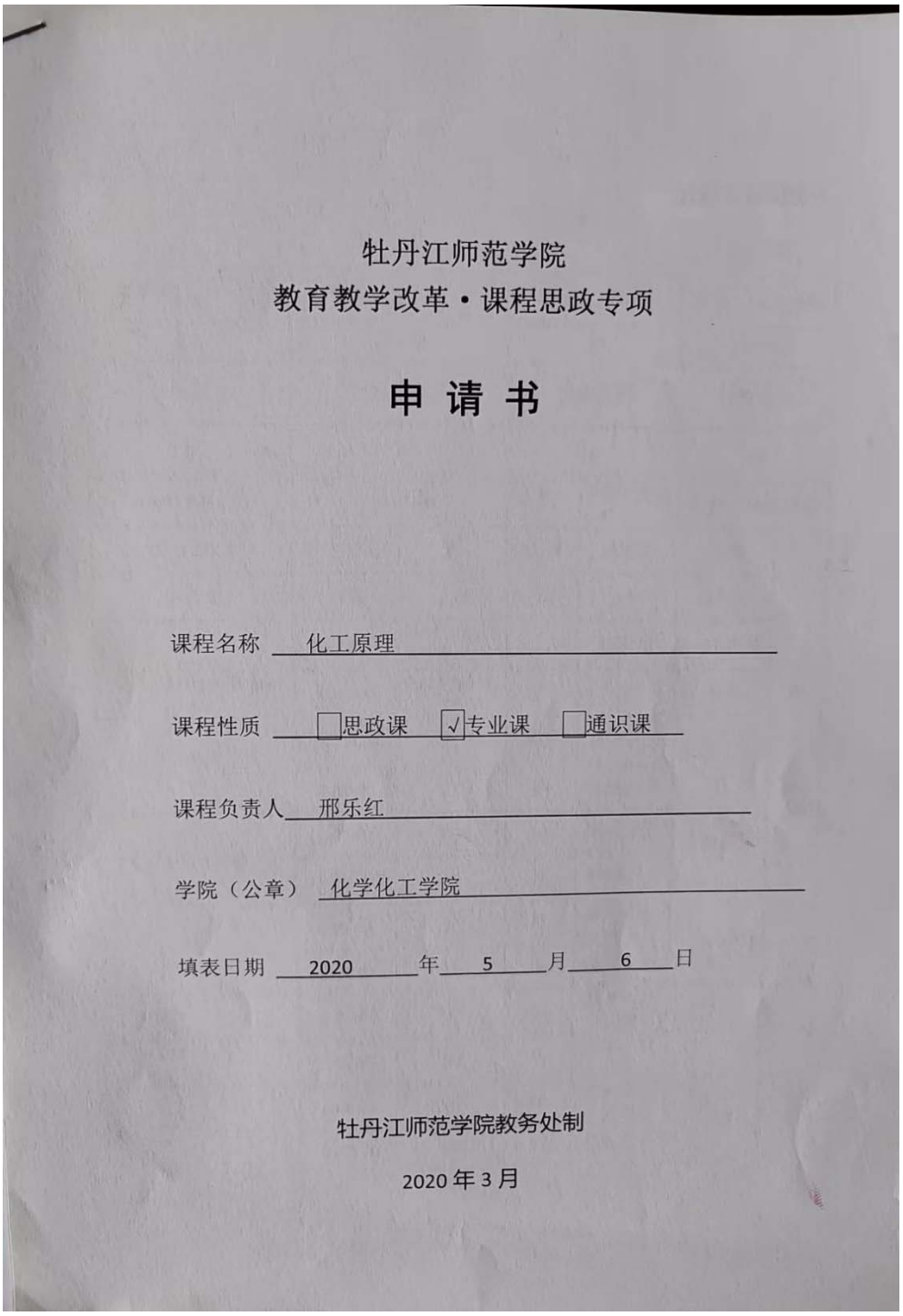

牡丹江师范学院
教育教学改革·课程思政专项

申 请 书

课程名称 化工原理

课程性质 □思政课 √专业课 □通识课

课程负责人 邢乐红

学院（公章） 化学化工学院

填表日期 2020 年 5 月 6 日

牡丹江师范学院教务处制

2020 年 3 月

2.工程教育专业认证背景下地方高校化工创新人才培养模式的研究与探索　牡丹江师范学院校级一般项目　负责人：邢乐红

牡丹江师范学院

教学改革项目经费卡

项目名称	教育专业认证背景下地方高校化工创新人才培养模式的研究与		
项目类型	校一般	项目编号	19-XJ21008
主持人	邢乐红	单　位	化学化工学院
项目经费	学校支持：3000元　　匹配经费：　　省拨经费：		
财务系统编号	1601121024		
财务处长签字	王宏		
教务处长签字	12/Fo21		

教务处公章　　财务处公章

年　月　日

填写说明：
1. 项目负责人详细安排预算项目，并严格执行；
2. 财务处按预算项目核销；
3. 计算机填写，A4纸双面打印，盖章后返教务处。

蒋舰教学改革项目（共 1 项）

1. 有机化学

牡丹江师范学院专项项目　　负责人：蒋舰

牡丹江师范学院

课程专项经费卡

项目名称	有机化学		
项目类型	线上线下混合式教程	项目编号	JK-2020015
主持人	蒋舰	单位	化学化工学院
项目经费	4000元		
财务系统编号	1699131015		
财务处长签字	王宏		
教务处长签字			

教务处公章　　财务处公章

年　月　日

填写说明：
1. 项目负责人用计算机填写项目信息和经费预算；
2. 财务处按预算项目核销；
3. A4纸双面打印。

教学改革论文（共 15 篇）

1.贾林艳,韩俊凤,左明辉,邵长斌,陈玉锋,邵艳秋.基于云班课的物理化学实验混合式教学模式探索**[J].**山东化工,**2021,50(01):217-218.**

2.刘素娟,邵艳秋,任玉兰,苏爽月,赵宇.移动 **APP** 辅助教学：分析化学实验“七步教学法”**[J].**牡丹江师范学院学报**(**自然科学版**),2020(01):75-77.**

3.云观,陈佳丽,蒋舰,邵艳秋.有机化学实验中废液及固废的处理**[J].**山东化工,**2020,49(05):257-258.**

4.邵艳秋,姜封庆,蔡雪,谭荣欣.高校化学实验室常见无机废液的处理方法**[J].**广东化工,**2019,46(05):263.**

5.邵艳秋,郑炜,云观,常玉莹.浅谈化学药品库的安全及管理**[J].**化工管理,**2019(04):124-125.**

6.邵艳秋,刘素娟,任玉兰,付大同.分析化学教学现状与 **PBL** 教学法的应用**[J].**牡丹江师范学院学报**(**自然科学版**),2015(04):74-76.**

7.任玉兰,邵艳秋,罗玉杰.讨论式教学法在仪器分析教学中的应用**[J].**教育与职业,**2014(21):151-152.**

8.刘素娟,廉波,邵艳秋,任玉兰,罗玉杰.高师院校分析化学实验教学改革与实践**[J].**牡丹江师范学院学报**(**自然科学版**),2012(01):62-63.**

9.邵艳秋,罗玉杰,任玉兰,刘素娟.分析化学教学改革谈**[J].**牡丹江师范学院学报**(**自然科学版**),2011(02):67-68.**

10.刘素娟,邵艳秋,任玉兰,罗玉杰.高等师范院校仪器分析实验课程改革与实践**[J].**牡丹江师范学院学报(自然科学版),**2011(01):74-75.**

11.邵艳秋,罗玉杰,廉波,任玉兰,刘素娟.能力培养视角下分析化学实验教学改革**[J].**鸡西大学学报,**2010,10(05):144-145.**

12.邵艳秋.化学师范生教学技能结构论析**[J].**黑龙江高教研究,**2008(08):119-120.**

13.邢乐红,王宜鑫,隋朝,肖同欣,赵玥,邵艳秋.工程教育专业认证背景下化学工程与工艺专业人才培养模式探索**[J].**教育现代化,**2020,7(07):11-12.**

14.邢乐红,王宜鑫,左明辉.工程教育专业认证背景下化学工程与工艺专业学生实践能力培养研究**[J].**山东化工,**2019,48(24):159-160.**

15.贾林艳,左明辉,韩俊凤,陈玉锋,邵长斌.《物理化学实验》课程思政探索与实践**[J].**广州化工,**2021,49(21):177-178.**

1.贾林艳,韩俊凤,左明辉,邵长斌,陈玉锋,邵艳秋.基于云班课的物理化学实验混合式教学模式探索[J].山东化工,2021,50(01):217-218.

基于云班课的物理化学实验混合式教学模式探索

贾林艳,韩俊凤,左明辉,邵长斌,陈玉锋,邵艳秋

(牡丹江师范学院 化学化工学院,黑龙江 牡丹江　157011)

摘要:混合式教学模式已成为高校教学改革的趋势之一。针对目前物理化学实验教学现状及存在的问题,探索基于云班课的混合式教学,详细阐述了传统教学与混合式教学的过程,混合式教学模式在物理化学实验教学中的应用,使得学生学习的积极性提高,创新能力和实践能力增强,课堂效率和教学效果大大提高。

关键词:混合式教学;物理化学实验;云班课

中图分类号:G642.423　　文献标识码:A　　文章编号:1008-021X(2021)01-0217-02

DOI:10.19319/j.cnki.issn.1008-021x.2021.01.096

Research on the Application of Mixed Teaching in Physical Chemistry Experiment Course Based on Cloud Class Platform

Jia Linyan, Han Junfeng, Zuo Minghui, Shao Changbin, Chen Yufeng, Shao Yanqiu

(College of Chemistry and Chemical Engineering, Mudanjiang Normal University, Mudanjiang　157011, China)

Abstract: Mixed teaching has become one of the important trends in the teaching development of college curriculum. Considering current situation and existing problems, mixed teaching in physical chemistry experiment course has been researched based on cloud class platform. The comparison on teaching process has been expounded between traditional teaching and mixed teaching. The new teaching mode not only has stimulated interest in learning, strengthened practical and innovation ability, but also has been effectively improved the quality of teaching.

Key words: mixed teaching; physical chemistry experiment; cloud class

随着互联网技术的快速发展,电脑、智能手机的普及,各种线上教学平台应运而生,为混合式教学提供了必备条件。教师必须跟上时代的步伐,利用“互联网+”平台,创新教学理念和教学方式[1]。混合式教学是目前教学改革的趋势之一,它是将传统教学与线上教学相结合的教学模式,是互联网与教育相融合的产物[2]。该教学模式既可以发挥教师的引导、启发、监控教学过程作用,又能够充分体现学生作为学习过程主体的主动性、积极性与创造性[3]。选择一个适宜的线上平台是决定混合式教学效果的重要因素。

云班课是一款免费移动智能教学 APP,很大程度上解除了教师在选择时的费用之忧,该软件有教师端和学生端,教师可以上传各种教学资源、创建题库、创建活动、进行轻直播等。上传的教学资源可以是文档和视频等资料;创建活动包括答疑探讨、测试、问卷调查、头脑风暴、作业任务等活动。

物理化学实验需要综合运用物理和化学的原理与技术,方法与仪器,以及数学运算工具,是一门理论性、实践性、综合性和研究性很强的课程[4],学生需掌握实验的基本原理、基本方法,通过实验的完成和数据处理,提高学生发现问题、分析问题和解决问题的能力,在实验中加强对学生的科研和创新能力的培养。

1　传统教学模式

由于受实验仪器台套数的限制,目前我校物理化学实验课程采用大循环模式,每个实验班 16 人左右,每个实验有 4 套仪器,即一位教师指导 16 人完成 4 个实验。教学模式可分为以下几个步骤:

1.1　学生课前预习

课前要求学生写预习报告。由于物理化学实验涉及的原理和实验技术较为深奥难懂,学生看教材很枯燥,大部分学生只是对照实验讲义采取摘抄的方式完成预习报告交差而已,对实验仪器设备的使用方法没有感官的认识,对实验每一步预期的测定结果及现象并没有系统了解,并未达到预习的目的,所以其实是对实验一无所知走进实验室。

1.2　课上实验

基本上采用灌输式教学模式。教师对实验目的、原理和实验步骤一一讲解,进行仪器操作演示,学生机械式地听讲。然后学生“抓中药式”按教材的实验步骤完成实验。由于前期预习不够充分,所以对实验过程出现的实验现象、测定的数据规律没有认识,当测定结果出现很大偏差时不能及时发现问题仍旧机械地做下去,最后得出错误的结论。

1.3　课后总结

下课后学生根据测定的实验结果处理实验数据,完成实验报告。由于实验数据处理有的较为复杂,有些学生不能自己独立完成,甚至有个别学生抄袭别人的报告一交了之。对实验中出现的误差不能认真分析。

1.4　课程考核方式

近年来已多次对实验成绩考核进行改革,但预习实验报告和实验报考仍占考核成绩地权重较高。这两部分都包含实验目的、实验原理、实验仪器与药品、实验步骤,学生基本上都是照书摘抄,数据处理和误差分析部分很多学生也是课后相互借鉴完成,无法实现培养学生独立进行数据处理、分析问题解决问题等能力的目标。

可以看出,传统的物理化学实验教学过程是以教师为中心,学生处于被动接受的地位,积极性不高,教学效果较差。因此,教师需要适应时代的发展,对实验教学进行改革与创新。

2　基于云班课的混合式教学模式

由于云班课具有使用便捷,师生均可随时随地在手机上使

收稿日期:2020-09-23

基金项目:牡丹江师范学院教学改革项目(19-XJ21029)(JK-2020014);黑龙江省高等教育教学改革一般研究项目(SJGY20190688)

作者简介:贾林艳(1971—),女,博士,牡丹江师范学院教授,硕士生导师,主要从事物理化学教学及稀土发光材料研究。

(C)1994-2021 China Academic Journal Electronic Publishing House. All rights reserved.　http://www.cnki.net

用的特点，所以被我们首选为线上平台。根据平台特点对物理化学实验进行了混合式教学模式改革。

2.1 课前准备

教师根据具体实验，将实验目的、原理、步骤和数据处理方法制成 Flash 或 PPt，然后将讲解内容录制成视频上传至云班课的资源中，同时在视频上提出一些问题供学生思考，这样既可以检验学生对知识内容掌握的程度，又加强了师生的互动性，上传到云班课班级资源中，这样学生可以利用课余时间在课前反复听老师的讲解，将实验原理和内容理解透彻，避免了传统教学中学生照方抓药的弊端。学生可以灵活利用课余时间，自主掌握学习进度，随时随地利用互联网观看上传的预习内容，并配合实验指导书对照学习。

2.2 课上活动

由于在课前学生已经高质量完成了预习，对实验内容已经心中有数，所以在课堂上，老师可以采用提问的方式检查学生的预习效果，加深学生对对重点内容的理解，这样大大缩短了讲解时间，学生有更充足的时间完成实验，老师根据学生的实验进度和出现的问题进行指导，学生对预习及实验过程中遇到的问题可以面对面地进行师生互动交流。实验过程中教师还可以针对每个实验进行实验扩展研究，如对凝固点降低法测定溶质的相对分子质量的实验，若以水为溶剂测定蔗糖分子量，冷冻剂直接用冰水是否可行？如果不行，该怎样解决？

2.3 课后总结

课后学生不仅要按要求进行数据处理和误差分析，完成实验报告，而更需要对实验现象及结果进行深入思考和讨论，这样才能加深对理论的理解。教师需要引导学生进行这样的思考，布置一些思考题，发布在云班课的“答疑讨论区”里，学生以小组形式讨论完成。如凝固点降低法测定溶质的相对分子质量的实验，学生的实验结果会有误差，这时可以引导学生思考“误差的来源有哪些？最大的误差来自哪里？如何可以减小误差？”。液体饱和蒸气压的测定实验中，可以提问“该实验装置是否可以测定固体的分解压？如何测定？”通过进行讨论答疑，学生进行深入思考，积极性有了很大提高，教师也可根据学生问答的情况了解学生对知识的掌握程度，对教学效果也心中有数。

2.4 课程考核

本次混合式教学实践中，对 2017 级专业学生采取的考核方式是：线上学习（包括观看平台资源、讨论和小组任务）占 20%，线下实验操作、课堂表现及实验报告占 40%，测试（包括理论和实验）占 40%。

3 教学反馈

目前混合式教学模式在物理化学实验课程中还在探索阶段，但与传统教学模式相比，已经显示出优越性。一方面，提高了学生学习的积极性。课前学生可以在线上听老师的讲解和完成思考题，使得预习的效果大大提高。其二，提高了课堂效率。由于线上预习的效果的提高，课堂上教师只需对实验原理和操作中难点加以强调，学生可把时间主要用在实验观察和思考上，对于复杂的数据处理可以在课堂通过老师的帮助顺利完成，避免学生课后因为数据处理困难而产生的实验报告抄袭现象。其三，学生独立思考和创新能力提高，团队合作意识增强。

4 结语

通过在线校化学、应用化学、化学工程与工艺三个专业的物理化学实验课实施基于云班课的混合式教学模式，教学效果已初见成效。学生学习的主动性和自觉性有了很大的提高，动手实践能力大大增强，增强了学生的综合能力和创新能力，探索了实验教学改革的新模式。

参考文献

[1] 王春燕，周丽梅，宋 强．“互联网 + ”时代大学基础化学课程教学方法的探索 [J]．山东化工，2017，23：125-126.

[2] 秦 楠．“互联网+”背景下混合式教学模式建构研究 [D]．济南：山东师范大学，2017.

[3] 何克抗．从 Blending Learning 看教育技术理论的新发展 [J]．电化教育研究，2004，3：3-15.

[4] 贺 婷，孟 涛，方 萍，等．“理论、实践与科研三位一体”物理化学实验教学改革 [J]．实验室研究与探索，2015，5：138-140.

（本文文献格式：贾林艳，陈俊凤，左明辉，等．基于云班课的物理化学实验混合式教学模式探索 [J]．山东化工，2021，50（1）：217-218.）

（上接第 216 页）

“第二课堂”，采用课堂教学与参加实际工作相结合的教学形式，实现学校与企业共同参与人才培养的过程[7]，这样不但可以巩固课上所学的理论基础知识，而且能够提高学生的环境认知能力。

3.4 实现教研有机结合

把科研引入教学活动当中是高校提高人才培养质量的新思路、新举措[8]。在实际教学工作中，教师应把教学和科研恰到好处地统一起来，充分发挥教学与科研协同育人的作用，鼓励学生在学习中参与科研[9]。比如，教师可以将自己的科研项目引入课堂，组织学生建立科学研究小组，通过项目的申报、立项、实施以及成果获得等诸多环节，让学生了解科学研究的全过程。此外，通过这种科研训练，也有助于提高学生数据检索、资料筛选、论文分析等方面的能力，这对以后好的解决大一学生文献检索能力不强的问题。

4 总结

本文通过对《环境学导论》课程教学目标达成情况进行分析，有效地反映了学生的学习状况，同时也反映出了课堂教学中的不足，高效率的课堂教学是所有教师共同追求的目标，要实现这一目标，除了在制定教学目标上下功夫外，还要做到充分挖掘和利用有利于学生发展的课程资源，不断完善课程内容体系，教学过程中要灵活运用多种教学手段，有效加强校企交流合作，打造联合培养新平台。除此之外，以科研项目、大学生创新创业项目等为依托，实现教学与实践、教学与科研的有机结合，在提高课程教学目标达成度的同时，也保证了人才培养的质量[10]。

参考文献

[1] 陈俊杰，倪建林，吴海燕，等．面向产出的课程目标达成情况评价与分析——以《流压与流力传动》课程为例 [J]．南方农业，2020，7：158-159.

[2] 曹永清．从“车间进校”到“企业课堂”——构建以企业为主导的深层次校企合作模式 [J]．广东教育：职教，2009，5：14-16.

[3] 徐永兴，陈芳芳，樊盛华．高校科研资源转化为教学资源的路径研究 [J]．黑龙江教育：高教研究与评估，2019，11：52-54.

[4] 杨淑欣，孙国军，王丽静．论高校教学与科研的互动 [J]．河北师范大学学报：教育科学版，2002，6：21-23.

[5] 冯爱妮，林 琳．构建本科课程评价方案的探索与实践 [J]．北京教育：高教，2017，9：79-81.

（本文文献格式：王艺璇，滕洪辉，杜百祥．基于教学目标达成度的“环境学导论”课程评价研究 [J]．山东化工，2021，50（1）：215-216+218.）

(C)1994-2021 China Academic Journal Electronic Publishing House. All rights reserved. http://www.cnki.net

2.刘素娟,邵艳秋,任玉兰,苏爽月,赵宇.移动 APP 辅助教学：分析化学实验“七步教学法”[J].牡丹江师范学院学报(自然科学版),2020(01):75-77.

文章编号:1003-6180(2020)01-0075-03

移动 APP 辅助教学：分析化学实验“七步教学法”

刘素娟,邵艳秋,任玉兰,苏爽月,赵 宇
(牡丹江师范学院 化学化工学院,黑龙江 牡丹江 157011)

摘 要:提出手机移动 APP 蓝墨云班课与分析化学实验课程深度融合的“七步教学法”.“七步教学法”分为课前预习过关测试、课堂提问激发兴趣、阴性惩罚奖励剥夺、实验操作拍照上传、及时表扬慎用批评、实验报告批改及时、课后总结提升内化.教学成果表明,“七步教学法”能有效激发学生的学习兴趣,充分调动学生学习积极性,提高学生学习自主性,线上与线下学习结合更加紧密,取得了较好的教学效果.

关键词:移动 APP;分析化学实验;七步教学法
DOI:10.13815/j.cnki.jmtc(ns).2020.01.017
[中图分类号]G642 [文献标志码]A

Mobile APP Assisted Teaching: " Seven-step Teaching Method' for Analytical Chemistry Experiment

LIU Sujuan,SHAO Yanqiu,REN Yulan,SU Shuangyue,ZHAO Yu
(College of Chemistry and Chemical Engineering, Mudanjiang Normal University, Mudanjiang 157011,China)

Abstract: This paper proposed a" seven-step teaching method' that integrates mobile APP blue ink cloud class with analytical chemistry experiment course. " Seven-step teaching method' was divided into pre-class pass test, classroom questions to stimulate interest, negative punishment and reward deprivation, experimental operation photos uploaded, timely praise and criticism, experimental report correction timely, after-class summary to improve internalization. The teaching results showed that the" seven-step teaching method' can effectively stimulate students' interest in learning, fully mobilize students' learning enthusiasm, and improve their autonomy in learning. The combination of online and offline learning was more closely, and had achieved a better teaching effect.

Key words: Mobile APP; Analytical Chemistry Experiment; Seven-step Teaching Method

收稿日期:2019-06-20
基金项目:黑龙江省青年科学基金项目(QC2014C009);牡丹江师范学院教改项目(18-XJ20066)
作者简介:刘素娟(1981-),女,山东鄄城人.副教授,硕士,硕士生导师,主要从事分析化学和材料合成研究;邵艳秋(1969-),女,黑龙江牡丹江人.教授,博士,主要从事材料合成研究;任玉兰(1971-),女,黑龙江牡丹江人.教授,博士,主要从事材料合成研究.

(C)1994-2020 China Academic Journal Electronic Publishing House. All rights reserved. http://www.cnki.net

移动终端逐渐走进高校大学生的学习和课堂教学中,深刻改变着广大教育教学工作者和学生对移动学习的认知.2018 年 4 月教育部印发的《教育信息化 2.0 行动计划》中指出,必须"依托各类智能设备及网络,积极开展智慧教育创新研究和示范,推动新技术支持下教育的模式变革和生态重构,成为传统课堂教学模式的有益补充."

蓝墨云班课是开发推广较早的教育类手机 APP,界面友好、功能全面,使用方便.笔者在教学中将手机 APP 蓝墨云班课与分析化学实验课程深度融,实施课前预习过关测试,课堂提问激发兴趣,同性惩罚奖励剥夺,实验操作拍照上传、及时表扬慎用批评,实验报告批改及时和课后总结提升内化的"七步教学法"教学,充分调动学生的学习自主性,激发学生的实验兴趣,发挥学生的主观能动性和教师的宏观调控作用.方便教师和学生及时充分沟通,提高学生的学习效率和教师的办公效率.图 1 为蓝墨云班课辅助下分析化学实验课程"七步教学法".

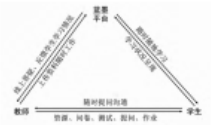

图 1　蓝墨云班课辅助下的"七步教学法"

1　课前预习,过关测试

实验预习是学习的重要环节.通过实验预习,学生对实验目的原理步骤等内容做到心中有数,既可以锻炼学生的资料查阅能力和自学能力,也有利于学生更有针对性地听老师讲解.化学实验有一定的危险性,学生做好预习有利于人身安全.比如测合金中镍含量的测定实验[1-2],教师可从中国知网上搜索一些与实验相关的资料文献,上传至平台,方便学生课前预习.笔者让学生把预习报告写好拍照上传至蓝墨云班课平台,随时掌握学生上传预习报告的情况.教师在蓝墨平台设置预习测试题,学生在写预习报告的同时必须完成测试题目并全部正确才可进入实验室上课,与传统方式比较,利用移动 APP 可有效监控学生预习情况,提高学生学习的自主性.

2　课堂提问,激发兴趣

蓝墨云班课平台有多种提问方式,如抢答、举手、小组评价、随机选择和定点选择等,互动方式丰富多样,这些功能都可以很好地调动学生的积极性.活跃课堂气氛.如教师用随机选择方式提问,学生不知道手机会抽到谁,所有人都会做准备,学生的注意力是高度集中的,这有利于提高课堂效率和学习效果.学生喜欢参与课堂活动,教师用抢答功能提问学生,学生产生强烈的主人翁精神和冒险的竞争精神.课堂气氛活跃而激烈.用小组评价功能提问学生时,学生分为若干小组,小组内成员既分工又协作,共同完成问题的解答,这种方式可以有效促进课堂中学生之间的互动.教师可以设定平台经验值与学生成绩呈正相关,给回答问题的学生加经验值.学生回答问题积极性就更高了,学生学习的积极性主动性被充分调动起来.

3　同性惩罚,奖励剥夺

同性惩罚和奖励剥夺是指每次实验课都告知学生有 20 分的操作分.如果操作错误就扣掉一些,这会影响课程的期末成绩.学生不希望被扣分,所以努力做到操作正确,慢慢就养成了正确的实验习惯.使用同性惩罚奖励剥夺的方式,学生的自我约束力明显增强.

4　实验操作,拍照上传

学生把分析化学实验中重点实验操作拍成照片或微视频,上传至蓝墨云班课平台.上传资料可以一直保留,学生随时可以到班课中找到自己和同学的照片或视频温习.每次实验课拍照两个基本操作,录两个实验操作微视频并上传至蓝墨云班课平台,学生都喜欢自己的实验操作动作更准确更优美,便会更严格要求自己,慢慢就养成严谨细致的实验操作习惯,也会对分析化学实验这门课程产生极大的热情.

5　及时表扬,慎用批评

教师要多关注学生,学生操作正确要及时表扬,一句"你操作的很正确,你实验做的很认真"也许会让他从此爱上分析化学实验这门课程,或许他从此走进科研的大门,或许他自己做老师时也会把这个法宝传承下去.你永远不会知道你的及时表扬会对学生产生多大的蝴蝶效应.批评不能言语过激,点到为止,看到学生有操作错误的地方指出来错在哪里以及怎样改正就可以了.

6　实验报告,批改及时

蓝墨云班课平台条件下,学生写完实验报告可以随时拍照上传,教师可以利用碎片时间批改,及时把问题和建议反馈给学生.教师提高了工作效率,节省了工作时间,就有更多的时间和精力用于教学内容的设计和教学模式的更新上.对于实验报告里面出现的问题,教师有了更多时间把问题及修改方案详细写清楚,方便学生理解和整改.

7　课后总结,提升内化

实验结束后,学生到讲台上对本次实验的学习收获进行总结,对自己的实验操作进行点评.这是学习效果内化提高阶段,通过总结和点评,学生锻炼了总结知识的能力,从他人的学习心得中得到启发,不仅可以正确评价自己,而且会激发起更高的学习积极性.

8　实践结果

经过一个学期的教学实践,2017 级参与分析化学实验与移动 APP 蓝墨云班课深度融合教学尝试的小组与常规方式授课小组相比较,学生分析化学实验期末平均成绩由 80 分以下提高到了 80 分以上.笔者调查了学生对"七步教学法"的态度,85%学生表示,"七步教学法"能够随时随地进行分析化学实验学习,96%的学生愿意花更多时间进行课前预习和课后复习,97%的学生认为这种教学法教会了他们如何自学,仅 1%学生明确表示不喜欢"七步教学法".

结语

利用移动终端手机 APP 蓝墨云班课平台建设和丰富实验教学资源,不仅可以拓宽实验教学的时间和空间,强化学生的主体地位,而且还为学生提供了自主学习平台和交流探讨平台,显著提高了分析化学实验的教育教学质量.实验教学是连接理论知识与实际应用的桥梁,是培养学生实践能力和创新意识的重要途径.[3-6]分析化学实验是一门重要专业必修课程,其基础性和综合性都很强.通过该课程的学习,学生可加深对分析化学严格的"量"的概念的理解,掌握分析化学实验的重要基本操作和技能.分析化学实验既可以培养学生严谨的科学态度以及实事求是的科学精神,培养学生科学分析解决实际问题的能力,为学生今后在学科领域内从事理论研究和实际工作打下基础.实践证明,手机 APP 辅助的"七步教学法"以学生为中心,线上线下学习结合,有效激发了学生的学习兴趣,培养了学生的创新能力.

参考文献

[1]李晓霞.基于 UMU 互动平台"互联网+"混动学习"探究模式"[J].实验技术与管理,2019,36(4):196-199.
[2]崔强.丁二酮肟重量法测定合锌生铁中镍含量分析过程中问题浅析[C].第 23 届全国铁合金学术研讨会论文集,2014:693-695.
[3]高娟,李萍,李学超,等.基于微信平台的工科大学物理教学[J].牡丹江师范学院学报,自然科学版,2019(2):72-74.
[4]马杰.MOOC 环境下 Ubuntu 系统教学成效分析[J].牡丹江师范学院学报,自然科学版,2018(4):69-72.

编辑:吴楠

(C)1994-2020 China Academic Journal Electronic Publishing House. All rights reserved.　http://www.cnki.net

(C)1994-2020 China Academic Journal Electronic Publishing House. All rights reserved.　http://www.cnki.net

3.云观,陈佳丽,蒋舰,邵艳秋.有机化学实验中废液及固废的处理[J].山东化工,2020,49(05):257-258.

有机化学实验中废液及固废的处理

云　观[1],陈佳丽[2],蒋　舰[1],邵艳秋[1]

(1.牡丹江师范学院 化学化工学院,黑龙江 牡丹江　157011;2.牡丹江龙江环保供水有限公司,黑龙江 牡丹江　157011)

摘要:本文总结了我校本科有机化学实验的实验项目及产生的废液、固废,并进行分类。通过中和至无毒化、蒸馏再利用、转化为其它实验的反应原料等环保安全的方法处理产生的废液、固废,可以减少有机化学实验对环境的污染,并且可以降低实验成本。

关键词:有机化学实验;废液;固废;处理办法

中图分类号:X703;X705　　文献标识码:B　　文章编号:1008－021X(2020)05－0257－02

DOI:10.19319/j.cnki.issn.1008-021x.2020.05.100

Treatment of Liquid and Solid Wastes in Organic Chemistry Experiments

Yun Guan[1], *Chen Jiali*[2], *Jiang Jian*[1], *Shao Yanqiu*[1]

(1. College of Chemistry and Chemical Engineering, Mudanjiang Normal University, Mudanjiang　157011, China;
2. Mudanjiang Longjiang Environmental Protection Water Supply Co., Ltd., Mudanjiang　157011, China)

Abstract: This paper summarizes the experimental items of organic chemistry experiment and the waste liquid and solid waste, and classifies them. The environmental protection and safety methods such as neutralization to non－toxicization, distillation and reuse, and conversion into other experimental reaction materials to deal with the waste liquid and solid waste can reduce the environmental pollution caused by organic chemistry experiments and reduce the experimental cost.

Key words: organic chemistry experiment; waste liquid; solid waste; treatment method

有机化学实验是本科教学中化学、生物、医学、高分子和材料科学等多专业的专业基础课,在有机化学实验中大多数实验都会产生废液及固废,如果在实验结束后不能及时处理实验产生的废弃物,将会对人体健康和环境造成危害和污染。目前绿色化学实验呼声渐高[1-3],进行环境无害的化学实验是化学实验教学领域的长期目标。本文主要介绍了本校本科有机化学相关实验时产生的废液、固废和处理办法。

1　有机化学实验中产生的废液及固废种类

根据现阶段本院本科生使用的教材[4],将其进行的全部有机化学实验的题目及废液固废类型进行了汇总,如表 1 所示。

表 1　有机化学实验项目及产生的主要废液固废

Table 1　Organic chemistry experiment topic and main waste liquid and solid waste

序号	实验项目	产生的主要废液及固废
序号	实验项目	产生的主要废液及固废
1	熔点的测定	液体石蜡
2	液态有机化合物折光率的测定	无
3	柱层析	无水乙醇、三氧化二铝粉料
4	重结晶提纯法	乙酰苯胺、活性炭
5	蒸馏和沸点测定	无水乙醇
6	分馏	丙酮、无水乙醇
7	环己烯的制备	环己烯、氯化钙
8	溴乙烷的制备	溴乙烷、硫酸
9	乙酸乙酯的制备	乙酸乙酯、硫酸镁
10	减压蒸馏	乙酸正丁酯
11	乙酰苯胺的制备	乙酰苯胺、乙酸、锌粉
12	茶叶中生物碱的提取	咖啡因、乙醇、茶叶

表 1(续)

序号	实验项目	产生的主要废液及固废
13	肉桂酸的合成	肉桂酸、苯甲醛
14	正丁醚的合成	正丁醚、硫酸、氯化钙
15	乙酸正丁酯的合成	乙酸正丁酯、乙酸、正丁醇、硫酸、硫酸镁
16	脲醛树脂的合成	脲醛树脂
17	甲基橙的合成	甲基橙、乙醇、乙醚
18	阿司匹林的制备	水杨酸
19	洗涤灵的制备	十二烷基硫酸钠

2　废液、固废类型及处理办法

2.1　废液及固废类型

2.1.1　干燥剂型

在实验环己烯的制备、乙酸乙酯的制备、正丁醚的合成、乙酸正丁酯的合成中,产生的氯化钙、硫酸镁废弃物均作为产品干燥时的干燥剂使用。这两种化学品在使用后均变为结晶水合物状态。

2.1.2　催化剂型

在正丁醚的合成实验和乙酸正丁酯的合成实验中,浓硫酸作为催化剂使用,在实验过程中会经过分液漏斗分出,成为废液。

2.1.3　反应原料型

在实验乙酰苯胺的制备、阿司匹林的制备、乙酸正丁酯、肉桂酸的制备中,乙酸、锌粉、水杨酸、正丁醇、苯甲醛五种有机物由于未完全反应,在进行除杂时,以杂质的形式被蒸馏或过滤出来形成废物。在实验茶叶中生物碱的提取中,乙醇作为萃取咖啡因的溶剂,在后期蒸馏时需蒸馏出大部分乙醇,成为废液。在实验溴乙烷的制备中,浓硫酸作为反应原料,过量和溴化钠进行反应,反应结束后剩余的硫酸分液漏斗分出,成为废液。

收稿日期:2019－12－17

基金项目:黑龙江省高等教育教学改革一般研究项目(SJGY20190688)

作者简介:云　观(1992—),助教,研究方向为有机化学与生物化学。

(C)1994-2020 China Academic Journal Electronic Publishing House. All rights reserved.　http://www.cnki.net

2.1.4 回收原料型

在实验蒸馏和沸点测定、分馏中，无水乙醇和丙酮作为实验式样进行使用，蒸馏和分馏出的无水乙醇和丙酮成为实验废液；在实验熔点的测定中，液体石蜡作为热浴液进行使用，多次使用后会被样品污染而成为废液；在实验柱层析中，无水乙醇作为洗脱剂使用，在洗去色谱柱和洗脱重甲基橙时会和样品混合形成废液；在所有的蒸馏和分馏操作中，均会用到碎瓷片充当沸石，使用过后成为固废。

2.1.5 反应产物型

在所有的有机合成制备中，得到的有机物产品由于纯度和学生操作严谨度不同，不能直接用作化学试剂，成为废液及固废。

2.1.6 泄露危险品型

在使用水银温度计时，因为学生误操作造成水银泄露，成为泄漏危险品型废液。

2.1.7 废弃剂型

在实验甲基橙的制备中，用到乙醚和乙醇进行洗涤甲基橙晶体，洗涤后成为废液。

2.1.8 碎玻璃型

学生在实验过程中，不可避免会造成玻璃仪器的打碎和损坏，形成固体废弃物。

2.2 废液及固废处理办法

2.2.1 中和无毒害处理

对于产生的干燥剂型、催化剂型、反应原料型、洗涤剂型废液及固废，可进行中和处理。采用碱性废液固废和酸性废液中和，也可采用药剂中和，即采用 Na_2CO_3、NaOH、石灰乳、碳酸钙、工业硫酸、盐酸等中和[5]。反应方程式为 $H^+ + OH^- \rightarrow H_2O$、$NaOH + HCl \rightarrow NaCl + H_2O$、$Na_2CO_3 + H_2SO_4 \rightarrow Na_2SO_4 + H_2O + CO_2\uparrow$，经过中和的废液可直接排放。对于产生的毒害性固废，例如温度计中水银，首先监督学生不要直接倒入下水道及垃圾箱，用硫磺粉覆盖于水银表面，生成无毒的硫化汞[6]，然后密封储存，交给有资质的废物处理企业进行处理。

2.2.2 蒸馏再利用处理

对于回收原料型废液，可进行再次利用，蒸馏和分馏操作产生的乙醇和丙酮、柱层析中流出来的乙醇，均可以收集起来再次蒸馏使用，蒸馏后的二次乙醇可用于清洗玻璃仪器，进行折光率测定的练习、蒸馏操作的练习等实验使用，使用过的沸石也可收集起来，使用二次乙醇浸泡洗涤，烘干后可再次使用。

2.2.3 安全储存作为其它实验的反应原料

反应产物型废液及固废按难处理，反应产物无法直接作为成品化学试剂使用，对于此类废液及固废，应选用合适的容器安全储存，一部分可作为其它实验的实验原料，例如合成的丙烯酸，可以在下一届学生进行熔点测定实验时作为待测样品使用；学生合成的乙酰苯胺，由于苯胺氧化，变为粉红色，可以利用其进行重结晶基础操作；合成的阿司匹林，可以作为样品进行分析化学实验，测定其产品纯度；实验中合成的乙酸正丁酯可储存起来，作为减压蒸馏实验的原材料；让学生练习减压蒸馏实验操作；学生合成的洗涤灵进一步处理，制成成品洗涤灵，用以洗刷实验室的玻璃仪器。

对于环己烯、溴乙烷、咖啡因、甲基橙等反应产物固废处理，将一部分交给有相关科研项目的教师，其通过柱色谱等方法将固废提纯后使用，可减少这些教师的科研开支；剩余的部分进行安全储存，然后交给有废物处理资质的企业进行安全处理。

2.2.4 损坏玻璃仪器的再利用和处理

对于损坏的玻璃仪器，首先对其评估，对于可修理可再利用的玻璃仪器，先将其清洗干净，送到仪器维修部门进行修理；对于不可修理的玻璃仪器，则作为固体废弃物进行储存，然后交给有固废处理资质的企业进行处理。

3 小结

采用上述处理措施，可减少有机化学实验中的废液、固废排放量，降低实验开支，节省实验低值易耗经费，有机化学实验应逐渐实现绿色化，还需要更多的化学教育工作者们进一步努力。

参考文献

[1] 宋胜芳. 绿色有机化学实验的探索和实践 [J]. 实验室研究与探索，2006(8)：989－991.
[2] 黄 丹，邓崇光. 论有机化学实验的绿色化 [J]. 实验室研究与探索，2001(5)：37－38.
[3] 杨腾芳，吴美芳，黄良保，等. "绿色化"有机化学实验教学实践和探讨 [J]. 实验室研究与探索，2002(3)：14－15.
[4] 曾和平. 有机化学实验 [M]. 4 版. 北京：高等教育出版社，2014.
[5] 刘 梅. 化学清洗废液的现场处理方法 [J]. 清洗世界，2007(10)：30－35.
[6] 宋晓勇. 血压计水银泄露时的正确处理方法 [J]. 医疗装备，2006(1)：13.

（本文文献格式：王 旭，陈世丽，肖 旭，等. 有机化学实验中废液及固废的处理 [J]. 山东化工，2020，49(5)：257－258.）

（上接第 256 页）

4 结论

（1）天然工况下，滑坡前缘局部发生缓慢蠕滑，暴雨工况下，由降位移产生滑动破坏，且滑坡整体安全系数不大，属于山滑坡是降雨-河水升因诱发的牵引式渐进破坏型滑坡，并且在暴雨工况下有整体滑动的可能。

（2）降雨入渗会降低滑坡的整体稳定性，河水将促进滑坡前部土滑段变形首先引起破坏，需要采取措施降低水对滑体前缘的影响，提高滑坡的整体稳定性。

（3）考虑滑坡的诱发因素，针对其破坏模式，建议采用如下防治措施：方案一：抗滑桩＋两排＋挡土墙＋截排水；方案二：削方＋抗滑桩＋一排＋挡土墙＋截排水。具体采用何种方案，应需考虑工程经济成本，比选确定。

参考文献

[1] 刘 杰，李 媛，杨旭东，等. 2000－2015 年全国地质灾害发育分布特征分析 [J]. 中国地质灾害与防治学报，2018，29(3)：1－7.
[2] 成永锋. 论水对滑坡的作用 [J]. 四川建筑，2004，24(1)：53－56.
[3] 丁秀丽，向喜琼，殷志达，等. 降雨型滑坡预报新方法 [J]. 岩石力学与工程学报，2004，23(21)：3738－3743.
[4] 邓合玉，陈 勇. 库水升降条件下滑坡变形及稳定机理研究 [J]. 三峡大学学报（自然科学版），2018，40(6)：34－38.
[5] 卢晓朗，姜雪川，杜 毅，等. 库水位下降条件下顺倾层滑坡稳定性分析 [J]. 中国地质灾害与防治学报，2017，28(3)：8－15.
[6] 曹 伟. 论库水位变化对土质滑坡稳定性的影响 [J]. 山西师范大学学报（自然科学版），2017，4：128－133.
[7] 中华人民共和国国土资源部. GB/T 32864-2016 滑坡防治工程勘查规范 [S]. 北京：中国标准出版社，2016：14－15.

（本文文献格式：侯 倩，尹晓刚，王晓娟，等. 河水与降雨诱发某堆积层滑坡的破坏模式与防治方案 [J]. 山东化工，2020，49(5)：254－256，258.）

(C)1994-2020 China Academic Journal Electronic Publishing House. All rights reserved. http://www.cnki.net

4.邵艳秋,姜封庆,蔡雪,谭荣欣.高校化学实验室常见无机废液的处理方法[J].广东化工,2019,46(05):263+262.

高校化学实验室常见无机废液的处理方法

邵艳秋，姜封庆，蔡雪，谭荣欣
(牡丹江师范学院化学化工学院，黑龙江牡丹江 157011)

[摘要]高校化学实验室每年都需要进行大量的无机实验，无机实验所产生有害无机废液对地球环境污染严重，该文主要介绍我校实验室所产生的无机废液，根据其化学性质进行了简单分类并提出环保安全的处理方法。

[关键词]实验室；无机废液；处理方法
[中图分类号]G4 [文献标识码]A [文章编号]1007-1865(2019)05-0263-01

Treatment Methods of Common Inorganic Waste Liquid in University Chemistry Laboratory

Shao Yanqiu, Jiang Fengqing, Cai Xue, Tan Rongxin
(Department of Chemistry, MudanjiangNormalUniversity, Mudanjiang 157011, China)

Abstract: A large number of inorganic experiments are carried out every year in chemical laboratories of colleges and universities. The harmful inorganic waste liquid produced by inorganic experiments has seriously polluted the earth environment.

Keywords: laboratory; inorganic waste; processing method

无机废液的处理是高校实验室三废处理中最难以解决的问题。首先无机废液的种类繁多，实验室在处理上有较大难度；其次，无机实验产生无机废液的数量较大；最后，高校缺乏系统的实验室废液处理的相关教育[1]，使得学生对于废液处理的并没有形成一个科学严谨的态度，导致学生做完实验直接将废液倒进实验室下水道，造成下水管道污染甚至对周围水质造成极大的影响[2]，该文根据高校实验室中常见无机废液的种类和特点整理出了相应的处理方法。

1 无机化学实验废液的产生及分类

高校化学实验室所产生的废液按其来源可以分为容器洗涤液和未反应完全或者新产生的实验余液。实验所产生余液的性质复杂，种类繁多，需要严格按要求处理。废液按成分一般可分为无机废液、有机废液和生化废液[3]。其中，对环境污染最为严重的是无机废液[4]，主要包括含有铬、铅、镉、氰、银、钡、铜、汞等废液。另外，实验室产生的酸碱废液也对环境也会造成一定的影响。这些废液对生活用水及环境危害极大[5]。因此，我校对无机化学实验产生的废液处理问题高度重视，采取了实验室自行处理及分类存放找专门机构集中处理的方式。本文根据无机废液的性质及相关文献介绍总结出了我们实验课所产生废液的自行处理方法。

2 无机实验废液处理的一般原则

实验教学倡导将绿色化学[6]、环保化学、安全化学[7]等理念融入教学之中。在制定教学大纲时根据国家专业目录培养学生的技能要求，尽量选择毒性小、污染少，废液排放量小、废液种类少、废液处理容易的实验项目以减少对环境的污染[8-9]。另外，在学生培养过程中加强学生对废液处理、废物循环再利用以及减少废物排放量的认识，强化环保化学理念。

要不断强化微型实验在教学中的实际应用，在能得到同样实验现象和实验结论的前提下，尽量减少实验耗材，所排放废液就会大大减少。所以我们在教学过程中根据具体实验要求尽量选择微型实验，从而降低实验室废液处理的压力。

对于排放的废液要按照小心收集、准确分类、安全存放和严格处理的要求进行处理。

优先选择花费小、操作简单、绿色安全的处理方法，而且要高度重视废液的回收再利用问题[10]。

3 无机实验废液处理的对策及方法

我校无机实验产生的废液种类主要有含铬、铅、镉、汞、银、钡、铜、锌、酸碱废液等几类，参照文献结合自身实验条件采取以下处理办法。

3.1 酸碱废液的处理

无机化学实验通常会产生酸性和碱性的物质，这类废液直接排放会造成水 pH 值的改变。如果水质酸度过高，会造成实验室管道腐蚀。一般在处理这类废液时先看其浓度，如果浓度较低，可稀释后直接排放，如果浓度过高，则需定期进行中和处理，达到国家污水排放标准(GB8978-1996)[11]后再进行排放。

3.2 含铬废液的处理

铬酸洗液是实验室常用的洗液，也是无机实验中含铬废液的主要产生来源；醋酸铬(Ⅱ)水合物的制备实验会产生含铬废液。其中 Cr(Ⅵ)是 Cr(Ⅲ)的毒性的 100 倍，所以，实验室废液处理一般是把高价铬离子转化为低价铬离子，水中 Cr(Ⅵ)排放要小于 0.5 ppm。一般处理方法是用铁氧体法除去铬，在含铬废液中加入硫酸亚铁作为还原剂，从而把高价铬还原为低价铬，pH 值调节后生成铬的氢氧化物沉淀，进行统一焚烧处理，剩余废液可简单稀释后直接倒入下水道。

3.3 含银废液的处理

含银废液中回收银的方法有很多，如沉淀法、电解法和离子交换法等，但最主要的是沉淀法。无机化学实验中常见非金属阴离子的分离与鉴定、常见阳离子的分离与鉴定、P区非金属元素(一)、P区非金属元素(二)和离子的鉴定和未知物的鉴别等实验产生含银废液，用沉淀法处理含银废液方便适用。此方法是在废液中加入Na_2SO_4等含有SO_4^{2-}的溶液，将废液中的Ag^+完全转化为相对应的Ag_2SO_4沉淀，然后进行过滤回收处理。各高校在无机实验中会产生大量的含银废液，可以在实验后对其进行集中的处理。

3.4 含铅、镉废液的处理

含铅废液和含镉废液也是化学实验室经常产生的毒性很强的无机废液，产生铅、镉废液的实验有碘化铅溶度积的测定、常见阳离子的分离与鉴定、P 区非金属元素(一)、P 区非金属元素(二)、离子的鉴定和未知物的鉴别、氢气的制备和铜相对原子量的测定等实验都产生铅、镉废液。实验室一般可以把废液中毒性强的铅离子和镉离子转化为无毒性的沉淀。首先把碱性物质加入到含铅、镉废液的废液中，然后调节废液的 pH 值为 8~10，加入共沉淀剂$FeSO_4$，使废液中的铅离子和镉离子生成相对应的沉淀物，最后把沉淀物进行焚烧处理[12]。

3.5 含汞废液的处理

离子的鉴定和未知物的鉴别这个实验产生汞废液。实验室处理废液的办法是调节废液的 pH 值至碱性，然后把大量的Na_2S加入到含汞废液中，从而使有毒的汞离子转化为无毒的沉淀。最后再加入大量的Na_2S和$FeSO_4$使其完全生成沉淀，静置 10 min 后，离心过滤的上层清液中汞离子浓度远低于排放标准后，可以安全的排放到外界，而所产生的沉淀则需要积累到一定数量后统一进行焚烧处理。

(下转第 262 页)

[收稿日期] 2019-01-28
[基金项目] 牡丹江师范学院教改项目(18-XJ20064)；黑龙江省教育厅科研备案项目(1352MSYB006)；牡丹江师范学院科研项目(JG2017001)
[作者简介] 邵艳秋(1969-)，女，吉林长春人，博士，主要研究方向为实验室建设与管理。

(C)1994-2019 China Academic Journal Electronic Publishing House. All rights reserved. http://www.cnki.net

毕竟物理化学这门比较抽象难懂，学生预习起来比较费劲，甚至有些学生提出根本看不懂，预习和不预习效果差别不是很大。时间长了，那些发前预习的几个同学也变得不爱预习了。这直接导致学生的课堂教学效果不是很理想。

对于化工 172 班由于采用了基于超星尔雅的学习管理及评价体系，平台上有视频有课件，根据教师的引导学生预习起来相对化工 171 班比较容易。同时，平台上师生之间可以互相交流讨论，针对不会的问题可以直接提出来，通过的教师的引导作答，使更多的学生参与到讨论中来，激发了学生的积极性，大大提高了预习的效果。虽然这个管理及评价体系不能完全的做到管理所有的学生，但是也少量够使 80 %的学生参与到其中，这跳了传统的教学方式，说明该体系对于学生学习起到了很大的督促作用。

课堂效果分析，两个班的教学效果差距很大，化工 171 班的学生课上回答问题的积极性不高，对于有些难的知识点不能够很好的掌握，甚至有一半的学生反映课堂上有些知识点听不懂，久而久之就越发的不愿意学习物理化学这门课程。课堂的上的气氛也越来越沉闷。对于化工 172 班，由于从刚开始学习物理化学这门课程的时候就开始应用超星尔雅的学习管理及评价体系，学生由开始被动的学习到变成习惯而变为主动的学习，课堂氛围良好，大部分同学能够针对教师课堂提出的问题作出回应，并且积极思考，能够融入的课堂当中。

课后反馈及评价，针对课堂学习情况，教师给学生留下课后思考题。化工 171 班的学生完成情况一般，个别同学下载就不做，有些学生直接抄学习好的同学。因此，学生的对课后思考题的反馈不能很好反应学生的学习情况，以此作为平时成绩的评价标准也不是很理想。对于化工 172 班，教师在平台上留下小测试习题，让学生在规定的时间内完成，系统自动评分，效果较好。同时还有课后讨论等这些都可以作为学生学习情况的评价标准。

教学效果分析，期中考试的时候，化工 171 班的平均成绩只有 58.5 分，有近一半不及格，甚至有个别学生出现了个位数，期中考试之后及时把超星尔雅的学习管理及评价体系应用到该班级，但是效果仍然没有化工 172 班好。还可能是前期养成的习惯很难纠正。而化工 172 班，期中考试只有 6 个不及格的，学习起步一目了然。因此，该系统的对于学生学习情况的管理起到非常重要的作用。同时，对于学生的学习的评价也更为公正客观。

4 总结

当今高速发展的信息化时代，网络的发展走进校园，基于超星尔雅的学习管理及评价体系不仅可以应用到物理化学这么课程，还能够应用到高校各个学科，在督促学生自主学习的同时，也对学生的学习的情况给予更公正的评价。

参考文献

[1]闫杰. 现代网络技术在继续教育中的应用[J]. 科教纵点，2015(2)：6-7.
[2]胡安辉. 现代网络技术教育特性探析[J]. 网络与信息工程，2004(3)：59-60.
[3]李承敬. 基于 CAS 协议的超星尔雅学习平台与高职教务系统融合研究[J]. 中国教育信息化，2016(9)：94-96.
[4]欧丽. 沈良忠. 在线课程的学生学习行为分析研究[J]. 电脑知识与技术，2018(14)：123-125.
[5]胡明. 任宇. 陈悦. 数字化校园中网络教学与资源共享管理平台的构建研究[J]. 中国医学教育技术，2019，33(01)：60-64.

(本文文献格式：王清龙，韩永纯. 现代网络技术在学生学习管理及评价体系中的应用——以物理化学为例[J]. 广东化工，2019，46 (5)：281-282)

(上接第 263 页)

3.6 含铜废液的处理

常见阳离子的分离与鉴定和由粗盐制备试剂级氯化钠这两个实验产生铜废液，处理时可以加入 Na_2SO_3 等含有 SO_3^{2-} 的溶液，把废液中的 Ba^{2+} 全部变成容易除去的 $BaSO_3$ 沉淀，然后进行过滤回收处理。

3.7 含铜废液的处理

常见阳离子的分离与鉴定和溶液的配制实验产生含铜废液，实验室在处理此类废液时可以加入 NaOH 等碱性溶液，然后调节溶液的 pH 值至碱性，把废液中 Cu^{2+} 转化为相对应的沉淀，然后对沉淀进行过滤回收处理。最后在滤液中要加入稀盐酸或者稀硫酸等酸类物质进行中和处理，直至溶液 pH 值调至 7 为止。

3.8 含铅废液的处理

常见非金属阴离子的分离与鉴定，氧化还原反应和氧化还原平衡，常见阳离子的分离与鉴定和离子的鉴定和未知物的鉴别等实验产生含锌废液，实验室在处理含锌的废液时可以通过加入 NaOH 等碱性溶液，使废液中的 Zn^{2+} 全部转化成 $Zn(OH)_2$ 沉淀，在滴加碱液时，要时刻注意控制碱液的滴量，因为碱液过多过少都会对沉淀转化率造成一定的影响，所以在加入 NaOH 时一定要不断地对 pH 试纸测试溶液的 pH 值。

3.9 含硫废液的处理

常见非金属阴离子的分离与鉴定实验产生含硫废液，实验室在处理此类废液时可以利用 H_2O_2 把含硫废液中的硫氧化为硫酸盐后，进行再利用，也可以把硫酸亚铁和石灰加入到含硫废液中，然后调节溶液 pH 值，控制其范围在 8~9，即可生成硫化铁沉淀，最后进行回收处理。

4 结语

本文结合高校所开设的实验所产生的废液找到适合的废液处理办法，具有可操作性，对实验室的安全健康发展以及环境的美好具有重要的意义。

参考文献

[1]吴欣. 高校实验废液的调查评价及清洁生产管理[J]. 四川环境，2005，24(5)：93-100.
[2]方海敏. 实验室二度排放研究总辨污染物直接排入下水道[N]. 南方都市报，2004-05-10.
[3]曾考华. 杨环二度综合治理，创建绿色化学实验室[J]. 实验技术与管理，2004，21(2)：139-142.
[4]陈斌. 高校化学实验室废液处理的必要性及方法研究[J]. 辽宁化工，2017，46(09)：917-919.
[5]吕春林. 赵慧芳. 王英. 高校化学实验室废液管理的必要性及处理方法[J]. 广东化工，2016，43(17)：138-139.
[6]曾吉方. 高中化学教学中绿色化学理念的渗透[J]. 中学生数理化(教与学)，2016(3).
[7]陈志斌. 唐亚文. 高等学校化学化工实验室安全教程[M]. 南京：南京大学出版社，2003.
[8]薛建英. 黄志斌. 高等学校实验室环境管理与安全[M]. 南京：南京大学出版社，2013.
[9]唐天国. 廖林川. 实验室安全与环境保护[M]. 成都：四川大学出版社，2014.
[10]兰贵闪. 余晓. 高校实验教学中产生的化学废物的回收及处理[J]. 大学化学，2016(06)：71-75.
[11]GB8978-1996. 污水综合排放标准[S].
[12]边艳明. 浅析实验室处理高校化学实验废液[J]. 科技创业月刊，2006(9)：78-79.

(本文文献格式：邵艳辉，崔树庆，徐雪，等. 高校化学实验室常见无机废液药处理方法[J]. 广东化工，2019，46(5)：282)

(C)1994-2019 China Academic Journal Electronic Publishing House. All rights reserved. http://www.cnki.net

5.邵艳秋,郑炜,云观,常玉莹.浅谈化学药品库的安全及管理[J].化工管理,2019(04):124-125.

安全生产

浅谈化学药品库的安全及管理

邵艳秋 郑炜 云观 常玉莹
(牡丹江师范学院化学化工学院,黑龙江 牡丹江 157011)

摘要:国家对高校实验室的安全越来越重视,尤其对集中存放化学试剂的药品库的安全要求越来越高。通过实践,牡丹江师范学院化学化工学院探索了一条较为合理的药品库管理办法,为兄弟院校药品库管理及安全提供了一些可操作的管理模式。

关键词:药品库;化学试剂;管理办法

1 化学实验室药品库管理的重要性

化学实验药品库管理与其它库房管理不同,很多种类繁多的大量的化学试剂及危险化学试剂较为长期的存放,一些易燃易爆的化学试剂如乙醚、丙酮极易自燃,在管理上存在着严重的安全隐患。近几年,有关实验室安全管理问题倍受关注,但仍有实验室安全事故发生。2018年11月11日,南京中医药大学翰林学院一实验室发生爆燃,造成多名师生受伤,给高校实验室管理又一次敲响警钟。如何增强高校实验室安全管理力度,建立一个科学有效的管理办法,是实验室工作的重中之重。具有化学专业的高等院校基本都有药品库,而加大对集中存放大量化学试剂药品库的管理力度至关重要。

2 药品库管理现存问题

2.1 管理制度不健全

在经过以评促改的教学评估过程,学校强化了实验室制度建设,根据要求建立了很多实验室管理制度,如实验室安全操作规程、实验室教师守则、实验室学生守则等管理制度先后上墙。8·12天津滨海新区危化品爆炸事故发生后,为了吸取教训,学校制定了危险化学品制度及应急预案。但这些制度有些没有列明详细的操作过程,有些则没有把安全制度落到实处,安全隐患很大。

2.2 长期积累的化学试剂较多

我校化学药品库已经有39年的历史,化学试剂品种更是多达1100多种。由于药品采购计划不够完善,随着实验内容的变化及毕业论文等科技活动内容的更新,造成了较多的化学试剂库存积压,长期不用。如:1-(2-吡啶偶氮)-2-萘酚,1-(2-吡啶偶氮)-2-萘酚,1,2-二溴乙烷,1,2-环己二胺四乙酸,DL-缬氨酸等几百种试剂长期不使用,都存放在药品库,给管理带来一定压力。

2.3 药品集中存放

药品库承担着整个学院实验运行的工作,涉及到各种性能的化学试剂的备用存放。受办学条件的限制,存放场所较少,很难做到试剂单独存放。除了剧毒药品,其他化学试剂基本都放在一个药品库,这样就对库管员及实验人员的人身健康带来威胁,一旦出现操作不当或者周围环境发生变化,就会造成火灾甚至爆炸[1]。

2.4 药品采购的统筹和计划

本校低值易耗采购工作基本上是每年一次,前几年由于重视程度不够,同时药品库的信息化管理比较落后,库房及时清点的不及时,对药品的数量和质量没有准确数据,统筹性和计划性做得不好,有些化学试剂库存较大。

3 药品库管理的改进措施及办法

3.1 健全制度,强化人员培训

为确保药品库的安全运行,严格的管理制度是必不可少的。为此,要制定化学品出入库制度、变质化学品处理及易致毒化学品等管理制度并上墙[2]。

库管员要有较强的专业知识,对化学试剂的性质及易发生的可能性危险有相当的了解,要具有应急解决问题的能力。库管员要定期进行培训,参加相关学术会议,不断积累经验,成为专业素质高、管理经验丰富的库管员。

3.2 化学试剂的采购和出入库管理

从耗材的采购到管理都要进行精细化管理,低值易耗采购前要对库存进行清点,将试剂的库存量下放给各课程组的实验准备人员,按照实验课所需要的药品上浮30%进行预算,确保学生上课因实验失败或者浪费带来的更多消耗使药品不足。药品入库管理双人负责,并进行详细记录和统计,入库单详细记录耗材的名称、数量、规格、生产商及质量验收情况[3]。

我们根据实际工作需要制定了四类药品出库单:毕业论文药品出库单,包括药品名称、规格、单价、出库量、使用量等,然后由学生填写姓名、学号及班级,毕业论文指导教师签字;教师及实验技术人员建立个人取药记录卡,每次领取药品除了填写基本试剂信息外,还要填上使用房间号及使用人,然后在个人的使用记录卡上进行登记;易制毒化学试剂列出一类、二类、三类出库单。实验课出库的药品一般严格按照学生人数算好使用量,如果实验课有少量剩余,就自存待用;毕业论文出库药品回收后进行特别标注,经过验纯后再入库。

管理员编制了方便管理的化学试剂电子文档,科学化的信息化数据管理便于清晰快速的了解实验室耗材的购买、使用和库存情况,能够及时更新耗材的消耗、出库、入库变化情况,避免重复购买导致的库存积压,做到了账物相符,账目始终在动态管理中。

(C)1994-2020 China Academic Journal Electronic Publishing House. All rights reserved. http://www.cnki.net

3.3 分类存放的管理措施

化学试剂状态和性能差异也很大，有的常温十分稳定，有的却非常活泼，有的受高温也不变质，有的极易变质。只有对化学试剂的性能深入了解，按照试剂特点来集中分类存放，才能做到安全地保管好试剂。这就要求库管人员熟知化学试剂的习性，并且掌握发生危险的紧急处理方法。我们根据化学试剂的形态、挥发性、毒性、危险性等分类，并按照一定顺序存放。无机类（细分为钾盐、钠盐、钙盐、镁盐等）；有机类（细分为醇类、酯类、酚类、糖类、指示剂等）；酸类（细分为盐酸、硫酸、硝酸、磷酸、乙酸等）；易制毒化学品单独集中存放。药品存放一定要做到以下几步：

（1）库房清洁干净，将所有试剂瓶都擦拭的干干净净。

（2）一些有毒的化学试剂如升汞或其他汞盐等剧毒药品，锁在剧毒保险柜里存放，双人双锁专人管理，并置于外库中。

（3）易燃、易爆的化学试剂单独存放在一个房间和区域，与人们经常活动的区域间隔一段距离。

（4）将一些能够实现有利的相互作用的化学试剂临近存放，如易燃的试剂旁边放一些阻燃剂，一旦有事故，能起到良好的控制效果；一些有不利相互作用的试剂的存放，如易发生氧化性爆炸的试剂，存放时要留出安全距离甚至隔离保存[4]。

3.4 化学药品库的场所管理

化学试剂药品库配有安全门和防盗窗等防盗措施，一旦药品流出就会给社会带来潜在的危害，特别是剧毒、易爆、易燃的药品，一定做到万无一失；药品库要有良好的的通风装置，防止有毒和易燃气体的长期积累达到一定的密度；为防止静电产生火灾的发生，药品库一定要安装防爆开关和防爆灯；药品库的灭火器等消防器材要及时更换，在数量和质量上达标。

4 结语

综上所述，本文针对普通高等学校中药品库管理过程中的问题进行了分析，并且结合工作实际要求，从采购到储存安全角度出发，提出有针对性的管理措施，为提升化学试剂的安全管理水平给出较为实用性的合理建议。

参考文献：

[1] 祁垒文. 化学室化学试剂及化学仪器的管理研究[J]. 智能化工,2018,(14):147-148.

[2] 高芳, 方红明, 罗志文, 等. 高校化学实验室安全管理与教育探索[J]. 广州化工,2018,46(20):111-113.

[3] 胡晓娜, 苗露蕊, 范淑君. 高校化学实验室规范化管理探究[J]. 化工管理,2018,(26):203-204.

[4] 郭红玉. 高校化学药品库的安全和网络化管理[J]. 化工时刊,2014,28(2):40-44.

项目基金：牡丹江师范学院教改项目(18-XJ20064)；黑龙江省教育厅科研备案项目(1352MSYB006)；牡丹江师范学院科研项目(JG2017001)。

危化品公路自提业务安全管理探析

王建军（中国石化化工销售有限公司华中分公司，湖北 武汉洪山区 430070）

摘要：文章通过对危化品公路运输业务管理实践的研究，探讨危化品销售企业在公路自提业务中的管理手段和方法，以期预防危化品公路运输中重大事故的发生。

关键词：危化品运输；自提；安全

0 引言

近年来，危化品运输安全重大、较大事故频发，造成大量人员伤亡和财产损失，具体情况见表1。

表1 危化品运输事故统计

序号	事故名称	受伤人数	死亡人数	直接经济损失
1	沪昆高速“7·19”特别重大道路交通危化品爆燃事故	6人	54人	5300万
2	晋济高速公路山西晋城段岩后隧道“3·1”特别重大道路交通危化品燃爆事故	12人	40人	8197万
3	金誉石化“6·5”罐车泄漏重大爆炸着火事故	9人	10人	4468万
4	滨州高新区“8.7”较大危化品违法运输事故	11人	5人	1100万

上述事故暴露出危化品公路运输单位存在如下5类主要问题：

（1）超范围违规经营。“以包代管”、“包而不管”问题严重，违规对融资经营危化品运输车辆只挂靠不管理，违规给不具备安全运输条件的危化品罐车充装货物。

（2）日常管理混乱。安全检查和隐患排查治理不彻底、不深入，安全教育培训流于形式，从业人员安全意识差、操作技能差，车辆司机和押运员对公司运输资质范围不清、对所运货物的性质不了解、习惯性违章操作。

（3）车辆设备管理混乱。购买不具备资格厂商的车辆及车辆设备，非法从事车辆改装和罐体加装，车辆行车记录长时期处于故障状态，罐体底部卸料管根部球阀长期处于开启状态，半挂车的罐体未安装紧急切断阀。

（4）疲劳驾驶失管失察。对道路运输车辆未进行动态监控，对所属驾驶员的疲劳驾驶行为未能及时发现和纠正。

（5）事故应急管理不到位。未按规定制定有针对性的应急处置预案，未定期组织从业人员开展应急救援演练，对驾驶员应急处置教育培训不到位，致使所属驾驶员出现险情时未采取正确的应急处置措施，直接导致事故发生或造成本人死亡。

1 监督管理措施

为坚决杜绝危化品运输重特大事故的发生，全面加强危化品安全管理工作，促进安全生产形势持续稳定好转，国务

(C)1994-2020 China Academic Journal Electronic Publishing House. All rights reserved. http://www.cnki.net

6.邵艳秋,刘素娟,任玉兰,付大同.分析化学教学现状与 PBL 教学法的应用[J].牡丹江师范学院学报(自然科学版),2015(04):74-76.

分析化学教学现状与 PBL 教学法的应用

邵艳秋[a],刘素娟[a],任玉兰[a],付大同[b]
(牡丹江师范学院 a.化学化工学院; b.教师教育学院, 黑龙江 牡丹江 157011)

摘 要:PBL 在普通化学专业分析化学教学中应用的优势是:有利于学生能力的培养和知识的灵活运用,有利于强化学生学习的内部动机,其理念代表着现代应用性专业教学发展的方向.教学中要特别注意 PBL 教学法的特点和适用条件,加强其与传统教学的结合,发挥各自的优势,弥补各自的不足,最终实现 PBL 教学法的真正作用.

关键词:PBL;教学法;分析化学

[中图分类号]G642.41 [文献标志码]A [文章编号]1003-6180(2015)04-0074-03

DOI:10.13815/j.cnki.jmtc(ns).2015.04.033

1 PBL 教学法与应用性专业教育

1969 年,美国神经病学教授 Barrows 首次提出 PBL(Problem-based learning)教学法,即基于问题教学法[1-3].与传统教学方法不同,PBL 强调以实际真实性问题为基础,以学生为中心,通过学生的主动探索和自主解决问题的活动来构建知识和发展能力.PBL 适合所有有着复杂未来职业情境的专业教育(比如医学专业教育).PBL 提出以后,首先应用于医学教育领域,其次应用于工科专业教学以及各种职业教育.国内普通化学专业分析化学课程对于 PBL 教学法也有诸多的尝试,从研究资料上看,多数是反映 PBL 教学法的成功经验和积极效果,而对于基于问题教学法的适用性和局限性讨论的不多.本文对分析化学课实施 PBL 教学改革的总体情况进行归纳和梳理,从利弊得失两个方面进行分析.

2 国内分析化学教学发展现状

分析化学作为一门表征和测量的科学,既是一门综合性科学,具有较强的系统性,同时也是指向各种职业情境的具有极强针对性、应用性的技术手段.[4-5]分析化学在教学上历来存在两种价值取向,一是强调对基础知识、基本理论的掌握;二是强调实际应用能力的培养.如何加强上述两方面的教学并协调二者之间的关系,就成为当前普通化学专业分析化学教学改革一个无法回避的问题.

每一种教学模式其教学目标都有着自己的定位.传统教学模式注重基础知识的掌握,强调教师主导下的班级集体教学,以保证知识传授的高效率;而建构主义等现代学习理论却认为,学生在传统教学模式下的学习完全是机械的、孤立的,所接受的知识也是难以应用的、无意义的,无助于培养学生的批判性思维、创新思维和解决问题的能力.建构主义强调通过大量实例教学,结合具体情境,让学生面对真实问题,积极探索,建构知识和发展能力.教师在教学过程中,不仅是传授知识和技能,更重要的是运用有效的教学策略引导学生去发现问题、解决问题.教师由学生学习的传授者和输出者,变为学生学习的指导者和促进者.两种教学观各执一面,而且当二者各自发展又相互博弈达到一定水平后,教学改革的空间已经变得极为狭小,成为教学质量提高的瓶颈,再也难以有所提高.再加上价值观念的对立,教学方式与内容的冲突,时间空间上难以协调,即便是常规教学也受到干扰.

当前国内普通化学专业分析化学教学上普遍存在如下几方面的问题:(1)内容膨胀,课时太少.随着实际领域中应用性需求的增长,很多测量分析的课题和手段不断反映到分析化学的教学当中.总体上,分析化学向有机化学拓展的趋势明显,手段上越来越重视仪器分析.内容增加了很多,相对课时并没有相应增加,现有课时无法满足教学需要,知识教学的任务繁重;(2)教学目标不清晰.来自应用领域的呼声是强调培养学生的能力,而学校教学在传统教学的重压之下也是心有余而力不足;(3)学生主体活动缺乏.活动是达到目标的途径.活动缺乏意味着有意义学习没有发生.迫于繁重的知识教学任务,分析化学常见的一种教学策略就是"灌输式",教师讲了又讲,学生基本处于一种被动接受的状态.没有独立的思考,没有动手尝试的机会,学生对知识的理解只能流于表面;(4)考核方法单一陈旧.分析化学教学过程中的考核太少,且主要是书面笔答方式,考查知识

收稿日期:2015-10-21
基金项目:黑龙江省教育厅科学技术研究项目(11551510);牡丹江师范学院校级教改立项重点项目(12-XJ14027);牡丹江师范学院案例教学改革专项项目(2013ALZX003)

(C)1994-2020 China Academic Journal Electronic Publishing House. All rights reserved. http://www.cnki.net

的简单呈现,对学生的能力培养缺乏积极的引导作用;(5)学生学习缺乏热情,学生不能理解当前的学习其实际意义是什么,学习没有动力.

3 PBL 在普通化学专业分析化学教学中的应用

面对传统教学存在的一些问题,也进行了一系列的改革尝试,其中之一是采用 PBL 教学法.由于人们思想上对 PBL 存在着不同的理解,在具体实施上存在较大的差异,实际效果上就有很大的不同.教学改革的核心问题是如何处理好传统教学模式与现代教学模式之间的关系.要想在传统教学的大背景下,成功实施 PBL 教学法,主要应采取以下具体措施:

3.1 问题核心

围绕各种实际问题安排教学,伴随问题的解决来掌握有关内容.问题的选择与设计至关重要,既要针对实际情境具有典型性、代表性,还要尽量涵盖所有重要的基本概念与原理,也就是既要有利于能力的培养,也要尽可能系统地掌握知识.一般可供选择的问题大致有五类:日常生活问题、学术探索问题、职业情境问题、社会环境问题以及信息技术问题.问题的设计要考虑到学生的兴趣和知识基础,也要具有一定的真实性和整体性,如"你知道煤碳的种类吗?它们是如何定价的?请你选择某一煤场的煤碳并测定该种煤碳燃烧热是多少大卡?""你了解国内某些江河重金属的污染情况吗?请你测定一下牡丹江流域江水重金属含量.""尿液成份的变化与人的身体状况有什么关系?尿液中有哪些有机成份可以检测?如何检测?"问题应具有一定的真实性和整体性,操作起来要有一定的难度,以问题为核心,一些关键问题会被反复提及,促进理解不断加深.如上述三个问题中都包含了"如何取样"的问题,而且各不相同.

3.2 作业前置

提前布置有关问题或作业.问题教学的一个重要条件就是学生必须要有充分的准备,所以作业前置能够较好地引导学习完成课下时间的自主学习,保持学生的注意力,提高课堂教学效率.作业前置所涉及到的问题可以是同一个问题的深入,也可以是与已有问题相关的新问题.

3.3 小组合作

PBL 教学法要求涉及的问题是真实的、整体的、具有相当的难度和复杂性,学生单独难以完成.需要小组成员共同完成课题,按能力特长分别承担不同的任务,发挥各自的优势,相互学习和借鉴.小组成员之间会产生特有的社会促进作用,对强化学习动机有着重要的积极影响.

3.4 反转课堂

反转课堂就是要把时间交还给学生,把主导权交给学生,让真正的学习发生在课堂以外更广阔的时间空间内,教师只是提供评价、检查,或者去帮助那些学习有困难的学生.反转课堂实现了个别化教学,实现了教学目标弹性化,增强了学生学习的自主性和责任感.PBL 课堂一定是反转课堂.

3.5 过程考核

以问题为核心的教学是一个各种活动极为丰富的过程,学生的学习融合在各种活动当中,所以对学生的考核要渗透到分析问题和解决问题的全过程.过程考核就是考核学生的各种学习活动,特别是考核活动的程度、表现、特点、情感、态度和能力.过程考核之"过程"既是指条件也是指对象,但主要是指对象.

4 经验启示——PBL 教学法的优势与适用性

从一些教改研究文献来看,人们对 PBL 教学法褒贬不一.大多数研究对 PBL 教学法的优点、作用都给予了高度的肯定,但分析化学课真正实施 PBL 教学法的案例却在不断减少.一些教师或教学单位能够表示理解并接受 PBL,但在实际教学中却并不使用.究其原因,是某些人认为 PBL 与传统教学模式全面冲突,难以实施;二是弊端突出,后果不良.

有人认为,PBL 教学法的缺点突出,其适用性有限.一是不利于基础知识学习,以问题为核心的学习导致学习内容零散、不系统,特别是对于那些基础原本就较差的学生来说,实施基于问题的学习,无异于饮鸩止渴;二是占用时间多,PBL 效率差,很难在特定的时间内完成预定的教学任务;三是要求高,PBL 对环境和硬件条件以及教师和学生的能力都有一定的要求.如要求学生要具有高度的自觉性和较强的独立自主能力,四是投入大,教师、学生的精力投入、仪器设备、资金投入都极为惊人;五是难实施.由于 PBL 教学法与传统教学体制多方面存在冲突,所以推行 PBL 教学法常常需要其他多种教学改革的配合与支持.

但也有人认为,PBL 的优势也是极为鲜明的.一是有利于能力的培养,有利于所学知识的灵活运用;二是有利于强化学生学习的内部动机,三是理念先进,代表着现代应用性专业教学发展的方向.

其实,当下重要的不是强调上述观点的冲突和对立,而是要深入研究 PBL 教学模式与传统教学模式如何有机结合.PBL 教学法与传统传授式教学也并不是完全不可调和的,二者对教学的要

(C)1994-2020 China Academic Journal Electronic Publishing House. All rights reserved. http://www.cnki.net

7.任玉兰,邵艳秋,罗玉杰.讨论式教学法在仪器分析教学中的应用[J].教育与职业,2014(21):151-152.

讨论式教学法在仪器分析教学中的应用

任玉兰　邵艳秋　罗玉杰

[摘要]文章介绍了讨论式教学法在仪器分析教学中的应用,探讨了讨论式教学法的教学策略,分析了讨论式教学法在培养学生的学习主动性和提高综合素质与能力方面的作用。

[关键词]讨论式教学　仪器分析　教学改革

[作者简介]任玉兰(1971-),女,山东平度人,牡丹江师范学院化学化工学院,副教授,研究方向为分析化学;邵艳秋(1969-),女,黑龙江穆棱人,牡丹江师范学院化学化工学院,教授,研究方向为分析化学;罗玉杰(1954-),女,山东莱州人,牡丹江师范学院化学化工学院,副教授,研究方向为分析化学。(黑龙江　牡丹江　157011)

[课题项目]本文系2011年牡丹江师范学院教育教学改革工程项目"《仪器分析(含实验)》课程体系改革与实践研究"的研究成果。(项目编号:11-XJ12066)

[中图分类号]G642　[文献标识码]A　[文章编号]1004-3985(2014)21-0151-02

DOI:10.13615/j.cnki.1004-3985.2014.21.066

仪器分析是高校化学类专业本科生的一门重要专业基础课,教学内容涉及化学、物理学、仪表电子学、数学和计算机科学等学科的知识,知识面广,综合性强,在培养大学生综合素质、创新意识及实践能力方面起着非常重要的作用。为进一步提高课堂的教学质量,激发学生的学习潜能,强化学生的科学素养,本教学团队尝试了将讨论式教学法应用于仪器分析的教学当中,颇有成效。

一、课程现状与讨论式教学法的提出

仪器分析是通过测量物质某些物理或物理化学性质、参数及其变化来确定物质的组成、含量及化学结构的分析方法的集合。分析方法种类多,涉及面广,难度大,不同类别的分析方法之间联系不多。如光学分析法是依据电磁辐射与物质之间的相互作用而建立起来的一类方法,而电化学分析法则是通过测量电参量及其变化来进行分析的一类方法。这两类方法所用的仪器各不相同,工作原理也不相通,使得学生在学习的过程中感到难度大、内容抽象、难于理解和掌握,对课程容易产生畏难情绪,学习缺乏主动性,考试时只会死记硬背,知其然而不知其所以然。

讨论式教学法是发挥学生的主体作用和教师的主导作用,发扬课堂教学中民主作风的一种课堂教学方法;是在教师的引导下,为实现一定的教学目标,通过预先的设计与组织,启发学生就特定问题发表自己的见解,以培养学生独立思考问题的能力和求学创新的精神;是学生以小组或全班为单位,通过讨论或辩论发现问题、获得知识、培养能力的一种课堂形式。这种教学模式有利于提高学生的学习主动性、积极性,培养学生的创新意识和创新能力。目前,讨论式教学法在大学课堂教学中已得到了广泛应用,国外一些著名大学也将其作为仅次于课堂讲授的第二教学手段。

二、讨论式教学法在仪器分析教学中的应用

针对仪器分析课程"杂、散、难"的特点,如何找出各知识点的关联,主干和分支的接界点,使课程学起来杂而不散、难而不繁是问题的关键之一。为此,笔者将"讨论式"教学法引入仪器分析教学中,并针对该方法的运用谈几点自己的体会。

1.精研教材,创设问题,想方设法提高学生的综合素质。将讨论式教学法应用于教学中,并取得良好教学效果的一个关键问题就是:如何合理地设计出要讨论的问题,以激发学生学习的潜能,提升学生的综合素质。问题设计得恰当与否,主要取决于教师对教材的理解程度,直接影响学生对教学内容理解的深度与广度。在设计讨论问题时,教师要把握以下几点:一是要充分研究教材,依据教学目的与要求,针对教学的重点与难点提出问

用教具教学,这样可以让学生直观地学习英语。如在讲复活节时,也可以带彩蛋、小兔子的玩具等与学生讲述一些习俗及传说。课堂教学可以采用多种形式的训练方法,如演讲辩论、英语游戏、讨论口译、情景对话、图片联想、续编故事等。通过各种学习形式,实现图文共享、声情并茂、视听融会,引导学生全身心地投入课堂学习。

英语口语教学,要立足实际,转变观念,开拓创新,通过TPR教学模式在口语教学的运用,有望充分有效地利用有限的课堂时间,加强师生互动,激发学生学习英语的兴趣,为学生搭建一个学习知识、提高能力、参与交际的平台。同时,锻炼他们的语言能力、思辨能力、创造能力及交际能力,以培养出适应社会需求的"学得好、用得上"的外语应用型人才。

[参考文献]

[1]杜利红.论英语口语教学中合作学习的组织策略[J].鸡西大学学报,2011(8).

[2]高丹丹.合作学习与大学英语口语教学[J].安徽文学(下半月),2010(7).

[3]张迅.创造模拟语境,合作提高口语——ESL英语口语教学的组织策略[J].考试周刊,2009(2).

[4]Asher J.Learning Another Language Through Actions(5th edn)[M].LosGatos,CA:Sky Oaks Productions,1996.

(C)1994-2021 China Academic Journal Electronic Publishing House. All rights reserved.　http://www.cnki.net

题，二是设计的问题要有衔接性，应深入浅出、环环相扣。三是要注意主干问题与分支问题在教学过程中的合理设计；四是要有总结性问题和引申性问题，以便于学生通过对教学内容的总结而使所学知识得到进一步升华与凝练。

例如，在仪器分析课程电解及库仑分析法这一章的学习中，笔者精心设计了八个问题（如图所示）。这八个问题包含了整个这一章的重点和难点。通过对这八个问题的讨论，学生总结出了这两种方法之间从定义的角度引申出的三点区别与四点联系。最后一个问题属于这一章的知识拓展问题。由于这门课程具有分析方法种类多、关联少的特点，因此尽量挖掘各方法之间的关联，也有助于学生对这门知识的理解与升华，使得学生本来觉得这门课程知识点散乱，但通过适当地比较发现它原来也是有一定规律性的。

电解及库仑分析法的教学设计图

2.启发思路，得出结论，循循善诱激发学生的自身潜能。要讨论的问题精心设计好了，下一步就是课堂教学，教师的引领作用是圆满完成教学任务的一个关键。以电解及库仑分析法这一章的教学为例，在第一个问题讨论结束后，涉及第二个问题的引入。教师可以利用第一个问题讨论的结果之一，即电解分析法与库仑分析法都用到了电解池，涉及待测组分的电解，那么什么情况下待测组分开始电解呢？这时适时提出一个名词，即分解电压。只有外加电压达到了分解电压时才开始电解，从而引入了第二个问题。问题二得出的是理论分解电压，而实际的分解电压又是什么情况呢，它们之间是通过过电位联系在一起的。这样环环相扣、循循善诱，推出了第三个问题。在教师精心的教学设计下，学生被一步步引领入科学的殿堂。依此类推，学生经过了充分的课前准备、热烈的课堂讨论，可以增进对知识点的深入理解。在课堂教学过程中，教师要注意两个问题，一是如何调动学生学习的积极性，激发学生的潜能；二是如何控制讨论的深度和广度，引发学生的求知欲。

3.精辟点评，及时总结，充分调动学生学习的积极性。讨论是否适时、适当、适量，能否达到预期的效果，也充分体现了一名教师的课堂管理艺术。要想上好一节成功的讨论课，那么在整个教学环节中，教师要遵循"四要"原则。一是在教学设计中，教师要充分考虑如何培养学生的创新意识，提高学生分析问题和解决问题的能力，激发学生学习的主动性和积极性。二是在讨论的过程中，教师要适当参与，与学生积极互动，共同讨论，努力营造主动探索、生动活泼的课堂氛围，并用恰当的语言进行精辟的点拨。三是教师要善于发现和保护学生的创新意识，使每个学生都能发挥自身潜能。对于想法新颖而又有理有据的学生，要充分给予肯定和鼓励，让创新意识的萌芽生根、成长，引导学生去"质疑、探究、合作"，以培养学生的创新能力与团队精神。四是在讨论结束时，教师要及时进行讨论内容的小结。对于回答错误的学生，教师应以鼓励为主，积极引导，对于回答正确的学生，教师应及时给予表扬，以增强学生的自信心。

三、教学中应注意的两个问题

1.以学生为本，重视学生主体性的发挥。讨论式教学法改革的目标是探索一种具体可行的方法与途径，打破以往教师讲、学生记的讲授式和满堂灌的教学模式，将教育教学转变为以学生发展为中心，注重学生科学素养各个方面的全面发展，使学生变被动学习为主动发展，从而促进学生创新意识、创新能力和实践能力的培养。因此，在讨论式教学中，教师要重视学生的主体地位，努力激发学生的创造性，使教学真正成为师生富有个性化的创造过程。以学生为主体，教师成为学生的组织者、引导者、合作者，师生之间应是平等的对话关系。从而学生不再是一个接受知识的容器，而是一个学习的主体。课堂不再是"一言堂"，而成为多声部的"合唱团"，教师不再是"独奏者"，而成为"伴奏者"，教师与学生一起演奏出一曲和谐美妙的乐章。

2.教师的引领作用是确保讨论的方向、进程与效果的关键。上一堂精彩的讨论课，与教师的努力是密不可分的，而教师的引领作用是实现良好教学效果的关键之一。课前，教师要精研教材，积极整合课程资源，确立讨论题目。课堂中，教师要积极引领，深入浅出，循循善诱，使学生真正地融入这次讨论中，师生都作为平等的个体参与知识和问题的探索。另外，学生主动参与、自主探究和自由创造，提高了学生的语言表达能力和交际能力。课后，教师要及时总结经验，查找不足。总之，教师恰到好处的引领能让学生受到启发，深刻领会到各知识点之间的联系，并能激发学生主动学习的意识。

通过讨论式教学法的引入，培养了学生独立思考的能力、运用知识解决问题的能力、独立获取知识的自主学习能力及语言表达能力。设计问题，集体讨论，活跃的课堂氛围，有助于减轻学生学习的压力，激发学生的求知欲，使学生注意力集中，思维活跃，有利于学生主动学习知识，对所学知识印象深刻、不易遗忘，极大地提高了学生的学习效率。

[参考文献]

[1]邓志芳，李春喜，刘晓东.仪器分析》课程教学改革的探索[J].实验科学与技术，2007(4).

[2]梁中贤.高校讨论式教学之管见[J].中国高等教育，2011(23).

[3]周润德，苏辉，石志广.讨论式教学方法在大学课堂中的运用研究[J].高等教育研究学报，2008(4).

(C)1994-2021 China Academic Journal Electronic Publishing House. All rights reserved. http://www.cnki.net

8.刘素娟,廉波,邵艳秋,任玉兰,罗玉杰.高师院校分析化学实验教学改革与实践[J].牡丹江师范学院学报(自然科学版),2012(01):62-63.

DOI:10.13815/j.cnki.jmtc(ns).2012.01.025

3 结论

通过 Packet Tracer5. 3 软件建立通信网基础课程模拟实验环境,开展通信网基础课程的实验教学,以 VOIP 网络和 DSL 接入网实验为例分析仿真实验过程,一方面解决了因缺乏实验设备无法开展通信网基础课程实验教学的问题,另一方面通过对各种类型的通信网络的仿真实验过程,加深学生对通信网基础课程中的概念、协议和网络原理的掌握和理解,培养和提高学生组建、使用和管理通信网的技能,达到通过实验教学促进理论教学的目的.

参考文献

[1]孙强,徐晨,黄勋."现代通信网"课程实验教学研究[J]. 电气电子教学学报,2009,31(6): 68-70.
[2]万晓林. 利用 PACKET TRACER 5.0 组建 CISCO 网络实训平台[J]. 电脑知识与技术,2009,5(21): 5914-5915.
[3]宋梦华. 基于 Packet Tracer 的虚拟通信仿真研究[J]. 天津职业院校联合学报,2010,12(2): 53-57.
[4]唐宝民,江凌云. 通信网技术基础[M]. 北京:人民邮电出版社,2009: 37-167,276-309.
[5]谢华. 通信网基础[M]. 北京:电子工业出版社,2007: 11-126,210-234.
[6]单家凌. VOIP 技术的实验设计与研究[J]. 实验室科学,2011,14(2):137-139.
[7]Cisco Packet Tracer 5. 3[EB/OL]. (2010-11-13)[2011-03-26] http://www. linuxidc. com/Linux/2010-11/29785. htm.

编辑:文心

高师院校分析化学实验教学改革与实践

刘素娟,廉 波,邵艳秋,任玉兰,罗玉杰
(牡丹江师范学院 化学化工学院,黑龙江 牡丹江 157011)

摘 要:介绍素质培养型实验教学体系的教学内容、教学方法、开放实验室、成绩评定等. 探讨在分析化学实验中培养具有科学思维方法和以动手能力较强的高素质人才.

关键词:分析化学;实验;人才培养

[中图分类号]G642 [文献标志码]A [文章编号]1003-6180(2012)01-0062-02

分析化学是化学的一个重要分支,广泛应用于地质普查、矿产勘探、冶金、化学工业、能源、农业、医药、临床化验、环境保护、商品检验、考古分析、法医刑侦鉴定等领域. 分析化学实验是分析化学的重要组成部分,在工农业生产、科学研究及国民经济各部门中起着重要的作用.[1-2]学生通过分析化学实验的学习,可加深对分析化学基础理论、基本知识的理解,正确和熟练地掌握化学实验的基本操作技能,提高观察、分析和解决实际问题的能力,培养学生严谨的工作作风和实事求是的科学态度,形成严格的"量"的概念,为学习后继课程和将来从事化学教学和科研等工作打下坚实的基础.[3-4]综合院校在录取研究生时常常认为,师范生理论成绩非常好,然而实验动手能力与解决实际问题的能力相对较差. 这种现象在一部分师范生中确实存在,有的学生研究生入学考试初试成绩名列前茅,但是在复试时因为实验操作而被一票否决. 所以,师范院校的化学分析实验要进行改革,以提高学生分析问题、解决问题的能力,提高学生分析归纳能力、创新精神和独立工作能力,为将来从事化学教学和科研工作打好基础. 为此,牡丹江师范学院化学化工学院分析化学课题组以"加强基础、开拓思维、提高素质、培养能力、注重创新"为指导思想,对实验内容、实验教学方式、实验条件和考核体制进行了改革,构建了全新的素质培养型实验教学体系,取得了良好的教学效果,达到了预期目的.

1 教学内容贴近生活,以提高学生的学习兴趣

兴趣是最好的老师,大多数学生对哪门课程感兴趣,哪门课程就能学好,就会主动学习和钻研. 分析课题组教师们认为,调整教学内容,使之更加贴近生活,学生会觉得分析化学实验离日常

收稿日期:2011-08-15
资助项目:牡丹江师范学院教改项目(11-XJ12067);牡丹江师范学院青年一般项目(QY201005)

(C)1994-2021 China Academic Journal Electronic Publishing House. All rights reserved. http://www.cnki.net

生活并不遥远，且学有所用。例如，食用白醋中 HAc 浓度的测定、蛋壳中碳酸钙含量的测定、自来水总硬度的测定、水果中抗坏血酸(Vc)含量的测定、阿司匹林的测定、安乃近含量测定等实验，学生就很感兴趣。

2 运用多种教学方法

活跃是课堂之魂，课堂时间是十分宝贵的，教师应在有限的时间内把学生的注意力集中起来，使课堂气氛活跃起来，最大限度地提高课堂效率，讨论式教学法就是一种行之有效的教学方法，首次使用新仪器时，教师边讲解边提问，通过演示规范正确的操作方法，告诉学生仪器的使用方法，紧紧吸引住学生的注意力，在后续的课堂教学中，教师抽时间让学生演示，让其他学生评价，这种教学方式可以极大地活跃课堂气氛，通过讨论，学生们相互补充，取长补短，活跃了课堂气氛，提高了教学效果及课堂效率，激发了学生学习的积极性和主动性，形成了浓厚的学习氛围，讨论式教学法使分析实验课堂活了，学生成为学习的主人，学生的表达能力得到了提高，可谓一举数得。

3 开放实验室

开放式实验可实现实验时间、实验内容和实验设备上的全方位开放，提高资源使用效率，开放式实验教学分为几个层次，第一层次——课堂理论教学的延伸和拓展，主要是为了夯实基础，学生通过查阅资料，对实验疑问用不同实验方法进行验证，实验过程中，指导教师不离开实验室，指导学生实验，解答学生问题，第二层次——鼓励一部分学生对实验进行改进或改造(如把某个实验改成微量型实验)，第三层次——对科研兴趣浓厚的学生，鼓励他们联系相关教师，参与教师的科学研究，由于这些实验内容反映了当代科学技术的发展水平，涉及的知识面广，学生可以初步品尝搞科研的酸甜苦辣，为他们以后的深造奠定基础。

通过大学生科技创新竞赛活动，提高学生做实验的兴趣与积极性，化学化工学院每年要举行分析化学实验技能大赛，通过这项活动，在一定程度上改变了学生重理论轻实验的态度，极大地调动了学生做实验的兴趣，也为参加省市和全国的化学实验技能大赛选拔了选手，使不同层次学生的实验动手能力、解决实际问题能力和创新能力进一步提高。

开放式实验教学涉及的知识面广，对教师的要求高，教师不仅要有本学科扎实的理论基础和实验技能，还要不断更新知识，这样才能胜任实验教学，可以说开放式教学提高了师资队伍业务水平。

4 改变考核机制，以考促学

分析化学实验成绩评定经过改革后，由以下部分组成：平时成绩、实验报告、操作考试、笔试，平时成绩包括实验预习、课堂提问、打扫卫生等，培养高素质人才要从点滴做起，从小事做起，打扫卫生虽然是一件小事，但也可以从一个侧面看出学生的素质，所以，要求学生做完实验后要达到“五光”——实验仪器光、实验台面光、水池光、实验室地面光、垃圾桶光，教师要求学生当堂写出实验报告，以最真实地反映实验情况，杜绝伪造实验数据的情况，操作考试，教师给出实验题目，学生自己查资料，写出实验方案，进行实验，教师根据整个实验过程打分，运用所学分析化学实验知识解决实际生活中问题并撰写小论文的学生，可以加附加分 10 分，通过改革，加强了考试指挥棒的作用，调动了学生做实验的积极性。

分析化学实验教学改革实践表明，学生的实验基本功更扎实了，求知欲望和对未知事物的探索精神得到较大的发展与提高，综合运用所学知识解决实际问题的能力增强，新的实验教学体系达到了知识与技能的传授以及能力与素质的培养相互促进的作用。

参考文献

[1] 崔凤灵，靳建华. 高师分析化学实验教学改革尝试[J]. 大学化学，2008(1)：25-28.
[2] 程生芳，王清江，宗俊，等. 以人为本实施分析化学实验教学改革[J]. 大学化学，2007(16)：20-23.
[3] 刘磊，李海军，王仕元. 高等院校实验教学改革与探索[J]. 牡丹江师范学院学报，自然科学版，2010(3)：68-70.
[4] 邓建军，孙少锐. 化工安全技术教学改革与实践[J]. 牡丹江师范学院学报，自然科学版，2011(12)：68-69.

编辑：琳莉

(C)1994-2021 China Academic Journal Electronic Publishing House. All rights reserved. http://www.cnki.net

9.邵艳秋,罗玉杰,任玉兰,刘素娟.分析化学教学改革谈[J].牡丹江师范学院学报(自然科学版),2011(02):67-68.

DOI:10.13815/j.cnki.jmtc(ns).2011.02.025
2011 年第 2 期 牡丹江师范学院学报(自然科学版) No.2,2011
(总第 75 期) Journal of Mudanjiang Normal University Total No.75

分析化学教学改革谈

邵艳秋,罗玉杰,任玉兰,刘素娟
(牡丹江师范学院 化学化工学院,黑龙江 牡丹江 157011)

摘 要:对分析化学课程的教材、教学内容、教学模式及评价方法四方面进行了改革,达到了提高学生学习的主动性、强化学生综合运用知识、培养学生创新能力的目的.

关键词:分析化学;教学改革

[中图分类号]G642.421 [文献标志码]A [文章编号]1003-6180(2011)02-0067-02

随着社会实际的需要和分析方法、技术、仪器的不断更新,需要及时进行分析化学教学改革,以适应当前高等教育的改革与发展.牡丹江师范学院化学化工学院贯彻"以人为本、重实践、求创新"的教育理念,对分析化学课程的教学方法和考试方法进行了改革和探索,达到了提高学生学习的主动性、强化学生综合运用知识的水平、提高学生创新能力的目的.

1 教材建设

教材建设是分析化学教学改革的重要环节.教材建设的目的就是要把 21 世纪分析化学立体多维的形象向学生展示出来[1].牡丹江师范学院化学化工学院应用化学专业的分析化学及其实验教学没有沿用师范教育专业的教材,而是根据专业特点,有针对性地选择了理论课和实验课的教材(如制药方向选择了李发美主编的《分析化学和分析化学实验》),理论课的授课内容较师范专业教材有很大变动(如在酸碱滴定法一章,选用盐酸吗啡的测定,实用性较强;实验课选用了阿司匹林的测定、药用氢氧化钠的测定等内容),教材的针对性强、专业性强、应用性强,增强了学生的学习兴趣,加深了学生对专业知识的理解.

2 教学内容改革

牡丹江师范学院化学化工学院为向学生展示分析化学丰富多彩的内容,尝试在教学内容上进行了改革.分析化学是一门方法学,需要对各种分析方法综合运用.现行的分析化学教材几乎都是按照分析方法进行编排的(如酸碱滴定、氧化还原滴定、络合滴定、沉淀滴定、重量分析、电位滴定、光谱分析、色谱分析等),通过按部就班地学习,分章节地掌握科学研究的方法、原理与步骤.我们对教学内容进行了改革,突出应用能力培养.以无机化合物、有机化合物的成分分析、结构分析为分析对象,体现了多学科交叉、实践性强、应用广泛的特点,引导学生学会在分析应用中获取理论知识,学会用全面的观点分析解决问题.课堂授课采用应用实例分析、多种方法对比分析、文献总结分析等方法进行讲解,获得了较好的教学效果.

3 教学方法改革

分析化学教学改革很关键的一步是教学模式的改革.教学改革实践表明,针对不同教学内容,通过预习、自学、探究、讨论等方法的有机结合,能提高学生学习的主动性.在分析化学教学中,从时间维度、空间内容维度、分析化学定位等多维度多角度讲解传授,取得了较好的教学效果.每一种分析方法采用简单回顾历史和展望未来导入,引发学生的学习兴趣,使他们知道现在丰富多彩的分析方法是如何发展起来的,明白还有许多问题有待改进和解决.如色谱分析的授课程序:从 1903 年俄国植物学家茨维特(Tswett)提出的分离植物色素讲起,给出流动相、固定相的空间图像→1941 年马丁(Martin)和辛格(Synge)发现液液色谱→1952 年詹姆斯(James)发现气相色谱→20 世纪 60 年代高效液相色谱法的发展[2].使学生明白,今天丰富多彩的色谱分析方法原来是从一百多年前的叶绿素分离发展起来的,使他们看到分析方法将来发展的方向,展现了分析化学生动活泼的立体形象,也可引起学生对分析化学的浓厚兴趣.

多种教学方法结合的教学模式克服了单纯讲授法的弊端,也避免了讨论式教学方法所带来的耗时太长、针对性不强的问题.在教学模式实施过程中,强调教学内容的特点,将适合讲授的内容通过启发式和总结性教学法传授给学生,将适合讨论的内容采用参与式和讨论式教学方法传授给学生,多种教学方法交叉灵活运用,最大限度地提高教学质量.

教学中要充分利用计算机辅助教学,减少书写板书的时间,增大课堂信息量,丰富教学内容.但也要避免将计算机作为主要教学工具,翻页式将教学内容呈现给学生,使得学生枯燥地看课件,降低了学生听课效率[3].如配位平衡中条件常数的计算公式较多,传统教学会出现板书书写时间长的问题,学生因只顾记笔记而不能及时理解内容,造成厌烦心理.教师如果先做好课件,从副反应定义出发,将公式分类,先给出各种有关金属离子副反应系数,再给出滴定剂 EDTA 副反应系数,最后给出总副反应系数.在这个过程中将条件

收稿日期:2011-02-04
基金项目:牡丹江师范学院教育教学改革工程一般项目(09YY-09293)

(C)1994-2021 China Academic Journal Electronic Publishing House. All rights reserved. http://www.cnki.net

形成常数的得来穿插介绍,脉络清晰,很容易让学生接受.

每位学生都有自己的一套学习方法和习惯,所以教学模式的选择非常重要.教师通过文献整理、案例查找做好课前准备,方能取得预期教学效果.

分析化学内容复杂繁多、丰富多彩,教师不可能通过规定学时把所有知识教给学生,而是要通过教学这把知识大门的钥匙,让学生自己去找知识.

4 教学评价方法改革

教学评价是教学改革的重要步骤,其评价方法改革在以下三个方面进行:

一是全面考核.考核分四部分:(1)课前提问;(2)作业;(3)月考;(4)期末考试.采用结构分制,分为平时考核成绩和期末考核成绩,平时考核占70%,期末占考核 30%.

二是全程考核.在整个教学期间,教师认真记录教学情况和学生的学习表现,随时对学生进行考核,并不断积累成绩.考核涉及教学过程的各种环节,特别是将每堂课的课前提问作为重中之重.

三是动态考核.学生考核的标准和内容并不是固定不变的,对不同的学生和不同的情境,考核的内容和标准应该有所变化.评价要看学生遇到问题时的处理方式和效果,看其分析问题和解决问题的能力.通过作业加强对学生的综合运用知识的能力和实际解决问题能力的培养.

总之,分析化学教学改革的目的是提高教学质量,通过改革使学生掌握分类、比较、分析、综合、归纳的科学方法,提高学生分析问题和解决问题的能力.当然,改革是一个不断完善的过程,要边创新,边实践,边总结,逐渐构建一个合理优化的教学体系.要以提高课堂教学质量为切入点,把它作为一项课题深入研究和总结,调动学生学习的积极性和主动性,从而提高学生综合运用知识的能力,培养有创新能力的高素质的人才.

参考文献

[1] 徐光宪.对分析化学教学的两点初浅看法[J].大学化学,2008,23(2):1.
[2] 张寒琦.仪器分析[M].北京:高等教育出版社,2009:26.
[3] 任秀莲,魏琦峰,张天云.定量分析化学教学改革与实践[J].大学化学,2006,21(5):17.
[4] 赵刚海,战春梅.高校理工科综合设计性实验教学质量评价的思考[J].牡丹江师范学院学报:自然科学版,2008(1):67-68.

编辑:琳莉

化工安全技术教学改革与实践

邓进军[1],孙少晨[2]
(1.大庆师范学院 化学化工学院,黑龙江 大庆 163712;2.沈阳市特种设备检测研究院,辽宁 沈阳 110035)

摘 要:针对化工安全技术教学存在的问题,提出教学改革的几点措施:一是正确利用有意注意和无意注意规律组织教学,二是采用灵活多变的教学方法,三是及时更新教学内容,四是采用多媒体教学手段,五是注重理论联系实际,最终达到使学生全面掌握化工安全技术课程内容的目的.

关键词:化工安全;教学;方法

[中图分类号]G642.421 [文献标志码]A [文章编号]1003-6180(2011)02-0068-02

随着社会的不断进步,思想的不断更新,学生对社会、对知识的认识和接受的方法也在不断改变,这就要求教师的教学手段必须与时俱进,跟上时代步伐,才能让学生更清晰、更快捷地掌握更多的知识.化工安全技术课程教学作为理论知识与实践知识相融合的产物,一方面知识和内容体系不断更新,另一方面课时不断减少.为了使学生掌握化工安全技术课程的内容,课堂教学不仅要有清晰的教学思路,还需要应用科学的教学模式[1].

目前的化工安全技术课教学存在以下问题:一是就学生而言,大部分学生是独生子女,家长事事顺着孩子的意愿,导致这部分学生意志力比较薄弱,比较任性,自制能力较差,上课不能长时间注意听讲,课堂接受能力差,对教师布置的作业常常敷衍了事或者照搬照抄,应付差事.二是就教师的教学而言,部分教师教学方法单一,容易使学生产生厌倦情绪和神经疲劳;教学方法呆板,不能适应学生求新求变的心理;语言重复罗嗦,枯燥无味,吸引不了学生的注意力.化工安全技术课程采用新的教学模式至关重要,只有采用科学的教学模式,才能让学生对高危行业的安全隐患有所认识,拥有安全意识和自我防护的意识.

1 利用注意规律组织教学

在教学中,凡需要学生注意和操作的活动,尽量赋予他们无意注意的特征[2].讲授的内容要难易适中,让学生既能听懂又要有新意,这是引起学生兴趣、维持学生注意的关键.在处理教材中的难

收稿日期:2010-09-05
基金项目:油田公司教育科研项目(sdqz-2009-jy-ky-002);大庆师范学院教改项目(JY0922)

(C)1994-2021 China Academic Journal Electronic Publishing House. All rights reserved. http://www.cnki.net

10.刘素娟,邵艳秋,任玉兰,罗玉杰.高等师范院校仪器分析实验课程改革与实践[J].牡丹江师范学院学报(自然科学版),2011(01):74-75.

DOI:10.13815/j.cnki.jmtc(ns).2011.01.023
2011 年第 1 期 牡丹江师范学院学报(自然科学版) No.1,2011
(总第 74 期) Journal of Mudanjiang Normal University Total No 74

高等师范院校仪器分析实验课程改革与实践

刘素娟,邵艳秋,任玉兰,罗玉杰
(牡丹江师范学院 化学化工学院,黑龙江 牡丹江 157011)

摘 要:分析了仪器分析实验课程的现状,提出高等师范院校仪器分析实验课程改革的思路:一是提高学生对仪器分析实验课程重要性的认识;二是增加反映新技术、新方法、新知识的实验;三是采用多样化教学模式授课;四是建立科学的考核评估体系;五是开放实验室;六是采用多媒体辅助教学.

关键词:仪器分析实验课程;改革;效率

[中图分类号]G642 [文献标志码]A [文章编号]1003-6180(2011)01-0074-02

仪器分析实验课程是师范院校化学专业的必修课,仪器分析实验教学的目的是要求学生掌握实验基础知识、基本操作技能、仪器分析的基本原理以及实验数据处理方法,注重对学生进行综合研究能力的训练,为学生的毕业设计及工作打下良好的基础.

1 仪器分析实验课程的现状

仪器分析实验课内容多,课时少(仅 36 学时).仪器分析实验的仪器大多价格昂贵,学校拥有的仪器设备数量有限,因此,大多数学校采用"大循环"实验."大循环"实验虽可解决人均实验台套数不足的矛盾,但往往会出现理论教学与实验教学不同步的问题.学生在没有理论基础的情况下开展实验影响教学质量.

2 仪器分析实验课程改革方案

笔者结合我校仪器分析实验课程教学情况,就高等师范院校仪器分析实验教学提出以下建议.

2.1 提高学生对仪器分析实验课程重要性的认识

仪器分析实验课是高等师范院校重要的专业基础课,对学生掌握现代大型仪器的原理、特点和应用具有重要意义.但普通高等师范院校的学生普遍存在轻视实验、动手能力差的现象,所以首先要解决当前仪器分析实验教学中普遍存在的"重理论轻实践"的问题,提高学生对仪器分析实验课程重要性的认识.

2.2 改革实验内容

仪器分析的经典内容在理论上比较成熟,但在实际应用上较陈旧,不适应现代分析化学的要求,因此,在实验教学内容方面要适当增加反映新技术、新方法、新知识的实验.根据本院现有的仪器及实验条件编写了实验教材,在原来经典、基础性实验的基础上增设了综合性实验、设计性实验及仪器分析实验技术的强化训练,提高学生用分析化学知识分析问题、解决实际问题的能力,更有效地培养学生的实践能力和创新能力.

2.3 采用多样化教学模式授课

一是根据实验内容合理安排实验顺序,如组织学生观看视频→模拟→实践(也可相互穿插进行),这样可以提高教学效率,激发学生学习兴趣;二是采用启发式和讨论式教学法,增强课堂教学的互动性,激活学生的思维,充分调动学生自主学习的积极性;三是结合多媒体手段和网络教学资源,扩大课堂容量,优化课堂教学;四是课后让学生完成趣味性较强的小课题,实现因材施教,培养学生的创新能力.

2.4 建立科学的考核评估体系

考核方式的改革可以带动学生学习方式的改变.比如期末综合考核:一是选择具有典型意义的样品测试学生的分析技能,按结果进行成绩评定;二是考核学生分析仪器基本操作和实验操作技能.教师要精心设计技能操作考核评分表,在完成实验项目训练后,要求学生按照评分标准进行自检、互检,对考核不合格的学生,要求其再训练,直到达标为止.

2.5 开放实验室

开放实验室,允许学生补做课堂上未掌握好、失败的实验.为了能让学生进一步加深对大型仪器的认识及运用,学生可以自选实验.开放实验室可促进学生参与到科研创新实验中来,培养学生的科研兴趣,充分利用实验室现有资源,提高仪器设备的利用率.

收稿日期:2010-09-29
基金项目:牡丹江师范学院基金项目(QY201005)

(C)1994-2021 China Academic Journal Electronic Publishing House. All rights reserved. http://www.cnki.net

2.6 采用多媒体辅助教学

使用现代信息技术辅助教学,解决由于仪器结构复杂、工作原理抽象、学生难以接受的问题,促进学生自主学习,提高学习效率.多媒体可将基本概念、基本原理、仪器内部结构直观地表现出来,使学生能够比较轻松地理解和掌握课程内容.

化学化工学院分析测试中心拥有的仪器种类较多,有傅立叶红外光谱仪、高效液相色谱仪、气相色谱仪、原子吸收分光光度计、紫外可见分光光度计、荧光分光光度计等大型仪器.这些仪器在教学中的应用加强了学生对仪器基本原理的理解、对分析方法的应用以及实际操作能力的提高.近三年的仪器分析实验教学改革调动了学生的积极性和主动性,为学生完成毕业论文打下了基础,也激发了学生从事科学研究的兴趣.

参考文献:

[1] 于凯.无机化学实验改革谈[J].牡丹江师范学院学报:自然科学版,2003(2):57.

[2] 曹延华,徐晓佳,李亦惠.基础化学实验教学改革与探索[J].牡丹江师范学院学报:自然科学版,2005(4):56.

编辑:琳莉

基于主体教育理论的数学实验教学

李石涛,滕 勇
(沈阳工业大学 基础部,辽宁 辽阳 111000)

摘 要: 阐述主体教育理论背景下的数学实验在教学观念、教学目的、教学方法、教学环节、教学活动、师生关系六个方面充分体现了学生的主体参与性、主体能动性、主体创造性,并通过具体的教学实例说明如何进行数学实验教学.

关键词: 主体教育;数学实验;教学方法

[中图分类号]TP391 [文献标志码]A [文章编号]1008-4150(2011)01-0075-03

20 世纪 80 年代初,我国的著名教育专家顾明远教授率先发表文章,提出"学生既是教育的客体,又是教育的主体"的重要观点,引起教育学界的一场大讨论,一些著名教授纷纷发表见解,支持并进一步阐发"学生是教育主体"的观点,形成了主体教育思想.与此同时,从 20 世纪 80 年代中下期开始,数学实验的思想和内容引入我国高等院校,在 20 世纪 90 年代,数学实验在一些院校中开始大规模开设,近几年,数学实验大有燎原之势[1].

主体教育理论自产生以来,对我国的教育教学改革产生了广泛而深入的影响.主体教育理论认为,人的主体性素质是现代社会人的核心素质,在教育中应该注重培养和发展人的主体性.所谓主体性,指学生在教师指导下积极主动学习时,表现出的一种主观能动性,表现在对外部世界的能动选择上,主要是受本人兴趣、需要以及所接受的外部要求的推动和支配,表现在自觉性、选择性上;另一方面表现在对外部信息的内部加工上,受本人原有知识经验、认知结构、情感意志、性格等制约,表现为自主性、创造性[2].在数学实验教学中,教师通过对数学实验教学的设计和课堂教学的组织,给学生提供数学实验的情境,恰当给予学生引导、帮助,创造反省活动过程和再认识数学事实的机会,来保证发挥学生的主体性.同时,学生的主体性主要体现在学生主动参与到数学实验教学的各种活动中,学生通过参与数学实验活动,形成数学概念,探索数学问题,寻求问题解决策略,独立思考,理解数学,领悟数学思想和方法,创造性地提出新问题并在解决问题过程中不断深化和发展.本文基于主体教育理论对数学实验教学进行研究,阐明数学实验课更能突出学生的主体地位,只有突出学生的主体性地位,数学实验课才能收到更好的效果.

收稿日期:2010-11-23
基金项目:辽宁省高等教育教学改革研究项目(2009);沈阳工业大学教育教学改革重点立项(200965)

(C)1994-2021 China Academic Journal Electronic Publishing House. All rights reserved. http://www.cnki.net

11.邵艳秋,罗玉杰,廉波,任玉兰,刘素娟.能力培养视角下分析化学实验教学改革[J].鸡西大学学报,2010,10(05):144-145.

DOI:10.16792/j.cnki.1672-6758.2010.05.065
第10卷 第5期 鸡西大学学报 Vol 10 No 5
2010年 10月 JOURNAL OF JIXI UNIVERSITY Oct 2010

文章编号:1672-6758(2010)05-0144-2

能力培养视角下分析化学实验教学改革

邵艳秋 罗玉杰 廉 波 任玉兰 刘素娟

摘 要:根据分析化学实验课的教学现状和存在问题,提出从实验教学内容、教学模式和方法及实验考核等方面进行改革,提高学生学习的主动性,强化学生创新能力和实验动手能力的培养。

关键词:分析化学实验;实验技能;教学改革
中图分类号:G642.0 **文献标识码**:A

分析化学是一门实践性很强的基础性学科,有着极为广泛的应用领域,如生命科学研究、环境治理、能源与材料、医学与食品检验、工业产品质量监控、毒品与法医鉴定等,几乎涉及人类生活的所有方面。近几年,社会对分析化学人才的需求不断增强,对人才质量的要求也在发生着变化,越来越看重分析化学工作者的动手能力、综合运用知识能力和实际解决问题能力等应用与实践能力。而分析化学的实验教学是培养学生基本实践能力的主要途径。分析化学实验教学应顺应实践领域的客观发展,加强对学生的实验基本技能、动手能力、综合运用知识的能力和实际解决问题的能力的培养。

传统分析化学的实验教学不论是在教学内容上,抑或是教学模式方法上,都与分析化学实践领域的客观要求有着相当的差距。主要表现在以下几个方面。

1.教学理念上,存在着"以教师为中心"、"以教材为中心"的倾向。传统分析化学的实验内容往往是教材预先设定好了的,教学中也是以教师的活动为主,因而学生极少拥有自己的思维空间和动手机会,这对学生的动手实践能力、综合运用知识的能力以及解决实际问题的能力的培养是极为不利的。

2.教学内容上,传统的分析化学的实验教学以重复教学教材中现成的"经典"实验的验证性实验为主,缺少开放性、综合性和设计性实验。传统实验教学中,实验的条件、过程、对象、结论都是已知的和明确的,学生只是照猫画虎地操作而已,缺乏热情和动机。

3.教学方法上,以教师的讲授和演示为主,学生被动地接受,简单重复和模仿。

4.教学过程上,在规定的时间内整齐划一地进行实验,无法满足不同层次学生的学习要求;过于重视操作的细节,而忽视操作技能的完整性,不利于技能的熟练化。

5.教学评价上,重理论而轻实践,重结果而轻过程。评价指标缺乏实用性,没有起到引导学生能力发展的作用。

针对上述存在的问题,我们分析化学教改小组经过细致的调研,对分析化学实验教学进行了多种尝试性改革,取得了较好的效果。主要有以下几个方面。

1.改革实验教学的内容。

我们将实验项目分为三大类:一是基础性实验;二是专业性实验;三是综合性实验。同时,它们也是实验教学的三个阶段。分析化学实验教学主要是要培养学生三项实验技能,即基础实验技能、专业实验技能和综合实验技能。

首先,合理优化实验项目,减少实验教学内容上的低层次重复。由于各个课程都强调自身的完整性,分析化学与其它基础课、专业课在实验教学上多有交叉,特别是分析化学与无机化学在基础性实验教学上有着很多类似的项目,多为验证性分析实验项目和定性实验项目,内容陈旧、单一。对此,我们大幅度减少验证性的基础实验项目,精选定量分析实验项目,并将设计性、综合性实验项目增加到一定的比例,尤其注意增加了能够体现现代分析化学实验技术的实验项目。

其次,注意选择与日常生活、生产密切相关的实际问题,结合到分析化学的实验教学中来,保持实验教学与实践领域的沟通与联系,体现应用性,突出时代感。例如,最早的分析化学实验的定性实验内容就占近三分之一学时,大多数离子鉴定的实验在无机化学实验中做过。我们在实验教改过程中将这部分 20学时的实验内容划掉,增添了很多应用性较强的实验内容。同时,对定量分析实验中的内容也进行了筛选,开设一些与日常生活相关的设计性实验,如蔬菜中维生素 C含量的测定,鸡蛋壳中碳酸钙及巨能钙中钙含量的测定、蜂蜜中金属离子含量的测定等内容。

第三,充分发挥现有仪器的使用率,开好仪器分析实验。当前实际应用领域中,仪器分析使用广泛,许多重要的分析化学课题都是由仪器分析完成的。会使用仪器进行实验分析是高级分析实验技能。例如,根据现在市售

作者简介:邵艳秋,博士,教授,牡丹江师范学院化学化工学院,黑龙江·牡丹江。邮政编码:157012
基金项目:牡丹江师范学院教育教学改革工程一般项目(项目编号:09YY-09293)

(C)1994-2021 China Academic Journal Electronic Publishing House. All rights reserved. http://www.cnki.n

的各种饮用水,用原子吸收方法分光光度法测定水中微量元素含量,用气相色谱法分析白酒中的甲醇,荧光光度法测定自来水中 Cl⁻离子含量等,这些实验都对学生动手能力的培养起很大的作用。

第四,结合教师的科研课题,不断精选、优化、更新实验教学内容,及时反应本学科领域的最新科技成果,保持实验教学的先进性、前沿性。如:牡丹江城市饮用水中金属离子的测定和消毒副产物的研究。这是我们教师的科研课题,我们将课题内容分解几部分,然后让学生自行选择,自愿选做。

2.改革实验教学的模式与方法。

首先,限制传统的以教师为中心、以内容为中心的讲授式教法,加强以学生为中心、以问题为中心的探究式学法。在以往教学中,教师讲得过多,要求过于严格和具体,实验的内容、条件、程序乃至结果都是事先规定和预知的,学生"照方抓药",机械操作,毫无乐趣和动力。开展开放性实验,围绕问题开展研究性学习,增强了学生学习的主动性和责任感。

其次,限制传统的师一生单向传授教学模式,加强现代的师一生、生一生多向合作学习模式。现代心理学认为,学生从他的伙伴那里学习的更多、更快,其中也包括失败的经验。实验中,鼓励学生相互沟通、协商与合作,往往能取得超乎寻常的效果。在开放实验的条件下,每一个学生所面对的问题是相似的,又都是不一样的,可以相互帮助,但很难抄袭实验结果。

第三,限制传统的统一、集中的教学模式,加强针对性、随机性教学模式。传统教学的问题就在于,教师讲解的时候,学生还没有真正开始进行实验或遇到问题,所以指导常常是无效的。教师的指导要"当其时",恰到好处。教师紧紧跟随学生的实验过程,随时进行有针对性的个别指导。指导的内容以出现的问题来确定,而不是依照教材的逻辑顺序。

第四,限制以知识传授为主的实验教学模式,加强以能力培养为核心的实验教学模式。如:我们在水的硬度测定实验里,让学生自己采集水样,可以取泉水、矿泉水、工厂排放废水,然后到实验室进行前处理,在让学生自己配置 EDTA标准溶液进行测定,让他们以环境工作者的心态来进行实验,大大调动了实验学习的主动性,增强了教学的目的性。再如,我们以前的实验都是由教辅人员将很多试剂配好,如去离子水的测定中,已经将阳离子和阴离子树脂处理好,学生上课时装柱后就实验,对树脂的前处理不会,这对他们能力培养是不利的,我们将树脂的前处理都交给学生,让他们对这一实验内容有全面的了解,离子交换分离实验的完整性得到充分体现,有利于提高学生的综合能力。

3.改革实验教学的评价方法。

一是全面考核。

采用多种测试的方法,全面考核学生的各种实验技能。如从考核的内容上设置了四个方面:(1)预习;(2)操作;(3)报告;(4)设计方案。从考核的结构上,采用结构分制,分为平时考核成绩和期末考核成绩,平时考核占70%,期末占30%。

二是全程考核。

在整个教学期间,教师认真记录教学情况和学生的学习表现,随时对学生进行考核,并不断积累成绩。考核涉及教学过程的各种环节,特别是实验课上的技能考核,作为重中之重。

三是动态考核。

对学生进行考核的标准和内容并不是固定不变的。对不同的学生,在不同的情境下,考核的内容和标准应该有所变化。不仅要看学生的实验是否成功,也要看学生遇到问题时的处理方式和效果。

总之,分析化学实验教学改革的目的是提高教学质量,通过改革提高学生分析问题和解决问题的能力。改革是一个不断完善的长期过程,要边创新,边实践,边总结,逐渐构建一个合理优化的教学体系。我们要以实验教学为切入点,把提高实验教学质量作为一项课题深入研究和总结,调动学生学习的积极性和主动性,从而提高学生在实验中动脑动手能力,培养有科学思维方法和创新能力的高素质的人才。

Reform of Experimental Teaching Reform Under the Perspective of Capability Cultivation

Shao Yanqiu Luo Yujie Lian Bo Ren Yulan Liu Sujuan

Abstract: This paper made an analysis on the current teaching situation and existing problems of experiment chemistry teaching. It focuses on the reform of the experimental teaching contents, the teaching modes and methods, and the experiment examination. The author believed these reform will improve the students' learning initiative, and strengthen students' innovation consciousness and practice ability.

Key words: analytical chemistry; experimental skills; teaching reform

Class No.: G642.0　　Document Mark: A

(责任编辑:郑英玲)

(C)1994-2021 China Academic Journal Electronic Publishing House. All rights reserved.　http://www.cnki.n

12.邵艳秋.化学师范生教学技能结构论析[J].黑龙江高教研究,2008(08):119-120.

2008年第 8期 黑龙江高教研究 No 8 2008
总第 172期 Heilongjiang Researches on Higher Education serial No 172

化学师范生教学技能结构论析

邵艳秋
(牡丹江师范学院 化学系,黑龙江 牡丹江 157012)

摘要:化学教学技能是化学教师素质的重要组成部分,也是提高化学教学质量的基本要素,教育部颁发的新课程标准对化学师范生教学技能的培养提出了新的要求。师范生化学教学技能可以分为基本技能、讲授技能和综合策略性技能。

关键词:教学技能;技能结构;课程标准
中图分类号:G655 **文献标志码**:A **文章编号**:1003-2614(2008)08-0119-02

一、化学教学技能的界定

教学技能是指教学者经过专门教育训练和长期教学实践的磨砺所形成的适应客观教学要求的、复杂的、自动化的活动方式和方法。教学技能既是一个人的教学才能在具体的教学过程中的表现,也是知识运用的一种结果。而化学教学技能又是一般教学技能在化学专业教学活动中的实际运用。任何一种有效的活动方式都离不开方法的运用,所以化学教学方法的熟练运用也是教学技能的范畴。具备一定的化学教学技能是化学课程教学质量的保证。新课标下化学教学技能包括课堂教学目标设计技能、教学方案设计能力、导入技能、语言与讲解技能、提问技能等。化学教学技能是制约教学质量的主要因素,所以仅仅掌握了化学专业知识是不能搞好化学教学的,还要培养和具备一定的化学教学技能。

二、化学教学技能的结构

化学教学技能作为一种自动化的活动方式,其构成是极为复杂的。因为教学活动不仅仅是教师的个别的、具体动作或者实验的操作,而是由化学知识、师生互动、化学实验设备、媒体设备等诸因素有机组成的活动的整体。所以,化学教学技能除教学者个人的动作和实验操作方面的技能以及化学知识的传授技能以外,还应该包括组织教学活动、升华教学效果的方法策略方面的技能。笔者认为,师范生化学教学技能可以分为化学教学的基本技能、化学知识的讲授技能和教学的综合策略性技能三个部分。

(一)化学教学的基本技能

化学教学的基本技能主要包括化学专业用语使用技能和示范性的实验技能。

1.专业用语使用技能

在所有化学用语中,符号用语、化学式用语和方程式用语是三种最主要的用语。化学用语要做到正确读出、规范书写和灵活运用。通过反复练习,师范生要能够准确完整地读出各种化学符号、数字、图形、字母,正确理解它们所代表的意义。对于化学式不仅能够正确地念出来和理解它们所代表的实际意义,还要能够熟练地掌握各种化学式的书写规则。分子式、简写式、结构式、电子式、示性式都有不同的书写要求,都应熟练地精确地掌握。写好化学式是写好化学方程式的基础,而化学方程式的书写和使用还往往涉及配平的问题,也必须熟练地掌握。

2.示范性的实验技能

实验技能一般包括实验的设计技能、实验过程的观察技能、操作技能以及实验结果的处理技能等。良好的实验技能是从事化学专业教学与研究的必要条件,而化学教师在具备这种实验技能的同时,还要使这种实验技能具有较强的示范性,以满足教学的需要。新课标要求下的实验技能的示范性应具有探究意义。笔者认为,实验技能的示范性要具有展示性和启发性两种功效,特别是启发性的功能。要通过教师的示范引发学生更多的思考,设置出问题的情境。

(二)化学知识的讲授技能

化学知识的讲授技能包括化学概念讲授技能和化学原理讲授技能。

1.化学概念讲授技能

化学知识的讲授中基本概念占了较大的比重,中学教材中涉及的概念极为丰富。整个教学内容基本上是以物质的结构为主线把物质的构成、性质、变化等方面的概念由简单到复杂、按一定的逻辑性组织起来的。所以如何让学生能够正确地、清晰地掌握这些概念是十分重要的,而这在很大程度上决定于教师的教学技能水平。因此,重视概念教学技能的培养是提高化学教学质量的关键因素。实施概念

收稿日期:2008-05-22
基金项目:黑龙江省教育厅科学技术研究项目(一般项目,项目编号:10541238)。
作者简介:邵艳秋,牡丹江师范学院化学系副教授,吉林大学物理化学专业博士研究生,研究方向为物理化学。
(C)1994-2021 China Academic Journal Electronic Publishing House. All rights reserved. http://www.cnki.net

教学的技能主要包括直观教学的技能、变式教学技能、启发式教学技能、概念的定义技能，以及为了练习和巩固概念而对问题情景的设计技能等方面。开展直观教学还要求教学者具备熟练使用多媒体设备的技能。在训练概念的传授技能时，首先要明确教学内容中都有哪些化学概念。一般来说，主要集中在物质的组成、物质的结构、物质的性质变化上，也包括各种化学量、化学术语、设备名称和操作技术的含义等。针对不同的概念选择有效的教学方法，熟练运用，最终就会形成一种技能。

2.化学原理讲授技能

化学原理讲授技能是以概念讲授技能为基础的，但比概念讲授技能更为复杂，因为原理揭示了概念与概念之间的内在联系。所以要讲好化学原理，首先要先讲好化学的概念。但化学原理教学也有着自身的要求，即在对基本概念的理解基础之上，通过联系社会生活的实际，或者提供典型的系列实验，引起学生的思考，通过分析综合、归纳总结等过程和方法，最终使学生相信原理的正确性。这是一个培养学生理论思维能力、探究能力和运用化学知识分析问题、解决问题能力的过程。

(三)化学教学的综合策略技能

化学教学的综合策略性技能是化学教学技能发展的较高级水平，它通常是熟练地、合理地综合运用了各种教学方法的结果，对教学效果起到事半功倍的加力作用，有利于培养学生学习的积极性和主动性，培养他们的思想情感、道德情操，从而达到“坏事变好事”、“教，是为了不教”等目的。这部分教学技能是新课程标准大力提倡的，又恰恰是被我们师范教育阶段所忽略的。

1.运用教学机智的技能

物质的结构、性质是极为复杂的，这也就使得化学与其他学科相比具有非同一般的复杂性和多样性，学生认识能力上也存在着较大的个体差异，加之新课标提倡的主体性教学模式，使化学课堂有着极大的偶然性和随机性。教师要随时准备处理课堂上可能发生的突发性事件。处理这些偶发突发事件对课堂教学来说既是挑战，也可能是个机遇。因为这些偶发突发事件往往也是教学过程中各种矛盾所造成的，存在着一定的必然性，处理好这些问题是突破教学难点、完成教学重点的好机会。教师要吃透教材充分备课，深入了解学生，丰富专业知识，做好面对突发事件的心理准备，还要学会一些应变技巧，如“因势利导法”、“曲线迂回法”、“反诘与幽默法”、“借尸还魂法”等。

2.课堂教学综合设计的技能

教学设计是教师必须掌握的最为重要的教学技能之一。化学师范生要学会在新的课程标准指导下，确定教学目标、处理教材内容、选择教学方法、设计教学过程。化学现象本来就不是孤立地存在于世界当中的，新的化学课程标准强调教学与生活与社会相联系，提供了许多能够用以设计探究式学生的各种问题情景和案例素材，怎样利用这些素材来设计探究式的综合性课程？这是化学师范生需要培养的教学技能。

3.进行思想教育、情感教育的技能

任何知识都具有多重属性。化学新课程标准将学习内容分为三个方面——知识性内容、技能性内容和体验性内容，其中特别强调体验性内容的学习。化学知识中包含着丰富的有价值的思想教育和情感教育的因素，善于挖掘和利用教学内容中可体验的素材，寓思想教育和情感教育于知识教学之中，这不仅仅是新课程标准的要求，也是高水平教学的体现。这一技能往往是我们师范生比较缺乏的。

4.促进学生发展的教育评价技能

教育评价不仅是检查教学质量、效果的措施，同时也是调动学生学习积极性、塑造良好的学习行为、促进学生全面发展的有力手段。化学新课程标准要求教学评价的多元化，“既要评价学生化学知识的掌握情况，更应重视对学生科学探究的能力、情感态度与价值观等方面的评价”，提倡以开放性的、以实际问题为内容的测验题目来考察学生的解决问题的能力。所以，编制内容多元化、答案开放性的测验试题是新课改要求教师具有的一项重要教学技能。

总之，教学技能是一个复杂的心理结构，具体体现在教学者身上时会有多种不同的组合和类型；对它不同的划分也体现了对教学技能的不同的理解。新课标下以探究为核心的多样化教学方式，以观念和理解为建构为本的现代教学观，必将有全新的对教学技能的理解，对化学师范生技能的培养提出新的要求，如何对师范生的教学技能进行培养，特别是课改所极力要求的综合策略性技能，是摆在高师化学教育面前的一项重要课题。

参考文献：

[1]李 敏，王树华.教师教学基本功[M].北京：中国人事出版社，1998：3.

[2]教育部.全日制义务教育化学课程标准：实验稿[S].北京：北京师范大学出版社，2001.

[3]教育部.基础教育课程改革纲要：试行[Z].2001.

[4]王 者.科学教育的目标与课程开发[J].外国教育研究，1993，(4)：20～23.

[5]李孝忠.能力心理学[M].北京：人民教育出版社，1980.

[6][美]桑特洛克(Santrock J.)教育心理学[M].陈红兵，等，译.南京：江苏教育出版社，2005.

(责任编辑：吴养泉)

(C)1994-2021 China Academic Journal Electronic Publishing House. All rights reserved. http://www.cnki.net

13.邢乐红,王宜鑫,隋朝,肖同欣,赵玥,邵艳秋.工程教育专业认证背景下化学工程与工艺专业人才培养模式探索[J].教育现代化,2020,7(07):11-12+22.

Education Modernization 教育现代化

DOI:10.16541/j.cnki.2095-8420.2020.07.005

工程教育专业认证背景下化学工程与工艺专业人才培养模式探索

邢乐红，王宜鑫，隋朝，肖同欣，赵玥，邵艳秋

（牡丹江师范学院 化学化工学院，黑龙江 牡丹江）

摘　要：根据工程教育专业认证标准相关要求，从人才培养目标与毕业要求的重新定位、课程体系设置、工程教育实践环节改革等方面，进行了我校化学工程与工艺专业人才培养方案改革，初步建立了“以学生为中心”“以目标为导向”“持续改进”的成果导向型人才培养新架构。

关键词：工程认证；化学工程与工艺；人才培养

本文引用格式：邢乐红，等．工程教育专业认证背景下化学工程与工艺专业人才培养模式探索[J]．教育现代化，2020,7(07):11-12,22.

一　引言

工程教育专业认证是由工程教育认证协会组织，基于工程教育国际互认体系标准，对高等学校开设的工科专业实施的专业认证，其目的是保证工程教育质量和保障教育质量持续改进[1]。工程教育国际互认体的内容主要包括工程教育标准、学历互认及工程资格互认等。工程教育国际互认体系是由《华盛顿协议》《都柏林协议》《悉尼协议》《亚太工程师计划》《工程技术员流动论坛议》《工程师流动论坛协议》六个国际重要协议所构成[2]。其中前三个协议主要规定了学历互认的相关要求，后面三个协议主要规定了工程技术人员职业技术资格互认的相关要求。这六个协议中最重要最具权威性的是1989年签署的《华盛顿协议》，该协议的主要内容包括两方面，一是工程教育认证体系具有可比性，二是通过认证的专业培养的毕业生获得的能力是等效的[3]。

我国于2006年开始进行工程教育认证，并由国家教育部授权成立了权威机构－全国工程教育专业认证专家委员会。2013年中国正式提交申请，并于同年6月顺利加入《华盛顿协议》，成为预备成员。2016年中国成为《华盛顿协议》正式成国[4]。开展工程教育专业认证的目的是为了不断提高工程教育质量，加快工程教育优化进程，提高我国工程教育的国际“地位”与国际竞争力。2006年底，我国高校化学工程与工艺专业开始了工程认证工作，2007年，清华大学和天津大学的化学工程与工艺专业按照国际标准率先通过工程教育专业认证。在此之后大批高校的化学工程与工艺专业申请国家工程教育认证并成功通过认证[5]。目前，高校已经意识到工程教育专业认证的重要性，以工程认证加快学科专业建设，提高高校人才培养质量和推动专业课程改革已势在必行[6]。牡丹江师范学院始建于1958年，是全国首批学士学位授予单位，现为黑龙江省东南部地区规模最大、综合实力最强的省属本科院校。本校化学工程与工艺专业于2011年开始招生，目前已有5届毕业生。本专业积极拓展与国内知名大学的学习交流，使得专业办学能力与水平稳步提高。我们有信心、有能力把本专业办成黑龙江省一流的专业，为东北老工业基地振兴和服务地方经济发展贡献力量。目前，本专业以工程认证为契机，对标工程认证标准，查找本专业的问题和不足，从人才培养目标与毕业要求的重新定位、课程体系设置、工程教育实践环节改革等方面，进行了我校化学工程与工艺专业人才培养方案改革，初步建立了“以学生为中心”“以目标为导向”“持续改进”的成果导向型人才培养新架构。

二　解读化学工程与工艺专业认证标准

化学工程与工艺专业全体教师，全面学习了解了认证标准相关内容，包括通用标准所包含的“七项指标”（专业目标、课程体系、支持条件、师资队伍、管理制度、学生发展、质量评价）共35个观测点（招生数量、录取分数、第一志愿生源、学生指导、就业率、就业性质与分布、具有吸引优秀生源的制度和措施、学生表现跟踪评估、考试内容与培养目标达成程度、转专业学分认定、培养目标内容、培养目标达成度与合理性、毕业要求内容、毕业要求如何通过教学活动实现、毕业要求达成度等）以及补充标准中对课程体系、师资队伍、支

基金项目：牡丹江师范学院教学改革项目（19-XJ21008）；牡丹江师范学院青年学术骨干项目（GG2018001）；黑龙江省高校青年创新人才培养计划项目（UNPYSCT-2016108）；牡丹江师范学院教学改革项目（18-XJ20064）；牡丹江师范学院国家级课题培育项目（GP2018002）；黑龙江省教育科学规划课题（GJC1316121）。

作者简介：邢乐红，女，山东武城县人，博士，副教授，牡丹江师范学院化学工程与工艺专业负责人。

(C)1994-2020 China Academic Journal Electronic Publishing House. All rights reserved. http://www.cnki.net

持条件等方面的补充要求19个观测点（课程设置、实践环节、综合设计、科技创新、毕业设计选题、内容、指导、师资专业背景、工程背景、实验条件、实践基地等），深刻体会工程教育专业认证的成果导向教育理念。并且强调了“以学生为中心”、“以目标为导向”、“持续改进”的核心理念。结合地域和本专业实际情况，做到以学生的培养为最终目标，课程内容和据对学生的期望而设计，师资与其它支撑条件有利于达成预期目标，能到毕业要求的达成支撑培养目标的达成，培养目标与毕业要求对日常教学活动起导向作用。建立了教学管理制度，进行常态性的评估与评价，通过质量监控与反馈机制对每一个常规教学活动进行评估，实现持续改进。

三　人才培养目标与毕业要求的重新定位

在全面了解认证内容的基础上，制定本专业人才培养目标和毕业要求。培养目标要符合学校定位和经济社会发展需求。培养目标内容主要包括两部分：一是明确本专业培养学生需要适应何种领域需求，具有哪些方面知识和能力，能在哪些行业部门从事哪些方面工作的人才；二是毕业五年左右在社会与专业领域的发展预期，包括解决复杂化工工程问题能力、团队意识、国际化视野、终身学习等方面。要定期按照计划评价培养目标的合理性，并根据评价结果的合理程度对培养目标适行改良修订。需要有企业或行业专家全程参与对培养目标的制定、评价与修订过程当中。本专业人才培养目标细则如下：培养德、智、体、美、劳全面发展，具备化学和化工方面的基本知识和基本技能，具有一定的创新意识和较强实践能力，能够适应未来职业和社会发展，能在化工、能源、材料、军工和科研机构等企事业单位从事工程设计、技术开发、生产管理、科学研究等工作的高素质应用型专门人才。

在充分了解专业认证通用标准中规定的十二条毕业要求（工程知识、研究、设计/开发解决方案、现代工具的应用、环境与可持续发展、个人与团队、项目管理、问题分析、职业规范、工程与社会、沟通交流和终身学习）的基础上结合本专业特点和实际情况，制定本专业人才培养的十二条毕业要求。并定期对毕业要求达成度进行评价，制定了《化学工程与工艺专业毕业要求达成度评价办法》对毕业要求达成度的评价频度、评价人、评价方法、记录等方面进行规范细致的规定，实现培养目标、毕业要求的持续改进。

四　课程体系改革

课程体系是本专业的育人总方案，是培养目标、毕业要求达成的依托与具体化，工程认证标准要求，要设置能够支持培养目标达成的合理课程，需要有行业或企业的专家参与本专业课程体系设计。课程体系内应包括各种教学课程，其中包含学科基础课至少占人才培养方案总学分的35%，专业基础课至少占人才培养方案总学分的30%，通识教育课至少占人才培养方案总学分的15%，实践环节与毕业设计（论文）至少占人才培养方案总学分的20%。本专业课程体系的考察点包括授课计划、大纲、课表、实验实践课程内容与效果、毕业论文选题、专业实践等环节。课程体系改革之前，大部分化工类核心课程的教学偏向于学生具备深厚的基础理论和专业知识的培养模式，缺少对学生解决复杂工程实际问题综合能力的培养。目前，通过对《化工原理》《化工热力学》《化工工艺学》《化学反应工程》《化工设计》等专业方向课程进行改革，已经解决复杂工程实际问题所需的综合能力分解于每门课程中进行培养。在课程教学过程中，教师设计难度适当的工程实际问题让学生独立或讨论解决。教师对学生完成情况进行指导、评价和总结。在不断的探索中，持续完善课程体系与毕业要求关系矩阵，各门课程对毕业要求的支撑情况，按照高、中、低三档分别进行分析和评价，并总结形成反馈信息，用于教学计划的修订和各教学环节的持续改进中，在课程体系设计时，加强校企合作，设置企业行业置换课程，还要注重多学科综合的学习能力。职业素质与责任感的培养。在课程设置上应更多地考虑多学科的交叉与融合，课程应与工程背景相关，为培养学生工程素质提供综合的知识背景。

五　工程教育实践环节改革与实践能力培养

实践环节是保证工程教育质量的关键，通过实践环节可培养学生的工程系统能力。实践中运用知识的能力，解决复杂工程问题的能力及管理决策能力，并通过合理统筹优化实践教学部分，激发学生的工程实践兴趣和勇于创新的精神，使学生的专业素质满足工程教育认证要求。化工专业的实践环节主要包括基础的四大化学实验、化工实验（化工原理实验、化工专业实验）、化工设计（化工单元设计、化工综合设计）、专业实习、双创训练、社会实践等。本专业从硬件和软件两个方面加强实践环节。硬件建设主要包括实验室平台维护、实践教学基地建设与维护。专业实习基地建设等方面。本专业正在积极申报“牡丹江师范学院中央财政支持地方高校改革发展资金2019年项目”，项目经费约120万元，用于建设“化学工程与工艺专业实验平台”。基于上述硬件平台，可以举办化工设计大赛、化工实验大赛、开展二课堂活动、创新创业活动等。软件建设是在实践教学计划和大纲的框架下，建立本专业实践教学过程与规范化的监察管理体系，加强对实践教学大纲与教学计划的实施力度，制定相对应的实践环节、方案以及管理规章制度，确保实践内容不走样、实践时间、实践场地及实践进程按部就班，相关责任细化到个人，使实践教学计划中规定的各个环节真正得到落实。

六　结语

牡丹江师范学院化学工程与工艺工程专业全体教师已深刻认识到工程认证的重要性，目前正在积极组织筹备工程认证的相关工作，坚持从专业建设工作入手，以专业认证标准为导向，健全工作体系，完善工作信标，将各指标落实于实际工作当中，对照认证内涵，积

（下转第22页）

(C)1994-2020 China Academic Journal Electronic Publishing House. All rights reserved.　http://www.cnki.net

冷凝器换热原理，设计了一种小型多通道蒸汽冷凝集液器，用于户外用集水及净水产品。顾鑫[9]等依据传热学相关知识，设计了有源滤波器户外散热装置，用于解决大热流密度下电子器件的散热。[10-14]

四　结论

综合利用校内实习平台开展学生实习，可以有效补充校外实习基地短板，达到高效实习目的。根据知识的难易程度及授课需要，针对不同年级学生多次开放房间空调器拆装平台，合理安排授课内容，有利于培养学生兴趣，提高学生创新创业能力。

参考文献

[1] 卢秀章. 本科高校专业实习存在问题及改革探索[J]. 高教学刊，2016(13):142-144.

[2] 马荷荷，张忠明，刘君. 改进高等工科院校生产实习工作的思考[J]. 高教学刊，2019(17):191-193.

[3] 马树军，王英蛟. 校内生产实习在“新工科”建设中的探索[J]. 科技创新导报，2018,15(17):195-197.

[4] 马斌，张雷，郭鹏，等. 基于校内汽车试验场搭建学科交叉教学实习平台模式初探[J]. 教育现代化，2019,6(26):106-107.

[5] 何水宁，王映华，张荣青，等. 燃料电池汽车供气系统[J]. 河南：CN207657807U,2018-07-27.

[6] 程艳晓，王凡，张军，等. 一种小型多通道蒸汽冷凝集液器[J]. 河南：CN208161305U,2018-11-30.

[7] 程艳晓，许培源，吴学红，等. 基于学业导师的创新型本科生阶梯式全历程培养模式的探索与实践[J]. 教育现代化，2019,6(52):1-246.

[8] 张金强，何水宁，王燕今，等. 一种有源滤波器稀释户外散热装置[P]. 河南省：CN208445008U,2019-01-29.

（上接第12页）

极进行本专业教育教学改革，调整培养计划，进行培养计划的整体设计，优化课程结构，加强教育实践，提高教师的工程实践水平，增强学生的团队精神训练，初步建立了“以学生为中心”、“以目标为导向”、“持续改进”的成果导向型人才培养新架构，希望在较短时间内通过工程教育专业认证，使本专业在更现范化的道路上不断发展，成为省级乃至国家级重点学科。

参考文献

[1] 郑答英，方岩雄，叶飞. 工程教育专业认证背景下的化学工程与工艺专业人才培养浅谈[J]. 广东化工，2016,43(333):188-189.

[2] 严云斌，陈彬，吴静娴，等. 工程教育专业认证背景下的化工专业工程教育培养机制探索[J]. 化工高等教育，2015,5:7-10.

[3] 戴炜珺，丁薇，赵蓉智，等. 专业认证背景下化学工程与工艺专业人才培养模式的探索[J]. 化工高等教育，2018,2:16-20.

[4] 朱佳妮，秦志宏，王月俭. 新工科背景下化工专业人才培养模式的探析[J]. 教育教学论坛，2018,6(24):217-218.

[5] 范方方，赵金和，刘其珍，等. 专业认证背景下创新型化工人才培养模式探索：山东化，2018,47:164-165.

（上接第10页）

给学生，从而提高学生的工程实践能力和创新能力。最后，有计划的选送青年教师到国外进行科研项目考察学习和交流访学，学习引进国外高水平院校的创新人才培养模式。总之，不管是引进的专职或兼职教师，还是培养的教师，可以有效地将他们自身的工程能力和经验，在教学过程中传递给学生，从而让学生在学习书本理论知识的同时，有效地提高动手能力和工程应用实践能力，从而培养学生的创新实践能力，保证创新型人才培养的顺利实施。

六　结语

培养科学基础厚、工程能力强、综合素质高的材料成型及控制工程人才，对于支撑服务以新技术、新业态、新产业、新模式为特点的新经济蓬勃发展具有十分重要的应用价值，也是新工科建设的必然要求和最终目标。因此，在新工科建设背景下，本项目提出创新培养模式，有利于材料成型及控制工程特色专业建设和人才培养，也对机械、汽车、电信、化工和计算机等工科专业创新培养模式的构建有一定的参考意义和应用价值。

参考文献

[1] 肖卓豪，李秀英，汪永进，等. 新工科背景下材料类本科专业认知体系建设初探[J]. 中国校外教育，2019(24):53-54.

[2] 史静，任东辉，李学平，等. “新工科”背景下工程能力创新型人才培养模式探究[J]. 科技视界，2018(14):41-42.

[3] 邵惠鹤，李春江，马晓君. 地方高校新工科人才创新创业能力培养模式研究[J]. 科技创业，2017(10):62-64.

[4] 史静，朱虹，段建东，等. 轮胎胎面磨耗和时间的全新发军——“新工科”模式对人才创新能力培养探究[J]. 教育与人才，2016(8):87-92.

[5] 李文秀，钟颖，于三三，等. 新工科背景下创新创业教育的实践探索[J]. 化工高等教育，2018(2):1-5.

[6] 林健. 新工科理念下的本硕博贯通功能材料课程体系建设思考[J]. 教育现代化，2019,6(45):19-21.

(C)1994-2020 China Academic Journal Electronic Publishing House. All rights reserved.　http://www.cnki.net

14.邢乐红,王宜鑫,左明辉.工程教育专业认证背景下化学工程与工艺专业学生实践能力培养研究[J].山东化工,2019,48(24):159-160.

DOI:10.19319/j.cnki.issn.1008-021x.2019.24.070

工程教育专业认证背景下化学工程与工艺专业学生实践能力培养研究

邢乐红*,王宜鑫,左明辉

(牡丹江师范学院 化学化工学院,黑龙江 牡丹江　157012)

摘要:实践教学是工程教育专业认证中的重要内容,是学生创新能力培养的基本保障。通过对实践教学中实验课程教学、专业实习、双创训练、二课堂活动等进行改革,学生的实验技能、创新能力和解决化工实际问题的能力得到了提高。

关键词:工程教育认证;化学工程与工艺专业;人才培养;实践能力

中图分类号:G642.0　　文献标识码:A　　文章编号:1008-021X(2019)24-0159-02

Exploration on the Practical Ability Cultivation of Chemical Engineering and Technology Specialty under the Engineering Education Accreditation

*Xing Lehong**, *Wang Yixin*, *Zuo Minghui*

(School of Chemistry and Chemical Engineering, Mudanjiang Normal University, Mudanjiang　157012, China)

Abstract: Practical teaching is an important content of the engineering education accreditation. Practical teaching is the important guarantee of students, innovation ability cultivation. Through reforms of practical teaching including experimental course teaching, professional practice, innovation and entrepreneurship training, the second class activity, the students, innovation and solving chemical engineering practical problems abilities have been enhanced.

Key words: engineering education accreditation; chemical engineering and technology specialty; talent cultivation; practical ability

工程教育专业认证是工程教育国际互认的基础,通过认证的专业所培养的毕业生获得的能力是等效的[1]。2006 年,我国高校的化学工程与工艺专业开始了工程教育专业认证的筹备工作。2007 年,清华大学和天津大学的化学工程与工艺专业按照国际标准要求,率先通过了工程教育专业认证。此后,中国石油大学、北京化工大学、大连理工大学、华东理工大学、浙江大学等大批高校的化学工程与工艺专业相继通过认证[2]。目前,越来越多的高校认识到工程认证的重要性,积极开展工程认证背景下的人才培养模式改革[3]。牡丹江师范学院化学工程与工艺专业于 2011 年开始招生,目前已有 5 届毕业生。本专业共有专任教师 6 人,其中具有博士学位教师 4 人,具有副高级职称教师 2 人,35 周岁以下青年教师 4 人,博士化率 66.7%。目前,本专业教师已充分认识到工程教育认证的重要性,积极开展相关的教育教学改革工作。

工程教育认证标准要求实践教学环节在人才培养方案中所占学分比例不少于总学分的 20%,是工程教育专业认证中的重要内容[4]。培养学生实践能力和创新能力是工程教育面临的主要问题之一。强化实践教学环节,规范学生实验操作技能,鼓励学生设计实验解决问题,支持学生参与科学研究,坚持实践教学与生产实际、社会实践相结合,对提高学生能力至关重要。这就要求在专业建设过程中要进一步深化实践教学改革,建立从实践中来、到实践中去和理论与实践紧密结合的高素质工程人才培养模式。本文以牡丹江师范学院化学工程与工艺专业为例,分析了工程教育专业认证背景下,化学工程与工艺专业学生实践能力培养的方法和措施。

1　实验课程教学

我校化学工程与工艺专业现开设的实验课程有,基础化学类实验课程(无机化学实验、有机化学实验、分析化学实验、物理化学实验)、化工专业类实验课程(化工原理实验、化工仿真实验、化工制图实验、化工综合实验)。在实验课程的教学工作中,首先要特别强调实验操作安全注意事项。基础化学类实验使用的药品有些具有毒性或强腐性,在实验项目的选择上,应尽量选择无毒安全,现象明显,对环境污染小的药品进行实验。对于有毒性或腐性蚀性药品要特别强调用法及注意事项,提高学生自我保护意识和安全生产意识。化工专业类实验常常会用到风机、泵等叶片式流体输送设备,要提醒学生将头发盘梳整理,以防卷入。塔设备在工作过程中需要加热,在数据记录时要小心不要烫伤等。在实验室安全教育之后,我们安排专门的实验室安全考试,考试成绩计入期末总成绩。经过以上措施,学生们的安全意识明显提高,安全生产的工程观念得到强化。

教学内容和教学方式方面,重视学生预习环节,由简单的上交实验报告,改变为由学生讲解实验目的、实验原理、教师针对实验目的和实验原理进行相关的提问,学生回答。教师发放课前预习小卷,学生回答小卷上的问题之后,才可以动手进行实验。实验步骤由学生结合预习的知识和现场实验装置对应之后,进行讲解,讲解基本合格的组,才可以做实验。通过上述改革之后,学生实验的主动性得到提高,实验课程教学效果明

收稿日期:2019-09-20

基金项目:牡丹江师范学院教学改革项目(19-XJ21008);牡丹江师范学院青年学术骨干项目(GG2018001);黑龙江省高校青年创新人才培养计划项目(UNPYSCT-2016108);黑龙江省教育教学改革项目(SJGY20190688)

作者简介:邢乐红(1983—),女,山东武城县人,博士,副教授,牡丹江师范学院化学工程与工艺专业负责人。

(C)1994-2020 China Academic Journal Electronic Publishing House. All rights reserved.　http://www.cnki.net

基础班。2019 年，我校 2016 级和 2017 级化学工程与工艺学生参加“欧贝尔”杯黑龙江省第二届大学生化工实验竞赛，获得省级二等奖两项。

2 专业实习

化工专业实习是化工专业实践教学中的重要环节，是学生初步了解化工生产实际情况的最直接有效的方式。我专业非常重视实习基地的建设与维护工作，目前我专业的实习基地主要有牡丹江吉控石油化工有限公司、内蒙古草卡生物科技有限公司、中节能香港有限公司黑龙江分公司、黑龙江省有色金属地质勘查七〇二队、北京八亿时空液晶科技股份有限公司。学生的实习时间为 2 至 3 个月，在实习期间，学生每天详细记录自己的实习情况和收获感想，形成实习日志，作为实习成绩评定的重要参考。学生实习期间的安全保障也是非常重要的。在实习开始之前，系主任会专门集中专业所有学生开实习动员会，会上主要强调实习期间的安全注意事项、工作纪律、成绩评定方法、实习材料撰写规范、常见问题等。通过专业实习，学生们普遍反映收获了很多生产实践知识，体会到了工作的辛苦和责任，为早日成为一名合格的工程师奠定了基础。

3 创新创业训练

创新创业训练是提高化工专业学生实践能力、培养工程观的重要手段。牡丹江师范学院化学工程与工艺专业非常重视学生创新创业工作。新生入学教育时，就鼓励学生关注大学生创新项目，学生一般会在大二、大三年级参加创新创业项目。目前，本专业每年都有若干学生主持或参加国家级和省级大学生创新项目。此外，我们还积极鼓励学生参加各级各类创新创业大赛。2018 年，我专业张秀彪等六名同学参加“全国高校商业精英挑战赛第八届创新创业竞赛全国总决赛”获得二等奖，指导教师蒋继贵获得优秀指导教师。金云鹏等四名同学参加了“2018 年黑龙江省互联网 + 大学生创新创业大赛”获得二等奖。

4 二课堂活动

第二课堂是第一课堂的基础上进行的课外学生科研活动，是学生科研能力增长的有效途径。在新生入学教育以及课下与学生交流的过程中发现，很多同学对科研有浓厚的兴趣，但如不知从何入手。我专业充分利用二课堂活动进行实验室开放，将教师个人科研项目中较为简单的部分交给本科生，作为他们的二课堂活动题目。将二课堂活动学生纳入课题组组会的讨论，让他们知道如何切入科研题目。充分发挥学生们的科研兴趣，参与到指导教师的科研活动中。实践发现，参与二课堂活动对学生大四毕业设计论文的顺利开展有促进作用。目前，我专业已有多名学生通过参加第二课堂活动成功发表了科研论文，为他们今后的工作和升学奠定了良好的基础。

5 结语

我校化学工程与工艺专业的工程认证工作已经在积极进行，全体专任教师正在积极组织准备工程认证的相关工作。实践教学环节的改革是建立“以学生为中心”“成果导向”型人才培养新架构的重要部分。本专业从实验课程教学、专业实习、双创训练、二课堂活动等入手进行实践教学环节教学改革，学生的实验技能、创新能力和解决化工实际问题的能力得到了提高。

参考文献

[1] 严宗诚，陈 韬，吴静娥，等. 工程教育专业认证背景下的化工专业工程教育的单机制探索 [J]. 化工高等教育，2015(5)：7－10.

[2] 张 芳，黄 芳，张慧东，等. 与工程教育专业认证接轨的应用型人才培养模式的研究与实践－以辽东学院化学工程与工艺专业为例 [J]. 山东化工，2015，44(17)：131－132.

[3] 朱佳媚，秦志宏，王丹伦. 新工科背景下化工专业人才培养模式的探析 [J]. 教育教学论坛，2018(26)：217－218.

[4] 王 雀，吴 熙，王 兵. 以课题制为核心的化工专业实习方式改革与实践 [J]. 化工高等教育，2018，36(2)：27－31.

（本文文献格式：邢乐红，王启鑫，左明辉. 工程教育专业认证背景下化学工程与工艺专业学生实践能力培养研究 [J]. 山东化工，2019，48(24)：159，160.）

（上接第 158 页）

似的。通过对滤液中的 (R) －A＋B 进行浓缩、真空干燥、中和、过滤、干燥等操作就可以得到 (R) －A。具体实验步骤如下：

(1) 将 rac－A(2.84g，10 mmol) 加入配有磁子的 100 mL 圆底烧瓶，加入 50 mL 丙酮，搅拌至溶解；

(2) 将 L－酒石酸 B(2.44g，10.5 mmol) 加入小单口瓶，向其中加入 30 mL 水，至全溶；

(3) 缓慢搅拌下，用一次性滴管将 L－酒石酸的水溶液缓慢滴加至 rac－A 的丙酮溶液，滴加结束以后，停止搅拌，静置 1 小时；

(4) 用砂芯漏斗抽滤，将列上层固体 1，用 20 mL 丙酮洗涤，将固体转移至小烧杯真空干燥；

(5) 滤液转入 250 mL 梨形瓶，旋蒸回收溶剂，瓶中剩余固体 2；

(6) 固体 1 和固体 2 分别加入 6 mL 二乙胺溶解，全部溶解以后，加入水使固体全部析出；

(7) 分别抽滤，将所得两个产品不能相互污染，将列 (S－A，1.39 g，产率 49%) 和 (R－A，1.34 g，产率 47%)，真空干燥，称重，计算产率。

(8) 用高效液相 (大赛赠手性柱 AD－H，流动相：正己烷/异丙醇 a 75/25，流速：1 mL/min，分别测试：S－A 和 (R－A 的 ee 值分别为 97% 和 99%。

以提高高校药学相关专业学生对手性药物相关知识的认知与理解，培养其手性拆分法操作技能为目的。本论文以一种经典的外消旋体拆分法－“联萘酚的手性拆分”作为教学素材，以 L－酒石酸为拆分剂，完成了对外消旋联萘二胺的拆分，两种对映体的产率 (ee 值) 分别为 49% (97%) 和 47% (99%)。该实验操作简便、现象及结论明确，适宜于作为实验实践教学参考素材。

参考文献

[1] 刘文强，李 莉. 手性药物及其中间体拆分方法的研究进展 [J]. 药学学报，2018，53(1)：37－46.

[2] 张来新，朱海云. 手性合成、手性拆分应分析分离科学及医药学中的应用 [J]. 合成材料老化与应用，2016，45(6)：102－105.

[3] Kenneth J. Brown, Matthew S. Berry, Joseph H. Murdoch. Synthesis of optically active 2,2′－dihalo－1,1′－binaphthyls via stable diazonium salts [J]. Journal of Organic Chemistry, 1983，50(22)：4345－4349.

[4] 陈光明，陈建敏，周长海. 手性联萘胺衍生物为配体的铜络合物催化下苯佐橡胺的不对称环丙烷化反应 [J]. 高等学校化学学报，1998，16(2)：216－219.

（本文文献格式：李 路，张志欣，王 涛. “联萘酚手性拆分”在药物合成实验教学中的应用 [J]. 山东化工，2019，48(24)：158，160.）

(C)1994-2020 China Academic Journal Electronic Publishing House. All rights reserved. http://www.cnki.net

15.贾林艳,左明辉,韩俊凤,陈玉锋,邵长斌.《物理化学实验》课程思政探索与实践[J].广州化工,2021,49(21):177-178+191.

《物理化学实验》课程思政探索与实践*

贾林艳，左明辉，韩俊凤，陈玉锋，邵长斌

（牡丹江师范学院化学化工学院，黑龙江 牡丹江 157011）

摘 要：为贯彻落实知识传授、能力培养、价值引领三位一体的课程目标，在物理化学实验教学中实施课程思政改革。本文详述了在实施课程思政的过程中，坚持以学生为中心，采用线上线下混合式教学模式，转变教育观念，建设课程思政团队，深入挖掘课程思政元素，探索思政元素融入教学中的方法及载体，促进学生思想道德水平和教学质量的提高，发挥专业课程在思政教育中的作用。

关键词：课程思政；物理化学实验；教学改革

中图分类号：G4 **文献标志码**：A **文章编号**：1001-9677(2021)021-0177-03

Practice of Course Ideology and Politics Education in Teaching Physical Chemistry Experiment*

JIA Lin-yan, ZUO Ming-hui, HAN Jun-feng, CHEN Yu-feng, SHAO Chang-bin
(College of Chemistry and Chemical Engineering, Mudanjiang Normal University, Heilongjiang Mudanjiang 157011, China)

Abstract: In order to carry out the course goal of imparting knowledge, cultivating ability and guiding value, ideology and politics innovation was put into Physical Chemistry experiment course. Setting up students-centered learning environment, the ideological and political reflection of curriculum education was explored, the combination of online and offline was studied, changing their teaching methods and integrating ideological and political elements with daily teaching. During Physical Chemistry experiment teaching, the methods can help promoting students' ideological and moral level, playing the role of professional courses in ideological and political education.

Key words: course ideology and politics; Physical Chemistry experiment; educational reform

课程思政是当前教育教学改革的重要内容之一。习近平总书记在全国高校思想政治工作会议上强调："要坚持把立德树人作为中心环节，把思想政治工作贯穿教育教学全过程，实现全程育人、全方位育人，努力开创我国高等教育事业发展新局面[1]。在总书记讲话精神的指引下，开启了我国高等学校课程思政改革建设的新局面，这就要求高校不仅要在思政课程上加强对学生的思想教育，还要坚持"大思政"的教育理念，充分发挥专业课程的思政教育作用，促进思政教育的改革发展。新时代要求我们回归教育的初心和本源，需要重视并重新定位专业课程的育人功能[2]，要把人才培养质量和效果放在首位，在工作中不能只谈"教学"，而是要脚踏实地关注"教育"。教师的根本任务是教书育人，可是在过去很长一段时间里，大部分专业课教师注重的是对学生专业知识的传授和技能培养，忽略了"育人"乃是所有教育工作者的神圣使命。

物理化学实验是高等学校开设的一门理论性、实践性和综合性很强的课程，在我校化学、应用化学、化学工程与工艺专业开设。该门课程运用物理化学的原理、技术和方法，通过实验操作和数据处理，使学生掌握基本原理、基本方法，加深对物理化学课程中理论、概念、原理的理解，培养学生理论联系实际的能力，提高分析问题和解决问题的能力，加强对学生的科研和创新能力的培养。传统教学中一般是教师讲解实验原理、实验过程，学生动手操作和数据处理，教师注重的是实验技能的培养，而没有重视对学生的思想道德教育和价值引领。当前互联网的飞速发展，各种网络信息和价值观影响着学生的思想，我们物理化学教学团队认真贯彻执行课程思政改革号召，在我校 2018 级物理化学实验课中进行课程思政探索实践，让学生通过课程的学习把知识技能上的"成长"和精神上的"成人"有机结合起来[3]。引导学生树立正确的人生观和世界观，做社会主义核心价值观的坚定信仰者、积极传播者和模范践行者。

1 思政团队建设

实施课程思政的关键是教师。"以教师为中心""以教为中心"的传统理念仍然根深蒂固，对课程思政理解不到位甚至偏颇[4]。这就需要教师首先要转变观念，提高自身的思政水平，充分发挥教师的积极性和主动性，坚持"教师主导，学生主体"的思想，不仅重视知识传授，更注重对学生进行德育教

* 基金项目：牡丹江师范学院教学改革项目(19-XJ21029，JK-20200140)；课程思政专项(KSCZ-2020033)。
第一作者：贾林艳(1971-)，女，博士，教授，主要从事物理化学教学和稀土材料研究。
(C)1994-2021 China Academic Journal Electronic Publishing House. All rights reserved. http://www.cnki.net

育，提高学生的思想道德水平和社会责任感。

1.1 理念转变 提升思政水平

为将课程思政落到实处，在原物理化学教学团队基础上建立物理化学课程思政团队，教师通过参加学校和学院组织的各类课程思政培训，深入学习体会课程思政建设的基本思想，转变教育观念，积极与思政课老师合作进行教学研究，努力学习辩证唯物主义、马克思主义基本原理，习近平新时代中国特色社会主义思想等，以此提高教师自身思想政治水平。

1.2 协作分工

根据人才培养方案，物理化学实验共开设 16 个实验，结合每个团队成员教师的优势，细化课程思政工作，将每个实验落实到人，深入挖掘思政元素，同时再进行集体备课，优化教学案例，修改完善教学大纲，探索课程思政在物理化学实验课中实施的形式和方法。在此基础上，团队成功申报校级物理化学（含实验）课程思政教学改革项目。

2 思政元素挖掘

课程思政不是简单的“课程+思政”，需要根据课程内容找出适宜思政元素，以适宜方式将其融入课程中。所以，思政元素的挖掘对课程思政实施的效果起关键作用。

2.1 辩证唯物主义认识论

化学是一门实验学科，物理化学的研究遵循一般的科学研究方法，“实践—认识—再实践—再认识”的过程，这就是辩证唯物主义的认识论，学生通过物理化学实验验证抽象深奥的理论，加深对理论知识的掌握，而理论的理解和应用又进一步激发了学生利用实验探索未知的勇气和信心，例如在饱和蒸气压测定实验中，学生通过测定不同温度下乙醇的饱和蒸气压，受深入理解了 Clausius-Clapeyron 方程、掌握沸点、饱和蒸气压、摩尔汽化热等概念；而且通过该实验单一反三，对可逆相变、相平衡、相变热都有更深的理解。

2.2 诚信求实，尊重科学

与其他基础实验相比，物理化学实验原理深奥、操作复杂、数据处理繁琐，所以实验结果往往与标准值产生很大的偏差甚至失败。如何对待实验失败，有些同学为了实验结果看起来“更好看”，甚至会编造实验数据，也有些同学会对实验失去兴趣，在这过程中，教师要及时发现问题，帮助找出失败的原因，探索误差的来源及减小或消除方法，注重对学生诚心求实，科学严谨、实事求是的科学作风的培养，建立良好的职业道德和社会责任感，同时给学生讲一些近年来国内外学术不端与造假丑闻事件，使学生从心底产生尊重科学、崇尚科学的意识，无论将来从事科学研究还是其他方面的工作，都应遵守诚心求实的科学作风。

2.3 爱国主义教育

爱国主义是社会主义核心价值观的重要内容之一，也是课程思政必不可少的元素。“科学是没有国界的，但科学家是有祖国的”。这是挂在我校实验室走廊的宣传版画内容。教学中根据实验相关内容通过实验拓展等项目融入科学家的爱国精神，不仅增强实验的趣味性而且使相关内容记忆理解深刻。例如界面移动法测定离子迁移数的实验[3]，我国著名物理化学家黄子卿在南京师范大学领导创新实行“体外测量对界面移动法测定离子迁移数的准确度的影响，并对实验装置做出改进，提高了测定的准确度并且发表了论文。同时还对他在其他方面的伟大成就进行介绍，如热力学温标水的三项点的测定值。国际上以此为标准确定绝对零度为 273.15K。科学家追求真理、精益求精的科学精神和爱国情怀，激发学生刻苦学习、努力钻研，立志为国家的发展贡献自己的力量。

2.4 节约能源，保护环境

电极制备及电池电动势的测定是一个经典的物理化学实验，电池在日常生活、工农业生产、航空航天各领域均有重要应用，所以对高性能电池的开发研究具有重要的理论意义和研究价值。课前布置学生查找关于电池的相关文献，了解电池的种类、发展历史及应用领域和电池材料的研究前沿，使学生意识到能源开发和节约能源的重要意义，平时学习生活中注意节约水电，深刻领悟“绿水青山就是金山银山”道理。实验中制备锌汞齐电极需用的硝酸亚汞溶液，学生认识到硝酸亚汞废液及擦拭电极后的棉花酸意去弃可能对环境造成的危害，了解含重金属废液的处理方法，增强环保意识。

2.5 团结协作，互助共赢

当今社会若想取得大的成绩仅凭个人的努力是无法完成的，需要团队合作。集体的力量，而学生中大部分是独生子女，家庭中的“小皇帝”，不善于与人沟通交流，缺乏合作意识，为了培养学生们的团结协作精神，在授课过程中有目的性培养这种能力，如针对设计性实验，采取分组形式共同完成文献检索、小组成员互相商量完成实验方案设计、实验过程要分工协作，遇到问题要共同探索解决，这样一个过程，不仅使学生分析问题解决问题的能力提高，而且使他们认识到团结协作在工作中的重要性。

3 思政元素融入方式

思政元素不能生硬、突兀引入课堂教学中，否则会起到相反效果，与教学内容有机地融合，自然展开，才容易引发学生的情感共鸣，达到预期的教育效果[4]。

首先，要充分发挥课堂的主渠道承载的立德树人的功能，使学生潜移默化地接受思政教育。教师结合课程教学内容寻找思想政治教育的融入点，秉承“润物细无声”的原则将思政教育潜移默化地充实到专业课程教学过程中。这就需要课程教师深入挖掘课程蕴含的思政教育资源，明确蕴含的正确世界观、人生观、价值观与职业道德等思政内容，在学生掌握物理化学的发展趋势、基本知识等基础上渗透辩证唯物主义和社会主义核心价值观等相关思政教育内容。

其次，课程思政不能仅仅局限于课堂上，物理化学实验日前采用混合式教学方式，注重学生课前和课后线上的学习，为此，我们针对实验内容布置相应的讨论题，以小组形式讨论完成报文，充分利用连带式在讨论题目中溶入课程思政内容，例如在学习双液系相图实验中，布置题目为“生活在极地地区的爱斯基摩人为什么在每年特定时间通过取同冰融化能够得到淡水呢？利用相图知识作出解释”。这样的问题一定会引起学生的好奇心，探知问题答案。经过课堂上实验完成异丙醇—环己烷双液系相图的绘制和课后问题的解答，可以使学生认识到实践是理论之源，是检验真理的唯一标准，理论与实践是相互促进的。

4 结 语

在物理化学实验教学中进行课程思政的初步探索，从教师转变观念着手，深入理解课程思政的重要性，深入挖掘思政元素，突出课程思政价值引领作用，我们总结完善切合的融入方式，将思政元素与课程内容有机融合，切实落实“全面育人”的方针政策。

（下转第 191 页）

1.5 从“抗疟药物分析”这一章加强学生对中国、中医药的认同感

说到抗疟药，必须讲到青蒿素及其衍生物，也必然引申到其结构的改造与质量控制。通过诺贝尔获得者屠呦呦如何从《肘后备急方》中发现青蒿素的提取方法，激发学生对中药宝库研发的探索热情及严谨的探究思路。

2 融入思政元素的方式与途径

当今，是互联网的时代，信息技术飞速发展的时代，高校的教学工作当然少不了对这些技术的使用与融入[5]，从之前多媒体、PPT 对课堂教学的成功改革，到现今超星技术、雨课堂技术的变革，微信公众号的发展，都极大地影响着教与学的课堂。

2.1 持续使用多媒体，利用雨课堂、录播教室功能，灵活优化教学方式

本课程践行“课程思政”已有两年的时间，参加过学校组织的教学比赛，已建立每堂课的视频，通过课程网站，学生可以自行反复学习与感悟。通过线下教学，将典型教学案例、比赛成果做到线下课堂，结合雨课堂功能，学生通过弹幕、做题等方式参与其中，一方面培养了学生对教师的尝切感与崇拜感（《荀子》讲“国将兴，必贵师而重傅，贵师重傅则法度存。”我国古代第一本教育专著的古训《学记》提到“宗其师信其道”。而教师也可以及时了解学生的动态，所思所想，加强了师生互动，拉近了师生间的距离。另一方面，雨课堂的直播与录播功能，学生可以课后反复学习与回味。

2.2 利用微信公众号建立第二课堂，将课程思政元素延伸

目前，建立了“CTGU 生物医药之家”微信公众平台，对药学事件的报道、实验室安全、科学研究探讨，中国优秀文化学习等方面进行发布，每周更新。既有客观的现实社会题材，也有师生的学习过程与心得，在很大程度上，提升了学生的自信心，表达能力，强化了师生间的情谊，每周一次的课题组会，都会有文化方面的习得，这是在课程教学当中不能实现的，而在第二课堂中，其学习内容与方式却变得灵活、多样，中国优秀传统文化中蕴含着大量“为人做事”的道理，在较高频率的课题组会学习中，学生在不知不觉中受到熏陶与感染，心态变得阳光、向上、向善，而组会后的习得与总结，会发布在公众号上，去影响更多的人。

3 结 语

本课程要求“要用好课堂教学这个主渠道”、“守好一段渠、种好责任田”的精神作风，采用多样化教学方法与授课形式，在各章节中充分挖掘、融入思想政治与道德情怀，以树立学生在制药行业的神圣使命感与荣誉感，增强学生对中华医药宝库的高度认可和探究热情，建立学生强烈的法律意识与社会责任意识，满足学生成长发展需求和期待[6]，与思想政治理论课同向同行，形成协同效应[7]。

运用中华优秀传统文化充实专业课程的“课程思政”[7]，并体现在学生每天都要使用的教材中，通过第二课堂的延伸，能够调物无声地提高学生的思想道德水平，潜移默化地传承我国优秀传统文化，因此具有重要意义。

所以要坚持育人导向，以“学生发展为中心”，在各教学环节，借用各方面的育人资源和育人力量，推动知识传授、能力培养与理想信念、价值理念、道德观念的教育有机结合，使思想政治工作体系贯通学科体系、教学体系、教材体系、管理体系，把我们的特色和优势有效转化为培养社会主义建设者和接班人的能力。

参考文献

[1] 李梅，李疆平．习近平德育思想探究[J]．思想理论教育导刊，2018（04）：20-24.

[2] 教育部办公厅《关于开展“三全育人”综合改革试点工作的通知》教思政厅函〔2018〕15 号[S]．2018-5-25.

[3] 国家药典委员会．中华人民共和国药典[M]．北京：中国医药科技出版社，2020.

[4] 何玉海．关于“课程思政”的本质内涵与实现路径的探索[J]．思想理论教育导刊，2019（10）：130-134.

[5] 张玉．运用中华优秀传统文化充实教材“课程思政”内容浅议[J]．新闻传播，2020（1）：77-79.

[6] 杨磊．从“思政课程”到“课程思政”的转变路径研究[J]．德育研究，2019（4）：22-25.

[7] 张烁．习近平在全国高校思想政治工作会议上强调 把思想政治工作贯穿教育教学全过程开创我国高等教育事业发展新局面[N]．人民日报，2016-12-09.

（上接第 178 页）

参考文献

[1] 习近平．全国高校思想政治工作会议上的讲话．http://www.xinhuanet.com//politics/2016-12/08.

[2] 张树永．高校化学类专业课程思政建设目标与实现途径刍议[J]．大学化学，2019，34（11）：4-9.

[3] 张进，刘利，姚思童．物理化学 MOOC 课程思政探索与实践[J]．大学化学，2021，36（X）：2010076/1-6.

[4] 王旭珍，王新平，王新荣，等．大道至简，润物无声—物理化学课程思政的实践[J]．大学化学，2019，34（11）：77-81.

[5] 孙文生，杨慕星．物理化学实验[M]．北京：高等教育出版社，2014：124-127.

(C)1994-2021 China Academic Journal Electronic Publishing House. All rights reserved. http://www.cnki.net

指导大学生创新创业项目目录
（共 66 项）

1.变废为宝：木耳菌糠有机化处理

黑龙江省大学生创新创业项目创新项目　　负责人：党文浩　李玉竹

2 东北地区土壤综合治理及应用

黑龙江省大学生创新创业项目创新项目　　负责人：董惠敏

3.白光 **LED** 用稀土发光材料的制备及颜色调控研究

黑龙江省大学生创新创业项目创新项目　　负责人：付玛　周爽

4.可用于污染物检测的金属锌配位聚合物光致变色材料的合成

黑龙江省大学生创新创业项目创新项目　　负责人：郭晓曼　孙紫月

5.生物炭的制备及其对 Bi_2WO_6 光催化剂改性研究

黑龙江省大学生创新创业项目创新项目　　负责人：姜鑫宇

6.钨酸铋及其复合光催化剂的制备和催化性能研究

黑龙江省大学生创新创业项目创新项目　　负责人：焦晶楠　沈勇

7.薄荷精油提取工艺的研究

黑龙江省大学生创新创业项目创新项目　　负责人：李敬怡　刘越

8.电沉积法制备镍基/生物炭复合电极耐蚀性能研究

牡丹江师范学院大学生创新创新项目　　负责人：　雒炜轩

9.金属离子催化的烷烃 **C-H** 键活化的理论探究

牡丹江师范学院大学生创新创新项目　　负责人：马艺嘉　刘晗

10.钢表面 **TD/SNC** 法热处理扩渗

牡丹江师范学院大学生创新创新项目　　负责人：马宇航

11.食品中常见人工合成甜味剂的检测技术研究

牡丹江师范学院大学生创新创新项目　　负责人：欧美怡 孙雨桐

12.聚苯胺重防腐涂料创业项目

牡丹江师范学院大学生创新创业项目　　负责人：吴远江 魏敏

13.废润滑油净化再生用静电吸附装置的研究

牡丹江师范学院大学生创新创业项目　　负责人：张佳璐

14.VOCs 环境污染中甲苯消除的研究

牡丹江师范学院大学生创新创新项目　　负责人：张悦

15.负载型二氧化钛的制备及污水处理光催化性能研究

黑龙江省大学生创新创业项目创新项目　　负责人：高红爽

16.臭氧鼓泡塔反应器内构件优化

黑龙江省大学生创新创业项目创新项目　　负责人：姜鹤

17.具有磁性和污染物检测双功能金属铜配合物的合成

黑龙江省大学生创新创业项目创新项目　　负责人：李彩云

18.以空心微珠为载体的纳米光催化剂的研发及宏量制备

黑龙江省大学生创新创业项目创新项目　　负责人：吕月珩

19.苯丙胺类违禁化学品拉曼光谱的密度泛函理论研究

黑龙江省大学生创新创业项目创新项目　　负责人：苏鑫

20.黄芪、丹参中药用成分的薄层色谱法提取分离测定

黑龙江省大学生创新创业项目创新项目　　负责人：陶蕊 周鹤淇

21.一种新型水性带锈转锈涂料的研发

黑龙江省大学生创新创业项目创新项目　　负责人：魏敏

22.改性氯氧化铋光催化剂的制备及性能研究

黑龙江省大学生创新创业项目创新项目　　负责人：徐佳鑫

23.黑龙江地区常见食用菌中胶原蛋白的提取

黑龙江省大学生创新创业项目创新项目　　负责人：张萌　郭朝阳

24. 耐水阻燃材料的制备与研究

黑龙江省大学生创新创业项目创新项目　　负责人：张宇

25. 烯烃与非化学计量分子的设计组装

黑龙江省大学生创新创业项目创新项目　　负责人：陈雪萌

26. 东北常见中药材中抗病毒成分的研究

黑龙江省大学生创新创业项目创新项目　　负责人：董鹏飞　刘越

27.电镀工艺对镍电极析氢性能影响研究

黑龙江省大学生创新创业项目创新项目　　负责人：董瑞

28.复杂基体中添加剂的高通量筛查及快速检测技术研究

黑龙江省大学生创新创业项目创新项目　　负责人：董芷蔓

29.环保型脲醛树脂的耐水性的改进研究

黑龙江省大学生创新创业项目创新项目　　负责人：付文惠　高阳

30.双极微弧氧化反应陶瓷膜层高温氧化性能研究

黑龙江省大学生创新创业项目创新项目　　负责人：范云龙

31.稀土掺杂氧化锌复合粉体的制备及光催化性能研究

黑龙江省大学生创新创业项目创新项目　　负责人：李红晶

32.金属铜化合物的制备及性能研究

黑龙江省大学生创新创业项目创新项目　　负责人：刘鸿雁

33.铜催化碳-碳键断裂及重组反应的机理研究

黑龙江省大学生创新创业项目创新项目　　负责人：罗红欣 李可忠

34.生物质基纳米复合材料在电化学传感器中的应用

黑龙江省大学生创新创业项目创新项目　　负责人：那博语

35.几种药物分子的 **SERS** 检测和理论研究

黑龙江省大学生创新创业项目创新项目　　负责人：倪佳瑶

36.基于含氮杂环配体的金属铜配合物的合成、磁性及生物活性研究

黑龙江省大学生创新创业项目创新项目　　负责人：茹莉莹

37.导电填料用纳米粉体的制备及其改性研究

黑龙江省大学生创新创业项目创新项目　　负责人：宋田园

38.基于“互联网＋”技术设计分析关药道地药材中抗癌活性成分的研究

黑龙江省大学生创新创业项目创新项目　　负责人：王悦 丁崇洪

39.二元三原子非金属计量分子与硼簇的设计组装

黑龙江省大学生创新创业项目创新项目　　负责人：王小倩

40.普鲁卡因药物-金属相互作用及其表面增强拉曼光谱的研究

黑龙江省大学生创新创业项目创新项目　　负责人：徐鑫

41.化妆品中重金属含量测定研究

黑龙江省大学生创新创业项目创新项目　　负责人：张宏玉

42.教育兴农-农村师范生教育教学技能-体化培养训练

黑龙江省大学生创新创业项目创新项目　　负责人：张月影 张艺

43.丙烷选择氧化制丙烯酸尾气中 **CO** 选择性脱除催化剂创业项目

黑龙江省大学生创新创业项目创业项目　　负责人：周启

44.金属掺杂富硼团簇的设计组装

黑龙江省大学生创新创业项目创新项目　　负责人：才洪雪

45.高灵敏 **SERS** 基底的制备及苏丹红的检测

黑龙江省大学生创新创业项目创新项目　　负责人：黄康乐

46.互联网＋背景下的大学生活动平台创新研究

黑龙江省大学生创新创业项目创新项目　　负责人：刘方鑫

47.吡虫啉表面增强拉曼光谱的研究

黑龙江省大学生创新创业项目创新项目　　负责人：潘佳琦

48.大学生教育教学实践能力创新训练

黑龙江省大学生创新创业项目创新项目　　负责人：孙晓春 何春雨

49.铋系含氧酸盐光催化剂的制备及改性研究

黑龙江省大学生创新创业项目创新项目　　负责人：谭鑫

50.水性汽车内饰胶粘剂创业项目

黑龙江省大学生创新创业项目创业项目　　负责人:于文卓 于泓

51.颜色可调控稀土掺杂荧光粉的制备及发光性能研究

黑龙江省大学生创新创业项目创新项目　　负责人：于文卓

52.金属卡宾催化碳碳形成机理理论研究

黑龙江省大学生创新创业项目创新项目　　负责人：张洪梅

53.磁性-生物活性双功能金属钴配合物分子材料的合成及性能研究

黑龙江省大学生创新创业项目创新项目　　负责人：赵一伦 唐怡

54.室温自交联木器拼板胶黏剂的研究开发

牡丹江师范学院大学生创新创业项目　　负责人：马悦

55.以空心微珠为载体的纳米光催化剂在自然光下性能研究

牡丹江师范学院大学生创新创业项目　　负责人:李欢欢

56.磁性-生物活性双功能金属镍配合物分子材料的合成及性能研究

黑龙江省大学生创新创业项目创新项目　　负责人：包双

57.铜催化碳碳形成机理理论研究

黑龙江省大学生创新创业项目创新项目　　负责人：张莹

58.新生态工艺生产环氧氯丙烷的工厂设计

黑龙江省大学生创新创业项目创业项目　　负责人:崔熙麟 罗坚

59.几种食品中添加剂含量的测定

黑龙江省大学生创新创业项目创新项目　　负责人:李晓龙 马幸玉

60.功能纳米材料的合成及其在电分析化学中的应用

黑龙江省大学生创新创业项目创新项目　　负责人：李自翔

61.改性铋系半导体光催化剂的制备及其性能研究

黑龙江省大学生创新创业项目创新项目　　负责人:刘同福

62.金银合金纳米粒子 **SERS** 基底的制备及非法食品添加剂检测研究

黑龙江省大学生创新创业项目创新项目　　负责人：王晓花

63.西玛津农药表面增强拉曼光谱的研究

黑龙江省大学生创新创业项目创新项目　　负责人：王宜鑫

64.清洁燃料油的研制与生产

黑龙江省大学生创新创业项目创业项目　　负责人:吴晗

65.金属杂化介孔材料制备及苯酚羟基化反应产物的反相高效液相色谱分析研究

黑龙江省大学生创新创业项目创新项目　　负责人：吴兆宇

66.连铸机结晶器表面电铸镍铁合金研究

牡丹江师范学院大学生创新创业项目　　负责人：王海鹏

2021 年大学生创新创业项目目录（14 项）

1.变废为宝：木耳菌糠有机化处理

黑龙江省大学生创新创业项目创新项目　　负责人：党文浩　李玉竹

2 东北地区土壤综合治理及应用

黑龙江省大学生创新创业项目创新项目　　负责人：董惠敏

3.白光 **LED** 用稀土发光材料的制备及颜色调控研究

黑龙江省大学生创新创业项目创新项目　　负责人：付玛　周爽

4.可用于污染物检测的金属锌配位聚合物光致变色材料的合成

黑龙江省大学生创新创业项目创新项目　　负责人：郭晓曼　孙紫月

5.生物炭的制备及其对 Bi_2WO_6 光催化剂改性研究

黑龙江省大学生创新创业项目创新项目　　负责人：姜鑫宇

6.钨酸铋及其复合光催化剂的制备和催化性能研究

黑龙江省大学生创新创业项目创新项目　　负责人：焦晶楠　沈勇

7.薄荷精油提取工艺的研究

黑龙江省大学生创新创业项目创新项目　　负责人：李敬怡　刘越

8.电沉积法制备镍基/生物炭复合电极耐蚀性能研究

牡丹江师范学院大学生创新创新项目　　负责人：　雒炜轩

9.金属离子催化的烷烃 **C-H** 键活化的理论探究

牡丹江师范学院大学生创新创新项目　　负责人：马艺嘉　刘晗

10.钢表面 **TD/SNC** 法热处理扩渗

牡丹江师范学院大学生创新创新项目　　负责人：马宇航

11.食品中常见人工合成甜味剂的检测技术研究

牡丹江师范学院大学生创新创新项目　　负责人：欧美怡　孙雨桐

12.聚苯胺重防腐涂料创业项目

牡丹江师范学院大学生创新创业项目　　负责人：吴远江　魏敏

13.废润滑油净化再生用静电吸附装置的研究

牡丹江师范学院大学生创新创业项目　　负责人：张佳璐

14.VOCs 环境污染中甲苯消除的研究

牡丹江师范学院大学生创新创新项目　　负责人：张悦

1.变废为宝：木耳菌糠有机化处理

黑龙江省大学生创新创业项目创新项目　　负责人：党文浩 李玉竹

项目编号：

黑龙江省大学生创新创业训练计划项目
立项申请书

所属高校（盖章）：

项目名称：变废为宝：木耳菌糠有机化处理

项目类别　☑创新训练　□创业训练

负 责 人：党文浩、李玉竹

所属学科：化　学

起止时间：2020.06-2021.06

项目经费：10000.00 元

填表日期：2021 年 6 月 14 日

黑龙江省教育厅制

2 东北地区土壤综合治理及应用

黑龙江省大学生创新创业项目创新项目　　负责人：董惠敏

项目编号：

黑龙江省大学生创新创业训练计划项目
立项申请书

所属高校（盖章）：牡丹江师范学院

项目名称：东北地区土壤综合治理及应用

项目类别　✓创新训练　□创业训练

负 责 人：董惠敏

所属学科：化　学

起止时间：2021.06-2022.06

项目经费：10000.00 元

填表日期：2021.06.13

黑龙江省教育厅制

3.白光 LED 用稀土发光材料的制备及颜色调控研究

黑龙江省大学生创新创业项目创新项目　　负责人：付玛 周爽

附件 1：

项目编号：_____

黑龙江省大学生创新创业训练计划项目
立项申请书

所属高校（盖章）：牡丹江师范学院

项目名称：白光 LED 用稀土发光材料的制备及颜色调控研究

项目类别　☑创新训练　□创业训练

负 责 人：付玛　周爽

所属学科：化　学

起止时间：2021. 6——2022. 12

项目经费：1.0 万元

填表日期：2021 年 6 月 10 日

黑龙江省教育厅制

4.可用于污染物检测的金属锌配位聚合物光致变色材料的合成

黑龙江省大学生创新创业项目创新项目　　负责人：郭晓曼 孙紫月

附件 1：

项目编号：_____

黑龙江省大学生创新创业训练计划项目
立项申请书

所属高校（盖章）：牡丹江师范学院

项目名称：可用于污染物检测的金属锌配位聚合物光致变色材料的合成

项目类别　√创新训练　□创业训练

负 责 人：郭晓曼 孙紫月

所属学科：化学

起止时间：2021.9-2022.9

项目经费：1 万元

填表日期：2021.6.15

黑龙江省教育厅制

5.生物炭的制备及其对 Bi_2WO_6 光催化剂改性研究

黑龙江省大学生创新创业项目创新项目　　负责人：姜鑫宇

项目编号：_____

黑龙江省大学生创新创业训练计划项目
立项申请书

所属高校（盖章）：牡丹江师范学院

项目名称：生物炭的制备及其对 Bi_2WO_6 光催化剂改性研究

项目类别　☑创新训练　□创业训练

负 责 人：姜鑫宇

所属学科：化学

起止时间：2021 年 6 月-2022 年 12 月

项目经费：1 万元

填表日期：2021 年 6 月 10 日

黑龙江省教育厅制

6.钨酸铋及其复合光催化剂的制备和催化性能研究

黑龙江省大学生创新创业项目创新项目　　负责人：焦晶楠 沈勇

附件 1：

项目编号：_____

黑龙江省大学生创新创业训练计划项目
立项申请书

所属高校（盖章）：牡丹江师范学院

项目名称：钨酸铋及其复合光催化剂的制备和催化性能研究

项目类别　☑创新训练　□创业训练

负 责 人：焦晶楠　沈勇

指导教师：邵艳秋

所属学科：化学

起止时间：2021 年 6 月-2023 年 6 月

项目经费：1 万元

填表日期：2021.06.15

黑龙江省教育厅制

7.薄荷精油提取工艺的研究

黑龙江省大学生创新创业项目创新项目　　负责人：李敬怡 刘越

项目编号：

黑龙江省大学生创新创业训练计划项目
立项申请书

所属高校（盖章）：牡丹江师范学院

项目名称：薄荷精油提取工艺的研究

项目类别　✓创新训练　□创业训练

负 责 人：李敬怡、刘越

所属学科：化　学

起止时间：2021.06-2022.06

项目经费：10000.00 元

填表日期：2021.06.13

黑龙江省教育厅制

8.电沉积法制备镍基/生物炭复合电极耐蚀性能研究

牡丹江师范学院大学生创新创新项目　　负责人：雒炜轩

附件 1：

项目编号：_____

黑龙江省大学生创新创业训练计划项目
立项申请书

所属高校（盖章）：牡丹江师范学院

项目名称：电沉积法制备镍基/生物炭复合电极耐蚀性能研究

项目类别　☑创新训练　□创业训练

负 责 人：雒炜轩

所属学科：化学工程与工艺

起止时间：2021.6-2022.6

项目经费：5000 元

填表日期：2021.6.11

黑龙江省教育厅制

9.金属离子催化的烷烃 C-H 键活化的理论探究

牡丹江师范学院大学生创新创新项目　　负责人：马艺嘉 刘晗

附件 1：

项目编号：_____

黑龙江省大学生创新创业训练计划项目
立项申请书

所属高校（盖章）：牡丹江师范学院

项目名称：金属离子催化的烷烃 C-H 键活化的理论探究

项目类别　☑创新训练　□创业训练

负 责 人：马艺嘉　刘晗

所属学科：化学

起止时间：2021 年 6 月-2022 年 6 月

项目经费：1 万

填表日期：2021 年 6 月 15 日

黑龙江省教育厅制

10.钢表面 TD/SNC 法热处理扩渗

牡丹江师范学院大学生创新创新项目　　负责人：马宇航

附件 1：

项目编号：_____

黑龙江省大学生创新创业训练计划项目
立项申请书

所属高校（盖章）：化学化工学院

项目名称：钢表面 TD/SNC 法热处理扩渗

项目类别　☑创新训练　□创业训练

负 责 人：马宇航

所属学科：化学工程与工艺

起止时间：

项目经费：一万

填表日期：2021.06

黑龙江省教育厅制

11.食品中常见人工合成甜味剂的检测技术研究

牡丹江师范学院大学生创新创新项目　　负责人：欧美怡　孙雨桐

附件 1：

项目编号：_____

黑龙江省大学生创新创业训练计划项目
立项申请书

所属高校（盖章）：牡丹江师范学院

项目名称：食品中常见人工合成甜味剂的检测技术研究

项目类别　☑创新训练　□创业训练

负 责 人：欧美怡　孙雨桐

所属学科：化学

起止时间：2021.06-2022.06

项目经费：0.5 万

填表日期：2021.06.16

黑龙江省教育厅制

12.聚苯胺重防腐涂料创业项目

牡丹江师范学院大学生创新创业项目　　负责人：吴远江 魏敏

附件 2：

项目编号：_____

黑龙江省大学生创业实践项目
立项申请书

所属高校（盖章）：牡丹江师范学院

项目名称：聚苯胺重防腐涂料创业项目

项目类别：创业实践

负 责 人：吴远江，魏敏

所属学科：化学

起止时间：2021.06-2023.06

项目经费：5 万

填表日期：2021 年 6 月 15 日

黑龙江省教育厅制

13.废润滑油净化再生用静电吸附装置的研究

牡丹江师范学院大学生创新创业项目　　负责人：张佳璐

附件 1：

项目编号：_____

黑龙江省大学生创新创业训练计划项目
立项申请书

所属高校（盖章）：牡丹江师范学院

项目名称：废润滑油净化再生用静电吸附装置的研究

项目类别　□创新训练　☑创业训练

负 责 人：张佳璐

所属学科：化学

起止时间：2021.07-2022.07

项目经费：3万

填表日期：2021.6

黑龙江省教育厅制

14.VOCs 环境污染中甲苯消除的研究

牡丹江师范学院大学生创新创新项目　　负责人：张悦

项目编号：_____

黑龙江省大学生创新创业训练计划项目
立项申请书

所属高校（盖章）：牡丹江师范学院

项目名称：VOCs 环境污染中甲苯消除的研究

项目类别　☑创新训练　□创业训练

负 责 人：张悦

所属学科：化学

起止时间：2021.07-2022.07

项目经费：0.5 万

填表日期：2021 年 06

黑龙江省教育厅制

2020 年大学生创新创业项目
目录（15 项）

1. 负载型二氧化钛的制备及污水处理光催化性能研究

黑龙江省大学生创新创业项目创新项目　　负责人：高红爽

2. 臭氧鼓泡塔反应器内构件优化

黑龙江省大学生创新创业项目创新项目　　负责人：姜鹤

3. 具有磁性和污染物检测双功能金属铜配合物的合成

黑龙江省大学生创新创业项目创新项目　　负责人：李彩云

4. 以空心微珠为载体的纳米光催化剂的研发及宏量制备

黑龙江省大学生创新创业项目创新项目　　负责人：吕月珩

5. 苯丙胺类违禁化学品拉曼光谱的密度泛函理论研究

黑龙江省大学生创新创业项目创新项目　　负责人：苏鑫

6. 黄芪、丹参中药用成分的薄层色谱法提取分离测定

黑龙江省大学生创新创业项目创新项目　　负责人：陶蕊 周鹤淇

7. 一种新型水性带锈转锈涂料的研发

黑龙江省大学生创新创业项目创新项目　　负责人：魏敏

8. 改性氯氧化铋光催化剂的制备及性能研究

黑龙江省大学生创新创业项目创新项目　　负责人：徐佳鑫

9. 黑龙江地区常见食用菌中胶原蛋白的提取

黑龙江省大学生创新创业项目创新项目　　负责人：张萌 郭朝阳

10. 耐水阻燃材料的制备与研究

黑龙江省大学生创新创业项目创新项目　　负责人：张宇

11. 烯烃与非化学计量分子的设计组装

黑龙江省大学生创新创业项目创新项目　　负责人：陈雪萌

12. 东北常见中药材中抗病毒成分的研究

黑龙江省大学生创新创业项目创新项目　　负责人：董鹏飞 刘越

13. 50.电镀工艺对镍电极析氢性能影响研究

黑龙江省大学生创新创业项目创新项目　　负责人：董瑞

14. 51.复杂基体中添加剂的高通量筛查及快速检测技术研究

黑龙江省大学生创新创业项目创新项目　　负责人：董芷蔓

15. 环保型脲醛树脂的耐水性的改进研究

黑龙江省大学生创新创业项目创新项目　　负责人：付文惠 高阳

1.负载型二氧化钛的制备及污水处理光催化性能研究

黑龙江省大学生创新创业项目创新项目　　负责人：高红爽

附件 1：

项目编号：_____

黑龙江省大学生创新创业训练计划项目
立项申请书

所属高校（盖章）：牡丹江师范学院

项目名称：负载型二氧化钛的制备及污水处理光催化性能研究

项目类别　☑创新训练　□创业训练

负 责 人：高红爽

所属学科：化　学

起止时间：2020. 5——2021. 5

项目经费：1.0 万元

填表日期：2020 年 5 月 10 日

黑龙江省教育厅制

2.臭氧鼓泡塔反应器内构件优化

黑龙江省大学生创新创业项目创新项目　　负责人：姜鹤

附件 1：

项目编号：_____

黑龙江省大学生创新创业训练计划项目
立项申请书

所属高校（盖章）：牡丹江师范学院

项目名称：臭氧鼓泡塔反应器内构件优化

项目类别　☑创新训练　□创业训练

负 责 人：姜鹤

所属学科：化学

起止时间：2020 年 6 月-2021 年 6 月

项目经费：1 万元

填表日期：2020 年 5 月 11 日

黑龙江省教育厅制

3.具有磁性和污染物检测双功能金属铜配合物的合成

黑龙江省大学生创新创业项目创新项目　　负责人：李彩云

附件 1：

项目编号：_____

黑龙江省大学生创新创业训练计划项目
立项申请书

所属高校（盖章）：牡丹江师范学院

项目名称：具有磁性和污染物检测双功能金属铜配合物的合成

项目类别　√创新训练　□创业训练

负 责 人：李彩云

所属学科：化学

起止时间：2020.9-2021.9

项目经费：1 万元

填表日期：2020.5.07

黑龙江省教育厅制

4.以空心微珠为载体的纳米光催化剂的研发及宏量制备

黑龙江省大学生创新创业项目创新项目　　负责人：吕月珩

附件 1：

项目编号：_____

黑龙江省大学生创新创业训练计划项目
立项申请书

所属高校（盖章）：化学化工学院

项目名称：以空心微珠为载体的纳米光催化剂的研发及宏量制备

项目类别　☑创新训练　□创业训练

负 责 人：吕月珩

所属学科：化学

起止时间：2020.06-2021.05

项目经费：一万

填表日期：2020.05

黑龙江省教育厅制

5.苯丙胺类违禁化学品拉曼光谱的密度泛函理论研究

黑龙江省大学生创新创业项目创新项目　　负责人：苏鑫

项目编号：_____

黑龙江省大学生创新创业训练计划项目
立项申请书

所属高校（盖章）：牡丹江师范学院

项目名称：苯丙胺类违禁化学品拉曼光谱的密度泛函理论研究

项目类别　☑创新训练　□创业训练

负 责 人：苏鑫

所属学科：化学

起止时间：2020.06-2021.06

项目经费：1万元

填表日期：2020.05

黑龙江省教育厅制

6.黄芪、丹参中药用成分的薄层色谱法提取分离测定

黑龙江省大学生创新创业项目创新项目　　负责人：陶蕊 周鹤淇

项目编号：_____

黑龙江省大学生创新创业训练计划项目
立项申请书

所属高校（盖章）：牡丹江师范学院

项目名称：黄芪、丹参中药用成分的薄层色谱法提取分离测定

项目类别　☑创新训练　□创业训练

负 责 人：陶蕊 周鹤淇

所属学科：分析化学

起止时间：2020 年 6 月—2021 年 6 月

项目经费：0.5 万

填表日期：2020 年 5 月 15 日

黑龙江省教育厅制

7.一种新型水性带锈转锈涂料的研发

黑龙江省大学生创新创业项目创新项目　　负责人：魏敏

附件 1：

项目编号：_____

黑龙江省大学生创新创业训练计划项目
立项申请书

所属高校（盖章）：牡丹江师范学院

项目名称：一种新型水性带锈转锈涂料的研发

项目类别　√创新训练　□创业训练

负 责 人：魏敏

所属学科：化学

起止时间：2020.06-2021.06

项目经费：10000 元

填表日期：2020 年 5 月 11 日

黑龙江省教育厅制

8.改性氯氧化铋光催化剂的制备及性能研究

黑龙江省大学生创新创业项目创新项目　　负责人：徐佳鑫

附件 1：

项目编号：_____

黑龙江省大学生创新创业训练计划项目
立项申请书

所属高校（盖章）：牡丹江师范学院

项目名称：改性氯氧化铋光催化剂的制备及性能研究

项目类别　☑创新训练　□创业训练

负 责 人：徐佳鑫

所属学科：化学

起止时间：2020 年 5 月-2021 年 12 月

项目经费：1 万元

填表日期：2020 年 5 月 10 日

黑龙江省教育厅制

9.黑龙江地区常见食用菌中胶原蛋白的提取

黑龙江省大学生创新创业项目创新项目　　负责人：张萌　郭朝阳

附件 1：

项目编号：_____

黑龙江省大学生创新创业训练计划项目
立项申请书

所属高校（盖章）：牡丹江师范学院

项目名称：黑龙江地区常见食用菌中胶原蛋白的提取

项目类别　☑创新训练　□创业训练

负 责 人：张萌　郭朝阳

所属学科：化学

起止时间：2020.7-2021.6

项目经费：0.5 万元

填表日期：2020 年 5 月 14 日

黑龙江省教育厅制

10.耐水阻燃材料的制备与研究

黑龙江省大学生创新创业项目创新项目　　负责人：张宇

附件 1：

项目编号：_____

黑龙江省大学生创新创业训练计划项目
立项申请书

所属高校（盖章）：牡丹江师范学院

项目名称：耐水阻燃材料的制备与研究

项目类别　☑创新训练　□创业训练

负 责 人：张宇

所属学科：化学

起止时间：2020.06-2021.06

项目经费：1 万元

填表日期：2020.05.15

黑龙江省教育厅制

11.烯烃与非化学计量分子的设计组装

黑龙江省大学生创新创业项目创新项目　　负责人：陈雪萌

项目编号：_____

黑龙江省大学生创新创业训练计划项目
立项申请书

所属高校（盖章）：_____

项目名称：烯烃与非化学计量分子的设计组装

项目类别　√创新训练　□创业训练

负 责 人：陈雪萌

所属学科：化学

起止时间：2020.05-2021.12

项目经费：10000 元

填表日期：2020.05.12

黑龙江省教育厅制

12.东北常见中药材中抗病毒成分的研究

黑龙江省大学生创新创业项目创新项目　　负责人：董鹏飞 刘越

项目编号：_____

黑龙江省大学生创新创业训练计划项目
立项申请书

所属高校（盖章）：牡丹江师范学院

项目名称：东北常见中药材中抗病毒成分的研究

项目类别　☑创新训练　□创业训练

负 责 人：董鹏飞、刘越

所属学科：分析化学

起止时间：2020.05-2021.05

项目经费：10000 元

填表日期：2020.05.09

黑龙江省教育厅制

13.电镀工艺对镍电极析氢性能影响研究

黑龙江省大学生创新创业项目创新项目　　负责人：董瑞

附件 1：

项目编号：_____

黑龙江省大学生创新创业训练计划项目
立项申请书

所属高校（盖章）：牡丹江师范学院

项目名称：电镀工艺对镍电极析氢性能影响研究

项目类别　√☑创新训练　□创业训练

负 责 人：董瑞

所属学科：化学工程与工艺

起止时间：2020.05-2021.05

项目经费：5000 元

填表日期：2020.05.09

黑龙江省教育厅制

14.复杂基体中添加剂的高通量筛查及快速检测技术研究

黑龙江省大学生创新创业项目创新项目　　负责人：董芷蔓

附件 1：

项目编号：_____

黑龙江省大学生创新创业训练计划项目
立项申请书

所属高校（盖章）：牡丹江师范学院

项目名称：复杂基体中添加剂的高通量筛查及快速检测技术研究

项目类别　☑创新训练　□创业训练

负 责 人：董芷蔓

所属学科：化学

起止时间：2020.09-2021.09

项目经费：10000 元

填表日期：2020.05.10

黑龙江省教育厅制

15.环保型脲醛树脂的耐水性的改进研究

黑龙江省大学生创新创业项目创新项目　　负责人：付文惠　高阳

附件 1：

项目编号：_____

黑龙江省大学生创新创业训练计划项目
立项申请书

所属高校（盖章）：　牡丹江师范学院

项目名称：　环保型脲醛树脂的耐水性的改进研究

项目类别　　☑创新训练　　□创业训练

负 责 人：　付文慧　高阳

所属学科：　化学

起止时间：　2020.06-2021.06

项目经费：　一万元

填表日期：　2020 年 5 月 13 日

黑龙江省教育厅制

2019 年大学生创新创业项目（共 14 项）

1.双极微弧氧化反应陶瓷膜层高温氧化性能研究

黑龙江省大学生创新创业项目创新项目　　负责人：范云龙

2.稀土掺杂氧化锌复合粉体的制备及光催化性能研究

黑龙江省大学生创新创业项目创新项目　　负责人：李红晶

3.金属铜化合物的制备及性能研究

黑龙江省大学生创新创业项目创新项目　　负责人：刘鸿雁

4.铜催化碳-碳键断裂及重组反应的机理研究

黑龙江省大学生创新创业项目创新项目　　负责人：罗红欣 李可忠

5.生物质基纳米复合材料在电化学传感器中的应用

黑龙江省大学生创新创业项目创新项目　　负责人：那博语

6.几种药物分子的 **SERS** 检测和理论研究

黑龙江省大学生创新创业项目创新项目　　负责人：倪佳瑶

7.基于含氮杂环配体的金属铜配合物的合成、磁性及生物活性研究

黑龙江省大学生创新创业项目创新项目　　负责人：茹莉莹

8.导电填料用纳米粉体的制备及其改性研究

黑龙江省大学生创新创业项目创新项目　　负责人：宋田园

9.基于“互联网＋”技术设计分析关药道地药材中抗癌活性成分的研究

黑龙江省大学生创新创业项目创新项目　　负责人：王悦 丁崇洪

10.二元三原子非金属计量分子与硼簇的设计组装

黑龙江省大学生创新创业项目创新项目　　负责人：王小倩

11.普鲁卡因药物-金属相互作用及其表面增强拉曼光谱的研究

黑龙江省大学生创新创业项目创新项目　　负责人：徐鑫

12.化妆品中重金属含量测定研究

黑龙江省大学生创新创业项目创新项目　　负责人：张宏玉

13.教育兴农-农村师范生教育教学技能-体化培养训练

黑龙江省大学生创新创业项目创新项目　　负责人：张月影 张艺

14.丙烷选择氧化制丙烯酸尾气中 **CO** 选择性脱除催化剂创业项目

黑龙江省大学生创新创业项目创业项目　　负责人：周启

1.双极微弧氧化反应陶瓷膜层高温氧化性能研究

黑龙江省大学生创新创业项目创新项目　　负责人：范云龙

项目编号：_____

黑龙江省大学生创新创业训练计划项目
立项申请书

所属高校（盖章）：化学化工学院

项目名称：**双极微弧氧化反应陶瓷膜层高温氧化性能研究**

项目类别　创新训练

负 责 人：范云龙

指导教师：郝国栋

所属学科：化学

起止时间：**2019.05-2020.12**

项目经费：1万

填表日期：**2019.05**

黑龙江省教育厅制

2.稀土掺杂氧化锌复合粉体的制备及光催化性能研究

黑龙江省大学生创新创业项目创新项目　　负责人：李红晶

附件 2：

项目编号：_____

黑龙江省大学生创新创业训练计划项目
立项申请书

所属高校（盖章）：牡丹江师范学院

项目名称：稀土掺杂氧化锌复合粉体的制备及光催化性能研究

项目类别　☑创新训练　□创业训练

负 责 人：李红晶

指导教师：贾林艳

所属学科：化　学

起止时间：2019.5——2020.12

项目经费：1.0 万元

填表日期：2019 年 5 月 6 日

黑龙江省教育厅制

3.金属铜化合物的制备及性能研究

黑龙江省大学生创新创业项目创新项目　　负责人：刘鸿雁

附件 1：

项目编号：_____

黑龙江省大学生创新创业训练计划项目
立项申请书

所属高校（盖章）：牡丹江师范学院

项目名称：金属铜化合物的制备及性能研究

项目类别　☑创新训练　□创业训练

负 责 人：刘鸿雁

指导教师：任玉兰

所属学科：化学

起止时间：2019 年 5 月-2020 年 12 月

项目经费：1 万元

填表日期：2019 年 5 月 10 日

黑龙江省教育厅制

4.铜催化碳-碳键断裂及重组反应的机理研究

黑龙江省大学生创新创业项目创新项目　　负责人：罗红欣 李可忠

项目编号：

黑龙江省大学生创新创业训练计划项目
立项申请书

所属高校（盖章）：　牡丹江师范学院

项目名称：铜催化碳-碳键断裂及重组反应的机理研究

项目类别　☑创新训练　☐创业训练

负 责 人：　罗红欣　　李可忠

指导教师：　左明辉

所属学科：　化学

起止时间：　2019 年 5 月-2020 年 12 月

项目经费：　1.0 万元

填表日期：　2019 年 5 月 10 日

黑龙江省教育厅制

5.生物质基纳米复合材料在电化学传感器中的应用

黑龙江省大学生创新创业项目创新项目　　负责人：那博语

附件 1：

项目编号：_____

黑龙江省大学生创新创业训练计划项目
立项申请书

所属高校（盖章）：牡丹江师范学院

项目名称：生物质基纳米复合材料在电化传感器中的应用

项目类别　√创新训练　□创业训练

负 责 人：那博语

指导教师：韩俊凤

所属学科：化学

起止时间：2019.7-2020.7

项目经费：1 万元

填表日期：2019.5.11

黑龙江省教育厅制

6.几种药物分子的 SERS 检测和理论研究

黑龙江省大学生创新创业项目创新项目　　负责人：倪佳瑶

附件 1：

项目编号：_____

黑龙江省大学生创新创业训练计划项目
立项申请书

所属高校（盖章）：牡丹江师范学院

项目名称：几种药物分子的 SERS 检测和理论研究

项目类别　☑创新训练　□创业训练

负 责 人：倪佳瑶

指导教师：陈玉锋

所属学科：化学

起止时间：2019.06-2020.06

项目经费：1.0 万元

填表日期：2019.05

黑龙江省教育厅制

7.基于含氮杂环配体的金属铜配合物的合成、磁性及生物活性研究

黑龙江省大学生创新创业项目创新项目　　负责人：茹莉莹

项目编号：_____

黑龙江省大学生创新创业训练计划项目
立项申请书

所属高校（盖章）：牡丹江师范学院

项目名称：基于含氮杂环配体的金属铜配合物的合成、磁性及生物活性研究

项目类别：√创新训练　□创业训练

负 责 人：茹莉莹

指导教师：崔术新

所属学科：化学

起止时间：2019.9-2020.9

项目经费：1 万元

填表日期：2019.5.10

黑龙江省教育厅制

8.导电填料用纳米粉体的制备及其改性研究

黑龙江省大学生创新创业项目创新项目　　负责人：宋田园

项目编号：_____

黑龙江省大学生创新创业训练计划项目
立项申请书

所属高校（盖章）：_____

项目名称：导电填料用纳米粉体的制备及其改性研究

项目类别　☑创新训练　□创业训练

负 责 人：宋田园

指导教师：付东升

所属学科：化学

起止时间：2019 年 5 月-2020 年 12 月

项目经费：1 万元

填表日期：2019 年 5 月 12 日

黑龙江省教育厅制

9.基于“互联网＋”技术设计分析关药道地药材中抗癌活性成分的研究

黑龙江省大学生创新创业项目创新项目　　负责人：王悦 丁崇洪

项目编号：_____

黑龙江省大学生创新创业训练计划项目
立项申请书

所属高校（盖章）：牡丹江师范学院

项目名称：基于“互联网+”技术设计分析关药道地药材中抗癌活性成分的研究

项目类别　☑创新训练　□创业训练

负 责 人：王 悦、 丁崇洪

指导教师：苏爽月

所属学科：化　学

起止时间：2019.06-2020.06

项目经费：10000.00 元

填表日期：2019.5.12

黑龙江省教育厅制

10.二元三原子非金属计量分子与硼簇的设计组装

黑龙江省大学生创新创业项目创新项目　　负责人：王小倩

附件 1：

项目编号：_____

黑龙江省大学生创新创业训练计划项目
立项申请书

所属高校（盖章）：牡丹江师范学院

项目名称：二元三原子非金属计量分子与硼簇的设计组装

项目类别　√创新训练　□创业训练

负 责 人：王小倩

指导教师：邵长斌

所属学科：化学

起止时间：2019.05-2020.12

项目经费：10000 元

填表日期：2019.05.13

黑龙江省教育厅制

11.普鲁卡因药物-金属相互作用及其表面增强拉曼光谱的研究

黑龙江省大学生创新创业项目创新项目　　负责人：徐鑫

附件 2：

项目编号：_____

黑龙江省大学生创新创业训练计划项目
立项申请书

所属高校（盖章）：牡丹江师范学院

项目名称：普鲁卡因药物-金属相互作用
及其表面增强拉曼光谱的研究

项目类别　☑创新训练　□创业训练

负 责 人：徐鑫

指导教师：庄志萍

所属学科：波谱学

起止时间：2019.05.——2020.05.

项目经费：10000 元

填表日期：2019.05.10

黑龙江省教育厅制

12.化妆品中重金属含量测定研究

黑龙江省大学生创新创业项目创新项目　　负责人：张宏玉

项目编号：_____

黑龙江省大学生创新创业训练计划项目
立项申请书

所属高校（盖章）　牡丹江师范学院

项目名称：化妆品中重金属含量测定研究

项目类别　☑创新训练　□创业训练

负 责 人：　张宏玉

指导教师：　汪洋

所属学科：　无机化学

起止时间：　2019 年 6 月-2020 年 6 月

项目经费：　0.5 万元

填表日期：　2019 年 5 月 11 日

黑龙江省教育厅制

13.教育兴农-农村师范生教育教学技能-体化培养训练

黑龙江省大学生创新创业项目创新项目　　负责人：张月影 张艺

项目编号：_____

黑龙江省大学生创新创业训练计划项目
立项申请书

所属高校（盖章）：牡丹江师范学院

项目名称：教育兴农--农村师范生
教育教学技能一体化培养训练

项目类别　☑创新训练　□创业训练

负 责 人：张月影　张艺

指导教师：王慧

所属学科：化学

起止时间：2019.5---2020.5

项目经费：一万元

填表日期：2019.5.13

黑龙江省教育厅制

14.丙烷选择氧化制丙烯酸尾气中 CO 选择性脱除催化剂创业项目

黑龙江省大学生创新创业项目创业项目　　负责人：周启

项目编号：_____

黑龙江省大学生创业实践项目
立项申请书

所属高校（盖章）：牡丹江师范学院

项目名称：丙烷选择氧化制丙烯酸尾气中 CO 选择性脱除催化剂创业项目

项目类别：创业实践

负 责 人：周启

指导教师：蔡雪

所属学科：化学

起止时间：2019 年 6 月—2021 年 6 月

项目经费：5 万元

填表日期：2019 年 5 月 6 日

黑龙江省教育厅制

2018 年大学生创新创业项目目录（10 项）

1.金属掺杂富硼团簇的设计组装

黑龙江省大学生创新创业项目创新项目　　负责人：才洪雪

2.高灵敏 **SERS** 基底的制备及苏丹红的检测

黑龙江省大学生创新创业项目创新项目　　负责人：黄康乐

3.互联网＋背景下的大学生活动平台创新研究

黑龙江省大学生创新创业项目创新项目　　负责人：刘方鑫

4.吡虫啉表面增强拉曼光谱的研究

黑龙江省大学生创新创业项目创新项目　　负责人：潘佳琦

5.大学生教育教学实践能力创新训练

黑龙江省大学生创新创业项目创新项目　　负责人：孙晓春 何春雨

6.铋系含氧酸盐光催化剂的制备及改性研究

黑龙江省大学生创新创业项目创新项目　　负责人：谭鑫

7.水性汽车内饰胶粘剂创业项目

黑龙江省大学生创新创业项目创业项目　　负责人:于文卓 于泓

8.颜色可调控稀土掺杂荧光粉的制备及发光性能研究

黑龙江省大学生创新创业项目创新项目　　负责人：于文卓

9.金属卡宾催化碳碳形成机理理论研究

黑龙江省大学生创新创业项目创新项目　　负责人：张洪梅

10.磁性-生物活性双功能金属钴配合物分子材料的合成及性能研究

黑龙江省大学生创新创业项目创新项目　　负责人：赵一伦 唐怡

1.金属掺杂富硼团簇的设计组装

黑龙江省大学生创新创业项目创新项目　　负责人：才洪雪

附件 1：

项目编号：_____

黑龙江省大学生创新创业训练计划项目
立项申请书

所属高校（盖章）：牡丹江师范学院

项目名称：金属掺杂富硼团簇的设计组装

项目类别　√创新训练　□创业训练

负 责 人：才洪雪

指导教师：邵长斌

所属学科：化学

起止时间：2018.09－2019.09

项目经费：10000 元

填表日期：2018.05.06

黑龙江省教育厅制

2.高灵敏 SERS 基底的制备及苏丹红的检测

黑龙江省大学生创新创业项目创新项目　　负责人：黄康乐

附件 1：

项目编号：_____

黑龙江省大学生创新创业训练计划项目
立项申请书

所属高校（盖章）：_____

项目名称：高灵敏 SERS 基底的制备及苏丹红的检测

项目类别　√创新训练　□创业训练

负 责 人：黄康乐

指导教师：陈玉锋、姜力

所属学科：化学

起止时间：2018.06-2019.06

项目经费：1.0 万元

填表日期：2018.05

黑龙江省教育厅制

3.互联网＋背景下的大学生活动平台创新研究

黑龙江省大学生创新创业项目创新项目　　负责人：刘方鑫

项目编号：_____

黑龙江省大学生创新创业训练计划项目
立项申请书

所属高校（盖章）：牡丹江师范学院

项目名称：互联网+背景下的大学生活动平台创新研究

项目类别　√创新训练　□创业训练

负 责 人：刘方鑫

指导教师：张晓祥

所属学科：880 教育学

起止时间：

项目经费：10000 元

填表日期：

黑龙江省教育厅制

4.吡虫啉表面增强拉曼光谱的研究

黑龙江省大学生创新创业项目创新项目　　负责人：潘佳琦

附件 1：

项目编号：_____

黑龙江省大学生创新创业训练计划项目
立项申请书

所属高校（盖章）：牡丹江师范学院

项目名称：吡虫啉表面增强拉曼光谱的研究

项目类别　☑创新训练　□创业训练

负 责 人：潘佳琦

指导教师：庄志萍

所属学科：化学

起止时间：2018.09——2019.09

项目经费：10000 元

填表日期：2018.05.04

黑龙江省教育厅制

5.大学生教育教学实践能力创新训练

黑龙江省大学生创新创业项目创新项目　　负责人：孙晓春 何春雨

附件 1：

项目编号：_____

黑龙江省大学生创新创业训练计划项目
立项申请书

所属高校（盖章）：牡丹江师范学院

项目名称：**大学生教育教学实践能力创新训练**

项目类别　√创新训练　□创业训练

负 责 人：孙晓春　何春雨

指导教师：王慧

所属学科：化学

起止时间：2018.5-2019.5

项目经费：10000

填表日期：2018.5.3

黑龙江省教育厅制

6.铋系含氧酸盐光催化剂的制备及改性研究

黑龙江省大学生创新创业项目创新项目　　负责人：谭鑫

附件 1：

项目编号：_____

黑龙江省大学生创新创业训练计划项目
立项申请书

所属高校（盖章）：牡丹江师范学院

项目名称：铋系含氧酸盐光催化剂的制备及改性研究

项目类别　☑创新训练　□创业训练

负 责 人：谭鑫

指导教师：任玉兰、赵平平

所属学科：化学

起止时间：2018 年 5 月-2019 年 12 月

项目经费：1 万元

填表日期：2018 年 5 月 3 日

黑龙江省教育厅制

7.水性汽车内饰胶粘剂创业项目

黑龙江省大学生创新创业项目创业项目　　负责人:于文卓 于泓

附件 2：

项目编号：_____

黑龙江省大学生创业实践项目
立项申请书

所属高校（盖章）：牡丹江师范学院

项目名称：水性汽车内饰胶黏剂创业项目

项目类别：创业实践

负 责 人：于文卓 于泓

指导教师：蒋舰 云观 郑伟 汪洋

所属学科：化学

起止时间：2018 年 6 月-2021 年 6 月

项目经费：5 万元

填表日期：2018 年 5 月 6 日

黑龙江省教育厅制

8.颜色可调控稀土掺杂荧光粉的制备及发光性能研究

黑龙江省大学生创新创业项目创新项目　　负责人：于文卓

附件 1：

项目编号：_____

黑龙江省大学生创新创业训练计划项目
立项申请书

所属高校（盖章）：牡丹江师范学院

项目名称：颜色可调控稀土掺杂荧光粉的制备及发光性能研究

项目类别　☑创新训练　□创业训练

负 责 人：于文卓

指导教师：贾林艳　邵长斌

所属学科：化　学

起止时间：2018.5——2019.4

项目经费：2.0 万元

填表日期：2018 年 5 月 6 日

黑龙江省教育厅制

9.金属卡宾催化碳碳形成机理理论研究

黑龙江省大学生创新创业项目创新项目　　负责人：张洪梅

附件 2：

项目编号：_____

黑龙江省大学生创新创业训练计划项目
立项申请书

所属高校（盖章）：牡丹江师范学院

项目名称：金属卡宾催化碳碳形成机理理论研究

项目类别　☑创新训练　☐创业训练

负 责 人：张洪梅

指导教师：左明辉

所属学科：化学

起止时间：2018 年 5 月-2019 年 5 月

项目经费：1.0 万元

填表日期：2018 年 5 月 1 日

黑龙江省教育厅制

10.磁性-生物活性双功能金属钴配合物分子材料的合成及性能研究

黑龙江省大学生创新创业项目创新项目　　负责人：赵一伦 唐怡

附件 1：

项目编号：_____

黑龙江省大学生创新创业训练计划项目
立项申请书

所属高校（盖章）：牡丹江师范学院

项目名称：磁性—生物活性双功能金属钴配合物分子材料的合成及性能研究

项目类别：√创新训练　□创业训练

负 责 人：赵一伦　唐怡

指导教师：崔术新

所属学科：化学

起止时间：2018.9-2019.9

项目经费：2 万元

填表日期：2018.4.26

黑龙江省教育厅制

2017 年指导大学生创新创业项目
目录（12 项）

1. 室温自交联木器拼板胶黏剂的研究开发

牡丹江师范学院大学生创新创业项目　　负责人：马悦

2. 以空心微珠为载体的纳米光催化剂在自然光下性能研究

牡丹江师范学院大学生创新创业项目　　负责人:李欢欢

3. 磁性-生物活性双功能金属镍配合物分子材料的合成及性能研究

黑龙江省大学生创新创业项目创新项目　　负责人：包双

4.铜催化碳碳形成机理理论研究

黑龙江省大学生创新创业项目创新项目　　负责人：张莹

5.新生态工艺生产环氧氯丙烷的工厂设计

黑龙江省大学生创新创业项目创业项目　　负责人:崔熙麟 罗坚

6.几种食品中添加剂含量的测定

黑龙江省大学生创新创业项目创新项目　　负责人:李晓龙 马幸玉

7. 功能纳米材料的合成及其在电分析化学中的应用

黑龙江省大学生创新创业项目创新项目　　负责人：李自翔

8. 改性铋系半导体光催化剂的制备及其性能研究

黑龙江省大学生创新创业项目创新项目　　负责人:刘同福

9.金银合金纳米粒子 **SERS** 基底的制备及非法食品添加剂检测研究

黑龙江省大学生创新创业项目创新项目　　负责人：王晓花

10.西玛津农药表面增强拉曼光谱的研究

黑龙江省大学生创新创业项目创新项目　　负责人：王宜鑫

11.清洁燃料油的研制与生产

黑龙江省大学生创新创业项目创业项目　　负责人：吴晗

12.金属杂化介孔材料制备及苯酚羟基化反应产物的反相高效液相色谱分析研究

黑龙江省大学生创新创业项目创新项目　　负责人：吴兆宇

1.室温自交联木器拼板胶黏剂的研究开发

牡丹江师范学院大学生创新创业项目　　负责人：马悦

项目编号：_____

牡丹江师范学院大学生科技创新项目
立项申请书

所在学院（盖章）：牡丹江师范学院

项目名称：室温自交联木器拼板胶黏剂的研究开发

负 责 人：马悦

指导教师：蒋舰 员涛 郭元平

所属学科：化学

起止时间：2017.11—2018.11

填表日期：2017.10.4

牡丹江师范学院创业就业指导中心制

2.以空心微珠为载体的纳米光催化剂在自然光下性能研究

牡丹江师范学院大学生创新创业项目　　负责人：李欢欢

项目编号：_____

牡丹江师范学院大学生科技创新项目
立项申请书

所在学院（盖章）：化学化工学院

项目名称：以空心微珠为载体的纳米光催化剂在自然光下性能研究

负 责 人：李欢欢

指导教师：郝国栋

所属学科：化学

起止时间：2017.10-2019.4

填表日期：2017.10

牡丹江师范学院创业就业指导中心制

3.磁性-生物活性双功能金属镍配合物分子材料的合成及性能研究

黑龙江省大学生创新创业项目创新项目　　负责人：包双

附件 2:

项目编号：_____

黑龙江省大学生创新创业训练计划项目
立项申请书

所属高校（盖章）：　牡丹江师范学院

项目名称：　磁性—生物活性双功能金属镍配合物分子材料的合成及性能研究

项目类别　　√创新训练□创业训练

负 责 人：　包双

指导教师：　崔术新

所属学科：　化学

起止时间：　2017.9-2018.9

项目经费：　2 万元

填表日期：　2017.5.1

黑龙江省教育厅制

4.铜催化碳碳形成机理理论研究

黑龙江省大学生创新创业项目创新项目　　负责人：张莹

附件 2：

项目编号：_____

黑龙江省大学生创新创业训练计划项目
立项申请书

所属高校（盖章）：牡丹江师范学院

项目名称：铜催化碳碳形成机理理论研究

项目类别　☑创新训练　☐创业训练

负 责 人：张莹

指导教师：左明辉

所属学科：化学

起止时间：2017 年 5 月-2018 年 5 月

项目经费：1.0 万元

填表日期：2017 年 5 月 11 日

黑龙江省教育厅制

5.新生态工艺生产环氧氯丙烷的工厂设计

黑龙江省大学生创新创业项目创业项目　　负责人:崔熙麟 罗坚

附件 2:

项目编号：_____

黑龙江省大学生创新创业训练计划项目
立项申请书

所属高校（盖章）：牡丹江师范学院

项目名称：新生态工艺生产环氧氯丙烷的工厂设计

项目类别　□创新训练　☑创业训练

负 责 人：崔熙麟　罗坚

指导教师：肖同欣

所属学科：化 学

起止时间：2017.9-2018.9

项目经费：10000 元

填表日期：2017 年 5 月 10 日

黑龙江省教育厅制

6.几种食品中添加剂含量的测定

黑龙江省大学生创新创业项目创新项目　　负责人：李晓龙 马幸玉

附件 2：

项目编号：_____

黑龙江省大学生创新创业训练计划项目
立项申请书

所属高校（盖章）：牡丹江师范学院

项目名称：几种食品中添加剂含量的测定

项目类别　☑创新训练　□创业训练

负 责 人：李晓龙 马幸玉

指导教师：苏爽月

所属学科：化　学

起止时间：2017.09-2018.09

项目经费：10000 元

填表日期：2017.5.6

黑龙江省教育厅制

7.功能纳米材料的合成及其在电分析化学中的应用

黑龙江省大学生创新创业项目创新项目　　负责人：李自翔

附件 2：

项目编号：_____

黑龙江省大学生创新创业训练计划项目
立项申请书

所属高校（盖章）：牡丹江师范学院

项目名称：功能纳米材料的合成及其在电分析化学中的应用

项目类别　√创新训练　□创业训练

负 责 人：李自翔

指导教师：韩俊凤

所属学科：化学

起止时间：2017.7-2018.7

项目经费：10000

填表日期：2017.5.10

黑龙江省教育厅制

8.改性铋系半导体光催化剂的制备及其性能研究

黑龙江省大学生创新创业项目创新项目　　负责人:刘同福

附件 2：

项目编号：_____

黑龙江省大学生创新创业训练计划项目
立项申请书

所属高校（盖章）：牡丹江师范学院

项目名称：改性铋系半导体光催化剂的制备及其性能研究

项目类别　√创新训练　□创业训练

负 责 人：刘同福

指导教师：任玉兰

所属学科：化　学

起止时间：2017.5-2018.12

项目经费：1 万元

填表日期：2017.5.10

黑龙江省教育厅制

9.金银合金纳米粒子 SERS 基底的制备及非法食品添加剂检测研究

黑龙江省大学生创新创业项目创新项目　　负责人：王晓花

附件 2：

项目编号：_____

黑龙江省大学生创新创业训练计划项目
立项申请书

所属高校（盖章）：牡丹江师范学院

项目名称：金银合金纳米粒子 SERS 基底的制备及非法食品添加剂检测研究

项目类别　☑创新训练　□创业训练

负 责 人：王晓花

指导教师：陈玉锋

所属学科：化学

起止时间：2017 年 6 月-2018 年 6 月

项目经费：1.0 万元

填表日期：2017 年 5 月

黑龙江省教育厅制

10.西玛津农药表面增强拉曼光谱的研究

黑龙江省大学生创新创业项目创新项目　　负责人：王宜鑫

附件 2：

项目编号：_____

黑龙江省大学生创新创业训练计划项目
立项申请书

所属高校（盖章）：_____

项目名称：西玛津农药表面增强拉曼光谱的研究

项目类别　☑创新训练　□创业训练

负 责 人：王宜鑫

指导教师：庄志萍

所属学科：分子光谱

起止时间：2017.05.11——2018.05.11

项目经费：10000 元

填表日期：2017.05.11

黑龙江省教育厅制

11.清洁燃料油的研制与生产

黑龙江省大学生创新创业项目创业项目　　负责人：吴晗

附件 3：

项目编号：

黑龙江省大学生创业实践项目
立项申请书

所属高校（盖章）：牡丹江师范学院

项目名称：清洁燃料油的研制与生产

项目类别：创业实践

负 责 人：吴 晗

指导教师：邵艳秋　王超宇

所属学科：化学工程与技术

起止时间：2017.5-2018.5

项目经费：50000 元

填表日期：2017 年 5 月 8 日

黑龙江省教育厅制

12.金属杂化介孔材料制备及苯酚羟基化反应产物的反相高效液相色谱分析研究

黑龙江省大学生创新创业项目创新项目　　负责人：吴兆宇

附件 2：

项目编号：_____

黑龙江省大学生创新创业训练计划项目
立项申请书

所属高校（盖章）：牡丹江师范学院

项目名称：金属杂化介孔材料制备及苯酚羟基化反应产物的反相高效液相色谱分析研究

项目类别　√创新训练　□创业训练

负 责 人：吴兆宇

指导教师：刘素娟

所属学科：化学

起止时间：2017.09-2018.09

项目经费：1 万元

填表日期：2017.05.09

黑龙江省教育厅制

2016 年指导大学生科研项目目录（1 项）

1.连铸机结晶器表面电铸镍铁合金研究

牡丹江师范学院大学生创新创业项目　　负责人：王海鹏

附件 2：

项目编号：_____

黑龙江省大学生创新创业训练计划项目
立项申请书

所属高校（盖章）：牡丹江师范学院

项目名称：连铸机结晶器表面电铸镍铁合金研究

项目类别　☑创新训练　□创业训练

负 责 人：王海鹏

指导教师：邢乐红

所属学科：化学

起止时间：2016. 10. 1 至 2017. 10. 1

项目经费：1 万元

填表日期：2016. 5. 4

黑龙江省教育厅制

指导学生发表论文（共 42 篇）

1.Shao Y, Jiang Z, Zhang Q, et al. Progress in nonmetal‐doped graphene electrocatalysts for the oxygen reduction reaction[J]. ChemSusChem, 2019, 12(10): 2133-2146.

2.Shao Y, Chang Y, Zhang S, et al. Impact of polymer backbone fluorination on the charge generation/recombination patterns and vertical phase segregation in bulk heterojunction organic solar cells[J]. Frontiers in chemistry, 2020, 8: 144.

3.邵艳秋,姜封庆,孙玺,常玉莹,王星月,宋冰,黄家辉.乙炔氢氯化反应铜基催化剂研究进展[J].塑料工业,2021,49(03):27-31.

4.王星月,邵艳秋,王丽杰,何冬青.Ag 负载对 $BiVO_4$ 半导体光诱导电荷传输行为调控及其光催化影响机理[J].化学工程师,2021,35(01):4-8.

5.邵艳秋,王丽杰,郑友进,于平,王星月.Ba^{2+}掺杂 $BiVO_4$ 光催化降解罗丹明 B 的性能研究[J].化工新型材料,2020,48(02):211-214.

6.邵艳秋,姜封庆,蔡雪,谭荣欣.高校化学实验室常见无机废液的处理方法[J].广东化工,2019,46(05):262-263.

7.邵艳秋,张宇婷,姜振双,刘素娟,任玉兰,王丽杰.水解剂氟化铵对 Fe-SBA-15 结构及催化性能的影响[J].无机盐工业,2019,51(09):97-101.

8.邵艳秋,于平,郑友进,王丽杰,王星月.氧化锌基阵列染料敏化太阳能电池研究进展[J].人工晶体学报,2019,48(10):1967-1975.

9.邵艳秋,张宇婷,王星月,常玉莹,孙家红.Fe-SBA-15 介孔分子筛的合成及其苯酚羟基化反应性能研究[J].山东化工,2019,48(20):1-2.

10.邵艳秋,张宇婷,芦原萱,刘素娟,任玉兰,苏爽月.不同疏水基固体酸 SBA-15-SO_3H 的合成及催化乙酸正丁酯研究[J].牡丹江师范学院学报(自然科学版),2017(04):48-51.

11.芦原萱,赵婷婷,陈玉刚,邵艳秋.疏水基团对介孔材料 SBA-15-SO_3H 催化性能的影响[J].牡丹江师范学院学报(自然科学版),2016(04):40-42.

12.盛琦,刘素娟,冯峰,邵艳秋,孙航.高效液相色谱法同时测定 8 种食品添加剂[J].湖北农业科学,2016,55(21):5620-5622.

13.邵艳秋,赵婷婷,付文婷,郑骐朋.氨基改性 SBA-15 介孔材料的制备及对 Pb(Ⅱ)的吸附性能研究[J].硅酸盐通报,2016,35(02):587-592.

14.赵婷婷,芦原萱,邵艳秋.NH_2-SBA-15 的制备及其对水中铅离子的吸附[J].牡丹江师范学院学报(自然科学版),2016(01):42-44.

15.邵艳秋,芦原萱,付文婷,苏爽月,郑炜.盐对氨基改性 SBA-15 吸附 Pb^{2+}性能的影响研究[J].硅酸盐通报,2016,35(11):3649-3653.

16.刘素娟,邵艳秋,崔术新,盛琦.反相高效液相色谱法快速测定 9 种食品添加剂[J].黑龙江畜牧兽医,2015(03):223-225.

17.郭美玲,赵婷婷,付文婷,邵艳秋.Cu-TiO_2/SBA-15 光催化剂的制备及光催化性能[J].黑龙江科技信息,2015(03):80.

18.Xing L H, Shi X T, Wang Y X, et al. Electrochemical Synthesis of Ni-SnO_2 Composite Electrodes for Hydrogen Evolution Reaction in Alkaline Solution[J]. Int. J. Electrochem. Sci, 2022, 17(220530): 2.

19.Xing L, Wang Y, Shi X, et al. Investigation of Pt/C and Pt-Ru/C Mixed Catalyst for DME Oxidation in Direct Dimethyl Ether Fuel Cells[J]. Int. J. Electrochem. Sci, 2020, 15: 10382-10391.

20.Xing L, Wang Y, Sui C, et al. Investigation of Pt/SnO_2/C Catalyst for Dimethyl Ether Oxidation in DDFC[J]. Int. J. Electrochem. Sci, 2020, 15: 2375-2384.

21.Xing L H, Yin G P, Du C Y, et al. Investigation on the durability of direct dimethyl ether fuel cell. Part II: Cathode degradation[J]. International Journal of Hydrogen Energy, 2017, 42(26): 16695-16699.

22.王宜鑫,邢乐红,石鑫婷,孟凡旭,张亮,董瑞.镀液中氨基磺酸镍质量浓度对电镀镍层析氢催化活性的影响[J].电镀与涂饰,2022,41(01):6-9.

23.邢乐红,王宜鑫,隋朝,肖同欣,赵玥,邵艳秋.工程教育专业认证背景下化学工程与工艺专业人才培养模式探索[J].教育现代化,2020,7(07):11-12.

24.邢乐红,王宜鑫,左明辉.工程教育专业认证背景下化学工程与工艺专业学生实践能力培养研究[J].山东化工,2019,48(24):159-160.

25.邢乐红,王宜鑫,王慧,左明辉,孙芳,梁志男.氨基乙酸对硫酸盐体系电镀镍-铁合金的影响[J].电镀与涂饰,2019,38(19):1039-1041.

26.邢乐红,黎德育,李宁,左明辉,李晶.抗坏血酸对硫酸盐体系镍–铁合金镀液稳定性的影响[J].电镀与涂饰,2018,37(12):526-528.

27.邢乐红,杨晶,王海鹏,达铭,李姗,崔术新.硫脲对低磷化学镀镍稳定性的影响[J].牡丹江师范学院学报(自然科学版),2016(03):41-42.

28.Zuo M , Wang H , Xu J , et al. Crystal structure of poly[bipyridine-N,N')-tetrakis(l-cyanido-N:C) dinickel(II)][J]. Acta Crystallographica, 2001, 71(6):709.

29.崔术新,张文文,沈金铭,茹莉莹,赵宇,徐宝,左明辉.铁镍双金属配合物[$Fe(2,2'\text{-}bpy)_2Ni(CN)_4]_n$的合成、晶体结构及磁性[J].硅酸盐学报,2020,48(06):919-924.

30.左明辉,沈金铭,徐杰,尹乾柱,崔术新.锌(Ⅱ)的一维配合物合成、晶体结构及其荧光性能研究[J].人工晶体学报,2019,48(07):1298-1302.

31.左明辉,沈金铭,尹乾柱,崔术新.氰基桥联金属镍配合物晶体的制备及其磁性[J].人工晶体学报,2018,47(09):1839-1842.

32.左明辉,何彦辉,许海霞,崔术新,邵长斌.水催化 HBrO 与 OH 自由基反应的微观机理[J].分子科学学报,2017,33(01):37-42.

33.Yang W, Jiang R, Liu C, et al. Triptycene-Based Porous Chalcogen-Bonded Organic Frameworks[J]. Crystal Growth & Design, 2021, 21(11): 6497-6503.

34.Cai X, Ma Y, Zhou Q, et al. Synergistic effects of phases in the selective oxidation of isobutane over supported $(NH_4)_3HPMo_{11}VO_{40}$ catalysts[J]. Reaction Kinetics, Mechanisms and Catalysis, 2021, 133(1): 293-308.

35.Wei C, Lu G, Guo C, et al. Ethylthio-substituted sandwich phthalocyaninato europium (III) semiconductors for sensing NO_2 and NH_3: Effect of the extended π-conjugate systems on tuning the conductivity and sensing behavior[J]. Organic Electronics, 2021, 93: 106151.

36.Cai X, Zhou Q, Ma Y, et al. Selective Removal of CO in Hydrocarbons-Rich Industrial Off-gases over CuO-$Ce_xZr_{1-x}O_2$ Catalysts [J]. Catalysis Surveys from Asia, 2021, 25(1): 68-75.

37. Cai X, Wei C, Dong J, et al. Dimeric phthalocyanine-involved double-decker complex-based electrochemical sensor for simultaneous detection of acetaminophen and ascorbic acid[J]. Journal of Materials Science: Materials in Electronics, 2019, 30(3): 1976-1983.

38.Cai X, Ning H. Crystal structure of di-μ-acetato-diacetatobis (μ-6, 6′-dimethoxy-2,2′-{[(propane-1,3-diylbis (azanylylidene)] bis (methanylylidene)} diphenolato) tetrazinc[J]. Acta Crystallographica Section E: Crystallographic Communications, 2015, 71(12): 217-218.

39.姜力,周启,陈玉锋,蔡雪.5,15-二(二茂铁基)-卟啉酞菁钇的结构和振

动光谱的密度泛函理论研究[J].原子与分子物理学报,2021,38(03):47-51.
40.孙守鹏,魏闯宇,宁桧,蔡雪.全波谱太能材料氟代酞菁锌分子ZnPc($C_{24}F_{48}$)的研究[J].牡丹江大学学报,2018,27(06):107-109.
41.宁桧,孙守鹏,蔡雪.轴向取代卟啉锌结构和光谱性质的研究[J].牡丹江师范学院学报(自然科学版),2017(01):39-42.
42.李梓萌,蔡雪.咔唑类取代酞菁锌染料敏化性能研究[J].牡丹江师范学院学报(自然科学版),2016(01):44-46.

邵艳秋指导学生发表论文目录（共 17 篇）

1.Shao Y, Jiang Z, Zhang Q, et al. Progress in nonmetal‐doped graphene electrocatalysts for the oxygen reduction reaction[J]. ChemSusChem, 2019, 12(10): 2133-2146.
2.Shao Y, Chang Y, Zhang S, et al. Impact of polymer backbone fluorination on the charge generation/recombination patterns and vertical phase segregation in bulk heterojunction organic solar cells[J]. Frontiers in chemistry, 2020, 8: 144.
3.邵艳秋,姜封庆,孙玺,常玉莹,王星月,宋冰,黄家辉.乙炔氢氯化反应铜基催化剂研究进展[J].塑料工业,2021,49(03):27-31.
4.王星月,邵艳秋,王丽杰,何冬青.Ag 负载对 $BiVO_4$ 半导体光诱导电荷传输行为调控及其光催化影响机理[J].化学工程师,2021,35(01):4-8.
5.邵艳秋,王丽杰,郑友进,于平,王星月.Ba^{2+}掺杂 $BiVO_4$ 光催化降解罗丹明 B 的性能研究[J].化工新型材料,2020,48(02):211-214.
6.邵艳秋,姜封庆,蔡雪,谭荣欣.高校化学实验室常见无机废液的处理方法[J].广东化工,2019,46(05):262-263.

7.邵艳秋,张宇婷,姜振双,刘素娟,任玉兰,王丽杰.水解剂氟化铵对Fe-SBA-15 结构及催化性能的影响[J].无机盐工业,2019,51(09):97-101.
8.邵艳秋,于平,郑友进,王丽杰,王星月.氧化锌基阵列染料敏化太阳能电池研究进展[J].人工晶体学报,2019,48(10):1967-1975.
9.邵艳秋,张宇婷,王星月,常玉莹,孙家红.Fe-SBA-15 介孔分子筛的合成及其苯酚羟基化反应性能研究[J].山东化工,2019,48(20):1-2.
10.邵艳秋,张宇婷,芦原萱,刘素娟,任玉兰,苏爽月.不同疏水基固体酸SBA-15-SO_3H 的合成及催化乙酸正丁酯研究[J].牡丹江师范学院学报(自然科学版),2017(04):48-51.
11.芦原萱,赵婷婷,陈玉刚,邵艳秋.疏水基团对介孔材料 SBA-15-SO_3H 催化性能的影响[J].牡丹江师范学院学报(自然科学版),2016(04):40-42.
12.盛琦,刘素娟,冯峰,邵艳秋,孙航.高效液相色谱法同时测定 8 种食品添加剂[J].湖北农业科学,2016,55(21):5620-5622.
13.邵艳秋,赵婷婷,付文婷,郑骐朋.氨基改性 SBA-15 介孔材料的制备及对 Pb(Ⅱ)的吸附性能研究[J].硅酸盐通报,2016,35(02):587-592.
14.赵婷婷,芦原萱,邵艳秋.NH_2-SBA-15 的制备及其对水中铅离子的吸附[J].牡丹江师范学院学报(自然科学版),2016(01):42-44.
15.邵艳秋,芦原萱,付文婷,苏爽月,郑炜.盐对氨基改性 SBA-15 吸附Pb^{2+}性能的影响研究[J].硅酸盐通报,2016,35(11):3649-3653.
16.刘素娟,邵艳秋,崔术新,盛琦.反相高效液相色谱法快速测定 9 种食品添加剂[J].黑龙江畜牧兽医,2015(03):223-225.
17.郭美玲,赵婷婷,付文婷,邵艳秋.Cu-TiO_2/SBA-15 光催化剂的制备及光催化性能[J].黑龙江科技信息,2015(03):80.

1.Shao Y, Jiang Z, Zhang Q, et al. Progress in nonmetal‐doped graphene electrocatalysts for the oxygen reduction reaction[J]. ChemSusChem, 2019, 12(10): 2133-2146.

MINIREVIEW WILEY-VCH

Progress in nonmetal-doped graphene electrocatalysts for oxygen reduction reaction

Yanqiu Shao,*[a, b] Zhenshuang Jiang,[a, b] Qiaoqiao Zhang,[b] and Jingqi Guan*[b]

Abstract: Due to the energy shortage and environmental pollution, green energy such as polymer electrolyte fuel cells and metal-air batteries plays a more and more important role, where the oxygen reduction reaction (ORR) is the rate-determining step. Development of high-efficiency and stable catalysts to facilitate ORR is of importance. Graphene is a new type of material with two-dimensional structure and high surface area, which shows wide applications in many fields. However, graphene with the zero bandgap property shows low electrocatalytic activity toward ORR. Introduction of some nonmetal atoms can change the electronic arrangement, generate active sites, and further improve the catalytic activity of graphene. It has been demonstrated that some nonmetal-doping strategies (such as nitrogen-doping, sulfur-doping, and phosphorus-doping) can promote the ORR activity. Herein, we summarize the recent development of nonmetal-doped graphene catalysts for ORR. Some common synthetic methods for the nonmetal-doped graphene materials are summarized, and the active sites and possible reaction mechanisms for ORR on various nonmetal-doped graphene catalysts are mainly discussed.

1. Introduction

Energy is very important for the development of the national economy and the improvement of people's living standards, which is an important factor directly affecting economic development. Since the beginning of the 21st century, the shortage of resources, environmental pollution, and greenhouse effect caused by the traditional energy utilization methods have become more and more prominent, the traditional energy structure and its utilization methods are increasingly difficult to meet the needs of human survival and development.[1] To address the increasingly serious energy crisis and environmental pollution problems, a variety of new green energy sources have been developed rapidly, including metal-air batteries and fuel cells.[2]

Under the urgent need for sustainable energy economy, electrochemical energy conversion technologies, such as polymer electrolyte membrane fuel cells (PEMFCs) and metal-air batteries, have become extremely important. The common feature of PEMFCs and metal-air batteries is that oxygen reduction reaction (ORR) is the basic support for their operation. The electrolytes can be divided into acidic electrolyte and alkaline electrolyte. Acidic electrolyte membrane promotes proton transfer from the anode to the cathode. In acidic electrolyte, ORR occurs either by four electrons reduction or by two electrons reduction.[3] The experimental results show that the four-electron reduction mechanism is dominant and advantageous because each oxygen molecule has four electrons. This route can avoid the formation of hydrogen peroxide in the electrode, which results in the membrane and ionic monomer degradation.[4] In alkaline electrolytes, hydroxyl ion is transferred from cathode to anode. In metal-air batteries or alkaline exchange membrane fuel cells, ORR process can also be carried out by two-step reduction (a total of four electrons), in which hydrogen peroxide can be directly or indirectly reduced to water.

At present, platinum is the only commercial catalyst, which shows high activity and stability under acidic conditions. Rapid oxygen reduction kinetics is indispensable in terms of performance. Acidic ORR is several orders of magnitude slower than anodic oxidation. Researchers found that ORR kinetics is more favorable under alkaline conditions. In the cathode reaction of the hydrogen fuel cell, the reduction of O_2 to H_2O requires 4 electrons and 4 protons.[5] The mechanism of this process is very complicated, and ORR dynamics usually limits the reaction rate and maximum power. In recent years, nonmetal-doped graphene materials have gained much attention in ORR. The electrochemical activity and durability of these nonmetal-doped graphene materials can be compared with traditional platinum supported on carbon black (Pt/C).[6] This is a breakthrough and a new milestone in the oxygen reduction reaction because it can substitute the expensive platinum and achieve appropriate power output.[7]

Graphene is a new type of two-dimensional grid structure material, which is composed of planar single-layer carbon atoms. It is the basic unit of other carbon allotropes, such as fullerenes, carbon nanotubes, and graphite. The theoretical specific surface area of graphene is as high as 2630 m^2/g.[4] It has excellent thermal conductivity and electronic conductivity and has a wide application prospect. At the basic level of graphene, it is a chemically specific hexagonal pattern of single-layer 2-carbon atoms.[8] However, the zero bandgap property of graphene decreases its catalytic activity.[9] Unmodified graphene shows low electrocatalytic activity for ORR and is not suitable for direct use as a cathode catalyst for the fuel cell.[2c] The introduction of heteroatoms into graphene can modify its electronic and electrochemical properties by changing the electron density in the graphene sheet. Heteroatom doped graphene can not only improve the electrical properties of graphene but also create more sites for ORR.[10] The theoretical and experimental results show that doped heteroatoms in graphene sp^2 orbital can effectively change the electronic arrangement, generate active sites and improve the catalytic activity.[3b] The doped elements mainly include N, P, O, and S. Nitrogen-doped graphene (NG) has been reported most

[a] Prof. Y. Shao, Z. Jiang
College of Chemistry and Chemical Engineering, Mu Danjiang Normal School, Mudanjiang 157011, China.
E-mail: shaoyanqiu1966@163.com
[b] Q. Zhang, Prof. J. Guan
College of Chemistry, Jilin University, Changchun 130012, China.
E-mail: guanjq@jlu.edu.cn

This article is protected by copyright. All rights reserved.

Accepted Manuscript

electrocatalysts.[101] Su et al. found that the catalytic activity of S/N-codoped 3d graphene undergoes mainly 4e transfer in 0.1 M KOH.[97]

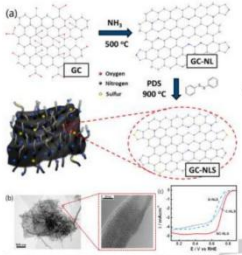

Figure 13. (a) Schematic illustration of the step-wise doping process to fabricate GC-NLS nanocomposites. (b) TEM images of the GC-NLS catalyst. (c) ORR polarization curves obtained in 0.1 M KOH showing the synergic effect of GC-NLS. Reprinted with permission from Ref.[97]. Copyright: 2014 American Chemical Society.

4. Summary and perspectives

Nonmetal-doped graphene materials have a great application prospect on energy catalysis due to their excellent catalytic activity and stability for ORR. Compared with graphene, nonmetal-doped graphene can not only improve the electron structure of graphene but also create more active sites for ORR. The two-dimensional structure and adjustable surface of graphene play an important role in doping different nonmetal elements, which provide good superiority to improve the stability and catalytic activity for ORR. Up to date, nitrogen, phosphorus, and sulfur doped graphene materials exhibit excellent ORR performance. Among them, nitrogen-doped graphene exhibits higher ORR activity than phosphorus and sulfur doped ones. Moreover, nitrogen-sulfur or nitrogen-phosphorus co-doped graphene can further enhance ORR performance.

However, the ORR activity of most of the nonmetal-doped graphene without metal active sites in acidic media is insufficient since they show high overpotential. The ORR activity can be significantly improved by assembling the nitrogen-doped graphene with N-doped carbon nanotubes due to the porous structures with a large surface area. Another familiar strategy to improve the ORR activity is introducing metal ions (e.g. Fe, Co) to the system. However, in the popular PEMFCs, the acid-corrosion resistance of most transition metals is less than carbon. Therefore, for commercialization of the fuel cell technology, improvement of the degree of graphitization is crucial to enhance the corrosion resistance of the nonmetal-doped graphene materials.

Currently, most of the research of ORR on nonmetal-doped graphene catalysts is carried out in alkaline media and is mainly remained in the experimental stage rather than the practical commercial applications of fuel cell. Since acidic PEMFCs are more practical than alkaline ones, development of efficient and stable nonmetal-doped graphene ORR catalysts operated in acid media is vital and urgent in future PEMFCs technologies.

Yanqiu Shao received her B.S in Chemistry from Mudanjiang Normal University and obtained her Ph.D in Physical Chemistry from Jilin University in China. She is currently a professor of Catalytic Principle and Functional Materials in Mudanjiang Normal University.

Zhenshuang Jiang received his B.S. degree from Mudanjiang Normal University in 2016. Currently, he is a Master candidate of Mudanjiang Normal University under the supervision of Prof. Yanqiu Shao. His research focuses on catalyst design for fuel cells and energy conversion.

Qiaoqiao Zhang received her B.S. degree from DaTong University in Shanxi in 2016. Currently, she is a Master candidate of Jilin University under the supervision of A/Prof. Jingqi Guan. Her research focuses on the synthesis of mononuclear-multinuclear catalysts for energy storage and conversion.

Jingqi Guan received his B.S. degree and Ph.D. degree from Jilin University in 2002 and 2007. He was promoted to associate professor of chemistry in Jilin University in 2009. He worked as a postdoctoral research fellow in the University of California at Berkeley from 2012 to 2013 and in the Dalian Institute of Chemical Physics from 2014 to 2018. His research interests focus on the synthesis of mononuclear-multinuclear catalysts for energy storage and conversion.

Accepted Manuscript

This article is protected by copyright. All rights reserved.

Acknowledgements

This work was supported by the Natural Science Foundation of Jilin Province (20180101291JC), Heilongjiang Education Department (1352 MSYB006), and Mudanjiang Normal University (JG2017001).

Conflict of interest

The authors declare no conflict of interest.

Keywords: Graphene • Nitrogen-doping • Oxidized carbon materials • Oxygen reduction reaction • Phosphorus-doping • Sulfur-doping • Fuel cell

[1] N. Recham, J.N. Chotard, L. Dupont, C. Delacourt, W. Walker, M. Armand, J.M. Tarascon, Nat. Mater. **2009**, *9*, 68.
[2] a) F. Cheng, J. Chen, Chem. Soc. Rev. **2012**, *41*, 2172-2192; b) Z.-L. Wang, D. Xu, J.-J. Xu, X.-B. Zhang, Chem. Soc. Rev. **2014**, *43*, 7746-7786; c) M.A. Rahman, X. Wang, C. Wen, J. Electrochem. Soc. **2013**, *160*, A1759-A1771; d) Y. Li, H. Dai, Chem. Soc. Rev. **2014**, *43*, 5257-5275; e) H. Kim, G. Jeong, Y.-U. Kim, J.-H. Kim, C.-M. Park, H.-J. Sohn, Chem. Soc. Rev. **2013**, *42*, 9011-9034; f) V. Neburchilov, H. Wang, J.J. Martin, W. Qu, J. Power Sources **2010**, *195*, 1271-1291; g) A. Kraytsberg, Y. Ein-Eli, Adv. Energy Mater. **2012**, *2*, 922-939; h) D.R. Egan, C. Ponce De Leon, R.J.K. Wood, R.L. Jones, K.R. Stokes, F.C. Walsh, J. Power Sources **2013**, *236*, 293-310.
[3] a) D. Yu, E. Nagelli, F. Du, L. Dai, J. Phys. Chem. Lett. **2010**, *1*, 2165-2173; b) Y. Zheng, Y. Jiao, M. Jaroniec, Y. Jin, S.Z. Qiao, Small **2012**, *8*, 3550-3566.
[4] a) J. Wu, X.Z. Yuan, J.J. Martin, H. Wang, J. Zhang, J. Shen, S. Wu, W. Merida, J. Power Sources **2008**, *184*, 104-119; b) T. Kinumoto, M. Inaba, Y. Nakayama, K. Ogata, R. Umebayashi, A. Tasaka, Y. Iriyama, T. Abe, Z. Ogumi, J. Power Sources **2006**, *158*, 1222-1228; c) R. Borup, J. Meyers, B. Pivovar, Y.S. Kim, R. Mukundan, N. Garland, D. Myers, M. Wilson, F. Garzon, D. Wood, P. Zelenay, K. More, K. Stroh, T. Zawodzinski, J. Boncella, J.E. Mcgrath, M. Inaba, K. Miyatake, M. Hori, K. Ota, Z. Ogumi, S. Miyata, A. Nishikata, Z. Siroma, Y. Uchimoto, K. Yasuda, K.-I. Kimijima, N. Iwashita, Chem. Rev. **2007**, *107*, 3904-3951.
[5] a) M.A. Patel, F. Luo, M.R. Khoshi, E. Rabie, Q. Zhang, C.R. Flach, R. Mendelsohn, E. Garfunkel, M. Szostak, H. He, ACS Nano **2016**, *10*, 2305-2315; b) D. Higgins, P. Zamani, A. Yu, Z. Chen, Energy Environ. Sci. **2016**, *9*, 357-390; c) Z. Yang, H. Nie, X.A. Chen, X. Chen, S. Huang, J. Power Sources **2013**, *236*, 238-249.
[6] a) D. Higgins, M.A. Hoque, M.H. Seo, R. Wang, F. Hassan, J.-Y. Choi, M. Pritzker, A. Yu, J. Zhang, Z. Chen, Adv. Funct. Mater. **2014**, *24*, 4325-4336; b) M.A. Hoque, F.M. Hassan, D. Higgins, J.-Y. Choi, M. Pritzker, S. Knights, S. Ye, Z. Chen, Adv. Mater. **2015**, *27*, 1229-1234; c) Y. Tan, C. Xu, G. Chen, N. Zheng, Q. Xie, Energy Environ. Sci. **2012**, *5*, 6923-6927; d) J. Zhu, M. Xiao, X. Zhao, C. Liu, J. Ge, W. Xing, Nano Energy **2015**, *13*, 316-326.
[7] a) X. Liu, L. Dai, Nat. Rev. Mater. **2016**, *1*, 16064; b) J. Zhang, L. Qu, G. Shi, J. Liu, J. Chen, L. Dai, Angew. Chem. Int. Ed. **2016**, *55*, 2230-2234.
[8] K.S. Novoselov, A.K. Geim, S.V. Morozov, D. Jiang, M.I. Katsnelson, I.V. Grigorieva, S.V. Dubonos, A.A. Firsov, Nature **2005**, *438*, 197.
[9] a) C. Biswas, Y.H. Lee, Adv. Funct. Mater. **2011**, *21*, 3806-3826; b) C. Huang, C. Li, G. Shi, Energy Environ. Sci. **2012**, *5*, 8848-8868.
[10] a) L. Qu, Y. Liu, J.-B. Baek, L. Dai, ACS Nano **2010**, *4*, 1321-1326; b) D. Yu, L. Wei, W. Jiang, H. Wang, B. Sun, Q. Zhang, K. Goh, R. Si, Y. Chen, Nanoscale **2013**, *5*, 3457-3464; c) S. Yang, X. Feng, X. Wang, K. Müllen, Angew. Chem. **2011**, *123*, 5451-5455; d) S. Yang, L. Zhi, K. Tang, X. Feng, J. Maier, K. Müllen, Adv. Funct. Mater. **2012**, *22*, 3634-3640; e) Z.-W. Liu, F. Peng, H.-J. Wang, H. Yu, W.-X. Zheng, J. Yang, Angew. Chem. Int. Ed. **2011**, *50*, 3257-3261.
[11] a) D. Geng, Y. Chen, Y. Chen, Y. Li, R. Li, X. Sun, S. Ye, S. Knights, Energy Environ. Sci. **2011**, *4*, 760-764; b) Z. Lin, M.-K. Song, Y. Ding, Y. Liu, M. Liu, C.-P. Wong, Phys. Chem. Chem. Phys. **2012**, *14*, 3381-3387; c) H. Fei, R. Ye, G. Ye, Y. Gong, Z. Peng, X. Fan, E.L.G. Samuel, P.M. Ajayan, J.M. Tour, ACS Nano **2014**, *8*, 10837-10843; d) J. Ma, Y. Duan, Z. Qin, J. Wang, W. Liu, M. Xu, S. Zhou, X. Cao, Neuroscience **2015**, *310*, 528-540; e) K.-J. Liu, T.-C. Chang, R.-Y. Yang, C.-E. Chen, S.-H. Ho, J.-Y. Tsai, T.-Y. Hsieh, O. Cheng, C.-T. Huang, Thin Solid Films **2014**, *572*, 39-43; f) Y. Li, Y. Li, E. Zhu, T. Mclouth, C.-Y. Chiu, X. Huang, Y. Huang, J. Am. Chem. Soc. **2012**, *134*, 12326-12329; g) J. Yang, C. Tian, L. Wang, H. Fu, J. Mater. Chem. **2011**, *21*, 3384-3390; h) E.J. Lim, S.M. Choi, M.H. Seo, Y. Kim, S. Lee, W.B. Kim, Electrochem. Commun. **2013**, *28*, 100-103; i) Y. Xie, J.-S. Liu, X. Je, W. Liu, F. Liu, Y. Yin, J. Gu, Z. Zou, Electrochim. Acta **2012**, *60*, 354-358.
[12] a) L. Wang, A. Ambrosi, M. Pumera, Angew. Chem. Int. Ed. **2013**, *52*, 13818-13821; b) X. Duan, J. Xu, Z. Wei, J. Ma, S. Guo, S. Wang, H. Liu, S. Dou, Adv. Mater. **2017**, *29*, 1701784.
[13] C.-K. Chang, S. Kataria, C.-C. Kuo, A. Ganguly, B.-Y. Wang, J.-Y. Hwang, K.-J. Huang, W.-H. Yang, S.-B. Wang, C.-H. Chuang, M. Chen, C.-I. Huang, W.-F. Pong, K.-J. Song, S.-J. Chang, J.-H. Guo, Y. Tai, M. Tsujimoto, S. Isoda, C.-W. Chen, L.-C. Chen, K.-H. Chen, ACS Nano **2013**, *7*, 1333-1341.
[14] a) L. Yan, M. Lin, C. Zeng, Z. Chen, S. Zhang, X. Zhao, A. Wu, Y. Wang, L. Dai, J. Qiu, M. Guo, Y. Liu, J. Mater. Chem. **2012**, *22*, 8367-8371; b) I.-Y. Jeon, Y.-R. Shin, G.-J. Sohn, H.-J. Choi, S.-Y. Bae, J. Mahmood, S.-M. Jung, J.-M. Seo, M.-J. Kim, D. Wook Chang, L. Dai, J.-B. Baek, Proc. Natl. Acad. Sci. **2012**, *109*, 5588.
[15] O.S. Kwon, S.J. Park, J.-Y. Hong, A.R. Han, J.S. Lee, J.S. Lee, J.H. Oh, J. Jang, ACS Nano **2012**, *6*, 1486-1493.
[16] Z. Sun, Z. Yan, J. Yao, E. Beitler, Y. Zhu, J.M. Tour, Nature **2010**, *468*, 549.
[17] I.-Y. Jeon, H.-J. Choi, M. Choi, J.-M. Seo, S.-M. Jung, M.-J. Kim, S. Zhang, L. Zhang, Z. Xia, L. Dai, N. Park, J.-B. Baek, Sci. Rep. **2013**, *3*, 1810.
[18] J. Xu, I.-Y. Jeon, J.-M. Seo, S. Dou, L. Dai, J.-B. Baek, Adv. Mater. **2014**, *26*, 7317-7323.
[19] a) H.-L. Guo, P. Su, X. Kang, S.-K. Ning, J. Mater. Chem. A **2013**, *1*, 2248-2255; b) Z.-S. Wu, A. Winter, L. Chen, Y. Sun, A. Turchanin, X. Feng, K. Müllen, Adv. Mater. **2012**, *24*, 5130-5135.
[20] Y. Su, Y. Zhang, X. Zhuang, S. Li, D. Wu, F. Zhang, X. Feng, Carbon **2013**, *62*, 296-301.
[21] Z. Liu, G. Chen, S. Siahrostami, Z. Chen, K. Liu, J. Xie, L. Liao, T. Wu, D. Lin, Y. Liu, T.F. Jaramillo, J.K. Nørskov, Y. Cui, Nat. Catal. **2018**, *1*, 156-162.
[22] C. Hu, L. Dai, Angew. Chem. Int. Ed. **2016**, *55*, 11736-11758.
[23] L. Dai, Y. Xue, L. Qu, H.-J. Choi, J.-B. Baek, Chem. Rev. **2015**, *115*, 4823-4892.
[24] L. Xue, Y. Li, X. Liu, Q. Liu, J. Shang, H. Duan, L. Dai, J. Shui, Nat. Commun. **2018**, *9*, 3819.
[25] J. Duan, S. Chen, M. Jaroniec, S.Z. Qiao, ACS Catal. **2015**, *5*, 5207-5234.
[26] a) Z. Yang, Z. Yao, G. Li, G. Fang, H. Nie, Z. Liu, X. Zhou, X.A. Chen, S. Huang, ACS Nano **2012**, *6*, 205-211; b) S. Zhong, L. Zhou, L. Wu, L. Tang, Q. He, J. Ahmed, J. Power Sources **2014**, *272*, 344-350; c) C. Han, X. Bo, Y. Zhang, M. Li, L. Guo, J. Power Sources **2014**, *272*, 267-276; d) H. Kim, K. Lee, S.I. Woo, Y. Jung, Phys. Chem. Chem. Phys. **2011**, *13*, 17505-17510; e) P.H. Matter, L. Zhang, U.S. Ozkan, J. Catal. **2006**, *239*, 83-96; f) R.A. Sidik, A.B. Anderson, N.P. Subramanian, S.P. Kumaraguru, B.N. Popov, J. Phys. Chem. B **2006**, *110*, 1787-1793; g) P.H. Matter, E. Wang, M. Arias, E.J. Biddinger, U.S. Ozkan, J. Mol. Catal. A: Chem. **2007**, *264*, 73-81; h) L. Yu, X. Pan, X. Cao, P. Hu, X. Bao, J. Catal. **2011**,

Accepted Manuscript

This article is protected by copyright. All rights reserved.

282, 183-190; i) Y. Zheng, Y. Jiao, J. Chen, J. Liu, J. Liang, A. Du, W. Zhang, Z. Zhu, S.C. Smith, M. Jaroniec, G.Q. Lu, S.Z. Qiao, J. Am. Chem. Soc. **2011**, *133*, 20116-20119.
[27] C.-S. Liu, X.-C. Liu, G.-C. Wang, R.-P. Liang, J.-D. Qiu, J. Electroanal. Chem. **2014**, *728*, 41-50.
[28] E. Gracia-Espino, X. Jia, T. Wågberg, J. Phys. Chem. C **2014**, *118*, 2804-2811.
[29] S. Zhao, H. Yin, L. Du, L. He, K. Zhao, L. Chang, G. Yin, H. Zhao, S. Liu, Z. Tang, ACS Nano **2014**, *8*, 12660-12668.
[30] Y. Wu, H. Yu, H. Wang, F. Peng, Chinese J. Catal. **2014**, *35*, 952-959.
[31] D. Usachov, O. Vilkov, A. Grüneis, D. Haberer, A. Fedorov, V.K. Adamchuk, A.B. Preobrajenski, P. Dudin, A. Barinov, M. Oehzelt, C. Laubschat, D.V. Vyalikh, Nano Lett. **2011**, *11*, 5401-5407.
[32] M. Yang, L. Zhou, J. Wang, Z. Liu, Z. Liu, J. Phys. Chem. C **2012**, *116*, 844-850.
[33] Z. Hou, X. Wang, T. Ikeda, K. Terakura, M. Oshima, M.-A. Kakimoto, Phys. Rev. B **2013**, *87*, 165401.
[34] P. Wu, P. Du, H. Zhang, C. Cai, Phys. Chem. Chem. Phys. **2013**, *15*, 6920-6928.
[35] a) A. Lherbier, A.R. Botello-Méndez, J.-C. Charlier, Nano Lett. **2013**, *13*, 1446-1450; b) A.R. Botello-Méndez, A. Lherbier, J.C. Charlier, Solid State Commun. **2013**, *175-176*, 90-100.
[36] T. Schiros, D. Nordlund, L. Pálová, D. Prezzi, L. Zhao, K.S. Kim, U. Wurstbauer, C. Gutierrez, D. Delongchamp, C. Jaye, D. Fischer, H. Ogasawara, L.G.M. Pettersson, D.R. Reichman, P. Kim, M.S. Hybertsen, A.N. Pasupathy, Nano Lett. **2012**, *12*, 4025-4031.
[37] Y. Zhang, J. Ge, L. Wang, D. Wang, F. Ding, X. Tao, W. Chen, Sci. Rep. **2013**, *3*, 2771.
[38] F. Pan, J. Jin, X. Fu, Q. Liu, J. Zhang, ACS App. Mater. Interfaces **2013**, *5*, 11108-11114.
[39] T. Ikeda, M. Boero, S.-F. Huang, K. Terakura, M. Oshima, J.-I. Ozaki, J. Phys. Chem. C **2008**, *112*, 14706-14709.
[40] Z. Lin, G.H. Waller, Y. Liu, M. Liu, C.-P. Wong, Nano Energy **2013**, *2*, 241-248.
[41] B. Zheng, J. Wang, F.-B. Wang, X.-H. Xia, Electrochem. Commun. **2013**, *28*, 24-26.
[42] a) J. Vazquez-Arenas, A. Galano, D.U. Lee, D. Higgins, A. Guevara-García, Z. Chen, J. Mater. Chem. A **2016**, *4*, 976-990; b) H.-P. Cong, P. Wang, M. Gong, S.-H. Yu, Nano Energy **2014**, *3*, 55-63.
[43] K.R. Lee, K.U. Lee, J.W. Lee, B.T. Ahn, S.I. Woo, Electrochem. Commun. **2010**, *12*, 1052-1055.
[44] Z.-H. Sheng, L. Shao, J.-J. Chen, W.-J. Bao, F.-B. Wang, X.-H. Xia, ACS Nano **2011**, *5*, 4350-4358.
[45] M. Sun, X. Wu, Z. Xie, X. Deng, J. Wen, Q. Huang, B. Huang, Carbon **2017**, *125*, 401-408.
[46] H. Zhang, Y. Wang, D. Wang, Y. Li, X. Liu, P. Liu, H. Yang, T. An, Z. Tang, H. Zhao, Small **2014**, *10*, 3371-3376.
[47] J. Sun, S.E. Lowe, L. Zhang, Y. Wang, K. Pang, Y. Wang, Y. Zhong, P. Liu, K. Zhao, Z. Tang, H. Zhao, Angew. Chem. Int. Ed. **2018**, *57*, 16511-16515.
[48] L. Lai, J.R. Potts, D. Zhan, L. Wang, C.K. Poh, C. Tang, H. Gong, Z. Shen, J. Lin, R.S. Ruoff, Energy Environ. Sci. **2012**, *5*, 7936-7942.
[49] D.W. Boukhvalov, Y.-W. Son, Nanoscale **2012**, *4*, 417-420.
[50] a) L. Zhang, Z. Xia, J. Phys. Chem. C **2011**, *115*, 11170-11176; b) L. Zhang, J. Niu, L. Dai, Z. Xia, Langmuir **2012**, *28*, 7542-7550.
[51] T. Xing, Y. Zheng, L.H. Li, B.C.C. Cowie, D. Gunzelmann, S.Z. Qiao, S. Huang, Y. Chen, ACS Nano **2014**, *8*, 6856-6862.
[52] a) K. Gong, F. Du, Z. Xia, M. Durstock, L. Dai, Science **2009**, *323*, 760; b) X. Bo, C. Han, Y. Zhang, L. Guo, ACS App. Mater. Interfaces **2014**, *6*, 3023-3030.
[53] C. Zhang, R. Hao, H. Liao, Y. Hou, Nano Energy **2013**, *2*, 88-97.
[54] D. Wei, Y. Liu, Y. Wang, H. Zhang, L. Huang, G. Yu, Nano Lett. **2009**, *9*, 1752-1758.
[55] W.A. Saidi, J. Phys. Chem. Lett. **2013**, *4*, 4160-4165.
[56] Z. Hou, X. Wang, T. Ikeda, K. Terakura, M. Oshima, M.-A. Kakimoto, S. Miyata, Phys. Rev. B **2012**, *85*, 165439.
[57] S. Kabir, K. Artyushkova, A. Serov, P. Atanassov, ACS App. Mater. Interfaces **2018**, *10*, 11623-11632.
[58] S. Chen, J. Duan, M. Jaroniec, S.Z. Qiao, Angew. Chem. Int. Ed. **2013**, *52*, 13567-13570.
[59] D. Guo, R. Shibuya, C. Akiba, S. Saji, T. Kondo, J. Nakamura, Science **2016**, *351*, 361.
[60] T. Mondal, A.K. Bhowmick, R. Krishnamoorti, Chem. Mater. **2015**, *27*, 716-725.
[61] a) Z. Zhang, K. Chi, F. Xiao, S. Wang, J. Mater. Chem. A **2015**, *3*, 12828-12835; b) X. Xiong, C. Yang, G. Wang, Y. Lin, X. Ou, J.-H. Wang, B. Zhao, M. Liu, Z. Lin, K. Huang, Energy Environ. Sci. **2017**, *10*, 1757-1763.
[62] G.-L. Tian, M.-Q. Zhao, D. Yu, X.-Y. Kong, J.-Q. Huang, Q. Zhang, F. Wei, Small **2014**, *10*, 2251-2259.
[63] a) D.-S. Yang, D. Bhattacharjya, S. Inamdar, J. Park, J.-S. Yu, J. Am. Chem. Soc. **2012**, *134*, 16127-16130; b) H. Peng, Z. Mo, S. Liao, H. Liang, L. Yang, F. Luo, H. Song, Y. Zhong, B. Zhang, Sci. Rep. **2013**, *3*, 1765; c) S.-A. Wohlgemuth, R.J. White, M.-G. Willinger, M.-M. Titirici, M. Antonietti, Green Chem. **2012**, *14*, 1515-1523; d) G.-L. Tian, Q. Zhang, B. Zhang, Y.-G. Jin, J.-Q. Huang, D.S. Su, F. Wei, Adv. Funct. Mater. **2014**, *24*, 5956-5961; e) Z. Chen, D. Higgins, A. Yu, L. Zhang, J. Zhang, Energy Environ. Sci. **2011**, *4*, 3167-3192; f) Y. Zhao, L. Yang, S. Chen, X. Wang, Y. Ma, Q. Wu, Y. Jiang, W. Qian, Z. Hu, J. Am. Chem. Soc. **2013**, *135*, 1201-1204; g) J.-S. Li, S.-L. Li, Y.-J. Tang, K. Li, L. Zhou, N. Kong, Y.-Q. Lan, J.-C. Bao, Z.-H. Dai, Sci. Rep. **2014**, *4*, 5130.
[64] S. Ratso, I. Kruusenberg, M. Vikkisk, U. Joost, E. Shulga, I. Kink, T. Kallio, K. Tammeveski, Carbon **2014**, *73*, 361-370.
[65] D.C. Higgins, M.A. Hoque, F. Hassan, J.-Y. Choi, B. Kim, Z. Chen, ACS Catal. **2014**, *4*, 2734-2740.
[66] J. Shui, M. Wang, F. Du, L. Dai, Sci. Adv. **2015**, *1*, e1400129.
[67] a) B. Dai, K. Chen, Y. Wang, L. Kang, M. Zhu, ACS Catal. **2015**, *5*, 2541-2547; b) J. Zhang, L. Dai, ACS Catal. **2015**, *5*, 7244-7253.
[68] D. Deng, X. Pan, L. Yu, Y. Cui, Y. Jiang, J. Qi, W.-X. Li, Q. Fu, X. Ma, Q. Xue, G. Sun, X. Bao, Chem. Mater. **2011**, *23*, 1188-1193.
[69] a) H.-W. Liang, X. Zhuang, S. Brüller, X. Feng, K. Müllen, Nat. Commun. **2014**, *5*, 4973; b) C.V. Rao, C.R. Cabrera, Y. Ishikawa, J. Phys. Chem. Lett. **2010**, *1*, 2622-2627; c) J. Wu, S. Ma, J. Sun, J.I. Gold, C. Tiwary, B. Kim, L. Zhu, N. Chopra, I.N. Odeh, R. Vajtai, A.Z. Yu, R. Luo, J. Lou, G. Ding, P.J.A. Kenis, P.M. Ajayan, Nat. Commun. **2016**, *7*, 13869; d) W. Ding, Z. Wei, S. Chen, X. Qi, T. Yang, J. Hu, D. Wang, L.-J. Wan, S.F. Alvi, L. Li, Angew. Chem. **2013**, *125*, 11971-11975.
[70] S. Wang, D. Yu, L. Dai, J. Am. Chem. Soc. **2011**, *133*, 5182-5185.
[71] S. Shanmugam, T. Osaka, Chem. Commun. **2011**, *47*, 4463-4465.
[72] Y. Tang, B.L. Allen, D.R. Kauffman, A. Star, J. Am. Chem. Soc. **2009**, *131*, 13200-13201.
[73] P.A. Denis, R. Faccio, A.W. Mombru, Chemphyschem **2009**, *10*, 715-722.
[74] A.Y.S. Eng, Z. Sofer, P. Šimek, J. Kosina, M. Pumera, Chem – Eur. J. **2013**, *19*, 15583-15592.
[75] J. Jin, F. Pan, L. Jiang, X. Fu, A. Liang, Z. Wei, J. Zhang, G. Sun, ACS Nano **2014**, *8*, 3313-3321.
[76] J. Liang, Y. Jiao, M. Jaroniec, S.Z. Qiao, Angew. Chem. **2012**, *124*, 11664-11668.
[77] A.S. Mayorov, R.V. Gorbachev, S.V. Morozov, L. Britnell, R. Jalil, L.A. Ponomarenko, P. Blake, K.S. Novoselov, K. Watanabe, T. Taniguchi, A.K. Geim, Nano Lett. **2011**, *11*, 2396-2399.
[78] L. Zhang, J. Niu, M. Li, Z. Xia, J. Phys. Chem. C **2014**, *118*, 3545-3553.
[79] Y. Zhang, M. Chu, L. Yang, W. Deng, Y. Tan, M. Ma, Q. Xie, Chem. Commun. **2014**, *50*, 6382-6385.
[80] J.-E. Park, Y.J. Jang, Y.J. Kim, M.-S. Song, S. Yoon, D.H. Kim, S.-J. Kim, Phys. Chem. Chem. Phys. **2014**, *16*, 103-109.
[81] a) L. Arroyo-Ramírez, D. Rodríguez, W. Otaño, C.R. Cabrera, ACS App. Mater. Interfaces **2012**, *4*, 2018-2024; b) M.E.M. Buan, N. Muthuswamy, J.C. Walmsley, D. Chen, M. Rønning, Carbon **2016**, *101*, 191-202.
[82] P.A. Denis, Comput. Mater. Sci. **2013**, *67*, 203-206.
[83] C. Zhang, N. Mahmood, H. Yin, F. Liu, Y. Hou, Adv. Mater. **2013**, *25*, 4932-4937.
[84] Y.-T. Wang, A.-H. Lu, H.-L. Zhang, W.-C. Li, J. Phys. Chem. C **2011**, *115*, 5413-5421.
[85] a) Z. Liu, F. Peng, H. Wang, H. Yu, J. Tan, L. Zhu, Catal. Commun. **2011**, *16*, 35-38; b) Z. Liu, F. Peng, H. Wang, H. Yu, W. Zheng, X. Wei, J. Nat. Gas Chem. **2012**, *21*, 257-264.
[86] G.A. Snook, P. Kao, A.S. Best, J. Power Sources **2011**, *196*, 1-12.
[87] Y. Wen, B. Wang, C. Huang, L. Wang, D. Hulicova-Jurcakova, Chem – Eur. J.

This article is protected by copyright. All rights reserved.

ChemSusChem 10.1002/cssc.201900060
MINIREVIEW WILEY-VCH

Eur. J. **2015**, *21*, 80-85.
[88] J.-I. Ozaki, N. Kimura, T. Anahara, A. Oya, Carbon **2007**, *45*, 1847-1853.
[89] L. Zhu, J. Wu, Q. Zhang, X. Li, Y. Li, X. Cao, J. Colloid Interface Sci. **2018**, *510*, 32-38.
[90] M.-S. Song, K.M. Lee, Y.R. Lee, I.Y. Kim, T.W. Kim, J.L. Gunjakar, S.-J. Hwang, J. Phys. Chem. C **2010**, *114*, 22134-22140.
[91] R. Li, Z. Wei, X. Gou, ACS Catal. **2015**, *5*, 4133-4142.
[92] J.P. Paraknowitsch, A. Thomas, Energy Environ. Sci. **2013**, *6*, 2839-2855.
[93] a) R. Li, W. Fan, G. Tian, H. Zhu, L. He, J. Cai, Q. Huang, Q. Cai, B. Li, Y. Bai, Z. Zhang, Y. Zhang, W. Wang, J. Li, F. Wei, H. Li, M. Jian, J. Li, Z. Zhang, R. Nielsen, D. Li, W. Gu, Z. Yang, Z. Xuan, O.A. Ryder, F.C.-C. Leung, Y. Zhou, J. Cao, X. Sun, Y. Fu, X. Fang, X. Guo, B. Wang, R. Hou, F. Shen, B. Mu, P. Ni, R. Lin, W. Qian, G. Wang, C. Yu, W. Nie, J. Wang, Z. Wu, H. Liang, J. Min, Q. Wu, S. Cheng, J. Ruan, M. Wang, Z. Shi, M. Wen, B. Liu, X. Ren, H. Zheng, D. Dong, K. Cook, G. Shan, H. Zhang, C. Kosid, X. Xie, Z. Lu, H. Zheng, Y. Li, C.C. Steiner, T.T.-Y. Lam, S. Lin, Q. Zhang, G. Li, J. Tian, T. Gong, H. Liu, D. Zhang, L. Fang, C. Ye, J. Zhang, W. Hu, A. Xu, Y. Ren, G. Zhang, M.W. Bruford, Q. Li, L. Ma, Y. Guo, N. An, Y. Hu, Y. Zheng, Y. Shi, Z. Li, Q. Liu, Y. Chen, J. Zhao, N. Qiu, S. Zhao, F. Tian, X. Wang, H. Wang, L. Xu, X. Liu, T. Vinar, Y. Wang, T.-W. Lam, S.-M. Yiu, S. Liu, H. Zhang, D. Li, Y. Huang, X. Wang, G. Yang, Z. Jiang, J. Wang, N. Qin, L. Li, J. Li, L. Bolund, K. Kristiansen, G.K.-S. Wong, M. Olson, X. Zhang, S. Li, H. Yang, J. Wang, J. Wang, Nature **2009**, *463*, 311; b) Z. Zhang, B. Lu, J. Hao, W. Yang, J. Tang, Chem. Commun. **2014**, *50*, 11554-11557.
[94] J. Wang, K. Huo, L. Ma, L. Tang, D. Li, X. Huang, Y. Yuan, C. Li, W. Wang, W. Guan, H. Chen, C. Jin, J. Wei, W. Zhang, Y. Yang, Q. Liu, Y. Zhou, C. Zhang, Z. Wu, W. Xu, Y. Zhang, T. Liu, D. Yu, Y. Zhang, L. Chen, D. Zhu, X. Zhong, L. Kang, X. Gan, X. Yu, Q. Ma, J. Yan, L. Zhou, Z. Liu, Y. Zhu, T. Zhou, F. He, X. Yang, Mol. Syst. Biol. **2011**, *7*, 536.
[95] Y. Meng, D. Voiry, A. Goswami, X. Zou, X. Huang, M. Chhowalla, Z. Liu, T. Asefa, J. Am. Chem. Soc. **2014**, *136*, 13554-13557.
[96] a) J. Chen, H. Zhang, P. Liu, Y. Li, G. Li, T. An, H. Zhao, Carbon **2015**, *92*, 339-347; b) J. Xu, Y. Zhao, C. Shen, L. Guan, ACS App. Mater. Interfaces **2013**, *5*, 12594-12601.
[97] C.H. Choi, S.H. Park, S.I. Woo, Green Chem. **2011**, *13*, 406-412.
[98] C. Hu, L. Dai, Adv. Mater. **2017**, *29*, 1604942.
[99] J. Li, Y. Zhang, X. Zhang, J. Huang, J. Han, Z. Zhang, X. Han, P. Xu, B. Song, ACS App. Mater. Interfaces **2017**, *9*, 398-405.
[100] J. Xu, G. Dong, C. Jin, M. Huang, L. Guan, ChemSusChem **2013**, *6*, 493-499.
[101] S.-A. Wohlgemuth, F. Vilela, M.-M. Titirici, M. Antonietti, Green Chem. **2012**, *14*, 741-749.

This article is protected by copyright. All rights reserved.

WILEY-VCH
Accepted Manuscript
Accepted Manuscript

2.Shao Y, Chang Y, Zhang S, et al. Impact of polymer backbone

fluorination on the charge generation/recombination patterns and vertical phase segregation in bulk heterojunction organic solar cells[J]. Frontiers in chemistry, 2020, 8: 144.

frontiers in Chemistry

ORIGINAL RESEARCH
published: 05 March 2020
doi: 10.3389/fchem.2020.00144

Impact of Polymer Backbone Fluorination on the Charge Generation/Recombination Patterns and Vertical Phase Segregation in Bulk Heterojunction Organic Solar Cells

Yanqiu Shao[1], Yuying Chang[1], Suju Zhang[1], Mingyue Bi[1], Shengjian Liu[2], Daliang Zhang[3], Shirong Lu[4] and Zhipeng Kan[4]**

[1] School of Chemistry and Chemical Engineering, Mudanjiang Normal University, Mudanjiang, China, [2] Guangzhou Key Laboratory of Materials for Energy Conversion and Storage, Guangdong Provincial Engineering Technology Research Center for Materials for Energy Conversion and Storage, School of Chemistry, South China Normal University (SCNU), Guangzhou, China, [3] Institute of Advanced Interdisciplinary Studies, Chongqing University, Chongqing, China, [4] Organic Semiconductor Research Center, Chongqing Institute of Green and Intelligent Technology, Chinese Academy of Sciences, Chongqing, China

OPEN ACCESS

Edited by:
Ergang Wang,
Chalmers University of Technology, Sweden

Reviewed by:
Lei Ying,
South China University of Technology, China
Hua Tan,
Xiangtan University, China

***Correspondence:**
Yanqiu Shao
shaoyanqiu1969@163.com
Zhipeng Kan
kanzhipeng@cigit.ac.cn

Specialty section:
This article was submitted to Physical Chemistry and Chemical Physics, a section of the journal Frontiers in Chemistry

Received: 16 December 2019
Accepted: 17 February 2020
Published: 05 March 2020

Citation:
Shao Y, Chang Y, Zhang S, Bi M, Liu S, Zhang D, Lu S and Kan Z (2020) Impact of Polymer Backbone Fluorination on the Charge Generation/Recombination Patterns and Vertical Phase Segregation in Bulk Heterojunction Organic Solar Cells. Front. Chem. 8:144. doi: 10.3389/fchem.2020.00144

Incorporating fluorine (–F) substituents along the main-chains of polymer donors and acceptors is an effective strategy toward efficient bulk-heterojunction (BHJ) solar cells. Specifically, F-substituted polymers often exhibit planar conformations, leading to favorable packing, and electronic coupling. However, the effects of fluorine substituents on the charge generation and recombination characteristics that determine the overall efficiency of BHJ active layers remain critically important issues to examine. In this report, two PBDT[2X]T polymer analogs –poly[4,8-bis[(2-ethylhexyl]oxy)benzo[1,2-*b*:4,5-*b*']dithiophene-thiophene] [PBDT[2H]T] and its F-substituted counterpart poly[4,8-bis((2-ethylhexyl)oxy)benzo[1,2-*b*:4,5-*b*']dithiophene-3,4-difluoro-thiophene] [PBDT[2F]T]—are studied to systematically examine how –F substituents impact the blend morphology, charge generation, carrier recombination and extraction in BHJ solar cells. Considering the large efficiency differences between PBDT[2H]T- and PBDT[2F]T-based BHJ devices, significant emphasis is given to characterizing the out-of-plane morphology of the blend films as vertical phase-separation characteristics are known to have dramatic effects on charge transport and carrier extraction in polymer-fullerene BHJ solar cells. Herein, we use electron energy loss spectroscopy (EELS) in tandem with charge transport characterization to examine PBDT[2X]T-fullerene blend films. Our analyses show that PBDT[2H]T and PBDT[2F]T possess very different charge generation, recombination and extraction characteristics, resulting from distinct aggregation, and phase-distribution within the BHJ blend films.

Keywords: bulk heterojunction, polymer backbone fluorination, charge generation and recombination, vertical phase segregation, organic solar cells

3.邵艳秋,姜封庆,蔡雪,谭荣欣.高校化学实验室常见无机废液的处理方法[J].广东化工,2019,46(05):262-263.

高校化学实验室常见无机废液的处理方法

邵艳秋，姜封庆，蔡雪，谭荣欣
(牡丹江师范学院化学化工学院，黑龙江牡丹江 157011)

[摘要]高校化学实验室每年都需要进行大量的无机实验，无机实验所产生有害无机废液对地球环境污染严重，该文主要介绍我校实验室所产生的无机废液，根据其化学性质进行了简单分类并提出环保安全的处理方法。
[关键词]实验室；无机废液；处理方法
[中图分类号]G4 [文献标识码]A [文章编号]1007-1865(2019)05-0263-01

Treatment Methods of Common Inorganic Waste Liquid in University Chemistry Laboratory

Shao Yanqiu, Jiang Fengqing, Cai Xue, Tan Rongxin
(Department of Chemistry, MudanjiangNormalUniversity, Mudanjiang 157011, China)

Abstract: A large number of inorganic experiments are carried out every year in chemical laboratories of colleges and universities. The harmful inorganic waste liquid produced by inorganic experiments has seriously polluted the earth environment.
Keywords: laboratory；inorganic waste；processing method

无机废液的处理是高校实验室三废处理中最难以解决的问题。首先无机废液的种类繁多，实验室在处理上有较大难度；其次，无机实验产生无机废液的数量较大；最后，高校缺乏系统的实验室废液处理的相关教育[1]，使得学生对于废液处理的并没有形成一个科学严谨的态度，导致学生做完实验直接将废液倒进实验室下水道，造成下水管道污染甚至对周围水质造成极大的影响[2]，该文根据高校实验室中常见无机废液的种类和特点整理出了相应的处理方法。

1 无机化学实验废液的产生及分类

高校化学实验室所产生的废液按其来源可以分为容器洗涤液和未反应完全或者新产生的实验余液。实验所产生余液的性质复杂，种类繁多，需要严格按要求处理。废液按成分一般可分为无机废液、有机废液和生化废液[3]。其中，对环境污染最为严重的是无机废液[4]，主要包括含有铬、铅、镉、氰、银、钡、铜、汞等废液。另外，实验室产生的酸碱废液也对环境也会造成一定的影响。这些废液对生活用水及环境危害极大[5]。因此，我校对无机化学实验产生的废液处理问题高度重视，采取了实验室自行处理及分类存放找专门机构集中处理的方式。本文根据无机废液的性质及相关文献介绍总结出了我们实验课所产生废液的自行处理方法。

2 无机实验废液处理的一般原则

实验教学倡导将绿色化学[6]、环保化学、安全化学[7]等理念融入教学之中。在制定教学大纲时根据国家专业目录培养学生的技能要求，尽量选择毒性小、污染少，废液排放量小、废液种类少、废液处理容易的实验项目以减少对环境的污染[8-9]。另外，在学生培养过程中加强学生对废液处理、废物循环再利用以及减少废物排放量的认识，强化环保化学理念。

要不断强化微型实验在教学中的实际应用，在能得到同样实验现象和实验结论的前提下，尽量减少实验耗材，所排放废液就会大大减少。所以我们在教学过程中根据具体实验要求尽量选择微型实验，从而降低实验室废液处理的压力。

对于排放的废液要按照小心收集、准确分类、安全存放和严格处理的要求进行处理。

优先选择花费小、操作简单、绿色安全的处理方法，而且要高度重视废液的回收再利用问题[10]。

3 无机实验废液处理的对策及方法

我校无机实验产生的废液种类主要有含铬、铅、镉、汞、银、钡、铜、锌、酸碱废液等几类，参照文献结合自身实验条件采取以下处理办法。

3.1 酸碱废液的处理

无机化学实验通常会产生酸性和碱性的物质，这类废液直接排放会造成水 pH 值的改变。如果水质酸度过高，会造成实验室管道腐蚀。一般在处理这类废液时先看其浓度，如果浓度较低，可稀释后直接排放，如果浓度过高，则需定期进行中和处理，达到国家污水排放标准(GB8978-1996)[11]后再进行排放。

3.2 含铬废液的处理

铬酸洗液是实验室常用的洗液，也是无机实验中含铬废液的主要产生来源；醋酸铬(Ⅱ)水合物的制备实验会产生含铬废液。其中 Cr(Ⅵ)是 Cr(Ⅲ)的毒性的 100 倍，所以，实验室废液处理一般是把高价铬离子转化为低价铬离子，水中 Cr(Ⅵ)排放要小于 0.5 ppm。一般处理方法是用铁氧体法除去铬，在含铬废液中加入硫酸亚铁作为还原剂，从而把高价铬还原为低价铬，pH 值调节后生成铬的氢氧化物沉淀，进行统一焚烧处理，剩余废液可简单稀释后直接倒入下水道。

3.3 含银废液的处理

含银废液中回收银的方法有很多，如沉淀法、电解法和离子交换法等，但最主要的是沉淀法。无机化学实验中常见非金属阴离子的分离与鉴定、常见阳离子的分离与鉴定、P区非金属元素(一)、P区非金属元素(二)和离子的鉴定和未知物的鉴别等实验产生含银废液，用沉淀法处理含银废液方便适用。此方法是在废液中加入Na_2SO_4等含有SO_4^{2-}的溶液，将废液中的Ag^+完全转化为相对应的Ag_2SO_4沉淀，然后进行过滤回收处理。各高校在无机实验中会产生大量的含银废液，可以在实验后对其进行集中的处理。

3.4 含铅、镉废液的处理

含铅废液和含镉废液也是化学实验室经常产生的毒性很强的无机废液，产生铅、镉废液的实验有碘化铅溶度积的测定、常见阳离子的分离与鉴定、P 区非金属元素(一)、P 区非金属元素(二)、离子的鉴定和未知物的鉴别、氢气的制备和铜相对原子量的测定等实验都产生铅、镉废液。实验室一般可以把废液中毒性强的铅离子和镉离子转化为无毒性的沉淀。首先把碱性物质加入到含铅、镉废液的废液中，然后调节废液的 pH 值为 8~10，加入共沉淀剂$FeSO_4$，使废液中的铅离子和镉离子生成相对应的沉淀物，最后把沉淀物进行焚烧处理[12]。

3.5 含汞废液的处理

离子的鉴定和未知物的鉴别这个实验产生汞废液。实验室处理废液的办法是调节废液的 pH 值至碱性，然后把大量的 Na_2S 加入到含汞废液中，从而使有毒的汞离子转化为无毒的沉淀。最后再加入大量的 Na_2S 和 $FeSO_4$ 使其完全生成沉淀，静置 10 min 后，离心过滤的上层清液中汞离子浓度远低于排放标准后，可以安全的排放到外界，而所产生的沉淀则需要积累到一定数量后统一进行焚烧处理。

(下转第 262 页)

[收稿日期] 2019-01-28
[基金项目] 牡丹江师范学院教改项目(18-XJ20064)；黑龙江省教育厅科研备案项目(1352MSYB006)；牡丹江师范学院科研项目(JG2017001)
[作者简介] 邵艳秋(1969-)，女，吉林长春人，博士，主要研究方向为实验室建设与管理。

(C)1994-2020 China Academic Journal Electronic Publishing House. All rights reserved. http://www.cnki.net

4.王星月,邵艳秋,王丽杰,何冬青.Ag 负载对 $BiVO_4$ 半导体光诱导电荷传输行为调控及其光催化影响机理[J].化学工程师,2021,35(01):4-8.

化 学 工 程 师
Sum 304 No. 1 Chemical Engineer 2021 年第 1 期

科研与开发

DOI:10.16247/j.cnki.23-1171/tq.20210104

Ag 负载对 $BiVO_4$ 半导体光诱导电荷传输行为调控及其光催化影响机理*

王星月[1,2],邵艳秋[1],王丽杰[2],何冬青[2]

(1.牡丹江师范学院,黑龙江 牡丹江 157000;2.黑龙江省科学院高技术研究院,黑龙江 哈尔滨 150001)

摘 要:利用半导体光催化剂降解水中的有机污染物一直是当今世界的研究热点。本文通过光沉积方法在哑铃状 $BiVO_4$ 半导体表面负载不同比例的 Ag 来调控 $BiVO_4$ 半导体的光诱导电荷载流子的传输动力学行为,并对 Ag/$BiVO_4$ 复合物的形貌等性质进行表征,同时在模拟太阳光下通过降解染料罗丹明 B(RhB)来评价 Ag/$BiVO_4$ 的降解效率。实验结果表明,少量 Ag 的负载即可将 $BiVO_4$ 半导体由 n 型电荷传输转变为 p 型电荷传输。具有 p 型半导体性质的 Ag/$BiVO_4$ 复合物与具有 n 型半导体性质的 $BiVO_4$ 相比,具有优异的光吸收性质及较高的比表面积,提高了材料的光吸收效率和增加了光催化反应的活性位点,从而具有较高的光催化降解效率,不同半导体类型的催化机理也被讨论。

关键词:$BiVO_4$;光沉积;电荷传输;光催化

中图分类号:X832 文献标识码:A

Regulation and photocatalytic effect of Ag loading on photoinduced charge transport behavior of $BiVO_4$ semiconductor*

WANG Xing-yue[1,2], SHAO Yan-qiu[1], WANG Li-jie[2], HE Dong-qing[2]

(1.Mudanjiang Normal University, Mudanjiang 157000, China;
2.Institute of Advanced Technology of Heilongjiang Academy of Sciences, Harbin 150020, China)

Abstract: The use of semiconductor photocatalysts to degrade organic pollutants in water has always been a research focus in the world.In this article, the $BiVO_4$ semiconductor type was regulated by the method of photodeposition with Ag loads of different proportions on the dumbbell $BiVO_4$ semiconductor surface, Ag/$BiVO_4$ compound properties were characterized. The degradation efficiency of Ag/$BiVO_4$ was evaluated by degrading RhB in simulated sunlight. The experimental results show that a small amount of Ag load can transform the $BiVO_4$ semiconductor from n-type to p-type, and the charge transfer properties of n-type $BiVO_4$ and p-type Ag/$BiVO_4$ complexes are also analyzed. With characteristics of p-type semiconductor Ag/$BiVO_4$ composites compared with $BiVO_4$ with characteristics of n-type semiconductor, excellent optical absorption properties and high specific surface area, improve the efficiency of the light absorption material and increases the active site of photocatalytic reaction, thus has the high efficiency of photocatalytic degradation, different types of semiconductor catalytic mechanism was also discussed.

Key words: $BiVO_4$; photodeposition; charge transfer; photocatalysis

环境污染已成为当今世界主要面临的难题之一,利用半导体光催化材料降解有机污染物从而改善环境污染,一直是科学界的研究热点。在众多的可见光半导体催化剂中,$BiVO_4$ 由于具有合适的带隙宽度(2.4eV),廉价,无污染等优点,成为新的研究热点。$BiVO_4$ 虽然具有合适的带隙,但仍然有载流子的迁移率低,可见光吸收范围不大等问题,为了克服以上问题,研究者们通过调控特定形貌,晶面、掺杂金属离子和非金属离子以及构建异质结等措施来克服 $BiVO_4$ 的固有缺陷[1]。韩国科学技术研究所的工作人员研究发现:与原始 $BiVO_4$ 相比,含 Ag 纳米复合材料 $BiVO_4$ 的光催化能力显著增强,并证明这是由于

收稿日期:2020-10-29

基金项目:黑龙江省省属高等学校基本科研业务费科研机构专项(1355JG015);牡丹江师范学院科研项目(JG201700l);牡丹江师范学院研究生科技创新项目(kjcx2019-97mdjnu)

作者简介:王星月(1996-),女,在读硕士研究生,从事钙钛矿型半导体光催化降解有机污染物的研究。

通信作者:邵艳秋(1969-),女,博士,硕士研究生导师,现主要从事多相催化材料研究。

(C)1994-2021 China Academic Journal Electronic Publishing House. All rights reserved. http://www.cnki.net

5.邵艳秋,王丽杰,郑友进,于平,王星月.Ba^{2+}掺杂 $BiVO_4$ 光催化降解罗丹明 B 的性能研究[J].化工新型材料,2020,48(02):211-214.

Ba^{2+}掺杂 $BiVO_4$ 光催化降解罗丹明 B 的性能研究

邵艳秋[1] 王丽杰[1,2*] 郑友进[2] 于 平[1,2] 王星月[1,2]

(1.牡丹江师范学院化学化工学院,牡丹江 157011;
2.黑龙江省新炭-基功能与超硬材料重点实验室,牡丹江 157011)

摘 要 利用半导体光催化剂解决环境污染问题是当今世界的研究热点。利用水热法制备了不同 Ba^{2+} 掺杂量的 $BiVO_4$ 光催化剂,并利用 X 射线粉末衍射(XRD)、扫描电子显微镜(SEM)和能量色散 X 射线光谱仪(EDS)表征手段研究其结构及形貌特征,同时通过降解罗丹明 B(RhB)评价其光催化活性。结果表明:制备的 $BiVO_4$ 具有哑铃状形貌,为单斜白钨矿结构。Ba^{2+} 可能取代了晶胞中 Bi^{3+} 的位置,不仅导致 $BiVO_4$ 晶体结构的变化,而且提高了 $BiVO_4$ 的光催化活性,最佳掺杂量样品 0.1 Ba^{2+}:$BiVO_4$ 在模拟太阳光的照射下 2h 的降解效率可达 31%,为进一步提高 $BiVO_4$ 的光催化活性提供了实验基础。

关键词 钒酸铋,掺杂,光催化降解,罗丹明 B

DOI:10.19817/j.cnki.issn1006-3536.2020.02.045

Study on photocatalytic degradation of Rh B by Ba^{2+} doped $BiVO_4$

Shao Yanqiu[1] Wang Lijie[1,2] Zheng Youjin[2] Yu Ping[1,2] Wang Xingyue[1,2]

(1.College of Chemistry and Chemical Engineering, Mudanjiang Normal University, Mudanjiang 157011; 2.Heilongjiang Province Key Laboratory of New Carbon-Base Functional and Superhard Material, Mudanjiang 157011)

Abstract The use of semiconductor photocatalysts to solve environmental pollution problems is a hot research topic in the world today. $BiVO_4$ photocatalysts with different Ba^{2+} doping amount were prepared by hydrothermal method, and their physical and chemical properties were studied by X-ray powder diffraction (XRD), scanning electron microscopy(SEM) and Energy dispersive X-ray spectrometer(EDS). At the same time, it's photocatalytic activity was evaluated by degradation of Rh B. The results shown that the prepared $BiVO_4$ had a dumbbell-like morphology and was a monoclinic scheelite structure. Ba^{2+} may replace the position of Bi^{3+} in the unit cell, which not only leaded to the change of $BiVO_4$ crystal structure, but also improved the photocatalytic activity of $BiVO_4$. The optimum doping amount of 0.1 Ba^{2+} : $BiVO_4$ can be degraded by 31% under simulated illumination for 2 hours. Further improving the photocatalytic activity of $BiVO_4$ provided an experimental basis.

Key words $BiVO_4$, doping, photocatalytic degradation, Rh B

能源短缺和环境污染已成为当今世界最棘手的问题。如何解决环境污染问题已经成为目前研究的重点和难点[1]。利用清洁能源太阳能,以半导体为载体进行光催化降解是解决环境污染的有效手段,作为半导体家族的重要一员,钒酸铋由于无毒、稳定性强、合适的能带结构(2.4eV),在光催化领域具有很大的应用前景[2]。但由于 $BiVO_4$ 具有光生电子-空穴对难分离、易复合等缺点,导致其光催化效率低,因此常需对其进行改性,如离子掺杂、构建异质结构、表面形貌修饰等方法来提高其光催化活性[3-5]。

离子掺杂是通过金属或非金属离子的掺杂,影响 $BiVO_4$ 的能带结构,降低光生电荷载流子传输的阻力,从而提高电荷载流子的分离效率来提高 $BiVO_4$ 的光催化活性。例如 Ge 等[6]掺杂的 Pd 以氧化钯的形式存在,提高了复合样品的光催化能力,在光照 15h 后可以完全降解甲基橙。其中 PdO 粒

基金项目:牡丹江师范学院科研项目(JG2017001);牡丹江师范学院研究生科技创新项目(kjcx2018-26mdjnu);黑龙江省教育厅科研备案项目(1352MSYYB006)

作者简介:邵艳秋(1969-),女,博士,教授,主要从事多相催化材料的研究。

联 系 人:王丽杰,女,硕士研究生,主要从事金属氧化物光催化降解有机污染物的研究。

(C)1994-2020 China Academic Journal Electronic Publishing House. All rights reserved. http://www.cnki.net

6.邵艳秋,姜封庆,蔡雪,谭荣欣.高校化学实验室常见无机废液的处理方法[J].广东化工,2019,46(05):262-263.

高校化学实验室常见无机废液的处理方法

邵艳秋，姜封庆，蔡雪，谭荣欣
(牡丹江师范学院化学化工学院，黑龙江牡丹江 157011)

[摘要]高校化学实验室每年都需要进行大量的无机实验，无机实验所产生有害无机废液对地球环境污染严重，该文主要介绍我校实验室所产生的无机废液，根据其化学性质进行了简单分类并提出环保安全的处理方法。

[关键词]实验室；无机废液；处理方法
[中图分类号]G4 [文献标识码]A [文章编号]1007-1865(2019)05-0263-01

Treatment Methods of Common Inorganic Waste Liquid in University Chemistry Laboratory

Shao Yanqiu, Jiang Fengqing, Cai Xue, Tan Rongxin
(Department of Chemistry, MudanjiangNormalUniversity, Mudanjiang 157011, China)

Abstract: A large number of inorganic experiments are carried out every year in chemical laboratories of colleges and universities. The harmful inorganic waste liquid produced by inorganic experiments has seriously polluted the earth environment.

Keywords: laboratory；inorganic waste；processing method

无机废液的处理是高校实验室三废处理中最难以解决的问题。首先无机废液的种类繁多，实验室在处理上有较大难度；其次，无机实验产生无机废液的数量较大；最后，高校缺乏系统的实验室废液处理的相关教育[1]，使得学生对于废液处理的并没有形成一个科学严谨的态度，导致学生做完实验直接将废液倒进实验室下水道，造成下水管道污染甚至对周围水质造成极大的影响[2]，该文根据高校实验室中常见无机废液的种类和特点整理出了相应的处理方法。

1 无机化学实验废液的产生及分类

高校化学实验室所产生的废液按其来源可以分为容器洗涤液和未反应完全或者新产生的实验余液。实验所产生余液的性质复杂，种类繁多，需要严格按要求处理。废液按成分一般可分为无机废液、有机废液和生化废液[3]。其中，对环境污染最为严重的是无机废液[4]，主要包括含有铬、铅、镉、氰、银、钡、铜、汞等废液。另外，实验室产生的酸碱废液也对环境也会造成一定的影响。这些废液对生活用水及环境危害极大[5]。因此，我校对无机化学实验产生的废液处理问题高度重视，采取了实验室自行处理及分类存放找专门机构集中处理的方式。本文根据无机废液的性质及相关文献介绍总结出了我们实验课所产生废液的自行处理方法。

2 无机实验废液处理的一般原则

实验教学倡导将绿色化学[6]、环保化学、安全化学[7]等理念融入教学之中。在制定教学大纲时根据国家专业目录培养学生的技能要求，尽量选择毒性小、污染少，废液排放量小、废液种类少、废液处理容易的实验项目以减少对环境的污染[8-9]。另外，在学生培养过程中加强学生对废液处理、废物循环再利用以及减少废物排放量的认识，强化环保化学理念。

要不断强化微型实验在教学中的实际应用，在能得到同样实验现象和实验结论的前提下，尽量减少实验耗材，所排放废液就会大大减少。所以我们在教学过程中根据具体实验要求尽量选择微型实验，从而降低实验室废液处理的压力。

对于排放的废液要按照小心收集、准确分类、安全存放和严格处理的要求进行处理。

优先选择花费小、操作简单、绿色安全的处理方法，而且要高度重视废液的回收再利用问题[10]。

3 无机实验废液处理的对策及方法

我校无机实验产生的废液种类主要有含铬、铅、镉、汞、银、钡、铜、锌、酸碱废液等几类，参照文献结合自身实验条件采取以下处理办法。

3.1 酸碱废液的处理

无机化学实验通常会产生酸性和碱性的物质，这类废液直接排放会造成水 pH 值的改变。如果水质酸度过高，会造成实验室管道腐蚀。一般在处理这类废液时先看其浓度，如果浓度较低，可稀释后直接排放，如果浓度过高，则需定期进行中和处理，达到国家污水排放标准(GB8978-1996)[11]后再进行排放。

3.2 含铬废液的处理

铬酸洗液是实验室常用的洗液，也是无机实验中含铬废液的主要产生来源；醋酸铬(Ⅱ)水合物的制备实验会产生含铬废液。其中 Cr(Ⅵ)是 Cr(Ⅲ)的毒性的 100 倍，所以，实验室废液处理一般是把高价铬离子转化为低价铬离子，水中 Cr(Ⅵ)排放要小于 0.5 ppm。一般处理方法是用铁氧体法除去铬，在含铬废液中加入硫酸亚铁作为还原剂，从而把高价铬还原为低价铬，pH 值调节后生成铬的氢氧化物沉淀，进行统一焚烧处理，剩余废液可简单稀释后直接倒入下水道。

3.3 含银废液的处理

含银废液中回收银的方法有很多，如沉淀法、电解法和离子交换法等，但最主要的是沉淀法。无机化学实验中常见非金属阴离子的分离与鉴定、常见阳离子的分离与鉴定、P区非金属元素(一)、P区非金属元素(二)和离子的鉴定和未知物的鉴别等实验产生含银废液，用沉淀法处理含银废液方便适用。此方法是在废液中加入Na_2SO_4等含有SO_4^{2-}的溶液，将废液中的Ag^+完全转化为相对应的Ag_2SO_4沉淀，然后进行过滤回收处理。各高校在无机实验中会产生大量的含银废液，可以在实验后对其进行集中的处理。

3.4 含铅、镉废液的处理

含铅废液和含镉废液也是化学实验室经常产生的毒性很强的无机废液，产生铅、镉废液的实验有碘化铅溶度积的测定、常见阳离子的分离与鉴定、P 区非金属元素(一)、P 区非金属元素(二)、离子的鉴定和未知物的鉴别、氢气的制备和铜相对原子量的测定等实验都产生铅、镉废液。实验室一般可以把废液中毒性强的铅离子和镉离子转化为无毒性的沉淀。首先把碱性物质加入到含铅、镉废液的废液中，然后调节废液的 pH 值为 8~10，加入共沉淀剂$FeSO_4$，使废液中的铅离子和镉离子生成相对应的沉淀物，最后把沉淀物进行焚烧处理[12]。

3.5 含汞废液的处理

离子的鉴定和未知物的鉴别这个实验产生汞废液。实验室处理废液的办法是调节废液的 pH 值至碱性，然后把大量的 Na_2S 加入到含汞废液中，从而使有毒的汞离子转化为无毒的沉淀。最后再加入大量的 Na_2S 和 $FeSO_4$ 使其完全生成沉淀，静置 10 min 后，离心过滤的上层清液中汞离子浓度远低于排放标准后，可以安全的排放到外界，而所产生的沉淀则需要积累到一定数量后统一进行焚烧处理。

(下转第 262 页)

[收稿日期] 2019-01-28
[基金项目] 牡丹江师范学院教改项目(18-XJ20064)；黑龙江省教育厅科研备案项目(1352MSYB006)；牡丹江师范学院科研项目(JG2017001)
[作者简介] 邵艳秋(1969-)，女，吉林长春人，博士，主要研究方向为实验室建设与管理。

(C)1994-2020 China Academic Journal Electronic Publishing House. All rights reserved. http://www.cnki.net

7.邵艳秋,张宇婷,姜振双,刘素娟,任玉兰,王丽杰.水解剂氟化铵对Fe-SBA-15结构及催化性能的影响[J].无机盐工业,2019,51(09):97-101.

第51卷 第9期 2019年9月 | 无机盐工业 INORGANIC CHEMICALS INDUSTRY | Vol.51 No.9 Sept.,2019

Doi:10.11962/1006-4990.2018-0562

水解剂氟化铵对Fe-SBA-15结构及催化性能的影响

邵艳秋[1,2],张宇婷[1,2],姜振双[1,2,3],刘素娟[1],任玉兰[1],王丽杰[1,2]

(1.牡丹江师范学院化学化工学院,黑龙江牡丹江 157011;2.黑龙江省新炭-基功能与超硬材料重点实验室;3.吉林大学化学学院)

摘　要:通过水热法制备了Fe-SBA-15介孔材料,探究了水解剂氟化铵对介孔材料结构及对苯酚羟基化反应的影响。采用X射线衍射(XRD)、红外光谱(FT-IR)和氮气吸附-脱附等方法对介孔材料进行了表征,用苯酚羟基化反应对改性后介孔材料的催化性能进行了研究。结果表明:改性后的介孔材料具有良好的催化性能,其中氟与硅物质的量比为0.03时制备的介孔材料的催化性能更为优良,在固定反应条件下苯酚转化率达到36.82%、苯二酚选择性达到81.76%。

关键词:水解剂;氟化铵;Fe-SBA-15;苯二酚;羟基化

中图分类号:O643　　**文献标识码**:A　　**文章编号**:1006-4990(2019)09-0097-05

Effects of hydrolysate NH_4F on structure and catalytic properties of Fe-SBA-15

Shao Yanqiu[1,2],Zhang Yuting[1,2],Jiang Zhenshuang[1,2,3],Liu Sujuan[1],Ren Yulan[1],Wang Lijie[1,2]

(1.*College of Chemistry and Chemical Engineering,Mudanjiang Normal University,Mudanjiang* 157011,*China*;2.*Heilongjiang Province Key Laboratory of New Carbon-Base Functional and Superhard Material*;3.*College of Chemistry,Jilin University*)

Abstract:Fe-SBA-15 mesoporous materials were prepared by hydrothermal synthesis,and the effect of hydrolysis agent NH_4F on the mesoporous materials structure and catalytic hydroxylation of phenol was explored.The mesoporous materials were characterized by X-ray diffraction(XRD),infrared spectroscopy(FT-IR) and N_2 adsorption desorption etc..The catalytic properties of modified mesoporous materials were studied by hydroxylation of phenol.The results indicated that the modified materials had good catalytic performance.When $n(F^-)/n(Si)=0.03$,the prepared mesoporous materials had better catalytic performance.Under the fixed reaction conditions,conversion of phenol and selectivity of dihydroxybenzene reached 36.82% and 81.76%,respectively.

Key words:hydrolysate;NH_4F;Fe-SBA-15;dihydroxybenzene;hydroxylation

SBA-15分子筛因具有较大的比表面积及有序的孔结构等优势使其在催化领域备受关注,纯硅SBA-15缺少酸性位点和活性中心,在应用上受到很大限制。通过分子筛表面Si—OH基团与活性组分之间的相互作用,将活性较高的成分引入孔道或骨架内来提高材料的活性一直受到关注和研究[1]。将金属引入分子筛孔道或骨架内可以提高分子筛的催化活性,但是引入的金属会对介孔结构造成一定的影响,所以在保证介孔材料有序孔结构的同时如何提高分子筛骨架内的金属含量是需要解决的问题[2-6]。研究发现,在氟离子存在的体系中,F^-既可以与过渡金属生成氟的配合物,还可以加快硅源的水解速率,有利于提高金属进入分子筛骨架中[7-8]。由于NH_4F受热会分解为氨和氟化氢,在材料制备过程中铵根对材料中铁的引入影响较小,并且NH_4F在分子筛中有一定的应用[9-10]。因此,笔者以NH_4F为水解剂,采用水热法制备了Fe-SBA-15(x)分子筛(x为氟与硅物质的量比),并探究了水解剂含量对材料结构和性能的影响。

1　实验部分

1.1　主要试剂

P123($EO_{20}PO_{70}EO_{20}$),Aldrich试剂;正硅酸乙酯

基金项目:黑龙江省教育厅科研备案项目(1352MSYYB006);牡丹江师范学院研究生科技创新项目(kjcx2017-09mdjmu);牡丹江师范学院科研项目(JG2017001);牡丹江师范学院大学生创新项目(201710233007)。

收稿日期:2019-03-27

作者简介:邵艳秋(1969—　),女,博士,教授,主要从事多相催化材料研究;E-mail:shaoyanqiu1969@163.com。

(C)1994-2019 China Academic Journal Electronic Publishing House. All rights reserved.　http://www.cnki.net

8.邵艳秋,于平,郑友进,王丽杰,王星月.氧化锌基阵列染料敏化太阳能电池研究进展[J].人工晶体学报,2019,48(10):1967-1975.

第48卷 第10期
2019年10月

人 工 晶 体 学 报
JOURNAL OF SYNTHETIC CRYSTALS

Vol. 48 No. 10
October, 2019

氧化锌基阵列染料敏化太阳能电池研究进展

邵艳秋[1],于 平[1,2],郑友进[2],王丽杰[1,2],王星月[1,2]
(1.牡丹江师范学院化学化工学院,牡丹江 157011; 2.黑龙江省新炭基功能与超硬材料重点实验室,牡丹江 157011)

摘要: ZnO基染料敏化太阳能电池(DSSCs)因其成本低、光电转换效率稳定、制备工艺简单且易于大规模生产等优势成为研究的热点。本文从形貌结构和优化方案两方面总结了近期ZnO阵列光阳极在DSSCs中的研究进展。通过分析不同形貌结构的ZnO阵列的优势和缺点来解释其对DSSCs影响的机理;通过总结ZnO阵列相关的掺杂、构筑异质结等优化方案获得了提高DSSCs光电转换效率的信息,为进一步提高DSSCs电池效率提供指导。

关键词: ZnO阵列; DSSCs; 光生电荷载流子; 光电转换效率
中图分类号: TM914.4 文献标识码: A 文章编号: 1000-985X(2019)10-1967-09
DOI:10.16553/j.cnki.issn1000-985x.2019.10.031

Research Progress of Zinc Oxide Based Array Dye-Sensitized Solar Cells

SHAO Yan-qiu[1], *YU Ping*[1,2], *ZHENG You-jin*[2], *WANG Li-jie*[1,2], *WANG Xing-yue*[1,2]
(1. School of Chemistry and Chemical Engineering, Mudanjiang Normal University, Mudanjiang 157011, China;
2. Heilongjiang Province Key Laboratory of New Carbon-Base Functional and Superhard Material, Mudanjiang 157011, China)

Abstract: ZnO-based dye-sensitized solar cells (DSSCs) have become the research hotspot due to their low cost, stable and efficient photoelectric conversion efficiency, simple preparation process and easy mass production. In this paper, the research progress of recent ZnO array photoanodes in DSSCs are summarized from the aspects of morphology structure and optimization scheme. By analyzing the advantages and disadvantages of ZnO array with different morphological structures, the mechanism of their effects on DSSCs is explained. By summarizing the doping and constructing heterojunctions of ZnO array, the information of improving the photoelectric conversion efficiency of DSSCs is obtained, which provides guidance for improving the efficiency of DSSCs.

Key words: ZnO array; DSSCs; photogenerated charge carry; photoelectric conversion efficiency

1 引 言

染料敏化太阳能电池(DSSCs)作为第三代新型高效太阳能电池具有工艺简单、成本低、无污染、效率高等优点,已成为人们研究的热点。经过不断的改进,DSSCs的光电转换效率已达到13%[1-4]。DSSCs的工作原理效仿植物光合作用,如图1。电极表面吸附在纳米级半导体材料上的染料被光照射受到激发后,将产生的电子注入到半导体的导带中,氧化态染料分子与电池中的还原性物质发生氧化-还原反应,被氧化的成分在电极上还原沉积,染料分子回到基态而重复使用[5]。纳米氧化物半导体作为光阳极在DSSCs中扮演着重要的角色,它不仅是吸附染料的重要载体,也是作为电荷分离和传输的载体,因此它应具有以下特点:(1)具有较大的比表面积,可吸附大量染料;(2)具备较高的电子迁移率,有利于光生电荷的传输,减少电荷载流子在传输过程中的复合。

TiO_2是经典的DSSCs光阳极材料,具有较高的光电转换效率,但由于热分散的影响及TiO_2较高的表面态密度,使得光生电子被其表面态能级俘获的几率增加,使TiO_2的扩散系数减小,电荷载流子的复合率增加,限制TiO_2基DSSCs的电池效率提高。ZnO的带隙宽为3.3 eV,激子结合能大且易形成高结晶态,有着与TiO_2相似的电子亲和性,电子迁移率也远超TiO_2,加之ZnO基光阳极价格低廉,制备方法简单多样,因此ZnO是有望取代TiO_2的理想光阳极材料[7-8]。然而,ZnO基DSSCs相较TiO_2的光电转换效率较低,主要原

基金项目:黑龙江省教育厅科研备案项目(1352MSYYB006);牡丹江师范学院研究生科技创新项目(kjcx2018-25mdjnu);牡丹江师范学院科研项目(JG2017001)

作者简介:邵艳秋(1969-),女,吉林省人,博士,教授。E-mail: shaoyanqiu1969@163.com

(C)1994-2021 China Academic Journal Electronic Publishing House. All rights reserved. http://www.cnki.net

9.邵艳秋,张宇婷,王星月,常玉莹,孙家红.Fe-SBA-15 介孔分子筛的合成及其苯酚羟基化反应性能研究[J].山东化工,2019,48(20):1-2.

科研与开发

Fe－SBA－15 介孔分子筛的合成及其苯酚羟基化反应性能研究

邵艳秋*，张宇婷，王星月，常玉莹，孙家红

（牡丹江师范学院 化学化工学院，黑龙江 牡丹江　157011）

摘要：以正硅酸乙酯（TEOS）为硅源，三氯化铁（$FeCl_3 \cdot 6H_2O$）为铁盐前驱体，三嵌段共聚物 P123 为模板剂，通过直接合成法制备介孔材料 Fe－SBA－15，考察不同 pH 调节剂对样品结构及催化性能的影响。X 射线衍射、傅立叶变换红外光谱和 N_2 吸附－脱附等表征结果显示：硅铁摩尔比为 50，pH 调节剂为氨水，pH 调节剂添加温度为 40℃时，所制备的样品介孔结构较好，铁的嫁接率达到 47.5%。以苯酚羟基化反应对样品进行催化活性评价，结果表明：当 pH 调节剂为氨水时，苯酚转化率及苯二酚选择性较高。

关键词：SBA－15；铁；尿素；氨水；苯酚

中图分类号：O643.32＋2　　文献标识码：A　　文章编号：1008－021X（2019）20－0001－02

Synthesis and Catalytic Properties of Iron Doped Mesoporous Material SBA－15

*Shao Yanqiu**，*Zhang Yuting*，*Wang Xingyue*，*Chang Yuying*，*Sun Jiahong*

（College of Chemistry and Chemical Engineering，Mu Danjiang Normal School，Mudanjiang　157011，China）

Abstract：Mesoporous material Fe－SBA－15 was prepared by direct synthesis using tetraethyl orthosilicate（TEOS）as silicon source，ferric chloride（$FeCl_3 \cdot 6H_2O$）as iron salt precursor and triblock copolymer P123 as template. The effects of different pH regulators on the structure and catalytic properties of the samples were investigated. The results of X－ray diffraction，Fourier transform infrared spectroscopy and N_2 adsorption－desorption characterization showed that the mesoporous structure of the prepared samples was better when the molar ratio of ferrosilicon was 50，the pH regulator was ammonia，and the temperature of adding the pH regulator was 40℃. The grafting rate of iron reached 47.5%. The hydroxylation of phenol was used to evaluate the catalytic activity of the sample. The results showed that the conversion of phenol and the selectivity of hydroquinone were higher when the pH regulator was ammonia water.

Key words：SBA－15；iron；urea；ammonia；phenol

DOI:10.19319/j.cnki.issn.1008-021x.2019.20.001

纯硅 SBA－15 具有规则孔径分布、较厚孔壁、较好的水热稳定性等优点，在催化、吸附分离、纳米组装等方面都有很大的应用价值，但在酸性较强的合成体系中很难将杂原子引入分子筛中[1]。Fe－SBA－15 介孔材料在催化反应中具有广泛应用，其制备方法可分为直接合成法和后合成法两大类[2]，直接合成法的关键是对合成体系酸度的调控，其会对铁的引入有较大影响。后合成法易造成活性组分发生团聚现象，从而对分子筛结构造成影响[3-5]。因此本文采用直接合成法制备 Fe－SBA－15 介孔分子筛，通过添加不同 pH 调节剂探究其对材料结构和催化性能的影响。

1　材料与方法

1.1　材料的制备

纯硅 SBA－15 的制备：SBA－15 分子筛的制备方法见参考文献[6]。

不同铁含量分子筛的制备[7]：称取 2g P123 溶解于 5mL 盐酸（10mol/L）和 50mL 去离子水中，搅拌至 P123 完全溶解后加入 4.5mL 正硅酸乙酯于 40℃下搅拌 4h，再加入一定量 $FeCl_3 \cdot 6H_2O$（其中硅铁摩尔比为 50），继续搅拌 30min，然后加入 pH 调节剂，继续升温至 40℃，待 pH 值在 5～6 之间后，将反应液转移至反应釜中，于 100℃下晶化 48h，然后冷却抽滤、洗涤烘干，最后在 550℃下焙烧 4h，即得到铁掺杂的 SBA－15 样品。

1.2　样品性能评价

在反应装置中加入 0.94g 苯酚、100mg 样品及 20mL 去离子水，升温至 60℃后缓慢滴加过氧化氢（体积分数为 30%），待反应至 1.5h 时将反应液离心处理，通过 LC－15C 型液相色谱仪对反应产物进行测定，利用外标法对产物中各组分含量进行分析[8]。

2　结果与分析

2.1　不同 pH 调节剂对样品结构的影响

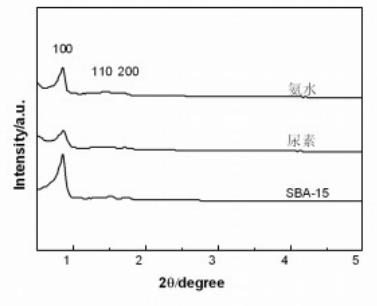

图 1　不同 pH 调节剂合成样品的 XRD 小角谱图

Fig. 1　XRD small angle spectra of synthetic samples with different pH regulators

图 1 为样品 XRD 小角图。由图可看出所制得的样品均出现 SBA－15 介孔分子筛中典型的 d（100）主衍射峰，表明样品具有六方介孔结构[9]。其中以尿素作为 pH 调节剂时，d（110）

收稿日期：2019－07－12

基金项目：黑龙江省教育厅科研备案项目（1352MSYYB006）

作者简介：邵艳秋（1969—），女，黑龙江牡丹江人，教授，博士，主要从事多相催化材料研究。

(C)1994-2020 China Academic Journal Electronic Publishing House. All rights reserved.　http://www.cnki.net

10.邵艳秋,张宇婷,芦原萱,刘素娟,任玉兰,苏爽月.不同疏水基固体酸 SBA-15-SO_3H 的合成及催化乙酸正丁酯研究[J].牡丹江师范学院学

报(自然科学版),2017(04):48-51.

文章编号:1003-6180(2017)04-0048-05

不同疏水基固体酸 SBA－15－SO_3H 的合成及催化乙酸正丁酯研究

邵艳秋[1,2],张宇婷[1,2],芦原萱[1,2],刘素娟[1],任玉兰[1],苏爽月[1]
(1.牡丹江师范学院 化学化工学院,黑龙江 牡丹江 157011;2.黑龙江省新炭-基功能与超硬材料重点实验室,黑龙江 牡丹江 157011)

摘 要:以 123 为模板剂,TEOS 为主要硅源,3－巯丙基三甲氧基硅烷、甲基三乙氧基硅烷、正辛基三乙氧基硅烷、N－十六烷基三乙氧基硅烷为有机硅源,采用直接法制备不同疏水基(甲基、辛基、十六烷基)固体酸,改变 TEOS 预水解时间,考察样品对乙酸正丁酯酯化反应的影响.采用 XRD、FT－IR 和 N_2 吸附-脱附等手段对样品进行表征.结果表明:随着疏水基有机硅烷链的增长,样品疏水性的增强,酯化率增大;TEOS 预水解时间为 180 min 时,样品的酯化率有所提高,最高可达 88.23%.

关键词:疏水;酯化;乙酸正丁酯;预水解时间

[中图分类号]O643 [文献标志码]A
DOI:10.13815/j.cnki.jmtc(ns).2017.04.013

Synthesis of Solid Acid SBA－15－SO_3H with different Hydrophobic Groups and Study on Catalytic Esterification of N-butyl Acetate

Shao Yan-qiu[1,2], Zhang Yu-ting[1,2], Lu Yuan-xuan[1,2],
Liu Su-juan[1], Ren Yu-lan[1], Su Shuang-yue[1]
(1. College of Chemistry and Chemical Engineering, Mu Danjiang Normal University, Mudanjiang 157011, China; 2. Heilongjiang Province Key Laboratory of New Carbon－Base Functional andSuperhard Material, Mudanjiang 157011, China)

Abstract: Containing different alkyl (methyl, octyl and cetyl) hydrophobic solid acid SBA－15－SO_3H was prepared by direct , in which Pluronic P123 was used as template, tetraethyl orthosilicate (TEOS) was adopted as silicon source and (3－Mercaptopropyl) trimethoxysilane、Methyltriethoxysilane、n－Octyltriethoxysilane、n－Hexadecyltriethoxysilane was utilized as coupling agent. And the contrast experiment was done, the prehydrolysis time of TEOS was changed, and the effect of sample on esterification of acetic acid was studied. All the materials were characterized by XRD, FT－IR and N_2 adsorption－desorption. The results show With the increase of the hydrophobic group, the increase of the hydrophobicity of the samples, the esterification rate increased; When the prehydrolys-

收稿日期:2017-09-15
基金项目:牡丹江市科学技术计划项目(Z2016g0001);牡丹江师范学院科研机构专项(JG2017001);黑龙江省教育厅科研备案项目(1352MSYYB006);黑龙江省自然科学学基金项目(E201341).
作者简介:邵艳秋(1969-),女,黑龙江牡丹江人.教授,博士,主要从事多相催化及催化材料;张宇婷(1993-),女,黑龙江鸡西人.研究生,主要从事介孔材料制备及应用研究;芦原萱(1990-),女,天津人.研究生,主要从事介孔材料制备及应用研究.

(C)1994-2020 China Academic Journal Electronic Publishing House. All rights reserved. http://www.cnki.net

11.芦原萱,赵婷婷,陈玉刚,邵艳秋.疏水基团对介孔材料 SBA-15-SO_3H 催化性能的影响[J].牡丹江师范学院学报(自然科学

版),2016(04):40-42.

文章编号:1003-6180(2016)04-0040-03

疏水基团对介孔材料 SBA-15-SO_3H 催化性能的影响

芦原萱,赵婷婷,陈玉刚,邵艳秋*
(牡丹江师范学院 化学化工学院,黑龙江 牡丹江 157011)

摘 要:采用直接合成方法制备含有不同量疏水基团-CH_3 固体酸 SBA-15-SO_3H. 通过 X 射线粉末衍射(XRD)、红外光谱(FT-IR) 和 N_2 吸附-脱附等手段对催化剂进行表征,并在乙酸正丁酯酯化反应中进行催化性能评价. 结果表明:随着疏水基团甲基含量的增加,样品的疏水性增强,酯化反应的酯化率有所提高,酯化率最高达到 75.89%.
关键词:疏水;固体酸;SBA-15;酯化反应

[中图分类号]Q74 [文献标志码]A
DOI:10.13815/j.cnki.jmtc(ns).2016.04.013

The Effect of Hydrophobic on the Catalytic Performance of Mesoporous Materials SBA-15-SO_3H

LU Yuan-xuan, ZHAO Ting-ting, CHEN Yu-gang, SHAO Yan-qiu
(College of Chemistry and Chemical Engineering Mu Danjiang Normal University, Mudanjiang 157011, China)

Abstract: Preparing the different amounts of hydrophobic group - CH_3 solid acid SBA-15-SO_3H by direct synthesis method. All the materials are characterized by X-ray diffraction (XRD), fourier transform infared spectroscopy (FT-IR) and N2 adsorption-desorption. The catalytic performance of the catalyst was evaluated in the esterification reation of N-butyl acetate. The result shows that the hydrophobicity of the samples strengthened with the increasing of content of the hydrophobic group, the rate of esterification improved, and the esterification rate reach the highest is up to 75.89%.
Key words: hydrophobic; solid acid; SBA-15; esterification

SBA-15 介孔分子筛因具有较大的比表面及孔径可调等特性,在合成材料上可以进行功能化修饰.[1]烷基磺酸功能化的介孔材料是一种良好的强酸性催化剂,受到很大关注.[2]产物生成水的有机酸催化反应导致催化剂失活及转化率低一直是研究者探讨的问题. 本文采用直接合成方法制备疏水性固体酸 SBA-15-SO_3H,考察其在正丁醇与冰乙酸酯化反应的催化性能.

1 实验部分

1.1 样品制备

以三嵌段聚合物 P123 为模板剂,正硅酸乙酯(TEOS)为主要硅源,3-巯丙基三甲氧基硅烷(MPTMS)和甲基三乙氧基硅烷(MTES)为有机硅源. 反应物摩尔组成:n(P123) : n(TEOS) : n(MPTMS) : n(MTES) : n(HCl) : n(H_2O) : n

收稿日期:2016-03-26
基金项目:黑龙江省教育厅科学技术研究资助项目(11551510);牡丹江师范学院研究生科技创新项目(yjsxscx2015-17mdjnu)
作者简介:芦原萱(1990-),女,天津人. 研究生,主要从事介孔材料及其应用研究;赵婷婷(1990-),女,黑龙江牡丹江人. 研究生,主要从事介孔材料及其应用研究;陈玉刚(1992-),男,云南宣威市人. 本科,主要从事介孔材料及其应用研究;邵艳秋(1969-),女,黑龙江牡丹江人. 教授,博士,主要从事多相催化材料研究.
通讯作者:邵艳秋

(C)1994-2022 China Academic Journal Electronic Publishing House. All rights reserved. http://www.cnki.net

12.盛琦,刘素娟,冯峰,邵艳秋,孙航.高效液相色谱法同时测定 8 种食品

添加剂[J].湖北农业科学,2016,55(21):5620-5622.

第 55 卷第 21 期 湖北农业科学 Vol. 55 No.21
2016 年 11 月 Hubei Agricultural Sciences Nov.,2016

高效液相色谱法同时测定 8 种食品添加剂

盛 琦,刘素娟,冯 峰,邵艳秋,孙 航
(牡丹江师范学院化学化工学院,黑龙江 牡丹江 157011)

摘要:建立对食品中 8 种添加剂(柠檬酸钠、乙酸、糖精钠、咖啡因、苯甲酸、对羟基苯甲酸乙酯、对羟基苯甲酸丙酯、对羟基苯甲酸丁酯)分离测定的高效液相色谱法。色谱柱为 Ultimate XB-C18(250 mm×4.6 mm,5 μm),流动相为甲醇和 0.02 mol/L 磷酸二氢钾溶液,梯度洗脱,流速为 1.5 mL/min,紫外-可见检测器可变波长程序检测,柱温 30 ℃,一次进样,15 min 内完成分析过程。方法简单,快速,对实际样品测定结果满意。

关键词:高效液相色谱;食品添加剂;同时测定
中图分类号:O657.7+2;TS202.3 文献标识码:A 文章编号:0439-8114(2016)21-5620-03
DOI:10.14088/j.cnki.issn0439-8114.2016.21.047

Simultaneous Determination of 8 Food Additives By HPLC

SHENG Qi, LIU Su-juan, FENG Feng, SHAO Yan-qiu, SUN Hang
(Department of Chemistry and Industry, Mudanjiang Normal University, Mudanjiang 157011, Heilongjiang, China)

Abstract: A high performance liquid chromatography(HPLC) was developed for the separating and determination of eight food additives(sodium citrate,acetic acid,saccharin sodium,caffeine,benzoic acid,ethyl p-hydroxybenzoate,propyl p-hydroxybenzoate, and butyl p-hydroxybenzoate. A Ultimate XB-C18 (250 mm×4.6 mm,5 μm) was used as separation column with methanol and 0.02 mol/L monopotassium phosphate solution as mobile phase in gradient elution. By variable wavelength UV-vis detection, the flow rate was 1.5 mL/min and the column temperature was 30 ℃. 8 additives could be separated in 15 min by one sampling. The method was fast,accurate,and the measured result of practical samples was satisfactory.

Key words: high performance liquid chromatography; food additives; simultaneous determination

食品添加剂适当使用可以改善食品质量,防止食物变质,保持食物营养[1,2],但乱用或滥用会损害消费者健康,研发食品添加剂快速检测方法有重要的现实意义。随着社会发展,食品安全逐渐得到重视,中国颁布了食品添加剂使用标准规范其使用[3]。检测食品添加剂的方法主要有液相色谱法、气相色谱法、毛细管电泳法、衍生光谱法和色谱-质谱联用方法[4-7],多存在检测标底较为单一的缺陷。本研究设计的梯度洗脱可变波长高效液相色谱法 1 次可检测 8 种添加剂,减少了药品和人工,缩短了检测时间。

1 材料与方法

1.1 仪器与试剂

LC-15C 性液相色谱仪 (日本岛津制作所);KQ-100E 型超声波清洗器(昆山市超声波仪器有限公司);TB-214 型电子分析天平 (北京赛多利斯仪器有限公司);8 种防腐剂柠檬酸钠、乙酸、糖精钠、咖啡因、苯甲酸、对羟基苯甲酸乙酯、对羟基苯甲酸丙酯、对羟基苯甲酸丁酯标准品均购自 Sigma 公司,其他试剂均为 HPLC 级;试验用水均为娃哈哈纯净水。

收稿日期:2015-12-01
资助项目:黑龙江省大学生创新创业训练计划项目(201410233004;201510233006);牡丹江师范学院青年一般项目(QY201316);黑龙江省教育厅面上项目(11551510)
作者简介:盛 琦(1993-),女,黑龙江双鸭山人,在读本科生;通信作者,刘素娟(1981-),女,山东聊城人,讲师,硕士,主要从事色谱研究。电话(13604607669)(电子信箱)liusujuan610@163.com。
(C)1994-2020 China Academic Journal Electronic Publishing House. All rights reserved. http://www.cnki.net

13.邵艳秋,赵婷婷,付文婷,郑骐朋.氨基改性 SBA-15 介孔材料的制备及对 Pb(Ⅱ)的吸附性能研究[J].硅酸盐通报,2016,35(02):587-592.

第 35 卷 第 2 期
2016 年 2 月
硅 酸 盐 通 报
BULLETIN OF THE CHINESE CERAMIC SOCIETY
Vol. 35 No. 2
February, 2016

氨基改性 SBA-15 介孔材料的制备及对 Pb(II)的吸附性能研究

邵艳秋[1,2],赵婷婷[1,2],付文婷[3],郑骐朋[2]
(1. 牡丹江师范学院化学化工学院,牡丹江 157011;2. 黑龙江省新炭基功能与超硬材料重点实验室,牡丹江 157011;3. 北京理工大学化学学院,北京 102488)

摘要:采用水热后嫁接的方法,分别制备出氨基、二氨基、三氨基改性的介孔二氧化硅吸附剂 N-SBA-15、2N-SBA-15、3N-SBA-15。采用 X-ray 衍射(XRD)、红外光谱(FT-IR)、N_2 吸附-脱附和扫描电镜(SEM)等方法对材料进行表征。讨论了吸附时间、体系 pH 值等因素对水中 Pb^{2+} 吸附性能的影响。结果表明:在纯硅 SBA-15 上嫁接的氨基越多,改性后材料对水中 Pb^{2+} 的吸附性能越好,当吸附 60 min、体系 pH 值为 5 时,材料对水中 Pb^{2+} 的吸附效率最佳,最大吸附率能达到 95% 左右。

关键词:胺基改性;SBA-15;吸附;铅离子
中图分类号:TQ173 文献标识码:A 文章编号:1001-1625(2016)02-0587-06
DOI:10.16552/j.cnki.issn1001-1625.2016.02.051

Preparation of Different Amino-modified SBA-15 and Its Adsorption Property to Pb^{2+}

SHAO Yan-qiu[1,2], *ZHAO Ting-ting*[1,2], *FU Wen-ting*[3], *ZHENG Qi-peng*[2]
(1. College of Chemistry and Chemical Engineering, Mu Danjiang Normal University, Mudanjiang 157011, China;
2. Heilongjiang Province Key Laboratory of New Carbon-Base Functional and Superhard Material, Mudanjiang 157011, China;
3. Department of Chemistry, Bejing Institute of Technology, Bejing 102488, China)

Abstract: The amino-modified SBA-15 (N-SBA-15), diamine-modified (2N-SBA-15) and triamino-modified (3N-SBA-15) were prepared by a hydrothermal grafting method. All mesoporous materials were characterized by X-ray diffraction (XRD), Fourier transform infrared spectroscopy (FT-IR), N_2 adsorption-desorption and SEM. Provide the evidence we need to make a disgussion among how the time and the pH of system influnce the absorption of Pb(II) ions in water. The result is that, modified materials shows a better adsorpting efficiency of Pb(II) ions in water when more amino grafted on the pure silicon SBA-15. When the adsorption is for 60 min, system pH is 5, the adsorption rate of mesoporous materials is the best, maximum adsorption rate can reach about 95%.

Key words: amino-modified; SBA-15; adsorption; Pb(II) ion

1 引 言

随着科学技术和工业化水平的迅速发展,大量有害金属和生活垃圾被排入水体中,对生态环境和人类的健康造成很大的危害。现如今,有效减少水体中重金属含量、净化污水的方法有许多,比如离子交换法、渗透

基金项目:黑龙江省教育厅科学技术研究资助项目(11551510);牡丹江师范学院超硬材料重点实验室开放课题资助项目(201401);牡丹江师范学院校级教改立项重点项目(12-XJ14027);黑龙江省自然科学学基金项目(E201341)
作者简介:邵艳秋(1969-),女,博士,教授.主要从事多相催化材料方面的研究.

(C)1994-2019 China Academic Journal Electronic Publishing House. All rights reserved. http://www.cnki.net

14.赵婷婷,芦原萱,邵艳秋.NH_2-SBA-15的制备及其对水中铅离子的吸附[J].牡丹江师范学院学报(自然科学版),2016(01):42-44.

NH_2-SBA-15 的制备及其对水中铅离子的吸附

赵婷婷[1,2],芦原萱[1],邵艳秋[2]
(1. 黑龙江省新炭-基功能与超硬材料重点实验室,黑龙江 牡丹江 157011;2. 牡丹江师范学院 化学化工学院,黑龙江 牡丹江 157011)

摘 要:以正硅酸乙酯为硅源,三嵌段聚合物 P123 为模板剂,采用一步合成法和后嫁接法制备氨基功能化 SBA-15,通过 X-ray 衍射(XRD)、红外光谱(FT-IR)和氮气吸附-脱附等手段对功能化前后的介孔材料进行表征,考察吸附时间和体系 pH 值等因素对 Pb^{2+} 吸附的影响. 结果表明:NH_2-SBA-15 已成功制备,且对 Pb^{2+} 吸附率能达到 90%左右,NH_2-SBA-15 对水中 Pb^{2+} 的最佳吸附时间为 60 min,最佳 pH 值为 5.

关键词:介孔材料;SBA-15;铅离子

[中图分类号]TQ170.8 [文献标志码]A [文章编号]1003-6180(2015)04-0042-03

DOI:10.13815/j.cnki.jmtc(ns).2016.01.017

随着现代技术的迅速发展和工业化水平的提高,越来越多的生活污水和工业生产中残留的废水排放到河流中,使水污染越来越严重.[1]水体中重金属难降解,所以比较难去除,因此,近年来如何去除污水中重金属是环境污染治理研究的热点之一.[2-3]水污染中重金属离子的处理方法有很多,其中吸附法因成本较低、去除效果理想、吸附剂可回收再利用等优点受到许多研究者的关注. 早在 20 世纪初就有关于重金属离子可被功能化介孔材料吸附的报道[4],University of California 的 Stucky 等用三嵌段聚合物 P123 合成了硅基介孔分子材料 SBA-15[5-6],随后,田志茗[7]等用改性的纯硅 SBA-15 吸附水中的重金属离子. 介孔二氧化硅具有很高的比表面积和孔容,但由于纯硅材料骨架全部由氧化硅构成,缺乏活性中心,无法发挥自身的多孔性能. 通过掺杂金属离子、引入无机物、嫁接有机官能团等方法,可有效地提高介孔材料对金属离子的吸附能力.[8]本文将氨基官能团嫁接到纯硅 SBA-15 上,增加了活性基团,有效地提高了对 Pb^{2+} 的吸附率.

1 实验

1.1 介孔材料 NH_2-SBA-15 的合成

一步法合成 采用正硅酸乙酯(TEOS)作反应体系硅源,三嵌段聚合物 P123 为模板剂,利用氨丙基三乙氧基硅烷(APTES)在一定条件下合成氨基功能化 SBA-15,其中,原料摩尔比为:P123∶HCl∶H_2O∶TEOS∶APTES=0.017∶6.1∶169.4∶(1-x)∶x. 得到的样品为直接合成的 NH_2-SBA-15.

后嫁接法合成 纯硅 SBA-15 参照文献[9]的方法进行制备,得到纯硅 SBA-15,取 1 g 样品倒入 30 mL 提前干燥的甲苯,滴加适量的 APTES,搅拌 24 h 后过滤,用甲苯、乙醇反复洗涤,得到后嫁接的 NH_2-SBA-15 样品.

1.2 样品的表征

采用 X 射线衍射仪(XRD)、红外光谱(FT-IR)和氮气吸附-脱附等方法对样品进行表征.

2 结果与讨论

2.1 结构分析

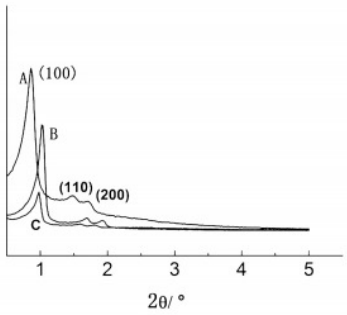

A:纯硅 SBA-15;B:直接合成 NH_2-SBA-15;
C:后嫁接 NH_2-SBA-15

图 1 样品 XRD 谱图

图 1 为氨基功能化前后介孔材料的 XRD 谱图. 从图中可以看出,在小角范围内都有 1 个强的(100)峰和 2 个弱的(110)(200)晶面衍射峰,这是典型有序六方介孔结构,说明在介孔材料嫁接氨基过程中,所合成的样品仍保持较好的介孔有序性,但峰的强度有所降低. 功能化后介孔材料的衍

收稿日期:2015-10-02
基金项目:牡丹江师范学院研究生科技创新项目(yjsxscx2014-16mdjnu)

(C)1994-2020 China Academic Journal Electronic Publishing House. All rights reserved. http://www.cnki.net

15.邵艳秋,芦原萱,付文婷,苏爽月,郑炜.盐对氨基改性 SBA-15 吸附 Pb^{2+} 性能的影响研究[J].硅酸盐通报,2016,35(11):3649-3653.

Doi:10.11962/1006-4990.2018-0562

水解剂氟化铵对Fe-SBA-15 结构及催化性能的影响

邵艳秋[1,2],张宇婷[1,2],姜振双[1,2,3],刘素娟[1],任玉兰[1],王丽杰[1,2]
(1.牡丹江师范学院化学化工学院,黑龙江牡丹江 157011;2.黑龙江省新炭-基功能与超硬材料重点实验室;3.吉林大学化学学院)

摘 要:通过水热法制备了 Fe-SBA-15 介孔材料,探究了水解剂氟化铵对介孔材料结构及对苯酚羟基化反应的影响。采用 X 射线衍射(XRD)、红外光谱(FT-IR)和氮气吸附-脱附等方法对介孔材料进行了表征,用苯酚羟基化反应对改性后介孔材料的催化性能进行了研究。结果表明:改性后的介孔材料具有良好的催化性能,其中氟与硅物质的量比为 0.03 时制备的介孔材料的催化性能更为优良,在固定反应条件下苯酚转化率达到 36.82%、苯二酚选择性达到 81.76%。

关键词:水解剂;氟化铵;Fe-SBA-15;苯二酚;羟基化
中图分类号:O643 **文献标识码**:A **文章编号**:1006-4990(2019)09-0097-05

Effects of hydrolysate NH_4F on structure and catalytic properties of Fe-SBA-15

Shao Yanqiu[1,2], Zhang Yuting[1,2], Jiang Zhenshuang[1,2,3], Liu Sujuan[1], Ren Yulan[1], Wang Lijie[1,2]
(1.*College of Chemistry and Chemical Engineering, Mudanjiang Normal University, Mudanjiang* 157011, *China*; 2.*Heilongjiang Province Key Laboratory of New Carbon-Base Functional and Superhard Material*; 3.*College of Chemistry, Jilin University*)

Abstract: Fe-SBA-15 mesoporous materials were prepared by hydrothermal synthesis, and the effect of hydrolysis agent NH_4F on the mesoporous materials structure and catalytic hydroxylation of phenol was explored. The mesoporous materials were characterized by X-ray diffraction (XRD), infrared spectroscopy (FT-IR) and N_2 adsorption desorption etc.. The catalytic properties of modified mesoporous materials were studied by hydroxylation of phenol. The results indicated that the modified materials had good catalytic performance. When $n(F^-)/n(Si)=0.03$, the prepared mesoporous materials had better catalytic performance. Under the fixed reaction conditions, conversion of phenol and selectivity of dihydroxybenzene reached 36.82% and 81.76%, respectively.

Key words: hydrolysate; NH_4F; Fe-SBA-15; dihydroxybenzene; hydroxylation

SBA-15 分子筛因具有较大的比表面积及有序的孔结构等优势使其在催化领域备受关注,纯硅 SBA-15 缺少酸性位点和活性中心,在应用上受到很大限制。通过分子筛表面 Si—OH 基团与活性组分之间的相互作用,将活性较高的成分引入孔道或骨架内来提高材料的活性一直受到关注和研究[1]。将金属引入分子筛孔道或骨架内可以提高分子筛的催化活性,但是引入的金属会对介孔结构造成一定的影响,所以在保证介孔材料有序孔结构的同时如何提高分子筛骨架内的金属含量是需要解决的问题[2-6]。研究发现,在氟离子存在的体系中,F^-既可以与过渡金属生成氟的配合物,还可以加快硅源的水解速率,有利于提高金属进入分子筛骨架中[7-8]。由于 NH_4F 受热会分解为氨和氟化氢,在材料制备过程中铵根对材料中铁的引入影响较小,并且 NH_4F 在分子筛中有一定的应用[9-10]。因此,笔者以 NH_4F 为水解剂,采用水热法制备了 Fe-SBA-15(x)分子筛(x 为氟与硅物质的量比),并探究了水解剂含量对材料结构和性能的影响。

1 实验部分

1.1 主要试剂

P123($EO_{20}PO_{70}EO_{20}$),Aldrich 试剂;正硅酸乙酯

基金项目:黑龙江省教育厅科研备案项目(1352MSYYB006);牡丹江师范学院研究生科技创新项目(kjcx2017-09mdjnu);牡丹江师范学院科研项目(JG2017001);牡丹江师范学院大学生创新项目(201710233007)。
收稿日期:2019-03-27
作者简介:邵艳秋(1969—),女,博士,教授,主要从事多相催化材料研究;E-mail:shaoyanqiu1969@163.com。

(C)1994-2019 China Academic Journal Electronic Publishing House. All rights reserved. http://www.cnki.net

16.刘素娟,邵艳秋,崔术新,盛琦.反相高效液相色谱法快速测定 9 种食品添加剂[J].黑龙江畜牧兽医,2015(03):223-225.

反相高效液相色谱法快速测定 9 种食品添加剂

刘素娟,邵艳秋,崔术新,盛　琦
(牡丹江师范学院 化学化工学院,黑龙江 牡丹江 157011)

中图分类号: S859.84; S816.7　文献标识码: B　文章编号: 1004-7034(2015)02-0223-03
DOI:10.13881/j.cnki.hljxmsy.2015.0235
关键词: 反相高效液相色谱; 快速测定; 食品添加剂; 标准曲线; 相关系数

摘　要: 为了同时检测食品中 9 种食品添加剂的含量,试验将 Ultimate XB-C_{18}(250 mm×4.6 mm, 5 μm)作为分离柱,以乙酸铵缓冲溶液-乙腈为流动相,梯度洗脱的方法进行检测。结果表明: 方法的相对标准偏差为 1.5%~4.1%,回收率为 93%~105%,各种食品添加剂的线性相关系数≥0.9987,具有较高的准确度和精密度,可用于实际样品的测定。

食品添加剂是有意识地少量添加于食品中,以改善食品的外观、风味、组织结构或贮存性质的非营养物质。随着生活水平的不断提高,人们对食品添加剂给食品安全带来的问题也越来越关注; 但是食品添加剂作为食品生产加工过程中常用的化学物质,违规及超限量使用事件时有发生,因此急需发展食品添加剂的高通量检测技术。

目前,对于食品添加剂的检测方法主要有高效液相色谱法[1]、紫外分光光度法[2]、离子色谱法[3]及液相色谱-质谱法[4-5]等。这些方法的分析时间较长,运用液相色谱-质谱方法虽然能准确地检测出添加剂,时间也有所缩短,但成本增加较多。研究应用反相高效液相色谱建立了能同时检测食品中国内外允许使用的 9 种食品添加剂的方法,结果表明,该方法简便、快速、准确、灵敏度高,为食品添加剂的检测提供了实用的技术手段,对于监测食品中添加剂的使用情况具有重要意义。

1　材料

1.1　试剂及仪器

9 种食品添加剂标准品,Sigma 公司生产; 其他试剂均为高效液相色谱级别。液相色谱仪(型号为 LC-15C),日本岛津公司生产; 超声波清洗器(型号为 KQ-100E),昆山市超声波仪器有限公司生产; 电动离心机(型号为 SBH-3),山东菏泽南城益发仪器厂生产; 电子分析天平(型号为 TB-214),北京赛多利斯仪器系统有限公司生产; 试验用水,均为娃哈哈纯净水。

收稿日期: 2014-07-25; 修回日期: 2014-09-21
基金项目: 黑龙江省教育厅面上项目(11551510); 黑龙江省青年科学基金项目(QC2014C009); 牡丹江师范学院青年一般项目(QY201316); 2013 年黑龙江省大学生创新项目
作者简介: 刘素娟(1981-),女,讲师,硕士,研究方向为高效液相色谱,liusujuan610@163.com.

1.2　色谱条件

液相色谱仪(型号为 LC-15C)、配备高压泵(型号为 LC-15C)、线脱气机(型号为 DGU-20A)、柱温箱(型号为 CTO-15C)、紫外-可见检测器(型号为 SPD-15C)、LCsolution15C 色谱工作站,均由牡丹江师范学院化学化工学院提供。HPLC 色谱柱为 Ultimate XB-C_{18}(250 mm×4.6 mm,5 μm); 流动相 A 为乙腈,流动相 B 为 0.02 mol/L 乙酸铵,梯度洗脱,见表 1。流速为 1.0 mL/min,检测时间为 0.01~5.00 min(254 nm)、5.00~5.01 min(230 nm)、5.01~11.50 min(230 nm)、11.50~11.51 min(254 nm)、11.51~18.00 min(254 nm),柱温为 30 ℃,进样量为 10 μL。

表 1　梯度洗脱　%

时间	乙腈	0.02 mol/L 乙酸铵水溶液
0.01 min	5	95
5.00 min	20	80
10.00 min	20	80
10.01 min	80	20
11.00 min	80	20
11.01 min	98	2
18.00 min	98	2

1.3　标准溶液制备

维生素 C、苯甲酸、山梨酸钾、糖精钠、咖啡因、对羟基苯甲酸甲酯、对羟基苯甲酸乙酯、对羟基苯甲酸丙酯、对羟基苯甲酸丁酯分别在甲醇和水的比例为

(C)1994-2022 China Academic Journal Electronic Publishing House. All rights reserved.　http://www.cnki.net

17.郭美玲,赵婷婷,付文婷,邵艳秋.Cu-TiO_2/SBA-15 光催化剂的制备及光催化性能[J].黑龙江科技信息,2015(03):80.

Cu - TiO_2/ SBA - 15 光催化剂的制备及光催化性能

郭美玲[1,2]　赵婷婷[1,2]　付文婷[3]　邵艳秋*

(1、牡丹江师范学院化学化工学院，黑龙江 牡丹江 157011　2、黑龙江省新炭-基功能与超硬材料重点实验室，黑龙江 牡丹江 157011
3、北京理工大学化学学院，北京 102488)

摘　要：以钛酸四正丁酯(TB)为钛源)和羧基改性的 SBA-15(COOH/SBA-15)及氯化铜经过溶剂热及焙烧处理制得 Cu-TiO_2/SBA-15 光催化剂。并采用 X 射线衍射(XRD)和 N_2 吸附脱附等对其进行了表征。以降解罗丹明 B 的实验研究了催化剂的光催化氧化性能。结果表明：少量铜离子掺杂对二氧化钛的结构无影响，且能显著提高催化剂的光催化性能。

关键词：光催化；Cu-TiO_2/SBA-15；实验

锐钛矿 TiO_2 的禁带宽度较宽(3.2eV)，只能被波长较短的紫外光激发，这样使得太阳能的利用率很低。此外，由于光激发产生的电子与空穴的复合，导致光量子效率很低。为了克服这些缺点，近年来，金属离子修饰 TiO_2 是提高其光催化活性的一条很好的途径，成为目前光催化技术的研究热点。本文将 TiO_2 负载在介孔 SiO_2 材料制得负载型 TiO_2/SBA-15 光催化剂，并用不同浓度的铜离子对 TiO_2 进行掺杂改性。最后对所制得的铜掺杂 COOH/SBA-15 光催化剂的催化活性进行评价。利用 COOH/SBA-15 与钛酸四正丁酯(TB)并混入一定量的氯化铜标准溶液，经过溶剂热处理和高温焙烧，得到 Cu-TiO_2/SBA-15 光催化剂。采用 XRD 和 N_2 吸附脱附进行表征，并以降解 RhB 的实验考察 Cu-TiO_2/SBA-15 的光催化性能。

1 实验

1.1 催化剂的制备及表征

将 2.0g P123 加入到 60mL 2.0mol·L^{-1} 的 HCl 溶液中，40℃恒温搅拌至 P123 完全溶解后缓慢加入 2-(氯基乙基三乙氧基硅烷(CETES)，继续搅拌 30min 后加入正硅酸乙酯(TEOS)，于 40℃恒温搅拌 24h 后移入特弗隆自压釜，在 100℃烘箱中老化 36h，所得产物经过滤、水洗和醇洗(无水乙醇)后于 60℃干燥得到氯基官能化 SBA-15(CN/SBA-15)，所得的 CN/SBA-15 加入到 150ml H_2SO_4 溶液中，95℃恒温搅拌 24h，过滤、水洗，80℃干燥即得到 COOH/SBA-15。将 COOH/SBA-15、氯化铜和钛酸四正丁酯(TB)分散于 25mL 无水乙醇中，搅拌 30min 后转移至聚四氟乙烯自压釜中，于 220℃下溶剂热处理 12h，所得到的产物经无水乙醇洗涤三次后，60℃干燥。最后，在 550℃下焙烧 5h 得到 Cu^{2+} 摩尔含量为 0.25at%、0.5at%、1.0at%、1.5at% Cu-TiO2/SBA-15 光催化剂。样品的 X 射线粉末衍射(XRD)分析在 D/max-2200/PC 型 X 射线衍射仪上进行。样品的比表面积和孔径分析在 3H-2000 型比表面及孔径分析仪上进行，样品在真空条件下于 200℃预脱气 3h 后，在 77.3K 下测定样品的 N_2 吸附-脱附等温线，由 BET 方程计算样品的比表面积，用等温线脱附分支以 BJH 方法计算孔径分布曲线。

1.2 光催化剂催化活性的评价

在光催化降解实验中，将 5mg TiO_2/SBA-15 催化剂置于 50ml 的 1× 10^{-5}mol/L 罗丹明 B 溶液，以 450w 自镇流高压汞灯作为光源，在搅拌下对反应进行光照，每隔 10min 取样，用紫外-可见分光光度计测定溶液的初始吸光度 A_0 和降解后的吸光度 A_t。

2 结果与讨论

2.1 光催化剂的晶型

从图 1 不同 Cu^{2+} 掺杂样品的小角 XRD 图，可以看出在 0.4°-3° 之间有三个明显的特征衍射峰，是典型的 SBA-15 二维六方结构的晶面衍射峰。随着铜的掺杂量的增加，(100)的衍射峰依然会出现，但峰强度会有所改变。由此可见，掺杂 Cu^{2+} 后对 SBA-15 的介孔结构没有很明显的影响。图 2 为不同含量的 Cu^{2+} 掺杂样品的广角 XRD 图，在 20°-70° 之间五个衍射峰，分别是锐钛矿晶面的衍射峰，说明 Cu-TiO_2/SBA-15 光催化剂表面的 TiO_2 颗粒为锐钛矿晶型。在 XRD 的图谱中，没有出现关于 CuO 的特征衍射峰，表明 Cu^{2+} 的掺杂不影响产物的形成，原因是 Cu^{2+} 取代 Ti^{4+} 进入二氧化钛中[4]。

2.2 N_2 吸附-脱附分析

图 3 给出了 0.5% Cu-TiO_2/SBA-15 的氮气吸附-脱附等温线。从

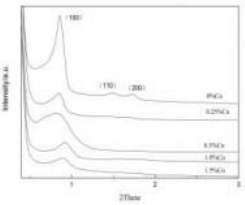

图 1 Cu-TiO_2/SBA-15 的小角 XRD

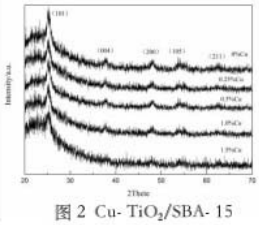

图 2 Cu-TiO_2/SBA-15 的广角 XRD

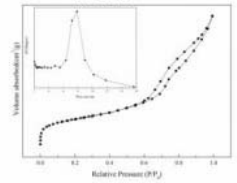

图 3 0.5% Cu-TiO_2/SBA-15 的氮气吸附-脱附等温线

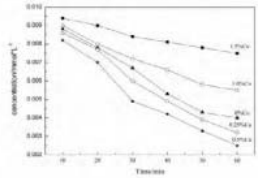

图 4 Cu-TiO_2/SBA-15 的催化效率

图中可以发现样品呈现出典型的 IV 型曲线，并且伴随着明显的滞后环，说明掺杂 Cu^{2+} 后分子筛 SBA-15 的孔道结构没有被破坏，样品的平均孔径为 8.39nm

2.3 光催化剂的催化效率

图 4 给出了不同 Cu^{2+} 掺杂样品的催化活性曲线。催化剂的光催化活性随着 Cu^{2+} 掺杂量的变化呈现出最佳值(0.5%)。由于 Cu^{2+} 和 Ti^{4+} 半径相近，Cu^{2+} 进入 TiO_2 晶格中取代 Ti^{4+}，Cu^{2+} 杂质能级形成了捕获阱，捕获光生载流子，从而降低了光生电子-空穴的复合几率[5]，提高了二氧化钛的光催化性能，而所形成捕获阱的数量取决于铜掺杂量。当铜掺杂量在合适范围内(0%~0.5%)，铜掺杂催化剂的催化性能随着铜浓度的增加而提高，当铜量超过最佳值(0.5%)后，反而导致二氧化钛的催化性能降低。

3 结论

利用 COOH/SBA-15 表面上高分散的羧基与钛酸四正丁酯(TB)的配合作用将 TB 锚定，并混入氯化铜，通过溶剂热处理及焙烧成功地制备出了不同掺杂量的 Cu-TiO_2/SBA-15。XRD 和 N_2 吸附脱附表明掺杂少量 Cu^{2+} 对二氧化钛晶体及 SBA-15 结构没有影响。在紫外光降解罗丹明 B (RhB)实验中，考察了铜掺杂量对催化行能的影响。实验结果表明：适量铜掺杂能够显著地改善二氧化钛光催化剂的催化性能。

参考文献

[1] Anpo,M;Yamashita,H;Ichihashi,Y.;Ehara,S.Photo catalytic reduction of CO_2 with H2O on various titanium oxide catalysts[J].Journal of Electro-analytical Chemistry.1995,396,21-26.

[2] 张立德.牟季美.纳米材料和纳米结构[M].北京:科学出版社,2001,135.

[3] Ikuma Y,Bessho H.Effect of Pt concentration on the production of hydrogen by a TiO_2 photocatalyst [J].Int. J Hydrogen Energy,2007,32:2689-2692.

基金项目：黑龙江省教育厅科学技术研究资助项目(11551510)；牡丹江师范学院超硬材料重点实验室开放课题资助项目(201401)；牡丹江师范学院校级教改立项重点项目(12-XJ14027)；黑龙江省自然科学学基金项目(E201341)。

通讯作者：邵艳秋(1969-)，女，教授，主要从事多相催化材料研究。

(C)1994-2022 China Academic Journal Electronic Publishing House. All rights reserved.　http://www.cnki.net

邢乐红指导学生发表论文目录（共 10 篇）

1.Xing L H, Shi X T, Wang Y X, et al. Electrochemical Synthesis of Ni-SnO_2 Composite Electrodes for Hydrogen Evolution Reaction in Alkaline Solution[J]. Int. J. Electrochem. Sci, 2022, 17(220530): 2.

2.Xing L, Wang Y, Shi X, et al. Investigation of Pt/C and Pt-Ru/C Mixed Catalyst for DME Oxidation in Direct Dimethyl Ether Fuel Cells[J]. Int. J. Electrochem. Sci, 2020, 15: 10382-10391.

3.Xing L, Wang Y, Sui C, et al. Investigation of Pt/SnO_2/C Catalyst for Dimethyl Ether Oxidation in DDFC[J]. Int. J. Electrochem. Sci, 2020, 15: 2375-2384.

4.Xing L H, Yin G P, Du C Y, et al. Investigation on the durability of direct dimethyl ether fuel cell. Part II: Cathode degradation[J]. International Journal of Hydrogen Energy, 2017, 42(26): 16695-16699.

5.王宜鑫,邢乐红,石鑫婷,孟凡旭,张亮,董瑞.镀液中氨基磺酸镍质量浓度对电镀镍层析氢催化活性的影响[J].电镀与涂饰,2022,41(01):6-9.

6.邢乐红,王宜鑫,隋朝,肖同欣,赵玥,邵艳秋.工程教育专业认证背景下化学工程与工艺专业人才培养模式探索[J].教育现代化,2020,7(07):11-12.

7.邢乐红,王宜鑫,左明辉.工程教育专业认证背景下化学工程与工艺专业学生实践能力培养研究[J].山东化工,2019,48(24):159-160.

8.邢乐红,王宜鑫,王慧,左明辉,孙芳,梁志男.氨基乙酸对硫酸盐体系电镀镍-铁合金的影响[J].电镀与涂饰,2019,38(19):1039-1041.

9.邢乐红,黎德育,李宁,左明辉,李晶.抗坏血酸对硫酸盐体系镍–铁合金

镀液稳定性的影响[J].电镀与涂饰,2018,37(12):526-528.
10.邢乐红,杨晶,王海鹏,达铭,李姗,崔术新.硫脲对低磷化学镀镍稳定性的影响[J].牡丹江师范学院学报(自然科学版),2016(03):41-42.

1.Xing L H, Shi X T, Wang Y X, et al. Electrochemical Synthesis of Ni-SnO_2 Composite Electrodes for Hydrogen Evolution Reaction in Alkaline Solution[J]. Int. J. Electrochem. Sci, 2022, 17(220530): 2.

Int. J. Electrochem. Sci., 17 (2022) Article Number: 220530, doi: 10.20964/2022.05.35

International Journal of
ELECTROCHEMICAL
SCIENCE
www.electrochemsci.org

Short Communication

Electrochemical Synthesis of Ni-SnO_2 Composite Electrodes for Hydrogen Evolution Reaction in Alkaline Solution

*Le-Hong Xing**, *Xin-Ting Shi, Yi-Xin Wang, Li Zhang, Xiao-Yan Xu, Fan-Xu Meng, Jing Li*

Heilongjiang Key Laboratory of Photoelectric Functional Materials, College of Chemistry and Chemical Engineering, Mudanjiang Normal University, Mudanjiang 157011, China
*E-mail: xinglehonghit@163.com

Received: 28 January 2022 / *Accepted:* 1 March 2022 / *Published:* 5 April 2022

In this work, high efficient Ni-SnO_2 electrodes were prepared for the alkaline hydrogen evolution reaction (HER) by a simple composite electroplating method from sulphamate bath containing SnO_2 nano-particles. The Ni-SnO_2 electrode was physically characterized by scanning electron microscopy (SEM), energy dispersive analysis of X-ray (EDAX), and X-ray diffraction (XRD). These physical characterization results revealed that the homemade SnO_2 particles (about 170 nm) were successfully co-deposited in coatings. The composited SnO_2 changed the surface morphology and phase structure of Ni matrix. The electrochemical activities and stabilities for HER were monitored by steady-state polarization, Tafel plots, electrochemical impedance spectroscopy (EIS) and chronopotentiometry technique. The activity was confirmed via the quantification of H_2 gases that evolved during chronopotentiometry study. The Ni-SnO_2 showed a higher catalytic activity for H_2 evolution, compared with Ni. The OH_{ads} on SnO_2 surface was benefit to the formation of adsorbed H_{ads} which is the rate-determining step for HER.

Keywords: Hydrogen evolution reaction; Electro-catalysis; Composite electroplating; Ni-SnO_2

1. INTRODUCTION

With the economic development and progress of industry, the energy crisis and environmental pollution have caused the global concern [1]. Driven by the growing concern, efforts have been made to develop new environmentally friendly energy sources. Hydrogen (H_2) is identified as the most potential energy carrier in future for its clean, renewable and high efficient characters [2,3]. Water is the cheapest and most rich resources of hydrogen, and water electrolysis is a sustainable and promising method for hydrogen production [4,5]. The development of the higher activity electrode materials is particularly important for water electrolysis. Nickel-based materials, such as Ni and Ni-M alloys, are prominent non-noble metal catalysts for their good electro-catalytic activity for HER and

2. Xing L, Wang Y, Shi X, et al. Investigation of Pt/C and Pt-Ru/C Mixed Catalyst for DME Oxidation in Direct Dimethyl Ether Fuel Cells[J]. Int. J. Electrochem. Sci, 2020, 15: 10382-10391.

Int. J. Electrochem. Sci., 15 **(2020)** 10382 – 10391, doi: 10.20964/2020.10.27

International Journal of
ELECTROCHEMICAL
SCIENCE
www.electrochemsci.org

Short Communication

Investigation of Pt/C and Pt-Ru/C Mixed Catalyst for DME Oxidation in Direct Dimethyl Ether Fuel Cells

*Lehong Xing**, *Yixin Wang, Xinting Shi, Rui Dong, Lin Wu*

College of Chemistry and Chemical Engineering, Mu Danjiang Normal University,
*E-mail: xinglehonghit@163.com

Received: 2 June 2020 / *Accepted:* 24 July 2020 / *Published:* 31 August 2020

The performance of Pt/C and Pt-Ru/C mixed catalyst has been studied for dimethyl ether (DME) oxidation in direct dimethyl ether fuel cells (DDFCs). Transmission Electron Microscopy (TEM) characterizations show that Pt and Pt-Ru particles (about 3.0 nm) are highly dispersed on their supports. The electrochemical activity of mixed catalyst was evaluated by polarization curve, amperometric current density – time technique, and electrochemical impedance spectroscopy (EIS). The results show that the activity of mixed catalyst is better than Pt/C toward DME oxidation. Pt-Ru/C in the mixed catalyst is helpful for reducing the catalyst poisoning effect, and simultaneously, Pt/C in the mixed catalyst can provide continuous Pt active sites for DME dehydrogenation. Too much Pt-Ru can reduce the catalytic activity. The optimal Pt-Ru content is 3.5 mg cm^{-2} Pt and 0.5 mg cm^{-2} Pt-Ru (metal loading) in anode catalyst layer.

Keywords: Direct dimethyl ether fuel cell; Dimethyl ether; Anode catalyst; Pt-Ru/C; Pt/C

1. INTRODUCTION

Direct type fuel cells which use formic acid, ethanol, formaldehyde, methanol and dimethyl ether (DME) as their fuel have been widely studied recently as potential new power sources [1-3]. These investigated direct type fuel cells are all have their own advantages [4,5]. The direct dimethyl ether fuel cell (DDFC) is one of the promising fuel cells [6]. Dimethyl ether (DME) is the simplest ether and there is no C-C bond in its molecular (CH_3OCH_3) [7]. The toxity of DME is low. DME gas can be compressed easily into liquid form, so that the transportation of DME is convenient. The energy density of DME is high and its fuel crossover effect is low [8,9]. However, DDFC still has some obstacles which hinder its practical applications. The major obstacle limits the performance of DDFC is the poor kinetics of DME oxidation, which mainly results from the week adsorption of DME on catalyst and the poisoning effect of Pt based catalyst [10]. The development of active catalyst towards DME oxidation is very necessary for DDFC. Pt-Ru/C and Pt/C are the two most commonly used anode catalyst for DDFC. Different

3.Xing L, Wang Y, Sui C, et al. Investigation of Pt/SnO_2/C Catalyst for Dimethyl Ether Oxidation in DDFC[J]. Int. J. Electrochem. Sci, 2020, 15: 2375-2384.

Int. J. Electrochem. Sci., 15 (2020) 2375 – 2384, doi: 10.20964/2020.03.26

International Journal of
ELECTROCHEMICAL
SCIENCE
www.electrochemsci.org

Short Communication

Investigation of Pt/SnO_2/C Catalyst for Dimethyl Ether Oxidation in DDFC

Lehong Xing[1,2,*], *Yixin Wang*[1], *Chao Sui*[1], *Na Zhang*[2]

[1] College of Chemistry and Chemical Engineering, Mu Danjiang Normal University, Mu Danjiang 157012 ,China
[2] School of Chemical Engineering and Technology, Harbin Institute of Technology, No. 92, West Da-Zhi Street, Harbin 150001 China
*E-mail: xinglehonghit@126.com

Received: 6 November 2019 / *Accepted:* 18 December 2019 / *Published:* 10 February 2020

The performance of Pt loading on SnO_2/C support catalyst has been investigated for dimethyl ether (DME) oxidation in direct dimethyl ether fuel cells (DDFCs). The transmission electron micrograph (TEM) tests show that the sizes of Pt particles loading on different supports (SnO_2/C and XC-72 carbon black) are nearly the same (3.2 nm). The cyclic voltammograms results reveal that Pt/SnO_2/C shows higher activity towards DME oxidation. DME prefers to be adsorbed on Pt/SnO_2/C surface. SnO_2 can adsorb OH_{ads} species which benefit to reduce the Pt poisoning effect. The maximum power density of DDFC has been enhanced by using Pt/SnO_2/C as the anodic catalyst. The electrochemical active surfaces (*EAS*) of different anodes are nearly the same. That is, the improvement of DDFC performance can be attributed to the enhanced activity of anode catalyst.

Keywords: Direct dimethyl ether fuel cell; Dimethyl ether; Anode catalyst; Supports; Pt/SnO_2/C

1. INTRODUCTION

At present, traditional energy resources such as coal, natural gas and oil are nearly exhausted. Fuel cells such as proton exchange membrane fuel cells (PEMFCs) and direct methanol fuel cells (DMFCs) have been widely studied to solve the potential energy crisis problems [1-3]. However, PEMFCs and DMFCs still have some obstacles which hinder their broad applications [4,5]. Dimethyl ether (DME) is a new attractive fuel for PEMFCs which has many advantages. The energy density of DME is high and its toxicity is low. DME has low fuel crossover effect [6]. The transportation of DME is convenient because it can be liquefied easily [7]. However, the major obstacle limits the performance of direct dimethyl ether fuel cell (DDFC) is the relatively slow kinetics of anodic DME oxidation. The improvement of catalyst activity towards DME oxidation is very important for DDFC [8]. Pt and Pt-M

4.Xing L H, Yin G P, Du C Y, et al. Investigation on the durability of direct dimethyl ether fuel cell. Part II: Cathode degradation[J]. International Journal of Hydrogen Energy, 2017, 42(26): 16695-16699.

INTERNATIONAL JOURNAL OF HYDROGEN ENERGY 42 (2017) 16695–16699

Available online at www.sciencedirect.com

ScienceDirect

journal homepage: www.elsevier.com/locate/he

Investigation on the durability of direct dimethyl ether fuel cell. Part II: Cathode degradation

Le-Hong Xing [a,b,*], *Ge-Ping Yin* [a], *Chun-Yu Du* [a], *Shu-Xin Cui* [b], *Ming-Hui Zuo* [b], *Hai-Peng Wang* [b]

[a] *State Key Laboratory of Urban Water Resource and Environment, School of Chemical Engineering and Technology, Harbin Institute of Technology, No. 92, West Da-Zhi Street, Harbin 150001, China*

[b] *College of Chemistry and Chemical Engineering, Mudanjiang Normal University, Mudanjiang 157012, China*

ARTICLE INFO

Article history:
Received 12 December 2016
Received in revised form
23 April 2017
Accepted 14 May 2017
Available online 17 June 2017

Keywords:
Direct dimethyl ether fuel cell
Durability test
Cathodic catalyst degradation
Electrochemical active surface
Dimethyl ether crossover

ABSTRACT

Cathodic Pt/C catalyst degradation for a direct dimethyl ether fuel cell (DDFC) has been investigated after a 70.5 h galvostatic operation at 60 °C under ambient pressure. The cathode electrochemical active surface (EAS) reduces from 349 to 267 cm^2 mg^{-1} Pt after durability test. Cathode EAS loss is associated with the growth of Pt catalyst particles. XRD and TEM results show that the particle size of cathodic Pt catalyst increases from an original value of 3.0 nm to 5.4 nm. Furthermore, the anode failure accelerates dimethyl ether (DME) crossover, and consequently, poisoning of catalyst by absorbed DME and/or intermediates aggravates the degradation of cathodic Pt/C catalyst. The effect of anode degradation on the long-term performance of DDFC has been reported in companion article (Part I).

© 2017 Hydrogen Energy Publications LLC. Published by Elsevier Ltd. All rights reserved.

Introduction

Recently, proton exchange membrane fuel cells (PEMFCs) [1–3], and direct methanol fuel cells (DMFCs) [4–6] have been investigated extensively for stationary and portable applications [7,8]. However, each of them has some shortcomings which limit their commercialization [9,10]. Dimethyl ether (DME) is known as a promising alternative fuel [11–13]. The transportation of DME is easier and safer than hydrogen because its physical properties are similar with liquefied petroleum gas (LPG) [14,15]. DME also has many advantages in comparison with methanol for its high energy density, low toxicity, and low fuel crossover [16–18]. Therefore, DME is a new proper fuel for fuel cells and has been receiving increasing attention recently [19–22].

Up to now, most of the research has been focused on the activity of anodic catalyst and the short-term performance of direct dimethyl ether fuel cell (DDFC) [23,24]. The long-term performance and durability of the membrane electrode assembly (MEA) for DDFC have not been investigated in detail. DDFC commercialization demands stable operation for at least thousands of hours, which is difficult to achieve [25]. The electrocatalyst is one of the major components of MEAs, and their stability plays an important role in the long-term operation of fuel cells [26,27]. Pt/C catalyst failure results from the corrosion of carbon support [28], the Ostwald ripening (dissolution and redeposition) of Pt particles [29], the coalescence

* *Corresponding author*. State Key Laboratory of Urban Water Resource and Environment, School of Chemical Engineering and Technology, Harbin Institute of Technology, No. 92, West Da-Zhi Street, Harbin 150001, China.
E-mail address: xinglehonghit@126.com (L.-H. Xing).
http://dx.doi.org/10.1016/j.ijhydene.2017.05.134
0360-3199/© 2017 Hydrogen Energy Publications LLC. Published by Elsevier Ltd. All rights reserved.

5.王宜鑫,邢乐红,石鑫婷,孟凡旭,张亮,董瑞.镀液中氨基磺酸镍质量浓度对电镀镍层析氢催化活性的影响[J].电镀与涂饰,2022,41(01):6-9.

第41卷 第1期 电镀与涂饰 ELECTROPLATING & FINISHING Vol.41 No.1

DOI: 10.19289/j.1004-227x.2022.01.002

镀液中氨基磺酸镍质量浓度对电镀镍层析氢催化活性的影响

王宜鑫，邢乐红*，石鑫婷，孟凡旭，张亮，董瑞

（牡丹江师范学院化学化工学院，黑龙江 牡丹江 157012）

摘要： 采用由10 g/L $NiCl_2·6H_2O$、30 g/L NH_4Cl和310～390 g/L $Ni(NH_2SO_3)_2·4H_2O$（氨基磺酸镍）组成的镀液（pH= 3.8），在温度35 ℃和电流密度3 A/dm^{2}的条件下电镀30 min，获得镍电极，研究了镀液中氨基磺酸镍质量浓度对镍镀层表面形貌和析氢催化活性的影响，结果表明，镀液中氨基磺酸镍质量浓度为350 g/L时，镍镀层结晶最细致，析氢催化活性和稳定性最佳。

关键词： 电镀镍；氨基磺酸镍；析氢反应；催化活性；稳定性

中图分类号： TQ153.12 **文献标志码：** A **文章编号：** 1004－227X (2022) 01－0006－04

Effect of mass concentration of nickel sulfamate in bath on catalytic activity of nickel coating for hydrogen evolution

WANG Yixin, XING Lehong *, SHI Xinting, MENG Fanxu, ZHANG Liang, DONG Rui

(School of Chemistry and Chemical Engineering, Mudanjiang Normal University, Mudanjiang 157012, China)

Abstract: A nickel electrode was obtained by electroplating nickel on pure copper in a bath (pH = 3.8) comprising $NiCl_2·6H_2O$ 10 g/L, NH_4Cl 30 g/L, and $Ni(NH_2SO_3)_2·4H_2O$ (nickel sulfamate) 310-390 g/L at temperature 35 ℃ and current density 3 A/dm^2 for 30 minutes. The effect of mass concentration of nickel sulfamate on surface morphology of the nickel coating and its catalytic activity for hydrogen evolution reaction was studied. The results showed that the nickel coating electroplated with nickel sulfamate 350 g/L was the finest and most compact with the best catalytic activity and stability in hydrogen evolution reaction.

Keywords: nickel electroplating; nickel sulfamate; hydrogen evolution reaction; catalytic activity; stability

氢能是一种高效的可再生清洁能源。氢气的制备方法主要有化石燃料法、电催化法、光催化法、微生物法等。其中电催化制氢具有纯度高、零污染、生产能力易调等优点，受到广泛关注[1-3]。电催化剂在电解制氢过程中起着至关重要的作用，电催化剂大多选用性能优异的铂族贵金属及其合金[4]。然而，铂族金属价格昂贵、丰度低，使其应用受限。金属镍有着较低的析氢过电位，析氢催化性能好，常被用作析氢催化剂[5-7]。电催化剂的制备方法主要有化学法、物理法、气相沉积法、电沉积法等[8-10]。电沉积法操作简单、快速，反应条件适中，成本低，因此被广泛应用。电镀镍时镀液中氨基磺酸镍浓度对镍镀层的性能有很大影响[11]。本文通过微观形貌分析以及极化曲线、塔菲尔曲线和计时电位曲线测量来研究氨基磺酸镍质量浓度对镀层析氢性能的影响。

1 实验

1.1 氨基磺酸盐体系电镀镍

1.1.1 前处理

选用5 cm × 4 cm的紫铜片作为基体，其前处理流程为：打磨→乙醇冲洗→20% NaOH溶液碱洗→10%（质量分数）盐酸洗→去离子水洗。

镍阳极使用前依次进行打磨、3 mol/L HCl溶液活化以及去离子水冲洗。

1.1.2 镀液配方和工艺条件

$NiCl_2·6H_2O$ 10 g/L，NH_4Cl 30 g/L，$Ni(NH_2SO_3)_2·4H_2O$（氨基磺酸镍）310～390 g/L，pH 3.8，温度35 ℃，电流密度3 A/dm^2，时间30 min。

收稿日期： 2021-05-17 **修回日期：** 2021-08-24

基金项目： 牡丹江师范学院国家培育项目（GP2021002）；黑龙江省牡丹江市科学技术局项目（SQ2020G115）；牡丹江师范学院课程专项项目（KCSZ-2020021）；黑龙江省大学生创新创业项目（202110233043）；牡丹江师范学院硕士研究生科技创新项目（lgcx2020-80mdjsu）。

第一作者： 王宜鑫（1993-），男，黑龙江宁安人，在读硕士研究生，主要研究方向为金属表面处理和表面改性。

通信作者： 邢乐红（1983-），女，山东武城人，博士，副教授，主要从事金属表面处理、化学电源等方面的研究。

引用格式： 王宜鑫，邢乐红，石鑫婷，等. 镀液中氨基磺酸镍质量浓度对电镀镍层析氢催化活性的影响[J]. 电镀与涂饰，2022，41(1)：6-9.

WANG Y X, XING L H, SHI X T, et al. Effect of mass concentration of nickel sulfamate in bath on catalytic activity of electroplated nickel coating for hydrogen evolution[J]. Electroplating & Finishing, 2022, 41(1): 6-9.

(C)1994-2022 China Academic Journal Electronic Publishing House. All rights reserved. http://www.cnki.net

6.邢乐红,王宜鑫,隋朝,肖同欣,赵玥,邵艳秋.工程教育专业认证背景下化学工程与工艺专业人才培养模式探索[J].教育现代

化,2020,7(07):11-12.

Education Modernization 教育现代化

DOI:10.16541/j.cnki.2095-8420.2020.07.005

工程教育专业认证背景下化学工程与工艺专业人才培养模式探索

邢乐红，王宜鑫，隋朝，肖同欣，赵玥，邵艳秋

（牡丹江师范学院 化学化工学院，黑龙江 牡丹江）

摘　要：根据工程教育专业认证标准相关要求，从人才培养目标与毕业要求的重新定位，课程体系设置，工程教育实践环节改革等方面，进行了我校化学工程与工艺专业人才培养方案改革，初步建立了“以学生为中心”“以目标为导向”“持续改进”的成果导向型人才培养新架构。

关键词：工程认证；化学工程与工艺；人才培养

本文引用格式：邢乐红，等．工程教育专业认证背景下化学工程与工艺专业人才培养模式探索[J]．教育现代化，2020,7(07):11-12,22.

一　引言

工程教育专业认证是由工程教育认证协会组织，基于工程教育国际互认体系标准，对高等学校开设的工科专业实施的专业认证，其目的是保证工程教育质量和保障教育质量持续改进[1]。工程教育国际互认体的内容主要包括工程教育标准，学历互认及工程资格互认等。工程教育国际互认体系是由《华盛顿协议》《都柏林协议》《悉尼协议》《亚太工程师计划》《工程技术员流动论坛议》《工程师流动论坛协议》六个国际重要协议所构成[2]。其中前三个协议主要规定了学历互认的相关要求，后面三个协议主要规定了工程技术人员职业技术资格互认的相关要求。这六个协议中最重要最具权威性的是1989年签署的《华盛顿协议》，该协议的主要内容包括两方面，一是工程教育认证体系具有可比性，二是通过认证的专业培养的毕业生获得的能力是等效的[3]。

我国于2006年开始进行工程教育认证，并由国家教育部授权成立了权威机构－全国工程教育专业认证专家委员会。2013年中国正式提交申请，并于同年6月顺利加入《华盛顿协议》，成为预备成员。2016年中国成为《华盛顿协议》正式成员[4]。开展工程教育专业认证的目的是为了不断提高工程教育质量，加快工程教育优化进程，提高我国工程教育的国际“地位”与国际竞争力。2006年底，我国高校化学工程与工艺专业开始了工程认证工作，2007年，清华大学和天津大学的化学工程与工艺专业按照国际标准率先通过工程教育专业认证。在此之后大批高校的化学工程与工艺专业申请国家工程教育认证并成功通过认证[5]。目前，高校已经意识到工程教育专业认证的重要性，以工程认证加快学科专业建设，提高高校人才培养质量和推动专业课程改革已势在必行[6]。牡丹江师范学院始建于1958年，是全国首批学士学位授予单位，现为黑龙江省东南部地区规模最大，综合实力最强的省属本科院校。本校化学工程与工艺专业于2011年开始招生，目前已有5届毕业生。本专业积极拓展与国内知名大学的学习交流，使得专业办学能力与水平稳步提高。我们有信心、有能力把本专业办成黑龙江省一流的专业，为东北老工业基地振兴和服务地方经济发展贡献力量。目前，本专业以工程认证为契机，对标工程认证标准，查找本专业的问题和不足，从人才培养目标与毕业要求的重新定位，课程体系设置，工程教育实践环节改革等方面，进行了我校化学工程与工艺专业人才培养方案改革，初步建立了“以学生为中心”“以目标为导向”“持续改进”的成果导向型人才培养新架构。

二　解读化学工程与工艺专业认证标准

化学工程与工艺专业全体教师，全面学习了解了认证标准相关内容，包括通用标准所包含的“七项指标”（专业目标，课程体系，支持条件，师资队伍，管理制度，学生发展，质量评价）共35个观测点（招生数量，录取分数，第一志愿生源，学生指导，就业率，就业性质与分布，具有吸引优秀生源的制度和措施，学生表现跟踪评估，考试内容与培养目标达成程度，转专业学分认定，培养目标内容，培养目标达成度与合理性，毕业要求内容，毕业要求如何通过教学活动实现，毕业要求达成度等）以及补充标准中对课程体系，师资队伍，支

基金项目：牡丹江师范学院教学改革项目（19-XJ21008）；牡丹江师范学院青年学术骨干项目（GG2018001）；黑龙江省高校青年创新人才培养计划项目（UNPYSCT-2016108）；牡丹江师范学院教学改革项目（18-XJ20064）；牡丹江师范学院国家级课题培育项目（GP2018002）；黑龙江省教育科学规划课题（GJC1316121）。

作者简介：邢乐红，女，山东武城县人，博士，副教授，牡丹江师范学院化学工程与工艺专业负责人。

(C)1994-2020 China Academic Journal Electronic Publishing House. All rights reserved. http://www.cnki.net

人才培养与机制创新

7.邢乐红,王宜鑫,左明辉.工程教育专业认证背景下化学工程与工艺专业学生实践能力培养研究[J].山东化工,2019,48(24):159-160.

DOI:10.19319/j.cnki.issn.1008-021x.2019.24.070

工程教育专业认证背景下化学工程与工艺专业学生实践能力培养研究

邢乐红*,王宜鑫,左明辉

(牡丹江师范学院 化学化工学院,黑龙江 牡丹江　157012)

摘要:实践教学是工程教育专业认证中的重要内容,是学生创新能力培养的基本保障。通过对实践教学中实验课程教学、专业实习、双创训练、二课堂活动等进行改革,学生的实验技能、创新能力和解决化工实际问题的能力得到了提高。

关键词:工程教育认证;化学工程与工艺专业;人才培养;实践能力

中图分类号:G642.0　　文献标识码:A　　文章编号:1008-021X(2019)24-0159-02

Exploration on the Practical Ability Cultivation of Chemical Engineering and Technology Specialty under the Engineering Education Accreditation

Xing Lehong , Wang Yixin , Zuo Minghui*

(School of Chemistry and Chemical Engineering, Mudanjiang Normal University, Mudanjiang　157012, China)

Abstract: Practical teaching is an important content of the engineering education accreditation. Practical teaching is the important guarantee of students, innovation ability cultivation. Through reforms of practical teaching including experimental course teaching, professional practice, innovation and entrepreneurship training, the second class activity, the students, innovation and solving chemical engineering practical problems abilities have been enhanced.

Key words: engineering education accreditation; chemical engineering and technology specialty; talent cultivation; practical ability

工程教育专业认证是工程教育国际互认的基础,通过认证的专业所培养的毕业生获得的能力是等效的[1]。2006 年,我国高校的化学工程与工艺专业开始了工程教育专业认证的筹备工作。2007 年,清华大学和天津大学的化学工程与工艺专业按照国际标准要求,率先通过了工程教育专业认证。此后,中国石油大学、北京化工大学、大连理工大学、华东理工大学、浙江大学等大批高校的化学工程与工艺专业相继通过认证[2]。目前,越来越多的高校认识到工程认证的重要性,积极开展工程认证背景下的人才培养模式改革[3]。牡丹江师范学院化学工程与工艺专业于 2011 年开始招生,目前已有 5 届毕业生。本专业共有专任教师 6 人,其中具有博士学位教师 4 人,具有副高级职称教师 2 人,35 周岁以下青年教师 4 人,博士化率 66.7%。目前,本专业教师已充分认识到工程教育认证的重要性,积极开展相关的教育教学改革工作。

工程教育认证标准要求实践教学环节在人才培养方案中所占学分比例不少于总学分的 20%,是工程教育专业认证中的重要内容[4]。培养学生实践能力和创新能力是工程教育面临的主要问题之一。强化实践教学环节,规范学生实验操作技能,鼓励学生设计实验解决问题,支持学生参与科学研究,坚持实践教学与生产实际、社会实践相结合,对提高学生能力至关重要。这就要求在专业建设过程中要进一步深化实践教学改革,建立从实践中来、到实践中去和理论与实践紧密结合的高素质工程人才培养模式。本文以牡丹江师范学院化学工程与工艺专业为例,分析了工程教育专业认证背景下,化学工程与工艺专业学生实践能力培养的方法和措施。

1　实验课程教学

我校化学工程与工艺专业现开设的实验课程有,基础化学类实验课程(无机化学实验、有机化学实验、分析化学实验、物理化学实验),化工专业类实验课程(化工原理实验、化工仿真实验、化工制图实验、化工综合实验)。在实验课程的教学工作中,首先要特别强调实验操作安全注意事项。基础化学类实验使用的药品有些具有毒性或强腐性,在实验项目的选择上,应尽量选择无毒安全,现象明显,对环境污染小的药品进行实验。对于有毒性或腐性蚀性药品要特别强调用法及注意事项,提高学生自我保护意识和安全生产意识。化工专业类实验常常会用到风机、泵等叶片式流体输送设备,要提醒学生将头发盘梳整理,以防卷入。塔设备在工作过程中需要加热,在数据记录时要小心不要烫伤等。在实验室安全教育之后,我们安排专门的实验室安全考试,考试成绩计入期末总成绩。经过以上措施,学生们的安全意识明显提高,安全生产的工程观念得到强化。

教学内容和教学方式方面,重视学生预习环节,由简单的上交实验报告,改变为由学生讲解实验目的、实验原理、教师针对实验目的和实验原理进行相关的提问,学生回答。教师发放课前预习小卷,学生回答小卷上的问题之后,才可以动手进行实验。实验步骤由学生结合预习的知识和现场实验装置对应之后,进行讲解,讲解基本合格的组,才可以做实验。通过上述改革之后,学生实验的主动性得到提高,实验课程教学效果明

收稿日期:2019-09-20

基金项目:牡丹江师范学院教学改革项目(19-XJ21008);牡丹江师范学院青年学术骨干项目(GG2018001);黑龙江省高校青年创新人才培养计划项目(UNPYSCT-2016108);黑龙江省教育教学改革项目(SJGY20190688)

作者简介:邢乐红(1983—),女,山东武城县人,博士,副教授,牡丹江师范学院化学工程与工艺专业负责人。

(C)1994-2020 China Academic Journal Electronic Publishing House. All rights reserved.　http://www.cnki.net

8.邢乐红,王宜鑫,王慧,左明辉,孙芳,梁志男.氨基乙酸对硫酸盐体系电镀镍-铁合金的影响[J].电镀与涂饰,2019,38(19):1039-1041.

第38卷 第19期 电镀与涂饰 Vol.38 No.19

DOI: 10.19289/j.1004-227x.2019.19.003

氨基乙酸对硫酸盐体系电镀镍–铁合金的影响

邢乐红*，王宜鑫，王慧，左明辉，孙芳，梁志男

（牡丹江师范学院化学化工学院，黑龙江 牡丹江 157012）

摘要： 在由 300 g/L $NiSO_4·6H_2O$、40 g/L $NiCl_2·6H_2O$、0.75 g/L $FeSO_4·7H_2O$、30 g/L H_3BO_3、8 mg/L 十二烷基磺酸钠组成的 Ni–Fe 合金电镀液(pH = 4.2)中，研究了氨基乙酸(0.00 ~ 0.60 g/L)对其稳定性及从中所得镀层性能的影响。结果表明，氨基乙酸可与 Fe^{2+}配位，抑制 Fe^{2+}的氧化，提高镀液稳定性，当氨基乙酸质量浓度为 0.20 g/L 时，镀液的稳定性最好，镀层的耐蚀性较好。

关键词： 镍–铁合金；电镀；硫酸盐；氨基乙酸；亚铁离子；稳定性；耐蚀性

中图分类号： TQ153.2　　**文献标志码：** A　　**文章编号：** 1004 – 227X (2019) 19 – 1039 – 08

Effect of glycine on electroplating of nickel–iron alloy in sulfate bath // XING Le-hong*, WANG Yi-xin, WANG Hui, ZUO Ming-hui, SUN Fang, LIANG Zhi-nan

Abstract: The effect of glycine (0.00-0.60 g/L) on the stability of a sulfate Ni–Fe alloy electroplating bath (pH = 4.2) comprising $NiSO_4·6H_2O$ 300 g/L, $NiCl_2·6H_2O$ 40 g/L, $FeSO_4·7H_2O$ 0.75 g/L, H_3BO_3 30 g/L, and sodium dodecyl sulfonate 8 mg/L, as well as the properties of the coatings obtained therefrom was studied. The results showed that the complexation of glycine with Fe^{2+} inhibits the oxidation of Fe^{2+}, improving the stability of plating bath. The bath containing glycine 0.20 g/L had the best stability, and the coatings prepared from it had good corrosion resistance.

Keywords: nickel–iron alloy; electroplating; sulfate; glycine; iron(II) ion; stability; corrosion resistance

First-author's address: School of Chemistry and Chemical Engineering, Mudanjiang Normal University, Mudanjiang 157012, China

连铸机拉坯时钢水通过结晶器冷却成型，对结晶器基体的磨损很大[1]。金属电沉积技术可改善结晶器表面性能，提高结晶器寿命[2]。电镀 Ni–Fe 合金镀层因具有硬度高、耐磨、耐腐蚀等优点，常被用作连铸机结晶器工作面的防护层[3-4]。硫酸盐体系电镀 Ni–Fe 镀液中的 Fe^{2+}稳定性较差，易被氧化成 Fe^{3+}，进而水解生成沉淀。该沉淀具有磁性，可进入镀层形成毛刺，影响镀层性能[5]。因此需要在镀液中添加 Fe^{2+}的稳定剂。柠檬酸可作为配位剂来稳定硫酸盐体系 Ni–Fe 合金镀液中的 Fe^{2+}[6]。氨基乙酸也是常用的电镀配位剂，但在 Ni–Fe 合金电镀中的应用鲜见报道。本文选用氨基乙酸作为稳定剂，以期获得性能良好的 Ni–Fe 合金镀层。

1 实验

1.1 硫酸盐体系电镀 Ni–Fe 合金

1.1.1 前处理

采用 8 cm × 5 cm 的低碳钢板作为基体，依次对其进行除油、热水洗 (80 °C)、酸洗和去离子水洗。除油液为 5 g/L 十二烷基磺酸钠水溶液，酸洗液为质量分数 5%的硫酸溶液。

1.1.2 镀液配方和工艺条件

在方形塑料镀槽中进行电镀，采用可溶性镍阳极。镀液组成和工艺条件为：$NiSO_4·6H_2O$ 300 g/L，$NiCl_2·6H_2O$ 40 g/L，$FeSO_4·7H_2O$ 0.75 g/L，H_3BO_3 30 g/L，十二烷基磺酸钠 8 mg/L，氨基乙酸 0.00 – 0.60 g/L，pH 4.2，温度 55 °C，电流密度 3.5 A/dm^2，空气搅拌，时间 30 min。

1.2 基础液氧化试验

在烧杯中进行基础液氧化试验。基础液与镀液的组成基本相同，但不含 Ni^{2+}，其原因是镀液中 Ni^{2+}

收稿日期：2019-03-25　　修回日期：2019-06-12

基金项目：黑龙江省高校青年创新人才培养计划项目（UNPYSCT-2016108）；牡丹江师范学院青年学术骨干项目（GG2018001）；牡丹江师范学院教改项目（19-XJ21008）；黑龙江省高等教育教学改革研究项目（SJGY20180519）；黑龙江省省属高等学校基本科研业务费科研项目（1352MSYY10007）。

作者简介：邢乐红（1983–），女，山东武城人，博士，副教授，主要从事金属表面处理、化学电源等方面的研究。

(C)1994-2019 China Academic Journal Electronic Publishing House. All rights reserved. http://www.cnki.net

9.邢乐红,黎德育,李宁,左明辉,李晶.抗坏血酸对硫酸盐体系镍–铁合金镀液稳定性的影响[J].电镀与涂饰,2018,37(12):526-528.

DOI: 10.19289/j.1004-227x.2018.12.002

抗坏血酸对硫酸盐体系镍–铁合金镀液稳定性的影响

邢乐红[1,2,*]，黎德育[2]，李宁[2]，左明辉[1]，李晶[1]

（1. 牡丹江师范学院化学化工学院，黑龙江 牡丹江 157012；
2. 哈尔滨工业大学化工学院，黑龙江 哈尔滨 150001）

摘要：研究了抗坏血酸对硫酸盐体系电镀 Ni–Fe 合金镀液稳定性的影响，镀液（pH = 4.2）组成为：$NiSO_4·6H_2O$ 300 g/L，$NiCl_2·6H_2O$ 40 g/L，$FeSO_4·7H_2O$ 0.75 g/L，H_3BO_3 30 g/L，十二烷基磺酸钠 8 mg/L，抗坏血酸 0.00 ~ 0.15 g/L。结果表明，抗坏血酸可抑制镀液中 Fe^{2+}的氧化。当抗坏血酸质量浓度为 0.10 g/L 时，镀液的稳定性最好，镀层的耐蚀性得到提高。

关键词：镍–铁合金；电镀；硫酸盐；抗坏血酸；亚铁离子；稳定性；耐蚀性

中图分类号：TQ153.2 **文献标志码：**A **文章编号：**1004 – 227X (2018) 12 – 0526 – 03

Effect of ascorbic acid on stability of sulfate nickel–iron alloy electroplating bath // XING Le-hong*, LI De-yu, LI Ning, ZUO Ming-hui, LI Jing

Abstract: The effect of ascorbic acid on stability of sulfate Ni–Fe alloy electroplating bath was studied. The bath composition is: $NiSO_4·6H_2O$ 300 g/L, $NiCl_2·6H_2O$ 40 g/L, $FeSO_4·7H_2O$ 0.75 g/L, H_3BO_3 30 g/L, sodium dodecyl sulfonate 8 mg/L, and ascorbic acid 0.00-0.15 g/L. It is shown that ascorbic acid has an inhibition effect on the oxidation of Fe^{2+}. The bath containing ascorbic acid 0.10 g/L has the best stability, and produces coatings with improved corrosion resistance.

Keywords: nickel–iron alloy; electroplating; sulfate; ascorbic acid; ferrous ion; stability; corrosion resistance

First-author's address: School of Chemistry and Chemical Engineering, Mudanjiang Normal University, Mudanjiang 157012, China

连铸机结晶器基体多采用 Cr–Zr–Cu 合金[1]。连铸机工作时，大量钢水快速、连续地通过结晶器冷却成型，钢水对结晶器内表面的冲击所造成的磨损很大。Ni–Fe 合金镀层具有优良的耐磨性、硬度及耐蚀性，因此常作为连铸机结晶器工作面的表面防护层来提高结晶器寿命[2]。结晶器表面电镀 Ni–Fe 合金主要采用氨基磺酸盐体系，其优点是镀液稳定性高，镀层内应力低，但成本高，电流效率低[3-4]。硫酸盐体系具有成本低、可大电流密度施镀等优点，成为近年来的研究热点[5]。目前，对硫酸盐体系电镀 Ni–Fe 合金的研究主要集中在镀液组成及工艺参数对镀层性能的影响上[6-7]，有关 Fe^{2+}稳定剂研究的报道较少。在硫酸盐体系镀液中，Fe^{2+}易被氧化成 Fe^{3+}，Fe^{3+}水解生成的沉淀会导致镀液浑浊，镀层性能变差，铁含量减少。因此需要在硫酸盐体系镀液中添加 Fe^{2+}的稳定剂。柠檬酸、EDTA（乙二胺四乙酸）等可作为配位剂来稳定硫酸盐体系 Ni–Fe 合金镀液中的 Fe^{2+} [8]。抗坏血酸具有还原性，是电镀铁中常用的稳定剂，但在 Ni–Fe 合金电镀中的应用鲜见报道。本文选用抗坏血酸作为稳定剂，以求获得性能良好的 Ni–Fe 合金镀层。

1 实验

1.1 硫酸盐电镀镍铁合金

1.1.1 前处理

采用尺寸为 8 cm × 5 cm 的低碳钢板作为基体，依次对其进行除油（5 g/L 十二烷基磺酸钠水溶液）、热水洗（80 °C）、酸洗（质量分数为 5%的硫酸溶液）和去离子水洗。

收稿日期：2018–05–16 **修回日期：**2018–06–11

基金项目：黑龙江省高校青年创新人才培养计划项目（UNPYSCT-2016108）；牡丹江师范学院青年学术骨干项目（GG2018001）；黑龙江省教育厅高等教育教学改革研究项目（SJGY20170156）；牡丹江师范学院教学改革研究项目（17-XJH19002）。

作者简介：邢乐红（1983–），女，山东武城县人，博士，讲师，主要从事金属表面处理及化学电源等方面的研究。

作者联系方式：(E-mail) xinglehonghit@126.com。

(C)1994-2020 China Academic Journal Electronic Publishing House. All rights reserved. http://www.cnki.net

10.邢乐红,杨晶,王海鹏,达铭,李姗,崔术新.硫脲对低磷化学镀镍稳定性的影响[J].牡丹江师范学院学报(自然科学版),2016(03):41-42.

文章编号:1003-6180(2016)03-0041-02

硫脲对低磷化学镀镍稳定性的影响

邢乐红,杨 晶,王海鹏,达 铭,李 姗,崔术新
(牡丹江师范学院 化学化工学院,黑龙江 牡丹江 157011)

摘 要:研究硫脲的加入对低磷化学镀镍镀液稳定性及镀层沉积速度的影响.实验结果表明,硫脲的加入对低磷化学镀镍镀液稳定性和沉积速度影响较大,当硫脲浓度为 3 mg/L 时,镀液的稳定性最好,镀层沉积速度最快.

关键词:低磷化学镀镍;硫脲;稳定性;沉积速度

[中图分类号]TP317.6 [文献标志码]A
DOI:10.13815/j.cnki.jmtc(ns).2016.03.014

Effect of Thiourea Addition on the Stability of Low-phosphorus Electroless Nickel Plating

XING Le-Hong, YANG Jing, Wang Hai-peng, DA Ming, LI Shang, CUI Shu-xin
(Mudanjiang Normal University School of Chemistry and Chemical Engineering, Mudanjiang, Heilongjiang, 157011)

Abstract: The effects of thiourea on the stability and deposition rate of low-phosphorus electroless nickel plating coating have been discussed. The results indicate that the concentration of thiourea can obviously affect the stability and deposition rate of low-phosphorus electroless nickel plating and the optimal concentration of thiourea in electrolyte is 3mg/L.

Key words: low-phosphorus electroless nickel plating; thiourea; stability; deposition rate

低磷化学镀镍具有高熔点、高硬度、良好的可焊性及脱模性[1-3],广泛用于能源、电子等领域元件的表面处理[4-5].化学镀镍溶液是一种具有自催化性质的热力学不稳定体系,镀液易受外来杂质及反应中间产物影响而发生不可逆自分解,导致镀液寿命减少甚至报废,加工成本升高,因此需要在镀镍液中添加稳定剂来提高镀液稳定性.稳定剂是化学镀镍自催化反应的毒化剂,加入稳定剂可抑制镀液的自发分解,使反应可控有序的进行.[6]微量的稳定剂即可达到稳定镀液的作用,不能过量,否则会降低镀速甚至不起镀.本文选用硫脲作为低磷化学镀镍液的稳定剂,以提高镀液稳定性,获得性能良好的镀层.

1 材料与方法

1.1 镀液组成及基本工艺

化学镀镍液的基本组成为:硫酸镍 27 g/L,乳酸 20 g/L,无水乙酸钠 20 g/L,次亚磷酸 21 g/L,十二烷基磺酸钠 5 mg/L.选用铜板作基体,对其进行除油、水洗、酸洗、弱侵蚀等基本处理后,进行化学镀(前处理工序及化学镀均在烧杯中进行).镀液温度为 85 ℃,pH 值 6.2.通过此工艺可获得磷含量低于 3 $wt\%$的低磷化学镀镍层.

1.2 镀速测定

化学镀镍层的沉积速度采用增重法测定[7],

收稿日期:2016-03-20
基金项目:黑龙江省青年科学基金项目(QC2014C009);黑龙江省大学生创新创业训练计划项目(201610233031);牡丹江市科学技术计划项目(G2013f1407);牡丹江师范学院博士启动金项目(MSB201208);牡丹江师范学院国家级重点创新预研项目(GY201201)
作者简介:邢乐红(1983-),女,山东武城人.讲师,博士,主要从事金属表面处理及化学电源等方面研究;杨晶(1994-),女,黑龙江大庆人.本科生,主要从事金属表面处理等方面研究;王海鹏(1994-),男,黑龙江鸡东人.本科生,主要从事金属表面处理等方面研究.

?1994-2017 China Academic Journal Electronic Publishing House. All rights reserved. http://www.cnki.net

崔术新指导学生发表论文目录（共 5 篇）

1.Zuo M , Wang H , Xu J , et al. Crystal structure of poly[bipyridine-N,N')-tetrakis(l-cyanido-N:C) dinickel(II)][J]. Acta Crystallographica, 2001, 71(6):709.

2.崔术新,张文文,沈金铭,茹莉莹,赵宇,徐宝,左明辉.铁镍双金属配合物 $[Fe(2,2'\text{-}bpy)_2Ni(CN)_4]_n$ 的合成、晶体结构及磁性[J].硅酸盐学报,2020,48(06):919-924.

3.左明辉,沈金铭,徐杰,尹乾柱,崔术新.锌(Ⅱ)的一维配合物合成、晶体结构及其荧光性能研究[J].人工晶体学报,2019,48(07):1298-1302.

4.左明辉,沈金铭,尹乾柱,崔术新.氰基桥联金属镍配合物晶体的制备及其磁性[J].人工晶体学报,2018,47(09):1839-1842.

5.左明辉,何彦辉,许海霞,崔术新,邵长斌.水催化 HBrO 与 OH 自由基反应的微观机理[J].分子科学学报,2017,33(01):37-42.

1.Zuo M, Wang H, Xu J, et al. Crystal structure of poly[2-2”bipyridine-N,N)-tetrakis(l-cyanido-N:C)dinickel(II)]][J]. Acta Crystallographica, 2001, 71(6):709.

CrossMark

research communications

Acta Cryst E CRYSTALLOGRAPHIC COMMUNICATIONS

ISSN 2056-9890

Crystal structure of poly[(2,2′-bipyridine-κ^2N,N')-tetrakis(μ-cyanido-κ^2N:C)dinickel(II)]

Minghui Zuo, Haiyu Wang, Jie Xu, Lingling Zhu and Shuxin Cui*

College of Chemistry and Chemical Engineering, Mu Danjiang Normal University, Mu Danjiang 157012, People's Republic of China. *Correspondence e-mail: cuisx981@163.com

Received 11 May 2015
Accepted 20 May 2015

Edited by M. Weil, Vienna University of Technology, Austria

Keywords: crystal structure; cyanide ligands; nickel; 2,2′-bipyridine; coordination polymer

CCDC reference: 1058883
Supporting information: this article has supporting information at journals.iucr.org

The polymeric title complex, $[Ni_2(CN)_4(C_{10}H_8N_2)]_n$, was obtained serendipitously under hydrothermal conditions. The asymmetric unit consists of one half of an $[Ni(CN)_4]^{2-}$ anion with the Ni^{2+} cation situated on an inversion centre, and one half of an $[Ni(2,2'\text{-bpy})]^{2+}$ cation (2,2′-bpy is 2,2′-bipyridine), with the second Ni^{2+} cation situated on a twofold rotation axis. The two Ni^{2+} cations exhibit different coordination spheres. Whereas the coordination of the metal in the anion is that of a slightly distorted square defined by four C-bound cyanide ligands, the coordination in the cation is that of a distorted octahedron defined by four N-bound cyanide ligands and two N atoms from the chelating 2,2′-bpy ligand. The two different Ni^{2+} cations are alternately bridged by the cyanide ligands, resulting in a two-dimensional structure extending parallel to (010). Within the sheets, π–π interactions between pyridine rings of neighbouring 2,2′-bpy ligands, with a centroid-to-centroid distance of 3.687 (3) Å, are present. The crystal packing is dominated by van der Waals forces. A weak C—H···N interaction between adjacent sheets is also observed.

1. Chemical context

Coordination metal complexes have been the subject of intensive investigation not only due to their potential application to material science as catalytic, conductive, luminescent, magnetic, porous, chiral or non-linear optical materials (Janiak *et al.*, 2003), but also because of their intriguing structural diversity (Kong *et al.*, 2008). The assembly of functional molecular building blocks into crystalline polymeric materials through coordination bonds or other weak interactions has many advantages over traditional stepwise syntheses and was demonstrated to be an effective approach to fabricating new materials (Kopotkov *et al.*, 2014). Using this approach, numerous materials with interesting structures and properties have been prepared through the reactions of cyanidometallate building blocks (Cui *et al.*, 2011; Zhang & Lachgar, 2015). These compounds show novel functionalities due to strong interactions mediated by the linear cyanide bridges. The probably oldest and most interesting example is the Prussian blue framework, $Fe_4[Fe(CN)_6]_3{\cdot}14H_2O$, and its analogues derived from the assembly of hexacyanidometalate anions $[M(CN)_6]$ and transition-metal ions (Li *et al.*, 2008). For instance, cyanide-bridged bimetallic assemblies were obtained from $K_4[Fe(CN)_6]$ as a source of cyanidometalate anions, metal cations, and aromatic nitrogen-containing ligands. These compounds show interesting magnetic and other properties that can be affected through the careful choice of the building-block components (Shen *et al.*, 2014).

OPEN ACCESS

2.崔术新,张文文,沈金铭,茹莉莹,赵宇,徐宝,左明辉.铁镍双金属配合物[Fe(2,2'-bpy)$_2$Ni(CN)$_4$]$_n$的合成、晶体结构及磁性[J].硅酸盐学报,2020,48(06):919-924.

第48卷第6期 硅 酸 盐 学 报 Vol. 48, No. 6
2020年6月 JOURNAL OF THE CHINESE CERAMIC SOCIETY June, 2020
http://www.gsyb.chpt.cnki.net DOI: 10.14062/j.issn.0454-5648.20190530

铁镍双金属配合物[Fe(2,2'-bpy)$_2$Ni(CN)$_4$]$_n$的合成、晶体结构及磁性

崔术新[1], 张文文[1], 沈金铭[1], 茹莉莹[1], 赵 宇[1], 徐 宝[2], 左明辉[1]
(1. 牡丹江师范学院化学化工学院, 黑龙江 牡丹江 157011; 2. 吉林师范大学数学学院, 吉林 四平 136000)

摘 要: 使用$K_4[Fe(CN)_6]$提供氰基阴离子和Fe^{2+}阳离子, 与$Ni(Ac)_2{\cdot}4H_2O$和2,2'-联吡啶(2,2'-bpy)在水热条件下反应制备了氰基桥连的双金属铁镍配合物[Fe(2,2'-bpy)$_2$Ni(CN)$_4$]$_n$(1), 用红外光谱、热重分析和X射线衍射对其进行表征。结果表明: 在配合物1中, $[Fe(2,2'\text{-bpy})_2]^{2+}$阳离子和$[Ni(CN)_4]^{2-}$阴离子通过氰基桥联形成$Fe^{2+}$、$Ni^{2+}$离子交替存在的一维锯齿链[Fe(2,2'-bpy)$_2$Ni(CN)$_4$]$_n$。热重分析显示, 双金属配合物[Fe(2,2'-bpy)$_2$Ni(CN)$_4$]$_n$有较好的热稳定性, 磁性测量表明, 配合物[Fe(2,2'-bpy)$_2$Ni(CN)$_4$]$_n$中金属铁镍离子间存在强的反铁磁相互作用。

关键词: 双金属配合物; 铁离子; 镍离子; 氰基; 磁性
中图分类号: 文献标志码: A 文章编号: 0454-5648(2020)06-0919-06
网络出版时间: 2020-03-24

Syntheses, Crystal Structures, and Magnetic Properties of Bimetallic Complex [Fe(2,2'-bpy)$_2$Ni(CN)$_4$]$_n$

CUI Shuxin[1], ZHANG Wenwen[1], SHEN Jinming[1], RU Liying[1], ZHAO Yi[1], XU Bao[2], ZUO Minghui[1]
(1. College of Chemical Engineering, Mudanjiang Normal University, Mudanjiang 157011, Heilongjiang, China;
2. College of Mathematics, Jilin Normal University, Siping 136000, Jilin, China)

Abstract: A complex [Fe(2,2'-bpy)$_2$Ni(CN)$_4$]$_n$ (1) was synthesized with $K_4[Fe(CN)_6]$ as a source of cyanide anions and Fe^{2+} cations, 2,2'-bipyridine (2,2'-bpy) and $Ni(Ac)_2{\cdot}4H_2O$ under hydrothermal condition. Based on the X-ray crystallographic studies, two cations Fe^{2+} and Ni^{2+} are alternately bridged by some cyanide ligands to form a 1D zigzag chain with 2,2'-bpy terminal ligands in complex 1. The thermogravimetric analysis shows that a bimetallic complex [Fe(2,2'-bpy)$_2$Ni(CN)$_4$]$_n$ has a good thermal stability. The magnetic measurement reveals an intense antiferromagnetic interaction between iron and nickel ions in complex 1.

Keywords: bimetallic complex; iron ion; nickel ion; cyanide; magnetism

金属配合物因在手性、非线性光学、催化、磁性等方面具有优良性能, 使其在功能材料领域具有较大的应用价值而受到当今科学家的广泛关注[1-4]。制备这类材料最成功的方法是利用过渡金属离子和有机配体进行自组装反应, 有机配体根据其在形成配合物时所起作用不同这可分为终端配体和桥联配体。研究表明: 合成金属配合物的桥联配体调控着磁中心的距离、轨道中电子云的重叠等, 这就要求配体要有良好的配位能力和较短的原子间距离。目前较为常用的桥联配体有氰基CN^-、羧酸根离子COO^-、草酸根离子$C_2O_4^{2-}$、叠氮离子N_3^-等, 其中氰基的C、N都具有良好的配位能力, 是目前自身距离最短的双原子桥, 作为2个金属中心之间磁相互作用的有效线性桥, 与过渡金属连接能形成结构多样、性能优良配合物。最古老的氰基配合物是普鲁士蓝体系$Fe_4[Fe(CN)_6]_3{\cdot}14H_2O$[5], 以及由六氰基金属离子$[M(CN)_6]^{n-}$和简单过渡金属离子组装而形成的单金属普鲁士蓝衍生物[6-11]。

收稿日期: 2019-07-24。 修订日期: 2019-10-11。
基金项目: 黑龙江省省属高等学校基本科研业务费科研项目(135SZD001, 1353MSYQN003)、牡丹江师范学院国家级课题培育项目(GPZ2018002)、黑龙江省青年科学基金(QC2016C009)、国家大学生创新创业项目(201910233002)资助。
第一作者: 崔术新(1978—), 女, 博士, 教授。

Received date: 2019-07-24. Revised date: 2019-10-11.
First author: CUI Shuxin (1978–), female, Ph.D., Professor.
E-mail: cuisx081@163.com

(C)1994-2020 China Academic Journal Electronic Publishing House. All rights reserved. http://www.cnki.net

3.左明辉,沈金铭,徐杰,尹乾柱,崔术新.锌(Ⅱ)的一维配合物合成、晶体结构及其荧光性能研究[J].人工晶体学报,2019,48(07):1298-1302.

第48卷 第7期 人 工 晶 体 学 报 Vol. 48 No. 7
2019年7月 JOURNAL OF SYNTHETIC CRYSTALS July, 2019

锌(II)的一维配合物合成、晶体结构及其荧光性能研究

左明辉,沈金铭,徐 杰,尹乾柱,崔术新
(牡丹江师范学院化学化工学院,牡丹江 157011)

摘要:通过回流加热法以吡啶-2,3-二羧酸(2,3-PDC)和2-甲基咪唑(DMIM)配体与金属Zn(II)离子反应合成了配合物 $[Zn(2,3\text{-}PDC)(H_2O)(DMIM)\cdot H_2O]_n$(1),用IR、热重分析和X-射线单晶衍射对配合物结构进行表征。X-射线研究结果显示配合物1中锌离子通过2,3-PDC配体桥联形成一维链结构。荧光光谱测量显示配合物的最大发射波长为473 nm。

关键词:吡啶-2,3-二羧酸;2-甲基咪唑;回流加热;晶体结构;荧光性质
中图分类号:O611 文献标识码:A 文章编号:1000-985X(2019)07-1298-05
DOI:10.16553/j.cnki.issn1000-985x.2019.07.019

Synthesis, Crystals Structure and Luminescence Properties of 1D Zn(II) Complex

ZUO Ming-hui, SHEN Jin-ming, XU Jie, YIN Qian-zhu, CUI Shu-xin
(College of Chemical Engineering, Mudanjiang Normal University, Mudanjiang 157011, China)

Abstract: The complex $[Zn(2,3\text{-}PDC)(H_2O)(DMIM)\cdot H_2O]_n$ (1) were synthesized based on obtained from 2,3-pyridinedicarboxylic acid (2,3-PDC), 2-methylimidazole (DMIM) and metal Zn^{2+} cations under the condition of reflux heating. The structure was characterized by IR, thermogravimetric analysis and single-crystal X-ray diffraction and fluorescence spectra. The X-ray crystallographic studies suggest that the Zn(II) ions in complex 1 are bridged by the 2,3-PDC ligands to form a one-dimensional chain. The fluorescence spectra of complex 1 show that there is a strong emission peak at 473 nm.

Key words: 2,3-pyridinedicarboxylic acid; 2-methylimidazole; reflux heating; crystal structure; luminescence property

1 引 言

近年来,通过金属离子和有机配体自组装而形成的金属有机配合物材料是十分活跃的研究领域。制备这类材料通常采用改变金属离子、配体及合成条件等途径,并运用晶体工程学原理可以实现对配合物组成、结构和功能的剪裁和调控,使其具有单纯无机或纯有机材料无法比拟的性能及用途[1-2]。常见配体中吡啶羧酸[3-4]、咪唑[5-6],吡啶及吡唑等含氮杂环化合物及其衍生物占有主要地位,该类化合物与金属离子之间存在着多种成键方式。由于该类氮杂环上可以引入不同取代基,配合物的结构及配位模式均能发生相应的变化,所以具有结构新颖的氮杂环配合物相继被合成,这些配合物被广泛应用于生物、药物、工业电化学等领域。同时,文献报道吡啶羧酸和咪唑混合配体有利于构建新型配合物[7-8]。我们的兴趣在于设计合成一类以吡啶羧酸和咪唑两种氮杂环化合物为配体的金属配合物,通过配体的晶体工程来调节其性质。本文中采用回流法以吡啶-2,3-二羧酸(2,3-PDC)作为桥联配体,Zn^{2+}作为金属阳离子以及2-甲基咪唑(DMIM)终端配

基金项目:黑龙江省教育厅备案项目(13532001);牡丹江师范学院国家级课题培育项目(GP2018002);国家大学生创新创业资助项目(201810233018);牡丹江师范学院研究生科技创新项目(kjcx2018-09mdjnu)
作者简介:左明辉(1978-),男,内蒙古自治区人,博士,副教授。E-mail:zuominh09@163.com
通讯作者:崔术新,博士,教授。E-mail:cuisx9810@163.com

(C)1994-2019 China Academic Journal Electronic Publishing House. All rights reserved. http://www.cnki.net

4.左明辉,沈金铭,尹乾柱,崔术新.氰基桥联金属镍配合物晶体的制备及其磁性[J].人工晶体学报,2018,47(09):1839-1842.

第47卷 第9期
2018年9月

人 工 晶 体 学 报
JOURNAL OF SYNTHETIC CRYSTALS

Vol.47 No.9
September,2018

氰基桥联金属镍配合物晶体的制备及其磁性

左明辉,沈金铭,尹乾柱,崔术新
(牡丹江师范学院化学化工学院,牡丹江 157011)

摘要:在水热条件下以$K_4[Fe(CN)_6]$作为氰根阴离子,Ni^{2+}作为金属阳离子以及2,2'-联吡啶(2,2'-bpy)为配体制备了金属镍配合物$[Ni_2(CN)_4(2,2'\text{-}bpy)]_n$(1),并用X-射线晶体衍射仪测定了其晶体结构。结果表明:在配合物1中$[Ni(CN)_4]^{2-}$阴离子和$[Ni(2,2'\text{-}bpy)]^{2+}$阳离子通过氰基交替链接成2-D层状结构,磁性测量表明配合物中镍离子间存在反铁磁相互作用。

关键词:水热法;镍配合物;氰基;磁性
中图分类号:O76 文献标识码:A 文章编号:1000-985X(2018)09-1839-04
DOI:10.16553/j.cnki.issn1000-985x.2018.09.014

Preparation and Magnetism of Nickel Complex Crystals with Cyanide Bridge

ZUO Ming-hui, SHEN Jin-ming, YIN Qian-zhu, CUI Shu-xin
(College of Chemistry and Chemical Engineering, Mudanjiang Normal University, Mudanjiang 157011, China)

Abstract: The complex $[Ni_2(CN)_4(2,2'\text{-}bpy)]_n$(1) have been synthesized based on obtained from $K_4[Fe(CN)_6]$ as a source of anions, metal Ni^{2+} cations, and 2,2'-bipyridine (2,2'-bpy) ligand under hydrothermal condition. The X-ray crystallographic studies suggested that the ations $[Ni(CN)_4]^{2-}$ and cations $[Ni(2,2'\text{-}bpy)]^{2+}$ are alternately bridged by the cyanide ligands to form a 2D layer with 2,2'-bpy terminal ligands in complex 1. Intramolecular antiferromagnetic interactions were observed in complex 1.

Key words: hydrothermal method; nickel complex; cyanide; magnetism

1 引 言

一直以来,金属配位化合物都受到各个领域的广泛关注,这不仅是因为它们在催化、导电、发光、磁性、多孔、手性或非线性光学材料等方面具有潜在的应用价值[1-4],也同时归因于它们有趣的结构多样性[5-7]。制备这类材料最成功的方法是利用过渡金属离子和两种类型的配体进行自组装反应,这两种配体中的一个作为终端配体,另一种作为桥联配体。相比于传统的分步合成法,水热法一步将功能性分子构筑元件组装为目标晶体材料具有更多优点,同时也被证明是制备新型材料的有效途径[8]。利用这种方法,越来越多具有迷人结构和重要性能的材料通过金属氰化物构筑元件的反应而制得的[9-12]。氰化物作为传递两个金属离子之间的磁相互作用的有效线性桥,是制备高自旋团簇的一种备选桥联配体[13-17]。同时,作为芳香族含氮配体的2,2'-联吡啶[18],由于其对金属阳离子和DNA的结合能力,被广泛应用于光化学剂[19],太阳能电池组件等有前途的的研究领域。由于线性氰化物桥产生的强相互作用,这些化合物往往能够表现出一些新颖的功能。我们的兴趣主要在于设计合成一类氰基桥联磁性金属配合物,通过金属离子或配体的晶体工程来调节其磁

基金项目:黑龙江省青年科学基金(QC2014C009);黑龙江省教育厅备案项目(1352MSYB003);牡丹江师范学院国家培育项目(GP2018001);黑龙江省高等学校青年创新人才资助项目(UNPYSCT-20016108);大学生创新创业资助项目(201710233004)
作者简介:左明辉(1978-),男,内蒙古自治区人,副教授。

(C)1994-2019 China Academic Journal Electronic Publishing House. All rights reserved. http://www.cnki.net

5.左明辉,何彦辉,许海霞,崔术新,邵长斌.水催化 HBrO 与 OH 自由基反应的微观机理[J].分子科学学报,2017,33(01):37-42.

第 33 卷第 1 期 分 子 科 学 学 报 Vol.33 No.1
2017 年 2 月 Journal of Molecular Science February 2017

[文章编号]1000-9035(2017)01-037-06
DOI:10.13563/j.cnki.jmolsci.2017.01.006

水催化HBrO与OH自由基反应的微观机理

左明辉*,何彦辉,许海霞,崔术新,邵长斌
(牡丹江师范学院化学化工学院,黑龙江 牡丹江 157011)

[摘 要] 采用密度泛函理论,分别在B3LYP/6-311++g(d,p)和B3LYP/aug-cc-PVTZ理论水平下,系统研究了无水和水催化的OH自由基与HBrO反应,即HBrO+OH和HBrO+OH+H_2O 2个反应的微观反应机理,给出了所有可能发生的反应路径,并指出能量最低的反应通道.对于没有水参与的反应,由于OH自由基进攻HBrO方式不同,存在顺式方向和反式方向2种进攻方式的反应路径;当有一分子水参与反应时,考虑HBrO…H_2O复合物与OH自由基的反应和HBrO与H_2O…OH复合物2种反应情况,共发现4条不同的反应路径.这2种反应的所有路径均是在OH自由基提取氢之前以氢键复合物形式存在,反应过程均为无势垒加合过程,总反应为放热反应.水对目标反应起催化作用,有效地降低了反应的势垒,可以加快OH自由基和HBrO的消耗速度.

[关键词] $HBrO_2$;自由基;反应机理;DFT
[中图分类号] O 641 [学科代码] 150·30 [文献标识码] A

0 引 言

目前,臭氧层破坏日益严重.大量的臭氧损失不仅发生在同温层,在对流层底部臭氧损耗也很严重[1-2],这一现象已经引起人们的普遍关注.有研究表明,这与OH自由基和卤素物种有很大的关系.次溴酸是同温层中BrO_x物种的临时存储器[3-4],同时对催化消除同温层的臭氧起到重要作用.次溴酸可以通过很多途径生成,例如:气相中HO_2与BrO的反应$HO_2+BrO\rightarrow HBrO+O_2$[4];或者硝酸溴的水解$BrONO_2(aq)+H_2O\rightarrow HBrO(aq)+HNO_3(aq)$[5].这为HBrO参与臭氧消耗提供了广泛的来源.

在紫外-可见光区,$\lambda>310$ nm[6-7]时,HBrO有很强的吸收,发生光解反应$HBrO+h\nu\rightarrow Br(^2P_J)+OH(^2\Pi)$,产生自由基Br和OH,可直接参与臭氧层破坏.由于HBrO很容易产生Br及OH等自由基,含溴自由基具有更大的臭氧破坏效率,能够大量消耗臭氧.溴对臭氧的消耗能力比氯对臭氧的消耗能力高2个数量级[8-10],因此,有关溴物种的反应对同温层和臭氧层都至关重要.这就表明,消除HBrO对减少臭氧层破坏有着至关重要的作用.

在燃烧化学和大气化学中,HO_2是一种重要的中间体,在催化臭氧层消耗中也起到重要作用,同时,考虑到同温层中含有丰富的OH自由基,它是大气中非常重要的一种活性中间体,因

收稿日期:2016-06-21
*通讯联系人.左明辉,E-mail: zuomh068@mails.jlu.edu.cn
黑龙江省教育厅科学技术研究资助项目(12531722);牡丹江师范学院省级预研资助项目(SY201222).

?1994-2017 China Academic Journal Electronic Publishing House. All rights reserved. http://www.cnki.net

蔡雪指导学生发表论文目录（共 10 篇）

1.Yang W, Jiang R, Liu C, et al. Triptycene-Based Porous Chalcogen-Bonded Organic Frameworks[J]. Crystal Growth & Design, 2021, 21(11): 6497-6503.

2.Cai X, Ma Y, Zhou Q, et al. Synergistic effects of phases in the selective oxidation of isobutane over supported $(NH_4)_3HPMo_{11}VO_{40}$ catalysts[J]. Reaction Kinetics, Mechanisms and Catalysis, 2021, 133(1): 293-308.

3.Wei C, Lu G, Guo C, et al. Ethylthio-substituted sandwich phthalocyaninato europium (III) semiconductors for sensing NO_2 and NH_3: Effect of the extended π-conjugate systems on tuning the conductivity and sensing behavior[J]. Organic Electronics, 2021, 93: 106151.

4.Cai X, Zhou Q, Ma Y, et al. Selective Removal of CO in Hydrocarbons-Rich Industrial Off-gases over $CuO\text{-}Ce_xZr_{1-x}O_2$ Catalysts [J]. Catalysis Surveys from Asia, 2021, 25(1): 68-75.

5. Cai X, Wei C, Dong J, et al. Dimeric phthalocyanine-involved double-decker complex-based electrochemical sensor for simultaneous detection of acetaminophen and ascorbic acid[J]. Journal of Materials Science: Materials in Electronics, 2019, 30(3): 1976-1983.

6.Cai X, Ning H. Crystal structure of di-μ-acetato-diacetatobis (μ-6, 6′-dimethoxy-2,2′-{[(propane-1,3-diylbis (azanylylidene)] bis (methanylylidene)} diphenolato) tetrazinc[J]. Acta Crystallographica Section E: Crystallographic Communications, 2015, 71(12): 217-218.

7.姜力,周启,陈玉锋,蔡雪.5,15-二(二茂铁基)-卟啉酞菁钇的结构和振动光谱的密度泛函理论研究[J].原子与分子物理学报,2021,38(03):47-51.

8.孙守鹏,魏闯宇,宁桧,蔡雪.全波谱太能材料氟代酞菁锌分子ZnPc($C_{24}F_{48}$)的研究[J].牡丹江大学学报,2018,27(06):107-109.

9.宁桧,孙守鹏,蔡雪.轴向取代卟啉锌结构和光谱性质的研究[J].牡丹江师范学院学报(自然科学版),2017(01):39-42.

10.李梓萌,蔡雪.咔唑类取代酞菁锌染料敏化性能研究[J].牡丹江师范学院学报(自然科学版),2016(01):44-46.

1.**Yang W, Jiang R, Liu C, et al. Triptycene-Based Porous Chalcogen-Bonded Organic Frameworks[J]. Crystal Growth & Design, 2021, 21(11): 6497-6503.**

CRYSTAL GROWTH & DESIGN

pubs.acs.org/crystal Article

Triptycene-Based Porous Chalcogen-Bonded Organic Frameworks

Wei Yang,* Rong Jiang, Chao Liu, Baoqiu Yu, Xue Cai,* and Hailong Wang

Cite This: *Cryst. Growth Des.* 2021, 21, 6497−6503 Read Online

ACCESS | Metrics & More | Article Recommendations | Supporting Information

ABSTRACT: Two chalcogen-bonded organic frameworks (denoted as CBOFs), CBOF-1 and CBOF-2, have been constructed by the self-assembly of a custom-made triptycenetris(2,1,3-benzoselendiazole) (TTB) as an organic building block. As revealed by the results of single crystal X-ray diffraction analysis, the combination of chalcogen bonding and Se···π interactions was conductive to the structural porosity of the obtained two compounds. In particular, CBOF-1 exhibited a 3D 4-connected **lvt** topological framework with TTB simplified as the 4-connected node. The open pore channels of CBOF-1 possessed a pore size of 4.2 Å, of which the theoretical accessible pore volume occupied 35.6% of the total volume. Structural porosity of CBOF-2 was filled by tetrahydrofuran molecules, and the accessible volume percentage was calculated for 29.5%. Due to the flexible structure, degassed CBOF-1 displayed permanent porosity using carbon dioxide as an absorbate at 196 K. In the present study, a new kind of porous organic framework with permanent porosity has been revealed.

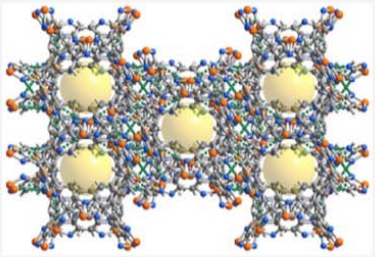

Downloaded via UNIV SCIENCE AND TECHNOLOGY BEIJING on December 3, 2021 at 01:20:24 (UTC).
See https://pubs.acs.org/sharingguidelines for options on how to legitimately share published articles.

INTRODUCTION

High order porous materials possess intriguing applications in the diverse realms such as gas storage, molecule separation, guest recognition, and heterogeneous catalysis, and so on.[1−5] Porous molecule-based crystalline materials such as metal−organic frameworks (MOFs)[6−9] and covalent organic frameworks (COFs)[10−16] are able to achieve the open functional voids with control of the size, shape, and uniformity as well as precise structural design from the atomic and molecular perspective. Besides polymeric MOFs and COFs via coordination and covalent interaction, respectively, hydrogen-bonded organic frameworks (HOFs)[17−24] and porous organic cages (POCs)[21−32] have been obtained by the self-assembly of discrete molecule modules with intrinsic or extrinsic voids through the weak hydrogen-bonding interaction and/or van der Waals force. Such reticular materials have been extensively fabricated and investigated in recent decades and have been found to be complementary to each other. Inspired by the development of diverse frameworks, exploring new and alternative approaches to construct porous molecule crystalline materials has attracted intense interest.

The anisotropic electron density distribution on the surface of atoms is an intrinsic characteristic of molecules, leading to an electron density that alternates between high and low around atoms. Thus, to stabilize the supramolecular assembly, the interactions between the negative and positive atoms/regions from different molecules are formed. Halogen bonding is generated by halogen atoms interacting with nucleophiles from elements of groups 13−16 in the periodic table, representing a kind of attractive interaction for the organization of molecular functional materials.[33,34] As pioneered by Prof. Barbour from discrete organic building blocks, such interaction has been used to produce porous halogen-bonded organic frameworks.[35−38] Alternatively, close chalcogen bonding contact has been found to occur between group 16 elements and nucleophiles.[39] In general, all sulfur, selenium, and tellurium atoms are able to form chalcogen bonds, and the bond strength is increased by following the increased polarizability of the chalcogen elements. The directionalities of chalcogen bonds are particularly similar to that of halogen bonds in terms of the crystal engineering thereof to a certain extent, enabling similar self-assembly behaviors.[40,41] As a result, prior research on halogen-bonded organic frameworks has provided inspiration for the present study, and for exploring the possibility of porous chalcogen-bonded organic frameworks. Notably, to the present knowledge, there are few examples of chalcogen-bonded organic assembly[42] and molecule capsules[43−46] with guest molecules included in the voids, and there has been no report on such materials with permanent porosity after solvent removal of solvent. Thus, the aforementioned direction of the corresponding research is of considerable significance.

In the present study, a new triptycene-containing organic linker, triptycenetris(2,1,3-benzoselendiazole) (TTB), was conceived and prepared, as shown in Scheme 1a. The

Received: August 17, 2021
Revised: October 3, 2021
Published: October 19, 2021

ACS Publications © 2021 American Chemical Society

https://doi.org/10.1021/acs.cgd.1c00942
Cryst. Growth Des. 2021, 21, 6497−6503

2..Cai X, Ma Y, Zhou Q, et al. Synergistic effects of phases in the selective oxidation of isobutane over supported $(NH_4)_3HPMo_{11}VO_{40}$ catalysts[J]. Reaction Kinetics, Mechanisms and Catalysis, 2021,

133(1): 293-308.

Reaction Kinetics, Mechanisms and Catalysis (2021) 133:293–308
https://doi.org/10.1007/s11144-021-01967-0

Synergistic effects of phases in the selective oxidation of isobutane over supported $(NH_4)_3HPMo_{11}VO_{40}$ catalysts

Xue Cai[1] · Yue Ma[1] · Qi Zhou[1] · Zitong Zhang[1] · Wenling Chu[2] · Weishen Yang[2]

Received: 3 February 2021 / Accepted: 15 March 2021 / Published online: 29 March 2021
© Akadémiai Kiadó, Budapest, Hungary 2021

Abstract
The supported 40 wt% $(NH_4)_3HPMo_{11}VO_{40}$ (APMV) catalysts over two different types of supports, supports-I ($Cs_3PMo_{12}O_{40}$, $Cs_{2.5}H_{0.5}PMo_{12}O_{40}$, $Cs_4PMo_{11}VO_{40}$ and $Cs_3HPMo_{11}VO_{40}$) and supports-II (CeO_2, WO_3/ZrO_2 and S-1 molecular sieve), were synthesized by deposition–precipitation method and further evaluated in the partial oxidation of isobutane to methacrylic acid (MAA) at 340 °C under atmospheric pressure. The fresh and used catalysts were characterized by N_2 adsorption/desorption, TG/DTG, XRD, FT-IR, Raman spectroscopy, pyridine- adsorption FT-IR and NH_3-TPD to investigate their structure, stability and surface acidity. The better results were obtained by impregnating 40 wt% active APMV phase onto the supports-I phase with same/similar Keggin structure, and it is believed that the formation of coherent interfaces between two structural well-matched phases with the same/similar Keggin anions greatly promotes interfacial transfer abilities of electrons and lattice oxygen, which is responsible for the efficient oxygen insertion to maximize MAA selectivity and conversion of isobutane. The current work provides a concept of phase synergy to design a promising catalyst for selective oxidation of isobutane.

Keywords Selective oxidation · Methacrylic acid · Synergetic effect · Heteropoly compounds

Introduction

Methacrylic acid (MAA) is an important organic chemical raw material for the production of methyl methacrylate (MMA), which is used as a monomer to produce poly methyl methacrylate (PMMA) and its derivatives. At present, the industrial

✉ Wenling Chu
cwl@dicp.ac.cn

[1] Mudanjiang Normal University, Mudanjiang 157011, China

[2] State Key Laboratory of Catalysis, Dalian Institute of Chemical Physics, Chinese Academy of Science, 457 Zhongshan Road, Dalian 116023, Liaoning, China

3.Wei C, Lu G, Guo C, et al. Ethylthio-substituted sandwich phthalocyaninato europium (III) semiconductors for sensing NO_2 and

NH_3: Effect of the extended π-conjugate systems on tuning the conductivity and sensing behavior[J]. Organic Electronics, 2021, 93: 106151.

Organic Electronics 93 (2021) 106151

Contents lists available at ScienceDirect

Organic Electronics

journal homepage: http://www.elsevier.com/locate/orgel

Ethylthio-substituted sandwich phthalocyaninato europium (III) semiconductors for sensing NO_2 and NH_3: Effect of the extended π-conjugate systems on tuning the conductivity and sensing behavior

Chuangyu Wei [a], Guang Lu [c], Chang Guo [a], Xuehui Lv [a], Xiangjie Tang [a], Qi Liu [a], Xue Cai [b,**], Yanli Chen [a,*], Jianzhuang Jiang [a,d,***]

[a] College of Science, China University of Petroleum (East China), Qingdao, 266580, China
[b] College of Chemistry and Chemical Engineering, Mudanjiang Normal University, Mudanjiang, 157011, China
[c] School of Chemistry and Biological Engineering, Shandong University of Science and Technology, Qingdao, 266510, China
[d] Beijing Key Laboratory for Science and Application of Functional Molecular and Crystalline Materials, Department of Chemistry, University of Science and Technology Beijing, Beijing, 100083, China

ARTICLE INFO

Keywords:
Sandwich-type phthalocyanine
π-conjugate system
Organic semiconductor
Solution-processed film
Gas sensing

ABSTRACT

By using the π-conjugated phthalocyanine macrocycle as the versatile building block, a series of five sandwich-type ethylthio substituted phthalocyaninato europium complexes, namely double-decker $Eu[Pc(SC_2H_5)_8]_2$ (**Pc-1**), triple-decker $Eu_2[Pc(SC_2H_5)_8]_3$ (**Pc-2**), and their corresponding dimers, $[Pc(SC_2H_5)_8]_2Eu_2[BiPc(SC_2H_5)_{12}]$ (**Pc-1@Pc-1**), $[Pc(SC_2H_5)_8]_3Eu_3[BiPc(SC_2H_5)_{12}]$ (**Pc-1@Pc-2**) and $[Pc(SC_2H_5)_8]_4Eu_4[BiPc(SC_2H_5)_{12}]$ (**Pc-2@Pc-2**), are synthesized and prepared into the solution-processed films by a simple quasi-Langmuir-Shäfer (QLS) method. Combination between the extending π-conjugated system in the longitudinal and transverse directions of Pc macrocycles and/or radical nature of **Pc-1** unit among different semiconducting molecules result in unusually small energy gaps (0.345–0.91 eV). Consequently, all of the semiconductors exhibit excellent conductivities. Among these materials, the conductivity for the radical species **Pc-1@Pc-1**, **Pc-1@Pc-2** and **Pc-1** is about 3–4 times larger than that for the non-radical compounds **Pc-2@Pc-2** and **Pc-2**. Moreover, the QLS films of five semiconductors take excellent linear responses for both oxidizing NO_2 (100–300 ppb) and reducing NH_3 (4–8.6 ppm). Respectively, the sensitivity (in % ppm^{-1}) gets increased in the order of **Pc-1** < **Pc-2** < **Pc-1@Pc-1** < **Pc-1@Pc-2** < **Pc-2@Pc-2** for NO_2, and **Pc-1@Pc-2** < **Pc-1** < **Pc-1@Pc-1** < **Pc-2@Pc-2** < **Pc-2** for NH_3. Depending on the highly extended π-conjugated systems, **Pc-2@Pc-2** and **Pc-2** films achieve the highest sensitivity of 208.2% ppm^{-1} and 0.97% ppm^{-1} to NO_2 and NH_3, respectively. In addition, with a less than 2 min response time within a limit of detection at 10 ppb for NO_2 and 0.48 ppm for NH_3, good reproducibility and selectivity have been revealed for the **Pc-2@Pc-2** and **Pc-2** films among the best gas sensors obtained so far for all the solution-processed films based on organic semiconductors in dry air at room temperature. More importantly, it is firstly demonstrated that the high NO_2 sensing is resulted from low Oxd_1, and high NH_3 sensing is resulted from high Red_1 among the sandwich Pc-based semiconductors.

1. Introduction

In recent years, organic semiconducting materials have been widely studied in the development of the profitable sensing systems for the sensitive detection of nitrogen-based hazardous gas due to their lower operating temperature, easier modulability of molecular properties, and solution processability compared with inorganic semiconductors [1–3]. Phthalocyanines (Pcs), as an important class of organic semiconductors, are a large series of heterocyclic conjugated molecules that possess unique electrical properties, high chemical stability, and tunable molecular orbital energies by the peripheral substituents and coordinated metals [4–6]. In particular, sandwich-type phthalocyanines, originating

* Corresponding author.
** Corresponding author.
*** Corresponding author. College of Science, China University of Petroleum (East China), Qingdao, 266580, China.
E-mail addresses: xuecai@mdjnu.edu.cn (X. Cai), yanlichen@upc.edu.cn (Y. Chen), jianzhuang@ustb.edu.cn (J. Jiang).

https://doi.org/10.1016/j.orgel.2021.106151
Received 13 February 2021; Received in revised form 12 March 2021; Accepted 12 March 2021
Available online 26 March 2021
1566-1199/© 2021 Elsevier B.V. All rights reserved.

4.Cai X, Zhou Q, Ma Y, et al. Selective Removal of CO in Hydrocarbons-Rich Industrial Off-gases over CuO-Ce_xZr_1 − xO_2 Catalysts [J]. Catalysis Surveys from Asia, 2021, 25(1): 68-75.

Catalysis Surveys from Asia
https://doi.org/10.1007/s10563-020-09314-4

ORIGINAL ARTICLE

Selective Removal of CO in Hydrocarbons-Rich Industrial Off-gases over CuO–$Ce_xZr_{1-x}O_2$ Catalysts

Xue Cai[1] · Qi Zhou[1] · Yue Ma[1] · Li Jiang[1] · Wenwen Yu[2,3] · Wenling Chu[2] · Rui Cai[2] · Weishen Yang[2]

Received: 4 August 2020 / Accepted: 23 September 2020
© Springer Science+Business Media, LLC, part of Springer Nature 2020

Abstract
The selective remove CO in industrial rich-hydrocarbon off-gases was performed over CuO–$Ce_xZr_{1-x}O_2$ (x = 0, 0.1, 0.5, 0.75, 0.9 and 1.0) mixed oxides. The effect of ceria content on the structure and catalytic properties of CuO–$Ce_xZr_{1-x}O_2$ compositions has been investigated, and the removal activity of CO is greatly dependent the structure of the support. Based on the characterizations from XRD, H_2-TPR, Raman spectra, XPS and CO-TPD, it can be found that the formation of ceria–zirconia solid solution induced by the introduction of ceria into zirconia leads to an increase in the amount of oxygen vacancies and the mobility of the lattice oxygen, and as a result, enhances the removal activity of catalysts towards CO. The lowest reaction temperature (~123 °C) for 100% conversion of CO remove was obtained over CuO–$Ce_{0.9}Zr_{0.1}O_2$ sample, which also exhibited the highest concentration of surface oxygen vacancy, the better reducibility and the highest low-temperature adsorption capacity of CO. This study presents a strategy to design a high-efficiency CuO-based catalyst by controlling the concentration of the surface oxygen vacancies.

Keywords Selective removal of CO · CuO–$Ce_xZr_{1-x}O_2$ ternary catalysts · Off-gas stream from propane oxidation · Oxygen vacancy sites

1 Introduction

Due to severe poisonous to the Pt catalysts used for the electrode materials, or due to a high risk of explosion in recycled industrial off-gases mixtures, the selective elimination of the undesirable CO in rich-hydrogen systems for the fuel cells or in recycled off-gas systems for the real-life chemical processes have attracted intensive attention in recent years. Particular attention has generally been paid to its application in selective remove of CO in off-gases from oxidation process of light alkanes with extremely exothermic properties, in which the lower conversion of alkane is necessary in order to efficiently decrease uncontrollable exotherm. As a result, recycled utilization of unconverted light-alkanes is one of the most cost-effective technologies for the industrial oxidation processes. To avoid explosion risk induced by the build-up in concentration of CO in recycled rich-hydrocarbons off-gases with complex components, one of the primary efforts is concentrated on selective oxidation removal of CO over the promising catalysts [1, 2].

In the past decades, various catalysts, such as precious metals [3], transition metal oxides [4, 5], have been investigated and exhibited excellent catalytic performances toward CO oxidation in rich-hydrogen systems for the fuel cells. As one of the most reactive catalysts, the binary supported metal oxide catalysts exhibit outstanding oxidation performance of CO due to the strong interaction between active metal species and supports [6]. Kleitz and colleagues [7] found that the tailored meso-structured CuO–CeO_2 catalysts exhibited the enhanced performance for preferential oxidation of CO at low temperature. Furthermore, it was found that [8] Cu–Fe mixed oxides with controlled composition showed a good performance in the CO oxidation reaction compared to a commercial Pt/Al_2O_3 catalyst used as a reference. ZrO_2 as an inert support shows high thermal stability

✉ Xue Cai
xuecai@mail.sdu.edu.cn

✉ Wenling Chu
cwl@dicp.ac.cn

[1] Mudanjiang Normal University, Mudanjiang 157011, China

[2] State Key Laboratory of Catalysis, Dalian Institute of Chemical Physics, Chinese Academy of Science, 457 Zhongshan Road, Dalian 116023, Liaoning, China

[3] University of Chinese Academy of Sciences, Beijing 100049, China

Published online: 01 October 2020

5.Cai X, Zhou Q, Ma Y, et al. Selective Removal of CO in Hydrocarbons-Rich Industrial Off-gases over CuO-Ce_xZr_1 − xO_2 Catalysts [J]. Catalysis Surveys from Asia, 2021, 25(1): 68-75.

Catalysis Surveys from Asia
https://doi.org/10.1007/s10563-020-09314-4

ORIGINAL ARTICLE

Selective Removal of CO in Hydrocarbons-Rich Industrial Off-gases over CuO–$Ce_xZr_{1-x}O_2$ Catalysts

Xue Cai[1] · Qi Zhou[1] · Yue Ma[1] · Li Jiang[1] · Wenwen Yu[2,3] · Wenling Chu[2] · Rui Cai[2] · Weishen Yang[2]

Received: 4 August 2020 / Accepted: 23 September 2020
© Springer Science+Business Media, LLC, part of Springer Nature 2020

Abstract
The selective remove CO in industrial rich-hydrocarbon off-gases was performed over CuO–$Ce_xZr_{1-x}O_2$ (x = 0, 0.1, 0.5, 0.75, 0.9 and 1.0) mixed oxides. The effect of ceria content on the structure and catalytic properties of CuO–$Ce_xZr_{1-x}O_2$ compositions has been investigated, and the removal activity of CO is greatly dependent the structure of the support. Based on the characterizations from XRD, H_2-TPR, Raman spectra, XPS and CO-TPD, it can be found that the formation of ceria–zirconia solid solution induced by the introduction of ceria into zirconia leads to an increase in the amount of oxygen vacancies and the mobility of the lattice oxygen, and as a result, enhances the removal activity of catalysts towards CO. The lowest reaction temperature (~123 °C) for 100% conversion of CO remove was obtained over CuO–$Ce_{0.9}Zr_{0.1}O_2$ sample, which also exhibited the highest concentration of surface oxygen vacancy, the better reducibility and the highest low-temperature adsorption capacity of CO. This study presents a strategy to design a high-efficiency CuO-based catalyst by controlling the concentration of the surface oxygen vacancies.

Keywords Selective removal of CO · CuO–$Ce_xZr_{1-x}O_2$ ternary catalysts · Off-gas stream from propane oxidation · Oxygen vacancy sites

1 Introduction

Due to severe poisonous to the Pt catalysts used for the electrode materials, or due to a high risk of explosion in recycled industrial off-gases mixtures, the selective elimination of the undesirable CO in rich-hydrogen systems for the fuel cells or in recycled off-gas systems for the real-life chemical processes have attracted intensive attention in recent years. Particular attention has generally been paid to its application in selective remove of CO in off-gases from oxidation process of light alkanes with extremely exothermic properties, in which the lower conversion of alkane is necessary in order to efficiently decrease uncontrollable exotherm. As a result, recycled utilization of unconverted light-alkanes is one of the most cost-effective technologies for the industrial oxidation processes. To avoid explosion risk induced by the build-up in concentration of CO in recycled rich-hydrocarbons off-gases with complex components, one of the primary efforts is concentrated on selective oxidation removal of CO over the promising catalysts [1, 2].

In the past decades, various catalysts, such as precious metals [3], transition metal oxides [4, 5], have been investigated and exhibited excellent catalytic performances toward CO oxidation in rich-hydrogen systems for the fuel cells. As one of the most reactive catalysts, the binary supported metal oxide catalysts exhibit outstanding oxidation performance of CO due to the strong interaction between active metal species and supports [6]. Kleitz and colleagues [7] found that the tailored meso-structured CuO–CeO_2 catalysts exhibited the enhanced performance for preferential oxidation of CO at low temperature. Furthermore, it was found that [8] Cu–Fe mixed oxides with controlled composition showed a good performance in the CO oxidation reaction compared to a commercial Pt/Al_2O_3 catalyst used as a reference. ZrO_2 as an inert support shows high thermal stability

✉ Xue Cai
xuecai@mail.sdu.edu.cn

✉ Wenling Chu
cwl@dicp.ac.cn

[1] Mudanjiang Normal University, Mudanjiang 157011, China

[2] State Key Laboratory of Catalysis, Dalian Institute of Chemical Physics, Chinese Academy of Science, 457 Zhongshan Road, Dalian 116023, Liaoning, China

[3] University of Chinese Academy of Sciences, Beijing 100049, China

Published online: 01 October 2020

6.Cai X, Ning H. Crystal structure of di-μ-acetato-diacetatobis (μ-6, 6′-dimethoxy-2,2′-{[(propane-1,3-diylbis (azanylylidene)] bis (methanylylidene)} diphenolato) tetrazinc[J]. Acta Crystallographica Section E: Crystallographic Communications, 2015, 71(12): 217-218.

Acta Cryst E CRYSTALLOGRAPHIC COMMUNICATIONS

OPEN ACCESS

ISSN 2056-9890

Crystal structure of di-μ-acetato-di-acetatobis(μ-6,6′-dimethoxy-2,2′-{[(propane-1,3-diylbis(azanylylidene)]-bis(methanylylidene)}diphenolato)tetra-zinc

Xue Cai* and Hui Ning

Department of Chemistry, Mudanjiang Normal University, Mudanjiang 157011, People's Republic of China. *Correspondence e-mail: xuecai@mail.sdu.edu.cn

Received 9 October 2015; accepted 29 October 2015

Edited by T. J. Prior, University of Hull, England

The tetranuclear title complex, $[Zn_4(C_{19}H_{20}N_2O_4)_2(CH_3COO)_4]$, is formed from two dinuclear motifs related by an inversion centre. The two crystallographically independent Zn^{II} ions in the asymmetric unit are in different coordination environments. One is square-based pyramidal with one O atom of an acetate group occupying the axial position and two N and O atoms of one bmspd [H_2bmspd = *N*,*N*′-bis(3-methoxysalicylidene)propylene-1,3-diamine] Schiff base ligand forming the basal plane. The other Zn^{II} atom is six-coordinated by four O atoms of the bmspd ligand forming the equatoral plane and two O atoms of different acetate groups located in the axial positions. As a result, the two phenolic planes of the bicompartmental Schiff base ligand are distorted slightly. However, the planes of the two Schiff base ligands are parallel. In addition, the Zn—N and Zn—O bond lengths span the reasonable ranges 2.062 (2)–2.073 (2) and 1.9261 (15)–2.4356 (16) Å, respectively. The Zn···Zn distances separated by phenolic O atoms are 3.2466 (4) Å while the Zn···Zn distances bridged by acetate groups are 5.9835 (6) Å. The tetranuclear moieties are connected by van der Waals interactions, and form a chain along *c* axis.

Keywords: crystal structure; zinc; Schiff base; acetate.

CCDC reference: 724776

1. Related literature

Metal-organic coordination complexes of *N*,*N*′-bis(salicylidene)ethylenediamine (salen) Schiff-base derivatives have been studied extensively within the fields of homogeneous catalysis (Wezenberg & Kleij, 2008), non-linear optics (Rigamonti *et al.*, 2006), magnetics (Yuan *et al.*, 2007) and biological metalloenzyme mimics (Laskin *et al.*, 2008).

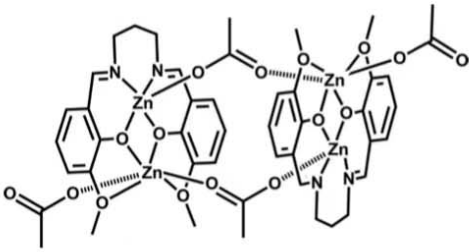

2. Experimental

2.1. Crystal data

$[Zn_4(C_{19}H_{20}N_2O_4)_2(C_2H_3O_2)_4]$
M_r = 1178.48
Triclinic, $P\overline{1}$
a = 10.4894 (9) Å
b = 10.7917 (9) Å
c = 11.9550 (11) Å
α = 103.425 (2)°
β = 94.323 (1)°
γ = 115.677 (1)°
V = 1162.17 (18) Å^3
Z = 1
Mo $K\alpha$ radiation
μ = 2.12 mm^{-1}
T = 298 K
0.15 × 0.10 × 0.08 mm

2.2. Data collection

Bruker SMART APEX CCD area-detector diffractometer
Absorption correction: multi-scan (*SADABS*; Sheldrick, 1996)
T_{min} = 0.742, T_{max} = 0.849
6281 measured reflections
4497 independent reflections
3969 reflections with $I > 2\sigma(I)$
R_{int} = 0.013

2.3. Refinement

$R[F^2 > 2\sigma(F^2)]$ = 0.024
$wR(F^2)$ = 0.071
S = 1.05
4497 reflections
318 parameters
H-atom parameters constrained
$\Delta\rho_{max}$ = 0.26 e Å^{-3}
$\Delta\rho_{min}$ = −0.27 e Å^{-3}

Data collection: *APEX2* (Bruker, 2004); cell refinement: *SAINT-Plus* (Bruker, 2001); data reduction: *SAINT-Plus*; program(s) used to solve structure: *SHELXTL* (Sheldrick, 2008); program(s) used to refine structure: *SHELXL97* (Sheldrick, 2008); molecular graphics: *XP* in *SHELXTL*; software used to prepare material for publication: *SHELXTL*.

Acknowledgements

The authors gratefully acknowledge the financial support provided by the Postdoctoral Science-Research Developmental Foundation of Heilongjiang Province (LBH-Q13170).

Supporting information for this paper is available from the IUCr electronic archives (Reference: PJ2024).

7.姜力,周启,陈玉锋,蔡雪.5,15-二(二茂铁基)-卟啉酞菁钇的结构和振动光谱的密度泛函理论研究[J].原子与分子物理学报,2021,38(03):47-51.

第38卷 第3期 原子与分子物理学报 Vol. 38 No. 3
2021年6月 JOURNAL OF ATOMIC AND MOLECULAR PHYSICS Jun. 2021

5,15－二(二茂铁基)－卟啉酞菁钇的结构和振动光谱的密度泛函理论研究

姜 力,周 启,陈玉锋,蔡 雪

(牡丹江师范学院 化学化工学院,牡丹江市 157000)

摘 要:本文选用混杂的B3LYP密度泛函理论方法,在Lanl2dz水平上,对5,15－二(二茂铁基)－卟啉酞菁钇[Por(Fc)$_2$]Y(Pc)的结构进行了优化,结果表明,5,15－二(二茂铁基)－卟啉酞菁钇呈现出三明治型构型,卟啉环与酞菁环呈穹型围绕在金属钇原子周围.对分子内主要的键长与键角进行了理论计算,通过频率计算,得到了5,15－二(二茂铁基)－卟啉酞菁钇[Por(Fc)$_2$]Y(Pc)的红外光谱图,与实验所得的红外光谱图进行比对,将理论计算和实验所得的光谱主要振动峰进行了线性回归拟合,相关系数为0.992,标准偏差为16.96.理论计算与实验所获得的红外光谱图基本一致,说明本文所选用的DFT理论计算方法是可行的.通过GaussView软件对5,15－二(二茂铁基)－卟啉酞菁钇的红外谱带简正振动模式进行了指认.此外,分析讨论了5,15－二(二茂铁基)－卟啉酞菁钇[Por(Fc)$_2$]Y(Pc)的分子静电势,确定了极大值与极小值的位置.对于研究5,15－二(二茂铁基)－卟啉酞菁钇分子的性质,提供了相应的理论基础.

关键词:卟啉酞菁;密度泛函理论;振动光谱;分子静电势

中图分类号:O641.4 文献标识码:A **DOI**:10.19855/j.1000-0364.2021.031007

Theoretical study on the structure and vibrational spectroscopy of 5,15－bis(ferrocenyl)－porphyrin yttrium phthalocyanine by density functional theory

JIANG Li, ZHOU Qi, CHEN Yu-Feng, CAI Xue

(Chemistry and Chemical Engineering Department, Mudanjiang Normal University, Mudanjiang 157000, China)

Abstract: In this paper, the structure of 5,15－bis(ferrocenyl)－porphyrin phthalocyanine yttrium [Por(Fc)$_2$]Y(Pc) molecule is optimized and calculated at density functional B3LYP level using Lanl2dz basis set. The results show that the 5,15－bis(ferrocenyl)－porphyrin yttrium phthalocyanine molecule exhibits a sandwich structure, and the porphyrin ring and the phthalocyanine ring are domed around the metal yttrium atom. The main bond lengths and bond angles in the molecule are calculated. IR spectrum was obtained from the calculation results of the frequencies, and compared with the experimental IR spectrum. By means of a line of best fit of the experimental IR frequencies versus the calculated ones in the range of 400～2000 cm^{-1}, the correlation coefficient and the standard deviation are found to be 0.992 and 16.96, respectively. The theoretical calculation is basically consistent with the infrared spectrogram obtained in the experiment, which indicates that the theoretical calculation method of DFT adopted is feasible in this paper. The vibrational mode was assigned on the basis of the GaussView. In addition, the molecular electrostatic potentialwere of [Por(Fc)$_2$]Y(Pc) were discussed based on the calculate results. This study provided a theoretical support for the analysis of [Por(Fc)$_2$]Y(Pc).

Key words: Porphyrin phthalocyanine; Density functional theory (DFT); Vibrational spectrum; Molecular electrostatic potential

收稿日期:2020-09-14
基金项目:黑龙江省教育厅基本科研业务费青年项目(1353MSYQN001);牡丹江师范学院科研项目(QN2019001)
作者简介:姜力(1987—),男,实验师.主要从事分子光谱研究.
通讯作者:蔡雪.E-mail:lijiang@mdjnu.edu.cn

(C)1994-2021 China Academic Journal Electronic Publishing House. All rights reserved. http://www.cnki.net

8.孙守鹏,魏闯宇,宁桧,蔡雪.全波谱太能材料氟代酞菁锌分子ZnPc($C_{24}F_{48}$)的研究[J].牡丹江大学学报,2018,27(06):107-109.

第 27 卷 第 6 期 牡丹江大学学报 Vol.27 No.6
2018 年 6 月 Journal of Mudanjiang University Jun. 2018

文章编号：1008-8717（2018）06-0107-03

全波谱太能材料氟代酞菁锌分子 ZnPc($C_{24}F_{48}$) 的研究

孙守鹏 魏闯宇 宁 桧 蔡 雪
（牡丹江师范学院化学化工学院，黑龙江 牡丹江 157011）

摘 要：在密度泛函理论和含时密度泛函理论的条件下对分子 ZnPc($C_{24}F_{48}$) 进行结构优化，模拟出分子的红外光谱和紫外吸收光谱，并对电子跃迁模式进行分析。通过电荷的比较设计出质子化模型 ZnPc($C_{24}F_{48}$)+H^+，通过计算模拟表明，该分子可以通过质子化对紫外光谱进行调节，因此该分子有成为全波谱太阳能吸波材料的潜力。

关键词：密度泛函；紫外吸收光谱；太阳能材料
中图分类号：O656.4 **文献标识码**：A
DOI:10.15907/j.cnki.23-1450.2018.06.033

Nature of Tunable Panchromatic Absorbing Material of ZnPc($C_{24}F_{48}$)

SUN Shou-peng, WEI Chuang-yu, NING Hui, CAI Xue
(Department of Chemstry, Mudanjiang Normal University, Mudanjiang, Heilongjiang 157011)

Abstract: Based on density functional theory and time-dependent density functional theory, we optimized the molecular structure of ZnPc($C_{24}F_{48}$), simulated the IR and UV spectra of molecules, and analyzed the mode of electron transition. Through the comparison of charge, we design the protonation model ZnPc($C_{24}F_{48}$)+H^+. Through the calculation and simulation, we can see that the molecule can regulate the UV spectrum through protonation, so the molecule has the potential to make full spectrum solar energy absorbing material.

Key words: density functional theory; UV spectrum; solar energy material

卟啉和酞菁的衍生物由于分子易于修改并且性能稳定，广泛应用于光电开关、分子导体、非线性光学等。[1-4] 酞菁分子属于有机大环结构，这种结构可以与金属形成金属配合物。近些年在实验化学的发展下，合成并深入研究了很多酞菁金属配合物的结构以及所具有的特殊性质。在 2012 年，Jiang's group 的齐冬冬博士曾经在全波谱太阳能吸波材料中发现了四吡咯稠合衍生物的两方面设计原则。[5] 本文选择了单晶分子，酞菁锌的氟原子取代的化合物 ZnPc($C_{24}F_{48}$)，在密度泛函理论的 B3LYP[6,7] 水平下，使用 6-311g(d,p) 基组，对该分子进行了结构的优化，并模拟出了该分子的红外光谱。在密度泛函理论的 PBE1PBE[8,9] 水平下，使用 6-311g(d,p) 基组，对该分子进行了紫外可见吸收光谱的模拟，所有的计算使用 Gaussian 09 D.01[10] 计算得到，通过利用 Multiwfn 4.3[11,12] 以半高全宽和高斯函数来对含时

收稿日期：2018-02-28
基金项目：牡丹江师范学院科研基金资助（gp201603）；黑龙江省教育厅科研项目（1352zd001）；牡丹江师范学院研究生科技创新项目（kjcx2016-15mdjnu）
作者简介：孙守鹏（1992-），男，黑龙江鸡西人，在读研究生，研究方向：酞菁化合物全谱吸收材料。
魏闯宇（1993-），女，黑龙江建三江人，在读研究生，研究方向：卟啉酞菁类化合物研究。
宁桧（1991-），辽宁丹东人，硕士，研究方向：卟啉化合物光谱性质研究。
通讯作者：蔡雪（1974-），女，吉林扶余人，牡丹江师范学院教授，博士，研究方向：卟啉酞菁化学。

(C)1994-2020 China Academic Journal Electronic Publishing House. All rights reserved. http://www.cnki.net

9.宁桧,孙守鹏,蔡雪.轴向取代卟啉锌结构和光谱性质的研究[J].牡丹江师范学院学报(自然科学版),2017(01):39-42.

文章编号:1003-6180(2017)01-0039-04

轴向取代卟啉锌结构和光谱性质的研究

宁 桧,孙守鹏,蔡 雪*
(牡丹江师范学院 化学化工学院,黑龙江 牡丹江 157011)

摘 要:在密度泛函理论 B3LYP 水平上,使用 6-31G 基组,对 ZnPor($C_{37}H_{39}O_3N$),ZnPor($C_{42}H_{39}O_3N$)和 ZnPor($C_{32}H_{39}O_4N$)分子结构进行优化,模拟出红外和紫外吸收光谱图,对这三个分子的结构和性质进行比较分析,实验结果表明,ZnPor($C_{42}H_{39}O_3N$)有做太阳能敏化剂的潜力.

关键词:卟啉锌;密度泛函理论;红外光谱;紫外光谱

[中图分类号]O656.4 [文献标志码]B
DOI:10.13315/j.cnki.jmtc(ns).2017.01.014

Structural and Spectroscopic Properties of Axially Substituted Porphyrin Zinc

NING Hui, SUN Shou-peng, CAI Xue*
(Mudanjiang Normal University Department of Chemistry, Mudanjiang 157011, China)

Abstract: In the density functional theory, B3LYP level, using 6-31G basis set, the structure of ZnPor($C_{37}H_{39}O_3N$), ZnPor($C_{42}H_{39}O_3N$) and ZnPor($C_{32}H_{39}O_4N$) molecules was optimized, simulate the infrared and ultraviolet absorption spectra, the structure and properties of these three molecules were compared and analyzed. Experimental results show that, ZnPor($C_{42}H_{39}O_3N$) has the potential to do solar sensitizer.

Key words: zinc porphyrin; density functional theory; Infrared spectrum; Ultraviolet spectrum

卟啉和金属卟啉类化合物受到生物学界,化学界和医学界的广泛关注[1-2]. 卟啉及金属卟啉类化合物广泛存在于动植物当中,具有特殊的生理活性. 早期的卟啉是从天然产物血红素和叶绿素中提取来的[3],叶绿体中的叶绿素就是含镁的卟啉化合物,由于卟啉类化合物对太阳光谱有着很好的吸收作用,其物理和化学性质也比较稳定,很适合作为光敏材料. 杨立国等人合成了几种轴向

收稿日期:2016-06-25
基金项目:黑龙江省博士后科研启动金资助项目(LBH-Q13170)
作者简介:宁桧(1990-),女,辽宁丹东人,硕士,主要从事卟啉类化合物光谱性质研究;孙守鹏(1992-),男,吉林德惠人,硕士,主要从事卟啉类化合物光谱性质研究;蔡雪(1974-),女,吉林扶余人,教授,博士,主要从事卟啉配合化学研究.
通讯作者:蔡雪

(C)1994-2021 China Academic Journal Electronic Publishing House. All rights reserved. http://www.cnki.net

10.李梓萌,蔡雪.咔唑类取代酞菁锌染料敏化性能研究[J].牡丹江师范学院学报(自然科学版),2016(01):44-46.

3 结论

(1) 采用两种方法——一步法和后嫁接法分别合成了 NH_2-SBA-15,合成的介孔材料对 Pb^{2+} 吸附均有大幅度的提高;后嫁接法合成的 NH_2-SBA-15 吸附效果更好. 通过 XRD、FT-IR 和 N_2 吸附-脱附等手段对材料进行表征,说明在合成过程中纯硅 SBA-15 的结构没有被破坏,仍保持良好的介孔有序性.

(2) 介孔材料对 Pb^{2+} 吸附与反应体系的 pH 值和吸附时间等因素有关. 批量实验表明:体系 pH 值较低时,相应的吸附率也低,pH 达到 5 时 Pb^{2+} 的吸附效果最佳;介孔材料对 Pb^{2+} 的吸附率随时间的增加而增大,60 min 为体系的最佳吸附时间,最佳吸附率能达到 90%左右.

参考文献

[1] 许秀琴, 朱勇, 杨挺, 等. 水体重金属的污染危害及其修复技术[J]. 污染防治技术, 2007, 20(4): 67-69.
[2] Zhao D Y, Feng J, Huo Q, et al. Triblock Copolymer Syntheses of Mesoporous Silica with Periodic 50 to 300 Angstrom Pores. Science[J]. Am. chem. soc,1998, 279: 548-552.
[3] 葛俊森, 梁渠. 水中重金属危害现状及处理方法[J]. 苏州化工, 2007, 35(5): 44-46.
[4] Feng X D, Fryxell G E, Wang L Q, et al. Functionalized Monolayers on Ordered Mesoporous Supports[J]. Science, 1997, 276: 923-926.
[5] Zhao D Y, Huo Q H, Feng J L, et al. Nonionic Triblock and Star Diblock Copolymer and Oligomeric Surfactant Syntheses of Highly Ordered Hydrothermally Stable Mesoporous Silica Structures[J]. Am. Chem. Soc, 1998, 120: 6024-6036.
[6] Zhao D Y, Huo Q H, Feng J L, et al. Triblock Copolymer Syntheses of Mesoporous Silica with Periodic 50 to 300 Angstrom Pores [J]. Science, 1998, 279: 548-552.
[7] 赵平平, 廉波. 银溶胶的制备、表征及应用[J]. 牡丹江师范学院学报: 自然科学版, 2014(3): 28-30.
[8] 杨华, 宋伟新, 王冰. CO-Nd 复合氧化物纳米微粒的制备及初步表征[J]. 牡丹江师范学院学报: 自然科学版, 2003(4): 19-21.
[9] 邵艳秋, 王虹苏, 管景奇, 等. 新型有机-无机杂化碱性介孔材料的合成[J]. 高等学校化学学报, 2013, 31(3): 592-596.

编辑:琳莉

咔唑类取代酞菁锌染料敏化性能研究

李梓萌,蔡 雪*

(牡丹江师范学院 化工学院,黑龙江 牡丹江 157011)

摘 要:理论计算模拟 $Zn[PcH_{15}R]$,$Zn[PcH_9R](NH_2)_6$ 和 $Zn[PcH_9R]F_6$ 的分子结构和原子电荷、HOMO与 LUMO 轨道以及红外光谱,发现取代后分子的能级差减小;R 基和吸电子基-F 的引入,增强了酞菁锌的染料敏化的性能. 说明 $Zn[PcH_{15}R]$和 $Zn[PcH_9R]F_6$ 这两种分子具有作为太阳能电池敏化剂的潜能.

关键词:酞菁;结构;光谱性质

[中图分类号]TG584 [文献标志码]A [文章编号]1003-6180(2016)01-0044-03

DOI:10.13815/j.cnki.jmtc(ns).2016.01.018

酞菁是人工合成的卟啉类似物,拥有比卟啉更大的共轭体系.[1] 由于卟啉化合物的特征吸收带多[2],且特征吸收带 Soret 带的摩尔吸光系数非常大,因此这类染料对太阳光有着很好的利用率,是未来在 DSC 中最具潜力的敏化剂之一.[3] 本研究选择具有共轭性的芳基类取代基-氮乙烯基咔唑(C14H11N)来取代酞菁. 在密度泛函理论(DFT)B3LYP 水平上使用 6-31(g)基组,研究 N-乙烯基咔唑 R(R=C4H11N)取代酞菁锌所得到的化合物,并将其周边引入吸电子基-F 和给电子基团-NH_2,进一步研究供电子基团和吸电子基团对乙烯基咔唑取代酞菁锌的影响.

酞菁锌分子的初始输入结构来自于以前的计算结果. 将酞菁锌分子的 β 位引入 R 取代基,运用密度泛函理论 B3LYP,采用 6-31g(d)基组对结构优化. 再将优化后的 $Zn[PcH_{15}R]$分子的周边

收稿日期:2015-10-30
基金项目:博士后研究人员落户黑龙江科研启动项目(LBH-Q13170)
通讯作者:蔡雪

(C)1994-2019 China Academic Journal Electronic Publishing House. All rights reserved. http://www.cnki.net

教材目录（2 部）

1.《大学基础化学实验》陈玉锋 邢乐红 邵长斌

2.《化工仿真实验》 肖同欣　云观

1.《大学基础化学实验》陈玉锋 邢乐红 邵长斌

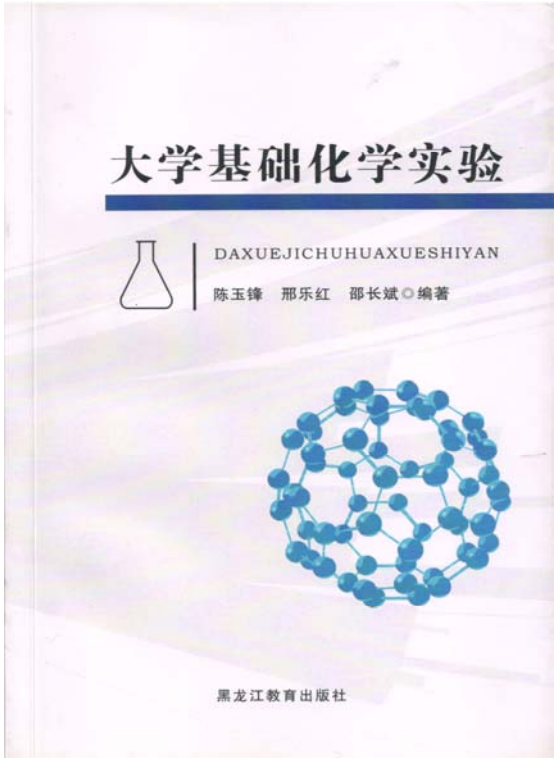

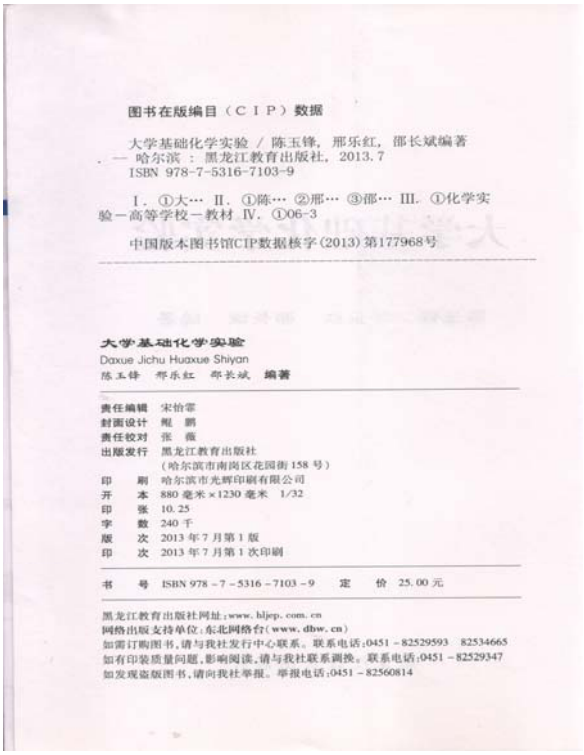
图书在版编目（CIP）数据

大学基础化学实验 / 陈玉锋，邢乐红，邵长斌编著
. — 哈尔滨 ： 黑龙江教育出版社，2013.7
ISBN 978-7-5316-7103-9

Ⅰ. ①大… Ⅱ. ①陈… ②邢… ③邵… Ⅲ. ①化学实验－高等学校－教材 Ⅳ. ①O6-3

中国版本图书馆CIP数据核字(2013)第177968号

大学基础化学实验
Daxue Jichu Huaxue Shiyan
陈玉锋 邢乐红 邵长斌 编著

责任编辑 宋怡霏
封面设计 靳 鹏
责任校对 张 薇
出版发行 黑龙江教育出版社
（哈尔滨市南岗区花园街158号）
印 刷 哈尔滨市光辉印刷有限公司
开 本 880毫米×1230毫米 1/32
印 张 10.25
字 数 240千
版 次 2013年7月第1版
印 次 2013年7月第1次印刷

书 号 ISBN 978-7-5316-7103-9 定 价 25.00元

黑龙江教育出版社网址：www.hljep.com.cn
网络出版支持单位：东北网络台（www.dbw.cn）
如需订购图书，请与我社发行中心联系。联系电话：0451-82529593 82534665
如有印装质量问题，影响阅读，请与我社联系调换。联系电话：0451-82529347
如发现盗版图书，请向我社举报。举报电话：0451-82560814

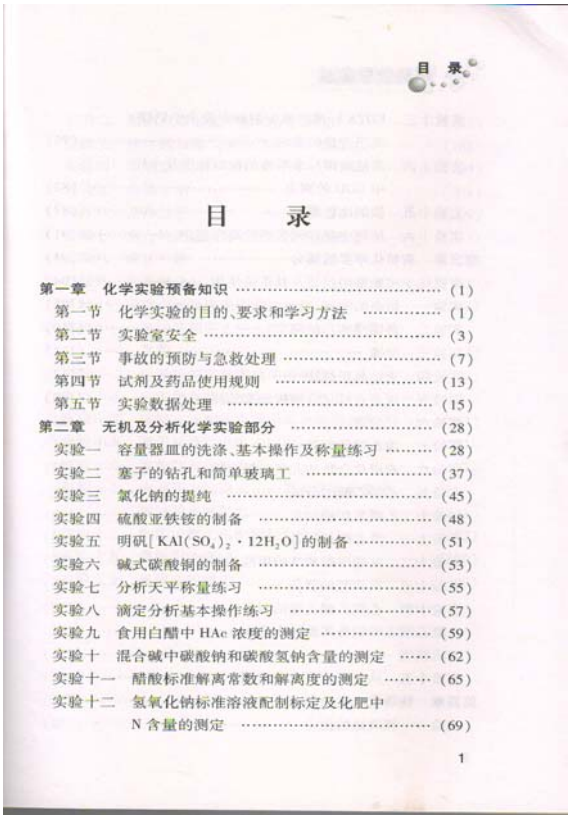
目 录

目 录

第一章 化学实验预备知识 …… (1)
第一节 化学实验的目的、要求和学习方法 …… (1)
第二节 实验室安全 …… (3)
第三节 事故的预防与急救处理 …… (7)
第四节 试剂及药品使用规则 …… (13)
第五节 实验数据处理 …… (15)
第二章 无机及分析化学实验部分 …… (28)
实验一 容量器皿的洗涤、基本操作及称量练习 …… (28)
实验二 塞子的钻孔和简单玻璃工 …… (37)
实验三 氯化钠的提纯 …… (45)
实验四 硫酸亚铁铵的制备 …… (48)
实验五 明矾[$KAl(SO_4)_2 \cdot 12H_2O$]的制备 …… (51)
实验六 碱式碳酸铜的制备 …… (53)
实验七 分析天平称量练习 …… (55)
实验八 滴定分析基本操作练习 …… (57)
实验九 食用白醋中 HAc 浓度的测定 …… (59)
实验十 混合碱中碳酸钠和碳酸氢钠含量的测定 …… (62)
实验十一 醋酸标准解离常数和解离度的测定 …… (65)
实验十二 氢氧化钠标准溶液配制标定及化肥中N含量的测定 …… (69)

1

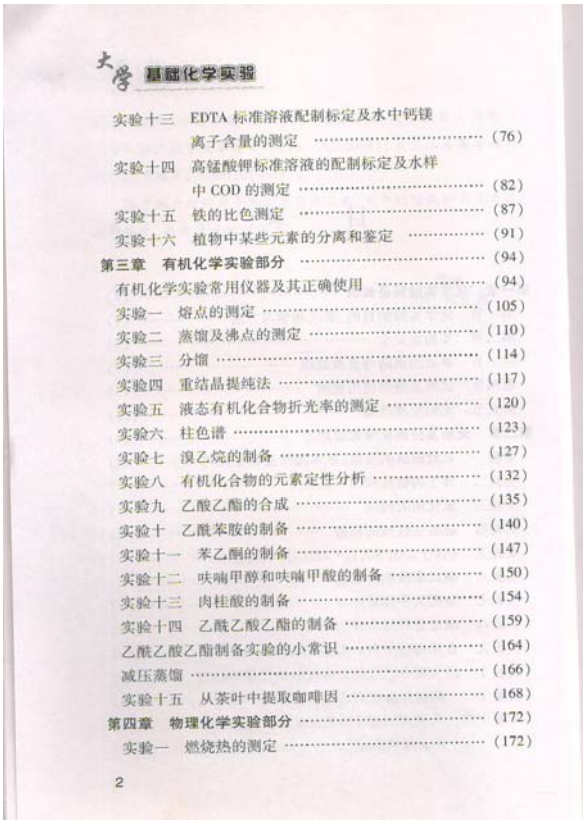
大学 基础化学实验

实验十三 EDTA 标准溶液配制标定及水中钙镁离子含量的测定 …… (76)
实验十四 高锰酸钾标准溶液的配制标定及水样中 COD 的测定 …… (82)
实验十五 铁的比色测定 …… (87)
实验十六 植物中某些元素的分离和鉴定 …… (91)
第三章 有机化学实验部分 …… (94)
有机化学实验常用仪器及其正确使用 …… (94)
实验一 熔点的测定 …… (105)
实验二 蒸馏及沸点的测定 …… (110)
实验三 分馏 …… (114)
实验四 重结晶提纯法 …… (117)
实验五 液态有机化合物折光率的测定 …… (120)
实验六 柱色谱 …… (123)
实验七 溴乙烷的制备 …… (127)
实验八 有机化合物的元素定性分析 …… (132)
实验九 乙酸乙酯的合成 …… (135)
实验十 乙酰苯胺的制备 …… (140)
实验十一 苯乙酮的制备 …… (147)
实验十二 呋喃甲醇和呋喃甲酸的制备 …… (150)
实验十三 肉桂酸的制备 …… (154)
实验十四 乙酰乙酸乙酯的制备 …… (159)
乙酰乙酸乙酯制备实验的小常识 …… (164)
减压蒸馏 …… (166)
实验十五 从茶叶中提取咖啡因 …… (168)
第四章 物理化学实验部分 …… (172)
实验一 燃烧热的测定 …… (172)

2

2.《化工仿真实验》 肖同欣　云观

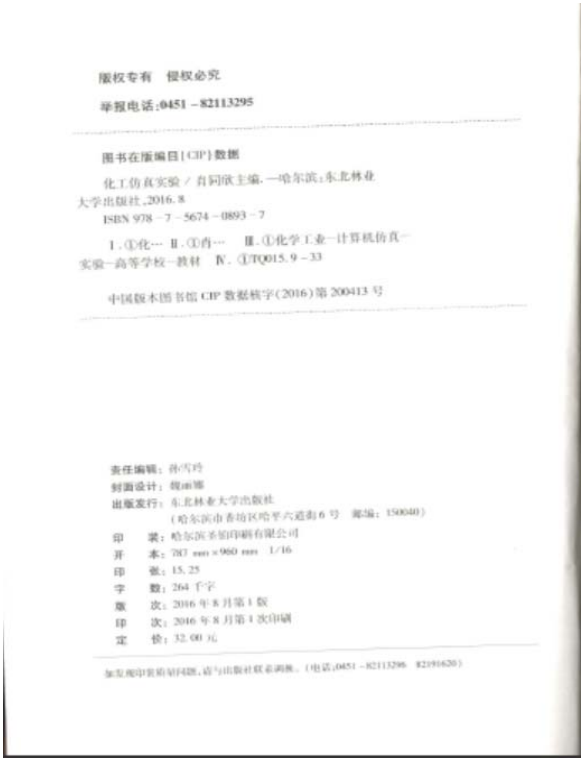
版权专有　侵权必究
举报电话:0451－82113295

图书在版编目(CIP)数据
化工仿真实验 / 肖同欣主编. —哈尔滨:东北林业大学出版社,2016.8
ISBN 978－7－5674－0893－7
Ⅰ.①化… Ⅱ.①肖… Ⅲ.①化学工业—计算机仿真—实验—高等学校—教材 Ⅳ.①TQ015.9－33
中国版本图书馆 CIP 数据核字(2016)第 200413 号

责任编辑:孙雪玲
封面设计:视由娜
出版发行:东北林业大学出版社
(哈尔滨市香坊区哈平六道街 6 号　邮编:150040)
印　　装:哈尔滨圣铂印刷有限公司
开　　本:787 mm×960 mm　1/16
印　　张:15.25
字　　数:264 千字
版　　次:2016 年 8 月第 1 版
印　　次:2016 年 8 月第 1 次印刷
定　　价:32.00 元

如发现印装质量问题,请与出版社联系调换。(电话:0451－82113296　82101620)

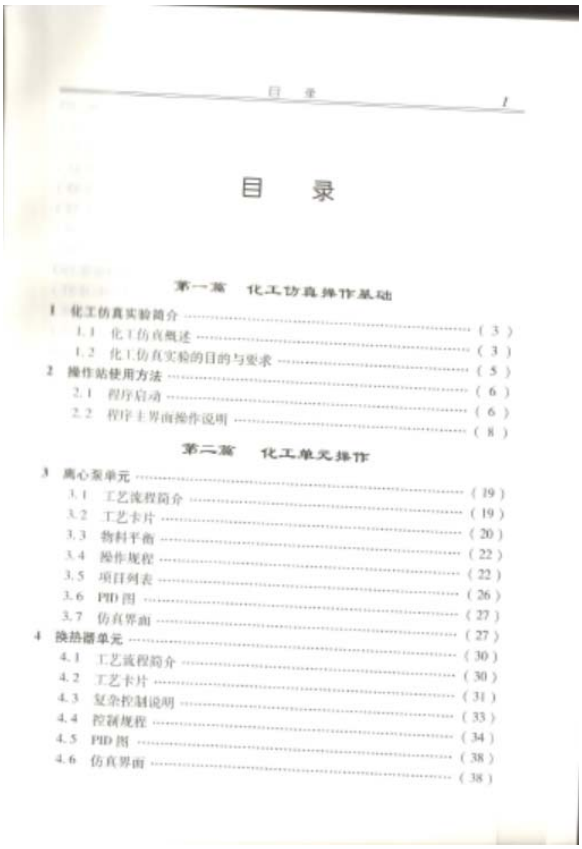

目　录　I

目　录

第一篇　化工仿真操作基础
1　化工仿真实验简介 …… (3)
1.1　化工仿真概述 …… (3)
1.2　化工仿真实验的目的与要求 …… (5)
2　操作站使用方法 …… (6)
2.1　程序启动 …… (6)
2.2　程序主界面操作说明 …… (8)
第二篇　化工单元操作
3　离心泵单元 …… (19)
3.1　工艺流程简介 …… (19)
3.2　工艺卡片 …… (20)
3.3　物料平衡 …… (22)
3.4　操作规程 …… (22)
3.5　项目列表 …… (26)
3.6　PID 图 …… (27)
3.7　仿真界面 …… (27)
4　换热器单元 …… (30)
4.1　工艺流程简介 …… (30)
4.2　工艺卡片 …… (31)
4.3　复杂控制说明 …… (33)
4.4　控制规程 …… (34)
4.5　PID 图 …… (38)
4.6　仿真界面 …… (38)

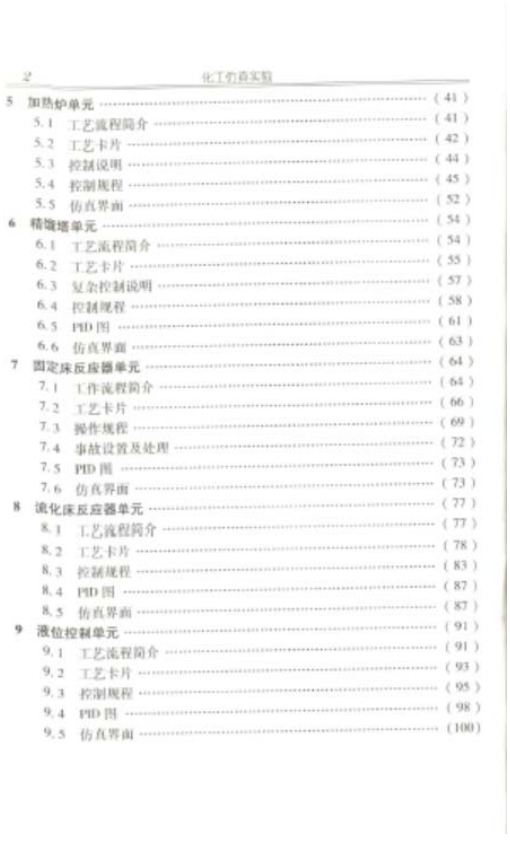

5　加热炉单元 …… (41)
5.1　工艺流程简介 …… (41)
5.2　工艺卡片 …… (42)
5.3　控制说明 …… (44)
5.4　控制规程 …… (45)
5.5　仿真界面 …… (52)
6　精馏塔单元 …… (54)
6.1　工艺流程简介 …… (54)
6.2　工艺卡片 …… (55)
6.3　复杂控制说明 …… (57)
6.4　控制规程 …… (58)
6.5　PID 图 …… (61)
6.6　仿真界面 …… (63)
7　固定床反应器单元 …… (64)
7.1　工作流程简介 …… (64)
7.2　工艺卡片 …… (66)
7.3　操作规程 …… (69)
7.4　事故设置及处理 …… (72)
7.5　PID 图 …… (73)
7.6　仿真界面 …… (73)
8　流化床反应器单元 …… (77)
8.1　工艺流程简介 …… (77)
8.2　工艺卡片 …… (78)
8.3　控制规程 …… (83)
8.4　PID 图 …… (87)
8.5　仿真界面 …… (87)
9　液位控制单元 …… (91)
9.1　工艺流程简介 …… (91)
9.2　工艺卡片 …… (93)
9.3　控制规程 …… (95)
9.4　PID 图 …… (98)
9.5　仿真界面 …… (100)

专著目录（5 部）

1、红色稀土硼酸盐发光材料的制备及发光性能　贾林艳

化学工业出版社 2018 年 5 月

2、直接二甲醚燃料电池膜电极制备技术与电池稳定性研究 邢乐红

新华出版社 2015 年 7 月

3、Ru 基催化剂催化消除 NO_x 的研究　隋朝 蔡雪

化学工业出版社 2019 年 5

4、酸碱双功能材料的合成研究

邵艳秋 黑龙江人民出版社 2014 年 7 月

5、二元富硼化合物的理论研究

邵长斌 化学工业出版社 2018 年 5 月

出版专著 5 部

1、红色稀土硼酸盐发光材料的制备及发光性能　　贾林艳

化学工业出版社 2018 年 5 月

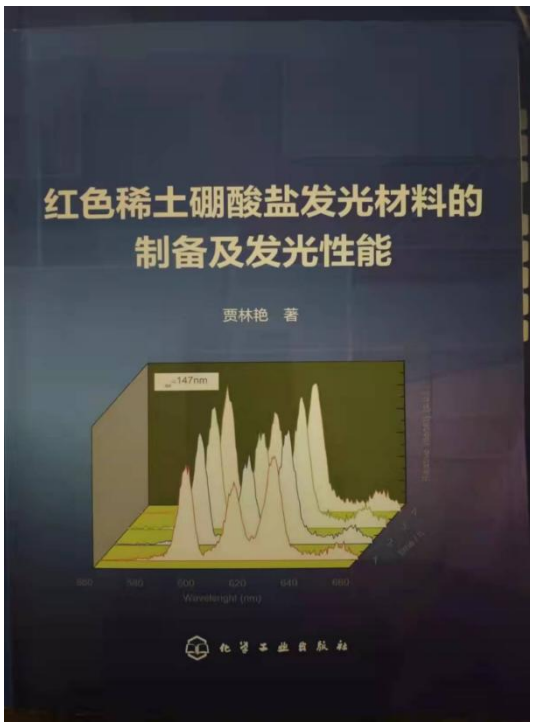

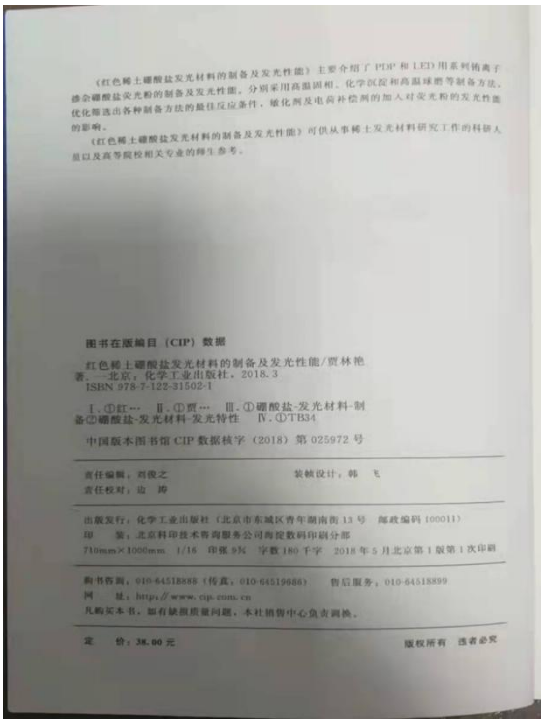

2、直接二甲醚燃料电池膜电极制备技术与电池稳定性研究 邢乐红

新华出版社 2015 年 7 月

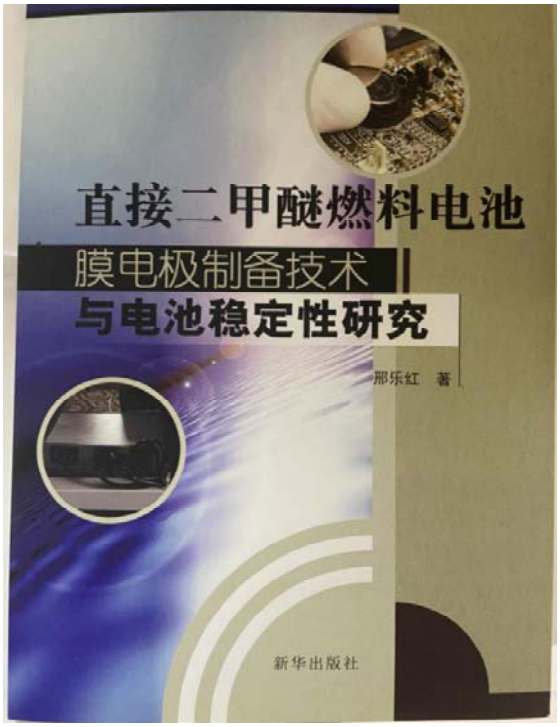

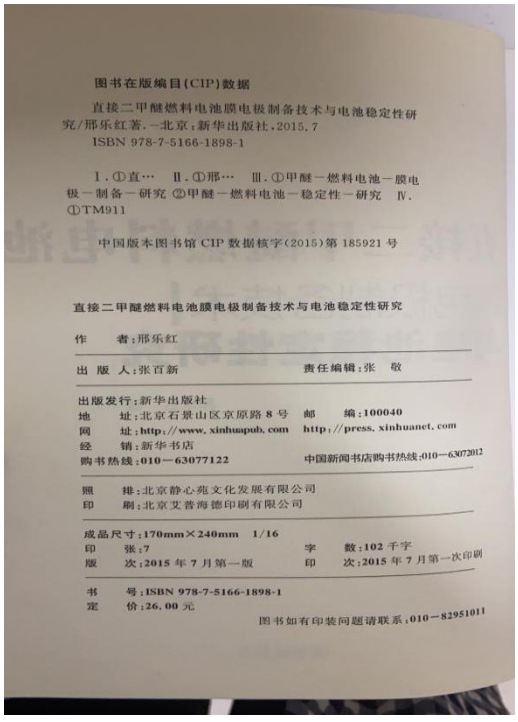

3、Ru 基催化剂催化消除 NO_x 的研究　隋朝 蔡雪

化学工业出版社 2019 年 5 月

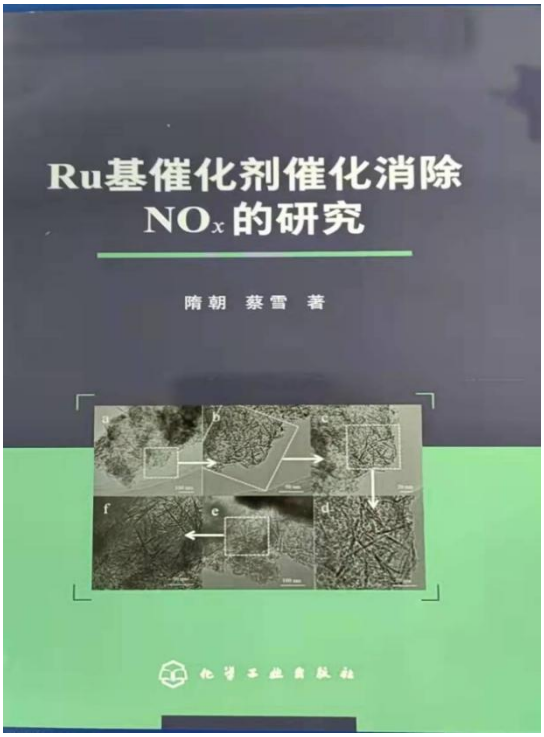

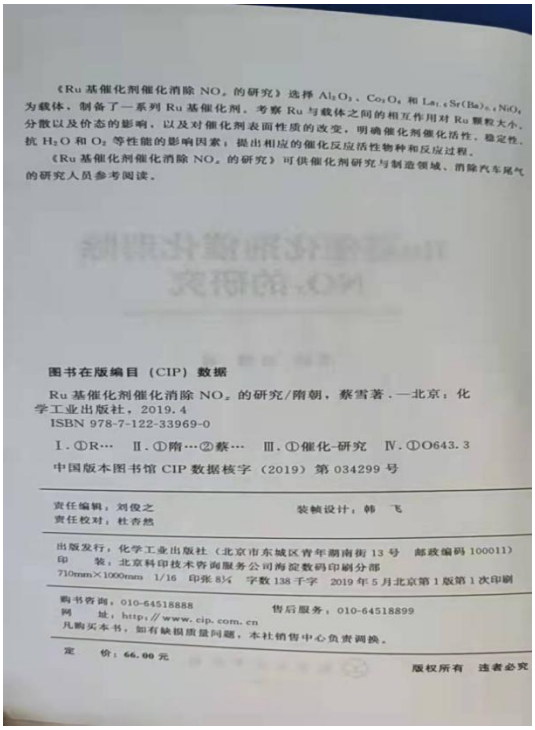
《Ru 基催化剂催化消除 NO_x 的研究》选择 Al_2O_3、Co_3O_4 和 $La_{1-x}Sr(Ba)_xNiO_3$ 为载体，制备了一系列 Ru 基催化剂。考察 Ru 与载体之间的相互作用对 Ru 颗粒大小、分散以及价态的影响，以及对催化剂表面性质的改变，明确催化剂催化活性、稳定性、抗 H_2O 和 O_2 等性能的影响因素；提出相应的催化反应活性物种和反应过程。

《Ru 基催化剂催化消除 NO_x 的研究》可供催化剂研究与制造领域、消除汽车尾气的研究人员参考阅读。

图书在版编目（CIP）数据

Ru 基催化剂催化消除 NO_x 的研究/隋朝，蔡雪著．—北京：化学工业出版社，2019.4

ISBN 978-7-122-33969-0

Ⅰ.①R… Ⅱ.①隋…②蔡… Ⅲ.①催化-研究 Ⅳ.①O643.3

中国版本图书馆 CIP 数据核字（2019）第 034299 号

责任编辑：刘俊之　　装帧设计：韩 飞

责任校对：杜杏然

出版发行：化学工业出版社（北京市东城区青年湖南街 13 号　邮政编码 100011）

印　　装：北京科印技术咨询服务公司海淀数码印刷分部

710mm×1000mm　1/16　印张 8¼　字数 138 千字　2019 年 5 月北京第 1 版第 1 次印刷

购书咨询：010-64518888　　售后服务：010-64518899

网　　址：http://www.cip.com.cn

凡购买本书，如有缺损质量问题，本社销售中心负责调换。

定　　价：66.00 元

版权所有　违者必究

4、酸碱双功能材料的合成研究

邵艳秋 黑龙江人民出版社 2014 年 7 月

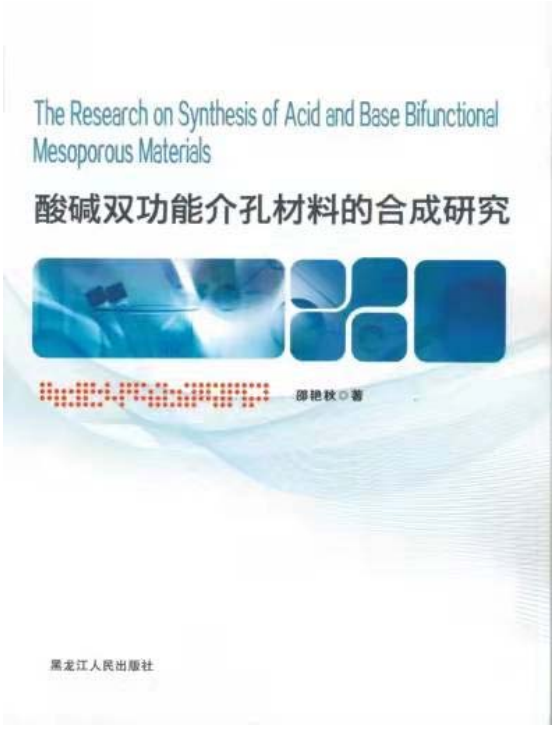

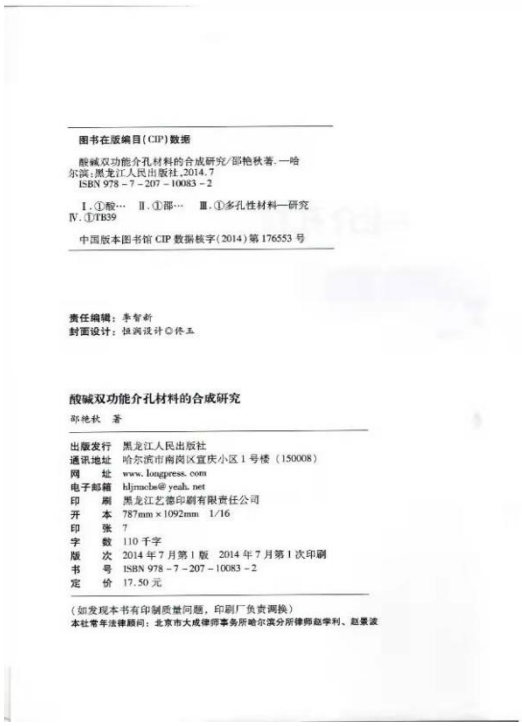
图书在版编目(CIP)数据
酸碱双功能介孔材料的合成研究/邵艳秋著. —哈尔滨:黑龙江人民出版社,2014.7
ISBN 978-7-207-10083-2
Ⅰ.①酸… Ⅱ.①邵… Ⅲ.①多孔性材料—研究 Ⅳ.①TB39
中国版本图书馆 CIP 数据核字(2014)第 176553 号
责任编辑:李智新
封面设计:恒润设计○佟玉
酸碱双功能介孔材料的合成研究
邵艳秋 著
出版发行 黑龙江人民出版社
通讯地址 哈尔滨市南岗区宣庆小区 1 号楼(150008)
网 址 www.longpress.com
电子邮箱 hljrmcbs@yeah.net
印 刷 黑龙江艺德印刷有限责任公司
开 本 787mm×1092mm 1/16
印 张 7
字 数 110 千字
版 次 2014 年 7 月第 1 版 2014 年 7 月第 1 次印刷
书 号 ISBN 978-7-207-10083-2
定 价 17.50 元
(如发现本书有印制质量问题,印刷厂负责调换)
本社常年法律顾问:北京市大成律师事务所哈尔滨分所律师赵学利、赵景波

5、二元富硼化合物的理论研究

邵长斌 化学工业出版社 2018 年 5 月

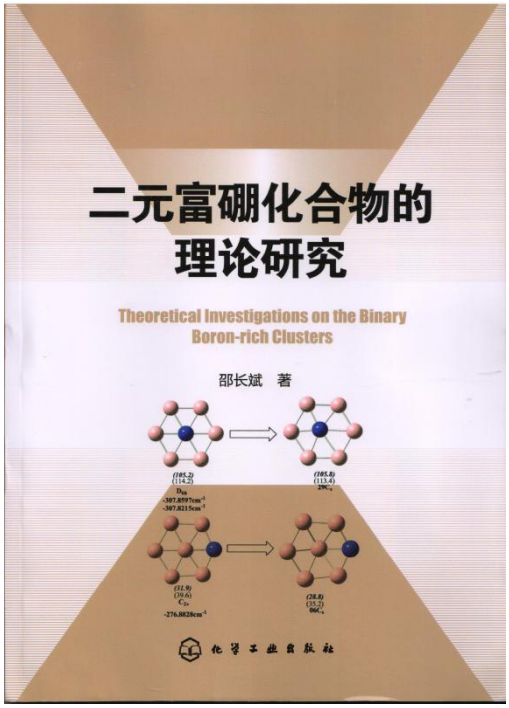

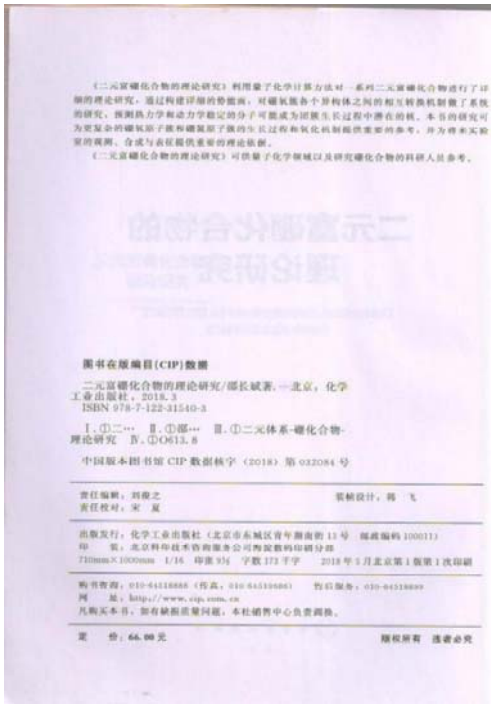
《二元富硼化合物的理论研究》利用量子化学计算方法对一系列二元富硼化合物进行了详细的理论研究,通过构建详细的势能面,对硼氢簇各个异构体之间的相互转换机制做了系统的研究,预测热力学和动力学稳定的分子可能成为团簇生长过程中潜在的核。本书的研究可为更复杂的硼氢原子簇和硼氢原子簇的生长过程和氧化机制提供重要的参考,并为将来实验室的预测、合成与表征提供重要的理论依据。
《二元富硼化合物的理论研究》可供量子化学领域以及研究硼化合物的科研人员参考。
图书在版编目(CIP)数据
二元富硼化合物的理论研究/邵长斌著. —北京:化学工业出版社,2018.3
ISBN 978-7-122-31540-3
Ⅰ.①二… Ⅱ.①邵… Ⅲ.①二元体系-硼化合物-理论研究 Ⅳ.①O613.8
中国版本图书馆 CIP 数据核字(2018)第 032084 号
责任编辑:刘俊之 装帧设计:韩 飞
责任校对:宋 夏
出版发行:化学工业出版社(北京市东城区青年湖南街 13 号 邮政编码 100011)
印 装:北京科印技术咨询服务公司数码印刷分部
710mm×1000mm 1/16 印张 9¼ 字数 173 千字 2018 年 5 月北京第 1 版第 1 次印刷
购书咨询:010-64518888(传真:010-64519686) 售后服务:010-64518899
网 址:http://www.cip.com.cn
凡购买本书,如有缺损质量问题,本社销售中心负责调换。
定 价:66.00 元
版权所有 违者必究

专利（共 3 项）

1.二甲醚燃料电池阳极微孔层的制备方法

发明专利　　邢乐红，马天方，肖同欣

2.一种耐湿热高温水性汽车门护板内饰胶黏剂及其制备方法

发明专利　　蒋舰，蔡雪

3.一种自动防止倒吸实验尾气吸收装置

实用新型专利　　郭元平，蔡雪，蒋舰

1.二甲醚燃料电池阳极微孔层的制备方法

发明专利　　邢乐红，马天方，肖同欣

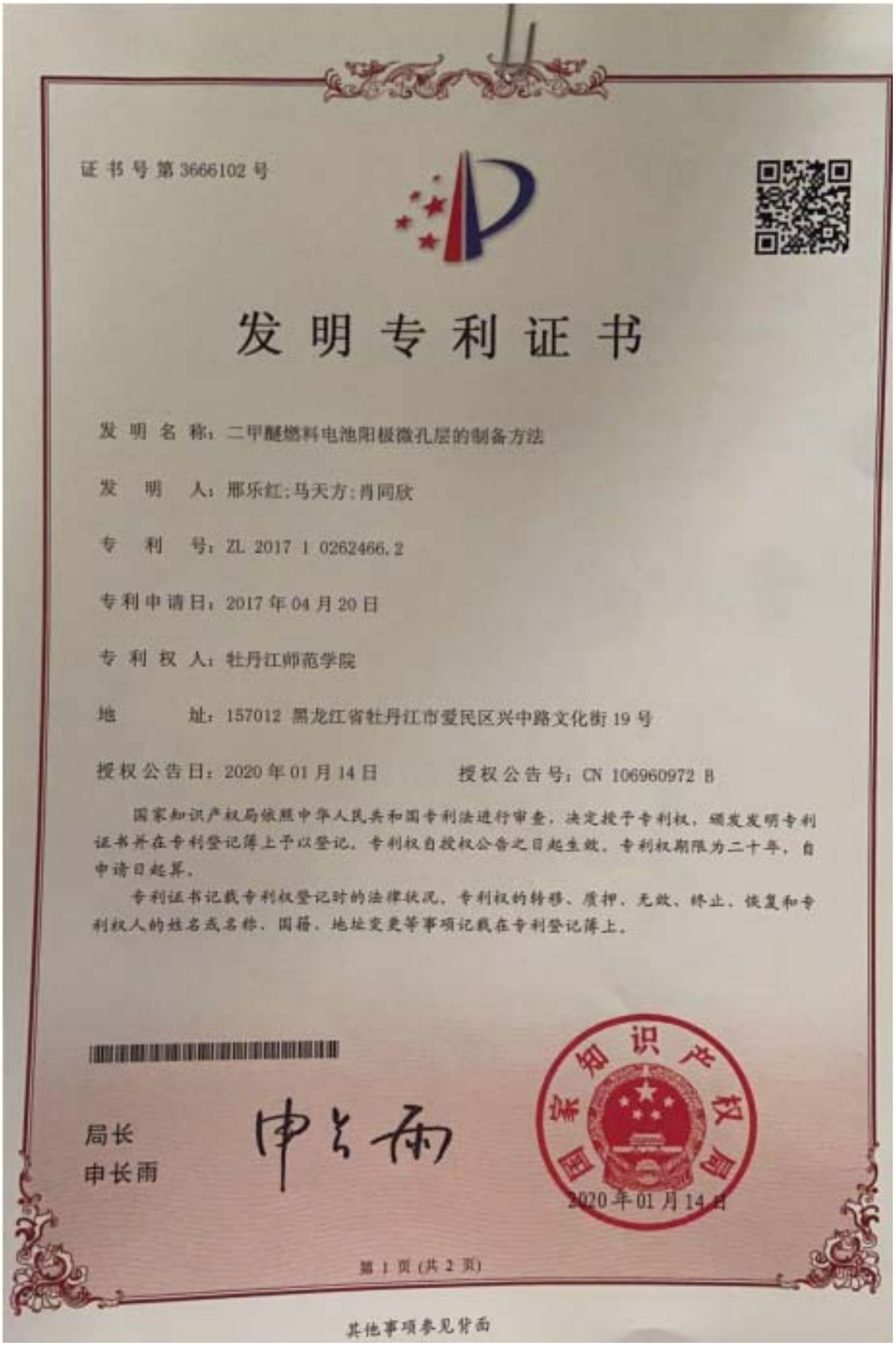

证书号第3666102号

发明专利证书

发明名称：二甲醚燃料电池阳极微孔层的制备方法

发明人：邢乐红;马天方;肖同欣

专利号：ZL 2017 1 0262466.2

专利申请日：2017年04月20日

专利权人：牡丹江师范学院

地址：157012 黑龙江省牡丹江市爱民区兴中路文化街19号

授权公告日：2020年01月14日　　授权公告号：CN 106960972 B

国家知识产权局依照中华人民共和国专利法进行审查，决定授予专利权，颁发发明专利证书并在专利登记簿上予以登记。专利权自授权公告之日起生效。专利权期限为二十年，自申请日起算。

专利证书记载专利权登记时的法律状况。专利权的转移、质押、无效、终止、恢复和专利权人的姓名或名称、国籍、地址变更等事项记载在专利登记簿上。

局长
申长雨

国家知识产权局

2020年01月14日

第1页(共2页)

其他事项参见背面

2.一种耐湿热高温水性汽车门护板内饰胶黏剂及其制备方法

发明专利　　蒋舰，蔡雪

国 家 知 识 产 权 局

130000

长春市高新开发区锦湖大路 13578 号三楼 328 房间 长春众邦菁华知识产权代理有限公司

李外(0431-81707878)

发文日：

2022 年 05 月 27 日

申请号或专利号：202010248781.1　　发文序号：2022052101178690

申请人或专利权人：牡丹江师范学院

发明创造名称：一种耐湿热耐高温水性汽车门护板内饰胶黏剂及其制备方法

授 予 发 明 专 利 权 通 知 书

1. 根据专利法第 39 条及实施细则第 54 条的规定，上述发明专利申请经实质审查，没有发现驳回理由，现作出授予专利权的通知。

申请人收到本通知书后，还应当依照办理登记手续通知书的内容办理登记手续。

申请人按期办理登记手续后，国家知识产权局将作出授予专利权的决定，颁发发明专利证书，并予以登记和公告。

期满未办理登记手续的，视为放弃取得专利权的权利。

法律、行政法规规定相应技术的实施应当办理批准、登记等手续的，应依照其规定办理。

2. 授予专利权的上述发明专利申请是以下列申请文件为基础的：

☐原始申请文件。☐分案申请递交日提交的文件。☒下列申请文件：

申请日提交的说明书摘要、说明书第 1-102 段；

2022 年 3 月 14 日提交的权利要求第 1-2 项。

3. 授予专利权的上述发明专利申请的名称：

☒未变更。

☐由__变更为上述名称。

4. ☐申请人于_____年_____月_____日提交专利号为_____的“放弃专利权声明”，经审查：

☐进入放弃专利权的程序。

☐未进入放弃专利权的程序。理由是：申请人声明放弃的专利与本发明专利申请不属于相同的发明创造。

5. ☐审查员依职权对申请文件修改如下：

注：在本通知书发出后收到的申请人主动修改的申请文件，不予考虑。

国家知识产权局 专利审查业务章

审查员：杨章静

审查部门：专利审查协[illegible]京中[illegible]学发明审查部

联系电话：010-53962975

210413 2020.3　纸件申请，回函请寄：100088 北京市海淀区蓟门桥西土城路 6 号　国家知识产权局专利局受理处收

电子申请，应当通过电子专利申请系统以电子文件形式提交相关文件。除另有规定外，以纸件等其他形式提交的文件视为未提交。

3.一种自动防止倒吸实验尾气吸收装置

实用新型专利　郭元平，蔡雪，蒋舰

证书号第14891936号

实用新型专利证书

实用新型名称：一种自动防止倒吸实验尾气吸收装置

发　明　人：郭元平;蔡雪;蒋舰

专　利　号：ZL 2021 2 0699015.7

专利申请日：2021年04月07日

专利权人：牡丹江师范学院

地　　址：157000 黑龙江省牡丹江市爱民区文化街191号

授权公告日：2021年11月30日　　授权公告号：CN 214916205 U

国家知识产权局依照中华人民共和国专利法经过初步审查，决定授予专利权，颁发实用新型专利证书并在专利登记簿上予以登记。专利权自授权公告之日起生效。专利权期限为十年，自申请日起算。

专利证书记载专利权登记时的法律状况。专利权的转移、质押、无效、终止、恢复和专利权人的姓名或名称、国籍、地址变更等事项记载在专利登记簿上。

局长
申长雨

国家知识产权局
2021年11月30日

第1页(共2页)

其他事项参见续页

科研项目（共 9 项）

1.改性介孔材料的制备对水中重金属的吸附研究

牡丹江师范学院科研项目　　负责人：邵艳秋

2.掺杂型半导体纳米材料的制备及光降解性能研究

黑龙江省教育厅备案项目　　负责人：邵艳秋

3.气液相燃料同时进料直接二甲醚燃料电池与阳极传质机制研究

牡丹江师范学院培育项目　　负责人：邢乐红

4.CeO_2**/C 载 Pt 阳极催化剂对直接二甲醚燃料电池性能影响研究**

牡丹江师范学院青年学术骨干项目　　负责人：邢乐红

5.绿色化学实验

牡丹江师范学院横向课题　　负责人：邢乐红

6.丙烷脱氢制丙烯催化剂研发

中国科学院大连化学物理研究所开放课题　　负责人：蔡雪

7.东北林蛙皮胶原蛋白提取工艺研究

牡丹江师范学院青年培育项目　　负责人：云观

8.东北林蛙消化系统消化酶的分析

牡丹江师范学院指导项目　　负责人：云观

9.新型超分子自组装离子液晶研究

黑龙江省教育厅项目　　负责人：蒋舰

邵艳秋科研项目目录（共 2 项）

1.改性介孔材料的制备对水中重金属的吸附研究

牡丹江师范学院科研项目　　负责人：邵艳秋

2.掺杂型半导体纳米材料的制备及光降解性能研究

黑龙江省教育厅备案项目　　负责人：邵艳秋

1.改性介孔材料的制备对水中重金属的吸附研究

项目类别	科研机构专项
项目编号	JG2017001

牡丹江师范学院科研项目

验　收　报　告

项目名称：改性介孔材料的制备及对水中重金属的吸附研究

承担单位：化学化工学院

负 责 人：邵艳秋

（2021 年 4 月10 日）

牡丹江师范学院制

2.掺杂型半导体纳米材料的制备及光降解性能研究

黑龙江省教育厅备案项目

申　请　书

自然科学类■　　社会科学类□

项目名称:掺杂型半导体纳米材料的制备及光降解性能研究
项目负责人:邵艳秋
联系电话:　13614608351
项目起止时间:2020.6-2022.12
申报单位(盖章):化学化工学院
填表日期:2020.5.7

牡丹江师范学院科研处制

邢乐红科研项目目录（共 3 项）

1.气液相燃料同时进料直接二甲醚燃料电池与阳极传质机制研究

牡丹江师范学院培育项目　　负责人：邢乐红

2.CeO_2/C 载 Pt 阳极催化剂对直接二甲醚燃料电池性能影响研究

牡丹江师范学院青年学术骨干项目　　负责人：邢乐红

3.绿色化学实验

牡丹江师范学院横向课题　　负责人：邢乐红

1.气液相燃料同时进料直接二甲醚燃料电池与阳极传质机制研究

牡丹江师范学院

科 研 经 费 卡

项目名称	气液相燃料同时进料直接二甲醚燃料电池与阳极传质机制研究		
项目类型	培育项目	项目编号	GP2021002
主持人	邢乐红	单位	化学化工学院

经费划拨情况　　财务系统编号：1303121002

拨款日期	年 月 日	年 月 日	年 月 日
到账经费	2万		
匹配经费			
总经费			
管理费			
财务处长签字	王宏		
科研处长签字			

科研处公章　　财务处公章

年 月 日

填写说明：
1. 项目信息、经费预算由项目负责人用计算机填写。
2. 经费划拨情况由科研处、财务处填写。
3. A 4 纸双面打印（建议使用卡纸等硬质纸张）

2.CeO_2/C 载 Pt 阳极催化剂对直接二甲醚燃料电池性能影响研究

牡丹江师范学院

科 研 经 费 卡

项目名称	CeO2/C载Pt阳极催化剂对直接二甲醚燃料电池性能影响研究		
项目类型	青年学术骨干项目	项目编号	GG2018001
主持人	邢乐红	单位	化学化工学院

经费划拨情况　　财务系统编号：D212220294 D21221581182029Y

拨款日期	2018年7月10日	年 月 日	年 月 日
到账经费	10000.00元		
匹配经费			
总经费	10000.00元		
管理费	500.00元		
财务处长签字	王宏		
科研处长签字			

科研处公章　　财务处公章

年 月 日

填写说明：
1. 项目信息、经费预算由项目负责人用计算机填写。
2. 经费划拨情况由科研处、财务处填写。
3. A4双面打印

3.绿色化学实验

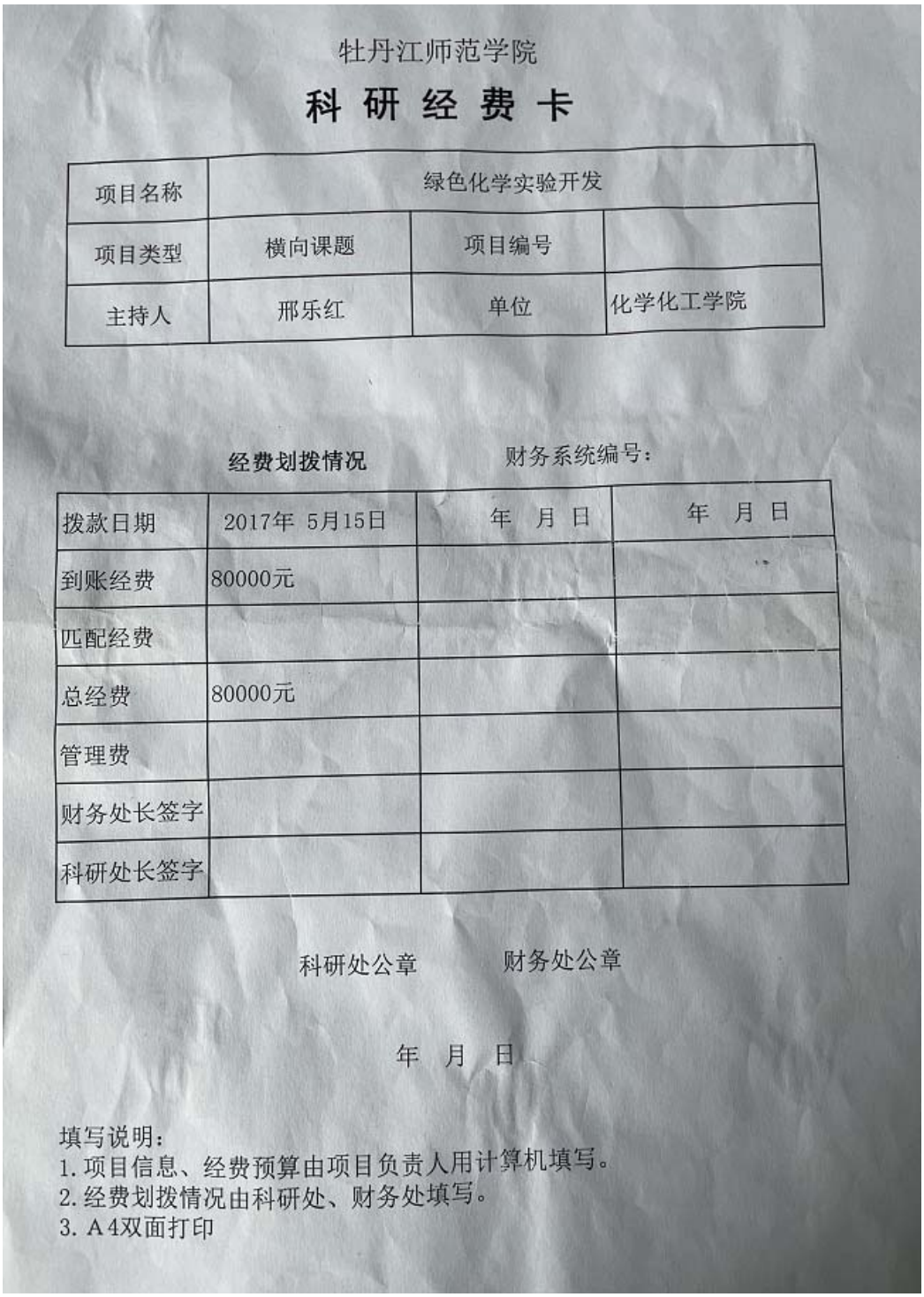

牡丹江师范学院

科 研 经 费 卡

项目名称	绿色化学实验开发		
项目类型	横向课题	项目编号	
主持人	邢乐红	单位	化学化工学院

经费划拨情况　　财务系统编号：

拨款日期	2017年 5月15日	年 月 日	年 月 日
到账经费	80000元		
匹配经费			
总经费	80000元		
管理费			
财务处长签字			
科研处长签字			

科研处公章　　财务处公章

年 月 日

填写说明：
1. 项目信息、经费预算由项目负责人用计算机填写。
2. 经费划拨情况由科研处、财务处填写。
3. A4双面打印

蔡雪科研论文项目（共 1 项）

1. 丙烷脱氢制丙烯催化剂研发

中国科学院大连化学物理研究所开放课题　　负责人：蔡雪

1. 丙烷脱氢制丙烯催化剂研发

中国科学院大连化学物理研究所

催化基础国家重点实验室

开放课题申请书

项目名称：丙烷脱氢制丙烯催化剂研发

申 请 者：蔡雪

所在单位：牡丹江师范学院

申请日期：2021.11.12

中国科学院大连化学物理研究所
催化基础国家重点实验室

云观科研项目目录（共 2 项）

1. 东北林蛙皮胶原蛋白提取工艺研究

牡丹江师范学院青年培育项目　　负责人：云　观

2. 东北林蛙消化系统消化酶的分析

牡丹江师范学院指导项目　　负责人：云　观

1.东北林蛙皮胶原蛋白提取工艺研究

牡丹江师范学院

科 研 经 费 卡

项目名称	东北林蛙皮胶原蛋白提取工艺研究		
项目类型	青年培育项目	项目编号	1353MSYQN005
主持人	云观	单位	化学化工学院

经费划拨情况　　财务系统编号：DJ1220773

拨款日期	2018年10月 日	年 月 日	年 月 日
到账经费	20000		
匹配经费			
总经费			
管理费	1000		
财务处长签字	王宏		
科研处长签字			

科研处公章　　财务处公章

年 月 日

填写说明：
1. 项目信息、经费预算由项目负责人用计算机填写。
2. 经费划拨情况由科研处、财务处填写。
3. A 4 纸双面打印（建议使用卡纸等硬质纸张）

2.东北林蛙消化系统消化酶的分析

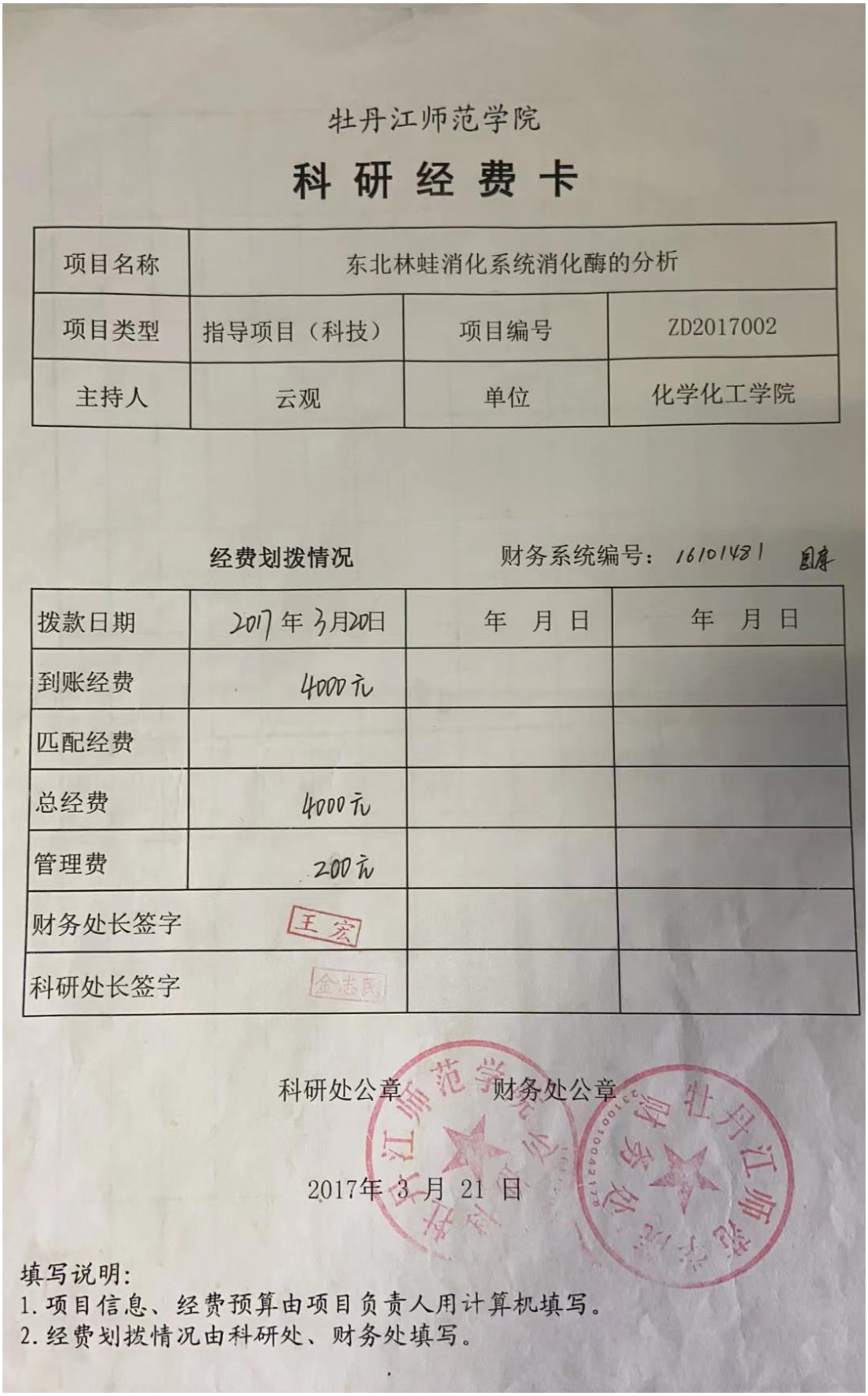

牡丹江师范学院

科 研 经 费 卡

项目名称	东北林蛙消化系统消化酶的分析		
项目类型	指导项目（科技）	项目编号	ZD2017002
主持人	云观	单位	化学化工学院

经费划拨情况　　财务系统编号：16101481

拨款日期	2017 年 3月20日	年 月 日	年 月 日
到账经费	4000元		
匹配经费			
总经费	4000元		
管理费	200元		
财务处长签字	王宏		
科研处长签字	金志良		

科研处公章　　财务处公章

2017年 3 月 21 日

填写说明:
1. 项目信息、经费预算由项目负责人用计算机填写。
2. 经费划拨情况由科研处、财务处填写。

蒋舰科研论文项目（共 1 项）

1.新型超分子自组装离子液晶研究

黑龙江省教育厅项目　　负责人：蒋舰

1.新型超分子自组装离子液晶研究

黑龙江省教育厅项目　　负责人：蒋舰

黑龙江省教育厅科研备案项目立项审批通知书

项目名称	新型超分子自组装离子液晶研究			项目负责人	蒋舰
项目编号	1352MSYYB010	项目类型	一般项目	项目起止时间	2017年5月—2020年5月
项目负责人所在单位	化学化工学院				
项目组成员（一）	郭元平	所在单位	牡丹江师范学院化学化工学院		
项目组成员（二）	廉波	所在单位	牡丹江师范学院化学化工学院		
项目组成员（三）		所在单位			
项目组成员（四）		所在单位			
项目组成员（五）		所在单位			
项目组成员（六）		所在单位			
项目组成员（七）		所在单位			
项目组成员（八）		所在单位			
项目组成员（九）		所在单位			
项目组成员（十）		所在单位			

牡丹江师范学院审批意见

经专家评审、校学术委员会研究决定，批准该项目列入黑龙江省教育厅2017年度科研备案项目（　一般项目　），资助经费（　1.4　）万元。

主管部门盖章

2017年6月10日

注：本表复印无效　　牡丹江师范学院2007年制表

高级别科研论文目录（共 14 篇 SCI 论文）

1.Shao Y, Jiang Z, Zhang Q, et al. Progress in nonmetal‐doped graphene electrocatalysts for the oxygen reduction reaction[J]. ChemSusChem, 2019, 12(10): 2133-2146. （SCI 检索收录一区，IF=8.869）

2.Shao Y, Chang Y, Zhang S, et al. Impact of polymer backbone fluorination on the charge generation/recombination patterns and vertical phase segregation in bulk heterojunction organic solar cells[J]. Frontiers in chemistry, 2020, 8: 144. （SCI 检索收录二区，IF=5.221）

3.Yang W, Jiang R, Liu C, et al. Triptycene-Based Porous Chalcogen-Bonded Organic Frameworks[J]. Crystal Growth & Design, 2021, 21(11): 6497-6503. （SCI 检索收录二区，IF=4.076）

4.Cai X, Ma Y, Zhou Q, et al. Synergistic efects of phases in the selective oxidation of isobutane over supported $(NH_4)_3HPMo_{11}VO_{40}$ catalysts[J]. Reaction Kinetics, Mechanisms and Catalysis, 2021, 133(1): 293-308. （SCI 检索收录四区，IF=1.762）

5.Cai X, Wei C, Dong J, et al. Dimeric phthalocyanine-involved double-decker complex-based electrochemical sensor for simultaneous detection of acetaminophen and ascorbic acid[J]. Journal of Materials Science: Materials in Electronics, 2019, 30(3): 1976-1983. （SCI 检索收录四区，IF=2.171）

6.Wei C, Lu G, Guo C, et al. Ethylthio-substituted sandwich phthalocyaninato europium (III) semiconductors for sensing NO_2 and NH_3: Effect of the extended π-conjugate systems on tuning the conductivity and sensing behavior[J]. Organic Electronics, 2021, 93: 106151. （SCI 检索收录三区，IF=3.721）

7.Cai X, Ning H. Crystal structure of di-μ-acetato-diacetatobis (μ-6, 6′-dimethoxy-2,2′-{[(propane-1,3-diylbis (azanylylidene)] bis

(methanylylidene)} diphenolato) tetrazinc[J]. Acta Crystallographica Section E: Crystallographic Communications, 2015, 71(12): 217-218.（SCI 检索收录四区，IF=0.278）

8.Cai X, Zhou Q, Ma Y, et al. Selective Removal of CO in Hydrocarbons-Rich Industrial Off-gases over CuO-Ce_xZr_1−xO_2 Catalysts [J]. Catalysis Surveys from Asia, 2021, 25(1): 68-75. （SCI 检索收录四区，IF=3.106）

9.Electrochemical Synthesis of Ni-SnO_2 Composite Electrodes for Hydrogen Evolution Reaction in Alkaline Solution 作者：邢乐红

10.Xing L H, Shi X T, Wang Y X, et al. Electrochemical Synthesis of Ni-SnO_2 Composite Electrodes for Hydrogen Evolution Reaction in Alkaline Solution[J]. Int. J. Electrochem. Sci, 2022, 17(220530): 2.（SCI 检索收录四区，IF=1.765）

11. Xing L, Wang Y, Shi X, et al. Investigation of Pt/C and Pt-Ru/C Mixed Catalyst for DME Oxidation in Direct Dimethyl Ether Fuel Cells[J]. Int. J. Electrochem. Sci, 2020, 15: 10382-10391.（SCI 检索收录四区，IF=1.765）

12. Xing L, Wang Y, Sui C, et al. Investigation of Pt/SnO_2/C Catalyst for Dimethyl Ether Oxidation in DDFC[J]. Int. J. Electrochem. Sci, 2020, 15: 2375-2384.（SCI 检索收录四区，IF=1.765）

13. Xing L H, Yin G P, Du C Y, et al. Investigation on the durability of direct dimethyl ether fuel cell. Part II: Cathode degradation[J]. International Journal of Hydrogen Energy, 2017, 42(26): 16695-16699.（SCI 检索收录二区，IF=5.816）

14.Jiang J. Observation of a 3-in-1 Russian-doll-like Complex in Solution[J]. Chemical Research in Chinese Universities, 2021: 1-3. （SCI 检索收录三区，IF=1.307）

1.Shao Y, Jiang Z, Zhang Q, et al. Progress in nonmetal‐doped graphene electrocatalysts for the oxygen reduction reaction[J]. ChemSusChem, 2019, 12(10): 2133-2146. （SCI 检索收录一区，IF=8.869）

ChemSusChem 10.1002/cssc.201900060

MINIREVIEW WILEY-VCH

Progress in nonmetal-doped graphene electrocatalysts for oxygen reduction reaction

Yanqiu Shao,*[a, b] Zhenshuang Jiang,[a, b] Qiaoqiao Zhang,[b] and Jingqi Guan*[b]

Abstract: Due to the energy shortage and environmental pollution, green energy such as polymer electrolyte fuel cells and metal-air batteries plays a more and more important role, where the oxygen reduction reaction (ORR) is the rate-determining step. Development of high-efficiency and stable catalysts to facilitate ORR is of importance. Graphene is a new type of material with two-dimensional structure and high surface area, which shows wide applications in many fields. However, graphene with the zero bandgap property shows low electrocatalytic activity toward ORR. Introduction of some nonmetal atoms can change the electronic arrangement, generate active sites, and further improve the catalytic activity of graphene. It has been demonstrated that some nonmetal-doping strategies (such as nitrogen-doping, sulfur-doping, and phosphorus-doping) can promote the ORR activity. Herein, we summarize the recent development of nonmetal-doped graphene catalysts for ORR. Some common synthetic methods for the nonmetal-doped graphene materials are summarized, and the active sites and possible reaction mechanisms for ORR on various nonmetal-doped graphene catalysts are mainly discussed.

1. Introduction

Energy is very important for the development of the national economy and the improvement of people's living standards, which is an important factor directly affecting economic development. Since the beginning of the 21st century, the shortage of resources, environmental pollution, and greenhouse effect caused by the traditional energy utilization methods have become more and more prominent, the traditional energy structure and its utilization methods are increasingly difficult to meet the needs of human survival and development.[1] To address the increasingly serious energy crisis and environmental pollution problems, a variety of new green energy sources have been developed rapidly, including metal-air batteries and fuel cells.[2]

Under the urgent need for sustainable energy economy, electrochemical energy conversion technologies, such as polymer electrolyte membrane fuel cells (PEMFCs) and metal-air batteries, have become extremely important. The common feature of PEMFCs and metal-air batteries is that oxygen reduction reaction (ORR) is the basic support for their operation. The electrolytes can be divided into acidic electrolyte and alkaline electrolyte. Acidic electrolyte membrane promotes proton transfer from the anode to the cathode. In acidic electrolyte, ORR occurs either by four electrons reduction or by two electrons reduction.[3] The experimental results show that the four-electron reduction mechanism is dominant and advantageous because each oxygen molecule has four electrons. This route can avoid the formation of hydrogen peroxide in the electrode, which results in the membrane and ionic monomer degradation.[4] In alkaline electrolytes, hydroxyl ion is transferred from cathode to anode. In metal-air batteries or alkaline exchange membrane fuel cells, ORR process can also be carried out by two-step reduction (a total of four electrons), in which hydrogen peroxide can be directly or indirectly reduced to water.

At present, platinum is the only commercial catalyst, which shows high activity and stability under acidic conditions. Rapid oxygen reduction kinetics is indispensable in terms of performance. Acidic ORR is several orders of magnitude slower than anodic oxidation. Researchers found that ORR kinetics is more favorable under alkaline conditions. In the cathode reaction of the hydrogen fuel cell, the reduction of O_2 to H_2O requires 4 electrons and 4 protons.[5] The mechanism of this process is very complicated, and ORR dynamics usually limits the reaction rate and maximum power. In recent years, nonmetal-doped graphene materials have gained much attention in ORR. The electrochemical activity and durability of these nonmetal-doped graphene materials can be compared with traditional platinum supported on carbon black (Pt/C).[6] This is a breakthrough and a new milestone in the oxygen reduction reaction because it can substitute the expensive platinum and achieve appropriate power output.[7]

Graphene is a new type of two-dimensional grid structure material, which is composed of planar single-layer carbon atoms. It is the basic unit of other carbon allotropes, such as fullerenes, carbon nanotubes, and graphite. The theoretical specific surface area of graphene is as high as 2630 m^2/g.[4] It has excellent thermal conductivity and electronic conductivity and has a wide application prospect. At the basic level of graphene, it is a chemically specific hexagonal pattern of single-layer 2-carbon atoms.[8] However, the zero bandgap property of graphene decreases its catalytic activity.[9] Unmodified graphene shows low electrocatalytic activity for ORR and is not suitable for direct use as a cathode catalyst for the fuel cell.[2c] The introduction of heteroatoms into graphene can modify its electronic and electrochemical properties by changing the electron density in the graphene sheet. Heteroatom doped graphene can not only improve the electrical properties of graphene but also create more sites for ORR.[10] The theoretical and experimental results show that doped heteroatoms in graphene sp^2 orbital can effectively change the electronic arrangement, generate active sites and improve the catalytic activity.[3b] The doped elements mainly include N, P, O, and S. Nitrogen-doped graphene (NG) has been reported most

[a] Prof. Y. Shao, Z. Jiang
College of Chemistry and Chemical Engineering, Mu Danjiang Normal School, Mudanjiang 157011, China.
E-mail: shaoyanqiu1969@163.com
[b] Q. Zhang, Prof. J. Guan
College of Chemistry, Jilin University, Changchun 130012, China.
E-mail: guanjq@jlu.edu.cn

This article is protected by copyright. All rights reserved.

Accepted Manuscript

frequently. In this review, graphene doped with different elements as non-metallic oxygen reduction catalyst is introduced.

2. Synthesis methods

There are many methods for preparing nonmetal-doped graphene materials, of which the heteroatom doping method can be divided into in-situ doping method and post-processing method. In-situ doping method is a vital strategy, which is the process of introducing heteroatoms in the process of graphene synthesis, and the whole process occurs simultaneously. Up to now, many preparation methods have been reported, which include chemical vapor deposition (CVD), plasma treatment, arc discharge, explosion, high-temperature heat treatment, and hydrothermal treatment, etc.[11] It should be noted that it is extremely difficult to remove the metal residues for some kinds of graphene, which might significantly influence the catalytic performance.[12] Herein, CVD and ball milling as in-situ doping methods, as well as wet chemical methods are mainly discussed.

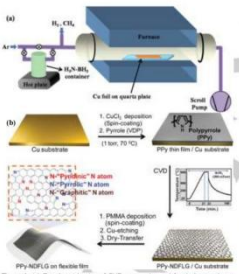

Figure 1. (a) Experimental setup of CVD commonly used for doping graphene. Reprinted with permission from Ref.[13]. Copyright: 2013 American Chemical Society. (b) N-doped graphene derived from a polypyrrole. Reprinted with permission from Ref.[19]. Copyright: 2012 American Chemical Society.

2.1. Chemical vapor deposition (CVD)

Chemical vapor deposition (CVD) is a kind of chemical technology, which mainly uses one or several vapor compounds or monomers containing thin film elements to generate thin films by chemical reaction on the substrate surface. It has some features, e.g. no need of high vacuum, gaseousness of reactants and by-products, low and fast film precipitation temperature, good crystallinity and compactness and complete structure of the obtained film, good adhesion to substrate, excellent step coverage, smooth deposition surface, broad scope of application of various metals, semiconductors, inorganic substances and organic matter, controllable material stoichiometric ratio batch production, and semi-continuous processing. As shown in Figure 1a,[13] precursors of solids, liquids or gases containing atoms are added to the growth furnace to synthesize them together with carbon sources. However, the CVD method involves high cost and is suitable for the synthesis of thin film graphene, but not suitable for commercial large-scale production.[14]

Polymers containing heteroatoms (sometimes embedded in a polymer matrix) are deposited directly on metal catalysts. The whole process is safe without the use of high-temperature gas, and moderate dopant can be achieved. Kwon et al.[15] synthesized pyrrole monomers vaporized on copper substrates in the presence of Cu^{2+} ions, followed by CVD growth (Figure 1b). The content of doped N is 3.14%, and the main pyrrole nitrogen may come from polypyrrole precursors. Sun et al.[16] found that the amount of N-doping reached 23.5% when the mixture of nitrogen-rich melamine and PMMA was directly spin-coated on the copper substrate at 1000°C at atmospheric pressure, where graphite N occupies the main part of the N-doped structure and the mobility of N-graphene is low (< 10 $cm^2 V^{-1} s^{-1}$).

2.2. Ball milling method

Ball milling is to strip graphite and crack C-C bonds, in which the newly formed activated carbon species react with dopants through mechanochemistry. As an energy-saving and efficient material preparation technology, it can obviously reduce the activation energy of reaction, refine the grain size, greatly improve the powder activity, improve the uniformity of particle distribution and the interface between reinforcer and matrix, promote the diffusion of solid ions, induce low temperature chemical reaction, and thus improve the compactness, electrical and thermal properties of materials. Zhang et al. prepared hydroxyl functionalized graphene by ball milling.[146] Jeon et al. studied graphene nanosheets as an efficient electronic catalyst for catalytic oxygen reduction. By ball milling, the stainless steel ball was rotated at high speed to produce enough kinetic energy. As a result, 36 kinds of activated carbon were formed at the edge of graphite crushing. These activated carbon have enough reaction ability to absorb halogen in sealed ball mill capsules.[17] Similarly, marginally selective graphene halide nanosheets (XGnFs, X = Cl, Br or I) were prepared by ball milling as anode materials for lithium-ion batteries.[18]

2.3. Wet chemical method

The synthetic method by the liquid reaction and chemical reaction is collectively referred to wet chemical method, such as coprecipitation chemical liquid deposition (CBD), electrochemical deposition (electroplating), sol-gel, etc. It has achieved rapid development in recent decades and is replacing some traditional ceramic generation methods. Due to small particle size, large specific surface area and high chemical activity, the ultra-fine ceramic powders prepared by wet chemical method show broad application prospects in heteroatom-doping carbon materials. The wet chemical method can be used to mix heteroatoms on 3D graphene gel with large surface area and pore structure.[19] For example, Wu et al. employed ammonia boron trifluoride for the co-doping of B and N.[186] RGO (reduced graphene oxide) aerogels doped with B and N were prepared by freeze-drying after reduction and self-assembly of GO sheets in hydrothermal conditions. Su et al. used nitrogen-sulfur codoped three-dimensional graphene skeleton as an efficient metal-free electrocatalyst for oxygen reduction reaction under hydrothermal conditions.[20]

3. Graphene doped with different nonmetals

3.1. Oxidized carbon materials

Graphene-based materials as the substitution of most metal-based catalysts in energy catalysis have been widely attended due to some superior properties. The oxidized carbon material, a new nonmental-based graphene catalyst, has begun to play a more and more important role in fuel cells. Lu et al. compared ORR performance on oxidized carbon materials and pure carbon materials, and found that the oxidized carbon materials exhibited higher catalytic activity and selectivity to H_2O_2 in alkaline or neutral medium for ORR.[21] The oxidized carbon materials can be obtained by chemical oxidation, in which some function groups with the oxygen atom generate. The oxidation process can contribute to some defects in the regular fabric of carbon materials, which can change the electronic structure, and further improve the ORR performance. Besides, the activity and selectivity are related to the content of oxygen, and the active sites of ORR on the oxidized carbon materials are the carbon atoms neighboring the oxygen atom in oxygen function groups.

In a word, the introduction of oxygen atom can influence the electronic distribution due to larger electrophilic ability of oxygen than carbon in the oxidized carbon materials. Consequently, the interaction between ORR intermediates and the active sites leads to a change. The existence of more active sites gives rise to rapid absorption of intermediates and further accelerates ORR.[22] Therefore, the oxidized carbon material is a vital nonmetal-doped graphene catalyst in ORR of fuel cells, which has great potential in the practical application.

3.2. Nitrogen-Doped Graphene (NG)

In recent years, researchers developed low-cost non-metallic carbon-based electrocatalysts for ORR[7a, 23]. It is reported that zigzag carbon can offer active sites for catalyzing efficiently the ORR.[24] The superior catalytic performance originates from the abundant defects of carbon. However, most of the pure carbon materials show relatively low ORR activity due to the absence of bandgap.[25] To improve the catalytic activity, the use of N-doping strategy is introduced. To date, nitrogen-doped carbon materials have been widely used as ORR catalysts due to their excellent electrocatalytic activity, low cost, good stability, and environmental protection.[19a, 26] The physical and chemical properties of N-doped graphene and undoped graphene are quite different. In the periodic table, nitrogen is adjacent to carbon. Because the electronegativity of N is greater than that of C, N atoms have ability to attract more electrons, and further change the electronic structure of graphene. It has been reported that N-doped graphene can be prepared from ammonia and graphene, which showed the best catalytic activity at 900 °C. The onset potential and half-wave potential of nitrogen-doped graphene were higher than those of industrial Pt/C catalyst.[27] Gracia-Espino et al. prepared a N-doped graphene by vapor deposition for ORR, which is carried out along the "quasi-four-electron" reaction path.[28] Zhao et al. synthesized a N-doped graphene material by the pyrolysis of MOFs.[29] Compared with pure graphene, the prepared doped graphene with high electroconductivity exhibits higher activity for ORR. Feng et al. used graphene oxide and NH_4HCO_3 as raw materials to prepare N-doped graphene. The nitrogen doping rate reached 12.75% at low temperature (150 °C), which is conducive to ORR.[30] Xin et al. prepared a nitrogen-doped graphene by high-temperature heat treatment and found the type of nitrogen atomization bond has a significant effect on the selectivity and catalytic activity. Graphitic nitrogen determines the limiting current density, while pyridinic nitrogen determines the onset potential in the process of the oxygen reduction reaction.

The possible bonding of N-doped graphene is shown in Figure 2a.[31] There are three kinds of nitrogen bond structure. Because the bond length of C-N is primarily the same, pyridinic-N and graphitic-N have little effect on the structure of graphene.[31] However, the pyrrolic-N of SP^3 bond destroys the planar structure of graphene. Pyridinic-N bond has the best stability in the presence of a single vacancy. If Stone-Wells defect and vacancy defect occur, pyridinic-N and graphitic-N have greater influence on ORR.[32] The electronegativity of N (3.04 at Paulin scale) is greater than that of C (2.55 at Paulin scale), which leads to the polarization of carbon network and thus affects the electrocatalytic performance of N-doped graphene.[24] N-doped graphene can conduct electricity by inhibiting the state density (DOS) near the bandgap near the Dirac point (Figure 2b).[26] The conductive behavior of nitrogen-doped graphene also depends on the configuration of N-doped graphene. For graphitic-N, three valence electrons of nitrogen form three s bonds with adjacent carbon atoms, one electron participates in the formation of π bond and the fifth electron participates in the π* state of the junction band. Each graphitic N can contribute 0.5 electrons to the π network of graphene lattice. For pyrrolidine-N, pyrrolidine forms at the defect sites and electrons can be extracted from graphene sheets into these defects, resulting in N-doping effect for the different bond types as compared to pristine graphene (Figure 2c).[26]

Paul et al. also pointed out that there were three chemical forms of nitrogen on the surface of nitrogen-doped graphene, namely pyridinic-N, pyrrolic-N and graphitic-N.[26a] Pyridinic-N refers to nitrogen atoms attached to two carbon atoms, corresponding to XPS binding energy of 402 to 405 eV. In addition to an electron supplied to the conjugated bond system, the N atom also has a lone pair of electrons, which can absorb O_2 molecule and their intermediates in the process of ORR, thus improving the catalytic efficiency. Pyrrolic-N is a nitrogen atom with two p electrons and conjugated with a pin bond system.

This article is protected by copyright. All rights reserved.

Graphitic-N refers to nitrogen which is linked to three C atoms. Some researchers believed that graphitic plays a key role in the electrocatalytic ORR.[33]

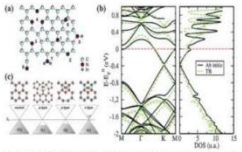

Figure 2. (a) Possible configurations of nitrogen dopants in graphene: 1-graphitic N, 2-pyridinic N, 3-single N pyridinic vacancy, 4-triple N pyridinic vacancy, 5-pyrrolic N, 6-interstitial N or adatom, 7-amine, and 8-nitrile. Reprinted with permission from Ref.[31]. Copyright: 2011 American Chemical Society. (b) *Ab initio* (thick black lines) and tight-binding (green dashed lines) band structures (left) and DOS (right) of a 10 × 10 graphene supercell containing one substitutional N dopant. Reprinted with permission from Ref.[264]. Copyright: 2013 American Chemical Society. (c) Computed doping effect of N dopant. Reprinted with permission from Ref.[26]. Copyright: 2012 American Chemical Society.

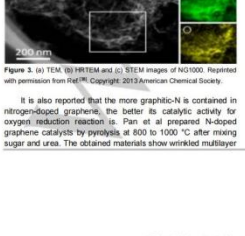

Figure 3. (a) TEM, (b) HRTEM and (c) STEM images of NG1000. Reprinted with permission from Ref.[36]. Copyright: 2013 American Chemical Society.

It is also reported that the more graphitic-N is contained in nitrogen-doped graphene, the better its catalytic activity for oxygen reduction reaction is. Pan et al prepared N-doped graphene catalysts by pyrolysis at 800 to 1000 °C after mixing sugar and urea. The obtained materials show wrinkled multilayer graphene structure (Figures 3a-c). The surface area can reach 565.1 $m^2 g^{-1}$ at 1000°C. Under the condition of 0.1 M KOH alkaline medium, the half-wave potential was 0.14 V vs Ag/AgCl, and Koutecky-Levich determined that the N-doped graphene material had a good mass transfer limiting current density at the potential of 0.25 V vs Ag/AgCl and the electron transfer number was 3.8.[35]

In addition, Ikeda et al. drew a conclusion that graphitic nitrogen is an energetic active site based on oxygen adsorption barrier and subsequent ORR process.[36] Geng et al. found that the ORR activity of the synthesized N-doped graphene with 2.8% N was high when the annealing temperature was 900 °C. X-ray photoelectron spectroscopy (XPS) analysis showed that the enhancement of ORR activity was attributed to the appropriate graphitization of N.[37a] Graphene oxide prepared by Hummers method was used to synthesize N-doped graphene with a suitable nitrogen source. When the number of N atoms in the pyrrole ring is large, polypyrrole can promote the electrochemical performance of graphene, which shows that natural formation has excellent catalytic activity and is beneficial to the formation of water through the four-electron path in alkaline electrolyte. At the same time, the stability of natural gas and the cross-durability of methanol are also excellent. Its performance is superior to that of commercial Pt/C catalyst, which proves that graphitic-N is very important in ORR.[60] Zhen and co-workers used similar methods to explore the effect of graphitic-N on ORR activity. The electrochemical tests showed that larger graphitic nitrogen configuration might have better electrocatalytic ORR activity.[61] Vazquez-Arenas and co-workers used DFT calculations to investigate the mechanism of ORR on N-doped graphene. It is proposed that the contact between a carbon atom and graphitic-N is an elementic defect, which promotes the adsorption and reduction of oxygen through electron transfer in the reaction process, thus playing the role of active center.[62]

Moreover, researchers have suggested that pyridinic-N is also a contributing factor to the electrocatalytic activity of ORR. Woo et al found that pyridinic-N improved the ORR activity under acidic conditions.[63] Xia's team used argon as a protective gas to annealed melamine to prepare N-doped graphene. The results showed that the pyridine-N component determined the electrocatalytic activity of N-doped graphene in a redox reaction.[64] Sun et al. developed a new method to prepare high concentration nitrogen doped platelet carbon nanofibers (plCNF). The chaotic edge of plCNF is clipped by high frequency etching technology, which produces many exposed edges and patterned edge points.[65] The pyridine-N atom is preferentially located. The electrochemical experiments show that the carbon atoms near pyridine-N can be used as the catalytic center of ORR, and the reaction process is dominated by 4e. The active sites on nitrogen-doped graphene can be determined by the changes of chemical composition before and after ORR. The activity of NG is related to the chemisorption ability of -OH group, which is formed on the carbon atom near pyridinic-N. It is found that the carbon atoms adjacent to pyridinic-N play an important role in ORR and are the main activity centers. Zhang et al. synthesized a N-doped carbon material by adopting a novel green strategy

without any starting chemicals, and the structure of nitrogen bond belongs to pyridinic-N.[66] Recently, Zhao and coworkers found that the N-HCβG catalyst possesses high ORR activity in both acid and alkaline conditions, in which the type of nitrogen is pyridinic-N.[67]

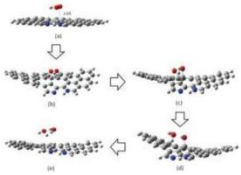

Figure 4. Optimized structure of each electron transformation in ORR: (a) initial position of OOH from N-graphene, (b) OOH adsorbs on the doped graphene, (c) O–O bond is broken, (d) one water molecule is generated, and (e) C–O bond is broken, and the second water molecule is generated. Gray, blue, red and small white balls represent C, N, O and H atoms, respectively. Reprinted with permission from Ref.[264]. Copyright: 2012 American Chemical Society.

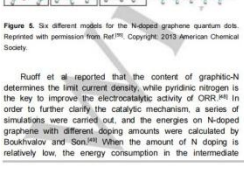

Figure 5. Six different models for the N-doped graphene quantum dots. Reprinted with permission from Ref.[59]. Copyright: 2013 American Chemical Society.

Ruoff et al. reported that the content of graphitic-N determines the limit current density, while pyridinic nitrogen is the key to improve the electrocatalytic activity of ORR.[68] In order to further clarify the catalytic mechanism, a series of simulations were carried out, and the energies on N-doped graphene with different doping amounts were calculated by Boukhvalov and Son.[69] When the amount of N doping is relatively low, the energy consumption in the intermediate process of ORR can be reduced and the energy barrier is lower than that on the platinum surface. The addition of nitrogen enlarges the positive spin density and charge density and enhances the catalytic activity.[63] The process can be carried out spontaneously on N-doped graphene. Interestingly, the calculated average reversible potential is 1.15 V vs. SHE, which is consistent with the experimental results (Figure 4). Meanwhile, multiple experiments revealed the influence of pyridinic-N position and microstructure on its catalytic efficiency.[61] A number of experiments have proved that ORR activity is related to the content of pyridine nitrogen.[12a, 44, 50a, 52]

It has also been suggested that pyridinic nitrogen and graphitic nitrogen simultaneously influence ORR activity.[46, 53] Wissam et al found that pyridinic and graphitic nitrogen are the most active sites. Ten graphene quantum-dots models for simulating nitrogen-doped graphene are presented, of which six models is shown in Figure 5.[59] In model A, C, and D, nitrogen doping its similar to graphite substitution, where nitrogen is located at different distances from the edge of graphene quantum dots. The model B has a similar pyridine type doping. Pyridine nitrogen is especially interesting because it has a pair of electrons besides one electron of the conjugated π bond. In E_1 nitrogen belongs to pyrrolidine doped five-membered rings.[59] Due to the mutual exclusion between nitrogen dopants, the aggregation of nitrogen on the original graphene is inhibited, therefore, the chemical properties of single nitrogen doping are expected to be widely used.[59]

Kabir et al. prepared nitrogen-doped graphene films by sacrifice support method.[57] The optimal doping temperature for is 850 °C, which showed good ORR activity (Figure 6). The content of nitrogen components such as graphitic-N, quaternary-N, nitrogen hydride, and pyridinic-N varies greatly with the pyrolysis temperature. The decrease of graphitic-N content and the increase of hydrogenation-N/pyridinic-N ratio would increase the ORR activity. The ORR mechanism steps on graphitic, hydrogenation and pyridinic nitrogen are proposed in Figures 6c-f.[57] Lu et al. prepared three-dimensional nitrogen-doped graphene (3D-NG@SiO_2).[58] It is suggested that nitrogen mainly exists in the form of pyridinic nitrogen by pyrolysis of poly (o-phenylenediamine) containing nitrogen precursor and silica gel. The initial potential of 3D-NG@SiO_2 was 0.08 V for ORR. The number of electron transfer is 3.92. This indicates that 3D-NG@SiO_2 mainly occurs through four-electron process. It is also proved that the catalyst has high activity, good durability and broad application prospects.

Guo et al.[28] clarified the possible mechanism of ORR on nitrogen-doped carbon materials by exploring the active sites of nitrogen-doped carbon materials for oxygen reduction. Lewis bases are formed by pyridinic N. First, oxygen molecules are adsorbed on carbon atoms next to the protonated pyridine N. Two possible approaches are proposed: one is the four-electron mechanism at a single site; the other is the 2 + 2 electron mechanism, which does not always occur at a single site. Titash Mondal et al.[60] synthesized nitrogen-doped graphene from heteroatomic polymers and proposed the mechanism of nitrogen-doped graphene (Figure 7). When the material was treated by high temperature, the chain breakage becomes active

This article is protected by copyright. All rights reserved.

and low molecular weight fragments are produced. The products formed by chain breaking are usually free radicals, which combine with each other to form new products.[81]

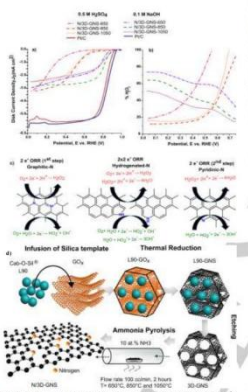

Figure 6. Hydrogen peroxide yield (%H_2O_2) and peroxyhydroxyl yield ($^*OOH$) of N-doped 3D-graphene nanosheet materials in (a) acid and (b) alkaline media. (c) ORR mechanism of graphitic, hydrogenation and pyridinic nitrogen. (d) ORR mechanism of graphitic, hydrogenation and pyridinic nitrogen. Reprinted with permission from Ref.[81]. Copyright: 2018 American Chemical Society.

Similar to nitrogen-doped graphene, nitrogen-doped carbon nanotubes have a larger specific surface area, higher conductivity and excellent catalytic activity for oxygen reduction.[82] Moreover, its low cost, high activity, and excellent durability are the advantages of ORR as a new electrocatalytic system.[10d, 37, 52a, 63] The hybrid composites of nitrogen-doped graphene and nitrogen-doped carbon nanotubes (NGCA) have been obtained via the in-situ synthesis method, which can further improve the catalytic performance for ORR.[64] The nitrogen-doped carbon nanotubes can not only be used as a high-speed electron conduction channel, but also effectively prevent the re-stacking of graphene, and greatly improve the specific surface area and conductivity of NGCA composite catalysts. As a result, the NGCA composite catalyst exhibits a four-electron reaction path, and its ORR activity at 0.75 V is six times as high as that of nitrogen-doped graphene. Besides, nitrogen-doped graphene-carbon nanotube composite catalyst could be also prepared by one-step chemical meteorological deposition.[83] Graphene and carbon nanotubes grow at the same time, resulting in a three-dimensional spatial structure. The specific surface area of graphene and carbon nanotubes reached 812.9 $m^2 g^{-1}$, and the conductivity reached 53.8 $s cm^{-1}$. Although the nitrogen content of the composite catalyst is only 0.53%, its oxygen reduction catalytic performance is very good, close to that of industrial Pt/C catalyst, and its long-term stability is much higher than that of Pt/C catalyst.

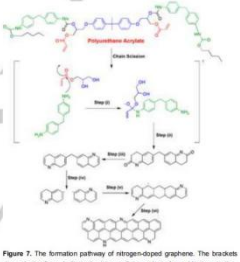

Figure 7. The formation pathway of nitrogen-doped graphene. The brackets shown in the figure indicate the intermediate products formed in the reaction. Reprinted with permission from Ref.[83]. Copyright: 2015 American Chemical Society.

In addition, the hybrid composites of nitrogen-doped graphene and nitrogen-doped carbon nanotubes also show superior ORR performance in acidic conditions. For example, Dai and coworkers synthesized a nitrogen-doped graphene/CNT catalyst, which exhibited high activity and stability in the acidic polymer electrolyte membrane fuel cells (PEMFCs).[66] The low-cost, metal-free, carbon-based ORR catalysts show promising practical application prospect for acidic PEMFCs.

In conclusions, N-doped graphene prepared by various methods is one of the most efficient metal-free ORR electrocatalysts.[52a, 57] The doped nitrogen atoms can affect the spin density and electron cloud distribution of adjacent carbon atoms and thus induce the formation of "active centers", which can directly participate in ORR.[44, 68] Up till now, there are still many controversies about the ORR active sites of N-doped graphene.[26d, 64] In addition to N-doped graphene, N-doped carbon nanostructures such as 3D N-containing polymer[69], N-doped carbon nanocapsules[70], N-CNT cups[71], and N-doped mesoporous carbon[72] also showed excellent activity in ORR electrocatalysis.[39]

3.3. Sulphur doped graphene

Since the electronegativity of S (2.58) and C (2.55) is similar, charge transfer can be ignored in the C-S bond. However, contrary to the zero spin density of undoped graphene, the mismatch between the outermost orbital of S and C leads to uneven spin density distribution on S-doped graphene. It was suggested that S-doped graphene was formed by defect formation and S bonds break in two steps. The S-doped graphene sheet could be a small bandgap semiconductor, more metalized than the original graphene.[73] Graphene doped with S has a higher resistance than original graphene.[74] Using first-principles calculations, Denis et al proposed that S-doped graphene is feasible for ORR, but its catalytic effect is not as good as that of nitrogen-doped graphene.[75] Jeon et al. found that covalently bonded S and oxidized S at the serrated and armchair-like edges of graphene nanometer salts obtained from ball-milling could lead to significant increase in spin density.[26a, 76] Xia et al. found that the change of atomic spin density plays an important role in oxygen reduction activity by density functional theory calculation.[77] Zhang et al. calculated the distribution of atomic charge and spin density as shown in Figure 8. When graphene is decorated by sulfur, graphene does not exhibit additional spin density because sulfur atoms do not introduce additional unpaired electrons. Charge density redistributes on S-doped graphene clusters with Stone-Wales defects. The positive charge densities of the carbon atoms 11, 15, 89 and 93 at the serrated edge are higher about 0.17 than other carbon atoms. It is speculated that these carbon atoms may be the catalytic sites of ORR. Adsorption calculations of OOH or O_2 at these sites show that both OOH and O_2 can be adsorbed on the sawtooth edge of graphene with Stone-Wales defects, but not on graphene without Stone-Wales defects. These active sites play an active role in promoting ORR. Figures 8c and 8d are similar in that the substituted sulfur atoms are located at the serrated edge. Atoms with high charge densities are also located at the sawtooth edge, and these atoms also generate spin densities. As shown in Figures 8e and 8f, the spin and charge densities of these sulfur oxide atom defective graphene structures are distributed on the edge of the armchair. Interestingly, the spin and charge densities of carbon atoms adjacent to sulfur oxide are also high. It is shown that sulfur-doped graphene clusters not only polarize more spin and charge density atoms with Stone-Wales defects, but also contribute to the catalysis of ORR. Similarly, as shown in Figure 8, atoms with higher charge density are distributed along the zigzag edge. Its value is less than 0.19. The authors tested these atoms with high charge density and spin density. The results show that atoms with charge density greater than 0.20 and spin density greater than 0.15 can absorb OOH or O_2, suggesting that they may be potential active centers of ORR. Figure 8h shows the charge density distribution on pure graphene clusters. It is found that there is no spin density on pure graphene clusters, and the maximum charge density is 0.17. OOH and O_2 cannot be adsorbed on carbon atoms. The results show that the catalytic activity of pure graphene is not good, which further proves that the graphene clusters doped with sulfur atoms have a positive effect on the catalytic activity of ORR.

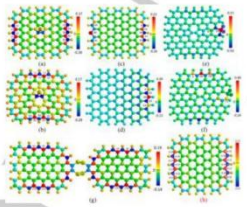

Figure 8. Atomic charge density and spin density distributions on the S-doped and pure graphene clusters. Atomic charge density distribution on S-adsorbed graphene clusters with (a) perfect structure and (b) one Stone-Wales defect; (c) atomic charge density and (d) spin density distributions on perfect graphene cluster with substituting S at the zigzag edge; (e) atomic charge density and (f) spin density on SO_2-doped graphene with a Stone-Wales defect; atomic charge density on (g) sulfur ring cluster connecting two pieces of graphene clusters and (h) pure graphene cluster. The colors of the balls stand for relative values of charge and spin density. The density decreases linearly from positive to negative values in the color order of red, orange, yellow, green, and blue. Sulfur and oxygen atoms are labeled with S and O, respectively. The unlabeled small and large balls represent H and C, respectively printed with permission from Ref.[78]. Copyright: 2014 American Chemical Society.

Sulfur-doped graphene can be obtained by using dibenzyl disulfide as sulfur source and graphene oxide as raw material. The ORR catalytic activity of S-graphene-600 is higher than that of graphene-600 (Figure 9a). The catalytic activity can be improved by enhancing the annealing temperature and the ORR activity of S- graphene-1050 is close to that of Pt/C (Figure 9). Recently, Zhang et al. prepared S-doped graphene by using carbon precursor of sulfonate ion exchange resin. The obtained S-doped graphene has similar electrocatalytic activity with Pt/C, but better stability and methanol resistance than the latter.[78] Most of the research showed that the onset potential and the number of electrons per oxygen transfer for S-doped graphene were similar to those for N-doped graphene. Xia et al. proposed a catalytic mechanism of ORR on S-doped graphene.[77] XPS

This article is protected by copyright. All rights reserved.

results show that doped S is mainly doped in the form of -C-S-C - or -C-SO_2-C-C- on the edge or surface of graphene.[79-80]

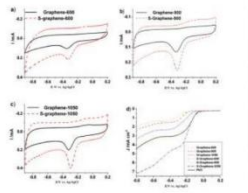

Figure 9. (a) Cyclic voltammetry curves of graphene-600 and S-graphene-600, (b) Cyclic voltammetry curves of graphene-900 and S-graphene-900, (c) Cyclic voltammetry curves of graphene-1050 and S-graphene-1050, (d) LSV curves of various graphene and Pt/C catalysts on a rotating glass-carbon disk. Reprinted with permission from Ref.[78a]. Copyright: 2012 American Chemical Society.

The ORR activity of pure graphene is very low, while S-doped graphene can enhance the charge and spin density, which is conducive to the adsorption of O_2. The active sites on these S-doped graphene clusters are those carbon atoms located at zigzag edges or near SO_2-doped structures, which have high positive charge density and spin density. It is known that the two-electron transfer pathway occurs on substituted sulfur atoms with high charge density, while the four-electron transfer pathway occurs on carbon atoms with high spin or charge density. Sulfur-doped graphene expands the family of metal-free carbon-based nanomaterials and becomes a new electrocatalyst to replace Pt in fuel cells.[10b, 21d] Even though the electrocatalytic activity of S-doped graphene for ORR is still lower than that of commercial Pt/C, the synergistic effect of sulfur and carbon materials on the development of metal-free ORR electrocatalysts provides a feasible strategy to design new ORR electrocatalysts.

3.4. Phosphorus doped graphene

It is proposed that nonmetallic atoms doped graphene can better regulate the electronic structure and thus improve the electrochemical properties of the oxygen reduction reaction. In order to improve the energy storage properties of graphene, various attempts have been made. Among them, the introduction of heteroatoms (O, N, S, B, and P) is one of the effective methods to improve the electrochemical performance of graphene electrode materials,[81] which has the advantage of changing the electronic properties of carbon materials and the influence of charge distribution on adjacent atoms.[10b] Doped heteroatoms generate induced charges and change the chemical adsorption by redistribution of charges. It can effectively weaken the O-O bond bonding, making the positively charged carbon atoms easy to attract electrons, thus promoting the ORR process.[5a, 52a] P-doped graphene can also improve the electron donor properties of carbon materials and thus enhances the catalytic activity.[82] The ORR activity of P-doped graphene was higher than that of non-doped graphene.[10b] Peng et al studied P-doped carbon nanospheres for ORR in both acidic and alkaline media and found that the ORR activity was higher in alkaline media, but the long-term stability of the materials was better in acidic media.[83] Zhang et al also found that P-doped graphene significantly improved the electrochemical performance of graphene in ORR and lithium-ion battery (LIB).[84] Liu et al synthesized P-doped graphene by pyrolysis of toluene and triphenylphosphine, which could be used as oxygen reduction catalyst.[10e, 63a, 85]

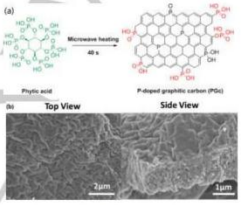

Figure 10. (a) Schematic diagram of preparing p-doped graphite carbon with phytic acid. (b) SEM images of PGC. Reprinted with permission from Ref.[84]. Copyright 2016 American Chemical Society.

In addition, it is found that P-doped graphene is more stable in air than N-doped graphene, and exhibits n-type semiconductor characteristics.[86] P-doped graphene can be applied in supercapacitors. For example, Yang et al used P-enriched activated carbon as a supercapacitor and found that P-enriched activated carbon can not only improve the performance and high capacitance of the supercapacitor but also broaden the potential of the battery in water electrolyte. Graphene oxide and phosphoric acid were treated at high temperature to enhance the voltage window of graphene. However, the capacitance of phosphor doped graphene is low, which is only 29 F/gat 1 A/g current density.[87] In 2016, Pate et al.[84] prepared P-doped porous carbon materials by microwave oven method. As shown in Figure 10a, the coordination of P atoms can be controlled.

This article is protected by copyright. All rights reserved.

This P-doped carbon has a special structure (Figure 10b). A porous carbon block is sandwiched between two shrunken graphene-like sheets. The reason for forming this structure may be that the diameter of P atom is larger than that of C atom and the doping of P atom causes local geometric stress in the carbon network around each P atom.

3.5. N/P codoped graphene

In addition to N-doped graphene as a non-metallic electrocatalyst, researchers have focused their attention on the non-metallic electrocatalyst with nitrogen and phosphorus as co-dopant.[81a, 86, 88] Zhu et al.[89] proposed that the nitrogen and phosphorus doped honeycomb carbon is an efficient electrocatalyst for ORR. The material was prepared by direct pyrolysis of popcorn in a static semi-open environment. It shows layered porous structure and the ORR is close to the standard Pt/C. The P/N codoped graphene prepared by pyrolysis of graphene and dicyandiamide mixture showed a marked increase in catalytic activity for ORR in phosphoric acid solution.[86] Nitrogen and phosphorus codoped graphene/carbon nanosheets (N, P-GCNS) were prepared by pyrolysis of the mixture of GO, polyaniline and phytic acid (Figure 11). Compared with N or P single-doped catalysts, N/P codoped graphene catalysts are more active.[81]

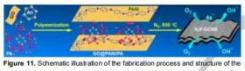

Figure 11. Schematic illustration of the fabrication process and structure of the N, P-GCNS bifunctional oxygen electrocatalyst. Reprinted with permission from Ref.[86]. Copyright: 2015 American Chemical Society.

3.6. N/S codoped graphene

In order to improve the interaction between doping elements and dopants, two kind of heteroatoms doped graphene can effectively solve this problem.[90] Heteroatoms codoped graphene as an electrocatalyst has a significant improvement in ORR.[85, 75, 91] In order to improve the catalytic activity of ORR, dopants are usually introduced into the carbon lattice.[78, 89b] Researchers have used two doped elements to adulterate graphene.[92a, 94] In the case of double doped carbon materials, S atoms can induce adjacent C and N atoms to polarize,[92b] it can form unique electronic distribution and further induce the synergistic effect.[86] N/S co-doped graphene can efficiently improve the catalytic activity of ORR.[28, 78, 95] Guan et al. prepared N and S co-doped graphene from pyrimidine and thiophene sites with enhanced ORR activity.[92c] Qiao et al proved this viewpoint correct by density functional theory calculation.[10d]

It is proposed that the three-dimensional voids on the graphite surface constitute its unique stratified structure.[96] It has high surface area, abundant active sites at the interface of electrochemical reaction, and good electron/electrolyte transport characteristics. Li et al. prepared S, N co-doped graphene carbon nanosheets by pyrolysis of melamine and dibenzyl sulfide.[96] The schematic diagram of the synthesis process of S, N co-doped graphene carbon nanosheets is presented in Figure 12a. Taking graphene nanosheets loaded with S_3N_4 as an example, the catalytic activity of graphene nanosheets annealed at 700, 800, 900 and 1000 °C was tested in the 0.1 M KOH electrolyte (Figure 12b). The results showed that the catalytic activity of S_3N_4 annealed at 900 °C was the best, which was higher than that of Pt/C. From Figures 12c and 12d, it can be concluded that the synergistic effect of S and N atoms in S and N co-doped carbon materials plays a key role in ORR in both alkaline and acidic media. Compared with single S or N doped graphene, S/N codoped graphene carbon nanosheets have higher ORR activity.

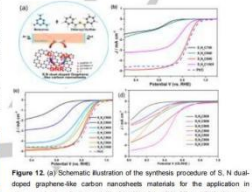

Figure 12. (a) Schematic illustration of the synthesis procedure of S, N dual-doped graphene-like carbon nanosheets materials for the application in oxygen reduction electrocatalysis. (b) LSV of the S_3N_4CT and Pt/C (20 wt %, E-TEK) at 1600 rpm. (c) LSV of the as-prepared S_3N_4C900 samples and Pt/C catalyst (20 wt %, E-TEK) at 1600 rpm. (d) LSV curves of S_3N_4C900 samples in O_2-saturated 0.5 M H_2SO_4 aqueous solution. Reprinted with permission from ref.[96]. Copyright: 2017 American Chemical Society.

Zheng et al. prepared sulfur-nitrogen co-doped graphene/CNT (GC) as shown in Figure 13a. Firstly, carbon nanotubes dispersed on graphene oxide surface were partially reduced by gas chromatography, and nitrogen was doped in ammonia at 500 °C. In the second step, nitrogen-doped gas chromatography was mixed with phenyl disulfide and heat-treated at 900 °C. It can be found that this distribution-by-distribution doping can significantly increase the nitrogen content. Even when the surface concentration of sulfur measured by XPS is only 0.23%, the beneficial effect on ORR is significant, and the change of GC structure after co-doping is minimal (Figure 13b). In 0.1 M KOH electrolyte (Figure 13c), the initial potential of GC-NLS is 0.85 V vs. RHE, which is 70 mV higher than that of co-doped graphene (G-NLS), and 50 mV higher than that of S/N co-doped CNTS (C-NLS). The half wave potential (0.72 V vs. RHE) also increased by 50 mV compared with that of C-NLS.[97] Wohlgemuth et al also found show that the introduction of sulfur atom can incrrase the structure defect, polarizability, and catalytic activity of ORR in alkaline condition.[93c, 100] N/S co-doped carbon foams with continuous and hierarchical structure show wide application prospects as ORR metal-free

This article is protected by copyright. All rights reserved.

Accepted Manuscript

electrocatalysts.[101] Su et al. found that the catalytic activity of S/N-codoped 3d graphene undergoes mainly 4e transfer in 0.1 M KOH.[97]

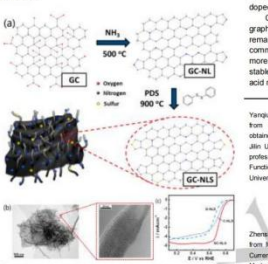

Figure 13. (a) Schematic illustration of the step-wise doping process to fabricate GC-NLS nanocomposites. (b) TEM images of the GC-NLS catalyst. (c) ORR polarization curves obtained in 0.1 M KOH showing the synergic effect of GC-NLS. Reprinted with permission from Ref.[97] Copyright: 2014 American Chemical Society.

4. Summary and perspectives

Nonmetal-doped graphene materials have a great application prospect on energy catalysis due to their excellent catalytic activity and stability for ORR. Compared with graphene, nonmetal-doped graphene can not only improve the electron structure of graphene but also create more active sites for ORR. The two-dimensional structure and adjustable surface of graphene play an important role in doping different nonmetal elements, which provide good superiority to improve the stability and catalytic activity for ORR. Up to date, nitrogen, phosphorus, and sulfur doped graphene materials exhibit excellent ORR performance. Among them, nitrogen-doped graphene exhibits higher ORR activity than phosphorus and sulfur doped ones. Moreover, nitrogen-sulfur or nitrogen-phosphorus co-doped graphene can further enhance ORR performance.

However, the ORR activity of most of the nonmetal-doped graphene without metal active sites in acidic media is insufficient since they show high overpotential. The ORR activity can be significantly improved by assembling the nitrogen-doped graphene with N-doped carbon nanotubes due to the porous structures with a large surface area. Another familiar strategy to improve the ORR activity is introducing metal ions (e.g. Fe, Co) to the system. However, in the popular PEMFCs, the acid-corrosion resistance of most transition metals is less than carbon. Therefore, for commercialization of the fuel cell technology, improvement of the degree of graphitization is crucial to enhance the corrosion resistance of the nonmetal-doped graphene materials.

Currently, most of the research of ORR on nonmetal-doped graphene catalysts is carried out in alkaline media and is mainly remained in the experimental stage rather than the practical commercial applications of fuel cell. Since acidic PEMFCs are more practical than alkaline ones, development of efficient and stable nonmetal-doped graphene ORR catalysts operated in acid media is vital and urgent in future PEMFCs technologies.

Yanqiu Shao received her B.S in Chemistry from Mudanjiang Normal University and obtained her Ph.D in Physical Chemistry from Jilin University in China. She is currently a professor of Catalytic Principle and Functional Materials in Mudanjiang Normal University.

Zhenshuang Jiang received his B.S. degree from Mudanjiang Normal University in 2016. Currently, he is a Master candidate of Mudanjiang Normal University under the supervision of Prof. Yanqiu Shao. His research focuses on catalyst design for fuel cells and energy conversion.

Qiaoqiao Zhang received her B.S. degree from DaTong University in Shanxi in 2018. Currently, she is a Master candidate of Jilin University under the supervision of A/Prof. Jingqi Guan. Her research focuses on the synthesis of mononuclear-multinuclear catalysts for energy storage and conversion.

Jingqi Guan received his B.S. degree and Ph.D. degree from Jilin University in 2002 and 2007. He was promoted to associate professor of chemistry in Jilin University in 2009. He worked as a postdoctoral research fellow in the University of California at Berkeley from 2012 to 2013 and in the Dalian Institute of Chemical Physics from 2014 to 2018. His research interests focus on the synthesis of mononuclear-multinuclear catalysts for energy storage and conversion.

This article is protected by copyright. All rights reserved.

Acknowledgements

This work was supported by the Natural Science Foundation of Jilin Province (20180101291JC), Heilongjiang Education Department (1352 MSYB006), and Mudanjiang Normal University (JG2017001).

Conflict of interest

The authors declare no conflict of interest.

Keywords: Graphene • Nitrogen-doping • Oxidized carbon materials • Oxygen reduction reaction • Phosphorus-doping • Sulfur-doping • Fuel cell

[1] N. Recham, J.N. Chotard, L. Dupont, C. Delacourt, W. Walker, M. Armand, J.M. Tarascon, Nat. Mater. **2009**, *9*, 68.
[2] a) F. Cheng, J. Chen, Chem. Soc. Rev. **2012**, *41*, 2172-2192; b) Z.-L. Wang, D. Xu, J.-J. Xu, X.-B. Zhang, Chem. Soc. Rev. **2014**, *43*, 7746-7786; c) M.A. Rahman, X. Wang, C. Wen, J. Electrochem. Soc. **2013**, *160*, A1759-A1771; d) Y. Li, H. Dai, Chem. Soc. Rev. **2014**, *43*, 5257-5275; e) H. Kim, G. Jeong, Y.-U. Kim, J.-H. Kim, C.-M. Park, H.-J. Sohn, Chem. Soc. Rev. **2013**, *42*, 9011-9034; f) V. Nebusholkin, H. Wang, J.J. Martin, W. Qu, J. Power Sources **2010**, *195*, 1271-1291; g) A. Kraytsberg, Y. Ein-Eli, Adv. Energy Mater. **2012**, *2*, 922-939; h) D.R. Egan, C. Ponce De León, R.J.K. Wood, R.L. Jones, K.R. Stokes, F.C. Walsh, J. Power Sources **2013**, *236*, 293-310.
[3] a) D. Yu, E. Nagelli, F. Du, L. Dai, J. Phys. Chem. Lett. **2010**, *1*, 2165-2173; b) Y. Zheng, Y. Jiao, M. Jaroniec, Y. Jin, S.Z. Qiao, Small **2012**, *8*, 3550-3566.
[4] a) J. Wu, X.Z. Yuan, J.J. Martin, H. Wang, J. Zhang, J. Shen, S. Wu, W. Merida, J. Power Sources **2008**, *184*, 104-119; b) T. Kinumoto, M. Inaba, Y. Nakayama, K. Ogata, R. Umebayashi, A. Tasaka, Y. Iriyama, T. Abe, Z. Ogumi, J. Power Sources **2006**, *158*, 1222-1228; c) R. Borup, J. Meyers, B. Pivovar, Y.S. Kim, R. Mukundan, N. Garland, D. Myers, M. Wilson, F. Garzon, D. Wood, P. Zelenay, K. More, K. Stroh, T. Zawodzinski, J. Boncella, J.E. Mcgrath, M. Inaba, K. Miyatake, M. Hori, K. Ota, Z. Ogumi, S. Miyata, A. Nishikata, Z. Siroma, Y. Uchimoto, K. Yasuda, K.-I. Kimijima, N. Iwashita, Chem. Rev. **2007**, *107*, 3904-3951.
[5] a) M.A. Patel, F. Luo, M.R. Khoshi, E. Rabie, Q. Zhang, C.R. Flach, R. Mendelsohn, E. Garfunkel, M. Szostak, H. He, ACS Nano **2016**, *10*, 2305-2315; b) D. Higgins, P. Zamani, A. Yu, Z. Chen, Energy Environ. Sci. **2016**, *9*, 357-390; c) Z. Yang, H. Nie, X.A. Chen, X. Chen, S. Huang, J. Power Sources **2013**, *236*, 238-249.
[6] a) D. Higgins, M.A. Hoque, M.H. Seo, R. Wang, F. Hassan, J.-Y. Choi, M. Pritzker, A. Yu, J. Zhang, Z. Chen, Adv. Funct. Mater. **2014**, *24*, 4324-4324; b) M.A. Hoque, F.M. Hassan, D. Higgins, J.-Y. Choi, M. Pritzker, S. Knights, S. Ye, Z. Chen, Adv. Mater. **2015**, *27*, 1229-1234; c) Y. Tan, C. Xu, G. Chen, N. Zheng, Q. Xie, Energy Environ. Sci. **2012**, *5*, 6923-6927; d) J. Zhu, M. Xiao, X. Zhao, C. Liu, J. Ge, W. Xing, Nano Energy **2015**, *13*, 318-326.
[7] a) X. Liu, L. Dai, Nat. Rev. Mater. **2016**, *1*, 16064; b) J. Zhang, L. Qu, G. Shi, J. Liu, J. Chen, L. Dai, Angew. Chem. Int. Ed. **2016**, *55*, 2230-2234.
[8] K.S. Novoselov, A.K. Geim, S.V. Morozov, D. Jiang, M.I. Katsnelson, I.V. Grigorieva, S.V. Dubonos, A.A. Firsov, Nature **2005**, *438*, 197.
[9] a) C. Biswas, Y.H. Lee, Adv. Funct. Mater. **2011**, *21*, 3806-3826; b) C. Huang, C. Li, G. Shi, Energy Environ. Sci. **2012**, *5*, 8848-8868.
[10] a) L. Qu, Y. Liu, J.-B. Baek, L. Dai, ACS Nano **2010**, *4*, 1321-1326; b) D. Yu, L. Wei, W. Jiang, H. Wang, B. Sun, Q. Zhang, K. Goh, R. Si, Y. Chen, Nanoscale **2013**, *5*, 3457-3464; c) S. Yang, X. Feng, X. Wang, K. Müllen, Angew. Chem. **2011**, *123*, 5413-5416; d) S. Yang, L. Zhi, K. Tang, X. Feng, J. Maier, K. Müllen, Adv. Funct. Mater. **2012**, *22*, 3634-3640; e) Z.-W. Liu, F. Peng, H.-J. Wang, H. Yu, W.-X. Zheng, J. Yang, Angew. Chem. Int. Ed. **2011**, *50*, 3257-3261.
[11] a) D. Geng, Y. Chen, Y. Chen, Y. Li, R. Li, X. Sun, S. Ye, S. Knights, Energy Environ. Sci. **2011**, *4*, 760-764; b) Z. Lin, M.-K. Song, Y. Ding, Y. Liu, M. Liu, C.-P. Wong, Phys. Chem. Chem. Phys. **2012**, *14*, 3381-3387; c) H. Fei, R. Ye, G. Ye, Y. Gong, Z. Peng, X. Fan, E.L.G. Samuel, P.M. Ajayan, J.M. Tour, ACS Nano **2014**, *8*, 10837-10843; d) J. Ma, Y. Duan, Z. Qin, J. Wang, W. Liu, M. Xu, S. Zhou, X. Cao, Neuroscience **2015**, *310*, 528-540; e) K.-J. Liu, T.-C. Chang, R.-Y. Yang, C.-E. Chen, S.-H. Ho, J.-Y. Tsai, T.-Y. Hsieh, O. Cheng, C.-T. Huang, Thin Solid Films **2014**, *572*, 39-43; f) Y. Li, Y. Zhu, T. Mclouth, C.-Y. Chiu, X. Huang, Y. Huang, J. Am. Chem. Soc. **2012**, *134*, 12326-12329; g) J. Yang, C. Tian, L. Wang, H. Fu, J. Mater. Chem. **2011**, *21*, 3384-3390; h) E.J. Lim, S.M. Choi, M.H. Seo, Y. Kim, S. Lee, W.B. Kim, Electrochem. Commun. **2013**, *28*, 100-103; i) Y. Xin, J.-G. Liu, X. Jie, W. Liu, F. Liu, Y. Yin, J. Gu, Z. Zou, Electrochim. Acta **2012**, *60*, 354-358.
[12] a) L. Wang, A. Ambrosi, M. Pumera, Angew. Chem. Int. Ed. **2013**, *52*, 13818-13821; b) X. Duan, J. Xu, Z. Wei, J. Ma, S. Guo, S. Wang, H. Liu, S. Dou, Adv. Mater. **2017**, *29*, 1701784.
[13] C.-K. Chang, S. Kataria, C.-C. Kuo, A. Ganguly, B.-Y. Wang, J.-Y. Hwang, K.-J. Huang, W.-H. Yang, S.-B. Wang, C.-H. Chuang, M. Chen, C.-I. Huang, W.-F. Pong, K.-J. Song, S.-J. Chang, J.-H. Guo, Y. Tai, M. Tsujimoto, S. Isoda, C.-W. Chen, L.-C. Chen, K.-H. Chen, ACS Nano **2013**, *7*, 1333-1341.
[14] a) L. Yan, M. Lin, C. Zeng, Z. Chen, S. Zhang, X. Zhao, A. Wu, Y. Wang, L. Dai, J. Qu, M. Guo, Y. Liu, J. Mater. Chem. **2012**, *22*, 8367-8371; b) I.-Y. Jeon, Y.-R. Shin, G.-J. Sohn, H.-J. Choi, S.-Y. Bae, J. Mahmood, S.-M. Jung, J.-M. Seo, M.-J. Kim, D. Wook Chang, L. Dai, J.-B. Baek, Proc. Natl. Acad. Sci. **2012**, *109*, 5588.
[15] O.S. Kwon, S.J. Park, J.-Y. Hong, A.R. Han, J.S. Lee, J.S. Lee, J.H. Oh, J. Jang, ACS Nano **2012**, *6*, 1486-1493.
[16] Z. Sun, Z. Yan, J. Yao, E. Beitler, Y. Zhu, J.M. Tour, Nature **2010**, *468*, 549.
[17] I.-Y. Jeon, H.-J. Choi, M. Choi, J.-M. Seo, S.-M. Jung, M.-J. Kim, S. Zhang, L. Zhang, Z. Xia, L. Dai, N. Park, J.-B. Baek, Sci. Rep. **2013**, *3*, 1810.
[18] J. Xu, I.-Y. Jeon, J.-M. Seo, S. Dou, L. Dai, J.-B. Baek, Adv. Mater. **2014**, *26*, 7317-7323.
[19] a) H.-L. Guo, P. Su, X. Kang, S.-K. Ning, J. Mater. Chem. A **2013**, *1*, 2248-2255; b) Z.-S. Wu, A. Winter, L. Chen, Y. Sun, A. Turchanin, X. Feng, K. Müllen, Adv. Mater. **2012**, *24*, 5130-5135.
[20] Y. Su, Y. Zhang, X. Zhuang, S. Li, D. Wu, F. Zhang, X. Feng, Carbon **2013**, *62*, 296-301.
[21] Z. Lu, G. Chen, S. Siahrostami, Z. Chen, K. Liu, J. Xie, L. Liao, T. Wu, D. Lin, Y. Liu, T.F. Jaramillo, J.K. Nørskov, Y. Cui, Nat. Catal. **2018**, *1*, 156-162.
[22] C. Hu, L. Dai, Angew. Chem. Int. Ed. **2016**, *55*, 11736-11758.
[23] L. Dai, Y. Xue, L. Qu, H.-J. Choi, J.-B. Baek, Chem. Rev. **2015**, *115*, 4823-4892.
[24] L. Xue, Y. Li, X. Liu, Q. Liu, J. Shang, H. Duan, L. Dai, J. Shui, Nat. Commun. **2018**, *9*, 3819.
[25] J. Duan, S. Chen, M. Jaroniec, S.Z. Qiao, ACS Catal. **2015**, *5*, 5207-5234.
[26] a) Z. Yang, Z. Yao, G. Li, G. Fang, H. Nie, Z. Liu, X. Zhou, X.A. Chen, S. Huang, ACS Nano **2012**, *6*, 205-211; b) S. Zhong, L. Zhou, L. Wu, L. Tang, Q. He, J. Ahmed, J. Power Sources **2014**, *272*, 344-350; c) C. Han, X. Bo, Y. Zhang, M. Li, L. Guo, J. Power Sources **2014**, *272*, 267-276; d) H. Kim, K. Lee, S.I. Woo, Y. Jung, Phys. Chem. Chem. Phys. **2011**, *13*, 17505-17510; e) P.H. Matter, L. Zhang, U.S. Ozkan, J. Catal. **2006**, *239*, 83-96; f) R.A. Sidik, A.B. Anderson, N.P. Subramaniam, S.P. Kumaraguru, B.N. Popov, J. Phys. Chem. B **2006**, *110*, 1787-1793; g) P.H. Matter, E. Wang, M. Arias, E.J. Biddinger, U.S. Ozkan, J. Mol. Catal. A: Chem. **2007**, *264*, 73-81; h) L. Yu, X. Pan, X. Cao, P. Hu, X. Bao, J. Catal. **2011**, *282*, 183-190; i) Y. Zheng, Y. Jiao, J. Chen, J. Liu, J. Liang, A. Du, W. Zhang, Z. Zhu, S.C. Smith, M. Jaroniec, G.Q. Lu, S.Z. Qiao, J. Am. Chem. Soc. **2011**, *133*, 20116-20119.
[27] C.-S. Liu, X.-C. Liu, G.-C. Wang, R.-P. Liang, J.-D. Qiu, J. Electroanal. Chem. **2014**, *728*, 41-50.
[28] E. Graciá-Espino, X. Jia, T. Wågberg, J. Phys. Chem. C **2014**, *118*, 2804-2811.
[29] S. Zhao, H. Yin, L. Du, L. He, K. Zhao, L. Chang, G. Yin, H. Zhao, S. Liu, Z. Tang, ACS Nano **2014**, *8*, 12660-12668.
[30] Y. Wu, H. Yu, H. Wang, F. Peng, Chinese J. Catal. **2014**, *35*, 952-959.
[31] D. Usachov, O. Vilkov, A. Grüneis, D. Haberer, A. Fedorov, V.K. Adamchuk, A.B. Preobrajenski, P. Dudin, A. Barinov, M. Oehzelt, C. Laubschat, D.V. Vyalikh, Nano Lett. **2011**, *11*, 5401-5407.
[32] M. Yang, L. Zhou, J. Wang, Z. Liu, Z. Liu, J. Phys. Chem. C **2012**, *116*, 844-850.
[33] Z. Hou, X. Wang, T. Ikeda, K. Terakura, M. Oshima, M.-A. Kakimoto, Phys. Rev. B **2013**, *87*, 165401.
[34] P. Wu, P. Du, H. Zhang, C. Cai, Phys. Chem. Chem. Phys. **2013**, *15*, 6920-6928.
[35] a) A. Lherbier, A.R. Botello-Méndez, J.-C. Charlier, Nano Lett. **2013**, *13*, 1446-1450; b) A.R. Botello-Méndez, A. Lherbier, J.C. Charlier, Solid State Commun. **2013**, *175-176*, 90-100.
[36] T. Schiros, D. Nordlund, L. Pálová, D. Prezzi, L. Zhao, K.S. Kim, U. Wurstbauer, C. Gutiérrez, D. Delongchamp, C. Jaye, D. Fischer, H. Ogasawara, L.G.M. Pettersson, D.R. Reichman, P. Kim, M.S. Hybertsen, A.N. Pasupathy, Nano Lett. **2012**, *12*, 4025-4031.
[37] Y. Zhang, J. Ge, L. Wang, D. Wang, F. Ding, X. Tao, W. Chen, Sci. Rep. **2013**, *3*, 2771.
[38] F. Pan, J. Jin, X. Fu, Q. Liu, J. Zhang, ACS App. Mater. Interfaces **2013**, *5*, 11108-11114.
[39] T. Ikeda, M. Boero, S.-F. Huang, K. Terakura, M. Oshima, J.-I. Ozaki, J. Phys. Chem. C **2008**, *112*, 14706-14709.
[40] Z. Lin, G.H. Waller, Y. Liu, M. Liu, C.-P. Wong, Nano Energy **2013**, *2*, 241-248.
[41] B. Zheng, J. Wang, F.-B. Wang, X.-H. Xia, Electrochem. Commun. **2013**, *28*, 24-26.
[42] a) J. Vazquez-Arenas, A. Galano, D.U. Lee, D. Higgins, A. Guevara-García, Z. Chen, J. Mater. Chem. A **2014**, *4*, 975-990; b) H.-P. Cong, P. Wang, M. Gong, S.-H. Yu, Nano Energy **2014**, *3*, 55-63.
[43] K.R. Lee, K.U. Lee, J.W. Lee, B.T. Ahn, S.I. Woo, Electrochem. Commun. **2010**, *12*, 1052-1055.
[44] Z.-H. Sheng, L. Shao, J.-J. Chen, W.-J. Bao, F.-B. Wang, X.-H. Xia, ACS Nano **2011**, *5*, 4350-4358.
[45] M. Sun, X. Wu, Z. Xie, X. Deng, J. Wen, Q. Huang, B. Huang, Carbon **2017**, *125*, 401-408.
[46] H. Zhang, Y. Wang, D. Wang, Y. Li, X. Liu, P. Liu, H. Yang, T. An, Z. Tang, H. Zhao, Small **2014**, *10*, 3371-3378.
[47] J. Sun, S.E. Lowe, L. Zhang, Y. Wang, K. Pang, Y. Wang, Y. Zhong, P. Liu, K. Zhao, Z. Tang, H. Zhao, Angew. Chem. Int. Ed. **2018**, *57*, 16511-16515.
[48] L. Lai, J.R. Potts, D. Zhan, L. Wang, C.K. Poh, C. Tang, H. Gong, Z. Shen, J. Lin, R.S. Ruoff, Energy Environ. Sci. **2012**, *5*, 7936-7942.
[49] D.W. Boukhvalov, Y.-W. Son, Nanoscale **2012**, *4*, 417-420.
[50] a) L. Zhang, Z. Xia, J. Phys. Chem. C **2011**, *115*, 11170-11176; b) L. Zhang, J. Niu, L. Dai, Z. Xia, Langmuir **2012**, *28*, 7552-7559.
[51] T. Xing, Y. Zheng, L.H. Li, B.C.C. Cowie, D. Gunzelmann, S.Z. Qiao, S. Huang, Y. Chen, ACS Nano **2014**, *8*, 6856-6862.
[52] a) K. Gong, F. Du, Z. Xia, M. Durstock, L. Dai, Science **2009**, *323*, 760; b) X. Bo, C. Han, Y. Zhang, L. Guo, ACS App. Mater. Interfaces **2014**, *6*, 3023-3030.
[53] C. Zhang, R. Hao, H. Liao, Y. Hou, Nano Energy **2013**, *2*, 88-97.
[54] D. Wei, Y. Liu, Y. Wang, H. Zhang, L. Huang, G. Yu, Nano Lett. **2009**, *9*, 1752-1758.
[55] W.A. Saidi, J. Phys. Chem. Lett. **2013**, *4*, 4160-4165.
[56] Z. Hou, X. Wang, T. Ikeda, K. Terakura, M. Oshima, M.-A. Kakimoto, S. Miyata, Phys. Rev. B **2012**, *85*, 165439.
[57] S. Kabir, K. Artyushkova, A. Serov, P. Atanassov, ACS App. Mater. Interfaces **2018**, *10*, 11623-11632.
[58] S. Chen, J. Duan, M. Jaroniec, S.Z. Qiao, Angew. Chem. Int. Ed. **2013**, *52*, 13567-13570.
[59] D. Guo, R. Shibuya, C. Akiba, S. Saji, T. Kondo, J. Nakamura, Science **2016**, *351*, 361.
[60] T. Mondal, A.K. Bhowmick, R. Krishnamoorti, Chem. Mater. **2015**, *27*, 716-725.
[61] a) Z. Zhang, K. Chi, F. Xiao, S. Wang, J. Mater. Chem. A **2015**, *3*, 12828-12835; b) X. Xiong, C. Yang, G. Wang, Y. Lin, X. Ou, J.-H. Wang, B. Zhao, M. Liu, Z. Lin, K. Huang, Energy Environ. Sci. **2017**, *10*, 1757-1763.
[62] G.-L. Tian, M.-Q. Zhao, D. Yu, X.-Y. Kong, J.-Q. Huang, Q. Zhang, F. Wei, Small **2014**, *10*, 2251-2259.
[63] a) D.-S. Yang, D. Bhattacharya, S. Inandan, J. Park, J.-S. Yu, J. Am. Chem. Soc. **2012**, *134*, 16127-16130; b) H. Peng, Z. Mo, S. Liao, H. Liang, L. Yang, F. Luo, H. Song, Y. Zhong, B. Zhang, Sci. Rep. **2013**, *3*, 1765; c) S.-A. Wohlgemuth, R.J. White, M.-G. Willinger, M.-M. Titirici, M. Antonietti, Green Chem. **2012**, *14*, 1515-1523; d) G.-L. Tian, Q. Zhang, B. Zhang, Y.-G. Jin, J.-Q. Huang, D.S. Su, F. Wei, Adv. Funct. Mater. **2014**, *24*, 5956-5961; e) Z. Chen, D. Higgins, A. Yu, L. Zhang, J. Zhang, Energy Environ. Sci. **2011**, *4*, 3167-3192; f) Y. Zhao, L. Yang, S. Chen, X. Wang, Y. Ma, Q. Wu, Y. Jiang, W. Qian, Z. Hu, J. Am. Chem. Soc. **2013**, *135*, 1201-1204; g) J.-S. Li, S.-L. Li, Y.-J. Tang, K. Li, L. Zhou, N. Kong, Y.-Q. Lan, J.-C. Bao, Z.-H. Dai, Sci. Rep. **2014**, *4*, 5130.
[64] S. Ratso, I. Kruusenberg, M. Vikkisk, U. Joost, E. Shulga, I. Kink, T. Kallio, K. Tammeveski, Carbon **2014**, *73*, 361-370.
[65] D.C. Higgins, M.A. Hoque, F. Hassan, J.-Y. Choi, B. Kim, Z. Chen, ACS Catal. **2014**, *4*, 2734-2740.
[66] J. Shui, M. Wang, F. Du, L. Dai, Sci. Adv. **2015**, *1*, e1400129.
[67] a) B. Dai, K. Chen, Y. Wang, L. Kang, M. Zhu, ACS Catal. **2015**, *5*, 2541-2547; b) J. Zhang, L. Dai, ACS Catal. **2015**, *5*, 7244-7253.
[68] D. Deng, X. Pan, L. Yu, Y. Cui, Y. Jiang, J. Qi, W.-X. Li, Q. Fu, X. Ma, Q. Xue, G. Sun, X. Bao, Chem. Mater. **2011**, *23*, 1188-1193.
[69] a) H.-W. Liang, X. Zhuang, S. Brüller, X. Feng, K. Müllen, Nat. Commun. **2014**, *5*, 4973; b) C.V. Rao, C.R. Cabrera, Y. Ishikawa, J. Phys. Chem. Lett. **2010**, *1*, 2622-2627; c) J. Wu, S. Ma, J. Sun, J.I. Gold, C. Tiwary, B. Kim, L. Zhu, N. Chopra, I.N. Odeh, R. Vajtai, A.Z. Yu, R. Luo, J. Lou, G. Ding, P.J.A. Kenis, P.M. Ajayan, Nat. Commun. **2016**, *7*, 13869; d) W. Ding, Z. Wei, S. Chen, X. Qi, T. Yang, J. Hu, D. Wang, L.-J. Wan, S.F. Alvi, L. Li, Angew. Chem. **2013**, *125*, 11971-11975.
[70] S. Wang, D. Yu, L. Dai, J. Am. Chem. Soc. **2011**, *133*, 5182-5185.
[71] S. Shanmugam, T. Osaka, Chem. Commun. **2011**, *47*, 4463-4465.
[72] Y. Tang, B.L. Allen, D.R. Kauffman, A. Star, J. Am. Chem. Soc. **2009**, *131*, 13200-13201.
[73] P.A. Denis, R. Faccio, A.W. Mombru, Chemphyschem **2009**, *10*, 715-722.
[74] A.Y.S. Eng, Z. Sofer, P. Šimek, J. Kosina, M. Pumera, Chem – Eur. J. **2013**, *19*, 15583-15592.
[75] J. Jin, F. Pan, L. Jiang, X. Fu, A. Liang, Z. Wei, J. Zhang, G. Sun, ACS Nano **2014**, *8*, 3313-3321.
[76] J. Liang, Y. Jao, M. Jaroniec, S.Z. Qiao, Angew. Chem. **2012**, *124*, 11664-11668.
[77] A.S. Mayorov, R.V. Gorbachev, S.V. Morozov, L. Britnell, R. Jalil, L.A. Ponomarenko, P. Blake, K.S. Novoselov, K. Watanabe, T. Taniguchi, A.K. Geim, Nano Lett. **2011**, *11*, 2396-2399.
[78] L. Zhang, J. Niu, M. Li, Z. Xia, J. Phys. Chem. C **2014**, *118*, 3545-3553.
[79] Y. Zhang, M. Chu, L. Yang, W. Deng, Y. Tan, M. Ma, Q. Xie, Chem. Commun. **2014**, *50*, 6382-6385.
[80] J.-E. Park, Y.J. Jang, Y.J. Kim, M.-S. Song, S. Yoon, D.H. Kim, S.-J. Kim, Phys. Chem. Chem. Phys. **2014**, *16*, 103-109.
[81] a) L. Arroyo-Ramírez, D. Rodríguez, W. Chaño, C.R. Cabrera, ACS App. Mater. Interfaces **2012**, *4*, 2018-2024; b) M.E.M. Buan, N. Muthuswamy, J.C. Walmsley, D. Chen, M. Rønning, Carbon **2016**, *101*, 191-202.
[82] P.A. Denis, Comput. Mater. Sci. **2013**, *67*, 203-206.
[83] C. Zhang, N. Mahmood, H. Yin, F. Liu, Y. Hou, Adv. Mater. **2013**, *25*, 4932-4937.
[84] Y.-T. Wang, A.-H. Lu, H.-L. Zhang, W.-C. Li, J. Phys. Chem. C **2011**, *115*, 5413-5421.
[85] a) Z. Liu, F. Peng, H. Wang, H. Yu, J. Tan, L. Zhu, Catal. Commun. **2011**, *16*, 35-38; b) Z. Liu, F. Peng, H. Wang, H. Yu, W. Zheng, X. Wei, J. Nat. Gas Chem. **2012**, *21*, 257-264.
[86] G.A. Snook, P. Kao, A.S. Best, J. Power Sources **2011**, *196*, 1-12.
[87] Y. Wen, B. Wang, C. Huang, L. Wang, D. Hulicova-Jurcakova, Chem – Eur. J. **2015**, *21*, 80-85.
[88] J.-I. Ozaki, N. Kimura, T. Anahara, A. Oya, Carbon **2007**, *45*, 1847-1853.
[89] L. Zhu, J. Wu, Q. Zhang, X. Li, Y. Li, X. Cao, J. Colloid Interface Sci. **2018**, *510*, 32-38.
[90] M.-S. Song, K.M. Lee, Y.R. Lee, I.Y. Kim, T.W. Kim, J.L. Gunjakar, S.-J. Hwang, J. Phys. Chem. C **2010**, *114*, 22134-22140.
[91] R. Li, Z. Wei, X. Gou, ACS Catal. **2015**, *5*, 4133-4142.
[92] J.P. Paraknowitsch, A. Thomas, Energy Environ. Sci. **2013**, *6*, 2839-2855.
[93] a) R. Li, W. Fan, G. Tian, H. Zhu, L. He, J. Cai, Q. Huang, Q. Cai, B. Li, Y. Bai, Z. Zhang, Y. Zhang, W. Wang, J. Li, F. Wei, H. Li, M. Jian, J. Li, Z. Zhang, R. Nielsen, D. Li, W. Gu, Z. Yang, Z. Xuan, O.A. Ryder, F.C.-C. Leung, Y. Zhou, J. Cao, X. Sun, Y. Fu, X. Fang, X. Guo, B. Wang, R. Hou, F. Shen, B. Han, N. Gao, N. Deng, Q. Wang, C. Yu, W. Nie, J. Wang, Z. Wu, H. Liang, J. Min, Q. Wu, S. Cheng, J. Ruan, M. Wang, Z. Shi, M. Wen, B. Liu, X. Ren, H. Zheng, D. Dong, K. Cook, G. Shan, H. Zhang, C. Kosid, X. Xie, Z. Lu, H. Zheng, Y. Li, C.C. Steiner, T.T.-Y. Lam, S. Lin, Q. Zhang, G. Li, J. Tian, T. Gong, H. Liu, D. Zhang, L. Fang, C. Ye, J. Zhang, W. Hu, A. Xu, Y. Ren, G. Zhang, M.W. Bruford, Q. Li, L. Ma, Y. Guo, N. An, Y. Hu, Y. Zheng, Y. Shi, Z. Li, Q. Liu, Y. Chen, J. Zhao, N. Qu, S. Zhao, F. Tian, X. Wang, H. Wang, L. Xu, X. Liu, T. Vinar, Y. Wang, T.-W. Lam, S.-M. Yiu, S. Liu, H. Zhang, D. Li, Y. Huang, X. Wang, G. Yang, Z. Jiang, J. Wang, N. Qin, L. Li, J. Li, L. Bolund, K. Kristiansen, G.K.-S. Wong, M. Olson, X. Zhang, S. Li, H. Yang, J. Wang, J. Wang, Nature **2009**, *463*, 311; b) Z. Zhang, B. Lu, J. Hao, W. Yang, J. Tang, Chem. Commun. **2014**, *50*, 11554-11557.
[94] J. Wang, K. Huo, L. Ma, L. Tang, D. Li, X. Huang, Y. Yuan, C. Li, W. Wang, W. Guan, H. Chen, C. Jin, J. Wei, W. Zhang, Y. Yang, Q. Liu, Y. Zhou, C. Zhang, Z. Wu, W. Xu, Y. Zhang, T. Liu, D. Yu, Y. Zhang, L. Chen, D. Zhu, X. Zhong, L. Kang, X. Gan, X. Yu, Q. Ma, J. Yan, L. Zhou, Z. Liu, Y. Zhu, T. Zhou, F. He, X. Yang, Mol. Syst. Biol. **2011**, *7*, 536.
[95] Y. Meng, D. Voiry, A. Goswami, X. Zou, X. Huang, M. Chhowalla, Z. Liu, T. Asefa, J. Am. Chem. Soc. **2014**, *136*, 13554-13557.
[96] a) J. Chen, H. Zhang, P. Liu, Y. Li, G. Li, T. An, H. Zhao, Carbon **2015**, *92*, 339-347; b) J. Xu, Y. Zhao, C. Shen, L. Guan, ACS App. Mater. Interfaces **2013**, *5*, 12594-12601.
[97] C.H. Choi, S.H. Park, S.I. Woo, Green Chem. **2011**, *13*, 406-412.
[98] C. Hu, L. Dai, Adv. Mater. **2017**, *29*, 1604942.
[99] J. Li, Y. Zhang, X. Zhang, J. Huang, J. Han, Z. Zhang, X. Han, P. Xu, B. Song, ACS App. Mater. Interfaces **2017**, *9*, 398-405.
[100] J. Xu, G. Dong, C. Jin, M. Huang, L. Guan, ChemSusChem **2013**, *6*, 493-499.
[101] S.-A. Wohlgemuth, F. Vilela, M.-M. Titirici, M. Antonietti, Green Chem. **2012**, *14*, 741-749.

This article is protected by copyright. All rights reserved.

2.Shao Y, Chang Y, Zhang S, et al. Impact of polymer backbone fluorination on the charge generation/recombination patterns and vertical phase segregation in bulk heterojunction organic solar cells[J]. Frontiers in chemistry, 2020, 8: 144. （SCI 检索收录二区，IF=5.221）

frontiers in Chemistry

ORIGINAL RESEARCH
published: 05 March 2020
doi: 10.3389/fchem.2020.00144

Impact of Polymer Backbone Fluorination on the Charge Generation/Recombination Patterns and Vertical Phase Segregation in Bulk Heterojunction Organic Solar Cells

Yanqiu Shao[1], Yuying Chang[1], Suju Zhang[1], Mingyue Bi[1], Shengjian Liu[2], Daliang Zhang[3], Shirong Lu[4] and Zhipeng Kan[4]**

[1] School of Chemistry and Chemical Engineering, Mudanjiang Normal University, Mudanjiang, China, [2] Guangzhou Key Laboratory of Materials for Energy Conversion and Storage, Guangdong Provincial Engineering Technology Research Center for Materials for Energy Conversion and Storage, School of Chemistry, South China Normal University (SCNU), Guangzhou, China, [3] Institute of Advanced Interdisciplinary Studies, Chongqing University, Chongqing, China, [4] Organic Semiconductor Research Center, Chongqing Institute of Green and Intelligent Technology, Chinese Academy of Sciences, Chongqing, China

OPEN ACCESS

Edited by:
Ergang Wang,
Chalmers University of Technology, Sweden

Reviewed by:
Lei Ying,
South China University of Technology, China
Hua Tan,
Xiangtan University, China

***Correspondence:**
Yanqiu Shao
shaoyanqiu1969@163.com
Zhipeng Kan
kanzhipeng@cigit.ac.cn

Specialty section:
This article was submitted to Physical Chemistry and Chemical Physics, a section of the journal Frontiers in Chemistry

Received: 16 December 2019
Accepted: 17 February 2020
Published: 05 March 2020

Citation:
Shao Y, Chang Y, Zhang S, Bi M, Liu S, Zhang D, Lu S and Kan Z (2020) Impact of Polymer Backbone Fluorination on the Charge Generation/Recombination Patterns and Vertical Phase Segregation in Bulk Heterojunction Organic Solar Cells. Front. Chem. 8:144. doi: 10.3389/fchem.2020.00144

Incorporating fluorine (–F) substituents along the main-chains of polymer donors and acceptors is an effective strategy toward efficient bulk-heterojunction (BHJ) solar cells. Specifically, F-substituted polymers often exhibit planar conformations, leading to favorable packing, and electronic coupling. However, the effects of fluorine substituents on the charge generation and recombination characteristics that determine the overall efficiency of BHJ active layers remain critically important issues to examine. In this report, two PBDT[2X]T polymer analogs –poly[4,8-bis((2-ethylhexyl)oxy)benzo[1,2-*b*:4,5-*b*']dithiophene-thiophene] [PBDT[2H]T] and its F-substituted counterpart poly[4,8-bis((2-ethylhexyl)oxy)benzo[1,2-*b*:4,5-*b*']dithiophene-3,4-difluoro-thiophene] [PBDT[2F]T]—are studied to systematically examine how –F substituents impact the blend morphology, charge generation, carrier recombination and extraction in BHJ solar cells. Considering the large efficiency differences between PBDT[2H]T- and PBDT[2F]T-based BHJ devices, significant emphasis is given to characterizing the out-of-plane morphology of the blend films as vertical phase-separation characteristics are known to have dramatic effects on charge transport and carrier extraction in polymer-fullerene BHJ solar cells. Herein, we use electron energy loss spectroscopy (EELS) in tandem with charge transport characterization to examine PBDT[2X]T-fullerene blend films. Our analyses show that PBDT[2H]T and PBDT[2F]T possess very different charge generation, recombination and extraction characteristics, resulting from distinct aggregation, and phase-distribution within the BHJ blend films.

Keywords: bulk heterojunction, polymer backbone fluorination, charge generation and recombination, vertical phase segregation, organic solar cells

INTRODUCTION

The substitution of π-conjugated polymer chains with fluorine (–F) substituents is an effective strategy in the design of polymer donors and acceptors for efficient bulk-heterojunction (BHJ) solar cells (Li et al., 2019). Of all considered benefits, recent studies have shown that F-substituted polymers are prone to adopt planar conformations, and favorable packing and electronic coupling patterns (Do et al., 2016; Tang et al., 2020) broader consensus emphasizes their propensity for higher backbone rigidity and a more pronounced tendency to aggregate on going from solutions to thin-film (Li et al., 2014, 2020; Fei et al., 2015) compared to their counterparts without –F substituents –material properties that can be taken advantage of in BHJ solar cell optimization processes (Liu et al., 2014).

In spite of the significant experimental work pursued to describe the correlations between –F substitutions in polymer main-chains and polymer performance in actual BHJ solar cells, direct connections between material structure and device efficiency are often difficult to make. Considering F-substituted polymers, some important questions remain, in particular with regard to how molecular scale effects directed by –F substituents can impact mesoscale morphologies, charge generation, and recombination patterns in BHJ thin films (Eisner et al., 2019). Since experimental methods are lacking to directly probe how functional group substitutions affect polymer main-chain packing and aggregation, computational methodologies must be employed to provide this level of description (Do et al., 2017). Quantum mechanical calculations can describe intrinsic *inter*-monomer torsion profiles, which govern the main-chain dihedral distribution in the bulk; whereas molecular dynamics (MD) simulations can provide information on main-chain packing arrangements in the bulk, and the propensity to form ordered π-π aggregates (Li et al., 2020). To further molecular-scale insights and qualitatively describe the types of aggregates that prevail in the bulk, solid-state nuclear magnetic resonance (SS-NMR) spectroscopy can be used to complement computational methodologies, providing an experimental analysis of the conformational landscape defined by the polymer main-chains in the bulk (Do et al., 2016). Based on this methodology, both theoretical and experimental studies on the influence of –F substitutions on *intra*- and *inter*-molecular interactions have shown that the higher polymer backbone planarity and rigidity are at the origin of local packing effects (to which relate binding energies and electronic coupling between neighboring chains), and that these result in distinct aggregation and charge transport patterns (Do et al., 2016). As an example, in poly(3-alkyl-4-fluoro)thiophenes (F-P3AT) (Fei et al., 2015) –F substitutions have been shown to raise the melting temperature and crystallization enthalpy of the P3AT analogs –variations in intrinsic material properties that are consistent with backbone planarization effects, inducing main-chain rigidity, and higher propensity for aggregation in the solid state. In turn, employing F-P3AT, field-effect transistor mobilities increased by a factor of 5 compared to P3AT-based transistors (Fei et al., 2015).

In polymer-based BHJ solar cells, –F substitutions of monomer units including: thiophenes (Jo et al., 2014; Wolf et al., 2015), **carbazoles** (Kim et al., 2014), **thienothiophenes** (Chen et al., 2009; Carsten et al., 2011), **benzothiadiazole** (Stuart et al., 2013; Yang et al., 2013; Kim et al., 2014), **benzotriazoles** (Price et al., 2011; Chen et al., 2019), **benzodithiophenes** (Chen et al., 2009; Jo et al., 2014; Wolf et al., 2015), **indacenodithiophenes** (Schroeder et al., 2012), **and anthradithiophenes** (Gundlach et al., 2008) have resulted in improved device efficiencies. Due to the strong inductive electron-withdrawing nature of –F substituents (element of highest electronegativity), F-substituted polymer donors possess lower-lying highest occupied molecular orbital (HOMO) energy levels than their counterparts without –F substituents –leading to higher open-circuit voltages (V_{OC}) in BHJ solar cells (Chen et al., 2009, 2019). Setting aside their important effect on the electronic properties of both polymer donors (Chen et al., 2009; Price et al., 2011; Schroeder et al., 2012; Stuart et al., 2013; Yang et al., 2013; Jo et al., 2014; Kim et al., 2014; Li et al., 2014; Wolf et al., 2015; Do et al., 2016; Kawashima et al., 2016) and acceptors (Liu et al., 2016, 2017), –F substitutions may also affect the preferential orientation of polymer aggregates relative to device substrates, impacting device performance in some instances (Stuart et al., 2013), although here we note that those effects are not well-understood to date, and there were reports with opposite conclusions (Kawashima et al., 2016). Most systematic studies of the effect of F-substituents in polymers (comparing F-substituted vs. unsubstituted, analogous model systems) have converged to the idea that device performance can vary dramatically when either donor or acceptor contain F-substituents in their main-chain (Jo et al., 2014; Wolf et al., 2015; Kawashima et al., 2016). Along those lines, several reports have shown that concurrent synthetic and device optimizations of fluorinated polymers can yield significant improvements in BHJ thin films as carrier mobilities increase, and that those improvements result in direct BHJ solar cell efficiency increments (Jo et al., 2014; Wolf et al., 2015). Using pump probe ultrafast spectroscopy, Gorenflot et al. (2018) reported the exciton dissociation, charge separation, and extraction in BHJ solar cells with fluorine substituents, and it was found that in the fluorinated polymer BHJ solar cells, the charge generation is about 40% higher than that of the non-fluorinated polymer BHJ solar cells, resulting from improved exciton diffusion to the heterojunction, in conjunction with more efficient charge separation and reduced geminate recombination losses (Gorenflot et al., 2018). However, the effects of the presence of F-substituted polymers on the charge generation and recombination characteristics in BHJ solar cells, and how those effects translate into practical device efficiency variations, remain critically important issues to examine. In addition, significant emphasis is given to characterize the "out-of-plane" morphology of the blend films, because vertical phase-separation characteristics are known to have dramatic effects on charge transport and carrier extraction in polymer-fullerene BHJ solar cells.

In this report, we examine the charge generation and recombination in two analogous model systems in BHJ solar cells: poly[4,8-bis((2-ethylhexyl)oxy)benzo[1,2-*b*:4,5-*b*']dithiophene-thiophene] [PBDT[2H]T] and its F-substituted counterpart poly[4,8-bis((2-ethylhexyl)oxy)benzo[1,2-*b*:4,5-*b*']dithiophene-3,4-difluoro-thiophene [PBDT[2F]T]. **(Chart 1)**

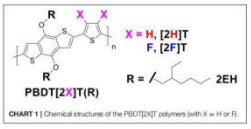

CHART 1 | Chemical structures of the PBDT[2X]T polymers (with X = H or F).

The PBDT[2X]T polymers dispersion index and molecular weight are shown in **Table S3**. Specifically, we systematically characterize carrier transport, recombination, and extraction across the BHJ devices and turn to morphological studies to establish a fuller understanding of how aggregation and vertical phase distributions impact the carrier dynamics, and in turn, BHJ solar cell efficiency.

RESULTS AND DISCUSSION

Optimized BHJ solar cells with direct device architecture were fabricated and tested under AM1.5G solar illumination (100 mW/cm^2). The PBDT[2X]T:PC$_{71}$BM blend solutions (ratio: 1:1.5, wt/wt) were cast from a hot chlorobenzene (CB; *ca.* 90°C) solution with 5 vol% 1-chloronaphthalene (CN) (cf. details in the SI; film thicknesses in the range 80–90 nm). The energy level diagram of PBDT[2H]T, PBDT[2F]T and PC$_{71}$BM in **Figure S2**. **Figure S3** accounts for the relative thin-film absorbance and solution absorption coefficients of the PBDT[2H]T and PBDT[2F]T. As shown in **Figure 1A** and **Table 1**, the optimized PBDT[2H]T:PC$_{71}$BM (2HT-based) and PBDT[2F]T:PC$_{71}$BM (2FT-based) BHJ solar cells achieved very distinct efficiencies and device statistics including standard deviations are provided in the Supplementary Information (**Tables S1, S2**; **Figure S1**). While the optimized 2HT-based devices achieved V_{OC} of *ca.* 0.77 V, modest $J_{SC}$of *ca.* 5.2 mA/cm^2, and fill-factors (*FFs*) of 60.1%, the 2FT-based counterpart yields a substantially higher J_{SC} of *ca.* 9.3 mA/cm^2, and a concurrently improved *FF* (73.3%) and V_{OC} (*ca.* 0.89 V). Overall, 2FT-based devices achieve a power conversion efficiency (PCE) improvement of more than two-fold, reaching up to 6.2% (*avg.* 6.1%) under the same film-casting conditions.

The large differences in J_{SC} values between 2HT- and 2FT-based BHJ solar cells (**Table 1**) are shown in the *J*-*V* curves provided in **Figure 1A**, and are consistent with the integrated current from the external quantum efficiency (EQE) spectra shown in **Figure 1B** (± 6%). In **Figure 1B**, 2FT-based devices show the most prominent spectral response in the range 350–600 nm, with EQE values reaching *ca.* 75% at 500 nm (EQE >60% in the range 350–580 nm). In comparison, EQE values in 2HT-based devices remain below 50% across the visible spectrum –observations implying that the substitution pattern in PBDT[2X]T correlates with significant variations in BHJ solar cell performance.

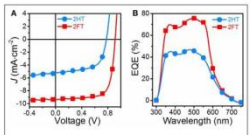

FIGURE 1 | **(A)** *J*-*V* curves and **(B)** EQE spectra for optimized 2HT- (blue) and 2FT-based (red) BHJ solar cells with PC$_{71}$BM as the acceptor; AM1.5G solar illumination (100 mW/cm^2).

TABLE 1 | PV performance of the 2HT- and 2FT-based BHJ solar cells[a,b].

	V_{OC} (V)	J_{SC} (mA/cm^2)	*FF* (%)	Avg. PCE (%)	Max. PCE (%)
2HT	0.77	5.2	60.1	2.4	2.7
2FT	0.89	9.3	73.3	6.1	6.2

[a]Average values across >10 devices across 3 substrates. [b]Device statistics in the Supplementary Information, **Table S1**.

The competition between charge recombination and extraction governs the *FF* in BHJ solar cells and in turn device PCE. Meanwhile, both the loss of photogenerated carriers by recombination and charge extraction processes are limited by the carrier mobilities of the blend film for holes and electrons. To estimate the electron and hole mobilities in optimized PBDT[2X]T:PC$_{71}$BM blend films, we measured the dark current density-voltage characteristics of single-carrier devices (see experimental details in the SI) and then fitted the data using the space-charge-limited current (SCLC) (Giulianini et al., 2010) model described by the Mott-Gurney law (with a small field dependent term), as in following equation (Mihailetchi et al., 2005).

$$J(V) = \frac{9}{8}\varepsilon_0\varepsilon_r\mu_0 \exp\left(0.89\beta\sqrt{\frac{V-V_{bi}}{L}}\right)\frac{(V-V_{bi})^2}{L^3} \quad (1)$$

where ε_0 and ε_r are the dielectric permittivity of a vacuum and the active layer, *L* is the thickness of the active layer, *V* is the applied voltage, V_{bi} is the built-in voltage, μ_0 is the zero-field mobility, and β is the field-activation factor.

Figure 2 shows the dark *J*-*V* characteristics of the electron-only diode in the configuration ITO/Al/2XT:PC$_{71}$BM/Al (**Figure 2A**) and that for the hole-only diode with the architecture ITO/MoO$_3$/2XT:PC$_{71}$BM/MoO$_3$/Ag (**Figure 2B**) (cf. additional details in the Supplementary Information, **Figure S4**). The fitting to the experimental results (solid lines in **Figure 2**; the parameters used in the fitting and films with other thickness are detailed in the Supplementary Information, **Figure S4**, **Tables S4** and **S5**) indicate that the electron mobility in the BHJ blend films with the 2HT and 2FT polymers is comparable: *ca.* 6.2 ×

10^{-4} cm^2 V^{-1}s^{-1} and 6.8 × 10^{-4} cm^2 V^{-1}s^{-1}, respectively. In contrast, the hole mobility in the 2HT- and 2FT-based blend films are an order of magnitude different: *ca.* 4.4 × 10^{-6} vs. 3.5 × 10^{-5} cm^2 V^{-1}s^{-1}, respectively. As a result, the carrier mobilities are significantly more balanced in 2FT-based devices –which represents an important parameter in explaining the performance differences observed between 2HT- and 2FT-based BHJ solar cells.

The charge collection probability, $P_c(I, V)$, is defined as the ratio between J_{SC} and saturated photocurrent density $J_{ph,sat}$ at reversed biases when the current density becomes independent of the applied voltage (cf. details in the Supplementary Information, **Figures S5, S6**) (Cowan et al., 2010; Mori et al., 2014).

Figure 3A shows the P_c ($I, -2V$) for the 2HT- and 2FT-based BHJ solar cells as a function of incident light intensity *I*. In both cases, the P_c values were almost independent of incident light intensity over the range 0.17–1.20 suns, yielding *ca.* 80% for 2FT-based devices and 95% for their 2FT counterparts. When the charge carrier density increases with increasing light intensity, the magnitude of the bimolecular recombination rate should also increase and the P_c should decrease at higher values of *I* if the device suffers non-negligible bimolecular recombination at short-circuit. Therefore, the independence of P_c on *I* suggests that neither 2FT- nor 2FT-based devices suffer from bimolecular recombination under the short-circuit conditions.

To further examine whether carrier recombination was limiting device efficiency to a different extent in 2HT- and 2FT-based devices, we turned to a characterization of J_{SC} and V_{OC} as a function of incident light intensity. **Figure 3B** provides the dependence of J_{SC} as a function of incident light intensity plotted in a log-log scale and fitted to a power law (solid lines). As reported in earlier work, a power law dependence of J_{SC}on incident light intensity *I* in BHJ solar cells is described by $J_{sc} \propto I^{\alpha}$ (Cowan et al., 2010; Koster et al., 2011; Kyaw et al., 2013). An exponential factor of $\alpha = 1$ (or near unity) is indicative of efficient carrier extraction prior to recombination at short-circuit. For 2HT-based devices, the power law fit to the J_{SC} vs. *I* data yields an α value of 0.94 ± 0.01, while for 2FT-based devices, the J_{SC} vs. *I* data fit yields an α value of 0.99 ± 0.01, indicating that carrier extraction proceeds with more recombination losses in 2HT-based BHJ solar cells. Therefore, through the analysis of P_c and the J_{SC} dependence on incident light intensity, 2HT-based devices suffer from two major losses channels thus far: (i) a relatively poor charge generation pattern reflected in the low J_{SC} (6 mA/cm^{-2}) and (ii) non-negligible recombination losses prior to extraction.

In parallel, **Figure 3C** depicts the variation of V_{OC} vs. *I* in a natural log-linear scale and fitted to $V_{oc} \propto n\frac{kT}{q}\ln(I)$ (Cowan et al., 2010; Kyaw et al., 2013), where *k*, *T*, and *q* are the Boltzmann constant, temperature in Kelvin, and the elementary charge, respectively. The parameter *n* (usually in the range of 1–2) accounts for the presence of carrier traps across the active layers or interfaces with the electrodes, and any deviations from $n = 1$ (trap-free condition) reflects the existence of trap-assisted recombination. As shown in **Figure 3C**, $n = 1.24$ and 1.27 were inferred for 2HT- and 2FT-based BHJ solar cells, respectively –implying that both 2HT- and 2FT-based devices suffer from trap-assisted recombination at open-circuit. To further our understanding of the charge recombination and extraction patterns in 2HT- and 2FT-based BHJ solar cells, we turned to transient photovoltage and photocurrent analyses.

Transient photovoltage (TPV) measurements and their analysis provide information regarding the non-geminate recombination of charges within devices. TPV measurements record the voltage decay transient of a device held at open-circuit under continuous illumination after being subject to a short perturbative light pulse; the photovoltage decay can be used as a direct measure of charge recombination kinetics in BHJ solar cells at open-circuit. One or two time constants, representative of carrier lifetime, can be obtained by fitting the decay kinetics with mono- or bi-exponential equations, suggesting that one or two recombination routes can co-exist, that can generally be assigned to either bimolecular or/and trap-assisted recombination (Li et al., 2011; Liang et al., 2018). TPV measurements were performed on the 2HT- and 2FT-based BHJ solar cells to characterize the non-geminate recombination profile in the two systems.

In both 2HT- and 2FT- based BHJ solar cells, mono-exponential fits to the experimental kinetics data were found to be appropriate fitting equations. **Figure 4A** shows the normalized TPV responses for a 2FT-based device subjected to several incident light intensities (Data fitting details reported in the Supplementary Information, see **Figure S7**). The single carrier lifetime figure derived from the TPV fitting of 2HT- and 2FT-based devices correlate with a single carrier recombination loss channel, here trap-assisted recombination as determined from the variation of V_{OC} with illumination intensity discussed in the previous section. **Figure 4B** plots the carrier lifetime as a function of V_{OC} for the 2HT- and 2FT-based BHJ solar cells. As expected, the carrier lifetime decreases with increasing V_{OC}, and the carrier lifetime at 1 sun is estimated as 2.3 and 2.0 μs (comparable) for 2HT- and 2FT-based devices, respectively.

Carrier transport and extraction across BHJ active layers can be examined via transient photocurrent (TPC) measurements (Hwang et al., 2009; McNeill et al., 2009; Li and McNeill, 2011; Li et al., 2011, 2013; Gao et al., 2014; Tremolet de Villers et al., 2014; Liang et al., 2019); analyses that are particularly relevant to the study of carrier traps and trap-assisted recombination in BHJ solar cells. In these analyses, the occurrence and extent of carrier traps across the active layer and/or at the interfaces between the BHJ blend film and the electrodes are reflected in the dependence of device current response and shape on light intensity. Instances of carrier traps concentrated at BHJ active layer/electrode interfaces and impinging on charge extraction have been discussed in recent studies (Hwang et al., 2009; McNeill et al., 2009; Li and McNeill, 2011; Tremolet de Villers et al., 2014). For example, in direct BHJ device configurations, fullerenes accumulating at the anode induce transient current peaks, greatly surpassing the steady-state current during rise events. Using concurrent experimental results and theoretical models, it has been shown that fullerenes act as hole-blocking layers, hindering hole extraction at the anode and, in turn, lowering BHJ solar cell efficiency (Tremolet de Villers et al., 2014). Here, we examine the turn-on and turn-off dynamics of the 2HT- and 2FT-based devices using long light pulse excitations (200 μs; cf. details in the SI), allowing the current density to reach steady-state conditions.

Figure 5 depicts the normalized transient photocurrent for optimized 2HT- and 2FT-based devices (cf. conditions given in **Table 1**); supplementary data can be found in the Supplementary Information (**Figure S8**). **Figure 6B** shows that the fast dynamics of the 2FT-based devices contrast with that for 2HT-based devices in **Figure 6A**. The rise/fall times on the order of 2 μs (i.e., the time required to reach 90% of the maximum current from an initial 10%) obtained from 2FT-based active layers (**Figure 6B**) are practically independent of light intensity. In comparison, the TPC curves for the 2HT-based devices show a significant dependence on light intensity, with a fast-initial transient photocurrent peak at higher light intensities followed by a second, slower photocurrent decay component leveling off at the steady-state current (at short-circuit) within *ca.* 150 μs (**Figure 6A**). Comparing the turn-off dynamics of the 2HT- and 2FT-based devices: the fast *ca.* 2 μs decay and the absence of pronounced photocurrent tail observed in 2FT-based active layers contrast with the persistent, light-intensity-dependent photocurrent tail observed in 2HT-based active layers, which suggests that carrier collection is delayed by deep traps for as long as 200 μs in the 2HT-based devices. In general, the slower dynamic component (beyond 205 μs, **Figures 5A,B**) becomes less prominent as light intensity increases, suggesting that the traps are filled at higher light intensities and, as a result, their impact on charge transport becomes less pronounced (McNeill et al., 2009; Li and McNeill, 2011). Based on earlier discussions and prior reports (Heumueller et al., 2014; Tremolet de Villers

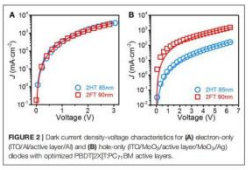

FIGURE 2 | Dark current density-voltage characteristics for **(A)** electron-only (ITO/Al/active layer/Al) and **(B)** hole-only (ITO/MoO$_3$/active layer/MoO$_3$/Ag) diodes with optimized PBDT[2X]T:PC$_{71}$BM active layers.

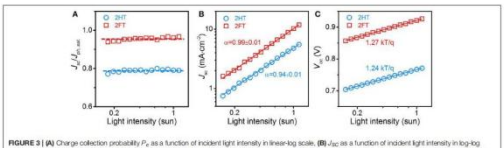

FIGURE 3 | **(A)** Charge collection probability P_c as a function of incident light intensity in linear-log scale, **(B)** J_{SC} as a function of incident light intensity in log-log scale, and **(C)** V_{OC} as a function of incident light intensity for the 2HT- and 2FT-based BHJ solar cells in linear-log scale. The solid lines in **(B,C)** correspond to fits to the data based on the equations $J_{sc} \propto I^{\alpha}$ and $V_{oc} \propto n\frac{kT}{q}\ln(I)$, respectively.

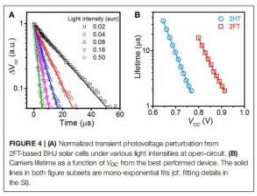

FIGURE 4 | **(A)** Normalized transient photovoltage perturbation from 2FT-based BHJ solar cells under various light intensities at open-circuit. **(B)** Carriers lifetime as a function of V_{OC} from the best performed device. The solid lines in both figure subsets are mono-exponential fits (cf. fitting details in the SI).

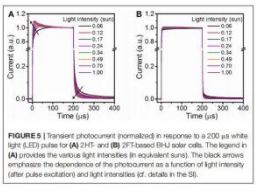

FIGURE 5 | Transient photocurrent (normalized) in response to a 200 μs white light (LED) pulse for **(A)** 2HT- and **(B)** 2FT-based BHJ solar cells. The legend in **(A)** provides the various light intensities (in equivalent suns). The black arrows emphasize the dependence of the photocurrent as a function of light intensity (after pulse excitation) and light intensities (cf. details in the SI).

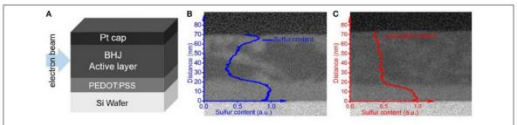

FIGURE 6 | (A) Schematic of the samples prepared for the cross-sectional TEM and EELS analyses. TEM cross-section images of the **(B)** 2HT- and **(C)** 2FT-based BHJ active layers cast on PEDOT:PSS and superimposed core-level sulfur analyses for the phase ratio mapping of polymer-rich (brighter regions) and fullerene-rich (darker regions) phases in the BHJ cross-section. The sulfur-content lines vs. distance from the substrate represented in subsets **(B,C)** capture the sulfur distribution averaged across the whole film cross section, and the distances are reported from the surface of the Si wafer (brightest layer) to the Pt capping layer (black).

et al., 2014; Pearson et al., 2016), the transient peak observed in 2HT-based devices may be the result of morphological effects buried within the active layer or occurring at the electrode interfaces. To probe those effects and provide a qualitative, macroscopic insight into the vertical distribution of polymer- and fullerene-rich domains across the optimized BHJ solar cells, we turned to electron energy loss spectroscopy (EELS) analyses performed from cross-sections of the BHJ thin films imaged by transmission electron microscopy (TEM) (cf. experimental details provided in the SI).

Figure 6 provides the EELS profiles collected from the cross-sections of BHJ thin films (cast from optimized conditions, see **Table 1**) with PBDT[2H]T (**Figure 6B**) and PBDT[2F]T (**Figure 6C**). Obtained from core-level sulfur analyses, the superimposed plots provide relative phase ratio mapping for the sulfur-rich—i.e., polymer-rich—and sulfur-deficient—i.e., fullerene-rich—regions in the BHJ cross-section. Here, we note that PEDOT:PSS interlayers were cast between the Si wafer (substrate) and the BHJ active layer to reproduce the morphology of the photoactive layers as obtained in actual BHJ solar cells; the high sulfur contents observed in the first *ca.* 20 nm distance from the Si wafer are thus consistent with the presence of the PEDOT:PSS. Beyond the PEDOT:PSS interface, the sulfur maps show two distinct phase distribution patterns for optimized 2HT- and 2FT-based BHJ active layers. On the one hand, **Figure 6B** suggests the existence of a gradient of polymer-rich phases across 2HT-based active layers on going from the PEDOT:PSS interface (anode) to the top interface (cathode in an actual BHJ device), with an apparent peak indicative of an accumulation of the polymer donor 2HT near the top interface (cathode). On the other hand, **Figure 6C** reflects a relatively uniform concentration profile of polymer and fullerene throughout the depth of the BHJ active layer. If supported by a more quantitative analysis of the vertical phase distribution in the BHJ active layers, the polymer-rich phase concentrated near the top interface (cathode) in 2HT-based active layers can hinder electron extraction by forming an electron-blocking layer. Concurrently, the apparently fullerene-rich phase concentrated near the PEDOT:PSS interface (anode) in 2HT-based active layers (**Figure 6B**) may be detrimental to hole extraction (hole-blocking layer).

CONCLUSION

To summarize, we systematically characterized the charge generation and recombination patterns in BHJ solar cells with PBDT[2H]T and its F-substituted counterpart PBDT[2F]T, and used EELS in tandem with charge transport characterization to examine PBDT[2X]T-fullerene blend films. The reduction in microsecond transient photocurrent allowed us to attribute the recombination losses in the 2HT-based BHJ solar cells to the hole extraction barrier/traps. However, the fluorinated polymer donor 2FT- based photoactive layer had a more uniformly distributed polymer/fullerene blend throughout most of the depth of the film with a thin fullerene accumulation layer at the anode, without showing the reduction in photocurrent. Thus, 2FT-based BHJ solar cells showed more efficient charge generation, extraction, and higher hole mobility compared with those of the 2HT-based BHJ solar cells, leading to higher V_{OC}, J_{SC}, FF, and overall device performance. The vertical phase segregation features of the 2HT- and 2FT-based BHJ solar cells were confirmed with EELS (sulfur mapping). The –F substituents impacted the polymer packing, which translates to the difference in aggregations from solution to film, thus the differences in polymer-fullerene phase mixing/composition in BHJ thin films. Our results provide an insight into the fluorination effects on the thin film BHJ compositions, especially the vertical phase, thus the device efficiency, providing a direct evidence of benefits from fluorination of polymers.

DATA AVAILABILITY STATEMENT

All datasets generated for this study are included in the article/supplementary material.

AUTHOR CONTRIBUTIONS

ZK, YS, YC, and SLu proposed the idea of this paper and contributed to analize the experiment results and wring the paper. YC and ZK contributed to the fabrication of the solar cells and characterization, DZ conducted the TEM. SLi contributed to the synthesis of the donor. SZ and MB conducted SCLC.

FUNDING

This work was financially supported by the National Natural Science Foundation of China (No. 61805245, 2180509), CAS Pioneer Hundred Talents Program (Y82A060Q10, Y92A160Q10), Recruitment Program of Global Experts (R52A199Z10), Higher education teaching reform of Heilongjiang Province of China (SJGY20190688), Heilongjiang Provincial Department of Education's Scientific Research Project (1352MSYYB006), Natural Science Foundation of Chongqing (cstc2015jcyjB0628 and cstc2017rgzn-zdyfX0030), the Guangdong Natural Science Foundation (No. 2016A030310428), and Guangzhou Science and Technology Foundation (No. 201904010361). Science and Technology Innovation Project of Mudanjiang Normal University (kjcx2019-22mdjnu).

SUPPLEMENTARY MATERIAL

The Supplementary Material for this article can be found online at: https://www.frontiersin.org/articles/10.3389/fchem.2020.00144/full#supplementary-material

REFERENCES

Carsten, B., Szarko, J. M., Son, H. J., Wang, W., Lu, L., He, F., et al. (2011). Examining the effect of the dipole moment on charge separation in donor-acceptor polymers for organic photovoltaic applications. *J. Am. Chem. Soc.* 133, 20468–20475. doi: 10.1021/ja208642b

Chen, H.-Y., Hou, J., Zhang, S., Liang, Y., Yang, G., Yang, Y., et al. (2009). Polymer solar cells with enhanced open-circuit voltage and efficiency. *Nat Photon* 3, 649–653. doi: 10.1038/nphoton.2009.192

Chen, Y., Zhang, Q., Du, M., Li, G., Li, Z., Huang, H., et al. (2019). Benzotriazole-based p-type polymers with thieno [3, 2-b] thiophene π-bridges and fluorine substituents to realize high Voc. *ACS Publ.* 1, 906–913. doi: 10.1021/acsapm.9b00156

Cowan, S. R., Roy, A., and Heeger, A. J. (2010). Recombination in polymer-fullerene bulk heterojunction solar cells. *Phys. Rev. B* 82:245207. doi: 10.1103/PhysRevB.82.245207

Do, K., Ravva, M. K., Wang, T., and Brédas, J.-L. (2017). Computational methodologies for developing structure–morphology–performance relationships in organic solar cells: a protocol review. *Chem. Mater.* 29, 346–354. doi: 10.1021/acs.chemmater.6b03111

Do, K., Saleem, Q., Ravva, M. K., Cruciani, F., Kan, Z., Wolf, J., et al. (2016). Impact of fluorine substituents on π-conjugated polymer main-chain conformations, packing, and electronic couplings. *Adv. Mater.* 28, 8197–8205. doi: 10.1002/adma.201601282

Eisner, F. D., Azzouzi, M., Fei, Z., Hou, X., Anthopoulos, T. D., Dennis, T. J. S., et al. (2019). Hybridization of local exciton and charge-transfer states reduces nonradiative voltage losses in organic solar cells. *J. Am. Chem. Soc.* 141, 6362–6374. doi: 10.1021/jacs.9b01465

Fei, Z., Boufflet, P., Wood, S., Wade, J., Moriarty, J., Gann, E., et al. (2015). Influence of backbone fluorination in regioregular poly (3-alkyl-4-fluoro) thiophenes. *J. Am. Chem. Soc.* 137, 6866–6879. doi: 10.1021/jacs.5b02785

Gao, F., Li, Z., Wang, J., Rao, A., Howard, I. A., Abrusci, A., et al. (2014). Trap-induced losses in hybrid photovoltaics. *ACS Nano* 8, 3213–3221. doi: 10.1021/nn501185b

Giulianini, M., Waclawik, E. R., Bell, J. M., and Motta, N. (2010). Temperature and electric field dependent mobility in poly (3-hexylthiophene) diodes. *J. Appl. Phys.* 108:014512. doi: 10.1063/1.3460111

Gorenflot, J., Paulke, A., Piersimoni, F., Wolf, J., Kan, Z., Cruciani, F., et al. (2018). From recombination dynamics to device performance: quantifying the efficiency of exciton dissociation, charge separation, and extraction in bulk heterojunction solar cells with fluorine-substituted polymer donors. *Adv. Energy Mater.* 8:1701678. doi: 10.1002/aenm.201701678

Gundlach, D. J., Boyer, J. E., Park, S. K., Subramanian, S., Jurchescu, O. D., Hamadani, B. H., et al. (2008). Contact-induced crystallinity for high-performance soluble acene-based transistors and circuits. *Nat. Mater.* 7, 216–221. doi: 10.1038/nmat2122

Hemmerlet, T., Mateker, W. R., Sachs-Quintana, I. T., Vandewal, K., Bartelt, J. A., Burke, T. M., et al. (2014). Reducing burn-in voltage loss in polymer solar cells by increasing the polymer crystallinity. *Energy Environ. Sci.* 7, 2974–2980. doi: 10.1039/C4EE01842G

Hwang, I., McNeill, C. R., and Greenham, N. C. (2009). Drift-diffusion modeling of photocurrent transients in bulk heterojunction solar cells. *J. Appl. Phys.* 106:094506. doi: 10.1063/1.3247547

Jo, J. W., Jung, J. W., Wang, H.-W., Kim, P., Russell, T. P., and Jo, W. H. (2014). Fluorination of polythiophene derivatives for high performance organic photovoltaics. *Chem. Mater.* 26, 4214–4220. doi: 10.1021/cm5022296

Kawashima, K., Fukuhara, T., Suda, Y., Suzuki, Y., Koganezawa, T., Yoshida, H., et al. (2016). Implication of fluorine atom on electronic properties, ordering structures, and photovoltaic performance in naphthobisthiadiazole-based semiconducting polymers. *J. Am. Chem. Soc.* 138, 10265–10275. doi: 10.1021/jacs.6b05418

Kim, J., Yun, M. H., Kim, G.-H., Lee, J., Lee, S. M., Ko, S.-J., et al. (2014). Synthesis of PCDTBT-based fluorinated polymers for high open-circuit voltage in organic photovoltaics: towards an understanding of relationships between polymer energy levels engineering and ideal morphology control. *ACS Appl. Mater. Interfaces* 6, 7523–7534. doi: 10.1021/am500891z

Konter, L. J., Kemerink, M., Wienk, M. M., Mateerová, K., and Janssen, R. A. (2011). Quantifying bimolecular recombination losses in organic bulk heterojunction solar cells. *Adv. Mater. Weinheim.* 23, 1670–1674. doi: 10.1002/adma.201004311

Kyaw, A. K., Wang, D. H., Gupta, V., Leong, W. L., Ke, L., Bazan, G. C., et al. (2013). Intensity dependence of current-voltage characteristics and recombination in high-efficiency solution-processed small-molecule solar cells. *ACS Nano* 7, 4569–4577. doi: 10.1021/nn401267x

Li, M., Bin, H., Jiao, X., Wienk, M. M., Yan, H., and Janssen, R. A. (2020). Controlling the microstructure of conjugated polymers in high-mobility monolayer transistors via the dissolution temperature. *Angew. Chem. Int. Ed.* 59, 846–852. doi: 10.1002/anie.201911311

Li, W., Albrecht, S., Yang, L., Roland, S., Tumbleston, J. R., McAfee, T., et al. (2014). Mobility-controlled performance of thick solar cells based on fluorinated copolymers. *J. Am. Chem. Soc.* 136, 15566–15576. doi: 10.1021/ja5067724

Li, W., Xiao, Z., Smith, J. A., Cai, L., Li, D., Kilbride, R. C., et al. (2019). Enhancing the efficiency of PTB7-Th: C60 : IDFIC-based ternary solar cells with versatile third components. *Appl. Phys. Rev.* 6:041405. doi: 10.1063/1.5125438

Li, Z., Gao, F., Greenham, N. C., and McNeill, C. R. (2011). Comparison of the operation of polymer/fullerene, polymer/polymer, and polymer/nanocrystal solar cells: a transient photocurrent and photovoltage study. *Adv. Funct. Mater.* 21, 1419–1431. doi: 10.1002/adfm.201002154

Li, Z., Lakhwani, G., Greenham, N. C., and McNeill, C. R. (2013). Voltage-dependent photocurrent transients of PTB7:PC70BM solar cells: experiment and numerical simulation. *J. Appl. Phys.* 114:034502. doi: 10.1063/1.4813612

Li, Z., and McNeill, C. R. (2011). Transient photocurrent measurements of PCDTBT:PC70BM and PCPDTBT:PC70BM solar cells: evidence for charge trapping in efficient polymer/fullerene blends. *J. Appl. Phys.* 109:074513. doi: 10.1063/1.3573394

Liang, R. Z., Babics, M., Seitkhan, A., Wang, K., Geraghty, P. B., Lopatin, S., et al. (2018). Additive-morphology interplay and loss channels in "all-small-molecule" bulk-heterojunction (BHJ) solar cells with the nonfullerene acceptor IDTTBM. *Adv. Funct. Mater.* 28:1705464. doi: 10.1002/adfm.201705464

Liang, R. Z., Zhang, Y., Savikhin, V., Babics, M., Kan, Z., Wohlfahrt, M., et al. (2019). Higher mobility and carrier lifetimes in solution-processable small-molecule ternary solar cells with 11% efficiency. *Adv. Energy Mater.* 9:1802856. doi: 10.1002/aenm.201802856

Liu, S., Kan, Z., Thomas, S., Cruciani, F., Brédas, J. L., and Beaujuge, P. M. (2016). Thieno [3, 4-c] pyrrole-4, 6-dione-3, 4-difluorothiophene polymer acceptors for efficient all-polymer bulk heterojunction solar cells. *Angew. Chem.* 128, 13190–13194. doi: 10.1002/ange.201604307

Liu, S., Song, X., Thomas, S., Kan, Z., Cruciani, F., Laquai, F., et al. (2017). Thieno [3, 4-c] pyrrole-4, 6-dione-based polymer acceptors for high open-circuit voltage all-polymer solar cells. *Adv. Energy Mater.* 7:1602574. doi: 10.1002/aenm.201602574

Liu, X., Gu, L., Zhang, Q., Wu, J., Long, Y., and Fan, Z. (2014). All-printable band-edge modulated ZnO nanowire photodetectors with ultra-high detectivity. *Nat. Commun.* 5, 1–9. doi: 10.1038/ncomms5007

McNeill, C. R., Hwang, I., and Greenham, N. C. (2009). Photocurrent transients in all-polymer solar cells: trapping and detrapping effects. *J. Appl. Phys.* 106:024507. doi: 10.1063/1.3177337

Mihailetchi, V. D., Wildeman, J., and Blom, P. W. (2005). Space-charge limited photocurrent. *Phys. Rev. Lett.* 94:126602. doi: 10.1103/PhysRevLett.94.126602

Mori, D., Benten, H., Okada, I., Ohkita, H., and Ito, S. (2014). Highly efficient charge-carrier generation and collection in polymer/polymer blend solar cells with a power conversion efficiency of 5.7%. *Energy Environ. Sci.* 7, 2939–2943. doi: 10.1039/C4EE01326C

Pearson, A. J., Hopkinson, P. E., Couderc, E., Domanski, K., Abdi-Jalebi, M., and Greenham, N. C. (2016). Critical light instability in CB/DIO processed PBDTTT-EFT:PC71BM organic photovoltaic devices. *Org. Electron.* 30, 225–236. doi: 10.1016/j.orgel.2015.12.024

Price, S. C., Stuart, A. C., Yang, L., Zhou, H., and You, W. (2011). Fluorine substituted conjugated polymer of medium band gap yields 7% efficiency in polymer–fullerene solar cells. *J. Am. Chem. Soc.* 133, 4625–4631. doi: 10.1021/ja1112595

Schroeder, B. C., Huang, Z., Ashraf, R. S., Smith, J., D'Angelo, P., Watkins, S. E., et al. (2012). Silaindacenodithiophene-based low band gap polymers – the effect of fluorine substitution on device performances and film morphologies. *Adv. Funct. Mater.* 22, 1663–1670. doi: 10.1002/adfm.201102941

Stuart, A. C., Tumbleston, J. R., Zhou, H., Li, W., Liu, S., Ade, H., et al. (2013). Fluorine substituents reduce charge recombination and drive structure and morphology development in polymer solar cells. *J. Am. Chem. Soc.* 135, 1806–1815. doi: 10.1021/ja309289u

Tang, H., Yan, C., Karethedath, S., Yin, H., Gao, Y., Gao, J., et al. (2020). Deciphering the role of fluorination: morphological manipulation prompts charge separation and reduces carrier recombination in all-small-molecule photovoltaics. *Solar RRL.* 2020:1900528. doi: 10.1002/solr.201900528

Tremolet de Villers, B. J., MacKenzie, R. C. I., Jasieniak, J. J., Treat, N. D., and Chabinyc, M. L. (2014). Linking vertical bulk-heterojunction composition and transient photocurrent dynamics in organic solar cells with solution-processed MoOx contact layers. *Adv. Energy Mater.* 4:1301290. doi: 10.1002/aenm.201301290

Wolf, J., Cruciani, F., El Labban, A., and Beaujuge, P. M. (2015). Wide band-gap 3,4-difluorothiophene-based polymer with 7% solar cell efficiency: an alternative to P3HT. *Chem. Mater.* 27, 4184–4187. doi: 10.1021/acs.chemmater.5b01530

Yang, L., Tumbleston, J. R., Zhou, H., Ade, H., and You, W. (2013). Disentangling the impact of side chains and fluorine substituents of conjugated donor polymers on the performance of photovoltaic blends. *Energy Environ. Sci.* 6, 316–326. doi: 10.1039/C2EE23233A

Conflict of Interest: The authors declare that the research was conducted in the absence of any commercial or financial relationships that could be construed as a potential conflict of interest.

Copyright © 2020 Shao, Chang, Zhang, Bi, Liu, Zhang, Lu and Kan. This is an open-access article distributed under the terms of the Creative Commons Attribution License (CC BY). The use, distribution or reproduction in other forums is permitted, provided the original author(s) and the copyright owner(s) are credited and that the original publication in this journal is cited, in accordance with accepted academic practice. No use, distribution or reproduction is permitted which does not comply with these terms.

3.Yang W, Jiang R, Liu C, et al. Triptycene-Based Porous Chalcogen-Bonded Organic Frameworks[J]. Crystal Growth & Design, 2021, 21(11): 6497-6503. （SCI 检索收录二区，IF=4.076）

CRYSTAL GROWTH & DESIGN

pubs.acs.org/crystal Article

Triptycene-Based Porous Chalcogen-Bonded Organic Frameworks

Wei Yang,* Rong Jiang, Chao Liu, Baoqiu Yu, Xue Cai,* and Hailong Wang

Cite This: *Cryst. Growth Des.* 2021, 21, 6497−6503 Read Online

ACCESS | Metrics & More | Article Recommendations | Supporting Information

Downloaded via UNIV SCIENCE AND TECHNOLOGY BEIJING on December 3, 2021 at 01:20:24 (UTC).
See https://pubs.acs.org/sharingguidelines for options on how to legitimately share published articles.

ABSTRACT: Two chalcogen-bonded organic frameworks (denoted as CBOFs), CBOF-1 and CBOF-2, have been constructed by the self-assembly of a custom-made triptycenetris(2,1,3-benzoselendiazole) (TTB) as an organic building block. As revealed by the results of single crystal X-ray diffraction analysis, the combination of chalcogen bonding and Se···π interactions was conductive to the structural porosity of the obtained two compounds. In particular, CBOF-1 exhibited a 3D 4-connected **lvt** topological framework with TTB simplified as the 4-connected node. The open pore channels of CBOF-1 possessed a pore size of 4.2 Å, of which the theoretical accessible pore volume occupied 35.6% of the total volume. Structural porosity of CBOF-2 was filled by tetrahydrofuran molecules, and the accessible volume percentage was calculated for 29.5%. Due to the flexible structure, degassed CBOF-1 displayed permanent porosity using carbon dioxide as an absorbate at 196 K. In the present study, a new kind of porous organic framework with permanent porosity has been revealed.

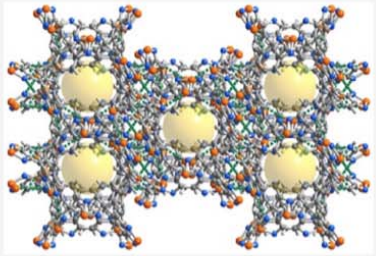

INTRODUCTION

High order porous materials possess intriguing applications in the diverse realms such as gas storage, molecule separation, guest recognition, and heterogeneous catalysis, and so on.[1−5] Porous molecule-based crystalline materials such as metal−organic frameworks (MOFs)[6−9] and covalent organic frameworks (COFs)[10−16] are able to achieve the open functional voids with control of the size, shape, and uniformity as well as precise structural design from the atomic and molecular perspective. Besides polymeric MOFs and COFs via coordination and covalent interaction, respectively, hydrogen-bonded organic frameworks (HOFs)[17−24] and porous organic cages (POCs)[21−32] have been obtained by the self-assembly of discrete molecule modules with intrinsic or extrinsic voids through the weak hydrogen-bonding interaction and/or van der Waals force. Such reticular materials have been extensively fabricated and investigated in recent decades and have been found to be complementary to each other. Inspired by the development of diverse frameworks, exploring new and alternative approaches to construct porous molecule crystalline materials has attracted intense interest.

The anisotropic electron density distribution on the surface of atoms is an intrinsic characteristic of molecules, leading to an electron density that alternates between high and low around atoms. Thus, to stabilize the supramolecular assembly, the interactions between the negative and positive atoms/regions from different molecules are formed. Halogen bonding is generated by halogen atoms interacting with nucleophiles from elements of groups 13−16 in the periodic table, representing a kind of attractive interaction for the organization of molecular functional materials.[33,34] As pioneered by Prof. Barbour from discrete organic building blocks, such interaction has been used to produce porous halogen-bonded organic frameworks.[35−38] Alternatively, close chalcogen bonding contact has been found to occur between group 16 elements and nucleophiles.[39] In general, all sulfur, selenium, and tellurium atoms are able to form chalcogen bonds, and the bond strength is increased by following the increased polarizability of the chalcogen elements. The directionalities of chalcogen bonds are particularly similar to that of halogen bonds in terms of the crystal engineering thereof to a certain extent, enabling similar self-assembly behaviors.[40,41] As a result, prior research on halogen-bonded organic frameworks has provided inspiration for the present study, and for exploring the possibility of porous chalcogen-bonded organic frameworks. Notably, to the present knowledge, there are few examples of chalcogen-bonded organic assembly[42] and molecule capsules[43−46] with guest molecules included in the voids, and there has been no report on such materials with permanent porosity after solvent removal of solvent. Thus, the aforementioned direction of the corresponding research is of considerable significance.

In the present study, a new triptycene-containing organic linker, triptycenetris(2,1,3-benzoselendiazole) (TTB), was conceived and prepared, as shown in Scheme 1a. The

Received: August 17, 2021
Revised: October 3, 2021
Published: October 19, 2021

ACS Publications © 2021 American Chemical Society

https://doi.org/10.1021/acs.cgd.1c00942
Cryst. Growth Des. 2021, 21, 6497−6503

Scheme 1. (a) Synthesis and Molecular Structure of Triptycene-Based Organic Linker of TTB for the Construction of Porous Supramolecular Frameworks. (b) Formation of Chalcogen-Bonded Ribbon-like Structure by 2,1,3-Benzoselendiazole

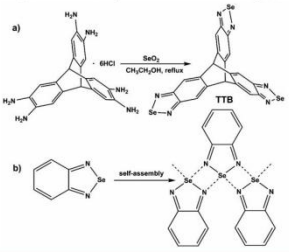

crystallization of TTB in different conditions resulted in the generation of two porous supramolecular frameworks, CBOF-1 and CBOF-2. The results of single crystal X-ray diffraction analysis revealed that CBOF-1 was formed by TTB building blocks through chalcogen bonding and Se···π interactions, thereby allowing for a structure containing open interconnecting channels with the size of 5.8 Å. CBOF-2 had a porous architecture containing 1D channels with a smaller diameter of 5.2 Å stabilized by chalcogen bonding and Se···π interactions. A hysteretic adsorption of CO_2 adsorbate at 196 K was monitored, indicating the flexible structure dynamics for the activated phase of CBOF-1. By using chalcogen bonding to construct porous supramolecular crystals with permanent porosity, a preliminary development has been presented in the present study.

EXPERIMENTAL SECTION

Synthesis of TTB. A mixture of hexaammonium triptycene hexachloride[47] (563.2 mg, 1.0 mmol) and 6 equiv of SeO_2 (666.0 mg, 6.0 mmol), and ethanol (40 mL) were added in a 100 mL flask. The mixture was refluxed for 12 h under nitrogen protection (Scheme 1). After cooling to room temperature, TTB was obtained through vacuum filtration and washed using 20 mL of ethanol. The product was dried at room temperature in a yield of 63%. ^{1}H NMR (400 MHz, $CDCl_3$): δ (ppm) 7.90 (s, 6H), 5.68 (s, 2H); ^{13}C NMR (100 MHz, $CDCl_3$): δ (ppm) 159.61, 141.85, 117.62, 52.29. Elemental analysis of TTB calcd. (%) for $C_{20}H_6N_6Se_3$: C 42.20, H 1.42, N 14.76; found: C 42.24, H 1.39, N 15.01. IR/cm^{-1} (KBr): 1640 (m) 1594 (s), 1439(m), 1286 (s), 881 (m), 759 (s). Single crystals of CBOF-1 and CBOF-2 were obtained by diffusing n-hexane into the chloroform and tetrahydrofuran solution, respectively, containing TTB (30 mg) at room temperature.

Crystallographic Measurement. An Oxford Diffraction Xcalibur, Eos, Gemini diffractometer with a Mo *Kα* radiation source (λ = 0.7107 Å) and Cu *Kα* radiation source (λ = 1.54178 Å) was used to collect crystallographic data for CBOF-1 and CBOF-2, respectively, at 150 K. The resolution and refinement of crystal structures of CBOF-1 and CBOF-2 relied on the SHELXS-2014 program.[48] The "SQUEEZE" command removed the disordered solvent molecules filled in the porosities of CBOF-1.[49] Table 1 summaries the parameters of unit cells and final refinement, and Table 2 exhibits the weak interaction in the supramolecular structures of CBOF-1 and CBOF-2. CCDC 2102442 and 2102443 for CBOF-1 and CBOF-2, respectively, which contain the supplementary crystallographic data, have free access from the Cambridge Crystallographic Data Centre *via* www.ccdc.cam.ac.uk/data_request/cif.

Table 1. Crystallographic and Refinement Parameters for Chalcogen-Bonded CBOF-1 and CBOF-1

crystal data	CBOF-1	CBOF-2
system	tetragonal	monoclinic
space group	$I\bar{4}2d$	$C2/c$
molecular formula[a]	$C_{20}H_6N_6Se_3$	$C_{21}H_{12}N_6O_{1.25}Se_3$
formula weight[a]	569.20	659.33
a/Å	16.5175(10)	23.3021(8)
b/Å	16.5175(10)	9.3111(3)
c/Å	18.5371(2)	44.7307(17)
α/deg	90	90
β/deg	90	96.949(3)
γ/deg	90	90
volume/Å^3	5057.44(8)	9833.8(6)
Z	8	16
density/g/cm^3	1.495	1.818
solvent-accessible[b] void space/%	35.8	29.5
theoretical pore volume/cm^3/g	0.24[a]	0.19[a]
refinement parameters	R_1 = 0.0481[c]	R_1 = 0.0724[c]
	wR_2 = 0.1556[c]	wR_2 = 0.1672[c]
CCDC No.	2102442	2102443

[a]Calculation based on the crystal structures using PLATON software. [b]$R_1 = \sum||F_o| - |F_c||/\sum|F_o|$. [c]$wR_2 = [\sum w(F_o^2 - F_c^2)^2/\sum w(F_o^2)^2]^{1/2}$.

Table 2. Chalcogen-Bonding Interactions in CBOF-1 and CBOF-2

Se···X	distance (Å)	symmetric code
1		
Se2···N1#1	3.323	$1.5 - y, 1 - x, -0.25 + z$
Se2···N1#2	3.323	$1.5 - y, 0.5 + x, 1.5 - z$
N1···Se#3	3.323	$-0.5 + y, 1.5 - x, 1.5 - z$
N1···Se#4	3.323	$1 - y, -x, 1 - z$
2		
Se1···N7	2.934	
N2···Se4	3.270	
Se1···N10#1	3.237	$1 - x, y, 1.5 - z$
Se2···O2#2	3.357	$x, 1 + y, z$
Se2···N6#3	3.356	$-0.5 + x, 0.5 + y, z$
Se3···O1#2	3.676	$x, 1 + y, z$
N5···Se6#4	3.733	$x, -y, -0.5 + z$
N6···Se2#5	3.356	$0.5 + x, -0.5 + y, z$
Se4···N7#6	3.763	$1.5 - x, 0.5 + y, 1.5 - z$
Se6···N5#4	3.733	$x, -y, -0.5 + z$
N10···Se1#1	3.237	$1 - x, y, 1.5 - z$
Se5···N7#7	3.644	$-0.5 + x, -0.5 + y, z$

RESULTS AND DISCUSSIONS

Design Principle and Synthesis of TTB. In order to construct a new kind of porous supramolecular framework through the self-assembly of organic modules, the Cambridge Structural Database for chalcogen-bonded crystal structures was explored. The formation of chalcogen bonds is preferred by 2,1,3-benzoselendiazole derivatives.[50] The possible ribbon-like connection is similar to that derived from 4,5-diiodobutitied benzimidazolone analogues through hydrogen-bonding.[51] Inspired by the prominent triptycene-based HOF with a considerably high specific surface area of 3020 m^2 g^{-1} pioneered by Prof. Mastalerz,[11] a new organic molecule was designed and prepared by incorporating the 2,1,3-benzoselendiazole unit into a rigid D_{3h}-symmetric triptycene structure. The reaction between hexaammonium triptycene hexachloride and selenium oxide led to TTB being used as a building block, as shown in Figures S1 and S2 (Supporting Information). The TTB molecule was optimized with the B3lyp 6-31g* basis set.[52−55] The surface electrostatic potential distribution map was obtained by using Multiwfn software[56] and VMD processing,[57] as presented in Figure S3 (Supporting Information). The different colors on the molecular electrostatic potential map represent the different electrostatic potentials of different regions. The surrounding nitrogen atoms exhibited a blue color, indicating negative electronegativity. Contrastingly, the surrounding selenium atoms displayed a red color, implying positive electronegativity. Such results suggest that Se atoms prefer to interact with electrophiles. The chalcogen bond between selenium and nitrogen atoms was expected to direct TTB into porous supramolecular frameworks. The crystallization of TTB in different conditions led to the formation of two compounds, CBOF-1 and CBOF-2.

Crystal Structures of 1 and 2. As revealed by the results of single crystal X-ray diffraction analysis in Figures 1 and 2, the two newly obtained supramolecular compounds, CBOF-1 and CBOF-2, had porous structures. CBOF-1 comes from the tetragonal system with $I\bar{4}2d$, as shown in Table 1, which also shows that the unit cell of CBOF-1 contained eight TTB molecules. Each TTB molecule was connected to the neighboring four modules through chalcogen-bonding interactions, as revealed in Figure 1a and Table 2. The distance of Se···N was 3.323 Å, which is in the normal region of the Se···N length.[58] The supramolecular moieties were further extended to a 3D supramolecular structure. TTB was approximately simplified as a 4-connected node, allowing for a $\{4^1\cdot8^2\}$ lvt net

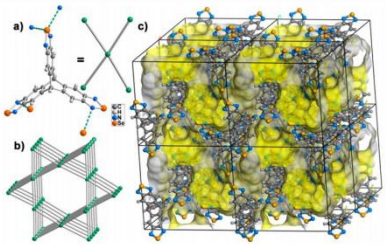

Figure 1. Crystal structures of CBOF-1 displaying (a) a TTB molecule (regarded as four-connected node) and corresponding weak connection with adjacent building blocks. (b) A simplified 4-connected topology linked through chalcogen bonding interactions. (c) A chalcogen-bonded structure showing the 3D channel pore surfaces highlighted as yellow/gray (inner/outer).

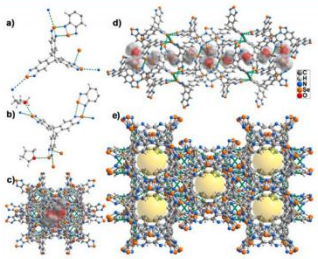

Figure 2. Crystal structures of CBOF-2 exhibiting (a, b) a TTB molecule with corresponding weak connection to adjacent building blocks. (c, d) A supramolecular tubular structure containing THF molecules in top and side view, respectively. (e) A chalcogen-bonded structure showing the 1D channels.

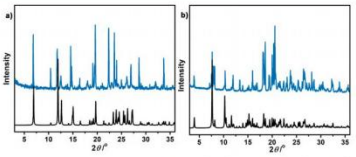

Figure 3. Comparison in powder X-ray diffraction patterns for as-synthesized (cyan) and simulated (black) CBOF-1 (a) and CBOF-2 (b), respectively.

topology (Figure 1b). Additionally, the neighbor TTB molecules were further linked by Se···π interactions to stabilize the porous structure, as shown in Figures 1c and S4 (Supporting Information). The porous channels interconnected with a size of 4.2 Å. The void accounted for 35.8% of the total volume, corresponding to the pore volume density of 0.24 cm^3 g^{-1}.

The diffusion of hexane into a THF solution of TTB produced CBOF-2, which originated from the monoclinic system with the $C2/c$ space group. There are two kinds of crystallographically dependent TTB molecules (Figure 2a,b). Both kinds of TTB linked with the other five organic building blocks *via* chalcogen-bonding interactions, with the Se···N length in the range of 2.934−3.733 Å. However, only one kind of TTB connected two THF molecules through Se···O interactions. Chalcogen bonds directed the formation of the porous tubular structure of CBOF-2 with the smallest size of 3.4 Å, and THF molecules were filled in the porosities of this compound (Figure 2c,d). Se···π interactions were also observed in CBOF-2, as presented in Figure S5 (Supporting Information). The tubular subunits were further assembled through chalcogen-bonding interactions, resulting in a 3D porous supramolecular structure shown in Figure 2e. Compared with CBOF-1, voids accounted for only 29.8% of the total pore volume of CBOF-2, and the pore volume density was 0.19 cm^3 g^{-1}.[59] The bulk materials for CBOF-1 and CBOF-2 were verified through a power X-ray diffractometer. The consistent powder X-ray diffraction (PXRD) patterns between the experiments and simulations for CBOF-1 and CBOF-2 illustrate the good purity thereof (Figure 3).

The thermal stability of these two compounds was determined, and the curves of temperature-dependent weigh

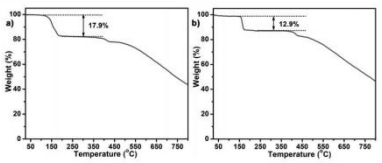

Figure 4. Thermogravimetric analysis curves of CBOF-1 (a) and CBOF-2 (b).

loss are shown in Figure 4. The solvent molecules filled in the porosities of CBOF-1 started to lose from ca. 105 to 195 °C, leading to 17.9% weight loss (Figure 4a). The TTB building block was decomposed at ca. 350 °C. Regarding CBOF-2, solvent molecules accounted for 12.9% of the total weight and escaped in the temperature region of 155−185 °C (Figure 4b). The higher temperature began to remove the solvent molecules in CBOF-1 than CBOF-2, which indicates the stronger solvent-framework interaction in the former compound. After degassing at room temperature, there was an obvious change observed in terms of the PXRD patterns of the as-synthesized sample and the activated sample for CBOF-1 (Figure S6, Supporting Information). Additionally, the crystallinity of activated CBOF-1 was significantly deteriorated. However, CBOF-1 exhibited the hysteretic CO_2 sorption behavior at 196 K with the uptake of 72 cm^3 g^{-1} at 760 mmHg (Figure 5). The profile indicates the flexible structure of

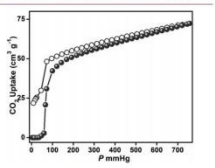

Figure 5. CO_2 sorption of CBOF-1 at 196 K.

CBOF-1. For CBOF-2, the sample was still crystalline after degassing at 150 °C according to the PXRD pattern (Figure S7, Supporting Information). Despite remaining crystalline, there was no gas sorption observed, even for the CO_2 adsorbate at 196 K, which could be attributed to the stable solvent molecules included in the porosity of CBOF-2.

CONCLUSIONS

In summary, two porous supramolecular frameworks have been successfully prepared from a triptycene derivative via chalcogen bonding and Se···π interactions. The crystal structures have been analyzed in detail. One compound exhibited a hysteretic adsorption of carbon dioxide at 196 K, indicating the presence of a dynamic activated framework. Such results show not only the ability of chalcogen bonding in producing porous molecule crystals but also the permanent porosity. The present study can provide a benchmark for the construction of new porous supramolecular frameworks with diverse applications.

ASSOCIATED CONTENT

Supporting Information

The Supporting Information is available free of charge at https://pubs.acs.org/doi/10.1021/acs.cgd.1c00942.

NMR spectra of TTB, check-cif, and powder XRD patterns of activated CBOF-1 and CBOF-2 (PDF)

Accession Codes

CCDC 2102442 and 2102443 contain the supplementary crystallographic data for this paper. These data can be obtained free of charge via www.ccdc.cam.ac.uk/data_request/cif, or by emailing data_request@ccdc.cam.ac.uk, or by contacting The Cambridge Crystallographic Data Centre, 12 Union Road, Cambridge CB2 1EZ, UK; fax: +44 1223 336033.

AUTHOR INFORMATION

Corresponding Authors

Wei Yang − *Beijing Key Laboratory for Science and Application of Functional Molecular and Crystalline Materials, Department of Chemistry and Chemical Engineering, School of Chemistry and Biological Engineering, University of Science and Technology Beijing, Beijing 100083, China;* orcid.org/0000-0001-5854-7568; Email: yangwei@ustb.edu.cn

Xue Cai − *Mudanjiang Normal University, Mudanjiang 157011, China;* Email: xuecai@mdjnu.edu.cn

Authors

Rong Jiang − *Beijing Key Laboratory for Science and Application of Functional Molecular and Crystalline Materials, Department of Chemistry and Chemical Engineering, School of Chemistry and Biological Engineering,*

University of Science and Technology Beijing, Beijing 100083, China

Chao Liu − *Beijing Key Laboratory for Science and Application of Functional Molecular and Crystalline Materials, Department of Chemistry and Chemical Engineering, School of Chemistry and Biological Engineering, University of Science and Technology Beijing, Beijing 100083, China*

Baoqin Yu − *Beijing Key Laboratory for Science and Application of Functional Molecular and Crystalline Materials, Department of Chemistry and Chemical Engineering, School of Chemistry and Biological Engineering, University of Science and Technology Beijing, Beijing 100083, China*

Hailong Wang − *Beijing Key Laboratory for Science and Application of Functional Molecular and Crystalline Materials, Department of Chemistry and Chemical Engineering, School of Chemistry and Biological Engineering, University of Science and Technology Beijing, Beijing 100083, China;* orcid.org/0000-0002-0138-2966

Complete contact information is available at: https://pubs.acs.org/10.1021/acs.cgd.1c00942

Notes

The authors declare no competing financial interest.

■ ACKNOWLEDGMENTS

Financial support from the Natural Science Foundation (NSF) of China (No. 21805005), Fundamental Research Funds for the Central Universities (No. FRF-TP-20-042A2), and University of Science and Technology Beijing is gratefully acknowledged. We are also very grateful for the help from Prof. Rui-Biao Lin at the Sun Yat-Sen University for the topology analysis.

■ REFERENCES

(1) Davis, M. E. Ordered Porous Materials for Emerging Applications. *Nature* **2002**, *417*, 813−821.
(2) Lin, R.; He, Y.; Li, P.; Wang, H.; Zhou, W.; Chen, B. Multifunctional Porous Hydrogen-Bonded Organic Framework Materials. *Chem. Soc. Rev.* **2019**, *48*, 1362−1389.
(3) Ding, M.; Flaig, R. W.; Jiang, H.; Yaghi, O. M. Carbon Capture and Conversion Using Metal-Organic Frameworks and MOF-based Materials. *Chem. Soc. Rev.* **2019**, *48*, 2783−2828.
(4) Geng, K.; He, T.; Liu, R.; Dalapati, S.; Tan, K. T.; Li, Z.; Tao, S.; Gong, Y.; Jiang, Q.; Jiang, D. Covalent Organic Frameworks: Design, Synthesis, and Functions. *Chem. Rev.* **2020**, *120*, 8814−8933.
(5) Zhao, M.; Yuan, K.; Wang, Y.; Li, G.; Guo, J.; Gu, L.; Hu, W.; Zhao, H.; Tang, Z. Metal−Organic Frameworks as Selectivity Regulators for Hydrogenation Reactions. *Nature* **2016**, *539*, 76−80.
(6) Yi, J.-D.; Si, D.-H.; Xie, R.; Yin, Q.; Zhang, M.-D.; Wu, Q.; Chai, G.-L.; Huang, Y.-B.; Cao, R. Conductive Two-Dimensional Phthalocyanine-based Metal−Organic Framework Nanosheets for Efficient Electroreduction of CO_2. *Angew. Chem., Int. Ed.* **2021**, *60*, 17108−17114.
(7) He, T.; Kong, X.-J.; Li, J.-R. Chemically Stable Metal−Organic Frameworks: Rational Construction and Application Expansion. *Acc. Chem. Res.* **2021**, *54*, 3083−3094.
(8) Lin, R.-B.; Li, L.; Zhou, H.-L.; Wu, H.; He, C.; Li, S.; Krishna, R.; Li, J.; Zhou, W.; Chen, B. Molecular Sieving of Ethylene from Ethane Using a Rigid Metal−Organic Framework. *Nat. Mater.* **2018**, *17*, 1128−1133.
(9) Wen, H.-M.; Liao, C.; Li, L. B.; Alsalme, A.; Alothman, Z.; Krishna, R.; Wu, H.; Zhou, W.; Hu, J.; Chen, B. A Metal−Organic Framework with Suitable Pore Size and Dual Functionalities for Highly Efficient Post-Combustion CO_2 Capture. *J. Mater. Chem. A* **2019**, *7*, 3128−3134.
(10) Guan, X.; Chen, F.; Fang, Q.; Qiu, S. Design and Applications of Three Dimensional Covalent Organic Frameworks. *Chem. Soc. Rev.* **2020**, *49*, 1357−1384.
(11) Wang, Z.; Yang, Y.; Zhao, Z.; Zhang, P.; Zhang, Y.; Liu, J.; Ma, S.; Cheng, P.; Chen, Y.; Zhang, Z. Green Synthesis of Olefin-linked Covalent Organic Frameworks for Hydrogen Fuel Cell Applications. *Nat. Commun.* **2021**, *12*, 1982.
(12) Qian, Y.; Li, D.; Han, Y.; Jiang, H.-L. Photocatalytic Molecular Oxygen Activation by Regulating Excitonic Effects in Covalent Organic Frameworks. *J. Am. Chem. Soc.* **2020**, *142*, 20763−20771.
(13) Lu, M.; Zhang, M.; Liu, C.-G.; Liu, J.; Shang, L.-J.; Wang, M.; Chang, J.-N.; Li, S.-L.; Lan, Y.-Q. Stable Dioxin-Linked Metallophthalocyanine Covalent Organic Frameworks as Photo-Coupled Electrocatalysts for CO_2 Reduction. *Angew. Chem., Int. Ed.* **2021**, *60*, 4864−4871.
(14) Dong, J.; Han, X.; Liu, Y.; Li, H.; Cui, Y. Metal−Covalent Organic Frameworks (MCOFs): A Bridge between Metal−Organic Frameworks and Covalent Organic Frameworks. *Angew. Chem., Int. Ed.* **2020**, *59*, 13722−13733.
(15) Zhang, M.-D.; Si, D.-H.; Yi, J.-D.; Zhao, S.-S.; Huang, Y.-B.; Cao, R. Conductive Phthalocyanine-Based Covalent Organic Framework for Highly Efficient Electroreduction of Carbon Dioxide. *Small* **2020**, *16*, 2005254.
(16) Han, B.; Ding, X.; Yu, B.; Wu, H.; Zhou, W.; Liu, W.; Wei, C.; Chen, B.; Qi, D.; Wang, H.; Wang, K.; Chen, Y.; Chen, B.; Jiang, J. Two-Dimensional Covalent Organic Frameworks with Cobalt(II)-Phthalocyanine Sites for Efficient Electrocatalytic Carbon Dioxide Reduction. *J. Am. Chem. Soc.* **2021**, *143*, 7104−7113.
(17) Zhang, X.; Li, L.; Wang, J.-X.; Wen, H.-M.; Krishna, R.; Wu, H.; Zhou, W.; Chen, Z.-N.; Li, B.; Qian, G.; Chen, B. Selective Ethane/Ethylene Separation in a Robust Microporous Hydrogen-Bonded Organic Framework. *J. Am. Chem. Soc.* **2020**, *142*, 633−640.
(18) Ye, Z.-M.; Zhang, X.-W.; Liao, P.-Q.; Xie, Y.; Xu, Y.-T.; Zhang, X.-F.; Wang, C.; Liu, D.-X.; Huang, N.-Y.; Qiu, Z.-H.; Zhou, D.-D.; He, C.-T.; Zhang, J.-P. A Hydrogen-Bonded net Hydrophobic Porous Molecular Crystal for Molecular-Sieving-like Separation of Butane and Isobutane. *Angew. Chem., Int. Ed.* **2020**, *59*, 23322−23328.
(19) Hisaki, I.; Xin, C.; Takahashi, K.; Nakamura, T. Designing Hydrogen-Bonded Organic Frameworks (HOFs) with Permanent Porosity. *Angew. Chem., Int. Ed.* **2019**, *58*, 11160−11170.
(20) Simard, M.; Su, D.; Wuest, J. D. Use of Hydrogen Bonds to Control Molecular Aggregation. Self-assembly of Three-Dimensional Networks with Large Chambers. *J. Am. Chem. Soc.* **1991**, *113*, 4696−4698.
(21) Luo, J.; Wang, J.-W.; Zhang, J.-H.; Lai, S.; Zhong, D.-C. Hydrogen-bonded Organic Frameworks: Design, Structures and Potential Applications. *CrystEngComm* **2018**, *20*, 5884−5898.
(22) Yu, B.; Li, L.; Liu, S.; Wang, H.; Liu, H.; Lin, C.; Liu, C.; Wu, H.; Zhou, W.; Li, X.; Wang, T.; Chen, B.; Jiang, J. Robust Biological Hydrogen-Bonded Organic Framework with Post-Functionalized Rhenium(I) Sites for Efficient Heterogeneous Visible-Light-Driven CO_2 Reduction. *Angew. Chem., Int. Ed.* **2021**, *60*, 8983−8989.
(23) Han, B.; Wang, H.; Wang, C.; Wu, H.; Zhou, W.; Chen, B.; Jiang, J. Postsynthetic Metalation of a Robust Hydrogen-Bonded Organic Framework for Heterogeneous Catalysis. *J. Am. Chem. Soc.* **2019**, *141*, 8737−8740.
(24) Yu, B.; Geng, S.; Wang, H.; Zhou, W.; Zhang, Z.; Chen, B.; Jiang, J. A Solid Transformation into Carboxyl Dimers Based on a Robust Hydrogen-Bonded Organic Framework for Propyne/Propylene Separation. *Angew. Chem., Int. Ed.* **2021**, DOI: 10.1002/anie.202110057.
(25) Tozawa, T.; Jones, J. T. A.; Swamy, S. I.; Jiang, S.; Adams, D. J.; Shakespeare, S.; Clowes, R.; Bradshaw, D.; Hasell, T.; Chong, S. Y.; Tang, C.; Thompson, S.; Parker, J.; Trewin, A.; Bacsa, J.; Slawin, A. M. Z.; Steiner, A.; Cooper, A. I. Porous Organic Cages. *Nat. Mater.* **2009**, *8*, 973−978.

(26) Su, K.; Wang, W.; Du, S.; Ji, C.; Zhou, M.; Yuan, D. Reticular Chemistry in the Construction of Porous Organic Cages. *J. Am. Chem. Soc.* **2020**, *142*, 18060−18072.
(27) Wang, H.; Jin, Y.; Sun, N.; Zhang, W.; Jiang, J. Post-synthetic Modification of Porous Organic Cages. *Chem. Soc. Rev.* **2021**, *50*, 8874−8886.
(28) McCaffrey, R.; Long, H.; Jin, Y.; Sanders, A.; Park, W.; Zhang, W. Template Synthesis of Gold Nanoparticles with an Organic Molecular Cage. *J. Am. Chem. Soc.* **2014**, *136*, 1782−1785.
(29) Mastalerz, M. Porous Shape-Persistent Organic Cage Compounds of Different Size, Geometry, and Function. *Acc. Chem. Res.* **2018**, *51*, 2411−2422.
(30) Wang, Z.; Sikdar, N.; Wang, S.; Li, X.; Yu, M.; Bu, X.; Chang, Z.; Zou, X.; Chen, Y.; Cheng, P.; Yu, K.; Zaworotko, M. J.; Zhang, Z. Soft Porous Crystal Based upon Organic Cages That Exhibit Guest-Induced Breathing and Selective Gas Separation. *J. Am. Chem. Soc.* **2019**, *141*, 9408−9414.
(31) Liu, C.; Liu, K.; Wang, C.; Liu, H.; Wang, H.; Su, H.; Li, X.; Chen, B.; Jiang, J. Elucidating Heterogeneous Photocatalytic Superiority of Microporous Porphyrin Organic Cage. *Nat. Commun.* **2020**, *11*, 1047.
(32) Sun, N.; Wang, C.; Wang, H.; Yang, L.; Jin, P.; Zhang, W.; Jiang, J. Multifunctional Tubular Organic Cage-Supported Ultrafine Palladium Nanoparticles for Sequential Catalysis. *Angew. Chem., Int. Ed.* **2019**, *58*, 18011−18016.
(33) Metrangolo, P.; Neukirch, H.; Pilati, T.; Resnati, G. Halogen Bonding Based Recognition Processes: A World Parallel to Hydrogen Bonding. *Acc. Chem. Res.* **2005**, *38*, 386−395.
(34) Gilday, L. C.; Robinson, S. W.; Barendt, T. A.; Langton, M. J.; Mullaney, B. R.; Beer, P. D. Halogen Bonding in Supramolecular Chemistry. *Chem. Rev.* **2015**, *115*, 7118−7195.
(35) Nikolayenko, V. I.; Castell, D. C.; van Heerden, D. P.; Barbour, L. J. Guest-Induced Structural Transformations in a Porous Halogen-Bonded Framework. *Angew. Chem., Int. Ed.* **2018**, *57*, 12086−12091.
(36) Gong, G.; Lv, S.; Han, J.; Xie, F.; Li, Q.; Xia, N.; Zeng, W.; Chen, Y.; Wang, L.; Wang, J.; Chen, S. Halogen-Bonded Organic Framework (XOF) Based on IodoniumBridged N···I+···N Interactions: A Type of Diphase Periodic Organic Network. *Angew. Chem., Int. Ed.* **2021**, *60*, 14831−14835.
(37) Pop, L.; Grosu, I. G.; Micliuş, M.; Hădade, N. D.; Pop, A.; Bende, A.; Terec, A.; Barbosu, M.; Grosu, I. Halogen-Bonded Organic Frameworks of Perfluoroiodo-and Perfluorodiiodobenzene with 2,2′,7,7′-Tetrapyridyl-9,9′-spirobifluorene. *Cryst. Growth Des.* **2021**, *21*, 1045−1054.
(38) Chonghoriboon, N.; Samakun, K.; Inprasit, T.; Kielar, F.; Dungkaew, W.; Wong, W.-Y.; Sung, H.-Y.; Ninković, D. B.; Zarić, S. D.; Chainok, K. Two-dimensional halogen-bonded organic frameworks based on the tetrabromobenzene-1,4-dicarboxylic acid building molecule. *CrystEngComm* **2020**, *22*, 24−34.
(39) Fourmigué, M.; Dhaka, A. Chalcogen bonding in crystalline dichalcogenides and selenocyanates From molecules of pharmaceutical interest to conducting materials. *Coord. Chem. Rev.* **2020**, *403*, 213094.
(40) Scilabra, P.; Terraneo, G.; Resnati, G. The Chalcogen Bond in Crystalline Solids: A World Parallel to Halogen Bond. *Acc. Chem. Res.* **2019**, *52*, 1313−1324.
(41) Strakova, K.; Assies, L.; Goujon, A.; Piazzolla, F.; Humeniuk, H. V.; Matile, S. Dithienothiophenes at Work: Access to Mechanosensitive Fluorescent Probes, Chalcogen-Bonding Catalysis, and Beyond. *Chem. Rev.* **2019**, *119*, 10977−11005.
(42) Gleiter, R.; Werz, D. B.; Rausch, B. J. A World Beyond Hydrogen Bonds? − Chalcogen-Chalcogen Interactions Yielding Tubular Structures. *Chem. - Eur. J.* **2003**, *9*, 2676−2683.
(43) Mehrparvar, S.; Wolper, C.; Gleiter, R.; Haberhauer, G. The Carbonyl Tellurazole Chalcogen Bond as a Molecular Recognition Unit: From Model Studies to Supramolecular Organic Frameworks. *Angew. Chem., Int. Ed.* **2020**, *59*, 17154−17161.
(44) Riwar, L.-J.; Trapp, N.; Root, K.; Zenobi, R.; Diederich, F. Supramolecular Capsules: Strong versus Weak Chalcogen Bonding. *Angew. Chem., Int. Ed.* **2018**, *57*, 17259−17264.
(45) Rahman, F.-U.; Tzeli, D.; Petsalakis, I. D.; Theodorakopoulos, G.; Ballester, P.; Rebek, J., Jr.; Yu, Y. Chalcogen Bonding and Hydrophobic Effects Force Molecules into Small Spaces. *J. Am. Chem. Soc.* **2020**, *142*, 5876−5883.
(46) Zhu, Y.-J.; Guo, Y.; Tang, M.-M.; Rebek, J., Jr.; Yu, Y. Dimeric Capsules Self-Assembled Through Halogen and Chalcogen Bonding. *Chem. Commun.* **2021**, *57*, 1543−1549.
(47) Mastalerz, M.; Sieste, S.; Cenić, M.; Oppel, I. M. Two-Step Synthesis of Hexaammonium Triptycene: An Air-Stable Building Block for Condensation Reactions to Extended Triptycene Derivatives. *J. Org. Chem.* **2011**, *76*, 6389−6393.
(48) Sheldrick, G. M. *SHELXL-2014*; University of Göttingen: Göttingen, Germany, 2014.
(49) Spek, A. L. Platon Squeeze: A Tool for the Calculation of the Disordered Solvent Contribution to the Calculated Structure Factors. *Acta Crystallogr., Sect. C: Struct. Chem.* **2015**, *71*, 9−18.
(50) Beniston, G.; Piguet, B.; Marrot, J.; Gommont, R. Supramolecular Association of 1,2,5-Chalcogenadiazoles: An Unexpected Self-assembled Dissymetric [Se/N]$_2$ Four-Membered Ring. *CrystEngComm* **2009**, *11*, 986−988.
(51) Mastalerz, M.; Oppel, I. M. Rational Construction of an Extrinsic Porous Molecular Crystal with an Extraordinary High Specific Surface Area. *Angew. Chem., Int. Ed.* **2012**, *51*, 5252−5255.
(52) Giannozzi, P.; Baroni, S.; Bonini, N.; Calandra, M.; Car, R.; Cavazzoni, C.; Ceresoli, D.; Chiarotti, G. L.; Cococcioni, M.; Dabo, I.; Dal Corso, A.; Fabris, S.; Fratesi, G.; de Gironcoli, S.; Gebauer, R.; Gerstmann, U.; Gougoussis, C.; Kokalj, A.; Lazzeri, M.; Martin-Samos, L.; Marzari, N.; Mauri, F.; Mazzarello, R.; Paolini, S.; Pasquarello, A.; Paulatto, L.; Sbraccia, C.; Scandolo, S.; Sclauzero, G.; Seitsonen, A. P.; Smogunov, A.; Umari, P.; Wentzcovitch, R. M. Quantum Espresso: a Modular and Open-source Software Project for Quantum Simulations of Materials. *J. Phys.: Condens. Matter* **2009**, *21*, 395502.
(53) Becke, A. D. Density-functional Exchange-energy Approximation with Correct Asymptotic Behavior. *Phys. Rev. A: At., Mol., Opt. Phys.* **1988**, *38*, 3098−3100.
(54) Hohenberg, P.; Kohn, W. Inhomogeneus Gas Electron. *Phys. Rev.* **1964**, *136*, B864−B871.
(55) Lee, C.; Yang, W.; Parr, R. G. Development of the Colle-Salvetti Correlation-energy formula into a functional of the electron density. *Phys. Rev. B: Condens. Matter Mater. Phys.* **1988**, *37*, 785−789.
(56) Lu, T.; Chen, F. Multiwfn: A Multifunctional Wavefunction Analyzer. *J. Comput. Chem.* **2012**, *33*, 580−592.
(57) Humphrey, W.; Dalke, A.; Schulten, K. VMD: Visual Molecular Dynamics. *J. Mol. Graphics* **1996**, *14*, 33−38.
(58) Ho, P. C.; Wang, J. Z.; Meloni, F.; Vargas-Baca, I. Chalcogen Bonding in Materials Chemistry. *Coord. Chem. Rev.* **2020**, *422*, 213464.
(59) Spek, A. L. *Platon, A Multipurpose Crystallographic Tool*; Utrecht University: Utrecht, The Netherlands, 2005.

4.Cai X, Ma Y, Zhou Q, et al. Synergistic efects of phases in the selective oxidation of isobutane over supported $(NH_4)_3HPMo_{11}VO_{40}$ catalysts[J]. Reaction Kinetics, Mechanisms and Catalysis, 2021, 133(1): 293-308.（SCI 检索收录四区，IF=1.762）

Reaction Kinetics, Mechanisms and Catalysis (2021) 133:293–308
https://doi.org/10.1007/s11144-021-01967-0

Synergistic effects of phases in the selective oxidation of isobutane over supported $(NH_4)_3HPMo_{11}VO_{40}$ catalysts

Xue Cai[1] · Yue Ma[1] · Qi Zhou[1] · Zitong Zhang[1] · Wenling Chu[2] · Weishen Yang[2]

Received: 3 February 2021 / Accepted: 15 March 2021 / Published online: 29 March 2021
© Akadémiai Kiadó, Budapest, Hungary 2021

Abstract
The supported 40 wt% $(NH_4)_3HPMo_{11}VO_{40}$ (APMV) catalysts over two different types of supports, supports-I ($Cs_3PMo_{12}O_{40}$, $Cs_{2.5}H_{0.5}PMo_{12}O_{40}$, $Cs_4PMo_{11}VO_{40}$ and $Cs_3HPMo_{11}VO_{40}$) and supports-II (CeO_2, WO_3/ZrO_2 and S-1 molecular sieve), were synthesized by deposition–precipitation method and further evaluated in the partial oxidation of isobutane to methacrylic acid (MAA) at 340 °C under atmospheric pressure. The fresh and used catalysts were characterized by N_2 adsorption/desorption, TG/DTG, XRD, FT-IR, Raman spectroscopy, pyridine- adsorption FT-IR and NH_3-TPD to investigate their structure, stability and surface acidity. The better results were obtained by impregnating 40 wt% active APMV phase onto the supports-I phase with same/similar Keggin structure, and it is believed that the formation of coherent interfaces between two structural well-matched phases with the same/similar Keggin anions greatly promotes interfacial transfer abilities of electrons and lattice oxygen, which is responsible for the efficient oxygen insertion to maximize MAA selectivity and conversion of isobutane. The current work provides a concept of phase synergy to design a promising catalyst for selective oxidation of isobutane.

Keywords Selective oxidation · Methacrylic acid · Synergetic effect · Heteropoly compounds

Introduction

Methacrylic acid (MAA) is an important organic chemical raw material for the production of methyl methacrylate (MMA), which is used as a monomer to produce poly methyl methacrylate (PMMA) and its derivatives. At present, the industrial

✉ Wenling Chu
cwl@dicp.ac.cn

[1] Mudanjiang Normal University, Mudanjiang 157011, China

[2] State Key Laboratory of Catalysis, Dalian Institute of Chemical Physics, Chinese Academy of Science, 457 Zhongshan Road, Dalian 116023, Liaoning, China

production of MAA usually adopts the acetone cyanohydrin method [1, 2], which suffers from many disadvantages such as the use of highly toxic HCN and the generation of a large amount of co-product ammonium bisulfate. On this regard, the partial oxidation of isobutane to MAA is a compelling alternative method due to the improved atom-economy, the inexpensive raw materials and negligible environmental impact. In this process, heteropoly compounds (HPCs) with Keggin-type structure have attracted great attention as effective catalysts due to the designed and controlled acidity and oxidizing ability [3–7].

Due to the low surface area of bulk HPCs and their poor thermal stability at high temperature, many attempts have been done to load the active HPCs component on a carrier with a large specific surface area, thereby increasing the catalytic efficiency and the stability by improving the catalyst dispersion [8–10]. Jing et al. impregnated 10–50 wt% $(NH_4)_3HPMo_{11}VO_{40}$ over $Cs_3PMo_{12}O_{40}$ and found that the conversion over pure HPC was 2.5% but it increased to 15.3% over the 40 wt%-supported catalysts, meanwhile the selectivity was 42% and 34% over supported and non-supported catalysts [11], respectively. It was reported that loading $H_4PMo_{11}VO_{40}$ on SiO_2 increased the maximum conversion that was five-times higher than that of unsupported one in partial oxidation of methacrolein, while the selectivity to MAA dropped and the stability was less [12]. The $(NH_4)_3HPMo_{11}VO_{40}$ catalyst supported on ZrO_2-modified SBA-15 exhibited high selectivity to CO_x (> 60%) coming from total oxidation of isobutane [11], leading to the rather low selectivity to MAA (1.6%). It is obvious that the catalytic activity and selectivity in the partial oxidation of isobutane to MAA are sensitive to support and catalyst dispersion. Besides increasing dispersion of active components, another way to improve the catalytic efficiency of the Keggin-type HPCs in the selective oxidation of isobutane to MAA, which has not been extensively explored up to know, is to search for synergetic effect between the supports and the active HPCs components.

Based on the above background, the aim of this study was to investigate the effects of phases synergy between active $(NH_4)_3HPMo_{11}VO_{40}$ (APMV) and different supports on the catalytic performance in selective oxidation of isobutane to methacrylic acid. In this work, we have purposely selected two different types of carriers, in which one type of supports (denoted as support-I) has similar primary structure with the active APMV catalyst, and another type of supports (denoted as support-II) has large specific surface areas but an obvious different structure with active APMV component, such as CeO_2, WO_3/ZrO_2, S-1 molecular sieve. Particular emphasis was given to a direct comparison in the structure and activity in order to elucidate synergetic effect of the phase due to well-match structure between active phase and support phase on the catalytic performance of the supported catalysts in the partial oxidation of isobutane to MAA.

Experimental

Preparation of catalysts

All supports investigated in this study, such as $Cs_xH_{3-x}PMo_{12}O_{40}$ (x = 2.5 and 3.0) [12, 13], $Cs_yH_{4-y}PMo_{11}VO_{40}$ (y = 4.0 and 3.0) [13], CeO_2 [14], WO_3/ZrO_2 [15] and S-1 molecular sieve [16] were prepared according to the corresponding literature.

$H_4PMo_{11}VO_{40}$ was synthesized as follows: 15.8 g of MoO_3 and 0.9 g of V_2O_5 were dissolved in 300 mL of deionized water and was heated to reflux at 150 °C in the oil bath. After 1 h, 1.2 g of H_3PO_4 (85 wt%) was added dropwise to the mixed solution above. The resulting mixture was kept at reflux for another 3 h with vigorous stirring to form a clear solution. The product was obtained by removing solvent under reduced pressure in a rotary evaporator at 60 °C, and further dried overnight at 80 °C in an oven.

A series of supported catalysts containing 40 wt% $(NH_4)_3HPMo_{11}VO_{40}$ (APMV) were prepared by the deposition–precipitation method. In a typical synthesis procedure, the carrier was suspended in 30 ml of deionized water, refluxed in a water bath at 40 °C, and stirred vigorously for 1 h. After 1 h, the aqueous solutions of NH_4NO_3 and $H_4PMo_{11}VO_{40}$ were simultaneously dropped into the suspension at a rate of 2 ml/min, stirred vigorously for 2 h, and rotary evaporated to obtain a precursor. All supported APMV catalysts were calcined in static air at 350 °C for 3 h.

As reference catalysts, bulk APMV was also synthesized by the same procedure without any support, and the phase mixtures of APMV + $Cs_3PMo_{12}O_{40}$ (weight ratio = 0.4:1.0) were obtained by mixing the respective powders and hand grinding them for 30 min.

Catalysts characterization

Thermogravimetric analysis (TGA) was performed using an instrument (NETZSCH STA 4493F) to monitor the thermal decomposition of the unsupported and supported catalysts (~ 10 mg) after calcined at 350 °C for 3 h. The catalyst was heated from room temperature to 600 °C or 800 °C at 10 °C/min under N_2 flow.

The phase structure of the as-synthesized catalysts was identified by X-ray diffraction (XRD, Rigaku D/MAX 2500/PC diffractometer) with Cu K_α radiation. Patterns were recorded in the 2θ range of 5°–40° at a scan speed of 5° min^{-1}.

Fourier transform infrared (FT-IR) spectra (Nicolet 6700 spectrometer) were recorded at a resolution of 4 cm^{-1} with 32scans.

The specific surface area was measured by N_2 adsorption at 77 K in a Quantachrome Autosorb instrument. First, the sample was degassed at 300 °C for 4 h. BET method was used to determine the specific surface areas of the samples.

Raman spectroscopy was conducted using a RamanScope Senterra spectrometer at a wavelength of 532 nm with a laser power of 0.02 mW and an acquisition time of 10 s.

The acid characteristics of the supported catalysts were studied by NH_3-temperature-programmed-desorption (NH_3-TPD), in which about 0.1 g of catalyst was pre-treated in a He flow (30 ml/min) at 200 °C for 1 h. After cooling to 100 °C, NH_3 was chemisorbed for another 1 h in a NH_3/He stream (30 ml/min). After purging the reactor with He to a flat baseline, the TPD profiles were recorded in a He flow from 100 to 600 °C at a rate of 10 °C/min using a TCD detector.

The IR spectra of adsorbed pyridine (Py-IR) were obtained on a Tensor27 (Bruker) FT-IR spectrophotometer. Before the test, a self-supporting sheet with a diameter of 13 mm was degassed at 350 °C for 0.5 h to remove physically adsorbed water. After

cooling to room temperature, the spectrum of the sample was recorded as a background spectrum. After that, the sample was exposed to pyridine vapor for 5 min, and then the IR spectrum of the pyridine adsorbed at room temperature was recorded. Subsequently, IR spectra were obtained by evacuating at 150 °C, 250 °C and 350 °C for 0.5 h to desorb the pyridine and then cooling to room temperature. The IR spectra of all samples were obtained by subtracting the background spectrum from the absorbance spectrum recorded after desorption of pyridine.

Selective oxidation of isobutane

The selective oxidation of isobutane is carried out in an atmospheric fixed-bed reactor, which is made of a quartz tube with an inner diameter of Φ10 mm and a length of 400 mm. The 20–40 mesh granular catalyst (~ 2 g) was loaded in the middle of the reactor. First, the catalyst is heated to 325 °C for a certain period of time under nitrogen flow. Then, the feedstock with molar ratio of isobutane/O_2/H_2O/N_2 = 27/13.5/10/49.5 was fed into the reactor at a total flow rate of 20 mL /min. Then the contact time was about 6 s. For isobutane oxidation, the reaction temperature was controlled at 340 °C. All gas products are analyzed online by a TCD gas chromatograph equipped with two continuous columns: Porapak Q column is used to separate hydrocarbons and CO_2, Molecular 13X separates O_2, N_2, and CO. Liquid products (such as acetone, methacrolein, acrylic acid and methacrylic acid) are collected by a cold trap for 2 h, and are quantitatively analyzed off-line by Aglinet 7890B gas chromatography with FID detector using a FFAP capillary column. All the reaction data were obtained within 2 h under steady state stream.

Results

TGA

The TG/DTG curves of unsupported and the supported APMV catalysts after calcined at 350 °C for 3 h are shown in Fig. 1, which exhibited two main steps along the 50–600 °C temperature range. In the case of bulk APMV, the first step in the TG curve was ascribed to the loss of physisorbed water (50–200 °C). The second weight loss was ascribed to the thermal decomposition of the APMV, which began to decompose at 340 °C and was completely decomposed at 480 °C. The same phenomenon was observed with supported APMV samples but the decomposition occurred at higher temperature with respect to bulk APMV. The thermal decomposition of the supported catalysts started at about 360 °C, which suggested that the thermal stability of the active APMV phase increased when supported.

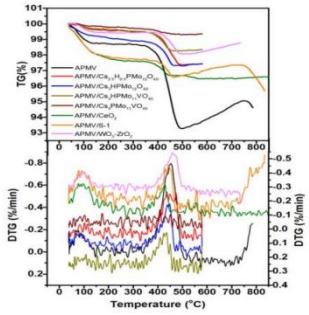

Fig. 1 Thermogravimetric analysis of unsupported and supported catalysts

XRD

The XRD patterns of supported 40 wt% APMV catalysts as well as different carriers are shown in Figs. 2 and S1. It can be seen from the patterns in Fig. 1 that pure bulk APMA exhibit diffraction peaks at 2θ = 10.5°, 18.4°, 23.7°, 26.1°, 30.2°, 35.6° and 38.9°, which are characteristic of the Keggin structure [17–19]. And two strong diffraction lines at 2θ = 15.1° and 21.4° could be attributed to characteristic NH_4^+ in APMA [20]. Specially, non-supported APMV catalyst showed weak MoO_3 crystal diffraction peaks at 28.5° and 34.4°, indicating its partial decomposition during the synthesis [21]. After supporting active APMV over the supports-I with similar primary structure, it is obvious that the diffraction peaks of NH_4^+ ions weakened and even disappeared due to the significant contribution of Keggin structure from the supports-I. More important, the diffraction peaks of MoO_3 crystal were not observed for the APMV/support-I catalysts, suggesting that the supports-I showed a stronger ability in stabilizing the active APMV phase.

In addition, for the 40 wt% APMV/support-II catalysts, in which CeO_2, WO_3/ZrO_2 and S-1 molecular sieve (just as shown in Fig. S1) have totally different structure with active APMV, the characteristic peaks attributed to the Keggin structure and NH_4^+ ions still exist but the intensity of these diffraction peaks significantly became weaker. But the diffraction peaks due to MoO_3 crystals were not still observed for the APMV/support-II catalysts, further indicating that the supports-II also exhibited stabilizing ability for APMA phase.

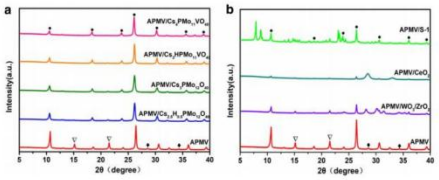

Fig. 2 XRD patterns of **a** APMV/support-I and **b** APMV/support-II: (filled circle) Keggin units and (filled diamond) MoO_3 and (inverted triangle) NH_4^+

Fig. S2 shows the XRD patterns of the used catalysts after 2 h of isobutane oxidation testing. It can be found that, compared to the fresh APMV/support catalysts, the diffraction patterns did not show any change in the phase composition or crystallinity, implying that there is no significant further decomposition of the Keggin structure during partial oxidation of isobutane under oxygen-poor conditions. This further suggested that the active APMV phase after impregnated on the supports exhibited excellent thermal stability.

FT-IR

FT-IR spectroscopy has been employed to determine the structural features of Keggin anion in the HPC catalysts. Fig. 3 gives the FT-IR spectra of the fresh supported catalysts with 40 wt% APMV loadings. All the catalysts showed obvious Keggin characteristic vibration bands at 1064, 961, 874 and 780 cm^{-1}, which are attributed to the stretching vibration of P–O, Mo=O_d, Mo–O_b–Mo and Mo–O_c–Mo [22], respectively. Furthermore, the bands at 1416 cm^{-1} assigned to the characteristic N–H vibration were also observed for all the as-synthetic supported catalysts [23, 24]. Obviously, the active APMV phase was well stabilized after loading on the various supports. For fresh bulk APMV sample, two characteristic splitting shoulder peaks at about 1080 cm^{-1} and 998 cm^{-1} are generally observed due to substitution of Mo in primary structure by V atom [25, 26]. However, these two splitting peaks disappeared after supporting APMV on $Cs_3PMo_{12}O_{40}$ and $Cs_{2.5}H_{0.5}PMo_{12}O_{40}$, further conforming the remarkable contribution of $[PMo_{12}O_{40}]^{3-}$ Keggin structure from the supports-I, which is in good agreement with results of XRD patterns shown in Fig. 2.

The FT-IR spectra of all used catalysts after selective oxidation of isobutane are shown in Fig. S3. It should be noted that all the characteristic band are retained, further illustrating that the intact Keggin structure in all synthesized catalysts in this

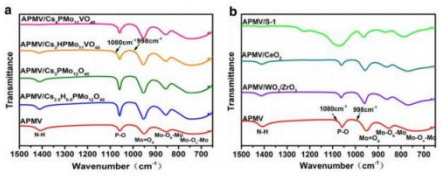

Fig. 3 FT-IR spectra of **a** APMV/support-I and **b** APMV/support-II

work is reserved after 2 h of testing, whether the active APMV is supported on supports-I with similar primary structure or on the supports-II with different structure features.

Raman spectroscopy and textural properties

The Raman spectra of the fresh supported catalysts are shown in Fig. 4. As shown by the well-known characteristic bands attributed to the following vibrations: δ(O–Mo–O) at 238 cm^{-1} and 255 cm^{-1}, δ(Mo–O–Mo) at 605 cm^{-1}, ν(Mo–O–Mo) at 878 cm^{-1}, 973 cm^{-1} and 959 cm^{-1}, and ν(Mo-O_t) at 990 cm^{-1}, the as-synthesized catalysts showed the existence of the Keggin structure [27]. And the absence of vibration bands at 818 and 660 cm^{-1} assigned to MoO_3 crystal [12, 28] further

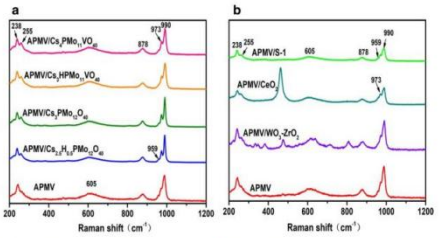

Fig. 4 Raman spectra of **a** APMV/support-I and **b** APMV/support-II

confirmed that the active APMV phase was well stabilized after loaded over the supports-I and supports-II.

The data of the specific surface area, total pore volume and pore diameter for the supports, pure APMV and the supported catalysts were listed in Table 1. The pore width distribution curves and the isotherm plots were shown in Figs. S4 and S5. It can be seen that the isotherms and the pore distribution of the 40 wt% APMV/support-I catalysts have significant difference compared to the supports-I themselves. And compared with the supports-I, the surface area of the supported samples decreased a lot due to the filling of APMV into the pores of supports-I besides APMV/$Cs_{2.0}H_{0.5}PMo_{12}O_{40}$ and APMV/$Cs_4PMo_{11}VO_{40}$ samples, both of which displayed a higher surface area than what is expected. This indicated that the APMV active phase partially contributes to the surface area of these two supported samples because APMV has a very high surface itself (40.35 m^2/g). Especially, for $Cs_4PMo_{11}VO_{40}$ support, the contribution of the active APMV to the surface area of the 40 wt% APMV/$Cs_4PMo_{11}VO_{40}$ catalyst is much more remarkable. In the case of the supports-II with larger specific surface area, there is no obvious change in the pore distribution and adsorption/desorption isotherms after loaded 40 wt% APMV on them. And the measured surface area and pore volume of the supported catalysts also decreased due to the block of porous structure of the supports-II by APMV. From above, it can be proposed that the active APMV phase over supports-II could exhibit the better dispersion than the APMV/supports-I.

NH_3-TPD

The NH_3-TPD technology was used to evaluate the surface acid properties of APMV catalysts supported on different carriers. It can be seen from Fig. 5 that all catalysts have similar desorption behavior of NH_3 and exhibit three types of acidic sites with different strength: weak acid sites at 100–250 °C, medium strong acid sites at 250–350 °C, and strong acid sites at 350–550 °C. Due to the release

Table 1 Textural properties of the supports, APMV and supported catalysts

Catalysts	Supports			Supported catalysts		
	S_{BET} (m^2/g)	V^a (cm^3/g)	D^b (nm)	S_{BET} (m^2/g)	V (cm^3/g)	D (nm)
APMV	–	–	–	40.35	0.052	5.91
APMV/$Cs_{2.5}H_{0.5}PMo_{12}O_{40}$	21.15	0.070	2.03	20.71	0.047	1.02
APMV/$Cs_3HPMo_{12}O_{40}$	97.89	0.117	4.82	37.72	0.070	1.03
APMV/$Cs_3HPMo_{11}VO_{40}$	37.56	0.062	7.00	26.31	0.085	1.56
APMV/$Cs_4PMo_{11}VO_{40}$	2.27	0.027	2.30	22.70	0.067	1.41
APMV/CeO_2	77.05	0.154	7.52	58.38	0.088	6.05
APMV/S-1	316.37	0.211	2.55	221.11	0.158	2.59
APMV/WO_3/ZrO_2	42.24	0.121	1.12	42.72	0.094	8.97

[a]V: The total pore volume at $p/p_0 = 0.99$

[b]D: Average pore size

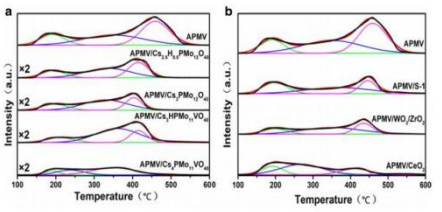

Fig. 5 NH_3-TPD profiles of **a** APMV/support-I and **b** APMV/support-II

of NH_3 from the decomposition of the ammonium cations in active APMV phase during the heating treatment, the amount of desorbed NH_3 was corrected by eliminating the theoretical values according to the literature [29] and the results were listed in Table 2. A significant different behavior was observed for the two types of supports, in which the APMV loading over supports-II exhibited the higher amount of weak acid sites and total acidity (mmol/g-cat). When calculating the density of acidic sites on the surface of supported catalysts (mmol/m^2-cat), the higher values were obtained for the APMV phase over supports-I, which was related to their relative lower specific surface area. From above, it can be concluded that the higher dispersion of active APMV on supports-II with the higher

Table 2 Amount of desorbed NH_3 on the surface of the supported catalyst

	Adsorption amount of NH_3 (μmol/g)			Total acidity	
	100–250 °C	250–350 °C	350–550 °C	(μmol/g)	(μmol/m^2)
APMV	234	185	501	920	23
APMV/$Cs_{2.5}H_{0.5}PMo_{12}O_{40}$	86	87	174	347	17
APMV/$Cs_3PMo_{12}O_{40}$	65	96	152	313	8
APMV/$Cs_3HPMo_{11}VO_{40}$	70	167	62	299	11
APMV/$Cs_4PMo_{11}VO_{40}$	80	81	31	192	8.5
APMV/CeO_2	185	142	65	396	7
APMV/WO_3/ZrO_2	104	100	156	360	11
APMV/S-1	174	98	218	490	2

surface area would expose the more acid sites, and finally led to the highest total acidity (mmol/g-cat) and the lower density of acid sites (mmol/m^2-cat).

Pyridine-adsorbed FT-IR spectra

The FT-IR spectra of pyridine-adsorbed catalysts can be carried out to further explore the presence of Brønsted and Lewis acid sites in as-synthesized samples. The spectra of the supported APMV catalysts recorded at 150 °C shows the presence of both Brønsted and Lewis acid sites (Fig. 6). Generally speaking, the bands at 1450 cm^{-1} and 1540 cm^{-1} in FT-IR spectra correspond to pyridine adsorbed on Brønsted (B) and Lewis (L) acidic sites of the catalyst surface, respectively [30]. And the absorption peak at 1488 cm^{-1} is related to the synergistic effect of B and L acid [31]. It is evident that B acidity is predominant for the APMV/support-I catalysts, but exhibiting rather poor L acidity. On the contrary, the L acidic sites on the surface of APMV/support-II catalysts were predominantly present and much higher than those on the APMV/support-I samples, suggesting that the Lewis acid sites might be mainly originated from the supports-II themselves or from interaction between the support-II and active APMV.

Additionally, the pyridine-IR spectra after outgassing at 250 °C and 350 °C was also investigated to estimate the strength of both B and L acidic centers on the supported catalysts (Figs. S6 and S7). Increasing evacuating temperature from 150 to 250 °C, there is no obvious change in the peak intensity of the B acid sites for all the as-synthesized catalysts but the amount of L acid sites over the APMV/support-II catalysts greatly decreased, indicating the weaker strength of L acidic sites from the contribution of the supports-II. Further increasing temperature to 350 °C, both the Brønsted and Lewis acidic sites over the supported-APMV catalysts still exist although their intensities decreased, clearly indicating the presence of strong acid sites. This is good agreement with the results of NH_3-TPD.

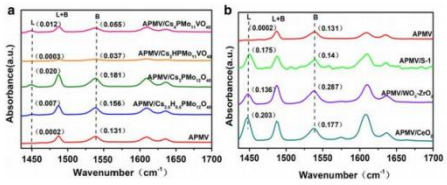

Fig. 6 FT-IR spectra of **a** APMV/support-I and **b** APMV/support-II after pyridine desorption at 150 °C. The B and L acidic amount in parentheses is calculated according to literature [32]

Selective oxidation of isobutane

The selective oxidation of isobutane over the 40 wt% APMV/support catalysts was studied at 340 °C under oxygen-poor condition with a feed ratio 27:13.5:10:49.5 (isobutane:O_2:H_2O:N_2). The results are presented in Table 3. The desirable products are methacrylic acid and methacrolein, and CO_2, CO, acetone, acetic acid and acrylic acid, trace amounts of ethylene and ethane are the side-products. The bulk APMV sample was active for selective oxidation of isobutane and exhibited 6.6% of isobutane conversion and 40.2% selectivity of desired products (MAA + MAL), whereas most of the pure supports were very poorly active and selective to MAA (Table S1). The significant increases were detected for the isobutane conversion and selectivity to MMA upon impregnating the active APMV on the supports-I with similar primary structure. And the highest yield in the desired products MAA + MAC (5.39%) was obtained with 40 wt% APMV/$Cs_3PMo_{12}O_{40}$ whereas it amounted to 4.58%, 3.98% and 3.06% with APMV/$Cs_{2.5}H_{0.5}PMo_{12}O_{40}$, APMV/$Cs_3HPMo_{11}VO_{40}$ and APMV/$Cs_4PMo_{11}VO_{40}$, respectively. Among them, it is interesting to note that inserting V into the primary structure of the supports resulted in slightly decrease in the selectivity to MAA. However, a remarkably negative effect was found when introducing active APMV onto the supports-II, in which almost no MAA was formed and the high selectivity to CO_x was observed. It is evident that catalyst activity and product selectivity in the isobutane oxidation to MAA are rather sensitive to the type of supports.

Discussion

It is well-known that, for the partial oxidation of isobutane to MAA, acidic-functional catalysts are necessary to activate the C-H bond and further promote desorption of MAA from the acidic surface [33–36]. Based on the results from NH_3-TPD

Table 3 Catalytic performance of 40 wt% APMV supported catalyst

Catalysts	Conv. of *i*-C_4H_{10} (%)	Selectivity (%)[a]							Yield of MAA + MAL(%)
		MAA	MAL	Actone	AcA	AA	CO	CO_2	
APMV	6.60	34.52	6.67	0.65	10.05	0.92	20.67	26.48	2.72
APMV/$Cs_{2.5}H_{0.5}PMo_{12}O_{40}$	9.03	44.23	6.46	1.06	8.30	1.51	16.60	21.78	4.58
APMV/$Cs_3PMo_{12}O_{40}$	11.34	43.01	4.52	0.94	8.32	1.40	17.27	24.49	5.39
APMV/$Cs_3HPMo_{11}VO_{40}$	9.79	35.23	5.38	0.78	9.79	1.42	20.36	27.00	3.98
APMV/$Cs_4PMo_{11}VO_{40}$	7.77	32.04	7.40	0.89	11.11	1.12	18.32	29.10	3.06
APMV + $Cs_3PMo_{12}O_{40}$	8.37	9.33	2.23	0.82	7.13	0.64	29.18	50.58	0.96
APMV/S-1	7.98	0.62	0.89	2.35	15.17	0.76	34.16	45.72	0.12
APMV/CeO_2	7.90	0.30	0.00	0.00	0.30	0.00	44.51	54.87	0.02
APMV/WO_3/ZrO_2	7.01	0.91	3.98	1.09	8.28	0.23	33.70	51.74	0.34

[a]*MAA* methacrylic acid, *MAL* methacrolein, *AcA* acetic acid, *AA* acrylic acid

(Fig. 5 and Table 2) and pyridine-adsorbed FT-IR spectra (Fig. 6), it can be found that, although the 40 wt% APMV/support-II catalysts possess much more amount of surface acidic sites (calculated by μmol/g) than the APMV/support-I catalysts, they exhibited the lower conversion of isobutane and the rather worst selectivity to MAA. However, if considering the acidic site density as μmol/m^2, it can be found from Fig. 7 that, although there is not totally linear relationship, a positive effect of NH_3 uptake (μmol/m^2) could be observed toward the catalytic activity (μmol/min m^2), which is defined as ($F_{isobutane} \times X_{isobutane}$)/($S_{BET} \times M_{cat}$) [11], and where $F_{isobutane}$, $X_{isobutane}$, S_{BET} and M_{cat} is the molar flowrate of isobutane, the conversion of isobutane, the specific surface area and the mass of catalyst, respectively. This emphasized that the amount of acidic sites per m^2, rather than that per gram, could play a role to a certain extent in determining the catalytic activity of partial oxidation of isobutane to MAA.

In addition, it has been reported [37] that the thermal stability of the active APMV phase could be a factor influencing the product distribution, in which the formation of MoO_3 from decomposition of active APMV phase is non-selective for the isobutane oxidation. Paul et al. attributed [11] the less selectivity of MAA over APMV/SiO_2 catalyst to the partial decomposition of the active phase to MoO_3 during the catalyst preparation. In our study, the results obtained by XRD, FT-IR and Raman spectra showed that the active APMV phase remained stable upon impregnated on the all as-synthesized supports, including supports-I and supports-II, in which almost no MoO_3 phase was detected. More importantly, there was virtually no change in the peak intensity of the Keggin structure for all used catalysts after isobutane oxidation and the absence of MoO_3 crystal was further confirmed by XRD and FT-IR spectra (Figs. S2 and S3). Thus, the significant difference in the distribution of the products in the case of the present study, especially the worst selectivity to MAA over the APMV/support-II catalysts, could not be attributed to the stability of the active phase.

For the partial oxidation of isobutane to MAA, redox properties have also an inevitable effect on the oxygen insertion reaction which generates the oxidized products. In our case, the improved catalytic performance was obtained over the 40 wt% APMV/support-I with the same primary structure, which might originated from a

Fig. 7 Correlation between the activity of isobutane partial oxidation and the acid site density of supported catalysts measured by NH_3-TPD

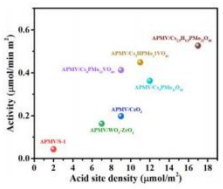

good synergetic effect between the similar primary polyoxometallate structure of the two phases. It is known [38] that, when the two phases contain same/similar lattice plane with each other, they are structurally closely matched. Thus, the optimal structure match between active APMV phase and the supports-I would lead to the formation of strong and coherent boundaries between lattices of the two phases [13]. For phase synergy to be effective, it is imperative that the contact between active phase and support phase must be intimate in order to facilitate their cooperation on an atomic scale or at least on a nanoscale, in which the interfacial transfer of electrons and active lattice oxygen species takes effect easily. Just as shown in Table 3, the catalyst (APMV + $Cs_3PMO_{12}O_{40}$) obtained by mechanically mixed active APMV and $Cs_3PMO_{12}O_{40}$ support exhibited rather poor selectivity in the desired products, which further identified the indispensability of intimate contact. Therefore, it appears reasonable to propose that the formation of coherent interfaces between two structural well-matched phases with the same/similar Keggin anions greatly promotes the transfer abilities of electrons and lattice oxygen, which is responsible for the efficient oxygen insertion to maximize MAA selectivity. This well-matched effect between the two phases, which is likely a major contributor to an increased selectivity in desired product MAA, has been discovered by dispersing active $Cs_2Te_{0.3}(VO)_{0.1}H_4PMo_{12}O_{40}$ over α-$La_2Mo_2O_9$ support [39]. Similarly, this might be the main reason why 40 wt% APMV/support-II catalysts gave the lowest selectivity to MAA as a consequence of the highly unmatched structure between active APMV and supports, resulting in difficulty for interfacial transfer of electrons and lattice oxygen, although the supports owned the higher surface area and more amount of surface acidic sites. As a result, the total oxidation reaction between isobutane and gaseous oxygen was dominant and led to the rather high selectivity to CO_x. Finally, as mentioned before, there was a slightly decrease in the selectivity to MAA when impregnating active APMV onto the containing-V supports-I with totally the same primary structure. It has been widely accepted [18, 31] that a certain amount of V species in the primary structure of HPCs possibly migrated into the secondary

Table 4 Catalytic performance of APMV and HPMV[a] supported catalyst

Catalysts	Temp. (°C)	Conv. of *i*-C_4H_{10} (%)	Selectivity (%)[b]				Refs.
			MAA	MAL	COx	others	
APMV	340	2.5	34.3	20.4	35.8	9.5	[11]
40wt%APMV/$Cs_5PMo_{12}O_{10}$	340	15.3	42.0	10.0	30.7	17.3	[11]
40wt%HPMV[a]/$Cs_3PMo_{12}O_{40}$	340	4.6	41.8	17.4	31.7	–	[40]
40wt%HPMV/$HCs_3PMo_{11}VO_{40}$	340	11.4	24.0	6.7	54.8	–	[40]
40wt%APMV/ZrO_2-SBA-15	340	6.6	1.6	9.6	63.5	25.3	[11]
40wt%APMV/SBA-15	340	5.0	9.7	18.0	42.0	30.3	[11]
50wt%HPMV/Ta_2O_5·nH_2O	350	8.7	3.5	1.0	–	–	[41]
50wt%HPMV/diatomaceous earth	350	7.9	3.6	1.1	–	–	[41]

[a]*HPMV* $H_4PMo_{11}VO_{40}$

[b]*MAA* methacrylic acid, *MAL* methacrolein, *AcA* acetic acid, and *AA* acrylic acid

structure during the partial oxidation of isobutane to MAA. However, it is not clear yet if this decrease in selectivity is related to the migration of V species or if it is due to the intrinsic properties of supports-I with V inserting the Keggin structure. Additional experimental works in the future are needed to further explain the reasons.

Table 4 represents the catalytic performance of supported 40–50 wt% APMV and HPMV ($H_4PMo_{11}VO_{40}$) catalysts studied earlier in the literature for selective oxidation of isobutane to MAA. Although the synergetic effect observed in our work has never been used to explain the difference in catalytic performance among these supported catalysts, it is obvious that the catalysts with the well-matched primary structure between the active HPC phase and the supports exhibited the more excellent activity and/or selectivity than those with completely mismatched structures. This further confirmed the possibility of explanation, for which the formation of a coherent interface between the phases would be favorable to lead to a synergetic effect.

Conclusions

The 40 wt% active APMV catalysts supported over two different types of supports (supports-I and supports-II) were synthesized and characterized, and their catalytic performance in partial oxidation of isobutane to MAA was also evaluated. It was found that 40 wt% APMV/support-I catalysts with similar primary structure exhibited far superior catalytic activity and selectivity than the 40 wt% APMV/support-II catalysts, which were poorly selective to MAA. As shown by physicochemical analyses, the thermal stability of the active phase was increased by impregnating active APMV over two types of supports, and the stability remains almost unchanged even after 2 h of catalytic testing. The well-matched primary structure between the active APMV phase and the support-I should be helpful for the development of a stronger bonding boundary which exhibited excellent electrons and lattice oxygen transfer abilities. The phase cooperation from the well-matched structure and/or the higher acid site density per unit surface area (μmol/m^2), not better dispersion of active phase, could have here a strong influence on the catalytic performance in partial oxidation of isobutane to MAA. The best catalytic performance with isobutane conversion of 11.3% and 5.39% yield in the desired products was achieved on the 40 wt% APMV/$Cs_3PMo_{12}O_{40}$ catalyst.

Supplementary Information The online version contains supplementary material available at https://doi.org/10.1007/s11144-021-01967-0.

Acknowledgements This work was supported by the National Natural Science Foundation of China (Grant No. 21673227), Scientific Group Research Project of Mudanjiang Normal University (No. D211220645), the Science and Technology Innovation Project of Mudanjiang Normal University (No. kjcx2020-16mdjnu).

Declarations

Conflict of interest There are no conflicts of interest to declare.

References

1. Jaber DMM, Jean-Luc D, Fabrizio C et al (2018) Catalysis for the synthesis of methacrylic acid and methyl methacrylate. Chem Soc Rev 47:7703–7738
2. Li B, Yan R, Diao Y et al (2013) Synthesis of methyl methacrylate by aldol condensation of methyl propionate with formaldehyde over acid–base bifunctional catalysts. Catal Lett 143:829–838
3. Wu S, Kan Q, Ding W et al (2012) Partial oxidation of isobutane to methacrolein over $Te_{(1.5+0.5x)}PMo_{12-x}V_xO_h$ heteropolycompounds with tellurium as counter cations. React Kinet Mech Cat 106:157–164
4. Song IK, Barteau MA (2004) Redox properties of Keggin-type heteropolyacid (HPA) catalysts: effect of counter-cation, heteroatom, and polyatom substitution. J Mol Catal A Chem 212:229–236
5. Kendell S, Brown T (2010) Datailed product and kinetic analysis for the low-pressure selective oxidation of isobutane over phosphomolybdic acid. React Kinet Mech Cat 99:251–268
6. Stuyven B, Emmerich J, Eloy P et al (2014) Molybdenum-vanadium -antimony mixed oxide catalyst for isobutane partial oxidation synthesized using magneto hydrodynamic forces. Appl Catal A Gen 474:18–25
7. Liu S, Chen L, Wang G et al (2016) Effects of Cs-substitution and partial reduction on catalytic performance of Keggin-type phosphomolybdic polyoxometalates for selective oxidation of isobutane. J Energy Chem 25:85–92
8. Kanno M, Miura YK, Yasukawa T et al (2011) 1-Molybdo-1-vanadophosphoricacid $H_4PMo_{11}VO_{40}$ supported on ammonia-modified silica as highly active and selective catalyst for oxidation of methacrolein. Catal Commun 13:59–62
9. Sebastien P, Wei C, Manzoor S et al (2010) Keggin-type $H_4PVMo_{11}O_{40}$-based catalysts for the isobutane selective oxidation. Sci Chin Chem 53:2039–2046
10. Paul S, Courtois VL, Vahnove D (1997) Kinetic investigation of isobutane selective oxidation over a heteropolyanion catalyst. Ind Eng Chem Res 36:3391–3399
11. Jing F, Katryniok B, Bordes-Richard E et al (2013) Improvement of the catalytic performance of supported $(NH_4)_3HPMo_{11}VO_{40}$ catalysts in isobutane selective oxidation. Catal Today 203:32–39
12. Kanno M, Yasukawa T, Ninomiya W et al (2010) Catalytic oxidation of methacrolein to methacrylic acid over silica-supported 11-molybdo-1-vanadophosphoric acid with different heteropolyacid loadings. J Catal 273:1–8
13. Zhou L, Wang L, Diao Y et al (2017) Cesium salts supported heteropoly acid for oxidation of methacrolein to methacrylic acid. Mol Catal 433:153–161
14. Ho C, Yu JC, Kwong T et al (2005) Morphology-controllable synthesis of mesoporous CeO_2 nano- and microstructures. Chem Mater 17:4514–4522
15. Cortés-Jácome MA, Toledo JA, Angeles-Chavez C et al (2005) Influence of synthesis methods on tungsten dispersion, structural deformation, and surface acidity in binary WO_3-ZrO_2 system. J Phys Chem B 109:22730–22739
16. Yang X, Huang L, Li J et al (2017) Fabrication of SiO_2@silicalite-1 and its use as a catalyst support. RSC Adv 7:11224–11230
17. Liao X, Wu D, Geng B et al (2017) Deep oxidative desulfurization catalyzed by $(NH_4)_nH_{4-n}PMo_{11}VO_{40}$ (x = 1, 2, 3, 4) using O_2 as an oxidant. RSC Adv 7:48454–48460
18. He J, Liu Y, Chu W et al (2018) Effect of V-containing precursors on the structure and catalytic performance of Cs-substituted phosphomolybdates for isobutane oxidation. Appl Catal A Gen 556:104–112
19. Guan J, Xu H, Jing S et al (2009) Selective oxidation of isobutane and isobutene over vanadium phosphorus oxides. Catal Commun 10:276–280
20. Jing F, Katryniok B, Dumeignil F et al (2014) Catalytic selective oxidation of isobutane to methacrylic acid on supported $(NH_4)_3HPMo_{11}VO_{40}$ catalysts. J Catal 309:121–135
21. Ballarini N, Candiracci F, Cavani F et al (2007) The dispersion of Keggin-type P/Mo polyoxometalates inside silica gel, and the preparation of catalysts for the oxidation of isobutane to methacrolein and methacrylic acid. Appl Catal A Gen 325:263–269
22. Zhou L, Wang L, Zhang S et al (2015) Effect of vanadyl species in Keggin-type heteropoly catalysts in selective oxidation of methacrolein to methacrylic acid. J Catal 329:431–440
23. Dermeche L, Thouvenot R, Hocine S et al (2009) Preparation and characterization of mixed ammonium salts of Keggin phosphomolybdate. Inorg Chim Acta 362:3896–3900

24. Laronze N, Marchal-Roch C, Guillou N et al (2003) Solid-state chemistry of ammonium and cesium 1-vanado-11-molybdophosphate and ammonium 12- molybdosilicate: application to oxidation catalysis. J Catal 220:172–181
25. Casarini D, Centi G, Jiru P et al (1993) Reactivity of molybdovanadophosphoric acids: influence of the presence of vanadium in the primary and secondary structure. J Catal 143:325–344
26. Dimitratos N, Védrine JC (2003) Properties of $Cs_{2.5}$ salts of transition metal M substituted Keggin-type $M_{1-x}PV_1M_xMo_{11-x}O_{40}$ heteropolyoxometallates in propane oxidation. Appl Catal A Gen 256:251–263
27. Huynh Q, Schuurman Y, Delichere P et al (2009) Study of Te and V as counter-cations in Keggin type phosphomolybdic polyoxometalate catalysts for isobutane oxidation. J Catal 261:166–176
28. Mezzogori R, Pigamo A (2001) Improved catalytic performance of Keggin-type polyoxometalates in the oxidation of isobutane to methacrylic acid under hydrocarbon-lean conditions using antimony-doped catalysts. Chem Eng J 82:33–42
29. Cao Y, Wang L, Zhou L et al (2017) $Cs(NH_4)_xH_{3-x}PMo_{11}VO_{40}$ catalyzed selective oxidation of methacrolein to methacrylic acid: effects of NH_4^+ on the structure and catalytic activity. Ind Eng Chem Res 56:653–664
30. Huang H, Yi D, Lu Y et al (2013) Study on the adsorption behavior and mechanism of dimethyl sulfide on silver modified bentonite by in situ FTIR and temperature-programmed desorption. Chem Eng J 225:447–455
31. Li XK, Zhao J, Ji W et al (2006) Effect of vanadium substitution in the cesium salts of Keggin-type heteropolyacids on propane partial oxidation. J Catal 237:58–66
32. Emeis CA (1993) Determination of integrated molar extinction coefficients for infrared-absorption bands of pyridine adsorbed on solid acid catalysts. J Catal 141:347–354
33. Busca G, Finocchio E, Ramis G et al (1996) On the role of acidity in catalytic oxidation. Catal Today 32:133–143
34. De Smet F, Ruiz P, Delmon B et al (2001) Rationalization of the catalytic behavior of lanthanide oxides and praseodymium molybdates in total and selective oxidation of isobutene. J Phys Chem B 105:12355–12363
35. Zhang H, Yan R, Yang L et al (2013) Investigation of Cu- and Fe-Doped $CsH_4PMo_{11}VO_{40}$ heteropoly compounds for the selective oxidation of methacrolein to methacrylic acid. Ind Eng Chem Res 52:4484–4490
36. Cavani F (1998) Heteropolycompound-based catalysts: a blend of acid and oxidizing properties. Catal Today 41:73–86
37. Jing F, Katryniok B, Bordes-Richard E et al (2015) Structural evolution under reaction conditions of supported $(NH_4)_3HPMo_{11}VO_{40}$ catalysts for the selective oxidation of isobutane. Catalysts 5:460–477
38. Grasselli RK (2001) Genesis of site isolation and phase cooperation in selective oxidation catalysis. Top Catal 15:93–104
39. Huynh Q, Selmi A, Corbel G et al (2009) Atypical synergetic effect between Te- and V-substituted phosphomolybdic cesium salt and LAMOX-type phases for the oxidation of isobutane into methacrylic acid. J Catal 266:64–70
40. Paul S, Chu W, Sultan M et al (2010) Keggin-type $H_4PVMo_{11}O_{40}$-based catalysts for the isobutane selective oxidation. Sci China 53:2039–2046
41. Ushikubo T (2003) Activation of propane and butanes over niobium-and tantalum-based oxide catalysts. Catal Today 78:79–84

Publisher's Note Springer Nature remains neutral with regard to jurisdictional claims in published maps and institutional affiliations.

5.Cai X, Wei C, Dong J, et al. Dimeric phthalocyanine-involved double-decker complex-based electrochemical sensor for simultaneous detection of acetaminophen and ascorbic acid[J]. Journal of Materials Science: Materials in Electronics, 2019, 30(3): 1976-1983. （SCI 检索收录四区，IF=2.171）

Journal of Materials Science: Materials in Electronics
https://doi.org/10.1007/s10854-018-0468-0

Dimeric phthalocyanine-involved double-decker complex-based electrochemical sensor for simultaneous detection of acetaminophen and ascorbic acid

Xue Cai[1] · Chuangyu Wei[1] · Jurong Dong[3] · Qi Liu[3] · Yanling Wu[3] · Guang Lu[2,4] · Yanli Chen[3] · Jianzhuang Jiang[2]

Received: 30 September 2018 / Accepted: 27 November 2018
© Springer Science+Business Media, LLC, part of Springer Nature 2018

Abstract
An electrochemical sensor for simultaneous detection of acetaminophen (APAP) and ascorbic acid (AA) is firstly developed by using the self-assembled film of a novel dimeric bis(phthalocyaninato) europium complex, [{Pc(SC_2H_5)$_8$}Eu{BiPc(SC_2H_5)$_{12}$}Eu{Pc(SC_2H_5)$_8$}] (**1**) coated onto ITO (fim-**1**/ITO) fabricated through a solution-processing quasi-LangmuirShäfer (QLS) protocol. A combination of unique sandwich molecular structure with extented π-conjugated system and *J*-type aggregates with quite uniform nanograins (ca. 15 nm) formed on ITO substrate render the film of **1** the excellent charge transfer ability and abundant electroactive sites, resulting in sensitive detection of APAP and AA with the good sensitivities of 254 and 85.6 mA μM^{-1} cm^{-2} and low detection limits of 1.3 and 3.7 μM for APAP and AA respectively. More importantly, a simultaneous determination of APAP and AA at a coexisting system of APAP and AA is also achieved with the still good sensitivities of 317 and 64.7 mA μM^{-1} cm^{-2}, and low detection limits of 1.0 and 4.9 μM for APAP and AA respectively. This work represents the first example of tetrapyrrole-based organic semiconductor electrochemical sensor for simultaneous detection of APAP and AA with excellent sensing performance, implying the great application potential of electroactive sandwich rare earth tetrapyrrole compounds in the nonenzymatic electrochemical sensors.

1 Introduction

As a commonly antipyretic and pain-relieving drug, acetaminophen (APAP) is contained in numerously OTC (over the counter) products [1]. However, an overdose of this drug can lead to the formation of some toxic metabolites in kidney (i.e., one of the most common pharmaceutical product poisonings at present.) [2]. Ascorbic acid (AA), as one of the most important vitamins, widely exists in various plants and participates in some important biological reactions such as cancer preventing, and improvement of immunity [3]. The deficiency of AA can result in different diseases, such as anemia, cataract and scurvy [4]. According to the previous researches, the adjunct presence of AA with APAP leads to intensified positive effects of APAP and its diminished toxicity [5]. The amount of APAP passed in urine will be reduced in high concentration of AA, which can rise the concentration of this drug in blood [6]. Therefore, the determination of APAP and AA in the presence of each other should be important in clinical medicine and health monitoring. A variety of methods have been used for the determination of APAP and AA in pharmaceuticals and biologicalfluids, such as high-performance liquid

Electronic supplementary material The online version of this article (https://doi.org/10.1007/s10854-018-0468-0) contains supplementary material, which is available to authorized users.

✉ Xue Cai
xuecai@mail.sdu.edu.cn

✉ Guang Lu
luguang_50366@126.com

✉ Yanli Chen
yanlichen@upc.edu.cn

Jianzhuang Jiang
jianzhuang@ustb.edu.cn

[1] College of Chemistry and Chemical Engineering, Mudanjiang Normal University, Mudanjiang 157011, China

[2] Beijing Key Laboratory for Science and Application of Functional Molecular and Crystalline Materials, Department of Chemistry, University of Science and Technology, Beijing, Beijing 100083, China

[3] School of Materials Science and Engineering, Institute of Advanced Materials, China University of Petroleum (East China), Qingdao 266580, China

[4] College of Chemical and Environmental Engineering, Shandong University of Science and Technology, Qingdao 266590, China

Published online: 11 December 2018

chromatography, gas chromatography, spectrophotometry, and electrochemical techniques [7–9]. Among the numerous detection methods, the electrochemical sensing technology has attracted increasing attention due to its superior characteristics of convenience, sensitivity and repeatability for monitoring these multiple analytes within the one sample [10, 11]. The key role of the improvement of electrochemical sensing technology is developing the sensitive, simple and low-cost electrode materials.

Phthalocyanine compounds are classified as interesting materials for sensing application depending on their electronic, optical and electrochemical properties [12]. The electrochemical sensors based on phthalocyanines have been used in the detection of dopamine, caffeic acid, and hydrogen peroxide for many years [13, 14]. Recently, Holanda et al., found that multi-walled carbon nanotubes-cobalt phthalocyanine-coated gold nanoparticles modified glassy carbon electrode presented good sensitivity and analytical stability for APAP detection [15]. However, the usage of gold nanoparticles and multi-walled carbon nanotubes are expensive, complicated in technology, which limit the practical application. On the other hand, although the graphene-modified electrodes used for electrochemical studies of APAP were found to have a poor response to APAP in PBS solution (pH 7.02) [16], the carbon based composite nanomaterial-modified electrodes employed for detection of APAP showed good sensitivity, selectivity, stability, and a low detection limit because of the unique electronic and catalytic properties of composite nanomaterials, such as ferrocene thiolate stabilized Fe_2O_3@Au nanoparticles coupling with graphene sheet/chitosan on a glassy carbon electrodes (GCEs) [17], GCEs modified with gold nanoparticles-multi-walled carbon nanotube [18], graphene-$CoFe_2O_4$ nanocomposite modified carbon paste electrode [19], TiO_2-graphene modified GCE [20], and single-wall CNT-dicetyl phosphate films [21]. However, in most cases, the behaviour of irreversible agglomerates for the large scale graphene usually has a negative impact on sensing performance [22]. Meanwhile the existence of dispersing agents in CNTs or graphene composite may be undesirable for many technological applications. Therefore, development of single-component phthalocyanine-based electrochemical sensor with high sensitivity for detecting APAP and AA simultaneously is highly desired but also challenging through the molecular design combinated with a simple device fabrication method.

Herein, a dimeric bis(phthalocyaninato) europium complex, [{Pc(SC$_2$H$_5$)$_8$}Eu{BiPc(SC$_2$H$_5$)$_{12}$}Eu{Pc(SC$_2$H$_5$)$_8$}] (**1**) {Pc(SC$_2$H$_5$)$_8$ = 2,3,9,10,16,17,23,24-octa(ethylthio) phthalocyanine, BiPc(SC$_2$H$_5$)$_{12}$ = bis[7,8,12,13,17,18-hexakis(ethylthio)-tribenzo[g,l,q]-5,10,15,20-tetraazaporphyrinate[b,e]benzene-linked binuclear phthalocyanine], was designed and synthesized, Scheme 1. The sandwich-type phthalocyanine in which lanthanide ions are bound to phthalocyanine rings, owning the accessibility of a range of oxidation states centered on the ligand [23]. The dimeric phthalocyanine framework with the sandwich double-decker structure further extends the π-conjugated system, enriches the oxidation states, which should enable this compound a good candidate for highly sensitive electrochemical sensors. Introducing the ethylthio substituents onto the periphery of phthalocyanine can improve the solubility, which is favorable for the solution-processing fabrication. Then, the electrochemical sensor based on the film of the dimeric phthalocyanine-involved double-decker complex was fabricteaed onto the ITO substrates by a simple QLS method [24]. The modified ITO electrode was revealed to have strong electrocatalytic activity toward APAP and AA simultaneously.

2 Experimental section

2.1 Materials and chemicals

1, 8-Diazabicyclo[5.4.0]undec-7-ene (DBU), acetaminophen (APAP) and ascorbic acid (AA) were purchased from Aldrich. The compounds of Eu(acac)$_3$·H$_2$O and 1, 2-benzenedicarbonitrile, 4, 5-ethylthio were prepared according to the literature methods [25]. The solvent *n*-pentanol was distilled from sodium. All other reagents and solvents were of reagent grade and used as received without further purification.

2.2 Measurements and characterizations

MALDI-TOF mass spectrum was recorded on the Bruker BIFLEX III ultra-high-resolution Fourier transform ion cyclotron resonance (FT-ICR) mass spectrometer with alpha-cyano-4-hudroxycinnamic acid as matrix (Fig. S1, Supplementary material). MALDI-TOF MS: an isotopic cluster peaking at m/z 3957.32, Calcd for **1**, [M]$^+$, 3959.15. ^{1}H NMR spectrum was recorded on the Bruker DPX 400 spectrometer in $CDCl_3$. The spectrum was referenced internally with residual $CDCl_3$ (δ 7.26). ^{1}H NMR (400 MHz, $CDCl_3$) δ: 14.54 (s, 2H, Pc ring), 12.32 (s, 4H, Pc ring), 10.90–11.40 (m, 16H, Pc* ring), 9.09 (m, 4H, Pc ring), 7.41 (m, 4H, Pc ring), 4.59–4.84 (m, 28H, SCH_2), 4.30–4.50 (m, 28H, SCH_2*), 1.07–1.20 (m, 84H, CH_3). Electrochemical measurements were carried out with a CHI760D voltammetric analyser and the detailed procedures please see our recently published papers [13, 26]. UV–Vis absorption spectra were recorded on the Hitachi U-3900 spectrophotometer. X-ray diffraction (XRD) experiments were carried out on the Rigaku D/max-B X-ray diffractometer with copper (K_α) radiation (λ = 1.5406 Å). Atomic force microscopic (AFM) image was obtained under ambient conditions by using a tapping mode with a Nanoscope III/Bioscope scanning probe microscope. Current–voltage (I–V) curve was collected using a Keysight B2910A precision source/measure unit with an incorporated voltage range supplied from − 10 to 10 V. Conductivity obtained by I–V curve can be calculated according to the report previously [27].

For characterizations, three kinds of substrates (SiO_2/Si, quartz, and ITO) were washed by deionized water, absolute ethyl alcohol, and dichloromethane, respectively. Films were deposited on different substrates by using QLS self-assembly method [24].

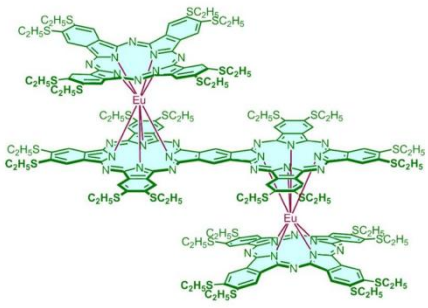

Scheme 1 Schematic molecular structures of [{Pc(SC$_2$H$_5$)$_8$}Eu{BiPc(SC$_2$H$_5$)$_{12}$}Eu{Pc(SC$_2$H$_5$)$_8$}] (**1**)

3 Results and discussion

3.1 Synthesis and characterization of [{Pc(SC$_2$H$_5$)$_8$}Eu{BiPc(SC$_2$H$_5$)$_{12}$}Eu{Pc(SC$_2$H$_5$)$_8$}] (1)

For the purpose of improving the solubility of phthalocyanine complex and preparing the solution-processing film, ethylthio substituents were introduced onto the periphery of the phthalocyanine ligand. This dimeric bisphthalocyanine compound was synthesized based on the published method [28]. Satisfactory ^{1}H NMR spectroscopic data in $CDCl_3$, MALDI-TOF mass were obtained for compound **1** (see Sect. 2 and Fig. S1, Supplementary material) Furthermore, the unique the dimeric bisphthalocyanine molecular structure let the redox states more various. As expected, the different pulse voltammogram (DPV) of **1** in dichloromethane shows two one-electron oxidations (Ox_1-Ox_2) and five one-electron reductions (Red_1–Red_5) (Fig. 1 and Table S1, Supplementary material), which is much more

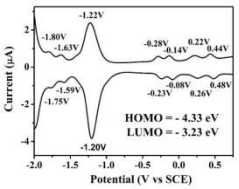

Fig. 1 Different pulse voltammogram (DPV) of **1** in dichloromethane at a scan rate of 20 mV s^{-1}

than monophthalocyanines, even normal bisphthalocyanines [29], consistent with the dimeric phthalocyanine-involved double-decker analogue reported previously [28].

3.2 Film characterization of [{Pc(SC$_2$H$_5$)$_8$}Eu{BiPc(SC$_2$H$_5$)$_{12}$}Eu{Pc(SC$_2$H$_5$)$_8$}] (1)

The film of **1** was fabricated by a simple QLS method. To clarify the microstructure and the morphology, the QLS film of **1** was characterized by UV–Vis, polarized UV–Vis absorption spetra, atomic force microscope (AFM) and X-ray diffraction (XRD). UV–Vis spectrum of the compound **1** in chloroform solution shows the Soret and Q bands at 316, 382, 585 and 699 nm respectively, Fig. 2a, with a typical nonaggregated molecular spectroscopic feature for dimeric phthalocyanine-involved double decker [30]. In comparison with the spectrum of chloroform solution, the Soret and Q bands of **1** in the QLS film red-shifted to 317 nm, 387 nm, 589 nm and 707 nm respectively, which indicate that the molecules of **1** in the QLS film take edge-to-edge (*J*-aggregate) packing mode according to exciton theory [31] and published results previously [32, 33] due to the strong exciton coupling between the adjacent dimeric bisphthalocyanine units. This is further comfirmed by polarized UV–Vis measurement [34], while the orientation angle of the phthalocyanine ring with respect to the substrate was estamited to be ca. 25.6° ± 5° (Fig. S2 and Table S2, Supplementary material). More evidence could be found in the out-of-plane (OOP) X-ray diffraction (XRD) pattern. As shown in Fig. 2b, the XRD spectra of the QLS film of **1** in the low-angle range showed one diffraction peak at 2θ = 5.98°, corresponding to a layer spacing of 1.48 nm. This is ascribed to the diffraction from (001) plane, showing a regular layered structure and good molecular ordering for this film. Based on the simulated energy-optimized double-decker molecular dimension of ca. 3.0 nm [35], the orientation angle of 29.5° was deduced (inset of Fig. 2b), which is consistent with the results obtained from the UV–Vis and polarized UV–Vis measurements. Therefore, the dimeric bisphthalocyanine molecules take an almost face-on stacking mode with orientation angle about 29.5° to the surface of the substrate in the QLS film, which provides a large contact area between phthalocynine rings and target analytes. Furthermore, the XRD diagram shows another diffraction peak at 0.31 nm, corresponding to the π–π stacking distance between neighboring molecules of **1** [33], indicating the valid intermolecular π–π interaction in the film. This in turn is expected to be beneficial for charge transport. On the other hand, AFM observation found that quite uniform nanograins (ca. 15 nm in diameter) formed in the QLS film of **1** with the root-mean-square (Rms) roughness value of 1.9 nm, Fig. 2c. This guaranteed the fewer defects localized around grain boundaries. Meanwhile small nanoparticles provide great specific surface area and numerous active sites for adsorption. As a result, good electrical conductivity and electrochemical sensing properties are expected. I-V measurements for the

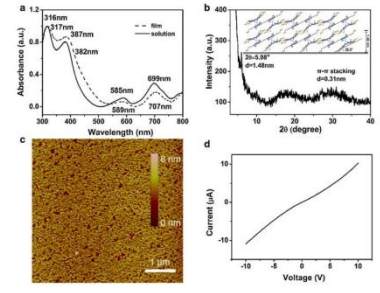

Fig. 2 **a** Electronic absorption spectra of **1** in $CHCl_3$ solution (solid line) and QLS film (dash line); **b** out-of-plane XRD pattern and **c** AFM phase image of the QLS film of **1**, **d** I–V curve

QLS film of **1** indeedly shown an excellent conductivity of 3.64×10^{-4} S cm^{-1}, Fig. 2d, further confirming good charge transfer capacity of the film. It is worth noting that although the current developed by the QLS film of **1** remains perfectly symmetrical, a slight non linearity in the I–V curve is exhibited, in agreement with the well reported space-charge-limited conduction (SCLC) found in phthalocyanine-based devices [36].

3.3 Electrochemical properties of [{Pc(SC$_2$H$_5$)$_8$}Eu{BiPc(SC$_2$H$_5$)$_{12}$}Eu{Pc(SC$_2$H$_5$)$_8$}] coated electrode

The electrochemical sensing behavior of both a bare ITO electrode and an ITO covered by the QLS film of **1** (denoted as film-**1**/ITO) were comparative investigate towards APAP and AA by cyclic voltammograms (CVs) in phosphate buffer solution (PBS at 0.1 M, pH 7.3), respectively, Fig. 3a, b. As expected, voltammograms registered in PBS using film-**1**/ITO did not show any detectable response (red line). This is also true for the CV response using bare ITO immersed in PBS containing APAP and AA, respectively (black line). In good contrast, the CV response of film-**1**/ITO towards APAP and AA in PBS show the significantly peaks at 0.45 V and 0.39 V, associated with the oxidation of the APAP and AA, respectively (blue line). These results confirm that the dimeric bisphthalocyanine **1** has electrocatalytic activity towards the APAP and AA. As shown in Fig. 3c, the arc diameter in Nyquist plots gets decreased from bare ITO to film-**1**/ITO (inset of Fig. 3c), indicating a lowered charge transfer resistance after film-**1** deposited on bare ITO electrode [37]. This in turn results in the better electrochemical sensing activity for this compound **1**.

The effect of scan rate on the electrochemical response for film-**1**/ITO toward APAP and AA was studied at different scan rate. As shown in Fig. 4, the oxidation peak currents of both APAP and AA were all linearly to the scan rate in the range of 20–200 mV s^{-1} suggesting that the oxidation reactions were controlled by surface adsorption process.

To investigate the relationship between oxidation peak current of film-**1**/ITO sensor and concentration of APAP and AA, differential pulse voltammetric (DPV) technique was carried out in the potential range of − 0.6 to 0.8 V in PBS (PH 7.3), Fig. 5. The intensity of current for the oxidation (I_p) process was proportional to the concentration of the analyte in the range from 1 to 100 μM for APAP and 10 to 1000 μM for AA, respectively, Fig. 5a, b. The linear regression equations were I_p (μA) = 0.2542 C_{APAP} (μM) + 0.2591 (R^2 = 0.9978), and I_p (μA) = 0.08562 C_{AA} (μM) + 1.041 (R^2 = 0.9968), Fig. 5c, d, resulting in the good sensitivity of 254 and 85.6 mA μM^{-1} cm^{-2} for APAP and AA, respectively. The lowest detection limit was estimated to be 1.3 and 3.7 μM for APAP and AA (S/N = 3), respectively, which

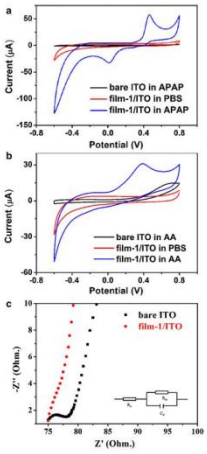

Fig. 3 CV curves of the film-**1**/ITO in 0.1M PBS (red), bare ITO (black) and film-**1**/ITO (blue) in 0.1M PBS containing 0.1 mM APAP (**a**) and 0.1 mM AA (**b**). Scan rate: 100 mV s^{-1}, **c** the EIS of bare ITO and film-**1**/ITO in PBS containing 5 mmol L^{-1} $[Fe(CN)_6]^{3-/4-}$. The inset shows the Randles equivaent circuit model

were comparable or even better than that of the previous reported electrochemical sensors for APAP and AA, (Tables S3, S4, Supplementary material). These indicated the the the dimeric phthalocyanine-involved double-decker is a promising sensor for simple, low-cost and sensitive detection of APAP and AA.

In addition, the peak currents were measured every 3 days on the same film-**1**/ITO electrode during 15 days, only a very little decay was found for the peak currents of APAP and AA with the respective values of 2.4% and 4%, respectively,

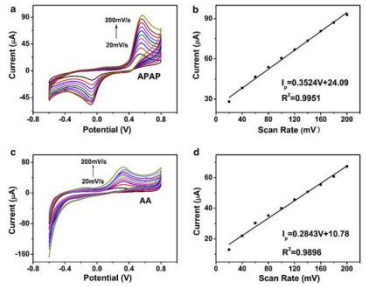

Fig. 4 CV curves at film-**I**/ITO in PBS containing the mixture of **a** 0.1 mM APAP and **c** 0.1 mM AA, with various scan rate between 20 and 200 mV s^{-1}, and the corresponding plots of peak current versus scan rate (**b**, **d**)

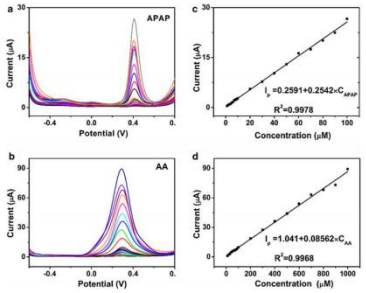

Fig. 5 DPV curves at film-**I**/ITO in PBS (PH 7.3) with varying concentrations from 1 to 100 μM for APAP (**a**) and 10–1000 μM for AA (**b**). The corresponding calibration plots for each testing sample are shown in the (**c**, **d**)

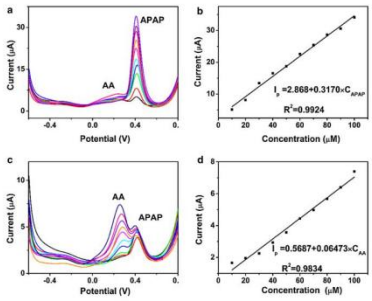

Fig. 6 DPV curves at film-**I**/ITO for simultaneous determination of APAP and AA in PBS (pH 7.3): **a** 100 μM AA with different concentrations of APAP, **c** 10 μM APAP with different concentrations of AA. The corresponding calibration plots for each testing sample are shown in the (**b**, **d**)

demonstrating the excellent reproducibility and stability of the film-**I**/ITO electrode, (Fig. S4, Supplementary material).

Furthermore, the simultaneous determination of APAP and AA at film-**I**/ITO was carried out by DPV technique. As shown in Fig. 6a, b, the electrochemical responses of APAP increased linearly along with the increased concentration of APAP from 10 to 100 μM under the same AA concentration of 100 μM. Similarly, the increasing AA concentration from 10 to 100 μM also causes the linearly increasing in current responses with the constant concentration of APAP (10 μM), Fig. 6c, d. Intreistingly, the linear regression equations are I_p (μA) = 0.3170 C_{APAP} (μM) + 2.868 (R^2 = 0.9924), and I_p (μA) = 0.06473 C_{AA} (μM) + 0.5687 (R^2 = 0.9834), resulting in the good sensitivity of 317 and 64.7 mA μM^{-1} cm^{-2} for APAP and AA, respectively. Obviously, upon co-existence of APAP and AA, a much higher sensitivity to APAP was achieved, while that was slight lower to AA, in comparison with those measured alone. These results not only exhibited that the film-**I**/ITO sensor can well distinguish and determine the APAP and AA when two analytes co-exist in PBS, but also shown that existence of AA can facilitate the detection of APAP. We noted that, very recently, using bimetallic Pd-Ag/rGO (reduced graphene oxide) nanocomposites on GCEs, a lower LOD (3.23 nM) for APAP detection has been reported by using a one-step procedure for the fabrication of modified electrodes [38]. The combination of good electrical conductivity and a large surface area of rGO with excellent electrochemical activity of noble metals should be response to this achievement. However, the relatively expensive Pd-Ag bimetals due to scarcity of precious metal resources produced globally might limit its large-scale application. With a more appropriate redox potential, simultaneous determination of APAP and AA can be achieved in the present case. The design and synthesis of new sandwich compounds with good conductivity and the optimization of the electrode fabrication are in progress.

4 Conclution

In summary, an efficient and sensitive electrochemical sensor based on the solution processing film of [{Pc(SC_2H_5)$_8$}Eu{BiPc(SC_2H_5)$_{12}$}Eu{Pc(SC_2H_5)$_8$}] (**1**) has been successfully developed for sensitive and selective simultaneous detection of APAP and AA. The [{Pc(SC_2H_5)$_8$}Eu{BiPc(SC_2H_5)$_{12}$}Eu{Pc(SC_2H_5)$_8$}] film-**I**/ITO electrode is revealed to exhibit linearly amperometric response towards both APAP and AA, with a high performance in terms of sensitivity, low detection limit and detection range. The present work opens a new way for the development of high-performance tetrapyrrole based nonenzymatic electrochemical sensor through molecular design and low-cost sensor fabrication technique.

Acknowledgements This work was financially supported by the National Natural Science Foundation of China (Nos. 21771192, 21631003 and 21371073), the Research Fund for Introduced Talents of China University of Petroleum (No. Y1510051), the Education Research Fund for Department of Heilongjiang Province (No. 1352DZ001), the Scientific Research Project of Mudanjiang Normal University (No. GP201603), the Science and Technology Innovation Project of Mudanjiang Normal University (No. kjcx2017-23mdjnu).

References

1. W.M. Lee, Hepatology **40**, 6–9 (2004)
2. A. Cernat, M. Tertis, R. Săndulescu, F. Bedioui, A. Cristea, C. Cristea, Anal. Chim. Acta **886**, 16–28 (2015)
3. X. Zuo, H. Zhang, N. Li, Sens. Actuators B **161**, 1074–1079 (2012)
4. D. Zhao, G. Yu, K. Tian, C. Xu, Biosens. Bioelectron. **82**, 119–126 (2016)
5. U. Grundmann, C. Wçmle, A. Biedler, S. Kreuer, M. Wrobel, W. Wilhelm, Anesth. Analg. **103**, 217–222 (2006)
6. A.A. Ensafi, H.K. Maleh, S. Mallakpour, Electroanalysis **3**, 666–675 (2012)
7. A.A. Abdelwahab, Y.B. Shim, Sens. Actuators B **221**, 659–665 (2015)
8. A.U. Alam, Y. Qin, M. Catalano, L. Wang, M.J. Kim, M.M.R. Howlader, N. Hu, M.J. Deen, ACS Appl. Mater. Interfaces **10**, 21411–21427 (2018)
9. B.G. Mahmoud, M. Khairy, F.A. Rashwan, C.E. Banks, Anal. Chem. **89**, 2170–2178 (2017)
10. X. Zhang, Y. Zhang, L. Ma, Sens. Actuators B **227**, 488–496 (2016)
11. X. Deng, Y. Fang, S. Lin, Q. Cheng, Q. Liu, X. Zhang, ACS Appl. Mater. Interfaces **9**, 3514–3523 (2017)
12. C. Pal, A.K. Sharma, A.N. Cammidge, M.J. Cook, A.K. Ray, J. Phys. Chem. B **117**, 15033–15040 (2013)
13. Z. Yu, L. Zou, Y. Chen, J. Jiang, ACS Appl. Mater. Interfaces **8**, 30398–30406 (2016)
14. H. Xu, J. Xiao, L. Yan, L. Zhu, B. Liu, J. Electroanal. Chem. **779**, 92–98 (2016)
15. L.F. de Holanda, F.WP. Ribeiro, C.P. Sousa,, P. de Lima-Neto, A.N. Correia, P. N. da Silva Casciano, J. Electroanal. Chem. **772**, 9–16 (2016)
16. X. Kang, J. Wang, H. Wu, J. Liu, I.A. Aksay, Y. Lin, Talanta, **81**, 754–759 (2010)
17. M. Liu, Q. Chen, C. Lai, Y. Zhang, J. Deng, H. Lin, S. Yao, Biosens. Bioelectron. **48**, 75–81 (2013)
18. T. Madrakian, E. Haghshenas, A. Afkhami, Sens. Actuators B **193**, 451–460 (2014)
19. A. Afkhami, H. Khoshsafar, H. Bagheri, T. Madrakian, Sens. Actuators B **203**, 909–918 (2014)
20. Y. Fan, J. Liu, H. Lu, Q. Zhang, Colloids Surf. B **85**, 289292 (2011)
21. D. Sun, H. Zhang, Microchim. Acta **158**, 131–136 (2007)
22. Y. Si, E.T. Samulski, Nano Lett. **8**, 1679–1682 (2008)
23. M.G. Martín, M.L. RodrÍguezMendez, J. A. de Saja, Langmuir **26**, 19217–1924 (2010)
24. Y. Chen, M. Bouvet, T. Sizun, Y. Gao, C. Plassard, E. Lesniewska, J. Jiang, Phys. Chem. Chem. Phys. **12**, 12851–12861 (2010)
25. M.J. Plater, A. Jeremiah, G. Bourhill, J. Chem. Soc. Perkin Trans. **1**, 91–96 (2002)
26. G. Lu, J. Li, S. Yan, W. Zhu, Z. Ou, K.M. Kadish, Inorg. Chem. **54**, 5795–5805 (2015)
27. H. Ahn, A. Chandekar, B. Kang, C. Sung, J.E. Whitten, Chem. Mater. **16**, 3274–3278 (2004)
28. G. Lu, K. Wang, X. Kong, H. Pan, J. Zhang, Y. Chen, J. Jiang, ChemElectroChem **5**, 605–609 (2018)
29. Y. Chen, D. Li, N. Yuan, J. Gao, R. Gu, G. Lu, M. Bouvet, J.Mater. Chem. **22**, 22142–22149 (2012)
30. K. Wang, D. Qi, H. Wang, W. Cao, W. Li, T. Liu, C. Duan, J. Jiang, Chem. A Eur. J. **19**, 11162–11166 (2013)
31. M. Kasha, H.R. Rawls, M.A. ElBayoumi, Pure Appl. Chem. **11**, 371–392 (1965)
32. Y. Chen, X. Kong, G. Lu, D. Qi, Y. Wu, X. Li, M. Bouvet, D. Sun, J. Jiang, Mater. Chem. Front. **2**, 1009–1016 (2018)
33. G. Lu, X. Kong, J. Sun, L. Zhang, Y. Chen, J. Jiang, Chem. Commun. **53**, 12754–12757 (2017)
34. M. Yoneyama, M. Sugi, M. Saito, K. Ikegama, S. Kuroda, S. Iizima, Jpn. J. Appl. Phys. **25**, 961 (1986)
35. H. Wang, X. Kong, S. Zhao, J. Wu, X. Li, Y. Chen, New J. Chem. **41**, 11955–11961 (2017)
36. V. Parra, J. Brunet, A. Pauly, M. Bouvet, Analyst **134**, 1776–1778 (2009)
37. L.A. Mercante, A. Pavinatto, L.E.O. Iwaki, V.P. Scagion, V. Zucolotto, O.N. Oliveira, L.H.C. Mattoso, D.S. Correa, ACS Appl. Mater. Interfaces **7**, 4784–4790 (2015)
38. Y.V.M. Reddy, S. Bathinapatla, T. Luczak, M. Osińska, H. Maseed, P. Ragavendra, L.S. Sarma, V.V.S.S. Srikanth, G. Madhavi, New J. Chem. **42**, 3137–3146 (2018)

6.Wei C, Lu G, Guo C, et al. Ethylthio-substituted sandwich phthalocyaninato europium (III) semiconductors for sensing NO_2 and NH_3: Effect of the extended π-conjugate systems on tuning the conductivity and sensing behavior[J]. Organic Electronics, 2021, 93: 106151.（SCI 检索收录三区，IF=3.721）

Organic Electronics 93 (2021) 106151

Contents lists available at ScienceDirect

Organic Electronics

journal homepage: http://www.elsevier.com/locate/orgel

Ethylthio-substituted sandwich phthalocyaninato europium (III) semiconductors for sensing NO_2 and NH_3: Effect of the extended π-conjugate systems on tuning the conductivity and sensing behavior

Chuangyu Wei [a], Guang Lu [c], Chang Guo [a], Xuehui Lv [a], Xiangjie Tang [a], Qi Liu [a], Xue Cai [b,**], Yanli Chen [a,*], Jianzhuang Jiang [a,d,***]

[a] College of Science, China University of Petroleum (East China), Qingdao, 266580, China
[b] College of Chemistry and Chemical Engineering, Mudanjiang Normal University, Mudanjiang, 157011, China
[c] School of Chemistry and Biological Engineering, Shandong University of Science and Technology, Qingdao, 266510, China
[d] Beijing Key Laboratory for Science and Application of Functional Molecular and Crystalline Materials, Department of Chemistry, University of Science and Technology Beijing, Beijing, 100083, China

ARTICLE INFO

Keywords:
Sandwich-type phthalocyanine
π-conjugate system
Organic semiconductor
Solution-processed film
Gas sensing

ABSTRACT

By using the π-conjugated phthalocyanine macrocycle as the versatile building block, a series of five sandwich-type ethylthio substituted phthalocyaninato europium complexes, namely double-decker $Eu[Pc(SC_2H_5)_8]_2$ (**Pc-1**), triple-decker $Eu_2[Pc(SC_2H_5)_8]_3$ (**Pc-2**), and their corresponding dimers, $[Pc(SC_2H_5)_8]_2Eu_2[BiPc(SC_2H_5)_{12}]$ (**Pc-1@Pc-1**), $[Pc(SC_2H_5)_8]_3Eu_3[BiPc(SC_2H_5)_{12}]$ (**Pc-1@Pc-2**) and $[Pc(SC_2H_5)_8]_4Eu_4[BiPc(SC_2H_5)_{12}]$ (**Pc-2@Pc-2**), are synthesized and prepared into the solution-processed films by a simple quasi-Langmuir-Shäfer (QLS) method. Combination between the extending π-conjugated system in the longitudinal and transverse directions of Pc macrocycles and/or radical nature of **Pc-1** unit among different semiconducting molecules result in unusually small energy gaps (0.345–0.91 eV). Consequently, all of the semiconductors exhibit excellent conductivities. Among these materials, the conductivity for the radical species **Pc-1@Pc-1**, **Pc-1@Pc-2** and **Pc-1** is about 3–4 times larger than that for the non-radical compounds **Pc-2@Pc-2** and **Pc-2**. Moreover, the QLS films of five semiconductors take excellent linear responses for both oxidizing NO_2 (100–300 ppb) and reducing NH_3 (4–8.6 ppm). Respectively, the sensitivity (in % ppm^{-1}) gets increased in the order of **Pc-1** < **Pc-2** < **Pc-1@Pc-1** < **Pc-1@Pc-2** < **Pc-2@Pc-2** for NO_2, and **Pc-1@Pc-2** < **Pc-1** < **Pc-1@Pc-1** < **Pc-2@Pc-2** < **Pc-2** for NH_3. Depending on the highly extended π-conjugated systems, **Pc-2@Pc-2** and **Pc-2** films achieve the highest sensitivity of 208.2% ppm^{-1} and 0.97% ppm^{-1} to NO_2 and NH_3, respectively. In addition, with a less than 2 min response time within a limit of detection at 10 ppb for NO_2 and 0.48 ppm for NH_3, good reproducibility and selectivity have been revealed for the **Pc-2@Pc-2** and **Pc-2** films among the best gas sensors obtained so far for all the solution-processed films based on organic semiconductors in dry air at room temperature. More importantly, it is firstly demonstrated that the high NO_2 sensing is resulted from low Oxd_1, and high NH_3 sensing is resulted from high Red_1 among the sandwich Pc-based semiconductors.

1. Introduction

In recent years, organic semiconducting materials have been widely studied in the development of the profitable sensing systems for the sensitive detection of nitrogen-based hazardous gas due to their lower operating temperature, easier modulability of molecular properties, and solution processability compared with inorganic semiconductors [1–3]. Phthalocyanines (Pcs), as an important class of organic semiconductors, are a large series of heterocyclic conjugated molecules that possess unique electrical properties, high chemical stability, and tunable molecular orbital energies by the peripheral substituents and coordinated metals [4–6]. In particular, sandwich-type phthalocyanines, originating

* Corresponding author.
** Corresponding author.
*** Corresponding author. College of Science, China University of Petroleum (East China), Qingdao, 266580, China.
E-mail addresses: xuecai@mdjnu.edu.cn (X. Cai), yanlichen@upc.edu.cn (Y. Chen), jianzhuang@ustb.edu.cn (J. Jiang).

https://doi.org/10.1016/j.orgel.2021.106151
Received 13 February 2021; Received in revised form 12 March 2021; Accepted 12 March 2021
Available online 26 March 2021
1566-1199/© 2021 Elsevier B.V. All rights reserved.

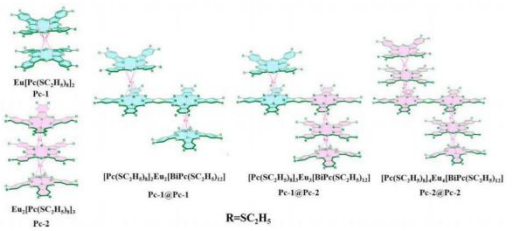

Scheme 1. Schematic molecular structures of **Pc-1**, **Pc-2**, **Pc-1@Pc-1**, **Pc-1@Pc-2** and **Pc-2@Pc-2**.

from the multiple Pc macrocyclic ligands complexed with rare earth metal ion(s) in one molecule, offer the most effective approach to adjust frontier molecular orbital energies, and thus the charge carrier density and mobility of the materials, due to the great number of possible substitution positions in the periphery of multiple Pc macrocycles and the intramolecular π-π interactions within these Pc chromophores [7]. Up to now, most organic semiconducting gas sensor show only one type of charge carrier's response behavior (either *p*- or n-type response) even though the ambipolar (both electron and hole) charge transport is an intrinsic nature of the pure organic semiconducting materials on the basis of theoretical considerations, and have ever been revealed by many organic filed effect transistor measurements. Since the ambipolar behavior of rare earth double decker phthalocyanine complexes was first reported in OFETs by G. Guillaud et al. [8], and the heteroleptic octanaphthoxy-substituted europium bisphthalocyanine was firstly found to show ambipolar charge-transporting gas sensing in 2016 [9], the development of novel ambipolar organic semiconductors towards sensor applications has aroused great research interest, as they are very cheap, mechanically flexible, and highly sensitive at room temperature (24–26 °C), without necessarily requiring micro-patterning of the individual *p*- and *n*-channel semiconductors [10–14]. In recent years, significant improvements on sensing performance have been achieved by different strategies, such as optimizing the film morphology [15], tuning the intra-/intermolecular interactions [11,16], and constructing sensing array or heterojunction devices [10,14,15,17–20]. More recently, through examining the NH_3 sensing nature of ambipolar thiophenoxy-substituted bis(phthalocyaninato) rare earth complexes, whether n-type or *p*-type response behaviors of ambipolar semiconductors has been found to be governed by the lower rather than the higher charge carrier density of the ambipolar organic semiconductors [20]. This is further corroborated by a *n*- and *p*-type responses to NO_2 and NH_3, respectively, for two ambipolar tris(phthalocyaninato) rare earth triple-deckers [11]. To effectively improve the sensing performance of sandwich-type phthalocyaninato rare earth ambipolar semiconductors, in-depth understanding of the correlations between molecular structure and gas sensing property is imperative. In addition, various methods, such as Langmuir-Blodgett (LB), Langmuir-Shäfer (LS), quasi-Langmuir-Shäfer (QLS) etc., have been employed to fabricate the thickness-controlled films for phthalocyanine-based sensing devices [7, 10,13,16,18]. Among them, the QLS technology developed by M. Bouvet and co-workers [22], is very attractive method, which can get well-organized films at the air-water interface without complicated apparatus.

In this study, we design and synthesize a series of ethylthio-substituted sandwich-type phthalocyaninato europium (III) complexes, double-decker $Eu[Pc(SC_4H_9)_8]_2$ (**Pc-1**), triple-decker $Eu_2[Pc(SC_4H_9)_8]_3$ (**Pc-2**), and their corresponding dimer combined with double- and/or triple-decker units via an edge-to-edge mode by a fusing benzene ring, $[Pc(SC_4H_9)_8]_2Eu_2[BiPc(SC_4H_9)_{12}]$ (**Pc-1@Pc-1**), $[Pc(SC_4H_9)_8]_2Eu_2[BiPc(SC_4H_9)_{12}]$ (**Pc-1@Pc-2**), and $[Pc(SC_4H_9)_8]Eu[BiPc(SC_4H_9)_{12}]$ (**Pc-2@Pc-2**), ([Pc(SC$_4$H$_9$)$_8$] = 2,3,9,10,16,17,23,24-octakis(ethylthio)-phthalocyanine, BiPc(SC$_4$H$_9$)$_{12}$ = bis[7,8,12,13,17,18-hexakis(ethylthio)tribenzo[g,l,q]-5,10,15,20-tetraazaporphyrinate [b,e]benzene-linked binuclear phthalocyaninate]), Scheme 1. The influence of the extending π-systems on the molecular redox potentials, conductivity, and gas sensing properties has been compared. The self-assembled films of the five compounds prepared by a solution-processed quasi-Langmuir-Shäfer (QLS) method were analyzed by UV–vis absorption spectra (UV–vis), X-ray diffraction (XRD), scanning electron microscope (SEM), and current-voltage (I–V) measurements. The redox potentials, energy gaps of the frontier electronic states, thin film microstructure/morphology, and molecular aggregation pattern in the QLS films of the five ambipolar semiconductors are systematically studied to comprehend the changes in sensing performance.

2. Experimental

2.1. Materials

1,8-Diazabicyclo[5.4.0]undec-7-ene (DBU), anhydrous 1,2,4-trichlorobenzene (TCB), and ethyl mercaptan were purchased from Aldrich. The compounds of $Eu(acac)_3{\cdot}H_2O$, 4,5-bisethylthio-1,2-dicyanobenzene were prepared according to the literature methods. CH_2Cl_2 for DPV studies was freshly distilled from CaH_2 under nitrogen. n-pentanol was distilled from sodium. All other reagents and solvents were of reagent grade and used as received without further purification. Column chromatography was carried out on silica gel (200–300 mesh) with the pure $CHCl_3$ as eluents.

2.2. Film preparation and measurement

The quasi-Langmuir-Shäfer (QLS) method [21] was employed to

prepare the pristine QLS films for $Eu[Pc(SC_4H_9)_8]_2$ (**Pc-1**), $Eu_2[Pc(SC_4H_9)_8]_3$ (**Pc-2**), $[Pc(SC_4H_9)_8]_2Eu_2[BiPc(SC_4H_9)_{12}]$ (**Pc-1@Pc-1**), $[Pc(SC_4H_9)_8]_2Eu_2[BiPc(SC_4H_9)_{12}]$ (**Pc-1@Pc-2**), and $[Pc(SC_4H_9)_8]Eu_1[BiPc(SC_4H_9)_{12}]$ (**Pc-2@Pc-2**) according to the published procedure [22, 23]. The detailed procedures were presented on the section of film-preparation in Supplementary materials. MALDI-TOF mass spectra were recorded on the Bruker BIFLEX III ultra-high-resolution Fourier transform ion cyclotron resonance (FT-ICR) mass spectrometer with alpha-cyano-4-hydroxycinnamic acid as matrix. ^{1}H NMR spectrums were recorded on the Bruker DPX 400 spectrometer in $CDCl_3$. The spectra were referenced internally with residual $CDCl_3$ (δ 7.26) relative to SiMe$_4$. Electrochemical measurements were carried out with a CHI760D voltammetric analyser and for the detailed procedures please see our recently published papers [24]. UV–vis and polarized UV–vis absorption spectra were recorded with a Hitachi U-3900 spectrophotometer. X-ray diffraction (XRD) experiments were carried out on a Bruker D8 ADVANCE with a Cu anode as the primary x-ray beam source (λ = 1.5406 Å). Scanning electron microscopy (SEM) images were obtained using Quant 250FEG. Current-voltage (I–V) curves were collected at room temperature using a Keysight B2910A precision source/measure unit with an incorporated voltage range supplied from −10 V to 10 V. Conductivity (σ) obtained by I-V curve can be calculated according to the repeated method reported in previous literature [25].

For characterizations, three kinds of substrates (SiO_2/Si, quartz, and ITO) were washed by deionized water, absolute ethyl alcohol, and dichloromethane, respectively. Films were deposited on different substrates by using QLS self-assembly method [22].

2.3. Synthesis details of Pc-1, Pc-2, Pc-1@Pc-1, Pc-1@Pc-2, Pc-2@Pc-2

$H_2Pc(SC_4H_9)_8$: 4,5-Bis(ethylthio)-1,2-dicyanobenzene (300 mg) was put in a micro reactor, the air was pumped out, and then nitrogen was purged. This process was repeated for three times (every 5 min). After this 3 mL dehydrated n-butanol as solvent and 5–6 drops of DBU were added. The reactor was then heated up to 140 °C and stirred for 10 h under N_2 protection. After the reaction was stopped, the product was recrystallized using a large amount of CH_3OH at room temperature for 5–6 h, then filtered. This step was repeated for five times to obtain a dark green solid. Yield: 200 mg (70%).

$Eu[Pc(SC_4H_9)_8]_2$ (**Pc-1**): $H_2Pc(SC_4H_9)_8$ (100 mg) and $Eu(acac)_3{\cdot}nH_2O$ (38.4 mg) were put in micro reactor, the air was pumped out, and then nitrogen was purged. This process was repeated for three times (every 5 min). After this 2 mL dehydrated n-pentanol as solvent and 5-6 drops of DBU were added. The reactor was then heated up to 180 °C and stirred for 8 h under N_2 protection. After the reaction was stopped, the product was recrystallized using a large amount of CH_3OH at room temperature for 5–6 h, then filtered. The residue left was chromatographed on a silica gel column with $CHCl_3$ as eluent. Recrystallization from $CHCl_3$ and methanol gave dark green powder. Yield: 86 mg (65%).

$Eu_2[Pc(SC_4H_9)_8]_3$ (**Pc-2**): $Eu[Pc(SC_4H_9)_8]_2$ (100 mg), $H_2Pc(SC_4H_9)_8$ (93 mg), and $Eu(acac)_3{\cdot}nH_2O$ (31.6 mg) were put in micro reactor, the air was pumped out, and then nitrogen was purged. This process was repeated for three times (every 5 min). After this 2 mL TCB as solvent was added. The reactor was then heated up to 210 °C and stirred for 8 h under N_2 protection. After the reaction was stopped, the product was recrystallized using a large amount of CH_3OH at room temperature for 5–6 h, then filtered. The residue left was chromatographed on a silica gel column with $CHCl_3$ as eluent. Recrystallization from $CHCl_3$ and methanol gave dark green powder. Yield: 53 mg (31.6%).

$[Pc(SC_4H_9)_8]_2Eu_2[BiPc(SC_4H_9)_{12}]$ (**Pc-1@Pc-1**): 4,5-Bisethylthio-1,2-dicyanobenzene (300 mg), bis(diiminoisoindoline) (17.1 mg), and $Eu(acac)_3{\cdot}nH_2O$ (108.9 mg) were put in micro reactor, the air was pumped out, and then nitrogen was purged. This process was repeated for three times (every 5 min). After this 4 mL dehydrated n-pentanol as solvent and 5–6 drops of DBU $H_2Pc(SC_4H_9)_8$ were added. The reactor was then heated up to 140 °C and stirred for 8 h under N_2 protection.

After the reaction was stopped, the product was recrystallized using a large amount of CH_3OH at room temperature for 5–6 h, then filtered. The residue left was chromatographed on a silica gel column with $CHCl_3$ as eluent. Recrystallization from $CHCl_3$ and methanol gave dark green powder. Yield: 107 mg (24.8%).

$[Pc(SC_4H_9)_8]_2Eu_2[BiPc(SC_4H_9)_{12}]$ (**Pc-1@Pc-2**): $[Pc(SC_4H_9)_8]_2Eu_2[BiPc(SC_4H_9)_{12}]$ (150 mg), $H_2Pc(SC_4H_9)_8$ (56.6 mg), and $Eu(acac)_3{\cdot}nH_2O$ (34.1 mg) were put in micro reactor, the air was pumped out, and then nitrogen was purged. This process was repeated for three times (every 5 min). After this 3 mL TCB as solvent and was added. The reactor was then heated up to 210 °C, stirred for 9 h under reflux, and protected with N_2 during the period. After the reaction was stopped, the product was recrystallized using a large amount of CH_3OH at room temperature for 5–6 h, then filtered. The residue left was chromatographed on a silica gel column with $CHCl_3$ as eluent. Recrystallization from $CHCl_3$ and methanol gave dark green powder. Yield: 7.0 mg (5.2%).

$[Pc(SC_4H_9)_8]Eu_1[BiPc(SC_4H_9)_{12}]$ (**Pc-2@Pc-2**): $[Pc(SC_4H_9)_8]_2Eu_2[BiPc(SC_4H_9)_{12}]$ (150 mg), $H_2Pc(SC_4H_9)_8$ (56.6 mg) and $Eu(acac)_3{\cdot}nH_2O$ (34.1 mg) were put in micro reactor, the air was pumped out, and then nitrogen was purged. This process was repeated for three times (every 5 min). After this 3 mL TCB as solvent and was added. The reactor was then heated up to 210 °C, stirred for 9 h under reflux, and protected with N_2 during the period. After the reaction was stopped, the product was recrystallized using a large amount of CH_3OH at room temperature for 5–6 h, then filtered. The residue left was chromatographed on a silica gel column with $CHCl_3$ as eluent. Recrystallization from $CHCl_3$ and methanol gave dark green powder. Yield: 6.0 mg (5%).

2.4. Gas sensing test

The films of five compounds were tested in a cuboid Teflon sensor chamber (about 30 cm^3 as internal volume). The desired NO_2, NH_3, H_2S, or CO_2 concentration was produced by diluting a mixture of NO_2/air (20 ppm NO_2, from Qingdao Ludong Gas., Ltd, China), NH_3/air (500 ppm NH_3, from Qingdao Ludong Gas., Ltd, China), H_2S/air (50 ppm H_2S, from Qingdao Ludong Gas., Ltd, China), or CO_2 (20 ppm CO_2, from Qingdao Ludong Gas., Ltd, China) with dry air using two CS200 Mass Flow Controllers. Total flows were 0.1 L min^{-1} for NO_2 or NH_3 and 2 L min^{-1} for diluent gas air, respectively. All tests were first exposed to synthetic air, followed by exposure to NO_2, NH_3, H_2S, or CO_2 gas at various concentrations, and the relative humidity is controlled at 0% (dry synthetic air), 35%, and 70%, respectively. In order to quantitatively analyze the sensor responses, the percent current change was calculated using the formula of $[(I_g-I_f)/I_f] \times 100$, where I_g is the initial current for each of exposure/recovery cycle and I_f is the current at the end of each exposure period. On the other hand, for gas sensing experiments, the samples were constantly polarized at 5 V.

3. Results and discussion

3.1. Design, synthesis and characterizations

The symmetrical ethylthio-substituted europium bis- and tris-phthalocyanines $Eu[Pc(SC_4H_9)_8]_2$ (**Pc-1**), $Eu_2[Pc(SC_4H_9)_8]_3$ (**Pc-2**), and their dimers combined with double- and/or triple-decker units via an edge-to-edge mode by a fusing benzene ring, $[Pc(SC_4H_9)_8]_2Eu_2[BiPc(SC_4H_9)_{12}]$ (**Pc-1@Pc-1**), $[Pc(SC_4H_9)_8]_2Eu_2[BiPc(SC_4H_9)_{12}]$ (**Pc-1@Pc-2**), and $[Pc(SC_4H_9)_8]Eu_1[BiPc(SC_4H_9)_{12}]$ (**Pc-2@Pc-2**) were successfully synthesized. The detailed synthesis procedures together with the structure characterization are described in the experimental section. An extended π-conjugated electronic/molecular structure can adjust the intra-/inter-molecular interactions, and thus the molecular orbital energies, resulting in gas sensing changes [26]. Adding ethylthio groups onto the periphery of phthalocyanine rings is expected to improve the solubility of the five compounds in conventional organic solvents. The MALDI-TOF mass spectra of the five compounds show intense molecular

Table 1
Half-wave redox potentials (V *vs* SCE) in CH_2Cl_2 containing 0.1 mol L^{-1} $[Bu_4N][ClO_4]$ together with the HOMO and LUMO levels of **Pc-1**, **Pc-2**, **Pc-1@Pc-1**, **Pc-1@Pc-2** and **Pc-2@Pc-2**.

Compounds	Red_3 (V)	Red_4 (V)	Red_3 (V)	Red_2 (V)	Red_1 (V)	$Ox1_1$ (V)	$Ox1_2$ (V)	$Ox1_3$ (V)	$Ox1_4$ (V)	LUMO(eV)	HOMO(eV)	$\Delta E^{opt}_{1/2}$ (V)[a]
Pc-1	–	−1.927	−1.584	−1.145	−0.134	0.260	–	–	–	−3.295[c]	−4.306[c]	0.394
Pc-2	–	–	–	−1.226	−0.735	0.236	0.515	0.920	1.050	−3.705[c]	−4.676[c]	0.971
Pc-1@Pc-1	−1.775	−1.610	−1.210	−0.255	−0.110	0.235	0.460	–	–	−3.230[c]	−4.330[c]	0.345
Pc-1@Pc-2	–	–	–	−0.852	−0.218	0.193	0.400	0.660	–	−3.588[c]	−4.222[c]	0.411
Pc-2@Pc-2	–	–	–	–	−0.762	0.148	0.305	0.584	0.664	−3.678[c]	−4.588[c]	0.910

[a] $\Delta E^{opt}_{1/2}(V) = = Ox1_1 - Red_1$.
[b] HOMO = −(Red_1+4.44 eV); and LUMO = −(Red_3+4.44 eV) [13].
[c] HOMO = −($Ox1_1$+4.44 eV); and LUMO = −(Red_1+4.44 eV) [7].
[d] HOMO = −(Red_1+4.44 eV); and LUMO = −(Red_3+4.44 eV) [9].

ion M^+ signals, Fig. S11 and Table S1. The five compounds were also characterized by ^{1}H NMR spectra with corresponding data summarized in Fig. S2† and Table S2†.

3.2. Electrochemical properties

The electrochemical behaviors of five sandwich complexes were investigated by differential pulse voltammetry (DPV) in CH_2Cl_2. The values of half-wave redox potential *vs* SCE are summarized in Table 1. These compounds exhibit the highly electrochemical behavior typical of the sandwich rare earth (III) phthalocyanines [13,27], with one to four quasi reversible one-electron oxidation(s) (labelled as $Ox1_1$–$Ox1_4$) and one to five quasi reversible one-electron reduction(s) (Red_1–Red_5) within the electrochemical window of CH_2Cl_2, Fig. S3†. All of these processes correspond to consecutive removal of electron from or addition to the Pc-based molecular orbitals since the oxidation/reduction of the central europium cation in these complexes does not occur in this electrochemical test window [28]. The five compounds show reversible oxidation and reduction waves, indicating the remarkable stability of the cationic and anionic species of these π-conjugated skeletons [29]. The effects of extended π-conjugate systems and the number of unpaired electrons in sandwich-type phthalocyaninato europium compounds are clearly disclosed by the changes in the half-wave potentials of the first oxidation ($Ox1_1$) and first reduction (Red_1), together with their difference ($\Delta E^{opt}_{1/2} = Ox1_1 - Red_1$, defined as the energy gap), of five kinds of sandwich phthalocyanine derivatives. As can be seen from Table 1 and Fig. S3†, extending the π-conjugated systems in the longitudinal and transverse directions of Pc macrocycles induces the first oxidation potential ($Ox1_1$) successively and gradually shifts toward the negative direction from **Pc-1** (0.260 V), **Pc-2** (0.236 V), **Pc-1@Pc-1** (0.235 V) **Pc-1@Pc-2** (0.193 V), to **Pc-2@Pc-2** (0.148 V), respectively. The lower the $Ox1_1$, the more susceptible the compound to oxidation. Consequently, **Pc-2@Pc-2** with maximum degree of conjugation exhibits the lowest $Ox1_1$ among the five compounds and therefore is the easiest one to be oxidized. Furthermore, both the conjugation degree and the number of free radical unit are crucial in determining the first reduction potentials of the five compounds. As can be seen, the increase in the conjugation degree also induces a negative shift for the first reduction (Red_1) from **Pc-2** (−0.735 V) to **Pc-2@Pc-2** (−0.762 V), and from **Pc-1** (−0.134 V), to **Pc-1@Pc-2** (−0.218 V), which makes **Pc-2@Pc-2** and **Pc-1@Pc-2** harder to be reduced than the original **Pc-2** and **Pc-1**, respectively. With an unpaired electron (so called as free radical) locating at the frontier molecular orbital of double-decker **Pc-1** unit [30], **Pc-1@Pc-1** exhibits the highest Red_1 (−0.110 V) among the five compounds. Consequently, tuning orbital energies in sandwich-type phthalocyaninato europium (III) semiconductors is successfully achieved by extending the 2D conjugate systems of sandwich-type phthalocyanines. Furthermore, the unusually small energy gaps ($\Delta E^{opt}_{1/2}$) of the set **Pc-1** (0.394 V), **Pc-1@Pc-1** (0.345 V), and **Pc-1@Pc-2** (0.411 V) also indicate their radical nature [28,31] compared to those for the non-radical **Pc-2** (0.971 V) and **Pc-2@Pc-2** (0.910 V). It is worth noting that the energy gaps for all these compounds are also far smaller than the room temperature bandgap of silicon, 1.1 eV [32], suggesting the good intrinsic semiconducting nature of the five sandwich-type Pc-based compounds. As a result, the highest occupied molecular orbital (HOMO) and the lowest unoccupied molecular orbital (LUMO) energy levels were estimated to be −4.306 and −3.295 eV for **Pc-1**, −4.676 and −3.705 eV for **Pc-2**, −4.330 and −3.230 eV for **Pc-1@Pc-1**, −4.222 and −3.588 eV for **Pc-1@Pc-2**, and −4.588 and −3.678 eV for **Pc-2@Pc-2**, respectively [13,16]. Consequently, the five compounds have HOMOs ranging from −4.306 to −4.676 eV and LUMOs ranging from −3.230 to −3.705 eV, which fall under the energy ranges required for ambipolar organic semiconductors [33], revealing the potential of the five compounds in ambipolar sensing devices.

3.3. Film microstructures and morphologies

The self-assembled films of the five compounds were obtained by a solution-based quasi-Langmuir-Shäfer (QLS) method [21]. UV–vis absorption spectra of the five compounds in both solution and the films are shown in Fig. 1 and their corresponding absorption maxima are compared in Table S3†. Similar to those reported for related sandwich rare earth phthalocyanines [13,34,35], the spectra in $CHCl_3$ solution show the intense Soret bands in the range of 316–388 nm and a Q-band at the 710, 669, 699, 684, and 689 nm for **Pc-1**, **Pc-2**, **Pc-1@Pc-1**, **Pc-1@Pc-2**, and **Pc-2@Pc-2**, respectively, attributed to the π-π* transitions. Obviously, compared with that of double-decker **Pc-1** in solution, the main Q-bands of **Pc-2**, **Pc-1@Pc-1**, **Pc-1@Pc-2**, and **Pc-2@Pc-2** in solution take blue-shifts dramatically by 41, 11, 26, and 21 nm, respectively. These results reveal an enhanced intramolecular π-π interaction between the Pc rings in the order of **Pc-2** > **Pc-1@Pc-2** > **Pc-2@Pc-2** > **Pc-1@Pc-1** > **Pc-1**. Note that the peaks found in the 572–585 nm region for **Pc-1**, **Pc-1@Pc-1**, and **Pc-1@Pc-2** are associated with the free radical structures of bis(phthalocyaninato) rare earth double-deckers having a semi-occupied HOMO orbital [13,36].

Interestingly, in the QLS film, the main Q absorption band of the double-decker **Pc-1** with a smallest intramolecular π-π interaction in solution (i.e. a non-aggregated state) blue-shifts to 687 nm, indicating the formation of *H*-type aggregation in the self-assembled film resulting from the strong intermolecular π-π interaction between **Pc-1** molecules [37]. However, as for other four sandwich-type compounds with the larger π-conjugate systems than **Pc-1**, their main Q bands assigned for the phthalocyanine ligands in the QLS films are all red shifted relative to those in solution, indicating the formation of *J*-type aggregation according to exciton theory [37] and published results previously [20, 38–40]. However, the red-shift of Q bands in the QLS films of other four compounds is different, showing a dependence on the number of the phthalocyanine ligands (or the size of molecules). For instance, in the QLS films, the main Q band is red shifted by 23, 8, 11, and 5 nm for **Pc-2**, **Pc-1@Pc-1**, **Pc-1@Pc-2**, and **Pc-2@Pc-2**, Fig. 1 and Table S3†, leading to the red-shift degree decreasing in the order of **Pc-2** > **Pc-1@Pc-2** > **Pc-1@Pc-1** > **Pc-2@Pc-2** in the QLS films and thus declined intermolecular interactions in the same order. Among the above four compounds that take the *J*-type aggregation in the film, **Pc-2@Pc-2** with a largest

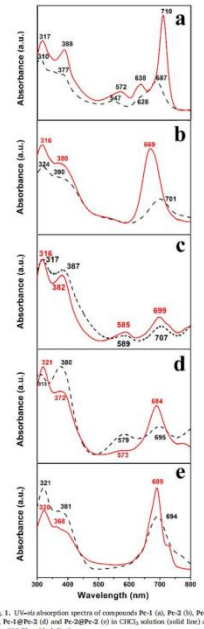

Fig. 1. UV–vis absorption spectra of compounds **Pc-1** (a), **Pc-2** (b), **Pc-1@Pc-1** (c), **Pc-1@Pc-2** (d) and **Pc-2@Pc-2** (e) in $CHCl_3$ solution (solid line) and their pure QLS films (dash line).

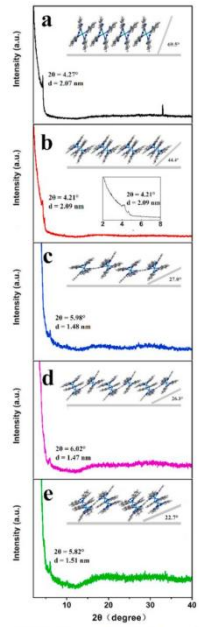

Fig. 2. The X-ray diffraction patterns of the QLS film of **Pc-1** (a), **Pc-2** (b), **Pc-1@Pc-1** (c), **Pc-1@Pc-2** (d) and **Pc-2@Pc-2** (e).

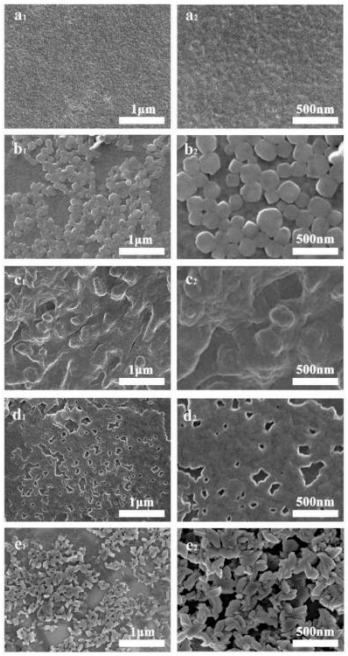

Fig. 3. SEM images for the films of **Pc-1** (a_1 and a_2), **Pc-2** (b_1 and b_2), **Pc-1@Pc-1** (c_1 and c_2), **Pc-1@Pc-2** (d_1 and d_2) and **Pc-2@Pc-2** (e_1 and e_2).

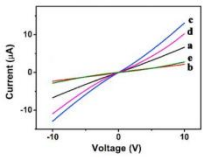

Fig. 4. I-V curves measured on the QLS films of the **Pc-1** (a), **Pc-2** (b), **Pc-1@Pc-1** (c), **Pc-1@Pc-2** (d) and **Pc-2@Pc-2** (e).

molecular backbone exhibits the smallest red-shift, while **Pc-2** with a smallest molecular backbone shows a largest red-shift. These results suggest that larger molecular backbones hinder the effective packing of sandwich phthalocyanine molecules along an edge-to-edge molecular stacking direction.

Furthermore, the orientation angles of the phthalocyanine ring with respect to the substrate in the QLS films of the five compounds were estimated to be ca. 69.1° for **Pc-1**, 44.1° for **Pc-2**, 25.6° for **Pc-1@Pc-1**, 24.9° for **Pc-1@Pc-2**, and 23.1° for **Pc-2@Pc-2**, respectively, by using a polarized UV–*vis* technique according to a literature method [7,22] (Fig. S4† and Table S4†), confirming that only **Pc-1** employs the *H*-type molecular stacking mode with a "face-to-face" orientation for the phthalocyanine molecules in the film and the other four compounds are of the *J*-type molecular stacking mode with an "edge-on" orientation for the phthalocyanine molecules in the film [41].

X-ray diffraction (XRD) patterns of the five kinds of films are shown in Fig. 2. In the low angle range ($2\theta = 2.8–9°$), the five films exhibit the (001) Bragg peak at $2\theta = 4.27°$, 4.21°, 5.98°, 6.02°, and 5.82°, respectively, corresponding to a periodic spacing distance of 2.07 nm, 2.09 nm, 1.47 nm, 1.48 nm, and 1.51 nm for **Pc-1**, **Pc-2**, **Pc-1@Pc-1**, **Pc-1@Pc-2**, and **Pc-2@Pc-2**, respectively, suggesting a regular layered structure exists in these films. Consequently, orientation angles of Pc rings with respect to the substrate surface of ca. 69.5°, 44.4°, 27.0°, 26.3°, and 22.7° are estimated for the respective films of **Pc-1**, **Pc-2**, **Pc-1@Pc-1**, **Pc-1@Pc-2**, and **Pc-2@Pc-2** based on their simulated molecular diagonal dimensions combined with the low-angle XRD results. These results are in good accordance with the calculated ones from the polarized UV–*vis* analysis of the films, further confirming the formation of *H*-aggregates for **Pc-1** and *J*-aggregates for the other four compounds **Pc-2**–**Pc-2@Pc-2** in the films. It is worth noting that along with the increase of conjugated systems, the angle between molecules and the substrate becomes smaller. This is in line with the results of the above-mentioned UV–*vis* analysis.

The SEM observation discloses the surface morphology change for the QLS films of the five compounds, Fig. 3. As can been seen from Fig. $3a_1$-$3a_2$, *H*-type aggregates in the **Pc-1** film show a fine film-structure containing uniformed nanoparticles distributed on the film-surface. The largest intermolecular interaction among the present *J*-type aggregates results in the uniformed disk-like nanoparticles with 200–300 nm in diameter on the surface of **Pc-2** film, Fig. $3b_1$-b_2. Further extending the π conjugate systems from **Pc-1@Pc-1** to **Pc-1@Pc-2** makes the formation of micro-sheets with an increased size depending on a slight increased intermolecular interaction from the former to the latter, Fig. $3c_1$-c_2 and Fig. $3d_1$-d_2. Furthermore, with the largest conjugate system and the smallest intermolecular interaction among the four kinds of the *J*-aggregates, **Pc-2@Pc-2** film displays the smallest uniformed nano-sheets with about 50 nm in width and 100–200 nm in length, Fig. $3e_1$-e_2. This unambiguously confirms that micro/nano-structures of the films including morphology and dimension are determined by the combination between molecular structure, patterns of molecular aggregation, and degree of intermolecular interaction.

3.4. Electrical and sensing properties

By means of the current-voltage (I–V) measurements, Fig. 4, the electronic conductivity of the **Pc-1**, **Pc-2**, **Pc-1@Pc-1**, **Pc-1@Pc-2** and **Pc-2@Pc-2** film is estimated to be about 2.02×10^{-4} S cm^{-1}, 6.00×10^{-5} S cm^{-1}, 3.64×10^{-4} S cm^{-1}, 3.42×10^{-4} S cm^{-1}, and 8.86×10^{-5} S cm^{-1}, respectively (it is noteworthy that the experiments were repeated for more than three times on different pieces of films) [21,25]. The results show that the films of all the five compounds are excellent semiconductors with the conductivity in the order of **Pc-1@Pc-1** > **Pc-1@Pc-2** > **Pc-1** > **Pc-2@Pc-2** > **Pc-2**. Apparently, the radical **Pc-1@Pc-1**, **Pc-1@Pc-2**, and **Pc-1** films exhibit higher intrinsic solid state conductivity on the order of 10^{-4} S cm^{-1}, compared to those for non-radical **Pc-2@Pc-2** and **Pc-2** films. The high conductivities of the set **Pc-1@Pc-1**, **Pc-1@Pc-2**, and **Pc-1** mostly result from the high densities of charge carriers induced by their small energy gaps ($\Delta E^{el}_{1/2}$ = 0.345, 0.411 and 0.394 V for **Pc-1@Pc-1**, **Pc-1@Pc-2** and **Pc-1**, respectively) [13,42]. While the large energy gaps ($\Delta E^{el}_{1/2}$) of **Pc-2@Pc-2** (0.910 V) and **Pc-2** (0.971 V) correspond to lower conductivities of the two non-radical semiconductors relative to those for the radical semiconductors. Consequently, a close correlation between the conductivity (σ) and energy gap (i.e. $\Delta E^{el}_{1/2}$) is revealed as follow: the smaller the energy gap in the frontier molecular orbital of the sandwich-type phthalocyanine-based semiconductor, the greater the conductivity. However, in comparison with the conductivity (2.02×10^{-4} S cm^{-1}) and energy gap (0.394 V) of **Pc-1**, indeed higher conductivity (3.42×10^{-4} S cm^{-1}) was obtained for **Pc-1@Pc-2** with a slightly larger energy gap of 0.411 V. At the first glance, it seems to contradict with the above "σ-$\Delta E^{el}_{1/2}$" relationship. However, it could be justified on the basis of the formation of different aggregates in the QLS films with red-shifted *J*-type absorption bands revealed for **Pc-1@Pc-2** and blue-shifted *H*-type absorption bands revealed for **Pc-1** [43–45]. The red-shift of all the absorption bands in thin solid film makes the energy gap of **Pc-1@Pc-2** appearing at lower wavelengths and thus $\Delta E^{el}_{1/2}$ in the film is expected to get smaller than that in solution. In good contrast, $\Delta E^{el}_{1/2}$ of **Pc-1** should be larger in the film than in solution depending on the blue-shifted absorptions in the solid state aggregates. As a result, a lower $\Delta E^{el}_{1/2}$ in the film should be achieved for **Pc-1@Pc-2** relative to that of **Pc-1** depending on the solid state stacking effect. Therefore, the conductivity is mainly governed by the energy gap (i.e. $\Delta E^{el}_{1/2}$) in addition to the solid state stacking effect for the sandwich-type phthalocyanine semiconductors.

To evaluate the gas sensing properties, the QLS films of the five compounds deposited onto the ITO interdigital electrodes/glass substrates were studied against NO_2 in the concentration range of 100–300 ppb, diluted with dry synthetic air at room temperature (24–26 °C). The sensing performance was controlled by a duty cycle with a constant dynamic exposure period of 2 min. And the corresponding recovery time, that is defined as the time required for the current recovering from I_{gas} to (95–99% × I_{air}) [46], varied from 1.2 to 35 min. Accordingly, recovery time varied depending on the concentration of the analyte [47]. Fig. $5a_1$-e_1 show the responses of the five kinds of films to NO_2 (i.e., an oxidizing gas) with an increase in their electrical resistance, demonstrating the *n*-type transport behavior of all the five compounds. This agrees with our previous studies on sandwich-type phthalocyaninato complexes [11,15,20,26]. The response (i.e. $(I_f-I_0)/I_0$) for the QLS films of the five compounds increases when exposed to NO_2 from 100 to 300 ppb in a linear manner with $R^2 \geq 0.96$, Fig. $5a_2$-e_2. As a consequence, such films can be used to quantitatively analyze the concentration of NO_2. Furthermore, the response for each concentration gradually increases in the order of **Pc-1** < **Pc-2** < **Pc-1@Pc-1** <

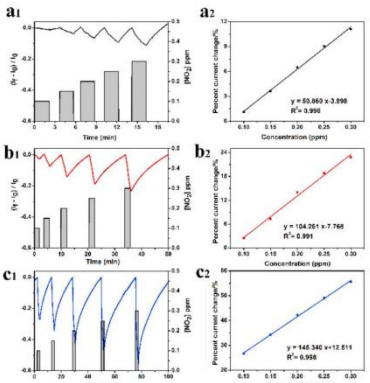

Fig. 5. The time-dependent current plots of film **Pc-1** (a_1), **Pc-2** (b_1), **Pc-1@Pc-1** (c_1), **Pc-1@Pc-2** (d_1) and **Pc-2@Pc-2** (e_1) and the corresponding sensor response varies linearly with different NO_2 concentration (a_2, b_2, c_2, d_2 and e_2).

Table 2
Sensitivity data for films of **Pc-1**–**Pc-2@Pc-2** in different detective ranges of NO_2 and NH_3.

Gas	Compound	Sensitivity (ppm^{-1})	LOD (ppm)	Response
NO_2 0.1–0.3 (ppm)	**Pc-1**	0.509	0.01	*n*-type
	Pc-2	1.043	0.01	
	PC-1@PC-1	1.453	0.01	
	PC-1@PC-2	1.902	0.04	
	PC-2@PC-2	2.082	0.01	
NH_3 4.0–8.6 (ppm)	**Pc-1**	0.0047	0.4	*p*-type
	Pc-2	0.0097	0.8	
	PC-1@PC-1	0.0059	0.5	
	PC-1@PC-2	0.0043	0.6	
	PC-2@PC-2	0.0087	0.7	

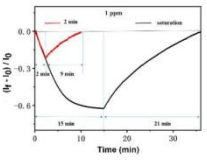

Fig. 6. The response of the devices for **Pc-2@Pc-2** under 1 ppm NO_2 exposure.

Pc-1@Pc-2 < **Pc-2@Pc-2**, with a slope (in ppm^{-1}) of 0.509, 1.043, 1.453, 1.902, and 2.082, respectively, Table 2. This order in sensitivity, matches well with the declined trend in the first oxidation potential ($Ox1_2$) for the five compounds, Table 1. As shown previously, the lower the $Ox1_2$, the easier the compound to be oxidized, and the higher the sensitivity of NO_2 detection. Consequently, $Ox1_2$ plays a crucial role in the sensitivities toward oxidative NO_2 for the five sandwich-type phthalocyaninato semiconductors. Comparing the sensor responses of the five semiconductors examined in this study, the largest π-conjugated molecular structure of **Pc-2@Pc-2** induces the lowest $Ox1_2$, achieving the highest sensitivity, which is more than 4 times higher than that of **Pc-1**. With the gradual extension of the π-conjugated molecular structures from **Pc-1**, **Pc-2**, **Pc-1@Pc-1**, **Pc-1@Pc-2**, to **Pc-2@Pc-2**, their sensitivities to the detection of NO_2 gas gets increased. This observation suggests that the sensitivity of the five sandwich-type phthalocyaninato semiconductors to NO_2 gas is mainly determined by their π-conjugated molecular structures rather than the intermolecular interactions in the films.

It should be noted that due to the limitations of our gas sensing measurement system, in order to obtain enough measurement period to reasonably evaluate the sensitivity of the sensors, a shorter dynamic exposure time of 2 min is adopted. Although a more sufficient exposure time than 2 min to reach the saturation region of the sensor response can exhibit a higher gas sensing response (for example, to 1 ppm NO_2, when the exposure time is 15 min, the response is significantly better than the 2 min exposure time), but the full recovery of the sensor becomes too slow (to 1 ppm NO_2 for 15 min its full recovery is 21 min), Fig. 6. In order to reduce recovery time, the primarily sensing response was examined by using 2-min doses at room temperature (24–26 °C).

It is worth noting that when the films of the five sandwich-type phthalocyaninato semiconductors are exposed to electron-donating NH_3 gas (4–8.6 ppm, step is 1.2 ppm), diluted with dry air (recovery period varied from 1 to 27.6 min), the positive response for all of the films was still observed, Fig. $7a_1$-e_1, indicating their *p*-type semiconducting behavior. Obviously, ambipolar (*n*- and *p*-type) responses towards oxidizing NO_2 and reducing NH_3 were discovered for the films of the five sandwich-type phthalocyaninato semiconductors. This is in line with the electrochemical measurement finding as mentioned above. Indeed, similar ambipolar responses have been found for the double-, triple-, and quadruple-decker sandwich phthalocyanines [18,22]. As can be seen in Fig. $7a_2$-e_2, a good linear correlation ($R^2 \geq 0.96$) was exhibited between the response and NH_3 concentrations with a slop of 0.0047, 0.0097, 0.0059, 0.0043, and 0.0087 ppm^{-1} for **Pc-1**, **Pc-2**, **Pc-1@Pc-1**, **Pc-1@Pc-2**, and **Pc-2@Pc-2**, respectively. The results show that both the first reduction (Red_1) and electronic structure have significant effect on the sensing characteristics for the five semiconductors. In the case of the three radical semiconductors, along with the gradually increase in Red_1 in the order of **Pc-1@Pc-2** (−0.218 V) < **Pc-1** (−0.134 V) < **Pc-1@Pc-1** (−0.110 V), the sensitivity to NH_3 increases in the same order of **Pc-1@Pc-2** (0.0043 ppm^{-1}) < **Pc-1** (0.0047 ppm^{-1}) < **Pc-1@Pc-1** (0.0059 ppm^{-1}), respectively. This is also true for the two non-radical semiconductors. A more positive Red_1 of **Pc-2** (−0.735 V) relative to **Pc-2@Pc-2** (−0.762 V) leads to a higher sensitivity of the former (0.0097 ppm^{-1}) than the latter (0.0087 ppm^{-1}). According to the previous experimental studies and density functional theory calculations on neutral radical lutetium bisphthalocyanine ($LuPc_2$), the unpaired electron on single molecular orbital of $LuPc_2$ is primarily of π-character that delocalizes over both macrocycles [48]. This should be also true for the neutral radical **Pc-1**, **Pc-1@Pc-1**, and **Pc-1@Pc-2**. Since both macrocycles of the radical rare earth bisphthalocyanines (i.e. **Pc-1** unit in the present case) bring negative charge from the unpaired electron on single molecular orbital, it counters productive to adsorb the negative charge-possessing N atom in NH_3. This should be responsible for the lower sensitivities to electron-donating NH_3 for the radical **Pc-1**, **Pc-1@Pc-1**, and **Pc-1@Pc-2** relative to that of non-radical **Pc-2** although the higher charge transfer ability (or conductivity) and Red_1 are revealed for the radical **Pc-1**, **Pc-1@Pc-1**, and **Pc-1@Pc-2** than the non-radical **Pc-2**.

On the other hand, the limit of detection (LOD) is also a crucial index for sensors, since trace concentrations of pollution gases that can lead to long-term environmental issues are more difficult to detect. The LOD of the five semiconductors to both NO_2 and NH_3 can be obtained from the sensitivity fitting curve when signal/noise equals to 3,[46,49] see Fig. $5a_2$-e_2 and $7a_2$-e_2, the details are shown in Supplementary materials. The calculated LOD values are down to 10–40 ppb and 0.48–0.89 ppm toward NO_2 and NH_3, respectively, for the films of the five ambipolar semiconductors, Table 2. This represents the lowest LOD for room-temperature NO_2 and NH_3 sensors measured in dry air among the organic chemiresistors reported so far [16]. It is worth noting that the sensor performance in this work is as good as the best results reported in the previous literature (Table S5†), for example some heterojunctions of Cu(F_{16}Pc)/$LuPc_2$ [50], polyaniline/$LuPc_2$ or poly(2,5-dimethoxyaniline)/$LuPc_2$[51] consisting of two semiconducting layers obtained by a combination of electrodeposition with vacuum sublimation, but simpler solution-processed films with only one semiconducting layer were used in the present case.

Towards future practical application, the selectivity, reproducibility, and stability of the films to NO_2 and NH_3 gas are also evaluated. As shown in Fig. S5† and S6†, no obvious response was detected for the five semiconductors to the electron-donating H_2S (100–300 ppb) and oxidation gas CO_2 (100–300 ppb) due likely to their weaker electron-donating ability than NH_3. Meanwhile the quite good reproducibility and stability towards 100 ppb of NO_2 gas and 4 ppm of NH_3 gas are revealed after five cycling tests upon the 2 min exposure time, Fig. S7†

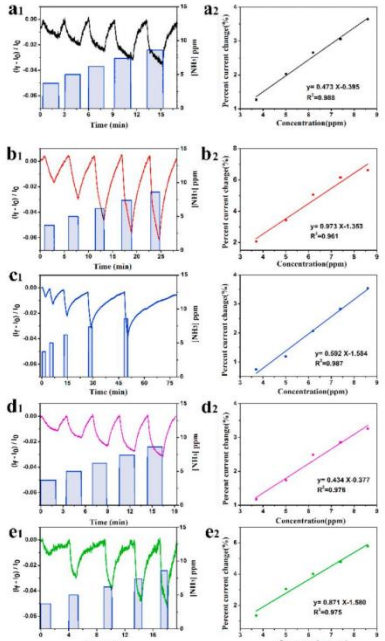

Fig. 7. The time-dependent current plots of film **Pc-1** (a_1), **Pc-2** (b_1), **Pc-1@Pc-1** (c_1), **Pc-1@Pc-2** (d_1) and **Pc-2@Pc-2** (e_1) and the corresponding sensor response varies linearly with different NH_3 concentration (a_2, b_2, c_2, d_2 and e_2).

and S8[8]. Furthermore, the effect of relative humidity (rh) on the relative response of **Pc-2@Pc-2** toward NO_2 and **Pc-2** toward NH_3 were also studied at 35% and 70% rh. This humidity range was chosen because the gas sensors operate within this broad humidity range in most of the practical applications. Representative response to 100 ppb NO_2 for **Pc-2@Pc-2** and to 4 ppm NH_3 for **Pc-2** is displayed in Fig. S9[8] and S10[8]. As can be seen from Fig. S9[8], toward 100 ppb NO_2, the relative response of **Pc-2@Pc-2** increases from 1.14 to 1.24 and 1.32 along with an increased rh value from 0% rh (i.e. dry synthetic air) to 35% rh and 70% rh, respectively. This is also true for the relative response of **Pc-2** to 4 ppm NH_3. As shown in Fig. S10[8], the response to NH_3 also increases along with the increased rh value due likely to an easier adsorption of NH_3 molecules on the surface of **Pc-2** film in a higher rh. And the recovery shows the slight dnfl in the high humidity due probably to the traps caused by the infiltration of the H_2O. Impressively, it has been found that the behavior of **Pc-2** toward NH_3 as a *p*- or n-type device, depends on the humidity contained in the atmosphere with a p-type response at 0% rh and n-type at 35% and 70% rh. So rh variation has a significant effect on sensing performance. This can be attributed to the competitive absorption kinetics of H_2O and NH_3 at higher rh, suppressing the electronic effects of the gas molecules [14,52,53].

It is noteworthy that the detecting ranges of 4–8.6 ppm to NH_3 and 100–300 ppb to NO_2 in the present case well cover the range required for detection in industrial pollution discharge (~10 ppm NH_3) and indoor air quality standard (~117 ppb NO_2) in China. This fact in combination with their highly sensitive and reproducible responses and low LODs suggests the very promising potential in practical application for the present sensors, especially **Pc-2@Pc-2** NO_2 sensor and **Pc-2** NH_3 sensor.

4. Conclusions

In summary, by extending 2D conjugate systems of sandwich-type rare earth phthalocyanines, the redox potentials, in particular the first oxidation (Oxd_1), first reduction (Red_1), and energy gap ($\Delta E^S{}_{1/2}$) are successfully tuned for the five kinds of sandwich-type phthalocyaninato europium (III) antipolar semiconductors. We have firstly demonstrated that the low first oxidation (Oxd_1), high first reduction (Red_1), and small energy gap ($\Delta E^S{}_{1/2}$) are the key factors for realizing highly sensitive NO_2 and NH_3 sensing as well as high conductivity, respectively, for the sandwich-type phthalocyaninato europium (III) ambipolar semiconductors. In particular, we produce the high-performance NO_2 and NH_3 organic chemiresistors with the QLS films of **Pc-2@Pc-2** and **Pc-2**, respectively. These devices show the high sensitivity, good reproducibility, nice selectivity, short response time, and low limit of detection to trace NO_2 and NH_3 gases present in dry air at room temperature (24–26 °C), representing the best performance achieved so far for solution-processed film of the organic chemiresistors. This work is truly helpful towards designing and fabricating new ambipolar phthalocyanine-based chemical sensors through extending π-conjugate systems of phthalocyanines with promising practical application potential.

Declaration of competing interest

The authors declare that they have no known competing financial interests or personal relationships that could have appeared to influence the work reported in this paper.

Acknowledgments

This work was supported by the National Natural Science Foundation of China (No.21771192), the Education Research Fund for Department of Heilongjiang Province (No.1352ZD201), the Scientific Research Project of Mudanjiang Normal University (No.GP201603), the Innovation and Entrepreneurship Project of Mudanjiang Normal University (No. CY2018008).

decker complex thin films and their comparative performances in ozone sensing, Phys. Chem. Chem. Phys. 12 (2010) 12851–12861, https://doi.org/10.1039/C0CP00381F.
[22] G. Lu, X. Kong, H. Wang, Y. Chen, C. Wei, Y. Chen, J. Jiang, A sandwich-type tetrakis(phthalocyaninato) europium-cadmium quadruple-decker: structure, ORET, and gas sensing properties, New J. Chem. 43 (2019) 15763–15767, https://doi.org/10.1039/C9NJ03542D.
[23] X. Cai, C. Wei, J. Dong, Q. Liu, Y. Wu, G. Lu, Y. Chen, J. Jiang, Dimeric phthalocyanine-involved double-decker complex-based electrochemical sensor for simultaneous detection of acetaminophen and ascorbic acid, J. Mater. Sci. Mater. Electron. 30 (2019) 1976–1983, https://doi.org/10.1007/s10854-018-04468-0.
[24] Z. Yu, L. Zou, Y. Chen, J. Jiang, (Pc)Ho[Pc(OEt)$_8$]Ho[trans-T (COOCH$_3$)$_4$PP]/GO hybrid film-based nonenzymatic H_2O_2 electrochemical sensor with excellent performance, ACS Appl. Mater. Interfaces 8 (2016) 30398–30406, https://doi.org/10.1021/acsami.6b08764.
[25] H. Ahn, A. Chandekar, B. Kang, C. Sung, J.E. Whitten, Electrical conductivity and vapor-sensing properties of ω(3-thienyl) alkanethiol-protected gold nanoparticle films, Chem. Mater. 16 (2004) 3274–3278, https://doi.org/10.1021/cm049794v.
[26] G. Lu, X. Kong, C. Wang, L. Zhao, D. Qi, Y. Jiang, S. Zhao, Y. Chen, J. Jiang, Optimizing the gas sensing properties of sandwich-type phthalocyaninato europium complex through extending the conjugated framework, Dyes Pigments 161 (2019) 240–246, https://doi.org/10.1016/j.dyepig.2018.09.063.
[27] G. Lu, M. Bai, R. Li, X. Zhang, C. Ma, P.C. Lo, J. Jiang, Lanthanide (III) double-decker complexes with octaphenoxy- or octathiophenoxyphthalocyaninato ligands-revealing the electron-withdrawing nature of the phenoxy and thiophenoxy groups in the double-decker complexes, Eur. J. Inorg. Chem. 18 (2006) 3703–3709, https://doi.org/10.1002/ejic.200606206.
[28] R. Wang, Y. Li, R. Li, D.Y. Cheng, P. Zhu, D.K. Ng, M. Bao, X. Cui, N. Kobayashi, J. Jiang, Heteroleptic rare earth double-decker complexes with naphthalocyaninato and phthalocyaninato ligands geneml synthesis, spectroscopic, and electrochemical chaacteristics, Inorg. Chem. 44 (2005) 2114–2120, https://doi.org/10.1021/ic048472w.
[29] X. Mu, W. Song, Y. Zhang, K. Ye, H. Zhang, Y. Wang, Controllable self-assembly of n-type semiconductors to microtubes and highly conductive ultralong microwires, Adv. Mater. 22 (2010) 4905–4909, https://doi.org/10.1002/adma.201002259.
[30] K. Wang, D. Qi, H. Wang, W. Cao, W. Li, T. Liu, C. Duan, J. Jiang, Binuclear phthalocyanine-based sandwich-type rare earth complexes: unprecedented two π-bridged bimolecul-enesil integrated SMMs, Chem. Eur J. 19 (2013) 11162–11166, https://doi.org/10.1002/chem.201301101.
[31] R. Murdey, M. Bouvet, M. Sumimoto, S. Sakaki, N. Sato, Direct observation of the energy gap in lutetium bisphthalocyanine thin films, Synth. Met. 159 (2009) 1677–1681, https://doi.org/10.1016/j.synthmet.2009.05.002.
[32] C. Kittel, Introduction to Solid State Physics, Wiley, New York, 1996. Reference to a chapter in an edited book.
[33] M.L. Tang, A.D. Reichardt, P. Wei, Z. Bao, Correlating carrier type with frontier molecular orbital energy levels in organic thin film transistors of functionalized acene derivatives, J. Am. Chem. Soc. 131 (2009) 5264–5273, https://doi.org/10.1021/ja809309h.
[34] G. Lu, X. Kong, J. Sun, L. Zhang, Y. Chen, J. Jiang, Solution-processed single crystal microwires of a novel dimeric phthalocyanine-involved triple-decker for high-performance ambipolar organic field effect transistors, Chem. Commun. 53 (2017) 12754–12757, https://doi.org/10.1039/C7CC08297F.
[35] G. Lu, X. Kong, P. Ma, K. Wang, Y. Chen, J. Jiang, Amphiphilic (phthalocyaninato) (porphyrinato) europium tripledecker nanoribbons with air-stable ambipolar OFET performance, ACS Appl. Mater. Interfaces 8 (2016) 6174–6182, https://doi.org/10.1021/acsami.5b12368.
[36] J. Xue, Y. Chen, J. Gao, L. Wan, T. Lei, P. Ma, J. Jiang, Synthesis, self-assembly, and semiconducting properties of phenanthrolinefused phthalocyanine derivatives, J. Mater. Chem. 22 (201 2) 221 42–221 49, https://doi.org/10.1039/C2JM32358C.
[37] M. Kasha, H.R. Rawls, M.A. El-Bayoumi, The exciton model in molecular spectroscopy, Pure Appl. Chem. 11 (1965) 371–392, https://doi.org/10.1351/pac196511030371.
[38] W.-H. Chen, W.-Y. Ko, Y.-S. Chen, C.-Y. Cheng, G.-M. Chan, K.-J. Lin, Growth of copper phthalocyanine rods on an plasmon electrodes through micelle disruption methods, Langmuir 26 (2010) 2191–2195, https://doi.org/10.1021/la903405a.
[39] B.M. Hassan, H. Li, N.B. McKeown, The control of molecular self-association in spin-coated films of substituted phthalocyanines, J. Mater. Chem. 10 (2000) 39–45, https://doi.org/10.1039/A903341F.
[40] K. Abdullah, Y. Chen, J. Jiang, Synthesis, Fabrication of self-assembled film and ambipolar chemical sensing properties of tripledecker (phthalocyaninato) (porphyrinato) europium complex, J. Porphyr. Phthalocyanines 21 (2017) 893–899, https://doi.org/10.1142/S1088424617500985.
[41] M.J. Plater, A. Jeremiah, G. Bourhill, Synthesis of soluble halogenated aryloxy substituted indium phthalocyanines, J. Chem. Soc., Perkin Trans. 1 1 (2002) 91–96, https://doi.org/10.1039/B107689M.
[42] M. Bouvet, V. Parra, C. Locatelli, H. Xiong, Electrical transduction in phthalocyanine-based gas sensors: from classical chemiresistors to new functional structures, J. Porphyr. Phthalocyanines 13 (2009) 84–91, https://doi.org/10.1142/S1088424609001935.
[43] H. Usta, C. Risko, Z. Wang, H. Huang, M.K. Deliomeroglu, A. Zhukhovitskiy, A. Facchetti, T.J. Marks, Design, synthesis, and characterization of ladder-type molecules and polymers. air-stable, solution-processable n-channel and ambipolar semiconductors for thin-film transistors via experiment and theory, J. Am. Chem. Soc. 131 (2009) 5586, https://doi.org/10.1021/ja809353s.
[44] Y. Zhang, X. Cai, Y. Zhou, X. Zhang, H. Xu, Z. Liu, X. Li, J. Jiang, Structures and spectroscopic properties of bis(phthalocyaninato) yttrium and lanthanum complexes: theoretical study based on density functional theory calculations, J. Phys. Chem. 111 (2007) 392–400, https://doi.org/10.1021/jp066155g.
[45] Y. Chen, D. Li, N. Yuan, J. Gao, R. Gu, G. Lu, M. Bouvet, Tuning the semiconducting nature of bis(phthalocyaninato) holmium complexes via peripheral substituents, J. Mater. Chem. 22 (2012) 22142–22149, https://doi.org/10.1039/C2JM35219B.
[46] Z. Wang, L. Huang, X. Zhu, X. Zhou, L. Chi, An ultrasensitive organic semiconductor NO_2 sensor based on crystalline TIPS-pentacene films, Adv. Mater. 29 (2017) 1703192, https://doi.org/10.1002/adma.201703192.
[47] K.Y. Ko, K. Park, S. Lee, Y. Kim, W.J. Woo, D. Kim, J.-G. Song, J. Park, H. Kim, Recovery improvement for large-area tungsten diselenide gas sensors, ACS Appl. Mater. Interfaces 10 (2018) 23916–23917, https://doi.org/10.1021/acsami.8b07034.
[48] R. Murdey, M. Bouvet, M. Sumimoto, S. Sakaki, N. Sato, Direct observation of the energy gap in lutetium bisphthalocyanine thin films, Synth. Met. 159 (2009) 1677–1681, https://doi.org/10.1016/j.synthmet.2009.05.002.
[49] R.G. Parkhamenko, A.S. Sukhikh, D.D. Klyamer, P.O. Krasnov, S.A. Gromilov, B. Kadem, A.K. Hassan, T.V. Basova, Thin films of unsubstituted and fluorinated palladium phthalocyanines: structure and sensor response toward ammonia and hydrogen, J. Phys. Chem. C 121 (2017) 1200–1209, https://doi.org/10.1021/acs.jpcc.6b10817.
[50] M. Matrea, B.M. Prest, J.-M. Suisse, M. Bouvet, Modulation of the organic heterojunction behavior, from electrografting to enhanced sensing properties, Sens. Actuators, B 299 (2019) 126968, https://doi.org/10.1016/j.snb.2019.126968.
[51] M. Matrea, M.-D. Tchangai, B.M. Prest, O. Heintz, F. Herbst, J.-M. Suisse, M. Bouvet, Low conductive electrodeposited poly(2,5-dimethoxyaniline) as a key material in a double lateral heterojunction, for sub-ppm ammonia sensing in humid atmosphere, ACS Sens. 4 (2019) 740–747, https://doi.org/10.1021/acssensors.9b00109.
[52] A. Wannebroucq, S. Ouedraogo, R. Meunier-Prest, J.-M. Suisse, M. Bayo, M. Bouvet, On the interest of antipolar materials for gas sensing, Sens. Actuators, B 258 (2018) 657–664, https://doi.org/10.1016/j.snb.2017.11.146.
[53] M. Matsuguchi, A. Okamoto, Y. Sakai, Effect of humidity on NH_3 gas sensitivity of polyaniline blend films, Sens. Actuators, B 94 (2003) 46–52, https://doi.org/10.1016/S0925-4005(03)00325-3.

Appendix A. Supplementary data

Supplementary data to this article can be found online at https://doi.org/10.1016/j.orgel.2021.106151.

References

[1] J. Cornil, J.-L. Brédas, J. Zaumseil, H. Sirringhaus, Ambipolar transport in organic conjugated materials, Adv. Mater. 19 (2007) 1791–1799, https://doi.org/10.1002/adma.200602922.
[2] Y. Zhang, J. Xia, F. Zhang, Z. Wang, Q. Liu, Ultrasensitive label-free homogeneous electrochemical aptasensor based on sandwich structure for thrombin detection, Sensor. Actuator. B Chem. 267 (2018) 412–418, https://doi.org/10.1016/j.snb.2018.04.092.
[3] J. Lu, Q. Meng, L. Zhang, Y. Liu, W. Liu, X. Zhang, Single crystal structure self-assembled nano-structure and semiconductor properties of a sandwich-type mixed (phthalocyaninato)(porphyrinato) europium triple-decker complex, Dyes Pigments 115 (2015) 1–6, https://doi.org/10.1016/j.dyepig.2014.12.005.
[4] D.D. Eley, Phthalocyanines as semiconductors, Nature 162 (1948), https://doi.org/10.1038/162819a0, 819-819.
[5] R.D. Gould, Structure and electrical conduction properties of phthalocyanine thin films, Coord. Chem. Rev. 156 (1996) 237–274, https://doi.org/10.1016/S0010-8545(96)01218-6.
[6] G. Guillaud, J. Simon, J.P. Germain, Metallophthalocyanines: gas sensors, resistors and field effect transistors, Coord. Chem. Rev. 178 (1998) 1433–1484, https://doi.org/10.1016/S0010-8545(98)00177-5.
[7] X. Kong, X. Zhang, D. Gao, D. Qi, Y. Chen, J. Jiang, Air stable ambipolar field-effect transistor based on a solution processed octanaphthoxy-substituted bis (phthalocyaninato) europium semiconductor with high and balanced carrier mobilities, Chem. Sci. 6 (2015) 1967–1972, https://doi.org/10.1039/C4SC03692K.
[8] G. Guillaud, M.A. Sadoun, M. Maitrot, J. Simon, M. Bouvet, Field-effect transistors based on intrinsic molecular semiconductors, Chem. Phys. Lett. 167 (1990) 503–506, https://doi.org/10.1016/0009-2614(90)85049-I.
[9] X. Kong, Z. Dong, Y. Wu, X. Li, Y. Chen, J. Jiang, High sensitive ambipolar response towards oxidizing NO_2 and reducing NH_3 based on bis(phthalocyaninato) europium semiconductors, Chin. J. Chem. 34 (2016) 975–982, https://doi.org/10.1002/cjoc.201600498.
[10] H. Wang, X. Kong, S. Zhao, J. Wu, X. Li, Y. Chen, High-performance ambipolar responses to oxidizing NO_2 and reducing NH_3 based on the self-assembled film of an amphiphilic tris(phthalocyaninato) europium complex, New J. Chem. 41 (2017) 11955–11961, https://doi.org/10.1039/C7NJ02796D.
[11] S. Liu, H. Wang, X. Wang, S. Li, H. Lin, Y. Chen, X. Li, Diverse sensor responses from two functionalized tris(phthalocyaninato)europium ambipolar semiconductors towards three oxidative and reductive gases, J. Mater. Chem. C 7 (2019) 424–433, https://doi.org/10.1039/C8TC05673E.
[12] X. Duan, Y. Zhang, H. Wang, F. Dai, G. Yang, Y. Chen, A phthalocyanine sensor array based on sensitivity and current changes for highly sensitive identification of three toxic gases at ppb levels, New J. Chem. 44 (2020) 13240–13246, https://doi.org/10.1039/d0nj02027g.
[13] G. Lu, X. Wang, X. Kong, H. Pan, J. Zhang, Y. Chen, J. Jiang, Binuclear phthalocyanine dimer-containing yttrium double-decker ambipolar semiconductor with sensitive response toward oxidizing NO_2 and reducing NH_3, ChemElectroChem 5 (2018) 605–609, https://doi.org/10.1002/celc.201701117.
[14] S. Ouedraogo, R. Meunier-Prest, A. Kumar, M. Bayodhungoura, M. Bouvet, Modulating the electrical properties of organic heterojunction devices based on phthalocyanines for ambipolar sensors, ACS Sens. 5 (2020) 1849–1857, https://doi.org/10.1021/acssensors.9b00871.
[15] Z. Dong, X. Kong, D. Qi, S. Zhao, X. Li, Y. Chen, J. Jiang, Polymorphism in the self-assembled nanostructures of a tris(phthalocyaninato) europium derivative: phase dependent semiconducting and NO_2 sensing behaviour, Org. Electron. 53 (2018) 127–134, https://doi.org/10.1016/j.orgel.2017.11.026.
[16] S. Zhao, X. Kong, X. Wang, X. Li, G. Yang, Y. Chen, Five-toning intermolecular and intramolecular interactions to build the films of tris(phthalocyaninato) rare earth complexes and their comparative performances in ambipolar gas sensing, IEEE Trans. Electron. Dev. 66 (2019) 1930–1936, https://doi.org/10.1109/TED.2019.2901807.
[17] Y. Wu, P. Ma, N. Wu, X. Kong, M. Bouvet, X. Li, Y. Chen, J. Jiang, Two-step solution-processed two-component bilayer phthalocyaninato copper-based heterojunctions with interesting ambipolar organic transiting and ethanol-sensing properties, Adv. Mater. Interfaces 3 (2016) 1600253, https://doi.org/10.1002/admi.201600253.
[18] J. Xue, Y. Chen, D. Qi, Y. Liu, J. Jiang, High-performance air-stable ambipolar organic field-effect transistor based on tris(phthalocyaninato) europium(III), Adv. Mater. 24 (2012) 1755–1758, https://doi.org/10.1002/adma.201200106.
[19] S.Z. Bisri, C. Piliego, J. Gao, M.A. Loi, Outlook and emerging semiconducting materials for ambipolar transistors, Adv. Mater. 26 (2014) 1176–1199, https://doi.org/10.1002/adma.201304280.
[20] Y. Chen, X. Kong, G. Lu, D. Qi, Y. Wu, X. Li, M. Bouvet, D. Sun, J. Jiang, The lower rather than higher density charge carrier determines the NH_3-sensing nature and sensitivity of ambipolar organic semiconductors, Mater. Chem. Front. 2 (2018) 1069–1016, https://doi.org/10.1039/C7QM00607A.
[21] Y. Chen, M. Bouvet, T. Sizun, Y. Gao, C. Plassard, E. Lesniewska, J. Jiang, Facile approaches to build ordered amphiphilic tris(phthalocyaninato) europium triple-

7.Cai X, Ning H. Crystal structure of di-μ-acetato-diacetatobis (μ-6, 6′-dimethoxy-2,2′-{[(propane-1,3-diylbis (azanylylidene)] bis (methanylylidene)} diphenolato) tetrazinc[J]. Acta Crystallographica Section E: Crystallographic Communications, 2015, 71(12): 217-218.（SCI 检索收录四区，IF=0.278）

CRYSTALLOGRAPHIC COMMUNICATIONS

OPEN ACCESS

ISSN 2056-9890

Crystal structure of di-μ-acetato-di-acetatobis(μ-6,6′-dimethoxy-2,2′-{[(propane-1,3-diylbis(azanylylidene)]-bis(methanylylidene)}diphenolato)tetra-zinc

Xue Cai* and Hui Ning

Department of Chemistry, Mudanjiang Normal University, Mudanjiang 157011, People's Republic of China. *Correspondence e-mail: xuecai@mail.sdu.edu.cn

Received 9 October 2015; accepted 29 October 2015

Edited by T. J. Prior, University of Hull, England

The tetranuclear title complex, $[Zn_4(C_{19}H_{20}N_2O_4)_2(CH_3COO)_4]$, is formed from two dinuclear motifs related by an inversion centre. The two crystallographically independent Zn^{II} ions in the asymmetric unit are in different coordination environments. One is square-based pyramidal with one O atom of an acetate group occupying the axial position and two N and O atoms of one bmspd [H_2bmspd = *N*,*N*′-bis(3-methoxysalicylidene)propylene-1,3-diamine] Schiff base ligand forming the basal plane. The other Zn^{II} atom is six-coordinated by four O atoms of the bmspd ligand forming the equatoral plane and two O atoms of different acetate groups located in the axial positions. As a result, the two phenolic planes of the bicompartmental Schiff base ligand are distorted slightly. However, the planes of the two Schiff base ligands are parallel. In addition, the Zn—N and Zn—O bond lengths span the reasonable ranges 2.062 (2)–2.073 (2) and 1.9261 (15)–2.4356 (16) Å, respectively. The Zn···Zn distances separated by phenolic O atoms are 3.2466 (4) Å while the Zn···Zn distances bridged by acetate groups are 5.9835 (6) Å. The tetranuclear moieties are connected by van der Waals interactions, and form a chain along *c* axis.

Keywords: crystal structure; zinc; Schiff base; acetate.

CCDC reference: 724776

1. Related literature

Metal-organic coordination complexes of *N*,*N*′-bis(salicylidene)ethylenediamine (salen) Schiff-base derivatives have been studied extensively within the fields of homogeneous catalysis (Wezenberg & Kleij, 2008), non-linear optics (Rigamonti *et al.*, 2006), magnetics (Yuan *et al.*, 2007) and biological metalloenzyme mimics (Laskin *et al.*, 2008).

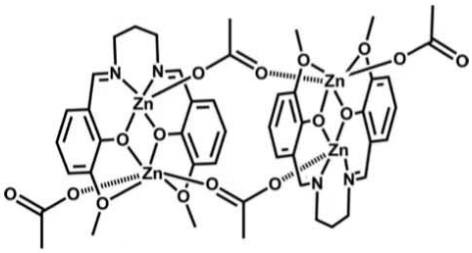

2. Experimental

2.1. Crystal data

$[Zn_4(C_{19}H_{20}N_2O_4)_2(C_2H_3O_2)_4]$
M_r = 1178.48
Triclinic, $P\overline{1}$
a = 10.4894 (9) Å
b = 10.7917 (9) Å
c = 11.9550 (11) Å
α = 103.425 (2)°
β = 94.323 (1)°
γ = 115.677 (1)°
V = 1162.17 (18) Å^3
Z = 1
Mo $K\alpha$ radiation
μ = 2.12 mm^{-1}
T = 298 K
0.15 × 0.10 × 0.08 mm

2.2. Data collection

Bruker SMART APEX CCD area-detector diffractometer
Absorption correction: multi-scan (*SADABS*; Sheldrick, 1996)
T_{min} = 0.742, T_{max} = 0.849
6281 measured reflections
4497 independent reflections
3969 reflections with $I > 2\sigma(I)$
R_{int} = 0.013

2.3. Refinement

$R[F^2 > 2\sigma(F^2)]$ = 0.024
$wR(F^2)$ = 0.071
S = 1.05
4497 reflections
318 parameters
H-atom parameters constrained
$\Delta\rho_{max}$ = 0.26 e Å^{-3}
$\Delta\rho_{min}$ = −0.27 e Å^{-3}

Data collection: *APEX2* (Bruker, 2004); cell refinement: *SAINT-Plus* (Bruker, 2001); data reduction: *SAINT-Plus*; program(s) used to solve structure: *SHELXTL* (Sheldrick, 2008); program(s) used to refine structure: *SHELXL97* (Sheldrick, 2008); molecular graphics: *XP* in *SHELXTL*; software used to prepare material for publication: *SHELXTL*.

Acknowledgements

The authors gratefully acknowledge the financial support provided by the Postdoctoral Science-Research Developmental Foundation of Heilongjiang Province (LBH-Q13170).

Supporting information for this paper is available from the IUCr electronic archives (Reference: PJ2024).

References

Bruker (2001). *SAINT-Plus*. Bruker AXS Inc., Madison, Wisconsin, USA.
Bruker (2004). *APEX2*. Bruker AXS Inc., Madison, Wisconsin, USA.
Laskin, I., Yang, Z. & Chu, I. K. (2008). *J. Am. Chem. Soc.* **130**, 3218–3220.
Rigamonti, L., Demartin, F., Forni, A., Righetto, S. & Pasini, A. (2006). *Inorg. Chem.* **45**, 10976–10989.
Sheldrick, G. M. (1996). *SADABS*. University of Göttingen, Germany.
Sheldrick, G. M. (2008). *Acta Cryst.* A**64**, 112–122.
Wezenberg, S. J. & Kleij, A. W. (2008). *Angew. Chem. Int. Ed.* **47**, 2354–2364.
Yuan, M., Zhao, F., Zhang, W., Wang, Z.-M. & Gao, S. (2007). *Inorg. Chem.* **46**, 11235–11242.

supporting information

Acta Cryst. (2015). E**71**, m217–m218 [https://doi.org/10.1107/S2056989015020551]

Crystal structure of di-μ-acetato-diacetatobis(μ-6,6′-dimethoxy-2,2′-[[(propane-1,3-diylbis(azanylylidene)]bis(methanylylidene)]diphenolato)tetrazinc

Xue Cai and Hui Ning

S1. Comment

The metal-organic coordination complexes of *N*,*N*′-bis(salicylidene)ethylenediamine (salen) Schiff-base derivatives were extensively studied within the field of homogeneous catalysis (Wezenberg *et al.*, 2008), nonlinear optic (Rigamonti *et al.*, 2006), magnetics (Yuan *et al.*, 2007), and biological metalloenzymes mimic (Laskin *et al.*, 2008). Recently, the compartmental salen ligands derived from the 2:1 condensation between 3-methoxysalicylaldehyde and corresponding diamines allowing for two metal ions located in dissimilar N_2O_2 and O_4 cavities bridged by phenolic oxygen atoms, which bring interesting magnetic phenomena and intriguing optical properties. Herein, a novel heterometallic tetranuclear (Zn_4) compound has been obtained by step-by-step method and its structure is described.

The compound is composed of two $[Zn_2(bmspd)(OAc)]^+$ ions bridged by two acetate ions. There are two kinds of symmetry-independent zinc ions in this compound. One zinc ion (Zn1) is located in a five-coordinated environment, as shown in Figure 1. The other kind of zinc ion (Zn2) is coordinated by the O_4 cavity in bmspd ligand and two oxygen atoms of acetate ions in pseudo-octahedral geometry. The neighbouring tetranuclear molecules form a two-dimensional supramolecular network by virtue of intermolecular π-π interactions. (Figure 2)

S2. Experimental

A mixture of metal-free Schiff-base ligand H_2bmspd (0.4 mmol 0.1368 g) and $Zn(OAc)_2{\cdot}2H_2O$ (0.4 mmol 0.0878 g) in methanol (20 ml) was stirred for 30 min at room temperature. Then, a solution of $Zn(OAc)_2{\cdot}2H_2O$ (0.4 mmol 0.0878 g) in methanol was added dropwise and the mixture was kept stirring for another 30 min at room temperature. Pale yellow block-shaped crystals for suitable for X-ray diffraction were obtained by slowly diffusing diethyl ether into the filtrate. The final mass of product was 0.0966 g.

S3. Refinement

The coordinates of the difference H atoms bound to C atoms were placed using the HFIX commands in *SHELXL-97*, with C—H distances of 0.93–0.97 Å. All H atoms were allowed for as riding atoms with U_{iso}(H) = 1.2U_{eq}(C) or 1.5U_{eq}(C). The orientation of hydrogen atoms of methyl groups of acetate was allowed to refine subject to geometric restraints.

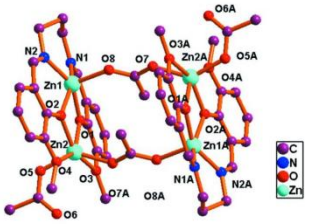

Figure 1

ORTEP diagram of molecular structure for complex $[Zn_4(bmspd)_2(OAc)_4]$ with atoms drawn as 50% probability ellipsoids.

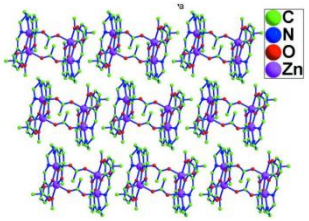

Figure 2

The perspective drawing of complex $[Zn_4(bmspd)_2(OAc)_4]$ packing in *ac* plane.

Di-μ-acetato-diacetatobis(*p*-6,6′-dimethoxy-2,2′-[[(propane-1,3-diylbis(azanylylidene)]bis(methanylylidene)]diphenolato)tetrazinc

Crystal data

$[Zn_4(C_{14}H_{20}N_2O_2)_2(C_2H_3O_2)_4]$	Z = 1
M_r = 1178.48	$F(000)$ = 604
Triclinic, $P\overline{1}$	D_x = 1.684 Mg m^{-3}
Hall symbol: -P 1	Mo $K\alpha$ radiation, λ = 0.71073 Å
a = 10.4894 (9) Å	Cell parameters from 4019 reflections
b = 10.7917 (9) Å	θ = 2.2–27.5°
c = 11.9559 (11) Å	μ = 2.12 mm^{-1}
α = 103.425 (2)°	T = 298 K
β = 94.323 (1)°	Block, yellow
γ = 115.677 (1)°	0.15 × 0.10 × 0.08 mm
V = 1162.17 (18) Å^3	

Data collection

Bruker SMART APEX CCD area-detector diffractometer	6281 measured reflections
	4497 independent reflections
Radiation source: fine-focus sealed tube	3969 reflections with $I > 2\sigma(I)$
Graphite monochromator	R_{int} = 0.013
Detector resolution: 0 pixels mm^{-1}	θ_{max} = 26.0°, θ_{min} = 1.8°
phi and ω scans	h = −6→12
Absorption correction: multi-scan (*SADABS*; Sheldrick, 1996)	k = −13→13
	l = −13→14
T_{min} = 0.742, T_{max} = 0.849	

Refinement

Refinement on F^2	Secondary atom site location: difference Fourier map
Least-squares matrix: full	
$R[F^2 > 2\sigma(F^2)]$ = 0.024	Hydrogen site location: inferred from neighbouring sites
$wR(F^2)$ = 0.071	
S = 1.05	H-atom parameters constrained
4497 reflections	$w = 1/[\sigma^2(F_o^2) + (0.0367P)^2 + 0.3975P]$ where $P = (F_o^2 + 2F_c^2)/3$
318 parameters	
0 restraints	$(\Delta/\sigma)_{max}$ = 0.006
Primary atom site location: structure-invariant direct methods	$\Delta\rho_{max}$ = 0.26 e Å^{-3}
	$\Delta\rho_{min}$ = −0.27 e Å^{-3}

Special details

Geometry. All e.s.d.'s (except the e.s.d. in the dihedral angle between two l.s. planes) are estimated using the full covariance matrix. The cell e.s.d.'s are taken into account individually in the estimation of e.s.d.'s in distances, angles and torsion angles; correlations between e.s.d.'s in cell parameters are only used when they are defined by crystal symmetry. An approximate (isotropic) treatment of cell e.s.d.'s is used for estimating e.s.d.'s involving l.s. planes.

Refinement. Refinement of F^2 against ALL reflections. The weighted *R*-factor *wR* and goodness of fit *S* are based on F^2, conventional *R*-factors *R* are based on *F*, with *F* set to zero for negative F^2. The threshold expression of $F^2 > \sigma(F^2)$ is used only for calculating *R*-factors(gt) *etc.* and is not relevant to the choice of reflections for refinement. *R*-factors based on F^2 are statistically about twice as large as those based on *F*, and *R*- factors based on ALL data will be even larger.

Fractional atomic coordinates and isotropic or equivalent isotropic displacement parameters (Å^2)

	x	y	z	U_{iso}*/U_{eq}
C1	0.5747 (2)	0.1717 (3)	0.1390 (2)	0.0479 (6)
H1A	0.5651	0.0938	0.1692	0.072*

H1B	0.5348	0.1350	0.0563	0.072*
H1C	0.5239	0.2186	0.1783	0.072*
C2	0.7601 (2)	0.3909 (2)	0.12186 (18)	0.0334 (4)
C3	0.6657 (2)	0.4234 (3)	0.0636 (2)	0.0431 (5)
H3	0.5666	0.3642	0.0497	0.052*
C4	0.7206 (3)	0.5459 (3)	0.0258 (2)	0.0540 (7)
H4	0.6577	0.5680	−0.0144	0.065*
C5	0.8656 (3)	0.6339 (3)	0.0473 (2)	0.0485 (6)
H5	0.9005	0.7136	0.0193	0.058*
C6	0.9640 (2)	0.6057 (2)	0.11148 (18)	0.0344 (5)
C7	0.9110 (2)	0.4824 (2)	0.14919 (17)	0.0288 (4)
C8	1.1149 (2)	0.7072 (2)	0.13321 (19)	0.0374 (5)
H8	1.1384	0.7791	0.0964	0.045*
C9	1.3647 (2)	0.8311 (2)	0.2054 (2)	0.0428 (5)
H9A	1.3563	0.9191	0.2172	0.051*
H9B	1.3959	0.8132	0.1316	0.051*
C10	1.4783 (2)	0.8521 (2)	0.3040 (2)	0.0438 (5)
H10A	1.4411	0.8567	0.3759	0.053*
H10B	1.5627	0.9436	0.3152	0.053*
C11	1.5238 (3)	0.7346 (3)	0.2830 (2)	0.0503 (6)
H11A	1.5415	0.7156	0.2039	0.060*
H11B	1.6138	0.7683	0.3370	0.060*
C12	1.4643 (2)	0.5208 (3)	0.33241 (19)	0.0396 (5)
H12	1.5642	0.5583	0.3466	0.048*
C13	1.3848 (2)	0.3817 (2)	0.35174 (18)	0.0362 (5)
C14	1.4677 (3)	0.3186 (3)	0.3880 (2)	0.0446 (6)
H14	1.5679	0.3689	0.4015	0.053*
C15	1.4038 (3)	0.1858 (3)	0.4035 (2)	0.0499 (6)
H15	1.4602	0.1465	0.4280	0.060*
C16	1.2532 (3)	0.1083 (3)	0.3828 (2)	0.0435 (5)
H16	1.2093	0.0169	0.3925	0.052*
C17	1.1699 (2)	0.1679 (2)	0.34775 (18)	0.0354 (5)
C18	1.2338 (2)	0.3069 (2)	0.33311 (17)	0.0310 (4)
C19	0.9443 (3)	−0.0457 (3)	0.3169 (3)	0.0661 (8)
H19A	0.8425	−0.0761	0.2991	0.099*
H19B	0.9686	−0.0585	0.3910	0.099*
H19C	0.9691	−0.1021	0.2566	0.099*
C20	0.7933 (2)	−0.0082 (2)	0.06099 (19)	0.0343 (4)
C21	0.7849 (2)	−0.1000 (3)	−0.0585 (2)	0.0422 (5)
H21A	0.7129	−0.1974	−0.0704	0.063*
H21B	0.8769	−0.0973	−0.0633	0.063*
H21C	0.7594	−0.0635	−0.1179	0.063*
C22	0.8649 (2)	0.3057 (2)	0.48569 (18)	0.0314 (4)
C23	1.0099 (3)	0.3370 (3)	0.5482 (2)	0.0493 (6)
H23A	1.0778	0.4354	0.5584	0.074*
H23B	1.0424	0.2747	0.5026	0.074*
H23C	1.0022	0.3208	0.6236	0.074*
N1	1.22093 (19)	0.71044 (18)	0.19729 (15)	0.0340 (4)

N2	1.41504 (19)	0.59888 (19)	0.29835 (16)	0.0359 (4)	
O1	0.99395 (15)	0.44590 (15)	0.20882 (13)	0.0329 (3)	
O2	1.14934 (15)	0.35966 (15)	0.30055 (13)	0.0343 (3)	
O3	0.72225 (16)	0.27149 (18)	0.15849 (17)	0.0488 (4)	
O4	1.02202 (17)	0.10166 (16)	0.32310 (15)	0.0437 (4)	
O5	0.89752 (18)	0.11959 (17)	0.09127 (14)	0.0436 (4)	
O6	0.7050 (2)	−0.0567 (2)	0.12112 (17)	0.0590 (5)	
O7	0.82953 (16)	0.25334 (17)	0.37574 (13)	0.0409 (4)	
O8	0.77997 (17)	0.33076 (18)	0.54407 (13)	0.0423 (4)	
Zn1	1.20447 (2)	0.56385 (2)	0.28798 (2)	0.02906 (8)	
Zn2	0.92824 (2)	0.25063 (2)	0.24271 (2)	0.02988 (8)	

Atomic displacement parameters (Å²)

	U^{11}	U^{22}	U^{33}	U^{12}	U^{13}	U^{23}
C1	0.0285 (12)	0.0518 (14)	0.0543 (15)	0.0087 (11)	0.0080 (10)	0.0197 (12)
C2	0.0322 (11)	0.0350 (11)	0.0342 (11)	0.0155 (9)	0.0064 (9)	0.0125 (9)
C3	0.0314 (12)	0.0494 (13)	0.0485 (13)	0.0184 (11)	0.0017 (10)	0.0174 (11)
C4	0.0471 (15)	0.0605 (16)	0.0624 (17)	0.0293 (13)	−0.0030 (12)	0.0281 (14)
C5	0.0517 (15)	0.0470 (14)	0.0532 (15)	0.0243 (12)	0.0024 (12)	0.0258 (12)
C6	0.0383 (12)	0.0344 (11)	0.0332 (11)	0.0177 (9)	0.0062 (9)	0.0136 (9)
C7	0.0311 (10)	0.0288 (10)	0.0270 (10)	0.0145 (8)	0.0052 (8)	0.0081 (8)
C8	0.0461 (13)	0.0308 (11)	0.0363 (11)	0.0151 (10)	0.0110 (10)	0.0164 (9)
C9	0.0401 (13)	0.0356 (12)	0.0433 (13)	0.0061 (10)	0.0100 (10)	0.0178 (10)
C10	0.0331 (12)	0.0387 (12)	0.0445 (13)	0.0024 (10)	0.0072 (10)	0.0141 (10)
C11	0.0302 (12)	0.0540 (15)	0.0619 (16)	0.0099 (11)	0.0159 (11)	0.0262 (13)
C12	0.0259 (11)	0.0473 (13)	0.0384 (12)	0.0149 (10)	0.0045 (9)	0.0046 (10)
C13	0.0352 (12)	0.0427 (12)	0.0292 (10)	0.0220 (10)	0.0001 (8)	0.0019 (9)
C14	0.0394 (13)	0.0543 (14)	0.0402 (12)	0.0284 (12)	−0.0019 (10)	0.0041 (11)
C15	0.0579 (16)	0.0616 (16)	0.0421 (13)	0.0432 (14)	−0.0025 (11)	0.0093 (11)
C16	0.0597 (16)	0.0434 (13)	0.0363 (12)	0.0326 (12)	0.0053 (11)	0.0113 (10)
C17	0.0424 (12)	0.0379 (11)	0.0291 (10)	0.0226 (10)	0.0064 (9)	0.0077 (9)
C18	0.0332 (11)	0.0353 (11)	0.0254 (10)	0.0193 (9)	0.0029 (8)	0.0048 (8)
C19	0.0645 (19)	0.0417 (15)	0.085 (2)	0.0146 (14)	0.0019 (16)	0.0313 (15)
C20	0.0313 (11)	0.0406 (12)	0.0349 (11)	0.0190 (10)	0.0052 (9)	0.0134 (9)
C21	0.0367 (12)	0.0430 (12)	0.0406 (12)	0.0185 (10)	0.0017 (10)	0.0035 (10)
C22	0.0355 (11)	0.0279 (10)	0.0316 (10)	0.0131 (9)	0.0107 (9)	0.0121 (8)
C23	0.0518 (15)	0.0672 (16)	0.0374 (12)	0.0374 (13)	0.0075 (11)	0.0111 (12)
N1	0.0332 (10)	0.0307 (9)	0.0325 (9)	0.0083 (8)	0.0084 (7)	0.0119 (7)
N2	0.0279 (9)	0.0393 (10)	0.0364 (10)	0.0125 (8)	0.0083 (7)	0.0100 (8)
O1	0.0255 (7)	0.0312 (7)	0.0399 (8)	0.0094 (6)	0.0001 (6)	0.0163 (6)
O2	0.0269 (7)	0.0315 (7)	0.0460 (9)	0.0138 (6)	0.0035 (6)	0.0149 (6)
O3	0.0254 (8)	0.0468 (9)	0.0741 (12)	0.0089 (7)	0.0038 (8)	0.0355 (9)
O4	0.0397 (9)	0.0345 (8)	0.0589 (10)	0.0168 (7)	0.0095 (8)	0.0182 (7)
O5	0.0423 (9)	0.0382 (9)	0.0384 (9)	0.0129 (7)	0.0064 (7)	0.0024 (7)
O6	0.0571 (11)	0.0699 (12)	0.0544 (11)	0.0260 (10)	0.0266 (9)	0.0283 (10)
O7	0.0369 (8)	0.0534 (9)	0.0281 (8)	0.0185 (7)	0.0093 (6)	0.0086 (7)
O8	0.0365 (9)	0.0551 (10)	0.0323 (8)	0.0206 (8)	0.0113 (7)	0.0077 (7)

Zn1	0.02476 (13)	0.02968 (13)	0.03096 (13)	0.00999 (10)	0.00664 (9)	0.01083 (10)
Zn2	0.02869 (14)	0.02835 (13)	0.02989 (13)	0.01035 (10)	0.00723 (10)	0.00921 (10)

Geometric parameters (Å, °)

C1—O3	1.412 (3)	C15—C16	1.398 (4)
C1—H1A	0.9600	C15—H15	0.9300
C1—H1B	0.9600	C16—C17	1.382 (3)
C1—H1C	0.9600	C16—H16	0.9300
C2—O3	1.362 (3)	C17—O4	1.370 (3)
C2—C3	1.378 (3)	C17—C18	1.414 (3)
C2—C7	1.416 (3)	C18—O2	1.322 (2)
C3—C4	1.394 (3)	C19—O4	1.418 (3)
C3—H3	0.9300	C19—H19A	0.9600
C4—C5	1.363 (4)	C19—H19B	0.9600
C4—H4	0.9300	C19—H19C	0.9600
C5—C6	1.417 (3)	C20—O6	1.226 (3)
C5—H5	0.9300	C20—O5	1.277 (3)
C6—C7	1.399 (3)	C20—C21	1.509 (3)
C6—C8	1.441 (3)	C21—H21A	0.9600
C7—O1	1.325 (2)	C21—H21B	0.9600
C8—N1	1.285 (3)	C21—H21C	0.9600
C8—H8	0.9300	C22—O8	1.253 (2)
C9—N1	1.482 (3)	C22—O7	1.259 (2)
C9—C10	1.514 (3)	C22—C23	1.501 (3)
C9—H9A	0.9700	C23—H23A	0.9600
C9—H9B	0.9700	C23—H23B	0.9600
C10—C11	1.515 (4)	C23—H23C	0.9600
C10—H10A	0.9700	N1—Zn1	2.0727 (17)
C10—H10B	0.9700	N2—Zn1	2.0616 (18)
C11—N2	1.479 (3)	O1—Zn1	2.0203 (14)
C11—H11A	0.9700	O1—Zn2	2.0639 (14)
C11—H11B	0.9700	O2—Zn2	2.0632 (14)
C12—N2	1.284 (3)	O2—Zn1	2.0676 (14)
C12—C13	1.452 (3)	O3—Zn2	2.4356 (16)
C12—H12	0.9300	O5—Zn2	1.9261 (15)
C13—C18	1.402 (3)	O7—Zn2	1.9635 (14)
C13—C14	1.415 (3)	O8—Zn1^{i}	2.0201 (15)
C14—C15	1.359 (4)	Zn1—O8^{i}	2.0201 (15)
C14—H14	0.9300		
O3—C1—H1A	109.5	C13—C18—C17	118.12 (19)
O3—C1—H1B	109.5	O4—C19—H19A	109.5
H1A—C1—H1B	109.5	O4—C19—H19B	109.5
O3—C1—H1C	109.5	H19A—C19—H19B	109.5
H1A—C1—H1C	109.5	O4—C19—H19C	109.5
H1B—C1—H1C	109.5	H19A—C19—H19C	109.5
O3—C2—C3	125.4 (2)	H19B—C19—H19C	109.5

O3—C2—C7	112.88 (18)	O6—C20—O5	124.8 (2)
C3—C2—C7	121.7 (2)	O6—C20—C21	120.8 (2)
C2—C3—C4	119.1 (2)	O5—C20—C21	114.42 (19)
C2—C3—H3	120.4	C20—C21—H21A	109.5
C4—C3—H3	120.4	C20—C21—H21B	109.5
C5—C4—C3	120.6 (2)	H21A—C21—H21B	109.5
C5—C4—H4	119.7	C20—C21—H21C	109.5
C3—C4—H4	119.7	H21A—C21—H21C	109.5
C4—C5—C6	121.0 (2)	H21B—C21—H21C	109.5
C4—C5—H5	119.5	O8—C22—O7	120.8 (2)
C6—C5—H5	119.5	O8—C22—C23	119.36 (19)
C7—C6—C5	119.1 (2)	O7—C22—C23	119.80 (19)
C7—C6—C8	123.83 (19)	C22—C23—H23A	109.5
C5—C6—C8	117.1 (2)	C22—C23—H23B	109.5
O1—C7—C6	123.77 (18)	H23A—C23—H23B	109.5
O1—C7—C2	117.92 (17)	C22—C23—H23C	109.5
C6—C7—C2	118.31 (18)	H23A—C23—H23C	109.5
N1—C8—C6	127.81 (19)	H23B—C23—H23C	109.5
N1—C8—H8	116.1	C8—N1—C9	115.46 (18)
C6—C8—H8	116.1	C8—N1—Zn1	125.35 (15)
N1—C9—C10	113.12 (18)	C9—N1—Zn1	119.19 (14)
N1—C9—H9A	109.0	C12—N2—C11	116.01 (19)
C10—C9—H9A	109.0	C12—N2—Zn1	124.81 (15)
N1—C9—H9B	109.0	C11—N2—Zn1	118.53 (15)
C10—C9—H9B	109.0	C7—O1—Zn1	129.06 (12)
H9A—C9—H9B	107.8	C7—O1—Zn2	125.64 (12)
C9—C10—C11	114.1 (2)	Zn1—O1—Zn2	105.29 (6)
C9—C10—H10A	108.7	C18—O2—Zn2	127.10 (13)
C11—C10—H10A	108.7	C18—O2—Zn1	129.24 (13)
C9—C10—H10B	108.7	Zn2—O2—Zn1	103.62 (6)
C11—C10—H10B	108.7	C2—O3—C1	119.07 (18)
H10A—C10—H10B	107.6	C2—O3—Zn2	113.52 (12)
N2—C11—C10	113.20 (19)	C1—O3—Zn2	127.31 (14)
N2—C11—H11A	108.9	C17—O4—C19	119.41 (19)
C10—C11—H11A	108.9	C20—O5—Zn2	120.25 (14)
N2—C11—H11B	108.9	C22—O7—Zn2	137.14 (14)
C10—C11—H11B	108.9	C22—O8—Zn1^{i}	135.32 (15)
H11A—C11—H11B	107.8	O1—Zn1—O8^{i}	109.18 (6)
N2—C12—C13	128.7 (2)	O1—Zn1—N2	149.75 (7)
N2—C12—H12	115.7	O8^{i}—Zn1—N2	98.57 (7)
C13—C12—H12	115.7	O1—Zn1—O2	75.35 (5)
C18—C13—C14	119.5 (2)	O8^{i}—Zn1—O2	100.83 (6)
C18—C13—C12	123.98 (19)	N2—Zn1—O2	88.08 (6)
C14—C13—C12	116.5 (2)	O1—Zn1—N1	88.64 (6)
C15—C14—C13	121.3 (2)	O8^{i}—Zn1—N1	103.96 (7)
C15—C14—H14	119.3	N2—Zn1—N1	96.30 (7)
C13—C14—H14	119.3	O2—Zn1—N1	153.84 (7)
C14—C15—C16	120.0 (2)	O5—Zn2—O7	137.44 (7)

8.Cai X, Zhou Q, Ma Y, et al. Selective Removal of CO in Hydrocarbons-Rich Industrial Off-gases over CuO-Ce_xZr_1 − xO_2 Catalysts [J]. Catalysis Surveys from Asia, 2021, 25(1): 68-75. （SCI 检索收录四区，IF=3.106）

Catalysis Surveys from Asia
https://doi.org/10.1007/s10563-020-09314-4

ORIGINAL ARTICLE

Selective Removal of CO in Hydrocarbons-Rich Industrial Off-gases over CuO–$Ce_xZr_{1-x}O_2$ Catalysts

Xue Cai[1] · Qi Zhou[1] · Yue Ma[1] · Li Jiang[1] · Wenwen Yu[2,3] · Wenling Chu[2] · Rui Cai[2] · Weishen Yang[2]

Received: 4 August 2020 / Accepted: 23 September 2020
© Springer Science+Business Media, LLC, part of Springer Nature 2020

Abstract
The selective remove CO in industrial rich-hydrocarbon off-gases was performed over CuO–$Ce_xZr_{1-x}O_2$ (x = 0, 0.1, 0.5, 0.75, 0.9 and 1.0) mixed oxides. The effect of ceria content on the structure and catalytic properties of CuO–$Ce_xZr_{1-x}O_2$ compositions has been investigated, and the removal activity of CO is greatly dependent the structure of the support. Based on the characterizations from XRD, H_2-TPR, Raman spectra, XPS and CO-TPD, it can be found that the formation of ceria–zirconia solid solution induced by the introduction of ceria into zirconia leads to an increase in the amount of oxygen vacancies and the mobility of the lattice oxygen, and as a result, enhances the removal activity of catalysts towards CO. The lowest reaction temperature (~123 ℃) for 100% conversion of CO remove was obtained over CuO–$Ce_{0.9}Zr_{0.1}O_2$ sample, which also exhibited the highest concentration of surface oxygen vacancy, the better reducibility and the highest low-temperature adsorption capacity of CO. This study presents a strategy to design a high-efficiency CuO-based catalyst by controlling the concentration of the surface oxygen vacancies.

Keywords Selective removal of CO · CuO–$Ce_xZr_{1-x}O_2$ ternary catalysts · Off-gas stream from propane oxidation · Oxygen vacancy sites

1 Introduction

Due to severe poisonous to the Pt catalysts used for the electrode materials, or due to a high risk of explosion in recycled industrial off-gases mixtures, the selective elimination of the undesirable CO in rich-hydrogen systems for the fuel cells or in recycled off-gas systems for the real-life chemical processes have attracted intensive attention in recent years. Particular attention has generally been paid to its application in selective remove of CO in off-gases from oxidation process of light alkanes with extremely exothermic properties, in which the lower conversion of alkane is necessary in order to efficiently decrease uncontrollable exotherm. As a result, recycled utilization of unconverted light-alkanes is one of the most cost-effective technologies for the industrial oxidation processes. To avoid explosion risk induced by the build-up in concentration of CO in recycled rich-hydrocarbons off-gases with complex components, one of the primary efforts is concentrated on selective oxidation removal of CO over the promising catalysts [1, 2].

In the past decades, various catalysts, such as precious metals [3], transition metal oxides [4, 5], have been investigated and exhibited excellent catalytic performances toward CO oxidation in rich-hydrogen systems for the fuel cells. As one of the most reactive catalysts, the binary supported metal oxide catalysts exhibit outstanding oxidation performance of CO due to the strong interaction between active metal species and supports [6]. Kleitz and colleagues [7] found that the tailored meso-structured CuO–CeO_2 catalysts exhibited the enhanced performance for preferential oxidation of CO at low temperature. Furthermore, it was found that [8] Cu–Fe mixed oxides with controlled composition showed a good performance in the CO oxidation reaction compared to a commercial Pt/Al_2O_3 catalyst used as a reference. ZrO_2 as an inert support shows high thermal stability

✉ Xue Cai
xuecai@mail.sdu.edu.cn

✉ Wenling Chu
cwl@dicp.ac.cn

[1] Mudanjiang Normal University, Mudanjiang 157011, China

[2] State Key Laboratory of Catalysis, Dalian Institute of Chemical Physics, Chinese Academy of Science, 457 Zhongshan Road, Dalian 116023, Liaoning, China

[3] University of Chinese Academy of Sciences, Beijing 100049, China

Published online: 01 October 2020

at higher temperature and further ZrO_2-supported CuO binary catalyst had a high CO conversion [9, 10]. However, there is little report about the selective removal of CO in rich-hydrocarbons off-gas streams with complicated compositions from industrial oxidation process of light alkanes.

Compared to CuO–CeO_2 and CuO–ZrO_2 binary systems, ternary Cu–Ce–Zr catalysts will exhibit distinct physico-chemical properties due to the formation of Ce–Zr solid solution, which plays a critical role in oxygen storage capacity and thermal stability. Especially, the combination of Ce^{4+} and Zr^{4+} ions is favorable to the formation of structural defects and the improvement in oxygen mobility, which is helpful for enhancing the catalytic performance.

Accordingly, in the present work, a series of CuO–$Ce_xZr_{1-x}O_2$ with varied Ce/Zr molar ratios were successfully synthesized. Their physico-chemical properties were investigated to identify the effect of the combination of Zr and Ce on the oxygen mobility and the formation of oxygen vacancies. Furthermore, using the selective oxidation removal of CO in off-gas from propane oxidation to acrylic acid as probe reaction, much more attention was devoted to investigating the role of varied Ce/Zr ratios on the reactivity of the catalysts for the selective removal of CO from complicated off-gas streams.

2 Experimental

2.1 Catalyst Preparation

$Ce_xZr_{1-x}O_2$ (x = 0, 0.1, 0.5, 0.75, 0.9 and 1.0) mixed metal oxide supports were prepared by a co-precipitation method. $Zr(NO_3)_4{\cdot}5H_2O$ and $Ce(NO_3)_3{\cdot}6H_2O$ with varied mole ratios were dissolved in 300 mL deionized water at room temperature under vigorous stirring. 0.5 mol/L $(NH_4)_2CO_3$ solution as the precipitation agent was added slowly into the precursor solution. After stirring for 4 h at room temperature, the precipitate was washed several times in deionized water, and then dried overnight at 120 ℃. The resulting powders were calcined at 500 ℃ for 4 h in air. The 5 wt% CuO–$Ce_xZr_{1-x}O_2$ samples were synthesized by a wet impregnation method. Each $Ce_xZr_{1-x}O_2$ powder was impregnated with copper nitrate $[Cu(NO_3)_2{\cdot}3H_2O]$ for 4 h, then dried at 72 ℃ and calcined at 400 ℃ for 4 h in an air atmosphere.

2.2 Catalyst Characterization

XRD patterns were collected using a Rigaku D/MAX 2500/PC diffractometer equipped with Cu Kα radiation (λ = 0.1542 nm) at 40 kV, 30 mA. Scan range is 10°–90° with scan speed of 5 °/min.

The BET surface areas were determined using a Quantachrome adsorption apparatus with nitrogen adsorption at 77 K. The samples were degassed at 300 ℃ for 3 h before test.

Elemental bulk composition was determined by X-ray fluorescence with a wavelength dispersive X-ray fluorescence spectrometer (ARL ADVANTXP) and the UNIQUANT software. The X-ray tube was set at 60 kV.

H_2-TPR experiments were undertaken in a quartz reactor, and about 50 mg of CuO–$Ce_xZr_{1-x}O_2$ sample was used for each measurement. Prior to the reduction, the catalyst was pretreated at 200 ℃ for 1 h in flowing He (20 mL/min) and then cooled to room temperature. After that, a 10% H_2/Ar mixture was allowed to flow through the sample and the temperature increased gradually to 800 ℃ with a ramp of 10 ℃/min. H_2 consumption was monitored using a thermal conduction detector (TCD).

The temperature-programmed desorption of CO (CO-TPD) was measured in a fixed bed reactor. The samples (70 mg) were loaded between quartz wool plugs in the middle of the reactor and pretreated by He (45 mL/min) with a rate of 10/min from room temperature (RT) to 200 ℃ for 1 h. And then the samples were cooled down to RT under the flow of He. The CO adsorption was performed at 50 ℃ under a flow rate of 30 mL/min for 1 h, then the samples were ramped to 700 ℃ at a linear heating rate of 10 ℃/min. The analysis of the effluent gases was carried out with a mass spectrometer.

Raman spectra were obtained on a Renishaw Raman spectrometer with 532 nm laser. The laser line power was about 0.3 mW.

The X-ray photoelectron spectroscopy (XPS) was measured with a Thermo Fisher ESCALAB 250 Xi spectrometer, with an X-ray source of Al Kα radiation of 1486.6 eV at 15 KV and 10.8 mA. The working pressure of the instrument was 7.1×10^{-9} Pa. The binding energies were calculated with reference to the energy of C 1s peak of contaminant carbon at 284.6 eV.

2.3 Catalytic Activity

The removal performance of CO over CuO–$Ce_xZr_{1-x}O_2$ samples was evaluated in a fixed-bed quartz reactor (i.d. 10 mm). The reaction feedstock is a simulated off-gas stream from selective oxidation of propane to acrylic acid process, which consists of 1.59% CO, 1.50% CO_2, 8.70% O_2, 0.02% C_3H_6, 0.02% C_3H_8, 0.46% C_3H_4O, 9.40% C_3H_4 and 78.31% N_2. Typically, 0.5 g catalyst (20–30 mesh) without any pretreatment was loaded into the reactor. The total flow rate of the simulated off-gas was 33.33 mL/min. The removal measurement of CO was performed by increasing the temperature from 50 to 300 ℃. CO conversion (%) and selectivity to CO removal were calculated according to the following equations:

$$\text{CO conversion (\%)} = ([CO]_{in} - [CO]_{out})/[CO]_{in},$$

$$\text{Selectivity to CO removal (\%)} = ([CO]_{in} - [CO]_{out})/2([O_2]_{in} - [O_2]_{out},$$

where $[CO]_{in}$, $[O_2]_{in}$ and $[CO]_{out}$, $[O_2]_{out}$ are the concentration of CO and O_2 from input and output of the reactor, respectively.

3 Results and Discussion

3.1 Catalyst Characterization

3.1.1 XRD

Figure 1 shows the XRD patterns of the CuO–$Ce_xZr_{1-x}O_2$ catalyst with varied Ce/Zr molar ratios, in which the theoretical Ce/Zr values are in good agreement with the actual results (listed in Table 1) from XRF characterization. XRD pattern of CuO–ZrO_2 sample corresponds to ZrO_2 consisting of a mixture of monoclinic and tetragonal phase. However, the introduction of Ce in a low concentration (Ce/Zr = 0.1) into the ZrO_2 structure stabilizes the tetragonal structure of zirconium oxide, and this stabilization of ZrO_2 structure by Ce was reported by other authors [11, 12]. With the further increase of Ce^{4+} incorporation, the CuO–$Ce_xZr_{1-x}O_2$ samples (x > 0.1) showed quite similar diffraction peaks to the CeO_2 cubic fluorite structure and no ZrO_2 phases were detected, indicating Zr^{4+} ions totally enter into CeO_2 lattice and a good single-phase cubic ceria–zirconia solid solution is formed. And the XRD diffraction peak shifted to a small angle due to lattice expansion caused by the substitution of Zr^{4+} cations (0.084 nm) with larger Ce^{4+} (0.097 nm) [13]. Furthermore, as shown in Fig. 1, the incorporation of Ce^{4+} into ZrO_2 also led to the weakening and broadening of the diffraction peaks, indicating that the grain size of the samples was reduced. Based on the Scherrer formula, the average crystal size of as-synthesized samples was calculated and the results in Table 1 showed that the crystallite sizes of CuO–$Ce_xZr_{1-x}O_2$ samples were in the range of 10–20 nm. Obviously, the addition of Ce significantly reduced the grain size and thus increased the BET surface area of the samples, and the highest BET surface area was observed over CuO–$Ce_{0.75}Zr_{0.25}O_2$. Finally, the absence of CuO reflection peaks in XRD pattern indicates that Cu species are highly dispersed on the ceria–zirconia solid solution, or the grain size is too small to be detected by XRD instrument [14].

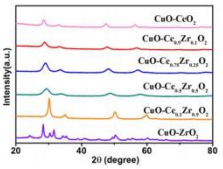

Fig. 1 XRD patterns of CuO–$Ce_xZr_{1-x}O$ catalysts

Table 1 Physico-chemical properties of CuO–$Ce_xZr_{1-x}O$ catalyst

Catalysts	S_{BET} (m^2/g)	Actual ratio of Ce/Zr[a]	Crystalline size (nm)[b]	A_{610}/A_{465}[c]	$Ce^{3+}/(Ce^{3+}+Ce^{4+})$[d] (%)	O_{ads}/O_{tot}[e] (%)	T_{100}[f] (°C)	Temperature window[g] (°C)
CuO–CeO_2	101.6	–	9.47	0.32	22.8	25.4	140	140–176
CuO–$Ce_{0.9}Zr_{0.1}O_2$	74.88	7.79	9.85	0.47	24.6	29.4	123	123–156
CuO–$Ce_{0.75}Zr_{0.25}O_2$	101.74	3.19	8.75	0.33	23.2	25.3	131	131–154
CuO–$Ce_{0.5}Zr_{0.5}O_2$	91.90	0.87	9.67	0.25	22.1	24.7	162	162–174
CuO–$Ce_{0.1}Zr_{0.9}O_2$	55.26	0.11	15.64	0.17	18.8	19.6	183	183–183
CuO–ZrO_2	33.18	0	20.62	–	–	15.1	191	191–191

[a] From the analysis of XRF files
[b] From Scherrer's formula of XRD files
[c] Concentration of oxygen vacancies from Raman spectra
[d] The relative ratio of Ce^{3+} species from Ce 3d XPS spectra
[e] Calculated by O 1s spectra of XPS files
[f] The temperature in which CO in off-gas stream is fully converted
[g] The temperature window is a temperature range in which full conversion of CO and ~ 100% CO selectivity wasobtained

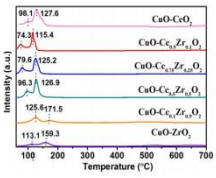

Fig. 2 H_2-TPR profiles of CuO–$Ce_xZr_{1-x}O$ catalysts

3.1.2 H_2-TPR

The redox properties of as-synthesized samples were examined by H_2-TPR and the results were shown in Fig. 2. All catalysts exhibited two reductive peaks, in which a shoulder peak located in the range of 70–110 ℃ and a major peak with a temperature of above 115 ℃. According to relevant literature reports [15, 16], the first low-temperature reduction peak is due to the reduction of the highly dispersed CuO species, which is strongly interacting with the $Ce_xZr_{1-x}O_2$ support, while the second peak can be attributed to the CuO species weakly associated with the supports [17]. The reductive temperatures of binary CuO–ZrO_2 and CuO–CeO_2 samples are 113.1 ℃, 159.3 ℃ and 98.1 ℃, 127.6℃, respectively. It can be seen from Fig. 2 that, except for CuO–$Ce_{0.1}Zr_{0.9}O_2$ sample with the stable ZrO_2 tetragonal structure shown by XRD, the reduction temperature of other ternary CuO–$Ce_xZr_{1-x}O_2$ samples gradually decreased with the increased of Ce content, indicating that the formation of the ceria–zirconia solid solution significantly improved the reducibility of the samples. Among the series of CuO–$Ce_xZr_{1-x}O_2$ samples with varied Ce/Zr ratios, CuO–$Ce_{0.9}Zr_{0.1}O_2$ catalyst presented the lowest reduction temperature, suggesting the better reducibility and oxygen mobility due to the improved synergism between Ce–Zr solid solution and Cu species [18]. It is possible that the highly dispersed CuO species with outstanding redox ability on the surface of Ce–Zr solid solution would be favorable to the enhancement in removal activity of CO in the industrial hydrocarbons-rich off-gas stream.

3.1.3 Raman Spectra

It has been reported [19] that the oxygen vacancies or defect sites play a significant role in determining the oxidation activity of CO. And Raman spectroscopy is a useful tool to characterize the defects and their surrounding chemical environment. Figure 3 showed the Raman spectra of as-synthesized CuO–$Ce_xZr_{1-x}O_2$ catalysts with varied Ce/Zr ratio. The CuO–ZrO_2 catalyst showed five main peaks at 336 cm^{-1}, 381 cm^{-1}, 475 cm^{-1}, 619 cm^{-1}, 636 cm^{-1}, which are attributed to the ZrO_2 support [20]. With the addition of Ce ions, the characteristic peaks of ZrO_2 weakened or further disappeared, but the peaks at 465 cm^{-1} assigned to the F_{2g} mode of the CeO_2 fluorite structure began to appear [21]. However, compared with those of pure CeO_2, the F_{2g} band of binary CuO–CeO_2 and ternary CuO–$Ce_xZr_{1-x}O_2$ catalysts became broader and weaker due to the deformation of the cubic CeO_2 induced by the strong interaction between Cu and Ce (Ce–Zr) or the formation of ceria–zirconia solid solution. Specially, a weak peak related to oxygen vacancies at ~ 610 cm^{-1} began to appear and became the stronger with doping Ce into ZrO_2 support. Generally, the ratio of the peak area at 610 cm^{-1} and 465 cm^{-1} (A_{610}/A_{465}) can be used to describe the relative concentration of oxygen vacancies [22, 23], and the results are listed in Table 1. Obviously, the concentration of oxygen vacancies over the ternary CuO–$Ce_xZr_{1-x}O_2$ catalysts is continuously increased with the amount of the doped Ce^{4+} into the ZrO_2 support. Although the binary CuO–CeO_2 exhibited the higher A_{610}/A_{465} value (0.32) due to the stronger interaction between copper and ceria [7, 24], the formation of ceria–zirconia solid solution would lead to the serious distortion of CeO_2 and induce the generation of more oxygen vacancies and defects [25]. And sample CuO–$Ce_{0.9}Zr_{0.1}O_2$ exhibited the highest A_{610}/A_{465} value (0.47) among series of as-synthesized catalysts. It was known that oxygen vacancies are benefit for improving the adsorption and activation of gas oxygen as well as the mobility of lattice oxygen [26], which is well consistent with H_2-TPR test.

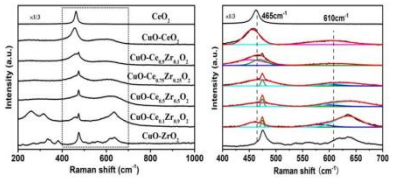

Fig. 3 Raman spectra of CuO–$Ce_xZr_{1-x}O$ catalyst samples and expansion of the hatched region

3.1.4 XPS Spectra

The further evidence for Ce doping into ZrO_2 to form oxygen vacancies could be achieved by O 1s XPS spectra shown in Fig. 4. The corresponding O 1s spectra show three characteristic peaks, which are assigned to the lattice oxygen species at 529.2–529.7 eV, the active oxygen vacancies at 531.1–531.3 eV and the chemisorbed oxygen species at ~ 532.2 eV including hydroxyl or carbonate, respectively [27, 28]. Many researchers have reported that the active oxygen vacancies play an important role in CO oxidations. For example, using quantitative temporal analysis, Widmann and colleagues [29] found that oxidation rate of CO was significantly strengthened by surface oxygen vacancies over Au/CeO_2 catalyst. Accordingly, the relative amount of O_{ads}/O_{tot} was calculated and the results were listed in Table 1. Similar with the information observed from Raman spectra, the concentration of surface oxygen vacancies is increased with doping Ce ions into ZrO_2 support for the ternary CuO–$Ce_xZr_{1-x}O_2$ samples. For the binary samples, the concentration of surface oxygen vacancies over CuO–CeO_2 is much higher than that of CuO–ZrO_2, suggesting that the strong interaction between copper and ceria is more favorable to the generation of oxygen vacancies.

Another conformation of the increase in the concentration of oxygen vacancies with respect to Ce incorporation can be found from Ce 3d XPS spectra of the CuO–$Ce_xZr_{1-x}O_2$ catalysts with varied Ce/Zr ratios, as shown in Fig. 5. Among the deconvoluted eight peaks, the peaks labeled as V′ and U′ correspond to the spin–orbit state of Ce^{3+} species, while other peaks are related to the Ce^{4+} species [30, 31]. The appearance of Ce^{3+} is an evidence of the generation of some oxygen vacancies induced by the reduction of Ce^{4+} [32, 33]. It is evident from Table 1 that the lower concentrations of Ce^{3+} on the surface of ternary CuO–$Ce_{0.1}Zr_{0.9}O_2$ can be convincingly attributed to the presence of the tetragonal ZrO_2 phase and the lowest amount of reducible Ce^{4+}. And the further increase of the doped Ce ions led to a gradual increase in the concentration of Ce^{3+} due to the generation of ceria–zirconia solid solution, suggesting the enhancement in the formation of surface oxygen defects/vacancies. As for the binary CuO–CeO_2 catalyst, the stronger interaction between copper and ceria is favorable to the generation of

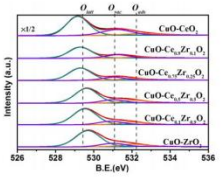

Fig. 4 XPS spectra of O 1s for the CuO/$Ce_xZr_{1-x}O$ catalyst samples

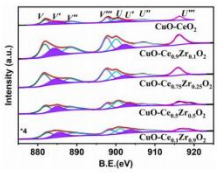

Fig. 5 XPS spectra of Ce 3d for the CuO–$Ce_xZr_{1-x}O$ catalyst samples

Ce^{3+} ions, which has been confirmed by many literatures [34, 35].

From the results above, it can conclude that the formation of ceria–zirconia solid solution facilitated the distortion of CeO_2 and created more oxygen vacancies over $CuO/Ce_xZr_{1-x}O_2$ samples, which were also confirmed by the evolution of Ce^{3+} and O_{vac} in XPS spectra and the increase in the peak area of A_{616} in Raman spectra.

3.1.5 CO-TPD

It has been reported [36, 37] that the adsorption of CO on the active sites of the CuO-based catalysts plays a key role in the oxidation removal process. Thus, we have further investigated the nature of catalyst surface by CO-TPD. Figure 6 gives the CO-TPD patterns of the catalysts with different ratios of Ce/Zr. The peak region below 110 ℃ can be assigned to the weakly chemisorbed CO species on the surface Cu^+ sites [38, 39]. As we can see, CuO–ZrO_2 and CuO–$Ce_{0.1}Zr_{0.9}O_2$ catalysts exhibited one smaller low-temperature desorption peak due to the presence of mixed ZrO_2 and tetragonal ZrO_2 phase, respectively. However, further incorporation of Ce cations into the ZrO_2 support led to the formation of one-phase ceria–zirconia solid solution, for which the amount of desorbed CO at low temperature is obviously increased. This trend gives the evidence that the a single-phase ceria–zirconia solid solution as the support is favorable to enhance the amount of adsorption sites for CO, indicating the presence of more active Cu^+ ions on the catalyst surface. This result is consistent with the higher reducibility over the CuO–$Ce_xZr_{1-x}O_2$ (x = 0.9, 0.75 and 0.5), as shown by the results of H_2-TPR.

Furthermore, it can be seen from Fig. 6 that the as-synthesized catalysts also exhibited a peak at temperature around 250–300 ℃, corresponding to the stronger adsorption of CO species by active metal on the surface. It can be found that, with the increase of Ce content, the desorption peak due to strong CO–metal bonds shifted to the lower temperature, and further gradually weakened and even disappeared. For CO oxidation, the chemisorption and activation of CO over active Cu^+ sites play an important role in the reaction between Cu^+–CO species and surface active oxygen species. The strong metal–CO bonds will severely inhibit the adsorption and activation of oxygen species, while the weakly adsorbed CO will significantly promote the adsorption of oxygen species, which is directly involved in the reaction process to oxidatively remove the CO adsorbed on Cu^+ sites. From above, it can be found that the CuO–$Ce_{0.9}Zr_{0.1}O_2$ catalyst owned the highest amount of weakly adsorbed CO and the negligible high-temperature peaks due to the strong CO–metal bonds, which is the main reason why the CuO–$Ce_{0.9}Zr_{0.1}O_2$ sample exhibited the best removal performance of CO in the off-gas stream from propane oxidation process, just as shown below.

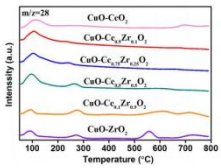

Fig. 6 CO-TPD profiles of all CuO–$Ce_xZr_{1-x}O_2$ catalysts

3.2 Catalytic Performance

Figure 7a displays the CO conversion during the removal process of CO in simulated off-gas over the CuO–$Ce_xZr_{1-x}O_2$ catalysts with varied Ce/Zr ratios. Here, the reaction temperature (T_{100}) corresponding to 100% CO conversion was used as an important criterion to evaluate the removal activity, the temperatures at which T_{100} obtained by each catalyst are listed in Table 1. It can be seen that the T_{100} values for CuO–ZrO_2 with a mixed phase structure and CuO–$Ce_{0.1}Zr_{0.9}O_2$ with a tetragonal structure are very close, nearly 190 ℃. The obvious lower removal activity of CO can be reasonably ascribed to their worst reducible nature as revealed in H_2-TPR results and the lowest concentration of oxygen vacancies as listed in Table 1. For binary CuO–CeO_2 catalyst, the T_{100} value is about 140 ℃. As the incorporation of more Ce into ZrO_2 support, a single-phase ceria–zirconia solid solution was formed and the corresponding temperature for T_{100} shifted to the lower temperature, and the lowest temperature of ~ 123 ℃ for 100% CO conversion could be achieved on the CuO–$Ce_{0.9}Zr_{0.1}O_2$ catalyst. The results indicate that, for the as-synthesized CuO–$Ce_xZr_{1-x}O_2$ catalysts, the removal activity of CO is significantly dependent on the structure of the supports.

For the selective removal of CO in off-gas from chemical processes, the operating temperature window of the catalysts is an important parameter for their industrial application. In general, it is defined as a temperature range in which 100% CO conversion and ~ 100% selectivity for CO removal is simultaneously obtained. Figure 7b shows the removal selectivity to CO over the series of CuO–$Ce_xZr_{1-x}O_2$ catalysts and the corresponding temperature window is listed in Table 1.

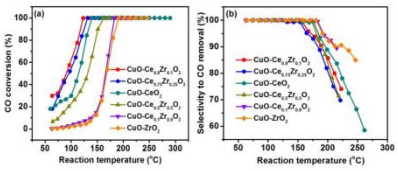

Fig. 7 CO conversion (**a**) and removal selectivity (**b**) as a function of reaction temperature over CuO–$Ce_xZr_{1-x}O_2$ catalysts

For binary CuO–ZrO_2 and ternary CuO–$Ce_{0.1}Zr_{0.9}O_2$ catalysts, no operating temperature window was observed. This may be ascribed to their higher T_{100} values, at which the olefins in off-gases, such as C_2H_4 and C_3H_6, began to be oxidized into CO_x. With the further introduction of Ce, the temperature window of ternary CuO–$Ce_xZr_{1-x}O_2$ catalysts is gradually increased with increasing x from 0.5 to 0.9. The binary CuO–CeO_2 catalyst exhibited the widest operating temperature window of about 35 ℃.

Based on the characteristic results above, such as XRD, H_2-TPR, Raman spectra and XPS analysis, it can be found that a single-phase ceria–zirconia solid solution was formed over the CuO–$Ce_xZr_{1-x}O_2$ (x = 0.9, 0.75 and 0.5) while a tetragonal ZrO_2 phase was developed over CuO–$Ce_{0.1}Zr_{0.9}O_2$. The formation of ceria–zirconia solid solution greatly increases the concentration of oxygen vacancies and the mobility of active oxygen species on the series of ternary CuO–$Ce_xZr_{1-x}O_2$ samples, which furthers enhances the reactivity of CO_{ad} weakly adsorbed on the Cu^+ active sites with the surface lattice oxygen. This means that the enhancement in the removal performance of CO over the CuO–$Ce_xZr_{1-x}O_2$ catalysts mainly originates from the facile activation of CO by the high concentration of oxygen vacancies due to the incorporation of Ce ions.

4 Conclusion

In summary, we have investigated the composition effect of series of CuO–$Ce_xZr_{1-x}O_2$ catalysts on the oxidative remove of CO in simulated off-gas from propane oxidation of acrylic acid. The structural characterizations showed that the incorporation of Ce into ZrO_2 support led to the formation of Ce–Zr solid solution, which caused the lattice distortion and induced more oxygen vacancy sites, and further promoted the mobility of lattice oxygen in the materials. The H_2-TPR investigation indicated that the reducibility of CuO–$Ce_xZr_{1-x}O_2$ samples gradually increased with the Ce content. The Raman and XPS spectra revealed that the CuO–$Ce_{0.9}Zr_{0.1}O_2$ sample owned the most abundant oxygen vacancies on the surface, which accelerated the adsorption of CO on the active copper sites and the activation of the oxygen species. These are the reasons why the CuO–$Ce_{0.9}Zr_{0.1}O_2$ sample exhibited the superior removal performance of CO in simulated off-gas from propane oxidation to acrylic acid.

Acknowledgements The authors are grateful for support from the Education Research Fund for Department of Heilongjiang Province (No. 1352D2001), the Scientific Research Project of Mudanjiang Normal University (No. GP201603), the National Natural Science Foundation of China (No. 21673227), the Science and Technology Innovation Project of Mudanjiang Normal University (No. kjcx2019-30mdjnu), Heilongjiang Province University Student Innovation and Entrepreneurship Training Program Project (No. 201910233025).

References

1 Chu WL, Liu YC, Wang HK, Cai R, Yang WS (2018) ChemCatChem 10(19):4292–4299
2 Yu WW, Zhou Q, Wang HK, Liu YC, Chu WL, Cai R, Yang WS (2020) J Mater Sci 55(6):2321–2332
3 Heo I, Yoon DY, Cho BK, Nam IS, Choung JW, Yoo S (2012) Appl Catal B 121:75–87
4 Shi L, Zhang G (2016) Catal Lett 146(8):1449–1456
5 Park ED, Lee D, Lee HC (2009) Catal Today 139(4):280–290
6 Moretti E, Molina AI, Sponchia G, Talon A, Frattini R, Rodriguez-Castellon E, Storaro L (2017) Appl Surf Sci 403:612–622
7 Yen H, Seo Y, Kaliaguine S, Kleitz F (2012) Angew Chem Int Ed 51(48):12032–12035
8 Yeste MP, Vidal H, Garcia-Cabeza AL, Hernandez-Garrido JC, Guerra FM, Cifredo GA, Gonzalez-Leal JM, Gatica JM (2018) Appl Catal A 552:58–69

9 Moretti E, Storaro L, Talon A, Lenarda M, Riello P, Frattini R, de Yuso MDM, Jimenez-Lopez A, Rodriguez-Castellon E, Tarozo F, Caballero A, Holgado JP (2011) Appl Catal B 102(3–4):627–637
10 Zhu J, Zhang LL, Deng Y, Liu B, Dong LH, Gao F, Sun KQ, Dong L, Chen Y (2010) Appl Catal B 96(3–4):449–457
11 Kaspar J, Fornasiero P, Hickey N (2003) Catal Today 77:419–449
12 Il'Ichev AN, Bykhovsky MY, Fattakhova ZT, Shashkin DP, Fedorova YE, Matyshak VA, Korchak VN (2019) Kinet Catal 60(5):661–671
13 Djinovic P, Batista J, Pintar A (2008) Appl Catal A 347(1):23–33
14 Wang Z, Qu Z, Quan X, Li Z, Wang H, Fan R (2013) Appl Catal B 134:153–166
15 Dong XF, Zou HB, Lin WM (2006) Int J Hydrog Energy 31(15):2337–2344
16 Manzoli M, Di Monte R, Boccuzzi F, Coluccia S, Kaspar J (2005) Appl Catal B 61(3–4):192–205
17 Fu GY, Mao DS, Sun S, Yu J, Yang ZQ (2015) J Ind Eng Chem 31:283–290
18 Li L, Song L, Chen CQ, Zhang YJ, Zhan YY, Lin XY, Zheng Q, Wang HD, Ma HX, Ding LH, Zhu W (2014) Int J Hydrog Energy 39(34):19570–19582
19 Davó-Quiñonero A, Bailón-García E, López-Rodríguez S, Juan-Juan J, Lozano-Castello D, García-Melchor M, Herrera FC, Pellegrin E, Escudero C, Bueno-Lopez A (2020) ACS Catal 10(11):6532–6545
20 Ratnasamy P, Srinivas D, Satyanarayana CVV, Manikandan P, Kumaran RSS, Sachin M, Shetti VN (2004) J Catal 221(2):455–465
21 Wang RG, Mutinda SI, Fang MH (2013) RSC Adv 3(42):19508–19514
22 Liyanage AD, Perera SD, Tan K, Chabal Y, Balkus KJ (2014) ACS Catal 4(2):577–584
23 Gao R, Zhang D, Maitarad P, Shi LY, Rungrotmongkol T, Li HR, Zhang JP, Cao WG (2013) J Phys Chem C 117(20):10502–10511
24 Li WG, Hu YJ, Jiang H, Yang S, Li CZ (2019) Mater Chem Phys 226:158–169
25 Reddy BM, Rao KN (2009) Catal Commun 10(9):1350–1353
26 Zhao W, Zhong Q (2014) RSC Adv 4(11):5653
27 Chen GZ, Song GL, Zhao W, Gao DW, Wei YW, Li CC (2018) Chem Eng J 352:64–70
28 Kocemba I, Rynkowski J, Gurgul J, Socha RP, Latka K, Krafft JM, Dzwigaj S (2016) Appl Catal A 519:16–26
29 Wang LC, Widmann D, Behm RJ (2015) Catal Sci Technol 5(2):925–941
30 Jiang N, Zhao YH, Qiu C, Shang KF, Lu N, Li J, Wu Y, Zhang Y (2019) Appl Catal B 259:118061
31 Zhang GL, Cheng X, Yang D, Yu G, Ma HM, Wang J, Wu HY, Yang ZG (2019) Fuel 258:116202
32 Zhou GG, Gong WT, Sun L, Wang X, Xiao W, Wang JW, Wang LG (2019) Materials 12(24):4041
33 Hassan S, Kumar R, Tiwari A, Song WY, van Haandel L, Pandey JK, Hensen E, Chowdhury B (2018) Mol Catal 451:238–246
34 Du PP, Wang WW, Jia CJ, Song QS, Huang YY, Si R (2016) Appl Catal A 518:87–101
35 Zhang XM, Tian PF, Tu WF, Zhang ZZ, Xu J, Han YF (2018) ACS Catal 8:5261–5275
36 Gamarra D, Munuera G, Hungría AB, Fernández-García M, Conesa JC, Midgley PA, Wang XQ, Hanson JC, Rodríguez JA, Martínez-Arias A (2007) J Phys Chem C 111(29):11026–11038
37 Hornés A, Hungría AB, Bera P, López Cámara A, Fernández-García M, Martínez-Arias A, Barrio L, Estrella M, Zhou G, Fonseca JJ, Hanson JC, Rodriguez JA (2010) J Am Chem Soc 132(1):34–35
38 Yao SY, Mudiyanselage K, Xu WQ, Johnston-Peck AC, Hanson JC, Wu TP, Stacchiola D, Rodriguez JA, Zhao HY, Beyer KA, Chapman KW, Chupas PJ, Martinez-Arias A, Si R, Bolin TB, Liu J, Senanayake SD (2014) ACS Catal 4(6):1650–1661
39 Svintsitskiy DA, Kardash TA, Stonkus OA, Slavinskaya EM, Stadnichenko AI, Koscheev SV, Chupakhin AP, Boronin AI (2013) J Phys Chem C 117(28):14588–14599

Publisher's Note Springer Nature remains neutral with regard to jurisdictional claims in published maps and institutional affiliations.

9.Electrochemical Synthesis of Ni-SnO_2 Composite Electrodes for Hydrogen Evolution Reaction in Alkaline Solution 作者：邢乐红

Int. J. Electrochem. Sci., 17 (2022) Article Number: 220530, doi: 10.20964/2022.05.35

International Journal of
ELECTROCHEMICAL
SCIENCE
www.electrochemsci.org

Short Communication

Electrochemical Synthesis of Ni-SnO_2 Composite Electrodes for Hydrogen Evolution Reaction in Alkaline Solution

Le-Hong Xing, Xin-Ting Shi, Yi-Xin Wang, Li Zhang, Xiao-Yan Xu, Fan-Xu Meng, Jing Li*

Heilongjiang Key Laboratory of Photoelectric Functional Materials, College of Chemistry and Chemical Engineering, Mudanjiang Normal University, Mudanjiang 157011, China
*E-mail: xinglehonghit@163.com

Received: 28 January 2022 / *Accepted:* 1 March 2022 / *Published:* 5 April 2022

In this work, high efficient Ni-SnO_2 electrodes were prepared for the alkaline hydrogen evolution reaction (HER) by a simple composite electroplating method from sulphamate bath containing SnO_2 nano-particles. The Ni-SnO_2 electrode was physically characterized by scanning electron microscopy (SEM), energy dispersive analysis of X-ray (EDAX), and X-ray diffraction (XRD). These physical characterization results revealed that the homemade SnO_2 particles (about 170 nm) were successfully co-deposited in coatings. The composited SnO_2 changed the surface morphology and phase structure of Ni matrix. The electrochemical activities and stabilities for HER were monitored by steady-state polarization, Tafel plots, electrochemical impedance spectroscopy (EIS) and chronopotentiometry technique. The activity was confirmed via the quantification of H_2 gases that evolved during chronopotentiometry study. The Ni-SnO_2 showed a higher catalytic activity for H_2 evolution, compared with Ni. The OH_{ads} on SnO_2 surface was benefit to the formation of adsorbed H_{ads} which is the rate-determining step for HER.

Keywords: Hydrogen evolution reaction; Electro-catalysis; Composite electroplating; Ni-SnO_2

1. INTRODUCTION

With the economic development and progress of industry, the energy crisis and environmental pollution have caused the global concern [1]. Driven by the growing concern, efforts have been made to develop new environmentally friendly energy sources. Hydrogen (H_2) is identified as the most potential energy carrier in future for its clean, renewable and high efficient characters [2,3]. Water is the cheapest and most rich resources of hydrogen, and water electrolysis is a sustainable and promising method for hydrogen production [4,5]. The development of the higher activity electrode materials is particularly important for water electrolysis. Nickel-based materials, such as Ni and Ni-M alloys, are prominent non-noble metal catalysts for their good electro-catalytic activity for HER and

sufficient corrosion resistance in alkaline solution [6-10]. Recently, Ni-based metallic oxide composite material has received considerable attention because it exhibits a number of advantages. For example, Zheng et. al. [11] investigated the effect of CeO_2 particles in Ni coatings on the activity of HER. The results show that the Ni based CeO_2 electrodes show higher HER activity and better stability than pure Ni. H_{ads} can easily adsorb on Ce atoms due to the presence of several half-filled and empty d orbitals. Kullaiah et. al. [12] prepared Ni-TiO_2 electrode by composite electroplating method. The addition of TiO_2 is benefit to the formation of tiny nickel grains and increased the number of active site. Besides CeO_2 and TiO_2, a lot of metallic oxides such as ZnO [13], Cu_2O [14], and MoO_2 [15] have been used as co-catalyst to enhance the activity of HER on Ni based materials. However, the effects of SnO_2 nano particles addition on the performance of HER have not been fully investigated yet. SnO_2 is considered to be an excellent co-catalyst for methanol oxidation, ethanol oxidation and O_2 reduction in fuel cells [16-18]. It is very stable in alkaline solutions, and can support sufficient OH_{ads} species. The OH_{ads} is benefit to the formation of adsorbed H_{ads} [19]. The catalytic activity can be enhanced when the formation of adsorbed H_{ads} is the rate-determining step for HER (Volmer step). According to the well known "volcano" curve, the strength of Ni-H bond is relatively weak, and the formation of H_{ads} is always the rate-determining step for HER (Volmer step) on Ni electrode [20]. In this study, the aim of work is to utilize SnO_2 to enhance the HER activity of Ni coating electrode. We first synthesized SnO_2 nano-particles by hydrolysis method. And then, these SnO_2 particles were suspended in nickel plating solution. The Ni-SnO_2 composite coating was prepared by composite electrodeposited method. Multiple physical and electrochemical tests were employed to investigate the effect of SnO_2 particles embed in Ni coating on the activity of HER.

2. EXPERIMENTAL

2.1. Preparation of Ni-SnO_2 electrode

Preparation of SnO_2 Nanoparticles: 5-hydrated tin tetrachloride ($SnCl_4·5H_2O$), sodium hydroxide, and ethanol were used as received without further purification. A sample of 17.53 g of $SnCl_4·5H_2O$ was dissolved in 50 ml ultrapure water (18.2 M Ω cm, Mill-Q Corp.). The pH value of the solution was adjusted to 7 with NaOH solution. Then, the solution was transferred into a stainless steel reactor (100 ml). The reactor was put in an electric oven and kept at 160 ℃ for 2 h. After cooling to room temperature, the obtained product was separated by centrifugation. The resulting powders were washed in sequence with ethanoic acid - ammonium acetate solution and pure ethanol, and then dried at 80 ℃ for 12 h in vacuum. The particle size of homemade SnO_2 was about 200 nm.

Preparation of Ni-SnO_2 composite electrode: The Ni-SnO_2 composite electrode was electrodeposited on 4×5 cm copper sheet by composite electrodeposition method. The plating electrolyte was composed of 350 g·L^{-1} Ni $(NH_2SO_3)_2·4H_2O$, 10 g·L^{-1} $NiCl_2·6H_2O$, 30 g·L^{-1} NH_4Cl and various different content of SnO_2 nanoparticles. These composite electrodes were named as Ni/SnO_2-1, Ni/SnO_2-2, Ni/SnO_2-3, Ni/SnO_2-4, which were obtained from the above electrolyte with 1 g·L^{-1}, 2 g·L^{-1}, 3 g·L^{-1}, 4 g·L^{-1} SnO_2 nanoparticles, respectively. The composite electrodeposition was carried out at

a current density of 3 A/dm^2, a temperature of 35 ℃ with a magnetic stirring at 850 rpm for 30 min.

2.2. Physical characterization

The morphology, crystal structure and the composition of the composite coatings were determined by SEM (Quanta 400, FEI), XRD (D8 Advance, Bruker) and EDAX, respectively.

2.3. Electrochemical measurements

Electrochemical studies including steady-state polarization, tafel plots, EIS and amperometric current density-time curves of the composite electrodes were conducted using electrochemical working station (PARSTAT 4000) in a standard three-electrode cell in 1 M NaOH solution. The composite electrodes were used as working electrode and 1 cm^2 platinum foil was served as counter electrode. Hg/HgO electrode was used as the reference electrode. The scan rate of steady-state polarization test was 5 mV·s^{-1}. The EIS was measured at -0.125 V (vs. SCE) in a frequency range from 100 kHz to 0.01 Hz with 6 ~ 12 points per decade. The amplitude of the AC-voltage was 0.005 V. All the electrochemical measurements were carried out at 25 ℃.

3. RESULTS AND DISCUSSION

Fig. 1 is the IR spectra of homemade SnO_2 nanoparticles. The characteristic peak in the range of 500-750 cm^{-1}, 1600 cm^{-1}, and 3430 cm^{-1} are assigned to Sn-O vibration, O-H bending vibration and O-H stretching vibration [16]. SnO_2 in composite electrodes can support abundant OH_{ads} species which are benefit to the formation of adsorbed H_{ads} during HER [21]. Fig. 2 is XRD patterns of SnO_2 nanoparticles. The SnO_2 nanoparticles show the major diffraction peaks of (110), (101), (111), (211), (301) and (321) [22]. The average size of SnO_2 particles were calculated from the most intense peak (110) according to Sherrer's Equation [23]. The particle size of SnO_2 was about 170 nm.

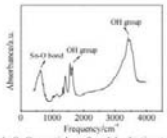

Figure 1. FTIR plot of homemade SnO_2 particles after dehydration treatment at 200 ℃ under vacuum condition.

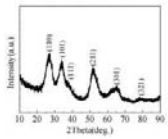

Figure 2. XRD analysis of SnO_2 nanoparticles.

The XRD patterns of Ni and Ni/SnO_2-3 electrodes are shown in Fig.3. The diffraction peaks for the two electrodes at 2θ about 44.5°, 51.8° and 76.4° can be attributed to Ni (111), Ni (200) and Ni (220). The peaks for Ni/SnO_2-3 electrode at about 26.6°, 33.8°, 38.7°, 51.7° and 54.3° can be well indexed to SnO_2 (JCPDS:41-1445). SnO_2 particles were successfully co-deposited in Ni matrix. The preferential orientation of Ni electrode is (200) crystal plane. The preferential orientation of Ni/SnO_2-3 electrode has been greatly changed to (111) crystal plane. Ni (111) plane was more benefit to the enhancement of electrocatalytic performance for HER than other planes [24,25]. The full width of half maximum values of Ni (111) and Ni (200) for pure Ni electrode is 0.193° and 0.233°, respectively. The two values for Ni/SnO_2-3 electrode are 0.204°and 0.303°, respectively. The diffraction peaks of Ni/SnO_2-3 electrode are broader than Ni. According to Sherrer's Equation, the crystallite size of composite electrode is smaller than that of Ni. The co-deposition of SnO_2 particles in Ni matrix has the effect of grain refinement.

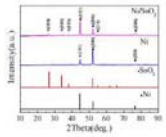

Figure 3. XRD patterns of Ni and Ni/SnO_2-3 electrodes.

SEM images of Ni and Ni/SnO_2 electrodes are shown in Fig.4. As shown in Fig.4(a) and (b), The Ni electrode shows a relatively bulky microstructure. The co-deposition of SnO_2 nano-particles makes the coating crystallization more meticulous and porous, which is benefit to increase of surface area. The white spherical particles in Fig.4(b) are SnO_2. The mean size of SnO_2 nano-particles is about

200 nm, which is consistent with the above XRD results. The presence of SnO_2 nano-particles in the composite electrode is confirmed via EDAX analysis. The amount of SnO_2 nano-particles incorporated in Ni/SnO_2-3 is approximately 4.7 wt%.

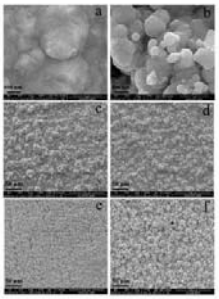

Figure 4. Low and high-magnification SEM images of electrode: (a) magnified Ni, (b) magnified Ni/SnO_2-3, (c) Ni/SnO_2-1, (d) Ni/SnO_2-2, (e) Ni/SnO_2-3, (f) Ni/SnO_2-4.

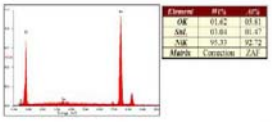

Figure 5. EDAX patterns of Ni/SnO_2-3 composite electrode and its quantitative analysis.

The electrocatalytic activity for HER on Ni/SnO_2 composite electrodes are tested by a series of electrochemical measures including cathode polarization curves, Tafel plots, and EIS. The corresponding parameters obtained from above electrochemical measurements are listed in Table 1.

Fig.6 (a) shows the cathode polarization curves of different electrodes. It is apparent that Ni/SnO_2-3 shows the highest catalytic activity, which demand the lowest overpotential of 427 mV to drive current densities of 10 mA cm^{-2}.

To further understand the mechanism of the HER, the Tafel plots in Fig.6 (b) are fitted to the classic Tafel equation (Eq. 1). The values of R^2 are greater than 0.99, which indicate that the calculated kinetic parameters listed in Table 1 adjust well to Tafel equation.

$$\eta = b\ log(j/j_0) \quad (1)$$

Here η is the cathode overpotential, b is the Tafel slope, j is current density and j_0 is the exchange current density. The j_0 in Table 1 represents the HER catalytic activity of the electrodes. As shown in Table 1, the j_0 values of these Ni/SnO_2 electrodes are all higher than that of pure Ni electrode. With the increase of the SnO_2 content in coatings, the values of j_0 for Ni/SnO_2 electrodes are first enhanced and then tend to decline. The catalytic activity of Ni/SnO_2-3 obtained from electrolyte with 3 g·L^{-1} SnO_2 nano-particles is the highest. The co-deposition of SnO_2 particles makes the grain size of the composite coating much finer than that of pure nickel. This fining effect is beneficial for HER. Too much SnO_2 co-deposit in the composite electrode may affect the electrode activity for its low electron conductivity. Tafel slope b is a significant parameter which can indicate the dominant HER mechanism on electrodes. As shown in Fig. 6(b) and Table 1, the b of the Ni and these Ni/SnO_2 composite electrodes are 120, 204, 199, 187 and 205 mV·dec^{-1}, respectively. According to the reported literature [26-29], the rate-determining steps of HER on above studied electrodes are Volmer reaction. The formation of H_{ads} determines Volmer reaction rate. SnO_2 in composite electrodes can support abundant OH_{ads} species. These OH_{ads} species can promote H_2O decomposition and H_{ads} formation by weakening the oxophilicity of the active site [30,31]. The SnO_2 and Ni interface benefits for the H_{ads} adsorption, but suppress the competitive H_2O_{ads} and OH_{ads} adsorption [32]. Hence, the Ni-SnO_2 showed a higher catalytic activity for H_2 evolution, compared with Ni.

The EIS measurements are carried out on Ni and Ni/SnO_2 electrodes at cathode potential of -0.125 V (vs. SCE) under HER operating conditions. The Nyquist diagrams are illustrated in Fig.6 (c). A widely used equivalent circuit is used to describe the HER process and the fitting results of the resistance elements are listed in Table1. The ohmic resistances (R_s) of these composite electrodes are all higher than that of Ni. SnO_2 co-deposit in the composite electrodes decrease the electron conductivity of electrode. The electrochemical reaction resistance (R_{ct}) of Ni/SnO_2-3 electrode is the lowest among all of studied electrodes. The bode phase angle plot obtained for these composite electrodes are presented in Fig.6 (d). All these plots abide by one-time-constant behavior, which is in good agreement with above mentioned equivalent circuits model given in Fig.6 (c). Also, the Ni/SnO_2-3 electrode has the lowest phase angle and impedance value, which confirms the enhanced HER rate.

The SnO_2 co-deposit in Ni electrodes can accelerate the HER process. Excessive SnO_2 in the composite electrodes decrease HER activity for the low electron conductivity of electrode. The Ni/SnO_2-3 with the optimal addition of SnO_2 in Ni shows the highest catalytic activity, which is coincident with the results of steady-state polarization in Fig.6 (a) and Tafel plots in Fig. 6 (b). C_{dl} is double layer capacitance which is associated with surface area of electrode [33,34]. The addition of SnO_2 raises the value of C_{dl}, which indicates that surface area of composite electrode has been increased. SnO_2 makes the Ni coating crystallization more tiny. The increase of active surface area

benefits for the formation of H_{ads}. This experimental finding is consistent with above SEM results.

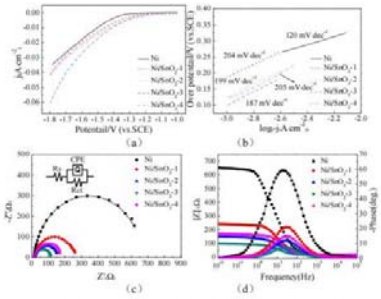

Figure 6. Electrochemical properties for HER on Ni and Ni/SnO_2 composite electrodes in 1 M NaOH. (a) Steady-state polarization curves, (b) Corresponding Tafel plots, (c) Nyquist diagrams (dots) and fitting diagrams (lines) based on possible equivalent circuits, (d) Bode plots.

Table 1. Electrocatalytic parameters obtained from above electrochemical measurements in 1 M NaOH solution.

	j_o (uA·cm^{-2})	b (mV·dec^{-1})	η_{10} (mV)	R_s (Ω)	R_{ct} (Ω)	C_{dl} (10^{-5} F·cm^{-2})
Ni	0.673	120	501	14.7	652.7	8.17
Ni/SnO_2-1	22.57	204	540	14.8	240.5	14.32
Ni/SnO_2-2	37.51	199	483	15.4	149.7	21.73
Ni/SnO_2-3	52.29	187	427	15.8	100.6	26.31
Ni/SnO_2-4	39.21	205	493	16.6	168.8	19.77

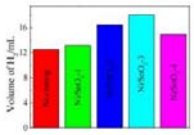

Figure 7. The volume of H_2 evolved on each studied electrode at cathode current density of 300 mA·cm^{-2} for 300 s

Fig. 7 shows the volume of H_2 gas evolved on each studied electrode for 300 s at a constant cathode current density of 300 mA·cm^{-2}. The Ni/SnO_2-3 electrode obtained from the electrolyte with 3 g·L^{-1} SnO_2 particles produces the maximum amount of H_2 (17.9 mL) compared to the other coatings. This result confirms that the Ni/SnO_2-3 shows the best activity for HER.

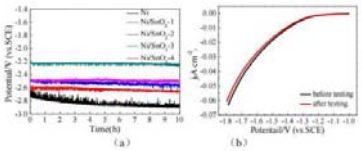

Figure 8. Stability tests of the composite electrodes. (a) The chronopotentiometry study at cathode current density of 100 mA·cm^{-2}, (b) Polarization curves of Ni/SnO_2-3 before and after 10 h chronopotentiometry test in 1 M NaOH solution.

The behavior of the electrode potential as a function of time at cathode current density of 100 mA·cm^{-2} is shown in Fig.8. The decrease of electrode potential for Ni, Ni/SnO_2-1, Ni/SnO_2-2, Ni/SnO_2-3, and Ni/SnO_2-4 is 323 mV, 54 mV, 101 mV, 34 mV and 49 mV, respectively. The HER stability of the composite electrode are all higher than pure Ni. The polarization curves of Ni/SnO_2-3 before and after 10 h stability test show negligible changes. The Ni/SnO_2-3 electrode demonstrates excellent stability.

The electrochemical properties of Ni/SnO_2 are compared with other composite materials reported in literatures. The comparison of these works is listed in Table 2. As shown in Table 2, the Ni/SnO_2 exhibits lower over potential [35-37] and higher exchange current density [38,39]. The

performance of hydrogen evolution with Ni/SnO_2 electrode catalyst is obvious higher than other reported composited materials.

Table 2. The activity of HER on different composite electrodes reported in literatures and this work

Electrode	Alkaline solution	b (mV·dec^{-1})	η (mV)	j_o (uA·cm^{-2})	Reference
Ni/SnO_2	1 M NaOH	187	427 (η_{10})	52.29	this work
Ni-Sn@C PNs	1 M NaOH	145	1230 (η_d)	-	[35]
(Ni-MoS_2)$_{3000}$	2mM $HClO_4$/ 0.1 M $NaClO_4$	120	680 ($\eta_{0.25}$)	8×10^{-4}	[36]
Cu/Cu_2O/ Ni NP	0.1 M H_2SO_4	50	456 (η_{10})	-	[37]
Ni-PAni	4 M KOH	-	-	3.47	[38]
Ni/WO_3	1 M KOH	124.7	-	5.88	[39]
Ni/B_2O_3	1 M KOH	128.8	-	2.29	[39]
Ni/SC	1 M KOH	116.9	-	2.43	[39]

4. CONCLUSIONS

The high efficient Ni-SnO_2 electrodes are fabricated by a simple low-cost composite electroplating method. Compared with pure Ni, the Ni/SnO_2 catalyst gives a higher catalytic activity and stability for HER. The co-deposition of SnO_2 in Ni coating makes metal crystallization finer and tinier, which increase the active surface area of electrode. The co-deposition of SnO_2 changes the preferential orientation of Ni to (111) crystal plane which is more benefit to the activity of HER. The OH_{ads} on SnO_2 surface facilitates the formation of adsorbed H_{ads} which is the rate-determining step for HER. SnO_2 is a promising co-catalyst to enhance the activity of HER on Ni based materials.

ACKNOWLEDGEMENT
This work was supported by the Mudanjiang Normal University Key Project (No. GP2021002), the Research Fund Project of Mudanjiang Science and Technology Project of Mudanjiang city (No. SQ2020JG115), the Teaching reform Projects of MuDanjiang Normal University (No. KCSZ-2020021), the Innovation Project of University Students (202110233043).

10.Xing L H, Shi X T, Wang Y X, et al. Electrochemical Synthesis of Ni-SnO_2 Composite Electrodes for Hydrogen Evolution Reaction in Alkaline Solution[J]. Int. J. Electrochem. Sci, 2022, 17(220530): 2.（SCI 检索收录四区，IF=1.765）

Int. J. Electrochem. Sci., 17 (2022) Article Number: 220530, doi: 10.20964/2022.05.35

International Journal of
ELECTROCHEMICAL
SCIENCE
www.electrochemsci.org

Short Communication

Electrochemical Synthesis of Ni-SnO_2 Composite Electrodes for Hydrogen Evolution Reaction in Alkaline Solution

*Le-Hong Xing**, *Xin-Ting Shi, Yi-Xin Wang, Li Zhang, Xiao-Yan Xu, Fan-Xu Meng, Jing Li*

Heilongjiang Key Laboratory of Photoelectric Functional Materials, College of Chemistry and Chemical Engineering, Mudanjiang Normal University, Mudanjiang 157011, China
*E-mail: xinglehonghit@163.com

Received: 28 January 2022 / *Accepted:* 1 March 2022 / *Published:* 5 April 2022

In this work, high efficient Ni-SnO_2 electrodes were prepared for the alkaline hydrogen evolution reaction (HER) by a simple composite electroplating method from sulphamate bath containing SnO_2 nano-particles. The Ni-SnO_2 electrode was physically characterized by scanning electron microscopy (SEM), energy dispersive analysis of X-ray (EDAX), and X-ray diffraction (XRD). These physical characterization results revealed that the homemade SnO_2 particles (about 170 nm) were successfully co-deposited in coatings. The composited SnO_2 changed the surface morphology and phase structure of Ni matrix. The electrochemical activities and stabilities for HER were monitored by steady-state polarization, Tafel plots, electrochemical impedance spectroscopy (EIS) and chronopotentiometry technique. The activity was confirmed via the quantification of H_2 gases that evolved during chronopotentiometry study. The Ni-SnO_2 showed a higher catalytic activity for H_2 evolution, compared with Ni. The OH_{ads} on SnO_2 surface was benefit to the formation of adsorbed H_{ads}, which is the rate-determining step for HER.

Keywords: Hydrogen evolution reaction; Electro-catalysis; Composite electroplating; Ni-SnO_2

1. INTRODUCTION

With the economic development and progress of industry, the energy crisis and environmental pollution have caused the global concern [1]. Driven by the growing concern, efforts have been made to develop new environmentally friendly energy sources. Hydrogen (H_2) is identified as the most potential energy carrier in future for its clean, renewable and high efficient characters [2,3]. Water is the cheapest and most rich resources of hydrogen, and water electrolysis is a sustainable and promising method for hydrogen production [4,5]. The development of the higher activity electrode materials is particularly important for water electrolysis. Nickel-based materials, such as Ni and Ni-M alloys, are prominent non-noble metal catalysts for their good electro-catalytic activity for HER and

sufficient corrosion resistance in alkaline solution [6-10]. Recently, Ni-based metallic oxide composite material has received considerable attention because it exhibits a number of advantages. For example, Zheng et. al. [11] investigated the effect of CeO_2 particles in Ni coatings on the activity of HER. The results show that the Ni based CeO_2 electrodes show higher HER activity and better stability than pure Ni. H_{ads} can easily adsorb on Ce atoms due to the presence of several half-filled and empty d orbitals. Kullaiah et. al. [12] prepared Ni-TiO_2 electrode by composite electroplating method. The addition of TiO_2 is benefit to the formation of tiny nickel grains and increased the number of active site. Besides CeO_2 and TiO_2, a lot of metallic oxides such as ZnO [13], Cu_2O [14], and MoO_2 [15] have been used as co-catalyst to enhance the activity of HER on Ni based materials. However, the effects of SnO_2 nano particles addition on the performance of HER have not been fully investigated yet. SnO_2 is considered to be an excellent co-catalyst for methanol oxidation, ethanol oxidation and O_2 reduction in fuel cells [16-18]. It is very stable in alkaline solutions, and can support sufficient OH_{ads} species. The OH_{ads} is benefit to the formation of adsorbed H_{ads} [19]. The catalytic activity can be enhanced when the formation of adsorbed H_{ads} is the rate-determining step for HER (Volmer step). According to the well known "volcano" curve, the strength of Ni-H bond is relatively weak, and the formation of H_{ads} is always the rate-determining step for HER (Volmer step) on Ni electrode [20]. In this study, the aim of work is to utilize SnO_2 to enhance the HER activity of Ni coating electrode. We first synthesized SnO_2 nano-particles by hydrolysis method. And then, these SnO_2 particles were suspended in nickel plating solution. The Ni-SnO_2 composite coating was prepared by composite electrodeposited method. Multiple physical and electrochemical tests were employed to investigate the effect of SnO_2 particles embed in Ni coating on the activity of HER.

2. EXPERIMENTAL

2.1. Preparation of Ni-SnO_2 electrode

Preparation of SnO_2 Nanoparticles: 5-hydrated tin tetrachloride ($SnCl_4{\cdot}5H_2O$), sodium hydroxide, and ethanol were used as received without further purification. A sample of 17.53 g of $SnCl_4{\cdot}5H_2O$ was dissolved in 50 ml ultrapure water (18.2 M Ω cm, Mill-Q Corp.). The pH value of the solution was adjusted to 7 with NaOH solution. Then, the solution was transferred into a stainless steel reactor (100 ml). The reactor was put in an electric oven and kept at 160 ℃ for 2 h. After cooling to room temperature, the obtained product was separated by centrifugation. The resulting powders were washed in sequence with ethanoic acid - ammonium acetate solution and pure ethanol, and then dried at 80 ℃ for 12 h in vacuum. The particle size of homemade SnO_2 was about 200 nm.

Preparation of Ni-SnO_2 composite electrode: The Ni-SnO_2 composite electrode was electrodeposited on 4×5 cm copper sheet by composite electrodeposition method. The plating electrolyte was composed of 350 g·L^{-1} Ni $(NH_2SO_3)_2{\cdot}4H_2O$, 10 g·L^{-1} $NiCl_2{\cdot}6H_2O$, 30 g·L^{-1} NH_4Cl and various different content of SnO_2 nanoparticles. These composite electrodes were named as Ni/SnO_2-1, Ni/SnO_2-2, Ni/SnO_2-3, Ni/SnO_2-4, which were obtained from the above electrolyte with 1 g·L^{-1}, 2 g·L^{-1}, 3 g·L^{-1}, 4 g·L^{-1} SnO_2 nanoparticles, respectively. The composite electrodeposition was carried out at

a current density of 3 A/dm^2, a temperature of 35 ℃ with a magnetic stirring at 850 rpm for 30 min.

2.2. Physical characterization

The morphology, crystal structure and the composition of the composite coatings were determined by SEM (Quanta 400, FEI), XRD (D8 Advance, Bruker) and EDAX, respectively.

2.3. Electrochemical measurements

Electrochemical studies including steady-state polarization, tafel plots, EIS and amperometric current density-time curves of the composite electrodes were conducted using electrochemical working station (PARSTAT 4000) in a standard three-electrode cell in 1 M NaOH solution. The composite electrodes were used as working electrode and 1 cm^2 platinum foil was served as counter electrode. Hg/HgO electrode was used as the reference electrode. The scan rate of steady-state polarization test was 5 mV·s^{-1}. The EIS was measured at -0.125 V (vs. SCE) in a frequency range from 100 kHz to 0.01 Hz with 6 ~ 12 points per decade. The amplitude of the AC-voltage was 0.005 V. All the electrochemical measurements were carried out at 25 ℃.

3. RESULTS AND DISCUSSION

Fig. 1 is the IR spectra of homemade SnO_2 nanoparticles. The characteristic peak in the range of 500-750 cm^{-1}, 1600 cm^{-1}, and 3430 cm^{-1} are assigned to Sn-O vibration, O-H bending vibration and O-H stretching vibration [16]. SnO_2 in composite electrodes can support abundant OH_{ads} species which are benefit to the formation of adsorbed H_{ads} during HER [21]. Fig. 2 is XRD patterns of SnO_2 nanoparticles. The SnO_2 nanoparticles show the major diffraction peaks of (110), (101), (111), (211), (301) and (321) [22]. The average size of SnO_2 particles were calculated from the most intense peak (110) according to Sherrer's Equation [23]. The particle size of SnO_2 was about 170 nm .

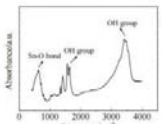

Figure 1. FTIR plot of homemade SnO_2 particles after dehydration treatment at 200 ℃ under vacuum condition.

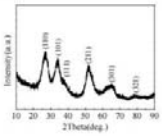

Figure 2. XRD analysis of SnO_2 nanoparticles.

The XRD patterns of Ni and Ni/SnO_2-3 electrodes are shown in Fig.3. The diffraction peaks for the two electrodes at 2θ about 44.5°, 51.8° and 76.4° can be attributed to Ni (111), Ni (200) and Ni (220). The peaks for Ni/SnO_2-3 electrode at about 26.6°, 33.8°, 38.7°, 51.7° and 54.3° can be well indexed to SnO_2 (JCPDS:41-1445). SnO_2 particles were successfully co-deposited in Ni matrix. The preferential orientation of Ni electrode is (200) crystal plane. The preferential orientation of Ni/SnO_2-3 electrode has been greatly changed to (111) crystal plane. Ni (111) plane was more benefit to the enhancement of electrocatalytic performance for HER than other planes [24,25]. The full width of half maximum values of Ni (111) and Ni (200) for pure Ni electrode is 0.193° and 0.233°, respectively. The two values for Ni/SnO_2-3 electrode are 0.204°and 0.303°, respectively. The diffraction peaks of Ni/SnO_2-3 electrode are broader than Ni. According to Sherrer's Equation, the crystallite size of composite electrode is smaller than that of Ni. The co-deposition of SnO_2 particles in Ni matrix has the effect of grain refinement.

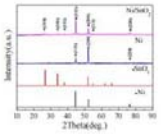

Figure 3. XRD patterns of Ni and Ni/SnO_2-3 electrodes.

SEM images of Ni and Ni/SnO_2 electrodes are shown in Fig.4. As shown in Fig.4(a) and (b), The Ni electrode shows a relatively bulky microstructure. The co-deposition of SnO_2 nano-particles makes the coating crystallization more meticulous and porous, which is benefit to increase of surface area. The white spherical particles in Fig.4(b) are SnO_2. The mean size of SnO_2 nano-particles is about

200 nm, which is consistent with the above XRD results. The presence of SnO_2 nano-particles in the composite electrode is confirmed via EDAX analysis. The amount of SnO_2 nano-particles incorporated in Ni/SnO_2-3 is approximately 4.7 wt%.

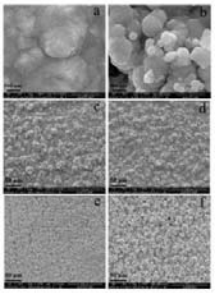

Figure 4. Low and high-magnification SEM images of electrode: (a) magnified Ni, (b) magnified Ni/SnO_2-3; (c) Ni/SnO_2-1; (d) Ni/SnO_2-2; (e) Ni/SnO_2-3; (f) Ni/SnO_2-4.

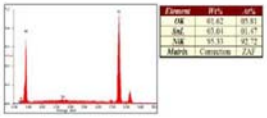

Figure 5. EDAX patterns of Ni/SnO_2-3 composite electrode and its quantitative analysis.

The electrocatalytic activity for HER on Ni/SnO_2 composite electrodes are tested by a series of electrochemical measures including cathode polarization curves, Tafel plots, and EIS. The corresponding parameters obtained from above electrochemical measurements are listed in Table 1.

Fig.6 (a) shows the cathode polarization curves of different electrodes. It is apparent that Ni/SnO_2-3 shows the highest catalytic activity, which demand the lowest overpotential of 427 mV to drive current densities of 10 mA cm^{-2}.

To further understand the mechanism of the HER, the Tafel plots in Fig.6 (b) are fitted to the classic Tafel equation (Eq. 1). The values of R^2 are greater than 0.99, which indicate that the calculated kinetic parameters listed in Table 1 adjust well to Tafel equation.

$$\eta = b\ log(j/j_0) \quad (1)$$

Here η is the cathode overpotential, b is the Tafel slope, j is current density and j_0 is the exchange current density. The j_0 in Table 1 represents the HER catalytic activity of the electrodes. As shown in Table 1, the j_0 values of these Ni/SnO_2 electrodes are all higher than that of pure Ni electrode. With the increase of the SnO_2 content in coatings, the values of j_0 for Ni/SnO_2 electrodes are first enhanced and then tend to decline. The catalytic activity of Ni/SnO_2-3 obtained from electrolyte with 3 g·L^{-1} SnO_2 nano-particles is the highest. The co-deposition of SnO_2 particles makes the grain size of the composite coating much finer than that of pure nickel. This fining effect is beneficial for HER. Too much SnO_2 co-deposit in the composite electrode may affect the electrode activity for its low electron conductivity. Tafel slope b is a significant parameter which can indicate the dominant HER mechanism on electrodes. As shown in Fig. 6(b) and Table 1, the b of the Ni and these Ni/SnO_2 composite electrodes are 120, 204, 199, 187 and 205 mV·dec^{-1}, respectively. According to the reported literature [26-29], the rate-determining steps of HER on above studied electrodes are Volmer reaction. The formation of H_{ads} determines Volmer reaction rate. SnO_2 in composite electrodes can support abundant OH_{ads} species. These OH_{ads} species can promote H_2O decomposition and H_{ads} formation by weakening the oxophilicity of the active site [30,31]. The SnO_2 and Ni interface benefits for the H_{ads} adsorption, but suppress the competitive H_2O_{ads} and OH_{ads} adsorption [32]. Hence, the Ni-SnO_2 showed a higher catalytic activity for H_2 evolution, compared with Ni.

The EIS measurements are carried out on Ni and Ni/SnO_2 electrodes at cathode potential of -0.125 V (vs. SCE) under HER operating conditions. The Nyquist diagrams are illustrated in Fig.6 (c). A widely used equivalent circuit is used to describe the HER process and the fitting results of the resistance elements are listed in Table1. The ohmic resistances (R_s) of these composite electrodes are all higher than that of Ni. SnO_2 co-deposit in the composite electrodes decrease the electron conductivity of electrode. The electrochemical reaction resistance (R_{ct}) of Ni/SnO_2-3 electrode is the lowest among all of studied electrodes. The bode phase angle plot obtained for these composite electrodes are presented in Fig.6 (d). All these plots abide by one-time-constant behavior, which is in good agreement with above mentioned equivalent circuits model given in Fig.6 (c). Also, the Ni/SnO_2-3 electrode has the lowest phase angle and impedance value, which confirms the enhanced HER rate.

The SnO_2 co-deposit in Ni electrodes can accelerate the HER process. Excessive SnO_2 in the composite electrodes decrease HER activity for the low electron conductivity of electrode. The Ni/SnO_2-3 with the optimal addition of SnO_2 in Ni shows the highest catalytic activity, which is coincident with the results of steady-state polarization in Fig.6 (a) and Tafel plots in Fig. 6 (b). C_{dl} is double layer capacitance which is associated with surface area of electrode [33,34]. The addition of SnO_2 raises the value of C_{dl}, which indicates that surface area of composite electrode has been increased. SnO_2 makes the Ni coating crystallization more tiny. The increase of active surface area

benefits for the formation of H_{ads}. This experimental finding is consistent with above SEM results.

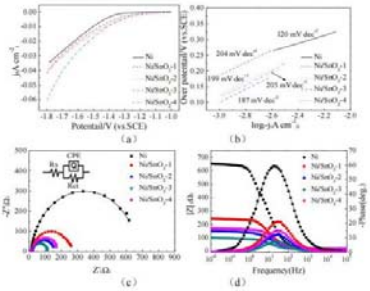

Figure 6. Electrochemical properties for HER on Ni and Ni/SnO_2 composite electrodes in 1 M NaOH. (a) Steady-state polarization curves, (b) Corresponding Tafel plots, (c) Nyquist diagrams (dots) and fitting diagrams (lines) based on possible equivalent circuits, (d) Bode plots.

Table 1. Electrocatalytic parameters obtained from above electrochemical measurements in 1 M NaOH solution.

	j_0 (uA·cm^{-2})	b (mV·dec^{-1})	η_{10} (mV)	R_s (Ω)	R_{ct} (Ω)	C_{dl} (10^{-4} F·cm^{-2})
Ni	0.673	120	501	14.7	652.7	8.17
Ni/SnO_2-1	22.57	204	540	14.8	240.5	14.32
Ni/SnO_2-2	37.51	199	483	15.4	149.7	21.73
Ni/SnO_2-3	52.29	187	427	15.8	100.6	26.31
Ni/SnO_2-4	39.21	205	493	16.6	168.8	19.77

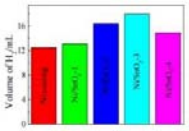

Figure 7. The volume of H_2 evolved on each studied electrode at cathode current density of 300 mA·cm^{-2} for 300 s

Fig. 7 shows the volume of H_2 gas evolved on each studied electrode for 300 s at a constant cathode current density of 300 mA·cm^{-2}. The Ni/SnO_2-3 electrode obtained from the electrolyte with 3 g·L^{-1} SnO_2 particles produces the maximum amount of H_2 (17.9 mL) compared to the other coatings. This result confirms that the Ni/SnO_2-3 shows the best activity for HER.

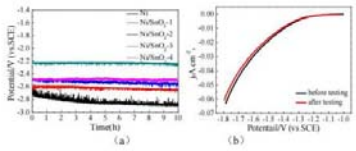

Figure 8. Stability tests of the composite electrodes. (a) The chronopotentiometry study at cathode current density of 100 mA·cm^{-2}. (b) Polarization curves of Ni/SnO2-3 before and after 10 h chronopotentiometry test in 1 M NaOH solution.

The behavior of the electrode potential as a function of time at cathode current density of 100 mA·cm^{-2} is shown in Fig.8. The decrease of electrode potential for Ni, Ni/SnO_2-1, Ni/SnO_2-2, Ni/SnO_2-3, and Ni/SnO_2-4 is 323 mV, 54 mV, 101 mV, 34 mV and 49 mV, respectively. The HER stability of the composite electrode are all higher than pure Ni. The polarization curves of Ni/SnO_2-3 before and after 10 h stability test show negligible changes. The Ni/SnO_2-3 electrode demonstrates excellent stability.

The electrochemical properties of Ni/SnO_2 are compared with other composite materials reported in literatures. The comparison of these works is listed in Table 2. As shown in Table 2, the Ni/SnO_2 exhibits lower over potential [35-37] and higher exchange current density [38,39]. The

performance of hydrogen evolution with Ni/SnO_2 electrode catalyst is obvious higher than other reported composited materials.

Table 2. The activity of HER on different composite electrodes reported in literatures and this work

Electrode	Alkaline solution	b (mV·dec^{-1})	η (mV)	j_0 (uA·cm^{-2})	Reference
Ni/SnO_2	1 M NaOH	187	427 (η_{10})	52.29	this work
Ni-Sn@C PNs	1 M NaOH	145	1230 (η_0)	-	[35]
(Ni-MoS_2)$_{1000}$	2mM $HClO_4$/ 0.1 M $NaClO_4$	120	680 ($\eta_{0.33}$)	8×10^{-4}	[36]
Cu/Cu_2O/ Ni NP	0.1 M H_2SO_4	50	456 (η_{10})	-	[37]
Ni-PAni	4 M KOH	-	-	3.47	[38]
Ni/WO_3	1 M KOH	124.7	-	5.88	[39]
Ni/Bi_2O_3	1 M KOH	128.8	-	2.29	[39]
Ni/SC	1 M KOH	116.9	-	2.43	[39]

4. CONCLUSIONS

The high efficient Ni-SnO_2 electrodes are fabricated by a simple low-cost composite electroplating method. Compared with pure Ni, the Ni/SnO_2 catalyst gives a higher catalytic activity and stability for HER. The co-deposition of SnO_2 in Ni coating makes metal crystallization finer and tinier, which increase the active surface area of electrode. The co-deposition of SnO_2 changes the preferential orientation of Ni to (111) crystal plane which is more benefit to the activity of HER. The OH_{ads} on SnO_2 surface facilitates the formation of adsorbed H_{ads} which is the rate-determining step for HER. SnO_2 is a promising co-catalyst to enhance the activity of HER on Ni based materials.

ACKNOWLEDGEMENT
This work was supported by the Mudanjiang Normal University Key Project (No. GP2021002), the Research Fund Project of Mudanjiang Science and Technology Project of Mudanjiang city (No. SQ2020JG115), the Teaching reform Projects of MuDanjiang Normal University (No. KCSZ-2020021), the Innovation Project of University Students (202110233043).

11. Xing L, Wang Y, Shi X, et al. Investigation of Pt/C and Pt-Ru/C Mixed Catalyst for DME Oxidation in Direct Dimethyl Ether Fuel Cells[J]. Int. J. Electrochem. Sci, 2020, 15: 10382-10391.（SCI 检索收录四区，IF=1.765）

Int. J. Electrochem. Sci., 15 **(2020)** 10382 – 10391, doi: 10.20964/2020.10.27

International Journal of
ELECTROCHEMICAL
SCIENCE
www.electrochemsci.org

Short Communication

Investigation of Pt/C and Pt-Ru/C Mixed Catalyst for DME Oxidation in Direct Dimethyl Ether Fuel Cells

*Lehong Xing**, *Yixin Wang*, *Xinting Shi*, *Rui Dong*, *Lin Wu*

College of Chemistry and Chemical Engineering, Mu Danjiang Normal University,
*E-mail: xinglehonghit@163.com

Received: 2 June 2020 / *Accepted:* 24 July 2020 / *Published:* 31 August 2020

The performance of Pt/C and Pt-Ru/C mixed catalyst has been studied for dimethyl ether (DME) oxidation in direct dimethyl ether fuel cells (DDFCs). Transmission Electron Microscopy (TEM) characterizations show that Pt and Pt-Ru particles (about 3.0 nm) are highly dispersed on their supports. The electrochemical activity of mixed catalyst was evaluated by polarization curve, amperometric current density – time technique, and electrochemical impedance spectroscopy (EIS). The results show that the activity of mixed catalyst is better than Pt/C toward DME oxidation. Pt-Ru/C in the mixed catalyst is helpful for reducing the catalyst poisoning effect, and simultaneously, Pt/C in the mixed catalyst can provide continuous Pt active sites for DME dehydrogenation. Too much Pt-Ru can reduce the catalytic activity. The optimal Pt-Ru content is 3.5 mg cm^{-2} Pt and 0.5 mg cm^{-2} Pt-Ru (metal loading) in anode catalyst layer.

Keywords: Direct dimethyl ether fuel cell; Dimethyl ether; Anode catalyst; Pt-Ru/C; Pt/C

1. INTRODUCTION

Direct type fuel cells which use formic acid, ethanol, formaldehyde, methanol and dimethyl ether (DME) as their fuel have been widely studied recently as potential new power sources [1-3]. These investigated direct type fuel cells are all have their own advantages [4,5]. The direct dimethyl ether fuel cell (DDFC) is one of the promising fuel cells [6]. Dimethyl ether (DME) is the simplest ether and there is no C-C bond in its molecular (CH_3OCH_3) [7]. The toxity of DME is low. DME gas can be compressed easily into liquid form, so that the transportation of DME is convenient. The energy density of DME is high and its fuel crossover effect is low [8,9]. However, DDFC still has some obstacles which hinder its practical applications. The major obstacle limits the performance of DDFC is the poor kinetics of DME oxidation, which mainly results from the week adsorption of DME on catalyst and the poisoning effect of Pt based catalyst [10]. The development of active catalyst towards DME oxidation is very necessary for DDFC. Pt-Ru/C and Pt/C are the two most commonly used anode catalyst for DDFC. Different

researchers have different conclusions about which one is more proper for DME oxidation. Liu [11] compare the performance of the two catalyst in DDFC. They find that Pt-Ru/C is better than Pt/C in low over potential range. Oppositely, Pt/C is better than Pt-Ru/C in high over potential range. In low over potential range, the anode needs OH supported by Ru to remove absorbed CO. In high over potential range, the absorbed CO can be oxidized immediately and the Ru addition decreases the continuous Pt active sites, which is harmful for DME oxidation. Kerangueven [12] find that Ru content in Pt-Ru has an important influence on the performance of DDFC. DDFC performs better with the decrease of Ru content in Pt-Ru. Tsutsumi [13] compare the two catalyst at different temperatures. The activity of Pt-Ru is better than Pt at high temperature, because the rate of DME oxidation reaction is relatively fast at high temperate and there are lots of adsorbed posing species generated on the surface of catalyst. Ru is helpful for the removal of posing intermediates. At low temperature, the activity of Pt is better than Pt-Ru, because the catalyst posing effect is not very significant. Li [14] consider that the catalyst activity of Pt-Ru is higher than Pt, and the optimal Pt to Ru ration is $Pt_{0.8}Ru_{0.2}$. Based on the above results, there are two different (positive and negative) effects of Ru on the activity of DME oxidation. The positive one is that Ru is helpful for the generation of oxygen-containing species. These oxygen-containing species can promote the catalyst activity when the oxidation of posing intermediates is the rate-determing step for DME oxidation reaction. The negative one is that the presence of Ru decreases the continuous Pt active sites, which is bad for DME adsorption and following dehydrogenation. It is very necessary to develop a catalyst which can make ideal balance between positive and negative effects. Besides, which one of these two effects (positive and negative) plays a major role in DME oxidation is strongly impacted by the operating conditions. Up to now, most of the researches about Pt-Ru/C and Pt/C catalyst are carrying out under high temperature and pressure. The performances of DDFCs with the two catalysts at lower than 100 ºC under ambient pressure have not been studied in detail. In this work, Pt-Ru/C is added into Pt/C to form a mixed catalyst for DME oxidation. We represent the first systematic study of the mixed catalyst with different Pt-Ru/C content at 60 ºC under ambient pressure. The mixed catalyst can provide continuous Pt active sites for DME dehydrogenation, and simultaneously provide oxygen-containing species for adsorbed intermediates oxidation. The influence of mixed catalyst on the performance of DDFC has been discussed based on the results of multiple physical and electrochemical tests.

2. EXPERIMENTAL

2.1. Preparation of catalyst

The 40 mass% Pt/C were synthesized by microwave-assisted polyol process [15]. 60 mg of pretreated carbon black (Vulcan XC-72) was ultrasonically dispersed in the solution containing 12 ml isopropyl alcohol and 48 ml glycol (EG) to form a uniform ink. 5.4 ml of 0.0386 mol L^{-1} H_2PtCl_6-EG solution dissolved in the above ink under stirring for 2h. 1 mol L^{-1} NaOH-EG solution was used to adjust the pH. The pH value of the solution was about 12. Afterwards, the solution was heated by a microwave oven (2450MHz, 800W) for 55s under argon gas protection. The solution was cooled down to ambient

temperature under stirring. Then 0.1 mol L^{-1} HNO_3 solution was used to adjust the pH. The pH value of the solution was about 3. The resulting catalyst was washed with ultrapure water, and then dried for 4 h at 80 ºC in vacuum. The 40 mass% Pt-Ru/C was synthesized in a similar way mentioned above with H_2PtCl_6-EG solution and $RuCl_3$-EG solution as precursors.

2.2. Preparation of Membrane electrode assembly (MEA)

The MEAs (5 cm^2) were prepared using a typical process which had been reported in detail previously[16]. The anode gas diffusion layers (GDLs) were wet-proofed carbon papers (Toray, TGP-H-060). The PTFE content in anode GDLs was 18 mass%. The wet-proofed cathode GDLs were composed of carbon papers and 1 mg cm^{-2} of Vulcan XC-72 carbon black. The PTFE content in cathode GDLs was 30 mass%. Pt/C and Pt-Ru/C mixed catalysts were used as the anode catalysts. The Pt and Pt-Ru loading of different MEAs are listed in Table 1. The total metal loading in anode catalyst layers of these MEAs are 4 mg cm^{-2}. The cathode catalyst was Pt/C (2 mg cm^{-2}). Nafion content in catalyst layers were 20 mass%.

Table 1. Components of anode catalyst layers for different MEAs.

Samples	Pt/ mg cm^{-2}	Pt-Ru/ mg cm^{-2}
MEA-1	4.0	0
MEA-2	3.5	0.5
MEA-3	3.8	0.2
MEA-4	3.0	1.0

2.3. Electrochemical measurements

2.3.1 Steady-state polarization curves

A Potentiostat/Galvanostat apparatus (Hokuto Denko Inc. HA-151) was employed to record the steady-state polarization curves of DME oxidation [17]. At the anode side, 1.5 mol L^{-1} DME solution was fed with a flow rate of 3 mL min^{-1}. Simultaneously, the humidified H_2 was supplied to cathode with a flow rate of 200 mL min^{-1}. The cathode served as a dynamic hydrogen electrode (DHE).

2.3.2 Electrochemical impedance spectra (EIS)

The EIS of the anodes was measured by an electrochemical analysis instrument (Shanghai Chen-Hua Instruments Corp., CHI 604B) under 0.45 V vs. DHE at 60 ºC. The amplitude of sinusoidal potential signal was 5mV. The frequencies were from 1 kHz to 0.01 Hz.

2.3.3 Amperometric i–t curves

The amperometric *i–t* curves of DME oxidation were measured by CHI 604B at 0.45 V vs. DHE. The anode and cathode reactants used in above electrochemical measurements (steady-state polarization curves, EIS, amperometric *i–t*) were all the same.

2.3.4 Fuel cell testing

The performances of DDFCs with different anode catalyst were tested using a commercial electrochemical station (Arbin Fuel Cell Testing System) at 60ºC under ambient pressure. During the test, 1.5 mol L^{-1} DME solution was fed at a flow rate of 3 mL min^{-1}, while humidified oxygen was supplied at a flow rate of 200 mL min^{-1}.

3. RESULTS AND DISCUSSION

TEM images and the nanoparticle size distribution diagrams of catalysts are presented in Fig. 1 and Fig. 2. The size distribution diagrams are obtained by random measurements of 100 particles. Pt and Pt-Ru alloy particles are highly dispersed on supports. The average particles sizes of the two catalysts are nearly the same (about 3 nm). Fig. 3 shows the polarization curves and the power density curves of MEAs with or without Ru in anode catalyst at 60 ºC. The maximum power density of the MEA1 and MEA2 is 40 mW cm^{-2} and 50 mW cm^{-2}, respectively. The performance of MEA with mixed catalyst is higher than that of Pt/C. The Ru in mixed catalyst provides oxygen-containing species which is helpful for the oxidation of absorbed intermediates and decrease the catalyst posing effect. The Pt/C in mixed catalyst provides continuous Pt active sites for DME oxidation. The mixed catalyst can make a balance between the positive and negative effects.

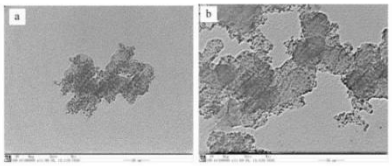

Figure 1. TEM images of catalysts: (a) Pt/C; (b) Pt-Ru/C.

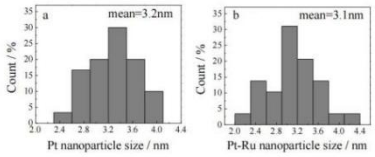

Figure 2. Size distribution diagrams of catalysts: (a) Pt/C ; (b) Pt-Ru/C.

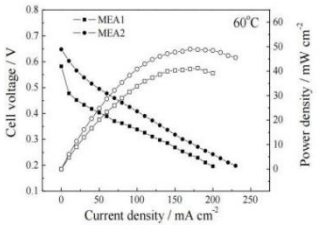

Figure 3. The polarization curves and the power density curves of the MEAs with different anode catalysts at 60 ºC: MEA1 with Pt/C ; MEA2 with the mixed catalysts.

Fig. 4 shows the polarization curves of DME oxidation at different anode. The performance of MEA2 is better than that of MEA1. MEA2 with the mixed catalysts exhibits lower polarization at anode. The Ru in mixed catalyst is benefit to decrease polarization and improve the performance of DDFC.

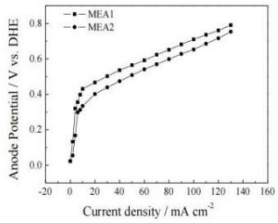

Figure 4. Steady-state polarization curves of DME oxidation reaction versus DHE.

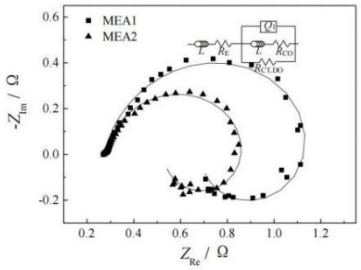

Figure 5. Electrochemical impedance spectra of DDFC anode with different catalyst (dots) and fitting diagrams using equivalent circuit (lines) at 0.45 V vs. DHE.

The EIS of anodes with different catalyst are shown in Fig.5. A possible equivalent circuit in Fig.5 is used to describe the anode process [18-20]. The fitting results analyzed by ZSimpWin software

are listed in Table 2. As seen in Fig.4, both MEA1 and MEA2 operate in low current region when the anode potential is 0.45 V vs. DHE. The mass transport polarization effect can be ignored in low current region. In Fig.5, the semicircle is due to DME oxidation reaction and the inductance in the low frequency region corresponds to the slow relaxation of CO_{ADS}. R_E is the ohmic resistance of anode. The R_E values of MEA1 and MEA2 are nearly the same. $R_{CT,DOR}$ is the charge transfer resistances of DME dehydrogenation. The $R_{CT,DOR}$ of MEA1 and MEA2 is 1.03 Ω and 0.64 Ω, respectively. R_{CO} is the charge transfer resistances of CO_{ADS} oxidation. The R_{CO} of MEA1 and MEA2 is 0.69 Ω and 0.41 Ω, respectively. The decrease of $R_{CT,DOR}$ means that DME dehydrogenation of MEA2 is easier than that of MEA1. The decrease of R_{CO} means that poisoning of the Pt in MEA2 is much more muted than that in MEA1. The total anode reaction resistance ($R_{R,A}$) of MEA1 and MEA2 is 0.41 Ω and 0.25 Ω, respectively. The increase of DDFC performance can be attributed to the decrease in the anode reaction resistance including DME dehydrogenation resistance and CO_{ADS} intermediate oxidation resistance.

Table 2. Fitting results of the resistance elements.

Resistances / Ω	MEA1	MEA2
R_E	0.27	0.28
$R_{CT,DOR}$	1.03	0.64
R_{CO}	0.69	0.41
$R_{R,A}=(R_{CT,DOR}^{-1}+R_{CO}^{-1})^{-1}$	0.41	0.25

The amperometric *i–t* curves in Fig. 6 are used to evaluate the activity of catalyst for DME oxidation. The final current density of MEA1 and MEA2 is 26 and 42 mA cm^{-2}, respectively. The electrocatalytic activity of the mixed catalyst is higher than Pt /C. There is less drop in activity of the mixed catalyst during the whole 1000s test, which indicate that the mixed catalyst can enhance the CO-tolerance ability for the existence of Pt-Ru/C. In addition, the mixed catalyst can supply continuous Pt active sites for DME oxidation by the existence of Pt /C.

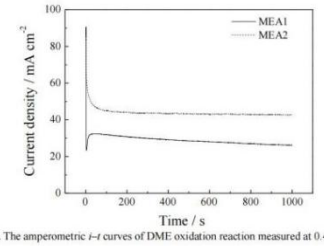

Figure 6. The amperometric *i–t* curves of DME oxidation reaction measured at 0.45 V vs. DHE.

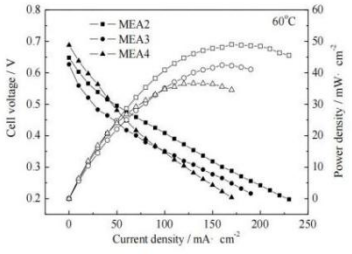

Figure 7. The polarization curves and the power density curves of MEAs with various Pt-Ru/C content in anode catalyst layer.

Fig. 7 shows the polarization curves and the power density curves of MEAs with different Pt-Ru/C content at anode. The Pt and Pt-Ru loading in anode catalyst layer of these MEAs are listed in Table 1. The MEAs perform firstly better and then worse with the increase of the Pt-Ru content in anode catalyst layer. The MEA2 with 3.5 mg cm^{-2} Pt and 0.5 mg cm^{-2} Pt-Ru in catalyst layer exists the highest

output performance, and its maximum power density is 50 mW cm^{-2}. The open circuit potentials and polarization curves (in low current density region) of different MEAs are enhanced with the increase of Ru content in anode catalyst layer. It indicates that, in low current density region, catalyst posing effect plays a major role in DME oxidation reaction. In high current density region, the oxidation of DME needs large amount of continuous Pt active sites. Too much Ru can reduce the continuous Pt active sites. The anode mixed catalyst with 3.5 mg cm^{-2} Pt and 0.5 mg cm^{-2} Pt-Ru in catalyst layer can provide continuous Pt active sites for DME dehydrogenation, and simultaneously provide oxygen-containing species to oxidize the poisoning adsorbed intermediates.

The new table has been made to compare the DME electrocatalysts described in literatures. The comparisons of these works are listed in table 3[7-10]. Comparing to these works in table 3, DDFC with Pt/C and Pt-Ru/C mixed catalyst shows higher performance under ambient pressure.

Table 3. The performances of DDFCs with different anode catalysts reported in literatures and this work

	Catalyst	The maximum power density/ mW cm^{-2}	Temperature/ °C	Pressure/bar	Reference
1	PtCu	13.5	80	1	21
2	Pt/C	60	80	3	22
3	PtRu	38	80	1	23
4	Pt/SnO_2/C	49.6	70	1	15
5	Mixed catalyst	60	60	1	this work

4. CONCLUSIONS

The mixed catalyst with Pt/C and Pt-Ru/C are prepared for DME oxidation in DDFC. TEM tests show that the average sizes of Pt and Pt-Ru alloy nanoparticles are nearly the same (about 3 nm). the EIS results show that the addition of Ru can reduce $R_{CT,DOR}$ and R_{CO} of DME oxidation reaction. The mixed catalyst is helpful for reducing the catalyst poisoning effect, and simultaneously can provide continuous Pt active sites for DME dehydrogenation. Too much content Pt-Ru in mixed catalyst can reduce the catalytic activity. DDFC with 3.5 mg cm^{-2} Pt and 0.5 mg cm^{-2} Pt-Ru in anode catalyst layer shows the highest performance (50 mW cm^{-2}).

ACKNOWLEDGEMENT
This work was supported by University Nursing Program for Young Scholars with the Young Scholars Programs of Mu Danjiang Normal University (GG2018001), Creative Talents in Heilongjiang Province (UNPYSCT-2016108), the Teaching reform Projects of Mu Danjiang Normal University (19-XJ21008, KCSZ2020021), Innovation Project of University Students (202010233015).

12. Xing L, Wang Y, Sui C, et al. Investigation of Pt/SnO_2/C Catalyst for Dimethyl Ether Oxidation in DDFC[J]. Int. J. Electrochem. Sci, 2020, 15: 2375-2384.（SCI 检索收录四区，IF=1.765）

Int. J. Electrochem. Sci., 15 **(2020)** 2375 – 2384, doi: 10.20964/2020.03.26

International Journal of
ELECTROCHEMICAL
SCIENCE
www.electrochemsci.org

Short Communication

Investigation of Pt/SnO_2/C Catalyst for Dimethyl Ether Oxidation in DDFC

Lehong Xing[1,2,*], *Yixin Wang*[1], *Chao Sui*[1], *Na Zhang*[2]

[1] College of Chemistry and Chemical Engineering, Mu Danjiang Normal University, Mu Danjiang 157012 ,China
[2] School of Chemical Engineering and Technology, Harbin Institute of Technology, No. 92, West Da-Zhi Street, Harbin 150001 China
*E-mail: xinglehonghit@126.com

Received: 6 November 2019 / *Accepted:* 18 December 2019 / *Published:* 10 February 2020

The performance of Pt loading on SnO_2/C support catalyst has been investigated for dimethyl ether (DME) oxidation in direct dimethyl ether fuel cells (DDFCs). The transmission electron micrograph (TEM) tests show that the sizes of Pt particles loading on different supports (SnO_2/C and XC-72 carbon black) are nearly the same (3.2 nm). The cyclic voltammograms results reveal that Pt/SnO_2/C shows higher activity towards DME oxidation. DME prefers to be adsorbed on Pt/SnO_2/C surface. SnO_2 can adsorb OH_{ads} species which benefit to reduce the Pt poisoning effect. The maximum power density of DDFC has been enhanced by using Pt/SnO_2/C as the anodic catalyst. The electrochemical active surfaces (*EAS*) of different anodes are nearly the same. That is, the improvement of DDFC performance can be attributed to the enhanced activity of anode catalyst.

Keywords: Direct dimethyl ether fuel cell; Dimethyl ether; Anode catalyst; Supports; Pt/SnO_2/C

1. INTRODUCTION

At present, traditional energy resources such as coal, natural gas and oil are nearly exhausted. Fuel cells such as proton exchange membrane fuel cells (PEMFCs) and direct methanol fuel cells (DMFCs) have been widely studied to solve the potential energy crisis problems [1-3]. However, PEMFCs and DMFCs still have some obstacles which hinder their broad applications [4,5]. Dimethyl ether (DME) is a new attractive fuel for PEMFCs which has many advantages. The energy density of DME is high and its toxicity is low. DME has low fuel crossover effect [6]. The transportation of DME is convenient because it can be liquefied easily [7]. However, the major obstacle limits the performance of direct dimethyl ether fuel cell (DDFC) is the relatively slow kinetics of anodic DME oxidation. The improvement of catalyst activity towards DME oxidation is very important for DDFC [8]. Pt and Pt-M

alloys are prominent catalysts for DDFCs [9]. Recently, metallic oxides have attracted increasing attention for catalytic researchers for their excellent co-catalyst effect [10]. In particular, tin dioxide (SnO_2) exhibits many advantages. SnO_2 shows high stability at anode. SnO_2 can adsorb sufficient OH_{ads} species. These OH_{ads} benefit to oxidize the poisoning intermediates generated during DME anodic oxidation reaction and release Pt active sites [11]. In addition, SnO_2 and SnO_2 based nanomaterials have been used as catalyst supports. The catalytic activity has been enhanced because of the strong metal-support interaction [12-14].

In this study, the aim of work is to utilize SnO_2 loaded on XC-72 carbon black as the catalyst support to enhance the DME oxidation activity. Firstly, homemade nano SnO_2/C composites are synthesized by hydrolysis method. Then, nano Pt particles are deposited on the SnO_2/C composites. The effects of catalyst supports on DME oxidation and the performance of DDFC have been discussed based on physical characterizations and electrochemical tests results.

2. EXPERIMENTAL

2.1. Preparation of catalyst

Preparation of nano SnO_2/C [15]: 64 mg of Dihydrate tin (II) halide were dissolved in the solution which was composed of 25 ml ethylene glycol (EG) and 1 ml water. 200 mg of carbon black (Vulcan, XC-72) was dispersed in another 25 ml EG. The two obtained solutions were mixed in a three-neckround-bottom flask. The mixture was kept at 190 ℃ for 3 h under stirring. Then, the mixture was cooled down to about 25 ℃. The products were filtered and washed 3 times. At last, the resulting powders were dried under vacuum condition. The theoretical content of SnO_2 in prepared supports was 20 wt. %.

Preparation of nano Pt based catalyst [15]: A 2.65 mL of H_2PtCl_6 - EG solution was diluted by 200 mL EG. The solution was adjusted to pH≈12 using NaOH-EG solution. An 80 mg of supports were dispersed into the solution under ultrasonic treatment for 0.5 h. Then the solution was refluxed for 4 h at 140 ◦C. The solution was cooled down to about 25 ℃ under stirring. Then the solution was adjusted to pH≈3 using 0.1 M HNO_3 solution. The homemade catalyst was washed 3 times, and then dried for 4 h at 80 ◦C under vacuum condition. As comparison, the 20 mass % Pt/C was prepared as reference catalyst.

2.2. MEA fabrication

The MEAs (5 cm^2) were prepared by the traditional methods which have been reported previously [16]. The wet-proofed Toray carbon papers were used as anode diffusion layers. The PTFE content of anode diffusion layers was 18 wt.%. The wet-proofed carbon papers coated with 1 mg cm^{-2} of carbon black and PTFE were used as the cathode diffusion layers. The PTFE content of cathode diffusion layers was 30 wt.%. The anodic catalysts of different MEAs were Pt/SnO_2/C and Pt/C, respectively. The cathodic catalysts of different MEAs were both Pt/C. In catalyst layer, the Pt loading was 2 mg cm^{-2}, and Nafion content was 20 wt.%.

2.3. Physical characterization

The morphology of catalyst was characterized by TEM (Hitachi H-7650). To examine and measure the content of SnO_2 in Pt/SnO_2/C, the chemical composition of the Pt/SnO_2/C was analyzed by EDAX techniques (HITACHIS-4700). The IR spectra (ThermoFisher- is10) were used to examine the OH_{ads} species on SnO_2 surface.

2.4. Electrochemical measurements

2.4.1 Cyclic voltammetry

Cyclic voltammetry (CV) measurements were conducted to evaluate anodic *EAS* [17]. During the test, humidified N_2 was pumped to the anode and humidified H_2 was pumped to the cathode. The cathode was used as a dynamic hydrogen electrode (DHE). The flow rate of N_2 and H_2 were both 200 mL min^{-1}. The CV measurements were performed from 0.05 V to 1.2 V (VS DHE). The scan rate was 0.01 V s^{-1}. The *EAS* of anodic catalyst could be calculated through Eq.(1):

$$EAS_H = \frac{Q_H}{[Pt]\times 0.21} \quad (1)$$

Where, Q_H was the charges due to hydrogen desorption, and [Pt] represented Pt loading on anode.

Another CV scan was conducted in a standard three-electrode cell. The CV scan was measured to compare the activity of the two homemade catalysts [18]. The glassy carbon disk (3 mm diam, CH Instrument, Inc) covered with catalyst was used as working electrode. 5μL of ultrasonically re-dispersed catalyst suspension (2 mg mL^{-1}) was spread on the glassy carbon disk. After drying in vacuum, the obtained electrode was coated with 5μL of 5 wt % Nafion solution to form a Nafion film. The counter electrode was platinum foil (1 cm^2). The reference electrode was a reversible hydrogen electrode (RHE). The CV scans were performed in the electrolyte of 0.5 mol L^{-1} H_2SO_4 containing 1.5 mol L^{-1} DME between 0.05 and 1.2 V (versus the RHE) at 25 ℃. The scan rate was 0.05 V s^{-1}.

2.4.2. Fuel cell tests.

The performances of MEAs fabricated with different anodic catalyst were tested by Arbin Fuel Cell Testing System at 70 ℃. The 1.5mol L^{-1} DME solution was the anodic fuel. The flow rate of DME solution was 3 mL min^{-1}. The humidified oxygen (200 mL min^{-1}) was fed to the cathode side under ambient pressure

3. RESULTS AND DISCUSSION

TEM images and the corresponding histograms of Pt/SnO_2/C and Pt/C are presented in Fig. 1 and Fig. 2. The corresponding histograms are obtained by random measurements of 200 Pt nanoparticles. The Pt particles are uniformly dispersed on SnO_2/C and carbon black supports. The average sizes of Pt

particles are nearly the same (3.2 nm) for the two catalysts.

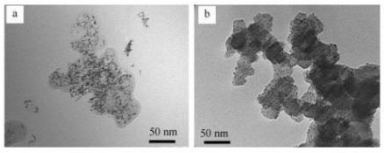

Figure 1. TEM images of Pt/SnO_2/C and Pt/C catalysts: (a) Pt/SnO_2/C; (b) Pt/C.

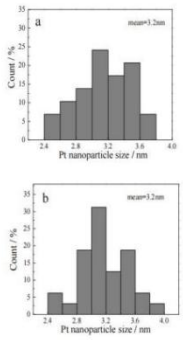

Figure 2. Size distribution of Pt/SnO_2/C and Pt/C catalysts: (a) Pt/SnO_2/C; (b) Pt/C.

The compositions of the Pt/SnO_2/C and Pt/C are analyzed by EDAX. The Pt content of Pt/SnO_2/C and Pt/C catalyst is 17.88 *wt*% and 18.42 *wt*%, respectively, which are approximately equal to the

theoretical Pt content in catalyst (20 *wt*%). The content of SnO_2 in prepared SnO_2/C composite is 18.60 *wt* %, which is almost equal to the theoretical value (20 *wt*%).

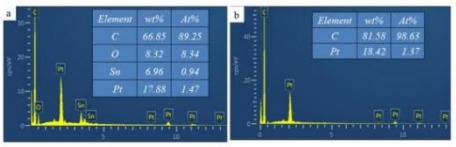

Figure 3 EDAX patterns of Pt/SnO_2/C and Pt/C catalysts and their quantitative analysis: (a) Pt/SnO_2/C; (b) Pt/C.

To compare the activity of Pt/SnO_2/C and Pt/C for DME oxidation, the cyclic voltammograms are recorded in 0.5 mol L^{-1} H_2SO_4 + 1.5 mol L^{-1} DME solution. The onset potential of DME oxidation on Pt/SnO_2/C is about 0.55 V.

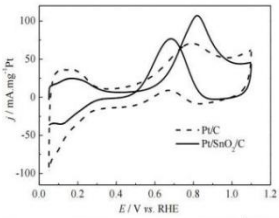

Figure 4. Cyclic voltammograms of DME electrooxidation in 0.5 mol L^{-1} H_2SO_4 + 1.5 mol L^{-1} DME aqueous solution on Pt/SnO_2/C and Pt/C catalysts. Scan rate: 0.05 V s^{-1}.

The peak current of DME oxidation on Pt/SnO_2/C is about 107 mA mg^{-1} Pt, which is much higher than that of Pt/C (70 mA mg^{-1} Pt). Thus, the Pt/SnO_2/C catalyst shows more excellent catalytic activity. G. Keranguéven [19] reports the CV curves of Pt-based catalysts in H_2SO_4 solutions with or without

DME. The peaks of CV curves with DME are suppressed during the H_2 adsorption and desorption potential range. The dissociative adsorption of DME suppresses H_2 adsorption and desorption in low potential range. Y. Liu [20] investigates the dissociative adsorption of DME and methanol in hydrogen range. The results show that both DME and methanol can absorb on catalyst and suppress the hydrogen adsorption and desorption reaction in low potential range. But the adsorption of DME is weaker than methanol. A fewer amount of DME molecules can be adsorbed and then dehydrogenated on catalyst compared with that of methanol. The activity of DME oxidation reaction is lower than methanol. The similar results have been reported by M. H. Shao [21], which use $HClO_4$ as the electrolyte. The improvement of the adsorption of DME on catalyst is very important for DDFC. As shown in Fig.4, the CV curve of $Pt/SnO_2/C$ has been suppressed during the H_2 adsorption and desorption potential range (from 0.03V to 0.28V). That is, the adsorption of DME on $Pt/SnO_2/C$ is easier than Pt/C in low potential range. The mechanism of DME electro-oxidation reported by Q. Zhang is as follows [22]:

$$CH_3–O–CH_3 + Pt \rightarrow Pt–C–O–CH_3 + H^+ + 2e^- \quad (2)$$
$$CH_3–O–CH_3 + Pt \rightarrow Pt–(CHOCH) – Pt + 4H^+ + 4e^- \quad (3)$$
$$Pt–C–O–CH_3 + H_2O \rightarrow Pt–COH + CH_3OH \quad (4)$$
$$Pt–(CHOCH)–Pt + H_2O \rightarrow 2Pt–CO + 4H^+ + 4e^- \quad (5)$$
$$Pt–COH \rightarrow Pt–CO + H^+ + e^- \quad (6)$$
$$CH_3OH + Pt \rightarrow Pt–CO + 4H^+ + 4e^- \quad (7)$$
$$Pt + H_2O \rightarrow Pt–OH_{ads} + H^+ + e^- \quad (8)$$
$$Pt–CO + Pt–OH_{ads} \rightarrow CO_2 + H^+ + e^- \quad (9)$$
$$Pt–COH + Pt–OH_{ads} \rightarrow CO_2 + H^+ + 2e^- \quad (10)$$

According to the above mechanism, the adsorption of DME on Pt is the first step of DME oxidation, which can significantly affect the reaction speed. $Pt/SnO_2/C$ is benefit to DME adsorption, which is a main cause for the increase in anodic catalyst activity. The IR spectra in Fig. 5 show the characteristic peak of SnO_2. The band in the range of 500-750 cm^{-1} is due to the Sn-O vibration. The band at about 1600 cm^{-1} is assigned to the bending vibration of O-H. The broad band at about 3430 cm^{-1} is stretching vibration of O-H. As shown in Fig. 5, there are sufficient OH_{ads} species existed on the surface of SnO_2. Many researchers have reported the intermediates generated during DME oxidation reaction. As shown in the Eq. (9) and (10), –CO and –COH are the poisoning intermediates adsorbed on Pt. Besides, other researchers consider that $-CH_2OCH_3$, -COOH and formaldehyde are the possible intermediates of DME oxidation reaction [21,23,24]. The OH_{ads} species on the surface of SnO_2 promote the oxidation of intermediates species which benefits to reduce the Pt poisoning effect and release Pt active sites. The dehydrogenation of DME on Pt surface needs three adjacent Pt active sites. The elimination of adsorbed intermediates species can increase the amount of adjacent Pt active sites, which is another cause for the increase in anodic catalyst activity.

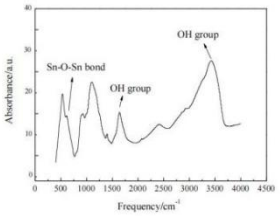

Figure 5. IR spectra of SnO_2 particles after dehydration treatment at 200 ℃ under vacuum condition.

Fig. 6 shows the polarization curves and the power density curves of MEAs with different anodic catalyst at 70 ℃. The maximum power density of the MEAs with $Pt/SnO_2/C$ and Pt/C anodic catalyst is 49.6 mW cm^{-2} and 33.6 mW cm^{-2}, respectively. Obviously, DDFC with $Pt/SnO_2/C$ anodic catalyst obtains higher output performance. $Pt/SnO_2/C$ is a proper anodic catalyst for DME, which can enhance the output performance of DDFC. The performances of DDFCs with different anode catalysts have been reported in many published literatures. The comparison of these works is listed in table 1[18,25-27]. Comparing to these works in table 1, the performance of DDFC with $Pt/SnO_2/C$ anode catalyst is obvious higher at relatively low temperature (70 ℃) and under relatively low pressure (1 bar).

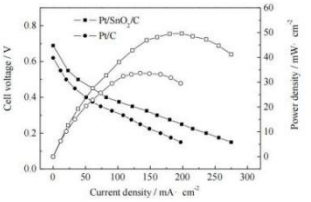

Figure 6. The polarization curves and the power density curves of the MEAs with various anode catalysts at 70 ℃.

Table 1. The performances of DDFCs with different anode catalysts reported in literatures and this work

	Catalyst	The maximum power density/ mW cm^{-2}	Temperature/ ℃	Pressure/bar	Reference
1	PtCu	13.5	80	1	7
2	Pt/C	60	80	3	8
3	Pt/MWNT	38.4	80	1	9
4	PtRu	38	80	1	10
5	$Pt/SnO_2/C$	49.6	70	1	Present work

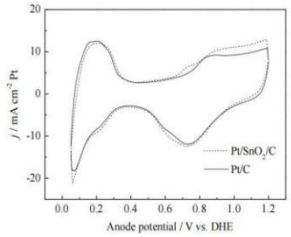

Figure 7. Cyclic voltammograms of anodes with various catalysts at a scan rate of 0.01V s^{-1}, in a potential range between 0.05 and 1.2V vs. DHE.

Fig.7 presents the anodic *EAS* of MEAs with different catalyst. The anodic *EAS* of MEA with $Pt/SnO_2/C$ catalyst is 81 m^2 g^{-1}Pt. The anodic *EAS* of the other MEA is 87 m^2 g^{-1}Pt. The *EAS* of different MEAs are nearly the same. The value of *EAS* represents the amount of Pt active sites in anode. That is, the MEAs with different catalyst have nearly the same amount of anodic Pt active sites. The enhancement of DDFC performance can be ascribed to the higher activity of anode catalyst.

4. CONCLUSIONS

$Pt/SnO_2/C$ catalyst with SnO_2/C as its supports has been prepared for DME electrooxidation in an acidic medium. TEM tests show that the average sizes of Pt particles are nearly the same (3.2 nm) for $Pt/SnO_2/C$ and Pt/C. The $Pt/SnO_2/C$ catalyst shows higher activity than Pt/C towards DME oxidation.

The adsorption of DME on $Pt/SnO_2/C$ is easier than Pt/C, which promotes the oxidation of DME. IR spectra results show that there are sufficient OH_{ads} species existed on the surface of SnO_2. These OH_{ads} species benefit to reduce the Pt poisoning effect and release Pt active sites. The maximum power density of DDFC with $Pt/SnO_2/C$ anodic catalyst is higher than DDFC with Pt/C anodic catalyst. DDFCs with different anodic catalyst have nearly the same anodic *EAS*. Therefore, the enhanced performance is attributed to the higher activity of $Pt/SnO_2/C$ for DME oxidation.

ACKNOWLEDGEMENT
This work was supported by University Nursing Program for Young Scholars with Creative Talents in Heilongjiang Province (UNPYSCT-2016108), the Young Scholars Programs of Mu Danjiang Normal University (GG2018001), the Teaching reform Projects of Mu Danjiang Normal University (19-XJ21008), the Scientific Research Fund of Heilongjiang Education Department (No. 1353ZD002), and the Scientific Research Projects of Mudanjiang Normal University (No.GP2019002).

References

1. L.Z. Yin, Q. Li, W.R. Chen, T.H. Wang, and H. Liu, *Int. J. Hydrogen Energy*, 11 (2019) 5499.
2. K.J. Reddy, and N. Sudhakar, *Int. J. Hydrogen Energy*, 44 (2019) 15355.
3. G.H. Gwak, D.H. Kim, S. Lee, and H. Ju, *Int. J. Hydrogen Energy*, 43 (2018) 13999.
4. C. Ouyang, X.L. Zhang, M.F. Wu, D.M. Xun, and P.P. Gao, *Int. J. Electrochem. Sci.*, 15 (2020) 80.
5. Y. Zhao, L.W. Chen, and Y.D. Meng, *Int. J. Electrochem. Sci.*, 14 (2019) 6826.
6. L.H. Xing, G.P. Yin, Z.B. Wang, S. Zhang, Y.Z. Gao, and C.Y. Du, *J. Power Sources*, 198 (2012) 170.
7. J.H. Yu, H.G. Choi, and S.M. Cho, *Electrochem. Commun.*, 7 (2005) 1385.
8. L. H. Xing, Y.Z. Gao, Z.B. Wang, C.Y. Du, and G.P. Yin, *Int. J. Hydrogen Energy*, 36 (2011) 11102.
9. U. Mondal, and G.D. Yadav, *J. CO_2 Util.*, 42 (2019) 16695.
10. W.J. Yuan, Y.F. Zhang, N.Y. Zhang, C.W. Yin, X.L. Zhang, and X.W. Liu, *Catal. Commun.*, 100 (2017) 66.
11. H. Zhang, C. Hu, X. He, L. Hong, G. Du, and Y. Zhang, *J. Power Sources*, 196 (2011) 4499.
12. W.Z. Hung, W.H. Chung, D.S. Tsai, D.P. Wilkinson, and Y.S. Huang, *Electrochim. Acta*, 55 (2010) 2116.
13. M.L. Dou, M. Hou, D. Liang, W.T. Lu, Z.G. Shao, and B.L. Yi, *Electrochim. Acta*, 92 (2013) 468.
14. Y. Fan, J.H. Liu, H.T. Lu, P. Huang, and D.L. Xiu, *Electrochim. Acta*, 76 (2012) 475.
15. N. Zhang, S. Zhang, C.Y. Du, Z.B. Wang, Y.Y. Shao, and K.F. Dong, *Electrochim. Acta*, 117 (2014) 413.
16. L.H. Xing, Z.B. Wang, C.Y. Du, and G.P. Yin, *Int. J. Energy Res.*, 36 (2012) 886.
17. L.H. Xing, G.P. Yin, C.Y. Du, S.X. Cui, M.H Zuo, and H.P. Wang, *Int. J. Hydrogen Energy*, 42 (2017) 16695.
18. K.D. Cai, G.P. Yin, J.J. Wang, and L.L. Lu, *Energy Fuels*, 23(2009) 903.
19. G. Kerangueven, C. Coutanceau , E. Sibert, J.M. Leger, and C. Lamy, *J. Power Sources*, 157 (2006) 318.
20. Y. Liu, M. Muraoka, S. Mitsushima, K.I. Ota, and N. Kamiya, *Electrochim. Acta*, 52 (2007) 5781.
21. M.H. Shao, J. Warren, N.S. Marinkovic, P.W. Faguy, and R.R. Adzic, *Electrochem. Commun.*, 7 (2005) 459.
22. Q. Zhang, Z.F. Li, S.W. Wang, W. Xing, R.J. Yu, and X.J Yu, *Electrochim. Acta*, 53 (2008) 8298.
23. G. Kerangueven, C. Coutanceau, E. Sibert, F. Hahn, J.M. Leger, and C. Lamy, *J. Appl.*

13. Xing L H, Yin G P, Du C Y, et al. Investigation on the durability of direct dimethyl ether fuel cell. Part II: Cathode degradation[J]. International Journal of Hydrogen Energy, 2017, 42(26): 16695-16699. （SCI 检索收录二区，IF=5.816）

INTERNATIONAL JOURNAL OF HYDROGEN ENERGY 42 (2017) 16695–16699

Available online at www.sciencedirect.com

ScienceDirect

journal homepage: www.elsevier.com/locate/he

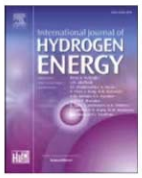

Investigation on the durability of direct dimethyl ether fuel cell. Part II: Cathode degradation

Le-Hong Xing [a,b,*], *Ge-Ping Yin* [a], *Chun-Yu Du* [a], *Shu-Xin Cui* [b], *Ming-Hui Zuo* [b], *Hai-Peng Wang* [b]

[a] *State Key Laboratory of Urban Water Resource and Environment, School of Chemical Engineering and Technology, Harbin Institute of Technology, No. 92, West Da-Zhi Street, Harbin 150001, China*

[b] *College of Chemistry and Chemical Engineering, Mudanjiang Normal University, Mudanjiang 157012, China*

ARTICLE INFO

Article history:
Received 12 December 2016
Received in revised form
23 April 2017
Accepted 14 May 2017
Available online 17 June 2017

Keywords:
Direct dimethyl ether fuel cell
Durability test
Cathodic catalyst degradation
Electrochemical active surface
Dimethyl ether crossover

ABSTRACT

Cathodic Pt/C catalyst degradation for a direct dimethyl ether fuel cell (DDFC) has been investigated after a 70.5 h galvostatic operation at 60 °C under ambient pressure. The cathode electrochemical active surface (EAS) reduces from 349 to 267 cm^2 mg^{-1} Pt after durability test. Cathode EAS loss is associated with the growth of Pt catalyst particles. XRD and TEM results show that the particle size of cathodic Pt catalyst increases from an original value of 3.0 nm to 5.4 nm. Furthermore, the anode failure accelerates dimethyl ether (DME) crossover, and consequently, poisoning of catalyst by absorbed DME and/or intermediates aggravates the degradation of cathodic Pt/C catalyst. The effect of anode degradation on the long-term performance of DDFC has been reported in companion article (Part I).

© 2017 Hydrogen Energy Publications LLC. Published by Elsevier Ltd. All rights reserved.

Introduction

Recently, proton exchange membrane fuel cells (PEMFCs) [1–3], and direct methanol fuel cells (DMFCs) [4–6] have been investigated extensively for stationary and portable applications [7,8]. However, each of them has some shortcomings which limit their commercialization [9,10]. Dimethyl ether (DME) is known as a promising alternative fuel [11–13]. The transportation of DME is easier and safer than hydrogen because its physical properties are similar with liquefied petroleum gas (LPG) [14,15]. DME also has many advantages in comparison with methanol for its high energy density, low toxicity, and low fuel crossover [16–18]. Therefore, DME is a new proper fuel for fuel cells and has been receiving increasing attention recently [19–22].

Up to now, most of the research has been focused on the activity of anodic catalyst and the short-term performance of direct dimethyl ether fuel cell (DDFC) [23,24]. The long-term performance and durability of the membrane electrode assembly (MEA) for DDFC have not been investigated in detail. DDFC commercialization demands stable operation for at least thousands of hours, which is difficult to achieve [25]. The electrocatalyst is one of the major components of MEAs, and their stability plays an important role in the long-term operation of fuel cells [26,27]. Pt/C catalyst failure results from the corrosion of carbon support [28], the Ostwald ripening (dissolution and redeposition) of Pt particles [29], the coalescence

* *Corresponding author*. State Key Laboratory of Urban Water Resource and Environment, School of Chemical Engineering and Technology, Harbin Institute of Technology, No. 92, West Da-Zhi Street, Harbin 150001, China.
E-mail address: xinglehonghit@126.com (L.-H. Xing).

http://dx.doi.org/10.1016/j.ijhydene.2017.05.134
0360-3199/© 2017 Hydrogen Energy Publications LLC. Published by Elsevier Ltd. All rights reserved.

due to the high surface energy of small Pt nanoparticles [30] and poisoning of catalysts by accumulated intermediates from DME electro-oxidation or impurities [31]. The cathodic catalyst in DDFC operates in a serious corrosive environment, such as high water content, low pH value, high temperature, high oxygen concentration and high potentials (0.6–1.2 V) [32]. The stability of catalyst is an important factor which can strongly impact the long-term performance of DDFC. In previous paper (part I) [33], we have reported the durability of anode catalyst for 70.5 h operation. The 70.5 h operation is composed of a 40.5 h operation beginning, and then cyclic voltammetry (CV) scans of the anode and cathode respectively, and another 30 h operation. In this paper (part II), we focus on exploring the durability of cathodic Pt/C catalyst for DDFC at the same condition. Electrochemical and physical characterizations are performed before and after the durability test, and their results are compared. Furthermore, the effect of DME crossover behavior on the cathodic catalyst deterioration is analyzed. The purpose of this study is to provide a better insight into the stability and changes of Pt/C catalysts under DDFC operating conditions and to investigate whether and how the anode degradation affects the performance of cathodic Pt/C catalyst by in situ CV and other techniques.

Experimental

MEA fabrication

The home-made MEA was fabricated by the gas diffusion layer-based method [33]. The working area of the MEA was 5 cm^2. The anode and cathode catalyst were both 40 wt.% Pt/C. The Pt loading of anode and cathode was 3.2 mg cm^{-2} and 2.5 mg cm^{-2}, respectively. The Nafion content was 20 wt.% in catalyst layers. The anode diffusion layers were wet-proofed Toray carbon papers (18 wt.% PTFE) coated with 1 mg cm^{-2} Vulcan XC-72 carbon blacks and 18 wt.% PTFE. The cathode diffusion layers were wet-proofed Toray carbon papers (30 wt.% PTFE) coated with 1 mg cm^{-2} Vulcan XC-72 carbon blacks and 30 wt.% PTFE. Nafion 115 polymer membranes (DuPont) were used to fabricate MEAs. The pretreated Nafion membranes sandwiched between anode and cathode and then the assemblies were hot pressed under a specific load of 100 kg cm^{-2} for 1.5 min at 135 °C.

Electrochemical measurements

Single fuel cell tests

The electrochemical tests of MEA were carried out by Fuel Cell Testing System (Arbin Instrument Corp.) using the single cell (Electrochemistry Corp.). All of the electrochemical measurements were carried out at 60 °C. The 1.5 mol L^{-1} DME solution was fed to the anode side with a flow rate of 3 mL min^{-1}. Pure oxygen was supplied to the cathode side with a flow rate of 200 mL min^{-1} under ambient pressure.

Cyclic voltammetry

Cyclic voltammetry (CV) scan was measured by a CHI 604B Electrochemical Analyzer (Shanghai Chen-Hua Instruments Corp. China) to evaluate the degradation of cathodic EAS. During the test, the cathode was protected by humidified N_2 at a flow rate of 200 mL min^{-1}. Simultaneously, the anode was fed with humidified H_2 at a flow rate of 200 mL min^{-1} as a dynamic hydrogen electrode (DHE). The CV sweep was performed at a scan rate of 0.01 V s^{-1} between 0.05 and 1.2 V (vs. the anode). The cathodic EAS at different conditions could be determined through Eq. (1), where [Pt] denoted Pt loading (mg cm^{-2}) on the electrode, Q_H represented the charge (mC cm^{-2}) for hydrogen desorption, and 0.21 was the required charge (mC cm^{-2}) to oxidize a monolayer of H_2 on bright Pt [34]. The similar CV tests were also employed to detect and eliminate the crossover DME and/or intermediates on cathodic Pt surface after the 40.5 h operation of the DDFC.

$$ESA_H = \frac{Q_H}{[Pt] \times 0.21} \quad (1)$$

DME crossover rate

The DME crossover rate was estimated by the limiting current density at the cathode. During the test, a 1.5 mol L^{-1} DME solution was fed to the anode at 3 mL min^{-1}. The linear sweep voltammetry (LSV) was performed at the cathode at a scan rate of 1 mV s^{-1} with a protection of pure N_2 at 200 mL min^{-1}. The anode was regarded as a DHE, because only the reduction of H^+ to H_2 took place at the anode. After the electrochemical tests, the used MEA was peeled carefully and cut into small pieces for further physical analysis [35,36].

Physical measurements

X-ray diffraction (XRD)

XRD analysis was conducted on the catalysts scraped from the fresh and aged cathode to characterize the changes of the Pt particles. The XRD patterns were recorded by a Japan D/max-rB X-ray diffractometer, using a Cu Kα radiation source at a tube current of 100 mA and a tube voltage of 40 kV, with a scan rate of 5° min^{-1}.

Transmission electron microscopy (TEM)

TEM for the catalyst samples was taken by a Hitachi H-7650 transmission electron microscope. Before taking the electron micrographs, the samples were finely ground and ultrasonically dispersed in isopropyl alcohol, and a drop of the resultant dispersion was deposited and dried on a standard copper grid coated with a polymer film.

Results and discussion

After the durability test, the maximum power density of DDFC drops dramatically from an initial value of 37 mW cm^{-2} to 12 mW cm^{-2} [33]. Cyclic voltammograms in Fig. 1 present the decay of cathodic EAS. The hydrogen desorption region on Pt catalyst decreases after the life test. The calculated EAS decreases from 349 to 267 cm^2 mg^{-1} Pt after 70.5 h operation. The EAS loss may result from the deterioration of Pt metal and the worse contact between the catalyst and the electrolyte. The CV results indicate that the cathode 'triple-phase boundaries' where the electrolyte, oxygen, and electrically connected Pt/C catalyst contact together in cathode, are decreasing after the life tests. The aging of cathodic catalyst would be one of the important reasons for the performance decay of DDFC cathode.

XRD patterns of cathodic Pt/C catalyst measured before and after the life test are shown in Fig. 2. The first diffraction peaks for cathode Pt/C at 2θ about 26° can be attributed to the hexagonal graphite structures (0 0 2) of the XC-72 carbon black support. The Pt has a face-centered cubic (fcc) structure showing the major diffraction peaks of Pt (1 1 1), Pt (2 0 0), Pt (2 2 0), Pt (3 1 1), Pt (2 2 2), and so on. The Pt (2 2 0) peak is chosen to calculate the mean particle size of fresh and aged Pt

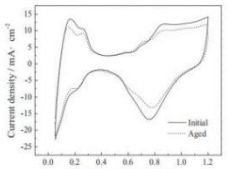

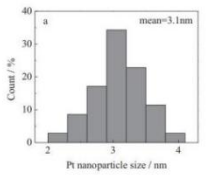

Fig. 1 – Cyclic voltammograms of Pt at the initial and aged cathode, at a scan rate of 0.01 V s^{-1}, in a potential range between 0.05 and 1.2 V vs. DHE.

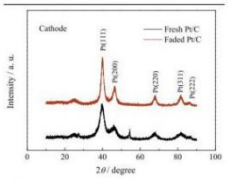

Fig. 2 – XRD patterns of cathodic catalysts before and after durability test.

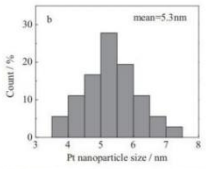

Fig. 4 – Histograms of particle size distributions of cathodic Pt catalyst before and after durability test: (a) initial Pt; (b) aged Pt.

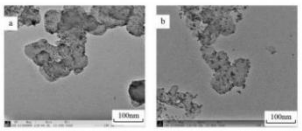

Fig. 3 – TEM images of cathodic Pt/C catalyst before and after durability test: (a) initial Pt/C; (b) aged Pt/C.

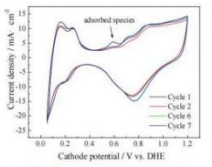

Fig. 5 – Cyclic voltammograms of cathode after 40.5 h operation, at a scan rate of 0.01 V s^{-1}, in a potential range between 0.05 and 1.2 V vs. DHE.

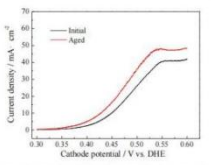

Fig. 6 – Linear sweep voltammograms of DME permeating through the membranes at the cathode before and after durability test.

catalysts according to Debye–Scherrer formula because it is isolated from the diffraction peaks of carbon support [37]. The particle size of cathodic catalyst grows from an original value of 3.0 nm to 5.4 nm. The sintering rate of cathodic catalyst is evidently high because small Pt particles are unstable in harsh corrosion operation environment of cathode. Besides, DME crossover may aggravate cathodic Pt degradation.

TEM images of the cathodic Pt/C catalyst before and after durability test are presented in Fig. 3 and the corresponding histograms are shown in Fig. 4. The dark black portions in Fig. 3 are Pt grains, and the gray portions are carbon support grains. The results show that Pt nanoparticles before durability test is small and even without agglomeration. After the durability test, Pt grains grow up evidently, which is consistent with the above XRD results. The growth of the Pt particles must be the main cause of the cathodic catalyst failure.

Fig. 5 shows the CV scans of cathode after 40.5 h operation. The adsorbed DME and/or intermediates species which accumulate on cathodic Pt surface would be oxidized after the CV scans. With an increasing cycling number, the oxidation peak of the adsorbed species gradually decreased. Simultaneously, the hydrogen desorption peak recovers. The CV profiles reach a steady state at the 6th cycle, and no further changes are observed from cycle 6 to cycle 7. It is indicated that the absorbed DME and/or intermediates have been fully oxidized. The poisoning of catalyst by adsorbed DME and/or intermediates species can debase the O_2 reduction reaction on Pt catalyst surface, which is another cause of the cathode catalyst failure.

The LSV curves for determining the DME crossover rate of fresh and faded cathode are shown in Fig. 6. At high cathode potential region, the DME electro-oxidation reaction is not dominated by the catalytic activity of the cathode, but governed by the DME permeation rate. The limiting current density of DME oxidation increases from about 41 mA cm^{-2} to 48 mA cm^{-2} after the durability test. The DME permeation rate gets higher after the durability test. It means that DME concentration at the interface between the anode and the membrane gets higher after the durability test, which caused by anode degradation. DME crossover is concomitant with performance loss of cathodic Pt due to the formation of mixed potential on cathodic catalyst. This mixed potential response [38] is also very deleterious and accelerates the sintering/degradation of cathodic Pt nanoparticles. Therefore, anode degradation is another factor which accelerates cathodic catalyst degradation.

Conclusions

The durability of cathodic Pt/C catalyst for DDFC has been investigated at a constant current density of 30 mA cm^{-2} for 70.5 h discontinuous operation under ambient pressure and at a cell temperature of 60 °C. The performance of cathodic Pt/C catalyst is decreased after the durability test. The cathodic EAS reduces from 349 to 267 cm^2 mg^{-1} Pt after 70.5 h operation. The particle size of cathodic Pt catalyst increased from an original value of 3.0 nm to 5.4 nm. The poisoning of catalyst by absorbed DME and/or intermediates is another cause of cathodic catalyst degradation. Furthermore, the anode decay accelerated the DME crossover and the severer poisoning of catalyst aggravated the degradation of the Pt/C cathodic catalyst in consequence.

Acknowledgment

This work is financially supported by Young Creative Talent Training Project of Heilongjiang Province (UNPYSCT-2016108), Preliminary Investigation Project of Mudanjiang Normal University (GY201201), Doctoral Research Fund of Mudanjiang Normal University (MSB201208), Innovation Project of University Students (201610233031) and Natural Science Foundation of Heilongjiang Province (QC2014C009).

REFERENCES

[1] Fletcher T, Thring R, Watkinson M. Int J Hydrogen Energy 2016;41:21503.
[2] Ye LC, Gao Y, Zhu SY, Zheng JS, Li P, Zheng JP. Int J Hydrogen Energy 2017;42:7241.
[3] Authayanun S, Saebea D, Patcharavorachot Y, Arpornwichanop A. Int J Hydrogen Energy 2017;42:1977.
[4] Wang ZB, Zuo PJ, Yin GP. Fuel Cells 2009;9:106.
[5] Lai QZ, Yin GP, Wang ZB, Du CY, Zuo PJ, Cheng XQ. Fuel Cells 2008;8:399.
[6] Zhao TS, Xu C, Chen R, Yang WW. Prog Energy Combust Sci 2009;35:275.
[7] Shen SY, Zhao TS, Xu JB. Energy Environ Sci 2011;4:1428.
[8] Xie F, Chen C, Meng H, Shen PK. Fuel Cells 2007;7:319.
[9] Shao YY, Liu J, Wang Y, Lin YH. J Mater Chem 2009;19:46.
[10] Liu P, Yin GP, Du CY. Electrochem Commun 2008;10:1471.
[11] Ileo P, Nagao M, Sano M, Hibino T. J Electrochem Soc 2008;155:B92.
[12] Li Q, Wu G, Johnston CM, Zelenay P. Electrocatalysis 2014;5:310.
[13] Li Q, Wen XD, Wu G, Chung HT, Gao R, Zelenay P. Angew Chem Int Ed 2015;127:7634.
[14] Cai KD, Wang C, Pu WH, Gao Y, Mao ZQ. Int J Hydrogen Energy 2012;37:12605.
[15] Semelsberger TA, Borup RL, Greene HL. J Power Sources 2006;156:497.
[16] Kerangueven G, Coutanceau C, Sibert E, Leger JM, Lamy C. J Power Sources 2006;157:318.
[17] Tong YJ, Lu IL, Zhang Y, Gao YZ, Yin GP, Osawa M, et al. J Phys Chem C 2007;111:3838.
[18] Liu Y, Murooka M, Mitsushima S, Ota KI, Kamiya I. Electrochim Acta 2007;52:5781.
[19] Lu LL, Yin GP, Tong YJ, Zhang Y, Gao YZ, Osawa M, et al. J Electroanal Chem 2008;619:143.
[20] Lu LL, Yin GP, Tong YJ, Zhang Y, Gao YZ, Osawa M, et al. J Electroanal Chem 2010;642:82.
[21] Tadao H, Yasuyuki T, Hiroyuki T, Naoaki T, Susumu Y. Electr Eng Jpn 2005;150:19.
[22] Zhang Y, Lu LL, Tong YJ, Osawa M, Ye S. Electrochim Acta 2008;53:6093.
[23] Lu LL, Yin GP, Wang ZB, Cai KD, Gao YZ. Catal Commun 2009;10:971.
[24] Yu JH, Choi HG, Cho SM. Electrochem Commun 2005;7:1385.
[25] Yoo JH, Choi HG, Chung CH, Cho SM. J Power Sources 2006;163:103.
[26] Jiang LH, Sun GQ, Wang SL, Wang GX, Xin Q, Zhou ZH, et al. Electrochem Commun 2005;7:663.
[27] Schmittinger WG, Vahidi A. J Power Sources 2008;180:1.
[28] Du CY, Chen M, Cao XY, Yin GP, Shi PF. Electrochem Commun 2009;11:486.
[29] Zhang SS, Yuan XZ, Wang HJ, Merida W, Zhu H, Shen J, et al. Int J Hydrogen Energy 2009;34:388.
[30] Zhang S, Shao YY, Yin GP, Lin YH. Angew Chem 2010;49:2211.
[31] Baturina OA, Swider-Lyons KE. J Electrochem Soc 2009;156:B1423.
[32] Wang ZB, Zuo PJ, Chu YY, Shao YY, Yin GP. Int J Hydrogen Energy 2009;34:4387.
[33] Xing LH, Yin GP, Wang ZB, Zhang S, Gao YZ, Du CY. J Power Sources 2012;198:170.
[34] Wu YN, Liao SJ, Su HN, Dang D, Liu B. Fuel Cells 2010;10:920.
[35] Ren XM, Springer TE, Zawodzinski TA, Gottesfeld S. J Electrochem Soc 2000;147:466.
[36] Xing LH, Gao YZ, Wang ZB, Du CY, Yin GP. Int J Hydrogen Energy 2011;36:11102.
[37] H Zhang Z, Ge JJ, Ma L, Liao JH, Lu TH, Xing W. Fuel Cells 2009;09:114.
[38] Hibino T, Kobayashi K. J Electrochem Soc 2014;5:H326.

14.Jiang J. Observation of a 3-in-1 Russian-doll-like Complex in Solution[J]. Chemical Research in Chinese Universities, 2021: 1-3.（SCI 检索收录三区，IF=1.307）

Letter

Observation of a 3-in-1 Russian-doll-like Complex in Solution

JIANG Jian✉

Received March 25, 2021
Accepted June 30, 2021
© Jilin University, The Editorial Department of Chemical Research in Chinese Universities and Springer-Verlag GmbH

Keywords Schiff-base macrocycle; Russian-doll-like; 3-in-1 complex; $CBPQT^{4+}$; Tetrathiafulvalene(TTF)

Supramolecular chemistry is based on non-covalent interactions that enable molecular recognition. By weak interactions, a large number of structures, such as rotaxane[1,2] and catenane[3,4], as well as more complex structures[5,6] have been assembled. The Borromean rings[5,6] and Schiff-base macrocycles[7,8] are becoming attractive in these years because of their diversity of structures and ability to self-assemble. Till now, researchers have reported a multitude of other fascinating supramolecular constructs[9,10].

In the recent years, so much attention has been paid to the synthesis and supramolecular chemistry of macrocycles constructed from Schiff base condensation[7,8]. Simple and elegant, this reaction can be used to attain large and functional macrocycles[7,8], as well as more complex structures[11]. These cycles are attractive for their supramolecular structure[12], liquid crystallinity[13], and potential for catalysis[14] and sensor[15].

We have reported that wide-mouthed Schiff-base macrocycle 1 and some related cycles bind organic cations in their interiors[12]. Remarkably, macrocycle 1 adopts a calixarene-like cone conformation with a very wide(ca. 1.23 nm×0.93 nm from semi-empirical calculations) opening that allows it to bind the macrocycle cyclobis(paraquat-*p*-phenylene)($CBPQT^{4+}$). From a Jobplot analysis, the host-guest complex($CBPQT^{4+}\subset$ 1) has a 1:1 stoichiometry and the binding constant is substantial[$(1.68\pm0.53)\times10^5$ $L\cdot mol^{-1}$].

By electrostatic attraction, macrocycle 1 and $CBPQT^{4+}$ (Fig.1) have been assembled to a unique ring-in-ring structure. The complex is a promising precursor for constructing Russian-doll-like superstructures, which have attracted so much attention in this decade. In recent years, although the assembly of Russian-doll-like structure is a target for supramolecular research, only a few cases of such structures have been reported[16–20], which may be attributed to the lack of large and suitable macrocycles. Among cases reported, however, to the best of our knowledge, there is no example of such hierarchical architectures assembled by Schiff-base macrocycle. Herein, we report the observation of a Russian-doll-like structure constructed by Schiff-base macrocycle, tetracationic cyclophane and a small organic molecule in solution.

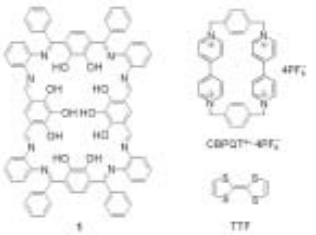

Fig.1 Structures of compounds 1, $CBPQT^{4+}\cdot4PF_6^-$ and TTF

Originally reported by Stoddart in 1988[21], $CBPQT^{4+}\cdot4PF_6^-$ has since aroused many interests to assemble varies of superstructures, such as host-guest complexes[22], rotaxanes[23] and catenanes[24]. In each case, the electron deficient $CBPQT^{4+}$ moiety interacts with the electron rich guest through electrostatic interactions. One notable example is its ability to form an inclusion structure with electron-rich tetrathiafulvalene(TTF), which shows a 1:1 stoichiometry[21] and the high binding constant in MeCN[25]. Formation of the host-guest complex encouraged us to study whether TTF can be bound inside the cavity of $CBPQT^{4+}$ in the complex $CBPQT^{4+}\subset$ 1 to form a unique Russian-doll-like 3-in-1 complex.

The ^1H NMR spectra of different assemblies of macrocycle 1, cyclobis(paraquat-*p*-phenylene), and tetrathiafulvalene in acetone-d_6 are exhibited in Fig.2. In the spectrum of macrocycle 1, the peaks at δ 14.47 and δ 14.35 are assigned to the hydroxyl protons. Adding $CBPQT^{4+}$ to the solution of macrocycle 1 resulted in the downfield shift to δ 14.76 and δ 14.67, respectively. Changes of chemical shift of hydroxyl protons indicated $CBPQT^{4+}$ was included inside macrocycle 1(the inclusion structure was proved by 2D ROESY NMR and MALDI-TOF MS[26]). When TTF was added to the solution, the two resonances further shifted to δ 14.79 and δ 14.78, respectively, indicating there is an interaction between tetrathiafulvalene and the ring-in-ring $CBPQT^{4+}\subset$ 1 structure.

✉ JIANG Jian
jianjiang@mdjnuedu.cn
School of Chemistry and Chemical Engineering, Mudanjiang Normal University, Mudanjiang 157000, P. R. China

Letter

Observation of a 3-in-1 Russian-doll-like Complex in Solution

JIANG Jian[✉]

Received March 25, 2021
Accepted June 30, 2021
© Jilin University, The Editorial Department of Chemical Research in Chinese Universities and Springer-Verlag GmbH

Keywords Schiff-base macrocycle; Russian-doll-like; 3-in-1 complex; CBPQT⁴⁺; Tetrathiafulvalene (TTF)

Supramolecular chemistry is based on non-covalent interactions that enable molecular recognition. By weak interactions, a large number of structures, such as rotaxane[1,2] and catenane[3,4], as well as more complex structures[5,6] have been assembled. The Borromean rings[5,6] and Schiff-base macrocycles[7,8] are becoming attractive in these years because of their diversity of structures and ability to self-assemble. Till now, researchers have reported a multitude of other fascinating supramolecular constructs[9-12].

In the recent years, so much attention has been paid to the synthesis and supramolecular chemistry of macrocycles constructed from Schiff base condensation[7,8]. Simple and elegant, this reaction can be used to attain large and functional macrocycles[7,8], as well as more complex structures[13]. These cycles are attractive for their supramolecular structure[8], liquid crystallinity[8], and potential for catalysis[8] and sensor[8].

We have reported that wide-mouthed Schiff-base macrocycle 1 and some related cycles bind organic cations in their interiors[8]. Remarkably, macrocycle 1 adopts a calixarene-like cone conformation with a very wide(ca. 1.23 nm×0.93 nm from semi-empirical calculations) opening that allows it to bind the macrocycle cyclobis(paraquat-*p*-phenylene)(CBPQT⁴⁺). From a Jobplot analysis, the host-guest complex(CBPQT⁴⁺⊂ 1) has a 1:1 stoichiometry and the binding constant is substantial[(1.68±0.53)×10⁶ L·mol⁻¹].

By electrostatic attraction, macrocycle 1 and CBPQT⁴⁺ (Fig.1) have been assembled to a unique ring-in-ring structure. The complex is a promising precursor for constructing Russian-doll-like superstructures, which have attracted so much attention in this decade. In recent years, although the assembly of Russian-doll-like structure is a target for supramolecular research, only a few cases of such structures have been reported[14-16], which may be attributed to the lack of large and suitable macrocycles. Among cases reported, however, to the best of our knowledge, there is no example of such hierarchical architectures assembled by Schiff-base macrocycle. Herein, we report the observation of a Russian-doll-like structure constructed by Schiff-base macrocycle, tetracationic cyclophane and a small organic molecule in solution.

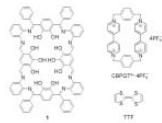

Fig.1 Structures of compounds 1, CBPQT⁴⁺·4PF6 and TTF

Originally reported by Stoddart in 1988[17], CBPQT⁴⁺·4PF6 has since aroused many interests to assemble varies of superstructures, such as host-guest complexes[18], rotaxane[19] and catenane[20]. In each case, the electron-deficient CBPQT⁴⁺ moiety interacts with the electron rich guest through electrostatic interactions. One notable example is its ability to form an inclusion structure with electron-rich tetrathiafulvalene(TTF), which shows a 1:1 stoichiometry[21] and the high binding constant in MeCN[18]. Formation of the host-guest complex encouraged us to study whether TTF can be bound inside the cavity of CBPQT⁴⁺ in the complex CBPQT⁴⁺⊂ 1 to form a unique Russian-doll-like 3-in-1 complex.

The ^{1}H NMR spectra of different assemblies of macrocycle 1, cyclobis(paraquat-*p*-phenylene), and tetrathiafulvalene in acetone-d_6 are exhibited in Fig.2. In the spectrum of macrocycle 1, the peaks at δ 14.47 and δ 14.35 are assigned to the hydroxyl protons. Adding CBPQT⁴⁺ to the solution of macrocycle 1 resulted in the downfield shift to δ 14.76 and δ 14.67, respectively. Changes of chemical shift of hydroxyl protons indicated CBPQT⁴⁺ was included inside macrocycle 1(the inclusion structure was proved by 2D ROESY NMR and MALDI-TOF MS[18]). When TTF was added to the solution, the two resonances further shifted to δ 14.79 and δ 14.70, respectively, indicating there is an interaction between tetrathiafulvalene and the ring-in-ring CBPQT⁴⁺⊂ 1 structure.

✉ JIANG Jian
Jiangjing@nenu.edu.cn
School of Chemistry and Chemical Engineering, Mudanjiang Normal University, Mudanjiang 157000, P. R. China

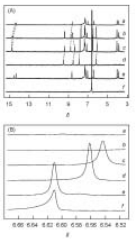

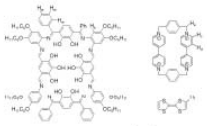

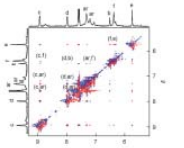

Fig.2 ^{1}H NMR spectra of different assemblies(macrocycle 1:CBPQT⁴⁺:TTF=1:1:4, molar ratio)(A) and amplified spectra around δ 6.6 from(A)(400 MHz, acetone-d_6, 298 K)(B)
a. Macrocycle 1; b. 1+CBPQT⁴⁺; c. 1+CBPQT⁴⁺+TTF; d. CBPQT⁴⁺+TTF; e. 1+TTF; f. TTF.

However, for the combination of macrocycle 1 and TTF, without CBPQT⁴⁺, no chemical shift change was observed for macrocycle 1 and TTF, which is shown in Fig.2(A) and (B). The reason for this is macrocycle 1 and tetrathiafulvalene are electron-rich structures, which are reluctant to form complex.

Addition of TTF to CBPQT⁴⁺ in solution caused chemical shift of TTF changed from δ 6.61 to δ 6.56 as shown in Fig.2(B), which indicates that a 1:1 complex was formed between CBPQT⁴⁺ and TTF as reported in the literature[18]. In the above solution, the resonance of TTF shifted further to δ 6.54 with the addition of macrocycle 1. Meanwhile, when macrocycle 1 was added, all four peaks of CBPQT⁴⁺ in TTF⊂CBPQT⁴⁺ complex shifted upfield. These changes of resonances for CBPQT⁴⁺ and TTF indicate macrocycle 1 has included both CBPQT⁴⁺ and TTF in its cavity and a Russian-doll-like 3-in-1 complex is formed. The 3-in-1 complex is grouped together by electrostatic attraction in electron-rich electron-deficient and electron-rich structures.

2D ROESY ^{1}H NMR spectrum(Fig.3) also proved the existence of the Russian-doll-like structure in solution. In Fig.3, cross-peaks between H_c and H_{ac}, H_d and H_b, H_d and H_{ac} are observed, which indicates macrocycle 1 includes CBPQT⁴⁺ inside its cavity. Couplings between H_d and H_a, H_d and H_b show that TTF is inside CBPQT⁴⁺. Spin-coupling between H_b and H_{ac} indicates TTF interacts with the aryl rings of macrocycle, consisting with the Russian-doll-like structure.

Fig.3 2D ROESY spectrum of the Russian-doll-like structure in 1:3 $CDCl_3/CD_3CN$ with a mixing time of 1.2 ms(400 MHz, 298 K)
Macrocycle 1: CBPQT⁴⁺:TTF= 1:3:4. The resonances around δ 7.2 are assigned to protons on ketimine phenyl and noted as "e".

Formation of hierarchical architecture was verified by MALDI-TOF mass spectrometry. In mass spectrum(Fig.4), we observe a peak attributed to [1+CBPQT⁴⁺+TTF+H₂O+3PF₆⁻]⁺, which proved the existence of 3-in-1 complex. In the spectrum, some other combinations would also be expected, including [CBPQT⁴⁺+3PF₆⁻]⁺, and [1+CBPQT⁴⁺+3PF₆⁻]⁺. Some additional peaks were not assigned, which might come from complexes with the matrix.

In our previous work[8,9], we found that structures like macrocycle 1 are very flexible and CBPQT⁴⁺ is movable

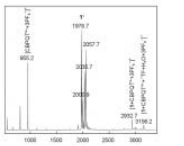

Fig.4 MALDI-TOF mass spectrum of the 3-in-1 complex

inside the macrocycle[8,9]. For this reason, the Russian-doll-like structure was simulated by inserting TTF⊂CBPQT⁴⁺ structure "from top" and "from bottom" of the macrocycle 1, and then energy-minimizing with PM3. Fig.5 exhibits one of conformations of our simulations(other simulation results are shown in the Electronic Supplementary Material of this paper). It indicates that three compounds can group together in the Russian-doll-like complex.

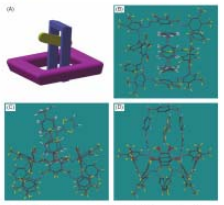

Fig.5 Graphical representation of 3-in-1 complex(A) and energy minimized(PM3) models of the Russian-doll-like structure with Spartan'08(B—D)
(B) The top view of one conformation; (C, D) side views of the conformation.

In summary, we proved by using NMR and mass spectrum that a 3-in-1 Russian-doll-like structure was assembled in solution. The development of complex architectures, such as these may open the route to innovative robust supramolecular designs. We are continuing to explore the host-guest chemistry in widemouthed Schiff base macrocycles.

Electronic Supplementary Material

Supplementary material is available in the online version of this article at https://doi.org/10.1007/s40242-021-1146-y.

Acknowledgements

This work was supported by the Archival Projects of the Department of Education of Heilongjiang Province, China(No.12653KSYY0010), the National Topic Cultivation Project of Mudanjiang Normal University, China(No.GP2020001) and the Key Project of Department of Education of Heilongjiang Province, China (No.12653KZD03).

The author thanks Prof. Mark J. MacLachlan(Department of Chemistry, University of British Columbia, CA) for support and discussions. The author also thanks the Natural Science and Engineering Research Council of Canada for the financial support while he worked in UBC, CA.

Conflicts of Interest

The authors declare no conflicts of interest.

References

[1] Tauba S., Komai Y., Fujikawa S., Nishiyama Y., *Chem. Eur. J.*, 2021, 27, 1966
[2] Li J., Han X.-N., Zhou H.-K., Han Y., Chen C.-F., *J. Org. Chem.*, 2020, 85, 11465
[3] Zhang Y., Chen G. C., Wang Y., Zhang X. J., Wang H. Y., Cao F. H., Sue A. C.-H., Li H., *Chem. Commun.*, 2018, 55, 11887
[4] Datta S., Kato Y., Higashiharaguchi S., Aratsu K., Isobe A., Saito T., Prabhu D. D., Kitamoto Y., Hallwass M. J., Smith A. J., Dalgliesh R., Mahmoudi N., Pesce L., Perego C., Pavan G. M., Yagai S., *Nature*, 2020, 583, 400
[5] Chen X. Y., Shen D., Cai K., Jiao Y., Wu H., Song B., Zhang L., Tan Y., Wang Y., Feng Y., Stern C. L., Stoddart J. F., *J. Am. Chem. Soc.*, 2020, 142, 20152
[6] Fernand Y., Huc I., *Acc. Chem. Res.*, 2018, 51, 970
[7] Gao W.-X., Feng H.-J., Lin Y.-J., Jin G.-X., *J. Am. Chem. Soc.*, 2019, 141, 9160
[8] Lu Y., Zhang H.-N., Jin G.-X., *Acc. Chem. Res.*, 2018, 51, 2148
[9] Chakraborty T., Mukherjee S., Parveen R., Chandra A., Samanta D., Das D., *New J. Chem.*, 2021, 45, 2050
[10] Cornelio G., Chierici E. P., Faita S., Sala S. D., *Angew. Chem.*, 2016, 55, 10330
[11] Zhang D. W., Wang H., Li Z. T., *Chem. J. Chinese Universities*, 2020, 41(6), 1139
[12] Zhang L., Li H. F., Chen P., Sun W., Yan P., *Chem. Res. Chinese Universities*, 2016, 32(4), 534
[13] Urbani M., Torres T., *Chem. Eur. J.*, 2008, 24, 6163
[14] Jiang J., MacLachlan M. J., *Org. Lett.*, 2018, 10, 1020
[15] Gubo S., Crane A. K., MacLachlan M. J., *Chem. Commun.*, 2011, 47, 1169
[16] Rees K. V., Love J. B., *Dalton Trans.*, 2021, 50, 1610
[17] Chaudhry M. T., Lalji F., MacLachlan M. J., *Chem. Commun.*, 2018, 54, 11869
[18] Chen Z., Goku S., White N., Lalji F., MacLachlan M. J., *Chem. Eur. J.*, 2016, 22, 17857
[19] Jiang J., Dong R. Y., MacLachlan M. J., *Chem. Commun.*, 2018, 51, 16205
[20] Rechac C., Carabyka, 2017, 7, 165
[21] Mathus S. J., Cameron S. A., Brooker S., *Inorg. Chem.*, 2018, 57, 2480
[22] Jiang J., MacLachlan M. J., *Chem. Commun.*, 2009, 5950
[23] Cai K., Lipke M. C., Liu Z., Nelson J., Cheng T., Shi Y., Cheng C., Shen D., Han J.-M., Vemuri S., Feng Y., Stern C. L., Goddard W. A., Wasielewski M. R., Stoddart J. F., *Nat. Commun.*, 2018, 9, 5275
[24] Rasmussen S. A.L., Gang J. G., Haver R., Odell B., Claridge T. D. W., Herz L. M., Anderson H. L., *J. Am. Chem. Soc.*, 2015, 137, 12713
[25] Dalgarno S. J., Fisher J., Raston C. L., *Chem. Eur. J.*, 2006, 12, 2772
[26] Dang H., Hashimoto Y., Kidera Y., Nagaoka A., Kobigai K., Kawahata M., Miyazawa T., Yamaguchi K., *Org. Le.*, 2015, 17, 2154
[27] Odell B., Reddington M. V., Slawin A. M. Z., Spencer N., Stoddart J. F., Williams D. J., *Angew. Chem. Int. Ed.*, 1988, 27, 1547
[28] Zhang D., Sato M. A., Lemaire L., Harmel W. Y., MacLachlan M. J., *Angew. Chem. Int. Ed.*, 2020, 59, 4703
[29] Wu Y., Frasconi M., Liu W.-G., Young R. M., Goddard W. A., Wasielewski M. R., Stoddart J. F., *J. Am. Chem. Soc.*, 2020, 142, 8530
[30] Grunder S., McGrier P. L., Whalley A. C., Boyle M. M., Stern C., Stoddart J. F., *J. Am. Chem. Soc.*, 2010, 132, 17691
[31] Philp D., Slawin A. M. Z., Spencer N., Stoddart J. F., Williams D. J., *J. Chem. Soc., Chem. Commun.*, 1991, 1584
[32] Nielsen M. B., Jeppesen J. O., Lau J., Lomholt C., Damgaard D., Jacobsen J. P., Becher J., Stoddart J. F., *J. Org. Chem.*, 2001, 66, 3559

科研论文（共 32 篇）

1.Shao Y, Chang Y, Zhang S, et al. Impact of polymer backbone fluorination on the charge generation/recombination patterns and vertical phase segregation in bulk heterojunction organic solar cells[J]. Frontiers in chemistry, 2020, 8: 144.

2.Shao Y, Jiang Z, Zhang Q, et al. Progress in nonmetal‐doped graphene electrocatalysts for the oxygen reduction reaction[J]. ChemSusChem, 2019, 12(10): 2133-2146.

3.邵艳秋,姜封庆,孙玺,常玉莹,王星月,宋冰,黄家辉.乙炔氢氯化反应铜基催化剂研究进展[J].塑料工业,2021,49(03):27-31.

4.邵艳秋,张宇婷,姜振双,刘素娟,任玉兰,王丽杰.水解剂氟化铵对Fe-SBA-15结构及催化性能的影响[J].无机盐工业,2019,51(09):97-101.

5.邵艳秋,于平,郑友进,王丽杰,王星月.氧化锌基阵列染料敏化太阳能电池研究进展[J].人工晶体学报,2019,48(10):1967-1975.

6.邵艳秋,赵婷婷,付文婷,郑骐朋.氨基改性 SBA-15 介孔材料的制备及对Pb(Ⅱ)的吸附性能研究[J].硅酸盐通报,2016,35(02):587-592.

7.邵艳秋,芦原萱,付文婷,苏爽月,郑炜.盐对氨基改性 SBA-15 吸附 Pb^{2+}性能的影响研究[J].硅酸盐通报,2016,35(11):3649-3653.

8.Yang W, Jiang R, Liu C, et al. Triptycene-Based Porous Chalcogen-Bonded Organic Frameworks[J]. Crystal Growth & Design, 2021, 21(11): 6497-6503.

9.Cai X, Ma Y, Zhou Q, et al. Synergistic effects of phases in the selective oxidation of isobutane over supported $(NH_4)_3HPMo_{11}VO_{40}$ catalysts[J]. Reaction Kinetics, Mechanisms and Catalysis, 2021, 133(1): 293-308.

10.Wei C, Lu G, Guo C, et al. Ethylthio-substituted sandwich phthalocyaninato

europium (III) semiconductors for sensing NO_2 and NH_3: Effect of the extended π-conjugate systems on tuning the conductivity and sensing behavior[J]. Organic Electronics, 2021, 93: 106151.

11.Cai X, Zhou Q, Ma Y, et al. Selective Removal of CO in Hydrocarbons-Rich Industrial Off-gases over CuO-Ce_xZr_1−xO_2 Catalysts [J]. Catalysis Surveys from Asia, 2021, 25(1): 68-75.

12.Cai X, Wei C, Dong J, et al. Dimeric phthalocyanine-involved double-decker complex-based electrochemical sensor for simultaneous detection of acetaminophen and ascorbic acid[J]. Journal of Materials Science: Materials in Electronics, 2019, 30(3): 1976-1983.

13.Cai X, Ning H. Crystal structure of di-μ-acetato-diacetatobis (μ-6, 6′-dimethoxy-2,2′-{[(propane-1,3-diylbis (azanylylidene)] bis (methanylylidene)} diphenolato) tetrazinc[J]. Acta Crystallographica Section E: Crystallographic Communications, 2015, 71(12): 217-218.

14.姜力,周启,陈玉锋,蔡雪.5,15-二(二茂铁基)-卟啉酞菁钇的结构和振动光谱的密度泛函理论研究[J].原子与分子物理学报,2021,38(03):47-51.

15.孙守鹏,魏闯宇,宁桧,蔡雪.全波谱太能材料氟代酞菁锌分子 ZnPc($C_{24}F_{48}$)的研究[J].牡丹江大学学报,2018,27(06):107-109.

16.宁桧,孙守鹏,蔡雪.轴向取代卟啉锌结构和光谱性质的研究[J].牡丹江师范学院学报(自然科学版),2017(01):39-42

17.李梓萌,蔡雪.咔唑类取代酞菁锌染料敏化性能研究[J].牡丹江师范学院学报(自然科学版),2016(01):44-46.

18.Xing L H, Shi X T, Wang Y X, et al. Electrochemical Synthesis of Ni-SnO_2 Composite Electrodes for Hydrogen Evolution Reaction in Alkaline Solution[J]. Int. J. Electrochem. Sci, 2022, 17(220530): 2.

19. Xing L, Wang Y, Shi X, et al. Investigation of Pt/C and Pt-Ru/C Mixed Catalyst for DME Oxidation in Direct Dimethyl Ether Fuel Cells[J]. Int. J. Electrochem. Sci, 2020, 15: 10382-10391.

20.Xing L, Wang Y, Sui C, et al. Investigation of Pt/SnO_2/C Catalyst for Dimethyl Ether Oxidation in DDFC[J]. Int. J. Electrochem. Sci, 2020, 15: 2375-2384.
21.Xing L H, Yin G P, Du C Y, et al. Investigation on the durability of direct dimethyl ether fuel cell. Part II: Cathode degradation[J]. International Journal of Hydrogen Energy, 2017, 42(26): 16695-16699.
22.王宜鑫,邢乐红,石鑫婷,孟凡旭,张亮,董瑞.镀液中氨基磺酸镍质量浓度对电镀镍层析氢催化活性的影响[J].电镀与涂饰,2022,41(01):6-9.
23.邢乐红,王宜鑫,王慧,左明辉,孙芳,梁志男.氨基乙酸对硫酸盐体系电镀镍-铁合金的影响[J].电镀与涂饰,2019,38(19):1039-1041.
24.邢乐红,黎德育,李宁,左明辉,李晶.抗坏血酸对硫酸盐体系镍–铁合金镀液稳定性的影响[J].电镀与涂饰,2018,37(12):526-528.
25.邢乐红,杨晶,王海鹏,达铭,李姗,崔术新.硫脲对低磷化学镀镍稳定性的影响[J].牡丹江师范学院学报(自然科学版),2016(03):41-42.
26.云观,郭朝阳,张萌.胶原蛋白提取及检测方法研究进展[J].山东化工,2022,51(07):70-72
27.云观,刘全菊,张可鑫,蒋舰.达夫反应法合成 2,4,6-三羟基苯-1,3,5-三甲醛反应条件研究[J].长春师范大学学报,2021,40(02):95-98.
28.云观,陈佳丽,蒋舰,邵艳秋.有机化学实验中废液及固废的处理[J].山东化工,2020,49(05):257-258.
29.云观,陈佳丽,刘艳爽,曹明星,杨春文.东北林蛙消化系统 LDH 同工酶表型的季节变化[J].黑龙江畜牧兽医,2018(01):215-217.
30.陈佳丽,云观,金建丽,杨松鹏,田新民.东北林蛙消化系统 SOD 和 POD 同工酶电泳分析[J].黑龙江畜牧兽医,2017(01):219-221.
31.Jiang J. Observation of a 3-in-1 Russian-doll-like Complex in Solution[J]. Chemical Research in Chinese Universities, 2021: 1-3.

32.李静,蒋舰,贠涛,邵艳秋.功能性离子液体的应用研究进展[J].黑龙江工业学院学报(综合版),2021,21(02):98-103.

邵艳秋发表科研论文目录（共 7 篇）

1.Shao Y, Chang Y, Zhang S, et al. Impact of polymer backbone fluorination on the charge generation/recombination patterns and vertical phase segregation in bulk heterojunction organic solar cells[J]. Frontiers in chemistry, 2020, 8: 144.

2.Shao Y, Jiang Z, Zhang Q, et al. Progress in nonmetal‐doped graphene electrocatalysts for the oxygen reduction reaction[J]. ChemSusChem, 2019, 12(10): 2133-2146.

3.邵艳秋,姜封庆,孙玺,常玉莹,王星月,宋冰,黄家辉.乙炔氢氯化反应铜基催化剂研究进展[J].塑料工业,2021,49(03):27-31.

4.邵艳秋,张宇婷,姜振双,刘素娟,任玉兰,王丽杰.水解剂氟化铵对Fe-SBA-15结构及催化性能的影响[J].无机盐工业,2019,51(09):97-101.

5.邵艳秋,于平,郑友进,王丽杰,王星月.氧化锌基阵列染料敏化太阳能电池研究进展[J].人工晶体学报,2019,48(10):1967-1975.

6.邵艳秋,赵婷婷,付文婷,郑骐朋.氨基改性 SBA-15 介孔材料的制备及对Pb(Ⅱ)的吸附性能研究[J].硅酸盐通报,2016,35(02):587-592.

7.邵艳秋,芦原萱,付文婷,苏爽月,郑炜.盐对氨基改性 SBA-15 吸附 Pb^{2+}性能的影响研究[J].硅酸盐通报,2016,35(11):3649-3653.

1.Shao Y, Chang Y, Zhang S, et al. Impact of polymer backbone fluorination on the charge generation/recombination patterns and vertical phase segregation in bulk heterojunction organic solar cells[J]. Frontiers in chemistry, 2020, 8: 144.

frontiers in Chemistry

ORIGINAL RESEARCH
published: 05 March 2020
doi: 10.3389/fchem.2020.00144

Impact of Polymer Backbone Fluorination on the Charge Generation/Recombination Patterns and Vertical Phase Segregation in Bulk Heterojunction Organic Solar Cells

Yanqiu Shao[1], Yuying Chang[1], Suju Zhang[1], Mingyue Bi[1], Shengjian Liu[2], Dallang Zhang[3], Shirong Lu[4] and Zhipeng Kan[4]**

[1] *School of Chemistry and Chemical Engineering, Mudanjiang Normal University, Mudanjiang, China,* [2] *Guangzhou Key Laboratory of Materials for Energy Conversion and Storage, Guangdong Provincial Engineering Technology Research Center for Materials for Energy Conversion and Storage, School of Chemistry, South China Normal University (SCNU), Guangzhou, China,* [3] *Institute of Advanced Interdisciplinary Studies, Chongqing University, Chongqing, China,* [4] *Organic Semiconductor Research Center, Chongqing Institute of Green and Intelligent Technology, Chinese Academy of Sciences, Chongqing, China*

OPEN ACCESS

Edited by:
Erjang Wang,
Chalmers University of Technology, Sweden

Reviewed by:
Lei Ying,
South China University of Technology, China
Hua Tan,
Xiangtan University, China

**Correspondence:*
Yanqiu Shao
shaoyanqiu1969@163.com
Zhipeng Kan
kanzhipeng@cigit.ac.cn

Specialty section:
This article was submitted to Physical Chemistry and Chemical Physics, a section of the journal Frontiers in Chemistry

Received: 16 December 2019
Accepted: 17 February 2020
Published: 05 March 2020

Citation:
Shao Y, Chang Y, Zhang S, Bi M, Liu S, Zhang D, Lu S and Kan Z (2020) Impact of Polymer Backbone Fluorination on the Charge Generation/Recombination Patterns and Vertical Phase Segregation in Bulk Heterojunction Organic Solar Cells. Front. Chem. 8:144. doi: 10.3389/fchem.2020.00144

Incorporating fluorine (–F) substituents along the main-chains of polymer donors and acceptors is an effective strategy toward efficient bulk-heterojunction (BHJ) solar cells. Specifically, F-substituted polymers often exhibit planar conformations, leading to favorable packing, and electronic coupling. However, the effects of fluorine substituents on the charge generation and recombination characteristics that determine the overall efficiency of BHJ active layers remain critically important issues to examine. In this report, two PBDT[2X]T polymer analogs –poly[4,8-bis((2-ethylhexyl)oxy)benzo[1,2-*b*:4,5-*b'*]dithiophene-thiophene] [PBDT[2H]T] and its F-substituted counterpart poly[4,8-bis((2-ethylhexyl)oxy)benzo[1,2-*b*:4,5-*b'*]dithiophene-3,4-difluoro-thiophene] [PBDT[2F]T]—are studied to systematically examine how –F substituents impact the blend morphology, charge generation, carrier recombination and extraction in BHJ solar cells. Considering the large efficiency differences between PBDT[2H]T- and PBDT[2F]T-based BHJ devices, significant emphasis is given to characterizing the out-of-plane morphology of the blend films as vertical phase-separation characteristics are known to have dramatic effects on charge transport and carrier extraction in polymer-fullerene BHJ solar cells. Herein, we use electron energy loss spectroscopy (EELS) in tandem with charge transport characterization to examine PBDT[2X]T-fullerene blend films. Our analyses show that PBDT[2H]T and PBDT[2F]T possess very different charge generation, recombination and extraction characteristics, resulting from distinct aggregation, and phase-distribution within the BHJ blend films.

Keywords: bulk heterojunction, polymer backbone fluorination, charge generation and recombination, vertical phase segregation, organic solar cells

INTRODUCTION

The substitution of π-conjugated polymer chains with fluorine (–F) substituents is an effective strategy in the design of polymer donors and acceptors for efficient bulk-heterojunction (BHJ) solar cells (Li et al., 2019). Of all considered benefits, recent studies have shown that F-substituted polymers are prone to adopt planar conformations, and favorable packing and electronic coupling patterns (Do et al., 2016; Tang et al., 2020) broader consensus emphasizes their propensity for higher backbone rigidity and a more pronounced tendency to aggregate on going from solutions to thin-film (Li et al., 2014, 2020; Fei et al., 2015) compared to their counterparts without –F substituents –material properties that can be taken advantage of in BHJ solar cell optimization processes (Liu et al., 2014).

In spite of the significant experimental work pursued to describe the correlations between –F substitutions in polymer main-chains and polymer performance in actual BHJ solar cells, direct connections between material structure and device efficiency are often difficult to make. Considering F-substituted polymers, some important questions remain, in particular with regard to how molecular scale effects directed by –F substituents can impact mesoscale morphologies, charge generation, and recombination patterns in BHJ thin films (Eisner et al., 2019). Since experimental methods are lacking to directly probe how functional group substitutions affect polymer main-chain packing and aggregation, computational methodologies must be employed to provide this level of description (Do et al., 2017). Quantum mechanical calculations can describe intrinsic *inter*-monomer torsion profiles, which govern the main-chain dihedral distribution in the bulk; whereas molecular dynamics (MD) simulations can provide information on main-chain packing arrangements in the bulk, and the propensity to form ordered π-π aggregates (Li et al., 2020). To further molecular-scale insights and qualitatively describe the types of aggregates that prevail in the bulk, solid-state nuclear magnetic resonance (SS-NMR) spectroscopy can be used to complement computational methodologies, providing an experimental analysis of the conformational landscape defined by the polymer main-chains in the bulk (Do et al., 2016). Based on this methodology, both theoretical and experimental studies on the influence of –F substitutions on *intra*- and *inter*-molecular interactions have shown that the higher polymer backbone planarity and rigidity are at the origin of local packing effects (to which relate binding energies and electronic coupling between neighboring chains), and that these result in distinct aggregation and charge transport patterns (Do et al., 2016). As an example, in poly(3-alkyl-4-fluoro)thiophenes (F-P3AT) (Fei et al., 2015) –F substitutions have been shown to raise the melting temperature and crystallization enthalpy of the P3AT analogs –variations in intrinsic material properties that are consistent with backbone planarization effects, inducing main-chain rigidity, and higher propensity for aggregation in the solid state. In turn, employing F-P3AT, field-effect transistor mobilities increased by a factor of 5 compared to P3AT-based transistors (Fei et al., 2015).

In polymer-based BHJ solar cells, –F substitutions of monomer units including: thiophenes (Jo et al., 2014; Wolf et al., 2015), **carbazoles** (Kim et al., 2014), **thienothiophenes** (Chen et al., 2009; Carsten et al., 2011), **benzothiadiazole** (Stuart et al., 2013; Yang et al., 2013; Kim et al., 2014), **benzotriazoles** (Price et al., 2011; Chen et al., 2019), **benzodithiophenes** (Chen et al., 2009; Jo et al., 2014; Wolf et al., 2015), **indacenodithiophenes** (Schroeder et al., 2012), **and anthradithiophenes** (Gundlach et al., 2008) have resulted in improved device efficiencies. Due to the strong inductive electron-withdrawing nature of –F substituents (element of highest electronegativity), F-substituted polymer donors possess lower-lying highest occupied molecular orbital (HOMO) energy levels than their counterparts without –F substituents –leading to higher open-circuit voltages (V_{OC}) in BHJ solar cells (Chen et al., 2009, 2019). Setting aside their important effect on the electronic properties of both polymer donors (Chen et al., 2009; Price et al., 2011; Schroeder et al., 2012; Stuart et al., 2013; Yang et al., 2013; Jo et al., 2014; Kim et al., 2014; Li et al., 2014; Wolf et al., 2015; Do et al., 2016; Kawashima et al., 2016) and acceptors (Liu et al., 2016, 2017), –F substitutions may also affect the preferential orientation of polymer aggregates relative to device substrates, impacting device performance in some instances (Stuart et al., 2013), although here we note that those effects are not well-understood to date, and there were reports with opposite conclusions (Kawashima et al., 2016). Most systematic studies of the effect of F-substituents in polymers (comparing F-substituted vs. unsubstituted, analogous model systems) have converged to the idea that device performance can vary dramatically when either donor or acceptor contain F-substituents in their main-chain (Jo et al., 2014; Wolf et al., 2015; Kawashima et al., 2016). Along those lines, several reports have shown that concurrent synthetic and device optimizations of fluorinated polymers can yield significant improvements in BHJ thin films as carrier mobilities increase, and that those improvements result in direct BHJ solar cell efficiency increments (Jo et al., 2014; Wolf et al., 2015). Using pump probe ultrafast spectroscopy, Gorenflot et al. (2018) reported the exciton dissociation, charge separation, and extraction in BHJ solar cells with fluorine substituents, and it was found that in the fluorinated polymer BHJ solar cells, the charge generation is about 40% higher than that of the non-fluorinated polymer BHJ solar cells, resulting from improved exciton diffusion to the heterojunction, in conjunction with more efficient charge separation and reduced geminate recombination losses (Gorenflot et al., 2018). However, the effects of the presence of F-substituted polymers on the charge generation and recombination characteristics in BHJ solar cells, and how those effects translate into practical device efficiency variations, remain critically important issues to examine. In addition, significant emphasis is given to characterize the "out-of-plane" morphology of the blend films, because vertical phase-separation characteristics are known to have dramatic effects on charge transport and carrier extraction in polymer-fullerene BHJ solar cells.

In this report, we examine the charge generation and recombination in two analogous model systems in BHJ solar cells: poly[4,8-bis((2-ethylhexyl)oxy)benzo[1,2-*b*:4,5-*b*']dithiophene-thieno[PBDT[2H]T] and its F-substituted counterpart poly[4,8-bis((2-ethylhexyl)oxy)benzo[1,2-*b*:4,5-*b*']dithiophene-3,4-difluoro-thiophene [PBDT[2F]T]. **(Chart 1)**

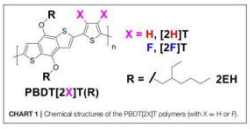

CHART 1 | Chemical structures of the PBDT[2X]T polymers (with X = H or F).

The PBDT[2X]T polymers dispersion index and molecular weight are shown in **Table S3**. Specifically, we systematically characterize carrier transport, recombination, and extraction across the BHJ devices and turn to morphological studies to establish a fuller understanding of how aggregation and vertical phase distributions impact the carrier dynamics, and in turn, BHJ solar cell efficiency.

RESULTS AND DISCUSSION

Optimized BHJ solar cells with direct device architecture were fabricated and tested under AM1.5G solar illumination (100 mW/cm^2). The PBDT[2X]T:PC$_{71}$BM blend solutions (ratio: 1:1.5, wt/wt) were cast from a hot chlorobenzene (CB; *ca.* 90°C) solution with 5 vol% 1-chloronaphthalene (CN) (cf. details in the SI; film thicknesses in the range 80–90 nm). The energy level diagram of PBDT[2H]T, PBDT[2F]T and PC$_{71}$BM in **Figure S2**. **Figure S3** accounts for the relative thin-film absorbance and solution absorption coefficients of the PBDT[2H]T and PBDT[2F]T. As shown in **Figure 1A** and **Table 1**, the optimized PBDT[2H]T:PC$_{71}$BM (2HT-based) and PBDT[2FT]T:PC$_{71}$BM (2FT-based) BHJ solar cells achieved very distinct efficiencies and device statistics including standard deviations are provided in the Supplementary Information (**Tables S1, S2**; **Figure S1**). While the optimized 2HT-based devices achieved V_{OC} of *ca.* 0.77 V, modest $J_{SC}$of *ca.* 5.2 mA/cm^2, and fill-factors (*FFs*) of 60.1%, the 2FT-based counterpart yields a substantially higher J_{SC} of *ca.* 9.3 mA/cm^2, and a concurrently improved *FF* (73.3%) and V_{OC} (*ca.* 0.89 V). Overall, 2FT-based devices achieve a power conversion efficiency (PCE) improvement of more than two-fold, reaching up to 6.2% (*avg.* 6.1%) under the same film-casting conditions.

The large differences in J_{SC} values between 2HT- and 2FT-based BHJ solar cells (**Table 1**) are shown in the *J-V* curves provided in **Figure 1A**, and are consistent with the integrated current from the external quantum efficiency (EQE) spectra shown in **Figure 1B** (± 6%). In **Figure 1B**, 2FT-based devices show the most prominent spectral response in the range 350–600 nm, with EQE values reaching *ca.* 75% at 500 nm (EQE >60% in the range 350–580 nm). In comparison, EQE values in 2HT-based devices remain below 50% across the visible spectrum –observations implying that the substitution pattern in PBDT[2X]T correlates with significant variations in BHJ solar cell performance.

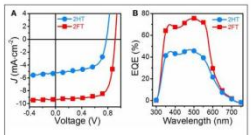

FIGURE 1 | **(A)** *J-V* curves and **(B)** EQE spectra for optimized 2HT- (blue) and 2FT-based (red) BHJ solar cells with PC$_{71}$BM as the acceptor; AM1.5G solar illumination (100 mW/cm^2).

TABLE 1 | PV performance of the 2HT- and 2FT-based BHJ solar cells[a,b].

	V_{OC} (V)	J_{SC} (mA/cm^2)	*FF* (%)	Avg. PCE (%)	Max. PCE (%)
2HT	0.77	5.2	60.1	2.4	2.7
2FT	0.89	9.3	73.3	6.1	6.2

[a]Average values across >10 devices across 3 substrates. [b]Device statistics in the Supplementary Information, **Table S1**.

The competition between charge recombination and extraction governs the *FF* in BHJ solar cells and in turn device PCE. Meanwhile, both the loss of photogenerated carriers by recombination and charge extraction processes are limited by the carrier mobilities of the blend film for holes and electrons. To estimate the electron and hole mobilities in optimized PBDT[2X]T:PC$_{71}$BM blend films, we measured the dark current density-voltage characteristics of single-carrier devices (see experimental details in the SI) and then fitted the data using the space-charge-limited current (SCLC) (Giulianini et al., 2010) model described by the Mott-Gurney law (with a small field dependent term), as in following equation (Mihailetchi et al., 2005).

$$J(V) = \frac{9}{8}\varepsilon_0\varepsilon_r\mu_0 \exp\left(0.89\beta\sqrt{\frac{V-V_{bi}}{L}}\right)\frac{(V-V_{bi})^2}{L^3} \quad (1)$$

where ε_0 and ε_r are the dielectric permittivity of a vacuum and the active layer, L is the thickness of the active layer, V is the applied voltage, V_{bi} is the built-in voltage, μ_0 is the zero-field mobility, and β is the field-activation factor.

Figure 2 shows the dark *J-V* characteristics of the electron-only diode in the configuration ITO/Al/2XT:PC$_{71}$BM/Al (**Figure 2A**) and that for the hole-only diode with the architecture ITO/MoO$_3$/2XT:PC$_{71}$BM/MoO$_3$/Ag (**Figure 2B**) (cf. additional details in the Supplementary Information, **Figure S4**). The fitting to the experimental results (solid lines in **Figure 2**; the parameters used in the fitting and films with other thickness are detailed in the Supplementary Information, **Figure S4**, **Tables S4** and **S5**) indicate that the electron mobility in the BHJ blend films with the 2HT and 2FT polymers is comparable: *ca.* 6.2 ×

10^{-4} cm^2 V^{-1}s^{-1} and 6.8 × 10^{-4} cm^2 V^{-1}s^{-1}, respectively. In contrast, the hole mobility in the 2HT- and 2FT-based blend films are an order of magnitude different: *ca.* 4.4 × 10^{-6} vs. 3.5 × 10^{-5} cm^2 V^{-1}s^{-1}, respectively. As a result, the carrier mobilities are significantly more balanced in 2FT-based devices –which represents an important parameter in explaining the performance differences observed between 2HT- and 2FT-based BHJ solar cells.

The charge collection probability, $P_c(I, V)$, is defined as the ratio between J_{SC} and saturated photocurrent density $J_{ph,sat}$ at reversed biases when the current density becomes independent of the applied voltage (cf. details in the Supplementary Information, **Figures S5**, **S6**) (Cowan et al., 2010; Mori et al., 2014).

Figure 3A shows the P_c (I, −2*V*) for the 2HT- and 2FT-based BHJ solar cells as a function of incident light intensity I. In both cases, the P_c values were almost independent of incident light intensity over the range 0.17–1.20 suns, yielding *ca.* 80% for 2HT-based devices and 95% for their 2FT counterparts. When the charge carrier density increases with increasing light intensity, the magnitude of the bimolecular recombination rate should also increase and the P_c should decrease at higher values of I if the device suffers non-negligible bimolecular recombination at short-circuit. Therefore, the independence of P_c on I suggests that neither 2HT- nor 2FT-based devices suffer from bimolecular recombination under the short-circuit conditions.

To further examine whether carrier recombination was limiting device efficiency to a different extent in 2HT- and 2FT-based devices, we turned to a characterization of J_{SC} and V_{OC} as a function of incident light intensity. **Figure 3B** provides the dependence of J_{SC} as a function of incident light intensity plotted in a log-log scale and fitted to a power law (solid lines). As reported in earlier work, a power law dependence of J_{SC}on incident light intensity I in BHJ solar cells is described by $J_{sc} \propto I^{\alpha}$ (Cowan et al., 2010; Koster et al., 2011; Kyaw et al., 2013). An exponential factor of $\alpha \approx 1$ (or near unity) is indicative of efficient carrier extraction prior to recombination at short-circuit. For 2HT-based devices, the power law fit to the J_{SC} vs. I data yields an α value of 0.94 ± 0.01, while for 2FT-based devices, the J_{SC} vs. I data fit yields an α value of 0.99 ± 0.01, indicating that carrier extraction proceeds with more recombination losses in 2HT-based BHJ solar cells. Therefore, through the analysis of P_c and the J_{SC} dependence on incident light intensity, 2HT-based devices suffer from two major losses channels thus far: (i) a relatively poor charge generation pattern reflected in the low J_{SC} (6 mA/cm^{-2}) and (ii) non-negligible recombination losses prior to extraction.

In parallel, **Figure 3C** depicts the variation of V_{OC} vs. I in a natural log-linear scale and fitted to $V_{oc} \propto n\frac{kT}{q}\ln(I)$ (Cowan et al., 2010; Kyaw et al., 2013), where k, T, and q are the Boltzmann constant, temperature in Kelvin, and the elementary charge, respectively. The parameter n (usually in the range of 1–2) accounts for the presence of carrier traps across the active layers or interfaces with the electrodes, and any deviations from $n = 1$ (trap-free condition) reflects the existence of trap-assisted recombination. As shown in **Figure 3C**, $n \approx 1.24$ and 1.27 were inferred for 2HT- and 2FT-based BHJ solar cells, respectively –implying that both 2HT- and 2FT-based devices suffer from trap-assisted recombination at open-circuit. To further our understanding of the charge recombination and extraction patterns in 2HT- and 2FT-based BHJ solar cells, we turned to transient photovoltage and photocurrent analyses.

Transient photovoltage (TPV) measurements and their analysis provide information regarding the non-geminate recombination of charges within devices. TPV measurements record the voltage decay transient of a device held at open-circuit under continuous illumination after being subject to a short perturbative light pulse; the photovoltage decay can be used as a direct measure of charge recombination kinetics in BHJ solar cells at open-circuit. One or two time constants, representative of carrier lifetime, can be obtained by fitting the decay kinetics with mono- or bi-exponential equations, suggesting that one or two recombination routes can co-exist, that can generally be assigned to either bimolecular or/and trap-assisted recombination (Li et al., 2011; Liang et al., 2018). TPV measurements were performed on the 2HT- and 2FT-based BHJ solar cells to characterize the non-geminate recombination profile in the two systems.

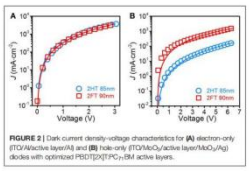

FIGURE 2 | Dark current density-voltage characteristics for **(A)** electron-only (ITO/Al/active layer/Al) and **(B)** hole-only (ITO/MoO$_3$/active layer/MoO$_3$/Ag) diodes with optimized PBDT[2X]T:PC$_{71}$BM active layers.

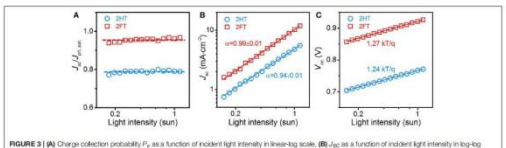

FIGURE 3 | **(A)** Charge collection probability P_c as a function of incident light intensity in linear-log scale, **(B)** J_{SC} as a function of incident light intensity in log-log scale, and **(C)** V_{OC} as a function of incident light intensity for the 2HT- and 2FT-based BHJ solar cells in linear-log scale. The solid lines in **(B,C)** correspond to fits to the data based on the equations $J_{sc} \propto I^{\alpha}$ and $V_{oc} \propto n\frac{kT}{q}\ln(I)$, respectively.

In both 2HT- and 2FT- based BHJ solar cells, mono-exponential fits to the experimental kinetics data were found to be appropriate fitting equations. **Figure 4A** shows the normalized TPV responses for a 2FT-based device subjected to several incident light intensities (Data fitting details reported in the Supplementary Information, see **Figure S7**). The single carrier lifetime figure derived from the TPV fitting of 2HT- and 2FT-based devices correlate with a single carrier recombination loss channel, here trap-assisted recombination as determined from the variation of V_{OC} with illumination intensity discussed in the previous section. **Figure 4B** plots the carrier lifetime as a function of V_{OC} for the 2HT- and 2FT-based BHJ solar cells. As expected, the carrier lifetime decreases with increasing V_{OC}, and the carrier lifetime at 1 sun is estimated as 2.3 and 2.0 μs (comparable) for 2HT- and 2FT-based devices, respectively.

Carrier transport and extraction across BHJ active layers can be examined via transient photocurrent (TPC) measurements (Hwang et al., 2009; McNeill et al., 2009; Li and McNeill, 2011; Li et al., 2011, 2013; Gao et al., 2014; Tremolet de Villers et al., 2014; Liang et al., 2019); analyses that are particularly relevant to the study of carrier traps and trap-assisted recombination in BHJ solar cells. In these analyses, the occurrence and extent of carrier traps across the active layer and/or at the interfaces between the BHJ blend film and the electrodes are reflected in the dependence of device current response and shape on light intensity. Instances of carrier traps concentrated at BHJ active layer/electrode interfaces and impinging on charge extraction have been discussed in recent studies (Hwang et al., 2009; McNeill et al., 2009; Li and McNeill, 2011; Tremolet de Villers et al., 2014). For example, in direct BHJ device configurations, fullerenes accumulating at the anode induce transient current peaks, greatly surpassing the steady-state current during rise events. Using concurrent experimental results and theoretical models, it has been shown that fullerenes act as hole-blocking layers, hindering hole extraction at the anode and, in turn, lowering BHJ solar cell efficiency (Tremolet de Villers et al., 2014). Here, we examine the turn-on and turn-off dynamics of the 2HT- and 2FT-based devices using long light pulse excitations (200 μs; cf. details in the SI), allowing the current density to reach steady-state conditions.

Figure 5 depicts the normalized transient photocurrent for optimized 2HT- and 2FT-based devices (cf. conditions given in **Table 1**); supplementary data can be found in the Supplementary Information (**Figure S8**). **Figure 6B** shows that the fast dynamics of the 2FT-based devices contrast with that for 2HT-based devices in **Figure 6A**. The rise/fall times on the order of 2 μs (i.e., the time required to reach 90% of the maximum current from an initial 10%) obtained from 2FT-based active layers (**Figure 6B**) are practically independent of light intensity. In comparison, the TPC curves for the 2HT-based devices show a significant dependence on light intensity, with a fast-initial transient photocurrent peak at higher light intensities followed by a second, slower photocurrent decay component leveling off at the steady-state current (at short-circuit) within *ca.* 150 μs (**Figure 6A**). Comparing the turn-off dynamics of the 2HT- and 2FT-based devices: the fast *ca.* 2 μs decay and the absence of pronounced photocurrent tail observed in 2FT-based active layers contrast with the persistent, light-intensity-dependent photocurrent tail observed in 2HT-based active layers, which suggests that carrier collection is delayed by deep traps for as long as 200 μs in the 2HT-based devices. In general, the slower dynamic component (beyond 205 μs, **Figures 5A,B**) becomes less prominent as light intensity increases, suggesting that the traps are filled at higher light intensities and, as a result, their impact on charge transport becomes less pronounced (McNeill et al., 2009; Li and McNeill, 2011). Based on earlier discussions and prior reports (Heumueller et al., 2014; Tremolet de Villers

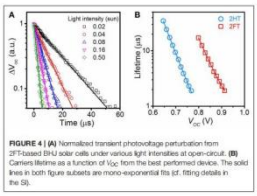

FIGURE 4 | **(A)** Normalized transient photovoltage perturbation from 2FT-based BHJ solar cells under various light intensities at open-circuit. **(B)** Carriers lifetime as a function of V_{OC} from the best performed device. The solid lines in both figure subsets are mono-exponential fits (cf. fitting details in the SI).

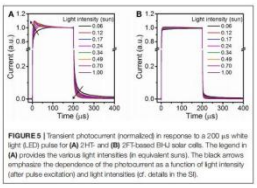

FIGURE 5 | Transient photocurrent (normalized) in response to a 200 μs white light (LED) pulse for **(A)** 2HT- and **(B)** 2FT-based BHJ solar cells. The legend in **(A)** provides the various light intensities (in equivalent suns). The black arrows emphasize the dependence of the photocurrent as a function of light intensity (after pulse excitation) and light intensities (cf. details in the SI).

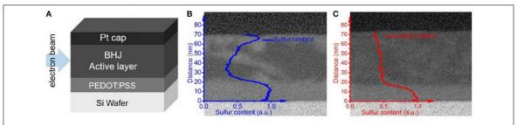

FIGURE 6 | (A) Schematic of the samples prepared for the cross-sectional TEM and EELS analyses. TEM cross-section images of the **(B)** 2HT- and **(C)** 2FT-based BHJ active layers cast on PEDOT:PSS and superimposed core-level sulfur analyses for the phase ratio mapping of polymer-rich (brighter regions) and fullerene-rich (darker regions) phases in the BHJ cross-section. The sulfur-content lines vs. distance from the substrate represented in subsets **(B,C)** capture the sulfur distribution averaged across the whole film cross section, and the distances are reported from the surface of the Si wafer (brightest layer) to the Pt capping layer (black).

et al., 2014; Pearson et al., 2016), the transient peak observed in 2HT-based devices may be the result of morphological effects buried within the active layer or occurring at the electrode interfaces. To probe those effects and provide a qualitative, macroscopic insight into the vertical distribution of polymer- and fullerene-rich domains across the optimized BHJ solar cells, we turned to electron energy loss spectroscopy (EELS) analyses performed from cross-sections of the BHJ thin films imaged by transmission electron microscopy (TEM) (cf. experimental details provided in the SI).

Figure 6 provides the EELS profiles collected from the cross-sections of BHJ thin films (cast from optimized conditions, see **Table 1**) with PBDT[2H]T (**Figure 6B**) and PBDT[2F]T (**Figure 6C**). Obtained from core-level sulfur analyses, the superimposed plots provide relative phase ratio mapping for the sulfur-rich—i.e., polymer-rich—and sulfur-deficient—i.e., fullerene-rich—regions in the BHJ cross-section. Here, we note that PEDOT:PSS interlayers were cast between the Si wafer (substrate) and the BHJ active layer to reproduce the morphology of the photoactive layers as obtained in actual BHJ solar cells; the high sulfur contents observed in the first *ca.* 20 nm distance from the Si wafer are thus consistent with the presence of the PEDOT:PSS. Beyond the PEDOT:PSS interface, the sulfur maps show two distinct phase distribution patterns for optimized 2HT- and 2FT-based BHJ active layers. On the one hand, **Figure 6B** suggests the existence of a gradient of polymer-rich phases across 2HT-based active layers on going from the PEDOT:PSS interface (anode) to the top interface (cathode in an actual BHJ device), with an apparent peak indicative of an accumulation of the polymer donor 2HT near the top interface (cathode). On the other hand, **Figure 6C** reflects a relatively uniform concentration profile of polymer and fullerene throughout the depth of the BHJ active layer. If supported by a more quantitative analysis of the vertical phase distribution in the BHJ active layers, the polymer-rich phase concentrated near the top interface (cathode) in 2HT-based active layers can hinder electron extraction by forming an electron-blocking layer. Concurrently, the apparently fullerene-rich phase concentrated near the PEDOT:PSS interface (anode) in 2HT-based active layers (**Figure 6B**) may be detrimental to hole extraction (hole-blocking layer).

CONCLUSION

To summarize, we systematically characterized the charge generation and recombination patterns in BHJ solar cells with PBDT[2H]T and its F-substituted counterpart PBDT[2F]T, and used EELS in tandem with charge transport characterization to examine PBDT[2X]T-fullerene blend films. The reduction in microsecond transient photocurrent allowed us to attribute the recombination losses in the 2HT-based BHJ solar cells to the hole extraction barrier/traps. However, the fluorinated polymer donor 2FT- based photoactive layer had a more uniformly distributed polymer/fullerene blend throughout most of the depth of the film with a thin fullerene accumulation layer at the anode, without showing the reduction in photocurrent. Thus, 2FT-based BHJ solar cells showed more efficient charge generation, extraction, and higher hole mobility compared with those of the 2HT-based BHJ solar cells, leading to higher V_{OC}, J_{SC}, FF, and overall device performance. The vertical phase segregation features of the 2HT- and 2FT-based BHJ solar cells were confirmed with EELS (sulfur mapping). The –F substituents impacted the polymer packing, which translates to the difference in aggregations from solution to film, thus the differences in polymer-fullerene phase mixing/composition in BHJ thin films. Our results provide an insight into the fluorination effects on the thin film BHJ compositions, especially the vertical phase, thus the device efficiency, providing a direct evidence of benefits from fluorination of polymers.

DATA AVAILABILITY STATEMENT

All datasets generated for this study are included in the article/supplementary material.

AUTHOR CONTRIBUTIONS

ZK, YS, YC, and SLu proposed the idea of this paper and contributed to analize the experiment results and wring the paper. YC and ZK contributed to the fabrication of the solar cells and characterization. DZ conducted the TEM. SLi contributed to the synthesis of the donor. SZ and MB conducted SCLC.

FUNDING

This work was financially supported by the National Natural Science Foundation of China (No. 61805245, 2180509), CAS Pioneer Hundred Talents Program (Y82A060Q10, Y92A160Q10), Recruitment Program of Global Experts (R52A199Z10), Higher education teaching reform of Heilongjiang Province of China (SJGY20190688), Heilongjiang Provincial Department of Education's Scientific Research Project (1352MSYYB006), Natural Science Foundation of Chongqing (cstc2015jcyjB0628 and cstc2017rgzn-zdyfX0030), the Guangdong Natural Science Foundation (No. 2016A030310428), and Guangzhou Science and Technology Foundation (No. 201904010361). Science and Technology Innovation Project of Mudanjiang Normal University (kjcx2019-22mdjnu).

SUPPLEMENTARY MATERIAL

The Supplementary Material for this article can be found online at: https://www.frontiersin.org/articles/10.3389/fchem.2020.00144/full#supplementary-material

REFERENCES

Carsten, B., Szarko, J. M., Son, H. J., Wang, W., Lu, L., He, F., et al. (2011). Examining the effect of the dipole moment on charge separation in donor-acceptor polymers for organic photovoltaic applications. *J. Am. Chem. Soc.* 133, 20468–20475. doi: 10.1021/ja208642b

Chen, H.-Y., Hou, J., Zhang, S., Liang, Y., Yang, G., Yang, Y., et al. (2009). Polymer solar cells with enhanced open-circuit voltage and efficiency. *Nat Photon* 3, 649–653. doi: 10.1038/nphoton.2009.192

Chen, Y., Zhang, Q., Du, M., Li, G., Li, Z., Huang, H., et al. (2019). Benzotriazole-based p-type polymers with thieno [3, 2-b] thiophene π-bridges and fluorine substituents to realize high Voc. *ACS Publ.* 1, 906–913. doi: 10.1021/acsapm.9b00156

Cowan, S. R., Roy, A., and Heeger, A. J. (2010). Recombination in polymer-fullerene bulk heterojunction solar cells. *Phys. Rev. B* 82:245207. doi: 10.1103/PhysRevB.82.245207

Do, K., Ravva, M. K., Wang, T., and Brédas, J.-L. (2017). Computational methodologies for developing structure–morphology–performance relationships in organic solar cells: a protocol review. *Chem. Mater.* 29, 346–354. doi: 10.1021/acs.chemmater.6b03111

Do, K., Saleem, Q., Ravva, M. K., Cruciani, F., Kan, Z., Wolf, J., et al. (2016). Impact of fluorine substituents on π-conjugated polymer main-chain conformations, packing, and electronic couplings. *Adv. Mater.* 28, 8197–8205. doi: 10.1002/adma.201601282

Eisner, F. D., Azzouzi, M., Fei, Z., Hou, X., Anthopoulos, T. D., Dennis, T. J. S., et al. (2019). Hybridization of local exciton and charge-transfer states reduces nonradiative voltage losses in organic solar cells. *J. Am. Chem. Soc.* 141, 6362–6374. doi: 10.1021/jacs.9b01465

Fei, Z., Boufflet, P., Wood, S., Wade, J., Moriarty, J., Gann, E., et al. (2015). Influence of backbone fluorination in regioregular poly (3-alkyl-4-fluoro) thiophenes. *J. Am. Chem. Soc.* 137, 6866–6879. doi: 10.1021/jacs.5b02785

Gao, F., Li, Z., Wang, J., Rao, A., Howard, I. A., Abrusci, A., et al. (2014). Trap-induced losses in hybrid photovoltaics. *ACS Nano* 8, 3213–3221. doi: 10.1021/nn501185b

Giulianini, M., Waclawik, E. R., Bell, J. M., and Motta, N. (2010). Temperature and electric field dependent mobility in poly (3-hexylthiophene) diodes. *J. Appl. Phys.* 108:014512. doi: 10.1063/1.3460111

Gorenflot, J., Paulke, A., Piersimoni, F., Wolf, J., Kan, Z., Cruciani, F., et al. (2018). From recombination dynamics to device performance: quantifying the efficiency of exciton dissociation, charge separation, and extraction in bulk heterojunction solar cells with fluorine-substituted polymer donors. *Adv. Energy Mater.* 8:1701678. doi: 10.1002/aenm.201701678

Gundlach, D. J., Royer, J. E., Park, S. K., Subramanian, S., Jurchescu, O. D., Hamadani, B. H., et al. (2008). Contact-induced crystallinity for high-performance soluble acene-based transistors and circuits. *Nat. Mater.* 7, 216–221. doi: 10.1038/nmat2122

Hemmerlet, T., Mateker, W. R., Sachs-Quintana, I. T., Vandewal, K., Bartelt, J. A., Burke, T. M., et al. (2014). Reducing burn-in voltage loss in polymer solar cells by increasing the polymer crystallinity. *Energy Environ. Sci.* 7, 2974–2980. doi: 10.1039/C4EE01842G

Hwang, I., McNeill, C. R., and Greenham, N. C. (2009). Drift-diffusion modeling of photocurrent transients in bulk heterojunction solar cells. *J. Appl. Phys.* 106:094506. doi: 10.1063/1.3247547

Jo, J. W., Jung, J. W., Wang, H.-W., Kim, P., Russell, T. P., and Jo, W. H. (2014). Fluorination of polythiophene derivatives for high performance organic photovoltaics. *Chem. Mater.* 26, 4214–4220. doi: 10.1021/cm5022296

Kawashima, K., Fukuhara, T., Suda, Y., Suzuki, Y., Koganezawa, T., Yoshida, H., et al. (2016). Implication of fluorine atom on electronic properties, ordering structures, and photovoltaic performance in naphthobisthiadiazole-based semiconducting polymers. *J. Am. Chem. Soc.* 138, 10265–10275. doi: 10.1021/jacs.6b05418

Kim, J., Yun, M. H., Kim, G.-H., Lee, J., Lee, S. M., Ko, S.-J., et al. (2014). Synthesis of PCDTBT-based fluorinated polymers for high open-circuit voltage in organic photovoltaics: towards an understanding of relationships between polymer energy levels engineering and ideal morphology control. *ACS Appl. Mater. Interfaces* 6, 7523–7534. doi: 10.1021/am500891z

Kotter, L. J., Kemerink, M., Wienk, M. M., Matarová, K., and Janssen, R. A. (2011). Quantifying bimolecular recombination losses in organic bulk heterojunction solar cells. *Adv. Mater. Weinheim.* 23, 1670–1674. doi: 10.1002/adma.201004311

Kyaw, A. K., Wang, D. H., Gupta, V., Leong, W. L., Ke, L., Bazan, G. C., et al. (2013). Intensity dependence of current-voltage characteristics and recombination in high-efficiency solution-processed small-molecule solar cells. *ACS Nano* 7, 4569–4577. doi: 10.1021/nn401267x

Li, M., Bin, H., Jiao, X., Wienk, M. M., Yan, H., and Janssen, R. A. (2020). Controlling the microstructure of conjugated polymers in high-mobility monolayer transistors via the dissolution temperature. *Angew. Chem. Int. Ed.* 59, 846–852. doi: 10.1002/anie.201911311

Li, W., Albrecht, S., Yang, L., Roland, S., Tumbleston, J. R., McAfee, T., et al. (2014). Mobility-controlled performance of thick solar cells based on fluorinated copolymers. *J. Am. Chem. Soc.* 136, 15566–15576. doi: 10.1021/ja5067724

Li, W., Xiao, Z., Smith, J. A., Cai, L., Li, D., Kilbride, R. C., et al. (2019). Enhancing the efficiency of PTB7-Th: C60 : IDFIC-based ternary solar cells with versatile third components. *Appl. Phys. Rev.* 6:041405. doi: 10.1063/1.5125438

Li, Z., Gao, F., Greenham, N. C., and McNeill, C. R. (2011). Comparison of the operation of polymer/fullerene, polymer/polymer, and polymer/nanocrystal solar cells: a transient photocurrent and photovoltage study. *Adv. Funct. Mater.* 21, 1419–1431. doi: 10.1002/adfm.201002154

Li, Z., Lakhwani, G., Greenham, N. C., and McNeill, C. R. (2013). Voltage-dependent photocurrent transients of PTB7:PC70BM solar cells: experiment and numerical simulation. *J. Appl. Phys.* 114:034502. doi: 10.1063/1.4813612

Li, Z., and McNeill, C. R. (2011). Transient photocurrent measurements of PCDTBT:PC70BM and PCPDTBT:PC70BM solar cells: evidence for charge trapping in efficient polymer/fullerene blends. *J. Appl. Phys.* 109:074513. doi: 10.1063/1.3573394

Liang, R. Z., Babics, M., Seitkhan, A., Wang, K., Geraghty, P. B., Lopatin, S., et al. (2018). Additive-morphology interplay and loss channels in "all-small-molecule" bulk-heterojunction (BHJ) solar cells with the nonfullerene acceptor IDTTBM. *Adv. Funct. Mater.* 28:1705464. doi: 10.1002/adfm.201705464

Liang, R. Z., Zhang, Y., Savikhin, V., Babics, M., Kan, Z., Wohlfahrt, M., et al. (2019). Higher mobility and carrier lifetimes in solution-processable small-molecule ternary solar cells with 11% efficiency. *Adv. Energy Mater.* 9:1802856. doi: 10.1002/aenm.201802856

Liu, S., Kan, Z., Thomas, S., Cruciani, F., Brédas, J. L., and Beaujuge, P. M. (2016). Thieno [3, 4-c] pyrrole-4, 6-dione-3, 4-difluorothiophene polymer acceptors for efficient all-polymer bulk heterojunction solar cells. *Angew. Chem.* 128, 13190–13194. doi: 10.1002/ange.201604307

Liu, S., Song, X., Thomas, S., Kan, Z., Cruciani, F., Laquai, F., et al. (2017). Thieno [3, 4-c] pyrrole-4, 6-dione-based polymer acceptors for high open-circuit voltage all-polymer solar cells. *Adv. Energy Mater.* 7:1602574. doi: 10.1002/aenm.201602574

Liu, X., Gu, L., Zhang, Q., Wu, J., Long, Y., and Fan, Z. (2014). All-printable band-edge modulated ZnO nanowire photodetectors with ultra-high detectivity. *Nat. Commun.* 5, 1–9. doi: 10.1038/ncomms5007

McNeill, C. R., Hwang, I., and Greenham, N. C. (2009). Photocurrent transients in all-polymer solar cells: trapping and detrapping effects. *J. Appl. Phys.* 106:024507. doi: 10.1063/1.3177337

Mihailetchi, V. D., Wildeman, J., and Blom, P. W. (2005). Space-charge limited photocurrent. *Phys. Rev. Lett.* 94:126602. doi: 10.1103/PhysRevLett.94.126602

Mori, D., Benten, H., Okada, I., Ohkita, H., and Ito, S. (2014). Highly efficient charge-carrier generation and collection in polymer/polymer blend solar cells with a power conversion efficiency of 5.7%. *Energy Environ. Sci.* 7, 2939–2943. doi: 10.1039/C4EE01326C

Pearson, A. J., Hopkinson, P. E., Couderc, E., Domanski, K., Abdi-Jalebi, M., and Greenham, N. C. (2016). Critical light instability in CB/DIO processed PBDTTT-EFT:PC71BM organic photovoltaic devices. *Org. Electron.* 30, 225–236. doi: 10.1016/j.orgel.2015.12.024

Price, S. C., Stuart, A. C., Yang, L., Zhou, H., and You, W. (2011). Fluorine substituted conjugated polymer of medium band gap yields 7% efficiency in polymer–fullerene solar cells. *J. Am. Chem. Soc.* 133, 4625–4631. doi: 10.1021/ja1112595

Schroeder, B. C., Huang, Z., Ashraf, R. S., Smith, J., D'Angelo, P., Watkins, S. E., et al. (2012). Silaindacenodithiophene-based low band gap polymers – the effect of fluorine substitution on device performances and film morphologies. *Adv. Funct. Mater.* 22, 1663–1670. doi: 10.1002/adfm.201102941

Stuart, A. C., Tumbleston, J. R., Zhou, H., Li, W., Liu, S., Ade, H., et al. (2013). Fluorine substituents reduce charge recombination and drive structure and morphology development in polymer solar cells. *J. Am. Chem. Soc.* 135, 1806–1815. doi: 10.1021/ja309289u

Tang, H., Yan, C., Karethedath, S., Yin, H., Gao, Y., Gao, J., et al. (2020). Deciphering the role of fluorination: morphological manipulation prompts charge separation and reduces carrier recombination in all-small-molecule photovoltaics. *Solar RRL.* 2020:1900528. doi: 10.1002/solr.201900528

Tremolet de Villers, B. J., MacKenzie, R. C. I., Jasieniak, J. J., Treat, N. D., and Chabinyc, M. L. (2014). Linking vertical bulk-heterojunction composition and transient photocurrent dynamics in organic solar cells with solution-processed MoOx contact layers. *Adv. Energy Mater.* 4:1301290. doi: 10.1002/aenm.201301290

Wolf, J., Cruciani, F., El Labban, A., and Beaujuge, P. M. (2015). Wide band-gap 3,4-difluorothiophene-based polymer with 7% solar cell efficiency: an alternative to P3HT. *Chem. Mater.* 27, 4184–4187. doi: 10.1021/acs.chemmater.5b01530

Yang, L., Tumbleston, J. R., Zhou, H., Ade, H., and You, W. (2013). Disentangling the impact of side chains and fluorine substituents of conjugated donor polymers on the performance of photovoltaic blends. *Energy Environ. Sci.* 6, 316–326. doi: 10.1039/C2EE23233A

Conflict of Interest: The authors declare that the research was conducted in the absence of any commercial or financial relationships that could be construed as a potential conflict of interest.

Copyright © 2020 Shao, Chang, Zhang, Bi, Liu, Zhang, Lu and Kan. This is an open-access article distributed under the terms of the Creative Commons Attribution License (CC BY). The use, distribution or reproduction in other forums is permitted, provided the original author(s) and the copyright owner(s) are credited and that the original publication in this journal is cited, in accordance with accepted academic practice. No use, distribution or reproduction is permitted which does not comply with these terms.

2.Shao Y, Jiang Z, Zhang Q, et al. Progress in nonmetal‐doped graphene electrocatalysts for the oxygen reduction reaction[J]. ChemSusChem, 2019, 12(10): 2133-2146.

ChemPubSoc Europe

DOI: 10.1002/cssc.201900060

CHEMSUSCHEM Minireviews

Progress in Nonmetal-Doped Graphene Electrocatalysts for the Oxygen Reduction Reaction

Yanqiu Shao,*[a, b] Zhenshuang Jiang,[a, b] Qiaoqiao Zhang,[b] and Jingqi Guan*[b]

Owing to energy shortages and environmental pollution, green energy sources such as polymer electrolyte fuel cells and metal–air batteries play a more and more important role, whereby the oxygen reduction reaction (ORR) is the rate-determining step. Development of high-efficiency and stable catalysts to facilitate the ORR is of importance. Graphene is a new type of material with two-dimensional structure and high surface area, which has wide-ranging applications in many fields. However, graphene with zero band gap shows low electrocatalytic activity toward the ORR. Introduction of nonmetal atoms can change the electronic arrangement, generate active sites, and further improve the catalytic activity of graphene. Some nonmetal-doping strategies (e.g., N, S, and P doping) can promote ORR activity. Herein, the recent development of nonmetal-doped graphene catalysts for ORR is reviewed. Some common synthetic methods for nonmetal-doped graphene materials are summarized, and the active sites and possible reaction mechanisms for ORR on various nonmetal-doped graphene catalysts are discussed.

Introduction

Energy is important for the development of national economies and the improvement of human living standards, which are important factors directly affecting economic development. Since the beginning of the 21st century, the shortage of resources, environmental pollution, and greenhouse effect caused by traditional energy utilization methods have become more and more prominent, and it is increasingly difficult for the traditional energy structure and its utilization methods to meet the needs of human survival and development.[1] To address the increasingly serious energy crisis and environmental pollution problems, a variety of new green energy sources have been developed, including metal–air batteries and fuel cells.[2]

Given the urgent need for a sustainable energy economy, electrochemical energy conversion technologies, such as polymer electrolyte membrane fuel cells (PEMFCs) and metal–air batteries, have become extremely important. The common feature of PEMFCs and metal–air batteries is that the oxygen reduction reaction (ORR) is the basis for their operation. The electrolytes can be divided into acidic and alkaline electrolytes. Acidic electrolytes promote proton transfer from the anode to the cathode. In acidic electrolyte, ORR occurs by four- or two-electron reduction.[3] The experimental results show that the four-electron reduction mechanism is dominant and advantageous, because each oxygen molecule has four electrons. This route can avoid the formation of hydrogen peroxide at the electrode, which results in degradation of the membrane and ionic monomer.[4] In alkaline electrolytes, hydroxyl ion is transferred from cathode to anode. In metal–air batteries and alkaline exchange membrane fuel cells, the ORR process can also occur by two-step reduction (total of four electrons), in which hydrogen peroxide can be directly or indirectly reduced to water.

At present, platinum is the only commercial catalyst that shows high activity and stability under acidic conditions. Rapid oxygen reduction kinetics is indispensable in terms of performance. Acidic ORR is several orders of magnitude slower than anodic oxidation. Researchers found that ORR kinetics is more favorable under alkaline conditions. In the cathode reaction of the hydrogen fuel cell, the reduction of O_2 to H_2O requires four electrons and four protons.[5] The mechanism of this process is very complicated, and ORR dynamics usually limits the reaction rate and maximum power. In recent years, nonmetal-doped graphene materials have gained much attention for ORR. The electrochemical activity and durability of these nonmetal-doped graphene materials can be compared with that of traditional platinum supported on carbon black (Pt/C).[6] This is a breakthrough and a new milestone in the ORR, because it can substitute the expensive platinum and achieve appropriate power output.[7]

Graphene is a two-dimensional grid-structured material composed of planar single-layer carbon atoms. It is the basic unit of other carbon allotropes, such as fullerenes, carbon nanotubes, and graphite. The theoretical specific surface area of graphene is as high as 2630 $m^2 g^{-1}$.[8] It has excellent thermal

[a] Prof. Y. Shao, Z. Jiang
College of Chemistry and Chemical Engineering
Mu Danjiang Normal University, Mudanjiang 157011 (P. R. China)
E-mail: shaoyanqiu1989@163.com
[b] Prof. Y. Shao, Z. Jiang, Q. Zhang, Prof. J. Guan
College of Chemistry, Jilin University
Changchun 130012 (P. R. China)
E-mail: guanjq@jlu.edu.cn
shaoyanqiu1989@163.com
The ORCID identification number(s) for the author(s) of this article can be found under:
https://doi.org/10.1002/cssc.201900060.

© 2019 Wiley-VCH Verlag GmbH & Co. KGaA, Weinheim

frequently. In this review, graphene doped with different elements as non-metallic oxygen reduction catalyst is introduced.

2. Synthesis methods

There are many methods for preparing nonmetal-doped graphene materials, of which the heteroatom doping method can be divided into in-situ doping method and post-processing method. In-situ doping method is a vital strategy, which is the process of introducing heteroatoms in the process of graphene synthesis, and the whole process occurs simultaneously. Up to now, many preparation methods have been reported, which include chemical vapor deposition (CVD), plasma treatment, arc discharge, explosion, high-temperature heat treatment, and hydrothermal treatment, etc.[11] It should be noted that it is extremely difficult to remove the metal residues for some kinds of graphene, which might significantly influence the catalytic performance.[12] Herein, CVD and ball milling as in-situ doping methods, as well as wet chemical methods are mainly discussed.

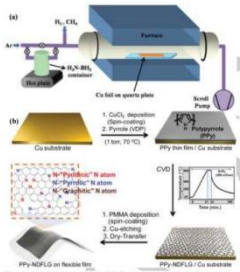

Figure 1. (a) Experimental setup of CVD commonly used for doping graphene. Reprinted with permission from Ref.[14]. Copyright 2013 American Chemical Society. (b) N-doped graphene derived from a polypyrrole. Reprinted with permission from Ref.[15]. Copyright: 2012 American Chemical Society.

2.1. Chemical vapor deposition (CVD)

Chemical vapor deposition (CVD) is a kind of chemical technology, which mainly uses one or several vapor compounds or monomers containing thin film elements to generate thin films by chemical reaction on the substrate surface. It has some features, e.g. no need of high vacuum, gaseousness of reactants and by-products, low and fast film precipitation temperature, good crystallinity and compactness and complete structure of the obtained film, good adhesion to substrate, excellent step coverage, smooth deposition surface, broad scope of application of various metals, semiconductors, inorganic substances and organic matter, controllable material stoichiometric ratio batch production, and semi-continuous processing. As shown in Figure 1a,[13] precursors of solids, liquids or gases containing atoms are added to the growth furnace to synthesize them together with carbon sources. However, the CVD method involves high cost and is suitable for the synthesis of thin film graphene, but not suitable for commercial large-scale production.[14]

Polymers containing heteroatoms (sometimes embedded in a polymer matrix) are deposited directly on metal catalysts. The whole process is safe without the use of high-temperature gas, and moderate dopant can be achieved. Kwon et al.[15] synthesized pyrrole monomers vaporized on copper substrates in the presence of $CuCl_2$ ions, followed by CVD growth (Figure 1b). The content of doped N is 3.14%, and the main pyrrole nitrogen may come from polypyrrole precursors. Sun et al[16] found that the amount of N-doping reached 23.5% when the mixture of nitrogen-rich melamine and PMMA was directly spin-coated on the copper substrate at 1000°C at atmospheric pressure, where graphite N occupies the main part of the N-doped structure and the mobility of N-graphene is low (< 10 cm^2 V^{-1} s^{-1}).

2.2. Ball milling method

Ball milling is to strip graphite and crack C-C bonds, in which the newly formed activated carbon species react with dopants through mechanochemistry. As an energy-saving and efficient material preparation technology, it can obviously reduce the activation energy of reaction, refine the grain size, greatly improve the powder activity, improve the uniformity of particle distribution and the interface between reinforcer and matrix, promote the diffusion of solid ions, induce low temperature chemical reaction, and thus improve the compactness, electrical and thermal properties of materials. Zhang et al. prepared hydroxyl functionalized graphene by ball milling.[1a,a] Jeon et al. studied graphene nanosheets as an efficient electronic catalyst for catalytic oxygen reduction. By ball milling, the stainless steel ball was rotated at high speed to produce enough kinetic energy. As a result, 36 kinds of activated carbon were formed at the edge of graphite crushing. These activated carbon have enough reaction ability to absorb halogen in sealed ball mill capsules.[17] Similarly, marginally selective graphene halide nanosheets (XGnPs, X = Cl, Br or I) were prepared by ball milling as anode materials for lithium-ion batteries.[18]

2.3. Wet chemical method

The synthetic method by the liquid reaction and chemical reaction is collectively referred to wet chemical method, such as coprecipitation chemical liquid deposition (CBD), electrochemical deposition (electroplating), sol-gel, etc. It has achieved rapid development in recent decades and is replacing some traditional ceramic generation methods. Due to small particle size, large specific surface area and high chemical activity, the ultra-fine ceramic powders prepared by wet chemical method show broad application prospects in heteroatom-doping carbon materials. The wet chemical method can be used to mix heteroatoms on 3D graphene gel with large surface area and pore structure.[19] For example, Wu et al. employed ammonia boron trifluoride for the co-doping of B and N.[19b] RGO (reduced graphene oxide) aerogels doped with B and N were prepared by freeze-drying after reduction and self-assembly of GO sheets in hydrothermal conditions. Su et al. used nitrogen-sulfur codoped three-dimensional graphene skeleton as an efficient metal-free electrocatalyst for oxygen reduction reaction under hydrothermal conditions.[20]

3. Graphene doped with different nonmetals

3.1. Oxidized carbon materials

Graphene-based materials as the substitution of most metal-based catalysts in energy catalysis have been widely attended due to some superior properties. The oxidized carbon material, a new nonmental-based graphene catalyst, has begun to play a more and more important role in fuel cells. Lu et al. compared ORR performance on oxidized carbon materials and pure carbon materials, and found that the oxidized carbon materials exhibited higher catalytic activity and selectivity to H_2O_2 in alkaline or neutral medium for ORR.[21] The oxidized carbon materials can be obtained by chemical oxidation, in which some function groups with the oxygen atom generate. The oxidation process can contribute to some defects in the regular fabric of carbon materials, which can change the electronic structure, and further improve the ORR performance. Besides, the activity and selectivity are related to the content of oxygen, and the active sites of ORR on the oxidized carbon materials are the carbon atoms neighboring the oxygen atom in oxygen function groups.

In a word, the introduction of oxygen atom can influence the electronic distribution due to larger electrophilic ability of oxygen than carbon in the oxidized carbon materials. Consequently, the interaction between ORR intermediates and the active sites leads to a change. The existence of more active sites gives rise to rapid absorption of intermediates and further accelerates ORR.[22] Therefore, the oxidized carbon material is a vital nonmetal-doped graphene catalyst in ORR of fuel cells, which has great potential in the practical application.

3.2. Nitrogen-Doped Graphene (NG)

In recent years, researchers developed low-cost non-metallic carbon-based electrocatalysts for ORR[7a, 23]. It is reported that zigzag carbon can offer active sites for catalyzing efficiently the ORR.[24] The superior catalytic performance originates from the abundant defects of carbon. However, most of the pure carbon materials show relatively low ORR activity due to the absence of bandgap.[25] To improve the catalytic activity, the use of N-doping strategy is introduced. To date, nitrogen-doped carbon materials have been widely used as ORR catalysts due to their excellent electrocatalytic activity, low cost, good stability, and environmental protection.[10a, 26] The physical and chemical properties of N-doped graphene and undoped graphene are quite different. In the periodic table, nitrogen is adjacent to carbon. Because the electronegativity of N is greater than that of C, N atoms have ability to attract more electrons, and further change the electronic structure of graphene. It has been reported that N-doped graphene can be prepared from ammonia and graphene, which showed the best catalytic activity at 900 °C. The onset potential and half-wave potential of nitrogen-doped graphene were higher than those of industrial Pt/C catalyst.[27] Gracia-Espino et al. prepared a N-doped graphene by vapor deposition for ORR, which is carried out along the "quasi-four-electron" reaction path.[28] Zhao et al. synthesized a N-doped graphene material by the pyrolysis of MOFs.[29] Compared with pure graphene, the prepared doped graphene with high electroconductivity exhibits higher activity for ORR. Feng et al. used graphene oxide and NH_4HCO_3 as raw materials to prepare N-doped graphene. The nitrogen doping rate reached 12.75% at low temperature (150 °C), which is conducive to ORR.[30] Xin et al. prepared a nitrogen-doped graphene by high-temperature heat treatment and found the type of nitrogen atomization bond has a significant effect on the selectivity and catalytic activity. Graphitic nitrogen determines the limiting current density; while pyridinic nitrogen determines the onset potential in the process of the oxygen reduction reaction.

The possible bonding of N-doped graphene is shown in Figure 2a.[31] There are three kinds of nitrogen bond structure. Because the bond length of C-N is primarily the same, pyridinic-N and graphitic-N have little effect on the structure of graphene.[32] However, the pyrrolic-N of SP^3 bond destroys the planar structure of graphene. Pyridinic-N bond has the best stability in the presence of a single vacancy. If Stone-Wells defect and vacancy defect occur, pyridinic-N and graphitic-N have greater influence on ORR.[33] The electronegativity of N (3.04 at Paulin scale) is greater than that of C (2.55 at Paulin scale), which leads to the polarization of carbon network and that affects the electrocatalytic performance of N-doped graphene.[34] N-doped graphene can conduct electricity by inhibiting the state density (DOS) near the bandgap near the Dirac point (Figure 2b).[35] The conductive behavior of nitrogen-doped graphene also depends on the configuration of N-doped graphene. For graphitic-N, three valence electrons of nitrogen form three s bonds with adjacent carbon atoms, one electron participates in the formation of π bond and the fifth electron participates in the π* state of the junction band. Each graphitic N can contribute 0.5 electrons to the π network of graphene lattice. For pyrrolidine-N, pyrrolidine forms at the defect sites and electrons can be extracted from graphene sheets into these defects, resulting in N-doping effect for the different bond types as compared to pristine graphene (Figure 2c).[36]

Paul et al. also pointed out that there were three chemical forms of nitrogen on the surface of nitrogen-doped graphene, namely pyridinic-N, pyrrolic-N and graphitic-N.[28a] Pyridinic-N refers to nitrogen atoms attached to two carbon atoms, corresponding to XPS binding energy of 402 to 405 eV. In addition to an electron supplied to the conjugated bond system, the N atom also has a lone pair of electrons, which can absorb O_2 molecule and their intermediates in the process of ORR, thus improving the catalytic efficiency. Pyrrolic-N is a nitrogen atom with two p electrons and conjugated with a pin bond system.

This article is protected by copyright. All rights reserved.

Graphitic-N refers to nitrogen which is linked to three C atoms. Some researchers believed that graphitic plays a key role in the electrocatalytic ORR.[37]

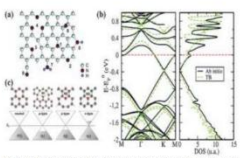

Figure 2. (a) Possible configurations of nitrogen dopants in graphene: 1-graphitic N, 2-pyridinic N, 3-single N pyridinic vacancy, 4-triple N pyridinic vacancy, 5-pyrrolic N, 6-interstitial N or adatom, 7-amine, and 8-nitrile. Reprinted with permission from Ref.[31]. Copyright: 2011 American Chemical Society. (b) *Ab initio* (thick black lines) and tight-binding (green dashed lines) band structures (left) and DOS (right) of a 10 × 10 graphite supercell containing one substitutional N dopant. Reprinted with permission from Ref.[39a]. Copyright: 2013 American Chemical Society. (c) Computed doping effect of N dopant. Reprinted with permission from Ref.[39a]. Copyright: 2012 American Chemical Society.

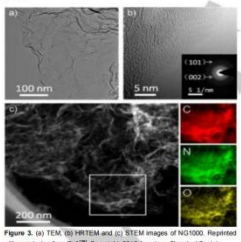

Figure 3. (a) TEM, (b) HRTEM and (c) STEM images of NG1000. Reprinted with permission from Ref.[39]. Copyright: 2013 American Chemical Society.

It is also reported that the more graphitic-N is contained in nitrogen-doped graphene, the better its catalytic activity for oxygen reduction reaction is. Pan et al prepared N-doped graphene catalysts by pyrolysis at 800 to 1000 °C after mixing sugar and urea. The obtained materials show wrinkled multilayer graphene structure (Figures 3a-c). The surface area can reach 565.1 m^2 g^{-1} at 1000°C. Under the condition of 0.1 M KOH alkaline medium, the half-wave potential was 0.14 V vs Ag/AgCl, and Koutecky-Levich determined that the N-doped graphene material had a good mass transfer limiting current density at the potential of 0.25 V vs Ag/AgCl and the electron transfer number was 3.8.[38]

In addition, Ikeda et al. drew a conclusion that graphitic nitrogen is an energetic active site based on oxygen adsorption barrier and subsequent ORR process.[39] Geng et al. found that the ORR activity of the synthesized N-doped graphene with 2.8% N was high when the annealing temperature was 900 °C. X-ray photoelectron spectroscopy (XPS) analysis showed that the enhancement of ORR activity was attributed to the appropriate graphitization of N.[11a] Graphene oxide prepared by Hummers method was used to synthesize N-doped graphene with a suitable nitrogen source. When the number of N atoms in the pyrrole ring is large, polypyrrole can promote the electrochemical performance of graphene, which shows that natural formation has excellent catalytic activity and is beneficial to the formation of water through the four-electron path in alkaline electrolyte. At the same time, the stability of natural gas and the cross-durability of methanol are also excellent. Its performance is superior to that of commercial Pt/C catalyst, which proves that graphitic-N is very important in ORR.[40] Zhen and co-workers used similar methods to explore the effect of graphitic-N on ORR activity. The electrochemical tests showed that larger graphitic nitrogen configuration might have better electrocatalytic ORR activity.[41] Vazquez-Arenas and co-workers used DFT calculations to investigate the mechanism of ORR on N-doped graphene. It is proposed that the contact between a carbon atom and graphitic-N is an electronic defect, which promotes the adsorption and reduction of oxygen through electron transfer in the reaction process, thus playing the role of active center.[42]

Moreover, researchers have suggested that pyridinic-N is also a contributing factor to the electrocatalytic activity of ORR. Woo et al found that pyridinic-N improved the ORR activity under acidic conditions.[43] Xia's team used argon as a protective gas to annealed melamine to prepare N-doped graphene. The results showed that the pyridine-N component determined the electrocatalytic activity of N-doped graphene in a redox reaction.[44] Sun et al. developed a new method to prepare high concentration nitrogen doped platelet carbon nanofibers (plCNF). The chaotic edge of pICNFs is clipped by high frequency etching technology, which produces many exposed edges and patterned edge points.[45] The pyridine-N atom is preferentially located. The electrochemical experiments show that the carbon atoms near pyridine-N can be used as the catalytic center of ORR, and the reaction process is dominated by 4e. The active sites on nitrogen-doped graphene can be determined by the changes of chemical composition before and after ORR. The activity of NG is related to the chemisorption ability of -OH group, which is formed on the carbon atom near pyridinic-N. It is found that the carbon atoms adjacent to pyridinic-N play an important role in ORR and are the main activity centers. Zhang et al. synthesized a N-doped carbon material by adopting a novel green strategy

This article is protected by copyright. All rights reserved.

without any starting chemicals, and the structure of nitrogen bond belongs to pyridinic-N.[46] Recently, Zhao and coworkers found that the N-HC@G catalyst possesses high ORR activity in both acid and alkaline conditions, in which the type of nitrogen is pyridinic-N.[47]

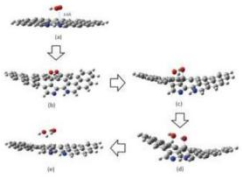

Figure 4. Optimized structure of each electron transformation in ORR: (a) initial position of OOH from N-graphene, (b) OOH adsorbs on the doped graphene, (c) O–O bond is broken, (d) one water molecule is generated, and (e) C–O bond is broken, and the second water molecule is generated. Gray, blue, red and small white balls represent C, N, O and H atoms, respectively. Reprinted with permission from Ref.[48a]. Copyright: 2012 American Chemical Society.

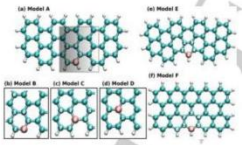

Figure 5. Six different models for the N-doped graphene quantum dots. Reprinted with permission from Ref.[39]. Copyright: 2013 American Chemical Society.

Ruoff et al reported that the content of graphitic-N determines the limit current density, while pyridinic nitrogen is the key to improve the electrocatalytic activity of ORR.[48] In order to further clarify the catalytic mechanism, a series of simulations were carried out, and the energies on N-doped graphene with different doping amounts were calculated by Boukhvalov and Son.[48b] When the amount of N doping is relatively low, the energy consumption in the intermediate process of ORR can be reduced and the energy barrier is lower than that on the platinum surface. The addition of nitrogen enlarges the positive spin density and charge density and enhances the catalytic activity.[50] The process can be carried out spontaneously on N-doped graphene. Interestingly, the calculated average reversible potential is 1.15 V vs. SHE, which is consistent with the experimental results (Figure 4). Meanwhile, multiple experiments revealed the influence of pyridinic-N position and microstructure on its catalytic efficiency.[51] A number of experiments have proved that ORR activity is related to the content of pyridine nitrogen.[10a, 48, 50a, 52]

It has also been suggested that pyridinic nitrogen and graphitic nitrogen simultaneously influence ORR activity.[46, 53] Wissam et al found that pyridinic and graphitic nitrogen are the most active sites. Ten graphene quantum-dots models for simulating nitrogen-doped graphene are presented, of which six models is shown in Figure 5.[39] In model A, C, and D, nitrogen doping is similar to graphite substitution, where nitrogen is located at different distances from the edge of graphene quantum dots. The model B has a similar pyridine type doping. Pyridine nitrogen is especially interesting because it has a pair of electrons besides one electron of the conjugated π bond. In E, nitrogen belongs to pyrrolidine doped five-membered rings.[50] Due to the mutual exclusion between nitrogen dopants, the aggregation of nitrogen on the original graphene is inhibited, therefore, the chemical properties of single nitrogen doping are expected to be widely used.[39]

Kabir et al. prepared nitrogen-doped graphene films by sacrifice support method.[51] The optimal doping temperature for is 850 °C, which showed good ORR activity (Figure 6). The content of nitrogen components such as graphitic-N, quaternary-N, nitrogen hydride, and pyridinic-N varies greatly with the pyrolysis temperature. The decrease of graphitic-N content and the increase of hydrogenation-N/pyridinic-N ratio would increase the ORR activity. The ORR mechanism steps on graphitic, hydrogenation and pyridinic nitrogen are proposed in Figures 6c-d.[51] Lu et al. prepared three-dimensional nitrogen-doped graphene (3D-NG@SiO_2).[10b] It is suggested that nitrogen mainly exists in the form of pyridinic nitrogen by pyrolysis of poly (o-phenylenediamine) containing nitrogen precursor and silica gel. The initial potential of 3D-NG@SiO_2 was 0.08 V for ORR. The number of electron transfer is 3.92. This indicates that 3D-NG@SiO_2 mainly occurs through four-electron process. It is also proved that the catalyst has high activity, good durability and broad application prospects.

Guo et al.[54] clarified the possible mechanism of ORR on nitrogen-doped carbon materials by exploring the active sites of nitrogen-doped carbon materials for oxygen reduction. Lewis bases are formed by pyridinic N. First, oxygen molecules are adsorbed on carbon atoms next to the protonated pyridine N. Two possible approaches are proposed: one is the four-electron mechanism at a single site; the other is the 2 + 2 electron mechanism, which does not always occur at a single site. Titash Mondal et al.[55] synthesized nitrogen-doped graphene from heteroatomic polymers and proposed the mechanism of nitrogen-doped graphene (Figure 7). When the material was treated by high temperature, the chain breakage becomes active

This article is protected by copyright. All rights reserved.

and low molecular weight fragments are produced. The products formed by chain breaking are usually free radicals, which combine with each other to form new products.[61]

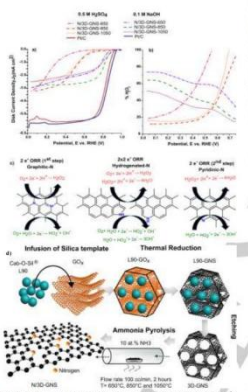

Figure 6. Hydrogen peroxide yield (%H_2O_2) and peroxyhydroxyl yield ($^*OH/O^*$) of N-doped 3D-graphene nanosheet materials in (a) acid and (b) alkaline media. (c) ORR mechanism of graphitic, hydrogenation and pyridinic nitrogen. (d) ORR mechanism of graphitic, hydrogenation and pyridinic nitrogen. Reprinted with permission from Ref.[57]. Copyright: 2018 American Chemical Society.

Similar to nitrogen-doped graphene, nitrogen-doped carbon nanotubes have a larger specific surface area, higher conductivity and excellent catalytic activity for oxygen reduction.[62] Moreover, its low cost, high activity, and excellent durability are the advantages of ORR as a new electrocatalytic system.[10d, 37, 52a, 63] The hybrid composites of nitrogen-doped graphene and nitrogen-doped carbon nanotubes (NGCA) have been obtained via the in-situ synthesis method, which can further improve the catalytic performance for ORR.[64] The nitrogen-doped carbon nanotubes can not only be used as a high-speed electron conduction channel, but also effectively prevent the re-stacking of graphene, and greatly improve the specific surface area and conductivity of NGCA composite catalysts. As a result, the NGCA composite catalyst exhibits a four-electron reaction path, and its ORR activity at 0.75 V is six times as high as that of nitrogen-doped graphene. Besides, nitrogen-doped graphene-carbon nanotube composite catalyst could be also prepared by one-step chemical meteorological deposition.[65] Graphene and carbon nanotubes grow at the same time, resulting in a three-dimensional spatial structure. The specific surface area of graphene and carbon nanotubes reached 812.9 $m^2 g^{-1}$, and the conductivity reached 53.8 $s cm^{-1}$. Although the nitrogen content of the composite catalyst is only 0.53%, its oxygen reduction catalytic performance is very good, close to that of industrial Pt/C catalyst, and its long-term stability is much higher than that of Pt/C catalyst.

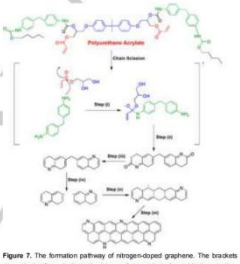

Figure 7. The formation pathway of nitrogen-doped graphene. The brackets shown in the figure indicate the intermediate products formed in the reaction. Reprinted with permission from Ref.[65]. Copyright: 2015 American Chemical Society.

In addition, the hybrid composites of nitrogen-doped graphene and nitrogen-doped carbon nanotubes also show superior ORR performance in acidic conditions. For example, Dai and coworkers synthesized a nitrogen-doped graphene/CNT catalyst, which exhibited high activity and stability in the acidic polymer electrolyte membrane fuel cells (PEMFCs).[66] The low-cost, metal-free, carbon-based ORR catalysts show promising practical application prospect for acidic PEMFCs.

In conclusions, N-doped graphene prepared by various methods is one of the most efficient metal-free ORR electrocatalysts.[52a, 67] The doped nitrogen atoms can affect the spin density and electron cloud distribution of adjacent carbon atoms and thus induce the formation of "active centers", which can directly participate in ORR.[44, 68] Up till now, there are still many controversies about the ORR active sites of N-doped graphene.[52c, 69] In addition to N-doped graphene, N-doped carbon nanostructures such as 3D N-containing polymer[67], N-doped carbon nanocapsules[70], N-CNT cups[71], and N-doped mesoporous carbon[72] also showed excellent activity in ORR electrocatalysis.[39]

3.3. Sulphur doped graphene

Since the electronegativity of S (2.58) and C (2.55) is similar, charge transfer can be ignored in the C-S bond. However, contrary to the zero spin density of undoped graphene, the mismatch between the outermost orbital of S and C leads to uneven spin density distribution on S-doped graphene. It was suggested that S-doped graphene was formed by defect formation and S bonds break in two steps. The S-doped graphene sheet could be a small bandgap semiconductor, more metalized than the original graphene.[73] Graphene doped with S has a higher resistance than original graphene.[74] Using first-principles calculations, Denis et al proposed that S-doped graphene is feasible for ORR, but its catalytic effect is not as good as that of nitrogen-doped graphene.[75] Jeon et al. found that covalently bonded S and oxidized S at the serrated and armchair-like edges of graphene nanometer salts obtained from ball-milling could lead to significant increase in spin density.[56a, 76] Xia et al. found that the change of atomic spin density plays an important role in oxygen reduction activity by density functional theory calculation.[77] Zhang et al. calculated the distribution of atomic charge and spin density as shown in Figure 8. When graphene is decorated by sulfur, graphene does not exhibit additional spin density because sulfur atoms do not introduce additional unpaired electrons. Charge density redistributes on S-doped graphene clusters with Stone-Wales defects. The positive charge densities of the carbon atoms 11, 15, 89 and 93 at the serrated edge are higher about 0.17 than other carbon atoms. It is speculated that these carbon atoms may be the catalytic sites of ORR. Adsorption calculations of OOH or O_2 at these sites show that both OOH and O_2 can be adsorbed on the sawtooth edge of graphene with Stone-Wales defects, but not on graphene without Stone-Wales defects. These active sites play an active role in promoting ORR. Figures 8c and 8d are similar in that the substituted sulfur atoms are located at the serrated edge. Atoms with high charge densities are also located at the sawtooth edge, and these atoms also generate spin densities. As shown in Figures 8e and 8f, the spin and charge densities of these sulfur oxide atom defective graphene structures are distributed on the edge of the armchair. Interestingly, the spin and charge densities of carbon atoms adjacent to sulfur oxide are also high. It is shown that sulfur-doped graphene clusters not only polarize more spin and charge density atoms with Stone-Wales defects, but also contribute to the catalysis of ORR. Similarly, as shown in Figure 8, atoms with higher charge density are distributed along the zigzag edge. Its value is less than 0.19. The authors tested these atoms with high charge density and spin density. The results show that atoms with charge density greater than 0.20 and spin density greater than 0.15 can absorb OOH or O_2, suggesting that they may be potential active centers of ORR. Figure 8h shows the charge density distribution on pure graphene clusters. It is found that there is no spin density on pure graphene clusters, and the maximum charge density is 0.17. OOH and O_2 cannot be adsorbed on carbon atoms. The results show that the catalytic activity of pure graphene is not good, which further proves that the graphene clusters doped with sulfur atoms have a positive effect on the catalytic activity of ORR.

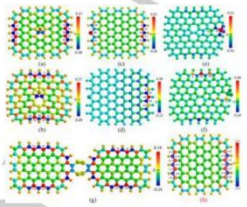

Figure 8. Atomic charge density and spin density distributions on the S-doped and pure graphene clusters. Atomic charge density distribution on S-adsorbed graphene clusters with (a) perfect structure and (b) one Stone-Wales defect; (c) atomic charge density and (d) spin density distributions on perfect graphene cluster with substituting S at the zigzag edge; (e) atomic charge density and (f) spin density on SO_2-doped graphene with a Stone-Wales defect; atomic charge density on (g) sulfur ring cluster connecting two pieces of graphene clusters and (h) pure graphene cluster. The colors of the balls stand for relative values of charge and spin density. The density decreases linearly from positive to negative values in the color order of red, orange, yellow, green, and blue. Sulfur and oxygen atoms are labeled with S and O, respectively. The unlabeled small and large balls represent H and C, respectively printed with permission from Ref.[78]. Copyright: 2014 American Chemical Society.

Sulfur-doped graphene can be obtained by using dibenzyl disulfide as sulfur source and graphene oxide as raw material. The ORR catalytic activity of S-graphene-600 is higher than that of graphene-600 (Figure 9a). The catalytic activity can be improved by enhancing the annealing temperature and the ORR activity of S- graphene-1050 is close to that of Pt/C (Figure 9). Recently, Zhang et al. prepared S-doped graphene by using carbon precursor of sulfonate ion exchange resin. The obtained S-doped graphene has similar electrocatalytic activity with Pt/C, but better stability and methanol resistance than the latter.[78] Most of the research showed that the onset potential and the number of electrons per oxygen transfer for S-doped graphene were similar to those for N-doped graphene. Xia et al. proposed a catalytic mechanism of ORR on S-doped graphene.[77] XPS

This article is protected by copyright. All rights reserved.

results show that doped S is mainly doped in the form of -C-S-C - or -C-SO_2-C-C- on the edge or surface of graphene.[79-83]

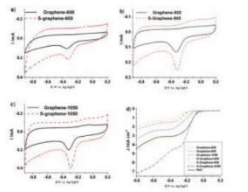

Figure 9. (a) Cyclic voltammetry curves of graphene-600 and S-graphene-600, (b) Cyclic voltammetry curves of graphene-900 and S-graphene-900, (c) Cyclic voltammetry curves of graphene-1050 and S-graphene-1050, (d) LSV curves of various graphene and Pt/C catalysts on a rotating glass-carbon disk. Reprinted with permission from Ref.[84]. Copyright: 2012 American Chemical Society.

The ORR activity of pure graphene is very low, while S-doped graphene can enhance the charge and spin density, which is conducive to the adsorption of O_2. The active sites on these S-doped graphene clusters are those carbon atoms located at zigzag edges or near SO_2-doped structures, which have high positive charge density and spin density. It is known that the two-electron transfer pathway occurs on substituted sulfur atoms with high charge density, while the four-electron transfer pathway occurs on carbon atoms with high spin or charge density. Sulfur-doped graphene expands the family of metal-free carbon-based nanomaterials and becomes a new electrocatalyst to replace Pt in fuel cells.[10b, 21d] Even though the electrocatalytic activity of S-doped graphene for ORR is still lower than that of commercial Pt/C, the synergistic effect of sulfur and carbon materials on the development of metal-free ORR electrocatalysts provides a feasible strategy to design new ORR electrocatalysts.

3.4. Phosphorus doped graphene

It is proposed that nonmetallic atoms doped graphene can better regulate the electronic structure and thus improve the electrochemical properties of the oxygen reduction reaction. In order to improve the energy storage properties of graphene, various attempts have been made. Among them, the introduction of heteroatoms (O, N, S, B, and P) is one of the effective methods to improve the electrochemical performance of graphene electrode materials,[85] which has the advantage of changing the electronic properties of carbon materials and the influence of charge distribution on adjacent atoms.[10b] Doped heteroatoms generate induced charges and change the chemical adsorption by redistribution of charges. It can effectively weaken the O-O bond bonding, making the positively charged carbon atoms easy to attract electrons, thus promoting the ORR process.[52a, 52d] P-doped graphene can also improve the electron donor properties of carbon materials and thus enhances the catalytic activity.[62] The ORR activity of P-doped graphene was higher than that of non-doped graphene.[10b] Peng et al studied P-doped carbon nanospheres for ORR in both acidic and alkaline media and found that the ORR activity was higher in alkaline media, but the long-term stability of the materials was better in acidic media.[52] Zhang et al also found that P-doped graphene significantly improved the electrochemical performance of graphene in ORR and lithium-ion battery (LIB).[64] Liu et al synthesized P-doped graphene by pyrolysis of toluene and triphenylphosphine, which could be used as oxygen reduction catalyst.[10e, 52a, 86]

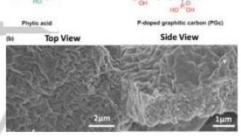

Figure 10. (a) Schematic diagram of preparing p-doped graphite carbon with phytic acid. (b) SEM images of PGC. Reprinted with permission from Ref.[64]. Copyright 2016 American Chemical Society.

In addition, it is found that P-doped graphene is more stable in air than N-doped graphene, and exhibits n-type semiconductor characteristics.[86] P-doped graphene can be applied in supercapacitors. For example, Yang et al used P-enriched activated carbon as a supercapacitor and found that P-enriched activated carbon can not only improve the performance and high capacitance of the supercapacitor but also broaden the potential of the battery in water electrolyte. Graphene oxide and phosphoric acid were treated at high temperature to enhance the voltage window of graphene. However, the capacitance of phosphor doped graphene is low, which is only 29 F/gat 1 A/g current density.[87] In 2016, Pate et al.[64] prepared P-doped porous carbon materials by microwave oven method. As shown in Figure 10a, the coordination of P atoms can be controlled.

This article is protected by copyright. All rights reserved.

This P-doped carbon has a special structure (Figure 10b). A porous carbon block is sandwiched between two shrunken graphene-like sheets. The reason for forming this structure may be that the diameter of P atom is larger than that of C atom and the doping of P atom causes local geometric stress in the carbon network around each P atom.

3.5. N/P codoped graphene

In addition to N-doped graphene as a non-metallic electrocatalyst, researchers have focused their attention on the non-metallic electrocatalyst with nitrogen and phosphorus as co-dopant.[87, 88, 89] Zhu et al.[89] proposed that the nitrogen and phosphorus doped honeycomb carbon is an efficient electrocatalyst for ORR. The material was prepared by direct pyrolysis of popcorn in a static semi-open environment. It shows layered porous structure and the ORR is close to the standard Pt/C. The P/N codoped graphene prepared by pyrolysis of graphene and dicyandiamide mixture showed a marked increase in catalytic activity for ORR in phosphoric acid solution.[88] Nitrogen and phosphorus codoped graphene/carbon nanosheets (N, P-GCNS) were prepared by pyrolysis of the mixture of GO, polyaniline and phytic acid (Figure 11). Compared with N or P single-doped catalysts, N/P codoped graphene catalysts are more active.[87]

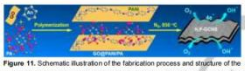

Figure 11. Schematic illustration of the fabrication process and structure of the N, P-GCNS bifunctional oxygen electrocatalyst. Reprinted with permission from Ref.[87]. Copyright: 2015 American Chemical Society.

3.6. N/S codoped graphene

In order to improve the interaction between doping elements and dopants, two kind of heteroatoms doped graphene can effectively solve this problem.[57] Heteroatoms codoped graphene as an electrocatalyst has a significant improvement in ORR.[85, 75, 90] In order to improve the catalytic activity of ORR, dopants are usually introduced into the carbon lattice.[78, 89b] Researchers have used two doped elements to adulterate graphene.[90a, 90] In the case of double doped carbon materials, S atoms can induce adjacent C and N atoms to polarize,[90] it can form unique electronic distribution and further induce the synergistic effect.[90] N/S co-doped graphene can efficiently improve the catalytic activity of ORR.[28, 78, 91] Guan et al. prepared N and S co-doped graphene from pyrimidine and thiophene sites with enhanced ORR activity.[92c] Qiao et al proved this viewpoint correct by density functional theory calculation.[10d]

It is proposed that the three-dimensional voids on the graphite surface constitute its unique stratified structure.[56] It has high surface area, abundant active sites at the interface of electrochemical reaction, and good electron/electrolyte transport characteristics. Li et al. prepared S, N co-doped graphene carbon nanosheets by pyrolysis of melamine and dibenzyl sulfide.[56] The schematic diagram of the synthesis process of S, N co-doped graphene carbon nanosheets is presented in Figure 12a. Taking graphene nanosheets loaded with S_3N_6 as an example, the catalytic activity of graphene nanosheets annealed at 700, 800, 900 and 1000 °C was tested in the 0.1 M KOH electrolyte (Figure 12b). The results showed that the catalytic activity of S_3N_6 annealed at 900 °C was the best, which was higher than that of Pt/C. From Figures 12c and 12d, it can be concluded that the synergistic effect of S and N atoms in S and N co-doped carbon materials plays a key role in ORR in both alkaline and acidic media. Compared with single S or N doped graphene, S/N codoped graphene carbon nanosheets have higher ORR activity.

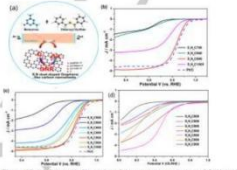

Figure 12. (a) Schematic illustration of the synthesis procedure of S, N dual-doped graphene-like carbon nanosheets materials for the application in oxygen reduction electrocatalysis. (b) LSV of the S_3N_6CT and Pt/C (20 wt %, E-TEK) at 1600 rpm. (c) LSV of the as-prepared S_3N_6C900 samples and Pt/C catalyst (20 wt %, E-TEK) at 1600 rpm. (d) LSV curves of S_3N_6C900 samples in O_2-saturated 0.5 M H_2SO_4 aqueous solution. Reprinted with permission from ref.[56]. Copyright: 2017 American Chemical Society.

Zheng et al. prepared sulfur-nitrogen co-doped graphene/CNT (GC) as shown in Figure 13a. Firstly, carbon nanotubes dispersed on graphene oxide surface were partially reduced by gas chromatography, and nitrogen was doped in ammonia at 500 °C. In the second step, nitrogen-doped gas chromatography was mixed with phenyl disulfide and heat-treated at 900 °C. It can be found that this distribution-by-distribution doping can significantly increase the nitrogen content. Even when the surface concentration of sulfur measured by XPS is only 0.23%, the beneficial effect on ORR is significant, and the change of GC structure after co-doping is minimal (Figure 13b). In 0.1 M KOH electrolyte (Figure 13c), the initial potential of GC-NLS is 0.85 V vs. RHE, which is 70 mV higher than that of co-doped graphene (G-NLS), and 50 mV higher than that of S/N co-doped CNTS (C-NLS). The half wave potential (0.72 V vs. RHE) also increased by 50 mV compared with that of C-NLS.[93] Wohlgemuth et al also found show that the introduction of sulfur atom can incrrase the structure defect, polarizability, and catalytic activity of ORR in alkaline condition.[93c, 100] N/S co-doped carbon foams with continuous and hierarchical structure show wide application prospects as ORR metal-free

This article is protected by copyright. All rights reserved.

Accepted Manuscript

electrocatalysts.[101] Su et al. found that the catalytic activity of S/N-codoped 3d graphene undergoes mainly 4e transfer in 0.1 M KOH.[97]

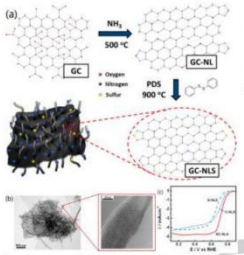

Figure 13. (a) Schematic illustration of the step-wise doping process to fabricate GC-NLS nanocomposites. (b) TEM images of the GC-NLS catalyst. (c) ORR polarization curves obtained in 0.1 M KOH showing the synergic effect of GC-NLS. Reprinted with permission from Ref.[94]. Copyright: 2014 American Chemical Society.

4. Summary and perspectives

Nonmetal-doped graphene materials have a great application prospect on energy catalysis due to their excellent catalytic activity and stability for ORR. Compared with graphene, nonmetal-doped graphene can not only improve the electron structure of graphene but also create more active sites for ORR. The two-dimensional structure and adjustable surface of graphene play an important role in doping different nonmetal elements, which provide good superiority to improve the stability and catalytic activity for ORR. Up to date, nitrogen, phosphorus, and sulfur doped graphene materials exhibit excellent ORR performance. Among them, nitrogen-doped graphene exhibits higher ORR activity than phosphorus and sulfur doped ones. Moreover, nitrogen-sulfur or nitrogen-phosphorus co-doped graphene can further enhance ORR performance.

However, the ORR activity of most of the nonmetal-doped graphene without metal active sites in acidic media is insufficient since they show high overpotential. The ORR activity can be significantly improved by assembling the nitrogen-doped graphene with N-doped carbon nanotubes due to the porous structures with a large surface area. Another familiar strategy to improve the ORR activity is introducing metal ions (e.g. Fe, Co) to the system. However, in the popular PEMFCs, the acid-corrosion resistance of most transition metals is less than carbon. Therefore, for commercialization of the fuel cell technology, improvement of the degree of graphitization is crucial to enhance the corrosion resistance of the nonmetal-doped graphene materials.

Currently, most of the research of ORR on nonmetal-doped graphene catalysts is carried out in alkaline media and is mainly remained in the experimental stage rather than the practical commercial applications of fuel cell. Since acidic PEMFCs are more practical than alkaline ones, development of efficient and stable nonmetal-doped graphene ORR catalysts operated in acid media is vital and urgent in future PEMFCs technologies.

Yanqiu Shao received her B.S in Chemistry from Mudanjiang Normal University and obtained her Ph.D in Physical Chemistry from Jilin University in China. She is currently a professor of Catalytic Principle and Functional Materials in Mudanjiang Normal University.

Zhenshuang Jiang received his B.S. degree from Mudanjiang Normal University in 2016. Currently, he is a Master candidate of Mudanjiang Normal University under the supervision of Prof. Yanqiu Shao. His research focuses on catalyst design for fuel cells and energy conversion.

Qiaoqiao Zhang received her B.S. degree from DaTong University in Shanxi in 2018. Currently, she is a Master candidate of Jilin University under the supervision of A/Prof. Jingqi Guan. Her research focuses on the synthesis of mononuclear-multinuclear catalysts for energy storage and conversion.

Jingqi Guan received his B.S. degree and Ph.D. degree from Jilin University in 2002 and 2007. He was promoted to associate professor of chemistry in Jilin University in 2009. He worked as a postdoctoral research fellow in the University of California at Berkeley from 2012 to 2013 and in the Dalian Institute of Chemical Physics from 2014 to 2018. His research interests focus on the synthesis of mononuclear-multinuclear catalysts for energy storage and conversion.

This article is protected by copyright. All rights reserved.

Acknowledgements

This work was supported by the Natural Science Foundation of Jilin Province (20180101291JC), Heilongjiang Education Department (1352 MSYB006), and Mudanjiang Normal University (JG2017001).

Conflict of interest

The authors declare no conflict of interest.

Keywords: Graphene • Nitrogen-doping • Oxidized carbon materials • Oxygen reduction reaction • Phosphorus-doping • Sulfur-doping • Fuel cell

[1] N. Recham, J.N. Chotard, L. Dupont, C. Delacourt, W. Walker, M. Armand, J.M. Tarascon, Nat. Mater. **2009**, *9*, 68.
[2] a) F. Cheng, J. Chen, Chem. Soc. Rev. **2012**, *41*, 2172-2192; b) Z.-L. Wang, D. Xu, J.-J. Xu, X.-B. Zhang, Chem. Soc. Rev. **2014**, *43*, 7746-7786; c) M.A. Rahman, X. Wang, C. Wen, J. Electrochem. Soc. **2013**, *160*, A1759-A1771; d) Y. Li, H. Dai, Chem. Soc. Rev. **2014**, *43*, 5257-5275; e) H. Kim, G. Jeong, Y.-U. Kim, J.-H. Kim, C.-M. Park, H.-J. Sohn, Chem. Soc. Rev. **2013**, *42*, 9011-9034; f) V. Nebuchinlov, H. Wang, J.J. Martin, W. Qu, J. Power Sources **2010**, *195*, 1271-1291; g) A. Kraytsberg, Y. Ein-Eli, Adv. Energy Mater. **2012**, *2*, 922-939; h) D.R. Egan, C. Ponce De León, R.J.K. Wood, R.L. Jones, K.R. Stokes, F.C. Walsh, J. Power Sources **2013**, *236*, 293-310.
[3] a) D. Yu, E. Nagelli, F. Du, L. Dai, J. Phys. Chem. Lett. **2010**, *1*, 2165-2173; b) Y. Zheng, Y. Jiao, M. Jaroniec, Y. Jin, S.Z. Qiao, Small **2012**, *8*, 3550-3566.
[4] a) J. Wu, X.Z. Yuan, J.J. Martin, H. Wang, J. Zhang, J. Shen, S. Wu, W. Merida, J. Power Sources **2008**, *184*, 104-119; b) T. Kinumoto, M. Inaba, Y. Nakayama, K. Ogata, R. Umebayashi, A. Tasaka, Y. Iriyama, T. Abe, Z. Ogumi, J. Power Sources **2006**, *158*, 1222-1228; c) R. Borup, J. Meyers, B. Pivovar, Y.S. Kim, R. Mukundan, N. Garland, D. Myers, M. Wilson, F. Garzon, D. Wood, P. Zelenay, K. More, K. Stroh, T. Zawodzinski, J. Boncella, J.E. Mcgrath, M. Inaba, K. Miyatake, M. Hori, K. Ota, Z. Ogumi, S. Miyata, A. Nishikata, Z. Siroma, Y. Uchimoto, K. Yasuda, K.-I. Kimijima, N. Iwashita, Chem. Rev. **2007**, *107*, 3904-3951.
[5] a) M.A. Patel, F. Luo, M.R. Khoshi, E. Rabie, Q. Zhang, C.R. Flach, R. Mendelsohn, E. Garfunkel, M. Szostak, H. He, ACS Nano **2016**, *10*, 2305-2315; b) D. Higgins, P. Zamani, A. Yu, Z. Chen, Energy Environ. Sci. **2016**, *9*, 357-390; c) Z. Yang, H. Nie, X.A. Chen, X. Chen, S. Huang, J. Power Sources **2013**, *236*, 238-249.
[6] a) D. Higgins, M.A. Hoque, M.H. Seo, R. Wang, F. Hassan, J.-Y. Choi, M. Pritzker, A. Yu, J. Zhang, Z. Chen, Adv. Funct. Mater. **2014**, *24*, 4324-4324; b) M.A. Hoque, F.M. Hassan, D. Higgins, J.-Y. Choi, M. Pritzker, S. Knights, S. Ye, Z. Chen, Adv. Mater. **2015**, *27*, 1229-1234; c) Y. Tan, C. Xu, G. Chen, N. Zheng, Q. Xie, Energy Environ. Sci. **2012**, *5*, 6923-6927; d) J. Zhu, M. Xiao, X. Zhao, C. Liu, J. Ge, W. Xing, Nano Energy **2015**, *13*, 318-326.
[7] a) X. Liu, L. Dai, Nat. Rev. Mater. **2016**, *1*, 16064; b) J. Zhang, L. Qu, G. Shi, J. Liu, J. Chen, L. Dai, Angew. Chem. Int. Ed. **2016**, *55*, 2230-2234.
[8] K.S. Novoselov, A.K. Geim, S.V. Morozov, D. Jiang, M.I. Katsnelson, I.V. Grigorieva, S.V. Dubonos, A.A. Firsov, Nature **2005**, *438*, 197.
[9] a) C. Biswas, Y.H. Lee, Adv. Funct. Mater. **2011**, *21*, 3806-3826; b) C. Huang, C. Li, G. Shi, Energy Environ. Sci. **2012**, *5*, 8848-8868.
[10] a) L. Qu, Y. Liu, J.-B. Baek, L. Dai, ACS Nano **2010**, *4*, 1321-1326; b) D. Yu, L. Wei, W. Jiang, H. Wang, B. Sun, Q. Zhang, K. Goh, R. Si, Y. Chen, Nanoscale **2013**, *5*, 3457-3464; c) S. Yang, X. Feng, X. Wang, K. Müllen, Angew. Chem. **2011**, *123*, 5453-5456; d) S. Yang, L. Zhi, K. Tang, X. Feng, J. Maier, K. Müllen, Adv. Funct. Mater. **2012**, *22*, 3634-3640; e) Z.-W. Liu, F. Peng, H.-J. Wang, H. Yu, W.-X. Zheng, J. Yang, Angew. Chem. Int. Ed. **2011**, *50*, 3257-3261.
[11] a) D. Geng, Y. Chen, Y. Chen, Y. Li, R. Li, X. Sun, S. Ye, S. Knights, Energy Environ. Sci. **2011**, *4*, 760-764; b) Z. Lin, M.-K. Song, Y. Ding, Y. Liu, M. Liu, C.-P. Wong, Phys. Chem. Chem. Phys. **2012**, *14*, 3381-3387; c) H. Fei, R. Ye, G. Ye, Y. Gong, Z. Peng, X. Fan, E.L.G. Samuel, P.M. Ajayan, J.M. Tour, ACS Nano **2014**, *8*, 10837-10843; d) J. Ma, Y. Duan, Z. Qin, J. Wang, W. Liu, M. Xu, S. Zhou, X. Cao, Neuroscience **2015**, *310*, 528-540; e) K.-J. Liu, T.-C. Chang, R.-Y. Yang, C.-E. Chen, S.-H. Ho, J.-Y. Tsai, T.-Y. Hsieh, O. Cheng, C.-T. Huang, Thin Solid Films **2014**, *572*, 39-43; f) Y. Li, Y. Li, E. Zhu, T. Mclouth, C.-Y. Chiu, X. Huang, Y. Huang, J. Am. Chem. Soc. **2012**, *134*, 12326-12329; g) J. Yang, C. Tian, L. Wang, H. Fu, J. Mater. Chem. **2011**, *21*, 3384-3390; h) E.J. Lim, S.M. Choi, M.H. Seo, Y. Kim, S. Lee, W.B. Kim, Electrochem. Commun. **2013**, *28*, 100-103; i) Y. Xin, J.-G. Liu, X. Jie, W. Liu, F. Liu, Y. Yin, J. Gu, Z. Zou, Electrochim. Acta **2012**, *60*, 354-358.
[12] a) L. Wang, A. Ambrosi, M. Pumera, Angew. Chem. Int. Ed. **2013**, *52*, 13818-13821; b) X. Duan, J. Xu, Z. Wei, J. Ma, S. Guo, S. Wang, H. Liu, S. Dou, Adv. Mater. **2017**, *29*, 1701784.
[13] C.-K. Chang, S. Kataria, C.-C. Kuo, A. Ganguly, B.-Y. Wang, J.-Y. Hwang, K.-J. Huang, W.-H. Yang, S.-B. Wang, C.-H. Chuang, M. Chen, C.-I. Huang, W.-F. Pong, K.-J. Song, S.-J. Chang, J.-H. Guo, Y. Tai, M. Tsujimoto, S. Isoda, C.-W. Chen, L.-C. Chen, K.-H. Chen, ACS Nano **2013**, *7*, 1333-1341.
[14] a) L. Yan, M. Lin, C. Zeng, Z. Chen, S. Zhang, X. Zhao, A. Wu, Y. Wang, L. Dai, J. Qu, M. Guo, Y. Liu, J. Mater. Chem. **2012**, *22*, 8367-8371; b) I.-Y. Jeon, Y.-R. Shin, G.-J. Sohn, H.-J. Choi, S.-Y. Bae, J. Mahmood, S.-M. Jung, J.-M. Seo, M.-J. Kim, D. Wook Chang, L. Dai, J.-B. Baek, Proc. Natl. Acad. Sci. **2012**, *109*, 5588.
[15] O.S. Kwon, S.J. Park, J.-Y. Hong, A.R. Han, J.S. Lee, J.S. Lee, J.H. Oh, J. Jang, ACS Nano **2012**, *6*, 1486-1493.
[16] Z. Sun, Z. Yan, J. Yao, E. Beitler, Y. Zhu, J.M. Tour, Nature **2010**, *468*, 549.
[17] I.-Y. Jeon, H.-J. Choi, M. Choi, J.-M. Seo, S.-M. Jung, M.-J. Kim, S. Zhang, L. Zhang, Z. Xia, L. Dai, N. Park, J.-B. Baek, Sci. Rep. **2013**, *3*, 1810.
[18] J. Xu, I.-Y. Jeon, J.-M. Seo, S. Dou, L. Dai, J.-B. Baek, Adv. Mater. **2014**, *26*, 7317-7323.
[19] a) H.-L. Guo, P. Su, X. Kang, S.-K. Ning, J. Mater. Chem. A **2013**, *1*, 2248-2255; b) Z.-S. Wu, A. Winter, L. Chen, Y. Sun, A. Turchanin, X. Feng, K. Müllen, Adv. Mater. **2012**, *24*, 5130-5135.
[20] Y. Su, Y. Zhang, X. Zhuang, S. Li, D. Wu, F. Zhang, X. Feng, Carbon **2013**, *62*, 296-301.
[21] Z. Lu, G. Chen, S. Siahrostami, Z. Chen, K. Liu, J. Xie, L. Liao, T. Wu, D. Lin, Y. Liu, T.F. Jaramillo, J.K. Nørskov, Y. Cui, Nat. Catal. **2018**, *1*, 156-162.
[22] C. Hu, L. Dai, Angew. Chem. Int. Ed. **2016**, *55*, 11736-11758.
[23] L. Dai, Y. Xue, L. Qu, H.-J. Choi, J.-B. Baek, Chem. Rev. **2015**, *115*, 4823-4892.
[24] L. Xue, Y. Li, X. Liu, Q. Liu, J. Shang, H. Duan, L. Dai, J. Shui, Nat. Commun. **2018**, *9*, 3819.
[25] J. Duan, S. Chen, M. Jaroniec, S.Z. Qiao, ACS Catal. **2015**, *5*, 5207-5234.
[26] a) Z. Yang, Z. Yao, G. Li, G. Fang, H. Nie, Z. Liu, X. Zhou, X.A. Chen, S. Huang, ACS Nano **2012**, *6*, 205-211; b) S. Zhong, L. Zhou, L. Wu, L. Tang, Q. He, J. Ahmed, J. Power Sources **2014**, *272*, 344-350; c) C. Han, X. Bo, Y. Zhang, M. Li, L. Guo, J. Power Sources **2014**, *272*, 267-276; d) H. Kim, K. Lee, S.I. Woo, Y. Jung, Phys. Chem. Chem. Phys. **2011**, *13*, 17505-17510; e) P.H. Matter, L. Zhang, U.S. Ozkan, J. Catal. **2006**, *239*, 83-96; f) R.A. Sidik, A.B. Anderson, N.P. Subramaniam, S.P. Kumaraguru, B.N. Popov, J. Phys. Chem. B **2006**, *110*, 1787-1793; g) P.H. Matter, E. Wang, M. Arias, E.J. Biddinger, U.S. Ozkan, J. Mol. Catal. A: Chem. **2007**, *264*, 73-81; h) L. Yu, X. Pan, X. Cao, P. Hu, X. Bao, J. Catal. **2011**, *282*, 183-190; i) Y. Zheng, Y. Jiao, J. Chen, J. Liu, J. Liang, A. Du, W. Zhang, Z. Zhu, S.C. Smith, M. Jaroniec, G.Q. Lu, S.Z. Qiao, J. Am. Chem. Soc. **2011**, *133*, 20116-20119.
[27] C.-S. Liu, X.-C. Liu, G.-C. Wang, R.-P. Liang, J.-D. Qiu, J. Electroanal. Chem. **2014**, *728*, 41-50.
[28] E. Gracia-Espino, X. Jia, T. Wågberg, J. Phys. Chem. C **2014**, *118*, 2804-2811.
[29] S. Zhao, H. Yin, L. Du, L. He, K. Zhao, L. Chang, G. Yin, H. Zhao, S. Liu, Z. Tang, ACS Nano **2014**, *8*, 12660-12668.
[30] Y. Wu, H. Yu, H. Wang, F. Peng, Chinese J. Catal. **2014**, *35*, 952-959.
[31] D. Usachov, O. Vilkov, A. Grüneis, D. Haberer, A. Fedorov, V.K. Adamchuk, A.B. Preobrajenski, P. Dudin, A. Barinov, M. Oehzelt, C. Laubschat, D.V. Vyalikh, Nano Lett. **2011**, *11*, 5401-5407.
[32] M. Yang, L. Zhou, J. Wang, Z. Liu, Z. Liu, J. Phys. Chem. C **2012**, *116*, 844-850.
[33] Z. Hou, X. Wang, T. Ikeda, K. Terakura, M. Oshima, M.-A. Kakimoto, Phys. Rev. B **2013**, *87*, 165401.
[34] P. Wu, P. Du, H. Zhang, C. Cai, Phys. Chem. Chem. Phys. **2013**, *15*, 6920-6928.
[35] a) A. Lherbier, A.R. Botello-Méndez, J.-C. Charlier, Nano Lett. **2013**, *13*, 1446-1450; b) A.R. Botello-Méndez, A. Lherbier, J.C. Charlier, Solid State Commun. **2013**, *175-176*, 90-100.
[36] T. Schiros, D. Nordlund, L. Pálová, D. Prezzi, L. Zhao, K.S. Kim, U. Wurstbauer, C. Gutiérrez, D. Delongchamp, C. Jaye, D. Fischer, H. Ogasawara, L.G.M. Pettersson, D.R. Reichman, P. Kim, M.S. Hybertsen, A.N. Pasupathy, Nano Lett. **2012**, *12*, 4025-4031.
[37] Y. Zhang, J. Ge, L. Wang, D. Wang, F. Ding, X. Tao, W. Chen, Sci. Rep. **2013**, *3*, 2771.
[38] F. Pan, J. Jin, X. Fu, Q. Liu, J. Zhang, ACS App. Mater. Interfaces **2013**, *5*, 11108-11114.
[39] T. Ikeda, M. Boero, S.-F. Huang, K. Terakura, M. Oshima, J.-I. Ozaki, J. Phys. Chem. C **2008**, *112*, 14706-14709.
[40] Z. Lin, G.H. Waller, Y. Liu, M. Liu, C.-P. Wong, Nano Energy **2013**, *2*, 241-248.
[41] S. Zheng, J. Wang, F.-B. Wang, X.-H. Xia, Electrochem. Commun. **2013**, *28*, 24-26.
[42] a) J. Vazquez-Arenas, A. Galano, D.U. Lee, D. Higgins, A. Guevara-Garcia, Z. Chen, J. Mater. Chem. A **2016**, *4*, 975-990; b) H.-P. Cong, P. Wang, M. Gong, S.-H. Yu, Nano Energy **2014**, *3*, 55-63.
[43] K.R. Lee, K.U. Lee, J.W. Lee, B.T. Ahn, S.I. Woo, Electrochem. Commun. **2010**, *12*, 1052-1055.
[44] Z.-H. Sheng, L. Shao, J.-J. Chen, W.-J. Bao, F.-B. Wang, X.-H. Xia, ACS Nano **2011**, *5*, 4350-4358.
[45] M. Sun, X. Wu, Z. Xie, X. Deng, J. Wen, Q. Huang, B. Huang, Carbon **2017**, *125*, 401-408.
[46] H. Zhang, Y. Wang, D. Wang, Y. Li, X. Liu, P. Liu, H. Yang, T. An, Z. Tang, H. Zhao, Small **2014**, *10*, 3371-3378.
[47] J. Sun, S.E. Lowe, L. Zhang, Y. Wang, K. Pang, Y. Wang, Y. Zhong, P. Liu, K. Zhao, Z. Tang, H. Zhao, Angew. Chem. Int. Ed. **2018**, *57*, 16511-16515.
[48] L. Lai, J.R. Potts, D. Zhan, L. Wang, C.K. Poh, C. Tang, H. Gong, Z. Shen, J. Lin, R.S. Ruoff, Energy Environ. Sci. **2012**, *5*, 7936-7942.
[49] D.W. Boukhvalov, Y.-W. Son, Nanoscale **2012**, *4*, 417-420.
[50] a) L. Zhang, Z. Xia, J. Phys. Chem. C **2011**, *115*, 11170-11176; b) L. Zhang, J. Niu, L. Dai, Z. Xia, Langmuir **2012**, *28*, 7552-7559.
[51] T. Xing, Y. Zheng, L.H. Li, B.C.C. Cowie, D. Gunzelmann, S.Z. Qiao, S. Huang, Y. Chen, ACS Nano **2014**, *8*, 6856-6862.
[52] a) K. Gong, F. Du, Z. Xia, M. Durstock, L. Dai, Science **2009**, *323*, 760; b) X. Bo, C. Han, Y. Zhang, L. Guo, ACS App. Mater. Interfaces **2014**, *6*, 3023-3030.
[53] C. Zhang, R. Hao, H. Liao, Y. Hou, Nano Energy **2013**, *2*, 88-97.
[54] D. Wei, Y. Liu, Y. Wang, H. Zhang, L. Huang, G. Yu, Nano Lett. **2009**, *9*, 1752-1758.
[55] W.A. Saidi, J. Phys. Chem. Lett. **2013**, *4*, 4160-4165.
[56] Z. Hou, X. Wang, T. Ikeda, K. Terakura, M. Oshima, M.-A. Kakimoto, S. Miyata, Phys. Rev. B **2012**, *85*, 165439.
[57] S. Kabir, K. Artyushkova, A. Serov, P. Atanassov, ACS App. Mater. Interfaces **2018**, *10*, 11623-11632.
[58] S. Chen, J. Duan, M. Jaroniec, S.Z. Qiao, Angew. Chem. Int. Ed. **2013**, *52*, 13567-13570.
[59] D. Guo, R. Shibuya, C. Akiba, S. Saji, T. Kondo, J. Nakamura, Science **2016**, *351*, 361.
[60] T. Mondal, A.K. Bhowmick, R. Krishnamoorti, Chem. Mater. **2015**, *27*, 716-725.
[61] a) Z. Zhang, K. Chi, F. Xiao, S. Wang, J. Mater. Chem. A **2015**, *3*, 12828-12835; b) X. Xiong, C. Yang, G. Wang, Y. Lei, X. Qu, J.-H. Wang, B. Zhao, M. Liu, Z. Lin, K. Huang, Energy Environ. Sci. **2017**, *10*, 1757-1763.
[62] G.-L. Tian, M.-Q. Zhao, D. Yu, X.-Y. Kong, J.-Q. Huang, Q. Zhang, F. Wei, Small **2014**, *10*, 2251-2259.
[63] a) D.-S. Yang, D. Bhattacharjya, S. Inamdar, J. Park, J.-S. Yu, J. Am. Chem. Soc. **2012**, *134*, 16127-16130; b) H. Feng, Z. Mo, S. Liao, H. Liang, L. Yang, F. Luo, H. Song, Y. Zhong, B. Zhang, Sci. Rep. **2013**, *3*, 1765; c) S.-A. Wohlgemuth, R.J. White, M.-G. Willinger, M.-M. Titirici, M. Antonietti, Green Chem. **2012**, *14*, 1515-1523; d) G.-L. Tian, Q. Zhang, B. Zhang, Y.-G. Jin, J.-Q. Huang, D.S. Su, F. Wei, Adv. Funct. Mater. **2014**, *24*, 5956-5961; e) Z. Chen, D. Higgins, A. Yu, L. Zhang, J. Zhang, Energy Environ. Sci. **2011**, *4*, 3167-3192; f) Y. Zhao, L. Yang, S. Chen, X. Wang, Y. Ma, Q. Wu, Y. Jiang, W. Qian, Z. Hu, J. Am. Chem. Soc. **2013**, *135*, 1201-1204; g) J.-S. Li, S.-L. Li, Y.-J. Tang, K. Li, L. Zhou, N. Kong, Y.-Q. Lan, J.-C. Bao, Z.-H. Dai, Sci. Rep. **2014**, *4*, 5130.
[64] S. Ratso, I. Kruusenberg, M. Viiksaa, U. Joost, E. Shulga, I. Kink, T. Kallio, K. Tammeveski, Carbon **2014**, *73*, 361-370.
[65] D.C. Higgins, M.A. Hoque, F. Hassan, J.-Y. Choi, B. Kim, Z. Chen, ACS Catal. **2014**, *4*, 2734-2740.
[66] J. Shui, M. Wang, F. Du, L. Dai, Sci. Adv. **2015**, *1*, e1400129.
[67] a) B. Dai, K. Chen, Y. Wang, L. Kang, M. Zhu, ACS Catal. **2015**, *5*, 2541-2547; b) J. Zhang, L. Dai, ACS Catal. **2015**, *5*, 7244-7253.
[68] D. Deng, X. Pan, L. Yu, Y. Cui, Y. Jiang, J. Qi, W.-X. Li, Q. Fu, X. Ma, Q. Xue, G. Sun, X. Bao, Chem. Mater. **2011**, *23*, 1188-1193.
[69] a) H.-W. Liang, X. Zhuang, S. Brüller, X. Feng, K. Müllen, Nat. Commun. **2014**, *5*, 4973; b) C.V. Rao, C.R. Cabrera, Y. Ishikawa, J. Phys. Chem. Lett. **2010**, *1*, 2622-2627; c) J. Wu, S. Ma, J. Sun, J.I. Gold, C. Tiwary, B. Kim, L. Zhu, N. Chopra, I.N. Odeh, R. Vajtai, A.Z. Yu, R. Luo, J. Lou, G. Ding, P.J.A. Kenis, P.M. Ajayan, Nat. Commun. **2016**, *7*, 13869; d) W. Ding, Z. Wei, S. Chen, X. Qi, T. Yang, J. Hu, D. Wang, L.-J. Wan, S.F. Alvi, L. Li, Angew. Chem. **2013**, *125*, 11971-11975.
[70] S. Wang, D. Yu, L. Dai, J. Am. Chem. Soc. **2011**, *133*, 5182-5185.
[71] S. Shanmugam, T. Osaka, Chem. Commun. **2011**, *47*, 4463-4465.
[72] Y. Tang, B.L. Allen, D.R. Kauffman, A. Star, J. Am. Chem. Soc. **2009**, *131*, 13200-13201.
[73] P.A. Denis, R. Faccio, A.W. Mombru, Chemphyschem **2009**, *10*, 715-722.
[74] A.Y.S. Eng, Z. Sofer, P. Šimek, J. Kosina, M. Pumera, Chem – Eur. J. **2013**, *19*, 15583-15592.
[75] J. Jin, F. Pan, L. Jiang, X. Fu, A. Liang, Z. Wei, J. Zhang, G. Sun, ACS Nano **2014**, *8*, 3313-3321.
[76] J. Liang, Y. Jiao, M. Jaroniec, S.Z. Qiao, Angew. Chem. **2012**, *124*, 11664-11668.
[77] A.S. Mayorov, R.V. Gorbachev, S.V. Morozov, L. Britnell, R. Jalil, L.A. Ponomarenko, P. Blake, K.S. Novoselov, K. Watanabe, T. Taniguchi, A.K. Geim, Nano Lett. **2011**, *11*, 2396-2399.
[78] L. Zhang, J. Niu, M. Li, Z. Xia, J. Phys. Chem. C **2014**, *118*, 3545-3553.
[79] Y. Zhang, M. Chu, L. Yang, W. Deng, Y. Tan, M. Ma, Q. Xie, Chem. Commun. **2014**, *50*, 6382-6385.
[80] J.-E. Park, Y.J. Jang, Y.J. Kim, M.-S. Song, S. Yoon, D.H. Kim, S.-J. Kim, Phys. Chem. Chem. Phys. **2014**, *16*, 103-109.
[81] a) L. Arroyo-Ramírez, D. Rodríguez, W. Otaño, C.R. Cabrera, ACS App. Mater. Interfaces **2012**, *4*, 2018-2024; b) M.E.M. Buan, N. Muthuswamy, J.C. Walmsley, D. Chen, M. Rønning, Carbon **2016**, *101*, 191-202.
[82] P.A. Denis, Comput. Mater. Sci. **2013**, *67*, 203-206.
[83] C. Zhang, N. Mahmood, H. Yin, F. Liu, Y. Hou, Adv. Mater. **2013**, *25*, 4932-4937.
[84] Y.-T. Wang, A.-H. Lu, H.-L. Zhang, W.-C. Li, J. Phys. Chem. C **2011**, *115*, 5413-5421.
[85] a) Z. Liu, F. Peng, H. Wang, H. Yu, J. Tan, L. Zhu, Catal. Commun. **2011**, *16*, 35-38; b) Z. Liu, F. Peng, H. Wang, H. Yu, W. Zheng, X. Wei, J. Nat. Gas Chem. **2012**, *21*, 257-264.
[86] G.A. Snook, P. Kao, A.S. Best, J. Power Sources **2011**, *196*, 1-12.
[87] Y. Wen, B. Wang, C. Huang, L. Wang, D. Hulicova-Jurcakova, Chem – Eur. J. **2015**, *21*, 80-85.
[88] J.-I. Ozaki, N. Kimura, T. Anahara, A. Oya, Carbon **2007**, *45*, 1847-1853.
[89] L. Zhu, J. Wu, Q. Zhang, X. Li, Y. Li, X. Cao, J. Colloid Interface Sci. **2018**, *510*, 32-38.
[90] M.-S. Song, K.M. Lee, Y.R. Lee, I.Y. Kim, T.W. Kim, J.L. Gunjakar, S.-J. Hwang, J. Phys. Chem. C **2010**, *114*, 22134-22140.
[91] R. Li, Z. Wei, X. Gou, ACS Catal. **2015**, *5*, 4133-4142.
[92] J.P. Paraknowitsch, A. Thomas, Energy Environ. Sci. **2013**, *6*, 2839-2855.
[93] a) R. Li, W. Fan, G. Tian, H. Zhu, L. He, J. Cai, Q. Huang, Q. Cai, B. Li, Y. Bai, Z. Zhang, Y. Zhang, W. Wang, J. Li, F. Hao, H. Li, M. Jian, J. Li, Z. Zhang, R. Nielsen, D. Li, W. Gu, Z. Yang, Z. Xuan, O.A. Ryder, F.C.-C. Leung, Y. Zhou, J. Cao, X. Sun, Y. Fu, X. Fang, X. Guo, B. Wang, R. Hou, F. Shen, B. Mu, P. Ni, R. Lin, W. Qian, G. Wang, C. Yu, W. Nie, J. Wang, Z. Wu, H. Liang, J. Min, Q. Wu, S. Cheng, J. Ruan, M. Wang, Z. Shi, M. Wen, B. Liu, X. Ren, H. Zheng, D. Dong, K. Cook, G. Shan, H. Zhang, C. Kosiol, X. Xie, Z. Lu, H. Zheng, Y. Li, C.C. Steiner, T.T.-Y. Lam, S. Lin, C. Zhang, G. Li, J. Tian, T. Gong, H. Liu, D. Zhang, L. Fang, C. Ye, J. Zhang, W. Hu, A. Xu, Y. Ren, G. Zhang, M.W. Bruford, Q. Li, L. Ma, Y. Guo, N. An, Y. Hu, Y. Zheng, Y. Shi, Z. Li, Q. Liu, Y. Chen, J. Zhao, N. Qu, S. Zhao, F. Tian, X. Wang, H. Wang, L. Xu, X. Liu, T. Vinar, Y. Wang, T.-W. Lam, S.-M. Yiu, S. Liu, H. Zhang, D. Li, Y. Huang, X. Wang, G. Yang, Z. Jiang, J. Wang, N. Qin, L. Li, J. Li, L. Bolund, K. Kristiansen, G.K.-S. Wong, M. Olson, X. Zhang, S. Li, H. Yang, J. Wang, J. Wang, Nature **2009**, *463*, 311; b) Z. Zhang, B. Lu, J. Hao, W. Yang, J. Tang, Chem. Commun. **2014**, *50*, 11554-11557.
[94] J. Wang, K. Huo, L. Ma, L. Tang, D. Li, X. Huang, Y. Yuan, C. Li, W. Wang, W. Guan, H. Chen, C. Jin, J. Wei, W. Zhang, Y. Yang, Q. Liu, Y. Zhou, C. Zhang, Z. Wu, W. Xu, Y. Zhang, T. Liu, D. Yu, Y. Zhang, L. Chen, D. Zhu, X. Zhong, L. Kang, X. Gan, X. Yu, Q. Ma, J. Yan, L. Zhou, Z. Liu, Y. Zhu, T. Zhou, F. He, X. Yang, Mol. Syst. Biol. **2011**, *7*, 536.
[95] Y. Meng, D. Voiry, A. Goswami, X. Zou, X. Huang, M. Chhowalla, Z. Liu, T. Asefa, J. Am. Chem. Soc. **2014**, *136*, 13554-13557.
[96] a) J. Chen, H. Zhang, P. Liu, Y. Li, G. Li, T. An, H. Zhao, Carbon **2015**, *92*, 339-347; b) J. Xu, Y. Zhao, C. Shen, L. Guan, ACS App. Mater. Interfaces **2013**, *5*, 12594-12601.
[97] C.H. Choi, S.H. Park, S.I. Woo, Green Chem. **2011**, *13*, 406-412.
[98] C. Hu, L. Dai, Adv. Mater. **2017**, *29*, 1604942.
[99] J. Li, Y. Zhang, X. Zhang, J. Huang, J. Han, Z. Zhang, X. Han, P. Xu, B. Song, ACS App. Mater. Interfaces **2017**, *9*, 398-405.
[100] J. Xu, G. Gong, C. Jin, M. Huang, L. Guan, ChemSusChem **2013**, *6*, 493-499.
[101] S.-A. Wohlgemuth, F. Vilela, M.-M. Titirici, M. Antonietti, Green Chem. **2012**, *14*, 741-749.

This article is protected by copyright. All rights reserved.

3.邵艳秋,姜封庆,孙玺,常玉莹,王星月,宋冰,黄家辉.乙炔氢氯化反应铜基催化剂研究进展[J].塑料工业,2021,49(03):27-31.8

乙炔氢氯化反应铜基催化剂研究进展*

邵艳秋[1,**]，姜封庆[1,2]，孙 玺[3]，常玉莹[2]，王星月[2]，宋 冰[1]，黄家辉[3,***]
(1. 牡丹江师范学院化学化工学院，黑龙江 牡丹江 157011；
2. 黑龙江省新型碳基功能与超硬材料重点实验室，黑龙江 牡丹江 157011；
3. 中国科学院大连化学物理研究所，辽宁 大连 116023)

摘要：开发乙炔氢氯化无汞催化剂对我国聚氯乙烯（PVC）工业具有重要意义，目前以金为代表的贵金属催化剂已经接近工业化应用，但其生产成本高限制了其市场推广，因此相对价廉的铜基催化剂受到广泛关注。主要从配体和载体改性等方面综述了科研人员对金属铜基催化剂在乙炔氢氯化反应中性能提升所做的工作，并且总结了含铜多金属催化剂在乙炔氢氯化反应中的研究进展，最后对铜催化剂工业发展前景进行了展望。

关键词：乙炔氢氯化；非贵金属；铜基催化剂；载体
中图分类号：TQ426 **文献标识码**：A **文章编号**：1005-5770（2021）03-0027-05
doi：10.3969/j.issn.1005-5770.2021.03.006 **开放科学（资源服务）标识码（OSID）**：

Research Progress of Copper Based Catalysts for Acetylene Hydrochlorination

SHAO Yan-qiu[1], JIANG Feng-qing[1,2], SUN Xi[3], CHANG Yu-ying[2], WANG Xing-yue[2], SONG Bing[1], HUANG Jia-hui[3]
(1. Department of Chemistry Mudanjiang Normal University, Mudanjiang 157011, China;
2. Key Laboratory of New Carbon-Based Functions and Superhard Materials, Mudanjiang 157011, China;
3. Dalian Institute of Chemical Physics, Chinese Academy of Sciences, Dalian 116023, China)

Abstract: The development of mercury-free acetylene hydrochlorination catalysts had great significance to Chinese polyvinyl chloride (PVC) industry. At present, precious metal catalysts represented by gold were chosen for industrial applications, but their high production costs limited their market promotion, therefore, relatively inexpensive copper-based catalysts had attracted widely attention. The performance improvement of metal copper-based catalysts in the hydrochlorination of acetylene was reviewed from the aspects of ligand and carrier modification. And the research progress of copper-containing multimetal catalysts in the hydrochlorination of acetylene were summarized, and finally the industrial development prospects of copper catalysts were prospected.

Keywords: Acetylene Hydrogen Chloride; Non Noble Metal; Copper-based Catalyst; Support

聚氯乙烯（PVC）具备抗老化、抗腐蚀、阻燃、易加工成型等优良性能，被广泛应用于建筑、家居、建材、服饰、医疗等生活中众多领域[1]。“富煤，贫油”的能源结构，导致我国主要通过电石法生产 PVC 的前驱体氯乙烯（VCM）。目前工业生产中仍使用的是传统的汞基催化剂[2]（其催化性能见表 1），但是汞催化剂随温度的升高易挥发，对人们的生活环境造成威胁。随着我国汞资源的日渐枯竭及“水俣公约”[3]的签署，我国将于 2022 年全面禁止汞基催化剂的使用，这使得无汞催化剂的开发备受关注。

Nkosi 和 Hutchings 等[4-6]研究发现 Au 作为催化剂在乙炔氢氯化反应中表现出优异的活性，受其启发的科研人员在乙炔氢氯化 Au 基催化剂开发上做了许多工作。但是金的成本过高，并不利于企业在行业中的竞争以及长期发展。Cu 由于其较低的价格，并且具有良好的热稳定性，被科研工作者广泛关注。Hutchings 教授曾猜测[4]，Cu^{2+} 具有较高的电极电势，有可能在乙炔氢氯化反应中会有突出表现。美国专利[5-6]率先公布了 Cu 作为主要活性组分催化乙炔氢氯化反应，后来我国的科研人员也对催化乙炔氢氯化反应的 Cu 基催化剂进行了大量的探索工作。天津大学、内蒙古大学、石河子大学、清华大学、中国科学院大连化学物理研究所等众多科研单位的学者通过不断尝试，取得许多有意义的研究成果。本文通过整理归纳目前国内外所取得的研究成果，概述了乙炔氢氯化单金属 Cu 基催化剂以及 Cu 作为助剂的多金属催化剂发展进程，并对非贵金属铜催化剂的开发及工业化应用进行总结和展望。

* 牡丹江师范学院科研项目（kjcx2019-98mdjnu），黑龙江省省属高等学校基本科研业务费科研机构专项（1355JG015），牡丹江师范学院省级大学生创新创业训练计划项目（202010233080）
** 通信作者 shaoyanqiu1969@163.com *** 通信作者 jiahuihuang@dicp.ac.cn
作者简介：邵艳秋，女，1969 年生，博士，教授，主要研究方向为功能材料。

(C)1994-2021 China Academic Journal Electronic Publishing House. All rights reserved. http://www.cnki.net

1 单金属铜基催化剂

张靖立等[7]采用球形活性碳（SAC）作为载体，通过等体积浸渍法制备了 Cu/SAC 催化剂。研究表明在 1 mol/L 盐酸、去离子水、氨水、乙二胺四种溶剂中，用 1 mol/L 盐酸制备的铜基催化剂活性最好。催化剂的表征数据表明用盐酸制备的 Cu/C 催化剂具有更好的表面分散性，虽然研究人员对溶剂的筛选有利于提高催化性能，但是过低的乙炔转化率及较差的催化剂稳定性仍然无法达到工业生产的需求，因此尝试通过添加配体和离子液体的方式对单金属铜基催化剂性能进行提升（相关催化剂催化性能详见表 1）。

表 1 配体及离子液体促进铜基催化剂催化性能

Tab 1 Ligand and ionic liquid promote the catalytic performance of copper-based catalysts

催化剂	Cu 质量分数/%	温度/℃	乙炔空速/h^{-1}	时间/h	转化率/%
$HgCl_2$/AC[8]	0	140	30	–	98
Cu/SAC[9]	15	180	180	10	68
MOF-Cu[10]	10	30	30	40	78
Cu-1HEDP/AC[11]	5	90	90	9	83.4
Cu-HMPA/SAC[12]	15	180	180	13	87.25
Cu-NMP/SAC[13]	12	180	180	12	94.2
$CuCl_2$–[PMIm]Cl[14]	–	140	370	12	39
[Hmpa]Cl-CuCl IL[15]	0.67	180	50	36	88
Cu@MOMTPPC/SAC[16]	15	180	180	48	92.2

1.1 配体及离子液体促进催化性能

有机配体特殊的结构可以与金属空轨道作用起到调控金属电子分布，稳定金属价态的作用，因此科研工作者将这种想法应用到了制备乙炔氯化铜基催化剂中，通过添加配体来增加铜基催化剂活性并提高催化剂稳定性，目前已经有报道通过合成金属有机框架材料（MOF）结构或者添加羟基亚乙基二膦酸（HEDP）、六甲基磷酰三胺（HMPA）、*N*-甲基吡咯烷酮（NMP）等配体提高催化剂性能，除了简单的有机配体外，科研工作者还采用离子液体来稳定金属铜制备了催化效果良好的铜基催化剂。（相关催化剂催化性能见表 1）

Wu 等[10]通过活性炭（AC）为载体，使用 MOF 结构合成了 MOF-Cu/AC 催化剂，其乙炔转化率为 78%。通过表征分析 MOF 结构可以增强催化剂对乙炔的吸附能力，并且具有良好的抗结焦能力。由于 MOF-Cu/AC 催化剂在高温以及低空速条件下催化活性仍然无法与汞催化剂相比，因此科研人员尝试通过添加配体的方式对单金属铜基催化剂活性进行提升。Wang 等[11]用含 P 配体 HEDP 制备了 Cu 的负载量为 5% 的 Cu-1HEDP/AC 催化剂。在乙炔空速［$GHSV$（C_2H_2）］= 90 h^{-1}的测试条件下，乙炔转化率可以达到 83.4%。Hu 等[12]选择了另外一种含 P 配体 HMPA，把铜的负载量增加到了 15%，制备了 15%Cu10%-HMPA/SAC 催化剂，在把乙炔空速增加到 180 h^{-1}后，乙炔转化率可以达到 87.25%，并且该催化剂在为期 100 h 的测验中可以保持长期稳定性，通过表征发现 HMPA 配体能够促进 Cu 物种在活性炭上的分散，抑制铜物种被还原，使其一直保持在高活性价态。除了含 P 配体外，含 N 配体同样得到了科研人员的关注。天津大学的 Han 等[13]在铜一系列吡咯烷酮配体中发现了催化效果最好的 NMP 配体，制备了 Cu 负载量为 12% 的 Cu-0.25NMP/SAC 催化剂，在 $GHSV$（C_2H_2）= 180 h^{-1}测试条件下，乙炔转化率可以达到 94.2%，基于此，科研人员认为吡咯烷酮配体（尤其是 NMP）可以成为高效、稳定、经济且环保的 Cu 催化剂有希望的候选者，并为进一步设计乙炔氯化催化剂提供了指导。

综上所述，以含铜 MOF 作为前驱体，或者添加 HEDP、HMPA、NMP 等配体，在乙炔氯化反应中可以起到促进 Cu 物种在活性炭上的分散以及抑制 Cu^{2+}被还原等积极作用，从而提高催化剂的表现，但是研究发现积碳是导致催化剂失活的重要原因，因此对积碳有抑制作用的离子液体受到科研人员的关注。

在 20 世纪初，第一个离子液体硝基乙胺走进了研究者们的视野，离子液体因具有导热性好、稳定性好、可重复利用等优点，在许多领域有所应用，研究表明，使用离子液体作为反应介质时，可以有效避免积碳引起的失活，近年来研究者们把离子液体应用到铜基催化剂的改性当中，从而获得了许多有价值的实验结果。Yu 等[14]在筛选了不同烷基链咪唑嗪基离子液体后，选择［PrMIm］Cl（1-丙基-3-甲基咪唑氯盐）作为反应媒介制备了催化剂，并得到了最佳的催化活性，相对于未改性的 $CuCl_2$/AC 催化剂催化活性仍然得到了提高，而 Ren 等[15]则把目光转向了氯代铜盐离子液体，在从众多氯代铜盐离子液体中发现了具有最佳催化性能的 *N*-甲基吡咯烷酮盐酸盐-0.60CuCl（［Hmmpa］Cl-0.60CuCl）离子液体催化剂，表征后发现该离子液体制备的催化剂具有更强的 HCl 吸附能力。Wang 等[16]通过（甲氧基甲基）三苯基氯化膦（MOMTPPC）离子液体制备的催化剂在乙炔氯化反应中，乙炔转化率可以达到 92.2%，在工业空速条件下乙炔转化率甚至可以达到 98.7%。这几乎可以和氯化汞催化剂相媲美，研究者们通过表征分析发现，MOMTPPC 离子液体的加入促进了 Cu 物种的分散、抑制了积碳，从而提高了催化活性。

离子液体在非贵金属铜基催化剂中的应用极具开创性，打破了固相催化体系的传统思维，使金属 Cu 原子得到更加充分的分散，并且铜离子与离子液体中离子间的相互作用对铜催化剂的活性位起到了一定的稳定作用。从而提高了铜基催化剂的催化活性以及稳定性。虽然离子液体可以很好地解决积碳问题，但是目前离子液体价格略高，并且实际应用到工业生产中也较为困难，如果可以进一步优化离子液体结构，降低成本将有望广阔的工业化前景。

1.2 载体改性促进催化性能

乙炔氯化反应的载体改性主要包括碳载体的杂原子改性以及碳纳米管和使用非碳载体。科研人员通过载体改性的手段可以对催化剂的催化性能进行提升。（相关催化剂催化性能如表 2 所示）

(C)1994-2021 China Academic Journal Electronic Publishing House. All rights reserved. http://www.cnki.net

表 2 载体改性促进铜基催化剂催化性能

Tab 2 Modified carrier promote the catalytic performance of copper-based catalysts

催化剂	Cu 质量分数/%	温度/℃	乙炔空速/h^{-1}	时间/h	转化率/%
Cu-g-C_3N_4/AC[17]	12	180	72	7.5	75
CuP/SAC[18]	15	140	30	82	97.2
Cu-NCNT[19]	5	180	180	3.3	45.8
Cu-Ru/MWCNTs[20]	6	180	180	4	51.6
Cu-CNTs[21]	1.58	180	180	48	98
$CuCl_2$/13X[22]	25	30	30	16	78
Cu/HY[23]	15	120	120	12	84
$AuCl_3$-$CuCl_2$/γ-Al_2O_3[24]	1	150	120	6	97

1.2.1 碳载体的杂原子改性

对于碳载体的杂原子改性主要是通过在载体上掺杂 N、P 等元素，通过这种方式可以达到提高金属铜与载体之间的作用力，促进活性组分分散、减少铜的团聚等作用，从而可以有效提高铜催化剂的催化活性。Zhao 等[17]选择在载体上掺杂 N 原子对催化剂进行改性，制备了 Cu-g-C_3N_4/AC 催化剂。研究表明，载体上 N 原子的改性对电子传输起到了积极的作用，促进了 Cu 物种的分散，并且增强了催化剂对 C_2H_2 的吸附量，从而催化剂的活性得到了极大的改善。Li 等[18]则通过在载体上掺杂 P 原子的方式对载体进行改性，研究发现 P 的掺杂可以有效抑制 Cu 物种在活性炭上的聚集、抑制活性物质 Cu^{2+}被还原，从而提升了催化活性以及稳定性。

通过 N、P 等杂原子对载体改性的方式，可以起到促进 Cu 物种在载体上的分散，抑制活性组分 Cu^{2+}被还原的作用，但是从根本上来讲，仍然无法对 Cu 活性中心结构产生改变，并不能大幅度的提高催化剂催化活性。同时，含 P、N 等元素的化合物污染环境，无法进行大规模工业化生产。所以，寻找一种环保、经济、高效的方式来改良铜催化剂是各大企业以及科研人员需要克服的一个难题。

1.2.2 碳纳米管及非碳载体

对于单金属铜基催化剂，除了对载体进行杂原子改性外，还可以通过碳纳米管、分子筛、氧化铝等载体材料提升其催化性能，碳纳米管因为其良好的物理化学性质成为了催化领域炙手可热的载体，Zhou 等[18]通过沉积法制备了 Cu 负载量为 5% 的新型 Cu-NCNT 催化剂，在 T= 180 ℃，$GHSV$（C_2H_2）= 180 h^{-1}，V_{HCl}∶$V_{C_2H_2}$= 1.1 的条件下对催化剂进行评价，其乙炔转化率为 45.8%，反应 3 h 后下降了 2%。研究者通过表征分析表明用氮掺杂的碳纳米管作为催化剂载体可以增加对乙炔的吸附量，并且可以有效的提高乙炔氯氧化活性。Xu 等[19]通过多级微纳复合结构的多壁碳纳米管（MWCNT）和王水浸渍合成的催化剂乙炔的转化率为 51.65%，氯乙烯的选择性可达到 99.93%。MWCNT 材料本身的乙炔氯氧化催化活性很低，但当与 Cu 合成催化剂时，催化活性得到大幅提升。蔡白雪等[20]通过酸处的碳纳米管制备的催化剂乙炔转化率稳定维持在 98%。对比于 Cu/AC 催化剂，该催化剂的催化活性和稳定性更好。碳纳米管材料制备的催化剂毒性小并且对环境友好，但是其催化活性仍然有待提高。

除了碳纳米管，分子筛也备受科研人员的关注。大连化物所的宋智甲等[21]在 300 ℃温度条件下制备了 Cu 负载量为 15% 的 $CuCl_2$/13X 催化剂。在 $GHSV$（C_2H_2）= 30 h^{-1}条件下，乙炔转化率为 78%，反应 16 h 后催化剂的转化率和选择性仍然趋于稳定，相博文等[22]同样将 Cu 负载量控制在 15%，并制备了分散为载体的 Cu/HY 催化剂，在乙炔空速是 $CuCl_2$/13X 催化剂 4 倍的条件下，乙炔转化率达到了 84%，且具有长期稳定性。通过表征分析发现，HY 分子筛的加入起到了抑制活性组分被还原以及抑制积碳的效果，从而提高了催化剂催化活性和稳定性。γ-Al_2O_3作为载体被科研人员应用在乙炔氯氧化反应催化剂的制备中。Zhao 等[23]研究发现 γ-Al_2O_3载体具有更好的机械强度和介孔（20～50 nm）结构，从而对催化剂活性进行提升，但是活催化剂稳定性不好，短时间内便会失活。如果后续研究可以解决失活过快以及成本过高的问题，该催化剂将更具实际应用价值。

单金属铜催化剂虽然可以通过使用配体和载体改性的方式提高催化剂的催化活性，但是催化活性与传统氯化汞催化剂和贵金属催化剂相比仍有差距，并且用碳纳米管、分子筛、氧化铝等载体改性工艺一般较为复杂，并不利于工业化的应用。如果后续研究可以简化合成条件并且不断优化催化剂活性，单金属铜基催化剂仍然有巨大发展空间。

2 铜作为助催化剂

多金属协同催化一直是催化剂改良常用的实验方法，掺杂的多金属之间可以产生相互的协同作用，防止活性组分被还原，稳定活性组分从而达到提高催化剂活性及稳定性的效果。铜在多金属催化剂中既可以充当主活性中心，又可以作为副活性中心发挥作用（相关催化剂催化性能见表 3）。

表 3 Cu 作助催化剂促进铜基催化剂催化性能

Tab 3 Cu used as auxiliary agent to promote the catalytic performance of copper-based catalysts

催化剂	Cu 质量分数/%	温度/℃	乙炔空速/h^{-1}	时间/h	转化率/%
Bi-Cu/C[25]	15	170	30	20	70
Cu-Bi-Ba/C[26]	12	140	90	4	66.4
Cu-Cs/AC[27]	1	200	50	200	92
Au-Cu1/AC（OAR）[28]	0.2	180	1 480	200	98.8
Au-Cu（Ⅲ）-Cu（Ⅱ）[29]	1	150	360	36	99.8
Au-Cu-SH/AC[30]	0.5	180	1 200	8	50.4
Au-Cu（Ⅱ）[31]	1	150	360	36	94.8
BaCu（Ⅱ）3Cu（Ⅱ）1/SAC[32]	0.1	170	180	48	99
Au-Cu-K/AC[33]	0.2	160	40	1 600	98

2.1 铜作主活性中心

当 Cu 作主活性中心时科研人员通常选择一种或多种非贵金属作为铜基催化剂的稳定成分。从而提高催化剂的稳定性。吕忠领等[25]用等体积浸渍法制备了 Cu 为主要活性组分，Bi 为稳定组分的 Bi-Cu/C 催化剂，其中 Cu 的负载量为 15%。通

(C)1994-2021 China Academic Journal Electronic Publishing House. All rights reserved. http://www.cnki.net

过固定床反应器对催化剂进行了评价，在反应 20 h 后乙炔的转化率仍可保持在 70% 以上。表征分析表明催化剂在载体表面均匀分散，并发现金属 Bi 对活性成分 Cu 有稳定作用。凌思等[26]用真空等体积浸渍法以及正交实验筛选出催化活性最好的 Cu-Bi-Ba/C 催化剂。研究表明 $BaCl_2$能与活性组分形成稳定的复合结构，在减少积碳量的同时，稳定了活性组分。综上所述非金属的加入虽然有利于 Cu 活性组分的稳定性，但是 Cu 作主活性中心的多金属催化剂的乙炔转化率仍然有待提高。

2.2 铜作副活性中心

铜在多金属催化剂中更多的是为贵金属提供相应的辅助作用，并不是充当主要的活性中心，研究人员们对此类催化剂进行了大量的研究。Zhai 等[27]制备了双非贵金属 Cu-Cs/AC 催化剂，并在 T= 200 ℃，$GHSV$（C_2H_2）= 50 h^{-1}，V_{HCl}/$V_{C_2H_2}$= 1.2 条件下进行了测试，反应 200 h 后，乙炔转化率为 92%。表征结果表明 Cs_2CuCl_3 结构不仅可以稳定活性组分 Cu^{2+}，并且可以增强对 HCl 的吸附能力。He 等[28]将有机王水（OAR）应用于催化剂的制备，与传统王水（AR）相比，通过 OAR 制备的双金属 Au-Cu 催化剂活性和稳定性更好，反应 200 h 后，乙炔转化率为 98.8%，通过表征分析表明 OAR 可以有效地固定硫和氯，并且机理研究表明，OAR 残留还可以稳定 Cu^{2+}物种，这项工作清楚地表明，这种催化剂的途径设计可以改善催化过程，除李小年外，还有许多其他科研人员对 Au-Cu/AC 催化剂进行了研究，Zhang 等[29]发现 Co（Ⅲ）和 Cu（Ⅱ）的协同作用增多了催化剂中的活性组分，并且增强了对反应物 HCl 的吸附能力，催化剂预估寿命超过 6 000 h，因此含 Cu 元素的三元催化剂具有很大的工业化应用前景。Hong 等[30]通过使用巯基乙酸钠和氢氧化钠溶液配置的混合溶液浸渍制备催化剂，与 1 mol/L HCl 制备 Au-Cu/AC 的催化剂相比，催化剂活性和稳定性都得到了提升。而内蒙古大学的 Du 等[31]通过超声浸渍法使活性成分更均匀地负载在载体上，在 $GHSV$（C_2H_2）= 720 h^{-1}的条件下，催化剂的乙炔转化率可以达到 97.4%。研究表明超声波利用典型的超声空化现象增强了质量传输以及整个浸渍溶液和催化剂载体孔的均匀热分布，Zhang 等[32]研究发现在催化剂中加入 Co 和 Cu 之后可以促进 Ru 物种的分散，并且 Cu（Ⅱ）可以有效抑制 Ru^{0}被还原。Wang 等[33]通过 KCl 的修饰制备了 Au-Cu/AC 催化剂，贵金属 Au 的添加量从 0.5% 降到 0.2%，并且提高了催化剂的性能，乙炔转化率可以达到 98%。通过表征分析表明，钾和铜的添加剂可以使金的活性物种恒好地分散并阻碍颗粒的聚集，在 Au-Cu-K/AC 催化剂中 Cu 在防止金属失活方面起着关键作用。在发明专利方面，众多科研人员[35-36]通过 Au、Ru、Pt 等贵金属与 Cu 搭配制备了许多催化效果良好的催化剂，当贵金属作为主活性中心，Cu 作副活性中心时，虽然催化剂的催化活性达到了氯化汞催化剂的水平，但是由于贵金属的加入，极大地提高了催化剂生产成本，并不利于投入到实际生产当中。

在乙炔氯氧化反应中金属 Cu 更多的是以贵金属铜助剂的形式存在，以 Cu 为主活性中心添加其他非贵金属的催化剂的催化效果上仍然不尽人意，有待提高，而 Cu 与贵金属制备的催化剂成本又过高，因此掺杂铜的多金属催化剂研究面对着很大的挑战。

3 总结与展望

Cu 基催化剂具备价格低以及热稳定性好等优点，虽然单组分 Cu 基催化剂的的活性不如传统的氯化汞催化剂以及贵金属 Au 基催化剂，但是通过添加配体以及离子液体的方式可以提升单金属铜基催化剂催化性能，随着离子液体更为深入的研究，通过改变离子液体结构提升性能，离子液体改性的非贵金属铜基催化剂也将具有实际应用价值。对于单金属 Cu 基催化剂而言，碳纳米管以及分子筛的使用将对其催化性能产生积极作用。随着科研人员对多金属铜基催化剂的研究也日益深入，研究发现多金属间的协同作用可以使铜基催化剂的催化活性得到改善。综上所述，坚信研制出高活性、高选择性、长寿命的工业化乙炔氯氧化铜基催化剂的愿望很快就会被研究者们实现。

参 考 文 献

[1] 郭燕燕. 乙炔氯氧化非贵金属无汞催化剂的研究 [D]. 呼和浩特：内蒙古大学，2014.
GUO Y Y. Study on non-precious metal mercury-free catalyst for acetylene hydrochlorination [D]. Hohhot: Mongolian University, 2014.

[2] ZHONG J W, XU Y P, LIU Z M. Heterogeneous non-mercury catalysts for acetylene hydrochlorination: progress, challenges, and opportunities [J]. Green Chemistry, 2018, 20: 2412-2427.

[3] NKOSI B, HUTCHINGS G J. Vapour phase hydrochlorination of acetylene with group VIII and IB metal chloride catalysts [J]. Applied Catalysis, 1988, 43: 33-39.

[4] HUTCHINGS G J. Vapor phase hydrochlorination of acetylene correlation of catalytic activity of supported metal chloride catalysts [J]. Journal of Catalysis, 1985, 96: 292-295.

[5] PERKINS G A. Preparation of vinyl chloride: US1934324 [P]. 1933-11-07.

[6] ARMIN J. Process for preparing vinyl chloride: US3113158 [P]. 1963-12-03.

[7] 张靖立，王富民，王录. 乙炔氢氯化过程中铜基催化剂的制备及催化性能 [J]. 化学工业与工程，2016，33（3）：19-24.
ZHANG X L, WANG F M, WANG L. Preparation and catalytic performance of copper-based catalysts in the process of acetylene hydrochlorination [J]. Chemical Industry and Engineering, 2016, 33 (3): 19-24.

[8] WU Y B, LI F X, LÜ Z P, et al. Synthesis and characterization of X-MOF/AC（X＝tin or copper）catalysts for the acetylene hydrochlorination [J]. Chemistry Select, 2019, 4 (32): 9403-9409.

[9] WANG X M, ZHU M Y, DAI B. Effect of phosphous ligand on cu-based catalysts for acetylene hydrochlorination [J]. ACS Sustainable Chemistry & Engineering, 2019, 7 (6): 6170-6177.

[10] HU Y B, WANG Y, WANG Y L, et al. High performance of supported Cu-based catalysts modulated via phosphamide coordination in acetylene hydrochlorination [J]. Applied Catalysis A: General, 2020, 591: 117408.

[11] HAN Y, WANG Y L, WANG Y, et al. Pyrrolidone ligand improved Cu-based catalysts with high performance for acetylene hydrochlorination [J]. Applied Organometallic Chemistry, 2020, 34: e6066.

[12] YU Y, YUE Y X, WANG B L, et al. Synergy between ionic liquids and $CuCl_2$ in gas-liquid phase reactions of acetylene hydrochlorination [J]. Catalysts, 2019, 9 (6): 504.

[13] REN Y F, WU B T, WANG F M, et al. Chlorocuprate (I) ionic liquid as an efficient and stable Cu-based catalyst for hydrochlorination of acetylene [J]. Catalysis Science & Technology, 2019, 9 (11): 2868-2878.

[14] WANG Y, NIAN Y, ZHANG J L, et al. MOMTPPC improved Cu-based heterogeneous catalyst with high efficiency for acetylene hydrochlorination [J]. Molecular Catalysis, 2019, 479: 55-65.

[15] ZHAO W L, ZHU M Y, DAI B. The preparation of Cu-g-C_3N_4/AC catalyst for acetylene hydrochlorination [J]. Catalysts, 2016, 6 (12): 193-202.

[16] LI H, WANG F M, CAI W F, et al. Hydrochlorination of acetylene using supported phosphorus doped Cu-based catalysts [J]. Catalysis Science & Technology, 2015, 5 (12): 5174-5184.

[17] ZHOU K, SI J K, JIA J C, et al. Reactivity enhancement of N-CNTs in green catalysis of C_2H_2 hydrochlorination by a Cu catalyst [J]. RSC Advances, 2014, 4 (15): 7766-7769.

[18] XU J T, ZHAO J, ZHANG T T, et al. Ultra-low Ru-promoted $CuCl_2$ as highly active catalyst for the hydrochlorination of acetylene [J]. RSC Advances, 2015, 5 (48): 38159-38163.

[19] 蔡白雪，甘霖，张祥剑，等. 新型微铜碳纳米管催化剂的制备及其对乙炔氢氯化反应的催化活性 [J]. 合成化学，2011，19（5）：622-625.
CAI B X, GAN Y, ZHANG X J, et al. Preparation of a novel copper-supported carbon nanotube catalyst and its catalytic activity for the hydrochlorination of acetylene [J]. Synthetic Chemistry, 2011, 19 (5): 622-625.

[20] 宋智甲，刘少峰，贺大威，等. $CuCl_2$/13X 催化剂在乙炔氢氯化反应中的应用 [J]. 中国科学：化学，2018，48（2）：186-195.
SONG Z J, LIU S F, HE D W, et al. Performance of $CuCl_2$/13X catalyst in acetylene hydrochlorination [J]. Science in China: Chemistry, 2018, 48 (2): 186-195.

[21] 相博文，王璐，王丰，等. Cu/HY 催化剂在乙炔氢氯化反应中的性能及其失活原因 [J]. 应用化学，2018，35（12）：1449-1456.
XIANG B W, WANG L, WANG F, et al. Deactivation of Cu/HY catalysts for acetylene hydrochlorination [J]. Applied Chemistry: 2018, 35 (12): 1449-1456.

[22] ZHAO J G, ZENG J J, CHENG X G, et al. An Au-Cu bimetal catalyst for acetylene hydrochlorination with renewable γ-Al_2O_3 as the support [J]. RSC Advances, 2015, 5 (22): 16727-16734.

[23] 吕忠领，丁英雁，秦玉才，等. Bi-Cu/C 催化剂在乙炔氢氯化反应中的催化性能 [J]. 石油炼制与化工，2016，47（10）：32-37.
LÜ Z L, DING Q W, QIN Y C, et al. Catalytic activity of Bi-Cu/C catalyst for acetylene hydrochlorination [J]. Petroleum Refining and Chemical Industry, 2016, 47 (10): 32-37.

[24] 凌思，吴广文，熊泽，等. 乙炔氢氯化反应用催化剂的制备及优化 [J]. 现代化工，2017，37（2）：86-89.
LING S, WU G W, XIONG Z, et al. Preparation and optimization of catalysts for acetylene hydrochlorination [J]. Modern Chemical, 2017, 37 (2): 86-89.

[25] ZHAI Y Y, ZHAO J, DI X X, et al. Carbon supported perovskite-like $CsCuCl_3$ nanoparticles: A highly active and cost-effective heterogeneous catalyst in the hydrochlorination of acetylene to vinyl chloride [J]. Catalysis Science & Technology, 2018 (8): 2901-2908.

[26] HE H H, ZHAO J, WANG B L, et al. Highly active AuCu-based catalysts for acetylene hydrochlorination prepared using organic aqua regia [J]. Materials (Basel, Switzerland), 2019, 12 (8): 1310-1322.

[27] ZHANG H Y, DAI B, LI W, et al. Non-mercury catalytic acetylene hydrochlorination over spherical activated-carbon-supported Au-Cu（Ⅲ）-Cu（Ⅱ）catalysts [J]. Journal of Catalysis, 2014, 316: 141-148.

[28] HONG G T, TIAN X H, JIANG B B, et al. Improvement of performance of a Au-Cu/AC catalyst using thiol for acetylene hydrochlorination reaction [J]. RSC Advances, 2016, 6 (5): 3806-3814.

[29] DU Y F, HU R S, JIA Y, et al. $CuCl_2$ promoted low-gold-content Au/C catalyst for acetylene hydrochlorination

（下转第 53 页）

(C)1994-2021 China Academic Journal Electronic Publishing House. All rights reserved. http://www.cnki.net

(C)1994-2021 China Academic Journal Electronic Publishing House. All rights reserved. http://www.cnki.net

4.邵艳秋,张宇婷,姜振双,刘素娟,任玉兰,王丽杰.水解剂氟化铵对Fe-SBA-15结构及催化性能的影响[J].无机盐工业,2019,51(09):97-101.

第51卷 第9期 无机盐工业 Vol.51 No.9
2019年9月 INORGANIC CHEMICALS INDUSTRY Sept.,2019

Doi:10.11962/1006-4990.2018-0562

水解剂氟化铵对Fe-SBA-15结构及催化性能的影响

邵艳秋[1,2],张宇婷[1,2],姜振双[1,2,3],刘素娟[1],任玉兰[1],王丽杰[1,2]
(1.牡丹江师范学院化学化工学院,黑龙江牡丹江 157011;2.黑龙江省新炭-基功能与超硬材料重点实验室;3.吉林大学化学学院)

摘 要:通过水热法制备了Fe-SBA-15介孔材料,探究了水解剂氟化铵对介孔材料结构及对苯酚羟基化反应的影响。采用X射线衍射(XRD)、红外光谱(FT-IR)和氮气吸附-脱附等方法对介孔材料进行了表征,用苯酚羟基化反应对改性后介孔材料的催化性能进行了研究。结果表明:改性后的介孔材料具有良好的催化性能,其中氟与硅物质的量比为0.03时制备的介孔材料的催化性能更为优良,在固定反应条件下苯酚转化率达到36.82%,苯二酚选择性达到81.76%。

关键词:水解剂;氟化铵;Fe-SBA-15;苯二酚;羟基化
中图分类号:O643 **文献标识码**:A **文章编号**:1006-4990(2019)09-0097-05

Effects of hydrolysate NH_4F on structure and catalytic properties of Fe-SBA-15

Shao Yanqiu[1,2],Zhang Yuting[1,2],Jiang Zhenshuang[1,2,3],Liu Sujuan[1],Ren Yulan[1],Wang Lijie[1,2]
(1.*College of Chemistry and Chemical Engineering,Mudanjiang Normal University,Mudanjiang* 157011,*China*;2.*Heilongjiang Province Key Laboratory of New Carbon-Base Functional and Superhard Material*;3.*College of Chemistry,Jilin University*)

Abstract:Fe-SBA-15 mesoporous materials were prepared by hydrothermal synthesis,and the effect of hydrolysis agent NH_4F on the mesoporous materials structure and catalytic hydroxylation of phenol was explored.The mesoporous materials were characterized by X-ray diffraction(XRD),infrared spectroscopy(FT-IR) and N_2 adsorption desorption etc..The catalytic properties of modified mesoporous materials were studied by hydroxylation of phenol.The results indicated that the modified materials had good catalytic performance.When $n(F^-)/n(Si)=0.03$,the prepared mesoporous materials had better catalytic performance.Under the fixed reaction conditions,conversion of phenol and selectivity of dihydroxybenzene reached 36.82% and 81.76%,respectively.

Key words:hydrolysate;NH_4F;Fe-SBA-15;dihydroxybenzene;hydroxylation

SBA-15分子筛因具有较大的比表面积及有序的孔结构等优势使其在催化领域备受关注,纯硅SBA-15缺少酸性位点和活性中心,在应用上受到很大限制。通过分子筛表面Si—OH基团与活性组分之间的相互作用,将活性较高的成分引入孔道或骨架内来提高材料的活性一直受到关注和研究[1]。将金属引入分子筛孔道或骨架内可以提高分子筛的催化活性,但是引入的金属会对介孔结构造成一定的影响,所以在保证介孔材料有序孔结构的同时如何提高分子筛骨架内的金属含量是需要解决的问题[2-6]。研究发现,在氟离子存在的体系中,F-既可以与过渡金属生成氟的配合物,还可以加快硅源的水解速率,有利于提高金属进入分子筛骨架中[7-8]。由于NH_4F受热会分解为氨和氟化氢,在材料制备过程中铵根对材料中铁的引入影响较小,并且NH_4F在分子筛中有一定的应用[9-10]。因此,笔者以NH_4F为水解剂,采用水热法制备了Fe-SBA-15(x)分子筛(x为氟与硅物质的量比),并探究了水解剂含量对材料结构和性能的影响。

1 实验部分

1.1 主要试剂

P123($EO_{20}PO_{70}EO_{20}$),Aldrich试剂;正硅酸乙酯

基金项目:黑龙江省教育厅科研备案项目(1352MSYYB006);牡丹江师范学院研究生科技创新项目(kjcx2017-09mdjsu);牡丹江师范学院科研项目(JG2017001);牡丹江师范学院大学生创新项目(201710233007)。
收稿日期:2019-03-27
作者简介:邵艳秋(1969—),女,博士,教授,主要从事多相催化材料研究;E-mail:shaoyanqiu1969@163.com。

(C)1994-2020 China Academic Journal Electronic Publishing House. All rights reserved. http://www.cnki.net

(TEOS)、九水合硝酸铁、氟化铵、苯酚、双氧水,均为国产分析纯试剂。

1.2 样品制备

称取 1 g P123 和定量的 NH_4F[$n(F^-)/n(Si)$=0、0.01、0.02、0.03、0.04、0.05]溶于 35 mL 盐酸(pH=1.5)中,得到溶液 A。将 2.3 mL TEOS、2.5 mL 去离子水和 0.207 0 g 硝酸铁在室温下预水解约 30 min,得到溶液 B。将溶液 A 缓慢滴加到溶液 B 中,在恒温 40 ℃下水浴搅拌 20 h,然后转移至反应釜中于 100 ℃晶化 24 h,待冷却至常温时进行抽滤和干燥,最后在 500 ℃焙烧 10 h 以去除模板剂,得到样品记作 Fe-SBA-15(x)介孔分子筛[18-21]。

1.3 样品表征

使用 D/max-2200/PC 型 X 射线衍射仪对材料的晶体结构进行表征;使用 Nicolet360 型红外光谱仪测定材料的 FT-TR 图;使用 3H-2000PS2 型比表面测试仪测定材料的比表面积及孔结构等参数;使用 FEI TECNAI F20 型透射电镜对材料进行微观结构测试;使用 LC-15C 型液相色谱仪测定物质的组成。

1.4 催化性能评价

在自制反应装置内,以苯酚羟基化反应来评价材料的催化性能。在烧瓶内加入定量的苯酚、水和催化剂,升温至所需温度,缓慢加入定量的过氧化氢(体积分数为 30%),反应至一定的时间,用 LC-15C 型液相色谱仪测定产物的组成,利用外标法对反应液中各组分含量进行分析。

2 结果与讨论

2.1 XRD 分析

图 1 为样品 XRD 谱图(小角)。由图 1 看出,加入 NH_4F 制备的 Fe-SBA-15 介孔材料在低角度 XRD 谱图中均出现较强的 d(100)衍射峰,这是 SBA-15 介孔分子筛的特征衍射峰,表明样品具有有序的二维六方介孔结构[21-23]。值得注意的是,铁掺杂的材料 d(100)主衍射峰均向低角度方向移动,这是因为 Fe 和 Si 原子半径不同,形成 Fe—O 和 Si—O 的键长不同导致的[20],这间接说明部分金属铁进入到分子筛骨架中。当 x 为 0、0.01、0.02、0.03 时,介孔分子筛出现 d(100)、d(110)、d(200)衍射峰,峰强度较高,峰形窄;随着 NH_4F 用量增加,d(100)衍射峰明显减弱,峰形宽化,d(110)、d(200)衍射峰消失。这说明在合成体系中加入适量水解剂 NH_4F 不会对介孔结构的有序性产生大的影响,材料仍保持二维六方介孔结构。但是加入过量的 NH_4F 会破坏介孔结构的有序性,可能是由于在合成体系中过量的 NH_4F 使硅源 TEOS 发生迅速的水解缩合,影响胶束的稳定性从而破坏材料的有序介孔结构。这一结果与 Stucky 之前的研究报道很相似[17]。

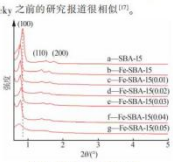

图 1 样品 XRD 谱图(小角)

2.2 FT-IR 分析

图 2 为样品 FT-IR 图。由图 2 可知,制备的材料与纯硅 SBA-15 分子筛吸收峰峰型相似,说明金属铁的引入并未对材料的二维六方介孔结构造成较大影响。在 798 cm^{-1} 和 1 088 cm^{-1} 附近分别对应 Si—O—Si 对称伸缩振动峰和非对称伸缩振动峰[18-20];1 631 cm^{-1}和 3 433 cm^{-1} 附近均有很强的吸收峰,这是吸附表面吸附水或吸附剂上 Si—OH 中的羟基振动峰[22];960 cm^{-1} 附近出现的吸收峰,Corma[22]认为其归属于 Si—OH 伸缩振动峰,但对于含铁的 SBA-15 分子筛而言,960 cm^{-1} 附近的吸收峰应是 Si—O—Fe/Si—OH 振动共同作用的结果[22]。随着氟化铵用量的增加,960 cm^{-1} 附近的吸收峰出现先增强后减弱的趋势,说明在引入相同含量铁的条件下,适量氟化铵的加入促进铁进入到分子筛骨架中,从而引起960 cm^{-1} 附近的吸收峰增强;随着氟化铵用量继续增加,过量的氟化铵引起正硅酸乙酯迅速

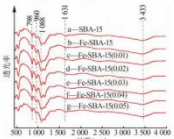

图 2 样品 FT-IR 图

地水解缩合破坏了材料的介孔结构,降低了金属铁进入分子筛骨架的可能性,从而使吸收峰强度减弱。

2.3 比表面积及孔结构分析

图 3 为样品 SBA-15、Fe-SBA-15、Fe-SBA-15(0.01)的 N_2 吸附-脱附等温线和孔径分布曲线。由图 3 可知,样品的 N_2 吸附-脱附等温线均属于Ⅳ型等温线,由于毛细管凝聚作用,p/p_0在 0.6~0.8 时出现较大 H1 型滞后环,说明加入少量 NH_4F 制备的样品仍具有有序介孔结构[19-20]。相比于 Fe-SBA-15,Fe-SBA-15(0.01)介孔材料的孔径分布更为集中,表明其具有更为均匀的孔道。

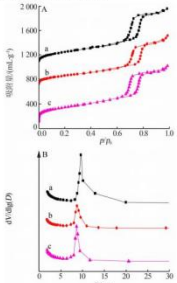

图 3 SBA-15(a)、Fe-SBA-15(b)、Fe-SBA-15(0.01)(c)样品 N_2 吸附-脱附等温线(A)和孔径分布曲线(B)

图 4 为样品 Fe-SBA-15(0.01~0.05)的 N_2 吸附-脱附等温线和孔径分布曲线。由图 4 看出,所制备的材料中,x≤0.03 样品的氮气吸附量有所降低,对应材料 BET 比表面积有所下降,孔径和孔体积变化较小;x 为 0.04 及 0.05 时滞后环向高压方向移动且闭合程度较差,样品氮气吸附量升高,说明过量加入氟化铵会对介孔材料孔道的规整度产生影响。

表 1 为样品比表面积及孔结构参数。由表 1 看出,与纯硅 SBA-15 相比,掺杂后的介孔材料 Fe-SBA-15(x)的比表面积、孔体积和平均孔直径虽有不同程度的降低,但仍保持了较大的比表面积。x>0.03 时,样品比表面积出现增大现象,结合样品 N_2 吸附-脱附等温线结果分析,过量氟化铵使部分正硅酸乙酯水解聚合速率迅速加快,材料孔道规整度下降,从而影响材料有序的介观结构,导致仅有少量金属铁被引入介孔分子筛中,所以材料在 x 为 0.04 和 0.05 时比表面积出现增大现象。

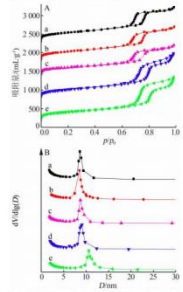

a—Fe-SBA-15(0.01);b—Fe-SBA-15(0.02);c—Fe-SBA-15(0.03);d—Fe-SBA-15(0.04);e—Fe-SBA-15(0.05)

图 4 Fe-SBA-15(x)样品的 N_2 吸附-脱附等温线(A)和孔径分布曲线(B)

表 1 样品比表面积与孔结构参数

样品	比表面积/($m^2 \cdot g^{-1}$)	孔体积/($cm^3 \cdot g^{-1}$)	平均孔直径/nm
SBA-15	880.84	1.57	7.94
Fe-SBA-15	843.44	1.14	5.39
Fe-SBA-15(0.01)	833.61	1.47	6.44
Fe-SBA-15(0.02)	783.44	1.32	6.67
Fe-SBA-15(0.03)	681.11	1.30	6.76
Fe-SBA-15(0.04)	699.96	1.47	6.82
Fe-SBA-15(0.05)	764.58	1.84	7.22

2.4 TEM 分析

图 5 为样品的 TEM 照片。由图 5 看出,相比于 x=0、0.05 材料,x=0.03 材料具有更为有序的介孔结构,且在几百纳米范围内具有连续孔道;其中 f 为垂直于 x=0.05 材料孔道方向拍摄,可以看出孔道规整度下降明显,表明过量加入 NH_4F 会对胶束的稳定性产生影响,破坏材料有序的介观结构[27]。所以,水解剂的添加量以 x=0.03 最佳。

(C)1994-2019 China Academic Journal Electronic Publishing House. All rights reserved. http://www.cnki.net

(C)1994-2019 China Academic Journal Electronic Publishing House. All rights reserved. http://www.cnki.net

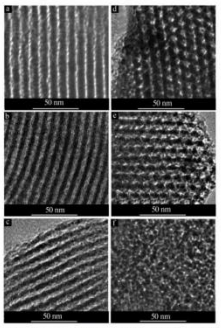

a、d—Fe-SBA-15;b、e—Fe-SBA-15(0.03);c、f—Fe-SBA-15(0.05)

图 5 样品 TEM 照片

2.5 材料中铁含量测定

表 2 为样品原子吸收数据。从表 2 看出,所制备的材料中均含有铁,随着氟离子用量增加,材料中的金属含量有所提高,其中 x=0.03 材料金属铁嫁接率最高,与 x=0 材料相比,金属铁嫁接率提高 17%;当 x>0.03 后,介孔分子筛中金属铁的嫁接率反而降低。这表明适量加入氟化铵,在保证材料有序介孔结构的同时,可以加快正硅酸乙酯的水解速率,使其与金属铁水解速率相近,从而促进材料中金属铁的引入。

表 2 样品原子吸收数据

样品	$[n(Fe)/n(Si)]$/%		嫁接率/%
	理论值	实际值	
Fe-SBA-15	5	2.37	47.4
Fe-SBA-15(0.01)	5	2.89	57.8
Fe-SBA-15(0.02)	5	3.04	60.8
Fe-SBA-15(0.03)	5	3.22	64.4
Fe-SBA-15(0.04)	5	2.51	50.2
Fe-SBA-15(0.05)	5	2.19	43.8

2.6 催化剂催化活性探究

表 3 为催化剂对苯酚羟基化反应的影响。采用高效液相色谱测定反应中苯酚、邻苯二酚及对苯二酚的含量[28]。固定反应条件:苯酚 0.94 g,水 20 mL,催化剂 0.05 g,反应温度为 50 ℃,过氧化氢(质量分数为 30%)为0.31 mL,反应时间为 3 h。

表 3 催化剂对苯酚羟基化反应的影响

催化剂	苯酚转化率/%	邻苯二酚选择性/%	对苯二酚选择性/%
SBA-15	1.35	—	—
Fe-SBA-15	23.61	37.25	29.73
Fe-SBA-15(0.01)	29.56	38.76	31.75
Fe-SBA-15(0.02)	33.17	40.13	32.63
Fe-SBA-15(0.03)	36.82	45.51	36.25
Fe-SBA-15(0.04)	21.47	19.70	11.57
Fe-SBA-15(0.05)	18.10	10.55	8.14

注:—表示未检测到。

由表3 看出,在苯酚羟基化反应中,以 SBA-15 为催化剂时,苯酚的转化率仅为 1.35%,反应产物并未检测到苯二酚的存在,引入铁后得到的催化剂对苯酚羟基化反应显示出较高的催化活性,因此推测金属铁为双氧水氧化苯酚制备苯二酚反应的催化中心。以 Fe-SBA-15 为催化剂时,苯酚转化率为 23.61%,苯二酚选择性为 66.98%。加入氟化铵制备的材料中,以 Fe-SBA-15(0.03)为催化剂时,苯酚羟基化反应效果最好,苯酚转化率为 36.82%,苯二酚选择性为 81.76%,与 Fe-SBA-15 催化剂相比,苯酚转化率和苯二酚选择性分别提高 13.21%和 14.78%。结合样品铁含量测定数据分析可知,在介孔材料合成过程中适量加入水解剂 NH_4F 有助于铁进入分子筛骨架,从而提高催化剂的反应活性。

2.7 含铁催化剂反应机理

在含铁催化剂作用下,双氧水氧化苯酚制苯二酚反应一般遵循自由基机理[29-31],见图 6。主要是过渡金属铁在三价和二价之间相互转化,催化双氧水产生羟基自由基,随后亲电进攻苯酚的邻位和对位,生成相应的邻苯二酚和对苯二酚,因此金属铁是产生羟基自由基的关键,表现为反应的催化中心。这与表 3 催化剂对苯酚羟基化反应影响实验结果的推测相符合。

图 6 苯酚制备苯二酚反应机理[28-31]

3 结论

采用水热法制备出一系列不同氟化铵添加量的 Fe-SBA-15(x)分子筛,由 XRD、TEM、BET、FT-IR 和 AAS(原子吸收光谱)等表征结果可知,适量加入氟化铵,在保证材料有序介孔结构和较大比表面积的同时,有利于金属铁进入到分子筛骨架或高度分散在分子筛表面,从而提高金属嫁接率,以苯酚羟基化反应为探针,发现金属铁为催化活性中心,较高的铁嫁接率对提高苯酚转化率和苯二酚选择性有较大影响,其中 Fe-SBA-15(0.03)分子筛表现出更为优良的催化活性,与 Fe-SBA-15 相比,苯酚转化率提高 13.21%,说明适量加入氟化铵有利于提高 Fe-SBA-15 分子筛的催化活性。

参考文献:

[1] 宗梁,黄英,赵阳.SBA-15 介孔材料的改性及应用[J].材料导报,2012,26(17):54-59.

[2] 代娜,周亚松,魏强,等.铝修饰改性对 SBA-15 分子筛性质及催化剂性能的影响[J].燃料化学学报,2013,41(12):1502-1506.

[3] Restrepo-Garcia J R,Baldovino-Medrano V G,Giraldo S A.Improving the selectivity in hydrocracking of phenanthrene over mesoporous Al-SBA-15 based Fe-W catalysts by enhancing mesoporosity and acidity[J].Applied Catalysis A:General,2016,510:98-109.

[4] Cruz P,Pérez Y,del Hierro I,et al.Copper,copper oxide nanoparticles and copper complexes supported on mesoporous SBA-15 as catalysts in the selective oxidation of benzyl alcohol in aqueous phase[J].Microporous and Mesoporous Materials,2016,220:136-147.

[5] Zhang J,Xin Z,Meng X,et al.Effect of MoO_3 on the heat resistant performances of nickel based MCM-41 methanation catalysts[J].Fuel,2014,116:25-33.

[6] Meloni D,Perra D,Monaci R,et al.Transesterification of Jatropha curcas oil and soybean oil on Al-SBA-15 catalysts[J].Applied Catalysis B:Environmental,2016,184:163-173.

[7] 裘式纶,庞文琴,张春田.溶酸性介质中 Fe-ZSM-5 型分子筛的合成与鉴定[J].无机化学学报,1988,4(4):11-19.

[8] Li Y,Zhang W,Zhang L,et al.Direct synthesis of Al-SBA-15 mesoporous materials via hydrolysis-controlled approach[J].Journal of Physical Chemistry B,2004,108,9739-9744.

[9] Zhang W H,Lu J Q,Han B,et al.Direct synthesis and characterization of titanium-substituted mesoporous molecular sieve SBA-15[J].Chemistry of Materials,2002,14:3413-3421.

[10] Boissière C,Larbot A,van der Lee A,et al.A new synthesis of mesoporous MSU-X silica controlled by a two-step pathway[J].Chemistry of Materials,2000,12(10):2902-2913.

[11] Li Y,Feng Z,Lian Y,et al.Direct synthesis of highly ordered Fe-SBA-15 mesoporous materials under weak acidic conditions[J].Microporous and Mesoporous Materials,2005,84:41-49.

[12] 张涛,冯秀娟,颜美,等.SBA-15 负载钯催化剂的制备及其在超临界二氧化碳介质中催化 Suzuki 偶联反应的研究[J].分子科学学报,2008,24(1):1-5.

[13] Zhao D,Feng J,Huo Q,et al.Triblock copolymer syntheses of mesoporous silica with periodic 50 to 300 angstrom pores[J].Science,1998,279(5350):548-552.

[14] 王华荣.氧化锌/SBA-15 复合材料制备及其光致发光性质[J].无机盐工业,2018,50(4):27-29.

[15] 明娟,王霞,王俊峰,等.金属改性 SBA-15 介孔分子筛水热稳定性研究[J].精细石油化工,2017,34(3):30-35.

[16] 闫宏宇,介孔 Fe、Al-SBA-15 的制备、表征及 NH_3-SCR 催化性能的研究[D].南京:南京理工大学,2015.

[17] Martinez F,Han Y J,Stucky G,et al.Synthesis and characterisation of iron-containing SBA-15 mesoporous silica[J].Studies in Surface Science and Catalysis,2002,142:1109-1116.

[18] Gao Q,Xu W,Xu Y,et al.Amino acid adsorption on mesoporous materials:influence of types of amino acids,modification of mesoporous materials,and solution conditions[J].Journal of Physical Chemistry B,2008,112(7):2261-2267.

[19] Xie W,Hu L.Biguanide-functionalized mesoporous SBA-15 silica as an efficient solid catalyst for interesterification of vegetable oils[J].Food Chemistry,2016,197,92-99.

[20] 徐玲,刘建华,郭兰兰,等.TiO_2-SBA-15 催化剂的制备、表征及光催化降解甲基橙[J].分子科学学报,2015,31(4):333-337.

[21] Wu M,Lin G,Chen D,et al.Sol-hydrothermal synthesis and hydrothermally structural evolution of nanocrystal titanium dioxide[J].Chemistry of Materials,2002,14(5):1974-1980.

[22] Corma A.From microporous to mesoporous molecular sieve materials and their use in catalysis[J].Chemical Reviews,1997,97(6):2373-2419.

[23] Guidotti M,Ravasio N,Psaro R,et al.Epoxidation on titanium-containing silicates,do structural features really affect the catalytic performance?[J].Journal of Catalysis,2003,214(2):242-250.

[24] Han Y J,Kim J M,Stucky G D.Preparation of noble metal nanowires using hexagonal mesoporous silica SBA-15[J].Chemistry of Materials,2000,12(8):2068-2069.

[25] Zhao D Y,Huo Q S,Feng J L,et al.Nonionic triblock and star diblock copolymer and oligomeric surfactant syntheses of highly ordered,hydrothermally stable,mesoporous silica structures[J].Journal of the American Chemical Society,1998,120:6024-6036.

[26] 李兆,Al-SBA-15 和 Fe-SBA-15 介孔材料的合成、表征及催化性能研究[D].大连:中国科学院大连化学物理研究所,2005.

[27] Pachamuthu M P,Srinivasan V V,Maheswari R,et al.The impact of the copper source on the synthesis of meso-structured CuTUD-1:A promising catalyst for phenol hydroxylation[J].Catalysis Science & Technology,2013,3(12):3335-3342.

[28] 陶明,刘华彦,俞汕雷,等.TS-1/蔗青石整体催化剂催化苯酚羟基化制苯二酚[J].工业催化,2017,25(2):46-51.

[29] Mohamed M M,Kinsa N A.Characterization of intrazeolitic Fe^{3+}-prepared by chemical vapor deposition of $[(C_6H_6)Fe(CO)_3]_2$ inside NaY and FSM-16 zeolites and their catalytic activities towards phenol hydroxylation[J].Materials Research Bulletin,2003,38(15):1993-2007.

[30] Choi J S,Yoon S S,Jang S H,et al.Phenol hydroxylation using Fe-MCM-41 catalysts[J].Catalysis Today,2006,111(3/4):280-287.

[31] 张晓晓.高结晶度和铁含量 FeAPO-5 分子筛的绿色合成及其苯酚羟基化性能研究[D].兰州:兰州理工大学,2018.

(C)1994-2019 China Academic Journal Electronic Publishing House. All rights reserved. http://www.cnki.net

(C)1994-2019 China Academic Journal Electronic Publishing House. All rights reserved. http://www.cnki.net

5.邵艳秋,于平,郑友进,王丽杰,王星月.氧化锌基阵列染料敏化太阳能电池研究进展[J].人工晶体学报,2019,48(10):1967-1975.

第48卷 第10期
2019年10月

人 工 晶 体 学 报
JOURNAL OF SYNTHETIC CRYSTALS

Vol.48 No.10
October,2019

氧化锌基阵列染料敏化太阳能电池研究进展

邵艳秋[1],于 平[1,2],郑友进[2],王丽杰[1,2],王星月[1,2]

(1.牡丹江师范学院化学化工学院,牡丹江 157011;2.黑龙江省新炭基功能与超硬材料重点实验室,牡丹江 157011)

摘要:ZnO基染料敏化太阳能电池(DSSCs)因其成本低、光电转换效率稳定、制备工艺简单且易于大规模生产等优势成为研究的热点。本文从形貌结构和优化方案两方面总结了近期ZnO阵列光阳极在DSSCs中的研究进展。通过分析不同形貌结构的ZnO阵列的优势和缺点来解释其对DSSCs影响的机理;通过总结ZnO阵列相关的掺杂、构筑异质结等优化方案获得了提高DSSCs光电转换效率的信息,为进一步提高DSSCs电池效率提供指导。

关键词:ZnO阵列;DSSCs;光生电荷载流子;光电转换效率

中图分类号:TM914.4 文献标识码:A 文章编号:1000-985X(2019)10-1967-09

DOI:10.16553/j.cnki.issn1000-985x.2019.10.031

Research Progress of Zinc Oxide Based Array Dye-Sensitized Solar Cells

SHAO Yan-qiu[1], *YU Ping*[1,2], *ZHENG You-jin*[2], *WANG Li-jie*[1,2], *WANG Xing-yue*[1,2]

(1. School of Chemistry and Chemical Engineering, Mudanjiang Normal University, Mudanjiang 157011, China;
2. Heilongjiang Province Key Laboratory of New Carbon-Base Functional and Superhard Material, Mudanjiang 157011, China)

Abstract: ZnO-based dye-sensitized solar cells (DSSCs) have become the research hotspot due to their low cost, stable and efficient photoelectric conversion efficiency, simple preparation process and easy mass production. In this paper, the research progress of recent ZnO array photoanodes in DSSCs are summarized from the aspects of morphology structure and optimization scheme. By analyzing the advantages and disadvantages of ZnO array with different morphological structures, the mechanism of their effects on DSSCs is explained. By summarizing the doping and constructing heterojunctions of ZnO array, the information of improving the photoelectric conversion efficiency of DSSCs is obtained, which provides guidance for improving the efficiency of DSSCs.

Key words: ZnO array; DSSCs; photogenerated charge carry; photoelectric conversion efficiency

1 引 言

染料敏化太阳能电池(DSSCs)作为第三代新型高效太阳能电池具有工艺简单、成本低、无污染、效率高等优点,已成为人们研究的热点。经过不断的改进,DSSCs的光电转换效率已达到13%[1-4]。DSSCs的工作原理效仿植物光合作用,如图1。电极表面吸附在纳米级半导体材料上的染料被光照射受到激发后,将产生的电子注入到半导体的导带中,氧化态染料分子与电池中的还原性物质发生氧化-还原反应,被氧化的成分在电极上还原沉积,染料分子回到基态而重复使用[5]。纳米氧化物半导体作为光阳极在DSSCs中扮演着重要的角色,它不仅是吸附染料的重要载体,也是作为电荷分离和传输的载体,因此它应具有以下特点:(1)具有较大的比表面积,可吸附大量染料;(2)具备较高的电子迁移率,有利于光生电荷的传输,减少电荷载流子在传输过程中的复合。

TiO_2是经典的DSSCs光阳极材料,具有较高的光电转换效率,但由于热分散的影响及TiO_2较高的表面态密度,使得光生电子被其表面态能级俘获的几率增加,使TiO_2的扩散系数减小,电荷载流子的复合率增加,限制TiO_2基DSSCs的电池效率提高。ZnO的带隙宽为3.3 eV,激子结合能大且易形成高结晶态,有着与TiO_2相似的电子亲和性,电子迁移率也远超TiO_2,加之ZnO基光阳极价格低廉,制备方法简单多样,因此ZnO是有望取代TiO_2的理想光阳极材料[6-8]。然而,ZnO基DSSCs相较TiO_2的光电转换效率较低,主要原

基金项目:黑龙江省教育厅科研备案项目(1352MSYYB006);牡丹江师范学院研究生科技创新项目(kjcx2018-25mdjsu);牡丹江师范学院科研项目(JG2017001)

作者简介:邵艳秋(1969-),女,吉林省人,博士,教授。E-mail:shaoyanqiu19696@163.com

(C)1994-2019 China Academic Journal Electronic Publishing House. All rights reserved. http://www.cnki.net

因为 ZnO 基光阳极在 N719 等酸性染料介质中不稳定，使电荷传输受阻，电子不能顺利注入 ZnO 的导带，而且光生电子从染料分子注入到 ZnO 的速率较低，导致光电转换效率降低[9]。为提高 ZnO 在酸性电解质中的稳定性和光生电子的传输速率，人们从形貌控制、掺杂、构筑异质结和量子点改性等方面入手进行研究。

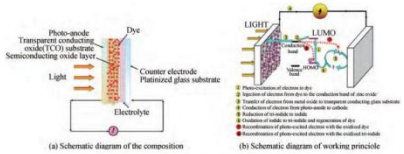

图 1 DSSCs 的组成示意图及工作原理图[9]

Fig. 1 Schematic diagram of the composition and working principle of the DSSCs[9]

2 基于 ZnO 阵列的 DSSCs

ZnO 的结合能是 60 meV，电子传输速率可达 200 ~ 1000 $cm^2/V \cdot s$[10]，其作为 n 型半导体有诸多优点。ZnO 的各向异性很强，可以通过控制溶液配比、反应温度、沉积时间等条件来控制其形貌，得到不同功能的 ZnO 材料，这在一定程度上减少了 DSSCs 的制作成本。因此从纳米 ZnO 阵列材料的结构入手，探讨零维、一维、二维以及三维的 ZnO 阵列对 DSSCs 性能的影响，这对 DSSCs 发展有非常重要的指导意义。

2.1 零维纳米 ZnO 阵列材料

零维 ZnO 阵列在 DSSCs 中应用广泛，其在 DSSCs 中的工作原理如图 2 所示。零维 ZnO 阵列 DSSCs 中的纳米粒子之间存在着较大的晶界，这种晶界形成的晶界势垒易增加电子和空穴的复合机率，使光生载流子的寿命降低，阻碍了 DSSCs 性能的提高。因此零维 ZnO 阵列 DSSCs 效率不及其他结构的 ZnO 基光阳极，但其普遍具有较大的比表面积，可以吸附大量的染料，从而直接影响材料的捕光效率。经过改性的零维 ZnO 阵列 DSSCs 具有很广阔的发展前景。德国化学家 During[11] 将羧基卟啉作为 ZnO 纳米粒子的互连体，增加连接性的同时还可以作为光活性顶层，改性后的 ZnO 基光阳极的效率提升了 46%。Giannouli 等[12] 将直径小于 50 nm 的 ZnO 纳米粒子与含有乙酰丙酮的蒸馏水混合以提高粒子孔隙率，降低 ZnO 粒子膏体的表面张力，最终光电转换效率达到 6.79%。单纯的 ZnO 聚合度很差[13-14]，针对这一问题科研工作者对 ZnO 纳米粒子进行包覆改性，包覆层不但可以作为光吸附剂或光感剂，还可以增加 ZnO 纳米粒子的聚合度，增加光吸收性能。Singh[15] 课题组用亚胺连接物和氯化钉包覆的 ZnO 作为光阳极使光电效率达到 3.83%。为了得到有序且厚度均一的核壳结构，研究者采用丝网印刷法和原子层沉积法调控包覆层厚度，这种核壳结构具有大量的有序介孔，比表面积大。因此可以增大染料的吸附率，而且电解液更容易浸入介孔中，增加了反应的活性位点。Zhang[17] 课题组用这种方法制备 TiO_2 包覆 ZnO 结构，光电转换效率为 3.7%，电流密度为 9.03 mA/cm^{-2}，开路电压为 0.649 V。Philip[16] 用多元醇水溶法制备了多孔 Ni-ZnO 结构，多元醇起到稳定剂的作用，同时也能抑制颗粒的生长，达到控制材料形貌的功能，这种多孔 Ni-ZnO 复合材料具有吸收率高、表面积大、结晶性强等优点，研究表明 Ni-ZnO 基 DSSCs 的光电转换效率为 0.416%，是改性前的 6 倍。

2.2 一维纳米 ZnO 阵列材料

垂直有序的一维纳米 ZnO 阵列可以为电子传输提供一个直接的通道，使光生电子能够快速抵达光阳极基底，这可以减少反向电子转移和激发态染料分子与氧化电解质之间的重组[18]。Guo 等[20] 用微波水溶法制备了能够快速生长且表面缺陷低的 ZnO 纳米线阵列，研究表明六次亚甲基四胺（HMTA）是减少表面缺陷的关键，此法还可以扩大 ZnO 纳米线阵列的比表面积，从而增加光的捕获量。Xu[21] 用交替循环法提高了

(C)1994-2021 China Academic Journal Electronic Publishing House. All rights reserved. http://www.cnki.net

ZnO 纳米线的长径比，最终光电转换效率达到 7%。He[22] 从结晶取向和微观结构入手，制备了具有高比表面积的超长 ZnO 纳米线阵列（如图 3），纳米线的高度为 25 μm，电转换效率达到 6.15%。

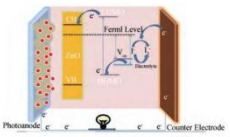

图 2 零维 ZnO 阵列 DSSCs 的示意图[15]

Fig. 2 Schematic representation of zero-dimension ZnO array DSSCs[15]

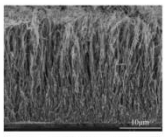

图 3 ZnO 纳米线阵列的 SEM 截面图[22]

Fig. 3 SEM cross-sectional view of ZnO nanowire arrays[22]

2.3 二维纳米 ZnO 阵列材料

与一维 ZnO 阵列相比，二维 ZnO 阵列因其空间结构上的优势，往往具有更大的比表面积。Ibrayev 等[23] 为了分析不同形貌对 DSSCs 性能的影响，分别用水溶法和电沉积法制备了一维 ZnO 纳米棒阵列和二维 ZnO 纳米片阵列，见图 4（a）和图 4（b）。结果显示纳米片相对于纳米棒有更大的比表面积，有利于染料的吸附。但纳米片中存在着大量缺陷，这些缺陷会降低 ZnO 的费米能级而成为电子捕获中心，纳米棒和纳米片的光电转换效率分别为 0.25% 和 0.5%。Chen 等[24] 用电沉积法制备 ZnO 纳米片，并用水热法在 ZnO 纳米片上制备了 ZnO 纳米棒，这种纳米片-纳米棒复合结构用 Cd 和 CdSe 共同敏化，最后应用于 DSSCs 的光阳极上，得到了 2.5% 的光电转化效率。Han 等[25] 用水热法制备了平均厚度 20 ~ 30 nm，尺寸为 100 nm 的 ZnO 纳米片，得到了 3.39% 的光电转换效率。Wang 等[26] 用水热法制备了 ZnO 纳米片，并用浸涂法将直径约为 20 nm 的 ZnO 纳米棒涂在厚度约为 20 ~ 30 μm 的 ZnO 纳米片的顶部，获得了 ZnO 纳米片-纳米棒复合结构，顶层的 ZnO 纳米棒提高了复合结构的光散射能力和染料吸附量，底层的单晶 ZnO 片状结构不仅可以为光生电子提供直接的通道以增加电子迁移率，二维结构还可以增加比表面积以增加染料的吸附量，使其光电转换效率由单一片状结构的 4.38% 提高至 7.95%。

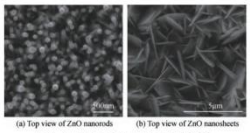

图 4 ZnO 纳米棒和 ZnO 纳米片的平面图[23]

Fig. 4 Top view of ZnO nanorods and ZnO nanosheets[23]

2.4 三维纳米 ZnO 阵列材料

三维结构的 ZnO 阵列通常是在一种形貌的纳米 ZnO 上进行形貌多样的分级生长，如枝状[27]、球状[28] 和花状[29] 等，多级结构有利于增大 ZnO 的比表面积，提高光散射效应。

Marimuthu 等[27] 先用溶胶-凝胶法制备 ZnO-TiO_2 种子层，然后在种子层上制备 ZnO 纳米线-枝状纳米针的三维花状阵列，如图 5 所示。枝状纳米针可以提供良好的光散射能力，紫外-可见光吸收分析发现花状阵

(C)1994-2021 China Academic Journal Electronic Publishing House. All rights reserved. http://www.cnki.net

列更容易吸附染料，纳米线和枝状纳米针的光电转换效率分别是 0.91% 和 1.47%。之后，Marimuthu 等[28] 用电沉积法制备了 ZnO 纳米微球，又用水溶法在微球表面制备了 ZnO 纳米棒，这种结构的三维阵列不仅可以增强比表面积和光散射效应，位于两种形貌之间的阻挡层可以防止反向电子的产生，一定程度上增大了 DSSCs 的光电转换效率。此外，三维阵列结构还可以使光生电子的寿命增长，减少电子-空穴的复合率。Saleem 等[29] 用低温水热法制备了三维花状 ZnO 阵列，其短路电流密度为 4.23 mA/cm^2，开路电压为 738 mV，填充系数为 0.74，光电转换效率为 2.23%。

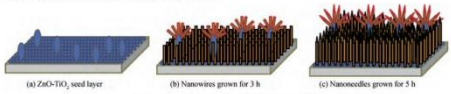

图 5 ZnO 纳米线-枝状纳米针结构的原理图[27]

Fig. 5 Schematic diagram of the ZnO nanostructures[27]

3 掺杂 ZnO 阵列的 DSSCs

3.1 金属掺杂 ZnO 阵列材料

一般将铂[30]，铝[31-32]，金[33] 等金属元素掺杂至 ZnO 纳米结构中提高材料的光电转换效率。如图 6 所示，与纯 ZnO 相比，杂原子的加入不但会改变 ZnO 的结晶度和晶格参数，还会引起晶格畸变，使其光学性质（如吸光度、扩散反射系数、带隙等）发生改变。这些改变或者引起导带下移，或者引起光谱红移，都可以扩大材料的吸光率，以增加 DSSCs 的效率。Parra[34] 用溶胶-凝胶法制备了 Al 掺杂的 ZnO 纳米盘，结果表明随着 Al^{3+} 离子的加入，晶粒尺寸和晶格常数降低，带隙发生改变，互相交错的纳米盘结构使材料的比表面积增大，更加利于染料的吸附。过渡金属的加入会减小带隙，改变 ZnO 的光电性能[35]。Kanimozhi[36] 用静电纺丝法制备了 Co 掺杂的 ZnO 纳米纤维，Co 的加入减少了光生电荷与染料或电解液的复合，提升了 DSSCs 的电流密度，将效率由原来的 1.63% 提升至 2.97%。研究发现在 ZnO 中掺入一定量的 Co 还会对材料的费米能级造成影响，并且纤维状的多孔结构更加利于染料的吸附以及增强光散射效应。此外不同染料的加入也可以扩大材料的吸光范围。Saboor[37] 用水热法制备了 Ag 掺杂 ZnO 纳米棒，用溴代邻苯三酚作为 DSSCs 的染料。研究表明，随着 Ag 加入量的不同，复合材料的带隙发生改变，溴代邻苯三酚的加入会使材料的吸收范围发生红移，扩大了材料的吸光范围。稀土元素的加入会改变 ZnO 的形貌，Choi[38] 用水热法在含有 Ce 的前驱体溶液中制备 ZnO 纳米线，溶液中充足的 Ce 能够使表面原本垂直排列的 ZnO 纳米线顶端带电，局部的静电作用造成 ZnO 纳米线弯曲或聚集，增加了染料的吸附能力，提高染料的负载率。

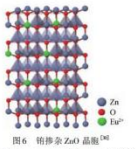

图 6 钡掺杂 ZnO 晶胞[38]

Fig. 6 Structure cell of Ba-doped ZnO[38]

3.2 非金属掺杂 ZnO 阵列材料

非金属掺杂可以改变 ZnO 的带隙，增加电子空穴的数量，从而提高 DSSCs 的性能。Roza 等[39] 用水热法以硝酸锌、HMT 以及二甲基硼酸为前驱体，通过控制退火温度，制备了 B 掺杂的管状 ZnO 纳米阵列（如图 7），制备的 DSSCs 具有较好的光电性能，光电转换效率为 0.29%，电流密度为 2.2 mA/cm^2，开路电压为 0.46 V。在此基础上，他们改进工艺后将光电转换效率提升至 0.67%，电流密度提升至 3.5 mA/cm^2，开路电压提升至 0.5 V[40]。

(C)1994-2021 China Academic Journal Electronic Publishing House. All rights reserved. http://www.cnki.net

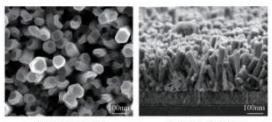

图 7 硼掺杂 ZnO 的 SEM 照片[39]

Fig. 7 FE-SEM images of B-doped ZnO[39]

4 异质结 ZnO 阵列材料

异质结可以加快电子传输速率、延长电子寿命、增强光的捕获能力。ZnO 异质结有体相异质结和贵金属沉积两种。体相异质结又分为同型异质结和异型异质结。其中异型异质结（p-n）在 DSSCs 中应用广泛，将 ZnO 与其他材料的各自优点相结合，从而提高光阳极材料的光电转换能力。与 ZnO 构筑异质结的半导体一般要求与 ZnO 有相似的晶体结构、相近的原子间距和热膨胀系数，如 TiO_2/ZnO 异质结[9-12]、ZnO/Cu_2O 异质结[42] 及石墨烯/ZnO 异质结[43]。TiO_2/ZnO 异质结的形式多种多样，John[44] 课题组制备了 TiO_2 纳米棒/ZnO 纳米薄膜异质结构，这种结构是以 FTO 上的 TiO_2 纳米棒为基底，再用浸涂法将由醋酸锌-二乙醇胺-乙醇组成的前驱体浸涂于 TiO_2 纳米棒上，最后用热分解法制备了 TiO_2-ZnO 复合薄膜异质结构，其光阳极的光电转换效率达到 4.36%，相对于单一的 TiO_2 纳米棒（3.10%）和 ZnO 纳米薄膜（0.63%），光电转化效率有大幅提升。表层的 ZnO 厚层比表面积较大，利于染料的吸附；底层的 TiO_2 纳米棒不仅为电子提供一个快速而直接的通道，也充当了一个阻断层，减少基底与电解液之间的电子复合。

核壳结构是常见的异质结构，除了可以提高光电流密度以外，涂覆的壳层可作为能量屏障，降低电子复合损失，使导带向下移动，增加电子注入量，提高电子注入效率。Hu[45] 用水热法制备了 ZnO/Nb_2O_5 核壳结构，Nb_2O_5 的加入使效率由原来的 0.856% 提升至 1.995%。Ebadi 等[46] 制备的 ZnO-TiO_2 核壳结构，其中 ZnO 作为 TiO_2 的壳，通过改变 ZnO 壳的形状和厚度，对染料敏化太阳能电池的光伏特性进行研究，其效率由原来的 4.66% 提高到 7.13%，以 ZnO 为核，TiO_2 为壳的异质结也达到不错的效果。Miles[47] 设计一种纳米片包覆 ZnO 纳米线掺杂有序介孔 TiO_2 的异质结构，用于制备准固态太阳能电池，制备流程如图 8 所示。他用电化学阳极氧化法制备了 ZnO 纳米线，然后采用该课题组之前发表过的水热法合成的 TiO_2 纳米片包覆 ZnO 纳米线结构，[48] 同时采用模版法设计有序介孔结构的 TiO_2[49]，最后将 ZnO 纳米线和 TiO_2 纳米片包覆的 ZnO 纳米线，分别引入 TiO_2[50] 的介孔中形成新的异质结构，通过控制二者的比例，提高异质结构的光电转换效率。测试表明，ZnO 纳米线掺杂介孔 TiO_2 光电转换效率最高可达 5.54%，TiO_2 纳米片包覆 ZnO 纳米线掺杂介孔 TiO_2 光电转换效率最高可达 7.46%。

另一种研究较为广泛的异质结构是分级结构。分级结构一般是将不同的物质或者结构以覆盖的方式进行制作，这样不仅能加厚纳米材料层以提高染料吸附率，而且复合不同的材料可以降低禁带高度以提高光电转换效率。Chamarzadeh 等[51] 在 TiO_2 纳米管上用溶胶-凝胶法制备出 TiO_2 纳米管负载 ZnO 纳米粒子的分级结构阵列，效率达到了 8.3%。

Zhou 等[52] 用水热法制备的 Cu_2O/ZnO 异质结构也得到了较高的光电转换效率，其光电转换效率可达 7.02%。这种异质结构光电转换效率的提高归因于材料的高比表面积和 Cu_2O/ZnO 双层膜异质结的孔隙结构。此外，Cu_2O 的加入可以弥补 ZnO 的固有缺陷，使得电荷转移的电阻降低，载荷量增加，延长电子寿命。石墨烯/3D-ZnO 结构是 Kilic 等[53] 用改良的 Hummers 法[54] 制备的氧化石墨烯浸涂在 FTO 基底上，再用水热法将 ZnO 三维结构长在石墨烯基底上得到的，这种异质结构的光电转换效率为 7.04%。

(C)1994-2021 China Academic Journal Electronic Publishing House. All rights reserved. http://www.cnki.net

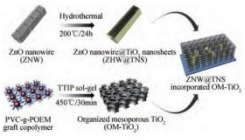

图 8 TiO_2 纳米片包覆 ZnO 纳米线掺杂有序介孔 TiO_2 的复合材料的制备流程[58]

Fig. 8 Schematic illustration of the fabrication of ZnO nanowire core surrounded by a shell of TiO_2 nanosheets incorporated organized mesoporous TiO_2[58]

除此之外，贵金属也被应用在 DSSCs 的光阳极中。一般来说，在光照下具有表面等离子体共振(SPR)效应的贵金属纳米颗粒会出现电子的集体振荡，这种效应可以增加染料的捕光能力，促进光阳极层载流子的生成。利用 SPR 效应，DSSCs 的光捕获能力可以显著提升[59-60]。Li[56-62] 在之前的工作基础上制备了 Au 包覆 ZnO 纳米粒子，其光阳极的光电转换效率达到了 8.91%，光电转换效率的提高归功于 SPR 效应。Lu 等[59] 将 Au 纳米粒子嵌入单晶 ZnO 纳米线阵列，由于 Au 纳米粒子的 SPR 效应产生强电场，染料的吸附得到了改善，使电池效率提高。Tan 等[60] 先用水热法制备了 ZnO 纳米线，又将其浸入氯金酸($HAuCl_4 \cdot 4H_2O$)溶液中，成功制备了 Au 修饰的 ZnO 纳米线，将光电转化效率由 0.576% 提升至 1.01%，光电转化效率的提升是由于 Au 纳米粒子在 520 nm 附近的 SPR 效应，促进了染料光吸收的改善，产生更多的电子，短路电流密度显著增加。

5 量子点改性 ZnO 阵列材料

近年来，无机半导体纳米晶(量子点)敏化太阳能电池是近年来发展起来的一种新型光伏器件，主要以光阳极为基础，利用无机半导体中的量子点敏化剂来吸收太阳光并产生光电子[61]。此外，由于克服了肖克利-奎伊瑟极限，量子点可使单个光子产生多个激子，使制备高效率电池成为可能[62]。Chen 等[63] 先用溶胶-凝胶法制备了氧化锌反蛋白石(ZnO IOs)，以其为模板制备了光阳极为网状结构的菁锌共敏化太阳能电池，可见光吸收波长提高至 750 nm。为了提高光电性能，运用连续离子吸附法将 CdS/CdSe 量子点涂覆在 ZnO IOs 光阳极上，光电性能从 4.01% 提高至 4.60%。Nayeri 等[64] 用磁控溅射法在 Al 掺杂的 ZnO 种子层上制备了 6 μm 高的 ZnO 纳米线，在此基底上覆盖了 CdS 纳米粒子以及 N719 染料，制备出了 ZnO/CdS 异质结 DSSCs(如图 9)，其光电效应达到了 2.68%。

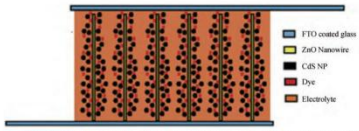

图 9 基于 ZnO 纳米线/CdS 纳米粒子/ N719 染料的量子点染料敏化太阳能电池原理图[64]

Fig. 9 Schematic illustration of QDSSC based on ZnO nanowire/CdS nanoparticle/N719 dye[64]

(C)1994-2021 China Academic Journal Electronic Publishing House. All rights reserved. http://www.cnki.net

6 结语与展望

综上所述，ZnO 基 DSSCs 在结构上可分为零维、一维、二维和三维模型。虽然零维 ZnO 粒子与粒子之间较大的晶界会阻碍光生电荷的传输，但是零维 ZnO 粒子较高的比表面积可以吸附大量的染料，这是影响电池效率的关键因素，因此经过改性的零维阵列 ZnO 基 DSSCs 具有很广阔的发展前景。一维阵列结构中光生载流子有唯一传输路径，避免了电荷载流子的多通道传输，但一维阵列结构的 ZnO 通常比表面积有限，因此具有高长径比的一维阵列往往会有较高的电池效率；二维阵列结构的 ZnO 不仅具有快速电子传输通道，结构上的优势使得二维 ZnO 阵列具有高比表面积；但就增加比表面积而言，人们偏向制备多级结构的三维 ZnO 阵列材料，如纳米棒-纳米片、纳米球-纳米棒等，这种不同结构的复合不仅可以增加比表面积，也可以增加材料的光散射效应，从而拓展对光的利用效率。此外，通过构筑异质结构、掺杂、量子点改性等优化方式都有方法成功制备出 ZnO 复合阵列。通过组成的调节，改变了 ZnO 晶格参数和晶粒尺寸，从而改变能量带隙。用掺杂型纳米结构调整 ZnO 的能带和表面状态被证明是一种改变 ZnO 光学和物理性质的有效方法。本文为进一步提高 DSSCs 的光电转换效率具有理论指导意义。

参 考 文 献

[1] Tsubomura H, Matsumura M, Nomura Y, et al. Dye Sensitised Zinc Oxide: Aqueous Electrolyte: Platinum Photocell [J]. Nature, 1976, 261: 402-403.

[2] Michael G. Solar Energy Conversion by Dye-Sensitized Photovoltaic Cells [J]. Inorganic Chemistry, 2005, 44 (20): 6841-6851.

[3] Memarian N, Concina I, Braga A, et al. Hierarchically Assembled ZnO Nanocrystallites for High-Efficiency Dye-Sensitized Solar Cells [J]. Angewandte Chemie-International Edition, 2011, 50 (51): 12321-12325.

[4] Brian O R, Michael G. A Low-Cost, High-Efficiency Solar Cell Based on Dye-Sensitized Colloidal TiO_2 Films [J]. Nature, 1991, 353 (6346): 737-740.

[5] Mathew S, Yella A, Gao P, et al. Dye-Sensitized Solar Cells with 13% Efficiency Achieved through the Molecular Engineering of Porphyrin Sensitizers [J]. Nature Chemistry, 2014, 6 (3): 242-247.

[6] Sengupta D, Das P, Mondal B, et al. Effects of Doping, Morphology and Film-Thickness of Photo-Anode Materials for Dye Sensitized Solar Cell Application-A Review [J]. Renewable and Sustainable Energy Reviews, 2016, 60: 356-376.

[7] Kim Y H, Lee J K, Song Y S, et al. Influence of TiO_2 Coating Thickness on Energy Conversion Efficiency of Dye-Sensitized Solar Cells [J]. Electronic Materials Letters, 2014, 10 (2): 445-449.

[8] Qiu J, Guo M, Wang X. Electrodeposition of Hierarchical ZnO Nanorod-Nanosheet Structures and Their Applications in Dye-Sensitized Solar Cells [J]. ACS Applied Materials & Interfaces, 2011, 3 (7): 2358-2367.

[9] Boro B, Gogoi B, Rajbongshi B, et al. Nano-Structured TiO_2/ZnO Nanocomposite for Dye-Sensitized Solar Cells Application: A Review [J]. Renewable and Sustainable Energy Reviews, 2018, 81: 2264-2270.

[10] Majumder T, Dhar S, Chakraborty P, et al. S, N Co-Doped Graphene Quantum Dots Decorated C-Doped ZnO Nanotaper Photoanodes for Solar Cells Applications [J]. Nano, 2019, 14 (1): 1950012.

[11] During J, Kunmann A, Killian M S, et al. Porphyrins as Multifunctional Interconnects in Networks of ZnO Nanoparticles and Their Application in Dye-Sensitized Solar Cells [J]. Chem. Photo. Chem., 2018, 2 (3): 213-222.

[12] Giannouli M, Govatsi K, Syrokostas G, et al. Factors Affecting the Power Conversion Efficiency in ZnO DSSCs: Nanowire vs. Nanoparticles [J]. Materials, 2018, 11 (3): 411.

[13] Liu Q, Wei Y, Shahid M Z, et al. Spectrum-Enhanced Au@ZnO Plasmonic Nanoparticles for Boosting Dye-Sensitized Solar Cell Performance [J]. Journal of Power Sources, 2018, 380: 142-148.

[14] Sun Y, Sun Y, Zhang T, et al. Complete Au@ZnO Core-Shell Nanoparticles With Enhanced Plasmonic Absorption Enabling Significantly Improved Photocatalysis [J]. Nanoscale, 2016, 8 (20): 10774-10782.

[15] Rajkumar C, Arulraj A. Seed Mediated Synthesis of Nanosized Zinc Oxide and Its Electron Transporting Activity in Dye-Sensitized Solar Cells [J]. Materials Research Express, 2018, 5 (1): 015029.

[16] Singh S, Singh A, Kaur N. Imine-Linked Receptors Decorated ZnO-Based Dye-Sensitized Solar Cells [J]. Bulletin of Materials Science, 2016, 39 (6): 1371-1379.

[17] Zhang D, Yoshida T, Furuta K, et al. Hydrothermal Preparation of Porous Nano-Crystalline TiO_2 Electrodes for Flexible Solar Cells [J]. Journal of Photochemistry and Photobiology A: Chemistry, 2004, 164 (1): 159-166.

[18] Philip M R, Babu R, Vasudevan K, et al. Enhanced Efficiency of Dye-Sensitized Solar Cells Based on Polyol-Synthesized Nickel-Zinc Oxide

(C)1994-2021 China Academic Journal Electronic Publishing House. All rights reserved. http://www.cnki.net

Composites [J]. Journal of Electronic Materials, 2019, 48 (1): 252-260.

[19] Xu C, Wu J, Desai U V, et al. Multilayer Assembly of Nanowire Arrays for Dye-Sensitized Solar Cells [J]. Journal of the American Chemical Society, 2011, 133 (21): 8122-8125.

[20] Guo H, Ding R, Li N, et al. Defects Controllable ZnO Nanowire Arrays by a Hydrothermal Growth Method for Dye-Sensitized Solar Cells [J]. Physica E: Low-Dimensional Systems and Nanostructures, 2019, 105: 156-161.

[21] Xu C, Gao D. Two-Stage Hydrothermal Growth of Long ZnO Nanowires for Efficient TiO_2 Nanotube-Based Dye-Sensitized Solar Cells [J]. Journal of Physical Chemistry C, 2012, 116 (12): 7236-7241.

[22] He D, Sheng X, Yang J, et al. [10-40] Oriented Multichannel ZnO Nanowire Arrays with Enhanced Optoelectronic Device Performance [J]. Journal of the American Chemical Society, 2014, 136 (48): 16772-16775.

[23] Ilnaye N K, Ilyasov B R, Mamayev D A. Influence of the Morphology of ZnO Nanostructures on Luminescent and Photovoltaic Properties [J]. Optics and Spectroscopy, 2017, 122 (3): 462-468.

[24] Chen Z, Li S, Wei C, et al. Preparation of ZnO Nanosheets-Nanorods Hierarchically Structured Films and Application in Quantum Dots Sensitized Solar Cells [J]. International Journal of Electrochemical Science, 2017, 12 (8): 7693-7701.

[25] Han S Y, Akhtar M S, Jung I, et al. ZnO Nanoflakes Nanomaterials Via Hydrothermal Process for Dye Sensitized Solar Cells [J]. Materials Letters, 2018, 230: 92-95.

[26] Cheng H, Wang Y, Guo P, et al. High-Efficiency Dye-Sensitized Solar Cells Based on a ZnO Nanorod/Nanosheet Hierarchical Structure [J]. Energy Technology, 2017, 6 (6): 1161-4167.

[27] Marimuthu T, Anandhan N, Thangamuthu R, et al. Facile Growth of ZnO Nanowire Arrays and Nanoneedle Arrays with Flower Structure on ZnO-TiO_2 Seed Layer for DSSC Applications [J]. Journal of Alloys and Compounds, 2017, 693: 1011-1019.

[28] Marimuthu T, Anandhan N, Thangamuthu R. A Facile Electrochemical-Hydrothermal Synthesis and Characterization of Zinc Oxide Hierarchical Structure for Dye Sensitized Solar Cell Applications [J]. Journal of Materials Science, 2018, 53 (17): 12441-12454.

[29] Saleem M, Ahmad M A, Fang L, et al. Solution-Derived ZnO Nanoflowers Based Photoelectrodes for Dye-sensitized Solar Cells [J]. Materials Research Bulletin, 2017, 96: 211-217.

[30] Fonseca A F V, Siqueira R L, Landers R, et al. A Theoretical and Experimental Investigation of Eu-Doped ZnO Nanorods and Its Application on Dye Sensitized Solar Cells [J]. Journal of Alloys and Compounds, 2018, 739: 939-947.

[31] Deng J, Wang M, Ye W, et al. CdS/CdSe-Sensitized Solar Cell Based on Al-Doped ZnO Nanoparticles Prepared by the Decomposition of Zinc Acetate Solid Solution [J]. Solid State Electronics, 2017, 127: 38-44.

[32] Sengupta D, Mondal B, Mukherjee K. Genesis of Flake-Like Morphology and Dye-Sensitized Solar Cell Performance of Al-Doped ZnO Particles: A Study [J]. Journal of Nanoparticle Research, 2017, 19 (3): 100.

[33] Tan W K, Ito T, Kawamura G, et al. Controlled Facile Fabrication of Plasmonic Enhanced Au-Decorated ZnO Nanowire Arrays Dye-Sensitized Solar Cells [J]. Materials Today Communications, 2017, 13: 354-358.

[34] Parra M R, Pandey P, Siddiqui H. et al. Evolution of ZnO Nanostructures as Hexagonal Disk: Implementation as Photoanode Material and Efficiency Enhancement in Al:ZnO Based Dye Sensitized Solar Cells [J]. Applied Surface Science, 2019, 470: 1130-4138.

[35] Fabbiyola S, Kennedy L J. Bandgap Engineering in Doped ZnO Nanostructures for Dye Sensitized Solar Cell Applications [J]. Journal of Nanoscience and Nanotechnology, 2019, 19 (5): 2963-2970.

[36] Kanimozhi G, Vinoth S, Kumar H, et al. A Novel Electrospun Cobalt-Doped Zinc Oxide Nanofibers as Photoanode for Dye-Sensitized Solar Cell [J]. Materials Research Express, 2019, 6 (2): 25041.

[37] Sabouri A, Shah S M, Hussain H. Band Gap Tuning and Applications of ZnO Nanorods in Hybrid Solar Cell: Ag-Doped Verses Sd-Doped ZnO Nanorods [J]. Materials Science in Semiconductor Processing, 2019, 93: 215-225.

[38] Choi S C, Sohn S H. Controllable Hydrothermal Synthesis of Bundled ZnO Nanowires Using Cerium Acetate Hydrate Precursors [J]. Physica E: Low-Dimensional Systems and Nanostructures, 2018, 104: 98-100.

[39] Reza L, Rahman M Y A, Umar A A, et al. Boron Doped ZnO Films for Dye-Sensitized Solar Cell (DSSC): Effect of Annealing Temperature [J]. Journal of Materials Science: Materials in Electronics, 2016, 27 (8): 8394-8401.

[40] Reza L, Rahman M Y A, Umar A A, et al. Multi-cycle Growth of Boron Doped ZnO Films as Photoanode for Dye-Sensitized Solar Cell (DSSC) [J]. International Journal of Electrochemical Science, 2016, 11 (12): 10965-10977.

[41] Feng Y, Chen J, Huang X, et al. A ZnO/TiO_2 Composite Nanorods Photoanode with Improved Performance for Dye-Sensitized Solar Cells [J]. Crystal Research and Technology, 2016, 51 (10): 548-553.

[42] Zhou X, Xie Y, Ma J, et al. Synthesis of Hierarchical Structure Cuprous Oxide by a Novel Two-Step Hydrothermal Method and the Effect of Its Addition on the Photovoltaic Properties of ZnO-Based Dye-Sensitized Solar Cells [J]. Journal of Alloys and Compounds, 2017, 721: 8-17.

[43] Kilic B, Turkdogan S, Astam A, et al. Graphene-Based Copper Oxide Thin Film Nanostructures as High-Efficiency Photocathode for P-Type Dye-Sensitized Solar Cells [J]. Journal of Photonics for Energy, 2017, 7 (4): 45502.

[44] John K A, Nadhanath J, Mallick S, et al. Electrochemical Synthesis of Novel Zn-Doped TiO_2 Nanotube/ZnO Nanoflake Heterostructure with

(C)1994-2021 China Academic Journal Electronic Publishing House. All rights reserved. http://www.cnki.net

Enhanced DSSC Efficiency [J]. Nano-Micro Letters, 2016, 8 (4): 381-387.

[45] Hu X, Wang H. ZnO/Nb_2O_5 Core/Shell Nanorod Array Photoanode for Dye-Sensitized Solar Cells [J]. Frontiers of Optoelectronics, 2018, 11 (3): 285-290.

[46] Ebadi M, Zarghami Z, Motevalli K. 40% Efficiency Enhancement in Solar Cells Using ZnO Nanorods as Shell Prepared Via Novel Hydrothermal Synthesis [J]. Physica E: Low-Dimensional Systems and Nanostructures, 2017, 87: 199-204.

[47] Miles D O, Lee C S, Cameron P J, et al. Hierarchical Growth of TiO_2 Nanosheets on Anodic ZnO Nanowires for High Efficiency Dye-Sensitized Solar Cells [J]. Journal of Power Sources, 2016, 325: 365-374.

[48] Miles D O, Cameron P J, Mattia D. Hierarchical 3D ZnO Nanowire Structures Via Fast Anodization of Zinc [J]. Journal of Materials Chemistry A, 2015, 3 (34): 17569-17577.

[49] Ramirez-Canon A, Miles D O, Cameron P J, et al. Zinc Oxide Nanostructured Films Produced Via Anodization: A Rational Design Approach [J]. RSC Advances, 2013, 3 (47): 25323-25330.

[50] Ahn S H, Chi W S, Park J T, et al. Direct Assembly of Preformed Nanoparticles and Graft Copolymer for the Fabrication of Micrometer-Thick, Organized TiO_2 Films: High Efficiency Solid-State Dye-Sensitized Solar Cells [J]. Advanced Materials, 2012, 24 (4): 519-522.

[51] Chamanzadeh Z, Noormohammadi M, Zahedifar M. Enhanced Photovoltaic Performance of Dye Sensitized Solar Cell Using TiO_2 and ZnO Nanoparticles on Top of Free Standing TiO_2 Nanotube Arrays [J]. Materials Science in Semiconductor Processing, 2017, 61: 107-113.

[52] Kilic B, Turkdogan S. Fabrication of Dye-Sensitized Solar Cells Using Graphene Sandwiched 3D-ZnO Nanostructures Based Photoanode and Pt-Free Pyrite Counter Electrode [J]. Materials Letters, 2017, 193: 195-198.

[53] Hummers W S, Offeman R E. Preparation of Graphitic Oxide [J]. Journal of the American Chemical Society, 1958, 80 (6): 1339.

[54] Dong H, Wu Z, El-Shafei A, et al. Ag-Encapsulated Au Plasmonic Nanorods for Enhanced Dye-Sensitized Solar Cell Performance [J]. Journal of Materials Chemistry A, 2015, 3 (8): 4659-4668.

[55] Fan G, Zhuo Q, Zhu J, et al. Plasmonic-Enhanced Polymer Solar Cells Incorporating Solution-Processable Au Nanoparticle-Adhered Graphene Oxide [J]. Journal of Materials Chemistry, 2012, 22 (31): 15614-15619.

[56] Liu Q, Wei Y, Shahid M Z, et al. Spectrum-Enhanced Au@ZnO Plasmonic Nanoparticles for Boosting Dye-Sensitized Solar Cell Performance [J]. Journal of Power Sources, 2018, 380: 142-148.

[57] Sun Y, Sun Y, Zhang T, et al. Complete Au@ZnO Core-Shell Nanoparticles with Enhanced Plasmonic Absorption Enabling Significantly Improved Photocatalysis [J]. Nanoscale, 2016, 8 (20): 10774-10782.

[58] Li G, Shuford K L, Chen M, et al. A Facile Polyol Route to Uniform Gold Octahedra with Tailorable Size and Their Optical Properties [J]. ACS Nano, 2008, 2 (9): 1769-1769.

[59] Lu M Y, Tsai C Y, Chen H A, et al. Plasmonic Enhancement of Au Nanoparticle-Embedded Single-Crystalline ZnO Nanowire Dye-Sensitized Solar Cells [J]. Nano Energy, 2016, 20: 264-271.

[60] Tan W K, Ito T, Kawamura G, et al. Controlled Facile Fabrication of Plasmonic Enhanced Au-Decorated ZnO Nanowire Arrays Dye-Sensitized Solar Cells [J]. Materials Today Communication, 2017, 13: 354-358.

[61] Liu Z, Huang J, Han J, et al. $CuInS_2$: A Promising Semiconductor Photo-Absorber Material for Quantum Dot Sensitized Solar Cells [J]. Physical Chemistry Chemical Physics, 2016, 18 (25): 16615-16620.

[62] Zhou C, Geng Y, Chen Q, et al. A Novel PbS/TiO_2 Composite Counter Electrode for CdS Quantum Dot-Sensitized ZnO Nanorods Solar Cells [J]. Materials Letters, 2016, 172: 171-174.

[63] Chen C, Cheng Y, Jin J, et al. CdS/CdSe Quantum Dots and ZnPc Dye Co-Sensitized Solar Cells with Au Nanoparticles/Graphene Oxide as Efficient Modified layer [J]. Journal of Colloid and Interface Science, 2016, 480: 49-56.

[64] Nayeri F D, Akhavanjad E, Ghomanvesiz M, et al. Dye Decorated ZnO-NWs/CdS-NPs Heterostructures for Efficiency Improvement of Quantum Dots Sensitized Solar Cell [J]. Superlattices and Microstructures, 2016, 91: 244-251.

(C)1994-2021 China Academic Journal Electronic Publishing House. All rights reserved. http://www.cnki.net

6.邵艳秋,赵婷婷,付文婷,郑骐朋.氨基改性 SBA-15 介孔材料的制备及对 Pb(Ⅱ)的吸附性能研究[J].硅酸盐通报,2016,35(02):587-592.

第35卷 第2期 硅 酸 盐 通 报 Vol. 35 No. 2
2016年2月 BULLETIN OF THE CHINESE CERAMIC SOCIETY February, 2016

氨基改性 SBA-15 介孔材料的制备及对 Pb(II)的吸附性能研究

邵艳秋[1,2],赵婷婷[1,2],付文婷[3],郑骐朋[2]
(1.牡丹江师范学院化学化工学院,牡丹江 157011;2.黑龙江省新炭基功能与超硬材料重点实验室,牡丹江 157011;3.北京理工大学化学学院,北京 102488)

摘要:采用水热后嫁接的方法,分别制备出氨基、二氨基、三氨基改性的介孔二氧化硅吸附剂 N-SBA-15、2N-SBA-15、3N-SBA-15。采用 X-ray 衍射(XRD)、红外光谱(FT-IR)、N_2 吸附-脱附和扫描电镜(SEM)等方法对材料进行表征。讨论了吸附时间、体系 pH 值等因素对水中 Pb^{2+} 吸附性能的影响。结果表明:在纯硅 SBA-15 上嫁接的氨基越多,改性后材料对水中 Pb^{2+} 的吸附性能越好,当吸附 60 min、体系 pH 值为 5 时,材料对水中 Pb^{2+} 的吸附效率最佳,最大吸附率能达到 95%左右。

关键词:胺基改性;SBA-15;吸附;铅离子
中图分类号:TQ173 **文献标识码**:A **文章编号**:1001-1625(2016)02-0587-06
DOI:10.16552/j.cnki.issn1001-1625.2016.02.051

Preparation of Different Amino-modified SBA-15 and Its Adsorption Property to Pb^{2+}

SHAO Yan-qiu[1,2], *ZHAO Ting-ting*[1,2], *FU Wen-ting*[3], *ZHENG Qi-peng*[2]
(1. College of Chemistry and Chemical Engineering, Mu Danjiang Normal University, Mudanjiang 157011, China;
2. Heilongjiang Province Key Laboratory of New Carbon-Base Functional and Superhard Material, Mudanjiang 157011, China;
3. Department of Chemistry, Beijing Institute of Technology, Beijing 102488, China)

Abstract: The amino-modified SBA-15 (N-SBA-15), diamine-modified (2N-SBA-15) and triamino-modified (3N-SBA-15) were prepared by a hydrothermal grafting method. All mesoporous materials were characterized by X-ray diffraction (XRD), Fourier transform infrared spectroscopy (FT-IR), N_2 adsorption-desorption and SEM. Provide the evidence we need to make a disgussion among how the time and the pH of system influnce the absorption of Pb(II) ions in water. The result is that, modified materials shows a better adsorpting efficiency of Pb(II) ions in water when more amino grafted on the pure silicon SBA-15. When the adsorption is for 60 min, system pH is 5, the adsorption rate of mesoporous materials is the best, maximum adsorption rate can reach about 95%.

Key words: amino-modified; SBA-15; adsorption; Pb(II) ion

1 引 言

随着科学技术和工业化水平的迅速发展,大量有害金属和生活垃圾被排入水体中,对生态环境和人类的健康造成很大的危害。现如今,有效减少水体中重金属含量、净化污水的方法有许多,比如离子交换法、渗透

基金项目:黑龙江省教育厅科学技术研究资助项目(11551530);牡丹江师范学院超硬材料重点实验室开放课题资助项目(201401);牡丹江师范学院校级教改立项重点项目(12-XJJ14027);黑龙江省自然科学学基金项目(E201341)
作者简介:邵艳秋(1969-),女,博士,教授.主要从事多相催化材料方面的研究.

(C)1994-2019 China Academic Journal Electronic Publishing House. All rights reserved. http://www.cnki.net

法、吸附法、电化学法、沉淀法、过滤法等，最为常用的就是吸附法[2,22]，其中吸附剂的选择一般认为是最理想的[3]。活性炭等常用的一些吸附剂存在价格偏高、再生困难等缺点，使吸附剂的使用受限，因此开发新型经济、易于分离的吸附剂成为研究重点[8]。介孔 SBA-15 具有高度有序的六方二维孔道[20]，孔径大小在 5 ~ 30 nm 范围[23]内，可调性能好。但是纯硅 SBA-15 因缺少活性基团，对水中 Pb(II) 吸附特别弱，所以，本文采用后嫁接法在纯硅 SBA-15 上嫁接不同量的氨基活性基团，对材料进行表征，探讨了嫁接前后材料对 Pb^{2+} 的吸附性能。

2 实 验

2.1 nN-SBA-15 的制备

纯硅 SBA-15 参照文献[6]的方法进行制备。分别取 1 g 合成材料加到圆底烧瓶中，在 120 ℃中干燥过夜，加入 30 mL 干燥处理的甲苯，分别加适量的 3-氨丙基三乙氧基硅烷(APTES)、N-3-(三甲氧基硅基)丙基乙二胺[N-3-(Trimethoxysily) propylethylenediamine]、二乙烯三胺基丙基三甲氧基硅烷(Trimethoxysilyl Propyl Diethylenetriami)，搅拌 24 h，过滤，用甲苯、乙醇多次洗涤，分别制备出氨基(N-SBA-15)、二氨基(2N-SBA-15)、三氨基(3N-SBA-15)样品。

机理 1 氨基功能化材料(N-SBA-15)的合成

Schemel Synthesis of amino-modified materials (N-SBA-15)

机理 2 二氨基功能化材料(2N-SBA-15)的合成

Scheme2 Synthesis of diamine-modified materials (2N-SBA-15)

机理 3 三氨基功能化材料(3N-SBA-15)的合成

Scheme3 Synthesis of triamino-modified materials (3N-SBA-15)

2.2 样品的表征

采用日本 D/max-2200/PC 型 X-ray 衍射仪测试材料介孔结构，小角 XRD 的扫描范围为 0.4° ~ 5°，步长为 0.02°。样品的傅立叶变换红外(FT-IR)光谱分析采用 Nicolet360 型光谱仪测定，使用 KBr 压片技术制样。在 3H-2000PS2 型吸附仪上测定样品的比表面和孔体积。

2.3 吸附实验和 Pb^{2+} 的测定方法

称取 50 mg 改性前后介孔材料加到 40 mL 100 mg/L 的 $Pb(NO_3)_2$ 溶液中，用磁力搅拌器搅拌一定时间，取上层清液，用 Z-8000 型原子吸收光谱仪测定残留的 Pb^{2+} 浓度。

3 结果与讨论

3.1 结构分析

图 1 是氨基功能化后材料与纯硅 SBA-15 的 XRD 谱图，制备材料都具有典型有序六方介孔结构[9]。从

(C)1994-2019 China Academic Journal Electronic Publishing House. All rights reserved. http://www.cnki.net

图中能观察到，纯硅 SBA-15 在 0.8° 有强的(100)晶面特征峰，功能化后的三个材料也在 0.8° ~ 0.9° 范围内有较强的特征峰，功能化后的介孔材料晶位向右偏移。随着氨基基团的增多，(100)、(110)和(200)衍射特征峰强度逐渐下降，说明接枝官能团后材料的有序性下降。3N-SBA-15 材料的(110)、(200)衍射峰已经基本观察不到，这是由于 SBA-15 的孔道被大量氨基填充造成的。

图 2 是纯硅 SBA-15、N-SBA-15、2N-SBA-15 和 3N-SBA-15 的红外谱图，可以看出 3442.75 cm^{-1} 周围都有一较宽的吸收峰，属于 Si-OH 的伸缩振动峰，798.37 cm^{-1} 和 1085.39 cm^{-1} 附近为分别对应 Si-O-Si 的对称伸缩振动峰和非对称伸缩振动峰[10]：1633.51 cm^{-1} 为水中-OH 的振动峰；2954.24 cm^{-1} 附近为 C-H 振动峰；1561.84 cm^{-1} 附近出现-NH_2 振动峰，说明是三个材料上都有氨基嫁接到 SBA-15 上。

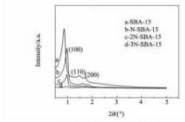

图 1 样品的 XRD 谱图

Fig. 1 XRD patterns of samples

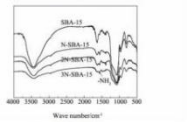

图 2 样品的红外谱图

Fig. 2 IR spectra of samples

改性后 SBA-15 中氨基含量通过酸碱滴定测定。分别称取 0.1g N-SBA-15、2N-SBA-15 或 3N-SBA-15 溶于 20 mL HCl(0.01 mol/L)溶液中，在室温下搅拌过夜，过滤，滤液用 0.01 mol/L NaOH 溶液滴定，滴定后计算氨基含量分别为 0.25 mmol/g、0.82 mmol/g 和 1.26 mmol/g。

图 3 为介孔材料氨基功能化前后氮气吸附-脱附等温线和孔径分布曲线。按照 IUPAC 划分方法，所有曲线都显示出 IV 型等温线和 H1 型滞后环，并且存在明显的毛细孔凝聚现象，是介孔结构[24]。随着嫁接氨基的增加，吸附等温线吸附分支的拐点向低相对压力方向移动的大，这是由于氨基引入的越多，介孔材料的孔道堵塞程度越大所导致的。表 1 给出了嫁接氨基前后 SBA-15 的比表面积等参数，从表中可以看出氨基功能化后的 SBA-4 的比表面积、孔径和孔体积均有所减小，这可能是因为引入的氨基基团占据一定空间，虽然嫁接氨基后 SBA-15 的孔道有一定程度的堵塞，但是由于嫁接的活性基团的增加，材料对水中 Pb^{2+} 的吸附越来越强。

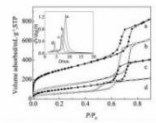

图 3 样品的 N_2 吸附-脱附等温线(a) SBA-15；(b) N-SBA-15；(c) 2N-SBA-15；(d) 3N-SBA-15

Fig. 3 Nitrogen adsorption-desorption isotherms of samples

表 1 介孔材料的结构参数

Tab. 1 Structural and physic-chemical properties of mesoporous material

Sample	Surface area/(m^2/g)	Pore volume/(cm^3/g)	Pore size/(nm)
SBA-15	874.49	1.27	9.42
N-SBA-15	637.55	0.84	7.61
2N-SBA-15	398.72	0.69	6.93
3N-SBA-15	188.47	0.42	3.57

(C)1994-2019 China Academic Journal Electronic Publishing House. All rights reserved. http://www.cnki.net

图 4 分别是 SBA-15、N-SBA-15、2N-SBA-15 和 3N-SBA-15 的 SEM 图片。从图中可以看出纯硅 SBA-15 属于高度有序的介孔材料，嫁接氨基后表面出现细小颗粒，说明有部分氨基嫁接在纯硅 SBA-15 表面上。从(b)和(c)中还可清晰的看到嫁接氨基后材料仍具有有序性，说明 N-SBA-15 和 2N-SBA-15 保持了良好的介孔有序性。材料(d)的有序性变得模糊，说明随着嫁接氨基含量的继续增加，纯硅 SBA-15 的有序性受到了一定的破坏。

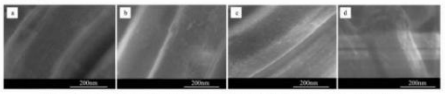

图 4 掺杂不同氨基的 SBA-15 扫描电镜照片(a) SBA-15；(b) N-SBA-15；(c) 2N-SBA-15；(d) 3N-SBA-15

Fig. 4 SEM images of SBA-15 with different-NH_2

3.2 吸附性能研究

3.2.1 pH 值对 Pb^{2+} 吸附的影响

体系 pH 值对介孔材料的吸附性能有较大的影响。温度恒定于 40 ℃，通过滴加 0.01 mol/L HCl 或 NaOH 调节 Pb^{2+} 的 pH 值，实验结果如图 5。结果表明：在其它反应条件一定时，纯硅 SBA-15 对水中 Pb^{2+} 的吸附率特别小，功能化后的 SBA-15 对 Pb^{2+} 的吸附率均有大幅度提升。从图中观察到，嫁接的氨基越多，改性后材料对水中 Pb^{2+} 的吸附效果越好。嫁接氨基后三种材料对水中 Pb^{2+} 的吸附趋势基本相同，当 pH <4 时，材料对水中 Pb^{2+} 的吸附率较小，pH 值达到 5 时吸附趋于平衡，3N-SBA-15 对水中 Pb^{2+} 的吸附率始终高于 2N-SBA-15 和 N-SBA-15，这是由于嫁接的氨基越多，介孔材料中的活性中心越多，对 Pb^{2+} 的吸附率就越高。

3.2.2 吸附时间对 Pb^{2+} 吸附的影响

吸附时间决定反应是否能达到饱和，通过批实验研究了 20 ~ 100 min、50 mg 嫁接氨基前后介孔材料对 100 mg/L $Pb(NO_3)_2$ 溶液中 Pb^{2+} 的吸附效果。从图 6 中能明显看到，当反应时间增大，纯硅 SBA-15 对水中 Pb^{2+} 的吸附没有太大变化，而嫁接氨基后材料对 Pb^{2+} 的吸附率大幅度增加，其中 3N-SBA-15 对水中 Pb^{2+} 的吸附性能最好，0 ~ 40 min 材料对 Pb^{2+} 的吸附率呈现律性增大，继续增加时间反应基本平衡，所以最佳吸附时间为 60 min。

图 5 溶液的 pH 值对吸附效率的影响

Fig. 5 Effect of solution pH value on adsorption efficiency

图 6 吸附时间对吸附率的影响

Fig. 6 Effect of contact time on adsorption efficiency

3.2.3 吸附温度对 Pb^{2+} 吸附的影响

图 7 是吸附温度对水中 Pb^{2+} 吸附的影响，温度对吸附率的影响不是很大，从图中可以看出吸附温度越

(C)1994-2019 China Academic Journal Electronic Publishing House. All rights reserved. http://www.cnki.net

高，材料对水中 Pb^{2+} 吸附率越大，当温度增大到一定程度，吸附率不再增加，吸附达到饱和，所以选择 40 ℃做为反应体系的最佳温度。

3.2.4 吸附动力学研究

吸附速率是研究吸附动力学的重要因素。本文选择了吸附性最好的材料 3N-SBA-15 进行动力学研究，图 8 为不同 Pb^{2+} 初始浓度下，3N-SBA-15 对 Pb^{2+} 的吸附量随时间的变化。当初始浓度增大，材料的吸附速率增大，即在短时间内吸附大量的 Pb^{2+}，原因是溶液的浓度高促使 Pb^{2+} 快速占据吸附剂的吸附位点，直到吸附达到饱和，吸附量不再增加。

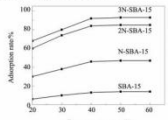

图 7 吸附温度对吸附率的影响

Fig. 7 Effect of contact temperature on adsorption efficiency

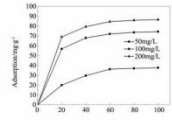

图 8 3N-SBA-15 对 Pb^{2+} 的吸附动力学研究

Fig. 8 Adsorption kinetics of 3N-SBA-15 for Pb^{2+}

4 结 论

本实验采用水热-后嫁接法分别合成了 N-SBA-15、2N-SBA-15 和 3N-SBA-15，嫁接氨基的 SBA-15 对 Pb^{2+} 吸附均有很大程度增加。嫁接氨基越多，改性后材料对 Pb^{2+} 的吸附效果越好，其中 3N-SBA-15 对 Pb^{2+} 吸附率能达到 95% 左右。通过 X-ray 衍射、红外光谱和氮气吸附-脱附等方法对改性前后的材料表征，说明在改性过程中纯硅 SBA-15 结构有一定程度紊乱，由于大量氨基的引入介孔的有序性有所下降，但随着活性基团的引入大大地增加了材料对水中 Pb^{2+} 吸附，说明介孔材料对水中 Pb^{2+} 的吸附靠的不仅仅是简单的物理吸附，而是通过嫁接上的-NH_2 或-NH-与 Pb^{2+} 之间发生络合作用的原因。

嫁接氨基前后材料对 Pb^{2+} 的吸附与反应体系 pH 值和反应时间等因素有关，通过批量实验得出：嫁接氨基后材料对 Pb^{2+} 的吸附很快，60 min 前后反应基本平衡；体系 pH 值从 3 增加到 7，嫁接氨基后的材料对水中 Pb^{2+} 的吸附率不断增大，当 pH 值达到 5 时，材料对 Pb^{2+} 的吸附率基本不变，即反应体系的最佳 pH 值为 5；吸附温度对吸附率的影响不是很大，本文选择的最佳温度为 40 ℃。

参 考 文 献

[1] Chen M S, Zhang C H, Xu J S, et al. Adsorption of Pb(Ⅱ) on three amine functionalized SBA-15 materials [J]. *Guangdong Chemical*, 2014, **41**(16): 40-42.

[2] Zaghouane-Boudiaf H, Boutahala M, Tiar C, et al. Treatment of 2, 4, 5-trichlorophenol by MgAl-SDBS organo-layered double hydroxides: Kinetic and equilibrium studies [J]. *Chemical Engineering Journal*, 2011, **173**(1): 36.

[3] Li B H, Yue Q L, Meng Z F, et al. Thermodynamic study of Cd(Ⅱ) ions adsorbed by amino-modified SBA-15 ordered mesoporous particles [J]. *Acta Scientiae Circumstantiae*, 2011, **31**(6): 1241-1247.

[4] 张春华, 陈满生, 许金生, 等. 多胺基功能化 SBA-15 材料对 Cd(Ⅱ)的吸收 [J]. 过程工程学报, 2014, **14**(4): 677-682.

[5] Bagshaw S A, Prouzet E, Pinnavaia T J. Templating of mesoporous molecular sieves by nonionic polyethylene oxide surfactants [J]. *Science (New York, NY)*, 1995, **269**(5228): 1242.

[6] Trindade F J, Rey J F Q, Breschintb S. Modification of molecular sieves MCM-41 and SBA-15 with covalently grafted pyromellitimide and 1, 4, 5, 8-naphthalenediimide [J]. *Journal of Colloid and Interface Science*, 2012, **368**(1): 34-40.

(C)1994-2019 China Academic Journal Electronic Publishing House. All rights reserved. http://www.cnki.net

7.邵艳秋,芦原萱,付文婷,苏爽月,郑炜.盐对氨基改性 SBA-15 吸附 Pb^{2+}性能的影响研究[J].硅酸盐通报,2016,35(11):3649-3653.

第35卷 第11期 硅 酸 盐 通 报 Vol. 35 No. 11
2016年11月 BULLETIN OF THE CHINESE CERAMIC SOCIETY November, 2016

盐对氨基改性 SBA-15 吸附 Pb^{2+} 性能的影响研究

邵艳秋[1,2],芦原萱[1,2],付文婷[3],苏爽月[1],郑 炜[1]
(1.牡丹江师范学院化学化工学院,牡丹江 157011;2.黑龙江省新炭-基功能与超硬材料重点实验室,牡丹江 157011;
3.北京理工大学化学学院,北京 102488)

摘要:以三嵌段共聚物 P123 作为模板剂,正硅酸乙酯(TEOS)为硅源,3-氨丙基三乙氧基硅烷(APTES)为偶联剂,采用嫁接法制备氨基化 SBA-15-KCl(n),并探究 n_{HCl} 与 n_{KCl} 的比对 Pb^{2+} 吸附效率的影响。采用 X 射线衍射(XRD)、透射电镜(TEM)、红外光谱(FT-IR)和 N_2 吸附-脱附等手段对合成的样品进行表征,通过实验对改性后介孔材料的吸附性能和影响因素进行研究。结果表明:改性后材料对 Pb^{2+} 吸附的最佳吸附时间为 60 min,体系 pH 值为 5,最佳吸附温度为 40 ℃,当 KCl 的加入量达到 0.0474 mol 即 n_{HCl}:n_{KCl} = 3:7 时,样品对 Pb^{2+} 吸附率最佳可在 95% 左右。

关键词:NH_2-SBA-15;KCl;吸附;Pb^{2+}
中图分类号:O643 文献标识码:A 文章编号:1001-1625(2016)11-3649-05
DOI:10.16552/j.cnki.issn1001-1625.2016.11.026

Effect of Salt on Amino-modified SBA-15 and Its Adsorption Property to Pb^{2+}

SHAO Yan-qiu[1,2], *LU Yuan-xuan*[1,2], *FU Wen-ting*[3], *SU Shuang-yue*[1], *ZHENG Wei*[1]
(1. College of Chemistry and Chemical Engineering, Mudanjiang Normal University, Mudanjiang 157011, China;
2. Heilongjiang Province Key Laboratory of New Carbon-Base Functional and Superhard Material, Mudanjiang 157011, China;
3. Department of Chemistry, Beijing Institute of Technology, Beijing 102488, China)

Abstract: Amino-functionalized mesoporous materials SBA-15-KCl (n) were prepared by employing a post-grafting method, in which Pluronic P123 was used as template, tetraethyl orthosilicate (TEOS) was adopted as silicon source and 3-aminopropyltrimethoxy-silane (APTES) was utilized as coupling agent. And the effect of ratio of n_{HCl} to n_{KCl} on the adsorption efficiency for Pb^{2+} was studied. All the materials were characterized by X-ray diffraction (XRD), transmission electron microscope (TEM), Fourier transform infrared spectroscopy (FT-IR) and N_2 adsorption-desorption. What's more, the adsorption properties and influencing factors of modified mesoporous materials were studied. The results show the optimal condition for Pb^{2+}: the adsorption time of the modified materials is 60 min, pH of the system is 5 and the optimal temperature is 40 ℃. When the amount of KCl is 0.0474 mol, which means n_{HCl}:n_{KCl} = 3:7, the samples achieve the maximum adsorption rate, about 95%, for Pb^{2+}.

Key words: NH_2-SBA-15; KCl; adsorption; Pb^{2+}

1 引 言

工业、生活废水中含有一些重金属元素,例如 Pb、Cr、Cu、Hg 等对人体健康有着极大危害,因此当今环

基金项目:牡丹江市科学技术计划项目(Z2016g0001);黑龙江省教育厅科学技术研究资助项目(11551510);牡丹江师范学院超硬材料重点实验室开放课题资助项目(201401);牡丹江师范学院校级教改立项重点项目(12-KJJ4027);黑龙江省自然科学学基金项目(E201341)

作者简介:邵艳秋(1969-),女,博士,教授.主要从事多相催化材料研究.

(C)1994-2019 China Academic Journal Electronic Publishing House. All rights reserved. http://www.cnki.net

境治理工作的重点之一是水中重金属元素的去除。处理含有重金属废水的方法有很多种，其中吸附法是一种最具应用潜力的污水处理方法。吸附法能高效去除废水中重金属离子，可回收[1-4]。氨基改性后的 SBA-15 介孔分子筛对废水中的重金属离子有很好的吸附性[4]。无机盐是一种强电解质，对表面活性剂胶束的形成有着显著的影响，加入适量的盐有助于介孔结构的形成[5-7]。本文采用嫁接法制备氨基化 SBA-15-KCl(n)，并探究 n_{HCl} 与 n_{KCl} 的比对 Pb^{2+} 吸附效率的影响。

2 实 验

2.1 实验试剂

三嵌段聚合物 $EO_{20}PO_{70}EO_{20}$，简称 P123，平均相对分子质量 5800，美国 Aldrich 公司生产；正硅酸乙酯，简称 TEOS，分析纯，广州市中杰化工科技有限公司生产；(3-氨丙基)三乙氧基硅烷，简称 APTES，纯度 > 98%，国药集团化学试剂有限公司生产；甲苯，分析纯，齐齐哈尔轻工学院试剂厂。

2.2 氨基化 SBA-15-KCl(n)的制备

以三嵌段聚合物 $EO_{20}PO_{70}EO_{20}$(P123)为模板剂，正硅酸乙酯(TEOS)为硅源，(3-氨丙基)三乙氧基硅烷(APTES)为有机硅源，具体合成 SBA-15-KCl(n)步骤参照文献[5]，其原料摩尔比为 n(P123)∶n(TEOS)∶n(KCl)∶n(HCl)∶$n(H_2O)$ = 0.017∶1.0∶X(0.66-6.1)∶6.72-X∶150.7-132.12，然后将制备好的样品倒入干燥过的甲苯溶液中，加入适量的(3-氨丙基)三乙氧基硅烷(APTES)，搅拌 24 h，用甲苯、无水乙醇反复抽滤，最后得到氨基嫁接量为 10% 的 SBA-15-KCl(n)。

2.3 样品的表征

采用日本 D/max-2200/PC 型 X-ray 衍射仪(XRD)，小角 XRD 的扫描范围为 0.4° ~ 5°，步长为 0.02°。在 FEI TECNAI F20 透射电镜(TEM)上观测样品的孔结构，加速电压为 200 kV。用 Nicolet360 型红外光谱仪进行傅立叶变换红外(FT-IR)光谱分析，采用 KBr 压片技术制样。在 3H-2000PS2 型吸附仪上测定样品的比表面和孔体积，在 -196 ℃(液氮温度)下进行吸附，N_2 为吸附质。

2.4 吸附实验和 Pb^{2+} 的测定方法

称取 20 mg 制备样品加到 30 mL 100 mg/L 的 $Pb(NO_3)_2$ 溶液中，搅拌特定时间，取上层清夜，用 Hitachi Z-5000 型原子吸收分光光度计测定残留的 Pb^{2+} 浓度。根据起始浓度和残留的浓度确定样品对 Pb^{2+} 的吸附效果。样品对 Pb^{2+} 的吸附效率计算方法如下：

$$r = \frac{c_0 - c_e}{c_0} \times 100\%$$

式中：r 为样品对 Pb^{2+} 的吸附效率，%；c_0 为 Pb^{2+} 的起始浓度，mg/L；c_e 为 Pb^{2+} 的残留浓度，mg/L。

3 结果与讨论

3.1 结构分析

图 1 为样品的 XRD 图，从图中可以看出，样品为典型的六方介孔结构[8]，在 0.8° ~ 0.9° 范围内存在较强的主要特征峰。与 NH_2-SBA-15 相比，随着 KCl 物质的量增加主要特征峰(100)峰和特征峰(110)、(200)衍射峰都有增强，表明孔道规整度优于 NH_2-SBA-15。当 KCl 的加入量达到 0.0542 mol(n_{HCl}∶n_{KCl} = 2∶8)时，主峰与特征峰明显减弱。

图 2 为样品的 FT-IR 谱图。798 cm^{-1} 和 1088 cm^{-1} 附近分别对应 Si-O-Si 的对称伸缩振动和非对称伸缩振动峰[9]；1631 cm^{-1} 和 3433 cm^{-1} 附近对应 Si-OH 振动峰[10]；2956 cm^{-1} 附近出现很小的吸收峰，该峰归属于 C-H 振动峰[11]；1560 cm^{-1} 附近出现吸收峰，该吸收峰属于 $-NH_2$ 振动峰[12]，这表明改性后的样品中已成功引入了氨基官能团。

图 3 为样品的 TEM 照片，图 3a 和图 3c 是分别从与 NH_2-SBA-15-KCl(0.0474 mol)样品介孔孔道相平行的方向和与介孔孔道相垂直的方向拍摄的，b 和 d 分别从与 NH_2-SBA-15-KCl(0.0542 mol)样品介孔孔道相平行的方向和与介孔孔道相垂直的方向拍摄的，说明两种材料在合成过程中仍然保持了纯硅 SBA-15 的有序介孔结构(图 3a、c 和图 3b、d)。从 TEM 看到介孔材料的孔径约为 5 ~ 7 nm 左右，这与氮气吸附-脱附等温线以及对应的孔分布基本相一致。从 TEM 可以看到，当 KCl 添加量增加时，材料有序性有所下降，但依然保持高度有序的六方结构。

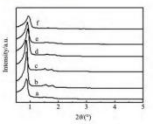

图 1 样品 XRD 图 (a) NH_2-SBA-15；(b) NH_2-SBA-15-KCl(0.0134 mol)；(c) NH_2-SBA-15-KCl(0.0270 mol)；(d) NH_2-SBA-15-KCl(0.0406 mol)；(e) NH_2-SBA-15-KCl(0.0474 mol)；(f) NH_2-SBA-15-KCl(0.0542 mol)

Fig. 1 XRD patterns of samples

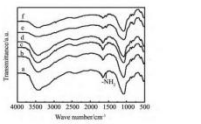

图 2 样品红外图(a) NH_2-SBA-15；(b) NH_2-SBA-15-KCl(0.0134 mol)；(c) NH_2-SBA-15-KCl(0.0270 mol)；(d) NH_2-SBA-15-KCl(0.0406 mol)；(e) NH_2-SBA-15-KCl(0.0474 mol)；(f) NH_2-SBA-15-KCl(0.0542 mol)

Fig. 2 FT-IR spectra of samples

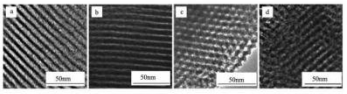

图 3 样品的 TEM 图(a、c) NH_2-SBA-15-KCl(0.0474 mol)；(b、d) NH_2-SBA-15-KCl(0.0542 mol)

Fig. 3 TEM images of samples

由图 4 可知，样品的 N_2 吸附-脱附等温曲线显示出 IV 型等温线和明显的 H1 滞后环，并且存在明显的毛细孔凝聚现象，表明样品为介孔结构，加入 KCl 后，滞后环向低压方向移动，这可能由于 KCl 的加入提高了氨基的嫁接率，介孔材料的孔道堵塞所致。

由表 1 可知，改性后的介孔分子筛其表面积、孔体积、孔径均减小，这可能是因为引入的氨基占有一定空间的结果。当 KCl 的加入量达到 0.0474 mol，即 n_{HCl}∶n_{KCl} = 3∶7 时，表面积与孔体积变化最大，这可能是当 n_{HCl}∶n_{KCl} = 3∶7 时，此时二者为最佳配比，形成的孔道规整度较高，从而提高了氨基的嫁接率，并且通过对样品的氨基含量分析可知，n_{HCl}∶n_{KCl} = 3∶7 时的氨基含量最高为 1.15 mmol·g^{-1}。

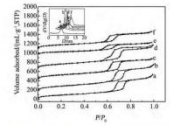

图 4 样品 N_2 吸附-脱附等温线(a) NH_2-SBA-15；(b) NH_2-SBA-15-KCl(0.0134 mol)；(c) NH_2-SBA-15-KCl(0.0270 mol)；(d) NH_2-SBA-15-KCl(0.0406 mol)；(e) NH_2-SBA-15-KCl(0.0474 mol)；(f) NH_2-SBA-15-KCl(0.0542 mol)

Fig. 4 Nitrogen adsorption-desorption isotherms of samples

(C)1994-2022 China Academic Journal Electronic Publishing House. All rights reserved. http://www.cnki.net

表 1 样品的孔结构参数及氨基含量分析

Tab. 1 Structural, physic-chemical properties and amino content analysis of samples

样品	n_{HCl}∶n_{KCl}	比表面/(m^2·g^{-1})	孔体积/(cm^3·g^{-1})	孔径/nm	氨基含量/(mmol·g^{-1})
NH_2-SBA-15	~	637.55	0.84	7.61	0.45
NH_2-SBA-15-KCl(0.0134 mol)	8∶2	442.30	0.84	5.40	0.65
NH_2-SBA-15-KCl(0.0270 mol)	6∶4	409.06	0.80	5.56	0.75
NH_2-SBA-15-KCl(0.0406 mol)	4∶6	378.94	0.88	5.43	1.03
NH_2-SBA-15-KCl(0.0474 mol)	3∶7	227.58	0.47	5.26	1.15
NH_2-SBA-15-KCl(0.0542 mol)	2∶8	317.16	0.66	5.43	0.93

3.2 吸附性能的研究

3.2.1 pH 值对 Pb^{2+} 吸附的影响

图 5 中 a ~ f 分别为改性后样品吸附水中 Pb^{2+} 的吸附率随 pH 值的变化曲线，将温度恒定于 40 ℃，通过滴加 0.01 mol/L HCl 或 NaOH 来调节 Pb^{2+} 的 pH 值，由图可知：NH_2-SBA-15 对水中 Pb^{2+} 的吸附率偏低，而氨基化 SBA-15-KCl(n)对 Pb^{2+} 的吸附率均有大幅度提升。当 pH < 4 时，样品对水中 Pb^{2+} 的吸附率较低，pH 值达到 5 时吸附趋于平衡，e 曲线对水中 Pb^{2+} 的吸附率始终最高，这一结果与前面的表征结果一致。

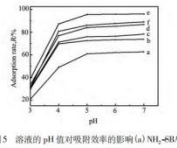

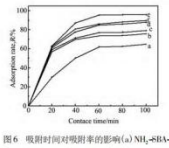

图 5 溶液的 pH 值对吸附效率的影响(a) NH_2-SBA-15；(b) NH_2-SBA-15-KCl(0.0134 mol)；(c) NH_2-SBA-15-KCl(0.0270 mol)；(d) NH_2-SBA-15-KCl(0.0406 mol)；(e) NH_2-SBA-15-KCl(0.0474 mol)；(f) NH_2-SBA-15-KCl(0.0542 mol)

Fig. 5 Effect of solution pH on adsorption efficiency

图 6 吸附时间对吸附率的影响(a) NH_2-SBA-15；(b) NH_2-SBA-15-KCl(0.0134 mol)；(c) NH_2-SBA-15-KCl(0.0270 mol)；(d) NH_2-SBA-15-KCl(0.0406 mol)；(e) NH_2-SBA-15-KCl(0.0474 mol)；(f) NH_2-SBA-15-KCl(0.0542 mol)

Fig. 6 Effect of contact time on adsorption efficiency

3.2.2 吸附时间对 Pb^{2+} 吸附的影响

图 6 中 a ~ f 分别为改性后样品吸附水中 Pb^{2+} 的吸附率随时间的变化曲线，由图可知：氨基化 SBA-15-KCl(n)对水中 Pb^{2+} 的吸附率与 NH_2-SBA-15 相比，吸附率均有所提高，当 KCl 的加入量达到 0.0474 mol，即 n_{HCl}∶n_{KCl} = 3∶7 时，此时的吸附效果最好，最高为 96.06%。0 ~ 60 min 样品对水中 Pb^{2+} 吸附率呈规律性增大，继续增加吸附时间反应趋于平衡，所以最佳吸附时间为 60 min。

3.2.3 吸附温度对 Pb^{2+} 吸附的影响

图 7 中 a ~ f 分别为改性后样品吸附水中 Pb^{2+} 的吸附率随温度的变化曲线，由图可知：氨基化 SBA-15-KCl(n)对水中 Pb^{2+} 的吸附率与 NH_2-SBA-15 相比，吸附率均有所提高，KCl 的加入量达到 0.0474 mol，即

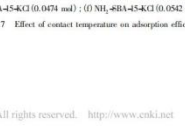

图 7 吸附温度对吸附率的影响(a) NH_2-SBA-15；(b) NH_2-SBA-15-KCl(0.0134 mol)；(c) NH_2-SBA-15-KCl(0.0270 mol)；(d) NH_2-SBA-15-KCl(0.0406 mol)；(e) NH_2-SBA-15-KCl(0.0474 mol)；(f) NH_2-SBA-15-KCl(0.0542 mol)

Fig. 7 Effect of contact temperature on adsorption efficiency

(C)1994-2022 China Academic Journal Electronic Publishing House. All rights reserved. http://www.cnki.net

n_{HCl}∶n_{KCl} = 3∶7 时，此时的吸附效果最好，最高为 95.94%。当吸附温度接近 40 ℃时，样品对水中 Pb^{2+} 的吸附基本达到饱和状态，继续升高温度，吸附率基本没有什么变化，所以选择 40 ℃做为吸附反应的最佳温度。

4 结 论

采用后嫁接法制备氨基化 SBA-15-KCl(n)，样品的结构没有被破坏，仍保持良好的介孔有序性。在吸附实验中，氨基化 SBA-15-KCl(n)介孔材料对 Pb^{2+} 的吸附率随时间的增加而增大，当吸附反应进行到 60 min 时，吸附基本趋于平衡，所以吸附反应的最佳吸附时间为 60 min；体系的 pH 值从 3 至 7，氨基化 SBA-15-KCl(n)介孔材料对水中 Pb^{2+} 的吸附率增大，当体系的 pH 值为 5 时，样品的吸附率基本保持不变，故体系的最佳 pH 值为 5；随着吸附温度的升高，氨基化 SBA-15-KCl(n)对水中 Pb^{2+} 吸附率增大，当吸附温度达到 40 ℃时，吸附反应趋于平衡，所以吸附反应的最佳温度为 40 ℃；当 KCl 的加入量为 0.0474 mol，即 n_{HCl}∶n_{KCl} = 3∶7 时，氨基化 SBA-15-KCl 对 Pb^{2+} 吸附率最高达到 95% 左右。

参 考 文 献

[1] 马玉芹. 功能化 SBA-15 纳米分子筛去除水中污染物的性能研究[D]. 长春：东北师范大学，2012.

[2] 王俊宏，刘军海，葛红光，等. SBA-15 的氨基化及对水中重金属铅(II)的吸附研究[J]. 科学技术与工程，2015，15(3)：170-173.

[3] 张春华，陈满生，许金生，等. 多胺基功能化 SBA-15 材料对 Cd(II)的吸附[J]. 过程工程学报，2014，14(4)：677-682.

[4] 赵婷婷，卢原雪，邵艳秋. NH_2-SBA-15 的制备及其对水中铅离子的吸附[J]. 牡丹江师范学院学报，2016，1：42-44.

[5] 赵会玲，赵超群，宋江闯，等. 离子对 SBA-15 形貌与孔道结构的影响[J]. 华东理工大学学报，2014，40(5)：59-64.

[6] Chen S Y, Cheng S. Acid-free synthesis of mesoporous silica using triblock copolymer as template with the aid of salt and alcohol[J]. *Chemistry of Materials*, 2007, **19**(12): 3041-3051.

[7] Newalkar B L, Komarneni S. Control over microporosity of ordered microporous-mesoporous silica SBA-15 framework under microwave-hydrothermal conditions: Effect of salt addition[J]. *Chemistry of Materials*, 2001, **13**(12): 4573-4579.

[8] 吴淑杰，黄家辉，吴建好，等. Al-HBA-15 介孔分子筛的合成、表征及其在苯酚叔丁基化反应中的催化性能[J]. 催化学报，2006，**27**(1)：9-14.

[9] Qiang G, Xu W, Yao X, et al. Amino acid adsorption on mesoporous materials: influence of types of amino acids, modification of mesoporous materials, and solution conditions[J]. *Journal of Physical Chemistry B*, 2008, **112**(7): 2261-2267.

[10] Wu M M, Lin G, Chen D H, et al. Sol-hydrothermal synthesis and hydrothermally structural evolution of nanocrystal titanium dioxide[J]. *Chem. Mater.*, 2002, **14**(5): 1974-1980.

[11] 徐应明，李军幸，戴晓华，等. 介孔分子筛表面功能膜的制备及对水体中铅污染的去除作用[J]. 应用化学，2002，**19**(10)：941-945.

[12] Nguyen T P B, Lee J W, Shim W G, et al. Synthesis of functionalized SBA-15 with ordered large pore size and its adsorption properties of BSA[J]. *Microp. Mesop. Mater.*, 2008, **110**(2-3): 560-569.

(C)1994-2022 China Academic Journal Electronic Publishing House. All rights reserved. http://www.cnki.net

蔡雪发表科研论文目录（共 **10** 篇）

1.Yang W, Jiang R, Liu C, et al. Triptycene-Based Porous Chalcogen-Bonded Organic Frameworks[J]. Crystal Growth & Design, 2021, 21(11): 6497-6503.

2.Cai X, Ma Y, Zhou Q, et al. Synergistic effects of phases in the selective oxidation of isobutane over supported $(NH_4)_3HPMo_{11}VO_{40}$ catalysts[J]. Reaction Kinetics, Mechanisms and Catalysis, 2021, 133(1): 293-308.

3.Wei C, Lu G, Guo C, et al. Ethylthio-substituted sandwich phthalocyaninato europium (III) semiconductors for sensing NO_2 and NH_3: Effect of the extended π-conjugate systems on tuning the conductivity and sensing behavior[J]. Organic Electronics, 2021, 93: 106151.

4.Cai X, Zhou Q, Ma Y, et al. Selective Removal of CO in Hydrocarbons-Rich Industrial Off-gases over $CuO\text{-}Ce_xZr_{1-x}O_2$ Catalysts [J]. Catalysis Surveys from Asia, 2021, 25(1): 68-75.

5.Cai X, Wei C, Dong J, et al. Dimeric phthalocyanine-involved double-decker complex-based electrochemical sensor for simultaneous detection of acetaminophen and ascorbic acid[J]. Journal of Materials Science: Materials in Electronics, 2019, 30(3): 1976-1983.

6.Cai X, Ning H. Crystal structure of di-μ-acetato-diacetatobis (μ-6, 6′-dimethoxy-2,2′-{[(propane-1,3-diylbis (azanylylidene)] bis (methanylylidene)} diphenolato) tetrazinc[J]. Acta Crystallographica Section E: Crystallographic Communications, 2015, 71(12): 217-218.

7.姜力,周启,陈玉锋,蔡雪.5,15-二(二茂铁基)-卟啉酞菁钇的结构和振动光谱的密度泛函理论研究[J].原子与分子物理学报,2021,38(03):47-51.

8.孙守鹏,魏闯宇,宁桧,蔡雪.全波谱太能材料氟代酞菁锌分子 $ZnPc(C_{24}F_{48})$ 的研究[J].牡丹江大学学报,2018,27(06):107-109.

9.宁桧,孙守鹏,蔡雪.轴向取代卟啉锌结构和光谱性质的研究[J].牡丹江师范学院学报(自然科学版),2017(01):39-42

10.李梓萌,蔡雪.咔唑类取代酞菁锌染料敏化性能研究[J].牡丹江师范学院学报(自然科学版),2016(01):44-46.

1.Yang W, Jiang R, Liu C, et al. Triptycene-Based Porous Chalcogen-Bonded Organic Frameworks[J]. Crystal Growth & Design, 2021, 21(11): 6497-6503.

CRYSTAL GROWTH & DESIGN

pubs.acs.org/crystal Article

Triptycene-Based Porous Chalcogen-Bonded Organic Frameworks

Wei Yang,* Rong Jiang, Chao Liu, Baoqiu Yu, Xue Cai,* and Hailong Wang

Cite This: *Cryst. Growth Des.* 2021, 21, 6497−6503 Read Online

ACCESS | Metrics & More | Article Recommendations | Supporting Information

ABSTRACT: Two chalcogen-bonded organic frameworks (denoted as CBOFs), CBOF-1 and CBOF-2, have been constructed by the self-assembly of a custom-made triptycenetris(2,1,3-benzoselendiazole) (TTB) as an organic building block. As revealed by the results of single crystal X-ray diffraction analysis, the combination of chalcogen bonding and Se···π interactions was conductive to the structural porosity of the obtained two compounds. In particular, CBOF-1 exhibited a 3D 4-connected **lvt** topological framework with TTB simplified as the 4-connected node. The open pore channels of CBOF-1 possessed a pore size of 4.2 Å, of which the theoretical accessible pore volume occupied 35.6% of the total volume. Structural porosity of CBOF-2 was filled by tetrahydrofuran molecules, and the accessible volume percentage was calculated for 29.5%. Due to the flexible structure, degassed CBOF-1 displayed permanent porosity using carbon dioxide as an absorbate at 196 K. In the present study, a new kind of porous organic framework with permanent porosity has been revealed.

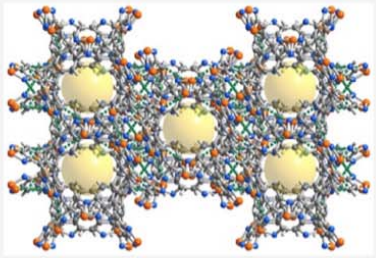

Downloaded via UNIV SCIENCE AND TECHNOLOGY BEIJING on December 3, 2021 at 01:20:24 (UTC).
See https://pubs.acs.org/sharingguidelines for options on how to legitimately share published articles.

INTRODUCTION

High order porous materials possess intriguing applications in the diverse realms such as gas storage, molecule separation, guest recognition, and heterogeneous catalysis, and so on.[1−5] Porous molecule-based crystalline materials such as metal−organic frameworks (MOFs)[6−9] and covalent organic frameworks (COFs)[10−16] are able to achieve the open functional voids with control of the size, shape, and uniformity as well as precise structural design from the atomic and molecular perspective. Besides polymeric MOFs and COFs via coordination and covalent interaction, respectively, hydrogen-bonded organic frameworks (HOFs)[17−24] and porous organic cages (POCs)[21−32] have been obtained by the self-assembly of discrete molecule modules with intrinsic or extrinsic voids through the weak hydrogen-bonding interaction and/or van der Waals force. Such reticular materials have been extensively fabricated and investigated in recent decades and have been found to be complementary to each other. Inspired by the development of diverse frameworks, exploring new and alternative approaches to construct porous molecule crystalline materials has attracted intense interest.

The anisotropic electron density distribution on the surface of atoms is an intrinsic characteristic of molecules, leading to an electron density that alternates between high and low around atoms. Thus, to stabilize the supramolecular assembly, the interactions between the negative and positive atoms/regions from different molecules are formed. Halogen bonding is generated by halogen atoms interacting with nucleophiles from elements of groups 13−16 in the periodic table, representing a kind of attractive interaction for the organization of molecular functional materials.[33,34] As pioneered by Prof. Barbour from discrete organic building blocks, such interaction has been used to produce porous halogen-bonded organic frameworks.[35−38] Alternatively, close chalcogen bonding contact has been found to occur between group 16 elements and nucleophiles.[39] In general, all sulfur, selenium, and tellurium atoms are able to form chalcogen bonds, and the bond strength is increased by following the increased polarizability of the chalcogen elements. The directionalities of chalcogen bonds are particularly similar to that of halogen bonds in terms of the crystal engineering thereof to a certain extent, enabling similar self-assembly behaviors.[40,41] As a result, prior research on halogen-bonded organic frameworks has provided inspiration for the present study, and for exploring the possibility of porous chalcogen-bonded organic frameworks. Notably, to the present knowledge, there are few examples of chalcogen-bonded organic assembly[42] and molecule capsules[43−46] with guest molecules included in the voids, and there has been no report on such materials with permanent porosity after solvent removal of solvent. Thus, the aforementioned direction of the corresponding research is of considerable significance.

In the present study, a new triptycene-containing organic linker, triptycenetris(2,1,3-benzoselendiazole) (TTB), was conceived and prepared, as shown in Scheme 1a. The

Received: August 17, 2021
Revised: October 3, 2021
Published: October 19, 2021

ACS Publications © 2021 American Chemical Society

https://doi.org/10.1021/acs.cgd.1c00942
Cryst. Growth Des. 2021, 21, 6497−6503

Scheme 1. (a) Synthesis and Molecular Structure of Triptycene-Based Organic Linker of TTB for the Construction of Porous Supramolecular Frameworks. (b) Formation of Chalcogen-Bonded Ribbon-like Structure by 2,1,3-Benzoselendiazole

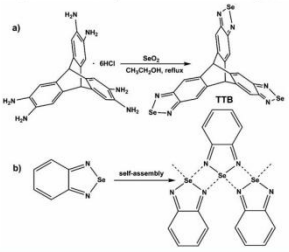

crystallization of TTB in different conditions resulted in the generation of two porous supramolecular frameworks, CBOF-1 and CBOF-2. The results of single crystal X-ray diffraction analysis revealed that CBOF-1 was formed by TTB building blocks through chalcogen bonding and Se···π interactions, thereby allowing for a structure containing open interconnecting channels with the size of 5.8 Å. CBOF-2 had a porous architecture containing 1D channels with a smaller diameter of 5.2 Å stabilized by chalcogen bonding and Se···π interactions. A hysteretic adsorption of CO_2 adsorbate at 196 K was monitored, indicating the flexible structure dynamics for the activated phase of CBOF-1. By using chalcogen bonding to construct porous supramolecular crystals with permanent porosity, a preliminary development has been presented in the present study.

EXPERIMENTAL SECTION

Synthesis of TTB. A mixture of hexaammonium triptycene hexachloride[47] (563.2 mg, 1.0 mmol) and 6 equiv of SeO_2 (666.0 mg, 6.0 mmol), and ethanol (40 mL) were added in a 100 mL flask. The mixture was refluxed for 12 h under nitrogen protection (Scheme 1). After cooling to room temperature, TTB was obtained through vacuum filtration and washed using 20 mL of ethanol. The product was dried at room temperature in a yield of 63%. ^{1}H NMR (400 MHz, $CDCl_3$): δ (ppm) 7.90 (s, 6H), 5.68 (s, 2H); ^{13}C NMR (100 MHz, $CDCl_3$): δ (ppm) 159.61, 141.85, 117.62, 52.29. Elemental analysis of TTB calcd. (%) for $C_{20}H_6N_6Se_3$: C 42.20, H 1.42, N 14.76; found: C 42.24, H 1.39, N 15.01. IR/cm^{-1} (KBr): 1640 (m) 1594 (s), 1439(m), 1286 (s), 881 (m), 759 (s). Single crystals of CBOF-1 and CBOF-2 were obtained by diffusing n-hexane into the chloroform and tetrahydrofuran solution, respectively, containing TTB (30 mg) at room temperature.

Crystallographic Measurement. An Oxford Diffraction Xcalibur, Eos, Gemini diffractometer with a Mo *Kα* radiation source (λ = 0.7107 Å) and Cu *Kα* radiation source (λ = 1.54178 Å) was used to collect crystallographic data for CBOF-1 and CBOF-2, respectively, at 150 K. The resolution and refinement of crystal structures of CBOF-1 and CBOF-2 relied on the SHELXS-2014 program.[48] The "SQUEEZE" command removed the disordered solvent molecules filled in the porosities of CBOF-1.[49] Table 1 summaries the parameters of unit cells and final refinement, and Table 2 exhibits the weak interaction in the supramolecular structures of CBOF-1 and CBOF-2. CCDC 2102442 and 2102443 for CBOF-1 and CBOF-2, respectively, which contain the supplementary crystallographic data, have free access from the Cambridge Crystallographic Data Centre *via* www.ccdc.cam.ac.uk/data_request/cif.

Table 1. Crystallographic and Refinement Parameters for Chalcogen-Bonded CBOF-1 and CBOF-1

crystal data	CBOF-1	CBOF-2
system	tetragonal	monoclinic
space group	$I\bar{4}2d$	$C2/c$
molecular formula[a]	$C_{20}H_6N_6Se_3$	$C_{21}H_{10}N_6O_{1.25}Se_3$
formula weight[a]	569.20	659.33
a/Å	16.5175(10)	23.3021(8)
b/Å	16.5175(10)	9.3111(3)
c/Å	18.5371(2)	44.7307(17)
α/deg	90	90
β/deg	90	96.949(3)
γ/deg	90	90
volume/Å^3	5057.44(8)	9833.8(6)
Z	8	16
density/g/cm^3	1.495	1.818
solvent-accessible[b] void space/%	35.8	29.5
theoretical pore volume/cm^3/g	0.24[a]	0.19[a]
refinement parameters	R_1 = 0.0481[c] wR_2 = 0.1556[c]	R_1 = 0.0724[d] wR_2 = 0.1672[c]
CCDC No.	2102442	2102443

[a]Calculation based on the crystal structures using PLATON software. [b]$R_1 = \sum||F_o| - |F_c||/\sum|F_o|$. [c]$wR_2 = [\sum w(F_o^2 - F_c^2)^2/\sum w(F_o^2)^2]^{1/2}$.

Table 2. Chalcogen-Bonding Interactions in CBOF-1 and CBOF-2

Se···X	distance (Å)	symmetric code
1		
Se2···N1#1	3.323	$1.5 - y, 1 - x, -0.25 + z$
Se2···N1#2	3.323	$1.5 - y, 0.5 + x, 1.5 - z$
N1···Se#3	3.323	$-0.5 + y, 1.5 - x, 1.5 - z$
N1···Se#4	3.323	$1 - y, -x, 1 - z$
2		
Se1···N7	2.934	
N2···Se4	3.270	
Se1···N10#1	3.237	$1 - x, y, 1.5 - z$
Se2···O2#2	3.357	$x, 1 + y, z$
Se2···N6#3	3.356	$-0.5 + x, 0.5 + y, z$
Se3···O1#2	3.676	$x, 1 + y, z$
N5···Se6#4	3.733	$x, -y, -0.5 + z$
N6···Se2#5	3.356	$0.5 + x, -0.5 + y, z$
Se4···N7#6	3.763	$1.5 - x, 0.5 + y, 1.5 - z$
Se6···N5#4	3.733	$x, -y, -0.5 + z$
N10···Se1#1	3.237	$1 - x, y, 1.5 - z$
Se5···N7#7	3.644	$-0.5 + x, -0.5 + y, z$

RESULTS AND DISCUSSIONS

Design Principle and Synthesis of TTB. In order to construct a new kind of porous supramolecular framework through the self-assembly of organic modules, the Cambridge Structural Database for chalcogen-bonded crystal structures was explored. The formation of chalcogen bonds is preferred by 2,1,3-benzoselendiazole derivatives.[50] The possible ribbon-like connection is similar to that derived from 4,5-diiodobutitied benzimidazolone analogues through hydrogen-bonding.[51] Inspired by the prominent triptycene-based HOF with a considerably high specific surface area of 3020 m^2 g^{-1} pioneered by Prof. Mastalerz,[11] a new organic molecule was designed and prepared by incorporating the 2,1,3-benzoselendiazole unit into a rigid D_{3h}-symmetric triptycene structure. The reaction between hexaammonium triptycene hexachloride and selenium oxide led to TTB being used as a building block, as shown in Figures S1 and S2 (Supporting Information). The TTB molecule was optimized with the B3lyp 6-31g* basis set.[52−55] The surface electrostatic potential distribution map was obtained by using Multiwfn software[56] and VMD processing,[57] as presented in Figure S3 (Supporting Information). The different colors on the molecular electrostatic potential map represent the different electrostatic potentials of different regions. The surrounding nitrogen atoms exhibited a blue color, indicating negative electronegativity. Contrastingly, the surrounding selenium atoms displayed a red color, implying positive electronegativity. Such results suggest that Se atoms prefer to interact with electrophiles. The chalcogen bond between selenium and nitrogen atoms was expected to direct TTB into porous supramolecular frameworks. The crystallization of TTB in different conditions led to the formation of two compounds, CBOF-1 and CBOF-2.

Crystal Structures of 1 and 2. As revealed by the results of single crystal X-ray diffraction analysis in Figures 1 and 2, the two newly obtained supramolecular compounds, CBOF-1 and CBOF-2, had porous structures. CBOF-1 comes from the tetragonal system with $I\bar{4}2d$, as shown in Table 1, which also shows that the unit cell of CBOF-1 contained eight TTB molecules. Each TTB molecule was connected to the neighboring four modules through chalcogen-bonding interactions, as revealed in Figure 1a and Table 2. The distance of Se···N was 3.323 Å, which is in the normal region of the Se···N length.[58] The supramolecular moieties were further extended to a 3D supramolecular structure. TTB was approximately simplified as a 4-connected node, allowing for a $\{4^1\cdot8^2\}$ lvt net

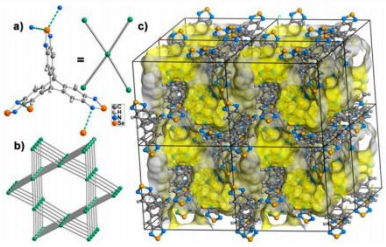

Figure 1. Crystal structures of CBOF-1 displaying (a) a TTB molecule (regarded as four-connected node) and corresponding weak connection with adjacent building blocks. (b) A simplified 4-connected topology linked through chalcogen bonding interactions. (c) A chalcogen-bonded structure showing the 3D channel pore surfaces highlighted as yellow/gray (inner/outer).

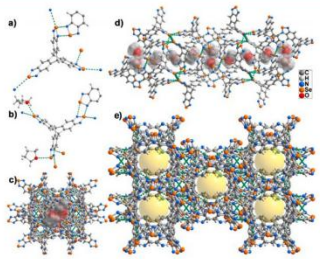

Figure 2. Crystal structures of CBOF-2 exhibiting (a, b) a TTB molecule with corresponding weak connection to adjacent building blocks. (c, d) A supramolecular tubular structure containing THF molecules in top and side view, respectively. (e) A chalcogen-bonded structure showing the 1D channels.

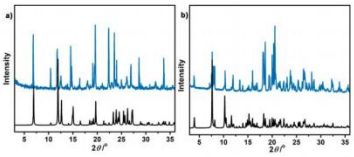

Figure 3. Comparison in powder X-ray diffraction patterns for as-synthesized (cyan) and simulated (black) CBOF-1 (a) and CBOF-2 (b), respectively.

topology (Figure 1b). Additionally, the neighbor TTB molecules were further linked by Se···π interactions to stabilize the porous structure, as shown in Figures 1c and S4 (Supporting Information). The porous channels interconnected with a size of 4.2 Å. The void accounted for 35.8% of the total volume, corresponding to the pore volume density of 0.24 cm^3 g^{-1}.

The diffusion of hexane into a THF solution of TTB produced CBOF-2, which originated from the monoclinic system with the $C2/c$ space group. There are two kinds of crystallographically dependent TTB molecules (Figure 2a,b). Both kinds of TTB linked with the other five organic building blocks *via* chalcogen-bonding interactions, with the Se···N length in the range of 2.934−3.733 Å. However, only one kind of TTB connected two THF molecules through Se···O interactions. Chalcogen bonds directed the formation of the porous tubular structure of CBOF-2 with the smallest size of 3.4 Å, and THF molecules were filled in the porosities of this compound (Figure 2c,d). Se···π interactions were also observed in CBOF-2, as presented in Figure S5 (Supporting Information). The tubular subunits were further assembled through chalcogen-bonding interactions, resulting in a 3D porous supramolecular structure shown in Figure 2e. Compared with CBOF-1, voids accounted for only 29.8% of the total pore volume of CBOF-2, and the pore volume density was 0.19 cm^3 g^{-1}.[59] The bulk materials for CBOF-1 and CBOF-2 were verified through a power X-ray diffractometer. The consistent powder X-ray diffraction (PXRD) patterns between the experiments and simulations for CBOF-1 and CBOF-2 illustrate the good purity thereof (Figure 3).

The thermal stability of these two compounds was determined, and the curves of temperature-dependent weigh

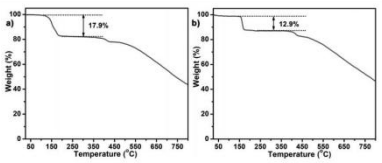

Figure 4. Thermogravimetric analysis curves of CBOF-1 (a) and CBOF-2 (b).

loss are shown in Figure 4. The solvent molecules filled in the porosities of CBOF-1 started to lose from ca. 105 to 195 °C, leading to 17.9% weight loss (Figure 4a). The TTB building block was decomposed at ca. 350 °C. Regarding CBOF-2, solvent molecules accounted for 12.9% of the total weight and escaped in the temperature region of 155−185 °C (Figure 4b). The higher temperature began to remove the solvent molecules in CBOF-1 than CBOF-2, which indicates the stronger solvent-framework interaction in the former compound. After degassing at room temperature, there was an obvious change observed in terms of the PXRD patterns of the as-synthesized sample and the activated sample for CBOF-1 (Figure S6, Supporting Information). Additionally, the crystallinity of activated CBOF-1 was significantly deteriorated. However, CBOF-1 exhibited the hysteretic CO_2 sorption behavior at 196 K with the uptake of 72 cm^3 g^{-1} at 760 mmHg (Figure 5). The profile indicates the flexible structure of

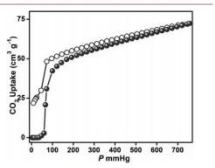

Figure 5. CO_2 sorption of CBOF-1 at 196 K.

CBOF-1. For CBOF-2, the sample was still crystalline after degassing at 150 °C according to the PXRD pattern (Figure S7, Supporting Information). Despite remaining crystalline, there was no gas sorption observed, even for the CO_2 adsorbate at 196 K, which could be attributed to the stable solvent molecules included in the porosity of CBOF-2.

CONCLUSIONS

In summary, two porous supramolecular frameworks have been successfully prepared from a triptycene derivative via chalcogen bonding and Se···π interactions. The crystal structures have been analyzed in detail. One compound exhibited a hysteretic adsorption of carbon dioxide at 196 K, indicating the presence of a dynamic activated framework. Such results show not only the ability of chalcogen bonding in producing porous molecule crystals but also the permanent porosity. The present study can provide a benchmark for the construction of new porous supramolecular frameworks with diverse applications.

ASSOCIATED CONTENT

Supporting Information

The Supporting Information is available free of charge at https://pubs.acs.org/doi/10.1021/acs.cgd.1c00942.

NMR spectra of TTB, check-cif, and powder XRD patterns of activated CBOF-1 and CBOF-2 (PDF)

Accession Codes

CCDC 2102442 and 2102443 contain the supplementary crystallographic data for this paper. These data can be obtained free of charge via www.ccdc.cam.ac.uk/data_request/cif, or by emailing data_request@ccdc.cam.ac.uk, or by contacting The Cambridge Crystallographic Data Centre, 12 Union Road, Cambridge CB2 1EZ, UK; fax: +44 1223 336033.

AUTHOR INFORMATION

Corresponding Authors

Wei Yang − *Beijing Key Laboratory for Science and Application of Functional Molecular and Crystalline Materials, Department of Chemistry and Chemical Engineering, School of Chemistry and Biological Engineering, University of Science and Technology Beijing, Beijing 100083, China;* orcid.org/0000-0001-5854-7568; Email: yangwei@ustb.edu.cn

Xue Cai − *Mudanjiang Normal University, Mudanjiang 157011, China;* Email: xuecai@mdjnu.edu.cn

Authors

Rong Jiang − *Beijing Key Laboratory for Science and Application of Functional Molecular and Crystalline Materials, Department of Chemistry and Chemical Engineering, School of Chemistry and Biological Engineering,*

University of Science and Technology Beijing, Beijing 100083, China

Chao Liu − *Beijing Key Laboratory for Science and Application of Functional Molecular and Crystalline Materials, Department of Chemistry and Chemical Engineering, School of Chemistry and Biological Engineering, University of Science and Technology Beijing, Beijing 100083, China*

Baoqin Yu − *Beijing Key Laboratory for Science and Application of Functional Molecular and Crystalline Materials, Department of Chemistry and Chemical Engineering, School of Chemistry and Biological Engineering, University of Science and Technology Beijing, Beijing 100083, China*

Hailong Wang − *Beijing Key Laboratory for Science and Application of Functional Molecular and Crystalline Materials, Department of Chemistry and Chemical Engineering, School of Chemistry and Biological Engineering, University of Science and Technology Beijing, Beijing 100083, China;* orcid.org/0000-0002-0138-2966

Complete contact information is available at: https://pubs.acs.org/10.1021/acs.cgd.1c00942

Notes

The authors declare no competing financial interest.

■ ACKNOWLEDGMENTS

Financial support from the Natural Science Foundation (NSF) of China (No. 21805005), Fundamental Research Funds for the Central Universities (No. FRF-TP-20-042A2), and University of Science and Technology Beijing is gratefully acknowledged. We are also very grateful for the help from Prof. Rui-Biao Lin at the Sun Yat-Sen University for the topology analysis.

■ REFERENCES

(1) Davis, M. E. Ordered Porous Materials for Emerging Applications. *Nature* **2002**, *417*, 813−821.
(2) Lin, R.; He, Y.; Li, P.; Wang, H.; Zhou, W.; Chen, B. Multifunctional Porous Hydrogen-Bonded Organic Framework Materials. *Chem. Soc. Rev.* **2019**, *48*, 1362−1389.
(3) Ding, M.; Flaig, R. W.; Jiang, H.; Yaghi, O. M. Carbon Capture and Conversion Using Metal-Organic Frameworks and MOF-based Materials. *Chem. Soc. Rev.* **2019**, *48*, 2783−2828.
(4) Geng, K.; He, T.; Liu, R.; Dalapati, S.; Tan, K. T.; Li, Z.; Tao, S.; Gong, Y.; Jiang, Q.; Jiang, D. Covalent Organic Frameworks: Design, Synthesis, and Functions. *Chem. Rev.* **2020**, *120*, 8814−8933.
(5) Zhao, M.; Yuan, K.; Wang, Y.; Li, G.; Guo, J.; Gu, L.; Hu, W.; Zhao, H.; Tang, Z. Metal−Organic Frameworks as Selectivity Regulators for Hydrogenation Reactions. *Nature* **2016**, *539*, 76−80.
(6) Yi, J.-D.; Si, D.-H.; Xie, R.; Yin, Q.; Zhang, M.-D.; Wu, Q.; Chai, G.-L.; Huang, Y.-B.; Cao, R. Conductive Two-Dimensional Phthalocyanine-based Metal−Organic Framework Nanosheets for Efficient Electroreduction of CO_2. *Angew. Chem., Int. Ed.* **2021**, *60*, 17108−17114.
(7) He, T.; Kong, X.-J.; Li, J.-R. Chemically Stable Metal−Organic Frameworks: Rational Construction and Application Expansion. *Acc. Chem. Res.* **2021**, *54*, 3083−3094.
(8) Lin, R.-B.; Li, L.; Zhou, H.-L.; Wu, H.; He, C.; Li, S.; Krishna, R.; Li, J.; Zhou, W.; Chen, B. Molecular Sieving of Ethylene from Ethane Using a Rigid Metal−Organic Framework. *Nat. Mater.* **2018**, *17*, 1128−1133.
(9) Wen, H.-M.; Liao, C.; Li, L. B.; Alsalme, A.; Alothman, Z.; Krishna, R.; Wu, H.; Zhou, W.; Hu, J.; Chen, B. A Metal−Organic Framework with Suitable Pore Size and Dual Functionalities for Highly Efficient Post-Combustion CO_2 Capture. *J. Mater. Chem. A* **2019**, *7*, 3128−3134.
(10) Guan, X.; Chen, F.; Fang, Q.; Qiu, S. Design and Applications of Three Dimensional Covalent Organic Frameworks. *Chem. Soc. Rev.* **2020**, *49*, 1357−1384.
(11) Wang, Z.; Yang, Y.; Zhao, Z.; Zhang, P.; Zhang, Y.; Liu, J.; Ma, S.; Cheng, P.; Chen, Y.; Zhang, Z. Green Synthesis of Olefin-linked Covalent Organic Frameworks for Hydrogen Fuel Cell Applications. *Nat. Commun.* **2021**, *12*, 1982.
(12) Qian, Y.; Li, D.; Han, Y.; Jiang, H.-L. Photocatalytic Molecular Oxygen Activation by Regulating Excitonic Effects in Covalent Organic Frameworks. *J. Am. Chem. Soc.* **2020**, *142*, 20763−20771.
(13) Lu, M.; Zhang, M.; Liu, C.-G.; Liu, J.; Shang, L.-J.; Wang, M.; Chang, J.-N.; Li, S.-L.; Lan, Y.-Q. Stable Dioxin-Linked Metallophthalocyanine Covalent Organic Frameworks as Photo-Coupled Electrocatalysts for CO_2 Reduction. *Angew. Chem., Int. Ed.* **2021**, *60*, 4864−4871.
(14) Dong, J.; Han, X.; Liu, Y.; Li, H.; Cui, Y. Metal−Covalent Organic Frameworks (MCOFs): A Bridge between Metal−Organic Frameworks and Covalent Organic Frameworks. *Angew. Chem., Int. Ed.* **2020**, *59*, 13722−13733.
(15) Zhang, M.-D.; Si, D.-H.; Yi, J.-D.; Zhao, S.-S.; Huang, Y.-B.; Cao, R. Conductive Phthalocyanine-Based Covalent Organic Framework for Highly Efficient Electroreduction of Carbon Dioxide. *Small* **2020**, *16*, 2005254.
(16) Han, B.; Ding, X.; Yu, B.; Wu, H.; Zhou, W.; Liu, W.; Wei, C.; Chen, B.; Qi, D.; Wang, H.; Wang, K.; Chen, Y.; Chen, B.; Jiang, J. Two-Dimensional Covalent Organic Frameworks with Cobalt(II)-Phthalocyanine Sites for Efficient Electrocatalytic Carbon Dioxide Reduction. *J. Am. Chem. Soc.* **2021**, *143*, 7104−7113.
(17) Zhang, X.; Li, L.; Wang, J.-X.; Wen, H.-M.; Krishna, R.; Wu, H.; Zhou, W.; Chen, Z.-N.; Li, B.; Qian, G.; Chen, B. Selective Ethane/Ethylene Separation in a Robust Microporous Hydrogen-Bonded Organic Framework. *J. Am. Chem. Soc.* **2020**, *142*, 633−640.
(18) Ye, Z.-M.; Zhang, X.-W.; Liao, P.-Q.; Xie, Y.; Xu, Y.-T.; Zhang, X.-F.; Wang, C.; Liu, D.-X.; Huang, N.-Y.; Qiu, Z.-H.; Zhou, D.-D.; He, C.-T.; Zhang, J.-P. A Hydrogen-Bonded net Hydrophobic Porous Molecular Crystal for Molecular-Sieving-like Separation of Butane and Isobutane. *Angew. Chem., Int. Ed.* **2020**, *59*, 23322−23328.
(19) Hisaki, I.; Xin, C.; Takahashi, K.; Nakamura, T. Designing Hydrogen-Bonded Organic Frameworks (HOFs) with Permanent Porosity. *Angew. Chem., Int. Ed.* **2019**, *58*, 11160−11170.
(20) Simard, M.; Su, D.; Wuest, J. D. Use of Hydrogen Bonds to Control Molecular Aggregation. Self-assembly of Three-Dimensional Networks with Large Chambers. *J. Am. Chem. Soc.* **1991**, *113*, 4696−4698.
(21) Luo, J.; Wang, J.-W.; Zhang, J.-H.; Lai, S.; Zhong, D.-C. Hydrogen-bonded Organic Frameworks: Design, Structures and Potential Applications. *CrystEngComm* **2018**, *20*, 5884−5898.
(22) Yu, B.; Li, L.; Liu, S.; Wang, H.; Liu, H.; Lin, C.; Liu, C.; Wu, H.; Zhou, W.; Li, X.; Wang, T.; Chen, B.; Jiang, J. Robust Biological Hydrogen-Bonded Organic Framework with Post-Functionalized Rhenium(I) Sites for Efficient Heterogeneous Visible-Light-Driven CO_2 Reduction. *Angew. Chem., Int. Ed.* **2021**, *60*, 8983−8989.
(23) Han, B.; Wang, H.; Wang, C.; Wu, H.; Zhou, W.; Chen, B.; Jiang, J. Postsynthetic Metalation of a Robust Hydrogen-Bonded Organic Framework for Heterogeneous Catalysis. *J. Am. Chem. Soc.* **2019**, *141*, 8737−8740.
(24) Yu, B.; Geng, S.; Wang, H.; Zhou, W.; Zhang, Z.; Chen, B.; Jiang, J. A Solid Transformation into Carboxyl Dimers Based on a Robust Hydrogen-Bonded Organic Framework for Propyne/Propylene Separation. *Angew. Chem., Int. Ed.* **2021**, DOI: 10.1002/anie.202110057.
(25) Tozawa, T.; Jones, J. T. A.; Swamy, S. I.; Jiang, S.; Adams, D. J.; Shakespeare, S.; Clowes, R.; Bradshaw, D.; Hasell, T.; Chong, S. Y.; Tang, C.; Thompson, S.; Parker, J.; Trewin, A.; Bacsa, J.; Slawin, A. M. Z.; Steiner, A.; Cooper, A. I. Porous Organic Cages. *Nat. Mater.* **2009**, *8*, 973−978.

(26) Su, K.; Wang, W.; Du, S.; Ji, C.; Zhou, M.; Yuan, D. Reticular Chemistry in the Construction of Porous Organic Cages. *J. Am. Chem. Soc.* **2020**, *142*, 18060−18072.
(27) Wang, H.; Jin, Y.; Sun, N.; Zhang, W.; Jiang, J. Post-synthetic Modification of Porous Organic Cages. *Chem. Soc. Rev.* **2021**, *50*, 8874−8886.
(28) McCaffrey, R.; Long, H.; Jin, Y.; Sanders, A.; Park, W.; Zhang, W. Template Synthesis of Gold Nanoparticles with an Organic Molecular Cage. *J. Am. Chem. Soc.* **2014**, *136*, 1782−1785.
(29) Mastalerz, M. Porous Shape-Persistent Organic Cage Compounds of Different Size, Geometry, and Function. *Acc. Chem. Res.* **2018**, *51*, 2411−2422.
(30) Wang, Z.; Sikdar, N.; Wang, S.; Li, X.; Yu, M.; Bu, X.; Chang, Z.; Zou, X.; Chen, Y.; Cheng, P.; Yu, K.; Zaworotko, M. J.; Zhang, Z. Soft Porous Crystal Based upon Organic Cages That Exhibit Guest-Induced Breathing and Selective Gas Separation. *J. Am. Chem. Soc.* **2019**, *141*, 9408−9414.
(31) Liu, C.; Liu, K.; Wang, C.; Liu, H.; Wang, H.; Su, H.; Li, X.; Chen, B.; Jiang, J. Elucidating Heterogeneous Photocatalytic Superiority of Microporous Porphyrin Organic Cage. *Nat. Commun.* **2020**, *11*, 1047.
(32) Sun, N.; Wang, C.; Wang, H.; Yang, L.; Jin, P.; Zhang, W.; Jiang, J. Multifunctional Tubular Organic Cage-Supported Ultrafine Palladium Nanoparticles for Sequential Catalysis. *Angew. Chem., Int. Ed.* **2019**, *58*, 18011−18016.
(33) Metrangolo, P.; Neukirch, H.; Pilati, T.; Resnati, G. Halogen Bonding Based Recognition Processes: A World Parallel to Hydrogen Bonding. *Acc. Chem. Res.* **2005**, *38*, 386−395.
(34) Gilday, L. C.; Robinson, S. W.; Barendt, T. A.; Langton, M. J.; Mullaney, B. R.; Beer, P. D. Halogen Bonding in Supramolecular Chemistry. *Chem. Rev.* **2015**, *115*, 7118−7195.
(35) Nikolayenko, V. I.; Castell, D. C.; van Heerden, D. P.; Barbour, L. J. Guest-Induced Structural Transformations in a Porous Halogen-Bonded Framework. *Angew. Chem., Int. Ed.* **2018**, *57*, 12086−12091.
(36) Geng, G.; Lv, S.; Han, J.; Xie, F.; Li, Q.; Xia, N.; Zeng, W.; Chen, Y.; Wang, L.; Wang, J.; Chen, S. Halogen-Bonded Organic Framework (XOF) Based on IodoniumBridged N···I+···N Interactions: A Type of Diphase Periodic Organic Network. *Angew. Chem., Int. Ed.* **2021**, *60*, 14831−14835.
(37) Pop, L.; Grosu, I. G.; Micliuş, M.; Hădade, N. D.; Pop, A.; Bende, A.; Terec, A.; Barbosu, M.; Grosu, I. Halogen-Bonded Organic Frameworks of Perfluoroiodo-and Perfluorodiiodobenzene with 2,2′,7,7′-Tetrapyridyl-9,9′-spirobifluorene. *Cryst. Growth Des.* **2021**, *21*, 1045−1054.
(38) Chongboriboon, N.; Samakun, K.; Inprasit, T.; Kielar, F.; Dungkaew, W.; Wong, W.-Y.; Sung, H.-Y.; Ninković, D. B.; Zarić, S. D.; Chainok, K. Two-dimensional halogen-bonded organic frameworks based on the tetrabromobenzene-1,4-dicarboxylic acid building molecule. *CrystEngComm* **2020**, *22*, 24−34.
(39) Fourmigué, M.; Dhaka, A. Chalcogen bonding in crystalline dichalcogenides and selenocyanates From molecules of pharmaceutical interest to conducting materials. *Coord. Chem. Rev.* **2020**, *403*, 213094.
(40) Scilabra, P.; Terraneo, G.; Resnati, G. The Chalcogen Bond in Crystalline Solids: A World Parallel to Halogen Bond. *Acc. Chem. Res.* **2019**, *52*, 1313−1324.
(41) Strakova, K.; Assies, L.; Goujon, A.; Piazzolla, F.; Humeniuk, H. V.; Matile, S. Dithienothiophenes at Work: Access to Mechanosensitive Fluorescent Probes, Chalcogen-Bonding Catalysis, and Beyond. *Chem. Rev.* **2019**, *119*, 10977−11005.
(42) Gleiter, R.; Werz, D. B.; Rausch, B. J. A World Beyond Hydrogen Bonds? − Chalcogen-Chalcogen Interactions Yielding Tubular Structures. *Chem. - Eur. J.* **2003**, *9*, 2676−2683.
(43) Mehrparvar, S.; Wolper, C.; Gleiter, R.; Haberhauer, G. The Carbonyl Tellurazole Chalcogen Bond as a Molecular Recognition Unit: From Model Studies to Supramolecular Organic Frameworks. *Angew. Chem., Int. Ed.* **2020**, *59*, 17154−17161.
(44) Riwar, L.-J.; Trapp, N.; Root, K.; Zenobi, R.; Diederich, F. Supramolecular Capsules: Strong versus Weak Chalcogen Bonding. *Angew. Chem., Int. Ed.* **2018**, *57*, 17259−17264.
(45) Rahman, F.-U.; Tzeli, D.; Petsalakis, I. D.; Theodorakopoulos, G.; Ballester, P.; Rebek, J., Jr.; Yu, Y. Chalcogen Bonding and Hydrophobic Effects Force Molecules into Small Spaces. *J. Am. Chem. Soc.* **2020**, *142*, 5876−5883.
(46) Zhu, Y.-J.; Guo, Y.; Tang, M.-M.; Rebek, J., Jr.; Yu, Y. Dimeric Capsules Self-Assembled Through Halogen and Chalcogen Bonding. *Chem. Commun.* **2021**, *57*, 1543−1549.
(47) Mastalerz, M.; Sieste, S.; Cenić, M.; Oppel, I. M. Two-Step Synthesis of Hexaammonium Triptycene: An Air-Stable Building Block for Condensation Reactions to Extended Triptycene Derivatives. *J. Org. Chem.* **2011**, *76*, 6389−6393.
(48) Sheldrick, G. M. *SHELXL-2014*; University of Göttingen: Göttingen, Germany, 2014.
(49) Spek, A. L. Platon Squeeze: A Tool for the Calculation of the Disordered Solvent Contribution to the Calculated Structure Factors. *Acta Crystallogr., Sect. C: Struct. Chem.* **2015**, *71*, 9−18.
(50) Beniston, G.; Pigot, B.; Marrot, J.; Gommont, R. Supramolecular Association of 1,2,5-Chalcogenadiazoles: An Unexpected Self-assembled Dissymetric [Se/N]$_2$ Four-Membered Ring. *CrystEngComm* **2009**, *11*, 986−988.
(51) Mastalerz, M.; Oppel, I. M. Rational Construction of an Extrinsic Porous Molecular Crystal with an Extraordinary High Specific Surface Area. *Angew. Chem., Int. Ed.* **2012**, *51*, 5252−5255.
(52) Giannozzi, P.; Baroni, S.; Bonini, N.; Calandra, M.; Car, R.; Cavazzoni, C.; Ceresoli, D.; Chiarotti, G. L.; Cococcioni, M.; Dabo, I.; Dal Corso, A.; Fabris, S.; Fratesi, G.; de Gironcoli, S.; Gebauer, R.; Gerstmann, U.; Gougoussis, C.; Kokalj, A.; Lazzeri, M.; Martin-Samos, L.; Marzari, N.; Mauri, F.; Mazzarello, R.; Paolini, S.; Pasquarello, A.; Paulatto, L.; Sbraccia, C.; Scandolo, S.; Sclauzero, G.; Seitsonen, A. P.; Smogunov, A.; Umari, P.; Wentzcovitch, R. M. Quantum Espresso: a Modular and Open-source Software Project for Quantum Simulations of Materials. *J. Phys.: Condens. Matter* **2009**, *21*, 395502.
(53) Becke, A. D. Density-functional Exchange-energy Approximation with Correct Asymptotic Behavior. *Phys. Rev. A: At., Mol., Opt. Phys.* **1988**, *38*, 3098−3100.
(54) Hohenberg, P.; Kohn, W. Inhomogeneus Gas Electron. *Phys. Rev.* **1964**, *136*, B864−B871.
(55) Lee, C.; Yang, W.; Parr, R. G. Development of the Colle-Salvetti Correlation-energy formula into a functional of the electron density. *Phys. Rev. B: Condens. Matter Mater. Phys.* **1988**, *37*, 785−789.
(56) Lu, T.; Chen, F. Multiwfn: A Multifunctional Wavefunction Analyzer. *J. Comput. Chem.* **2012**, *33*, 580−592.
(57) Humphrey, W.; Dalke, A.; Schulten, K. VMD: Visual Molecular Dynamics. *J. Mol. Graphics* **1996**, *14*, 33−38.
(58) Ho, P. C.; Wang, J. Z.; Meloni, F.; Vargas-Baca, I. Chalcogen Bonding in Materials Chemistry. *Coord. Chem. Rev.* **2020**, *422*, 213464.
(59) Spek, A. L. *Platon, A Multipurpose Crystallographic Tool*; Utrecht University: Utrecht, The Netherlands, 2005.

2.Cai X, Ma Y, Zhou Q, et al. Synergistic effects of phases in the selective oxidation of isobutane over supported $(NH_4)_3HPMo_{11}VO_{40}$ catalysts[J]. Reaction Kinetics, Mechanisms and Catalysis, 2021, 133(1): 293-308.

Reaction Kinetics, Mechanisms and Catalysis (2021) 133:293–308
https://doi.org/10.1007/s11144-021-01967-0

Synergistic effects of phases in the selective oxidation of isobutane over supported $(NH_4)_3HPMo_{11}VO_{40}$ catalysts

Xue Cai[1] · Yue Ma[1] · Qi Zhou[1] · Zitong Zhang[1] · Wenling Chu[2] · Weishen Yang[2]

Received: 3 February 2021 / Accepted: 15 March 2021 / Published online: 29 March 2021
© Akadémiai Kiadó, Budapest, Hungary 2021

Abstract
The supported 40 wt% $(NH_4)_3HPMo_{11}VO_{40}$ (APMV) catalysts over two different types of supports, supports-I ($Cs_3PMo_{12}O_{40}$, $Cs_{2.5}H_{0.5}PMo_{12}O_{40}$, $Cs_4PMo_{11}VO_{40}$ and $Cs_3HPMo_{11}VO_{40}$) and supports-II (CeO_2, WO_3/ZrO_2 and S-1 molecular sieve), were synthesized by deposition–precipitation method and further evaluated in the partial oxidation of isobutane to methacrylic acid (MAA) at 340 °C under atmospheric pressure. The fresh and used catalysts were characterized by N_2 adsorption/desorption, TG/DTG, XRD, FT-IR, Raman spectroscopy, pyridine- adsorption FT-IR and NH_3-TPD to investigate their structure, stability and surface acidity. The better results were obtained by impregnating 40 wt% active APMV phase onto the supports-I phase with same/similar Keggin structure, and it is believed that the formation of coherent interfaces between two structural well-matched phases with the same/similar Keggin anions greatly promotes interfacial transfer abilities of electrons and lattice oxygen, which is responsible for the efficient oxygen insertion to maximize MAA selectivity and conversion of isobutane. The current work provides a concept of phase synergy to design a promising catalyst for selective oxidation of isobutane.

Keywords Selective oxidation · Methacrylic acid · Synergetic effect · Heteropoly compounds

Introduction

Methacrylic acid (MAA) is an important organic chemical raw material for the production of methyl methacrylate (MMA), which is used as a monomer to produce poly methyl methacrylate (PMMA) and its derivatives. At present, the industrial

✉ Wenling Chu
cwl@dicp.ac.cn

[1] Mudanjiang Normal University, Mudanjiang 157011, China

[2] State Key Laboratory of Catalysis, Dalian Institute of Chemical Physics, Chinese Academy of Science, 457 Zhongshan Road, Dalian 116023, Liaoning, China

production of MAA usually adopts the acetone cyanohydrin method [1, 2], which suffers from many disadvantages such as the use of highly toxic HCN and the generation of a large amount of co-product ammonium bisulfate. On this regard, the partial oxidation of isobutane to MAA is a compelling alternative method due to the improved atom-economy, the inexpensive raw materials and negligible environmental impact. In this process, heteropoly compounds (HPCs) with Keggin-type structure have attracted great attention as effective catalysts due to the designed and controlled acidity and oxidizing ability [3–7].

Due to the low surface area of bulk HPCs and their poor thermal stability at high temperature, many attempts have been done to load the active HPCs component on a carrier with a large specific surface area, thereby increasing the catalytic efficiency and the stability by improving the catalyst dispersion [8–10]. Jing et al. impregnated 10–50 wt% $(NH_4)_3HPMo_{11}VO_{40}$ over $Cs_3PMo_{12}O_{40}$ and found that the conversion over pure HPC was 2.5% but it increased to 15.3% over the 40 wt%-supported catalysts, meanwhile the selectivity was 42% and 34% over supported and non-supported catalysts [11], respectively. It was reported that loading $H_4PMo_{11}VO_{40}$ on SiO_2 increased the maximum conversion that was five-times higher than that of unsupported one in partial oxidation of methacrolein, while the selectivity to MAA dropped and the stability was less [12]. The $(NH_4)_3HPMo_{11}VO_{40}$ catalyst supported on ZrO_2-modified SBA-15 exhibited high selectivity to CO_x (> 60%) coming from total oxidation of isobutane [11], leading to the rather low selectivity to MAA (1.6%). It is obvious that the catalytic activity and selectivity in the partial oxidation of isobutane to MAA are sensitive to support and catalyst dispersion. Besides increasing dispersion of active components, another way to improve the catalytic efficiency of the Keggin-type HPCs in the selective oxidation of isobutane to MAA, which has not been extensively explored up to know, is to search for synergetic effect between the supports and the active HPCs components.

Based on the above background, the aim of this study was to investigate the effects of phases synergy between active $(NH_4)_3HPMo_{11}VO_{40}$ (APMV) and different supports on the catalytic performance in selective oxidation of isobutane to methacrylic acid. In this work, we have purposely selected two different types of carriers, in which one type of supports (denoted as support-I) has similar primary structure with the active APMV catalyst, and another type of supports (denoted as support-II) has large specific surface areas but an obvious different structure with active APMV component, such as CeO_2, WO_3/ZrO_2, S-1 molecular sieve. Particular emphasis was given to a direct comparison in the structure and activity in order to elucidate synergetic effect of the phase due to well-match structure between active phase and support phase on the catalytic performance of the supported catalysts in the partial oxidation of isobutane to MAA.

Experimental

Preparation of catalysts

All supports investigated in this study, such as $Cs_xH_{3-x}PMo_{12}O_{40}$ (x = 2.5 and 3.0) [12, 13], $Cs_yH_{4-y}PMo_{11}VO_{40}$ (y = 4.0 and 3.0) [13], CeO_2 [14], WO_3/ZrO_2 [15] and S-1 molecular sieve [16] were prepared according to the corresponding literature.

$H_4PMo_{11}VO_{40}$ was synthesized as follows: 15.8 g of MoO_3 and 0.9 g of V_2O_5 were dissolved in 300 mL of deionized water and was heated to reflux at 150 °C in the oil bath. After 1 h, 1.2 g of H_3PO_4 (85 wt%) was added dropwise to the mixed solution above. The resulting mixture was kept at reflux for another 3 h with vigorous stirring to form a clear solution. The product was obtained by removing solvent under reduced pressure in a rotary evaporator at 60 °C, and further dried overnight at 80 °C in an oven.

A series of supported catalysts containing 40 wt% $(NH_4)_3HPMo_{11}VO_{40}$ (APMV) were prepared by the deposition–precipitation method. In a typical synthesis procedure, the carrier was suspended in 30 ml of deionized water, refluxed in a water bath at 40 °C, and stirred vigorously for 1 h. After 1 h, the aqueous solutions of NH_4NO_3 and $H_4PMo_{11}VO_{40}$ were simultaneously dropped into the suspension at a rate of 2 ml/min, stirred vigorously for 2 h, and rotary evaporated to obtain a precursor. All supported APMV catalysts were calcined in static air at 350 °C for 3 h.

As reference catalysts, bulk APMV was also synthesized by the same procedure without any support, and the phase mixtures of APMV + $Cs_3PMo_{12}O_{40}$ (weight ratio = 0.4:1.0) were obtained by mixing the respective powders and hand grinding them for 30 min.

Catalysts characterization

Thermogravimetric analysis (TGA) was performed using an instrument (NETZSCH STA 4493F) to monitor the thermal decomposition of the unsupported and supported catalysts (~ 10 mg) after calcined at 350 °C for 3 h. The catalyst was heated from room temperature to 600 °C or 800 °C at 10 °C/min under N_2 flow.

The phase structure of the as-synthesized catalysts was identified by X-ray diffraction (XRD, Rigaku D/MAX 2500/PC diffractometer) with Cu K_α radiation. Patterns were recorded in the 2θ range of 5°–40° at a scan speed of 5° min^{-1}.

Fourier transform infrared (FT-IR) spectra (Nicolet 6700 spectrometer) were recorded at a resolution of 4 cm^{-1} with 32scans.

The specific surface area was measured by N_2 adsorption at 77 K in a Quantachrome Autosorb instrument. First, the sample was degassed at 300 °C for 4 h. BET method was used to determine the specific surface areas of the samples.

Raman spectroscopy was conducted using a RamanScope Senterra spectrometer at a wavelength of 532 nm with a laser power of 0.02 mW and an acquisition time of 10 s.

The acid characteristics of the supported catalysts were studied by NH_3-temperature-programmed-desorption (NH_3-TPD), in which about 0.1 g of catalyst was pre-treated in a He flow (30 ml/min) at 200 °C for 1 h. After cooling to 100 °C, NH_3 was chemisorbed for another 1 h in a NH_3/He stream (30 ml/min). After purging the reactor with He to a flat baseline, the TPD profiles were recorded in a He flow from 100 to 600 °C at a rate of 10 °C/min using a TCD detector.

The IR spectra of adsorbed pyridine (Py-IR) were obtained on a Tensor27 (Bruker) FT-IR spectrophotometer. Before the test, a self-supporting sheet with a diameter of 13 mm was degassed at 350 °C for 0.5 h to remove physically adsorbed water. After

cooling to room temperature, the spectrum of the sample was recorded as a background spectrum. After that, the sample was exposed to pyridine vapor for 5 min, and then the IR spectrum of the pyridine adsorbed at room temperature was recorded. Subsequently, IR spectra were obtained by evacuating at 150 °C, 250 °C and 350 °C for 0.5 h to desorb the pyridine and then cooling to room temperature. The IR spectra of all samples were obtained by subtracting the background spectrum from the absorbance spectrum recorded after desorption of pyridine.

Selective oxidation of isobutane

The selective oxidation of isobutane is carried out in an atmospheric fixed-bed reactor, which is made of a quartz tube with an inner diameter of Φ10 mm and a length of 400 mm. The 20–40 mesh granular catalyst (~ 2 g) was loaded in the middle of the reactor. First, the catalyst is heated to 325 °C for a certain period of time under nitrogen flow. Then, the feedstock with molar ratio of isobutane/O_2/H_2O/N_2 = 27/13.5/10/49.5 was fed into the reactor at a total flow rate of 20 mL /min. Then the contact time was about 6 s. For isobutane oxidation, the reaction temperature was controlled at 340 °C. All gas products are analyzed online by a TCD gas chromatograph equipped with two continuous columns: Porapak Q column is used to separate hydrocarbons and CO_2, Molecular 13X separates O_2, N_2, and CO. Liquid products (such as acetone, methacrolein, acrylic acid and methacrylic acid) are collected by a cold trap for 2 h, and are quantitatively analyzed off-line by Aglinet 7890B gas chromatography with FID detector using a FFAP capillary column. All the reaction data were obtained within 2 h under steady state stream.

Results

TGA

The TG/DTG curves of unsupported and the supported APMV catalysts after calcined at 350 °C for 3 h are shown in Fig. 1, which exhibited two main steps along the 50–600 °C temperature range. In the case of bulk APMV, the first step in the TG curve was ascribed to the loss of physisorbed water (50–200 °C). The second weight loss was ascribed to the thermal decomposition of the APMV, which began to decompose at 340 °C and was completely decomposed at 480 °C. The same phenomenon was observed with supported APMV samples but the decomposition occurred at higher temperature with respect to bulk APMV. The thermal decomposition of the supported catalysts started at about 360 °C, which suggested that the thermal stability of the active APMV phase increased when supported.

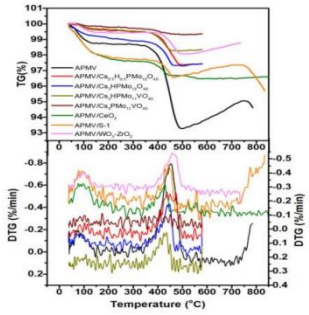

Fig. 1 Thermogravimetric analysis of unsupported and supported catalysts

XRD

The XRD patterns of supported 40 wt% APMV catalysts as well as different carriers are shown in Figs. 2 and S1. It can be seen from the patterns in Fig. 1 that pure bulk APMA exhibit diffraction peaks at 2θ = 10.5°, 18.4°, 23.7°, 26.1°, 30.2°, 35.6° and 38.9°, which are characteristic of the Keggin structure [17–19]. And two strong diffraction lines at 2θ = 15.1° and 21.4° could be attributed to characteristic NH_4^+ in APMA [20]. Specially, non-supported APMV catalyst showed weak MoO_3 crystal diffraction peaks at 28.5° and 34.4°, indicating its partial decomposition during the synthesis [21]. After supporting active APMV over the supports-I with similar primary structure, it is obvious that the diffraction peaks of NH_4^+ ions weakened and even disappeared due to the significant contribution of Keggin structure from the supports-I. More important, the diffraction peaks of MoO_3 crystal were not observed for the APMV/support-I catalysts, suggesting that the supports-I showed a stronger ability in stabilizing the active APMV phase.

In addition, for the 40 wt% APMV/support-II catalysts, in which CeO_2, WO_3/ZrO_2 and S-1 molecular sieve (just as shown in Fig. S1) have totally different structure with active APMV, the characteristic peaks attributed to the Keggin structure and NH_4^+ ions still exist but the intensity of these diffraction peaks significantly became weaker. But the diffraction peaks due to MoO_3 crystals were not still observed for the APMV/support-II catalysts, further indicating that the supports-II also exhibited stabilizing ability for APMA phase.

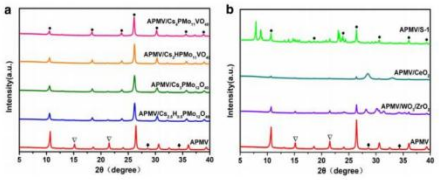

Fig. 2 XRD patterns of **a** APMV/support-I and **b** APMV/support-II: (filled circle) Keggin units and (filled diamond) MoO_3 and (inverted triangle) NH_4^+

Fig. S2 shows the XRD patterns of the used catalysts after 2 h of isobutane oxidation testing. It can be found that, compared to the fresh APMV/support catalysts, the diffraction patterns did not show any change in the phase composition or crystallinity, implying that there is no significant further decomposition of the Keggin structure during partial oxidation of isobutane under oxygen-poor conditions. This further suggested that the active APMV phase after impregnated on the supports exhibited excellent thermal stability.

FT-IR

FT-IR spectroscopy has been employed to determine the structural features of Keggin anion in the HPC catalysts. Fig. 3 gives the FT-IR spectra of the fresh supported catalysts with 40 wt% APMV loadings. All the catalysts showed obvious Keggin characteristic vibration bands at 1064, 961, 874 and 780 cm^{-1}, which are attributed to the stretching vibration of P–O, Mo=O_d, Mo–O_b–Mo and Mo–O_c–Mo [22], respectively. Furthermore, the bands at 1416 cm^{-1} assigned to the characteristic N–H vibration were also observed for all the as-synthetic supported catalysts [23, 24]. Obviously, the active APMV phase was well stabilized after loading on the various supports. For fresh bulk APMV sample, two characteristic splitting shoulder peaks at about 1080 cm^{-1} and 998 cm^{-1} are generally observed due to substitution of Mo in primary structure by V atom [25, 26]. However, these two splitting peaks disappeared after supporting APMV on $Cs_3PMo_{12}O_{40}$ and $Cs_{2.5}H_{0.5}PMo_{12}O_{40}$, further conforming the remarkable contribution of $[PMo_{12}O_{40}]^{3-}$ Keggin structure from the supports-I, which is in good agreement with results of XRD patterns shown in Fig. 2.

The FT-IR spectra of all used catalysts after selective oxidation of isobutane are shown in Fig. S3. It should be noted that all the characteristic band are retained, further illustrating that the intact Keggin structure in all synthesized catalysts in this

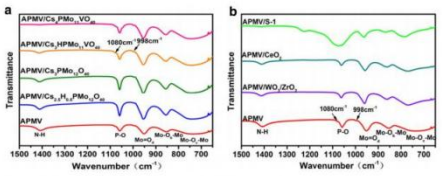

Fig. 3 FT-IR spectra of **a** APMV/support-I and **b** APMV/support-II

work is reserved after 2 h of testing, whether the active APMV is supported on supports-I with similar primary structure or on the supports-II with different structure features.

Raman spectroscopy and textural properties

The Raman spectra of the fresh supported catalysts are shown in Fig. 4. As shown by the well-known characteristic bands attributed to the following vibrations: δ(O–Mo–O) at 238 cm^{-1} and 255 cm^{-1}, δ(Mo–O–Mo) at 605 cm^{-1}, ν(Mo–O–Mo) at 878 cm^{-1}, 973 cm^{-1} and 959 cm^{-1}, and ν(Mo-O_t) at 990 cm^{-1}, the as-synthesized catalysts showed the existence of the Keggin structure [27]. And the absence of vibration bands at 818 and 660 cm^{-1} assigned to MoO_3 crystal [12, 28] further

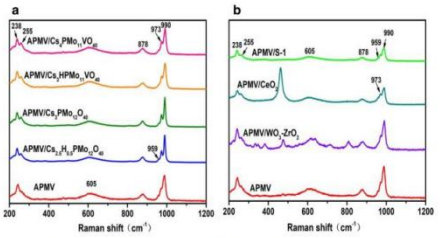

Fig. 4 Raman spectra of **a** APMV/support-I and **b** APMV/support-II

confirmed that the active APMV phase was well stabilized after loaded over the supports-I and supports-II.

The data of the specific surface area, total pore volume and pore diameter for the supports, pure APMV and the supported catalysts were listed in Table 1. The pore width distribution curves and the isotherm plots were shown in Figs. S4 and S5. It can be seen that the isotherms and the pore distribution of the 40 wt% APMV/support-I catalysts have significant difference compared to the supports-I themselves. And compared with the supports-I, the surface area of the supported samples decreased a lot due to the filling of APMV into the pores of supports-I besides APMV/$Cs_{2.0}H_{0.5}PMo_{12}O_{40}$ and APMV/$Cs_4PMo_{11}VO_{40}$ samples, both of which displayed a higher surface area than what is expected. This indicated that the APMV active phase partially contributes to the surface area of these two supported samples because APMV has a very high surface itself (40.35 m^2/g). Especially, for $Cs_4PMo_{11}VO_{40}$ support, the contribution of the active APMV to the surface area of the 40 wt% APMV/$Cs_4PMo_{11}VO_{40}$ catalyst is much more remarkable. In the case of the supports-II with larger specific surface area, there is no obvious change in the pore distribution and adsorption/desorption isotherms after loaded 40 wt% APMV on them. And the measured surface area and pore volume of the supported catalysts also decreased due to the block of porous structure of the supports-II by APMV. From above, it can be proposed that the active APMV phase over supports-II could exhibit the better dispersion than the APMV/supports-I.

NH_3-TPD

The NH_3-TPD technology was used to evaluate the surface acid properties of APMV catalysts supported on different carriers. It can be seen from Fig. 5 that all catalysts have similar desorption behavior of NH_3 and exhibit three types of acidic sites with different strength: weak acid sites at 100–250 °C, medium strong acid sites at 250–350 °C, and strong acid sites at 350–550 °C. Due to the release

Table 1 Textural properties of the supports, APMV and supported catalysts

Catalysts	Supports			Supported catalysts		
	S_{BET} (m^2/g)	V^a (cm^3/g)	D^b (nm)	S_{BET} (m^2/g)	V (cm^3/g)	D (nm)
APMV	–	–	–	40.35	0.052	5.91
APMV/$Cs_{2.5}H_{0.5}PMo_{12}O_{40}$	21.15	0.070	2.03	20.71	0.047	1.02
APMV/$Cs_3HPMo_{12}O_{40}$	97.89	0.117	4.82	37.72	0.070	1.03
APMV/$Cs_3HPMo_{11}VO_{40}$	37.56	0.062	7.00	26.31	0.085	1.56
APMV/$Cs_4PMo_{11}VO_{40}$	2.27	0.027	2.30	22.70	0.067	1.41
APMV/CeO_2	77.05	0.154	7.52	58.38	0.088	6.05
APMV/S-1	316.37	0.211	2.55	221.11	0.158	2.59
APMV/WO_3/ZrO_2	42.24	0.121	1.12	42.72	0.094	8.97

[a]V: The total pore volume at $p/p_0 = 0.99$

[b]D: Average pore size

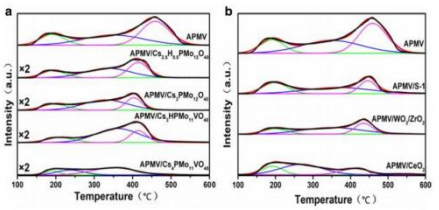

Fig. 5 NH_3-TPD profiles of **a** APMV/support-I and **b** APMV/support-II

of NH_3 from the decomposition of the ammonium cations in active APMV phase during the heating treatment, the amount of desorbed NH_3 was corrected by eliminating the theoretical values according to the literature [29] and the results were listed in Table 2. A significant different behavior was observed for the two types of supports, in which the APMV loading over supports-II exhibited the higher amount of weak acid sites and total acidity (mmol/g-cat). When calculating the density of acidic sites on the surface of supported catalysts (mmol/m^2-cat), the higher values were obtained for the APMV phase over supports-I, which was related to their relative lower specific surface area. From above, it can be concluded that the higher dispersion of active APMV on supports-II with the higher

Table 2 Amount of desorbed NH_3 on the surface of the supported catalyst

	Adsorption amount of NH_3 (μmol/g)			Total acidity	
	100–250 °C	250–350 °C	350–550 °C	(μmol/g)	(μmol/m^2)
APMV	234	185	501	920	23
APMV/$Cs_{2.5}H_{0.5}PMo_{12}O_{40}$	86	87	174	347	17
APMV/$Cs_3PMo_{12}O_{40}$	65	96	152	313	8
APMV/$Cs_3HPMo_{11}VO_{40}$	70	167	62	299	11
APMV/$Cs_4PMo_{11}VO_{40}$	80	81	31	192	8.5
APMV/CeO_2	185	142	65	396	7
APMV/WO_3/ZrO_2	104	100	156	360	11
APMV/S-1	174	98	218	490	2

surface area would expose the more acid sites, and finally led to the highest total acidity (mmol/g-cat) and the lower density of acid sites (mmol/m^2-cat).

Pyridine-adsorbed FT-IR spectra

The FT-IR spectra of pyridine-adsorbed catalysts can be carried out to further explore the presence of Brønsted and Lewis acid sites in as-synthesized samples. The spectra of the supported APMV catalysts recorded at 150 °C shows the presence of both Brønsted and Lewis acid sites (Fig. 6). Generally speaking, the bands at 1450 cm^{-1} and 1540 cm^{-1} in FT-IR spectra correspond to pyridine adsorbed on Brønsted (B) and Lewis (L) acidic sites of the catalyst surface, respectively [30]. And the absorption peak at 1488 cm^{-1} is related to the synergistic effect of B and L acid [31]. It is evident that B acidity is predominant for the APMV/support-I catalysts, but exhibiting rather poor L acidity. On the contrary, the L acidic sites on the surface of APMV/support-II catalysts were predominantly present and much higher than those on the APMV/support-I samples, suggesting that the Lewis acid sites might be mainly originated from the supports-II themselves or from interaction between the support-II and active APMV.

Additionally, the pyridine-IR spectra after outgassing at 250 °C and 350 °C was also investigated to estimate the strength of both B and L acidic centers on the supported catalysts (Figs. S6 and S7). Increasing evacuating temperature from 150 to 250 °C, there is no obvious change in the peak intensity of the B acid sites for all the as-synthesized catalysts but the amount of L acid sites over the APMV/support-II catalysts greatly decreased, indicating the weaker strength of L acidic sites from the contribution of the supports-II. Further increasing temperature to 350 °C, both the Brønsted and Lewis acidic sites over the supported-APMV catalysts still exist although their intensities decreased, clearly indicating the presence of strong acid sites. This is good agreement with the results of NH_3-TPD.

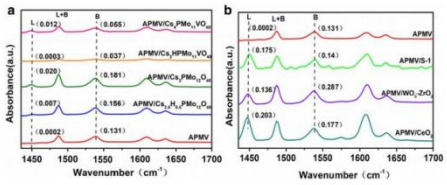

Fig. 6 FT-IR spectra of **a** APMV/support-I and **b** APMV/support-II after pyridine desorption at 150 °C. The B and L acidic amount in parentheses is calculated according to literature [32]

Selective oxidation of isobutane

The selective oxidation of isobutane over the 40 wt% APMV/support catalysts was studied at 340 °C under oxygen-poor condition with a feed ratio 27:13.5:10:49.5 (isobutane:O_2:H_2O:N_2). The results are presented in Table 3. The desirable products are methacrylic acid and methacrolein, and CO_2, CO, acetone, acetic acid and acrylic acid, trace amounts of ethylene and ethane are the side-products. The bulk APMV sample was active for selective oxidation of isobutane and exhibited 6.6% of isobutane conversion and 40.2% selectivity of desired products (MAA + MAL), whereas most of the pure supports were very poorly active and selective to MAA (Table S1). The significant increases were detected for the isobutane conversion and selectivity to MMA upon impregnating the active APMV on the supports-I with similar primary structure. And the highest yield in the desired products MAA + MAC (5.39%) was obtained with 40 wt% APMV/$Cs_3PMo_{12}O_{40}$ whereas it amounted to 4.58%, 3.98% and 3.06% with APMV/$Cs_{2.5}H_{0.5}PMo_{12}O_{40}$, APMV/$Cs_3HPMo_{11}VO_{40}$ and APMV/$Cs_4PMo_{11}VO_{40}$, respectively. Among them, it is interesting to note that inserting V into the primary structure of the supports resulted in slightly decrease in the selectivity to MAA. However, a remarkably negative effect was found when introducing active APMV onto the supports-II, in which almost no MAA was formed and the high selectivity to CO_x was observed. It is evident that catalyst activity and product selectivity in the isobutane oxidation to MAA are rather sensitive to the type of supports.

Discussion

It is well-known that, for the partial oxidation of isobutane to MAA, acidic-functional catalysts are necessary to activate the C-H bond and further promote desorption of MAA from the acidic surface [33–36]. Based on the results from NH_3-TPD

Table 3 Catalytic performance of 40 wt% APMV supported catalyst

Catalysts	Conv. of *i*-C_4H_{10} (%)	Selectivity (%)[a]							Yield of MAA + MAL(%)
		MAA	MAL	Actone	AcA	AA	CO	CO_2	
APMV	6.60	34.52	6.67	0.65	10.05	0.92	20.67	26.48	2.72
APMV/$Cs_{2.5}H_{0.5}PMo_{12}O_{40}$	9.03	44.23	6.46	1.06	8.30	1.51	16.60	21.78	4.58
APMV/$Cs_3PMo_{12}O_{40}$	11.34	43.01	4.52	0.94	8.32	1.40	17.27	24.49	5.39
APMV/$Cs_3HPMo_{11}VO_{40}$	9.79	35.23	5.38	0.78	9.79	1.42	20.36	27.00	3.98
APMV/$Cs_4PMo_{11}VO_{40}$	7.77	32.04	7.40	0.89	11.11	1.12	18.32	29.10	3.06
APMV + $Cs_3PMo_{12}O_{40}$	8.37	9.33	2.23	0.82	7.13	0.64	29.18	50.58	0.96
APMV/S-1	7.98	0.62	0.89	2.35	15.17	0.76	34.16	45.72	0.12
APMV/CeO_2	7.90	0.30	0.00	0.00	0.30	0.00	44.51	54.87	0.02
APMV/WO_3/ZrO_2	7.01	0.91	3.98	1.09	8.28	0.23	33.70	51.74	0.34

[a]*MAA* methacrylic acid, *MAL* methacrolein, *AcA* acetic acid, *AA* acrylic acid

(Fig. 5 and Table 2) and pyridine-adsorbed FT-IR spectra (Fig. 6), it can be found that, although the 40 wt% APMV/support-II catalysts possess much more amount of surface acidic sites (calculated by μmol/g) than the APMV/support-I catalysts, they exhibited the lower conversion of isobutane and the rather worst selectivity to MAA. However, if considering the acidic site density as μmol/m^2, it can be found from Fig. 7 that, although there is not totally linear relationship, a positive effect of NH_3 uptake (μmol/m^2) could be observed toward the catalytic activity (μmol/min m^2), which is defined as $(F_{isobutane} \times X_{isobutane})/(S_{BET} \times M_{cat})$ [11], and where $F_{isobutane}$, $X_{isobutane}$, S_{BET} and M_{cat} is the molar flowrate of isobutane, the conversion of isobutane, the specific surface area and the mass of catalyst, respectively. This emphasized that the amount of acidic sites per m^2, rather than that per gram, could play a role to a certain extent in determining the catalytic activity of partial oxidation of isobutane to MAA.

In addition, it has been reported [37] that the thermal stability of the active APMV phase could be a factor influencing the product distribution, in which the formation of MoO_3 from decomposition of active APMV phase is non-selective for the isobutane oxidation. Paul et al. attributed [11] the less selectivity of MAA over APMV/SiO_2 catalyst to the partial decomposition of the active phase to MoO_3 during the catalyst preparation. In our study, the results obtained by XRD, FT-IR and Raman spectra showed that the active APMV phase remained stable upon impregnated on the all as-synthesized supports, including supports-I and supports-II, in which almost no MoO_3 phase was detected. More importantly, there was virtually no change in the peak intensity of the Keggin structure for all used catalysts after isobutane oxidation and the absence of MoO_3 crystal was further confirmed by XRD and FT-IR spectra (Figs. S2 and S3). Thus, the significant difference in the distribution of the products in the case of the present study, especially the worst selectivity to MAA over the APMV/support-II catalysts, could not be attributed to the stability of the active phase.

For the partial oxidation of isobutane to MAA, redox properties have also an inevitable effect on the oxygen insertion reaction which generates the oxidized products. In our case, the improved catalytic performance was obtained over the 40 wt% APMV/support-I with the same primary structure, which might originated from a

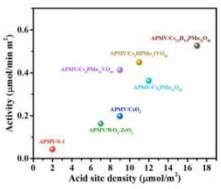

Fig. 7 Correlation between the activity of isobutane partial oxidation and the acid site density of supported catalysts measured by NH_3-TPD

good synergetic effect between the similar primary polyoxometallate structure of the two phases. It is known [38] that, when the two phases contain same/similar lattice plane with each other, they are structurally closely matched. Thus, the optimal structure match between active APMV phase and the supports-I would lead to the formation of strong and coherent boundaries between lattices of the two phases [13]. For phase synergy to be effective, it is imperative that the contact between active phase and support phase must be intimate in order to facilitate their cooperation on an atomic scale or at least on a nanoscale, in which the interfacial transfer of electrons and active lattice oxygen species takes effect easily. Just as shown in Table 3, the catalyst (APMV + $Cs_3PMO_{12}O_{40}$) obtained by mechanically mixed active APMV and $Cs_3PMO_{12}O_{40}$ support exhibited rather poor selectivity in the desired products, which further identified the indispensability of intimate contact. Therefore, it appears reasonable to propose that the formation of coherent interfaces between two structural well-matched phases with the same/similar Keggin anions greatly promotes the transfer abilities of electrons and lattice oxygen, which is responsible for the efficient oxygen insertion to maximize MAA selectivity. This well-matched effect between the two phases, which is likely a major contributor to an increased selectivity in desired product MAA, has been discovered by dispersing active $Cs_2Te_{0.3}(VO)_{0.1}H_4PMo_{12}O_{40}$ over α-$La_2Mo_2O_9$ support [39]. Similarly, this might be the main reason why 40 wt% APMV/support-II catalysts gave the lowest selectivity to MAA as a consequence of the highly unmatched structure between active APMV and supports, resulting in difficulty for interfacial transfer of electrons and lattice oxygen, although the supports owned the higher surface area and more amount of surface acidic sites. As a result, the total oxidation reaction between isobutane and gaseous oxygen was dominant and led to the rather high selectivity to CO_x. Finally, as mentioned before, there was a slightly decrease in the selectivity to MAA when impregnating active APMV onto the containing-V supports-I with totally the same primary structure. It has been widely accepted [18, 31] that a certain amount of V species in the primary structure of HPCs possibly migrated into the secondary

Table 4 Catalytic performance of APMV and HPMV[a] supported catalyst

Catalysts	Temp. (°C)	Conv. of *i*-C_4H_{10} (%)	Selectivity (%)[b]				Refs.
			MAA	MAL	COx	others	
APMV	340	2.5	34.3	20.4	35.8	9.5	[11]
40wt%APMV/$Cs_3PMo_{12}O_{40}$	340	15.3	42.0	10.0	30.7	17.3	[11]
40wt%HPMV[a]/$Cs_3PMo_{12}O_{40}$	340	4.6	41.8	17.4	31.7	–	[40]
40wt%HPMV/$HCs_3PMo_{11}VO_{40}$	340	11.4	24.0	6.7	54.8	–	[40]
40wt%APMV/ZrO_2-SBA-15	340	6.6	1.6	9.6	63.5	25.3	[11]
40wt%APMV/SBA-15	340	5.0	9.7	18.0	42.0	30.3	[11]
50wt%HPMV/Ta_2O_5·nH_2O	350	8.7	3.5	1.0	–	–	[41]
50wt%HPMV/diatomaceous earth	350	7.9	3.6	1.1	–	–	[41]

[a]*HPMV* $H_4PMo_{11}VO_{40}$

[b]*MAA* methacrylic acid, *MAL* methacrolein, *AcA* acetic acid, and *AA* acrylic acid

structure during the partial oxidation of isobutane to MAA. However, it is not clear yet if this decrease in selectivity is related to the migration of V species or if it is due to the intrinsic properties of supports-I with V inserting the Keggin structure. Additional experimental works in the future are needed to further explain the reasons.

Table 4 represents the catalytic performance of supported 40–50 wt% APMV and HPMV ($H_4PMo_{11}VO_{40}$) catalysts studied earlier in the literature for selective oxidation of isobutane to MAA. Although the synergetic effect observed in our work has never been used to explain the difference in catalytic performance among these supported catalysts, it is obvious that the catalysts with the well-matched primary structure between the active HPC phase and the supports exhibited the more excellent activity and/or selectivity than those with completely mismatched structures. This further confirmed the possibility of explanation, for which the formation of a coherent interface between the phases would be favorable to lead to a synergetic effect.

Conclusions

The 40 wt% active APMV catalysts supported over two different types of supports (supports-I and supports-II) were synthesized and characterized, and their catalytic performance in partial oxidation of isobutane to MAA was also evaluated. It was found that 40 wt% APMV/support-I catalysts with similar primary structure exhibited far superior catalytic activity and selectivity than the 40 wt% APMV/support-II catalysts, which were poorly selective to MAA. As shown by physicochemical analyses, the thermal stability of the active phase was increased by impregnating active APMV over two types of supports, and the stability remains almost unchanged even after 2 h of catalytic testing. The well-matched primary structure between the active APMV phase and the support-I should be helpful for the development of a stronger bonding boundary which exhibited excellent electrons and lattice oxygen transfer abilities. The phase cooperation from the well-matched structure and/or the higher acid site density per unit surface area (μmol/m^2), not better dispersion of active phase, could have here a strong influence on the catalytic performance in partial oxidation of isobutane to MAA. The best catalytic performance with isobutane conversion of 11.3% and 5.39% yield in the desired products was achieved on the 40 wt% APMV/$Cs_3PMo_{12}O_{40}$ catalyst.

Supplementary Information The online version contains supplementary material available at https://doi.org/10.1007/s11144-021-01967-0.

Acknowledgements This work was supported by the National Natural Science Foundation of China (Grant No. 21673227), Scientific Group Research Project of Mudanjiang Normal University (No. D211220645), the Science and Technology Innovation Project of Mudanjiang Normal University (No. kjcx2020-16mdjnu).

Declarations

Conflict of interest There are no conflicts of interest to declare.

References

1. Jaber DMM, Jean-Luc D, Fabrizio C et al (2018) Catalysis for the synthesis of methacrylic acid and methyl methacrylate. Chem Soc Rev 47:7703–7738
2. Li B, Yan R, Diao Y et al (2013) Synthesis of methyl methacrylate by aldol condensation of methyl propionate with formaldehyde over acid–base bifunctional catalysts. Catal Lett 143:829–838
3. Wu S, Kan Q, Ding W et al (2012) Partial oxidation of isobutane to methacrolein over $Te_{(1.5+0.5x)}PMo_{12-x}V_xO_n$ heteropolycompounds with tellurium as counter cations. React Kinet Mech Cat 106:157–164
4. Song IK, Barteau MA (2004) Redox properties of Keggin-type heteropolyacid (HPA) catalysts: effect of counter-cation, heteroatom, and polyatom substitution. J Mol Catal A Chem 212:229–236
5. Kendell S, Brown T (2010) Datailed product and kinetic analysis for the low-pressure selective oxidation of isobutane over phosphomolybdic acid. React Kinet Mech Cat 99:251–268
6. Stuyven B, Emmerich J, Eloy P et al (2014) Molybdenum-vanadium -antimony mixed oxide catalyst for isobutane partial oxidation synthesized using magneto hydrodynamic forces. Appl Catal A Gen 474:18–25
7. Liu S, Chen L, Wang G et al (2016) Effects of Cs-substitution and partial reduction on catalytic performance of Keggin-type phosphomolybdic polyoxometalates for selective oxidation of isobutane. J Energy Chem 25:85–92
8. Kanno M, Miura YK, Yasukawa T et al (2011) 1-Molybdo-1-vanadophosphoricacid $H_4PMo_{11}VO_{40}$ supported on ammonia-modified silica as highly active and selective catalyst for oxidation of methacrolein. Catal Commun 13:59–62
9. Sebastien P, Wei C, Manzoor S et al (2010) Keggin-type $H_4PVMo_{11}O_{40}$-based catalysts for the isobutane selective oxidation. Sci Chin Chem 53:2039–2046
10. Paul S, Courtois VL, Vahnove D (1997) Kinetic investigation of isobutane selective oxidation over a heteropolyanion catalyst. Ind Eng Chem Res 36:3391–3399
11. Jing F, Katryniok B, Bordes-Richard E et al (2013) Improvement of the catalytic performance of supported $(NH_4)_3HPMo_{11}VO_{40}$ catalysts in isobutane selective oxidation. Catal Today 203:32–39
12. Kanno M, Yasukawa T, Ninomiya W et al (2010) Catalytic oxidation of methacrolein to methacrylic acid over silica-supported 11-molybdo-1-vanadophosphoric acid with different heteropolyacid loadings. J Catal 273:1–8
13. Zhou L, Wang L, Diao Y et al (2017) Cesium salts supported heteropoly acid for oxidation of methacrolein to methacrylic acid. Mol Catal 433:153–161
14. Ho C, Yu JC, Kwong T et al (2005) Morphology-controllable synthesis of mesoporous CeO_2 nano- and microstructures. Chem Mater 17:4514–4522
15. Cortés-Jácome MA, Toledo JA, Angeles-Chavez C et al (2005) Influence of synthesis methods on tungsten dispersion, structural deformation, and surface acidity in binary WO_3-ZrO_2 system. J Phys Chem B 109:22730–22739
16. Yang X, Huang L, Li J et al (2017) Fabrication of SiO_2@silicalite-1 and its use as a catalyst support. RSC Adv 7:11224–11230
17. Liao X, Wu D, Geng B et al (2017) Deep oxidative desulfurization catalyzed by $(NH_4)_xH_{4-x}PMo_{11}VO_{40}$ (x = 1, 2, 3, 4) using O_2 as an oxidant. RSC Adv 7:48454–48460
18. He J, Liu Y, Chu W et al (2018) Effect of V-containing precursors on the structure and catalytic performance of Cs-substituted phosphomolybdates for isobutane oxidation. Appl Catal A Gen 556:104–112
19. Guan J, Xu H, Jing S et al (2009) Selective oxidation of isobutane and isobutene over vanadium phosphorus oxides. Catal Commun 10:276–280
20. Jing F, Katryniok B, Dumeignil F et al (2014) Catalytic selective oxidation of isobutane to methacrylic acid on supported $(NH_4)_3HPMo_{11}VO_{40}$ catalysts. J Catal 309:121–135
21. Ballarini N, Candiracci F, Cavani F et al (2007) The dispersion of Keggin-type P/Mo polyoxometalates inside silica gel, and the preparation of catalysts for the oxidation of isobutane to methacrolein and methacrylic acid. Appl Catal A Gen 325:263–269
22. Zhou L, Wang L, Zhang S et al (2015) Effect of vanadyl species in Keggin-type heteropoly catalysts in selective oxidation of methacrolein to methacrylic acid. J Catal 329:431–440
23. Dermeche L, Thouvenot R, Hocine S et al (2009) Preparation and characterization of mixed ammonium salts of Keggin phosphomolybdate. Inorg Chim Acta 362:3896–3900

24. Laronze N, Marchal-Roch C, Guillou N et al (2003) Solid-state chemistry of ammonium and cesium 1-vanado-11-molybdophosphate and ammonium 12- molybdosilicate: application to oxidation catalysis. J Catal 220:172–181
25. Casarini D, Centi G, Jiru P et al (1993) Reactivity of molybdovanadophosphoric acids: influence of the presence of vanadium in the primary and secondary structure. J Catal 143:325–344
26. Dimitratos N, Védrine JC (2003) Properties of $Cs_{2.5}$ salts of transition metal M substituted Keggin-type $M_{1-x}PV_xM_yMo_{11-y}O_{40}$ heteropolyoxometallates in propane oxidation. Appl Catal A Gen 256:251–263
27. Huynh Q, Schuurman Y, Delichere P et al (2009) Study of Te and V as counter-cations in Keggin type phosphomolybdic polyoxometalate catalysts for isobutane oxidation. J Catal 261:166–176
28. Mezzogori R, Pigamo A (2001) Improved catalytic performance of Keggin-type polyoxometalates in the oxidation of isobutane to methacrylic acid under hydrocarbon-lean conditions using antimony-doped catalysts. Chem Eng J 82:33–42
29. Cao Y, Wang L, Zhou L et al (2017) $Cs(NH_4)_xH_{3-x}PMo_{11}VO_{40}$ catalyzed selective oxidation of methacrolein to methacrylic acid: effects of NH_4^+ on the structure and catalytic activity. Ind Eng Chem Res 56:653–664
30. Huang H, Yi D, Lu Y et al (2013) Study on the adsorption behavior and mechanism of dimethyl sulfide on silver modified bentonite by in situ FTIR and temperature-programmed desorption. Chem Eng J 225:447–455
31. Li XK, Zhao J, Ji W et al (2006) Effect of vanadium substitution in the cesium salts of Keggin-type heteropolyacids on propane partial oxidation. J Catal 237:58–66
32. Emeis CA (1993) Determination of integrated molar extinction coefficients for infrared-absorption bands of pyridine adsorbed on solid acid catalysts. J Catal 141:347–354
33. Busca G, Finocchio E, Ramis G et al (1996) On the role of acidity in catalytic oxidation. Catal Today 32:133–143
34. De Smet F, Ruiz P, Delmon B et al (2001) Rationalization of the catalytic behavior of lanthanide oxides and praseodymium molybdates in total and selective oxidation of isobutene. J Phys Chem B 105:12355–12363
35. Zhang H, Yan R, Yang L et al (2013) Investigation of Cu- and Fe-Doped $CsH_4PMo_{11}VO_{40}$ heteropoly compounds for the selective oxidation of methacrolein to methacrylic acid. Ind Eng Chem Res 52:4484–4490
36. Cavani F (1998) Heteropolycompound-based catalysts: a blend of acid and oxidizing properties. Catal Today 41:73–86
37. Jing F, Katryniok B, Bordes-Richard E et al (2015) Structural evolution under reaction conditions of supported $(NH_4)_3HPMo_{11}VO_{40}$ catalysts for the selective oxidation of isobutane. Catalysts 5:460–477
38. Grasselli RK (2001) Genesis of site isolation and phase cooperation in selective oxidation catalysis. Top Catal 15:93–104
39. Huynh Q, Selmi A, Corbel G et al (2009) Atypical synergetic effect between Te- and V-substituted phosphomolybdic cesium salt and LAMOX-type phases for the oxidation of isobutane into methacrylic acid. J Catal 266:64–70
40. Paul S, Chu W, Sultan M et al (2010) Keggin-type $H_4PVMo_{11}O_{40}$-based catalysts for the isobutane selective oxidation. Sci China 53:2039–2046
41. Ushikubo T (2003) Activation of propane and butanes over niobium-and tantalum-based oxide catalysts. Catal Today 78:79–84

Publisher's Note Springer Nature remains neutral with regard to jurisdictional claims in published maps and institutional affiliations.

3.Wei C, Lu G, Guo C, et al. Ethylthio-substituted sandwich phthalocyaninato europium (III) semiconductors for sensing NO_2 and NH_3: Effect of the extended π-conjugate systems on tuning the conductivity and sensing behavior[J]. Organic Electronics, 2021, 93: 106151.

Organic Electronics 93 (2021) 106151

Contents lists available at ScienceDirect

Organic Electronics

journal homepage: http://www.elsevier.com/locate/orgel

Ethylthio-substituted sandwich phthalocyaninato europium (III) semiconductors for sensing NO_2 and NH_3: Effect of the extended π-conjugate systems on tuning the conductivity and sensing behavior

Chuangyu Wei [a], Guang Lu [c], Chang Guo [a], Xuehui Lv [a], Xiangjie Tang [a], Qi Liu [a], Xue Cai [b,**], Yanli Chen [a,*], Jianzhuang Jiang [a,d,***]

[a] College of Science, China University of Petroleum (East China), Qingdao, 266580, China
[b] College of Chemistry and Chemical Engineering, Mudanjiang Normal University, Mudanjiang, 157011, China
[c] School of Chemistry and Biological Engineering, Shandong University of Science and Technology, Qingdao, 266510, China
[d] Beijing Key Laboratory for Science and Application of Functional Molecular and Crystalline Materials, Department of Chemistry, University of Science and Technology Beijing, Beijing, 100083, China

ARTICLE INFO

Keywords:
Sandwich-type phthalocyanine
π-conjugate system
Organic semiconductor
Solution-processed film
Gas sensing

ABSTRACT

By using the π-conjugated phthalocyanine macrocycle as the versatile building block, a series of five sandwich-type ethylthio substituted phthalocyaninato europium complexes, namely double-decker $Eu[Pc(SC_2H_5)_8]_2$ (**Pc-1**), triple-decker $Eu_2[Pc(SC_2H_5)_8]_3$ (**Pc-2**), and their corresponding dimers, $[Pc(SC_2H_5)_8]_2Eu_2[BiPc(SC_2H_5)_{12}]$ (**Pc-1@Pc-1**), $[Pc(SC_2H_5)_8]_3Eu_3[BiPc(SC_2H_5)_{12}]$ (**Pc-1@Pc-2**) and $[Pc(SC_2H_5)_8]_4Eu_4[BiPc(SC_2H_5)_{12}]$ (**Pc-2@Pc-2**), are synthesized and prepared into the solution-processed films by a simple quasi-Langmuir-Shäfer (QLS) method. Combination between the extending π-conjugated system in the longitudinal and transverse directions of Pc macrocycles and/or radical nature of **Pc-1** unit among different semiconducting molecules result in unusually small energy gaps (0.345–0.91 eV). Consequently, all of the semiconductors exhibit excellent conductivities. Among these materials, the conductivity for the radical species **Pc-1@Pc-1**, **Pc-1@Pc-2** and **Pc-1** is about 3–4 times larger than that for the non-radical compounds **Pc-2@Pc-2** and **Pc-2**. Moreover, the QLS films of five semiconductors take excellent linear responses for both oxidizing NO_2 (100–300 ppb) and reducing NH_3 (4–8.6 ppm). Respectively, the sensitivity (in % ppm^{-1}) gets increased in the order of **Pc-1** < **Pc-2** < **Pc-1@Pc-1** < **Pc-1@Pc-2** < **Pc-2@Pc-2** for NO_2, and **Pc-1@Pc-2** < **Pc-1** < **Pc-1@Pc-1** < **Pc-2@Pc-2** < **Pc-2** for NH_3. Depending on the highly extended π-conjugated systems, **Pc-2@Pc-2** and **Pc-2** films achieve the highest sensitivity of 208.2% ppm^{-1} and 0.97% ppm^{-1} to NO_2 and NH_3, respectively. In addition, with a less than 2 min response time within a limit of detection at 10 ppb for NO_2 and 0.48 ppm for NH_3, good reproducibility and selectivity have been revealed for the **Pc-2@Pc-2** and **Pc-2** films among the best gas sensors obtained so far for all the solution-processed films based on organic semiconductors in dry air at room temperature. More importantly, it is firstly demonstrated that the high NO_2 sensing is resulted from low Oxd_1, and high NH_3 sensing is resulted from high Red_1 among the sandwich Pc-based semiconductors.

1. Introduction

In recent years, organic semiconducting materials have been widely studied in the development of the profitable sensing systems for the sensitive detection of nitrogen-based hazardous gas due to their lower operating temperature, easier modulability of molecular properties, and solution processability compared with inorganic semiconductors [1–3]. Phthalocyanines (Pcs), as an important class of organic semiconductors, are a large series of heterocyclic conjugated molecules that possess unique electrical properties, high chemical stability, and tunable molecular orbital energies by the peripheral substituents and coordinated metals [4–6]. In particular, sandwich-type phthalocyanines, originating

* Corresponding author.
** Corresponding author.
*** Corresponding author. College of Science, China University of Petroleum (East China), Qingdao, 266580, China.
E-mail addresses: xuecai@mdjnu.edu.cn (X. Cai), yanlichen@upc.edu.cn (Y. Chen), jianzhuang@ustb.edu.cn (J. Jiang).

https://doi.org/10.1016/j.orgel.2021.106151
Received 13 February 2021; Received in revised form 12 March 2021; Accepted 12 March 2021
Available online 26 March 2021
1566-1199/© 2021 Elsevier B.V. All rights reserved.

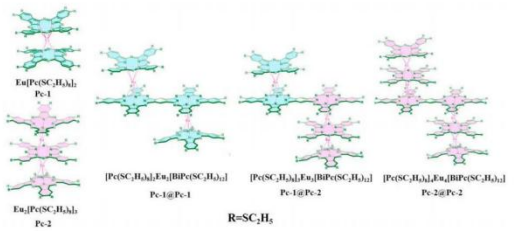

Scheme 1. Schematic molecular structures of **Pc-1**, **Pc-2**, **Pc-1@Pc-1**, **Pc-1@Pc-2** and **Pc-2@Pc-2**.

from the multiple Pc macrocyclic ligands complexed with rare earth metal ion(s) in one molecule, offer the most effective approach to adjust frontier molecular orbital energies, and thus the charge carrier density and mobility of the materials, due to the great number of possible substitution positions in the periphery of multiple Pc macrocycles and the intramolecular π-π interactions within these Pc chromophores [7]. Up to now, most organic semiconducting gas sensor show only one type of charge carrier's response behavior (either *p*- or n-type response) even though the ambipolar (both electron and hole) charge transport is an intrinsic nature of the pure organic semiconducting materials on the basis of theoretical considerations, and have ever been revealed by many organic filed effect transistor measurements. Since the ambipolar behavior of rare earth double decker phthalocyanine complexes was first reported in OFETs by G. Guillaud et al. [8], and the heteroleptic octanaphthoxy-substituted europium biphthalocyanine was firstly found to show ambipolar charge-transporting gas sensing in 2016 [9], the development of novel ambipolar organic semiconductors towards sensor applications has aroused great research interest, as they are very cheap, mechanically flexible, and highly sensitive at room temperature (24–26 °C), without necessarily requiring micro-patterning of the individual *p*- and *n*-channel semiconductors [10–14]. In recent years, significant improvements on sensing performance have been achieved by different strategies, such as optimizing the film morphology [15], tuning the intra-/intermolecular interactions [11,16], and constructing sensing array or heterojunction devices [10,14,15,17–20]. More recently, through examining the NH_3 sensing nature of ambipolar thiophenoxy-substituted bis(phthalocyaninato) rare earth complexes, whether *n*-type or *p*-type response behaviors of ambipolar semiconductors has been found to be governed by the lower rather than the higher charge carrier density of the ambipolar organic semiconductors [20]. This is further corroborated by a *n*- and *p*-type responses to NO_2 and NH_3, respectively, for two ambipolar tris(phthalocyaninato) rare earth triple-deckers [11]. To effectively improve the sensing performance of sandwich-type phthalocyaninato rare earth ambipolar semiconductors, in-depth understanding of the correlations between molecular structure and gas sensing property is imperative. In addition, various methods, such as Langmuir-Blodgett (LB), Langmuir-Shäfer (LS), quasi-Langmuir-Shäfer (QLS) etc., have been employed to fabricate the thickness-controlled films for phthalocyanine-based sensing devices [7, 10,13,16,18]. Among them, the QLS technology developed by M. Bouvet and co-workers [22], is very attractive method, which can get well-organized films at the air-water interface without complicated apparatus.

In this study, we design and synthesize a series of ethylthio-substituted sandwich-type phthalocyaninato europium (III) complexes, double-decker $Eu[Pc(SC_4H_9)_8]_2$ (**Pc-1**), triple-decker $Eu_2[Pc(SC_4H_9)_8]_2$ (**Pc-2**), and their corresponding dimer combined with double- and/or triple-decker units via an edge-to-edge mode by a fusing benzene ring, $[Pc(SC_4H_9)_8]_2Eu_2[BiPc(SC_2H_5)_{12}]$ (**Pc-1@Pc-1**), $[Pc(SC_4H_9)_8]_2Eu_2[$*i*-$BiPc(SC_2H_5)_{12}]$ (**Pc-1@Pc-2**), and $[Pc(SC_4H_9)_8]_4Eu_4[BiPc(SC_2H_5)_{12}]$ (**Pc-2@Pc-2**). ($[Pc(SC_4H_9)_8]$ = 2,3,9,10,16,17,23,24-octakis(ethylthio)-phthalocyanine, $BiPc(SC_2H_5)_{12}$ = bis[7,8,12,13,17,18-hexakis(ethylthio)tribenzo[g,l,q]-5,10,15,20-tetraazaporphyrinate [b,e]benzene-linked binuclear phthalocyaninate]), Scheme 1. The influence of the extending π-systems on the molecular redox potentials, conductivity, and gas sensing properties have been compared. The self-assembled films of the five compounds prepared by a solution-processed quasi-Langmuir-Shäfer (QLS) method were analyzed by UV–vis absorption spectra (UV–vis), X-ray diffraction (XRD), scanning electron microscope (SEM), and current-voltage (I–V) measurements. The redox potentials, energy gaps of the frontier electronic states, thin film microstructure/morphology, and molecular aggregation pattern in the QLS films of the five ambipolar semiconductors are systematically studied to comprehend the changes in sensing performance.

2. Experimental

2.1. Materials

1,8-Diazabicyclo[5.4.0]undec-7-ene (DBU), anhydrous 1,2,4-trichlorobenzene (TCB), and ethyl mercaptan were purchased from Aldrich. The compounds of $Eu(acac)_3{\cdot}H_2O$, 4,5-bisethylthio-1,2-dicyanobenzene were prepared according to the literature methods. CH_2Cl_2 for DPV studies was freshly distilled from CaH_2 under nitrogen. n-pentanol was distilled from sodium. All other reagents and solvents were of reagent grade and used as received without further purification. Column chromatography was carried out on silica gel (200–300 mesh) with the pure $CHCl_3$ as eluents.

2.2. Film preparation and measurement

The quasi-Langmuir-Shäfer (QLS) method [21] was employed to prepare the pristine QLS films for $Eu[Pc(SC_4H_9)_8]_2$ (**Pc-1**), $Eu_2[Pc(SC_4H_9)_8]_2$ (**Pc-2**), $[Pc(SC_4H_9)_8]_2Eu_2[BiPc(SC_2H_5)_{12}]$ (**Pc-1@Pc-1**), $[Pc(SC_4H_9)_8]_2Eu_2[BiPc(SC_2H_5)_{12}]$ (**Pc-1@Pc-2**), and $[Pc(SC_4H_9)_8]_4Eu_4[$*i*-$BiPc(SC_2H_5)_{12}]$ (**Pc-2@Pc-2**) according to the published procedure [22, 23]. The detailed procedures were presented on the section of film-preparation in Supplementary materials. MALDI-TOF mass spectra were recorded on the Bruker BIFLEX III ultra-high-resolution Fourier transform ion cyclotron resonance (FT-ICR) mass spectrometer with alpha-cyano-4-hudroxycinnamic acid as matrix. ^1H NMR spectrums were recorded on the Bruker DPX 400 spectrometer in $CDCl_3$. The spectra were referenced internally with residual $CDCl_3$ (δ 7.26) relative to SiMe$_4$. Electrochemical measurements were carried out with a CHI760D voltammetric analyser and for the detailed procedures please see our recently published papers [24]. UV–vis and polarized UV–vis absorption spectra were recorded with a Hitachi U-3900 spectrophotometer. X-ray diffraction (XRD) experiments were carried out on a Bruker D8 ADVANCE with a Cu anode as the primary x-ray beam source (λ = 1.5406 Å). Scanning electron microscopy (SEM) images were obtained using Quant 250FEG. Current-voltage (I–V) curves were collected at room temperature using a Keysight B2910A precision source/measure unit with an incorporated voltage range supplied from −10 V to 10 V. Conductivity (σ) obtained by I-V curve can be calculated according to the reported method reported in previous literature [23].

For characterizations, three kinds of substrates (SiO_2/Si, quartz, and ITO) were washed by deionized water, absolute ethyl alcohol, and dichloromethane, respectively. Films were deposited on different substrates by using QLS self-assembly method [22].

2.3. Synthesis details of *Pc-1*, *Pc-2*, *Pc-1@Pc-1*, *Pc-1@Pc-2*, *Pc-2@Pc-2*

$H_2Pc(SC_4H_9)_8$: 4,5-Bis(ethylthio)-1,2-dicyanobenzene (300 mg) was put in a micro reactor, the air was pumped out, and then nitrogen was purged. This process was repeated for three times (every 5 min). After this 3 mL dehydrated n-butanol as solvent and 5–6 drops of DBU were added. The reactor was then heated up to 140 °C and stirred for 10 h under N_2 protection. After the reaction was stopped, the product was recrystallized using a large amount of CH_3OH at room temperature for 5–6 h, then filtered. This step was repeated for five times to obtain a dark green solid. Yield: 200 mg (79%).

Eu[Pc(SC$_4$H$_9$)$_8$]$_2$ (Pc-1): $H_2Pc(SC_4H_9)_8$ (100 mg) and $Eu(acac)_3{\cdot}nH_2O$ (38.4 mg) were put in micro reactor, the air was pumped out, and then nitrogen was purged. This process was repeated for three times (every 5 min). After this 2 mL dehydrated n-pentanol as solvent and 5–6 drops of DBU were added. The reactor was then heated up to 180 °C and stirred for 8 h under N_2 protection. After the reaction was stopped, the product was recrystallized using a large amount of CH_3OH at room temperature for 5–6 h, then filtered. The residue left was chromatographed on a silica gel column with $CHCl_3$ as eluent. Recrystallization from $CHCl_3$ and methanol gave dark green powder. Yield: 86 mg (65%).

Eu$_2$[Pc(SC$_4$H$_9$)$_8$]$_2$ (Pc-2): $Eu[Pc(SC_4H_9)_8]_2$ (100 mg), $H_2Pc(SC_4H_9)_8$ (93 mg), and $Eu(acac)_3{\cdot}nH_2O$ (31.6 mg) were put in micro reactor, the air was pumped out, and then nitrogen was purged. This process was repeated for three times (every 5 min). After this 2 mL TCB as solvent and 5–6 drops of DBU $H_2Pc(SC_4H_9)_8$ were added. The reactor was then heated up to 210 °C and stirred for 8 h under N_2 protection. After the reaction was stopped, the product was recrystallized using a large amount of CH_3OH at room temperature for 5–6 h, then filtered. The residue left was chromatographed on a silica gel column with $CHCl_3$ as eluent. Recrystallization from $CHCl_3$ and methanol gave dark green powder. Yield: 50 mg (24.8%).

[Pc(SC$_4$H$_9$)$_8$]$_2$Eu$_2$[BiPc(SC$_2$H$_5$)$_{12}$] (Pc-1@Pc-1): $[Pc(SC_4H_9)_8]_2Eu_2[$*i*-$BiPc(SC_2H_5)_{12}]$ (150 mg), $H_2Pc(SC_2H_5)_8$ (56.6 mg), and $Eu(acac)_3{\cdot}nH_2O$ (34.1 mg) were put in micro reactor, the air was pumped out, and then nitrogen was purged. This process was repeated for three times (every 5 min). After this 3 mL TCB as solvent and 5–6 drops of DBU were added. The reactor was then heated up to 210 °C, stirred for 9 h under reflux, and protected with N_2 during the period. After the reaction was stopped, the product was recrystallized using a large amount of CH_3OH at room temperature for 5–6 h, then filtered. The residue left was chromatographed on a silica gel column with $CHCl_3$ as eluent. Recrystallization from $CHCl_3$ and methanol gave dark green powder. Yield: 7.0 mg (5.2%).

[Pc(SC$_4$H$_9$)$_8$]$_2$Eu$_2$[BiPc(SC$_2$H$_5$)$_{12}$] (Pc-1@Pc-2): $[Pc(SC_4H_9)_8]_2Eu_2[$*i*-$BiPc(SC_2H_5)_{12}]$ (150 mg), $H_2Pc(SC_2H_5)_8$ (56.6 mg) and $Eu(acac)_3{\cdot}nH_2O$ (34.1 mg) were put in micro reactor, the air was pumped out, and then nitrogen was purged. This process was repeated for three times (every 5 min). After this 3 mL TCB as solvent and 5–6 drops of DBU were added. The reactor was then heated up to 210 °C, stirred for 9 h under reflux, and protected with N_2 during the period. After the reaction was stopped, the product was recrystallized using a large amount of CH_3OH at room temperature for 5–6 h, then filtered. The residue left was chromatographed on a silica gel column with $CHCl_3$ as eluent. Recrystallization from $CHCl_3$ and methanol gave dark green powder. Yield: 6.0 mg (5%).

2.4. Gas sensing test

The films of five compounds were tested in a cuboid Teflon sensor chamber (about 30 cm^3 as internal volume). The desired NO_2, NH_3, H_2S, or CO_2 concentration was produced by diluting a mixture of NO_2/air (20 ppm NO_2, from Qingdao Ludong Gas., Ltd, China), NH_3/air (500 ppm NH_3, from Qingdao Ludong Gas., Ltd, China), H_2S/air (50 ppm H_2S, from Qingdao Ludong Gas., Ltd, China), or CO_2 (20 ppm CO_2, from Qingdao Ludong Gas., Ltd, China) with dry air using two CS200 Mass Flow Controllers. Total flows were 0.1 L min^{-1} for NO_2 or NH_3 and 2 L min^{-1} for diluent gas air, respectively. All tests were first exposed to synthetic air, followed by exposure to NO_2, NH_3, H_2S, or CO_2 gas at various concentrations, and the relative humidity is controlled at 0% (dry synthetic air), 35%, and 70%, respectively. In order to quantitatively analyze the sensor responses, the percent current change was calculated using the formula of $[(I_0-I_f)/I_0] \times 100$, where I_0 is the initial current for each of exposure/recovery cycle and I_f is the current at the end of each exposure period. On the other hand, for gas sensing experiments, the samples were constantly polarized at 5 V.

3. Results and discussion

3.1. Design, synthesis and characterizations

The symmetrical ethylthio-substituted europium bis- and tris-phthalocyanines $Eu[Pc(SC_2H_5)_8]_2$ (**Pc-1**), $Eu_2[Pc(SC_2H_5)_8]_3$ (**Pc-2**), and their dimers combined with double- and/or triple-decker units via an edge-to-edge mode by a fusing benzene ring, $[Pc(SC_2H_5)_8]_2Eu_2[BiPc(SC_2H_5)_{12}]$ (**Pc-1@Pc-1**), $[Pc(SC_2H_5)_8]_2Eu_2[BiPc(SC_2H_5)_{12}]$ (**Pc-1@Pc-2**), and $[Pc(SC_2H_5)_8]_4Eu_4[BiPc(SC_2H_5)_{12}]$ (**Pc-2@Pc-2**) were successfully synthesized. The detailed synthesis procedures together with the structure characterization are described in the experimental section. An extended π-conjugated electronic/molecular structure can adjust the intra-/inter-molecular interactions, and thus the molecular orbital energies, resulting in gas sensing changes [26]. Adding ethylthio groups onto the periphery of phthalocyanine rings is expected to improve the solubility of the five compounds in conventional organic solvents. The MALDI-TOF mass spectra of the five compounds show intense molecular

Table 1
Half-wave redox potentials (V vs SCE) in CH_2Cl_2 containing 0.1 mol L^{-1} $[Bu_4N][ClO_4]$ together with the HOMO and LUMO levels of **Pc-1**, **Pc-2**, **Pc-1@Pc-1**, **Pc-1@Pc-2** and **Pc-2@Pc-2**.

Compounds	Red_4 (V)	Red_4 (V)	Red_3 (V)	Red_2 (V)	Red_1 (V)	Oxd_1 (V)	Oxd_2 (V)	Oxd_3 (V)	Oxd_4 (V)	LUMO(eV)	HOMO(eV)	$\Delta E^{1}_{1/2}$ (V)[a]
Pc-1	–	−1.927	−1.554	−1.145	−0.134	0.260	–	–	–	−3.295[b]	−4.306[b]	0.394
Pc-2	–	–	–	−1.226	−0.735	0.236	0.515	0.920	1.050	−3.705[c]	−4.676[c]	0.971
Pc-1@Pc-1	−1.775	−1.610	−1.210	−0.255	−0.110	0.235	0.460	–	–	−3.230[c]	−4.330[c]	0.345
Pc-1@Pc-2	–	–	–	−0.852	−0.218	0.193	0.400	0.660	–	−3.588[b]	−4.222[c]	0.411
Pc-2@Pc-2	–	–	–	–	−0.762	0.148	0.305	0.504	0.664	−3.678[c]	−4.588[c]	0.910

[a] $\Delta E^{1}_{1/2}$(V) = = Oxd_1 − Red_1.
[b] HOMO = −(Red_1+4.44 eV); and LUMO = −(Red_4+4.44 eV) [18].
[c] HOMO = −(Oxd_1+4.44 eV); and LUMO = −(Red_1+4.44 eV) [7].
[d] HOMO = −(Red_1+4.44 eV); and LUMO = −(Red_4+4.44 eV) [9].

ion M$^+$ signals, Fig. S31 and Table S1. The five compounds were also characterized by ^1H NMR spectra with corresponding data summarized in Fig. S2† and Table S2†.

3.2. Electrochemical properties

The electrochemical behaviors of five sandwich complexes were investigated by differential pulse voltammetry (DPV) in CH_2Cl_2. The values of half-wave redox potential *vs* SCE are summarized in Table 1. These compounds exhibit the highly electrochemical behavior typical of the sandwich rare earth (III) phthalocyanines [13,27], with one to four quasi reversible one-electron oxidation(s) (labelled as Oxd_1–Oxd_4) and one to five quasi reversible one-electron reduction(s) (Red_1–Red_5) within the electrochemical window of CH_2Cl_2, Fig. S3†. All of these processes correspond to consecutive removal of electron from or addition to the Pc-based molecular orbitals since the oxidation/reduction of the central europium cation in these complexes does not occur in this electrochemical test window [28]. The five compounds show reversible oxidation and reduction waves, indicating the remarkable stability of the cationic and anionic species of these π-conjugated skeletons [29]. The effects of extended π-conjugate systems and the number of unpaired electrons in sandwich-type phthalocyaninato europium compounds are clearly disclosed by the changes in the half-wave potentials of the first oxidation (Oxd_1) and first reduction (Red_1), together with their difference ($\Delta E^{1}_{1/2}$ = Oxd_1−Red_1, defined as the energy gap), of five kinds of sandwich phthalocyanine derivatives. As can be seen from Table 1 and Fig. S3†, extending the π-conjugated systems in the longitudinal and transverse directions of Pc macrocycles induces the first oxidation potential (Oxd_1) successively and gradually shifts toward the negative direction from **Pc-1** (0.260 V), **Pc-2** (0.236 V), **Pc-1@Pc-1** (0.235 V) **Pc-1@Pc-2** (0.193 V), to **Pc-2@Pc-2** (0.148 V), respectively. The lower the Oxd_1, the more susceptible the compound to oxidation. Consequently, **Pc-2@Pc-2** with maximum degree of conjugation exhibits the lowest Oxd_1 among the five compounds and therefore is the easiest one to be oxidized. Furthermore, both the conjugation degree and the number of free radical unit are crucial in determining the first reduction potentials of the five compounds. As can be seen, the increase in the conjugation degree also induces a negative shift for the first reduction (Red_1) from **Pc-2** (−0.735 V) to **Pc-2@Pc-2** (−0.762 V), and from **Pc-1** (−0.134 V), to **Pc-1@Pc-2** (−0.218 V), which makes **Pc-2@Pc-2** and **Pc-1@Pc-2** harder to be reduced than the original **Pc-2** and **Pc-1**, respectively. With an unpaired electron (so called as free radical) locating at the frontier molecular orbital of double-decker **Pc-1** unit [30], **Pc-1@Pc-1** exhibits the highest Red_1 (−0.110 V) among the five compounds. Consequently, tuning orbital energies in sandwich-type phthalocyaninato europium (III) semiconductors is successfully achieved by extending the 2D conjugate systems of sandwich-type phthalocyanines. Furthermore, the unusually small energy gaps ($\Delta E^{1}_{1/2}$) of the set **Pc-1** (0.394 V), **Pc-1@Pc-1** (0.345 V), and **Pc-1@Pc-2** (0.411 V) also indicate their radical nature [28,31] compared to those for the non-radical **Pc-2** (0.971 V) and **Pc-2@Pc-2** (0.910 V). It is worth noting that the energy gaps for all these compounds are also far smaller than the room temperature bandgap of silicon, 1.1 eV [32], suggesting the good intrinsic semiconducting nature of the five sandwich-type Pc-based compounds. As a result, the highest occupied molecular orbital (HOMO) and the lowest unoccupied molecular orbital (LUMO) energy levels were estimated to be −4.306 and −3.295 eV for **Pc-1**, −4.676 and −3.705 eV for **Pc-2**, −4.330 and −3.230 eV for **Pc-1@Pc-1**, −4.222 and −3.588 eV for **Pc-1@Pc-2**, and −4.588 and −3.678 eV for **Pc-2@Pc-2**, respectively [13,16]. Consequently, the five compounds have HOMOs ranging from −4.306 to −4.676 eV and LUMOs ranging from −3.230 to −3.705 eV, which fall under the energy range required for ambipolar organic semiconductors [33], revealing the potential of the five compounds in ambipolar sensing devices.

3.3. Film microstructures and morphologies

The self-assembled films of the five compounds were obtained by a solution-based quasi-Langmuir-Shäfer (QLS) method [21]. UV–vis absorption spectra of the five compounds in both solution and the films are shown in Fig. 1 and their corresponding absorption maxima are compared in Table S3†. Similar to those reported for related sandwich rare earth phthalocyanines [13,34,35], the spectra in $CHCl_3$ solution show the intense Soret bands in the range of 316–388 nm and a Q-band at the 710, 669, 699, 684, and 689 nm for **Pc-1**, **Pc-2**, **Pc-1@Pc-1**, **Pc-1@Pc-2**, and **Pc-2@Pc-2**, respectively, attributed to the π-π* transitions. Obviously, compared with that of double-decker **Pc-1** in solution, the main Q-bands of **Pc-2**, **Pc-1@Pc-1**, **Pc-1@Pc-2**, and **Pc-2@Pc-2** in solution take blue-shifts dramatically by 41, 11, 26, and 21 nm, respectively. These results reveal an enhanced intramolecular π-π interaction between the Pc rings in the order of **Pc-2** > **Pc-1@Pc-2** > **Pc-2@Pc-2** > **Pc-1@Pc-1** > **Pc-1**. Note that the peaks found in the 572–585 nm region for **Pc-1**, **Pc-1@Pc-1**, and **Pc-1@Pc-2** are associated with the free radical structures of bis(phthalocyaninato) rare earth double-deckers having a semi-occupied HOMO orbital [13,36].

Interestingly, in the QLS film, the main Q absorption band of the double-decker **Pc-1** with a smallest intramolecular π-π interaction in solution (*i.e.* a non-aggregated state) blue-shifts to 687 nm, indicating the formation of *H*-type aggregation in the self-assembled film resulting from the strong intermolecular π-π interaction between **Pc-1** molecules [37]. However, as for other four sandwich-type compounds with the larger π-conjugate systems than **Pc-1**, their main Q bands assigned for the phthalocyanine ligands in the QLS films are all red shifted relative to those in solution, indicating the formation of *J*-type aggregation according to exciton theory [37] and published results previously [20, 38–40]. However, the red-shift of Q bands in the QLS films of other four compounds is different, showing a dependence on the number of the phthalocyanine ligands (or the size of molecules). For instance, in the QLS films, the main Q band is red-shifted by 23, 8, 11, and 5 nm for **Pc-2**, **Pc-1@Pc-1**, **Pc-1@Pc-2**, and **Pc-2@Pc-2**, Fig. 1 and Table S3†, leading to the red-shift degree decreasing in the order of **Pc-2** > **Pc-1@Pc-2** > **Pc-1@Pc-1** > **Pc-2@Pc-2** in the QLS films and thus declined intermolecular interactions in the same order. Among the above four compounds that take the *J*-type aggregation in the film, **Pc-2@Pc-2** with a largest

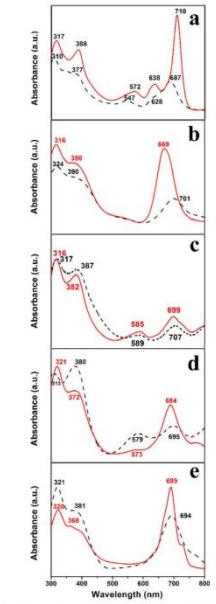

Fig. 1. UV–*vis* absorption spectra of compounds **Pc-1** (a), **Pc-2** (b), **Pc-1@Pc-1** (c), **Pc-1@Pc-2** (d) and **Pc-2@Pc-2** (e) in $CHCl_3$ solution (solid line) and their pure QLS films (dash line).

After the reaction was stopped, the product was recrystallized using a large amount of CH_3OH at room temperature for 5–6 h, then filtered. The residue left was chromatographed on a silica gel column with $CHCl_3$ as eluent. Recrystallization from $CHCl_3$ and methanol gave dark green powder. Yield: 107 mg (24.8%).

[Pc(SC$_4$H$_9$)$_8$]$_2$Eu$_2$[BiPc(SC$_2$H$_5$)$_{12}$] (Pc-1@Pc-2): $[Pc(SC_4H_9)_8]_2Eu_2[$*i*-$BiPc(SC_2H_5)_{12}]$ (150 mg), $H_2Pc(SC_2H_5)_8$ (56.6 mg), and $Eu(acac)_3{\cdot}nH_2O$ (34.1 mg) were put in micro reactor, the air was pumped out, and then nitrogen was purged. This process was repeated for three times (every 5 min). After this 3 mL TCB as solvent and 5–6 drops of DBU were added. The reactor was then heated up to 210 °C, stirred for 9 h under reflux, and protected with N_2 during the period. After the reaction was stopped, the product was recrystallized using a large amount of CH_3OH at room temperature for 5–6 h, then filtered. The residue left was chromatographed on a silica gel column with $CHCl_3$ as eluent. Recrystallization from $CHCl_3$ and methanol gave dark green powder. Yield: 7.0 mg (5.2%).

[Pc(SC$_4$H$_9$)$_8$]$_2$Eu$_2$[BiPc(SC$_2$H$_5$)$_{12}$] (Pc-2@Pc-2): $[Pc(SC_4H_9)_8]_2Eu_2[$*i*-$BiPc(SC_2H_5)_{12}]$ (150 mg), $H_2Pc(SC_2H_5)_8$ (56.6 mg) and $Eu(acac)_3{\cdot}nH_2O$ (34.1 mg) were put in micro reactor, the air was pumped out, and then nitrogen was purged. This process was repeated for three times (every 5 min). After this 3 mL TCB as solvent and 5–6 drops of DBU were added. The reactor was then heated up to 210 °C, stirred for 9 h under reflux, and protected with N_2 during the period. After the reaction was stopped, the product was recrystallized using a large amount of CH_3OH at room temperature for 5–6 h, then filtered. The residue left was chromatographed on a silica gel column with $CHCl_3$ as eluent. Recrystallization from $CHCl_3$ and methanol gave dark green powder. Yield: 6.0 mg (5%).

The films of five compounds were tested in a cuboid Teflon sensor chamber (about 30 cm^3 as internal volume). The desired NO_2, NH_3, H_2S, or CO_2 concentration was produced by diluting a mixture of NO_2/air (20 ppm NO_2, from Qingdao Ludong Gas., Ltd, China), NH_3/air (500 ppm NH_3, from Qingdao Ludong Gas., Ltd, China), H_2S/air (50 ppm H_2S, from Qingdao Ludong Gas., Ltd, China), or CO_2 (20 ppm CO_2, from Qingdao Ludong Gas., Ltd, China) with dry air using two CS200 Mass Flow Controllers. Total flows were 0.1 L min^{-1} for NO_2 or NH_3 and 2 L min^{-1} for diluent gas air, respectively. All tests were first exposed to synthetic air, followed by exposure to NO_2, NH_3, H_2S, or CO_2 gas at various concentrations, and the relative humidity is controlled at 0% (dry synthetic air), 35%, and 70%, respectively. In order to quantitatively analyze the sensor responses, the percent current change was calculated using the formula of $[(I_0-I_f)/I_0] \times 100$, where I_0 is the initial current for each of exposure/recovery cycle and I_f is the current at the end of each exposure period. On the other hand, for gas sensing experiments, the samples were constantly polarized at 5 V.

3. Results and discussion

3.1. Design, synthesis and characterizations

The symmetrical ethylthio-substituted europium bis- and tris-phthalocyanines $Eu[Pc(SC_2H_5)_8]_2$ (**Pc-1**), $Eu_2[Pc(SC_2H_5)_8]_3$ (**Pc-2**), and their dimers combined with double- and/or triple-decker units via an edge-to-edge mode by a fusing benzene ring, $[Pc(SC_2H_5)_8]_2Eu_2[BiPc(SC_2H_5)_{12}]$ (**Pc-1@Pc-1**), $[Pc(SC_2H_5)_8]_2Eu_2[BiPc(SC_2H_5)_{12}]$ (**Pc-1@Pc-2**), and $[Pc(SC_2H_5)_8]_4Eu_4[BiPc(SC_2H_5)_{12}]$ (**Pc-2@Pc-2**) were successfully synthesized. The detailed synthesis procedures together with the structure characterization are described in the experimental section. An extended π-conjugated electronic/molecular structure can adjust the intra-/inter-molecular interactions, and thus the molecular orbital energies, resulting in gas sensing changes [26]. Adding ethylthio groups onto the periphery of phthalocyanine rings is expected to improve the solubility of the five compounds in conventional organic solvents. The MALDI-TOF mass spectra of the five compounds show intense molecular

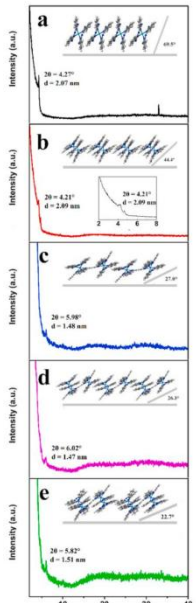

Fig. 2. The X-ray diffraction patterns of the QLS film of **Pc-1** (a), **Pc-2** (b), **Pc-1@Pc-1** (c), **Pc-1@Pc-2** (d) and **Pc-2@Pc-2** (e).

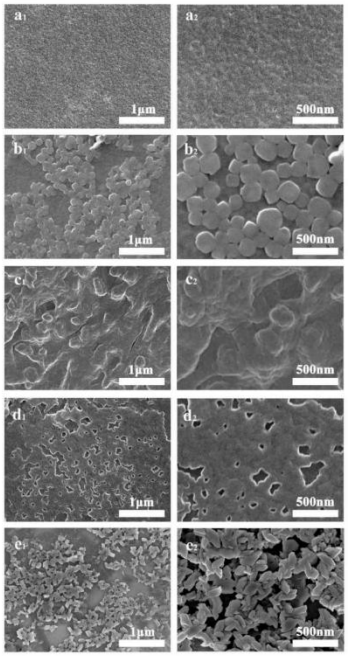

Fig. 3. SEM images for the films of **Pc-1** (a_1 and a_2), **Pc-2** (b_1 and b_2), **Pc-1@Pc-1** (c_1 and c_2), **Pc-1@Pc-2** (d_1 and d_2) and **Pc-2@Pc-2** (e_1 and e_2).

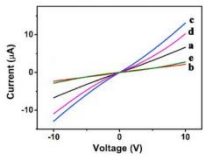

Fig. 4. I-V curves measured on the QLS films of the **Pc-1** (a), **Pc-2** (b), **Pc-1@Pc-1** (c), **Pc-1@Pc-2** (d) and **Pc-2@Pc-2** (e).

molecular backbone exhibits the smallest red-shift, while **Pc-2** with a smallest molecular backbone shows a largest red-shift. These results suggest that larger molecular backbones hinder the effective packing of sandwich phthalocyanine molecules along an *edge-to-edge* molecular stacking direction.

Furthermore, the orientation angles of the phthalocyanine ring with respect to the substrate in the QLS films of the five compounds were estimated to be ca. 69.1° for **Pc-1**, 44.1° for **Pc-2**, 25.6° for **Pc-1@Pc-1**, 24.9° for **Pc-1@Pc-2**, and 23.1° for **Pc-2@Pc-2**, respectively, by using a polarized UV–vis technique according to a literature method [7,22] (Fig. S4† and Table S4†), confirming that only **Pc-1** employs the *H*-type molecular stacking mode with a "face-to-face" orientation for the phthalocyanine molecules in the film and the other four compounds are of the *J*-type molecular stacking mode with an "edge-on" orientation for the phthalocyanine molecules in the film [41].

X-ray diffraction (XRD) patterns of the five kinds of films are shown in Fig. 2. In the low angle range ($2\theta = 2.6$–$9°$), the five films exhibit the (001) Bragg peak at $2\theta = 4.27°$, 4.21°, 5.98°, 6.02°, and 5.82°, respectively, corresponding to a periodic spacing distance of 2.07 nm, 2.09 nm, 1.47 nm, 1.48 nm, and 1.51 nm for **Pc-1**, **Pc-2**, **Pc-1@Pc-1**, **Pc-1@Pc-2**, and **Pc-2@Pc-2**, respectively, suggesting a regular layered structure exists in these films. Consequently, orientation angles of Pc rings with respect to the substrate surface of ca. 69.5°, 44.4°, 27.0°, 26.3°, and 22.7° are estimated for the respective films of **Pc-1**, **Pc-2**, **Pc-1@Pc-1**, **Pc-1@Pc-2**, and **Pc-2@Pc-2** based on their simulated molecular diagonal dimensions combined with the low-angle XRD results. These results are in good accordance with the calculated ones from the polarized UV–*vis* analysis of the films, further confirming the formation of *H*-aggregates for **Pc-1** and *J*-aggregates for the other four compounds **Pc-2**–**Pc-2@Pc-2** in the films. It is worth noting that along with the increase of conjugated systems, the angle between molecules and the substrate becomes smaller. This is in line with the results of the above-mentioned UV–vis analysis.

The SEM observation discloses the surface morphology change for the QLS films of the five compounds, Fig. 3. As can been seen from Fig. $3a_1$-$3a_2$, *H*-type aggregates in the **Pc-1** film show a fine film-structure containing uniformed nanoparticles distributed on the film-surface. The largest intermolecular interaction among the present *J*-type aggregates results in the uniformed disk-like nanoparticles with 200–300 nm in diameter on the surface of **Pc-2** film, Fig. $3b_1$-b_2. Further extending the π conjugate systems from **Pc-1@Pc-1** to **Pc-1@Pc-2** makes the formation of micro-sheets with an increased size depending on a slight increased intermolecular interaction from the former to the latter, Fig. $3c_1$-c_2 and Fig. $3d_1$-d_2. Furthermore, with the largest conjugate system and the smallest intermolecular interaction among the four kinds of the *J*-aggregates, **Pc-2@Pc-2** film displays the smallest uniformed nano-sheets with about 50 nm in width and 100–200 nm in length, Fig. $3e_1$-e_2. This unambiguously confirms that micro/nano-structures of the films including morphology and dimension are determined by the combination between molecular structure, patterns of molecular aggregation, and degree of intermolecular interaction.

3.4. Electrical and sensing properties

By means of the current-voltage (I–V) measurements, Fig. 4, the electronic conductivity of the **Pc-1**, **Pc-2**, **Pc-1@Pc-1**, **Pc-1@Pc-2** and **Pc-2@Pc-2** film is estimated to be about 2.02×10^{-4} S cm^{-1}, 6.00×10^{-5} S cm^{-1}, 3.64×10^{-4} S cm^{-1}, 3.42×10^{-4} S cm^{-1}, and 8.86×10^{-5} S cm^{-1}, respectively (it is noteworthy that the experiments were repeated for more than three times on different pieces of films) [21,25]. The results show that the films of all the five compounds are excellent semiconductors with the conductivity in the order of **Pc-1@Pc-1** > **Pc-1@Pc-2** > **Pc-1** > **Pc-2@Pc-2** > **Pc-2**. Apparently, the radical **Pc-1@Pc-1**, **Pc-1@Pc-2**, and **Pc-1** films exhibit higher intrinsic solid state conductivity on the order of 10^{-4} S cm^{-1}, compared to those for non-radical **Pc-2@Pc-2** and **Pc-2** films. The high conductivities of the set **Pc-1@Pc-1**, **Pc-1@Pc-2**, and **Pc-1** mostly result from the high densities of charge carriers induced by their small energy gaps ($\Delta E^{el}_{1/2}$ = 0.345, 0.411 and 0.394 V for **Pc-1@Pc-1**, **Pc-1@Pc-2** and **Pc-1**, respectively) [13,42]. While the large energy gaps ($\Delta E^{el}_{1/2}$) of **Pc-2@Pc-2** (0.910 V) and **Pc-2** (0.971 V) correspond to lower conductivities of the two non-radical semiconductors relative to those for the radical semiconductors. Consequently, a close correlation between the conductivity (σ) and energy gap (i.e. $\Delta E^{el}_{1/2}$) is revealed as follow: the smaller the energy gap in the frontier molecular orbital of the sandwich-type phthalocyanine-based semiconductor, the greater the conductivity. However, in comparison with the conductivity (2.02×10^{-4} S cm^{-1}) and energy gap (0.394 V) of **Pc-1**, indeed higher conductivity (3.42×10^{-4} S cm^{-1}) was obtained for **Pc-1@Pc-2** with a slightly larger energy gap of 0.411 V. At the first glance, it seems to contradict with the above "σ-$\Delta E^{el}_{1/2}$" relationship. However, it could be justified on the basis of the formation of different aggregates in the QLS films with red-shifted *J*-type absorption bands revealed for **Pc-1@Pc-2** and blue-shifted *H*-type absorption bands revealed for **Pc-1** [43–45]. The red-shift of all the absorption bands in thin solid film makes the energy gap of **Pc-1@Pc-2** appearing at lower wavelengths and thus $\Delta E^{el}_{1/2}$ in the film is expected to get smaller than that in solution. In good contrast, $\Delta E^{el}_{1/2}$ of **Pc-1** should be larger in the film than in solution depending on the blue-shifted absorptions in the solid state aggregates. As a result, a lower $\Delta E^{el}_{1/2}$ in the film should be achieved for **Pc-1@Pc-2** relative to that of **Pc-1** depending on the solid state stacking effect. Therefore, the conductivity is mainly governed by the energy gap (i.e. $\Delta E^{el}_{1/2}$) in addition to the solid state stacking effect for the sandwich-type phthalocyanine semiconductors.

To evaluate the gas sensing properties, the QLS films of the five compounds deposited onto the ITO interdigital electrodes/glass substrates were studied against NO_2 in the concentration range of 100–300 ppb, diluted with dry synthetic air at room temperature (24–26 °C). The sensing performance was controlled by a duty cycle with a constant dynamic exposure period of 2 min. And the corresponding recovery time, that is defined as the time required for the current recovering from I_{gas} to (95–99% × I_{air} [46], varied from 1.2 to 35 min. Accordingly, recovery time varied depending on the concentration of the analyte [47]. Fig. $5a_1$-e_1 show the responses of the five kinds of films to NO_2 (i.e., an oxidizing gas) with an increase in their electrical resistance, demonstrating the *n*-type transport behavior of all the five compounds. This agrees with our previous studies on sandwich-type phthalocyaninato complexes [11,13,20,26]. The response (i.e. $(I_f\text{-}I_g)/I_g$) for the QLS films of the five compounds increases when exposed to NO_2 from 100 to 300 ppb in a linear manner with $R^2 \geq 0.96$, Fig. $5a_2$-e_2. As a consequence, such films can be used to quantitatively analyze the concentration of NO_2. Furthermore, the response for each concentration gradually increases in the order of **Pc-1** < **Pc-2** < **Pc-1@Pc-1** <

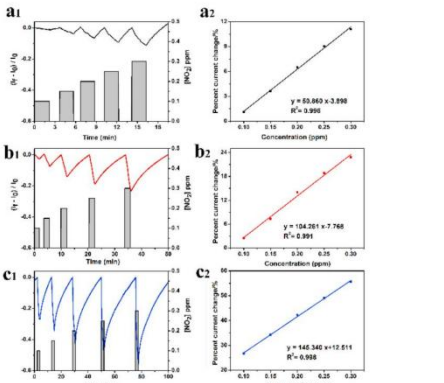

Fig. 5. The time-dependent current plots of film **Pc-1** (a_1), **Pc-2** (b_1), **Pc-1@Pc-1** (c_1), **Pc-1@Pc-2** (d_1) and **Pc-2@Pc-2** (e_1) and the corresponding sensor response varies linearly with different NO_2 concentration (a_2, b_2, c_2, d_2 and e_2).

Table 2
Sensitivity data for films of **Pc-1**−**Pc-2@Pc-2** in different detective ranges of NO_2 and NH_3.

Gas	Compound	Sensitivity (ppm^{-1})	LOD (ppm)	Response
NO_2 0.1–0.3 (ppm)	Pc-1	0.509	0.01	*n*-type
	Pc-2	1.043	0.01	
	PC-1@PC-1	1.453	0.01	
	PC-1@PC-2	1.902	0.04	
	PC-2@PC-2	2.082	0.01	
NH_3 4.0–8.6 (ppm)	Pc-1	0.0047	0.4	*p*-type
	Pc-2	0.0097	0.8	
	PC-1@PC-1	0.0059	0.5	
	PC-1@PC-2	0.0043	0.6	
	PC-2@PC-2	0.0087	0.7	

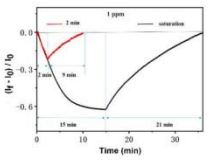

Fig. 6. The response of the devices for **Pc-2@Pc-2** under 1 ppm NO_2 exposure.

Pc-1@Pc-2 < **Pc-2@Pc-2**, with a slope (in ppm^{-1}) of 0.509, 1.043, 1.453, 1.902, and 2.082, respectively, Table 2. This order in sensitivity, matches well with the declined trend in the first oxidation potential ($Ox1_2$) for the five compounds, Table 1. As shown previously, the lower the $Ox1_2$, the easier the compound to be oxidized, and the higher the sensitivity of NO_2 detection. Consequently, $Ox1_2$ plays a crucial role in the sensitivities toward oxidative NO_2 for the five sandwich-type phthalocyaninato semiconductors. Comparing the sensor responses of the five semiconductors examined in this study, the largest π-conjugated molecular structure of **Pc-2@Pc-2** induces the lowest $Ox1_2$, achieving the highest sensitivity, which is more than 4 times higher than that of **Pc-1**. With the gradual extension of the π-conjugated molecular structures from **Pc-1**, **Pc-2**, **Pc-1@Pc-1**, **Pc-1@Pc-2**, to **Pc-2@Pc-2**, their sensitivities to the detection of NO_2 gas gets increased. This observation suggests that the sensitivity of the five sandwich-type phthalocyaninato semiconductors to NO_2 gas is mainly determined by their π-conjugated molecular structures rather than the intermolecular interactions in the films.

It should be noted that due to the limitations of our gas sensing measurement system, in order to obtain enough measurement period to reasonably evaluate the sensitivity of the sensors, a shorter dynamic exposure time of 2 min is adopted. Although a more sufficient exposure time than 2 min to reach the saturation region of the sensor response can exhibit a higher gas sensing response (for example, to 1 ppm NO_2, when the exposure time is 15 min, the response is significantly better than the 2 min exposure time), but the full recovery of the sensor becomes too slow (to 1 ppm NO_2 for 15 min its full recovery is 21 min), Fig. 6. In order to reduce recovery time, the primarily sensing response was examined by using 2-min doses at room temperature (24–26 °C).

It is worth noting that when the films of the five sandwich-type phthalocyaninato semiconductors are exposed to electron-donating NH_3 gas (4–8.6 ppm, step is 1.2 ppm), diluted with dry air (recovery period varied from 1 to 27.6 min), the positive response for all of the films was still observed, Fig. $7a_1$-e_1, indicating their *p*-type semiconducting behavior. Obviously, ambipolar (*n*- and *p*-type) responses towards oxidizing NO_2 and reducing NH_3 were discovered for the films of the five sandwich-type phthalocyaninato semiconductors. This is in line with the electrochemical measurement finding as mentioned above. Indeed, similar ambipolar responses have been found for the double-, triple-, and quadruple-decker sandwich phthalocyanines [18,22]. As can be seen in Fig. $7a_2$-e_2, a good linear correlation ($R^2 \geq 0.96$) was exhibited between the response and NH_3 concentrations with a slop of 0.0047, 0.0097, 0.0059, 0.0043, and 0.0087 ppm^{-1} for **Pc-1**, **Pc-2**, **Pc-1@Pc-1**, **Pc-1@Pc-2**, and **Pc-2@Pc-2**, respectively. The results show that both the first reduction (Red_1) and electronic structure have significant effect on the sensing characteristics for the five semiconductors. In the case of the three radical semiconductors, along with the gradually increase in Red_1 in the order of **Pc-1@Pc-2** (−0.218 V) < **Pc-1** (−0.134 V) < **Pc-1@Pc-1** (−0.110 V), the sensitivity to NH_3 increases in the same order of **Pc-1@Pc-2** (0.0043 ppm^{-1}) < **Pc-1** (0.0047 ppm^{-1}) < **Pc-1@Pc-1** (0.0059 ppm^{-1}), respectively. This is also true for the two non-radical semiconductors. A more positive Red_1 of **Pc-2** (−0.735 V) relative to **Pc-2@Pc-2** (−0.762 V) leads to a higher sensitivity of the former (0.0097 ppm^{-1}) than the latter (0.0087 ppm^{-1}). According to the previous experimental studies and density functional theory calculations on neutral radical lutetium bisphthalocyanine ($LuPc_2$), the unpaired electron on single molecular orbital of $LuPc_2$ is primarily of π-character that delocalizes over both macrocycles [48]. This should be also true for the neutral radical **Pc-1**, **Pc-1@Pc-1**, and **Pc-1@Pc-2**. Since both macrocycles of the radical rare earth bisphthalocyanines (i.e. **Pc-1** unit in the present case) bring negative charge from the unpaired electron on single molecular orbital, it counters productive to adsorb the negative charge-possessing N atom in NH_3. This should be responsible for the lower sensitivities to electron-donating NH_3 for the radical **Pc-1**, **Pc-1@Pc-1**, and **Pc-1@Pc-2** relative to that of non-radical **Pc-2** although the higher charge transfer ability (or conductivity) and Red_1 are revealed for the radical **Pc-1**, **Pc-1@Pc-1**, and **Pc-1@Pc-2** than the non-radical **Pc-2**.

On the other hand, the limit of detection (LOD) is also a crucial index for sensors, since trace concentrations of pollution gases that can lead to long-term environmental issues are more difficult to detect. The LOD of the five semiconductors to both NO_2 and NH_3 can be obtained from the sensitivity fitting curve when signal/noise equals to 3,[46,49] see Fig. $5a_2$-e_2 and $7a_2$-e_2, the details are shown in Supplementary materials. The calculated LOD values are down to 10–40 ppb and 0.48–0.89 ppm toward NO_2 and NH_3, respectively, for the films of the five ambipolar semiconductors, Table 2. This represents the lowest LOD for room-temperature NO_2 and NH_3 sensors measured in dry air among the organic chemiresistors reported so far [16]. It is worth noting that the sensor performance in this work is as good as the best results reported in the previous literature (Table S5†), for example some heterojunctions of Cu(F_{16}Pc)/$LuPc_2$ [50], polyaniline/$LuPc_2$ or poly(2,5-dimethoxyaniline)/$LuPc_2$[51] consisting of two semiconducting layers obtained by a combination of electrodeposition with vacuum sublimation, but simpler solution-processed films with only one semiconducting layer were used in the present case.

Towards future practical application, the selectivity, reproducibility, and stability of the films to NO_2 and NH_3 gas are also evaluated. As shown in Fig. S5† and S6†, no obvious response was detected for the five semiconductors to the electron-donating H_2S (100–300 ppb) and oxidation gas CO_2 (100–300 ppb) due likely to their weaker electron-donating ability than NH_3. Meanwhile the quite good reproducibility and stability towards 100 ppb of NO_2 gas and 4 ppm of NH_3 gas are revealed after five cycling tests upon the 2 min exposure time, Fig. S7†

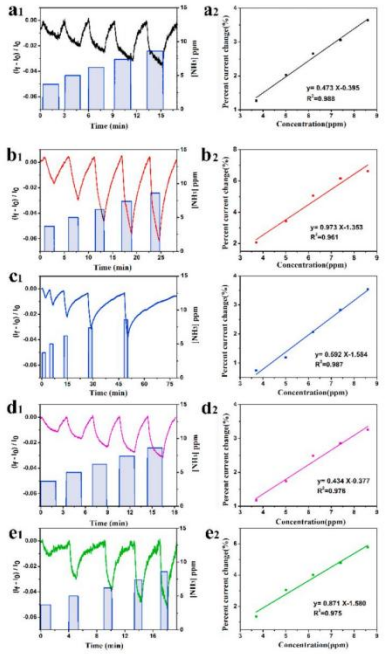

Fig. 7. The time-dependent current plots of film **Pc-1** (a_1), **Pc-2** (b_1), **Pc-1@Pc-1** (c_1), **Pc-1@Pc-2** (d_1) and **Pc-2@Pc-2** (e_1) and the corresponding sensor response varies linearly with different NH_3 concentration (a_2, b_2, c_2, d_2 and e_2).

and S8[7]. Furthermore, the effect of relative humidity (rh) on the relative response of **Pc-2@Pc-2** toward NO_2 and **Pc-2** toward NH_3 were also studied at 35% and 70% rh. This humidity range was chosen because the gas sensors operate within this broad humidity range in most of the practical applications. Representative response to 100 ppb NO_2 for **Pc-2@Pc-2** and to 4 ppm NH_3 for **Pc-2** is displayed in Fig. S9[7] and S10[7]. As can be seen from Fig. S9[7], toward 100 ppb NO_2, the relative response of **Pc-2@Pc-2** increases from 1.14 to 1.24 and 1.32 along with an increased rh value from 0% rh (i.e. dry synthetic air) to 35% rh and 70% rh, respectively. This is also true for the relative response of **Pc-2** to 4 ppm NH_3. As shown in Fig. S10[7], the response to NH_3 also increases along with the increased rh value due likely to an easier adsorption of NH_3 molecules on the surface of **Pc-2** film in a higher rh. And the recovery shows the slight dnift in the high humidity due probably to the traps caused by the infiltration of the H_2O. Impressively, it has been found that the behavior of **Pc-2** toward NH_3 as a *p*- or *n*-type device, depends on the humidity contained in the atmosphere with a *p*-type response at 0% rh and *n*-type at 35% and 70% rh. So rh variation has a significant effect on sensing performance. This can be attributed to the competitive absorption kinetics of H_2O and NH_3 at higher rh, suppressing the electronic effects of the gas molecules [14,52,53].

It is noteworthy that the detecting ranges of 4–8.6 ppm to NH_3 and 100–300 ppb to NO_2 in the present case well cover the range required for detection in industrial pollution discharge (~10 ppm NH_3) and indoor air quality standard (~117 ppb NO_2) in China. This fact in combination with their highly sensitive and reproducible responses and low LODs suggests the very promising potential in practical application for the present sensors, especially **Pc-2@Pc-2** NO_2 sensor and **Pc-2** NH_3 sensor.

4. Conclusions

In summary, by extending 2D conjugate systems of sandwich-type rare earth phthalocyanines, the redox potentials, in particular the first oxidation (Oxd_1), first reduction (Red_1), and energy gap ($\Delta E^S_{1/2}$) are successfully tuned for the five kinds of sandwich-type phthalocyaninato europium (III) anbipolar semiconductors. We have firstly demonstrated that the low first oxidation (Oxd_1), high first reduction (Red_1), and small energy gap ($\Delta E^S_{1/2}$) are the key factors for realizing highly sensitive NO_2 and NH_3 sensing as well as high conductivity, respectively, for the sandwich-type phthalocyaninato europium (III) ambipolar semiconductors. In particular, we produce the high-performance NO_2 and NH_3 organic chemiresistors with the QLS films of **Pc-2@Pc-2** and **Pc-2**, respectively. These devices show the high sensitivity, good reproducibility, nice selectivity, short response time, and low limit of detection to trace NO_2 and NH_3 gases present in dry air at room temperature (24–26 °C), representing the best performance achieved so far for solution-processed film of the organic chemiresistors. This work is truly helpful towards designing and fabricating new ambipolar phthalocyanine-based chemical sensors through extending π-conjugate systems of phthalocyanines with promising practical application potential.

Declaration of competing interest

The authors declare that they have no known competing financial interests or personal relationships that could have appeared to influence the work reported in this paper.

Acknowledgments

This work was supported by the National Natural Science Foundation of China (No.21771192), the Education Research Fund for Department of Heilongjiang Province (No.13521D201), the Scientific Research Project of Mudanjiang Normal University (No.GP201603), the Innovation and Entrepreneurship Project of Mudanjiang Normal University (No. CY2018008).

Appendix A. Supplementary data

Supplementary data to this article can be found online at https://doi.org/10.1016/j.orgel.2021.106151.

References

[1] J. Cornil, J.-L. Brédas, J. Zaumseil, H. Sirringhaus, Ambipolar transport in organic conjugated materials, Adv. Mater. 19 (2007) 1791–1799, https://doi.org/10.1002/adma.200602922.

[2] Y. Zhang, J. Xia, F. Zhang, Z. Wang, Q. Liu, Ultrasensitive label-free homogeneous electrochemical aptasensor based on sandwich structure for thrombin detection, Sensor. Actuator. B Chem. 267 (2018) 412–418, https://doi.org/10.1016/j.snb.2018.04.035.

[3] J. Lu, Q. Meng, L. Zhang, Y. Liu, W. Liu, X. Zhang, Single crystal structure self-assembled nano-structure and semiconductor properties of a sandwich-type mixed (phthalocyaninato)(porphyrinato) europium triple-decker complex, Dyes Pigments 115 (2015) 1–6, https://doi.org/10.1016/j.dyepig.2014.12.005.

[4] D.D. Eley, Phthalocyanines as semiconductors, Nature 162 (1948), https://doi.org/10.1038/162819a0, 819-819.

[5] R.D. Gould, Structure and electrical conduction properties of phthalocyanine thin films, Coord. Chem. Rev. 156 (1996) 237–274, https://doi.org/10.1016/S0010-8545(96)01258-6.

[6] G. Guillaud, J. Simon, J.P. Germain, Metallophthalocyanines: gas sensors, resistors and field effect transistors, Coord. Chem. Rev. 178 (1998) 1433–1484, https://doi.org/10.1016/S0010-8545(98)00177-5.

[7] X. Kong, X. Zhang, D. Gao, D. Qi, Y. Chen, J. Jiang, Air stable ambipolar field-effect transistor based on a solution processed octasubstituted/unsubstituted bis (phthalocyaninato) europium semiconductor with high and balanced carrier mobilities, Chem. Sci. 6 (2015) 1967–1972, https://doi.org/10.1039/C4SC03492B.

[8] G. Guillaud, M.A. Sadoun, M. Maitrot, J. Simon, M. Bouvet, Field-effect transistors based on intrinsic molecular semiconductors, Chem. Phys. Lett. 167 (1990) 503–506, https://doi.org/10.1016/0009-2614(90)85049-F.

[9] X. Kong, Z. Dong, Y. Wu, X. Li, Y. Chen, J. Jiang, High sensitive ambipolar response towards oxidizing NO_2 and reducing NH_3 based on bis(phthalocyaninato) europium semiconductors, Chin. J. Chem. 34 (2016) 975–982, https://doi.org/10.1002/cjoc.201600498.

[10] H. Wang, X. Kong, S. Zhao, J. Wu, X. Li, Y. Chen, High-performance ambipolar responses to oxidizing NO_2 and reducing NH_3 based on the self-assembled film of an amphiphilic tris(phthalocyaninato) europium complex, New J. Chem. 41 (2017) 11935–11941, https://doi.org/10.1039/C7NJ02706D.

[11] S. Liu, H. Wang, X. Wang, S. Li, H. Liu, Y. Chen, X. Li, Diverse sensor responses from two functionalized tris(phthalocyaninato)europium ambipolar semiconduction towards three oxidative and reductive gases, J. Mater. Chem. C 7 (2019) 424–433, https://doi.org/10.1039/C8TC05670E.

[12] X. Duan, Y. Zhang, H. Wang, F. Dai, G. Yang, Y. Chen, A phthalocyanine sensor array based on sensitivity and current changes for highly sensitive identification of three toxic gases at ppb levels, New J. Chem. 44 (2020) 13240–13248, https://doi.org/10.1039/d0nj02027g.

[13] G. Lu, K. Wang, X. Kong, H. Pan, J. Zhang, Y. Chen, J. Jiang, Binuclear phthalocyanine dimer-containing yttrium double-decker ambipolar semiconductor with sensitive response toward oxidizing NO_2 and reducing NH_3, ChemElectroChem 5 (2018) 605–609, https://doi.org/10.1002/cplu.201701117.

[14] S. Oundrazgo, R. Mesnier-Prest, A. Kumar, M. Bayodhungura, M. Bouvet, Modulating the electrical properties of organic heterojunction devices based on phthalocyanines for ambipolar sensors, ACS Sens. 5 (2020) 1849–1857, https://doi.org/10.1021/acssensors.0c00877.

[15] Z. Dong, X. Kong, D. Qi, S. Zhao, X. Li, Y. Chen, J. Jiang, Polymorphism in the self-assembled nanostructures of a tris(phthalocyaninato) europium derivative: phase dependent semiconducting and NO_2 sensing behaviour, Org. Electron. 53 (2018) 127–134, https://doi.org/10.1016/j.orgel.2017.11.026.

[16] S. Zhao, X. Kong, X. Wang, X. Li, G. Yang, Y. Chen, Fine-tuning intermolecular and intramolecular interactions to build the films of tris(phthalocyaninato) rare earth complexes and their comparative performances in ambipolar gas sensing, IEEE Trans. Electron. Dev. 66 (2019) 1930–1936, https://doi.org/10.1109/TED.2019.2901807.

[17] Y. Wu, P. Ma, N. Wu, X. Kong, M. Bouvet, X. Li, Y. Chen, J. Jiang, Two-step solution-processed two-component bilayer phthalocyaninato copper-based heterojunctions with interesting ambipolar organic transiting and ethanol-sensing properties, Adv. Mater. Interfaces 3 (2016) 1600253, https://doi.org/10.1002/admi.201600253.

[18] J. Kan, Y. Chen, D. Qi, Y. Liu, J. Jiang, High-performance air-stable ambipolar organic field-effect transistor based on tris(phthalocyaninato) europium(III), Adv. Mater. 24 (2012) 1755–1758, https://doi.org/10.1002/adma.201200036.

[19] S.Z. Bisri, C. Piliego, J. Gao, M.A. Loi, Outlook and emerging semiconducting materials for ambipolar transistors, Adv. Mater. 26 (2014) 1176–1199, https://doi.org/10.1002/adma.201304280.

[20] Y. Chen, X. Kong, G. Lu, D. Qi, Y. Wu, X. Li, M. Bouvet, D. Sun, J. Jiang, The lower rather than higher density charge carrier determines the NH_3-sensing nature and sensitivity of ambipolar organic semiconductors, Mater. Chem. Front. 2 (2018) 1009–1016, https://doi.org/10.1039/C7QM00607A.

[21] Y. Chen, M. Bouvet, T. Sizun, Y. Gao, C. Plassard, E. Lesniewska, J. Jiang, Facile approaches to build ordered amphiphilic tris(phthalocyaninato) europium triple-

decker complex thin films and their comparative performances in ozone sensing, Phys. Chem. Chem. Phys. 12 (2010) 12861–12861, https://doi.org/10.1039/C0CP90038F.

[22] G. Lu, X. Kong, H. Wang, Y. Chen, C. Wei, Y. Chen, J. Jiang, A sandwich-type tetrakis(phthalocyaninato) europium-cadmium quadruple-decker: structure, OFET, and gas sensing properties, New J. Chem. 43 (2019) 15763–15767, https://doi.org/10.1039/C9NJ03542D.

[23] X. Cui, C. Wei, J. Dong, Q. Liu, Y. Wu, G. Lu, Y. Chen, J. Jiang, Dimeric phthalocyanine-involved double-decker complex-based electrochemical sensor for simultaneous detection of acetaminophen and ascorbic acid, J. Mater. Sci. Mater. Electron. 30 (2019) 1976–1983, https://doi.org/10.1007/s10854-018-0168-8.

[24] Z. Yu, L. Zou, Y. Chen, J. Jiang, (Pc)Ru(Pc)Ru(trans-7 (COOCH$_2$)$_2$PP)/GO hybrid film-based nonenzymatic H_2O_2 electrochemical sensor with excellent performance, ACS Appl. Mater. Interfaces 8 (2016) 30398–30406, https://doi.org/10.1021/acsami.6b08760.

[25] H. Ahn, A. Chandekar, B. Kang, C. Sung, J.E. Whitten, Electrical conductivity and vapor-sensing properties of ω(3-thienyl) alkanethiol-protected gold nanoparticle films, Chem. Mater. 16 (2004) 3274–3278, https://doi.org/10.1021/cm049794s.

[26] G. Lu, X. Kong, C. Wang, L. Zhao, D. Qi, Y. Jiang, S. Zhao, Y. Chen, J. Jiang, Optimizing the gas sensing properties of sandwich-type phthalocyaninato europium complex through extending the conjugated framework, Dyes Pigments 161 (2019) 240–246, https://doi.org/10.1016/j.dyepig.2018.09.062.

[27] G. Lu, M. Bai, R. Li, X. Zhang, C. Ma, P.C. Lo, J. Jiang, Lanthanide (III) double-decker complexes with octaphenoxy- or octathiophenoxyphthalocyaninato ligands-revealing the electron-withdrawing nature of the phenoxy and thiophenoxy groups in the double-decker complexes, Eur. J. Inorg. Chem. 18 (2006) 3703–3709, https://doi.org/10.1002/ejic.200601295.

[28] R. Wang, Y. Li, R. Li, D.Y. Cheng, P. Zhu, D.K. Ng, M. Bao, X. Cui, N. Kobayashi, J. Jiang, Heteroleptic rare earth double-decker complexes with naphthalocyaninato and phthalocyaninato ligands general synthesis, spectroscopic, and electrochemical characteristics, Inorg. Chem. 44 (2005) 2114–2120, https://doi.org/10.1021/ic048472u.

[29] X. Mu, W. Song, Y. Zhang, K. Ye, H. Zhang, Y. Wang, Controllable self-assembly of n-type semiconductors to microtubes and highly conductive ultralong microwires, Adv. Mater. 22 (2010) 4905–4909, https://doi.org/10.1002/adma.201002259.

[30] K. Wang, D. Qi, H. Wang, W. Cao, W. Li, T. Liu, C. Duan, J. Jiang, Binuclear phthalocyaninato-based sandwich-type rare earth complexes: unprecedented two π-bridged binuclear-metal integrated SMMs, Chem. Eur. J. 19 (2013) 11162–11166, https://doi.org/10.1002/chem.201301101.

[31] R. Murdey, M. Bouvet, M. Sumimoto, S. Sakaki, N. Sato, Direct observation of the energy gap in lutetium bisphthalocyanine thin films, Synth. Met. 159 (2009) 1677–1681, https://doi.org/10.1016/j.synthmet.2009.05.002.

[32] C. Kittel, Introduction to Solid State Physics, Wiley, New York, 1996. Reference to a chapter in an edited book.

[33] M.L. Tang, A.D. Reichardt, P. Wei, Z. Bao, Correlating carrier type with frontier molecular orbital energy levels in organic thin film transistors of functionalized acene derivatives, J. Am. Chem. Soc. 131 (2009) 5264–5273, https://doi.org/10.1021/ja809659b.

[34] G. Lu, X. Kong, J. Sun, L. Zhang, Y. Chen, J. Jiang, Solution-processed single-crystal microsheets of a novel dimeric phthalocyanine-involved triple-decker for high-performance ambipolar organic field effect transistors, Chem. Commun. 53 (2017) 12754–12757, https://doi.org/10.1039/C7CC08797E.

[35] G. Lu, X. Kong, P. Ma, K. Wang, Y. Chen, J. Jiang, Amphiphilic (phthalocyaninato) (porphyrinato) europium tripledecker nanoribbons with air-stable ambipolar OFET performance, ACS Appl. Mater. Interfaces 8 (2016) 6174–6182, https://doi.org/10.1021/acsami.5b12368.

[36] J. Kan, Y. Chen, J. Gao, L. Wan, T. Lei, P. Ma, J. Jiang, Synthesis, self-assembly, and semiconducting properties of phenanthrolinefused phthalocyanine derivatives, J. Mater. Chem. 22 (201 2) 221 42–221 49, https://doi.org/10.1039/C2JM32358C.

[37] M. Kasha, H.R. Rawls, M.A. El-Bayoumi, The exciton model in molecular spectroscopy, Pure Appl. Chem. 11 (1965) 371–392, https://doi.org/10.1351/pac196511030371.

[38] W.-H. Chen, W.-Y. Ku, Y.-S. Chen, C.-Y. Cheng, C.-M. Chan, K.-J. Lin, Growth of copper phthalocyanine rods on an plasmon electrodes through micelle disruption methods, Langmuir 26 (2010) 2191–2195, https://doi.org/10.1021/la903455a.

[39] B.M. Hassan, H. Li, N.B. McKeown, The control of molecular self-association in spin-coated films of substituted phthalocyanines, J. Mater. Chem. 10 (2000) 39–45, https://doi.org/10.1039/A903341I.

[40] K. Abdullah, Y. Chen, J. Jiang, Synthesis, Fabrication of self-assembled film and ambipolar chemical sensing properties of tripledecker (phthalocyaninato) (porphyrinato) europium complex, J. Porphyr. Phthalocyanines 21 (2017) 893–899, https://doi.org/10.1142/S1088424617500985.

[41] M.J. Plater, A. Jeremiah, G. Bourhill, Synthesis of soluble halogenated aryloxy substituted indium phthalocyanines, J. Chem. Soc., Perkin Trans. 1 1 (2002) 91–96, https://doi.org/10.1039/B107689M.

[42] M. Bouvet, V. Parra, C. Locatelli, H. Xiang, Electrical transduction in phthalocyanine-based gas sensors: from classical chemiresistors to new functional structures, J. Porphyr. Phthalocyanines 13 (2009) 84–91, https://doi.org/10.1142/S1088424609000196.

[43] H. Usta, C. Risko, Z. Wang, H. Huang, M.K. Deliomeroglu, A. Zhukhovitskiy, A. Facchetti, T.J. Marks, Design, synthesis, and characterization of ladder-type molecules and polymers. air-stable, solution-processable n-channel and ambipolar semiconductors for thin-film transistors via experiment and theory, J. Am. Chem. Soc. 131 (2009) 5586, https://doi.org/10.1021/ja809555x.

[44] Y. Zhang, X. Cai, Y. Zhou, X. Zhang, H. Xu, Z. Liu, X. Li, J. Jiang, Structures and spectroscopic properties of bis(phthalocyaninato) yttrium and lanthanum complexes: theoretical study based on density functional theory calculations, J. Phys. Chem. 111 (2007) 392–400, https://doi.org/10.1021/jp066152y.

[45] Y. Chen, D. Li, N. Yuan, J. Gao, R. Gu, G. Lu, M. Bouvet, Tuning the semiconducting nature of bis(phthalocyaninato) holmium complexes via peripheral substituents, J. Mater. Chem. 22 (201 2) 221 42–221 49, https://doi.org/10.1039/C2JM35219B.

[46] Z. Wang, L. Huang, X. Zhu, X. Zhou, L. Chi, An ultrasensitive organic semiconductor NO_2 sensor based on crystalline TIPS-pentacene films, Adv. Mater. 29 (2017) 1703192, https://doi.org/10.1002/adma.201703192.

[47] K.Y. Ko, K. Park, S. Lee, Y. Kim, W.J. Woo, D. Kim, J.-G. Song, J. Park, H. Kim, Recovery improvement for large-area tungsten diselenide gas sensors, ACS Appl. Mater. Interfaces 10 (2018) 23915–23917, https://doi.org/10.1021/acsami.8b07034.

[48] R. Murdey, M. Bouvet, M. Sumimoto, S. Sakaki, N. Sato, Direct observation of the energy gap in lutetium bisphthalocyanine thin films, Synth. Met. 159 (2009) 1677–1681, https://doi.org/10.1016/j.synthmet.2009.05.002.

[49] R.G. Parkhomenko, A.S. Sukhikh, D.D. Klyamer, P.O. Krasnov, S.A. Gromilov, B. Kadem, A.K. Hassan, T.V. Basova††, Thin films of unsubstituted and fluorinated palladium phthalocyanines: structure and sensor response toward ammonia and hydrogen, J. Phys. Chem. C 121 (2017) 1200–1209, https://doi.org/10.1021/acs.jpcc.6b10867.

[50] M. Matteo, R.M. Prest, J.-M. Suisse, M. Bouvet, Modulation of the organic heterojunction behavior, from electrograffing to enhanced sensing properties, Sens. Actuators, B 299 (2019) 126968, https://doi.org/10.1016/j.snb.2019.126968.

[51] M. Matteo, M.-D. Tchangai, R.M. Prest, O. Heintz, F. Herbst, J.-M. Suisse, M. Bouvet, Low conductive electrodeposited poly(2,5-dimethoxyaniline) as a key material in a double lateral heterojunction, for sub-ppm ammonia sensing in humid atmosphere, ACS Sens. 4 (2019) 740–747, https://doi.org/10.1021/acssensors.9b00109.

[52] A. Wannebroucq, S. Oudrhiogo, R. Meunier-Prest, J.-M. Suisse, M. Bayo, M. Bouvet, On the interest of ambipolar materials for gas sensing, Sens. Actuators, B 258 (2018) 657–664, https://doi.org/10.1016/j.snb.2017.11.146.

[53] M. Matsuguchi, A. Okamoto, Y. Sakai, Effect of humidity on NH_3 gas sensitivity of polyaniline blend films, Sens. Actuators, B 94 (2003) 46–52, https://doi.org/10.1016/S0925-4005(03)00325-3.

4.Cai X, Zhou Q, Ma Y, et al. Selective Removal of CO in Hydrocarbons-Rich Industrial Off-gases over CuO-$Ce_xZr_{1-x}O_2$ Catalysts [J]. Catalysis Surveys from Asia, 2021, 25(1): 68-75.

Catalysis Surveys from Asia
https://doi.org/10.1007/s10563-020-09314-4

ORIGINAL ARTICLE

Selective Removal of CO in Hydrocarbons-Rich Industrial Off-gases over CuO–$Ce_xZr_{1-x}O_2$ Catalysts

Xue Cai[1] · Qi Zhou[1] · Yue Ma[1] · Li Jiang[1] · Wenwen Yu[2,3] · Wenling Chu[2] · Rui Cai[2] · Weishen Yang[2]

Received: 4 August 2020 / Accepted: 23 September 2020
© Springer Science+Business Media, LLC, part of Springer Nature 2020

Abstract
The selective remove CO in industrial rich-hydrocarbon off-gases was performed over CuO–$Ce_xZr_{1-x}O_2$ (x = 0, 0.1, 0.5, 0.75, 0.9 and 1.0) mixed oxides. The effect of ceria content on the structure and catalytic properties of CuO–$Ce_xZr_{1-x}O_2$ compositions has been investigated, and the removal activity of CO is greatly dependent the structure of the support. Based on the characterizations from XRD, H_2-TPR, Raman spectra, XPS and CO-TPD, it can be found that the formation of ceria–zirconia solid solution induced by the introduction of ceria into zirconia leads to an increase in the amount of oxygen vacancies and the mobility of the lattice oxygen, and as a result, enhances the removal activity of catalysts towards CO. The lowest reaction temperature (~123 ℃) for 100% conversion of CO remove was obtained over CuO–$Ce_{0.9}Zr_{0.1}O_2$ sample, which also exhibited the highest concentration of surface oxygen vacancy, the better reducibility and the highest low-temperature adsorption capacity of CO. This study presents a strategy to design a high-efficiency CuO-based catalyst by controlling the concentration of the surface oxygen vacancies.

Keywords Selective removal of CO · CuO–$Ce_xZr_{1-x}O_2$ ternary catalysts · Off-gas stream from propane oxidation · Oxygen vacancy sites

1 Introduction

Due to severe poisonous to the Pt catalysts used for the electrode materials, or due to a high risk of explosion in recycled industrial off-gases mixtures, the selective elimination of the undesirable CO in rich-hydrogen systems for the fuel cells or in recycled off-gas systems for the real-life chemical processes have attracted intensive attention in recent years. Particular attention has generally been paid to its application in selective remove of CO in off-gases from oxidation process of light alkanes with extremely exothermic properties, in which the lower conversion of alkane is necessary in order to efficiently decrease uncontrollable exotherm. As a result, recycled utilization of unconverted light-alkanes is one of the most cost-effective technologies for the industrial oxidation processes. To avoid explosion risk induced by the build-up in concentration of CO in recycled rich-hydrocarbons off-gases with complex components, one of the primary efforts is concentrated on selective oxidation removal of CO over the promising catalysts [1, 2].

In the past decades, various catalysts, such as precious metals [3], transition metal oxides [4, 5], have been investigated and exhibited excellent catalytic performances toward CO oxidation in rich-hydrogen systems for the fuel cells. As one of the most reactive catalysts, the binary supported metal oxide catalysts exhibit outstanding oxidation performance of CO due to the strong interaction between active metal species and supports [6]. Kleitz and colleagues [7] found that the tailored meso-structured CuO–CeO_2 catalysts exhibited the enhanced performance for preferential oxidation of CO at low temperature. Furthermore, it was found that [8] Cu–Fe mixed oxides with controlled composition showed a good performance in the CO oxidation reaction compared to a commercial Pt/Al_2O_3 catalyst used as a reference. ZrO_2 as an inert support shows high thermal stability

✉ Xue Cai
xuecai@mail.sdu.edu.cn

✉ Wenling Chu
cwl@dicp.ac.cn

[1] Mudanjiang Normal University, Mudanjiang 157011, China

[2] State Key Laboratory of Catalysis, Dalian Institute of Chemical Physics, Chinese Academy of Science, 457 Zhongshan Road, Dalian 116023, Liaoning, China

[3] University of Chinese Academy of Sciences, Beijing 100049, China

Published online: 01 October 2020

at higher temperature and further ZrO_2-supported CuO binary catalyst had a high CO conversion [9, 10]. However, there is little report about the selective removal of CO in rich-hydrocarbons off-gas streams with complicated compositions from industrial oxidation process of light alkanes.

Compared to CuO–CeO$_2$ and CuO–ZrO$_2$ binary systems, ternary Cu–Ce–Zr catalysts will exhibit distinct physico-chemical properties due to the formation of Ce–Zr solid solution, which plays a critical role in oxygen storage capacity and thermal stability. Especially, the combination of Ce^{4+} and Zr^{4+} ions is favorable to the formation of structural defects and the improvement in oxygen mobility, which is helpful for enhancing the catalytic performance.

Accordingly, in the present work, a series of CuO–$Ce_xZr_{1-x}O_2$ with varied Ce/Zr molar ratios were successfully synthesized. Their physico-chemical properties were investigated to identify the effect of the combination of Zr and Ce on the oxygen mobility and the formation of oxygen vacancies. Furthermore, using the selective oxidation removal of CO in off-gas from propane oxidation to acrylic acid as probe reaction, much more attention was devoted to investigating the role of varied Ce/Zr ratios on the reactivity of the catalysts for the selective removal of CO from complicated off-gas streams.

2 Experimental

2.1 Catalyst Preparation

$Ce_xZr_{1-x}O_2$ (x = 0, 0.1, 0.5, 0.75, 0.9 and 1.0) mixed metal oxide supports were prepared by a co-precipitation method. $Zr(NO_3)_2{\cdot}5H_2O$ and $Ce(NO_3)_3{\cdot}6H_2O$ with varied mole ratios were dissolved in 300 mL deionized water at room temperature under vigorous stirring. 0.5 mol/L $(NH_4)_2CO_3$ solution as the precipitation agent was added slowly into the precursor solution. After stirring for 4 h at room temperature, the precipitate was washed several times in deionized water, and then dried overnight at 120 ℃. The resulting powders were calcined at 500 ℃ for 4 h in air. The 5 wt% CuO–$Ce_xZr_{1-x}O_2$ samples were synthesized by a wet impregnation method. Each $Ce_xZr_{1-x}O_2$ powder was impregnated with copper nitrate [$Cu(NO_3)_2{\cdot}3H_2O$] for 4 h, then dried at 72 ℃ and calcined at 400 ℃ for 4 h in an air atmosphere.

2.2 Catalyst Characterization

XRD patterns were collected using a Rigaku D/MAX 2500/PC diffractometer equipped with Cu Kα radiation (λ = 0.1542 nm) at 40 kV, 30 mA. Scan range is 10°–90° with scan speed of 5 °/min.

The BET surface areas were determined using a Quantachrome adsorption apparatus with nitrogen adsorption at 77 K. The samples were degassed at 300 ℃ for 3 h before test.

Elemental bulk composition was determined by X-ray fluorescence with a wavelength dispersive X-ray fluorescence spectrometer (ARL ADVANTXP) and the UNIQUANT software. The X-ray tube was set at 60 kV.

H_2-TPR experiments were undertaken in a quartz reactor, and about 50 mg of CuO–$Ce_xZr_{1-x}O_2$ sample was used for each measurement. Prior to the reduction, the catalyst was pretreated at 200 ℃ for 1 h in flowing He (20 mL/min) and then cooled to room temperature. After that, a 10% H_2/Ar mixture was allowed to flow through the sample and the temperature increased gradually to 800 ℃ with a ramp of 10 ℃/min. H_2 consumption was monitored using a thermal conduction detector (TCD).

The temperature-programmed desorption of CO (CO-TPD) was measured in a fixed bed reactor. The samples (70 mg) were loaded between quartz wool plugs in the middle of the reactor and pretreated by He (45 mL/min) with a rate of 10/min from room temperature (RT) to 200 ℃ for 1 h. And then the samples were cooled down to RT under the flow of He. The CO adsorption was performed at 50 ℃ under a flow rate of 30 mL/min for 1 h, then the samples were ramped to 700 ℃ at a linear heating rate of 10 ℃/min. The analysis of the effluent gases was carried out with a mass spectrometer.

Raman spectra were obtained on a Renishaw Raman spectrometer with 532 nm laser. The laser line power was about 0.3 mW.

The X-ray photoelectron spectroscopy (XPS) was measured with a Thermo Fisher ESCALAB 250 Xi spectrometer, with an X-ray source of Al Kα radiation of 1486.6 eV at 15 KV and 10.8 mA. The working pressure of the instrument was 7.1×10^{-5} Pa. The binding energies were calculated with reference to the energy of C 1s peak of contaminant carbon at 284.6 eV.

2.3 Catalytic Activity

The removal performance of CO over CuO–$Ce_xZr_{1-x}O_2$ samples was evaluated in a fixed-bed quartz reactor (i.d. 10 mm). The reaction feedstock is a simulated off-gas stream from selective oxidation of propane to acrylic acid process, which consists of 1.59% CO, 1.50% CO_2, 8.70% O_2, 0.02% C_2H_6, 0.02% C_2H_4, 0.46% C_3H_8, 9.40% C_3H_6 and 78.31% N_2. Typically, 0.5 g catalyst (20–30 mesh) without any pretreatment was loaded into the reactor. The total flow rate of the simulated off-gas was 33.33 mL/min. The removal measurement of CO was performed by increasing the temperature from 50 to 300 ℃. CO conversion (%) and selectivity to CO removal were calculated according to the following equations:

$$\text{CO conversion (\%)} = ([CO]_{in} - [CO]_{out})/[CO]_{in},$$

$$\text{Selectivity to CO removal (\%)} = ([CO]_{in} - [CO]_{out})/2([O_2]_{in} - [O_2]_{out}),$$

where $[CO]_{in}$, $[O_2]_{in}$ and $[CO]_{out}$, $[O_2]_{out}$ are the concentration of CO and O_2 from input and output of the reactor, respectively.

3 Results and Discussion

3.1 Catalyst Characterization

3.1.1 XRD

Figure 1 shows the XRD patterns of the CuO–$Ce_xZr_{1-x}O_2$ catalyst with varied Ce/Zr molar ratios, in which the theoretical Ce/Zr values are in good agreement with the actual results (listed in Table 1) from XRF characterization. XRD pattern of CuO–ZrO_2 sample corresponds to ZrO_2 consisting of a mixture of monoclinic and tetragonal phase. However, the introduction of Ce in a low concentration (Ce/Zr = 0.1) into the ZrO_2 structure stabilizes the tetragonal structure of zirconium oxide, and this stabilization of ZrO_2 structure by Ce was reported by other authors [11, 12]. With the further increase of Ce^{4+} incorporation, the CuO–$Ce_xZr_{1-x}O_2$ samples (x > 0.1) showed quite similar diffraction peaks to the CeO_2 cubic fluorite structure and no ZrO_2 phases were detected, indicating Zr^{4+} ions totally enter into CeO_2 lattice and a good single-phase cubic ceria–zirconia solid solution is formed. And the XRD diffraction peak shifted to a small angle due to lattice expansion caused by the substitution of Zr^{4+} cations (0.084 nm) with larger Ce^{4+} (0.097 nm) [13]. Furthermore, as shown in Fig. 1, the incorporation of Ce^{4+} into ZrO_2, also led to the weakening and broadening of the diffraction peaks, indicating that the grain size of the samples was reduced. Based on the Scherrer formula, the average crystal size of as-synthesized samples was calculated and the results in Table 1 showed that the crystallite sizes of CuO–$Ce_xZr_{1-x}O_2$ samples were in the range of 10–20 nm. Obviously, the addition of Ce significantly reduced the grain size and thus increased the BET surface area of the samples, and the highest BET surface area was observed over CuO–$Ce_{0.75}Zr_{0.25}O_2$. Finally, the absence of CuO reflection peaks in XRD pattern indicates that Cu species are highly dispersed on the ceria–zirconia solid solution, or the grain size is too small to be detected by XRD instrument [14].

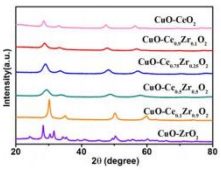

Fig. 1 XRD patterns of CuO–$Ce_xZr_{1-x}O$ catalysts

Table 1 Physico-chemical properties of CuO–$Ce_xZr_{1-x}O$ catalyst

Catalysts	S_{BET} (m^2/g)	Actual ratio of Ce/Zr[a]	Crystalline size (nm)[b]	A_{610}/A_{465}[c]	Ce^{3+}/(Ce^{3+}+Ce^{4+})[d] (%)	O_{ads}/O_{tot}[e] (%)	T_{100}[f] (°C)	Temperature window[g] (°C)
CuO–CeO_2	101.6	–	9.47	0.32	22.8	25.4	140	140–176
CuO–$Ce_{0.9}Zr_{0.1}O_2$	74.88	7.79	9.85	0.47	24.6	29.4	123	123–156
CuO–$Ce_{0.75}Zr_{0.25}O_2$	101.74	3.19	8.75	0.33	23.2	25.3	131	131–154
CuO–$Ce_{0.5}Zr_{0.5}O_2$	91.90	0.87	9.67	0.25	22.1	24.7	162	162–174
CuO–$Ce_{0.1}Zr_{0.9}O_2$	55.26	0.11	15.64	0.17	18.8	19.6	183	183–183
CuO–ZrO_2	33.18	0	20.62	–	–	15.1	191	191–191

[a] From the analysis of XRF files
[b] From Scherrer's formula of XRD files
[c] Concentration of oxygen vacancies from Raman spectra
[d] The relative ratio of Ce^{3+} species from Ce 3d XPS spectra
[e] Calculated by O 1s spectra of XPS files
[f] The temperature in which CO in off-gas stream is fully converted
[g] The temperature window is a temperature range in which full conversion of CO and ~ 100% CO selectivity wasobtained

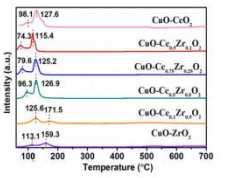

Fig. 2 H_2-TPR profiles of CuO–$Ce_xZr_{1-x}O$ catalysts

3.1.2 H_2-TPR

The redox properties of as-synthesized samples were examined by H_2-TPR and the results were shown in Fig. 2. All catalysts exhibited two reductive peaks, in which a shoulder peak located in the range of 70–110 ℃ and a major peak with a temperature of above 115 ℃. According to relevant literature reports [15, 16], the first low-temperature reduction peak is due to the reduction of the highly dispersed CuO species, which is strongly interacting with the $Ce_xZr_{1-x}O_2$ support, while the second peak can be attributed to the CuO species weakly associated with the supports [17]. The reductive temperatures of binary CuO–ZrO_2 and CuO–CeO_2 samples are 113.1 ℃, 159.3 ℃ and 98.1 ℃, 127.6℃, respectively. It can be seen from Fig. 2 that, except for CuO–$Ce_{0.1}Zr_{0.9}O_2$ sample with the stable ZrO_2 tetragonal structure shown by XRD, the reduction temperature of other ternary CuO–$Ce_xZr_{1-x}O_2$ samples gradually decreased with the increased of Ce content, indicating that the formation of the ceria–zirconia solid solution significantly improved the reducibility of the samples. Among the series of CuO–$Ce_xZr_{1-x}O_2$ samples with varied Ce/Zr ratios, CuO–$Ce_{0.5}Zr_{0.5}O_2$ catalyst presented the lowest reduction temperature, suggesting the better reducibility and oxygen mobility due to the improved synergism between Ce–Zr solid solution and Cu species [18]. It is possible that the highly dispersed CuO species with outstanding redox ability on the surface of Ce–Zr solid solution would be favorable to the enhancement in removal activity of CO in the industrial hydrocarbons-rich off-gas stream.

3.1.3 Raman Spectra

It has been reported [19] that the oxygen vacancies or defect sites play a significant role in determining the oxidation activity of CO. And Raman spectroscopy is a useful tool to characterize the defects and their surrounding chemical environment. Figure 3 showed the Raman spectra of as-synthesized CuO–$Ce_xZr_{1-x}O_2$ catalysts with varied Ce/Zr ratio. The CuO–ZrO_2 catalyst showed five main peaks at 336 cm^{-1}, 381 cm^{-1}, 475 cm^{-1}, 619 cm^{-1}, 636 cm^{-1}, which are attributed to the ZrO_2 support [20]. With the addition of Ce ions, the characteristic peaks of ZrO_2 weakened or further disappeared, but the peaks at 465 cm^{-1} assigned to the F_{2g} mode of the CeO_2 fluorite structure began to appear [21]. However, compared with those of pure CeO_2, the F_{2g} band of binary CuO–CeO_2 and ternary CuO–$Ce_xZr_{1-x}O_2$ catalysts became broader and weaker due to the deformation of the cubic CeO_2 induced by the strong interaction

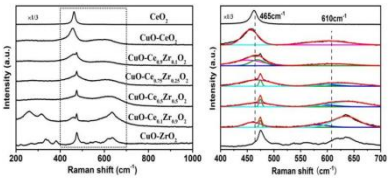

Fig. 3 Raman spectra of CuO–$Ce_xZr_{1-x}O$ catalyst samples and expansion of the hatched region

between Cu and Ce (Ce–Zr) or the formation of ceria–zirconia solid solution. Specially, a weak peak related to oxygen vacancies at ~610 cm^{-1} began to appear and became the stronger with doping Ce into ZrO_2 support. Generally, the ratio of the peak area at 610 cm^{-1} and 465 cm^{-1} (A_{610}/A_{465}) can be used to describe the relative concentration of oxygen vacancies [22, 23], and the results are listed in Table 1. Obviously, the concentration of oxygen vacancies over the ternary CuO–$Ce_xZr_{1-x}O_2$ catalysts is continuously increased with the amount of the doped Ce^{4+} into the ZrO_2 support. Although the binary CuO–CeO_2 exhibited the higher A_{610}/A_{465} value (0.32) due to the stronger interaction between copper and ceria [7, 24], the formation of ceria–zirconia solid solution would lead to the serious distortion of CeO_2 and induce the generation of more oxygen vacancies and defects [25]. And sample CuO–$Ce_{0.9}Zr_{0.1}O_2$ exhibited the highest A_{610}/A_{465} value (0.47) among series of as-synthesized catalysts. It was known that oxygen vacancies are benefit for improving the adsorption and activation of gas oxygen as well as the mobility of lattice oxygen [26], which is well consistent with H_2-TPR test.

3.1.4 XPS Spectra

The further evidence for Ce doping into ZrO_2 to form oxygen vacancies could be achieved by O 1s XPS spectra shown in Fig. 4. The corresponding O 1s spectra show three characteristic peaks, which are assigned to the lattice oxygen species at 529.2–529.7 eV, the active oxygen vacancies at 531.1–531.3 eV and the chemisorbed oxygen species at ~ 532.2 eV including hydroxyl or carbonate, respectively [27, 28]. Many researchers have reported that the active oxygen vacancies play an important role in CO oxidations. For example, using quantitative temporal analysis, Widmann and colleagues [29] found that oxidation rate of CO was significantly strengthened by surface oxygen vacancies over Au/CeO_2 catalyst. Accordingly, the relative amount of O_{ads}/O_{tot} was calculated and the results were listed in Table 1. Similar with the information observed from Raman spectra, the concentration of surface oxygen vacancies is increased with doping Ce ions into ZrO_2 support for the ternary CuO–$Ce_xZr_{1-x}O_2$ samples. For the binary samples, the concentration of surface oxygen vacancies over CuO–CeO_2 is much higher than that of CuO–ZrO_2, suggesting that the strong interaction between copper and ceria is more favorable to the generation of oxygen vacancies.

Another conformation of the increase in the concentration of oxygen vacancies with respect to Ce incorporation can be found from Ce 3d XPS spectra of the CuO–$Ce_xZr_{1-x}O_2$ catalysts with varied Ce/Zr ratios, as shown in Fig. 5. Among the deconvoluted eight peaks, the peaks labeled as V′ and U′ correspond to the spin-orbit state of Ce^{3+} species, while other peaks are related to the Ce^{4+} species [30, 31]. The appearance of Ce^{3+} is an evidence of the generation of some oxygen vacancies induced by the reduction of Ce^{4+} [32, 33]. It is evident from Table 1 that the lower concentrations of Ce^{3+} on the surface of ternary CuO–$Ce_{0.1}Zr_{0.9}O_2$ can be convincingly attributed to the presence of the tetragonal ZrO_2 phase and the lowest amount of reducible Ce^{3+}. And the further increase of the doped Ce ions led to a gradual increase in the concentration of Ce^{3+} due to the generation of ceria–zirconia solid solution, suggesting the enhancement in the formation of surface oxygen defects/vacancies. As for the binary CuO–CeO_2 catalyst, the stronger interaction between copper and ceria is favorable to the generation of

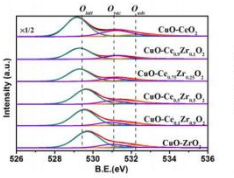

Fig. 4 XPS spectra of O 1s for the CuO/$Ce_xZr_{1-x}O$ catalyst samples

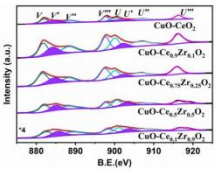

Fig. 5 XPS spectra of Ce 3d for the CuO–$Ce_xZr_{1-x}O$ catalyst samples

Ce^{3+} ions, which has been confirmed by many literatures [34, 35].

From the results above, it can conclude that the formation of ceria–zirconia solid solution facilitated the distortion of CeO_2 and created more oxygen vacancies over $CuO/Ce_xZr_{1-x}O_2$ samples, which were also confirmed by the evolution of Ce^{3+} and O_{vac} in XPS spectra and the increase in the peak area of A_{610} in Raman spectra.

3.1.5 CO-TPD

It has been reported [36, 37] that the adsorption of CO on the active sites of the CuO-based catalysts plays a key role in the oxidation removal process. Thus, we have further investigated the nature of catalyst surface by CO-TPD. Figure 6 gives the CO-TPD patterns of the catalysts with different ratios of Ce/Zr. The peak region below 110 ℃ can be assigned to the weakly chemisorbed CO species on the surface Cu^+ sites [38, 39]. As we can see, CuO–ZrO_2 and CuO–$Ce_{0.1}Zr_{0.9}O_2$ catalysts exhibited one smaller low-temperature desorption peak due to the presence of mixed ZrO_2 and tetragonal ZrO_2 phase, respectively. However, further incorporation of Ce cations into the ZrO_2 support led to the formation of one-phase ceria–zirconia solid solution, for which the amount of desorbed CO at low temperature is obviously increased. This trend gives the evidence that the a single-phase ceria–zirconia solid solution as the support is favorable to enhance the amount of adsorption sites for CO, indicating the presence of more active Cu^+ ions on the catalyst surface. This result is consistent with the higher reducibility over the CuO–$Ce_xZr_{1-x}O_2$ (x = 0.9, 0.75 and 0.5), as shown by the results of H_2-TPR.

Furthermore, it can be seen from Fig. 6 that the as-synthesized catalysts also exhibited a peak at temperature around 250–300 ℃, corresponding to the stronger adsorption of CO species by active metal on the surface. It can be found that, with the increase of Ce content, the desorption peak due to strong CO–metal bonds shifted to the lower temperature, and further gradually weakened and even disappeared. For CO oxidation, the chemisorption and activation of CO over active Cu^+ sites play an important role in the reaction between Cu^+–CO species and surface active oxygen species. The strong metal–CO bonds will severely inhibit the adsorption and activation of oxygen species, while the weakly adsorbed CO will significantly promote the adsorption of oxygen species, which is directly involved in the reaction process to oxidatively remove the CO adsorbed on Cu^+ sites. From above, it can be found that the CuO–$Ce_{0.9}Zr_{0.1}O_2$ catalyst owned the highest amount of weakly adsorbed CO and the negligible high-temperature peaks due to the strong CO–metal bonds, which is the main reason why the CuO–$Ce_{0.9}Zr_{0.1}O_2$ sample exhibited the best removal performance of CO in the off-gas stream from propane oxidation process, just as shown below.

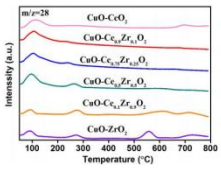

Fig. 6 CO-TPD profiles of all CuO–$Ce_xZr_{1-x}O_2$ catalysts

3.2 Catalytic Performance

Figure 7a displays the CO conversion during the removal process of CO in simulated off-gas over the CuO–$Ce_xZr_{1-x}O_2$ catalysts with varied Ce/Zr ratios. Here, the reaction temperature (T_{100}) corresponding to 100% CO conversion was used as an important criterion to evaluate the removal activity, the temperatures at which T_{100} obtained by each catalyst are listed in Table 1. It can be seen that the T_{100} values for CuO–ZrO_2 with a mixed phase structure and CuO–$Ce_{0.1}Zr_{0.9}O_2$ with a tetragonal structure are very close, nearly 190 ℃. The obvious lower removal activity of CO can be reasonably ascribed to their worst reducible nature as revealed in H_2-TPR results and the lowest concentration of oxygen vacancies as listed in Table 1. For binary CuO–CeO_2 catalyst, the T_{100} value is about 140 ℃. As the incorporation of more Ce into ZrO_2 support, a single-phase ceria–zirconia solid solution was formed and the corresponding temperature for T_{100} shifted to the lower temperature, and the lowest temperature of ~ 123 ℃ for 100% CO conversion could be achieved on the CuO–$Ce_{0.9}Zr_{0.1}O_2$ catalyst. The results indicate that, for the as-synthesized CuO–$Ce_xZr_{1-x}O_2$ catalysts, the removal activity of CO is significantly dependent on the structure of the supports.

For the selective removal of CO in off-gas from chemical processes, the operating temperature window of the catalysts is an important parameter for their industrial application. In general, it is defined as a temperature range in which 100% CO conversion and ~ 100% selectivity for CO removal is simultaneously obtained. Figure 7b shows the removal selectivity to CO over the series of CuO–$Ce_xZr_{1-x}O_2$ catalysts and the corresponding temperature window is listed in Table 1.

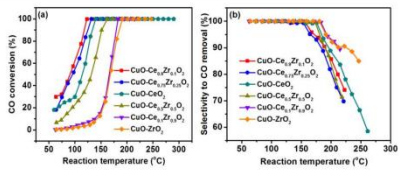

Fig. 7 CO conversion (**a**) and removal selectivity (**b**) as a function of reaction temperature over CuO–$Ce_xZr_{1-x}O_2$ catalysts

For binary CuO–ZrO_2 and ternary CuO–$Ce_{0.1}Zr_{0.9}O_2$ catalysts, no operating temperature window was observed. This may be ascribed to their higher T_{100} values, at which the olefins in off-gases, such as C_3H_6 and C_2H_4, began to be oxidized into CO_x. With the further introduction of Ce, the temperature window of ternary CuO–$Ce_xZr_{1-x}O_2$ catalysts is gradually increased with increasing x from 0.5 to 0.9. The binary CuO–CeO_2 catalyst exhibited the widest operating temperature window of about 35 ℃.

Based on the characteristic results above, such as XRD, H_2-TPR, Raman spectra and XPS analysis, it can be found that a single-phase ceria–zirconia solid solution was formed over the CuO–$Ce_xZr_{1-x}O_2$ (x = 0.9, 0.75 and 0.5) while a tetragonal ZrO_2 phase was developed over CuO–$Ce_{0.1}Zr_{0.9}O_2$. The formation of ceria–zirconia solid solution greatly increases the concentration of oxygen vacancies and the mobility of active oxygen species on the series of ternary CuO–$Ce_xZr_{1-x}O_2$ samples, which furthers enhances the reactivity of CO_{ad} weakly adsorbed on the Cu^+ active sites with the surface lattice oxygen. This means that the enhancement in the removal performance of CO over the CuO–$Ce_xZr_{1-x}O_2$ catalysts mainly originates from the facile activation of CO by the high concentration of oxygen vacancies due to the incorporation of Ce ions.

4 Conclusion

In summary, we have investigated the composition effect of series of CuO–$Ce_xZr_{1-x}O_2$ catalysts on the oxidative remove of CO in simulated off-gas from propane oxidation of acrylic acid. The structural characterizations showed that the incorporation of Ce into ZrO_2 support led to the formation of Ce–Zr solid solution, which caused the lattice distortion and induced more oxygen vacancy sites, and further promoted the mobility of lattice oxygen in the materials. The H_2-TPR investigation indicated that the reducibility of CuO–$Ce_xZr_{1-x}O_2$ samples gradually increased with the Ce content. The Raman and XPS spectra revealed that the CuO–$Ce_{0.9}Zr_{0.1}O_2$ sample owned the most abundant oxygen vacancies on the surface, which accelerated the adsorption of CO on the active copper sites and the activation of the oxygen species. These are the reasons why the CuO–$Ce_{0.9}Zr_{0.1}O_2$ sample exhibited the superior removal performance of CO in simulated off-gas from propane oxidation to acrylic acid.

Acknowledgements The authors are grateful for support from the Education Research Fund for Department of Heilongjiang Province (No. 1352IZD001), the Scientific Research Project of Mudanjiang Normal University (No. GP201603), the National Natural Science Foundation of China (No. 21673227), the Science and Technology Innovation Project of Mudanjiang Normal University (No. kjcx2019-30mdjnu), Heilongjiang Province University Student Innovation and Entrepreneurship Training Program Project (No. 201910233025).

References

1 Chu WL, Liu YC, Wang HK, Cai R, Yang WS (2018) ChemCatChem 10(19):4292–4299
2 Yu WW, Zhou Q, Wang HK, Liu YC, Chu WL, Cai R, Yang WS (2020) J Mater Sci 55(6):2321–2332
3 Heo I, Yoon DY, Cho BK, Nam IS, Choung JW, Yoo S (2012) Appl Catal B 121:75–87
4 Shi L, Zhang G (2016) Catal Lett 146(8):1449–1456
5 Park ED, Lee D, Lee HC (2009) Catal Today 139(4):280–290
6 Moretti E, Molina AI, Sponchia G, Talon A, Fratini R, Rodriguez-Castellon E, Storaro L (2017) Appl Surf Sci 403:612–622
7 Yen H, Seo Y, Kaliaguine S, Kleitz F (2012) Angew Chem Int Ed 51(48):12032–12035
8 Yeste MP, Vidal H, Garcia-Cabeza AL, Hernandez-Garrido JC, Guerra FM, Cifredo GA, Gonzalez-Leal JM, Gatica JM (2018) Appl Catal A 552:58–69

9 Moretti E, Storaro L, Talon A, Lenarda M, Riello P, Frattini R, de Yuso MDM, Jimenez-Lopez A, Rodriguez-Castellon E, Ternero F, Caballero A, Holgado JP (2011) Appl Catal B 102(3–4):627–637
10 Zhu J, Zhang LL, Deng Y, Liu B, Dong LH, Gao F, Sun KQ, Dong L, Chen Y (2010) Appl Catal B 96(3–4):449–457
11 Kaspar J, Fornasiero P, Hickey N (2003) Catal Today 77:419–449
12 Il'ichev AN, Bykhovsky MY, Fattakhova ZT, Shashkin DP, Fedorova YE, Matyshak VA, Korchak VN (2019) Kinet Catal 60(5):661–671
13 Djinovic P, Batista J, Pintar A (2008) Appl Catal A 347(1):23–33
14 Wang Z, Qu Z, Quan X, Li Z, Wang H, Fan R (2013) Appl Catal B 134:153–166
15 Dong XF, Zou HB, Lin WM (2006) Int J Hydrog Energy 31(15):2337–2344
16 Manzoli M, Di Monte R, Boccuzzi F, Coluccia S, Kaspar J (2005) Appl Catal B 61(3–4):192–205
17 Fu GY, Mao DS, Sun S, Yu J, Yang ZQ (2015) J Ind Eng Chem 31:283–290
18 Li L, Song L, Chen CQ, Zhang YJ, Zhan YY, Lin XY, Zheng Q, Wang HD, Ma HX, Ding LH, Zhu W (2014) Int J Hydrog Energy 39(34):19570–19582
19 Daroi-Quiñonero A, Bailón-García E, López-Rodríguez S, Juan-Juan J, Lozano-Castello D, Garcia-Melchor M, Herrera FC, Pellegrin E, Escudero C, Bueno-Lopez A (2020) ACS Catal 10(11):6532–6545
20 Ratnasamy P, Srinivas D, Satyanarayana CVV, Manikandan P, Kumaran RSS, Sachin M, Shetti VN (2004) J Catal 221(2):455–465
21 Wang RG, Mutinda SI, Fang MH (2013) RSC Adv 3(42):19508–19514
22 Liyanage AD, Perera SD, Tan K, Chabal Y, Balkus KJ (2014) ACS Catal 4(2):577–584
23 Gao R, Zhang D, Maitarad P, Shi LY, Rungrotmongkol T, Li HR, Zhang JP, Cao WG (2013) J Phys Chem C 117(20):10502–10511
24 Li WG, Hu YJ, Jiang H, Yang S, Li CZ (2019) Mater Chem Phys 226:158–169
25 Reddy BM, Rao KN (2009) Catal Commun 10(9):1350–1353
26 Zhao W, Zhong Q (2014) RSC Adv 4(11):5653
27 Chen GZ, Song GL, Zhao W, Gao DW, Wei YW, Li CC (2018) Chem Eng J 352:64–70
28 Kocemba I, Rynkowski J, Gurgul J, Socha RP, Latka K, Krafft JM, Dzwigaj S (2016) Appl Catal A 519:16–26
29 Wang LC, Widmann D, Behm RJ (2015) Catal Sci Technol 5(2):925–941
30 Jiang N, Zhao YH, Qiu C, Shang KF, Lu N, Li J, Wu Y, Zhang Y (2019) Appl Catal B 259:118061
31 Zhang GL, Cheng X, Yang D, Yu G, Ma HM, Wang J, Wu HY, Yang ZG (2019) Fuel 258:116202
32 Zhou GG, Geng WT, Sun L, Wang X, Xiao W, Wang JW, Wang LG (2019) Materials 12(24):4041
33 Hassan S, Kumar R, Tiwari A, Song WY, van Haandel L, Pandey JK, Hensen E, Chowdhury B (2018) Mol Catal 451:236–246
34 Du PP, Wang WW, Jia CJ, Song QS, Huang YY, Si R (2016) Appl Catal A 518:87–101
35 Zhang XM, Tian PF, Tu WF, Zhang ZZ, Xu J, Han YF (2018) ACS Catal 8:5261–5275
36 Gamarra D, Munuera G, Hungría AB, Fernández-García M, Conesa JC, Midgley PA, Wang XQ, Hanson JC, Rodríguez JA, Martínez-Arias A (2007) J Phys Chem C 111(29):11026–11038
37 Hornés A, Hungría AB, Bera P, López Cámara A, Fernández-García M, Martínez-Arias A, Barrio L, Estrella M, Zhou G, Fonseca JJ, Hanson JC, Rodriguez JA (2010) J Am Chem Soc 132(1):34–35
38 Yao SY, Mudiyanselage K, Xu WQ, Johnston-Peck AC, Hanson JC, Wu TP, Stacchiola D, Rodriguez JA, Zhao HY, Beyer KA, Chapman KW, Chupas PJ, Martinez-Arias A, Si R, Bolin TB, Liu J, Senanayake SD (2014) ACS Catal 4(6):1650–1661
39 Sviridenkova EA, Kurdash TA, Simkus OA, Slavinskaya EM, Stadnichenko AI, Koscheev SV, Chupakhin AP, Boronin AI (2013) J Phys Chem C 117(28):14588–14599

Publisher's Note Springer Nature remains neutral with regard to jurisdictional claims in published maps and institutional affiliations.

5. Cai X, Wei C, Dong J, et al. Dimeric phthalocyanine-involved double-decker complex-based electrochemical sensor for simultaneous detection of acetaminophen and ascorbic acid[J]. Journal of Materials Science: Materials in Electronics, 2019, 30(3): 1976-1983.

Journal of Materials Science: Materials in Electronics
https://doi.org/10.1007/s10854-018-0468-0

Dimeric phthalocyanine-involved double-decker complex-based electrochemical sensor for simultaneous detection of acetaminophen and ascorbic acid

Xue Cai[1] · Chuangyu Wei[1] · Jurong Dong[3] · Qi Liu[3] · Yanling Wu[3] · Guang Lu[2,4] · Yanli Chen[3] · Jianzhuang Jiang[2]

Received: 30 September 2018 / Accepted: 27 November 2018
© Springer Science+Business Media, LLC, part of Springer Nature 2018

Abstract
An electrochemical sensor for simultaneous detection of acetaminophen (APAP) and ascorbic acid (AA) is firstly developed by using the self-assembled film of a novel dimeric bis(phthalocyaninato) europium complex, [{$Pc(SC_2H_5)_8$}Eu{$BiPc(SC_2H_5)_{12}$}Eu{$Pc(SC_2H_5)_8$}] (**1**) coated onto ITO (fim-**1**/ITO) fabricated through a solution-processing quasi-LangmuirShäfer (QLS) protocol. A combination of unique sandwich molecular structure with extented π-conjugated system and *J*-type aggregates with quite uniform nanograins (ca. 15 nm) formed on ITO substrate render the film of **1** the excellent charge transfer ability and abundant electroactive sites, resulting in sensitive detection of APAP and AA with the good sensitivities of 254 and 85.6 mA μM^{-1} cm^{-2} and low detection limits of 1.3 and 3.7 μM for APAP and AA respectively. More importantly, a simultaneous determination of APAP and AA at a coexisting system of APAP and AA is also achieved with the still good sensitivities of 317 and 64.7 mA μM^{-1} cm^{-2}, and low detection limits of 1.0 and 4.9 μM for APAP and AA respectively. This work represents the first example of tetrapyrrole-based organic semiconductor electrochemical sensor for simultaneous detection of APAP and AA with excellent sensing performance, implying the great application potential of electroactive sandwich rare earth tetrapyrrole compounds in the nonenzymatic electrochemical sensors.

Electronic supplementary material The online version of this article (https://doi.org/10.1007/s10854-018-0468-0) contains supplementary material, which is available to authorized users.

✉ Xue Cai
xuecai@mail.sdu.edu.cn

✉ Guang Lu
luguang_50366@126.com

✉ Yanli Chen
yanlichen@upc.edu.cn

Jianzhuang Jiang
jianzhuang@ustb.edu.cn

[1] College of Chemistry and Chemical Engineering, Mudanjiang Normal University, Mudanjiang 157011, China

[2] Beijing Key Laboratory for Science and Application of Functional Molecular and Crystalline Materials, Department of Chemistry, University of Science and Technology, Beijing, Beijing 100083, China

[3] School of Materials Science and Engineering, Institute of Advanced Materials, China University of Petroleum (East China), Qingdao 266580, China

[4] College of Chemical and Environmental Engineering, Shandong University of Science and Technology, Qingdao 266590, China

1 Introduction

As a commonly antipyretic and pain-relieving drug, acetaminophen (APAP) is contained in numerously OTC (over the counter) products [1]. However, an overdose of this drug can lead to the formation of some toxic metabolites in kidney (i.e., one of the most common pharmaceutical product poisonings at present.) [2]. Ascorbic acid (AA), as one of the most important vitamins, widely exists in various plants and participates in some important biological reactions such as cancer preventing, and improvement of immunity [3]. The deficiency of AA can result in different diseases, such as anemia, cataract and scurvy [4]. According to the previous researches, the adjunct presence of AA with APAP leads to intensified positive effects of APAP and its diminished toxicity [5]. The amount of APAP passed in urine will be reduced in high concentration of AA, which can rise the concentration of this drug in blood [6]. Therefore, the determination of APAP and AA in the presence of each other should be important in clinical medicine and health monitoring. A variety of methods have been used for the determination of APAP and AA in pharmaceuticals and biologicalfluids, such as high-performance liquid

Published online: 11 December 2018

chromatography, gas chromatography, spectrophotometry, and electrochemical techniques [7–9]. Among the numerous detection methods, the electrochemical sensing technology has attracted increasing attention due to its superior characteristics of convenience, sensitivity and repeatability for monitoring these multiple analytes within the one sample [10, 11]. The key role of the improvement of electrochemical sensing technology is developing the sensitive, simple and low-cost electrode materials.

Phthalocyanine compounds are classified as interesting materials for sensing application depending on their electronic, optical and electrochemical properties [12]. The electrochemical sensors based on phthalocyanines have been used in the detection of dopamine, caffeic acid, and hydrogen peroxide for many years [13, 14]. Recently, Holanda et al., found that multi-walled carbon nanotubes-cobalt phthalocyanine-coated gold nanoparticles modified glassy carbon electrode presented good sensitivity and analytical stability for APAP detection [15]. However, the usage of gold nanoparticles and multi-walled carbon nanotubes are expensive, complicated in technology, which limit the practical application. On the other hand, although the graphene-modified electrodes used for electrochemical studies of APAP were found to have a poor response to APAP in PBS solution (pH 7.02) [16], the carbon based composite nanomaterial-modified electrodes employed for detection of APAP showed good sensitivity, selectivity, stability, and a low detection limit because of the unique electronic and catalytic properties of composite nanomaterials, such as ferrocene thiolate stabilized Fe_3O_4@Au nanoparticles coupling with graphene sheet/chitosan on a glassy carbon electrodes (GCEs) [17], GCEs modified with gold nanoparticles-multi-walled carbon nanotube [18], graphene-$CoFe_2O_4$ nanocomposite modified carbon paste electrode [19], TiO_2-graphene modified GCE [20], and single-wall CNT-dicetyl phosphate films [21]. However, in most cases, the behaviour of irreversible agglomerates for the large scale graphene usually has a negative impact on sensing performance [22]. Meanwhile the existence of dispersing agents in CNTs or graphene composite may be undesirable for many technological applications. Therefore, development of single-component phthalocyanine-based electrochemical sensor with high sensitivity for detecting APAP and AA simultaneously is highly desired but also challenging through the molecular design combinated with a simple device fabrication method.

Herein, a dimeric bis(phthalocyaninato) europium complex, [{Pc(SC$_2$H$_5$)$_8$}Eu{BiPc(SC$_2$H$_5$)$_{12}$}Eu{Pc(SC$_2$H$_5$)$_8$}] (**1**) {Pc(SC$_2$H$_5$)$_8$ = 2,3,9,10,16,17,23,24-octa(ethylthio) phthalocyaninate, BiPc(SC$_2$H$_5$)$_{12}$ = bis[7,8,12,13,17,18-hexakis(ethylthio)-tribenzo[g,l,q]-5,10,15,20-tetraazaporphyrinate[b,e]benzene-linked binuclear phthalocyanine], was designed and synthesized, Scheme 1. The sandwich-type phthalocyanine in which lanthanide ions are bound to phthalocyanine rings, owning the accessibility of a range of oxidation states centered on the ligand [23]. The dimeric phthalocyanine framework with the sandwich double-decker structure further extends the π-conjugated system, enriches the oxidation states, which should enable this compound a good candidate for highly sensitive electrochemical sensors. Introducing the ethylthio substituents onto the periphery of phthalocyanine can improve the solubility, which is favorable for the solution-processing fabrication. Then, the electrochemical sensor based on the film of the dimeric phthalocyanine-involved double-decker complex was fabricteaed onto the ITO substrates by a simple QLS method [24]. The modified ITO electrode was revealed to have strong electrocatalytic activity toward APAP and AA simultaneously.

2 Experimental section

2.1 Materials and chemicals

1, 8-Diazabicyclo[5.4.0]undec-7-ene (DBU), acetaminophen (APAP) and ascorbic acid (AA) were purchased from Aldrich. The compounds of Eu(acac)$_3$·H$_2$O and 1, 2-benzenedicarbonitrile, 4, 5-ethylthio were prepared according to the literature methods [25]. The solvent *n*-pentanol was distilled from sodium. All other reagents and solvents were of reagent grade and used as received without further purification.

2.2 Measurements and characterizations

MALDI-TOF mass spectrum was recorded on the Bruker BIFLEX III ultra-high-resolution Fourier transform ion cyclotron resonance (FT-ICR) mass spectrometer with alpha-cyano-4-hudroxycinnamic acid as matrix (Fig. S1, Supplementary material). MALDI-TOF MS: an isotopic cluster peaking at m/z 3957.32, Calcd for **1**, $[M]^+$, 3959.15. ^{1}H NMR spectrum was recorded on the Bruker DPX 400 spectrometer in $CDCl_3$. The spectrum was referenced internally with residual $CDCl_3$ (δ 7.26). ^{1}H NMR (400 MHz, $CDCl_3$) δ: 14.54 (s, 2H, Pc ring), 12.32 (s, 4H, Pc ring), 10.90–11.40 (m, 16H, Pc ring), 9.09 (m, 4H, Pc ring), 7.41 (m, 4H, Pc ring), 4.59–4.84 (m, 28H, SCH_2), 4.30–4.50 (m, 28H, SCH_2), 1.07–1.20 (m, 84H, CH_3). Electrochemical measurements were carried out with a CHI760D voltammetric analyser and the detailed procedures please see our recently published papers [13, 26]. UV–Vis absorption spectra were recorded on the Hitachi U-3900 spectrophotometer. X-ray diffraction (XRD) experiments were carried out on the Rigaku D/max-B X-ray diffractometer with copper (K_α) radiation (λ = 1.5406 Å). Atomic force microscopic (AFM) image was obtained under ambient conditions by using a tapping mode with a Nanoscope III/Bioscope scanning probe microscope. Current–voltage (I–V) curve was collected using a Keysight B2910A precision source/measure unit with an incorporated voltage range supplied from − 10 to 10 V. Conductivity obtained by I–V curve can be calculated according to the report previously [27].

For characterizations, three kinds of substrates (SiO_2/Si, quartz, and ITO) were washed by deionized water, absolute ethyl alcohol, and dichloromethane, respectively. Films were deposited on different substrates by using QLS self-assembly method [24].

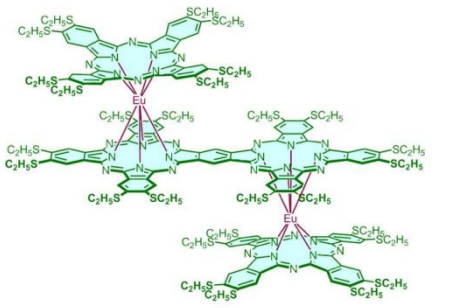

Scheme 1 Schematic molecular structures of [{Pc(SC$_2$H$_5$)$_8$}Eu{BiPc(SC$_2$H$_5$)$_{12}$}Eu{Pc(SC$_2$H$_5$)$_8$}] (**1**)

3 Results and discussion

3.1 Synthesis and characterization of [{Pc(SC$_2$H$_5$)$_8$}Eu{BiPc(SC$_2$H$_5$)$_{12}$}Eu{Pc(SC$_2$H$_5$)$_8$}] (1)

For the purpose of improving the solubility of phthalocyanine complex and preparing the solution-processing film, ethylthio substituents were introduced onto the periphery of the phthalocyanine ligand. This dimeric bisphthalocyanine compound was synthesized based on the published method [28]. Satisfactory ^{1}H NMR spectroscopic data in $CDCl_3$, MALDI-TOF mass were obtained for compound **1** (see Sect. 2 and Fig. S1, Supplementary material) Furthermore, the unique the dimeric bisphthalocyanine molecular structure let the redox states more various. As expected, the different pulse voltammogram (DPV) of **1** in dichloromethane shows two one-electron oxidations (Oxd_1-Oxd_2) and five one-electron reductions (Red_1–Red_5) (Fig. 1 and Table S1, Supplementary material), which is much more

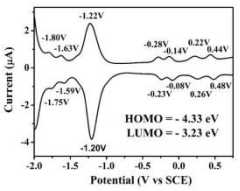

Fig. 1 Different pulse voltammogram (DPV) of **1** in dichloromethane at a scan rate of 20 mV s^{-1}

than monophthalocyanines, even normal bisphthalocyanines [29], consistent with the dimeric phthalocyanine-involved double-decker analogue reported previously [28].

3.2 Film characterization of [{Pc(SC$_2$H$_5$)$_8$}Eu{BiPc(SC$_2$H$_5$)$_{12}$}Eu{Pc(SC$_2$H$_5$)$_8$}] (1)

The film of **1** was fabricated by a simple QLS method. To clarify the microstructure and the morphology, the QLS film of **1** was characterized by UV–Vis, polarized UV–Vis absorption spetra, atomic force microscope (AFM) and X-ray diffraction (XRD). UV–Vis spectrum of the compound **1** in chloroform solution shows the Soret and Q bands at 316, 382, 585 and 699 nm respectively, Fig. 2a, with a typical nonaggregated molecular spectroscopic feature for dimeric phthalocyanine-involved double decker [30]. In comparison with the spectrum of chloroform solution, the Soret and Q bands of **1** in the QLS film red-shifted to 317 nm, 387 nm, 589 nm and 707 nm respectively, which indicate that the molecules of **1** in the QLS film take edge-to-edge (*J*-aggregate) packing mode according to exciton theory [31] and published results previously [32, 33] due to the strong exciton coupling between the adjacent dimeric bisphthalocyanine units. This is further comfirmed by polarized UV–Vis measurement [34], while the orientation angle of the phthalocyanine ring with respect to the substrate was estamited to be ca. 25.6° ± 5° (Fig. S2 and Table S2, Supplementary material). More evidence could be found in the out-of-plane (OOP) X-ray diffraction (XRD) pattern. As shown in Fig. 2b, the XRD spectra of the QLS film of **1** in the low-angle range showed one diffraction peak at 2θ = 5.98°, corresponding to a layer spacing of 1.48 nm. This is ascribed to the diffraction from (001) plane, showing a regular layered structure and good molecular ordering for this film. Based on the simulated energy-optimized double-decker molecular dimension of ca. 3.0 nm [35], the orientation angle of 29.5° was deduced (inset of Fig. 2b), which is consistent with the results obtained from the UV–Vis and polarized UV–Vis measurements. Therefore, the dimeric bisphthalocyanine molecules take an almost face-on stacking mode with orientation angle about 29.5° to the surface of the substrate in the QLS film, which provides a large contact area between phthalocyanine rings and target analytes. Furthermore, the XRD diagram shows another diffraction peak at 0.31 nm, corresponding to the π–π stacking distance between neighboring molecules of **1** [33], indicating the valid intermolecular π–π interaction in the film. This in turn is expected to be beneficial for charge transport. On the other hand, AFM observation found that quite uniform nanograins (ca. 15 nm in diameter) formed in the QLS film of **1** with the root-mean-square (Rms) roughness value of 1.9 nm, Fig. 2c. This guaranteed the fewer defects localized around grain boundaries. Meanwhile small nanoparticles provide great specific surface area and numerous active sites for adsorption. As a result, good electrical conductivity and electrochemical sensing properties are expected. I-V measurements for the

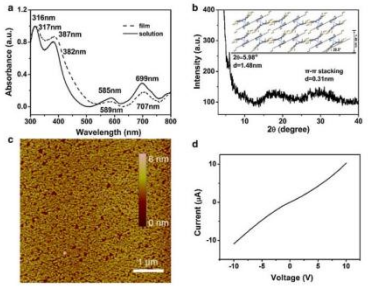

Fig. 2 **a** Electronic absorption spectra of **1** in $CHCl_3$ solution (solid line) and QLS film (dash line); **b** out-of-plane XRD pattern and **c** AFM phase image of the QLS film of **1**, **d** I–V curve

QLS film of **1** indeedly shown an excellent conductivity of 3.64×10^{-4} S cm^{-1}, Fig. 2d, further confirming good charge transfer capacity of the film. It is worth noting that although the current developed by the QLS film of **1** remains perfectly symmetrical, a slight non linearity in the I–V curve is exhibited, in agreement with the well reported space-charge-limited conduction (SCLC) found in phthalocyanine-based devices [36].

3.3 Electrochemical properties of [{Pc(SC$_2$H$_5$)$_8$}Eu{BiPc(SC$_2$H$_5$)$_{12}$}Eu{Pc(SC$_2$H$_5$)$_8$}] coated electrode

The electrochemical sensing behavior of both a bare ITO electrode and an ITO covered by the QLS film of **1** (denoted as film-**1**/ITO) were comparative investigate towards APAP and AA by cyclic voltammograms (CVs) in phosphate buffer solution (PBS at 0.1 M, pH 7.3), respectively, Fig. 3a, b. As expected, voltammograms registered in PBS using film-**1**/ITO did not show any detectable response (red line). This is also true for the CV response using bare ITO immersed in PBS containing APAP and AA, respectively (black line). In good contrast, the CV response of film-**1**/ITO towards APAP and AA in PBS show the significantly peaks at 0.45 V and 0.39 V, associated with the oxidation of the APAP and AA, respectively (blue line). These results confirm that the dimeric bisphthalocyanine **1** has electrocatalytic activity towards the APAP and AA. As shown in Fig. 3c, the arc diameter in Nyquist plots gets decreased from bare ITO to film-**1**/ITO (inset of Fig. 3c), indicating a lowered charge transfer resistance after film-**1** deposited on bare ITO electrode [37]. This in turn results in the better electrochemical sensing activity for this compound **1**.

The effect of scan rate on the electrochemical response for film-**1**/ITO toward APAP and AA was studied at different scan rate. As shown in Fig. 4, the oxidation peak currents of both APAP and AA were all linearly to the scan rate in the range of 20–200 mV s^{-1} suggesting that the oxidation reactions were controlled by surface adsorption process.

To investigate the relationship between oxidation peak current of film-**1**/ITO sensor and concentration of APAP and AA, differential pulse voltammetric (DPV) technique was carried out in the potential range of − 0.6 to 0.8 V in PBS (PH 7.3), Fig. 5. The intensity of current for the oxidation (I_p) process was proportional to the concentration of the analyte in the range from 1 to 100 μM for APAP and 10 to 1000 μM for AA, respectively, Fig. 5a, b. The linear regression equations were I_p (μA) = 0.2542 C_{APAP} (μM) + 0.2591 (R^2 = 0.9978), and I_p (μA) = 0.08562 C_{AA} (μM) + 1.041 (R^2 = 0.9968), Fig. 5c, d, resulting in the good sensitivity of 254 and 85.6 mA μM^{-1} cm^{-2} for APAP and AA, respectively. The lowest detection limit was estimated to be 1.3 and 3.7 μM for APAP and AA (S/N = 3), respectively, which

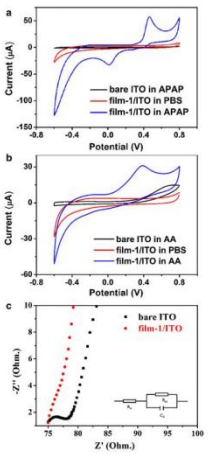

Fig. 3 CV curves of the film-**1**/ITO in 0.1M PBS (red), bare ITO (black) and film-**1**/ITO (blue) in 0.1M PBS containing 0.1 mM APAP (**a**) and 0.1 mM AA (**b**). Scan rate: 100 mV s^{-1}, **c** the EIS of bare ITO and film-**1**/ITO in PBS containing 5 mmol L^{-1} $[Fe(CN)_6]^{3-/4-}$. The inset shows the Randles equivalent circuit model

were comparable or even better than that of the previous reported electrochemical sensors for APAP and AA, (Tables S3, S4, Supplementary material). These indicated the the the dimeric phthalocyanine-involved double-decker is a promising sensor for simple, low-cost and sensitive detection of APAP and AA.

In addition, the peak currents were measured every 3 days on the same film-**1**/ITO electrode during 15 days, only a very little decay was found for the peak currents of APAP and AA with the respective values of 2.4% and 4%, respectively,

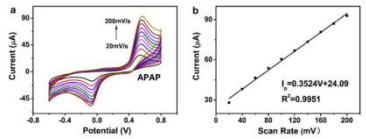

Fig. 4 CV curves at film-**I**/ITO in PBS containing the mixture of **a** 0.1 mM APAP and **c** 0.1 mM AA, with various scan rate between 20 and 200 mV s^{-1}; and the corresponding plots of peak current versus scan rate (**b**, **d**)

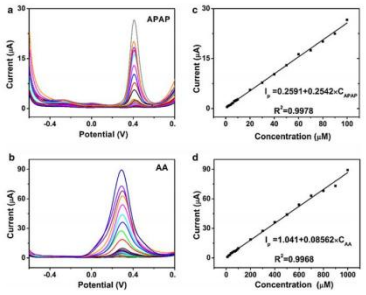

Fig. 5 DPV curves at film-**I**/ITO in PBS (PH 7.3) with varying concentrations from 1 to 100 μM for APAP (**a**) and 10–1000 μM for AA (**b**). The corresponding calibration plots for each testing sample are shown in the (**c**, **d**)

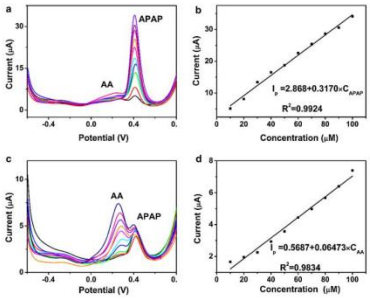

Fig. 6 DPV curves at film-**I**/ITO for simultaneous determination of APAP and AA in PBS (pH 7.3): **a** 100 μM AA with different concentrations of APAP, **c** 10 μM APAP with different concentrations of AA. The corresponding calibration plots for each testing sample are shown in the (**b**, **d**)

demonstrating the excellent reproducibility and stability of the film-**I**/ITO electrode, (Fig. S4, Supplementary material).

Furthermore, the simultaneous determination of APAP and AA at film-**I**/ITO was carried out by DPV technique. As shown in Fig. 6a, b, the electrochemical responses of APAP increased linearly along with the increased concentration of APAP from 10 to 100 μM under the same AA concentration of 100 μM. Similarly, the increasing AA concentration from 10 to 100 μM also causes the linearly increasing in current responses with the constant concentration of APAP (10 μM), Fig. 6c, d. Intreistingly, the linear regression equations are I_p (μA) = 0.3170 C_{APAP} (μM) + 2.868 (R^2 = 0.9924), and I_p (μA) = 0.06473 C_{AA} (μM) + 0.5687 (R^2 = 0.9834), resulting in the good sensitivity of 317 and 64.7 mA $μM^{-1}$ cm^{-2} for APAP and AA, respectively. Obviously, upon co-existence of APAP and AA, a much higher sensitivity to APAP was achieved, while that was slight lower to AA, in comparison with those measured alone. These results not only exhibited that the film-**I**/ITO sensor can well distinguish and determine the APAP and AA when two analytes co-exist in PBS, but also shown that existence of AA can facilitate the detection of APAP. We noted that, very recently, using bimetallic Pd-Ag/rGO (reduced graphene oxide) nanocomposites on GCEs, a lower LOD (3.23 nM) for APAP detection has been reported by using a one-step procedure for the fabrication of modified electrodes [38]. The combination of good electrical conductivity and a large surface area of rGO with excellent electrochemical activity of noble metals should be response to this achievement. However, the relatively expensive Pd-Ag bimetals due to scarcity of precious metal resources produced globally might limit its large-scale application. With a more appropriate redox potential, simultaneous determination of APAP and AA can be achieved in the present case. The design and synthesis of new sandwich compounds with good conductivity and the optimization of the electrode fabrication are in progress.

4 Conclution

In summary, an efficient and sensitive electrochemical sensor based on the solution processing film of [{Pc(SC_2H_5)$_8$}Eu{BiPc(SC_2H_5)$_{12}$}Eu{Pc(SC_2H_5)$_8$}] (**1**) has been successfully developed for sensitive and selective simultaneous detection of APAP and AA. The [{Pc(SC_2H_5)$_8$}Eu{BiPc(SC_2H_5)$_{12}$}Eu{Pc(SC_2H_5)$_8$}] film-**I**/ITO electrode is revealed to exhibit linearly amperometric response towards both APAP and AA, with a high performance in terms of sensitivity, low detection limit and detection range. The present work opens a new way for the development of high-performance tetrapyrrole based nonenzymatic electrochemical sensor through molecular design and low-cost sensor fabrication technique.

Acknowledgements This work was financially supported by the National Natural Science Foundation of China (Nos. 21771192,

21631003 and 21371073), the Research Fund for Introduced Talents of China University of Petroleum (No. Y1510051), the Education Research Fund for Department of Heilongjiang Province (No. 1352DZ0001), the Scientific Research Project of Mudanjiang Normal University (No. GP201603), the Science and Technology Innovation Project of Mudanjiang Normal University (No. kjcx2017-23mdjnu).

References

1. W.M. Lee, Hepatology **40**, 6–9 (2004)
2. A. Cernat, M. Tertis, R. Săndulescu, F. Bedioui, A. Cristea, C. Cristea, Anal. Chim. Acta **886**, 16–28 (2015)
3. X. Zuo, H. Zhang, N. Li, Sens. Actuators B **161**, 1074–1079 (2012)
4. D. Zhao, G. Yu, K. Tian, C. Xu, Biosens. Bioelectron. **82**, 119–126 (2016)
5. U. Grundmann, C. Wçrnle, A. Bieñler, S. Kreuer, M. Wrobel, W. Wilhelm, Anesth. Analg. **103**, 217–222 (2006)
6. A.A. Ensafi, H.K. Maleh, S. Mallakpour, Electroanalysis **3**, 666–675 (2012)
7. A.A. Abdelwahab, Y.B. Shim, Sens. Actuators B **221**, 659–665 (2015)
8. A.U. Alam, Y. Qin, M. Catalano, L. Wang, M.J. Kim, M.M.R. Howlader, N. Hu, M.J. Deen, ACS Appl. Mater. Interfaces **10**, 21411–21427 (2018)
9. B.G. Mahmoud, M. Khairy, F.A. Rashwan, C.E. Banks, Anal. Chem. **89**, 2170–2178 (2017)
10. X. Zhang, Y. Zhang, L. Ma, Sens. Actuators B **227**, 488–496 (2016)
11. X. Deng, Y. Fang, S. Lin, Q. Cheng, Q. Liu, X. Zhang, ACS Appl. Mater. Interfaces **9**, 3514–3523 (2017)
12. C. Pal, A.K. Sharma, A.N. Cammidge, M.J. Cook, A.K. Ray, J. Phys. Chem. B **117**, 15033–15040 (2013)
13. Z. Yu, L. Zou, Y. Chen, J. Jiang, ACS Appl. Mater. Interfaces **8**, 30398–30406 (2016)
14. H. Xu, J. Xiao, L. Yan, L. Zhu, B. Liu, J. Electroanal. Chem. **779**, 92–98 (2016)
15. L.F. de Holanda, F.WP. Ribeiro, C.P. Sousa,, P. de Lima-Neto, A.N. Correia, P. N. da Silva Casciano. J. Electroanal. Chem. **772**, 9–16 (2016)
16. X. Kang, J. Wang, H. Wu, J. Liu, I.A. Aksay, Y. Lin, Talanta, **81**, 754–759 (2010)
17. M. Liu, Q. Chen, C. Lai, Y. Zhang, J. Deng, H. Lin, S. Yao, Biosens. Bioelectron. **48**, 75–81 (2013)
18. T. Madrakian, E. Haghshenas, A. Afkhami, Sens. Actuators B **193**, 451–460 (2014)
19. A. Afkhami, H. Khoshsafar, H. Bagheri, T. Madrakiana, Sens. Actuators B **203**, 909–918 (2014)
20. Y. Fan, J. Liu, H. Lu, Q. Zhang, Colloids Surf. B **85**, 289292 (2011)
21. D. Sun, H. Zhang, Microchim. Acta **158**, 131–136 (2007)
22. Y. Si, E.T. Samulski, Nano Lett. **8**, 1679–1682 (2008)
23. M.G. Martin, M.L. RodrÍguezMendez, J. A. de Saja, Langmuir **26**, 19217–1924 (2010)
24. Y. Chen, M. Bouvet, T. Sizun, Y. Gao, C. Plassard, E. Lesniewska, J. Jiang, Phys. Chem. Chem. Phys. **12**, 12851–12861 (2010)
25. M.J. Plater, A. Jeremiah, G. Bourhill, J. Chem. Soc. Perkin Trans. **1**, 91–96 (2002)
26. G. Lu, J. Li, S. Yan, W. Zhu, Z. Ou, K.M. Kadish, Inorg. Chem. **54**, 5795–5805 (2015)
27. H. Ahn, A. Chandekar, B. Kang, C. Sung, J.E. Whitten, Chem. Mater. **16**, 3274–3278 (2004)
28. G. Lu, K. Wang, X. Kong, H. Pan, J. Zhang, Y. Chen, J. Jiang, ChemElectroChem **5**, 605–609 (2018)
29. Y. Chen, D. Li, N. Yuan, J. Gao, R. Gu, G. Lu, M. Bouvet, J.Mater. Chem. **22**, 22142–22149 (2012)
30. K. Wang, D. Qi, H. Wang, W. Cao, W. Li, T. Liu, C. Duan, J. Jiang, Chem. A Eur. J. **19**, 11162–11166 (2013)
31. M. Kasha, H.R. Rawls, M.A. ElBayoumi, Pure Appl. Chem. **11**, 371–392 (1965)
32. Y. Chen, X. Kong, G. Lu, D. Qi, Y. Wu, X. Li, M. Bouvet, D. Sun, J. Jiang, Mater. Chem. Front. **2**, 1009–1016 (2018)
33. G. Lu, X. Kong, J. Sun, L. Zhang, Y. Chen, J. Jiang, Chem. Commun. **53**, 12754–12757 (2017)
34. M. Yoneyama, M. Sugi, M. Saito, K. Ikegama, S. Kuroda, S. Iizima, Jpn. J. Appl. Phys. **25**, 961 (1986)
35. H. Wang, X. Kong, S. Zhao, J. Wu, X. Li, Y. Chen, New J. Chem. **41**, 11955–11961 (2017)
36. V. Parra, J. Brunet, A. Pauly, M. Bouvet, Analyst **134**, 1776–1778 (2009)
37. L.A. Mercante, A. Pavinatto, L.E.O. Iwaki, V.P. Scagion, V. Zucolotto, O.N. Oliveira, L.H.C. Maitoso, D.S. Correa, ACS Appl. Mater. Interfaces **7**, 4784–4790 (2015)
38. Y.V.M. Reddy, S. Bathinapurla, T. Luczak, M. Osińska, H. Maseed, P. Ragavendra, L.S. Sarma, V.V.S.S. Srikanth, G. Madhavi, New J. Chem. **42**, 3137–3146 (2018)

6.Cai X, Ning H. Crystal structure of di-μ-acetato-diacetatobis (μ-6, 6′-dimethoxy-2,2′-{[(propane-1,3-diylbis (azanylylidene)] bis (methanylylidene)} diphenolato) tetrazinc[J]. Acta Crystallographica Section E: Crystallographic Communications, 2015, 71(12): 217-218.

Acta Cryst E CRYSTALLOGRAPHIC COMMUNICATIONS

OPEN ACCESS

ISSN 2056-9890

Crystal structure of di-μ-acetato-di-acetatobis(μ-6,6′-dimethoxy-2,2′-{[(propane-1,3-diylbis(azanylylidene)]-bis(methanylylidene)}diphenolato)tetra-zinc

Xue Cai* and Hui Ning

Department of Chemistry, Mudanjiang Normal University, Mudanjiang 157011, People's Republic of China. *Correspondence e-mail: xuecai@mail.sdu.edu.cn

Received 9 October 2015; accepted 29 October 2015

Edited by T. J. Prior, University of Hull, England

The tetranuclear title complex, $[Zn_4(C_{19}H_{20}N_2O_4)_2(CH_3COO)_4]$, is formed from two dinuclear motifs related by an inversion centre. The two crystallographically independent Zn^{II} ions in the asymmetric unit are in different coordination environments. One is square-based pyramidal with one O atom of an acetate group occupying the axial position and two N and O atoms of one bmspd [H_2bmspd = *N*,*N*′-bis(3-methoxysalicylidene)propylene-1,3-diamine] Schiff base ligand forming the basal plane. The other Zn^{II} atom is six-coordinated by four O atoms of the bmspd ligand forming the equatoral plane and two O atoms of different acetate groups located in the axial positions. As a result, the two phenolic planes of the bicompartmental Schiff base ligand are distorted slightly. However, the planes of the two Schiff base ligands are parallel. In addition, the Zn—N and Zn—O bond lengths span the reasonable ranges 2.062 (2)–2.073 (2) and 1.9261 (15)–2.4356 (16) Å, respectively. The Zn···Zn distances separated by phenolic O atoms are 3.2466 (4) Å while the Zn···Zn distances bridged by acetate groups are 5.9835 (6) Å. The tetranuclear moieties are connected by van der Waals interactions, and form a chain along *c* axis.

Keywords: crystal structure; zinc; Schiff base; acetate.

CCDC reference: 724776

1. Related literature

Metal-organic coordination complexes of *N*,*N*′-bis(salicylidene)ethylenediamine (salen) Schiff-base derivatives have been studied extensively within the fields of homogeneous catalysis (Wezenberg & Kleij, 2008), non-linear optics (Rigamonti *et al.*, 2006), magnetics (Yuan *et al.*, 2007) and biological metalloenzyme mimics (Laskin *et al.*, 2008).

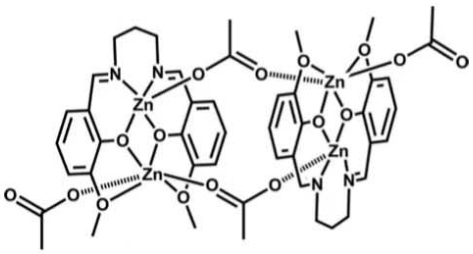

2. Experimental

2.1. Crystal data

$[Zn_4(C_{19}H_{20}N_2O_4)_2(C_2H_3O_2)_4]$
M_r = 1178.48
Triclinic, $P\overline{1}$
a = 10.4894 (9) Å
b = 10.7917 (9) Å
c = 11.9550 (11) Å
α = 103.425 (2)°
β = 94.323 (1)°
γ = 115.677 (1)°
V = 1162.17 (18) Å^3
Z = 1
Mo $K\alpha$ radiation
μ = 2.12 mm^{-1}
T = 298 K
0.15 × 0.10 × 0.08 mm

2.2. Data collection

Bruker SMART APEX CCD area-detector diffractometer
Absorption correction: multi-scan (*SADABS*; Sheldrick, 1996)
T_{min} = 0.742, T_{max} = 0.849
6281 measured reflections
4497 independent reflections
3969 reflections with $I > 2\sigma(I)$
R_{int} = 0.013

2.3. Refinement

$R[F^2 > 2\sigma(F^2)]$ = 0.024
$wR(F^2)$ = 0.071
S = 1.05
4497 reflections
318 parameters
H-atom parameters constrained
$\Delta\rho_{max}$ = 0.26 e Å^{-3}
$\Delta\rho_{min}$ = −0.27 e Å^{-3}

Data collection: *APEX2* (Bruker, 2004); cell refinement: *SAINT-Plus* (Bruker, 2001); data reduction: *SAINT-Plus*; program(s) used to solve structure: *SHELXTL* (Sheldrick, 2008); program(s) used to refine structure: *SHELXL97* (Sheldrick, 2008); molecular graphics: *XP* in *SHELXTL*; software used to prepare material for publication: *SHELXTL*.

Acknowledgements

The authors gratefully acknowledge the financial support provided by the Postdoctoral Science-Research Developmental Foundation of Heilongjiang Province (LBH-Q13170).

Supporting information for this paper is available from the IUCr electronic archives (Reference: PJ2024).

References

Bruker (2001). *SAINT-Plus*. Bruker AXS Inc., Madison, Wisconsin, USA.
Bruker (2004). *APEX2*. Bruker AXS Inc., Madison, Wisconsin, USA.
Laskin, I., Yang, Z. & Chu, I. K. (2008). *J. Am. Chem. Soc.* **130**, 3218–3220.
Rigamonti, L., Demartin, F., Forni, A., Righetto, S. & Pasini, A. (2006). *Inorg. Chem.* **45**, 10976–10989.
Sheldrick, G. M. (1996). *SADABS*. University of Göttingen, Germany.
Sheldrick, G. M. (2008). *Acta Cryst.* A**64**, 112–122.
Wezenberg, S. J. & Kleij, A. W. (2008). *Angew. Chem. Int. Ed.* **47**, 2354–2364.
Yuan, M., Zhao, F., Zhang, W., Wang, Z.-M. & Gao, S. (2007). *Inorg. Chem.* **46**, 11235–11242.

supporting information

Acta Cryst. (2015). E**71**, m217–m218 [https://doi.org/10.1107/S2056989015020551]

Crystal structure of di-μ-acetato-diacetatobis(μ-6,6′-dimethoxy-2,2′-{[(propane-1,3-diylbis(azanylylidene)]bis(methanylylidene)}diphenolato)tetrazinc

Xue Cai and Hui Ning

S1. Comment

The metal-organic coordination complexes of *N*,*N*′-bis(salicylidene)ethylenediamine (salen) Schiff-base derivatives were extensively studied within the field of homogeneous catalysis (Wezenberg *et al.*, 2008), nonlinear optic (Rigamonti *et al.*, 2006), magnetics (Yuan *et al.*, 2007), and biological metalloenzymes mimic (Laskin *et al.*, 2008). Recently, the compartmental salen ligands derived from the 2:1 condensation between 3-methoxysalicylaldehyde and corresponding diamines allowing for two metal ions located in dissimilar N_2O_2 and O_4 cavities bridged by phenolic oxygen atoms, which bring interesting magnetic phenomena and intriguing optical properties. Herein, a novel heterometallic tetranuclear $(Zn)_4$ compound has been obtained by step-by-step method and its structure is described.

The compound is composed of two $[Zn_2(bmspd)(OAc)]^+$ ions bridged by two acetate ions. There are two kinds of symmetry-independent zinc ions in this compound. One zinc ion (Zn1) is located in a five-coordinated environment, as shown in Figure 1. The other kind of zinc ion (Zn2) is coordinated by the O_5 cavity in bmspd ligand and two oxygen atoms of acetate ions in pseudo-octahedral geometry. The neighbouring tetranuclear molecules form a two-dimensional supramolecular network by virtue of intermolecular π-π interactions. (Figure 2)

S2. Experimental

A mixture of metal-free Schiff-base ligand H_2bmspd (0.4 mmol 0.1368 g) and $Zn(OAc)_2{\cdot}2H_2O$ (0.4 mmol 0.0878 g) in methanol (20 ml) was stirred for 30 min at room temperature. Then, a solution of $Zn(OAc)_2{\cdot}2H_2O$ (0.4 mmol 0.0878 g) in methanol was added dropwise and the mixture was kept stirring for another 30 min at room temperature. Pale yellow block-shaped crystals for suitable for X-ray diffraction were obtained by slowly diffusing diethyl ether into the filtrate. The final mass of product was 0.0966 g.

S3. Refinement

The coordinates of the difference H atoms bound to C atoms were placed using the HFIX commands in *SHELXL-97*, with C—H distances of 0.93–0.97 Å. All H atoms were allowed for as riding atoms with U_{iso}(H) = 1.2U_{eq}(C) or 1.5U_{eq}(C). The orientation of hydrogen atoms of methyl groups of acetate was allowed to refine subject to geometric restraints.

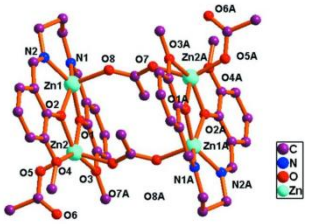

Figure 1
ORTEP diagram of molecular structure for complex $[Zn_4(bmspd)_2(OAc)_4]$ with atoms drawn as 50% probability ellipsoids.

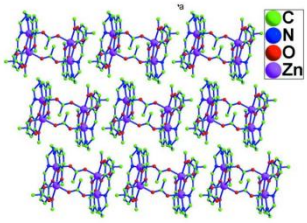

Figure 2
The perspective drawing of complex $[Zn_4(bmspd)_2(OAc)_4]$ packing in *ac* plane.

Di-μ-acetato-diacetatobis(μ-6,6′-dimethoxy-2,2′-{[(propane-1,3-diylbis(azanylylidene)]bis(methanylylidene)}diphenolato)tetrazinc

Crystal data

$[Zn_4(C_{17}H_{16}N_2O_4)_2(C_2H_3O_2)_4]$	Z = 1
M_r = 1178.48	$F(000)$ = 604
Triclinic, $P\overline{1}$	D_x = 1.684 Mg m^{-3}
Hall symbol: -P 1	Mo $K\alpha$ radiation, λ = 0.71073 Å
a = 10.4894 (9) Å	Cell parameters from 4019 reflections
b = 10.7917 (9) Å	θ = 2.2–27.5°
c = 11.9550 (11) Å	μ = 2.12 mm^{-1}
α = 103.425 (2)°	T = 298 K
β = 94.323 (1)°	Block, yellow
γ = 115.677 (1)°	0.15 × 0.10 × 0.08 mm
V = 1162.17 (18) Å^3	

Data collection

Bruker SMART APEX CCD area-detector diffractometer	6281 measured reflections 4497 independent reflections
Radiation source: fine-focus sealed tube	3969 reflections with $I > 2\sigma(I)$
Graphite monochromator	R_{int} = 0.013
Detector resolution: 0 pixels mm^{-1}	θ_{max} = 26.0°, θ_{min} = 1.8°
phi and ω scans	h = −6→12
Absorption correction: multi-scan (*SADABS*; Sheldrick, 1996)	k = −13→13 l = −13→14
T_{min} = 0.742, T_{max} = 0.849	

Refinement

Refinement on F^2	Secondary atom site location: difference Fourier map
Least-squares matrix: full	Hydrogen site location: inferred from neighbouring sites
$R[F^2 > 2\sigma(F^2)]$ = 0.024	H-atom parameters constrained
$wR(F^2)$ = 0.071	$w = 1/[\sigma^2(F_o^2) + (0.0367P)^2 + 0.3975P]$ where $P = (F_o^2 + 2F_c^2)/3$
S = 1.05	$(\Delta/\sigma)_{max}$ = 0.006
4497 reflections	$\Delta\rho_{max}$ = 0.26 e Å^{-3}
318 parameters	$\Delta\rho_{min}$ = −0.27 e Å^{-3}
0 restraints	
Primary atom site location: structure-invariant direct methods	

Special details

Geometry. All e.s.d.'s (except the e.s.d. in the dihedral angle between two l.s. planes) are estimated using the full covariance matrix. The cell e.s.d.'s are taken into account individually in the estimation of e.s.d.'s in distances, angles and torsion angles; correlations between e.s.d.'s in cell parameters are only used when they are defined by crystal symmetry. An approximate (isotropic) treatment of cell e.s.d.'s is used for estimating e.s.d.'s involving l.s. planes.

Refinement. Refinement of F^2 against ALL reflections. The weighted R-factor wR and goodness of fit S are based on F^2, conventional R-factors R are based on F, with F set to zero for negative F^2. The threshold expression of $F^2 > \sigma(F^2)$ is used only for calculating R-factors(gt) *etc.* and is not relevant to the choice of reflections for refinement. R-factors based on F^2 are statistically about twice as large as those based on F, and R- factors based on ALL data will be even larger.

Fractional atomic coordinates and isotropic or equivalent isotropic displacement parameters (Å^2)

	x	y	z	U_{iso}*/U_{eq}
C1	0.5747 (2)	0.1717 (3)	0.1390 (2)	0.0479 (6)
H1A	0.5651	0.0938	0.1692	0.072*

H1B	0.5348	0.1350	0.0563	0.072*
H1C	0.5239	0.2186	0.1783	0.072*
C2	0.7601 (2)	0.3909 (2)	0.12186 (18)	0.0334 (4)
C3	0.6657 (2)	0.4234 (3)	0.0636 (2)	0.0431 (5)
H3	0.5666	0.3642	0.0497	0.052*
C4	0.7206 (3)	0.5459 (3)	0.0258 (2)	0.0540 (7)
H4	0.6577	0.5680	−0.0144	0.065*
C5	0.8656 (3)	0.6339 (3)	0.0473 (2)	0.0485 (6)
H5	0.9005	0.7136	0.0193	0.058*
C6	0.9640 (2)	0.6057 (2)	0.11148 (18)	0.0344 (5)
C7	0.9110 (2)	0.4824 (2)	0.14919 (17)	0.0288 (4)
C8	1.1149 (2)	0.7072 (2)	0.13321 (19)	0.0374 (5)
H8	1.1384	0.7791	0.0964	0.045*
C9	1.3647 (2)	0.8311 (2)	0.2054 (2)	0.0428 (5)
H9A	1.3563	0.9191	0.2172	0.051*
H9B	1.3959	0.8132	0.1316	0.051*
C10	1.4783 (2)	0.8521 (2)	0.3040 (2)	0.0438 (5)
H10A	1.4411	0.8567	0.3759	0.053*
H10B	1.5627	0.9436	0.3152	0.053*
C11	1.5238 (3)	0.7346 (3)	0.2830 (2)	0.0503 (6)
H11A	1.5415	0.7156	0.2039	0.060*
H11B	1.6138	0.7683	0.3370	0.060*
C12	1.4643 (2)	0.5208 (3)	0.33241 (19)	0.0396 (5)
H12	1.5642	0.5583	0.3466	0.048*
C13	1.3848 (2)	0.3817 (2)	0.35174 (18)	0.0362 (5)
C14	1.4677 (3)	0.3186 (3)	0.3880 (2)	0.0446 (6)
H14	1.5679	0.3689	0.4015	0.053*
C15	1.4038 (3)	0.1858 (3)	0.4035 (2)	0.0499 (6)
H15	1.4602	0.1465	0.4280	0.060*
C16	1.2532 (3)	0.1083 (3)	0.3828 (2)	0.0435 (5)
H16	1.2093	0.0169	0.3925	0.052*
C17	1.1699 (2)	0.1679 (2)	0.34775 (18)	0.0354 (5)
C18	1.2338 (2)	0.3069 (2)	0.33311 (17)	0.0310 (4)
C19	0.9443 (3)	−0.0457 (3)	0.3169 (3)	0.0661 (8)
H19A	0.8425	−0.0761	0.2991	0.099*
H19B	0.9686	−0.0585	0.3910	0.099*
H19C	0.9691	−0.1021	0.2566	0.099*
C20	0.7933 (2)	−0.0082 (2)	0.06099 (19)	0.0343 (4)
C21	0.7849 (2)	−0.1000 (3)	−0.0585 (2)	0.0422 (5)
H21A	0.7129	−0.1974	−0.0704	0.063*
H21B	0.8769	−0.0973	−0.0633	0.063*
H21C	0.7594	−0.0635	−0.1179	0.063*
C22	0.8649 (2)	0.3057 (2)	0.48569 (18)	0.0314 (4)
C23	1.0099 (3)	0.3370 (3)	0.5482 (2)	0.0493 (6)
H23A	1.0778	0.4354	0.5584	0.074*
H23B	1.0424	0.2747	0.5026	0.074*
H23C	1.0022	0.3208	0.6236	0.074*
N1	1.22093 (19)	0.71044 (18)	0.19729 (15)	0.0340 (4)

N2	1.41504 (19)	0.59888 (19)	0.29835 (16)	0.0359 (4)	
O1	0.99395 (15)	0.44590 (15)	0.20882 (13)	0.0329 (3)	
O2	1.14934 (15)	0.35966 (15)	0.30055 (13)	0.0343 (3)	
O3	0.72225 (16)	0.27149 (18)	0.15849 (17)	0.0488 (4)	
O4	1.02202 (17)	0.10166 (16)	0.32310 (15)	0.0437 (4)	
O5	0.89752 (18)	0.11959 (17)	0.09127 (14)	0.0436 (4)	
O6	0.7050 (2)	−0.0567 (2)	0.12112 (17)	0.0590 (5)	
O7	0.82953 (16)	0.25334 (17)	0.37574 (13)	0.0409 (4)	
O8	0.77997 (17)	0.33076 (18)	0.54407 (13)	0.0423 (4)	
Zn1	1.20447 (2)	0.56385 (2)	0.28798 (2)	0.02906 (8)	
Zn2	0.92824 (2)	0.25063 (2)	0.24271 (2)	0.02988 (8)	

Atomic displacement parameters (Å²)

	U^{11}	U^{22}	U^{33}	U^{12}	U^{13}	U^{23}
C1	0.0285 (12)	0.0518 (14)	0.0543 (15)	0.0087 (11)	0.0080 (10)	0.0197 (12)
C2	0.0322 (11)	0.0350 (11)	0.0342 (11)	0.0155 (9)	0.0064 (9)	0.0125 (9)
C3	0.0314 (12)	0.0494 (13)	0.0485 (13)	0.0184 (11)	0.0017 (10)	0.0174 (11)
C4	0.0471 (15)	0.0605 (16)	0.0624 (17)	0.0293 (13)	−0.0030 (12)	0.0281 (14)
C5	0.0517 (15)	0.0470 (14)	0.0532 (15)	0.0243 (12)	0.0024 (12)	0.0258 (12)
C6	0.0383 (12)	0.0344 (11)	0.0332 (11)	0.0177 (9)	0.0062 (9)	0.0136 (9)
C7	0.0311 (10)	0.0288 (10)	0.0270 (10)	0.0145 (8)	0.0052 (8)	0.0081 (8)
C8	0.0461 (13)	0.0308 (11)	0.0363 (11)	0.0151 (10)	0.0110 (10)	0.0164 (9)
C9	0.0401 (13)	0.0356 (12)	0.0433 (13)	0.0061 (10)	0.0100 (10)	0.0178 (10)
C10	0.0331 (12)	0.0387 (12)	0.0445 (13)	0.0024 (10)	0.0072 (10)	0.0141 (10)
C11	0.0302 (12)	0.0540 (15)	0.0619 (16)	0.0099 (11)	0.0159 (11)	0.0262 (13)
C12	0.0259 (11)	0.0473 (13)	0.0384 (12)	0.0149 (10)	0.0045 (9)	0.0046 (10)
C13	0.0352 (12)	0.0427 (12)	0.0292 (10)	0.0220 (10)	0.0001 (8)	0.0019 (9)
C14	0.0394 (13)	0.0543 (14)	0.0402 (12)	0.0284 (12)	−0.0019 (10)	0.0041 (11)
C15	0.0579 (16)	0.0616 (16)	0.0421 (13)	0.0432 (14)	−0.0025 (11)	0.0093 (11)
C16	0.0597 (16)	0.0434 (13)	0.0363 (12)	0.0326 (12)	0.0053 (11)	0.0113 (10)
C17	0.0424 (12)	0.0379 (11)	0.0291 (10)	0.0226 (10)	0.0064 (9)	0.0077 (9)
C18	0.0332 (11)	0.0353 (11)	0.0254 (10)	0.0193 (9)	0.0029 (8)	0.0048 (8)
C19	0.0645 (19)	0.0417 (15)	0.085 (2)	0.0146 (14)	0.0019 (16)	0.0313 (15)
C20	0.0313 (11)	0.0406 (12)	0.0349 (11)	0.0190 (10)	0.0052 (9)	0.0134 (9)
C21	0.0367 (12)	0.0430 (12)	0.0406 (12)	0.0185 (10)	0.0017 (10)	0.0035 (10)
C22	0.0355 (11)	0.0279 (10)	0.0316 (10)	0.0131 (9)	0.0107 (9)	0.0121 (8)
C23	0.0518 (15)	0.0672 (16)	0.0374 (12)	0.0374 (13)	0.0075 (11)	0.0111 (12)
N1	0.0332 (10)	0.0307 (9)	0.0325 (9)	0.0083 (8)	0.0084 (7)	0.0119 (7)
N2	0.0279 (9)	0.0393 (10)	0.0364 (10)	0.0125 (8)	0.0083 (7)	0.0100 (8)
O1	0.0255 (7)	0.0312 (7)	0.0399 (8)	0.0094 (6)	0.0001 (6)	0.0163 (6)
O2	0.0269 (7)	0.0315 (7)	0.0460 (9)	0.0138 (6)	0.0035 (6)	0.0149 (6)
O3	0.0254 (8)	0.0468 (9)	0.0741 (12)	0.0089 (7)	0.0038 (8)	0.0355 (9)
O4	0.0397 (9)	0.0345 (8)	0.0589 (10)	0.0168 (7)	0.0095 (8)	0.0182 (7)
O5	0.0423 (9)	0.0382 (9)	0.0384 (9)	0.0129 (7)	0.0064 (7)	0.0024 (7)
O6	0.0571 (11)	0.0699 (12)	0.0544 (11)	0.0260 (10)	0.0266 (9)	0.0283 (10)
O7	0.0369 (8)	0.0534 (9)	0.0281 (8)	0.0185 (7)	0.0093 (6)	0.0086 (7)
O8	0.0365 (9)	0.0551 (10)	0.0323 (8)	0.0206 (8)	0.0113 (7)	0.0077 (7)

Zn1	0.02476 (13)	0.02968 (13)	0.03096 (13)	0.00999 (10)	0.00664 (9)	0.01083 (10)
Zn2	0.02869 (14)	0.02835 (13)	0.02989 (13)	0.01035 (10)	0.00723 (10)	0.00921 (10)

Geometric parameters (Å, °)

C1—O3	1.412 (3)	C15—C16	1.398 (4)
C1—H1A	0.9600	C15—H15	0.9300
C1—H1B	0.9600	C16—C17	1.382 (3)
C1—H1C	0.9600	C16—H16	0.9300
C2—O3	1.362 (3)	C17—O4	1.370 (3)
C2—C3	1.378 (3)	C17—C18	1.414 (3)
C2—C7	1.416 (3)	C18—O2	1.322 (2)
C3—C4	1.394 (3)	C19—O4	1.418 (3)
C3—H3	0.9300	C19—H19A	0.9600
C4—C5	1.363 (4)	C19—H19B	0.9600
C4—H4	0.9300	C19—H19C	0.9600
C5—C6	1.417 (3)	C20—O6	1.226 (3)
C5—H5	0.9300	C20—O5	1.277 (3)
C6—C7	1.399 (3)	C20—C21	1.509 (3)
C6—C8	1.441 (3)	C21—H21A	0.9600
C7—O1	1.325 (2)	C21—H21B	0.9600
C8—N1	1.285 (3)	C21—H21C	0.9600
C8—H8	0.9300	C22—O8	1.253 (2)
C9—N1	1.482 (3)	C22—O7	1.259 (2)
C9—C10	1.514 (3)	C22—C23	1.501 (3)
C9—H9A	0.9700	C23—H23A	0.9600
C9—H9B	0.9700	C23—H23B	0.9600
C10—C11	1.515 (4)	C23—H23C	0.9600
C10—H10A	0.9700	N1—Zn1	2.0727 (17)
C10—H10B	0.9700	N2—Zn1	2.0616 (18)
C11—N2	1.479 (3)	O1—Zn1	2.0203 (14)
C11—H11A	0.9700	O1—Zn2	2.0639 (14)
C11—H11B	0.9700	O2—Zn2	2.0632 (14)
C12—N2	1.284 (3)	O2—Zn1	2.0676 (14)
C12—C13	1.452 (3)	O3—Zn2	2.4356 (16)
C12—H12	0.9300	O5—Zn2	1.9261 (15)
C13—C18	1.402 (3)	O7—Zn2	1.9635 (14)
C13—C14	1.415 (3)	O8—Zn1^{i}	2.0201 (15)
C14—C15	1.359 (4)	Zn1—O8^{i}	2.0201 (15)
C14—H14	0.9300		
O3—C1—H1A	109.5	C13—C18—C17	118.12 (19)
O3—C1—H1B	109.5	O4—C19—H19A	109.5
H1A—C1—H1B	109.5	O4—C19—H19B	109.5
O3—C1—H1C	109.5	H19A—C19—H19B	109.5
H1A—C1—H1C	109.5	O4—C19—H19C	109.5
H1B—C1—H1C	109.5	H19A—C19—H19C	109.5
O3—C2—C3	125.4 (2)	H19B—C19—H19C	109.5

O3—C2—C7	112.88 (18)	O6—C20—O5	124.8 (2)
C3—C2—C7	121.7 (2)	O6—C20—C21	120.8 (2)
C2—C3—C4	119.1 (2)	O5—C20—C21	114.42 (19)
C2—C3—H3	120.4	C20—C21—H21A	109.5
C4—C3—H3	120.4	C20—C21—H21B	109.5
C5—C4—C3	120.6 (2)	H21A—C21—H21B	109.5
C5—C4—H4	119.7	C20—C21—H21C	109.5
C3—C4—H4	119.7	H21A—C21—H21C	109.5
C4—C5—C6	121.0 (2)	H21B—C21—H21C	109.5
C4—C5—H5	119.5	O8—C22—O7	120.8 (2)
C6—C5—H5	119.5	O8—C22—C23	119.36 (19)
C7—C6—C5	119.1 (2)	O7—C22—C23	119.80 (19)
C7—C6—C8	123.83 (19)	C22—C23—H23A	109.5
C5—C6—C8	117.1 (2)	C22—C23—H23B	109.5
O1—C7—C6	123.77 (18)	H23A—C23—H23B	109.5
O1—C7—C2	117.92 (17)	C22—C23—H23C	109.5
C6—C7—C2	118.31 (18)	H23A—C23—H23C	109.5
N1—C8—C6	127.81 (19)	H23B—C23—H23C	109.5
N1—C8—H8	116.1	C8—N1—C9	115.46 (18)
C6—C8—H8	116.1	C8—N1—Zn1	125.35 (15)
N1—C9—C10	113.12 (18)	C9—N1—Zn1	119.19 (14)
N1—C9—H9A	109.0	C12—N2—C11	116.01 (19)
C10—C9—H9A	109.0	C12—N2—Zn1	124.81 (15)
N1—C9—H9B	109.0	C11—N2—Zn1	118.53 (15)
C10—C9—H9B	109.0	C7—O1—Zn1	129.06 (12)
H9A—C9—H9B	107.8	C7—O1—Zn2	125.64 (12)
C9—C10—C11	114.1 (2)	Zn1—O1—Zn2	105.29 (6)
C9—C10—H10A	108.7	C18—O2—Zn2	127.10 (13)
C11—C10—H10A	108.7	C18—O2—Zn1	129.24 (13)
C9—C10—H10B	108.7	Zn2—O2—Zn1	103.62 (6)
C11—C10—H10B	108.7	C2—O3—C1	119.07 (18)
H10A—C10—H10B	107.6	C2—O3—Zn2	113.52 (12)
N2—C11—C10	113.20 (19)	C1—O3—Zn2	127.31 (14)
N2—C11—H11A	108.9	C17—O4—C19	119.41 (19)
C10—C11—H11A	108.9	C20—O5—Zn2	120.25 (14)
N2—C11—H11B	108.9	C22—O7—Zn2	137.14 (14)
C10—C11—H11B	108.9	C22—O8—Zn1^{i}	135.32 (15)
H11A—C11—H11B	107.8	O1—Zn1—O8^{i}	109.18 (6)
N2—C12—C13	128.7 (2)	O1—Zn1—N2	149.75 (7)
N2—C12—H12	115.7	O8^{i}—Zn1—N2	98.57 (7)
C13—C12—H12	115.7	O1—Zn1—O2	75.35 (5)
C18—C13—C14	119.5 (2)	O8^{i}—Zn1—O2	100.83 (6)
C18—C13—C12	123.98 (19)	N2—Zn1—O2	88.08 (6)
C14—C13—C12	116.5 (2)	O1—Zn1—N1	88.64 (6)
C15—C14—C13	121.3 (2)	O8^{i}—Zn1—N1	103.96 (7)
C15—C14—H14	119.3	N2—Zn1—N1	96.30 (7)
C13—C14—H14	119.3	O2—Zn1—N1	153.84 (7)
C14—C15—C16	120.0 (2)	O5—Zn2—O7	137.44 (7)

7.姜力,周启,陈玉锋,蔡雪.5,15-二(二茂铁基)-卟啉酞菁钇的结构和振动光谱的密度泛函理论研究[J].原子与分子物理学报,2021,38(03):47-51.

第38卷 第3期 原 子 与 分 子 物 理 学 报 Vol. 38 No. 3
2021年6月 JOURNAL OF ATOMIC AND MOLECULAR PHYSICS Jun. 2021

5,15－二(二茂铁基)－卟啉酞菁钇的结构和振动光谱的密度泛函理论研究

姜 力,周 启,陈玉锋,蔡 雪

(牡丹江师范学院 化学化工学院,牡丹江市 157000)

摘 要:本文选用混杂的B3LYP密度泛函理论方法,在Lanl2dz水平上,对5,15－二(二茂铁基)－卟啉酞菁钇〖Por(Fc)$_2$〗Y(Pc)的结构进行了优化,结果表明,5,15－二(二茂铁基)－卟啉酞菁钇呈现出三明治型构型,卟啉环与酞菁环呈穹型围绕在金属钇原子周围.对分子内主要的键长与键角进行了理论计算,通过频率计算,得到了5,15－二(二茂铁基)－卟啉酞菁钇〖Por(Fc)$_2$〗Y(Pc)的红外光谱图,与实验所得的红外光谱图进行比对,将理论计算和实验所得的光谱主要振动峰进行了线性回归拟合,相关系数为0.992,标准偏差为16.96.理论计算与实验所获得的红外光谱图基本一致,说明本文所选用的DFT理论计算方法是可行的.通过GaussView软件对5,15－二(二茂铁基)－卟啉酞菁钇的红外谱带简正振动模式进行了指认.此外,分析讨论了5,15－二(二茂铁基)－卟啉酞菁钇〖Por(Fc)$_2$〗Y(Pc)的分子静电势,确定了极大值与极小值的位置.对于研究5,15－二(二茂铁基)－卟啉酞菁钇分子的性质,提供了相应的理论基础.

关键词:卟啉酞菁;密度泛函理论;振动光谱;分子静电势
中图分类号:O641.4 文献标识码:A **DOI**:10.19855/j.1000-0364.2021.031007

Theoretical study on the structure and vibrational spectroscopy of 5,15－bis(ferrocenyl)－porphyrin yttrium phthalocyanine by density functional theory

JIANG Li, ZHOU Qi, CHEN Yu-Feng, CAI Xue

(Chemistry and Chemical Engineering Department, Mudanjiang Normal University, Mudanjiang 157000, China)

Abstract: In this paper, the structure of 5,15－bis(ferrocenyl)－porphyrin phthalocyanine yttrium 〖Por(Fc)$_2$〗Y(Pc) molecule is optimized and calculated at density functional B3LYP level using Lanl2dz basis set. The results show that the 5,15－bis(ferrocenyl)－porphyrin yttrium phthalocyanine molecule exhibits a sandwich structure, and the porphyrin ring and the phthalocyanine ring are domed around the metal yttrium atom. The main bond lengths and bond angles in the molecule are calculated. IR spectrum was obtained from the calculation results of the frequencies, and compared with the experimental IR spectrum. By means of a line of best fit of the experimental IR frequencies versus the calculated ones in the range of 400～2000 cm^{-1}, the correlation coefficient and the standard deviation are found to be 0.992 and 16.96, respectively. The theoretical calculation is basically consistent with the infrared spectrogram obtained in the experiment, which indicates that the theoretical calculation method of DFT adopted is feasible in this paper. The vibrational mode was assigned on the basis of the GaussView. In addition, the molecular electrostatic potentialwere of 〖Por(Fc)$_2$〗Y(Pc) were discussed based on the calculate results. This study provided a theoretical support for the analysis of 〖Por(Fc)$_2$〗Y(Pc).

Key words: Porphyrin phthalocyanine; Density functional theory (DFT); Vibrational spectrum; Molecular electrostatic potential

收稿日期:2020-09-14
基金项目:黑龙江省教育厅基本科研业务费青年项目(1353MSYQN001);牡丹江师范学院科研项目(QN2019001)
作者简介:姜力(1987—),男,实验师.主要从事分子光谱研究.
通讯作者:蔡雪.E-mail:lijiang@mdjnu.edu.cn

(C)1994-2021 China Academic Journal Electronic Publishing House. All rights reserved. http://www.cnki.net

1 引 言

卟啉和酞菁作为最常见也是最重要的四吡咯衍生物，由于其具有比较独特的光、电、磁性质，引起了科学家们的广泛关注[1,2]. 它们是一类具有18π电子的多吡咯共轭化合物，可以同多种稀土金属配位构成双层或三层的三明治型配合物[3]，在这些分子中，彼此之间被拉到很近距离的两个或三个共轭 π 体系之间相互作用，再加上稀土金属中心固有的性质[4]，使这些配合物表现出三明治型结构独特的性质，使它们在分子电子学，分子信息储存，气体传感，电致变色和有机场效应晶体管等方面具有广泛应用[5-8].

密度泛函理论(density functional theory，DFT)与实验数据相结合的方法，常被用来研究分子的几何构型和振动光谱[9-11]，由于 B3LYP 方法对计算资源要求不高并且具有较高的精确度，所以该方法在理论计算上应用较广泛. Seog Woo 等人研究合成了 5－二茂铁－15－苯基－2，8，12，18－四乙基－3，7，13，17－四甲基卟啉(1)，并分别与 $Zn(OAc)_2 \cdot 2H_2O$ 和 $MnCl_2 \cdot 4H_2O$ 金属化反应得到 Zn(1)、Mncl(1). 在 0.29、0.22、0.37 V 下，(1)、Zn(1)、Mncl(1)的循环伏安图显示了二茂铁的可逆单电子氧化过程[12]. Boyd 等人合成了 5，15－二(二茂铁)－2，8，12，18－四叔丁基－3，7，13，17－四甲基卟啉并得到了其镍的配合物，发现该配合物呈 syn 构型分布，在两个二茂铁基团之间存在电子耦合[13]. 尽管有四吡咯配合物体系中引入二茂铁基团的很多例子被报道过，但在其三明治型配合物结构框架中引入二茂铁基团并同时混杂卟啉与酞菁的例子却很少. 本文采用混杂的 B3LYP 密度泛函方法[14,15]，在 Lanl2dz 基组水平上，计算 5，15－二(二茂铁基)－卟啉酞菁钇分子 $[Por(Fc)_2]Y(Pc)$ 的红外光谱，与实验所得的红外光谱图进行了比对，利用 Gauss-View 软件对 5，15－二(二茂铁基)－卟啉酞菁钇 $[Por(Fc)_2]Y(Pc)$ 的简正振动模式进行了指认归属[16]，分析研究了 5，15－二(二茂铁基)－卟啉酞菁钇 $[Por(Fc)_2]Y(Pc)$ 的分子表面静电势.

2 理论计算和实验

值得提及的是，由于 $[Por(Fc)_2]Y(Pc)$ 分子中既包含稀土金属钇又含有过渡金属铁，再加上整个分子体系的所有原子共有 129 个之多，对于这样复杂的分子结构，一些小的基组如被大家熟知并被广泛使用的 6－31G(d)基组不能被用来计算. 因此在本文工作中选择了 Lanl2dz 基组[17]，在计算过程的能量最小化环节采用了使用冗余内坐标的 Berny 运算法则，全部计算过程采用默认的收敛标准，在前面步骤产生的能量最小化结构基础上进行了正则坐标分析[18-19]，计算所得的振动光谱频率用 0.9614 校正系数进行校正[20]. 理论计算采用 Gaussian09 量子化学程序包[21]，分子构型用 GaussView 6.0 构造，利用 Gaussian 09 程序包，在 B3LYP/Lanl2dz 水平上对 5，15－二(二茂铁基)－卟啉酞菁钇 $[Por(Fc)_2]Y(Pc)$ 的几何结构进行优化和频率计算，简正振动模式分析指认归属采用 GaussView 软件完成.

5，15－二(二茂铁基)－卟啉酞菁钇分子 $[Por(Fc)_2]Y(Pc)$ 的红外光谱(IR)采集使用 BIORAD FIS－165 分析仪，波数范围为 4000－400 cm^{-1}，分辨率是 2 cm^{-1}. 所有数据处理采用软件 NGSLabSpec1－Origin 中的 Baseline correction 进行处理，并用 Origin 8.0 工具作图.

3 结果与讨论

3.1 分子结构及优化

优化结果中没有发现虚频，表明优化得到的结构是 5，15－二(二茂铁基)－卟啉酞菁钇 $[Por(Fc)_2]Y(Pc)$ 的稳定构型(见图 1). 计算结果表明，优化后的分子结构对称性属于 C_2. 金属钇原子被夹入卟啉环与酞菁环之间，形成三明治型结构，两个环扭曲成碟子状，一个碟子相对于另一个扭曲了 45 度[22]，$N_6N_8N_9N_7$，$N_{12}N_{10}N_{11}N_{13}$ 的二面角均接近 0.00°，中心钇原子与酞菁环的四个异吲哚氮原子及卟啉环的四个吡咯氮原子配位形成四方反棱柱的配位结构(见图 2)，O 代表四个异吲哚(吡咯环)氮原子平面的中心. 由于引入了两个二茂铁基团，在卟啉环 meso 位发生取代，引起吡咯环的扭曲变形，与酞菁环之间空间位阻效应的相互影响，异吲哚也发生扭曲，伴随着两个二茂铁基团垂直于卟啉环各自相向旋转 45 度，卟啉环与酞菁环以金属钇原子为中心呈弯型围绕在其周围(见图 3).

3.2 5，15－二(二茂铁基)－卟啉酞菁钇 $[Por(Fc)_2]Y(Pc)$ 的红外谱带振动归属

$[Por(Fc)_2]Y(Pc)$ 分子由 129 个原子组成，

(C)1994-2021 China Academic Journal Electronic Publishing House. All rights reserved.　http://www.cnki.net

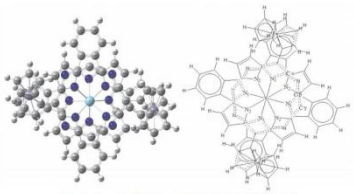

图 1　5，15－二(二茂铁基)－卟啉酞菁钇分子结构模型示意图

Fig. 1　Optimized structure of $[Por(Fc)_2]Y(Pc)$

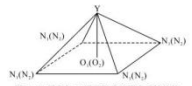

图 2　Y 原子与 N 原子组成的四方反棱柱体几何构型

Fig. 2　Geometrical configuration of tetragonal antiprism made of Y and N

表 1　Y 原子到 N 原子(异吲哚、吡咯环)平面的距离(Å)，主键长(Å)、键角(°)

Table 1　The calculated distances from Y to nitrogen plane (isoindole ring, pyrrole ring) and the main bond lengths and bond angles of $[Por(Fc)_2]Y(Pc)$. (Bond length unit: Å Bond angle unit:°)

R_{Y-N1}	$R_{N1-C\alpha}$	R_{Y-N1}	$R_{C\alpha-N}$	$\angle N_1YN_2$	$\angle YN_1C_\alpha$
1.53	1.37	2.51	1.33	105.18	123.97
R_{Y-O2}	$R_{N2-C\beta}$	R_{Y-N2}	$R_{C\beta-C\gamma}$	$\angle N_2YN_3$	$\angle YN_2C_\beta$
1.31	1.38	2.45	1.38	117.94	119.81

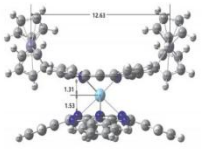

图 3　5，15－二(二茂铁基)－卟啉酞菁钇部分原子间距离示意图

Fig. 3　Optimized distances between some atoms in $[Por(Fc)_2]Y(Pc)$

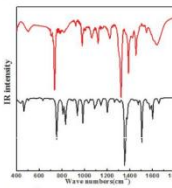

图 4　$[Por(Fc)_2]Y(Pc)$ 理论计算和实验的红外光谱图(红色为实验，黑色为计算)

Fig. 4　The theoretical (black) and experimental (red) IR spectrum of $[Por(Fc)_2]Y(Pc)$

共有 381 个简正振动模式. 利用 GaussView 软件对 5，15－二(二茂铁基)－卟啉酞菁钇的简正振动模式进行指认归属. 本文选取 $[Por(Fc)_2]Y(Pc)$ 分子 2000－400 cm^{-1} 的理论计算和实验数据作红外光谱图(见图 4)，理论计算和实验所得的红外光谱图基本上是一致的. 对理论计算和实验光谱主要振动峰进行了线性回归拟合[23](见图 5)，结果表明，相关系数为 0.992，标准偏差 16.96，两者吻合较好，说明本文所选取的 DFT

(C)1994-2021 China Academic Journal Electronic Publishing House. All rights reserved.　http://www.cnki.net

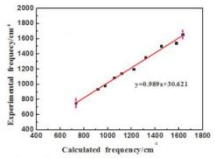

图 5　$[Por(Fc)_2]Y(Pc)$ 主要实验和理论计算频率线性回归拟合

Fig. 5　The linear regression fitting between main experimental and theoretical IR frequencies of $[Por(Fc)_2]Y(Pc)$

理论计算方法以及水平是可行的.

通过对红外谱图分析 466 cm^{-1} 的红外峰被指认归属于二茂铁茂环的面外摇摆以及吡咯环的面内摇摆振动；755 cm^{-1} 是红外谱图中的次强峰，被指认归属于异吲哚 C－H 面外弯曲振动，吡咯环 C－N－C 的面外弯曲振动；809 cm^{-1} 被指认为吡咯环 C－H 面外弯曲振动；830 cm^{-1} 归属于二茂铁茂环 C－H 面外弯曲以及吡咯环 C－N－C 的面内弯曲振动；935cm^{-1}归属于二茂铁茂环 C－H 面内弯曲以及吡咯环 C－H 面外弯曲振动. 985 cm^{-1}被指认归属于吡咯环的 C－H 面内弯曲，C－N－C 面内弯曲振动以及二茂铁茂环 C－H 面内弯曲振动；1201 cm^{-1}被指认为吡咯环 C－H 面内弯曲，C－N－C 面内弯曲振动；1355 cm^{-1}是红外谱图的最强峰，归属于吡咯环 C－C 伸缩、C－N－C 面内弯曲振动以及异吲哚 C－H 面内弯曲振动；1374 cm^{-1}的红外峰被指认为吡咯环的 C－N－C 面内弯曲振动，异吲哚 C－H 面内弯曲振动；1505 cm^{-1}是红外谱图的较强峰，被指认归属于异吲哚 C－H 面内弯曲振动；1599 cm^{-1}红外峰被指认为吡咯环 C－C 伸缩，C－H 面内弯曲振动.

3.3 5，15－二(二茂铁基)－卟啉酞菁钇 $[Por(Fc)_2]Y(Pc)$ 的分子表面静电势

空间中某一点的静电势是指将单位正电荷从无穷远移动到该点所需的功. 在原子核和电子共存的分子系统中，原子核和电子都会影响分子的静电势. 因此，分子周围空间与原子核距离不同的点静电势也不同. 静电势对于研究分子之间的静电相互作用，预测反应位点和预测分子性质具有重要意义. 分子静电势图上的不同颜色表示具有不同静电势的区域. 其中，红色，黄色，绿色和蓝色表示电负性逐渐降低. 蓝色区域具有更大的负静电势，而红色区域具有更大的正静电势. 白色区域的静电势接近零. 红色区域表示带负电的区域，即电子的密集区域，该区域更容易受到亲电试剂的攻击. 蓝色区域表示带正电荷的区域，更容易受到亲核试剂的攻击. 分子表面静电势分布图[24](见图 6)分析结果表明，5，15－二(二茂铁基)－卟啉酞菁钇分子存在极小值点 34 个，最小点位于吡咯环上的 N_{13} 原子处；极大值点 53 个，最大点位于异吲哚苯环上与 C_{46} 相连的 H_{75} 原子上.

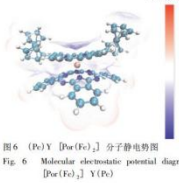

图 6　(Pc)Y $[Por(Fc)_2]$ 分子静电势图

Fig. 6　Molecular electrostatic potential diagram of $[Por(Fc)_2]Y(Pc)$

4 结 论

选用混杂的 B3LYP 密度泛函方法，在 Lanl2dz 水平下，对 5，15－二(二茂铁基)－卟啉酞菁钇 $[Por(Fc)_2]Y(Pc)$ 的结构进行了优化，对分子内主要的键长与键角进行了计算，通过频率计算，获得了 5，15－二(二茂铁基)－卟啉酞菁钇 $[Por(Fc)_2]Y(Pc)$ 的红外光谱，理论计算与实验所得的红外光谱图基本上是一致的，对理论计算和实验光谱主要振动峰进行了线性回归拟合，相关系数为 0.992，标准偏差为 16.69，两者吻合较好，说明本文选取的 DFT 理论计算方法是可靠的，并结合 GaussView 软件对 5，15－二(二茂铁基)－卟啉酞菁钇 $[Por(Fc)_2]Y(Pc)$ 的简正振动模式进行了指认归属. 此外，分析并讨论了 5，15－二(二茂铁基)－卟啉酞菁钇 $[Por(Fc)_2]Y(Pc)$ 的分子静电势. 对研究 5，15－二(二茂铁基)－卟啉酞菁钇 $[Por(Fc)_2]Y(Pc)$ 分子的性质，提供了理论基础.

(C)1994-2021 China Academic Journal Electronic Publishing House. All rights reserved.　http://www.cnki.net

参考文献：

[1] Wong C P, Robert F V, William D H. Lanthanide porphyrin complexes. potential new class of nuclear magnetic resonance dipolar probe [J]. *J. Am. Chem. Soc.*, 1974, 96: 7149.

[2] Yang X D, Sun J Z, Wang M, *et al*. Research progress in porphyrin and its derivatives as organic photoelectric materials [J]. *J. Funct. Mater.*, 2003, 34: 113 (in Chinese) [杨新国，孙景志，汪茫，等. 卟啉类光电功能材料研究进展 [J]. 功能材料，2003, 34: 113]

[3] Kinn L S, Moskalev P N, Makashev Yu A. Formation of phthalocyanines of rare－earth elements [J]. *J. Inorg. Chem.*, 1965, 10: 1065.

[4] Wong C P. New metalloporphyrins thorium and yttrium complexes of tetraphenylporphin [J]. *Tetrahydron Lett.*, 1975, 16: 2637.

[5] Komatsu T, Ohta K, Fujimoto T, *et al*. Chromic materials. part 1. －liquid－crystalline behaviour and electrochromism in bis (octakis－n－alkylphthalocyaninato) lutetium (III) complexes [J]. *J. Mater. Chem.*, 1994, 4: 533.

[6] Madru R, Guilland G, Maitrot M, *et al*. The first field effect transistor based on an intrinsic molecular semiconductor [J]. *J. Chem. Phys Lett.*, 1987, 142: 103.

[7] Marks T. Electrically conductive metallomacrocyclic assemblies [J]. *Science.*, 1985, 227: 881.

[8] Wright J D. Gas adsorption on phthalocyanines and its effects on electrical properties [J]. *Prog. Surf. Sci.*, 1989, 31: 1.

[9] Eichhorn H. Mesomorphic phthalocyanines, tetraazaporphyrins, porphyrins and triphenylenes as charge－transporting materials [J]. *J. Porphyrins Phthalocyanines.*, 2000, 4: 88.

[10] Wright J D. Gas adsorption on phthalocyanines and its effects on electrical properties [J]. *Prog. Surf. Sci.*, 1989, 31: 1.

[11] Leznoff C C, Lever A B, *et al*. Phthalocyanines: properties and applications [J]. *Advanced Materials.*, 2010, 5: 942.

[12] Seog W R, Byung B P, Youngkyu D, *et al*. Electronic and NMR properties of meso－monosubstituted ferrocenylporphyrin: evidence of p－conjugation between porphyrin and ferrocene [J]. *Polyhedron.*, 2000, 19: 1961.

[13] Boyd P D, Burnell A K, Campbell W M, *et al*. Synthesis, structure and properties of ferrocene functionalized porphyrins [J]. *Chem. Commun.*, 1999, 9: 637.

[14] Popova A, Christov M, Raicheva S, *et al*. Adsorption and inhibitive properties of benzimidazole derivatives in acid mild steel corrosionCorrosion [J]. *Science.*, 2004, 46: 1333.

[15] Read A E, Curtiss A L, Weinhold F. Intermolecular interactions from a natural bond orbital, donor－acceptor viewpoint [J]. *Chem. Rev.*, 1988, 88: 899.

[16] Sundaragansan N, Dominic B J, Settu K. [J]. *Spectrochim. Acta* A, 2007, 66: 381.

[17] Shirk J S, Pong R G, Hanack M, *et al*. Effect of axial substitution on the optical limiting properties of indium phthalocyanines [J]. *J. Phys. Chem.* A, 2000, 104: 1438.

[18] Dong S. Synthesis, characterization and spectroscople properties of phthalocyanines and their metal complexes with electro－active functional groups [D]. *Jinan: Shandong University*, 2010 (in Chinese) [董帅. 电子活性基团修饰的酞菁类化合物及其金属配合物的合成、表征和光谱性质 [D]. 济南：山东大学，2010]

[19] Zhang Y X. Quantum chemistry study of the structures, properties and semiconductor performance of phthalocyanine complexes [D]. *Jinan: Shandong University*, 2009 (in Chinese) [张跃兴. 酞菁类配合物的构效关系及其半导体性质的量子化学研究 [D]. 济南：山东大学，2009]

[20] Alecu I M, Zheng J, Zhao Y, Truhlar D G. Computational thermochemistry: scale factor databases and scale factors for vibrational frequencies obtained from electronic model chemistries [J]. *J. Chem. Theory Comput.*, 2010, 6: 2872.

[21] Frisch M J, Trucks G W, Schlegel H B, *et al*. Gaussian 09, Revision D. 01 [CP]. Wallingford CT: Gaussian, Inc., 2013.

[22] Cai X. *Structures, spectrum properties and OFET performance of phthalocyanine complexes based on density functional theory calculations* [D]. Jinan: Shandong University, 2009 (in Chinese) [蔡雪. 在密度泛函理论基础上研究酞菁类化合物的结构、光谱及OFET性质 [D]. 济南：山东大学，2009]

[23] Chen Y F, Shao C B, Zuo M H, *et al*. Theoretical study on vibrational spectroscopy of 2－Mercapto－5－nitrobenzimidazole by density functional theory [J]. *Spectrosc. Spect. Anal.*, 2019, 39: 3047 (in Chinese) [陈玉锋，邵长斌，左明辉，等. 2－巯基－5－硝基苯并咪唑振动光谱的密度泛函理论研究 [J]. 光谱学与光谱分析，2019，39：3047]

[24] Lu T, Chen F W. Multiwfn: a multifunctional wavefunction analyzer [J]. *J. Comput. Chem.*, 2012, 33: 580.

(C)1994-2021 China Academic Journal Electronic Publishing House. All rights reserved.　http://www.cnki.net

8.孙守鹏,魏闯宇,宁桧,蔡雪.全波谱太能材料氟代酞菁锌分子ZnPc($C_{24}F_{48}$)的研究[J].牡丹江大学学报,2018,27(06):107-109.

第 27 卷 第 6 期 牡丹江大学学报 Vol.27 No.6
2018 年 6 月 Journal of Mudanjiang University Jun. 2018

文章编号：1008-8717（2018）06-0107-03

全波谱太能材料氟代酞菁锌分子 ZnPc($C_{24}F_{48}$) 的研究

孙守鹏 魏闯宇 宁 桧 蔡 雪
（牡丹江师范学院化学化工学院，黑龙江 牡丹江 157011）

摘 要：在密度泛函理论和含时密度泛函理论的条件下对分子 ZnPc($C_{24}F_{48}$) 进行结构优化，模拟出分子的红外光谱和紫外吸收光谱，并对电子跃迁模式进行分析。通过电荷的比较设计出质子化模型 ZnPc($C_{24}F_{48}$)+H^+，通过计算模拟表明，该分子可以通过质子化对紫外光谱进行调节，因此该分子有成为全波谱太阳能吸波材料的潜力。

关键词：密度泛函；紫外吸收光谱；太阳能材料
中图分类号：O656.4 **文献标识码**：A
DOI:10.15907/j.cnki.23-1450.2018.06.033

Nature of Tunable Panchromatic Absorbing Material of ZnPc($C_{24}F_{48}$)

SUN Shou-peng, WEI Chuang-yu, NING Hui, CAI Xue
(Department of Chemstry, Mudanjiang Normal University, Mudanjiang, Heilongjiang 157011)

Abstract: Based on density functional theory and time-dependent density functional theory, we optimized the molecular structure of ZnPc($C_{24}F_{48}$), simulated the IR and UV spectra of molecules, and analyzed the mode of electron transition. Through the comparison of charge, we design the protonation model ZnPc($C_{24}F_{48}$)+H^+. Through the calculation and simulation, we can see that the molecule can regulate the UV spectrum through protonation, so the molecule has the potential to make full spectrum solar energy absorbing material.

Key words: density functional theory; UV spectrum; solar energy material

卟啉和酞菁的衍生物由于分子易于修改并且性能稳定，广泛应用于光电开关、分子导体、非线性光学等。[1-4] 酞菁分子属于有机大环结构，这种结构可以与金属形成金属配合物。近些年在实验化学的发展下，合成并深入研究了很多酞菁金属配合物的结构以及所具有的特殊性质。在 2012 年，Jiang's group 的齐冬冬博士曾经在全波谱太阳能吸波材料中发现了四吡咯稠合衍生物的两方面设计原则。[5] 本文选择了单晶分子，酞菁锌的氟原子取代的化合物 ZnPc($C_{24}F_{48}$)，在密度泛函理论的 B3LYP[6,7] 水平下，使用 6-311g(d,p) 基组，对该分子进行了结构的优化，并模拟出了该分子的红外光谱。在密度泛函理论的 PBE1PBE[8,9] 水平下，使用 6-311g(d,p) 基组，对该分子进行了紫外可见吸收光谱的模拟，所有的计算使用 Gaussian 09 D.01[10] 计算得到，通过利用 Multiwfn 4.3[11,12] 以半高全宽和高斯函数来对含时

收稿日期：2018-02-28
基金项目：牡丹江师范学院科研基金资助（gp201603）；黑龙江省教育厅科研项目（1352zd001）；牡丹江师范学院研究生科技创新项目（kjcx2016-15mdjnu）
作者简介：孙守鹏（1992-），男，黑龙江鸡西人，在读研究生，研究方向：酞菁化合物全谱吸收材料。
魏闯宇（1993-），女，黑龙江建三江人，在读研究生，研究方向：卟啉酞菁类化合物研究。
宁桧（1991-），辽宁丹东人，硕士，研究方向：卟啉化合物光谱性质研究。
通讯作者：蔡雪（1974-），女，吉林扶余人，牡丹江师范学院教授，博士，研究方向：卟啉酞菁化学。

(C)1994-2020 China Academic Journal Electronic Publishing House. All rights reserved. http://www.cnki.net

密度泛函理论下利用 Gaussian 09 D.01 计算得到激发态的结果进行展宽。光捕获效率（LHE）、跃迁模式和轨道贡献都是通过 TD-analysis 1.13 [15] 版本得到的。单个质子化模型同样通过 PBE1PBE 泛函和使用 6-311g(d,p) 基组。对该分子进行了紫外可见吸收光谱的模拟并利用 Gaussian 09 D.01 和 Multiwfn 4.3 处理得到。

高斯函数的表达式为：

$$G(\omega)=\frac{1}{c\sqrt{2\pi}}e^{\frac{(\omega-\omega_i)^2}{2c^2}}$$

$$c=\frac{FWHM}{2\sqrt{2\ln 2}}$$

基态和激发态之间的总电子密度转移($\sum f_{m\to n}$)，采用的计算公式：

$$f_{m\to n}=\frac{c_{m\to n}^2}{\sum_i^2}(\rho_n-\rho_m)$$

式中 n 和 m 在 MO(m) → MO(n) 跃迁模式中，m 轨道和 n 轨道的电子密度，是该跃迁在 TDDFT 方程中的正交系数，这样一来就可以被看作该跃迁模式在相关吸收峰中的贡献比例。从而把各个吸收峰看成是各个相关跃迁模式的线性组合。

1 结果与讨论

1.1 分子结构

图 1 ZnPc($C_{28}F_{48}$) 分子结构图

图 1 是酰胺锌衍生化合物 ZnPc($C_{28}F_{48}$) 的分子结构图，该分子是由酰胺分子外围拥有八个六氟代丙烷基，中心的金属是过渡金属锌。该分子的对称性是 C_{4v}。并且在优化后的频率计算中没有出现虚频，这说明该分子的结构稳定且可以认为是在 B3LYP 泛函和 6-311g(d,p) 基组条件下计算得到的能量最低的构型。

从表 1 中可以看出，ZnPc($C_{28}F_{48}$) 的分子的 meso-N 和内部的 N 原子的电荷数是不一致的，N^1 是与 Zn 配位的原子，而 N3 是与酰胺内的 C 原子相连的。尽管如此，N^1 原子的电荷依旧小于周围取代基的 F 原子。因此可知，如果按照 2016 年，Y. G. Gorbunova 的团队发现的酰胺锌分子，再加入一定测量的酸后，紫外可见吸收光谱将会发生红移。因此通过电荷的分析来看，ZnPc($C_{28}F_{48}$) 的分子中也同样具有作为可调控太阳能吸波材料的潜力。

表 1 ZnPc($C_{28}F_{48}$) 分子主要的键长与键角

单位 Å/°	ZnPc($C_{28}F_{48}$)
Zn	1.532
N^1	−0.836
N^3	−0.386
C^2	0.521
F^5	−0.183
F^{10}	−0.183
∠ $Zn-N^1-C^2$	125
∠ $C^2-C^3-F^5$	117
∠ $C^2-C^3-F^{10}$	110

1.2 红外吸收光谱

在密度泛函理论下计算优化后得到的红外吸收光谱。所用数据都使用红外校正系数 0.9614 进行校正得到。

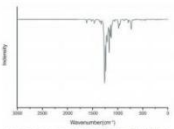

图 2 ZnPc($C_{28}F_{48}$) 分子的红外吸收光谱图

图 2 是通过计算模拟并经过校正的分子 ZnPc($C_{28}F_{48}$) 的红外吸收光谱图。从图 2 中可以看出，ZnPc($C_{28}F_{48}$) 在 946cm^{-1} 的有一个吸收峰，该吸收峰属于 C-C 伸缩振动；在 703cm^{-1} 处的吸收峰属于酰胺环面内摇摆振动；在 1124cm^{-1} 和 1176cm^{-1} 处的吸收峰，都归属于 C-F 伸缩振动；在 1161cm^{-1}，1208cm^{-1} 和 1224cm^{-1} 处的吸收峰，属于氟代异丙基的 C-C 伸缩振动。

1.3 紫外吸收光谱与跃迁分析

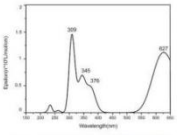

图 3 ZnPc($C_{28}F_{48}$) 分子的紫外吸收光谱图

从 300nm 到 450nm 的吸收峰比较宽，实际上通过含时密度泛函计算得到结果中，主要的吸收峰是在 309nm，345nm 和 376nm 等吸收峰共同形成的。ZnPc($C_{28}F_{48}$) 分子的 Q 带吸收峰的位置在 627nm，从紫外光谱中可以发现 Q 带的范围较广，如果将分子放入到溶剂氯仿中，Q 带的吸收峰范围会更快，并且从表 2 中发现，Q 带的吸收峰的光捕获效率（LHE）是达到了 76%。

表 2 ZnPc($C_{28}F_{48}$) 分子真空下电子跃迁

波长与光捕获效率	跃迁模型和贡献百分比
309nm(f=0.73	(38%)489(HOMO−10) → 500(LUMO)
LHE=81%	(26%)499(HOMO) → 505(LUMO+5)
	(25%)495(HOMO−4) → 501(LUMO+1)
345nm(f=0.32)	(43%)495(HOMO−4) → 500(LUMO)
LHE=52%	(26%)493(HOMO−7) →501(LUMO+1)
	(19%)489(HOMO−1) →501(LUMO+1)
376nm(f=0.24)	(51%)498(HOMO−1) →501(LUMO+1)
LHE=0%	(44%)497(HOMO−2) → 500(LUMO)
627nm(f=0.62)	(95%)499(HOMO) → 500(LUMO)
LHE=76%	

从表 2 中可以看出，分子的第 499 号轨道是 HOMO 轨道（最高占据轨道），第 500 号轨道是 LUMO 轨道（最低未占据轨道）。在波长为 309nm 处，光捕获效率达到了 81%，贡献比大于 10% 的有三种跃迁模式：分别是电子从 HOMO−10 跃迁到 LUMO；电子从 HOMO 跃迁到 LUMO+5；电子从 HOMO−4 跃迁到 LUMO+1。波长为 345nm 的光捕获效率为 52%，贡献比大于 10% 同样有三种跃迁模式：分别是电子从 HOMO−4 跃迁到 LUMO；电子从 HOMO−7 跃迁到 LUMO+1；电子从 HOMO−1 跃迁到 LUMO+1。然而波长为 376nm 的光捕获效率却为 0%，贡献比大于 10% 同样有两种跃迁模式：分别是电子从 HOMO−1 跃迁到 LUMO+1；电子从 HOMO−2 跃迁到 LUMO。波长为 627nm 的光捕获效率为 76%，贡献比大于 10% 同样有一种跃迁模式：电子从 HOMO 跃迁到 LUMO。

图 4 ZnPc($C_{28}F_{48}$)+H$^+$ 分子结构图

根据以上的条件，设计如图 4 的质子化分子模型 ZnPc($C_{28}F_{48}$)+H$^+$，虽然 F 比 N 的电负性大，但是质子在进攻分子的时候，依旧更容易靠近酰胺大环的 meso-N 原子上。

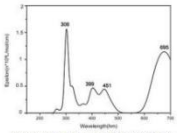

图 5 ZnPc($C_{28}F_{48}$) +H$^+$ 的紫外吸收光谱图

从 300nm 到 500nm 的吸收峰比 ZnPc($C_{28}F_{48}$) 宽 50nm，通过含时密度泛函计算得到结果中，主要的吸收峰是在 306nm，399nm 和 451nm 等吸收峰共同形成的，整个吸收峰有所红移。ZnPc($C_{28}F_{48}$) 分子的 Q 带吸收峰的位置在 627nm，但是质子化模型红移到了 695nm，即 Q 吸收带也发生了红移。从图 3 和图 5 对比可以看出，质子化的模型比分子吸收峰更宽。

表 3 ZnPc($C_{28}F_{48}$)+H$^+$ 分子真空下电子跃迁

波长与光捕获效率	跃迁模型和贡献百分比
306nm(f=0.60	(45%)488(HOMO−11) →500(LUMO)
LHE=75%	(26%)491(HOMO−8) → 505(LUMO+1)
399nm(f=0.27)	(64%)496(HOMO−3) → 500(LUMO)
LHE=46%	(19%)497(HOMO−2) → 500(LUMO+1)
	(10%)494(HOMO−5) → 500(LUMO)
451nm(f=0.14)	(83%)497(HOMO−2) → 500(LUMO)
LHE=28%	(13%)498(HOMO−1) → 501(LUMO+1)
695nm(f=0.61)	(98%)499(HOMO) → 500(LUMO)
LHE=76%	

从表 3 中可以看出，分子的第 499 号轨道是 HOMO 轨道（最高占据轨道），第 500 号轨道是 LUMO 轨道（最低未占据轨道）。在波长为 306nm 处，光捕获效率达到了 75%，贡献比大于 10% 的有两种跃迁模式：分别是电子从 HOMO−11 跃迁到 LUMO；电子从 HOMO−8 跃迁到 LUMO+1。波长为 399nm 的光捕获效率为 46%，贡献比大于 10% 同样有三种跃迁模式：分别是电子从 HOMO−3 跃迁到 LUMO；电子从 HOMO−2 跃迁到 LUMO+1；电子从 HOMO−5 跃迁到 LUMO。然而波长为 451nm 的光捕获效率却为 28%，贡献比大于 10% 同样有两种跃迁模式：分别是电子从 HOMO−2 跃迁到 LUMO；电子从 HOMO−1 跃迁到 LUMO+1。波长为 627nm 的光捕获效率为 76%，贡献比大于 10% 同样有一种跃迁模式：电子从 HOMO 跃迁到 LUMO。

2 结论

分子 ZnPc($C_{28}F_{48}$) 选自 CCDC 的单晶分子，该分子通过计算得到了分子的结构，键长键角，红外吸收光谱以及紫外吸收光谱，并且通过 TD-analysis 对含时密度泛函理论的条件下计算的结果进

（下转第 113 页）

(C)1994-2020 China Academic Journal Electronic Publishing House. All rights reserved. http://www.cnki.net

[2] Marques JP,Written;Wu YF,Trans.Pattern Recognition Concepts,Methods and Applications.2nd ed.Beijing: TsinghuaUniversity Press,2002.51-74(in Chinese).

[3] 郁启鹏.K-means 算法初始聚类中心选择的优化[J]. 计算机系统应用 ,2017,26(5):170-174.

[4] 顾洪博. 基于孤立点和初始质心的 k 均值算法的改进与应用 [J]. 陕西理工学院学报 ,2009,9(4) :45-49.

[5] 李金涛 , 艾萍 . 基于 K means 聚类算法的改进 [J]. 国外电子测量技术 ,2017,36(6): 9-13,21.

[6] 袁方 , 周志勇 . 初始聚类中心优化的 k-means 算法 [J]. 计算机工程 ,2007,33(3):65-66.

[7] 赖玉霞 , 刘建平 .K-means 算法的初始聚类中心的优化 [J]. 计算机工程与应用 ,2008, 44(10):147-149.

[8] 顾洪博 , 张继怀 . 聚类算法初始聚类中心的优化 [J]. 西安工程大学学报 ,2010,24(2):222-226.

[9] 何佳知 , 谢颖华 . 基于密度的优化初始聚类中心 K-means 算法研究 [J]. 微型机与应用 ,2015,34(19) :17-19.

（上接第 109 页）

行了跃迁分析。然后设计质子进攻 meso-N 的模型 ZnPc($C_{28}F_{48}$)+H$^+$，得到紫外吸收光谱，通过二者的光谱比较发现质子化模型发生了红移，吸收光谱变宽。因此通过在分子中加入酸会对分子 ZnPc($C_{28}F_{48}$) 的光谱，会导致分子光谱的红移和变宽。综上所述，ZnPc($C_{28}F_{48}$) 有可能适合做全波谱太阳能吸波材料。

参考文献：

[1] Tsuda A and Osuka A. Fully Conjugated Porphyrin Tapes with Electronic Absorption Bands That Reach into Infrared [J]. Science, 2001, (293): 79-82.

[2] Peumans P, Yakimov A and Forrest S R. Small molecular weight organic thin-film photodetectors and solar cells [J]. J. Appl. Phys., 2003, (93): 3693-3723.

[3] Hiramoto M, Fujiwara H and Yokoyama M. Pin like behavior in three-layered organic solar cells having a co-deposited interlayer of pigments [J]. J. Appl. Phys., 1992, (72): 3781-3787.

[4] Allen C M, Sharman W M and Van Lier J E. Current status of phthalocyanines in the photodynamic therapy of cancer [J]. J. Porphyrins Phthalocyanines, 2001, (5): 161-169.

[5] Qi D, Zhang L and Jiang J. Toward Panchromatic Organic Functional Molecules: Density Functional Theory Study on the Nature of the Broad UV-Visible-NIR Spectra of Substituted Tetra(azulene) porphyrins [J]. J. Mol. Graphics Modell. 2012, (38): 304-313.

[6]Becke A D. Density-functional thermochemistry. III. The role of exact exchange. J. Chem. Phys. 1993, 98 (7): 5648- 5652.

[7] C. Lee; W. Yang and R. G. Parr. Development of the Colle-Salvetti correlation -energy formula into a functional of the electron density. Phys. Rev. B 1988, 37: 785-789.

[8] J.P. Perdew; K. Burke; and M. Ernzerhof. Generalized Gradient Approximation Made Simple. Phys. Rev.Lett. 1996, 77: 3865-3868.

[9]J. P. Perdew; K. Burke; and M. Ernzerhof. Generalized Gradient Approximation Made Simple. Phys. Rev. Lett., 1997, 78: 1396.

[10] M. J. Frisch; G. W. Trucks; H. B. Schlegel; G. E. Scuseria; M. A. Robb; J. R. Cheeseman; G. Scalmani; V. Barone; B. Mennucci; G. A. Petersson; H. Nakatsuji; M. Caricato; X. Li; H. P. Hratchian; A. F. Izmaylov; J. Bloino; G. Zheng; J. L. Sonnenberg; M. Hada; M. Ehara; K. Toyota; R. Fukuda; J. Hasegawa; M. Ishida; T. Nakajima; Y. Honda; O. Kitao; H. Nakai; T. Vreven; J. A. Montgomery; Jr.; J. E. Peralta; F. Ogliaro; M. Bearpark; J. J. Heyd; E. Brothers; K. N. Kudin; V. N. Staroverov; T. Keith; R. Kobayashi; J. Normand; K. Raghavachari; A. Rendell; J. C. Burant; S. S. Iyengar; J. Tomasi; M. Cossi; N. Rega; J. M. Millam; M. Klene; J. E. Knox; J. B. Cross; V. Bakken; C. Adamo; J. Jaramillo; R. Gomperts; R. E. Stratmann; O. Yazyev; A. J. Austin; R. Cammi; C. Pomelli; J. W. Ochterski; R. L. Martin; K. Morokuma; V. G. Zakrzewski; G. A. Voth; P. Salvador; J. J. Dannenberg; S. Dapprich; A. D. Daniels;O. Farkas; J. B. Foresman; J. V. Ortiz; J. Cioslowski; and D. J. Fox. Gaussian 09, Revision D.01, Gaussian, Inc.: Pittsburgh, PA, 2009.

[11] T. Lu and F. Chen. Multiwfn: A multifunctional wavefunction analyzer. J. Comput. Chem. 2012, 33 (5), 580-592.

[12] Multiwfn--A Multifunctional Wavefunction Analyzer (for Windows 64it) Version 3.4(dev), Project leader: Tian Lu (Beijing Kein Research Center for Natural Sciences), 2017.

[13] D. Qi. TD-Analy Program (ver1.13), Beijing Key Laboratory for Science and Application of Functional Molecular and Crystalline Materials, Department of Chemistry, University of Science and Technology Beijing, 2014, Beijing, China.

(C)1994-2020 China Academic Journal Electronic Publishing House. All rights reserved. http://www.cnki.net

9.宁桧,孙守鹏,蔡雪.轴向取代卟啉锌结构和光谱性质的研究[J].牡丹江师范学院学报(自然科学版),2017(01):39-42.

文章编号:1003-6180(2017)01-0039-04

轴向取代卟啉锌结构和光谱性质的研究

宁 桧,孙守鹏,蔡 雪*
(牡丹江师范学院 化学化工学院,黑龙江 牡丹江 157011)

摘 要:在密度泛函理论 B3LYP 水平上,使用 6-31G 基组,对 ZnPor($C_{37}H_{39}O_3N$),ZnPor($C_{42}H_{39}O_3N$)和 ZnPor($C_{32}H_{39}O_4N$)分子结构进行优化,模拟出红外和紫外吸收光谱图,对这三个分子的结构和性质进行比较分析,实验结果表明,ZnPor($C_{42}H_{39}O_3N$)有做太阳能敏化剂的潜力.

关键词:卟啉锌;密度泛函理论;红外光谱;紫外光谱

[中图分类号]O656.4 [文献标志码]B
DOI:10.13315/j.cnki.jmtc(ns).2017.01.014

Structural and Spectroscopic Properties of Axially Substituted Porphyrin Zinc

NING Hui,SUN Shou-peng,CAI Xue*
(Mudanjiang Normal University Department of Chemistry,Mudanjiang 157011,China)

Abstract:In the density functional theory,B3LYP level,using 6-31G basis set,the structure of ZnPor($C_{37}H_{39}O_3N$),ZnPor($C_{42}H_{39}O_3N$) and ZnPor($C_{32}H_{39}O_4N$) molecules was optimized,simulate the infrared and ultraviolet absorption spectra,the structure and properties of these three molecules were compared and analyzed. Experimental results show that,ZnPor($C_{42}H_{39}O_3N$) has the potential to do solar sensitizer.

Key words:zinc porphyrin; density functional theory;Infrared spectrum;Ultraviolet spectrum

卟啉和金属卟啉类化合物受到生物学界,化学界和医学界的广泛关注[1-2].卟啉及金属卟啉类化合物广泛存在于动植物当中,具有特殊的生理活性.早期的卟啉是从天然产物血红素和叶绿素中提取来的[3],叶绿体中的叶绿素就是含镁的卟啉化合物.由于卟啉类化合物对太阳光谱有着很好的吸收作用,其物理和化学性质也比较稳定,很适合作为光敏材料.杨立国等人合成了几种轴向

收稿日期:2016-06-25
基金项目:黑龙江省博士后科研启动金资助项目(LBH-Q13170)
作者简介:宁桧(1990-),女,辽宁丹东人,硕士,主要从事卟啉类化合物光谱性质研究,孙守鹏(1992-),男,吉林德惠人,硕士,主要从事卟啉类化合物光谱性质研究,蔡雪(1974-),女,吉林扶余人,教授,博士,主要从事卟啉配合化学研究.
通讯作者:蔡雪

(C)1994-2021 China Academic Journal Electronic Publishing House. All rights reserved. http://www.cnki.net

取代金属卟啉类衍生物分子，对分子进行了表征、绝对构型的指认以及分子手性的识别等研究[1-2]，但是未对分子的性质进行理论研究。因此，本文直接采用合成的单晶分子，在密度泛函理论 B3LYP 水平上，使用 6-31G 基组[3-4]，对三种轴向取代卟啉类衍生物分子进行理论计算，优化其结构，模拟出红外和紫外吸收光谱图，并对光谱图进行比较分析。本实验计算全部使用 Gaussian09[5] 软件完成，使用 Origin 软件绘图。

1　结果与讨论

1.1　分子结构

图 1　ZnPor($C_{37}H_{29}O_3N$)分子结构图

(左：分子侧面，右：分子正面)

图 2　ZnPor($C_{42}H_{37}O_3N$)分子结构图

(左：分子侧面，右：分子正面)

图 3　ZnPor($C_{42}H_{39}O_4N$)分子结构图

(左：分子侧面，右：分子正面)

图 1　分子结构图

如图 1 所示，轴向取代吡啶的 5,15-二(2-羟基萘基)-10-苯基-20-(4-羟基苯基)卟啉锌为 ZnPor($C_{37}H_{29}O_3N$)，轴向取代苯丙氨酸甲酯的 5,15-二(3-羟基萘基)-10-苯基-20-(4-羟基苯基)卟啉锌为 ZnPor($C_{42}H_{37}O_3N$)，轴向取代苯丙氨酸甲酯的 5-苯基-10-(2-羟基萘基)-15-(4-羟基苯基)卟啉锌为 ZnPor($C_{42}H_{39}O_4N$)。这三种分子的轴向和 meso 位引入取代基后，都不再呈平面结构。通过理论计算，ZnPor($C_{37}H_{29}O_3N$)，ZnPor($C_{42}H_{37}O_3N$)和 ZnPor($C_{42}H_{39}O_4N$)的红外吸收光谱均无虚频。

表 1　分子的主要键参数　　Å/°

	ZnPor($C_{37}H_{29}O_3N$)	ZnPor($C_{42}H_{37}O_3N$)	ZnPor($C_{42}H_{39}O_4N$)
Zn-N_2	2.053	2.055	2.052
C_6-N_2	1.384	1.387	1.382
C_9-N_2	1.383	1.381	1.382
C_7-C_{13}	1.382	1.379	1.377
C_{13}-C_{15}	1.401	1.404	1.401
$\angle C_6$-Zn-N_2	87.98	87.96	87.51
$\angle C_9$-N_2-C_6	106.79	106.73	106.45
$\angle C_{11}$-C_{10}-C_{39}	121.29	124.95	125.11
$\angle C_7$-C_{39}-H_{41}	121.06	125.09	125.48

表 1 为三个分子的主要键参数，ZnPor($C_{37}H_{29}O_3N$)与 ZnPor($C_{42}H_{37}O_3N$)分子的 meso 位引入的取代基相同，而轴向引入取代基不同。ZnPor($C_{42}H_{37}O_3N$)与 ZnPor($C_{42}H_{39}O_4N$)分子的轴向取代基相同，meso 位 ZnPor($C_{42}H_{39}O_4N$)比 ZnPor($C_{42}H_{37}O_3N$)少引入一个羟基萘基团，通过比较发现，取代基对键长和键角都产生了影响，但影响较小。

1.2　红外吸收光谱图

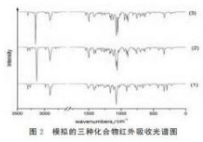

图 2　模拟的三种化合物红外吸收光谱图

(C)1994-2021 China Academic Journal Electronic Publishing House. All rights reserved.　http://www.cnki.net

图 2 模拟了 ZnPor($C_{37}H_{29}O_3N$)，ZnPor($C_{37}H_{37}O_3N$)和 ZnPor($C_{42}H_{39}O_4N$)这三个化合物的红外光谱图。从光谱图中可以发现，ZnPor($C_{37}H_{37}O_3N$)在 1 025 cm^{-1} 处出现吸收峰，该吸收峰属于卟啉环的 C—H 摇摆振动，该振动模式下，ZnPor($C_{37}H_{29}O_3N$)的吸收峰出现在 1 005 cm^{-1} 处，与 ZnPor($C_{42}H_{37}O_3N$)相比，发生了蓝移，ZnPor($C_{37}H_{29}O_3N$)的吸收峰也出现在 1 025 cm^{-1} 处，与 ZnPor($C_{42}H_{37}O_3N$)相比，吸收峰几乎没有变化。ZnPor($C_{37}H_{29}O_3N$)在 2 934 cm^{-1} 处出现吸收峰，该吸收峰归属于轴向吡啶环的 C—H 伸缩振动，是吡啶的特征吸收峰。ZnPor($C_{37}H_{29}O_3N$)在 1 134 cm^{-1} 处出现吸收峰，吸收峰归属于吡咯环的 C—N 伸缩振动，该振动模式下，ZnPor($C_{37}H_{29}O_3N$)红移到 1 156 cm^{-1} 处，ZnPor($C_{37}H_{39}O_4N$)的吸收峰出现在 1 150 cm^{-1} 处，与 ZnPor($C_{42}H_{37}O_3N$)相比，发生蓝移。ZnPor($C_{42}H_{37}O_3N$)和 ZnPor($C_{42}H_{39}O_4N$)均在 1 128 cm^{-1} 处出现吸收峰，归属于轴向苯丙氨酸甲酯中的 C—O 伸缩振动，该吸收峰为酯的特征吸收峰。ZnPor($C_{42}H_{37}O_3N$)与 ZnPor($C_{37}H_{29}O_3N$)和 ZnPor($C_{42}H_{39}O_4N$)相比发生红移，说明 ZnPor($C_{42}H_{37}O_3N$)可能具有更好的做太阳能敏化剂的潜力，也说明轴向取代比 meso 位取代对金属卟啉分子的影响更大一些。

1.3　紫外吸收光谱图

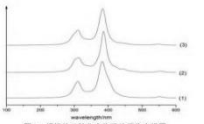

图 3　模拟的三种化合物紫外吸收光谱图

图 3 模拟出 ZnPor($C_{37}H_{29}O_3N$)，ZnPor($C_{42}H_{37}O_3N$)和 ZnPor($C_{42}H_{39}O_4N$)这三个化合物的紫外吸收光谱图。通常情况下，卟啉和金属卟啉类化合物会在 420 nm 波长附近出现强吸收峰，称之为 Soret 带(B 带)，在 500～750 nm 波长范围内，称之为 Q 带。由光谱图可以看出，三种化合物在可见光区都有明显的吸收，紫外-可见吸收光谱差别较小，说明取代基对卟啉锌类化合物紫外-可见吸收光谱影响不大。

ZnPor($C_{37}H_{29}O_3N$)在 S 带的最强吸收峰出现在 308 nm 和 386 nm 处，在 Q 带的强吸收峰出现在 554 nm 处。ZnPor($C_{42}H_{37}O_3N$)在 S 带的最强吸收峰出现在 313 nm 和 386 nm 处，在 Q 带的吸收峰出现在 558 nm 处。ZnPor($C_{37}H_{29}O_3N$)在 S 带的最强吸收峰 310 nm 和 383 nm 处，在 Q 带的强吸收峰出现在 548 nm 处。ZnPor($C_{42}H_{37}O_3N$)与其他两种化合物相比，Q 带发生红移。

表 2　三个化合物的主要电子跃迁

名称	波长/nm	系统
ZnPor($C_{37}H_{29}O_3N$)	386.0=0.385	98.4%|28(H)→29(L)+30(H)→31(L)
	308.0=0.433	59.3%|28(H)→29(L)+30(H)→31(L)
		18.3%|28(H)→30(H)+29%|31(L)
	554.0=0.403	98.4%|28(H)→29(L)+30(H)→31(L)
	313.0=0.351	58.4%|28(H)→29(L)+30(H)→31(L)
ZnPor($C_{42}H_{37}O_3N$)	386.0=0.453	98.3%|30(H)→29(L)+30(H)→31(L)
		98.1%|28(H)→29(L)+30(H)→31(L)
	558.0=0.381	98.4%|30(H)→31(L)
		98.6%|28(H)→29(L)+30(H)→31(L)
	310.0=0.223	98.4%|30(H)→29(L)+30(H)→31(L)
		98.4%|28(H)→29(L)+30(H)→31(L)
ZnPor($C_{42}H_{39}O_4N$)	383.0=0.453	98.3%|30(H)→29(L)+30(H)→31(L)
		98.1%|28(H)→29(L)+30(H)→31(L)
	554.0=0.403	98.4%|30(H)→31(L)
	313.0=0.351	98.4%|28(H)→29(L)+30(H)→31(L)

表 2 模拟了三种化合物的主要吸收波长和电子跃迁数值，由表 2 可知，ZnPor($C_{37}H_{29}O_3N$)在 308 nm 处，主要是电子从 HOMO－11 跃迁到 LUMO＋1，贡献率是 87%；在 386 nm 处，主要是

(C)1994-2021 China Academic Journal Electronic Publishing House. All rights reserved.　http://www.cnki.net

电子从 HOMO－1 跃迁到 LUMO＋1，贡献率是 34%，电子从 HOMO－1 跃迁到 LUMO＋2，贡献率是 18%；在 554 nm 处，主要是电子从 HOMO跃迁到 LUMO，贡献率是 67%。ZnPor($C_{42}H_{37}O_3N$)在 313 nm 处，主要是电子从 HOMO－11跃迁到 LUMO＋1，贡献率是 87%；在 386 nm 处，主要是电子从 HOMO－1 跃迁到 LUMO，贡献率是 19%，电子从 HOMO 跃迁到 LUMO＋1，贡献率是 12%，电子从 HOMO－1 跃迁到 LUMO＋1，贡献率是 8%；在 558 nm 处，主要是电子从 HOMO 跃迁到 LUMO，贡献率是 65%，电子从 HOMO－1 跃迁到 LUMO＋1，贡献率是 34%。ZnPor($C_{42}H_{39}O_4N$)在 310 nm 处，主要是电子从 HOMO－9 跃迁到 LUMO，贡献为 67%，电子从 HOMO－1 跃迁到 LUMO＋3，贡献率是 10%；在 383 nm 处，主要是电子从 HOMO－1 跃迁到 LUMO，贡献率是 34%，电子从 HOMO 跃迁到 LUMO＋1，贡献率是 18%，电子从 HOMO－1 跃迁到 LUMO＋1，贡献率是 17%；在 548 nm 处，主要是电子从 HOMO 跃迁到 LUMO，贡献率是 44%，电子从 HOMO－1 跃迁到 LUMO＋1，贡献率是 22%。

2　结论

笔者从 CCDC 数据库中获得 ZnPor($C_{37}H_{29}O_3N$)，ZnPor($C_{42}H_{37}O_3N$)和 ZnPor($C_{42}H_{39}O_4N$)3 个分子的晶体结构[2]，对这三种化合物的分子结构、键长键角、红外吸收光谱、紫外吸收光谱和电子跃迁进行模拟与分析，比较了轴向和 meso 位连有取代基对金属卟啉化合物所产生的影响。红外和紫外吸收光谱图中，对这三种化合物的吸收峰进行了指认。在紫外吸收光谱图中，ZnPor($C_{37}H_{29}O_3N$)，ZnPor($C_{42}H_{37}O_3N$)和 ZnPor($C_{42}H_{39}O_4N$)，均在 Q 带出现了吸收峰，表明分子在可见光范围内有较强的响应，ZnPor($C_{42}H_{37}O_3N$)与其他两种化合物比，发生了红移。在红外吸收光谱图中，ZnPor($C_{42}H_{37}O_3N$)与 ZnPor($C_{37}H_{29}O_3N$)相比，发生了红移，ZnPor($C_{42}H_{37}O_3N$)与 ZnPor($C_{42}H_{39}O_4N$)相比，吸收峰的变化较小，说明轴向取代比 meso 位取代对金属卟啉分子的影响更大。综上所述，ZnPor($C_{42}H_{37}O_3N$)更有可能做为太阳能敏化剂。

参考文献

[1] W. M. Campbell, K. W. Jolley, P. Wagner. Highly Efficient Porphyrin Sensitizers for Dye－Sensitized Solar Cells [J]. Phys. Chem. C, 2007(11): 11760-11762.

[2] 朱英，张学俊. 卟啉类染料敏化剂的研究进展[J]. 山西化工，2013,33(5):35-39.

[3] 杨建东，王都留. 卟啉及金属卟啉化合物的合成及应用研究进展[J]. 首都师范大学学报，自然科学版，2012,(33):14-18.

[4] H. Fiesher. Die Chemie des pyrrols[M]. AKademic Verlagsgesellschft Liepzig, 1937,2(1),158.

[5] Ligao Yang, Mengliang Zhu, Yangjian Liu, et al. Chiral dinaphthylporphyrin with C2 symmetry: synthesis, resolution, And enantio-discrimination by single-crystal X-ray diffraction analysis[J]. Tetrahedron Letters, 2014(55), 3377-3380.

[6] Wang H L, Wang K, Bian Y Z, et al. Mixed (phthalocyaninato)(porphyrinato) heterometal complexes with sandwich quadruple-decker molecular structure [J]. Chem. Commun., 2011(47), 6879-6881.

[7] 闫峰，蔡雪. α位β位取代酰菁锌化合物结构与性质研究[J]. 牡丹江师范学院学报，自然科学版，2015(1):23-24.

[8] 胡星娜，徐尚. 中位取代卟啉锌结构及光谱性质研究[J]. 牡丹江师范学院学报，自然科学版，2016(1):49-51.

[9] M. J. Frisch, G. W. Trucks, H. B. Schlegel, et al. Gaussian 09, Revision D. 01, Gaussian Inc. Pittsburgh PA, 2013.

编辑：琳莉

(C)1994-2021 China Academic Journal Electronic Publishing House. All rights reserved.　http://www.cnki.net

10.李梓萌,蔡雪.咔唑类取代酞菁锌染料敏化性能研究[J].牡丹江师范学院学报(自然科学版),2016(01):44-46.

3 结论

(1) 采用两种方法——一步法和后嫁接法分别合成了 NH_2-SBA-15,合成的介孔材料对 Pb^{2+} 吸附均有大幅度的提高;后嫁接法合成的 NH_2-SBA-15 吸附效果更好. 通过 XRD、FT-IR 和 N_2 吸附-脱附等手段对材料进行表征,说明在合成过程中纯硅 SBA-15 的结构没有被破坏,仍保持良好的介孔有序性.

(2) 介孔材料对 Pb^{2+} 吸附与反应体系的 pH 值和吸附时间等因素有关. 批量实验表明:体系 pH 值较低时,相应的吸附率也低,pH 达到 5 时 Pb^{2+} 的吸附效果最佳;介孔材料对 Pb^{2+} 的吸附率随时间的增加而增大,60 min 为体系的最佳吸附时间,最佳吸附率能达到 90%左右.

参考文献

[1] 许秀琴, 朱勇, 杨挺, 等. 水体重金属的污染危害及其修复技术[J]. 污染防治技术, 2007, 20(4): 67-69.

[2] Zhao D Y, Feng J, Huo Q, et al. Triblock Copolymer Syntheses of Mesoporous Silica with Periodic 50 to 300 Angstrom Pores. Science[J]. Am. chem. soc,1998, 279: 548-552.

[3] 葛俊森, 梁渠. 水中重金属危害现状及处理方法[J]. 苏州化工, 2007, 35(5): 44-46.

[4] Feng X D, Fryxell G E, Wang L Q, et al. Functionalized Monolayers on Ordered Mesoporous Supports[J]. Science, 1997, 276: 923-926.

[5] Zhao D Y, Huo Q H, Feng J L, et al. Nonionic Triblock and Star Diblock Copolymer and Oligomeric Surfactant Syntheses of Highly Ordered Hydrothermally Stable Mesoporous Silica Structures[J]. Am. Chem. Soc, 1998, 120: 6024-6036.

[6] Zhao D Y, Huo Q H, Feng J L, et al. Triblock Copolymer Syntheses of Mesoporous Silica with Periodic 50 to 300 Angstrom Pores [J]. Science, 1998, 279: 548-552.

[7] 赵平平, 廉波. 银溶胶的制备、表征及应用[J]. 牡丹江师范学院学报: 自然科学版, 2014(3): 28-30.

[8] 杨华, 宋伟新, 王冰. CO—Nd 复合氧化物纳米微粒的制备及初步表征[J]. 牡丹江师范学院学报: 自然科学版, 2003(4): 19-21.

[9] 邵艳秋, 王虹苏, 管景奇, 等. 新型有机-无机杂化碱性介孔材料的合成[J]. 高等学校化学学报, 2013, 31(3): 592-596.

编辑:琳莉

咔唑类取代酞菁锌染料敏化性能研究

李梓萌,蔡 雪*

(牡丹江师范学院 化工学院,黑龙江 牡丹江 157011)

摘 要:理论计算模拟 $Zn[PcH_{15}R]$,$Zn[PcH_9R](NH_2)_6$ 和 $Zn[PcH_9R]F_6$ 的分子结构和原子电荷、HOMO与 LUMO 轨道以及红外光谱,发现取代后分子的能级差减小;R 基和吸电子基-F 的引入,增强了酞菁锌的染料敏化的性能. 说明 $Zn[PcH_{15}R]$和 $Zn[PcH_9R]F_6$ 这两种分子具有作为太阳能电池敏化剂的潜能.

关键词:酞菁;结构;光谱性质

[中图分类号]TG584 [文献标志码]A [文章编号]1003-6180(2016)01-0044-03

DOI:10.13815/j.cnki.jmtc(ns).2016.01.018

酞菁是人工合成的卟啉类似物,拥有比卟啉更大的共轭体系.[1] 由于卟啉化合物的特征吸收带多[2],且特征吸收带 Soret 带的摩尔吸光系数非常大,因此这类染料对太阳光有着很好的利用率,是未来在 DSC 中最具潜力的敏化剂之一.[3] 本研究选择具有共轭性的芳基类取代基-氮乙烯基咔唑(C14H11N)来取代酞菁. 在密度泛函理论(DFT)B3LYP 水平上使用 6-31(g)基组,研究 N-乙烯基咔唑 R(R=C4H11N)取代酞菁锌所得到的化合物,并将其周边引入吸电子基-F 和给电子基团-NH_2,进一步研究供电子基团和吸电子基团对乙烯基咔唑取代酞菁锌的影响.

酞菁锌分子的初始输入结构来自于以前的计算结果. 将酞菁锌分子的 β 位引入 R 取代基,运用密度泛函理论 B3LYP,采用 6-31g(d)基组对结构优化. 再将优化后的 $Zn[PcH_{15}R]$分子的周边

收稿日期:2015-10-30
基金项目:博士后研究人员落户黑龙江科研启动项目(LBH—Q13170)
通讯作者:蔡雪

(C)1994-2019 China Academic Journal Electronic Publishing House. All rights reserved. http://www.cnki.net

位置引入吸电子基团-F 和给电子基团-NH_2，用同样的基组和方法对 Zn[PcH_8R]F_8 和 Zn[PcH_8R](NH_2)$_8$ 这两个分子进行结构优化，计算用 Gaussian09 软件完成。

1 结果与讨论

1.1 分子结构

通过模拟计算得出，未取代的 $ZnPcH_{16}$ 化合物具有 D_{4h} 的分子对称性和平面结构，将 N-乙烯基咔唑取代 $ZnPcH_{16}$ 的 β 位 H 原子以后，Zn[$PcH_{15}R$]不再呈平面结构，同样将 6 个—NH_2 和 6 个-F 取代 Zn[$PcH_{15}R$]的 6 个 H 原子以后，Zn[PcH_8R](NH_2)$_8$ 和 Zn[PcH_8R]F_8 这两个分子也不再呈平面结构，如图 1 所示。

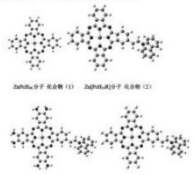

$ZnPcH_{16}$分子 化合物 (1)　Zn[$PcH_{15}R$]分子 化合物 (2)

Zn[PcH_8R](NH_2)$_8$分子 化合物 (3)　Zn[PcH_8R]F_8分子 化合物 (4)

图 1 分子结构图

表 1 锌离子到四个异吲哚中氮原子组成的平面主要键角键长

	$ZnPcH_{16}$	Zn[$PcH_{15}R$]	Zn[PcH_8R](NH_2)$_8$	Zn[PcH_8R]F_8
R_{Zn-N_1}	2.862 8	2.814 9	2.814 8	2.814 4
R_{Zn-N_2}	2.835 5	1.990 1	1.992 8	1.990 1
$R_{N_1-C_1}$	1.396 1	1.373 1	1.371 8	1.372 1
$R_{N_2-C_2}$	1.346 8	1.329 8	1.331 6	1.329 2
$\angle Zn-N_1-C_1$	125.33	125.27	125.28	125.39
$\angle C_1-C_2-C_3$	132.44	132.21	132.32	132.19

为了能更好地研究取代后的分子结构较未取代 $ZnPcH_{16}$ 分子结构发生的变化，选取比较具有代表性原子之间的距离和相对应的键角的量值，通过比较发现，由于取代基 R(N-乙烯基咔唑)的引入，使金属 Zn 到四个异吲哚 N，的距离减小，且四个异吲哚中由四个氮原子组成的平面环的半径也相应减小，R_{Zn-N_1} 由未取代的 2.024 5 Å 变化到 R 基取代后的 1.990 1 Å，同理，R_{Zn-N_2} 从 2.862 8 Å 变化到 2.814 9 Å，说明取代基 R 的引入，使酞菁锌分子的环内半径减小。当 Zn[$PcH_{15}R$]分子的周边连接了-NH_2 和-F 以后，Zn[PcH_8R](NH_2)$_8$ 和 Zn[PcH_8R]F_8 分子的环内半径与 Zn[$PcH_{15}R$]分子半径相比变化非常小，几乎可以忽略不计，说明供电子基-NH_2 和吸电子基-F 的引入对 R 基取代后的酞菁锌分子的结构并无太大影响。通过表 1 还可看出，Zn[PcH_8R]分子与未取代的 $ZnPcH_{16}$ 分子的键角 $\angle C_1-C_2-C_3$ 由 132.04°变化到 132.21°，$\angle Zn-N_1-C_1$ 由 125.23°变化到125.27°，取代后角度变化非常小，说明取代基 R 的引入造成的酞菁分子平面扭曲可以忽略不计。

1.2 原子电荷

表 2 酞菁锌化合物的主要原子电荷

	$ZnPcH_{16}$	Zn[$PcH_{15}R$]	Zn[PcH_8R](NH_2)$_8$	Zn[PcH_8R]F_8
Zn^{2+}	1.243	0.947	0.938	0.951
N_1	−0.440	−0.722	−0.720	−0.722
N_2	0.087	−0.559	−0.565	−0.559
C_1	−0.600	0.408	0.400	0.406
C_2	0.203	0.675	0.678	0.676
C_3	−0.597	−0.272	−0.273	−0.272
H_1	0.259	0.252	0.247	0.252
H_2	0.204	0.231	0.228	0.231

表 2 为模拟酞菁锌化合物的主要原子 Mulliken 电荷，当 R 是具有吸电子的取代基时，会使 Zn^{2+}、N_1、N_2 和 H 原子的电荷变正[5]，而当 R 是具有给电子性质的取代基时，会使这些原子电荷变负。[5]通过观察表 2 可知，Zn[$PcH_{15}R$]取代后的酞菁锌化合物 Zn^{2+}、N_1、N_2 和 H 原子的电荷相对于未取代的 $ZnPcH_{16}$ 化合物的电荷变负，Zn^{2+}由原来的 1.243 e 变到 0.947 e，N_1 由−0.468 e变到−0.722 e，N_2 由 0.087 e 变到−0.559 e，同理，H 也由未取代的 0.259 e 变到 0.152 e，说明连接的 R 取代基是具有供电子性质的取代基，这里 Zn[PcH_8R](NH_2)$_8$ 的 Zn^{2+}变化也非常大，除了由于 R 基供电子基团以外，还因为在 Zn[PcH_8R]的基础上又引入了 6 个具有供电子性质的-NH_2，所以使 Zn^{2+}、N_1、N_2 这些原子的电荷变得更负，Zn^{2+}由最开始的 1.243 e 变到了现在的 0.938 e，而 Zn[PcH_8R]F_8，由于在引入了 R 基的基础上又引入了 6 个具有吸电子效应的 F 原子，与 R 基形成了具有推拉电子结构的分子，所以其 Zn^{2+}的原子电荷的变化相对小一些，由原来的 1.234 e 变到了 0.953 e。

1.3 分子轨道能量

$ZnPcH_{16}$、Zn[$PcH_{15}R$]、Zn[PcH_8R](NH_2)$_8$ 和 Zn[PcH_8R]F_8 的 HOMO 和 LUMO 轨道能量见图 2。在化合物 $ZnPcH_{16}$、Zn[$PcH_{15}R$]、Zn[PcH_8R](NH_2)$_8$ 和 Zn[PcH_8R]F_8 中，HOMO 到 LUMO 的轨道能极差分别是 2.201 4 ev、2.116 7 ev、2.07 ev 和 2.107 ev，这表明相对于化合物 $ZnPcH_{16}$ 而言，取代后的三种化合物的能级差都不同程度地减小，说明这三种化合物的 Q 带相对于未取代的酞菁锌化合物的 Q 带都发生了一定程度的红移，酞菁锌化合物所连接的取代基团使 Q 带发生红移，可看出取代后的三种化合物更有利于吸收光子，在作为敏化剂分子方面具有更大的可能，这与以前的研究结果是一致的。[6]

(C)1994-2019 China Academic Journal Electronic Publishing House. All rights reserved. http://www.cnki.net

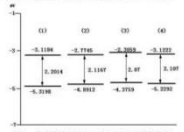

图 2 化合物的 HOMO 和 LUMO 轨道能级图

1.4 红外光谱

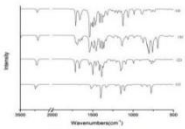

图 3 模拟的 4 种化合物的红外光谱图

模拟化合物 $ZnPcH_{16}$、Zn[$PcH_{15}R$]、Zn[PcH_8R](NH_2)$_8$ 和 Zn[PcH_8R]F_8 的红外光谱见图 3，可以看出，R 基取代后的三种化合物相较于未取代的 $ZnPcH_{16}$ 分子而言，吸收峰的数目增加了，原因是分子对称性的降低，其中(2)和(4)化合物相较于化合物(1)的红外光谱都发生了一定程度的红移。在模拟的红外光谱 1 500～1 000 cm^{-1}区域内，化合物(1)的最强红外吸收光谱位于1 393.5 cm^{-1}处，化合物(2)的最强吸收峰在 1 411 cm^{-1}处，此处的吸收峰归属于 R 取代基中 C—C 和 C—N 的伸缩振动以及碳碳双键的 C—H 的摇摆振动，化合物(3)的最强吸收峰在 815 cm^{-1}处，归属于 C—C 和 C—N 的伸缩振动，同时还包括 NH_2 中 N—H 的摇摆振动，不过此化合物的最强吸收峰并没有发生红移，化合物(4)的最强吸收峰在 1 531 cm^{-1}处，归属于四个异吲哚中 C—C 键的伸缩振动以及中间大环的 C—N 键的伸缩振动，所以，化合物(2)和(4)可以使吸收光谱发生红移，说明该物质具有作为太阳能敏化剂的潜力。

2 结论

研究结果表明，N—乙烯基咔唑(R 基)的引入对酞菁锌的几何结构、电子结构和光谱性质都发生了一定程度的影响，因为 R 基是具有芳香性的取代基，所以当 R 基取代了酞菁锌的 H 原子以后，使酞菁锌的共轭程度增加，通过理论模拟发现，Zn[$PcH_{15}R$]分子的 HOMO-LUMO 能级差减小，与未取代的酞菁锌分子的红外光谱比较也发生了红移，说明 Zn[$PcH_{15}R$]分子有作为染料敏化剂的可能，这与以前的研究结果是一致的。在 Zn[$PcH_{15}R$]分子的周边位置引入具有供电子性质的-NH_2 和具有吸电子性质的-F 原子以后，计算结果显示这两个分子的HOMO-LUMO 能极差与未取代的酞菁锌的能极差相比也同样减小了，Zn[PcH_8R]F_8 分子的红外光谱也发生了红移。比较 Zn[$PcH_{15}R$]和 Zn[PcH_8R]F_8 这两个分子的红外光谱，发现 R 基取代后的酞菁锌分子在连接具有吸电子-F 原子以后，其红外光谱的红移程度更大，说明 Zn[PcH_8R]F_8 分子中 R 基与-F 原子形成的推拉电子结构更有利于光电转化效率的提高。综上说明，Zn[$PcH_{15}R$]和 Zn[PcH_8R]F_8 这两个分子具有作为太阳能电池敏化剂的潜能。

参考文献

[1] 张云峰，刘涛，薛慧玲，等. 染料敏化太阳能电池的研究进展[J]. 四川师范大学学报(自然科学版)，2014，37 (4)，631-641.
[2] T. F. Ma, W. Zheng, X. Cui. 九—乙基咔唑—N—氧化物结构和光谱性质的理论研究[J]. 牡丹江师范学院学报(自然科学版)，2014 (4)：63.
[3] 朱英，张学俊. 咔唑类染料敏化剂的研究进展[J]. 山西化工，2013.33(5)：35-39.
[4] 韩建东，王都留. 咔唑及金属咔唑化合物的合成及应用研究进展[J]. 首都师范大学学报(自然科学版)，2012(33)，14-18.
[5] F. Yao, X. Cui, 9-位取代酞菁锌化合物结构与性质研究[J]. 牡丹江师范学院学报(自然科学版)，2015(1)，62.
[6] 徐明生，李振国，阚福麟，等. 纳米与能源，酞菁及其应用[J]. 材料科学与工程，1999(04)，1-6.

编辑：琳莉

(C)1994-2019 China Academic Journal Electronic Publishing House. All rights reserved. http://www.cnki.net

邢乐红发表科研论文目录（共 8 篇）

1.Xing L H, Shi X T, Wang Y X, et al. Electrochemical Synthesis of Ni-SnO_2 Composite Electrodes for Hydrogen Evolution Reaction in Alkaline Solution[J]. Int. J. Electrochem. Sci, 2022, 17(220530): 2.

2. Xing L, Wang Y, Shi X, et al. Investigation of Pt/C and Pt-Ru/C Mixed Catalyst for DME Oxidation in Direct Dimethyl Ether Fuel Cells[J]. Int. J. Electrochem. Sci, 2020, 15: 10382-10391.

3.Xing L, Wang Y, Sui C, et al. Investigation of Pt/SnO_2/C Catalyst for Dimethyl Ether Oxidation in DDFC[J]. Int. J. Electrochem. Sci, 2020, 15: 2375-2384.

4.Xing L H, Yin G P, Du C Y, et al. Investigation on the durability of direct dimethyl ether fuel cell. Part II: Cathode degradation[J]. International Journal of Hydrogen Energy, 2017, 42(26): 16695-16699.

5.王宜鑫,邢乐红,石鑫婷,孟凡旭,张亮,董瑞.镀液中氨基磺酸镍质量浓度对电镀镍层析氢催化活性的影响[J].电镀与涂饰,2022,41(01):6-9.

6.邢乐红,王宜鑫,王慧,左明辉,孙芳,梁志男.氨基乙酸对硫酸盐体系电镀镍-铁合金的影响[J].电镀与涂饰,2019,38(19):1039-1041.

7.邢乐红,黎德育,李宁,左明辉,李晶.抗坏血酸对硫酸盐体系镍–铁合金镀液稳定性的影响[J].电镀与涂饰,2018,37(12):526-528.

8.邢乐红,杨晶,王海鹏,达铭,李姗,崔术新.硫脲对低磷化学镀镍稳定性的影响[J].牡丹江师范学院学报(自然科学版),2016(03):41-42.

1. **Xing L H, Shi X T, Wang Y X, et al. Electrochemical Synthesis of Ni-SnO_2 Composite Electrodes for Hydrogen Evolution Reaction in Alkaline Solution[J]. Int. J. Electrochem. Sci, 2022, 17(220530): 2.**

Int. J. Electrochem. Sci., 17 (2022) Article Number: 220530, doi: 10.20964/2022.05.35

International Journal of
ELECTROCHEMICAL
SCIENCE
www.electrochemsci.org

Short Communication

Electrochemical Synthesis of Ni-SnO_2 Composite Electrodes for Hydrogen Evolution Reaction in Alkaline Solution

*Le-Hong Xing**, *Xin-Ting Shi, Yi-Xin Wang, Li Zhang, Xiao-Yan Xu, Fan-Xu Meng, Jing Li*

Heilongjiang Key Laboratory of Photoelectric Functional Materials, College of Chemistry and Chemical Engineering, Mudanjiang Normal University, Mudanjiang 157011, China
*E-mail: xinglehonghit@163.com

Received: 28 January 2022 / *Accepted:* 1 March 2022 / *Published:* 5 April 2022

In this work, high efficient Ni-SnO_2 electrodes were prepared for the alkaline hydrogen evolution reaction (HER) by a simple composite electroplating method from sulphamate bath containing SnO_2 nano-particles. The Ni-SnO_2 electrode was physically characterized by scanning electron microscopy (SEM), energy dispersive analysis of X-ray (EDAX), and X-ray diffraction (XRD). These physical characterization results revealed that the homemade SnO_2 particles (about 170 nm) were successfully co-deposited in coatings. The composited SnO_2 changed the surface morphology and phase structure of Ni matrix. The electrochemical activities and stabilities for HER were monitored by steady-state polarization, Tafel plots, electrochemical impedance spectroscopy (EIS) and chronopotentiometry technique. The activity was confirmed via the quantification of H_2 gases that evolved during chronopotentiometry study. The Ni-SnO_2 showed a higher catalytic activity for H_2 evolution, compared with Ni. The OH_{ads} on SnO_2 surface was benefit to the formation of adsorbed H_{ads} which is the rate-determining step for HER.

Keywords: Hydrogen evolution reaction; Electro-catalysis; Composite electroplating; Ni-SnO_2

1. INTRODUCTION

With the economic development and progress of industry, the energy crisis and environmental pollution have caused the global concern [1]. Driven by the growing concern, efforts have been made to develop new environmentally friendly energy sources. Hydrogen (H_2) is identified as the most potential energy carrier in future for its clean, renewable and high efficient characters [2,3]. Water is the cheapest and most rich resources of hydrogen, and water electrolysis is a sustainable and promising method for hydrogen production [4,5]. The development of the higher activity electrode materials is particularly important for water electrolysis. Nickel-based materials, such as Ni and Ni-M alloys, are prominent non-noble metal catalysts for their good electro-catalytic activity for HER and

sufficient corrosion resistance in alkaline solution [6-10]. Recently, Ni-based metallic oxide composite material has received considerable attention because it exhibits a number of advantages. For example, Zheng et. al. [11] investigated the effect of CeO_2 particles in Ni coatings on the activity of HER. The results show that the Ni based CeO_2 electrodes show higher HER activity and better stability than pure Ni. H_{ads} can easily adsorb on Ce atoms due to the presence of several half-filled and empty d orbitals. Kullaiah et. al. [12] prepared Ni-TiO_2 electrode by composite electroplating method. The addition of TiO_2 is benefit to the formation of tiny nickel grains and increased the number of active site. Besides CeO_2 and TiO_2, a lot of metallic oxides such as ZnO [13], Cu_2O [14], and MoO_2 [15] have been used as co-catalyst to enhance the activity of HER on Ni based materials. However, the effects of SnO_2 nano particles addition on the performance of HER have not been fully investigated yet. SnO_2 is considered to be an excellent co-catalyst for methanol oxidation, ethanol oxidation and O_2 reduction in fuel cells [16-18]. It is very stable in alkaline solutions, and can support sufficient OH_{ads} species. The OH_{ads} is benefit to the formation of adsorbed H_{ads} [19]. The catalytic activity can be enhanced when the formation of adsorbed H_{ads} is the rate-determining step for HER (Volmer step). According to the well known "volcano" curve, the strength of Ni-H bond is relatively weak, and the formation of H_{ads} is always the rate-determining step for HER (Volmer step) on Ni electrode [20]. In this study, the aim of work is to utilize SnO_2 to enhance the HER activity of Ni coating electrode. We first synthesized SnO_2 nano-particles by hydrolysis method. And then, these SnO_2 particles were suspended in nickel plating solution. The Ni-SnO_2 composite coating was prepared by composite electrodeposited method. Multiple physical and electrochemical tests were employed to investigate the effect of SnO_2 particles embed in Ni coating on the activity of HER.

2. EXPERIMENTAL

2.1. Preparation of Ni-SnO_2 electrode

Preparation of SnO_2 Nanoparticles: 5-hydrated tin tetrachloride ($SnCl_4{\cdot}5H_2O$), sodium hydroxide, and ethanol were used as received without further purification. A sample of 17.53 g of $SnCl_4{\cdot}5H_2O$ was dissolved in 50 ml ultrapure water (18.2 M Ω cm, Mill-Q Corp.). The pH value of the solution was adjusted to 7 with NaOH solution. Then, the solution was transferred into a stainless steel reactor (100 ml). The reactor was put in an electric oven and kept at 160 ℃ for 2 h. After cooling to room temperature, the obtained product was separated by centrifugation. The resulting powders were washed in sequence with ethanoic acid - ammonium acetate solution and pure ethanol, and then dried at 80 ℃ for 12 h in vacuum. The particle size of homemade SnO_2 was about 200 nm.

Preparation of Ni-SnO_2 composite electrode: The Ni-SnO_2 composite electrode was electrodeposited on 4×5 cm copper sheet by composite electrodeposition method. The plating electrolyte was composed of 350 $g{\cdot}L^{-1}$ Ni $(NH_2SO_3)_2{\cdot}4H_2O$, 10 $g{\cdot}L^{-1}$ $NiCl_2{\cdot}6H_2O$, 30 $g{\cdot}L^{-1}$ NH_4Cl and various different content of SnO_2 nanoparticles. These composite electrodes were named as Ni/SnO_2-1, Ni/SnO_2-2, Ni/SnO_2-3, Ni/SnO_2-4, which were obtained from the above electrolyte with 1 $g{\cdot}L^{-1}$, 2 $g{\cdot}L^{-1}$, 3 $g{\cdot}L^{-1}$, 4 $g{\cdot}L^{-1}$ SnO_2 nanoparticles, respectively. The composite electrodeposition was carried out at

a current density of 3 A/dm^2, a temperature of 35 ℃ with a magnetic stirring at 850 rpm for 30 min.

2.2. Physical characterization

The morphology, crystal structure and the composition of the composite coatings were determined by SEM (Quanta 400, FEI), XRD (D8 Advance, Bruker) and EDAX, respectively.

2.3. Electrochemical measurements

Electrochemical studies including steady-state polarization, tafel plots, EIS and amperometric current density-time curves of the composite electrodes were conducted using electrochemical working station (PARSTAT 4000) in a standard three-electrode cell in 1 M NaOH solution. The composite electrodes were used as working electrode and 1 cm^2 platinum foil was served as counter electrode. Hg/HgO electrode was used as the reference electrode. The scan rate of steady-state polarization test was 5 $mV{\cdot}s^{-1}$. The EIS was measured at -0.125 V (vs. SCE) in a frequency range from 100 kHz to 0.01 Hz with 6 − 12 points per decade. The amplitude of the AC-voltage was 0.005 V. All the electrochemical measurements were carried out at 25 ℃.

3. RESULTS AND DISCUSSION

Fig. 1 is the IR spectra of homemade SnO_2 nanoparticles. The characteristic peak in the range of 500-750 cm^{-1}, 1600 cm^{-1}, and 3430 cm^{-1} are assigned to Sn-O vibration, O-H bending vibration and O-H stretching vibration [16]. SnO_2 in composite electrodes can support abundant OH_{ads} species which are benefit to the formation of adsorbed H_{ads} during HER [21]. Fig. 2 is XRD patterns of SnO_2 nanoparticles. The SnO_2 nanoparticles show the major diffraction peaks of (110), (101), (111), (211), (301) and (321) [22]. The average size of SnO_2 particles were calculated from the most intense peak (110) according to Sherrer's Equation [23]. The particle size of SnO_2 was about 170 nm .

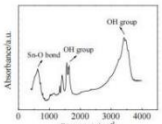

Figure 1. FTIR plot of homemade SnO_2 particles after dehydration treatment at 200 ℃ under vacuum condition.

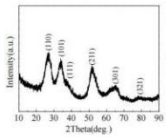

Figure 2. XRD analysis of SnO_2 nanoparticles.

The XRD patterns of Ni and Ni/SnO_2-3 electrodes are shown in Fig.3. The diffraction peaks for the two electrodes at 2θ about 44.5°, 51.8° and 76.4° can be attributed to Ni (111), Ni (200) and Ni (220). The peaks for Ni/SnO_2-3 electrode at about 26.6°, 33.8°, 38.7°, 51.7° and 54.3° can be well indexed to SnO_2 (JCPDS:41-1445). SnO_2 particles were successfully co-deposited in Ni matrix. The preferential orientation of Ni electrode is (200) crystal plane. The preferential orientation of Ni/SnO_2-3 electrode has been greatly changed to (111) crystal plane. Ni (111) plane was more benefit to the enhancement of electrocatalytic performance for HER than other planes [24,25]. The full width of half maximum values of Ni (111) and Ni (200) for pure Ni electrode is 0.193° and 0.233°, respectively. The two values for Ni/SnO_2-3 electrode are 0.204°and 0.303°, respectively. The diffraction peaks of Ni/SnO_2-3 electrode are broader than Ni. According to Sherrer's Equation, the crystallite size of composite electrode is smaller than that of Ni. The co-deposition of SnO_2 particles in Ni matrix has the effect of grain refinement.

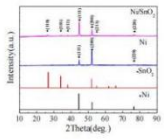

Figure 3. XRD patterns of Ni and Ni/SnO_2-3 electrodes.

SEM images of Ni and Ni/SnO_2 electrodes are shown in Fig.4. As shown in Fig.4(a) and (b), The Ni electrode shows a relatively bulky microstructure. The co-deposition of SnO_2 nano-particles makes the coating crystallization more meticulous and porous, which is benefit to increase of surface area. The white spherical particles in Fig.4(b) are SnO_2. The mean size of SnO_2 nano-particles is about

200 nm, which is consistent with the above XRD results. The presence of SnO_2 nano-particles in the composite electrode is confirmed via EDAX analysis. The amount of SnO_2 nano-particles incorporated in Ni/SnO_2-3 is approximately 4.7 wt%.

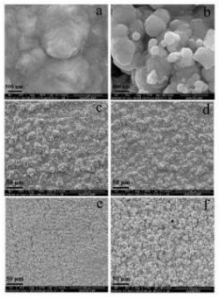

Figure 4. Low and high-magnification SEM images of electrode: (a) magnified Ni, (b) magnified Ni/SnO_2-3; (c) Ni/SnO_2-1, (d) Ni/SnO_2-2; (e) Ni/SnO_2-3; (f) Ni/SnO_2-4.

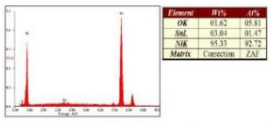

Element	Wt%	At%
OK	01.62	05.81
SnL	03.04	01.47
NiK	95.33	92.72
Matrix	Correction	ZAF

Figure 5. EDAX patterns of Ni/SnO_2-3 composite electrode and its quantitative analysis.

The electrocatalytic activity for HER on Ni/SnO_2 composite electrodes are tested by a series of electrochemical measures including cathode polarization curves, Tafel plots, and EIS. The corresponding parameters obtained from above electrochemical measurements are listed in Table 1.

Fig.6 (a) shows the cathode polarization curves of different electrodes. It is apparent that Ni/SnO_2-3 shows the highest catalytic activity, which demand the lowest overpotential of 427 mV to drive current densities of 10 mA cm^{-2}.

To further understand the mechanism of the HER, the Tafel plots in Fig.6 (b) are fitted to the classic Tafel equation (Eq. 1). The values of R^2 are greater than 0.99, which indicate that the calculated kinetic parameters listed in Table 1 adjust well to Tafel equation.

$$\eta = b\,log(j/j_0) \qquad (1)$$

Here η is the cathode overpotential, b is the Tafel slope, j is current density and j_0 is the exchange current density. The j_0 in Table 1 represents the HER catalytic activity of the electrodes. As shown in Table 1, the j_0 values of these Ni/SnO_2 electrodes are all higher than that of pure Ni electrode. With the increase of the SnO_2 content in coatings, the values of j_0 for Ni/SnO_2 electrodes are first enhanced and then tend to decline. The catalytic activity of Ni/SnO_2-3 obtained from electrolyte with 3 g L^{-1} SnO_2 nano-particles is the highest. The co-deposition of SnO_2 particles makes the grain size of the composite coating much finer than that of pure nickel. This fining effect is beneficial for HER. Too much SnO_2 co-deposit in the composite electrode may affect the electrode activity for its low electron conductivity. Tafel slope b is a significant parameter which can indicate the dominant HER mechanism on electrodes. As shown in Fig. 6(b) and Table 1, the b of the Ni and these Ni/SnO_2 composite electrodes are 120, 204, 199, 187 and 205 mV dec^{-1}, respectively. According to the reported literature [26-29], the rate-determining steps of HER on above studied electrodes are Volmer reaction. The formation of H_{ads} determines Volmer reaction rate. SnO_2 in composite electrodes can support abundant OH_{ads} species. These OH_{ads} species can promote H_2O decomposition and H_{ads} formation by weakening the oxophilicity of the active site [30,31]. The SnO_2 and Ni interface benefits for the H_{ads} adsorption, but suppress the competitive H_2O_{ads} and OH_{ads} adsorption [32]. Hence, the Ni-SnO_2 showed a higher catalytic activity for H_2 evolution, compared with Ni.

The EIS measurements are carried out on Ni and Ni/SnO_2 electrodes at cathode potential of -0.125 V (vs. SCE) under HER operating conditions. The Nyquist diagrams are illustrated in Fig.6 (c). A widely used equivalent circuit is used to describe the HER process and the fitting results of the resistance elements are listed in Table1. The ohmic resistances (R_s) of these composite electrodes are all higher than that of Ni. SnO_2 co-deposit in the composite electrodes decrease the electron conductivity of electrode. The electrochemical reaction resistance (R_{ct}) of Ni/SnO_2-3 electrode is the lowest among all of studied electrodes. The bode phase angle plot obtained for these composite electrodes are presented in Fig.6 (d). All these plots abide by one-time-constant behavior, which is in good agreement with above mentioned equivalent circuits model given in Fig.6 (c). Also, the Ni/SnO_2-3 electrode has the lowest phase angle and impedance value, which confirms the enhanced HER rate.

The SnO_2 co-deposit in Ni electrodes can accelerate the HER process. Excessive SnO_2 in the composite electrodes decrease HER activity for the low electron conductivity of electrode. The Ni/SnO_2-3 with the optimal addition of SnO_2 in Ni shows the highest catalytic activity, which is coincident with the results of steady-state polarization in Fig.6 (a) and Tafel plots in Fig. 6 (b). C_{dl} is double layer capacitance which is associated with surface area of electrode [33,34]. The addition of SnO_2 raises the value of C_{dl}, which indicates that surface area of composite electrode has been increased. SnO_2 makes the Ni coating crystallization more tiny. The increase of active surface area

benefits for the formation of H_{ads}. This experimental finding is consistent with above SEM results.

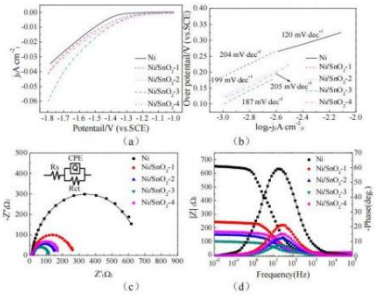

Figure 6. Electrochemical properties for HER on Ni and Ni/SnO_2 composite electrodes in 1 M NaOH. (a) Steady-state polarization curves, (b) Corresponding Tafel plots, (c) Nyquist diagrams (dots) and fitting diagrams (lines) based on possible equivalent circuits, (d) Bode plots.

Table 1. Electrocatalytic parameters obtained from above electrochemical measurements in 1 M NaOH solution.

	j_o ($uA\cdot cm^{-2}$)	b ($mV\cdot dec^{-1}$)	η_{10} (mV)	R_s (Ω)	R_{ct} (Ω)	C_{dl} ($10^{-3}\,F\cdot cm^{-2}$)
Ni	0.673	120	501	14.7	652.7	8.17
Ni/SnO_2-1	22.57	204	540	14.8	240.5	14.32
Ni/SnO_2-2	37.51	199	483	15.4	149.7	21.73
Ni/SnO_2-3	52.29	187	427	15.8	100.6	26.31
Ni/SnO_2-4	39.21	205	493	16.6	168.8	19.77

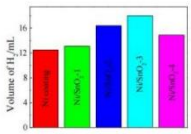

Figure 7. The volume of H_2 evolved on each studied electrode at cathode current density of 300 mA·cm^{-2} for 300 s

Fig. 7 shows the volume of H_2 gas evolved on each studied electrode for 300 s at a constant cathode current density of 300 mA·cm^{-2}. The Ni/SnO_2-3 electrode obtained from the electrolyte with 3 g·L^{-1} SnO_2 particles produces the maximum amount of H_2 (17.9 mL) compared to the other coatings. This result confirms that the Ni/SnO_2-3 shows the best activity for HER.

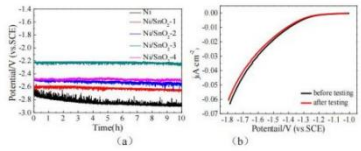

Figure 8. Stability tests of the composite electrodes. (a) The chronopotentiometry study at cathode current density of 100 mA·cm^{-2}, (b) Polarization curves of Ni/SnO_2-3 before and after 10 h chronopotentiometry test in 1 M NaOH solution.

The behavior of the electrode potential as a function of time at cathode current density of 100 mA·cm^{-2} is shown in Fig.8. The decrease of electrode potential for Ni, Ni/SnO_2-1, Ni/SnO_2-2, Ni/SnO_2-3, and Ni/SnO_2-4 is 323 mV, 54 mV, 101 mV, 34 mV and 49 mV, respectively. The HER stability of the composite electrode are all higher than pure Ni. The polarization curves of Ni/SnO_2-3 before and after 10 h stability test show negligible changes. The Ni/SnO_2-3 electrode demonstrates excellent stability.

The electrochemical properties of Ni/SnO_2 are compared with other composite materials reported in literatures. The comparison of these works is listed in Table 2. As shown in Table 2, the Ni/SnO_2 exhibits lower over potential [35-37] and higher exchange current density [38,39]. The

performance of hydrogen evolution with Ni/SnO_2 electrode catalyst is obvious higher than other reported composited materials.

Table 2. The activity of HER on different composite electrodes reported in literatures and this work

Electrode	Alkaline solution	b ($mV\cdot dec^{-1}$)	η (mV)	j_0 ($uA\cdot cm^{-2}$)	Reference
Ni/SnO_2	1 M NaOH	187	427 (η_{10})	52.29	this work
Ni-Sn@C PNs	1 M NaOH	145	1230 (η_5)	-	[35]
(Ni-MoS_2)$_{1000}$	2mM $HClO_4$/ 0.1 M $NaClO_4$	120	680 ($\eta_{0.15}$)	8×10^{-4}	[36]
Cu/Cu_2O/ Ni NP	0.1 M H_2SO_4	50	456 (η_{10})	-	[37]
Ni-PAni	4 M KOH	-	-	3.47	[38]
Ni/WO_3	1 M KOH	124.7	-	5.88	[39]
Ni/Bi_2O_3	1 M KOH	128.8	-	2.29	[39]
Ni/SC	1 M KOH	116.9	-	2.43	[39]

4. CONCLUSIONS

The high efficient Ni-SnO_2 electrodes are fabricated by a simple low-cost composite electroplating method. Compared with pure Ni, the Ni/SnO_2 catalyst gives a higher catalytic activity and stability for HER. The co-deposition of SnO_2 in Ni coating makes metal crystallization finer and tinier, which increase the active surface area of electrode. The co-deposition of SnO_2 changes the preferential orientation of Ni to (111) crystal plane which is more benefit to the activity of HER. The OH_{ads} on SnO_2 surface facilitates the formation of adsorbed H_{ads} which is the rate-determining step for HER. SnO_2 is a promising co-catalyst to enhance the activity of HER on Ni based materials.

ACKNOWLEDGEMENT
This work was supported by the Mudanjiang Normal University Key Project (No. GP2021002), the Research Fund Project of Mudanjiang Science and Technology Project of Mudanjiang city (No. SQ2020JG115), the Teaching reform Projects of MuDanjiang Normal University (No. KCSZ-2020021), the Innovation Project of University Students (202110233043).

2. Xing L, Wang Y, Shi X, et al. Investigation of Pt/C and Pt-Ru/C Mixed Catalyst for DME Oxidation in Direct Dimethyl Ether Fuel Cells[J]. Int. J. Electrochem. Sci, 2020, 15: 10382-10391.

Int. J. Electrochem. Sci., 15 **(2020)** 10382 – 10391, doi: 10.20964/2020.10.27

International Journal of
ELECTROCHEMICAL
SCIENCE
www.electrochemsci.org

Short Communication

Investigation of Pt/C and Pt-Ru/C Mixed Catalyst for DME Oxidation in Direct Dimethyl Ether Fuel Cells

*Lehong Xing**, *Yixin Wang*, *Xinting Shi*, *Rui Dong*, *Lin Wu*

College of Chemistry and Chemical Engineering, Mu Danjiang Normal University,
*E-mail: xinglehonghit@163.com

Received: 2 June 2020 / *Accepted:* 24 July 2020 / *Published:* 31 August 2020

The performance of Pt/C and Pt-Ru/C mixed catalyst has been studied for dimethyl ether (DME) oxidation in direct dimethyl ether fuel cells (DDFCs). Transmission Electron Microscopy (TEM) characterizations show that Pt and Pt-Ru particles (about 3.0 nm) are highly dispersed on their supports. The electrochemical activity of mixed catalyst was evaluated by polarization curve, amperometric current density – time technique, and electrochemical impedance spectroscopy (EIS). The results show that the activity of mixed catalyst is better than Pt/C toward DME oxidation. Pt-Ru/C in the mixed catalyst is helpful for reducing the catalyst poisoning effect, and simultaneously, Pt/C in the mixed catalyst can provide continuous Pt active sites for DME dehydrogenation. Too much Pt-Ru can reduce the catalytic activity. The optimal Pt-Ru content is 3.5 mg cm^{-2} Pt and 0.5 mg cm^{-2} Pt-Ru (metal loading) in anode catalyst layer.

Keywords: Direct dimethyl ether fuel cell; Dimethyl ether; Anode catalyst; Pt-Ru/C; Pt/C

1. INTRODUCTION

Direct type fuel cells which use formic acid, ethanol, formaldehyde, methanol and dimethyl ether (DME) as their fuel have been widely studied recently as potential new power sources [1-3]. These investigated direct type fuel cells are all have their own advantages [4,5]. The direct dimethyl ether fuel cell (DDFC) is one of the promising fuel cells [6]. Dimethyl ether (DME) is the simplest ether and there is no C-C bond in its molecular (CH_3OCH_3) [7]. The toxity of DME is low. DME gas can be compressed easily into liquid form, so that the transportation of DME is convenient. The energy density of DME is high and its fuel crossover effect is low [8,9]. However, DDFC still has some obstacles which hinder its practical applications. The major obstacle limits the performance of DDFC is the poor kinetics of DME oxidation, which mainly results from the week adsorption of DME on catalyst and the poisoning effect of Pt based catalyst [10]. The development of active catalyst towards DME oxidation is very necessary for DDFC. Pt-Ru/C and Pt/C are the two most commonly used anode catalyst for DDFC. Different

researchers have different conclusions about which one is more proper for DME oxidation. Liu [11] compare the performance of the two catalyst in DDFC. They find that Pt-Ru/C is better than Pt/C in low over potential range. Oppositely, Pt/C is better than Pt-Ru/C in high over potential range. In low over potential range, the anode needs OH supported by Ru to remove absorbed CO. In high over potential range, the absorbed CO can be oxidized immediately and the Ru addition decreases the continuous Pt active sites, which is harmful for DME oxidation. Kerangueven [12] find that Ru content in Pt-Ru has an important influence on the performance of DDFC. DDFC performs better with the decrease of Ru content in Pt-Ru. Tsutsumi [13] compare the two catalyst at different temperatures. The activity of Pt-Ru is better than Pt at high temperature, because the rate of DME oxidation reaction is relatively fast at high temperate and there are lots of adsorbed posing species generated on the surface of catalyst. Ru is helpful for the removal of posing intermediates. At low temperature, the activity of Pt is better than Pt-Ru, because the catalyst posing effect is not very significant. Li [14] consider that the catalyst activity of Pt-Ru is higher than Pt, and the optimal Pt to Ru ration is $Pt_{0.8}Ru_{0.2}$. Based on the above results, there are two different (positive and negative) effects of Ru on the activity of DME oxidation. The positive one is that Ru is helpful for the generation of oxygen-containing species. These oxygen-containing species can promote the catalyst activity when the oxidation of posing intermediates is the rate-determing step for DME oxidation reaction. The negative one is that the presence of Ru decreases the continuous Pt active sites, which is bad for DME adsorption and following dehydrogenation. It is very necessary to develop a catalyst which can make ideal balance between positive and negative effects. Besides, which one of these two effects (positive and negative) plays a major role in DME oxidation is strongly impacted by the operating conditions. Up to now, most of the researches about Pt-Ru/C and Pt/C catalyst are carrying out under high temperature and pressure. The performances of DDFCs with the two catalysts at lower than 100 ºC under ambient pressure have not been studied in detail. In this work, Pt-Ru/C is added into Pt/C to form a mixed catalyst for DME oxidation. We represent the first systematic study of the mixed catalyst with different Pt-Ru/C content at 60 ºC under ambient pressure. The mixed catalyst can provide continuous Pt active sites for DME dehydrogenation, and simultaneously provide oxygen-containing species for adsorbed intermediates oxidation. The influence of mixed catalyst on the performance of DDFC has been discussed based on the results of multiple physical and electrochemical tests.

2. EXPERIMENTAL

2.1. Preparation of catalyst

The 40 mass% Pt/C were synthesized by microwave-assisted polyol process [15]. 60 mg of pretreated carbon black (Vulcan XC-72) was ultrasonically dispersed in the solution containing 12 ml isopropyl alcohol and 48 ml glycol (EG) to form a uniform ink. 5.4 ml of 0.0386 mol L^{-1} H_2PtCl_6-EG solution dissolved in the above ink under stirring for 2h. 1 mol L^{-1} NaOH-EG solution was used to adjust the pH. The pH value of the solution was about 12. Afterwards, the solution was heated by a microwave oven (2450MHz, 800W) for 55s under argon gas protection. The solution was cooled down to ambient

temperature under stirring. Then 0.1 mol L^{-1} HNO_3 solution was used to adjust the pH. The pH value of the solution was about 3. The resulting catalyst was washed with ultrapure water, and then dried for 4 h at 80 ºC in vacuum. The 40 mass% Pt-Ru/C was synthesized in a similar way mentioned above with H_2PtCl_6-EG solution and $RuCl_3$-EG solution as precursors.

2.2. Preparation of Membrane electrode assembly (MEA)

The MEAs (5 cm^2) were prepared using a typical process which had been reported in detail previously[16]. The anode gas diffusion layers (GDLs) were wet-proofed carbon papers (Toray, TGP-H-060). The PTFE content in anode GDLs was 18 mass%. The wet-proofed cathode GDLs were composed of carbon papers and 1 mg cm^{-2} of Vulcan XC-72 carbon black. The PTFE content in cathode GDLs was 30 mass%. Pt/C and Pt-Ru/C mixed catalysts were used as the anode catalysts. The Pt and Pt-Ru loading of different MEAs are listed in Table 1. The total metal loading in anode catalyst layers of these MEAs are 4 mg cm^{-2}. The cathode catalyst was Pt/C (2 mg cm^{-2}). Nafion content in catalyst layers were 20 mass%.

Table 1. Components of anode catalyst layers for different MEAs.

Samples	Pt/ mg cm^{-2}	Pt-Ru/ mg cm^{-2}
MEA-1	4.0	0
MEA-2	3.5	0.5
MEA-3	3.8	0.2
MEA-4	3.0	1.0

2.3. Electrochemical measurements

2.3.1 Steady-state polarization curves

A Potentiostat/Galvanostat apparatus (Hokuto Denko Inc. HA-151) was employed to record the steady-state polarization curves of DME oxidation [17]. At the anode side, 1.5 mol L^{-1} DME solution was fed with a flow rate of 3 mL min^{-1}. Simultaneously, the humidified H_2 was supplied to cathode with a flow rate of 200 mL min^{-1}. The cathode served as a dynamic hydrogen electrode (DHE).

2.3.2 Electrochemical impedance spectra (EIS)

The EIS of the anodes was measured by an electrochemical analysis instrument (Shanghai Chen-Hua Instruments Corp., CHI 604B) under 0.45 V vs. DHE at 60 ºC. The amplitude of sinusoidal potential signal was 5mV. The frequencies were from 1 kHz to 0.01 Hz.

2.3.3 Amperometric i–t curves

The amperometric *i–t* curves of DME oxidation were measured by CHI 604B at 0.45 V vs. DHE. The anode and cathode reactants used in above electrochemical measurements (steady-state polarization curves, EIS, amperometric *i–t*) were all the same.

2.3.4 Fuel cell testing

The performances of DDFCs with different anode catalyst were tested using a commercial electrochemical station (Arbin Fuel Cell Testing System) at 60ºC under ambient pressure. During the test, 1.5 mol L^{-1} DME solution was fed at a flow rate of 3 mL min^{-1}, while humidified oxygen was supplied at a flow rate of 200 mL min^{-1}.

3. RESULTS AND DISCUSSION

TEM images and the nanoparticle size distribution diagrams of catalysts are presented in Fig. 1 and Fig. 2. The size distribution diagrams are obtained by random measurements of 100 particles. Pt and Pt-Ru alloy particles are highly dispersed on supports. The average particles sizes of the two catalysts are nearly the same (about 3 nm). Fig. 3 shows the polarization curves and the power density curves of MEAs with or without Ru in anode catalyst at 60 ºC. The maximum power density of the MEA1 and MEA2 is 40 mW cm^{-2} and 50 mW cm^{-2}, respectively. The performance of MEA with mixed catalyst is higher than that of Pt/C. The Ru in mixed catalyst provides oxygen-containing species which is helpful for the oxidation of absorbed intermediates and decrease the catalyst posing effect. The Pt/C in mixed catalyst provides continuous Pt active sites for DME oxidation. The mixed catalyst can make a balance between the positive and negative effects.

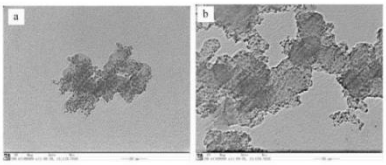

Figure 1. TEM images of catalysts: (a) Pt/C; (b) Pt-Ru/C.

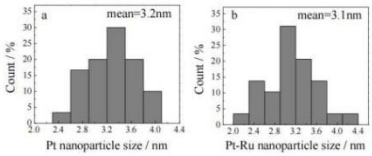

Figure 2. Size distribution diagrams of catalysts: (a) Pt/C ; (b) Pt-Ru/C.

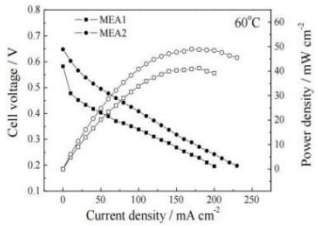

Figure 3. The polarization curves and the power density curves of the MEAs with different anode catalysts at 60 ºC: MEA1 with Pt/C ; MEA2 with the mixed catalysts.

Fig. 4 shows the polarization curves of DME oxidation at different anode. The performance of MEA2 is better than that of MEA1. MEA2 with the mixed catalysts exhibits lower polarization at anode. The Ru in mixed catalyst is benefit to decrease polarization and improve the performance of DDFC.

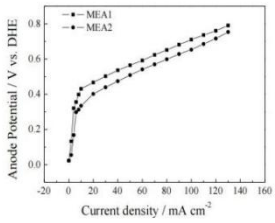

Figure 4. Steady-state polarization curves of DME oxidation reaction versus DHE.

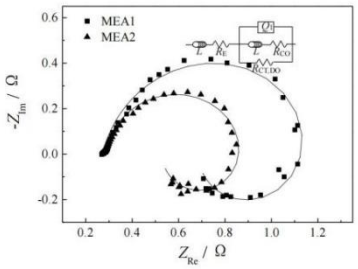

Figure 5. Electrochemical impedance spectra of DDFC anode with different catalyst (dots) and fitting diagrams using equivalent circuit (lines) at 0.45 V vs. DHE.

The EIS of anodes with different catalyst are shown in Fig.5. A possible equivalent circuit in Fig.5 is used to describe the anode process [18-20]. The fitting results analyzed by ZSimpWin software

are listed in Table 2. As seen in Fig.4, both MEA1 and MEA2 operate in low current region when the anode potential is 0.45 V vs. DHE. The mass transport polarization effect can be ignored in low current region. In Fig.5, the semicircle is due to DME oxidation reaction and the inductance in the low frequency region corresponds to the slow relaxation of CO_{ADS}. R_E is the ohmic resistance of anode. The R_E values of MEA1 and MEA2 are nearly the same. $R_{CT,DOR}$ is the charge transfer resistances of DME dehydrogenation. The $R_{CT,DOR}$ of MEA1 and MEA2 is 1.03 Ω and 0.64 Ω, respectively. R_{CO} is the charge transfer resistances of CO_{ADS} oxidation. The R_{CO} of MEA1 and MEA2 is 0.69 Ω and 0.41 Ω, respectively. The decrease of $R_{CT,DOR}$ means that DME dehydrogenation of MEA2 is easier than that of MEA1. The decrease of R_{CO} means that poisoning of the Pt in MEA2 is much more muted than that in MEA1. The total anode reaction resistance ($R_{R,A}$) of MEA1 and MEA2 is 0.41 Ω and 0.25 Ω, respectively. The increase of DDFC performance can be attributed to the decrease in the anode reaction resistance including DME dehydrogenation resistance and CO_{ADS} intermediate oxidation resistance.

Table 2. Fitting results of the resistance elements.

Resistances / Ω	MEA1	MEA2
R_E	0.27	0.28
$R_{CT,DOR}$	1.03	0.64
R_{CO}	0.69	0.41
$R_{R,A}=(R_{CT,DOR}^{-1}+R_{CO}^{-1})^{-1}$	0.41	0.25

The amperometric *i–t* curves in Fig. 6 are used to evaluate the activity of catalyst for DME oxidation. The final current density of MEA1 and MEA2 is 26 and 42 mA cm^{-2}, respectively. The electrocatalytic activity of the mixed catalyst is higher than Pt /C. There is less drop in activity of the mixed catalyst during the whole 1000s test, which indicate that the mixed catalyst can enhance the CO-tolerance ability for the existence of Pt-Ru/C. In addition, the mixed catalyst can supply continuous Pt active sites for DME oxidation by the existence of Pt /C.

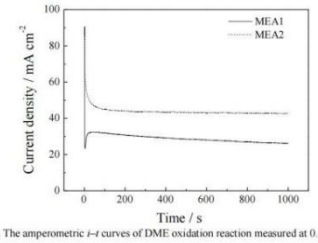

Figure 6. The amperometric *i–t* curves of DME oxidation reaction measured at 0.45 V vs. DHE.

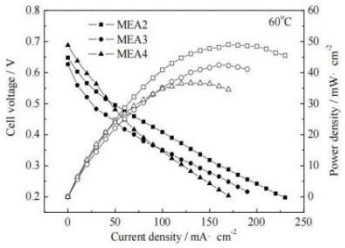

Figure 7. The polarization curves and the power density curves of MEAs with various Pt-Ru/C content in anode catalyst layer.

Fig. 7 shows the polarization curves and the power density curves of MEAs with different Pt-Ru/C content at anode. The Pt and Pt-Ru loading in anode catalyst layer of these MEAs are listed in Table 1. The MEAs perform firstly better and then worse with the increase of the Pt-Ru content in anode catalyst layer. The MEA2 with 3.5 mg cm^{-2} Pt and 0.5 mg cm^{-2} Pt-Ru in catalyst layer exists the highest

output performance, and its maximum power density is 50 mW cm^{-2}. The open circuit potentials and polarization curves (in low current density region) of different MEAs are enhanced with the increase of Ru content in anode catalyst layer. It indicates that, in low current density region, catalyst posing effect plays a major role in DME oxidation reaction. In high current density region, the oxidation of DME needs large amount of continuous Pt active sites. Too much Ru can reduce the continuous Pt active sites. The anode mixed catalyst with 3.5 mg cm^{-2} Pt and 0.5 mg cm^{-2} Pt-Ru in catalyst layer can provide continuous Pt active sites for DME dehydrogenation, and simultaneously provide oxygen-containing species to oxidize the poisoning adsorbed intermediates.

The new table has been made to compare the DME electrocatalysts described in literatures. The comparisons of these works are listed in table 3[7-10]. Comparing to these works in table 3, DDFC with Pt/C and Pt-Ru/C mixed catalyst shows higher performance under ambient pressure.

Table 3. The performances of DDFCs with different anode catalysts reported in literatures and this work

	Catalyst	The maximum power density/ mW cm^{-2}	Temperature/ ℃	Pressure/bar	Reference
1	PtCu	13.5	80	1	21
2	Pt/C	60	80	3	22
3	PtRu	38	80	1	23
4	$Pt/SnO_2/C$	49.6	70	1	15
5	Mixed catalyst	60	60	1	this work

4. CONCLUSIONS

The mixed catalyst with Pt/C and Pt-Ru/C are prepared for DME oxidation in DDFC. TEM tests show that the average sizes of Pt and Pt-Ru alloy nanoparticles are nearly the same (about 3 nm). the EIS results show that the addition of Ru can reduce $R_{CT,DOR}$ and R_{CO} of DME oxidation reaction. The mixed catalyst is helpful for reducing the catalyst poisoning effect, and simultaneously can provide continuous Pt active sites for DME dehydrogenation. Too much content Pt-Ru in mixed catalyst can reduce the catalytic activity. DDFC with 3.5 mg cm^{-2} Pt and 0.5 mg cm^{-2} Pt-Ru in anode catalyst layer shows the highest performance (50 mW cm^{-2}).

ACKNOWLEDGEMENT
This work was supported by University Nursing Program for Young Scholars with the Young Scholars Programs of Mu Danjiang Normal University (GG2018001), Creative Talents in Heilongjiang Province (UNPYSCT-2016108), the Teaching reform Projects of Mu Danjiang Normal University (19-XJ21008, KCSZ2020021), Innovation Project of University Students (202010233015).

3.Xing L, Wang Y, Sui C, et al. Investigation of Pt/SnO_2/C Catalyst for Dimethyl Ether Oxidation in DDFC[J]. Int. J. Electrochem. Sci, 2020, 15: 2375-2384.

Int. J. Electrochem. Sci., 15 (2020) 2375 – 2384, doi: 10.20964/2020.03.26

International Journal of
ELECTROCHEMICAL
SCIENCE
www.electrochemsci.org

Short Communication

Investigation of Pt/SnO_2/C Catalyst for Dimethyl Ether Oxidation in DDFC

Lehong Xing[1,2,*], *Yixin Wang*[1], *Chao Sui*[1], *Na Zhang*[2]

[1] College of Chemistry and Chemical Engineering, Mu Danjiang Normal University, Mu Danjiang 157012 ,China
[2] School of Chemical Engineering and Technology, Harbin Institute of Technology, No. 92, West Da-Zhi Street, Harbin 150001 China
*E-mail: xinglehonghit@126.com

Received: 6 November 2019 / *Accepted:* 18 December 2019 / *Published:* 10 February 2020

The performance of Pt loading on SnO_2/C support catalyst has been investigated for dimethyl ether (DME) oxidation in direct dimethyl ether fuel cells (DDFCs). The transmission electron micrograph (TEM) tests show that the sizes of Pt particles loading on different supports (SnO_2/C and XC-72 carbon black) are nearly the same (3.2 nm). The cyclic voltammograms results reveal that Pt/SnO_2/C shows higher activity towards DME oxidation. DME prefers to be adsorbed on Pt/SnO_2/C surface. SnO_2 can adsorb OH_{ads} species which benefit to reduce the Pt poisoning effect. The maximum power density of DDFC has been enhanced by using Pt/SnO_2/C as the anodic catalyst. The electrochemical active surfaces (*EAS*) of different anodes are nearly the same. That is, the improvement of DDFC performance can be attributed to the enhanced activity of anode catalyst.

Keywords: Direct dimethyl ether fuel cell; Dimethyl ether; Anode catalyst; Supports; Pt/SnO_2/C

1. INTRODUCTION

At present, traditional energy resources such as coal, natural gas and oil are nearly exhausted. Fuel cells such as proton exchange membrane fuel cells (PEMFCs) and direct methanol fuel cells (DMFCs) have been widely studied to solve the potential energy crisis problems [1-3]. However, PEMFCs and DMFCs still have some obstacles which hinder their broad applications [4,5]. Dimethyl ether (DME) is a new attractive fuel for PEMFCs which has many advantages. The energy density of DME is high and its toxicity is low. DME has low fuel crossover effect [6]. The transportation of DME is convenient because it can be liquefied easily [7]. However, the major obstacle limits the performance of direct dimethyl ether fuel cell (DDFC) is the relatively slow kinetics of anodic DME oxidation. The improvement of catalyst activity towards DME oxidation is very important for DDFC [8]. Pt and Pt-M

alloys are prominent catalysts for DDFCs [9]. Recently, metallic oxides have attracted increasing attention for catalytic researchers for their excellent co-catalyst effect [10]. In particular, tin dioxide (SnO_2) exhibits many advantages. SnO_2 shows high stability at anode. SnO_2 can adsorb sufficient OH_{ads} species. These OH_{ads} benefit to oxidize the poisoning intermediates generated during DME anodic oxidation reaction and release Pt active sites [11]. In addition, SnO_2 and SnO_2 based nanomaterials have been used as catalyst supports. The catalytic activity has been enhanced because of the strong metal-support interaction [12-14].

In this study, the aim of work is to utilize SnO_2 loaded on XC-72 carbon black as the catalyst support to enhance the DME oxidation activity. Firstly, homemade nano SnO_2/C composites are synthesized by hydrolysis method. Then, nano Pt particles are deposited on the SnO_2/C composites. The effects of catalyst supports on DME oxidation and the performance of DDFC have been discussed based on physical characterizations and electrochemical tests results.

2. EXPERIMENTAL

2.1. Preparation of catalyst

Preparation of nano SnO_2/C [15]: 64 mg of Dihydrate tin (II) halide were dissolved in the solution which was composed of 25 ml ethylene glycol (EG) and 1 ml water. 200 mg of carbon black (Vulcan, XC-72) was dispersed in another 25 ml EG. The two obtained solutions were mixed in a three-neckround-bottom flask. The mixture was kept at 190 ℃ for 3 h under stirring. Then, the mixture was cooled down to about 25 ℃. The products were filtered and washed 3 times. At last, the resulting powders were dried under vacuum condition. The theoretical content of SnO_2 in prepared supports was 20 wt. %.

Preparation of nano Pt based catalyst [15]: A 2.65 mL of H_2PtCl_6 - EG solution was diluted by 200 mL EG. The solution was adjusted to pH≈12 using NaOH-EG solution. An 80 mg of supports were dispersed into the solution under ultrasonic treatment for 0.5 h. Then the solution was refluxed for 4 h at 140 ◦C. The solution was cooled down to about 25 ℃ under stirring. Then the solution was adjusted to pH≈3 using 0.1 M HNO_3 solution. The homemade catalyst was washed 3 times, and then dried for 4 h at 80 ◦C under vacuum condition. As comparison, the 20 mass % Pt/C was prepared as reference catalyst.

2.2. MEA fabrication

The MEAs (5 cm^2) were prepared by the traditional methods which have been reported previously [16]. The wet-proofed Toray carbon papers were used as anode diffusion layers. The PTFE content of anode diffusion layers was 18 wt.%. The wet-proofed carbon papers coated with 1 mg cm^{-2} of carbon black and PTFE were used as the cathode diffusion layers. The PTFE content of cathode diffusion layers was 30 wt.%. The anodic catalysts of different MEAs were Pt/SnO_2/C and Pt/C, respectively. The cathodic catalysts of different MEAs were both Pt/C. In catalyst layer, the Pt loading was 2 mg cm^{-2}, and Nafion content was 20 wt.%.

2.3. Physical characterization

The morphology of catalyst was characterized by TEM (Hitachi H-7650). To examine and measure the content of SnO_2 in Pt/SnO_2/C, the chemical composition of the Pt/SnO_2/C was analyzed by EDAX techniques (HITACHIS-4700). The IR spectra (ThermoFisher- is10) were used to examine the OH_{ads} species on SnO_2 surface.

2.4. Electrochemical measurements

2.4.1 Cyclic voltammetry

Cyclic voltammetry (CV) measurements were conducted to evaluate anodic *EAS* [17]. During the test, humidified N_2 was pumped to the anode and humidified H_2 was pumped to the cathode. The cathode was used as a dynamic hydrogen electrode (DHE). The flow rate of N_2 and H_2 were both 200 mL min^{-1}. The CV measurements were performed from 0.05 V to 1.2 V (VS DHE). The scan rate was 0.01 V s^{-1}. The *EAS* of anodic catalyst could be calculated through Eq.(1):

$$EAS_H = \frac{Q_H}{[Pt]\times 0.21} \quad (1)$$

Where, Q_H was the charges due to hydrogen desorption, and [Pt] represented Pt loading on anode.

Another CV scan was conducted in a standard three-electrode cell. The CV scan was measured to compare the activity of the two homemade catalysts [18]. The glassy carbon disk (3 mm diam, CH Instrument, Inc) covered with catalyst was used as working electrode. 5μL of ultrasonically re-dispersed catalyst suspension (2 mg mL^{-1}) was spread on the glassy carbon disk. After drying in vacuum, the obtained electrode was coated with 5μL of 5 wt % Nafion solution to form a Nafion film. The counter electrode was platinum foil (1 cm^2). The reference electrode was a reversible hydrogen electrode (RHE). The CV scans were performed in the electrolyte of 0.5 mol L^{-1} H_2SO_4 containing 1.5 mol L^{-1} DME between 0.05 and 1.2 V (versus the RHE) at 25 ℃. The scan rate was 0.05 V s^{-1}.

2.4.2. Fuel cell tests.

The performances of MEAs fabricated with different anodic catalyst were tested by Arbin Fuel Cell Testing System at 70 ℃. The 1.5mol L^{-1} DME solution was the anodic fuel. The flow rate of DME solution was 3 mL min^{-1}. The humidified oxygen (200 mL min^{-1}) was fed to the cathode side under ambient pressure

3. RESULTS AND DISCUSSION

TEM images and the corresponding histograms of Pt/SnO_2/C and Pt/C are presented in Fig. 1 and Fig. 2. The corresponding histograms are obtained by random measurements of 200 Pt nanoparticles. The Pt particles are uniformly dispersed on SnO_2/C and carbon black supports. The average sizes of Pt

particles are nearly the same (3.2 nm) for the two catalysts.

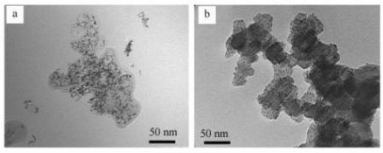

Figure 1. TEM images of Pt/SnO_2/C and Pt/C catalysts: (a) Pt/SnO_2/C; (b) Pt/C.

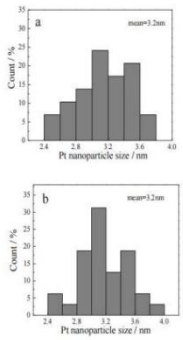

Figure 2. Size distribution of Pt/SnO_2/C and Pt/C catalysts: (a) Pt/SnO_2/C; (b) Pt/C.

The compositions of the Pt/SnO_2/C and Pt/C are analyzed by EDAX. The Pt content of Pt/SnO_2/C and Pt/C catalyst is 17.88 *wt*% and 18.42 *wt*%, respectively, which are approximately equal to the

theoretical Pt content in catalyst (20 *wt*%). The content of SnO_2 in prepared SnO_2/C composite is 18.60 *wt* %, which is almost equal to the theoretical value (20 *wt*%).

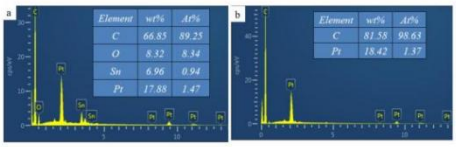

Figure 3 EDAX patterns of Pt/SnO_2/C and Pt/C catalysts and their quantitative analysis: (a) Pt/SnO_2/C; (b) Pt/C.

To compare the activity of Pt/SnO_2/C and Pt/C for DME oxidation, the cyclic voltammograms are recorded in 0.5 mol L^{-1} H_2SO_4 + 1.5 mol L^{-1} DME solution. The onset potential of DME oxidation on Pt/SnO_2/C is about 0.55 V.

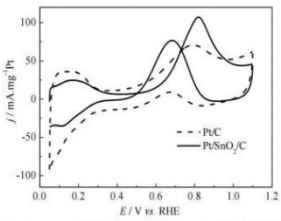

Figure 4. Cyclic voltammograms of DME electrooxidation in 0.5 mol L^{-1} H_2SO_4 + 1.5 mol L^{-1} DME aqueous solution on Pt/SnO_2/C and Pt/C catalysts. Scan rate: 0.05 V s^{-1}.

The peak current of DME oxidation on Pt/SnO_2/C is about 107 mA mg^{-1} Pt, which is much higher than that of Pt/C (70 mA mg^{-1} Pt). Thus, the Pt/SnO_2/C catalyst shows more excellent catalytic activity. G. Kerangueven [19] reports the CV curves of Pt-based catalysts in H_2SO_4 solutions with or without

DME. The peaks of CV curves with DME are suppressed during the H_2 adsorption and desorption potential range. The dissociative adsorption of DME suppresses H_2 adsorption and desorption in low potential range. Y. Liu [20] investigates the dissociative adsorption of DME and methanol in hydrogen range. The results show that both DME and methanol can absorb on catalyst and suppress the hydrogen adsorption and desorption reaction in low potential range. But the adsorption of DME is weaker than methanol. A fewer amount of DME molecules can be adsorbed and then dehydrogenated on catalyst compared with that of methanol. The activity of DME oxidation reaction is lower than methanol. The similar results have been reported by M. H. Shao [21], which use $HClO_4$ as the electrolyte. The improvement of the adsorption of DME on catalyst is very important for DDFC. As shown in Fig.4, the CV curve of $Pt/SnO_2/C$ has been suppressed during the H_2 adsorption and desorption potential range (from 0.03V to 0.28V). That is, the adsorption of DME on $Pt/SnO_2/C$ is easier than Pt/C in low potential range. The mechanism of DME electro-oxidation reported by Q. Zhang is as follows [22]:

$$CH_3–O–CH_3 + Pt \rightarrow Pt–C–O–CH_3 + H^+ + 2e^- \quad (2)$$

$$CH_3–O–CH_3 + Pt \rightarrow Pt–(CHOCH) – Pt + 4H^+ + 4e^- \quad (3)$$

$$Pt–C–O–CH_3 + H_2O \rightarrow Pt–COH + CH_3OH \quad (4)$$

$$Pt–(CHOCH)–Pt + H_2O \rightarrow 2Pt–CO + 4H^+ + 4e^- \quad (5)$$

$$Pt–COH \rightarrow Pt–CO + H^+ + e^- \quad (6)$$

$$CH_3OH + Pt \rightarrow Pt–CO + 4H^+ + 4e^- \quad (7)$$

$$Pt + H_2O \rightarrow Pt–OH_{ads} + H^+ + e^- \quad (8)$$

$$Pt–CO + Pt–OH_{ads} \rightarrow CO_2 + H^+ + e^- \quad (9)$$

$$Pt–COH + Pt–OH_{ads} \rightarrow CO_2 + H^+ + 2e^- \quad (10)$$

According to the above mechanism, the adsorption of DME on Pt is the first step of DME oxidation, which can significantly affect the reaction speed. $Pt/SnO_2/C$ is benefit to DME adsorption, which is a main cause for the increase in anodic catalyst activity. The IR spectra in Fig. 5 show the characteristic peak of SnO_2. The band in the range of 500-750 cm^{-1} is due to the Sn-O vibration. The band at about 1600 cm^{-1} is assigned to the bending vibration of O-H. The broad band at about 3430 cm^{-1} is stretching vibration of O-H. As shown in Fig. 5, there are sufficient OH_{ads} species existed on the surface of SnO_2. Many researchers have reported the intermediates generated during DME oxidation reaction. As shown in the Eq. (9) and (10), –CO and –COH are the poisoning intermediates adsorbed on Pt. Besides, other researchers consider that $-CH_2OCH_3$, -COOH and formaldehyde are the possible intermediates of DME oxidation reaction [21,23,24]. The OH_{ads} species on the surface of SnO_2 promote the oxidation of intermediates species which benefits to reduce the Pt poisoning effect and release Pt active sites. The dehydrogenation of DME on Pt surface needs three adjacent Pt active sites. The elimination of adsorbed intermediates species can increase the amount of adjacent Pt active sites, which is another cause for the increase in anodic catalyst activity.

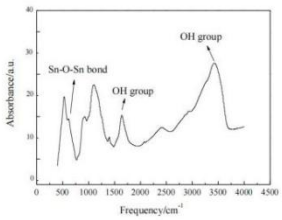

Figure 5. IR spectra of SnO_2 particles after dehydration treatment at 200 ºC under vacuum condition.

Fig. 6 shows the polarization curves and the power density curves of MEAs with different anodic catalyst at 70 ºC. The maximum power density of the MEAs with $Pt/SnO_2/C$ and Pt/C anodic catalyst is 49.6 mW cm^{-2} and 33.6 mW cm^{-2}, respectively. Obviously, DDFC with $Pt/SnO_2/C$ anodic catalyst obtains higher output performance. $Pt/SnO_2/C$ is a proper anodic catalyst for DME, which can enhance the output performance of DDFC. The performances of DDFCs with different anode catalysts have been reported in many published literatures. The comparison of these works is listed in table 1[18,25-27]. Comparing to these works in table 1, the performance of DDFC with $Pt/SnO_2/C$ anode catalyst is obvious higher at relatively low temperature (70 ºC) and under relatively low pressure (1 bar).

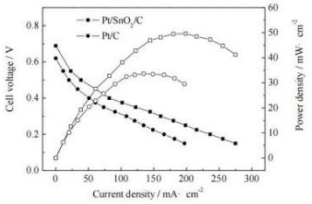

Figure 6. The polarization curves and the power density curves of the MEAs with various anode catalysts at 70 ºC.

Table 1. The performances of DDFCs with different anode catalysts reported in literatures and this work

	Catalyst	The maximum power density/ mW cm^{-2}	Temperature/ ºC	Pressure/bar	Reference
1	PtCu	13.5	80	1	7
2	Pt/C	60	80	3	8
3	Pt/MWNT	38.4	80	1	9
4	PtRu	38	80	1	10
5	$Pt/SnO_2/C$	49.6	70	1	Present work

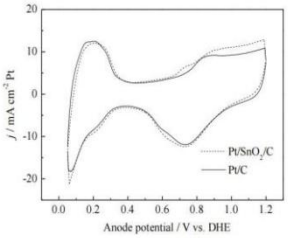

Figure 7. Cyclic voltammograms of anodes with various catalysts at a scan rate of 0.01V s^{-1}, in a potential range between 0.05 and 1.2V vs. DHE.

Fig.7 presents the anodic *EAS* of MEAs with different catalyst. The anodic *EAS* of MEA with $Pt/SnO_2/C$ catalyst is 81 m^2 g^{-1}Pt. The anodic *EAS* of the other MEA is 87 m^2 g^{-1}Pt. The *EAS* of different MEAs are nearly the same. The value of *EAS* represents the amount of Pt active sites in anode. That is, the MEAs with different catalyst have nearly the same amount of anodic Pt active sites. The enhancement of DDFC performance can be ascribed to the higher activity of anode catalyst.

4. CONCLUSIONS

$Pt/SnO_2/C$ catalyst with SnO_2/C as its supports has been prepared for DME electrooxidation in an acidic medium. TEM tests show that the average sizes of Pt particles are nearly the same (3.2 nm) for $Pt/SnO_2/C$ and Pt/C. The $Pt/SnO_2/C$ catalyst shows higher activity than Pt/C towards DME oxidation.

The adsorption of DME on $Pt/SnO_2/C$ is easier than Pt/C, which promotes the oxidation of DME. IR spectra results show that there are sufficient OH_{ads} species existed on the surface of SnO_2. These OH_{ads} species benefit to reduce the Pt poisoning effect and release Pt active sites. The maximum power density of DDFC with $Pt/SnO_2/C$ anodic catalyst is higher than DDFC with Pt/C anodic catalyst. DDFCs with different anodic catalyst have nearly the same anodic *EAS*. Therefore, the enhanced performance is attributed to the higher activity of $Pt/SnO_2/C$ for DME oxidation.

ACKNOWLEDGEMENT

This work was supported by University Nursing Program for Young Scholars with Creative Talents in Heilongjiang Province (UNPYSCT-2016108), the Young Scholars Programs of Mu Danjiang Normal University (GG2018001), the Teaching reform Projects of Mu Danjiang Normal University (19-XJ21008), the Scientific Research Fund of Heilongjiang Education Department (No. 1353ZD002), and the Scientific Research Projects of Mudanjiang Normal University (No.GP2019002).

References

1. L.Z. Yin, Q. Li, W.R. Chen, T.H. Wang, and H. Liu, *Int. J. Hydrogen Energy*, 11 (2019) 5499.
2. K.J. Reddy, and N. Sudhakar, *Int. J. Hydrogen Energy*, 44 (2019) 15355.
3. G.H. Gwak, D.H. Kim, S. Lee, and H. Ju, *Int. J. Hydrogen Energy*, 43 (2018) 13999.
4. C. Ouyang, X.L. Zhang, M.F. Wu, D.M. Xun, and P.P. Gao, *Int. J. Electrochem. Sci.*, 15 (2020) 80.
5. Y. Zhao, L.W. Chen, and Y.D. Meng, *Int. J. Electrochem. Sci.*, 14 (2019) 6826.
6. L.H. Xing, G.P. Yin, Z.B. Wang, S. Zhang, Y.Z. Gao, and C.Y. Du, *J. Power Sources*, 198 (2012) 170.
7. J.H. Yu, H.G. Choi, and S.M. Cho, *Electrochem. Commun.*, 7 (2005) 1385.
8. L. H. Xing, Y.Z. Gao, Z.B. Wang, C.Y. Du, and G.P. Yin, *Int. J. Hydrogen Energy*, 36 (2011) 11102.
9. U. Mondal, and G.D. Yadav, *J. CO_2 Util.*, 42 (2019) 16695.
10. W.J. Yuan, Y.F. Zhang, N.Y. Zhang, C.W. Yin, X.L. Zhang, and X.W. Liu, *Catal. Commun.*, 100 (2017) 66.
11. H. Zhang, C. Hu, X. He, L. Hong, G. Du, and Y. Zhang, *J. Power Sources*, 196 (2011) 4499.
12. W.Z. Hung, W.H. Chung, D.S. Tsai, D.P. Wilkinson, and Y.S. Huang, *Electrochim. Acta*, 55 (2010) 2116.
13. M.L. Dou, M. Hou, D. Liang, W.T. Lu, Z.G. Shao, and B.L. Yi, *Electrochim. Acta*, 92 (2013) 468.
14. Y. Fan, J.H. Liu, H.T. Lu, P. Huang, and D.L. Xiu, *Electrochim. Acta*, 76 (2012) 475.
15. N. Zhang, S. Zhang, C.Y. Du, Z.B. Wang, Y.Y. Shao, and K.F. Dong, *Electrochim. Acta*, 117 (2014) 413.
16. L.H. Xing, Z.B. Wang, C.Y. Du, and G.P. Yin, *Int. J. Energy Res.*, 36 (2012) 886.
17. L.H. Xing, G.P. Yin, C.Y. Du, S.X. Cui, M.H Zuo, and H.P. Wang, *Int. J. Hydrogen Energy*, 42 (2017) 16695.
18. K.D. Cai, G.P. Yin, J.J. Wang, and L.L. Lu, *Energy Fuels*, 23(2009) 903.
19. G. Kerangueven, C. Coutanceau , E. Sibert, J.M. Leger, and C. Lamy, *J. Power Sources*, 157 (2006) 318.
20. Y. Liu, M. Muraoka, S. Mitsushima, K.I. Ota, and N. Kamiya, *Electrochim. Acta*, 52 (2007) 5781.
21. M.H. Shao, J. Warren, N.S. Marinkovic, P.W. Faguy, and R.R. Adzic, *Electrochem. Commun.*, 7 (2005) 459.
22. Q. Zhang, Z.F. Li, S.W. Wang, W. Xing, R.J. Yu, and X.J Yu, *Electrochim. Acta*, 53 (2008) 8298.
23. G. Kerangueven, C. Coutanceau, E. Sibert, F. Hahn, J.M. Leger, and C. Lamy, *J. Appl.*

4.Xing L H, Yin G P, Du C Y, et al. Investigation on the durability of direct dimethyl ether fuel cell. Part II: Cathode degradation[J]. International Journal of Hydrogen Energy, 2017, 42(26): 16695-16699.

INTERNATIONAL JOURNAL OF HYDROGEN ENERGY 42 (2017) 16695–16699

Available online at www.sciencedirect.com

ScienceDirect

journal homepage: www.elsevier.com/locate/he

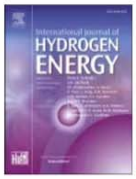

Investigation on the durability of direct dimethyl ether fuel cell. Part II: Cathode degradation

Le-Hong Xing [a,b,*], *Ge-Ping Yin* [a], *Chun-Yu Du* [a], *Shu-Xin Cui* [b], *Ming-Hui Zuo* [b], *Hai-Peng Wang* [b]

[a] *State Key Laboratory of Urban Water Resource and Environment, School of Chemical Engineering and Technology, Harbin Institute of Technology, No. 92, West Da-Zhi Street, Harbin 150001, China*

[b] *College of Chemistry and Chemical Engineering, Mudanjiang Normal University, Mudanjiang 157012, China*

ARTICLE INFO

Article history:
Received 12 December 2016
Received in revised form
23 April 2017
Accepted 14 May 2017
Available online 17 June 2017

Keywords:
Direct dimethyl ether fuel cell
Durability test
Cathodic catalyst degradation
Electrochemical active surface
Dimethyl ether crossover

ABSTRACT

Cathodic Pt/C catalyst degradation for a direct dimethyl ether fuel cell (DDFC) has been investigated after a 70.5 h galvostatic operation at 60 °C under ambient pressure. The cathode electrochemical active surface (EAS) reduces from 349 to 267 cm^2 mg^{-1} Pt after durability test. Cathode EAS loss is associated with the growth of Pt catalyst particles. XRD and TEM results show that the particle size of cathodic Pt catalyst increases from an original value of 3.0 nm to 5.4 nm. Furthermore, the anode failure accelerates dimethyl ether (DME) crossover, and consequently, poisoning of catalyst by absorbed DME and/or intermediates aggravates the degradation of cathodic Pt/C catalyst. The effect of anode degradation on the long-term performance of DDFC has been reported in companion article (Part I).

© 2017 Hydrogen Energy Publications LLC. Published by Elsevier Ltd. All rights reserved.

Introduction

Recently, proton exchange membrane fuel cells (PEMFCs) [1–3], and direct methanol fuel cells (DMFCs) [4–6] have been investigated extensively for stationary and portable applications [7,8]. However, each of them has some shortcomings which limit their commercialization [9,10]. Dimethyl ether (DME) is known as a promising alternative fuel [11–13]. The transportation of DME is easier and safer than hydrogen because its physical properties are similar with liquefied petroleum gas (LPG) [14,15]. DME also has many advantages in comparison with methanol for its high energy density, low toxicity, and low fuel crossover [16–18]. Therefore, DME is a new proper fuel for fuel cells and has been receiving increasing attention recently [19–22].

Up to now, most of the research has been focused on the activity of anodic catalyst and the short-term performance of direct dimethyl ether fuel cell (DDFC) [23,24]. The long-term performance and durability of the membrane electrode assembly (MEA) for DDFC have not been investigated in detail. DDFC commercialization demands stable operation for at least thousands of hours, which is difficult to achieve [25]. The electrocatalyst is one of the major components of MEAs, and their stability plays an important role in the long-term operation of fuel cells [26,27]. Pt/C catalyst failure results from the corrosion of carbon support [28], the Ostwald ripening (dissolution and redeposition) of Pt particles [29], the coalescence

* *Corresponding author*. State Key Laboratory of Urban Water Resource and Environment, School of Chemical Engineering and Technology, Harbin Institute of Technology, No. 92, West Da-Zhi Street, Harbin 150001, China.
E-mail address: xinglehonghit@126.com (L.-H. Xing).

http://dx.doi.org/10.1016/j.ijhydene.2017.05.134
0360-3199/© 2017 Hydrogen Energy Publications LLC. Published by Elsevier Ltd. All rights reserved.

due to the high surface energy of small Pt nanoparticles [30] and poisoning of catalysts by accumulated intermediates from DME electro-oxidation or impurities [31]. The cathodic catalyst in DDFC operates in a serious corrosive environment, such as high water content, low pH value, high temperature, high oxygen concentration and high potentials (0.6–1.2 V) [32]. The stability of catalyst is an important factor which can strongly impact the long-term performance of DDFC. In previous paper (part I) [33], we have reported the durability of anode catalyst for 70.5 h operation. The 70.5 h operation is composed of a 40.5 h operation beginning, and then cyclic voltammetry (CV) scans of the anode and cathode respectively, and another 30 h operation. In this paper (part II), we focus on exploring the durability of cathodic Pt/C catalyst for DDFC at the same condition. Electrochemical and physical characterizations are performed before and after the durability test, and their results are compared. Furthermore, the effect of DME crossover behavior on the cathodic catalyst deterioration is analyzed. The purpose of this study is to provide a better insight into the stability and changes of Pt/C catalysts under DDFC operating conditions and to investigate whether and how the anode degradation affects the performance of cathodic Pt/C catalyst by in situ CV and other techniques.

Experimental

MEA fabrication

The home-made MEA was fabricated by the gas diffusion layer-based method [33]. The working area of the MEA was 5 cm^2. The anode and cathode catalyst were both 40 wt.% Pt/C. The Pt loading of anode and cathode was 3.2 mg cm^{-2} and 2.5 mg cm^{-2}, respectively. The Nafion content was 20 wt.% in catalyst layers. The anode diffusion layers were wet-proofed Toray carbon papers (18 wt.% PTFE) coated with 1 mg cm^{-2} Vulcan XC-72 carbon blacks and 18 wt.% PTFE. The cathode diffusion layers were wet-proofed Toray carbon papers (30 wt.% PTFE) coated with 1 mg cm^{-2} Vulcan XC-72 carbon blacks and 30 wt.% PTFE. Nafion 115 polymer membranes (DuPont) were used to fabricate MEAs. The pretreated Nafion membranes sandwiched between anode and cathode and then the assemblies were hot pressed under a specific load of 100 kg cm^{-2} for 1.5 min at 135 °C.

Electrochemical measurements

Single fuel cell tests

The electrochemical tests of MEA were carried out by Fuel Cell Testing System (Arbin Instrument Corp.) using the single cell (Electrochemistry Corp.). All of the electrochemical measurements were carried out at 60 °C. The 1.5 mol L^{-1} DME solution was fed to the anode side with a flow rate of 3 mL min^{-1}. Pure oxygen was supplied to the cathode side with a flow rate of 200 mL min^{-1} under ambient pressure.

Cyclic voltammetry

Cyclic voltammetry (CV) scan was measured by a CHI 604B Electrochemical Analyzer (Shanghai Chen-Hua Instruments Corp. China) to evaluate the degradation of cathodic EAS. During the test, the cathode was protected by humidified N_2 at a flow rate of 200 mL min^{-1}. Simultaneously, the anode was fed with humidified H_2 at a flow rate of 200 mL min^{-1} as a dynamic hydrogen electrode (DHE). The CV sweep was performed at a scan rate of 0.01 V s^{-1} between 0.05 and 1.2 V (vs. the anode). The cathodic EAS at different conditions could be determined through Eq. (1), where [Pt] denoted Pt loading (mg cm^{-2}) on the electrode, Q_H represented the charge (mC cm^{-2}) for hydrogen desorption, and 0.21 was the required charge (mC cm^{-2}) to oxidize a monolayer of H_2 on bright Pt [34]. The similar CV tests were also employed to detect and eliminate the crossover DME and/or intermediates on cathodic Pt surface after the 40.5 h operation of the DDFC.

$$ESA_{Pt} = \frac{Q_H}{[Pt] \times 0.21} \quad (1)$$

DME crossover rate

The DME crossover rate was estimated by the limiting current density at the cathode. During the test, a 1.5 mol L^{-1} DME solution was fed to the anode at 3 mL min^{-1}. The linear sweep voltammetry (LSV) was performed at the cathode at a scan rate of 1 mV s^{-1} with a protection of pure N_2 at 200 mL min^{-1}. The anode was regarded as a DHE, because only the reduction of H^+ to H_2 took place at the anode. After the electrochemical tests, the used MEA was peeled carefully and cut into small pieces for further physical analysis [35,36].

Physical measurements

X-ray diffraction (XRD)

XRD analysis was conducted on the catalysts scraped from the fresh and aged cathode to characterize the changes of the Pt particles. The XRD patterns were recorded by a Japan D/max-rB X-ray diffractometer, using a Cu Kα radiation source at a tube current of 100 mA and a tube voltage of 40 kV, with a scan rate of 5° min^{-1}.

Transmission electron microscopy (TEM)

TEM for the catalyst samples was taken by a Hitachi H-7650 transmission electron microscope. Before taking the electron micrographs, the samples were finely ground and ultrasonically dispersed in isopropyl alcohol, and a drop of the resultant dispersion was deposited and dried on a standard copper grid coated with a polymer film.

Results and discussion

After the durability test, the maximum power density of DDFC drops dramatically from an initial value of 37 mW cm^{-2} to 12 mW cm^{-2} [33]. Cyclic voltammograms in Fig. 1 present the decay of cathodic EAS. The hydrogen desorption region on Pt catalyst decreases after the life test. The calculated EAS decreases from 349 to 267 cm^2 mg^{-1} Pt after 70.5 h operation. The EAS loss may result from the deterioration of Pt metal and the worse contact between the catalyst and the electrolyte. The CV results indicate that the cathode 'triple-phase boundaries' where the electrolyte, oxygen, and electrically connected Pt/C catalyst contact together in cathode, are decreasing after the life tests. The aging of cathodic catalyst would be one of the important reasons for the performance decay of DDFC cathode.

XRD patterns of cathodic Pt/C catalyst measured before and after the life test are shown in Fig. 2. The first diffraction peaks for cathode Pt/C at 2θ about 26° can be attributed to the hexagonal graphite structures (0 0 2) of the XC-72 carbon black support. The Pt has a face-centered cubic (fcc) structure showing the major diffraction peaks of Pt (1 1 1), Pt (2 0 0), Pt (2 2 0), Pt (3 1 1), Pt (2 2 2), and so on. The Pt (2 2 0) peak is chosen to calculate the mean particle size of fresh and aged Pt

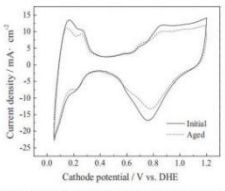

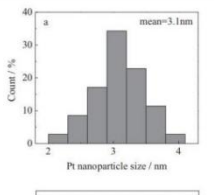

Fig. 1 – Cyclic voltammograms of Pt at the initial and aged cathode, at a scan rate of 0.01 V s^{-1}, in a potential range between 0.05 and 1.2 V vs. DHE.

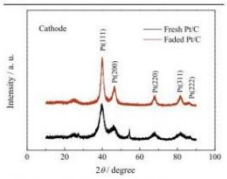

Fig. 2 – XRD patterns of cathodic catalysts before and after durability test.

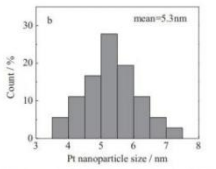

Fig. 4 – Histograms of particle size distributions of cathodic Pt catalyst before and after durability test: (a) initial Pt; (b) aged Pt.

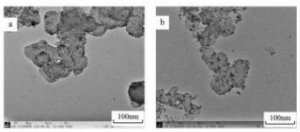

Fig. 3 – TEM images of cathodic Pt/C catalyst before and after durability test: (a) initial Pt/C, (b) aged Pt/C.

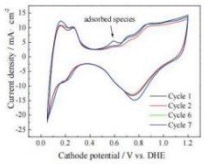

Fig. 5 – Cyclic voltammograms of cathode after 40.5 h operation, at a scan rate of 0.01 V s^{-1}, in a potential range between 0.05 and 1.2 V vs. DHE.

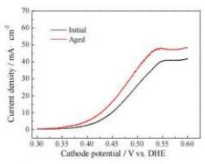

Fig. 6 – Linear sweep voltammograms of DME permeating through the membranes at the cathode before and after durability test.

catalysts according to Debye–Scherrer formula because it is isolated from the diffraction peaks of carbon support [37]. The particle size of cathodic catalyst grows from an original value of 3.0 nm to 5.4 nm. The sintering rate of cathodic catalyst is evidently high because small Pt particles are unstable in harsh corrosion operation environment of cathode. Besides, DME crossover may aggravate cathodic Pt degradation.

TEM images of the cathodic Pt/C catalyst before and after durability test are presented in Fig. 3 and the corresponding histograms are shown in Fig. 4. The dark black portions in Fig. 3 are Pt grains, and the gray portions are carbon support grains. The results show that Pt nanoparticles before durability test is small and even without agglomeration. After the durability test, Pt grains grow up evidently, which is consistent with the above XRD results. The growth of the Pt particles must be the main cause of the cathodic catalyst failure.

Fig. 5 shows the CV scans of cathode after 40.5 h operation. The adsorbed DME and/or intermediates species which accumulate on cathodic Pt surface would be oxidized after the CV scans. With an increasing cycling number, the oxidation peak of the adsorbed species gradually decreased. Simultaneously, the hydrogen desorption peak recovers. The CV profiles reach a steady state at the 6th cycle, and no further changes are observed from cycle 6 to cycle 7. It is indicated that the absorbed DME and/or intermediates have been fully oxidized. The poisoning of catalyst by adsorbed DME and/or intermediates species can debase the O_2 reduction reaction on Pt catalyst surface, which is another cause of the cathode catalyst failure.

The LSV curves for determining the DME crossover rate of fresh and faded cathode are shown in Fig. 6. At high cathode potential region, the DME electro-oxidation reaction is not dominated by the catalytic activity of the cathode, but governed by the DME permeation rate. The limiting current density of DME oxidation increases from about 41 mA cm^{-2} to 48 mA cm^{-2} after the durability test. The DME permeation rate gets higher after the durability test. It means that DME concentration at the interface between the anode and the membrane gets higher after the durability test, which caused by anode degradation. DME crossover is concomitant with performance loss of cathodic Pt due to the formation of mixed potential on cathodic catalyst. This mixed potential response [38] is also very deleterious and accelerates the sintering/degradation of cathodic Pt nanoparticles. Therefore, anode degradation is another factor which accelerates cathodic catalyst degradation.

Conclusions

The durability of cathodic Pt/C catalyst for DDFC has been investigated at a constant current density of 30 mA cm^{-2} for 70.5 h discontinuous operation under ambient pressure and at a cell temperature of 60 °C. The performance of cathodic Pt/C catalyst is decreased after the durability test. The cathodic EAS reduces from 349 to 267 cm^2 mg^{-1} Pt after 70.5 h operation. The particle size of cathodic Pt catalyst increased from an original value of 3.0 nm to 5.4 nm. The poisoning of catalyst by absorbed DME and/or intermediates is another cause of cathodic catalyst degradation. Furthermore, the anode decay accelerated the DME crossover and the severer poisoning of catalyst aggravated the degradation of the Pt/C cathodic catalyst in consequence.

Acknowledgment

This work is financially supported by Young Creative Talent Training Project of Heilongjiang Province (UNPYSCT-2016108), Preliminary Investigation Project of Mudanjiang Normal University (GY201201), Doctoral Research Fund of Mudanjiang Normal University (MSB201208), Innovation Project of University Students (201610233031) and Natural Science Foundation of Heilongjiang Province (QC2014C009).

REFERENCES

[1] Fletcher T, Thring R, Watkinson M. Int J Hydrogen Energy 2016;41:21503.
[2] Ye LC, Gao Y, Zhu SY, Zheng JS, Li P, Zheng JP. Int J Hydrogen Energy 2017;42:7241.
[3] Authayanun S, Saebea D, Patcharavorachot Y, Assabumrungrat S, Arpornwichanop A. Int J Hydrogen Energy 2017;42:1977.
[4] Wang ZB, Zuo PJ, Yin GP. Fuel Cells 2009;9:106.
[5] Lai QZ, Yin GP, Wang ZB, Du CY, Zuo PJ, Cheng XQ. Fuel Cells 2008;8:399.
[6] Zhao TS, Xu C, Chen R, Yang WW. Prog Energy Combust Sci 2009;35:275.
[7] Shen SY, Zhao TS, Xu JB. Energy Environ Sci 2011;4:1428.
[8] Xie F, Chen C, Meng H, Shen PK. Fuel Cells 2007;7:319.
[9] Shao YY, Liu J, Wang Y, Lin YH. J Mater Chem 2009;19:46.
[10] Liu F, Yin GP, Du CY. Electrochem Commun 2008;10:1471.
[11] Heo P, Nagao M, Sano M, Hibino T. J Electrochem Soc 2008;155:B92.
[12] Li Q, Wu G, Johnston CM, Zelenay P. Electrocatalysis 2014;5:330.
[13] Li Q, Wen XD, Wu G, Chung HT, Gao R, Zelenay P. Angew Chem Int Ed 2015;127:7634.
[14] Cai KD, Wang C, Pu WH, Gao Y, Mao ZQ. Int J Hydrogen Energy 2012;37:12605.
[15] Senselsberger TA, Borup RL, Greene HL. J Power Sources 2006;156:497.
[16] Kerangueven G, Coutanceau C, Sibert E, Leger JM, Lamy C. J Power Sources 2006;157:318.
[17] Tong YJ, Lu LL, Zhang Y, Gao YZ, Yin GP, Osawa M, et al. J Phys Chem C 2007;111:18836.
[18] Liu Y, Murooka M, Mitsushima S, Ota KI, Kamiya I. Electrochim Acta 2007;52:5781.
[19] Lu LL, Yin GP, Tong YJ, Zhang Y, Gao YZ, Osawa M, et al. J Electroanal Chem 2008;619:143.
[20] Lu LL, Yin GP, Tong YJ, Zhang Y, Gao YZ, Osawa M, et al. J Electroanal Chem 2010;642:82.
[21] Tadao H, Yasuyuki T, Hiroyuki T, Naoaki T, Susumu Y. Electr Eng Jpn 2009;150:19.
[22] Zhang Y, Lu LL, Tong YJ, Osawa M, Ye S. Electrochim Acta 2008;53:6093.
[23] Lu LL, Yin GP, Wang ZB, Cai KD, Gao YZ. Catal Commun 2009;10:971.
[24] Yu JH, Choi HG, Cho SM. Electrochem Commun 2005;7:1385.
[25] Yoo JH, Choi HG, Chung CH, Cho SM. J Power Sources 2006;163:103.
[26] Jiang LH, Sun GQ, Wang SL, Wang GX, Xin Q, Zhou ZH, et al. Electrochem Commun 2005;7:603.
[27] Schmittinger WG, Vahidi A. J Power Sources 2008;180:1.
[28] Du CY, Chen M, Cao XY, Yin GP, Shi PF. Electrochem Commun 2009;11:496.
[29] Zhang SS, Yuan XZ, Wang HJ, Merida W, Zhu H, Shen J, et al. Int J Hydrogen Energy 2009;34:388.
[30] Zhang S, Shao YY, Yin GP, Lin YH. Angew Chem 2010;49:2211.
[31] Baturina OA, Swider-Lyons KE. J Electrochem Soc 2009;156:B1425.
[32] Wang ZB, Zuo PJ, Chu YY, Shao YY, Yin GP. Int J Hydrogen Energy 2009;34:4387.
[33] Xing LH, Yin GP, Wang ZB, Zhang S, Gao YZ, Du CY. J Power Sources 2012;198:170.
[34] Wu YN, Liao SJ, Su HN, Dang D, Liu B. Fuel Cells 2010;10:930.
[35] Ren XM, Springer TE, Zawodzinski TA, Gottesfeld S. J Electrochem Soc 2000;147:466.
[36] Xing LH, Gao YZ, Wang ZB, Du CY, Yin GP. Int J Hydrogen Energy 2011;36:11102.
[37] H Zhang Z, Ge JJ, Ma L, Liao JH, Lu TH, Xing W. Fuel Cells 2009;09:114.
[38] Hibino T, Kobayashi K. J Electrochem Soc 2014;5:H326.

5.王宜鑫,邢乐红,石鑫婷,孟凡旭,张亮,董瑞.镀液中氨基磺酸镍质量浓度对电镀镍层析氢催化活性的影响[J].电镀与涂饰,2022,41(01):6-9.

第41卷 第1期 电镀与涂饰 ELECTROPLATING & FINISHING Vol.41 No.1

DOI: 10.19289/j.1004-227x.2022.01.002

镀液中氨基磺酸镍质量浓度对电镀镍层析氢催化活性的影响

王宜鑫，邢乐红*，石鑫婷，孟凡旭，张亮，董瑞

（牡丹江师范学院化学化工学院，黑龙江 牡丹江 157012）

摘要： 采用由10 g/L $NiCl_2·6H_2O$、30 g/L NH_4Cl和310～390 g/L $Ni(NH_2SO_3)_2·4H_2O$（氨基磺酸镍）组成的镀液（pH=3.8），在温度35 ℃和电流密度3 A/dm² 的条件下电镀30 min，获得镍电极。研究了镀液中氨基磺酸镍质量浓度对镍镀层表面形貌和析氢催化活性的影响。结果表明，镀液中氨基磺酸镍质量浓度为350 g/L时，镍镀层结晶最细致，析氢催化活性和稳定性最佳。

关键词： 电镀镍；氨基磺酸镍；析氢反应；催化活性；稳定性

中图分类号： TQ153.12 **文献标志码：** A **文章编号：** 1004－227X(2022)01－0006－04

Effect of mass concentration of nickel sulfamate in bath on catalytic activity of nickel coating for hydrogen evolution

WANG Yixin, XING Lehong *, SHI Xinting, MENG Fanxu, ZHANG Liang, DONG Rui

(School of Chemistry and Chemical Engineering, Mudanjiang Normal University, Mudanjiang 157012, China)

Abstract: A nickel electrode was obtained by electroplating nickel on pure copper in a bath (pH = 3.8) comprising $NiCl_2·6H_2O$ 10 g/L, NH_4Cl 30 g/L, and $Ni(NH_2SO_3)_2·4H_2O$ (nickel sulfamate) 310-390 g/L at temperature 35 ℃ and current density 3 A/dm² for 30 minutes. The effect of mass concentration of nickel sulfamate on surface morphology of the nickel coating and its catalytic activity for hydrogen evolution reaction was studied. The results showed that the nickel coating electroplated with nickel sulfamate 350 g/L was the finest and most compact with the best catalytic activity and stability in hydrogen evolution reaction.

Keywords: nickel electroplating; nickel sulfamate; hydrogen evolution reaction; catalytic activity; stability

氢能是一种高效的可再生清洁能源。氢气的制备方法主要有化石燃料法、电催化法、光催化法、微生物法等。其中电催化制氢具有纯度高、零污染、生产能力易调等优点，受到广泛关注[1-3]。电催化剂在电解制氢过程中起着至关重要的作用，电催化剂大多选用性能优异的铂族贵金属及其合金[4]。然而，铂族金属价格昂贵、丰度低，使其应用受限。金属镍有着较低的析氢过电位，析氢催化性能好，常被用作析氢催化剂[5-7]。电催化剂的制备方法主要有化学法、物理法、气相沉积法、电沉积法等[8-10]。电沉积法操作简单、快速，反应条件适中，成本低，因此被广泛应用。电镀镍时镀液中氨基磺酸镍浓度对镍镀层的性能有很大影响[11]。本文通过微观形貌分析以及极化曲线、塔菲尔曲线和计时电位曲线测量来研究氨基磺酸镍质量浓度对镀层析氢性能的影响。

1 实验

1.1 氨基磺酸盐体系电镀镍

1.1.1 前处理

选用5 cm×4 cm的紫铜片作为基体，其前处理流程为：打磨→乙醇冲洗→20% NaOH溶液碱洗→10%（质量分数）盐酸洗→去离子水洗。

镍阳极使用前依次进行打磨、3 mol/L HCl溶液活化以及去离子水冲洗。

1.1.2 镀液配方和工艺条件

$NiCl_2·6H_2O$ 10 g/L，NH_4Cl 30 g/L，$Ni(NH_2SO_3)_2·4H_2O$（氨基磺酸镍）310～390 g/L，pH 3.8，温度35 ℃，电流密度3 A/dm²，时间30 min。

收稿日期： 2021-05-17 **修回日期：** 2021-08-24

基金项目： 牡丹江师范学院国家培育项目（GP2021002）；黑龙江省牡丹江市科学技术局项目（SQ2020G115）；牡丹江师范学院课程专项项目（KCSZ-2020021）；黑龙江省大学生创新创业项目（202110230043）；牡丹江师范学院硕士研究生科技创新项目（lgcx2020-80mdjsu）。

第一作者： 王宜鑫（1997-），男，黑龙江宁安人，在读硕士研究生，主要研究方向为金属表面处理和表面改性。

通信作者： 邢乐红（1983-），女，山东武城人，博士，副教授，主要从事金属表面处理、化学电源等方面的研究。

引用格式： 王宜鑫，邢乐红，石鑫婷，等. 镀液中氨基磺酸镍质量浓度对电镀镍层析氢催化活性的影响[J]. 电镀与涂饰，2022，41(1)：6-9.

WANG Y X, XING L H, SHI X T, et al. Effect of mass concentration of nickel sulfamate in bath on catalytic activity of electroplated nickel coating for hydrogen evolution[J]. Electroplating & Finishing, 2022, 41(1): 6-9.

(C)1994-2022 China Academic Journal Electronic Publishing House. All rights reserved. http://www.cnki.net

1.2　性能检测与表征方法

采用 FEI QUANTA FEG 400 热场发射扫描电子显微镜 (SEM) 观察镀层的表面形貌。

采用 PARSTAT 4000 电化学工作站测量镀镍层在 1 mol/L NaOH 溶液中的析氢极化曲线、塔菲尔 (Tafel) 曲线和计时电位曲线。镀层的有效面积为 0.785 cm^2，辅助电极为 1 cm × 1 cm × 0.1 mm 的铂片电极，参比电极为饱和甘汞电极 (SCE)。极化曲线测量的扫描速率为 5 mV/s。计时电位曲线测量的电流密度为 100 mA/cm^2，时间 5 h。

2　结果与讨论

2.1　氨基磺酸镍质量浓度对镀层微观形貌的影响

由图 1 可知，当氨基磺酸镍质量浓度为 350 g/L 时，镍镀层的晶粒最细致。

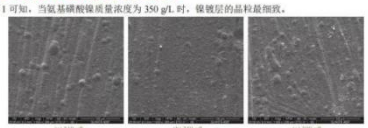

(a) 310 g/L　(b) 350 g/L　(c) 390 g/L

图 1　氨基磺酸镍质量浓度不同时所得镍镀层的微观形貌

Figure 1　Micromorphologies of nickel coatings electroplated with different mass concentrations of nickel sulfamate

2.2　氨基磺酸镍质量浓度对镀层析氢性能的影响

2.2.1　析氢极化曲线分析

由图 2 可知，随氨基磺酸镍质量浓度增大，镍镀层的析氢极化曲线先正移后负移，说明镍镀层的析氢电位先减小后增大，即电催化析氢性能先改善后变差。氨基磺酸镍质量浓度为 350 g/L 时，镍镀层在相同电位下的析氢电流密度最大，电催化析氢性能最好。可能是因为氨基磺酸镍质量浓度为 350 g/L 时镍层结晶最细致，比表面积大，析氢活性位点多，有利于氢在电极表面的吸附和脱附。

2.2.2　塔菲尔曲线分析

图 3 示出了在不同氨基磺酸镍质量浓度下所得镀层在 1 mol/L NaOH 溶液中的 Tafel 曲线。Tafel 曲线斜率 (b) 能够反映电极的催化活性，b 越小说明析氢反应越快。b 也是判断电极析氢反应机制的重要依据，析氢反应机制包括 Volmer、Tafel 和 Heyrovsky 步骤[12]，见式 (1) – (3)。其中，M 为电极材料，H_{ads} 为氢吸附原子。

$$\text{Volmer 步骤}\quad M + H_2O + e^- \rightarrow M\text{-}Had_S + OH^- \tag{1}$$

$$\text{Tafel 步骤}\quad 2M\text{-}H_{ads} \rightarrow 2M + H_2 \tag{2}$$

$$\text{Heyrovsky 步骤}\quad M\text{-}H_{ads} + H_2O + e^- \rightarrow M + H_2 + OH^- \tag{3}$$

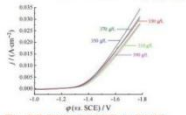

图 2　氨基磺酸镍质量浓度不同时所得镍镀层在 1 mol/L NaOH 溶液中的析氢极化曲线

Figure 2　Polarization curves of hydrogen evolution reaction in 1 mol/L NaOH solution for nickel coatings electroplated with different mass concentrations of nickel sulfamate

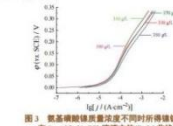

图 3　氨基磺酸镍质量浓度不同时所得镍镀层在 1 mol/L NaOH 溶液中的 Tafel 曲线

Figure 3　Tafel plots in 1 mol/L NaOH solution for nickel coatings electroplated with different mass concentrations of nickel sulfamate

(C)1994-2022 China Academic Journal Electronic Publishing House. All rights reserved.　http://www.cnki.net

$M\text{-}H_{ads}$ 为反应的中间产物。当析氢反应动力学过程的反应速率控制步骤为 Volmer 反应、Heyrovsky 反应或 Tafel 反应时，各自的 b 分别约为 120、40 和 30 mV/dec [13]。

采用式 (4) 对图 3 进行拟合得到相应的析氢反应电催化参数，列于表 1。

$$\eta = b\lg\frac{j}{j_0} \tag{4}$$

式中，η 为电极的析氢过电位，j 为电流密度，j_0 为交换电流密度。

表 1　Tafel 曲线拟合得到的析氢反应电催化参数

Table 1　Electrocatalytic parameters of hydrogen evolution reaction fitted from Tafel plots

ρ(氨基磺酸镍) / (g·L^{-1})	b / (mV·dec^{-1})	j_0 / (μA·cm^{-2})	η_{10} / mV	η_{100} / mV
310	128	0.586	541.71	669.71
330	124	0.608	522.79	646.79
350	120	0.673	500.64	620.64
370	122	0.618	513.49	635.49
390	123	0.594	519.82	642.82

注：η_{10} 和 η_{100} 分别为电极在 10 mA/cm^2 和 100 mA/cm^2 时的析氢过电位。

从表 1 可知，镍镀层的 b 均在 120 mV/dec 左右，说明电极表面的析氢反应动力学过程受 Volmer 反应步骤控制。交换电流密度是衡量电极析氢催化活性的重要参数，交换电流密度越高，电流对镀层电位的影响越小，说明镀层析氢性能越好。氨基磺酸镍质量浓度为 350 g/L 时，镍镀层的交换电流密度最高，析氢催化活性最好，与析氢极化曲线分析结果一致。

2.2.3　计时电位曲线分析

由图 4 和表 2 可知，氨基磺酸镍质量浓度为 350 g/L 时，所得的镍镀层在 100 mA/cm^2 下连续电解 5 h 的计时电位曲线基本保持稳定，电位衰减较小，稳定性较好。

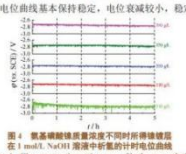

图 4　氨基磺酸镍质量浓度不同时所得镍镀层在 1 mol/L NaOH 溶液中析氢的计时电位曲线

Figure 4　Chronopotentiometric curves of hydrogen evolution reaction in 1 mol/L NaOH solution for nickel coatings electroplated with different mass concentrations of nickel sulfamate

表 2　计时电位曲线拟合得到的析氢反应电催化参数

Table 2　Electrocatalytic parameters of hydrogen evolution reaction fitted from chronopotentiometric curves

ρ(氨基磺酸镍) / (g·L^{-1})	φ_0 (vs. SCE) / V	φ_5 (vs. SCE) / V	$\Delta\varphi$ / V
310	−2.692	−2.789	0.097
330	−2.741	−2.768	0.027
350	−2.760	−2.784	0.024
370	−2.740	−2.768	0.028
390	−2.717	−2.755	0.038

注：φ_0 和 φ_5 分别为电极电解 5 h 前、后电极的析氢电位，$\Delta\varphi = \varphi_0 - \varphi_5$。

图 5 是氨基磺酸镍质量浓度为 350 g/L 时所得镍镀层电解 5 h 前后的极化曲线。可见两条极化曲线十分接近。在 0.01 A/cm^2 的阴极电流密度下，析氢 5 h 后镀层的析氢过电位仅增大约 11 mV，说明镍镀层在 1 mol/L NaOH 溶液中具有较理想的析氢稳定性。

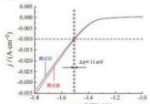

图 5　镍镀层在 1 mol/L NaOH 溶液中电解 5 h 前后的析氢极化曲线

Figure 5　Polarization curves of hydrogen evolution reaction on nickel coating before and after electrolysis in 1 mol/L NaOH solution for 5 hours

(C)1994-2022 China Academic Journal Electronic Publishing House. All rights reserved.　http://www.cnki.net

3　结论

氨基磺酸镍质量浓度为 350 g/L 时制备出的镍镀层结晶最细致，在 1 mol/L NaOH 溶液中表现出最好的电催化析氢性能和较好的稳定性。

参考文献：

[1] 陈云锟, 何湘柱, 曾树勋, 等. 复合电沉积制备镍–石墨烯电极及其电催化析氢性能研究[J]. 电镀与涂饰, 2020, 39 (1): 7-11.
CHEN Y Y, HE X Z, ZENG S X, et al . Preparation of nickel–reduced graphene oxide electrode by composite electrodeposition and study on its electrocatalytic activity for hydrogen evolution [J]. Electroplating & Finishing, 2020, 39 (1): 7-11.

[2] 闫巍, 余智勇, 李新杰, 等. 钛/石墨烯/镍–铁合金析氢电极的制备及其析氢性能[J]. 电镀与涂饰, 2017, 36 (7): 337-341.
YAN W, YU Z Y, LI X J, et al. Preparation and hydrogen evolution performance of titanium/reduced graphene oxide/nickel–iron alloy electrode [J]. Electroplating & Finishing, 2017, 36 (7): 337-341.

[3] 闫巍, 余智勇, 周亚欢, 等. 钛基镍–铁合金电极的制备及其析氢性能[J]. 电镀与涂饰, 2016, 35 (21): 1097-1102.
YAN W, YU Z Y, ZHOU Y H, et al. Preparation of nickel–iron alloy electrode on titanium substrate and its hydrogen evolution performance [J]. Electroplating & Finishing, 2016, 35 (21): 1097-1102.

[4] JIANG P J, LV Y, CHEN C M, et al. A facile route to synthesize Pt-WO_3 nanosheets with enhanced electrochemical performance for HER [J]. Journal of Electrochemistry, 2019, 25 (5): 562-570.
蒋鹏杰, 吕巍, 陈昌鑫, 等. Pt–WO_3 纳米片的合成及其电催化析氢性能研究[J]. 电化学, 2019, 25 (5): 562-570.

[5] 柴多, 贾予腾, 赵明, 等. 铜基梯度镍电沉积层的制备及析氢性能研究[J]. 电镀与涂饰, 2019, 38 (13): 641-646.
CHAI D, JIA Y T, ZHAO M, et al. Preparation of gradient nickel coating on copper by electrodeposition and study on its hydrogen evolution property [J]. Electroplating & Finishing, 2019, 38 (13): 641-646.

[6] 王华, 段成林. 电沉积方法制备镍硫析氢电极及其电化学性能[J]. 电镀与涂饰, 2011, 30 (8): 1-5.
WANG H, DUAN C L. Preparation of nickel–sulfur electrode by electrodeposition and its electrochemical performance [J]. Electroplating & Finishing, 2011, 30 (8): 1-5.

[7] 姚素薇, 姚丽娜, 张卫国, 等. 镍–钨/二氧化锆纳米复合电极析氢性能的研究[J]. 电镀与涂饰, 2009, 28 (2): 1-3.
YAO S W, YAO Y W, ZHANG W G, et al. Study of hydrogen evolution on nickel–tungsten/zirconia nanocomposite electrode [J]. Electroplating & Finishing, 2009, 28 (2): 1-3.

[8] 高平. 钛铁镍化学镀 Ni–Mo–P 镀层的形貌和耐腐蚀性能[J]. 电镀与精饰, 2021, 43 (4): 30-34.
GAO P. Morphology and corrosion resistance of Ni–Mo–P coatings on NiFeB prepared by electroless plating [J]. Plating & Finishing, 2021, 43 (4): 30-34.

[9] 谢北洋, 晏石林, 何旭, 等. 碳纳米管改性泡沫镍/环氧树脂复合材料阻尼性能[J]. 复合材料学报, 2017, 34 (6): 1325-1333.
XIE B P, YAN S L, HE X, et al. Damping property of Ni foam/epoxy resin composites modified with carbon nanotubes [J]. Acta Materiae Compositae Sinica, 2017, 34 (6): 1325-1333.

[10] 杜艳, 陈洪龄, 陈日志, 等. 高活性纳米镍催化剂的制备及其催化性能研究[J]. 高校化学工程学报, 2004, 18 (4): 515-518.
DU Y, CHEN H L, CHEN R Z, et al. Synthesis of nickel nanoparticles and the study of its catalytic performance [J]. Journal of Chemical Engineering of Chinese Universities, 2004, 18 (4): 515-518.

[11] 邢宏红, 黎德育, 李宁, 等. 镀液组成对硫酸盐镀锌镀层性能的影响[J]. 电镀与涂饰, 2016, 35 (7): 351-353.
XING L H, LI D Y, LI N, et al. Effect of bath composition on properties of zinc coating electroplated from a sulfate bath [J]. Electroplating & Finishing, 2016, 35 (7): 351-353.

[12] SAFIZADEH F, GHALI E, HOULACHI G. Electrocatalysis developments for hydrogen evolution reaction in alkaline solutions – a review [J]. International Journal of Hydrogen Energy, 2015, 40 (1): 256-274.

[13] TAN H, LIU Z H, CHAO D L, et al. Partial nitridation-induced electrochemistry enhancement of ternary oxide nanosheets for fiber energy storage device [J]. Advanced Energy Materials, 2018, 8 (21): 1800685.

(C)1994-2022 China Academic Journal Electronic Publishing House. All rights reserved.　http://www.cnki.net

6.邢乐红,王宜鑫,王慧,左明辉,孙芳,梁志男.氨基乙酸对硫酸盐体系电镀镍-铁合金的影响[J].电镀与涂饰,2019,38(19):1039-1041.

第38卷 第19期 电镀与涂饰 Vol.38 No.19

DOI: 10.19289/j.1004-227x.2019.19.003

氨基乙酸对硫酸盐体系电镀镍-铁合金的影响

邢乐红*，王宜鑫，王慧，左明辉，孙芳，梁志男

（牡丹江师范学院化学化工学院，黑龙江 牡丹江 157012）

摘要：在由 300 g/L $NiSO_4·6H_2O$、40 g/L $NiCl_2·6H_2O$、0.75 g/L $FeSO_4·7H_2O$、30 g/L H_3BO_3、8 mg/L 十二烷基磺酸钠组成的 Ni–Fe 合金电镀液(pH = 4.2)中，研究了氨基乙酸(0.00 ~ 0.60 g/L)对其稳定性及从中所得镀层性能的影响。结果表明，氨基乙酸可与 Fe^{2+}配位，抑制 Fe^{2+}的氧化，提高镀液稳定性。当氨基乙酸质量浓度为 0.20 g/L 时，镀液的稳定性最好，镀层的耐蚀性较好。

关键词：镍–铁合金；电镀；硫酸盐；氨基乙酸；亚铁离子；稳定性；耐蚀性

中图分类号：TQ153.2　　**文献标志码：**A　　**文章编号：**1004 – 227X(2019)19 – 1039 – 03

Effect of glycine on electroplating of nickel–iron alloy in sulfate bath // XING Le-hong*, WANG Yi-xin, WANG Hui, ZUO Ming-hui, SUN Fang, LIANG Zhi-nan

Abstract: The effect of glycine (0.00-0.60 g/L) on the stability of a sulfate Ni–Fe alloy electroplating bath (pH = 4.2) comprising $NiSO_4·6H_2O$ 300 g/L, $NiCl_2·6H_2O$ 40 g/L, $FeSO_4·7H_2O$ 0.75 g/L, H_3BO_3 30 g/L, and sodium dodecyl sulfonate 8 mg/L, as well as the properties of the coatings obtained therefrom was studied. The results showed that the complexation of glycine with Fe^{2+} inhibits the oxidation of Fe^{2+}, improving the stability of plating bath. The bath containing glycine 0.20 g/L had the best stability, and the coatings prepared from it had good corrosion resistance.

Keywords: nickel–iron alloy; electroplating; sulfate; glycine; iron(II) ion; stability; corrosion resistance

First-author's address: School of Chemistry and Chemical Engineering, Mudanjiang Normal University, Mudanjiang 157012, China

连铸机拉坯时钢水通过结晶器冷却成型，对结晶器基体的磨损很大[1]。金属电沉积技术可改善结晶器表面性能，提高结晶器寿命[2]。电镀 Ni–Fe 合金镀层因具有硬度高、耐磨、耐腐蚀等优点，常被用作连铸机结晶器工作面的防护层[3-4]。硫酸盐体系电镀 Ni–Fe 镀液中的 Fe^{2+}稳定性较差，易被氧化成 Fe^{3+}，进而水解生成沉淀。该沉淀具有磁性，可进入镀层形成毛刺，影响镀层性能[5]。因此需要在镀液中添加 Fe^{2+}的稳定剂。柠檬酸可作为配位剂来稳定硫酸盐体系 Ni–Fe 合金镀液中的 Fe^{2+}[6]。氨基乙酸也是常用的电镀配位剂，但在 Ni–Fe 合金电镀中的应用鲜见报道。本文选用氨基乙酸作为稳定剂，以期获得性能良好的 Ni–Fe 合金镀层。

1　实验

1.1　硫酸盐体系电镀 Ni–Fe 合金

1.1.1　前处理

采用 8 cm × 5 cm 的低碳钢板作为基体，依次对其进行除油、热水洗(80 °C)、酸洗和去离子水洗。除油液为 5 g/L 十二烷基磺酸钠水溶液，酸洗液为质量分数 5%的硫酸溶液。

1.1.2　镀液配方和工艺条件

在方形塑料镀槽中进行电镀，采用可溶性镍阳极。镀液组成和工艺条件为：$NiSO_4·6H_2O$ 300 g/L，$NiCl_2·6H_2O$ 40 g/L，$FeSO_4·7H_2O$ 0.75 g/L，H_3BO_3 30 g/L，十二烷基磺酸钠 8 mg/L，氨基乙酸 0.00 – 0.60 g/L，pH 4.2，温度 55 °C，电流密度 3.5 A/dm^2，空气搅拌，时间 30 min。

1.2　基础液氧化试验

在烧杯中进行基础液氧化试验。基础液与镀液的组成基本相同，但不含 Ni^{2+}，其原因是镀液中 Ni^{2+}

收稿日期：2019-03-25　　修回日期：2019-06-12

基金项目：黑龙江省高校青年创新人才培养计划项目(UNPYSCT-2016108)；牡丹江师范学院青年学术骨干项目(GG2018001)；牡丹江师范学院教改项目(19-XJ21008)；黑龙江省高等教育教学改革研究项目(SJGY20180519)；黑龙江省省属高等学校基本科研业务费科研项目(1352MSYY8007)。

作者简介：邢乐红(1983–)，女，山东武城人，博士，副教授，主要从事金属表面处理、化学电源等方面的研究。

(C)1994-2019 China Academic Journal Electronic Publishing House. All rights reserved.　http://www.cnki.net

浓度很高，颜色很深，不加 Ni^{2+}更容易观察 Fe^{2+}的氧化过程和 $Fe(OH)_3$沉淀的生成情况[5]。随着氧化时间的延长，基础液由无色透明变为淡黄色，最后变成红褐色。

1.3 性能检测和表征方法

采用 721 型分光光度计测定基础液中 Fe^{2+}的浓度，显色剂为 100 g/L 硫氰酸钠溶液，波长 480 nm[7]。

采用上海仪器五厂的 4XC 型金相显微镜观察 Ni–Fe 合金镀层的微观形貌。

采用上海辰华 CHI660 电化学工作站测量 Ni–Fe 合金镀层在 3.5% NaCl 溶液中的塔菲尔(Tafel)曲线，镀层的有效面积为 1 cm^2，辅助电极为 1 cm × 1 cm 的铂片电极，参比电极为饱和甘汞电极(SCE)，扫描速率为 10 mV/s。

2 结果与讨论

2.1 氨基乙酸的加入对 Fe^{2+}稳定性的影响

向基础液中加入 0.30 g/L 氨基乙酸，分别测定空气搅拌 30、60、90、120 和 150 min 时基础液中 Fe^{2+}的质量浓度，并与不含稳定剂的基础液的氧化情况进行对比，结果如图 1 所示。基础液中加入氨基乙酸后 Fe^{2+}的质量浓度明显下降，说明 Fe^{2+}的氧化受到抑制。因此，可以使用氨基乙酸作为 Fe^{2+}的稳定剂。

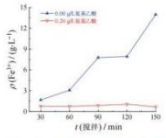

图 1 加入 0.30 g/L 氨基乙酸对镀液中 Fe^{2+}含量的影响

Figure 1 Effect of the addition of 0.30 g/L glycine on content of Fe^{2+} in plating bath

2.2 氨基乙酸质量浓度对 Fe^{2+}稳定性的影响

在基础液中分别加入 0.00、0.10、0.20、0.40 和 0.60 g/L 氨基乙酸，调节基础液 pH 为 4.2，温度 55 ℃，分析空气搅拌 30 min 后基础液中 Fe^{2+}的质量浓度，结果如图 2 所示。随着氨基乙酸质量浓度的增大，基础液中 Fe^{2+}的质量浓度降低，氨基乙酸质量浓度为 0.20 g/L 时镀液中 Fe^{2+}的质量浓度最低，继续增大氨基乙酸的质量浓度，Fe^{2+}的质量浓度并无明显变化。所以选择氨基乙酸的质量浓度为 0.20 g/L。

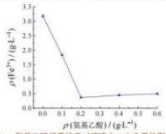

图 2 氨基乙酸质量浓度对镀液中 Fe^{2+}含量的影响

Figure 2 Effect of mass concentration of glycine on content of Fe^{2+} in plating bath

2.3 氨基乙酸的加入对 Ni–Fe 合金镀层微观形貌的影响

由图 3 可知，从不含稳定剂的镀液中所得镀层结晶粗大，加入稳定剂后镀层细致平整。这可能是由于加入的氨基乙酸可与 Fe^{2+}配位，令 Fe^{2+}的氧化受到抑制，Fe^{2+}水解生成的磁性沉淀对镀层性能的影响减弱。

(C)1994-2019 China Academic Journal Electronic Publishing House. All rights reserved. http://www.cnki.net

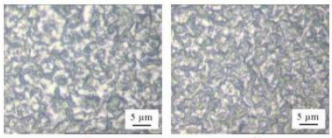

图 3 从含 0.00 g/L (a)和 0.20 g/L (b)氨基乙酸的镀液中所得 Ni–Fe 合金镀层的微观形貌

Figure 3 Microscopic morphologies Ni–Fe alloy coatings obtained from the plating baths with 0.00 g/L (a) and 0.20 g/L (b) glycine, respectively

2.4 氨基乙酸的加入对 Ni–Fe 合金镀层耐蚀性的影响

对图 4 中的 Tafel 曲线进行拟合，得到从不含氨基乙酸镀液中所得镀层的腐蚀电位和腐蚀电流密度分别为−0.173 V 和 2.315 × 10^{-3} A/cm^2，从含 0.20 g/L 氨基乙酸镀液中所得 Ni–Fe 合金镀层的腐蚀电位和腐蚀电流密度分别为−0.149 V 和 8.626 × 10^{-6} A/cm^2，可见后者的耐蚀性更好。

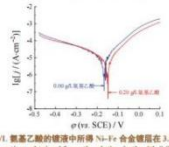

图 4 从含 0.00 g/L 和 0.20 g/L 氨基乙酸的镀液中所得 Ni–Fe 合金镀层在 3.5% NaCl 溶液中的 Tafel 曲线

Figure 4 Tafel plots for Ni–Fe alloy coatings obtained from the plating bath with 0.00 g/L and 0.20 g/L glycine, respectively

3 结论

研究了硫酸盐体系电镀 Ni–Fe 合金镀液中加入氨基乙酸对镀液稳定性和镀层微观形貌的影响。结果表明：氨基乙酸可与镀液中的 Fe^{2+}配位，提高 Fe^{2+}的稳定性。氨基乙酸质量浓度为 0.20 g/L 时，镀液的抗氧化能力最高，得到的 Ni–Fe 合金镀层质量最好。

参考文献：

[1] 王建福, 李光强, 朱诚意, 等. 表面改性技术在连铸结晶器上的应用进展[J]. 电镀与涂饰, 2005, 24 (12): 58-62.

[2] 何联质. 功能性超厚镍铁合金电镀工艺的研究[J]. 电镀与涂饰, 2002, 21 (2): 1-3.

[3] 杨金芳, 龚竹青, 邓湘元, 等. Ni–Fe 合金电镀的研究进展[J]. 电镀与涂饰, 2005, 24 (5): 23-27.

[4] 舒霞, 吴玉程, 王文芳, 等. 电沉积 Ni–Fe 合金镀层腐蚀性能研究[J]. 金属功能材料, 2006, 13 (3): 20-23.

[5] 邢乐红, 李宁, 黎德育, 等. 抗坏血酸对硫酸盐体系镍–铁合金镀液稳定性的影响[J]. 电镀与涂饰, 2018, 37 (12): 526-528.

[6] 杨绮琴, 王伟郁, 高喜, 等. 葡萄糖酸盐体系电镀镍铁合金的研究[J]. 电镀与涂饰, 1985, 4 (3): 17-23.

[7] 国家武. 镍–铁合金镀液中硫酸亚铁和 Fe^{3+}的快速分析[J]. 电镀与精饰, 2010, 32 (8): 42-44.

[编辑：周新莉]

(C)1994-2019 China Academic Journal Electronic Publishing House. All rights reserved. http://www.cnki.net

7.邢乐红,黎德育,李宁,左明辉,李晶.抗坏血酸对硫酸盐体系镍–铁合金镀液稳定性的影响[J].电镀与涂饰,2018,37(12):526-528.

第37卷 第12期 电镀与涂饰 ELECTROPATING & FINISHING Vol.37 No.12

DOI: 10.19289/j.1004-227x.2018.12.002

抗坏血酸对硫酸盐体系镍–铁合金镀液稳定性的影响

邢乐红[1,2,*]，黎德育[2]，李宁[2]，左明辉[1]，李晶[1]

（1. 牡丹江师范学院化学化工学院，黑龙江 牡丹江 157012；
2. 哈尔滨工业大学化工学院，黑龙江 哈尔滨 150001）

摘要：研究了抗坏血酸对硫酸盐体系电镀Ni–Fe合金镀液稳定性的影响，镀液(pH = 4.2)组成为：$NiSO_4·6H_2O$ 300 g/L，$NiCl_2·6H_2O$ 40 g/L，$FeSO_4·7H_2O$ 0.75 g/L，H_3BO_3 30 g/L，十二烷基磺酸钠8 mg/L，抗坏血酸0.00～0.15 g/L。结果表明，抗坏血酸可抑制镀液中Fe^{2+}的氧化。当抗坏血酸质量浓度为0.10 g/L时，镀液的稳定性最好，镀层的耐蚀性得到提高。

关键词：镍–铁合金；电镀；硫酸盐；抗坏血酸；亚铁离子；稳定性；耐蚀性

中图分类号：TQ153.2 **文献标志码：**A **文章编号：**1004－227X (2018) 12－0526－03

Effect of ascorbic acid on stability of sulfate nickel–iron alloy electroplating bath // XING Le-hong*, LI De-yu, LI Ning, ZUO Ming-hui, LI Jing

Abstract: The effect of ascorbic acid on stability of sulfate Ni–Fe alloy electroplating bath was studied. The bath composition is: $NiSO_4·6H_2O$ 300 g/L, $NiCl_2·6H_2O$ 40 g/L, $FeSO_4·7H_2O$ 0.75 g/L, H_3BO_3 30 g/L, sodium dodecyl sulfonate 8 mg/L, and ascorbic acid 0.00-0.15 g/L. It is shown that ascorbic acid has an inhibition effect on the oxidation of Fe^{2+}. The bath containing ascorbic acid 0.10 g/L has the best stability, and produces coatings with improved corrosion resistance.

Keywords: nickel–iron alloy; electroplating; sulfate; ascorbic acid; ferrous ion; stability; corrosion resistance

First-author's address: School of Chemistry and Chemical Engineering, Mudanjiang Normal University, Mudanjiang 157012, China

连铸机结晶器基体多采用Cr–Zr–Cu合金[1]。连铸机工作时，大量钢水快速、连续地通过结晶器冷却成型，钢水对结晶器内表面的冲击所造成的磨损很大。Ni–Fe合金镀层具有优良的耐磨性、硬度及耐蚀性，因此常作为连铸机结晶器工作面的表面防护层来提高结晶器寿命[2]。结晶器表面电镀Ni–Fe合金主要采用氨基磺酸盐体系，其优点是镀液稳定性高，镀层内应力低，但成本高，电流效率低[3-4]。硫酸盐体系具有成本低、可大电流密度施镀等优点，成为近年来的研究热点[5]。目前，对硫酸盐体系电镀Ni–Fe合金的研究主要集中在镀液组成及工艺参数对镀层性能的影响上[6-7]，有关Fe^{2+}稳定剂研究的报道较少。在硫酸盐体系镀液中，Fe^{2+}易被氧化成Fe^{3+}，Fe^{3+}水解生成的沉淀会导致镀液浑浊，镀层性能变差，铁含量减少。因此需要在硫酸盐体系镀液中添加Fe^{2+}的稳定剂。柠檬酸、EDTA(乙二胺四乙酸)等可作为配位剂来稳定硫酸盐体系Ni–Fe合金镀液中的Fe^{2+} [8]。抗坏血酸具有还原性，是电镀铁中常用的稳定剂，但在Ni–Fe合金电镀中的应用鲜见报道。本文选用抗坏血酸作为稳定剂，以求获得性能良好的Ni–Fe合金镀层。

1 实验

1.1 硫酸盐电镀镍铁合金

1.1.1 前处理

采用尺寸为8 cm × 5 cm的低碳钢板作为基体，依次对其进行除油(5 g/L十二烷基磺酸钠水溶液)、热水洗(80 °C)、酸洗(质量分数为5%的硫酸溶液)和去离子水洗。

收稿日期：2018–05–16 **修回日期：**2018–06–11

基金项目：黑龙江省高校青年创新人才培养计划项目（UNPYSCT-2016108）；牡丹江师范学院青年学术骨干项目（GG2018001）；黑龙江省教育厅高等教育教学改革研究项目（SJGY20170156）；牡丹江师范学院教学改革研究项目（17-XJH19002）。

作者简介：邢乐红（1983–），女，山东武城县人，博士，讲师，主要从事金属表面处理及化学电源等方面的研究。

作者联系方式：(E-mail) xinglehonghit@126.com。

(C)1994-2020 China Academic Journal Electronic Publishing House. All rights reserved. http://www.cnki.net

1.1.2　镀液配方和工艺条件

在方形塑料镀槽中进行电镀，采用可溶性镍阳极。镀液组成和工艺条件为：硫酸镍 ($NiSO_4·6H_2O$) 300 g/L，氯化镍 ($NiCl_2·6H_2O$) 40 g/L，硫酸亚铁 ($FeSO_4·7H_2O$) 0.75 g/L，硼酸 30 g/L，十二烷基磺酸钠 8 mg/L，抗坏血酸 0.00 ~ 0.15 g/L，pH 4.2，温度 55 ℃，电流密度 3.5 A/dm^2，空气搅拌，时间 30 min。

1.2　基础液氧化实验

在烧杯中进行基础液氧化实验。随着实验时间的延长，基础液由无色透明变成淡黄，最后生成红褐色 $Fe(OH)_3$ 沉淀。基础液只用于氧化实验，其组成与镀液基本相同，但不含 Ni^{2+}，因为镀液含高浓度的 Ni^{2+} 而呈深绿色，导致氧化实验过程中不容易观察到 Fe^{2+} 的氧化和 $Fe(OH)_3$ 沉淀的生成情况。

1.3　性能检测和表征方法

采用 721 型分光光度计测定基础液中 Fe^{3+} 的质量浓度，显色剂为 100 g/L 硫氰酸钠溶液，波长 480 nm [9]。利用日立 S-4700 型扫描电子显微镜 (SEM) 观察 Ni–Fe 合金镀层的微观形貌。

采用上海辰华 CHI660 电化学工作站测量 Ni–Fe 合金镀层 (有效面积 1 cm^2) 在 3.5% NaCl 溶液中的塔菲尔曲线，以 1 cm × 1 cm 的铂片为辅助电极，饱和甘汞电极 (SCE) 为参比电极，扫描速率为 10 mV/s。

2　结果与讨论

2.1　抗坏血酸的加入对 Fe^{3+} 稳定性的影响

向基础液中加入 0.05 g/L 抗坏血酸，分别测定空气搅拌 30、60、90、120 和 150 min 时基础液中 Fe^{3+} 的质量浓度，并与不含稳定剂的基础液的氧化情况进行对比，结果如图 1 所示。基础液中加入抗坏血酸后 Fe^{3+} 的质量浓度明显下降，说明 Fe^{2+} 的氧化受到抑制，因此，可以使用抗坏血酸作为 Fe^{2+} 的稳定剂。

2.2　抗坏血酸质量浓度对 Fe^{3+} 稳定性的影响

在基础液中分别加入 0.00、0.03、0.05、0.10 和 0.15 g/L 抗坏血酸，测定空气搅拌 30 min 后基础液中 Fe^{3+} 的质量浓度，结果如图 2 所示。随着抗坏血酸质量浓度的增大，基础液中 Fe^{3+} 的质量浓度降低，抗坏血酸质量浓度在 0.10 g/L 左右时镀液中 Fe^{3+} 的质量浓度最低，继续增大抗坏血酸的质量浓度后，Fe^{3+} 的质量浓度并无明显变化。所以选择抗坏血酸的质量浓度为 0.10 g/L。

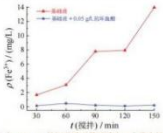

图 1　加入 0.05 g/L 抗坏血酸对基础液中 Fe^{3+} 稳定性的影响

Figure 1　Effect of the addition of 0.05 g/L ascorbic acid on stability of Fe^{3+} in basic solution

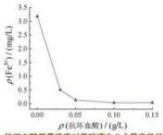

图 2　抗坏血酸质量浓度对基础液中 Fe^{3+} 稳定性的影响

Figure 2　Effect of the mass concentration of ascorbic acid on stability of Fe^{3+} in basic solution

2.3　抗坏血酸的加入对 Ni–Fe 合金镀层微观形貌的影响

由图 3 可知，不含稳定剂的镀液中所得镀层疏松多孔，这可能是由于在无稳定剂的情况下，镀液中的 Fe^{2+} 易被氧化成 Fe^{3+}，Fe^{3+} 水解生成的磁性沉淀易被夹杂在镀层中，使得镀层产生针孔和毛刺。镀液中加入具有还原性的抗坏血酸后，镀液中 Fe^{3+} 的氧化受到抑制，使镀液稳定性提高，故所得镀层细致、平整。

2.4　抗坏血酸的加入对 Ni–Fe 合金镀层耐蚀性的影响

采用电化学工作站自带软件对图 4 中的塔菲尔曲线进行拟合，得到从不含抗坏血酸镀液中所得镀层的腐蚀电位和腐蚀电流密度分别为−0.163 V 和 2.25 × 10^{-5} A/cm^2，从含 0.10 g/L 抗坏血酸镀液中所得 Ni–Fe 合金镀层的腐蚀电位和腐蚀电流密度分别为−0.147 V 和 8.97 × 10^{-6} A/cm^2，可见后者的耐蚀性更好。

(C)1994-2022 China Academic Journal Electronic Publishing House. All rights reserved.　http://www.cnki.net

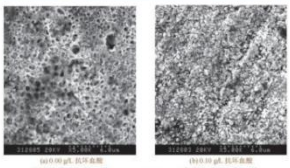

(a) 0.00 g/L 抗坏血酸 (a) 0.00 g/L Ascorbic acid　(b) 0.10 g/L 抗坏血酸 (b) 0.10 g/L Ascorbic acid

图 3　加入 0.10 g/L 抗坏血酸对 Ni–Fe 合金镀层表面微观形貌的影响

Figure 3　Effect of the addition of 0.10 g/L ascorbic acid on surface morphology of Ni–Fe alloy coating

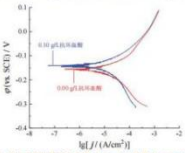

图 4　从不含和含 0.10 g/L 抗坏血酸的镀液中所得 Ni–Fe 合金镀层在 3.5% NaCl 溶液中的塔菲尔曲线

Figure 4　Tafel plots in 3.5% NaCl solution for Ni–Fe alloy coatings obtained from the bath without or with 0.10 g/L ascorbic acid

3　结论

研究了硫酸盐体系电镀 Ni–Fe 合金镀液中抗坏血酸的加入对镀液稳定性及镀层微观形貌、耐蚀性等方面的影响。结果表明：抗坏血酸的加入可以提高镀液中 Fe^{2+} 的稳定性，抗坏血酸质量浓度在 0.10 g/L 左右时镀液的抗氧化能力最好。在镀液中加入 0.10 g/L 抗坏血酸作为稳定剂时所得 Ni–Fe 合金镀层的微观形貌和耐蚀性均得到改善。

参考文献：

[1]　刘芳, 刘变升, 陶兴启, 等. 结晶器铜板表面处理的研究进展[J]. 表面技术, 2006, 35 (3): 1-3, 16.
[2]　樊自拴, 潘继民, 孙斗松, 等. 结晶器失效分析和表面处理技术的研究进展[J]. 特造技术, 2004, 25 (12): 952-954.
[3]　SRIVASTAVA H K. Microstructure of nickel electrodeposited from a nickel sulfamate/formamide bath [J]. Metal Finishing, 1995, 93 (5): 20-27.
[4]　KIM D J, KIM M J, KIM J S, et al. Material characteristics of Ni–P–B electrodeposits obtained from a sulfonate solution [J]. Surface and Coatings Technology, 2008, 202 (12): 2519-2526.
[5]　LEE T R, CHANG L W, CHEN C H. Effect of electrolyte temperature on composition and phase structure of nanocrystalline Fe-Ni alloys prepared by direct current electrodeposition [J]. Surface and Coatings Technology, 2012, 207: 523-528.
[6]　杨金贝, 龚竹青, 邓意元, 等. Ni–Fe 合金电镀的研究进展[J]. 电镀与涂饰, 2005, 24 (5): 23-27.
[7]　舒霞, 吴玉程, 王文芳, 等. 电沉积 Ni–Fe 合金镀层腐蚀性能研究[J]. 金属功能材料, 2006, 13 (3): 20-23.
[8]　梁振兴, 梁国栋, 谢国佩, 等. NT 镍铁合金电镀工艺研究报告[J]. 电镀与涂饰, 1988, 7 (2): 1-22.
[9]　郭崇武. 镍–铁合金镀液中硫酸亚铁和 Fe^{3+} 的快速分析[J]. 电镀与精饰, 2010, 32 (8): 42-44.

[编辑：周新莉]

(C)1994-2022 China Academic Journal Electronic Publishing House. All rights reserved.　http://www.cnki.net

8.邢乐红,杨晶,王海鹏,达铭,李姗,崔术新.硫脲对低磷化学镀镍稳定性的影响[J].牡丹江师范学院学报(自然科学版),2016(03):41-42.

文章编号:1003-6180(2016)03-0041-02

硫脲对低磷化学镀镍稳定性的影响

邢乐红,杨 晶,王海鹏,达 铭,李 姗,崔术新
(牡丹江师范学院 化学化工学院,黑龙江 牡丹江 157011)

摘 要:研究硫脲的加入对低磷化学镀镍镀液稳定性及镀层沉积速度的影响.实验结果表明,硫脲的加入对低磷化学镀镍镀液稳定性和沉积速度影响较大,当硫脲浓度为 3 mg/L 时,镀液的稳定性最好,镀层沉积速度最快.

关键词:低磷化学镀镍;硫脲;稳定性;沉积速度

[中图分类号]TP317.6 [文献标志码]A
DOI:10.13815/j.cnki.jmtc(ns).2016.03.014

Effect of Thiourea Addition on the Stability of Low-phosphorus Electroless Nickel Plating

XING Le-Hong, YANG Jing, Wang Hai-peng, DA Ming, LI Shang, CUI Shu-xin
(Mudanjiang Normal University School of Chemistry and Chemical Engineering, Mudanjiang, Heilongjiang, 157011)

Abstract: The effects of thiourea on the stability and deposition rate of low-phosphorus electroless nickel plating coating have been discussed. The results indicate that the concentration of thiourea can obviously affect the stability and deposition rate of low-phosphorus electroless nickel plating and the optimal concentration of thiourea in electrolyte is 3mg/L.

Key words: low-phosphorus electroless nickel plating; thiourea; stability; deposition rate

低磷化学镀镍具有高熔点、高硬度、良好的可焊性及脱模性[1-3],广泛用于能源、电子等领域元件的表面处理[4-5].化学镀镍溶液是一种具有自催化性质的热力学不稳定体系,镀液易受外来杂质及反应中间产物影响而发生不可逆自分解,导致镀液寿命减少甚至报废,加工成本升高,因此需要在镀镍液中添加稳定剂来提高镀液稳定性.稳定剂是化学镀镍自催化反应的毒化剂,加入稳定剂可抑制镀液的自发分解,使反应可控有序的进行.[6]微量的稳定剂即可达到稳定镀液的作用,不能过量,否则会降低镀速甚至不起镀.本文选用硫脲作为低磷化学镀镍液的稳定剂,以提高镀液稳定性,获得性能良好的镀层.

1 材料与方法

1.1 镀液组成及基本工艺

化学镀镍液的基本组成为:硫酸镍 27 g/L,乳酸 20 g/L,无水乙酸钠 20 g/L,次亚磷酸 21 g/L,十二烷基磺酸钠 5 mg/L.选用铜板作基体,对其进行除油、水洗、酸洗、弱侵蚀等基本处理后,进行化学镀(前处理工序及化学镀均在烧杯中进行).镀液温度为 85 ℃,pH 值 6.2.通过此工艺可获得磷含量低于 3 $wt\%$的低磷化学镀镍层.

1.2 镀速测定

化学镀镍层的沉积速度采用增重法测定[7],

收稿日期:2016-03-20
基金项目:黑龙江省青年科学基金项目(QC2014C009);黑龙江省大学生创新创业训练计划项目(201610233031);牡丹江市科学技术计划项目(G2013f1407);牡丹江师范学院博士启动金项目(MSB201208),牡丹江师范学院国家级重点创新预研项目(GY201201)
作者简介:邢乐红(1983-),女,山东武城人,讲师,博士,主要从事金属表面处理及化学电源等方面研究;杨晶(1994-),女,黑龙江大庆人,本科生,主要从事金属表面处理等方面研究;王海鹏(1994-),男,黑龙江鸡东人,本科生,主要从事金属表面处理等方面研究.

?1994-2017 China Academic Journal Electronic Publishing House. All rights reserved. http://www.cnki.net

按公式(1)计算.

$$v = \frac{m_2 - m_1 + \Delta m}{2\rho \cdot s \cdot t} \times 10^4 . \qquad (1)$$

式(1)中,v 为沉积速度(μm/h),ρ 为镀层的密度(g/cm³),t 为施镀时间(h),s 为试片面积(cm²),m_2 为镀片镀后质量(g),m_1 为镀片初始的质量(g),Δm 为处理时损失的铜片质量(g).

1.3　镀液稳定性测定

用 $PdCl_2$ 滴定法[9]测量不同浓度不同稳定剂的稳定性,在恒温 60 ℃的条件下,在 50 mL 镀液中加入 1 mL $PdCl_2$ 溶液,测量镀液从滴入氯化钯到其分解的时间(镀液变黑或者变浑浊的时间),比较分解时间的长短,判断稳定性的好坏.分解越慢,时间越长,稳定性越好.

2　结果与讨论

2.1　硫脲对镀液稳定性的影响

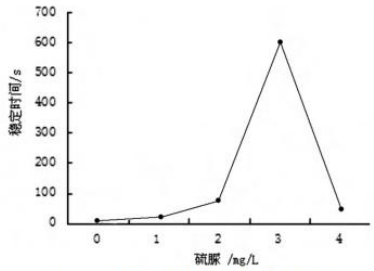

图 1　硫脲浓度对镀液稳定性的影响

在不含稳定剂的镀液中分别加入浓度为 0,1,2,3,4 mg/L 的硫脲作为稳定剂.用 $PdCl_2$ 滴定法测量不同浓度不同稳定剂的稳定性,结果如图 1 所示.由图 1 可以看出,随着硫脲浓度的增加镀液稳定性先增大后减小,当硫脲浓度为 3 mg/L 时,镀液稳定性最好.当硫脲浓度大于 4 mg/L 时,镀液不再起镀.

2.2　硫脲对镀速的影响

在不含稳定剂的镀液中分别加入浓度为 0,1,2,3,4 mg/L 的硫脲作为稳定剂.测量不同硫脲浓度条件下化学镀镍液的镀速.结果见图 2.由图 2 可以看出,随着硫脲浓度的增加,镀液镀速先增大后减小,当硫脲浓度为 3 mg/L 时,镀速最高.

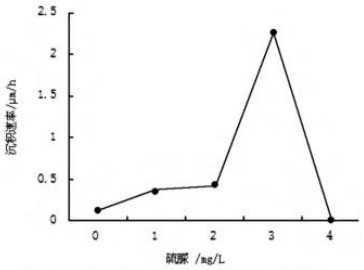

图 2　硫脲浓度对镀层沉积速度的影响

2.3　硫脲对镀层外观的影响

在不含稳定剂的镀液中加入浓度为 3 mg/L 的硫脲,恒温 85 ℃,施镀时间为 60 min,获得的镀层外观形貌如图 3 所示.由图 3 可见,当镀液中硫脲浓度为 3 mg/L 时,镀层表面细致平滑,外观质量良好.

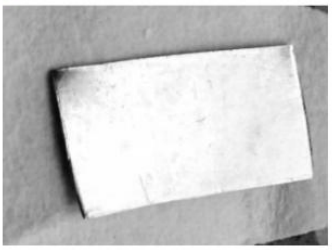

图 3　硫脲对镀层外观的影响

3　结论

研究了低磷化学镀镍液中稳定剂对镀液稳定性及镀层沉积速度的影响,结果表明,随着镀液中硫脲浓度的增加,镀液稳定性和镀层沉积速度均先增大后减小,当硫脲浓度为 3 mg/L 时,镀液的稳定性最好,镀层沉积速度最快,可获得性能良好的镀层.

参考文献

[1] 邢乐红,王冰,廉波. 低磷化学镀镍光亮剂研究[J]. 牡丹江师范学院学报:自然科学版,2015(2):35-36.
[2] 贾林艳,韩俊凤,马杰. 尖晶石 LiMn2O4 的低热固态反应法合成及其表征[J]. 牡丹江师范学院学报:自然科学版,2009(4):17-18.
[3] 郑振,李宁,黎德育等. 低磷化学镀镍液补加方式对镀层的影响[J]. 材料保护,2010,43(5):37-39.
[4] Lehong Xing, Yunzhi Gao, Zhenbo Wang, et al. Effect of anode diffusion layer fabricated with mesoporous carbon on the performance of direct dimethyl ether fuel cell [J]. International Journal of Hydrogen Energy, 2011, 36(17): 11102-11107.
[5] Lehong Xing, Zhenbo Wang, Chunyu Du, et al. The Influence of anode diffusion layer on the performance of direct dimethyl ether fuel cell [J]. International Journal of Energy Research, 2012, 36(7): 886-890.
[6] 郑振,李宁,黎德育. 稳定剂对低磷化学镀镍液及镀层的影响[J]. 电镀与环保,2009,29(1):30-33.
[7] 夏承钰. 酸性化学镀镍沉积速度的研究[J]. 材料保护,1996,29(1):4-7.

编辑:琳莉

?1994-2017 China Academic Journal Electronic Publishing House. All rights reserved.　http://www.cnki.net

云观发表科研论文目录（共 5 篇）

1.云观,郭朝阳,张萌.胶原蛋白提取及检测方法研究进展[J].山东化工,2022,51(07):70-72

2.云观,刘全菊,张可鑫,蒋舰.达夫反应法合成 2,4,6-三羟基苯-1,3,5-三甲醛反应条件研究[J].长春师范大学学报,2021,40(02):95-98.

3.云观,陈佳丽,蒋舰,邵艳秋.有机化学实验中废液及固废的处理[J].山东化工,2020,49(05):257-258.

4.云观,陈佳丽,刘艳爽,曹明星,杨春文.东北林蛙消化系统 LDH 同工酶表型的季节变化[J].黑龙江畜牧兽医,2018(01):215-217.

5.陈佳丽,云观,金建丽,杨松鹏,田新民.东北林蛙消化系统 SOD 和 POD 同工酶电泳分析[J].黑龙江畜牧兽医,2017(01):219-221.

1.云观,郭朝阳,张萌.胶原蛋白提取及检测方法研究进展[J].山东化工,2022,51(07):70-72

专论与综述

胶原蛋白提取及检测方法研究进展

云观，郭朝阳，张萌

（牡丹江师范学院，黑龙江 牡丹江 157011）

摘要：胶原蛋白是人体的重要组成部分，具有良好的理化和生物学特性。胶原蛋白作为蛋白质资源，广泛应用于化妆品工业、食品行业、医学生物美容行业等。文章对胶原蛋白的提取方法以及检测方法进行了介绍，旨在为相关领域的研究提供参考，以期为胶原蛋白相关产品的研发提供帮助。

关键词：胶原蛋白；提取方法；检测方法

中图分类号：TQ936.2 文献标识码：A 文章编号：1008-021X(2022)07-0070-03

DOI:10.19319/j.cnki.issn.1008-021x.2022.07.001

Research Progress on Extraction Methods and Detection Methods of Collagen

Yun Guan, Guo Chaoyang, Zhang Meng

(Mudanjiang Normal University, Mudanjiang 157011, China)

Abstract: Collagen is an important part of the human body, and an important part of human body. It has good physical, chemical and biological characteristics. Collagen, as a protein resource, is widely used in cosmetics industry, food industry, medical and biological beauty industry, etc. In this paper, the extraction methods and detection methods of collagen were introduced, aiming to provide reference for the research in related fields, in order to provide help for the research and development of collagen-related products.

Key words: collagen; extraction method; detection method

胶原蛋白是天然的高分子蛋白质，是多细胞生物体内分布最广，含量最多的功能性蛋白质，在人体中约占体重的 6%，占总蛋白质的 25%～30%[1-2]。具有良好的理化性能，普遍存在于动物的结缔组织中，是皮肤的支持组织，可保持皮肤细腻，增强弹性并提高细胞的储水能力，有极好的生物降解性[3-4]。胶原蛋白是一种特殊的三螺旋结构蛋白质的统称，不同的胶原蛋白类型在分布上有着不同的特点，性质上也存在不同[5-6]。普通蛋白一般是双螺旋结构，但胶原蛋白为三螺旋结构，且胶原蛋白含有羟脯氨酸，是胶原蛋白的特性成分之一[7]。胶原蛋白理化性质稳定，具有出色的营养特性与加工性能，其广泛的应用使得被越来越多的行业所需要，也促使越来越多的人对胶原蛋白的提取及检测进行更深入的研究，以找出新的方法，既避免资源浪费又可以不污染环境。

1 胶原蛋白的提取

1.1 样品预处理

由于脂肪等物质在提取胶原蛋白时会产生影响，所以样品需要进行预先处理。目前经常使用的预处理办法有 4 种，包括酶解法、复合盐溶液与脂肪酶联合脱脂法、脱脂液法以及有机溶液萃取法。例如周艳华等人[8]在大鲵皮中提取胶原蛋白时，将大鲵皮浸泡在 10%的正丁醇溶液中 24 h 来去除脂肪。王萌萌等人[9]以林蛙皮为原料，用浓度为 9%的脂肪酶进行脱脂，脱脂后所得结果理想，提取的胶原蛋白不仅结构完整且提取率最高达到 80.1%。马艳等人[10]在鸡翅脱脂的研究中，运用脂肪酶、$NaHCO_3$ 与 NaCl 复合盐溶液，分别进行了三组实验（碱性脂肪酶作用、复合盐溶液作用、酶和复合盐溶液共同作用方法），发现使用复合盐溶液与脂肪酶联合脱脂的效果较好，脱脂率可达到 70.88%。一些样品中还存在色素及非胶原物质，现阶段经常采用 NaOH 溶液来去除。周瑞等人[11]从暗纹东方鲀鱼皮中提取胶原蛋白时，将鱼皮浸泡在 0.1 mol/L NaOH 溶液中 24 h除去色素以及非胶原蛋白物质。傅燕凤等人[12]从淡水鱼的鱼皮中提取胶原蛋白时，分别加入了 1%，2.5%，5%，7.5%氯化钠溶液，在 5 ℃下连续搅拌 24 h 发现，对于淡水鱼中的鲢鱼和鳙鱼来说脱除杂蛋白的最佳盐浓度为 2.9%，对于草鱼来说，脱除杂蛋白的最佳盐浓度为 5%。在从水产动物的皮、骨、鳞、肌肉等部位提取胶原蛋白时，除了脱脂、去除非胶原蛋白以及色素外，对水产动物部分组织器官还需要进行除盐、除钙的处理。在从鱼鳞中提取胶原蛋白时，可以通过加入乙二胺四乙酸来除去过多的钙离子[13-14]。从水产脊椎动物软骨中提取胶原蛋白时，除上述除盐、除钙和脱脂处理外，还需要用盐酸胍去除多糖物质。在从棘皮类动物如海参、海胆、海星和鲍鱼[15]中提取胶原蛋白时，也需要去除其中所含的钙离子以及多糖。

1.2 胶原蛋白的溶出

1.2.1 碱提取法

碱提法是利用碱性物质通过浸渍处理，使胶原蛋白中含有-OH 和-SH 的氨基酸不稳定从而进行提取胶原蛋白。梁文伟等人[16]从皮料的皮屑中提取胶原蛋白时，在 NaOH 用量为 9%、水解时间 6 h、温度 120 ℃的条件下提取率可达 87.45%。温慧芳等人[17]从鲟鱼皮中提取胶原蛋白时，在 1∶10 的料液比、1.6%的 CaOH 浓度、70 ℃水解 9 h 条件下，提取率能够达到 79.67%。碱提取法步骤相对复杂，并且由于经过碱液的浸泡、冲洗、悬浮、加热和离心等步骤，得到的胶原蛋白相对分子质量较低并且含量较少[18]，利用率不高，而且还会造成肽键的水解，

收稿日期：2021-09-10

基金项目：黑龙江省教育厅基本科研业务费（1353MSYQN005）：东北林蛙皮胶原蛋白提取工艺研究；黑龙江省大学生创新创业训练项目（202010233034）：黑龙江地区常见食用菌中胶原蛋白的提取

作者简介：云观，硕士研究生，讲师，研究方向为生物化学及有机化学。

如果肽键水解的程度大,就会生成有毒的 D-型氨基酸。所以在实际提取中,如果想提取相对分子质量大、结构相对完整,并且相对更安全的胶原蛋白,利用碱法与其他方法相结合,或者运用碱性物质对样品进行预处理的情况相对更多。

1.2.2　酸提取法

酸提取法,其主要是通过破坏盐键和酉夫键,从而引起胶原纤维溶解,需要胶原蛋白在低浓度酸性的条件下达到。目前研究中常用的酸有乙酸、盐酸、草酸、柠檬酸和乳酸五种酸[18]。周维等人[19]从鲢纹东方鲀鱼皮中提取胶原蛋白时,将处理后的鱼皮浸泡在 0.5 mol/L 的乙酸溶液中 48 h,后经过盐析、离心和透析等步骤,最后发现酸提取法提取的胶原蛋白提取率相对较低,这主要是因为由提取胶原蛋白螺旋交联,使得酸溶剂下其溶解度降低[18]。目前实验中通常将酸与酶混合使用,来达到更高的提取率以及更完整的胶原蛋白结构。

1.2.3　热水浸提法

热水提取法的应用原理是由于蛋白质可在水中溶解,在样品经过一系列预处理后,将其浸入一定温度的水中,水温升高则胶原蛋白的溶解程度也在不断增大,浸提一段时间后再对其进行纯化最终获得胶原蛋白。但这个方法对温度的要求十分严格,胶原蛋白的结构并不稳定,一旦提取温度过高,胶原蛋白便会失去其分子活性[18],胶原蛋白特有的三螺旋结构就会失去,所得的胶原蛋白结构变化,其应用价值及对生物的利用率也随之降低。但若提取温度不足,则会导致提取的胶原蛋白非不完全,最终使胶原蛋白的提取率降低。周瑞等人[18]从鱼皮中提取胶原蛋白时将处理好的鱼皮在 80 ℃水中浸 6 h,后进行离心,得到胶原蛋白,通过整个实验结果的对比,虽然热水浸提的提取率比较高,但是所得胶原蛋白已经变性为明胶。

1.2.4　酶解提取法

酶解提取是在一定的条件下,运用不同的蛋白酶,从而得到酶溶性胶原蛋白的方法,目前研究中常用的酶基本分为三大类,即动物蛋白酶、植物蛋白酶以及微生物蛋白酶。张百刚等人[18]从龟甲中提取胶原蛋白时,先用乙酸乙酯进行脱脂,再用胃蛋白酶进行酶解,得出在 40 ℃,pH 值 1.5 的环境下,4%的酶用量,酶解 5 h,提取率最高,达 11.08%。刘静波等人[18]从黑长耳中提取胶原蛋白时,调节 pH 值为 8.0,添加 8%碱蛋白酶,酶解 2 h,提取率可达 1.09%。杨辉等人[18]从安康鱼肠道中提取胶原蛋白时,利用胃蛋白酶在 pH 值 1.9 的条件下提取 4 h,胶原蛋白的得率可达 11.3%。

1.2.5　复合法提取

在提取过程中为了得到更高的胶原蛋白提取率,同时保证胶原蛋白结构完整且应用性良好,设计了一系列的复合方法来达到此目的。目前常见的复合法有:酸与酶复合法、酸与热水复合法、酶与酶复合法等。李祇雨等人[18]通过鱼鳞提取胶原蛋白的研究中,利用 15%柠檬酸和 0.6 g 胃蛋白酶复合,将样品在 4 ℃下浸泡 24 h,这种情况下胶原蛋白的提取率高,约达 87.94%,且结构保持良好。张鹏程等人[18]从鲢鱼中提取胶原蛋白时,运用酸、热水和酶三种物质复合,先将样品用醋酸溶液浸泡后放入 100 ℃沸水中将其完全溶解,后加入胃蛋白酶,得出在加入 5%醋酸,浸泡 48 h 前点 1.5 h 并加入胃蛋白酶酶解 6 h 的条件下胶原蛋白提取率达最高,为 58.56%。冯玲玲等人[18]从翁中提取胶原蛋白时先用 pH 值 2.0~2.5 的盐酸溶液浸泡 14 h,之后再利用胃蛋白酶在酸性条件下进行酶解,最后所得出胶原蛋白提取量达 1.96%,占其总蛋白质的 39.22%。

2　胶原蛋白的检测

2.1　胶原蛋白种类的鉴别

目前对胶原蛋白蛋白种类的鉴别主要有四种方法,分别是:傅里叶红外光谱检测法、紫外光谱分析法、磷酸缓冲盐溶液检测法以及组织化学染色法。

2.1.1　傅里叶红外光谱检测法

红外光谱检测的原理是通过光源发出的光进行反射,产生干涉光,分束器与干涉光会合后经过样品池,使干涉光含有样品的信息,再经过傅里叶变换对信号进行处理,最终得到透过率和吸收度与波数和波长关系的光谱图,再根据官能团的特征吸收来判定未知样品中存在哪些官能团,从而确定未知物的化学组成。应用此方法在 ATR 支架上扫描得出胶原蛋白样品的红外吸收光谱图,得到谱图之后根据不同波数确定酰胺的Ⅰ带、Ⅱ带、Ⅲ带。Chiaomaria S[18]等人经研究得出结论,胶原蛋白三螺旋结构及氨基酸序列与酰胺三种带的伸缩振动直接相关,酰胺Ⅲ带峰位与波长范围为 1 400~1 454 cm^{-1} 的峰值比例为 1.0 时,制有完整的胶原蛋白三螺旋结构。

2.1.2　紫外吸收光谱法

胶原蛋白中存在的可在紫外吸收光谱中出现吸收峰的不饱和键有-CO-NH-、-COOH、C_6H_6 以及多元芳香环,氨具具等人[18]总结出由于-CO-NH-的存在,绝大部分蛋白质在低于 280 nm 波长下和 280 nm 波长处有强吸收峰,但是不含有色氨酸只含有酰基酪氨酸的胶原蛋白只在 230 nm 下出现强吸收,因此只需检测检测蛋白质在 280 nm 处是否无明显吸收峰,而在 200~230 nm 处出现强吸收峰,若是该种情况,则可以认为该种蛋白质中存在胶原蛋白。通过胶原蛋白的紫外分析来确定胶原蛋白的性质在不少文献中有提及。例如周维等人[18]在研究鲢纹东方鲀鱼皮胶原蛋白的提取及其物性时对比了 5 种处理方法,探究得到胶原蛋白均在 235 nm 左右有强吸收峰,经酶处理后胶原蛋白的紫外吸收能力明显增强且其结构并不会被破坏。

2.1.3　磷酸缓冲盐溶液和组织化学染色法

磷酸缓冲盐溶液是由磷酸盐溶液溶于蒸馏水中后,用 1 mol/L 的 NaOH 溶液校正酸碱度后,再经蒸馏水稀释得到的溶液,将胶原蛋白试样与磷酸盐缓冲溶液混合,在 4 ℃下该试样会呈现液态,而升高温度的在 36 ℃时试样呈现固态,根据胶原蛋白在该种条件下的特征可鉴别它的存在。

组织化学染色法包括 V.G 染色法、天狼星红染色法和复合染色法。V.G 染色法不用于单纯鉴别胶原蛋白,天狼星红法则用来鉴定胶原蛋白的类型,天狼星红能与胶原蛋白特异性结合,同时,可对结合后的物质用 NaOH 进行离心和洗脱后在 540 nm 下测定其吸光度,以测定胶原蛋白含量。复合染色法则是由于胶原蛋白中含有较多的碱性氨基酸,因此可与染料性质为酸性的物质强烈反映。

2.2　胶原蛋白含量的鉴定

2.2.1　高效液相色谱法

高效液相色谱法应用高压输液系统,将极性不同的单一溶剂或混合溶剂-缓冲液等流动相泵入色谱柱,色谱柱中装有固定相,各组成成分被分离后进入检测器进行检测,以此对样品进行分析。周静段已经有研究人员应用此方法来测定鸡皮、鲫龟甲和鲶皮中胶原蛋白的含量以及鲫鱼不同组织中的胶原蛋白含量[20-22]。

2.2.2　紫外分光光度法

紫外分光光度法通过测定样品的吸光度,以波长和吸光度的关系绘制待测物的光谱与对照光谱比较或测定两个特定波长的吸收值来鉴别物质。在测定胶原蛋白的含量时,可以在 230 nm 下测定已知胶原蛋白浓度溶液的吸光度,绘制 A-c 曲线,再将待测试样在 230 nm 处测定其吸光度,再根据标准曲线得出胶原蛋白的含量。

2.2.3　邻羟基联吡啶法

胶原蛋白在强酸或强碱条件下经高温水解会将组织脯氨酸,再利用氯胺 T 氧化羟脯氨酸,生成含有吡咯环的氧化物,

(C)1994-2022 China Academic Journal Electronic Publishing House. All rights reserved.　http://www.cnki.net

剩余的氯胺 T 用高氯酸去除,在一定温度下该氧化物会与对二氨基苯甲醛反应,生成红色的特征产物,在 558 nm 处检出,与标准曲线比较定量,即可确定羟脯氨酸的浓度,从而计算胶原蛋白的含量。

3　展望

胶原蛋白应用领域广泛,我国博大的生物资源为胶原蛋白的提取提供了便利条件,并且胶原蛋白的提取也使我国的生物利用率得到了一定的提高,胶原蛋白提取的研究从一定程度上也解决了环境问题,食品加工过程中 30%的废弃物由骨骼、鳞片等构成,其中都蕴藏着大量的胶原蛋白,但目前仍存在一些理论与实际结合的困难,例如新产品的开发以及应用。而且在胶原蛋白的纯化上也存在一定的问题需要解决,研究与发现胶原蛋白潜在的生理活性与功能并且提高纯化技术是当前所紧缺对的,随着胶原蛋白的提取与使用在不断地扩展,其将为我国经济、环境方面都带来可观收益。随着科技进步和社会发展速度的加快,胶原蛋白产品的使用会越来越受欢迎也会变得越来越重要,随着进一步深入对胶原蛋白的研究,鉴定胶原蛋白的方法将愈发简便准确。

参考文献

[1]　RAMA P, VIJAYALAKSHMI M, JAYASHMAN R, et al. Extraction of collagen from cat fish (tachysurus maculatus) by pepsin digestion and preparation and characterization of collagen chitosan sheet [J]. International Journal of Pharmacy and Pharmaceutical, 2010,2(4) :133-137.

[2]　QUERESHI S, MIHASKE A, RAUT D, et al. Extraction and partial characterization of collagen from different animal skins [J]. Agricultural & Biological Chemistry, 2010,2(9) : 28-31.

[3]　陈毅军,刘正乔.胶原蛋白提取及其纺丝工艺研究现状[J].山东纺织科技,2016,57(5):54-56.

[4]　MARLENA G W, LESZEK K, SLAWOMIR M, et al. Comparison of thermal properties of fish collagen and bovine collagen in the temperature range 298 - 670 K [J]. Materials Science & Engineering C, 2007,3(6):465-471.

[5]　周婷,杨恒,王鑫,等.酶解技术提取动物组织中的胶原蛋白及其肽的研究进展[J].食品工业科技,2020,41(15):332-338.

[6]　FAUZI M B, LOKANATHAN Y, AMINUDDIN B S, et al. Ovine tendon collagen: extraction, characterisation and fabrication of thin films for tissue engineering applications [J]. Materials Science&Engineering,2016,66:163-171.

[7]　ZHOU C, LI Y, YU X, et al. Extraction and characterization of chicken feet soluble collagen [J]. LWT-Food Science and Technology,2016,74:145-153.

[8]　周艳华,张鹏飞,李涛,等.干制大鲵皮胶原蛋白提取工艺优化[J].食品工业,2020,41(1):1-4.

[9]　王丽丽,刘仁杰,陈光.鲟皮胶原蛋白提取工艺的优化与相关性质研究[J].食品科技,2017,42(6):237-242.

[10]　马艳,李春保,王志轩,等.鸡翅提酸技术研究[J].肉类工业,2007(2):21-23.

[11]　周瑞,李若男,周丽莎,等.超反东方鲀鱼皮胶原蛋白的提取及其特性[J].水产学报,2020,44(8):1349-1359.

[12]　傅鹰凤,汪月新,杨承刚,等.淡水鱼鱼皮胶原蛋白的提取[J].上海水产大学学报,2004(2):146-150.

[13]　ALI A M M, KISHIMURA H, BENJAKUL S, et al. Extraction efficiency and characteristics of acid and pepsin solubile collagens from the skin of golden carp (probarbus jullieni) as affected by ultrasonication [J]. Process Biochemistry,2018,66:237-244.

[14]　CHEN S, CHEN H, XIE Q, et al. Rapid isolation of high purity pepsin - soluble type I collagen from scales of red drum fish (Sciaenops ocellatus) [J]. Food Hydrocoll, 2016, 52:468-477.

[15]　DONG X, YUAN Q, 陈 H, et al. Isolation and characterization of pepsin-soluble collagen from abalone (Haliotis discus hannai) gastropod muscle part Ⅱ [J]. Food Science and Technology Research,2012,18(2):271-278.

[16]　梁文伟,王志杰,杜飞.碱法水解皮革废屑提取胶原蛋白及其用于纸张的增强[J].造纸科学与技术,2010(5):39-41.

[17]　温慧芳,赵利,陈丽丽,等.碱法提取(鲫)鱼皮胶原蛋白工艺优化的研究[J].食品工业科技,2015(19):233-236.

[18]　DING J F, LI Y Y, XU J J, et al. Study on effect of jellyfish collagen hydrolysate on anti-fatigue and anti - oxidation [J]. Food Hydrocoll, 2011,25:1350-1353.

[19]　徐灿时,李正军.鱼鳞胶原蛋白的提取技术[J].西部皮革,2016,32(19):27-30.

[20]　于丽,肖刚,陈海华.鱼皮胶原蛋白的提取工艺及特性研究[J].上海医药,2019,40(3):70-73.

[21]　赵烁,曹敏杰,王晶,等.水产动物源胶原蛋白的提取及应用研究进展[J].食品安全质量检测学报,2020,11(22):8157-8165.

[22]　张百刚,梁海荣,冯再平,等.龟甲胶原蛋白的提取工艺研究[J].江西农业学报,2020,32(5):83-87.

[23]　刘静波,赵曙宁,林松毅,等.鹅解法提取黑木耳中胶原蛋白的工艺优化[J].农业工程学报,2012,28(13):282-286.

[24]　杨辉,赵新宇,解海洋,等.安康鱼肠中胶原蛋白与多糖的提取与保湿性[J].皮革与化工,2020,37(1):25-28.

[25]　李秋南,刘红梅,李彦,等.鱼鳞胶原蛋白提取线造中鱼蛋白的回收与表征[J].食品工业科技,2021,42(9):179-185.

[26]　张鹏程,左宝金,冷向阳.鲢鱼胶原蛋白提取条件优化[J].延边大学农学学报,2020,42(1):69-75.

[27]　冯玲玲,冯进,李春阳.海鲈Ⅰ型胶原蛋白的提取及结构特性研究[J].食品工业科技,2021,42(7):15-21.

[28]　CHIARAMARIA S, LISA V, ELISA M, et al. FTIR investigation of the secondary structure of type I collagen: new insight into the amide III band [J]. Spectrochimica Acta Part A: Molecular and Biomolecular Spectroscopy, 2020, 229:118006.

[29]　夏其昌.蛋白质化学研究技术与进展[M].北京:科学出版社,1997.

[30]　丁瑞敏,周华峰,李晋高,等.高效液相色谱-蒸发光散射法测定鲢皮中胶原蛋白的含量[J].日用化学工业,2017,47(11):639-662.

[31]　黄宝玉,下欢,吴海红,等.高效液相色谱法检测鲫鱼不同组织中的胶原蛋白含量[J].食品科学,2015,36(14):65-69.

[32]　吴玉琼,徐红霞,胡永乐,等.木瓜蛋白酶提取鲢皮胶原蛋白的工艺研究[J].武夷学院学报,2015,34(6):26-30.

(本文文献格式:云观,鄂朝阳,张晓.胶原蛋白提取及检测方法研究进展[J].山东化工,2022,51(7):70-72.)

(全文 8100 字)

(C)1994-2022 China Academic Journal Electronic Publishing House. All rights reserved.　http://www.cnki.net

2.云观,刘全菊,张可鑫,蒋舰.达夫反应法合成 2,4,6-三羟基苯-1,3,5-三甲醛反应条件研究[J].长春师范大学学报,2021,40(02):95-98.

第 40 卷 第 2 期 长春师范大学学报 2021 年 2 月
Vol.40 No.2 Journal of Changchun Normal University Feb.2021

达夫反应法合成 2,4,6－三羟基苯－1,3,5－三甲醛反应条件研究

云　观,刘全菊,张可鑫,蒋　舰

(牡丹江师范学院化学化工学院,黑龙江 牡丹江 157000)

[摘　要]2,4,6－三羟基苯－1,3,5－三甲醛是合成共价有机框架材料和超分子结构的重要中间体,在合成中有很多应用。经达夫反应合成 2,4,6－三羟基苯－1,3,5－三甲醛具有操作简单、产物易分离等优点。本文通过对酸性介质、反应温度、反应时间、水解试剂等因素对目标化合物产率的影响,确定了合成 2,4,6－三羟基苯－1,3,5－三甲醛的最佳反应条件。

[关键词]2,4,6－三羟基苯－1,3,5－三甲醛;达夫反应;间苯三酚;六次甲基四胺;三氟乙酸

[中图分类号]O625.41　[文献标志码]A　[文章编号]2095－7602(2021)02－0095－04

共价有机框架材料(COF)越来越引起研究者的关注[1]。2,4,6－三羟基苯－1,3,5－三甲醛(图 1)因其对称的结构,及其分子上含有的三个活泼的醛基和三个羟基,常用来合成共价有机框架材料[2-8]。2,4,6－三羟基苯－1,3,5－三甲醛不但可用来构建框架材料,其独特的分子结构也引起超分子化学家的兴趣,用以合成多种超分子结构[9-11]。

2,4,6－三羟基苯－1,3,5－三甲醛作为一种重要的有机试剂,其合成一般采用达夫反应(Duff reaction)来完成[12],虽然反应的产率较低,但可一步完成,且产物易于分离。达夫反应[13-16]又称"六亚甲基四胺甲酰化反应",是在酸性介质中,用六次甲基四胺(乌洛托品)对芳香族化合物进行甲酰化,从而生成芳香醛。此反应为亲电取代反应,亲电试剂为六次甲基四胺在酸性条件下衍生出来的亚胺正离子,甲酰基来源于六次甲基四胺中的亚甲基单元,该反应最初产物为芳香亚胺离子,经水解后得到芳香醛。用达夫反应合成 2,4,6－三羟基苯－1,3,5－三甲醛的反应方程式如图 2 所示。

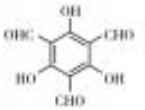

图 1　2,4,6－三羟基苯－1,3,5－三甲醛的分子结构

图 2　2,4,6－三羟基苯－1,3,5－三甲醛的合成反应方程式

由于文献上报道的达夫反应可在不同酸性介质中进行[13-16],合成不同的芳香醛所需反应温度不同[10-11],反应时间也不同[13-16],因此,分析不同反应条件对产率的影响,研究 2,4,6－三羟基苯－1,3,5－三甲醛的最佳合成条件,对合成该化合物有重要的意义。

[收稿日期]2020－07－15

[基金项目]黑龙江省教育厅备案项目"新型超分子自组装离子液晶研究"(1352MSYYB010)。

[作者简介]云观,男,助教,硕士,从事有机化学及生物化学研究。

[通讯作者]蒋舰,男,讲师,博士,从事超分子化学研究。

1 实验部分

1.1 仪器与试剂

核磁共振波谱仪(Bruker Avance 400,大连化学物理所)。

六次甲基四胺、间苯三酚购自阿拉丁(上海)试剂有限公司,两种试剂使用前在50℃下真空干燥3 h;三氟乙酸购自阿拉丁(上海)试剂有限公司,使用前未进行其他处理;二氯甲烷、无水硫酸镁购自国药集团化学试剂有限公司,使用前未进行其他处理。

1.2 2,4,6-三羟基苯-1,3,5-三甲醛的制备

分别准确称量六次甲基四胺20.550 g(147 mmol),干燥的间苯三酚6.014 g(49 mmol),放入250 mL三口瓶中,在氮气保护下,用注射器加入90 mL有机酸,反应在油浴下电磁搅拌,用秒表监控反应时间,反应混合物在100℃下搅拌2 h,向反应体系中加入水解试剂(3 mol/L HCl),水解1 h后停止反应。待体系温度降到室温,用G4砂芯漏斗过滤掉不溶性杂质,滤液用100 mL二氯甲烷萃取3次,合并有机层并用无水硫酸镁干燥,过滤,然后将滤液旋转蒸发得黄色固体,即为产物2,4,6-三羟基苯-1,3,5-三甲醛,产物纯度可达95%。产物可通过减压升华进一步纯化,纯化后产品为乳白色固体。

1.3 化合物表征

采用氢谱核磁共振对制备的化合物进行表征,测定化合物的结构和纯度。

2 结果和讨论

2.1 酸性介质对产率的影响

达夫反应制备芳香醛的反应过程中,六次甲基四胺需要进行两次质子化[9],因此介质酸的强度对反应的影响很大。文献报道中,达夫反应通常在醋酸或三氟乙酸中进行,我们分别对这两种有机酸进行研究,实验结果如表1所示。

表1 酸性介质对产率的影响

酸性介质	反应温度/℃	反应时间/min	水解试剂	产率/%
三氟乙酸	100	120	3 mol/L HCl	12.3
醋酸	90	120	3 mol/L HCl	0.0
醋酸	100	120	3 mol/L HCl	0.0
醋酸	118	120	3 mol/L HCl	0.0
醋酸	118	240	3 mol/L HCl	0.0

从表1可知,以三氟乙酸为介质,反应后可得到2,4,6-三羟基苯-1,3,5-三甲醛。但以醋酸为介质,在不同的反应条件下,都只能得到少量黄色液体,经氢谱核磁共振检测表明,黄色液体中不含有目标产物,因此以醋酸为反应介质,无法得到2,4,6-三羟基苯-1,3,5-三甲醛。醋酸和三氟乙酸的结构相似,但醋酸的酸性远小于三氟乙酸,因此醋酸的弱酸性导致该反应无法进行。

2.2 反应温度对产率的影响

反应的发生程度很大程度上取决于反应温度,因此反应温度是影响产率的一个重要因素。以三氟乙酸为酸性介质,反应时间为2 h,以3 mol/L HCl为水解试剂,考察温度对反应产率的影响,实验结果如表2所示。

表2 反应温度对产率的影响

反应温度/℃	产率/%
80	4.2
90	11.6
100	12.3
120	11.5

(C)1994-2021 China Academic Journal Electronic Publishing House. All rights reserved. http://www.cnki.net

由表2可知,反应在80℃时产率很低,随着温度提高,反应产率逐渐增大,当温度达到100℃时,产率达到12.3%。但继续升高温度,产率下降且产物颜色加深,氢谱核磁共振显示,产物中杂质增多,其原因可能是高温下发生聚合反应,所以该反应的最佳反应温度为100℃。

2.3 反应时间对产率的影响

由于化学动力学的原因,反应产率与反应时间密切相关。在100℃下,以三氟乙酸为酸性介质,以3 mol/L HCl为水解试剂,考察了反应时间对反应产率的影响,实验结果如表3所示。

表3 反应时间对产率的影响

反应时间/min	产率/%
30	2.3
60	9.7
120	12.3
180	11.5
240	10.8

随着时间的增加,产率逐渐增大,当反应时间大于2 h,继续增加反应时间,产率开始减小,反应体系颜色逐渐加深,并且处理后产物中的杂质增加。因此,从表3中可以看出,反应最佳时间为2 h,时间延长会导致副反应增加。

2.4 水解试剂对产率的影响

达夫反应的最初产物是芳香亚胺类结构,进行水解后才能得到芳香醛,水解试剂一般使用去离子水[9]或稀盐酸[3]。以三氟乙酸为酸性介质,反应温度100℃,反应时间为2 h,分别以去离子水和3 mol/L HCl为水解试剂,考察水解试剂对反应产率的影响,实验结果如表4所示。

表4 水解试剂对产率的影响

水解试剂	产率/%
去离子水	11.4
3 mol/L HCl	12.3

从表4可以看出,以去离子水和稀盐酸作水解试剂的产率相差不大,但稀盐酸略好,这可能因为酸性条件下亚胺的水解是可逆反应,酸性越强,平衡越倾向于生成芳香醛。

2.5 升华温度对升华产率的影响

反应结束后,经过后处理,可得到纯度达95%的2,4,6-三羟基苯-1,3,5-三甲醛,为了得到更纯的产物可进行减压升华。本研究考察了在油泵减压下(真空度约0.2 kPa),不同升华温度对升华产率(升华后的质量与升华前质量的比值)的影响,结果如表5所示。

表5 升华温度对升华产率的影响

升华温度/℃	升华时间/min	升华产率/%
120	120	42.3
140	120	46.5
160	120	69.1
180	120	47.2

实验结果表明,随着升华温度的增加,升华产率逐渐增大,当温度达到160℃时,升华产率达到69.1%,继续升高温度,产物迅速碳化,升华产率下降。

本研究也考察了延长升华时间对升华产率的影响,在升华温度为160℃时,将升华时间延长到3 h,产率未见增加,因此升华的最佳时间为2 h。

2.6 产品的^{1}H NMR表征

产品的核磁共振氢谱化学位移(400 MHz,$CDCl_3$)δ:14.10(s,3H),10.14(s,3H),与2,4,6-三羟基苯-1,3,5-三甲醛的结构一致。

3 结论

以间苯三酚、六次甲基四胺为反应物,经达夫反应合成了2,4,6-三羟基苯-1,3,5-三甲醛,并得到了适宜的反应条件:三氟乙酸为酸性介质,反应温度100℃,反应时间2 h,以3 mol/L HCl为水解试剂进行水解,2,4,6-三羟基苯-1,3,5-三甲醛的产率为12.3%,纯度为95%。继续提纯可使用减压升华的方法,升华温度为160℃,升华时间2 h。

[参考文献]

[1] LIU X G, HUANG D L, LAI C, et al. Recent advances in covalent organic frameworks (COFs) as a smart sensing material [J]. Chemical Society Reviews, 2019(48): 5266-5302.

[2] KAGZMAREK A M, LIU Y Y, KAGZMAREK M K, et al. Developing luminescent ratiometric thermometers based on a covalent organic framework (COF) [J]. Angewandte Chemie International Edition, 2020(59): 2-11.

[3] SHEN J, ZHANG H, SU Y L, et al. Polydopamine-modulated covalent organic framework membranes for molecular separation [J]. Journal of Material Chemistry, 2019(7): 18063-18071.

[4] DAUGHERTY M C, YITAKU E, LI R L, et al. Improved synthesis of beta-ketoenamine-linked covalent organic frameworks via monomer exchange reactions [J]. Chemical Communications, 2019(55): 2680-2683.

[5] ALBACETE P, MARTINEZ J, LI X, et al. Layer-stacking-driven fluorescence in a two-dimensional imine-linked covalent organic framework [J]. Journal of the American Chemical Society, 2018(140): 12922-12929.

[6] PETRYK M, SZYMKOWIAK J, GIERCZYK B, et al. Chiral, triformylphenol-derived salen-type [3+6] organic cages [J]. Organic & Biomolecular Chemistry, 2016(14): 7495-7499.

[7] CHONG J H, SAUER M, PATRICK B O, et al. Highly stable keto-enamine salicylideneanilines [J]. Organic Letters, 2003(5): 3823-3826.

[8] DUFF J C, BILL E J. Reactions between hexamethylenetetramine and phenolic compounds [J]. Journal of the American Chemical Society, 1932: 1987-1988.

[9] SMITH W E. Formylation of aromatic compounds with hexamethylenetramine and trifluoracetic acid [J]. Journal of Organic Chemistry, 1972(37): 3972-3973.

[10] 赵莹燕, 王李和, 李效军. Duff反应法合成5-壬基水杨醛 [J]. 化学工业与工程, 2014(31): 22-25.

[11] ANDREW A A, THOMAS G, SCOTT A, et al. A convenient one-step synthesis of 2-hydroxy-1,3,5-benzenetricarbaldehyde [J]. Synthetic Communications, 2000(30): 3227-3232.

Studies on Reaction Conditions for the Synthesis of Triformylphloroglucinol by Duff Reaction

YUN Guan, LIU Quan-jie, ZHANG Ke-xin, JIANG Jian

(College of Chemistry and Chemical Engineering, Mudanjiang Normal University, Mudanjiang 157000, China)

Abstract: Triformylphloroglucinol is an important intermediate in the synthesis of covalent organic framework materials and supramolecular structures. The synthesis of triformylphloroglucinol with Duff reaction methods has the advantages of simple operation and easy separation. The optimum reaction conditions for synthesis of triformylphloroglucinol were studied. The effects of acidic medium, reaction temperature, reaction time and other factors on the yield of the target compound were discussed in this paper.

Key words: triformylphloroglucinol; Duff reaction; phloroglucinol; hexamethylenetramine; trifluoracetic acid

3.云观,陈佳丽,蒋舰,邵艳秋.有机化学实验中废液及固废的处理[J].山东化工,2020,49(05):257-258.

有机化学实验中废液及固废的处理

云　观[1],陈佳丽[2],蒋　舰[1],邵艳秋[1]

(1. 牡丹江师范学院 化学化工学院,黑龙江 牡丹江　157011;2. 牡丹江龙江环保供水有限公司,黑龙江 牡丹江　157011)

摘要:本文总结了我校本科有机化学实验的实验项目及产生的废液、固废,并进行分类。通过中和至无毒化、蒸馏再利用、转化为其它实验的反应原料等环保安全的方法处理产生的废液、固废,可以减少有机化学实验对环境的污染,并且可以降低实验成本。

关键词:有机化学实验;废液;固废;处理办法

中图分类号:X703;X705　　文献标识码:B　　文章编号:1008-021X(2020)05-0257-02

DOI:10.19319/j.cnki.issn.1008-021x.2020.05.100

Treatment of Liquid and Solid Wastes in Organic Chemistry Experiments

Yun Guan[1], *Chen Jiali*[2], *Jiang Jian*[1], *Shao Yanqiu*[1]

(1. College of Chemistry and Chemical Engineering, Mudanjiang Normal University, Mudanjiang　157011, China;
2. Mudanjiang Longjiang Environmental Protection Water Supply Co., Ltd., Mudanjiang　157011, China)

Abstract: This paper summarizes the experimental items of organic chemistry experiment and the waste liquid and solid waste, and classifies them. The environmental protection and safety methods such as neutralization to non-toxicization, distillation and reuse, and conversion into other experimental reaction materials to deal with the waste liquid and solid waste can reduce the environmental pollution caused by organic chemistry experiments and reduce the experimental cost.

Key words: organic chemistry experiment; waste liquid; solid waste; treatment method

有机化学实验是本科教学中化学、生物、医学、高分子和材料科学等多专业的专业基础课,在有机化学实验中大多数实验都会产生废液及固废,如果在实验结束后不能及时处理实验产生的废弃物,将会对人体健康和环境造成危害和污染。目前绿色化学实验呼声渐高[1-3],进行环境无害的化学实验是化学实验教学领域的长期目标。本文主要介绍了本校本科有机化学相关实验时产生的废液、固废和处理办法。

1　有机化学实验中产生的废液及固废种类

根据现阶段本院本科生使用的教材[4],将其进行的全部有机化学实验的题目及废液固废类型进行了汇总,如表 1 所示。

表 1　有机化学实验项目及产生的主要废液固废

Table 1　Organic chemistry experiment topic and main waste liquid and solid waste

序号	实验项目	产生的主要废液及固废
序号	实验项目	产生的主要废液及固废
1	熔点的测定	液体石蜡
2	液态有机化合物折光率的测定	无
3	柱层析	无水乙醇、三氧化二铝粉末
4	重结晶提纯法	乙酰苯胺、活性炭
5	蒸馏和沸点测定	无水乙醇
6	分馏	丙酮、无水乙醇
7	环己烯的制备	环己烯、氯化钙
8	溴乙烷的制备	溴乙烷、硫酸
9	乙酸乙酯的制备	乙酸乙酯、硫酸镁
10	减压蒸馏	乙酸正丁酯
11	乙酰苯胺的制备	乙酰苯胺、乙酸、锌粉
12	茶叶中生物碱的提取	咖啡因、乙醇、茶叶

表 1(续)

序号	实验项目	产生的主要废液及固废
13	肉桂酸的合成	肉桂酸、苯甲醛
14	正丁醚的合成	正丁醚、硫酸、氯化钙
15	乙酸正丁酯的合成	乙酸正丁酯、乙酸、正丁醇、硫酸、硫酸镁
16	聚醋树脂的合成	聚醋树脂
17	甲基橙的合成	甲基橙、乙醇、乙醚
18	阿司匹林的制备	水杨酸
19	洗涤灵的制备	十二烷基硫酸钠

2　废液、固废类型及处理办法

2.1　废液及固废类型

2.1.1　干燥剂型

在实验环己烯的制备、乙酸乙酯的制备、正丁醚的合成、乙酸正丁酯的合成中,产生的氯化钙、硫酸镁废弃物均作为产品干燥时的干燥剂使用。这两种化学品在使用后均变为结晶水合物状态。

2.1.2　催化剂型

在正丁醚的合成实验和乙酸正丁酯的合成实验中,浓硫酸作为催化剂使用,在实验过程中会经过分液漏斗分出,成为废液。

2.1.3　反应原料型

在实验乙酰苯胺的制备、阿司匹林的制备、乙酸正丁酯、肉桂酸的制备中,乙酸、锌粉、水杨酸、正丁醇、苯甲醛五种有机物由于未完全反应,在进行除杂时,以杂质的形式被蒸馏或过滤出来形成废物。在实验茶叶中生物碱的提取中,乙醇作为萃取咖啡因的溶剂,在后期蒸馏时需蒸馏出大部分乙醇,成为废液。在实验溴乙烷的制备中,浓硫酸作为反应原料,过量和溴化钠进行反应,反应结束后剩余的硫酸分液漏斗分出,成为废液。

收稿日期:2019-12-17

基金项目:黑龙江省高等教育教学改革一般研究项目(SJGY20190688)

作者简介:云　观(1992—),助教,研究方向为有机化学与生物化学。

2.1.4 回收原料型

在实验蒸馏和沸点测定、分馏中，无水乙醇和丙酮作为实验式样进行使用，蒸馏和分馏出的无水乙醇和丙酮成为实验废液。在实验熔点的测定中，液体石蜡作为热溶液进行使用，多次使用后会被样品污染而成为废液。在实验柱层析中，无水乙醇作为洗脱剂使用，在洞洗色谱柱和洗脱亚甲基蓝时会和样品混合形成废液。在所有的蒸馏和分馏操作中，均会用到碎瓷片充当沸石，使用过后成为固废。

2.1.5 反应产物型

在所有的有机合成制备中，得到的有机物产品由于纯度和学生操作严谨度不同，不能直接用作化学试剂，成为废液及固废。

2.1.6 泄露危险品型

在使用水银温度计时，因为学生误操作造成水银泄露，成为泄漏危险品型废液。

2.1.7 洗涤剂型

在实验甲基橙的制备中，用到乙醚和乙醇进行洗涤甲基橙晶体，洗涤后成为废液。

2.1.8 碎玻璃型

学生在实验过程中，不可避免会造成玻璃仪器的打碎和损坏，形成固体废弃物。

2.2 废液及固废处理办法

2.2.1 中和无毒害处理

对于产生的干燥剂型、催化剂型、反应原料型、洗涤剂型废液及固废，可进行中和处理，采用碱性废液固废和酸性废液中和；也可采用药剂中和，即采用 Na_2CO_3、NaOH、石灰乳、碳酸钙、工业硫酸、盐酸等中和[8]，反应方程式为：$H^+ + OH^- \rightarrow H_2O$，$NaOH + HCl \rightarrow NaCl + H_2O$，$Na_2CO_3 + H_2SO_4 \rightarrow Na_2SO_4 + H_2O + CO_2\uparrow$，经过中和的废液可直接排放。对于产生的毒害性固废，例如温度计中水银，首先监督学生不要直接倒入下水道及垃圾箱，用硫磺粉覆盖于水银表面，生成无毒的硫化汞[9]，然后密封储存，交给有资质的废物处理企业进行处理。

2.2.2 蒸馏再利用处理

对于回收原料型废液，可进行再次利用。蒸馏和分馏操作产生的乙醇和丙酮，柱层析中洗脱用的乙醇，均可以收集起来再次蒸馏使用。蒸馏后的二次乙醇可用于清洗玻璃仪器，进行折光率测定的练习、蒸馏操作的练习等实验使用。使用过的沸石也可收集起来，使用二次乙醇浸泡清洗，烘干后可再次使用。

2.2.3 安全储存作为其它实验的反应原料

反应产物型废液及固废较难处理，反应产物无法直接作为成品化学试剂使用。对于此类废液及固废，应选用合适的容器安全储存，一部分可作为其它实验的实验原料。例如合成的肉桂酸，可以在下一届学生进行熔点测定实验时作为待测样品使用；学生合成的乙酰苯胺，由于苯胺氧化，变为粉红色，可以利用其进行重结晶基础操作；合成的阿司匹林，可以作为样品进行分析化学实验，测定其产品纯度；实验中合成的乙酸正丁酯可储存起来，作为减压蒸馏实验的原材料，让学生练习减压蒸馏实验操作；学生合成的洗涤灵进一步处理，制成成品洗涤灵，用以洗刷实验室的玻璃仪器。

对于环己烯、溴乙烷、咖啡因、甲基橙等反应产物固废处理，将一部分交给有相关科研项目的教师，其通过柱色谱等方法将固废提纯后使用，可减少这些教师的科研开支；剩余的部分进行安全储存，然后交给有废物处理资质的企业进行安全处理。

2.2.4 损坏玻璃仪器的再利用和处理

对于损坏的玻璃仪器，首先对其评估，对于可修理可再利用的玻璃仪器，先将其清洗干净，送到仪器维修部门进行修理；对于不可修理的玻璃仪器，则作为固体废弃物进行储存，然后交给有固废处理资质的企业进行处理。

3 小结

采用上述处理措施，可减少有机化学实验中的废液、固废排放量，降低实验开支，节省实验低值易耗经费。有机化学实验应逐渐实现绿色化，还需要更多的化学教育工作者们进一步努力。

参考文献

[1] 宋柱等. 绿色有机化学实验的探索和实践 [J]. 实验室研究与探索，2006(8)：989－991.
[2] 黄 丹，范崇允. 论有机化学实验的绿色化 [J]. 实验室研究与探索，2001(5)：37－38.
[3] 陆婉芳，吴美芳，黄良保，等. "绿色化"有机化学实验教学实践和探讨 [J]. 实验室研究与探索，2002(3)：14－15.
[4] 曾和平. 有机化学实验 [M]. 4 版. 北京：高等教育出版社，2014.
[5] 刘 炀. 化学清洗废液的现场处理方法 [J]. 清洗世界，2007(10)：30－35.
[6] 宋晓英. 血压计水银泄露时的正确处理方法 [J]. 医疗装备，2006(1)：13.

(本文文献格式：云 观，陈佳丽，蒋 靓，等. 有机化学实验中废液及固废的处理 [J]. 山东化工，2020，49(5)：257－258.)

(上接第 256 页)

4 结论

(1) 天然工况下，滑坡前缘局部发生缓慢蠕滑，暴雨工况下，该部位将产生滑动破坏，且滑坡整体安全裕度不大。猫子山滑坡是降雨、河水外因诱发的牵引式渐进破坏型滑坡，并且在暴雨工况下有整体滑动的可能。

(2) 降雨入渗会降低滑坡的整体稳定性，河水将促进滑坡前部主滑段变形甚至引起破坏。需要采取措施隔离水对滑体前缘的影响，提高滑坡的整体稳定性。

(3) 考虑滑坡的诱发因素，针对其破坏模式，建议采用如下防治措施。方案一：抗滑桩(两排)＋挡土墙＋截排水；方案二：耐方＋抗滑桩(一排)＋挡土墙＋截排水。具体采用何种方案，尚需考虑工程经济成本，比选确定。

参考文献

[1] 房 浩，李 媛，杨旭东，等. 2000－2015 年全国地质灾害发育分布特征分析 [J]. 中国地质灾害与防治学报，2018，29(5)：1－7.
[2] 成永刚. 论水对滑坡的作用 [J]. 四川建筑，2004，24(1)：53－54.
[3] 丁继新，尚彦军，杨志法，等. 降雨型滑坡预报新方法 [J]. 岩石力学与工程学报，2004，23(21)：3738－3743.
[4] 邓合玉，陈 勇. 库水升降条件下滑坡变形失稳机理研究 [J]. 三峡大学学报(自然科学版)，2018，40(6)：34－38.
[5] 尹晓萌，晏鄂川，杜 毅，等. 库水位下降条件下堆积层滑坡稳定性分析 [J]. 中国地质灾害与防治学报，2007，28(3)：8－15.
[6] 曹 伟. 论库水位变化对土质滑坡稳定性的影响 [J]. 山西师范大学学报(自然科学版)，2017(4)：128－133.
[7] 中华人民共和国国土资源部. GB/T 32864 2016 滑坡防治工程勘查规范 [S]. 北京：中国标准出版社，2016：14－15.

(本文文献格式：侯 倩，尹晓萌，王晓娟，等. 河水与降雨诱发某堆积层滑坡的破坏模式与防治方案 [J]. 山东化工，2020，49(5)：254－256，258.)

(C)1994-2020 China Academic Journal Electronic Publishing House. All rights reserved. http://www.cnki.net

4.云观,陈佳丽,刘艳爽,曹明星,杨春文.东北林蛙消化系统 LDH 同工酶表型的季节变化[J].黑龙江畜牧兽医,2018(01):215-217.

黑龙江畜牧兽医 2018(01):215-217 特种动物研究

DOI:10.13881/j.cnki.hljxmsy.2017.01.0136

东北林蛙消化系统 LDH 同工酶表型的季节变化

云 观,陈佳丽,刘艳爽,曹明星,杨春文*

(牡丹江师范学院,黑龙江 牡丹江 157011)

中图分类号:S865.3; Q55 文献标识码:B 文章编号:1004-7034(2018)01-0215-03

摘 要:为了解小兴安岭地区不同季节东北林蛙消化系统中食道、胃、肠道和肝脏的乳酸脱氢酶(LDH)同工酶的分布情况和活性,试验采用聚丙烯酰胺凝胶垂直板电泳对其进行分离分析。结果表明:东北林蛙消化系统4种器官组织中 LDH 同工酶共分离出电泳迁移率为 0.299~0.153,基因型为 C'4、CC'3、C2C'2、C3C'、C4、AB2C、B4、B'4、A2C2、A2B2、A2B'2、A3B、A4 的 LDH_1~LDH_{13}的 13 条谱带。4种器官组织在不同季节分离出的谱带数不同,在春季食道、胃、肠道和肝脏中均分离出 11 条谱带,夏季分别分离出 10,10,11,9 条谱带,秋季分别分离出 4,4,5,5 条谱带,冬季分别分离出 7,6,6,6 条谱带。电泳迁移率为 0.255,0.242 的 LDH_6 和 LDH_7 为冬季特有谱带。各组织中 LDH_{13} 活性均最强。LDH 同工酶的分布和活性具有明显的组织特异性,在不同季节的各组织器官中的表达程度不同,呈现多态性,具有季节性的差异。

关键词:东北林蛙;消化系统;聚丙烯酰胺凝胶电泳;乳酸脱氢酶(LDH);同工酶

东北林蛙(*Rana dybowskii*)原称中国林蛙(*Ranachensinensis*),属两栖纲无尾目蛙科蛙亚科 c 蛙属[1]。已被列入我国重点保护野生动物名录,属国家Ⅱ级保护动物,濒危野生动植物物种国际贸易公约(CITES)将其列入附录Ⅱ[2]。

乳酸脱氢酶(lactate dehydrogenase,LDH)参与糖酵解途径,是催化乳酸和丙酮酸相互转化的一种重要酶,几乎存在于所有组织中[3-4]。

关于东北林蛙 LDH 同工酶的相关研究已有很多报道[5-10],但对其季节变化的研究尚未见报道。本研究采用聚丙烯酰胺凝胶垂直板电泳方法,对东北林蛙春、夏、秋、冬四个季节消化系统中 LDH 同工酶进行分离、分析,以期为东北林蛙全人工养殖及进一步开发利用和深入研究提供基础数据。

1 材料

1.1 试验动物

东北林蛙于2015年1,5,8,10月份捕自黑龙江省小兴安岭地区铁力林业局的3年生健康成体蛙。

1.2 试验药品

丙烯酰胺、甲叉双丙烯酰胺、琼脂糖、三羟甲基氨基甲烷、乳酸钠,国药集团化学试剂有限公司生产;氯化硝基四氮唑蓝、氧化型辅酶Ⅰ、甲硫吩嗪,上海玉博生物科技有限公司生产;氯化钠、磷酸二氢钾、磷酸氢二钾、甘油、冰乙酸,天津博迪化工有限公司生产。以上药品均为国产分析纯或生化试剂。

1.3 试验仪器

三恒多用电泳仪(型号为 Eep3000)、水浴锅(型号为 HWS28),上海一恒科技有限公司生产;垂直板电泳槽(型号为 DYY—Ⅲ),北京六一仪器厂生产;和泰超纯水机,山东博科生物产业有限公司生产;高速冷冻离心机,(型号为 OULTER™ALLegra ™64R Centrifuge)Beckman 公司生产;电子天平(型号为 BP211D),德国塞多利斯公司生产;微量移液枪(SL-10、SL-100),RAININ Pipetlite Magetic Assist Pipette 公司生产;凝胶成像系统(型号为 MultiImage™ Light Cabinet),Alpha Innotech 公司生产。

2 方法

采用常规聚丙烯酰胺凝胶垂直板电泳方法[10],对东北林蛙消化系统(食道、胃、肠道和肝脏)中 LDH 同工酶进行分离、分析,并参照参考文献[12]对 LDH 同工酶进行染色,凝胶成像系统拍照并保存电泳图谱。电泳图谱下端为阳极,上端为阴极,LDH 同工酶命名顺序按阳极至阴极的顺序。

3 结果与分析

通过对东北林蛙的消化系统 LDH 同工酶进行电泳分析,参照参考文献[5,8-9]确定谱带位置并对酶

收稿日期:2017-01-07;修回日期:2017-11-29

基金项目:牡丹江师范学院科技项目(ZD2017002);黑龙江省高校科技创新团队项目"森林啮齿动物种群崩溃机理及控制技术研究"

作者简介:云 观(1992—),男,硕士研究生,研究方向为动物生理生化,wxcj90@126.com。

* 通信作者:杨春文(1958—),男,教授,博士,研究方向为动物生态学,wxjj90@126.com。

(C)1994-2021 China Academic Journal Electronic Publishing House. All rights reserved. http://www.cnki.net

谱进行分析，计算电泳迁移率[18]。

3.1 LDH 同工酶电泳结果

东北林蛙消化系统4种器官组织共分离出13种LDH同工酶谱带，春、夏、秋、冬季分别分离出11、11、5、7条谱带（见图1）。谱带分布和电泳迁移率见表1。

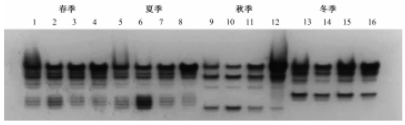

注：1-16分别表示春、夏、秋、冬不同季节中的食道、胃、肠道和肝脏；从下至上顺序是从阳极到阴极的顺序。

图1 东北林蛙消化系统LDH同工酶电泳结果

表1 东北林蛙消化系统LDH同工酶谱带分布及电泳迁移率

基因型	谱带	电泳迁移率	春季				夏季				秋季				冬季			
			食道	胃	肠道	肝脏	食道	胃	肠道	肝脏	食道	胃	肠道	肝脏	食道	胃	肠道	肝脏
A4	LDH_{A4}	0.153																
A3B	LDH_{A3B}	0.178																
A2B'2	$LDH_{A2B'2}$	0.191																
A2B2	LDH_{A2B2}	0.204																
A2C2	LDH_{A2C2}	0.217																
B'4	$LDH_{B'4}$	0.229																
B4	LDH_{B4}	0.242																
AB2C	LDH_{AB2C}	0.255																
C4	LDH_{C4}	0.261																
C3C'	$LDH_{C3C'}$	0.274																
C2C'2	$LDH_{C2C'2}$	0.280																
CC'3	$LDH_{CC'3}$	0.287																
C'4	$LDH_{C'4}$	0.299																

注：电泳迁移率0.299~0.153的顺序是从阳极到阴极的顺序，-表示有谱带分布，谱带深浅表示酶活性的大小。

3.2 LDH 同工酶的谱带分布

由图1、表1可见，东北林蛙消化系统4种器官组织共分离出电泳迁移率为0.299~0.153的LDH_1~LDH_{11}的13条谱带，参照参考文献[6,8]确定基因型分别为C'4、CC'3、C2C'2、C3C'、C4、AB2C、B4、B'4、A2C2、A2B2、A2B'2、A3B、A4。

春季东北林蛙食道、胃、肠道和肝脏中共分离出电泳迁移率分别为0.299~0.261和0.229~0.153的LDH_1~LDH_5和LDH_8~LDH_{11}的11条谱带，且基因型相同。夏季共分离出电泳迁移率为0.299~0.261和0.229~0.153的LDH_1~LDH_5和LDH_8~LDH_{11}的11条谱带，夏季食道和胃中缺失LDH_{11}，肝脏中缺失LDH_8和LDH_{11}。秋季共分离出电泳迁移率为0.299、0.229、0.204、0.191、0153的LDH_1、LDH_5、LDH_8、LDH_{11}、LDH_{10}的5条谱带，食道和胃缺失LDH_{10}。冬季共分离出电泳迁移率为0.261~0.242、0.217、0.204、0.178、0.153的LDH_1~LDH_5、LDH_8、LDH_{10}、LDH_{11}的7条谱带，胃、肠道和肝脏中缺失LDH_8。电泳迁移率为0.255和0.242的LDH_5和LDH_8是冬季特有谱带。

3.3 LDH 同工酶的活性分析

由图1、表1表可见，4种器官组织中LDH同工酶在春季、夏季、秋季和冬季均有表达，但表达强度各不相同。电泳迁移率为0.153的LDH_{A4}为4个季节各组织中共有谱带，其中食道LDH同工酶活性为冬季>春季>秋季>夏季，胃LDH同工酶活性为秋季>冬季>夏季>春季，肠道LDH同工酶活性为冬季>秋季>夏季>春季，肝脏LDH同工酶活性为秋季>夏季>春季>冬季。同一组织，不同季节之间LDH同工酶活性的表达强度也不同，食道的LDH同工酶活性为春季>夏季>冬季>秋季，胃的LDH同工酶活性为夏季>春季>冬季>秋季，肠道的LDH同工酶活性为夏季>春季>冬季>秋季，肝脏的LDH同工酶活性为秋季>春季>夏季>冬季>秋季，胃的LDH同工酶活性为夏季>春季>冬季>秋季，肠道的LDH同工酶活性为夏季>春季>冬季>秋季，肝脏的LDH同工酶活性为秋季>春季>夏季>冬季。同一季节，不同组织中LDH同工酶活性的表达强度不同，春季LDH同工酶活性为肝脏>胃>食道>肠道，夏季和秋季LDH同工酶活性为肝脏>胃>肠道>食道，冬季LDH同工酶活性为肠道>肝脏>食道>胃。

4 讨论

春、夏、秋和冬各季节LDH同工酶在东北林蛙消化系统中均有表达。春季东北林蛙消化系统相对其他3个季节分离出的谱带数最多，其食道、胃、肠道和肝脏均分离出LDH_1~LDH_5、LDH_8~LDH_{11}的11条谱带。从电泳图谱上可以看出，春季和夏季LDH-C基因控制的谱带表达完全，春季消化系统由冬眠进入复苏季节或是机体调控机制应激反应的表现，与春季繁殖功能相适应。夏季东北林蛙肝脏活性LDH_A>LDH_5，这与夏季代谢力高、觅食量大有关。秋季东北林蛙食道和胃只有LDH_5、LDH_8、LDH_{10}、LDH_{11}表达，肠道和肝脏同时有LDH_{A4}表达，与潜入冬眠的时期代谢减弱有关。冬季东北林蛙食道有基因型为A2C2的LDH_{A4}谱带，为冬眠状态的谱带特征。LDH_5和LDH_8为冬季特有条带，且LDH_5活性最高，这与韩雅莉[18]和李永通等[19]报道结果相符。秋季和冬季LDH-C基因分别表达出LDH_1和LDH_5，这区别于春、夏季的季节代谢变化和繁殖特征。通过基因型LDH-C的表达特点看出，基因调控通过季节变化在LDH同工酶谱带特征上表现出来。

在肝脏中LDH_{A4}对乳酸的亲和力弱，糖酵解反应活跃的组织中含量较高，这与肝组织是耐缺氧器官是相适应的[5,8]。高浓度的LDH_1对满足组织在低氧或缺氧状态下的能量需要是非常重要的[18]。LDH1对乳酸的亲和力强，主要催化乳酸氧化成为丙酮酸而进入三羧酸循环，用以能量供应，这与东北林蛙所处的生态位有关，是其代谢需要而相适应的环境决定的。LDH_1可有效地防止乳酸产生而引起的疲劳，同时又不防碍对乳酸的利用。不同季节消化系统中LDH_{A4}的活性均远远高于LDH_1，说明在其消化系统中有活跃的糖酵解反应，与两栖动物处于进化树相对低的位置或者是其消化系统在进化过程中的不完善密切相关[15-16]。东北林蛙被分为4个亚种，在中国分布较广泛，且变异很大[20-21]。本研究结果与张辉等[20]、刘学龙等[19]的报道结果有所不同，这可能与研究材料的取材地点不同有关，亚种不同，基因表达特点也不同。

5 结论

东北林蛙的消化系统LDH同工酶在不同季节、不同组织中的表达有明显差异。谱带分布与季节有显著相关性。根据东北林蛙消化系统LDH同工酶基因表达的季节性特征，推测其基因表达的差异与环境因素影响具有相关性。不同组织中所呈现的特异性同工酶谱与其特定生理功能和代谢类型密切相关。因此，可根据东北林蛙消化系统中LDH同工酶的表型分布差异分析季节变化对东北林蛙食性、消化、繁殖等代谢特征的影响。

参考文献：

[1] 费梁.中国动物志:两栖纲(下)(无尾目 蛙科)[M].北京:科学出版社,2009.

[2] 王志坚.国家林业局令第七号——国家保护的有益的或者有重要经济、科学研究价值的陆生野生动物名录[J].野生动物,2000,31(5):40-42.

[3] 张碧霞.乳酸脱氢酶对垂性静脉的诊断意义[J].国际检验医学杂志,2010,31(10):1172-1173.

[4] YU C F. Gel Electrophoresis Analysis of lactate dehydrogenase isozymes(LDH) in the serum of rabbit[J]. Chinese J Rabbit Farming,1995,31(1):20-26.

[5] 刘学龙,陶玉琍,崔鹏鹏.长白山区中国林蛙乳酸脱氢酶同工酶多态性的研究[J].黑龙江畜牧兽医,2004(9):8-10.

[6] 田新民,金建湘,石兰英,等.低温胁迫下东北林蛙不同组织乳酸脱氢酶活性分析[J].黑龙江畜牧兽医,2013(11上):107-109.

[7] 李勋,赵文阁,付红霞,等.黑龙江省五种无尾两栖类的同工酶研究[J].哈尔滨师范大学自然科学学报,1994,10(4):63-69.

[8] 张辉,吴清江.中国林蛙乳酸脱氢酶多基因系统及基因间遗传联关系的研究[J].遗传学报,1996,23(1):11-17.

[9] 崔鹏鹏,陶玉琍,刘学龙,等.长白山区中国林蛙乳酸脱氢酶的同工酶初步研究[J].黑龙江畜牧兽医,2004(2):51.

[10] 韩雅莉.中国林蛙六种组织乳酸脱氢酶同工酶的研究[J].内蒙古农牧学院学报,1992,13(4):55-59.

[11] 李建武,萧能杰,余瑞元,等.生物化学实验原理和方法[M].北京:北京大学出版社,1994.

[12] 陈毓荃.生物化学试验方法和技术[M].北京:科学出版社,2002.

[13] 金建湘,林春文,田新民,等.北骨骼蝶翼期不同组织 SOD 和 LDH 同工酶分析[J].黑龙江农学报,2015,24(1):23-27.

[14] 李永通,吴至康.贵州北部四种两栖类乳酸脱氢酶同工酶的比较研究[J].动物学研究,1991,12(2):193-198.

[15] 金建湘,林春文,金志民.刺蛹乳酸脱氢酶和超氧化物歧化酶同工酶的研究[J].中国林副特产,2005,(3):42-44.

[16] 邢克洲,陈子强,李一飞.东方粉蝶不同发育阶段乳酸脱氢酶同工酶的变化[J].动物学杂志,1992,27(4):18-21.

[17] 魏刚,陈服官,徐宁,等.中国林蛙 *Rana chaninensis* 系统发育及物种形成和分化的研究[J].动物学报,1990,36(1):76-81.

[18] 魏刚,陈服官,徐宁,等.中国林蛙新亚种研究[J].动物分类学报,1991,16(3):295-302.

[19] 刘学龙,陶玉琍,崔鹏鹏.长白山区中国林蛙乳酸脱氢酶同工酶多态性的研究[J].实验研究,2004,46(9):8-10.

(C)1994-2021 China Academic Journal Electronic Publishing House. All rights reserved. http://www.cnki.net

(C)1994-2021 China Academic Journal Electronic Publishing House. All rights reserved. http://www.cnki.net

5.陈佳丽,云观,金建丽,杨松鹏,田新民.东北林蛙消化系统SOD和POD同工酶电泳分析[J].黑龙江畜牧兽医,2017(01):219-221.

其间夹杂有杯状细胞,牛和水牛的胆囊固有层内分布较多的腺体,而猪和肉食动物的较少[5,9]。有研究表明,扬子鳄[8]、鳖[9]、丹顶鹤[10]、胡子鲶[11]的胆囊壁固有层内无腺体。由此可见,黑熊胆囊壁的黏膜固有层不同于禽类、鱼类、爬行类动物,与牛胆囊壁的结构相似,与猪、肉食动物不同,但黏膜上皮细胞间未观察到杯状细胞。

通常认为,动物胆囊的主要功能是储存和浓缩胆汁,华田苗等[6]、朱平等[7]通过光镜或电镜观察认为,丹顶鹤和扬子鳄胆囊上皮细胞中充满分泌颗粒,因此胆囊上皮细胞不仅有吸收功能而且还具有分泌功能。此外,孔小明等[10]研究表明,黄牛和水牛胆囊壁固有层内均有腺体,黄体的腺体明显多于水牛,且认为腺体可分为浆液腺、黏液腺、混合腺[1-2]。试验结果表明,黑熊胆囊壁黏膜上皮和固有层内管状腺上皮细胞胞浆内均含有大量的PAS反应强阳性的微细颗粒,而且在黏膜上皮表面和管状腺腺腔内可见少量PAS反应强阳性物质,说明这些上皮细胞不仅有吸收功能,还具有分泌功能,而且黏膜上皮和固有层管状腺上皮细胞胞浆内的物质呈PAS反应强阳性,说明其分泌物中均含有黏多糖,这些分泌物与胆汁形成、分泌中的作用机制还有待于进一步研究。

参考文献:
[1] 马逸清,徐利,胡锦矗.中国熊类资源数量估计及保护对策[J].生命科学研究,1998,2(3):205-211.
[2] 曹识.熊猫繁育业与野生动物保护关系研究[D].哈尔滨:东北林业大学,2014.
[3] KONG X M, CHENG S J, BELKHIRI M, et al. A comparative study of gallbladder histochemistry in B. Bubalis and B. Taurus [J]. Acta Zoologica Sinica, 2000, 46(2):121-129.
[4] 李继承.组织学与胚胎学[M].杭州:浙江大学出版社,2003.
[5] 沈霞芬.家畜组织学与胚胎学[M].北京:中国农业出版社,2010.
[6] 华田苗,陈士超,陈世辉,等.扬子鳄胆囊的组织学研究[J].解剖学杂志,2001,24(2):125-127.
[7] 赵万鹏,赵宏霞,英冬梅.鳖胰腺和胆囊组织学的初步观察[J].信阳师范学院学报(自然科学版),2006,19(3):300-302.
[8] 朱平,姜叔诚.丹顶鹤胆囊的显微观察[J].动物学杂志,1998,33(6):26-28.
[9] 乐雅文,刘翠敏,郭志荣.胡子鲶(*Clarias fuscus Lacepede*)肝脏、胆囊以及胰脏组织学的初步研究[J].内蒙古大学学报(自然科学版),2001,32(4):439-411.
[10] 周艳.熊猫无管引流采胆技术的研究[D].哈尔滨:东北林业大学,2012.
[11] 孔小明,高作信,郑明学.不同品种和年龄牛胆囊的比较组织学研究[J].畜牧兽医学报,1993,24(6):532-536.

(015)

东北林蛙消化系统SOD和POD同工酶电泳分析

陈佳丽,云 观,金建丽,杨松鹏,田新民
(牡丹江师范学院 生命科学与技术学院,黑龙江 牡丹江 157011)

中图分类号:S865.9;Q554 文献标识码:B 文章编号:1004-7034(2017)01-0219-03
DOI:10.13881/j.cnki.hljxmsy.2017.0169
关键词:东北林蛙;聚丙烯酰胺凝胶电泳;超氧化物歧化酶(SOD);过氧化物酶(POD);同工酶

摘 要:为了对东北林蛙的人工养殖和深入研究提供基础的生理生化指标依据,试验采用聚丙烯酰胺凝胶垂直板电泳方法,对东北林蛙春季消化系统中食道、胃、肠道、肝脏4种器官组织的超氧化物歧化酶(SOD)和过氧化物酶(POD)同工酶进行分离、分析。结果表明:东北林蛙消化系统中共分离出SOD_1~SOD_6、电泳迁移率为0.649~0.034的16条谱带;共分离出POD_1~POD_{13}、电泳迁移率为0.814~0.093的13条谱带。4种器官组织中SOD和POD活性顺序相同,均为肝脏>食道>胃>肠道。

收稿日期:2015-11-02;修回日期:2016-11-23
基金项目:牡丹江师范学院研究生科技创新项目(yjscxcx2015-11mdjnu);牡丹江师范学院科研项目指导项目(科技)(ZD2017002);黑龙江省教育厅科学技术项目(12541836)
作者简介:陈佳丽(1990-),女,硕士研究生,研究方向为动物生理生化,wcxjl@126.com.
通信作者:金建丽(1959-),女,教授,本科,研究方向为动物生理生化,wcxjl@126.com.

东北林蛙(*Rana dybowskii*)属两栖纲无尾目蛙科蛙亚科蛙属[1],已被列入国家保护的有益的或者有重要经济、科学研究价值的陆生野生动物名录[2]。东北林蛙是传统药用动物,又是营养丰富的美味食品,是重要的经济类动物。

超氧化物歧化酶(Superoxide dismutase,SOD)是催化超氧阴离子自由基(O^{2-})发生歧化反应的一类

金属酶，是机体最重要的抗氧化防御酶类。其基本功能是清除生物体内过高浓度的超氧阴离子自由基，保持体内自由基的代谢平衡，从而保持细胞正常的代谢不受破坏[1]。过氧化物酶（Peroxidase，POD）存在于细胞的过氧化物体内，其主要功能是清除氨基酸分解代谢及糖醛酸合成代谢等过程中形成的过氧化物。在肝细胞中数量特别多，过氧化物酶体的标志酶是过氧化氢酶，它的作用主要是将过氧化氢水解，对细胞起保护作用[2]。

关于动物体的不同器官组织同工酶的研究已有研究报道[3-8]，但对东北林蛙消化系统中 SOD 和 POD 同工酶研究尚未见报道。研究采用聚丙烯酰胺凝胶垂直板电泳方法，对东北林蛙春季消化系统中食道、胃、肠道、肝脏 4 种器官组织的 SOD 和 POD 同工酶进行分离、分析，为东北林蛙的人工养殖、解决圈养越冬、疾病和食物等问题的深入研究提供生理生化指标。

1 材料

东北林蛙，捕自黑龙江省小兴安岭地区的健康成年个体。

2 方法

采用常规聚丙烯酰氨凝胶垂直板电泳方法[9]，对东北林蛙消化系统（食道、胃、肠道、肝脏）中 SOD 和 POD 同工酶进行分离、分析，并进行染色[9]。凝胶成像系统拍照，保存电泳。为体现电泳重复性，每个样本分别在相邻泳道点样 3～4 次。电泳图下端为阳极，上端为阴极，SOD 和 POD 同工酶命名顺序按阳极至阴极顺序。电泳迁移率的计算见参考文献[10]。

3 结果与分析

通过对东北林蛙的消化系统（食道、胃、肠道、肝脏）中 SOD 和 POD 同工酶进行电泳分析，得到电泳图谱。

3.1 SOD 同工酶电泳结果与分析

食道、胃、肠道、肝脏中分别分离出 8、6、4、11 条谱带，其活性依次为肝脏＞食道＞胃＞肠道，其中肝脏的 SOD 活性最强且谱带数最多，见表 1。东北林蛙的消化系统中共分离出 SOD_1～SOD_{16}，电泳迁移率为 0.649～0.034 的 16 条谱带，见图 1。

由表 1、图 1 可知：食道、胃、肠道、肝脏的共有谱带为 SOD_7、SOD_{11}，电泳迁移率分别为 0.628、0.135。电泳迁移率为 0.230、0.209、0.034 的 SOD_4、SOD_{10}、SOD_{16} 谱带为食道特有谱带，电泳迁移率为 0.649、0.074 的 SOD_1、SOD_{14} 谱带为肠道特有谱带，电泳迁移率为 0.601、0.453、0.297、0.176 的 SOD_3、SOD_5、SOD_6、SOD_8、SOD_{13} 谱带为肝脏特有谱带。

3.2 POD 同工酶电泳结果与分析

食道、胃、肠道、肝脏中分别分离出 7、7、5、10 条谱带，见表 2。POD 在消化系统中共分离出电泳迁移率为 0.814～0.093 的 13 条谱带，即 POD_1～POD_{13}，见图 2。

表 1 SOD 同工酶谱带分布和电泳迁移率

项目	电泳迁移率	食道	胃	肠道	肝脏
SOD_1	0.034	—			
SOD_2	0.054	—	—		—
SOD_3	0.074			—	
SOD_4	0.088	—	—		—
SOD_5	0.135	—	—	—	—
SOD_6	0.176				—
SOD_7	0.209	—			
SOD_8	0.230	—			
SOD_9	0.250		—		—
SOD_{10}	0.277		—		—
SOD_{11}	0.297				—
SOD_{12}	0.453				—
SOD_{13}	0.500	—			—
SOD_{14}	0.601				—
SOD_{15}	0.628	—	—	—	—
SOD_{16}	0.649				—

注：电泳迁移率 0.649～0.034 的顺序是从阳极到阴极的顺序，表示 SOD 电泳谱带在此处有分布，谱带颜色深浅代表蛋白质含量的高低。

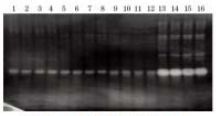

1～4. 食道；5～8. 胃；9～12. 肠道；13～16. 肝脏；从下至上顺序是从阳极到阴极。

图 1 SOD 同工酶电泳结果

由表 2、图 2 可知：POD_1、POD_3、POD_6、POD_9 谱带为食道、胃、肠道、肝脏中共有谱带，电泳迁移率分别为 0.707、0.657、0.500、0.443；食道和胃的 POD 谱带相同均有 POD_2、POD_4、POD_5～POD_7、POD_8、POD_{10} 谱带，但酶活性有差异，即食道＞胃；肝脏特有 6 条谱带，是电泳迁移率分别为 0.814、0.628、0.407、0.143、0.114、0.093 的 POD_1、POD_2、POD_8、POD_{11}、POD_{12}、POD_{13}；肠道有 POD_2、POD_3、POD_5～POD_7 5 条谱带，电泳迁移率分别为 0.707、0.657、0.543、0.500、0.443，缺失带数较多，POD 相对活性最弱且动物具有吞噬功能的白细胞等含有丰富的过氧化物酶，因此在血液丰富、白细胞及吞噬细胞含量较多的肝脏中 POD 同工酶的表达较强，进一步说明同工酶的表达和活性与组织功能相一致[12]。

表 2 POD 同工酶谱带分布和电泳迁移率

项目	电泳迁移率	食道	胃	肠道	肝脏
POD_1	0.093				—
POD_2	0.114				—
POD_3	0.143				—
POD_4	0.257	—	—		
POD_5	0.286	—	—		
POD_6	0.407				—
POD_7	0.443	—	—	—	—
POD_8	0.500	—	—	—	—
POD_9	0.543	—	—	—	
POD_{10}	0.628				—
POD_{11}	0.657	—	—	—	—
POD_{12}	0.707	—	—	—	—
POD_{13}	0.814				—

注：电泳迁移率 0.814～0.093 的顺序是从阳极到阴极的顺序，表示 POD 电泳谱带在此处有分布，谱带颜色深浅代表蛋白质含量的高低。

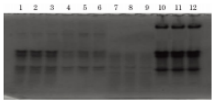

1～3. 食道；4～6. 胃；7～9. 肠道；10～12. 肝脏；从下至上顺序是从阳极到阴极。

图 2 POD 同工酶电泳结果

谱带数最少。

食道、胃部、肝脏 POD 在电泳迁移率为 0.443 的 POD_7 谱带活力最强，肠道 POD 在电泳迁移率为 0.543 的 POD_9 谱带活力最强。消化系统中 POD 活性依次为肝脏＞食道＞胃＞肠道，其中肝脏的 POD 活性最强且谱带数最多。

4 讨论

在生理状态下，SOD 自由基的产生和清除处于动态平衡，任何原因导致自由基产生过多或自由基清除不力均可使自由基浓度平稳加，进而引发 DNA 断裂、脂质过氧化、酶蛋白失活等，从而引起机体氧化应激反应。在这些活性氧产生及转化中，SOD 等起着非常重要的作用[13]。SOD 清除 O^{2-} 的能力与其含量和活性有关[14]。

东北林蛙的 SOD 和 POD 在肝脏中含量最多且活性最强，说明肝脏在机体酶反应中起到很重要的作用。SOD 是催化 O^{2-} 发生歧化反应的一类金属酶，是机体最重要的抗氧化防御酶类。POD 主要功能是清除氨基酸分解代谢及糖醛酸合成代谢等过程中形成的过氧化物，酶的作用分工明确，春季动物复苏，但是氧气供应仍然不足，糖酵解功能过程增强，POD 水解过氧化氢细胞毒性物质能力增强。电泳图谱体现出这一点。这一方面更能体现出春季正直动物的繁殖季节，觅食和寻求异性等活动达到高峰。这一结论与姚登邦等[15]的研究结论相一致。

5 结论

SOD 和 POD 同工酶在东北林蛙消化系统中均有表达；在消化系统的各组织内和组织间谱带分布和酶活性均存在较大差异，SOD 和 POD 同工酶的活性均在肝脏中表达最强；各组织中均存在谱带缺失现象。这些差异是由有关基因表达和调控的差异造成的[16]。

参考文献：

[1] 费梁. 中国动物志：两栖纲（下卷）（无尾目 蛙科）[M]. 北京：科学出版社，2009.

[2] 王志宝. 国家保护的有益的或者有重要经济、科学研究价值的陆生野生动物名录 [J]. 野生动物，2000 (5)：70.

[3] 徐立红，张甬元，陈宜瑜. 分子生态毒理学研究进展及其在水环境保护中的意义 [J]. 水生生物学报，1995，19 (2)：171－185.

[4] 陈晓虹，王林英，曹文元. 阿霉素小鼠红两种动物酯酶、过氧化物酶同工酶的比较研究 [J]. 动物学杂志，2000，35 (5)：19－23.

[5] 赵晓平，常顺利，刘晓光. 家鸽不同组织同工酶的初步研究 [J]. 四川动物，2008，27 (6)：1017－1020.

[6] 陈瑶. 达唐鲫四种鱼类三种同工酶的组织分布及基因位点分析 [D]. 呼和浩特：内蒙古农业大学，2006.

[7] 邓楚平，刘楚辉. 赤点石斑鱼 4 种同工酶的组织分布及基因位点分析 [J]. 浙江海洋学院学报（自然科学版），2004，23 (2)：103－106.

[8] 李淑武，蒋艳，金福元，等. 生物化学实验原理和方法 [M]. 北京：北京大学出版社，1994.

[9] 陈毓荃. 生物化学实验方法和技术 [M]. 北京：北京大学出版社，2002.

[10] 杨晓苏，贵州几种野生鱼类染色体组型与酯酶同工酶研究 [M]. 贵阳：贵州大学，2007.

[11] 黄宏华，贾书英，Cd、Hg 对蟾蜍肝匀浆超氧化物歧化酶活性及其同工酶的影响 [J]. 四川动物，2005，24 (2)：152－156.

[12] 陈晓虹，王林英，曹文元. 阿霉素小鼠两种动物酯酶-过氧化物酶同工酶的比较研究 [J]. 动物学杂志，2000，35 (5)：19－23.

[13] 姚登邦，于红娟，张建伟，等. 不同季节高脂肪氧乳酸菌发酵活力和同工酶谱 [J]. 中国应用生理学杂志，2007，23 (3)：365－369.

(015)

(C)1994-2021 China Academic Journal Electronic Publishing House. All rights reserved. http://www.cnki.net

(C)1994-2021 China Academic Journal Electronic Publishing House. All rights reserved. http://www.cnki.net

蒋舰发表科研论文目录（共 2 篇）

1.Jiang J. Observation of a 3-in-1 Russian-doll-like Complex in Solution[J]. Chemical Research in Chinese Universities, 2021: 1-3.

2.李静,蒋舰,负涛,邵艳秋.功能性离子液体的应用研究进展[J].黑龙江工业学院学报(综合版),2021,21(02):98-103.

1.Jiang J. Observation of a 3-in-1 Russian-doll-like Complex in Solution[J]. Chemical Research in Chinese Universities, 2021: 1-3.

Letter

Observation of a 3-in-1 Russian-doll-like Complex in Solution

JIANG Jian[✉]

Received March 25, 2021
Accepted June 30, 2021
© Jilin University, The Editorial Department of Chemical Research in Chinese Universities and Springer-Verlag GmbH

Keywords Schiff-base macrocycle; Russian-doll-like; 3-in-1 complex; $CBPQT^{4+}$; Tetrathiafulvalene(TTF)

Supramolecular chemistry is based on non-covalent interactions that enable molecular recognition. By weak interactions, a large number of structures, such as rotaxane[1,2] and catenane[3,4], as well as more complex structures[5,6] have been assembled. The Borromean rings[5,6] and Schiff-base macrocycles[7,8] are becoming attractive in these years because of their diversity of structures and ability to self-assemble. Till now, researchers have reported a multitude of other fascinating supramolecular constructs[9,10].

In the recent years, so much attention has been paid to the synthesis and supramolecular chemistry of macrocycles constructed from Schiff base condensation[8,11,12]. Simple and elegant, this reaction can be used to attain large and functional macrocycles[13,14], as well as more complex structures[15]. These cycles are attractive for their supramolecular structure[16], liquid crystallinity[16], and potential for catalysis[17] and sensor[18].

We have reported that wide-mouthed Schiff-base macrocycle 1 and some related cycles bind organic cations in their interiors[19]. Remarkably, macrocycle 1 adopts a calixarene-like cone conformation with a very wide(ca. 1.23 nm×0.93 nm from semi-empirical calculations) opening that allows it to bind the macrocycle cyclobis(paraquat-*p*-phenylene)($CBPQT^{4+}$). From a Jobplot analysis, the host-guest complex($CBPQT^{4+}\subset$ 1) has a 1:1 stoichiometry and the binding constant is substantial[$(1.68\pm0.53)\times10^5$ $L\cdot mol^{-1}$].

By electrostatic attraction, macrocycle 1 and $CBPQT^{4+}$ (Fig.1) have been assembled to a unique ring-in-ring structure. The complex is a promising precursor for constructing Russian-doll-like superstructures, which have attracted so much attention in this decade. In recent years, although the assembly of Russian-doll-like structure is a target for supramolecular research, only a few cases of such structures have been reported[20–24], which may be attributed to the lack of large and suitable macrocycles. Among cases reported, however, to the best of our knowledge, there is no example of such hierarchical architectures assembled by Schiff-base macrocycle. Herein, we report the observation of a Russian-doll-like structure constructed by Schiff-base macrocycle, tetracationic cyclophane and a small organic molecule in solution.

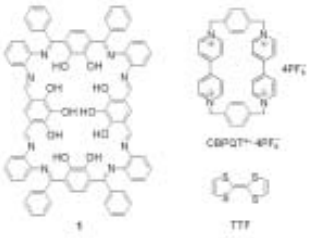

Fig.1 Structures of compounds 1, $CBPQT^{4+}\cdot4PF_6^-$ and TTF

Originally reported by Stoddart in 1988[25], $CBPQT^{4+}\cdot4PF_6^-$ has since aroused many interests to assemble varies of superstructures, such as host-guest complexes[26], rotaxanes[27] and catenanes[28]. In each case, the electron deficient $CBPQT^{4+}$ moiety interacts with the electron rich guest through electrostatic interactions. One notable example is its ability to form an inclusion structure with electron-rich tetrathiafulvalene(TTF), which shows a 1:1 stoichiometry[25] and the high binding constant in MeCN[29]. Formation of the host-guest complex encouraged us to study whether TTF can be bound inside the cavity of $CBPQT^{4+}$ in the complex $CBPQT^{4+}\subset$ 1 to form a unique Russian-doll-like 3-in-1 complex.

The ^1H NMR spectra of different assemblies of macrocycle 1, cyclobis(paraquat-*p*-phenylene), and tetrathiafulvalene in acetone-d_6 are exhibited in Fig.2. In the spectrum of macrocycle 1, the peaks at δ 14.47 and δ 14.35 are assigned to the hydroxyl protons. Adding $CBPQT^{4+}$ to the solution of macrocycle 1 resulted in the downfield shift to δ 14.76 and δ 14.67, respectively. Changes of chemical shift of hydroxyl protons indicated $CBPQT^{4+}$ was included inside macrocycle 1(the inclusion structure was proved by 2D ROESY NMR and MALDI-TOF MS[23]). When TTF was added to the solution, the two resonances further shifted to δ 14.79 and δ 14.78, respectively, indicating there is an interaction between tetrathiafulvalene and the ring-in-ring $CBPQT^{4+}\subset$ 1 structure.

✉ JIANG Jian
jianjiang@mdjnuedu.cn
School of Chemistry and Chemical Engineering, Mudanjiang Normal University, Mudanjiang 157000, P. R. China

https://doi.org/10.1007/s40242-021-1146-y

Letter

Observation of a 3-in-1 Russian-doll-like Complex in Solution

JIANG Jian[✉]

Received March 25, 2021
Accepted June 30, 2021
© Jilin University, The Editorial Department of Chemical Research in Chinese Universities and Springer-Verlag GmbH

Keywords Schiff-base macrocycle; Russian-doll-like; 3-in-1 complex; CBPQT⁴⁺; Tetrathiafulvalene(TTF)

Supramolecular chemistry is based on non-covalent interactions that enable molecular recognition. By weak interactions, a large number of structures, such as rotaxane[1,2] and catenane[3,4], as well as more complex structures[5,6] have been assembled. The Borromean rings[5,6] and Schiff-base macrocycles[7,8] are becoming attractive in these years because of their diversity of structures and ability to self-assemble. Till now, researchers have reported a multitude of other fascinating supramolecular constructs[9,10].

In the recent years, so much attention has been paid to the synthesis and supramolecular chemistry of macrocycles constructed from Schiff base condensation[7,8]. Simple and elegant, this reaction can be used to attain large and functional macrocycles[7,8], as well as more complex structures[11]. These cycles are attractive for their supramolecular structure[8], liquid crystallinity[8], and potential for catalysis[12] and sensor[13].

We have reported that wide-mouthed Schiff-base macrocycle 1 and some related cycles bind organic cations in their interiors[12]. Remarkably, macrocycle 1 adopts a calixarene-like cone conformation with a very wide(ca. 1.23 nm×0.93 nm from semi-empirical calculations) opening that allows it to bind the macrocycle cyclobis(paraquat-*p*-phenylene)(CBPQT⁴⁺). From a Jobplot analysis, the host-guest complex(CBPQT⁴⁺⊂ 1) has a 1:1 stoichiometry and the binding constant is substantial[(1.68±0.53)×10⁶ L·mol⁻¹].

By electrostatic attraction, macrocycle 1 and CBPQT⁴⁺ (Fig.1) have been assembled to a unique ring-in-ring structure. The complex is a promising precursor for constructing Russian-doll-like superstructures, which have attracted so much attention in this decade. In recent years, although the assembly of Russian-doll-like structure is a target for supramolecular research, only a few cases of such structures have been reported[14–16], which may be attributed to the lack of large and suitable macrocycles. Among cases reported, however, to the best of our knowledge, there is no example of such hierarchical architectures assembled by Schiff-base macrocycle. Herein, we report the observation of a Russian-doll-like structure constructed by Schiff-base macrocycle, tetracationic cyclophane and a small organic molecule in solution.

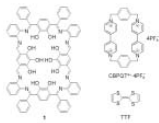

Fig.1 Structures of compounds 1, CBPQT⁴⁺·4PF6⁻ and TTF

Originally reported by Stoddart in 1988[17], CBPQT⁴⁺·4PF6⁻ has since aroused many interests to assemble varies of superstructures, such as host-guest complexes[18], rotaxane[19] and catenane[20]. In each case, the electron-deficient CBPQT⁴⁺ moiety interacts with the electron rich guest through electrostatic interactions. One notable example is its ability to form an inclusion structure with electron-rich tetrathiafulvalene(TTF), which shows a 1:1 stoichiometry[21] and the high binding constant in MeCN[18]. Formation of the host-guest complex encouraged us to study whether TTF can be bound inside the cavity of CBPQT⁴⁺ in the complex CBPQT⁴⁺⊂ 1 to form a unique Russian-doll-like 3-in-1 complex.

The ^{1}H NMR spectra of different assemblies of macrocycle 1, cyclobis(paraquat-*p*-phenylene), and tetrathiafulvalene in acetone-d_6 are exhibited in Fig.2. In the spectrum of macrocycle 1, the peaks at δ 14.47 and δ 14.35 are assigned to the hydroxyl protons. Adding CBPQT⁴⁺ to the solution of macrocycle 1 resulted in the downfield shift to δ 14.76 and δ 14.67, respectively. Changes of chemical shift of hydroxyl protons indicated CBPQT⁴⁺ was included inside macrocycle 1(the inclusion structure was proved by 2D ROESY NMR and MALDI-TOF MS[18]). When TTF was added to the solution, the two resonances further shifted to δ 14.79 and δ 14.70, respectively, indicating there is an interaction between tetrathiafulvalene and the ring-in-ring CBPQT⁴⁺⊂ 1 structure.

✉ JIANG Jian
Jianjiang@nenu.edu.cn
School of Chemistry and Chemical Engineering, Mudanjiang Normal University, Mudanjiang 157000, P. R. China

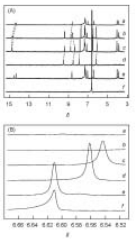

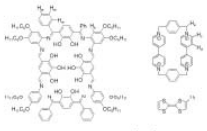

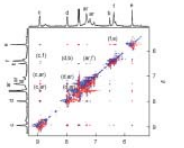

Fig.2 ^{1}H NMR spectra of different assemblies(macrocycle 1:CBPQT⁴⁺:TTF=1:1:4, molar ratio)(A) and amplified spectra around δ 6.8 from(A)(400 MHz, acetone-d_6, 298 K)(B)
a. Macrocycle 1; b. 1+CBPQT⁴⁺; c. 1+CBPQT⁴⁺+TTF; d. CBPQT⁴⁺+TTF; e. 1+TTF; f. TTF.

However, for the combination of macrocycle 1 and TTF, without CBPQT⁴⁺, no chemical shift change was observed for macrocycle 1 and TTF, which is shown in Fig.2(A) and (B). The reason for this is macrocycle 1 and tetrathiafulvalene are electron-rich structures, which are reluctant to form complex.

Addition of TTF to CBPQT⁴⁺ in solution caused chemical shift of TTF changed from δ 6.61 to δ 6.56 as shown in Fig.2(B), which indicates that a 1:1 complex was formed between CBPQT⁴⁺ and TTF as reported in the literature[18]. In the above solution, the resonance of TTF shifted further to δ 6.54 with the addition of macrocycle 1. Meanwhile, when macrocycle 1 was added, all four peaks of CBPQT⁴⁺ in TTF⊂CBPQT⁴⁺ complex shifted upfield. These changes of resonances for CBPQT⁴⁺ and TTF indicate macrocycle 1 has included both CBPQT⁴⁺ and TTF in its cavity and a Russian-doll-like 3-in-1 complex is formed. The 3-in-1 complex is grouped together by electrostatic attraction in electron-rich electron-dificient and electron-rich structures.

2D ROESY ^{1}H NMR spectrum(Fig.3) also proved the existence of the Russian-doll-like structure in solution. In Fig.3, cross-peaks between H_c and H_{ac}, H_d and H_b, H_d and H_{ac} are observed, which indicates macrocycle 1 includes CBPQT⁴⁺ inside its cavity. Couplings between H_d and H_a, H_d and H_b show that TTF is inside CBPQT⁴⁺. Spin-coupling between H_b and H_{ac} indicates TTF interacts with the aryl rings of macrocycle, consisting with the Russian-doll-like structure.

Fig.3 2D ROESY spectrum of the Russian-doll-like structure in 1:3 $CDCl_3/CD_3CN$ with a mixing time of 1.2 ms(400 MHz, 298 K)
Macrocycle 1: CBPQT⁴⁺:TTF=1:1:4. The resonances around δ 7.2 are assigned to protons on ketimine phenyl and noted as "e".

Formation of hierarchical atchitechture was verified by MALDI-TOF mass spectrometry. In mass spectrum(Fig.4), we observe a peak attributed to [1+CBPQT⁴⁺+TTF+H₂O+3PF6⁻]⁺, which proved the existence of 3-in-1 complex. In the spectrum, some other combinations would also be expected, including [CBPQT⁴⁺+3PF6⁻]⁺, and [1+CBPQT⁴⁺+3PF6⁻]⁺. Some additional peaks were not assigned, which might come from complexes with the matrix.

In our previous work[8,12], we found that structures like macrocycle 1 are very flexible and CBPQT⁴⁺ is movable

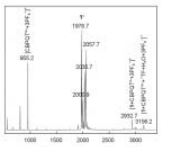

Fig.4 MALDI-TOF mass spectrum of the 3-in-1 complex

inside the macrocycle[18]. For this reason, the Russian-doll-like structure was simulated by inserting TTF⊂CBPQT⁴⁺ structure "from top" and "from bottom" of the macrocycle 1, and then energy-minimizing with PM3. Fig.5 exhibits one of conformations of our simulations(other simulation results are shown in the Electronic Supplementary Material of this paper). It indicats that three compounds can group together in the Russian-doll-like complex.

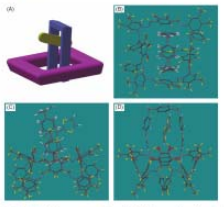

Fig.5 Graphical representation of 3-in-1 complex(A) and energy minimized(PM3) models of the Russian-doll-like structure with Spartan'08(B—D)
(B) The top view of one conformation; (C, D) side views of the conformation.

In summary, we proved by using NMR and mass spectrum that a 3-in-1 Russian-doll-like structure was assembled in solution. The development of complex architectures, such as these may open the route to innovative robust supramolecular designs. We are continuing to explore the host-guest chemistry in widemouthed Schiff base macrocycles.

Electronic Supplementary Material

Supplementary material is available in the online version of this article at https://doi.org/10.1007/s40242-021-1146-y.

Acknowledgements

The work was supported by the Archival Projects of the Department of Education of Heilongjiang Province, China(No.12653KFY180.10), the National Topic Cultivation Project of Mudanjiang Normal University, China(No.GP2020001) and the Key Project of Department of Education of Heilongjiang Province, China (No.12531C003).
The author thanks Prof. Mark J. MacLachlan(Department of Chemistry, University of British Columbia, CA) for support and discussions. The author also thanks the Natural Science and Engineering Research Council of Canada for the financial support while he worked in UBC, CA.

Conflicts of Interest

The authors declare no conflicts of interest.

References

[1] Tauba S., Komai Y., Fujikawa S., Nishiyama Y., *Chem. Eur. J.*, 2021, 27, 1966
[2] Li J., Han X.-N., Zhou H.-K., Han Y., Chen C.-F., *J. Org. Chem.*, 2020, 85, 11465
[3] Zhang Y., Chen G. C., Wang Y., Zhang X. J., Wang H. Y., Cao F. H., Sue A. C.-H., Li H., *Chem. Commun.*, 2018, 55, 11887
[4] Datta S., Kato Y., Higashiharaguchi S., Aratsu K., Isobe A., Saito T., Prabhu D. D., Kitamoto Y., Hallenbeck M. J., Smith A. J., Dalgliesh R., Mahmood N., Pesce L., Perego C., Pavan G. M., Yagai S., *Nature*, 2020, 583, 400
[5] Chen X. Y., Shen D., Cai K., Jiao Y., Wu H., Song B., Zhang L., Tan Y., Wang Y., Feng Y., Stern C. L., Stoddart J. F., *J. Am. Chem. Soc.*, 2020, 142, 20152
[6] Ferrand Y., Huc I., *Acc. Chem. Res.*, 2018, 51, 970
[7] Gao W.-X., Feng H.-J., Lin Y.-J., Jin G.-X., *J. Am. Chem. Soc.*, 2019, 141, 9160
[8] Lu Y., Zhang H.-N., Jin G.-X., *Acc. Chem. Res.*, 2018, 51, 2148
[9] Chakraborty T., Mukherjee S., Parveen R., Chandra A., Samanta D., Das D., *New J. Chem.*, 2021, 45, 2050
[10] Cornelio G., Chierici E. P., Falla S., Bella S. D., *Inorg. Chem.*, 2016, 55, 10330
[11] Zhang D. W., Wang H., Li Z. T., *Chem. J. Chinese Universities*, 2020, 41(6), 1139
[12] Zhang L., Li H. F., Chen P., Sun W., Yan P., *Chem. Res. Chinese Universities*, 2016, 32(4), 534
[13] Urbani M., Torres T., *Chem. Eur. J.*, 2020, 26, 1683
[14] Jiang J., MacLachlan M. J., *Org. Lett.*, 2019, 12, 1020
[15] Gubo S., Crane A. K., MacLachlan M. J., *Chem. Commun.*, 2011, 47, 1169
[16] Rees K. V., Love J. B., *Dalton Trans.*, 2021, 50, 1610
[17] Chaudhry M. T., Lalji F., MacLachlan M. J., *Chem. Commun.*, 2018, 54, 11869
[18] Chen Z., Goku S., White N., Lalji F., MacLachlan M. J., *Chem. Eur. J.*, 2016, 22, 17857
[19] Jiang J., Dong R. Y., MacLachlan M. J., *Chem. Commun.*, 2018, 54, 10205
[20] Rechina C., Carabyna, 2017, 7, 165
[21] Mathua S. J., Cameron S. A., Brooker S., *Inorg. Chem.*, 2018, 57, 2480
[22] Jiang J., MacLachlan M. J., *Chem. Commun.*, 2009, 5950
[23] Cai K., Lipke M. C., Liu Z., Nelson J., Cheng T., Shi Y., Cheng C., Shen D., Han J.-M., Vemuri S., Feng Y., Stern C. L., Goddard W. A., Wasielewski M. R., Stoddart J. F., *Nat. Commun.*, 2018, 9, 5275
[24] Rasmussen S. A.L., Gang J. G., Haver R., Odell B., Claridge T. D. W., Herz L. M., Anderson H. L., *J. Am. Chem. Soc.*, 2015, 137, 12713
[25] Dalgarno S. J., Fisher J., Raston C. L., *Chem. Eur. J.*, 2006, 12, 2772
[26] Dang H., Hashimoto Y., Kidera Y., Nagaoka A., Kobigai K., Kawahata M., Miyazawa T., Yamaguchi K., *Org. Le.*, 2015, 17, 2154
[27] Odell B., Reddington M. V., Slawin A. M. Z., Spencer N., Stoddart J. F., Williams D. J., *Angew. Chem. Int. Ed.*, 1988, 27, 1547
[28] Zhang D., Sato M. A., Lemaire L., Harmel W. Y., MacLachlan M. J., *Angew. Chem. Int. Ed.*, 2020, 59, 4703
[29] Wu Y., Frasconi M., Liu W.-G., Young R. M., Goddard W. A., Wasielewski M. R., Stoddart J. F., *J. Am. Chem. Soc.*, 2020, 142, 8530
[30] Grunder S., McEwer P. L., Whalley A. C., Boyle M. M., Stern C., Stoddart J. F., *J. Am. Chem. Soc.*, 2013, 135, 17691
[31] Philp D., Slawin A. M. Z., Spencer N., Stoddart J. F., Williams D. J., *J. Chem. Soc., Chem. Commun.*, 1991, 1584
[32] Nielsen M. B., Jeppesen J. O., Lau J., Lomholt C., Damgaard D., Jacobsen J. P., Becher J., Stoddart J. F., *J. Org. Chem.*, 2001, 66, 3559

2.李静,蒋舰,贠涛,邵艳秋.功能性离子液体的应用研究进展[J].黑龙江工业学院学报(综合版),2021,21(02):98-103.

第21卷 第2期 黑龙江工业学院学报 Vol.21 No.2
2021年2月 JOURNAL OF HEILONGJIANG UNIVERSITY OF TECHNOLOGY Feb. 2021

文章编号:2096-3874(2021)02-0098-06

功能性离子液体的应用研究进展

李 静,蒋 舰,贠 涛,邵艳秋

(牡丹江师范学院,黑龙江 牡丹江 157000)

摘 要:室温离子液体是一种仅由阳离子和阴离子组成的液体,在化学工业中表现出其作为溶剂和催化剂的独特性质,引起了科学家的关注。离子液体的阴阳离子可以通过引入特殊基团形成功能性离子液体,由于其对环境友好,在许多行业中作为绿色催化剂而被广泛使用。针对近几年离子液体在催化反应中的应用、吸收CO_2方面的应用以及燃料中脱硫反应的应用进行论述,同时对离子液体作为绿色化溶剂的发展前景进行了展望。

关键词:离子液体;脱硫;应用;催化;吸收

中图分类号:TQ413 文献标识码:A

DOI:10.16792/j.cnki.1672-6758.2021.02.018

离子液体(Ionic Liquids,ILS)是由不对称的阳离子和各种阴离子组成的多原子有机盐,一般由有机阳离子(如烷基铵离子、烷基磷离子、N-烷基吡啶、N',N'-二烷基咪唑)和无机阴离子(如BF_4^-,PF_6^-,SbF_6^-,$CF_3SO_3^-$等)组成。

随着离子液体研究应用的不断深入,离子液体的可设计性为各个领域的应用发展带来了新的契机。通过在常规离子液体阴阳离子上带有特殊功能的官能团,可形成带有某种性能和应用设计的功能化离子液体。离子液体作为一种新型功能化材料,应用于催化反应[1]、电化学反应[2-3]、生物物质[4]以及材料化学[5]等领域,在反应中无需助催化剂和其他溶剂,具有反应条件温和,稳定性高,且对环境无污染、绿色环保等优点。

1 离子液体在催化反应中的应用

由于离子液体特殊的物理性质和化学性质,通过对阴离子和阳离子的设计来合成功能性离子液体,引入功能性基团来实现离子液体在更多不同领域的应用价值。近年来,离子液体被广泛应用于Diels-Alder反应、Friedel-Crafts反应、过渡金属催化反应、区域选择性烷基化反应[6]等催化反应。

1.1 咪唑类离子液体的应用

咪唑类离子液体是工业界最常用的一类离子液体。离子液体检测不到蒸气压,不可燃,热稳定性高,可以回收[7],常温下一般表现出液体的性质,被誉为新型环境友好的电解质[8],广泛用于无机、有机和高分子化合物的优良溶剂[9]。咪唑离子液体作为溶剂可以从水中去除有毒重金属,近年来将其应用于聚合物改性方面的阻燃剂,受到了广泛的关注[10]。

大多数报道的离子液体,如咪唑类、吡啶类和季铵盐类等为阳离子,四氟硼酸盐、六氟磷酸盐和杂多钨酸盐等为阴离子。然而上述阴离子易水解,易产生引起腐蚀基底的有毒产物氟化氢,而且生物毒性较大,同时降解过程中所产生的中间体物质对环境的污染性极大。

Para[11]等研究了无机电解质对咪唑类离子液体表面张力的影响,结果表明单价阴离子会导致阳离子表面活性剂溶液的表面张力降低。Ma[12]等人通过使用多种咪唑类离子液体作为化学反应的催化剂和溶剂,并将其应用于酯化反应和

作者简介:李静,硕士,助教,牡丹江师范学院。研究方向:有机合成和应用。

基金项目:黑龙江省省属高等学校基本科研业务费科研项目(项目编号:1354MSYQN032);牡丹江师范学院科研项目(项目编号:QN2020007)。

(C)1994-2021 China Academic Journal Electronic Publishing House. All rights reserved. http://www.cnki.net

Friedel－Crafts 烷基化和酰基化反应。利用无限稀释后的活性系数来判断离子液体对有机反应的催化活性或物质转化的影响。通过建立离子液体中溶质无限稀释时的活度系数模型，并通过定量分析离子液体对物质结构的影响来比较不同咪唑型离子液体对反应的影响程度。

李思田[15]等合成 1－乙烯基－3－正丁基溴代咪唑离子液体，并且分别用 1－乙烯基－3－正丁基溴代咪唑离子液体、1－甲基－3－丁基溴代咪唑离子液体和 1－乙基－3－丁基溴代咪唑离子液体与模拟油按照体积比 1∶1 进行搅拌混合，取上层液体进行萃合量分析，计算脱萘率。实验表明乙烯基取代的咪唑类离子液体脱萘率最高，原因主要在于乙烯基取代的咪唑阳离子正电荷对萘芳环之间产生 π－π 相互作用，从而使萘的 π－电子云极化，导致进入离子液体相内被分离。实验还讨论了利用不同添加剂对离子液体脱萘效果的影响，实验证明在 β－环糊精协同作用下，离子液体作为脱除剂来萃取溶剂油中的萘的效果最好。

Diels－Alder 反应广泛应用于有机合成和化学工业中，是一类具有高度的“原子经济性”的反应[14]。均相反应存在催化剂用量大、产物不易分离、污染环境、回收率低等诸多缺点，而离子液体具有一些独有的物理化学性质，可在该反应中作为催化剂和溶剂，可在反应中反复循环使用并对环境友好。因此离子液体被认为是均相反应有机溶剂良好的替代品，而且已经成功应用于有机合成反应[16]。

李昌志[16]等研究了合成 1－丁基－3－甲基咪唑氯［bmim］Cl）、1－乙基－3－甲基咪唑溴二烷基咪唑（［emim］Br）、丁基吡啶溴（［bpy］Br）和乙基吡啶溴（［etpy］Br）与 $ZnCl_2$ 构成的具有 Lewis 酸性的离子液体体系，将其作为催化剂和反应介质，通过月桂烯与丙烯醛的 Diels－Alder 反应快速高区域选择性地合成了对位柑青醛。该实验从 $ZnCl_2$ 含量、反应温度、离子液体用量、反应时间和溶剂种类变量因素来考察离子液体体系对反应速率和产率的影响，实验证明该体系下的产率和对位柑青醛区域选择性高，并对离子液体重复性使用做了相关实验，离子液体可以回收使用 4 次，其催化活性和区域选择性基本保持不变。该离子液体对湿气不敏感，反应结束后产物与离子液体很容易分离，且分离后的离子液体可重复使用，这些优点使反应体系具有良好的工业应用价值。

Kalyan Ramesh[17]等开发了一种在深度共晶溶剂（deep eutectic solvents，DESs）中通过 Diels－Alder（DA）电击反应，用咪唑系室离子液体对还原氧化石墨烯（rGO）进行共价功能化的有效方法。首先，用聚氯甲基苯乙烯－马来酸酐－糠酸胺和甲基咪唑反应制备了含糠酰和咪唑的室离子液体；然后，在无催化剂的超声作用下，在深共晶溶剂（DES）中通过 DA 反应将聚离子液体（PVF－IL）s）直接接枝在还原氧化石墨烯表面。最后，用 FT－IR、TGA、拉曼光谱、XPS、SEM 和 TEM 对杂化材料进行了表征。利用循环伏安法（CV）和电化学阻抗谱（EIS）研究了杂化材料的电容和电化学行为。在 CV 中，rGO－p（F－IL）杂化产物的电容最大。EIS 的扩散电阻低于还原氧化石墨烯。表明该杂化产物具有良好的电化学电容行为。

1.2 氨基酸类离子液体的应用

氨基酸离子液体由于其独特的酸碱行为及生物学意义，经常将其作为合成化学中的模板和生物大分子的稳定剂应用于不同领域，是一类特殊的离子液体。这些离子液体的物理化学性质可以很容易地改变。不同的氨基酸组合作为阴离子和阳离子来修改不同类型的分子和离子的相互作用。这样他们可以提供丰富的信息分子水平用于理解更复杂的生物过程。

Wei Jie[18]等人以甘氨酸作为阴离子，醚基咪唑基团作为阳离子合成了一种新型离子液体 1－甲氧乙基－3－甲基咪唑甘氨酸［MOEMIM］［Gly］，并通过实验证明了该离子液体的物理化学性质。根据离子液体［MOEMIM］［Gly］的摩尔表面 Gibbs 自由能，改进了传统的 Eötvös 经验方程，使得方程具有更明确的物理意义。

Gong[19]等对 CO_2 转化反应的催化能力进行了测试，该实验在 1 个标准大压力下，以改性氨基酸离子液体为催化剂，将二氧化碳环加成环氧化物，有效地合成了环状碳酸盐。以三乙胺为辅助催化剂，大大提高了 L－脯氨酸基离子液体的催化活性，在室压下，温度为 90℃条件下，无有机溶剂和金属成分的情况下，循环碳酸盐的分离产率可达 97%，该实验对 CO_2 的去除开辟了新的道路。

岳爽[20]等利用一种带氨基的阳离子含有氨基酸的功能化离子液体，并利用该离子液体催化二氧化碳与环氧化合物合成环状碳酸酯。该反应具有产量高、活性强、反应条件温和、稳定性高且对环境无污染、绿色环保等优点。

环内酯是合成有价值产品的重要有机中间物，包括聚合物、合成香料、杀菌剂和植物生长调节剂[21]，而环酮的 Baeyer－Villiger 氧化已经成为形成内脂最重要的途径之一。通过 Baeyer－Villiger 法工业生产内脂常用的过氧化酸作为氧化剂，但是这类氧化剂存在实质性的缺点：安全系数低、腐蚀设备和产品回收困难等。使用环境友好型氧化剂如过氧化氢和分子氧来氧化是目前研究人员最为感兴趣的氧化剂[22]。Yu Fengli[23]利用多种氨基酸与多种质子酸反应，制备出一系列氨基酸离子液体，并将其作为催化剂，过氧化氢为氧化剂来催化环酮的 Baeyer－Villiger 氧化反应。通过正交实验证明了在底物：催化剂：过氧化氢物质的量比为 1∶0.06∶4，反应温度 60℃，催化氧化进行 6h 为最佳反应时间。环戊酮的转化率为 96.57%，δ－戊内酯的收率为 70.51%。该实验经过 4 次循环后，催化活性仍然没有降低。

2 离子液体吸收 CO_2 的应用

毫无疑问，石油、煤炭和天然气在未来几年仍将是全球主要的燃料和化学原料来源。最近的天然气被认为是这些材料中最清洁的。因此正在被加速消耗[24]。

尽管天然气被誉为清洁燃料，但它通常会受到各种不良物质的污染，尤其是二氧化碳和硫化氢。随着低硫天然气储量的枯竭，高硫天然气的利用率将会增加。由于掺合的二氧化碳降低了天然气的燃料价值，在酸性气体中存在的大量二氧化碳迫使其在燃烧前被去除。酸性气体的燃料价值较低，再加上二氧化碳和全球变暖之间的联系，二氧化碳的有效捕获成为了全世界的热点。研究人员已经开发了各种吸附、膜分离等方法，用于去除工业气体中的二氧化碳。其中，化学吸收，尤其是用烷烃醇胺水洗涤，是最发达、最常用的方法之一[25]。

夏裘文[26]等人采用两步法合成一种新型多氨基功能化离子液体 1－氨丙基－3－甲基咪唑赖氨酸［APmim］［Lys］，采用单因素法研究浓度和温度对离子液体吸收 CO_2 效果的影响。探讨了离子液体的循环稳定性。结果发现：在 30℃时，质量分数为 20% 的［APmim］［Lys］离子吸收具有较好的吸收效果，对 CO_2 的吸收量可达 1.72mol/molIL，经过 7 次循环吸收－解吸操作，吸收率仍高于 89.5%，具有良好的循环稳定性。

夏裘文[26]等人 2019 年合成了 1－氨丙基－3－甲基咪唑甘氨酸盐［APmim］［Gly］离子液体与 N－甲基二乙醇胺 MDEA 溶液对比，研究了压力为 1MPa、不同质量分数的离子液体两在不同温度下对 CO_2 的吸收能力，并进行多次循环再生。结果显示：在 30℃时，质量分数为 20% 的［APmim］［Gly］具有最佳的吸收能力，对 CO_2 的吸收量可达 1.32mol/molIL，远高于 MDEA。同时该离子液体具有良好的再生能力，经 6 次循环其吸收率可高达 92.4%。

Chen[27]等用疏水二氧化硅纳米颗粒包裹乙二醇或甘油的功能化离子液体溶液，形成流动性快速捕获二氧化碳的微米颗粒。制备无水“干离子液体”（D－IL）。无水 D－IL 不仅具有离子液体的稳定性和“干物质”的微尺寸这两种物质的优点，而且有效地克服了离子液体的高粘度和含水溶液的干物质失水的缺点。该实验研究了 D－IL 的二氧化碳捕获能力和捕获率，并与相应的解决方案进行了比较。结果证实，D－IL 具有显著的较高的二氧化碳捕获速度、优异的吸收能力和相当大的再生效率。其微米结构可以完全克服高粘度的阻力。从而表现出任务特定的离子液体的化学特性。

Wu[28]等通过实验方法和理论计算，研究了离子液体中烟气对二氧化碳和二氧化硫的吸收情况。单种离子液体，如［NH_4emim］［BF_4］和［C_4mim］［OAc］，在不受二氧化硫干扰的模拟烟气中都表现出良好的二氧化碳吸收性能。然而，二氧化硫更有可能与 IL 的活性位点发生反应。当二氧化硫在烟气中时，单个离子液体对二氧化碳的吸收能力将受到显著抑制。吸收过程中 CO_2 和 SO_2 之间存在竞争关系。由于 SO_2 和 ILS 的相互作用能较强，单个 ILS 更倾向于捕获 SO_2 而不是去除 CO_2。实验和计算结果表明，［OAc］阴离子和［NH_4emim］阳离子是 CO_2 和 SO_2 吸收的主要活性中心。低吸收值的 IL－SO_2 或 IL－CO_2 系统通常意味着低吸收容量。因此，对于 IL 混合物［C_4mim］［OAc］/［NH_4emim］［BF_4］，量子计算结果表明，［NH_4emim］［BF_4］可能更容易吸收烟气中的 SO_2，而［C_4mim］［OAc］很容易去除 CO_2。

3 离子液体脱硫反应的应用

在过去的几十年里，由于燃料的燃烧污染严重，人们对燃料脱硫是否符合规定给予了很大的关注。虽然加氢脱硫（HDS）可以有效的去除硫醇、硫化物和二硫化物，但对耐火材料中含硫化合物的去除率却很低。由于它们的立体位阻，HDS 通常要求严格操作条件和高成本来实现超深脱硫的燃料。因此，人们开发出更多可供选择的超深脱硫工艺，如吸附、萃取、生物脱硫、氧化等。在这些方法中，氧化脱硫（ODS）与萃取相结合的脱硫被认为是一种脱硫方法最有希望的过程。有机硫化合物如 DBT 及其衍生物，可选择性氧化成它们对应的亚砜和砜，然而，实验中使用的萃取剂通常是易燃和挥发性有机化合物，这就导致额外的安全和环境问题。

离子液体催化剂因其制备简单、结构可设计、蒸气压低、毒性小、稳定性高、溶解性能独特、易分离、不易燃易爆等优点而受到人们的广泛关注。室温离子液体作为分离、有机合成和催化的新一代绿色溶剂的潜力和应用得到了广泛的应用，引起了业界和学术界的广泛关注[29]。最近，很多文章都报道了使用离子液体去除燃料中含硫化合物，但是硫的去除效率都相当低，仅在 10% ~40% 之间[30]。

为了提高脱硫效率，采用萃取法和氧化脱硫工艺相结合。在这些过程中，以过氧化氢为氧化剂、离子液体［BMIM］［PF_6］、［BMIM］［BF_4］和 $Me_3NCH_2C_6H_4Cl \cdot 2ZnCl_2$ 离子液体为萃取剂，乙酸和 $Na_2MoO_4 \cdot 2H_2O$ 为外加催化剂，整个体系硫的去除率可达 90.0% 以上。但该实验必须在高温下或在大量离子液体浓度下进行。Gao[31]等分别采用 Brønsted 酸性离子液体［BMIM］［HSO_4］和［C_4Py］［HSO_4］作为催化剂和提取剂对模型柴油进行脱硫处理实验。含 DBT 型柴油机 90 分钟室温脱硫可达到 99.6%，明显优于 IL 简易提取脱硫。［BMIM］［HSO_4］可用于回收多达 6 次，并且脱硫率没有明显降低。利用［BMIM］［HSO_4］与催化氧化工艺相结合的萃取可作为 HDS 工艺的补充技术。

周杰[32]合成了 3 种 N－甲基吡咯烷酮离子液体［HMMP］$FeCl_4$、［HMMP］$CoCl_4$、［HMMP］$ZnCl_4$，并将其用于模拟汽油中噻吩的萃取脱除。实验表明：30℃下，三种离子液体脱硫能力的强弱顺序为：［HMMP］$FeCl_4$ >［HMMP］$CoCl_4$ >［HMMP］$ZnCl_4$。以脱硫能力最强的［HMMP］$FeCl_4$ 为催化剂，在优化条件下，单程脱硫率为 70.7%，经 4 次萃取后，模拟汽油中硫含量降至 61μg/g，总脱硫率为 95.6%。

离子液体是一种新型溶剂，与传统溶剂相比，离子液体具有较高的从汽油和柴油中提取芳烃硫和芳烃化合物的能力。Usarala Dosman－ahn[33]研究了离子液体在溶剂萃取法提取汽油和柴油中有机硫化合物时的脱硫性能。

离子液体（ILS）被认为是经典加氢脱硫过程的新替代技术的夹带剂，或用于低浓度芳烃硫化合物的深度脱硫。石油工业面临的挑战是减少燃料中蒙发的芳烃硫化合物，如噻吩、苯并噻吩、甲基二苯并噻吩、4,6－二苯并噻吩硫醇、硫醚和二硫化物。随着美国和欧洲新颁低硫含量的法规出台，柴油深度脱硫已成为一个重要的行业课题。具有特定的、选择的阳离子和阴离子的离子液体可能是液体－液体萃取模型燃料中硫化合物的候选之一，它们适用于在一个萃取步骤中，在质量分数范围内有效地去除模型燃料中所有形式的硫。由于离子液体可能再循环，可以考虑在工业中使用离子液体进行后续的萃取步骤。然而，进一步研究不同萃取量的离子液体对不同汽油和柴油的萃取效果，将得到更为乐观的结论。

4 结论与展望

环境友好型离子液体的研发成为绿色工程中研究领域的一大热点。离子液体因其特殊的物理、化学性质使得离子液体作为催化剂广泛应用于催化反应、电化学反应、化学合成、化学分析等领域。同时，通过改变离子液体中离子类型来合成出功能性不同的离子液体，并将其应用于催化吸收二氧化碳和燃料脱硫等绿色化学工程中。另一方面，离子液体因其价格昂贵，难以实现工业化大规模使用。离子液体废弃液对环境是否有影响也需要深入研究，特别应注重离子液体作为环境友好型溶剂代替有机溶剂的应用研究。

参考文献

[1] Zhao H. Innovative applications of ionic liquids as “green”engineeringliquids[J]. Chem Eng Commun, 2006,193(12):1660－1677.

[2] 维娜，李冰冰，许华梅，等. NiCoP 材料的制备及电化学转氨性能研究[J]. 黑龙江工业学院学报（综合版），2020,11(20):70－74.

[3] 孙喜雪，孙明轩，方亚林，等. 染料敏化太阳能电池骨轴对电极研究进展[J]. 化工进展，2016,35(10):3236－3250.

[4] Xue Z, He D, Xie X. Poly(ethylene oxide)－based electrolytes forlithium－ion batteries[J]. J Mater Chem A, 2015,3:1039.

[5] Mattyjd. Eadie, KennethR. Seddon. Ionicliquids. Green solvents for the future[J]. Pure Appl. Chem. ,2000,72(7):1391－1398.

[6] Peng, J. J. ,Shi, F. ,Gu, Y. L. , et al. Highly selective and green aqueous－Ionic liquid biphasic hdroxylation of benzene to phenol with hydrogen peroxide[J]. Green Chem. , 2003,5(2):224－226.

[7] Rogers R D. Materials science: reflections on ionic liquids[J]. Nature,2007,447(7147):917－918.

[8] Brenna M K,Heather Y L,Thomas J F, etal. Physical chemistry of ionic liquids[J]. Physical Chemistry Chemical Physics,2010,12(8):1648.

[9] Lewandowski A, Galinski M. Carbon－ionic liquid doublelayer capacitors[J]. Journal of Physics and Chemistry of Solids,2004,65(2－3):281－286.

[10] Chen S J,Wang C L,Li J. Effect of alkyl groups in organic part of polyoxo－metalates based ionic liquids on properties of flame retardant polypropylene[J]. Themochimica Acta,2016,631:51－58.

[11] Pan G, Jurek E, Wanzyniski P. The Hofmeister Series Effect in Adsorption of Cationic Surfactants:Theoretical Description and Experimental Results[J]. Adv Colloid Interface Sci,2006,122(1－3):39－55.

[12] Ma Zheng, Dong Xiaxia, Hu Yufeng, et al. Effect of Ionic Liquids on Organic Reactions Based on Activity Coefficients at Infinite Dilution[J]. Chinese Journal of Chemical Engineering,2013,21(12):1370－1375.

[13] 李思田，徐洋，姚琼. β－环糊精协同乙醇基咪唑离子液体脱除溶剂油中的萘[J]. 化工进展，2020,39(4):1321－1328.

[14] T. Fischer, A. Sethi, T. Welton, et al. Diels－Alder Reactions in Room－Temprature Ionic Liquids[J]. Tetrahedron Letters, 1999,40(4):793－796.

[15] Lu Jun, Li Yingying, Yang Ling, et al. Study on the condensation reactions between aromatic aldehydes and thiohaibutanic acid[J]. Org Chem,2008,28(9):958－960.

[16] 李昌志，杨爱红，ZnCl2 离子液体中高区域选择性合成柑橙醛[J]. 催化学报，2005(03):194－198.

[17] Kalyan Ramesh, Sonita A. P. Sharo, Dong Woo Kim, etal. Ultrasound－accelerated covalent－functionalization of reduced graphene oxide with imidazolium－based poly(ionic liquid) s by Diels－Alder click reaction for supercapacitors[J]. Reactive and Functional Polymers,2020,152:104605.

[18] Wei Jie, Dong Hexin, Chen Xia, etal. Physicochemical Properties of 1－Methoxyethyl－3－Methylimidazolium Glycine[J]. Acta Phys. Chim. Sin. ,2018,34(8):927－932.

[19] Gong Qing, etc. Synthesis of Cyclic Carbonate From Carbon Dioxideand Epoxide Using Amino Acid Ionic Liquid Under1 atm Pressure[J]. Aust. J. Chem. 2012,65:381－386.

[20] 岳爽，郝秀佳，李俊. 一种加离子带氨基的含有氨基酸的离子液体及其制备方法和应用: CN108794400A[P]. 2018－11－13[2021－03－23].

[21] Bedkessel A, Andreae M. R. M. Efficient Catalytic Methods for the Baeyer－Villiger Oxidation and Epoxidation with Hydrogen Peroxide[J]. Tetrahedron Lett,2001,42(12):2293－2295.

[22] Zhang Qinghua, Wang Shudeng. Baeyer－Villiger oxidation of ketones with hydrogen peroxide catalyzed by Sn－aniline complex[J]. Chinese Chemical Letters,2007,18(1):4－6.

[23] Yu Fengli, Chi Yujie, Gao Chong, et al. Baeyer－Villiger Oxidation of Cyclic Ketones Catalyzed by Amino Acid Ionic Liquids[J]. Chem. Res. Chinese Universities, 2020, 36(5):865－869.

(C)1994-2022 China Academic Journal Electronic Publishing House. All rights reserved.　http://www.cnki.net

实验室安全培训及考试

9:36

学院活动|化学化工学院举办实验室安全考试

化学化工学院 青春铁系人

2019-09-27 20:51

为进一步加强化学化工学院实验室安全管理工作，提高学生实验室安全责任意识，学院于2019年9月26日中午12：20在文科楼115开展了实验室安全知识考试。参加本次考试的是2019级全体新生，学习部全体成员负责监考。

9:36

化学化工学院实验室安全知识测试

化学化工学院团委 青春铁系人

2016-11-24 14:49

化学化工学院实验室安全知识测试

为检测同学们对实验室安全方面知识和技能的掌握程度，2016年11月23日，化学化工学院学习部举办“实验室安全知识”测试。

考试进行时

11月23日中午12点10分至13点10分，全体

9:36

化学化工学院学习部“安全知识”考试

化学化工学院 青春铁系人

2017-10-18 20:56

2017 年 10 月 18日，为配合学校本科教学合格安全意识，建设平安和谐校园，进一步强化大学生推进化学系科学实验、安全实验、安全教学的建设，化学化工学院精心组织了这次实验室安全知识考试 。

本次试题包含实验室操作规则、安全防护、事故处理方法等

9:35

学院活动丨安全无小事，时刻记心中--实验室安全知识竞赛

青春铁系人 2021-11-14 23:42

为进一步增强我院学生安全意识，普及实验室安全知识，营造“人人懂安全、人人管安全，人人要安全”的学习氛围，化学化工学院于11月14日在文科楼115举办了实验室安全知识竞赛。

9:36

学院活动|长鸣安全警钟，携手安全实验

化学化工学院 青春铁系人

2019-09-04 19:31

为了使化学新生更好的了解实验室基本安全常识、强化学生实验室安全意识、加强实验室管理，学院于2019年9月3日晚7：00在五角楼103进行实验室安全教育，有副院长邵艳秋老师主持并做实验室安全教育；由学院实践部主任兼19级工艺班主任云观老师做实验室安全事故案例警示培训讲座。2019级全体新生参加。

9:36

青春铁系人 >

告、早处理”的工作原则，提高快速反应和应急处理能力，切实做好我院学生安全的各项预防工作，保障安全事故的及时处理，提高学院学生管理水平。

化学化工学院于2021年11月3日12：30在理工楼564召开学生安全工作会议。学院党委书记邵艳秋、团总支书记王虎、辅导员侯玉爽、辅导员助理金云鹏及学生会团总支部分学生干部，2019级、2020级、2021级全体学生线上参加会议。

本次会议从寝室安全、网络诈骗安全、心理健康安全、严禁赌博、严禁吸毒、实验室安全六个方面对同学们提出要求。

联合培养协议

联合培养证书

学生 马悦 ，性别 女 ，自 2019.5 至 2022.1 ，
在中国科学院大连化学物理研究所 [illegible] 专业学习。
特此证明。

中国科学院大连化学物理研究所
中国科学院大学能源学院

所长：刘中民
日期：2022.1.18

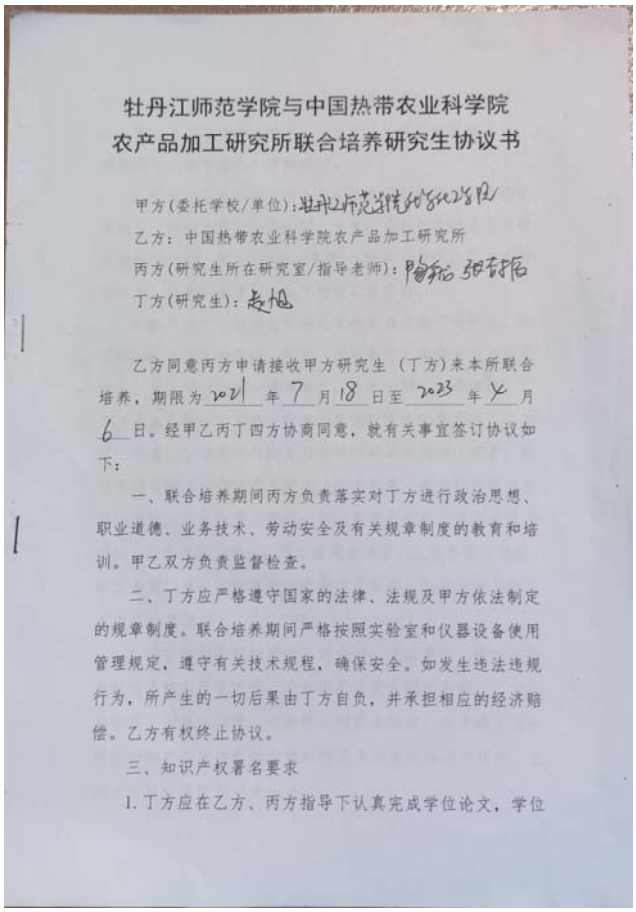

牡丹江师范学院与中国热带农业科学院
农产品加工研究所联合培养研究生协议书

甲方(委托学校/单位)：牡丹江师范学院
乙方：中国热带农业科学院农产品加工研究所
丙方(研究生所在研究室/指导老师)：陶金花 [illegible]
丁方(研究生)：赵旭

乙方同意丙方申请接收甲方研究生（丁方）来本所联合培养，期限为 2021 年 7 月 18 日至 2023 年 6 月 6 日。经甲乙丙丁四方协商同意，就有关事宜签订协议如下：

一、联合培养期间丙方负责落实对丁方进行政治思想、职业道德、业务技术、劳动安全及有关规章制度的教育和培训。甲乙双方负责监督检查。

二、丁方应严格遵守国家的法律、法规及甲方依法制定的规章制度。联合培养期间严格按照实验室和仪器设备使用管理规定，遵守有关技术规程，确保安全。如发生违法违规行为，所产生的一切后果由丁方自负，并承担相应的经济赔偿。乙方有权终止协议。

三、知识产权署名要求

1. 丁方应在乙方、丙方指导下认真完成学位论文，学位

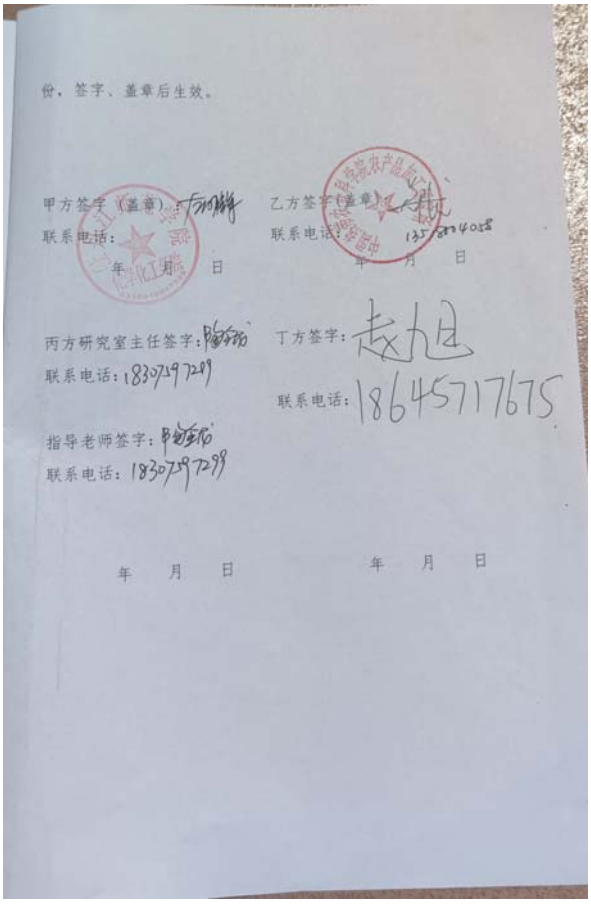

份，签字、盖章后生效。

甲方签字（盖章）：
联系电话：
年 月 日

乙方签字（盖章）：
联系电话：
年 月 日

丙方研究室主任签字：陶金花
联系电话：18307297209

丁方签字：赵旭
联系电话：18645717675

指导老师签字：陶金花
联系电话：18307297209

年 月 日

年 月 日

校企合作成果

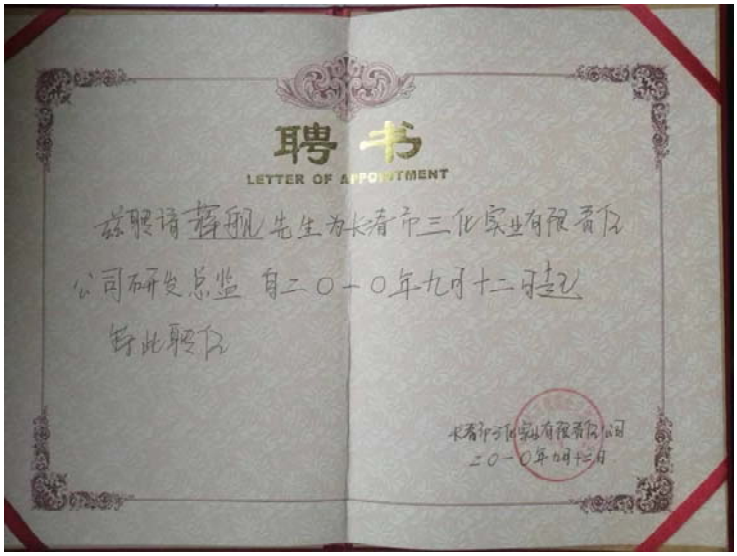

聘书

LETTER OF APPOINTMENT

兹聘请薛飚先生为长春市三化实业有限责任公司研发总监 自二〇一〇年九月十二日起

特此聘任

长春市三化实业有限责任公司

二〇一〇年九月十二日

国家知识产权局

130000

长春市高新开发区锦湖大路 1357H 号三楼 328 房间 长春众邦菁华知识产权代理有限公司

李外(0431-81707878)

发文日：

2022 年 05 月 27 日

申请号或专利号：202010248781.1　　发文序号：2022052101178690

申请人或专利权人：牡丹江师范学院

发明创造名称：一种耐湿热耐高温水性汽车门护板内饰胶黏剂及其制备方法

授予发明专利权通知书

1. 根据专利法第 39 条及实施细则第 54 条的规定，上述发明专利申请经实质审查，没有发现驳回理由，现作出授予专利权的通知。

申请人收到本通知书后，还应当依照办理登记手续通知书的内容办理登记手续。

申请人按期办理登记手续后，国家知识产权局将作出授予专利权的决定，颁发发明专利证书，并予以登记和公告。

期满未办理登记手续的，视为放弃取得专利权的权利。

法律、行政法规规定相应技术的实施应当办理批准、登记等手续的，应依照其规定办理。

2. 授予专利权的上述发明专利申请是以下列申请文件为基础的：

☐原始申请文件。☐分案申请递交日提交的文件。☒下列申请文件：

申请日提交的说明书摘要、说明书第 1-102 段；

2022 年 3 月 14 日提交的权利要求第 1-2 项。

3. 授予专利权的上述发明专利申请的名称：

☒未变更。

☐由__变更为上述名称。

4. ☐申请人于_____年_____月_____日提交专利号为_____的“放弃专利权声明”，经审查：

☐进入放弃专利权的程序。

☐未进入放弃专利权的程序。理由是：申请人声明放弃的专利与本发明专利申请不属于相同的发明创造。

5. ☐审查员依职权对申请文件修改如下：

注：在本通知书发出后收到的申请人主动修改的申请文件，不予考虑。

国家知识产权局 专利审查业务章

审查员：杨章静

审查部门：专利审查[illegible]京中[illegible]发明审查部

联系电话：010-53962975

210413 2020.3　纸件申请，回函请寄：100088 北京市海淀区蓟门桥西土城路 6 号　国家知识产权局专利局受理处收

电子申请，应当通过电子专利申请系统以电子文件形式提交相关文件，除另有规定外，以纸件等其他形式提交的文件视为未提交。

化学专业获批黑龙江省一流本科专业建设点

2019年度省级一流本科专业建设点公示名单

序号	学校名称	专业名称
1	哈尔滨工业大学	国际经济与贸易
2	哈尔滨工业大学	社会学
3	哈尔滨工业大学	俄语
4	哈尔滨工业大学	数学与应用数学
5	哈尔滨工业大学	应用化学
6	哈尔滨工业大学	生物技术
7	哈尔滨工业大学	材料成型及控制工程
8	哈尔滨工业大学	工业设计
9	哈尔滨工业大学	材料化学
10	哈尔滨工业大学	高分子材料与工程
11	哈尔滨工业大学	光电信息科学与工程
12	哈尔滨工业大学	电磁场与无线技术
13	哈尔滨工业大学	物联网工程
14	哈尔滨工业大学	建筑环境与能源应用工程
15	哈尔滨工业大学	道路桥梁与渡河工程

序号	学校名称	专业名称
216	牡丹江师范学院	英语
217	牡丹江师范学院	化学
218	牡丹江师范学院	思想政治教育
219	牡丹江师范学院	生物技术

光电功能材料实验室获批黑龙江省重点实验室

关于2021年度拟备案黑龙江省重点实验室名单的公示

DATANG 高新认定服务 2021-11-01 15:34

各有关单位：

为推进黑龙江省重点实验室建设和发展，按照全省科技工作会议和《黑龙江省重点实验室管理办法》（黑科发〔2016〕43号）部署要求，现对2021年度拟备案的省重点实验室予以公示（名单见附件）。公示时间为2021年11月1日至2021年11月5日。

如对公示名单有异议，请在公示期内以书面形式实名向省科技厅基础研究处或科技监督与诚信建设处反映，并提供必要的证明材料。反映情况的材料要客观准确、依据确凿，对匿名或无具体事实根据的举报，不予受理。

基础研究处：0451-82632603；

科技监督与诚信建设处：0451-82628025；

地址：哈尔滨市南岗区中山路202号。

黑龙江省科学技术厅

2020年10月29日

2021 年度拟备案省重点实验室名单

序号	实验室名称	申报单位	实验室主任
1	黑龙江省寒地作物基因资源发掘与种质创新重点实验室	中国科学院东北地理与农业生态研究所农业技术中心	卜庆云
2	黑龙江省聚烯烃新材料重点实验室	东北石油大学	王俊
3	黑龙江省主要农作物生物育种重点实验室	北大荒垦丰种业股份有限公司	刘辉
4	黑龙江省低碳清洁能源动力技术重点实验室	哈尔滨工程大学	李彦军
5	黑龙江省麦类作物品种改良重点实验室	黑龙江省农业科学院作物资源研究所	宋庆杰
6	黑龙江省 CO_2 资源化利用与能源催化材料重点实验室	哈尔滨理工大学	张凤鸣
7	黑龙江省肿瘤免疫学重点实验室	哈尔滨医科大学附属肿瘤医院	张艳桥
8	黑龙江省乳酸菌遗传与代谢工程重点实验室	东北农业大学	孟祥晨
9	黑龙江省重症医学重点实验室	哈尔滨医科大学附属第一医院	赵鸣雁
10	黑龙江省林源活性物质生态利用重点实验室	东北林业大学	赵修华
11	黑龙江省微纳敏感器件与系统重点实验室	黑龙江大学	赵晓锋
12	黑龙江省光电功能材料重点实验室	牡丹江师范学院	姜建壮
13	黑龙江省中药质量研究与评价重点实验室	黑龙江省药品检验研究院	笔雪艳
14	黑龙江省兽医免疫学重点实验室	中国农业科学院哈尔滨兽医研究所	翁长江
15	黑龙江省新能源汽车重点实验室	哈尔滨工业大学	崔淑梅

注：按照实验室负责人姓氏笔画排名。